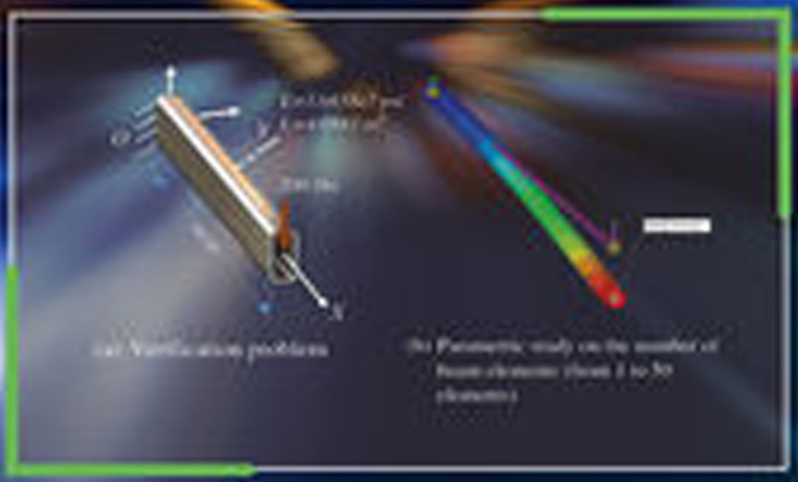
WALTER D. PILKEY | DEBORAH F. PILKEY | ZHUMING BI

PETERSON'S STRESS CONCENTRATION FACTORS

FOURTH EDITION



WILEY

PETERSON'S STRESS CONCENTRATION FACTORS

PETERSON'S STRESS CONCENTRATION FACTORS

Fourth Edition

WALTER D. PILKEY, DEBORAH F. PILKEY, ZHUMING BI

WILEY

This edition first published 2020

© 2020 John Wiley & Sons, Inc.

All rights reserved. No part of this publication may be reproduced, stored in a retrieval system, or transmitted, in any form or by any means, electronic, mechanical, photocopying, recording or otherwise, except as permitted by law. Advice on how to obtain permission to reuse material from this title is available at http://www.wiley.com/go/permissions.

The right of Zhuming Bi to be identified as the author of this work has been asserted in accordance with law.

Registered Office
John Wiley & Sons, Inc., 111 River Street, Hoboken, NJ 07030, USA

Editorial Office
John Wiley & Sons, Inc., 111 River Street, Hoboken, NJ 07030, USA

For details of our global editorial offices, customer services, and more information about Wiley products visit us at www.wiley.com.

Wiley also publishes its books in a variety of electronic formats and by print-on-demand. Some content that appears in standard print versions of this book may not be available in other formats.

Limit of Liability/Disclaimer of Warranty
While the publisher and authors have used their best efforts in preparing this work, they make no representations or warranties with respect to the accuracy or completeness of the contents of this work and specifically disclaim all warranties, including without limitation any implied warranties of merchantability or fitness for a particular purpose. No warranty may be created or extended by sales representatives, written sales materials or promotional statements for this work. The fact that an organization, website, or product is referred to in this work as a citation and/or potential source of further information does not mean that the publisher and authors endorse the information or services the organization, website, or product may provide or recommendations it may make. This work is sold with the understanding that the publisher is not engaged in rendering professional services. The advice and strategies contained herein may not be suitable for your situation. You should consult with a specialist where appropriate. Further, readers should be aware that websites listed in this work may have changed or disappeared between when this work was written and when it is read. Neither the publisher nor authors shall be liable for any loss of profit or any other commercial damages, including but not limited to special, incidental, consequential, or other damages.

Library of Congress Cataloging-in-Publication Data is Available:

ISBN 9781119532514 (Hardback)
ISBN 9781119532538 (ePDF)
ISBN 9781119532521 (ePub)

Cover Design: Wiley
Cover Images: Car lights on highway © BABAROGA/Shutterstock, Structure of verification
Courtesy of Zhuming Bi, Parametric study Courtesy of Zhuming Bi

Set in 10/12pt and TimesLTStd by SPi Global, Chennai, India

10 9 8 7 6 5 4 3 2 1

CONTENTS

INDEX TO THE STRESS CONCENTRATION FACTORS **xv**

PREFACE FOR THE FOURTH EDITION **xxxi**

PREFACE FOR THE THIRD EDITION **xxxiii**

PREFACE FOR THE SECOND EDITION **xxxv**

1 FUNDAMENTALS OF STRESS ANALYSIS **1**

1.1 Stress Analysis in Product Design / 2
1.2 Solid Objects Under Loads / 4
1.3 Types of Materials / 6
1.4 Materials Properties and Testing / 7
1.4.1 Tensile and Compression Tests / 8
1.4.2 Hardness Tests / 8
1.4.3 Shear Tests / 13
1.4.4 Fatigue Tests / 14
1.4.5 Impact Tests / 16

1.5 Static and Fatigue Failures / 17
1.6 Uncertainties, Safety Factors, and Probabilities / 19
1.7 Stress Analysis of Mechanical Structures / 21
1.7.1 Procedure of Stress Analysis / 21
1.7.2 Geometric Discontinuities of Solids / 21
1.7.3 Load Types / 23
1.7.4 Stress and Representation / 24
1.7.4.1 Simple Stress / 26
1.7.4.2 General Stresses / 26
1.7.4.3 Principal Stresses and Directions / 27
1.8 Failure Criteria of Materials / 30
1.8.1 Maximum Shear Stress (MSS) Theory / 30
1.8.2 Distortion Energy (DE) Theory / 32
1.8.3 Maximum Normal Stress (MNS) Theory / 34
1.8.4 Ductile and Brittle Coulomb-Mohr (CM) Theory / 36
1.8.5 Modified-Mohr (MM) Theory / 37
1.8.6 Guides for Selection of Failure Criteria / 37
1.9 Stress Concentration / 39
1.9.1 Selection of Nominal Stresses as Reference / 42
1.9.2 Accuracy of Stress Concentration Factors / 45
1.9.3 Decay of Stress away from the Peak Stress / 46
1.10 Stress Concentration as a Two-Dimensional Problem / 46
1.11 Stress Concentration as a Three-Dimensional Problem / 47
1.12 Plane and Axisymmetric Problems / 49
1.13 Local and Nonlocal Stress Concentration / 52
1.14 Multiple Stress Concentration / 57
1.15 Principle of Superposition for Combined Loads / 61
1.16 Notch Sensitivity / 64
1.17 Design Relations for Static Stress / 69
1.17.1 Ductile Materials / 69
1.17.2 Brittle Materials / 71
1.18 Design Relations for Alternating Stress / 72
1.18.1 Ductile Materials / 72
1.18.2 Brittle Materials / 73
1.19 Design Relations for Combined Alternating and Static Stresses / 74
1.19.1 Ductile Materials / 74
1.19.2 Brittle Materials / 77

1.20 Limited Number of Cycles of Alternating Stress / 78
1.21 Stress Concentration Factors and Stress Intensity Factors / 79
1.22 Selection of Safety Factors / 83
References / 85

2 NOTCHES AND GROOVES 89

2.1 Notation / 89
2.2 Stress Concentration Factors / 90
2.3 Notches in Tension / 92
2.3.1 Opposite Deep Hyperbolic Notches in an Infinite Thin Element; Shallow Elliptical, Semicircular, U-Shaped, or Keyhole-Shaped Notches in Semi-Infinite Thin Elements; Equivalent Elliptical Notch / 92
2.3.2 Opposite Single Semicircular Notches in a Finite-Width Thin Element / 94
2.3.3 Opposite Single U-Shaped Notches in a Finite-Width Thin Element / 94
2.3.4 Finite-Width Correction Factors for Opposite Narrow Single Elliptical Notches in a Finite-Width Thin Element / 95
2.3.5 Opposite Single V-Shaped Notches in a Finite-Width Thin Element / 95
2.3.6 Single Notch on One Side of a Thin Element / 96
2.3.7 Notches with Flat Bottoms / 96
2.3.8 Multiple Notches in a Thin Element / 96
2.3.9 Analytical Solutions for Stress Concentration Factors for Notched Bars / 98
2.4 Depressions in Tension / 98
2.4.1 Hemispherical Depression (Pit) in the Surface of a Semi-Infinite Body / 98
2.4.2 Hyperboloid Depression (Pit) in the Surface of a Finite-Thickness Element / 98
2.4.3 Opposite Shallow Spherical Depressions (Dimples) in a Thin Element / 99
2.5 Grooves in Tension / 100
2.5.1 Deep Hyperbolic Groove in an Infinite Member (Circular Net Section) / 100
2.5.2 U-Shaped Circumferential Groove in a Bar of Circular Cross Section / 100
2.5.3 Flat-Bottom Grooves / 100
2.5.4 Closed-Form Solutions for Grooves in Bars of Circular Cross Section / 100
2.6 Bending of Thin Beams with Notches / 101
2.6.1 Opposite Deep Hyperbolic Notches in an Infinite Thin Element / 101
2.6.2 Opposite Semicircular Notches in a Flat Beam / 101
2.6.3 Opposite U-Shaped Notches in a Flat Beam / 101
2.6.4 V-Shaped Notches in a Flat Beam Element / 102
2.6.5 Notch on One Side of a Thin Beam / 102

2.6.6 Single or Multiple Notches with Semicircular or Semielliptical Notch Bottoms / 102
2.6.7 Notches with Flat Bottoms / 103
2.6.8 Closed-Form Solutions for Stress Concentration Factors for Notched Beams / 103
2.7 Bending of Plates with Notches / 103
2.7.1 Various Edge Notches in an Infinite Plate in Transverse Bending / 103
2.7.2 Notches in a Finite-Width Plate in Transverse Bending / 104
2.8 Bending of Solids with Grooves / 104
2.8.1 Deep Hyperbolic Groove in an Infinite Member / 104
2.8.2 U-Shaped Circumferential Groove in a Bar of Circular Cross Section / 104
2.8.3 Flat-Bottom Grooves in Bars of Circular Cross Section / 105
2.8.4 Closed-Form Solutions for Grooves in Bars of Circular Cross Section / 105
2.9 Direct Shear and Torsion / 106
2.9.1 Deep Hyperbolic Notches in an Infinite Thin Element in Direct Shear / 106
2.9.2 Deep Hyperbolic Groove in an Infinite Member / 106
2.9.3 U-Shaped Circumferential Groove in a Bar of Circular Cross Section Subject to Torsion / 106
2.9.4 V-Shaped Circumferential Groove in a Bar of Circular Cross Section Under Torsion / 108
2.9.5 Shaft in Torsion with Grooves with Flat Bottoms / 108
2.9.6 Closed-Form Formulas for Grooves in Bars of Circular Cross Section Under Torsion / 109
2.10 Test Specimen Design for Maximum K_t for a Given *r/D* or *r/H* / 109
References / 109
Charts / 113

3 SHOULDER FILLETS 167

3.1 Notation / 167
3.2 Stress Concentration Factors / 169
3.3 Tension (Axial Loading) / 170
3.3.1 Opposite Shoulder Fillets in a Flat Bar / 170
3.3.2 Effect of Length of Element / 170
3.3.3 Effect of Shoulder Geometry in a Flat Member / 170
3.3.4 Effect of a Trapezoidal Protuberance on the Edge of a Flat Bar / 171
3.3.5 Fillet of Noncircular Contour in a Flat Stepped Bar / 172
3.3.6 Stepped Bar of Circular Cross Section with a Circumferential Shoulder Fillet / 175

3.3.7 Tubes / 176
3.3.8 Stepped Pressure Vessel Wall with Shoulder Fillets / 176
3.4 Bending / 177
3.4.1 Opposite Shoulder Fillets in a Flat Bar / 177
3.4.2 Effect of Shoulder Geometry in a Flat Thin Member / 177
3.4.3 Elliptical Shoulder Fillet in a Flat Member / 177
3.4.4 Stepped Bar of Circular Cross Section with a Circumferential Shoulder Fillet / 177
3.5 Torsion / 178
3.5.1 Stepped Bar of Circular Cross Section with a Circumferential Shoulder Fillet / 178
3.5.2 Stepped Bar of Circular Cross Section with a Circumferential Shoulder Fillet and a Central Axial Hole / 178
3.5.3 Compound Fillet / 179
3.6 Methods of Reducing Stress Concentration at a Shoulder / 180
References / 182
Charts / 184

4 HOLES 209

4.1 Notation / 209
4.2 Stress Concentration Factors / 211
4.3 Circular Holes with In-Plane Stresses / 214
4.3.1 Single Circular Hole in an Infinite Thin Element in Uniaxial Tension / 214
4.3.2 Single Circular Hole in a Semi-Infinite Element in Uniaxial Tension / 217
4.3.3 Single Circular Hole in a Finite-Width Element in Uniaxial Tension / 218
4.3.4 Effect of Length of Element / 218
4.3.5 Single Circular Hole in an Infinite Thin Element under Biaxial In-Plane Stresses / 219
4.3.6 Single Circular Hole in a Cylindrical Shell with Tension or Internal Pressure / 220
4.3.7 Circular or Elliptical Hole in a Spherical Shell with Internal Pressure / 223
4.3.8 Reinforced Hole Near the Edge of a Semi-Infinite Element in Uniaxial Tension / 223
4.3.9 Symmetrically Reinforced Hole in a Finite-Width Element in Uniaxial Tension / 226
4.3.10 Nonsymmetrically Reinforced Hole in a Finite-Width Element in Uniaxial Tension / 227
4.3.11 Symmetrically Reinforced Circular Hole in a Biaxially Stressed Wide, Thin Element / 227

4.3.12 Circular Hole with Internal Pressure / 235
4.3.13 Two Circular Holes of Equal Diameter in a Thin Element in Uniaxial Tension or Biaxial In-Plane Stresses / 236
4.3.14 Two Circular Holes of Unequal Diameter in a Thin Element in Uniaxial Tension or Biaxial In-Plane Stresses / 241
4.3.15 Single Row of Equally Distributed Circular Holes in an Element in Tension / 243
4.3.16 Double Row of Circular Holes in a Thin Element in Uniaxial Tension / 243
4.3.17 Symmetrical Pattern of Circular Holes in a Thin Element in Uniaxial Tension or Biaxial In-Plane Stresses / 244
4.3.18 Radially Stressed Circular Element with a Ring of Circular Holes, with or without a Central Circular Hole / 245
4.3.19 Thin Element with Circular Holes with Internal Pressure / 246
4.4 Elliptical Holes in Tension / 247
4.4.1 Single Elliptical Hole in Infinite- and Finite-Width Thin Elements in Uniaxial Tension / 250
4.4.2 Width Correction Factor for a Cracklike Central Slit in a Tension Panel / 252
4.4.3 Single Elliptical Hole in an Infinite, Thin Element Biaxially Stressed / 253
4.4.4 Infinite Row of Elliptical Holes in Infinite- and Finite-Width Thin Elements in Uniaxial Tension / 263
4.4.5 Elliptical Hole with Internal Pressure / 263
4.4.6 Elliptical Holes with Bead Reinforcement in an Infinite Thin Element under Uniaxial and Biaxial Stresses / 263
4.5 Various Configurations with In-Plane Stresses / 263
4.5.1 Thin Element with an Ovaloid; Two Holes Connected by a Slit under Tension; Equivalent Ellipse / 263
4.5.2 Circular Hole with Opposite Semicircular Lobes in a Thin Element in Tension / 265
4.5.3 Infinite Thin Element with a Rectangular Hole with Rounded Corners Subject to Uniaxial or Biaxial Stress / 266
4.5.4 Finite-Width Tension Thin Element with Round-Cornered Square Hole / 267
4.5.5 Square Holes with Rounded Corners and Bead Reinforcement in an Infinite Panel under Uniaxial and Biaxial Stresses / 267
4.5.6 Round-Cornered Equilateral Triangular Hole in an Infinite Thin Element Under Various States of Tension / 267
4.5.7 Uniaxially Stressed Tube or Bar of Circular Cross Section with a Transverse Circular Hole / 267

4.5.8 Round Pin Joint in Tension / 268
4.5.9 Inclined Round Hole in an Infinite Panel Subjected to Various States of Tension / 269
4.5.10 Pressure Vessel Nozzle (Reinforced Cylindrical Opening) / 270
4.5.11 Spherical or Ellipsoidal Cavities / 271
4.5.12 Spherical or Ellipsoidal Inclusions / 272
4.6 Holes in Thick Elements / 274
4.6.1 Countersunk Holes / 276
4.6.2 Cylindrical Tunnel / 277
4.6.3 Intersecting Cylindrical Holes / 278
4.6.4 Rotating Disk with a Hole / 279
4.6.5 Ring or Hollow Roller / 281
4.6.6 Pressurized Cylinder / 281
4.6.7 Pressurized Hollow Thick Cylinder with a Circular Hole in the Cylinder Wall / 282
4.6.8 Pressurized Hollow Thick Square Block with a Circular Hole in the Wall / 283
4.6.9 Other Configurations / 283
4.7 Orthotropic Thin Members / 284
4.7.1 Orthotropic Panel with an Elliptical Hole / 284
4.7.2 Orthotropic Panel with a Circular Hole / 286
4.7.3 Orthotropic Panel with a Crack / 286
4.7.4 Isotropic Panel with an Elliptical Hole / 286
4.7.5 Isotropic Panel with a Circular Hole / 286
4.7.6 More Accurate Theory for $a/b < 4$ / 287
4.8 Bending / 288
4.8.1 Bending of a Beam with a Central Hole / 288
4.8.2 Bending of a Beam with a Circular Hole Displaced from the Center Line / 289
4.8.3 Curved Beams with Circular Holes / 289
4.8.4 Bending of a Beam with an Elliptical Hole; Slot with Semicircular Ends (Ovaloid); or Round-Cornered Square Hole / 290
4.8.5 Bending of an Infinite- and a Finite-Width Plate with a Single Circular Hole / 290
4.8.6 Bending of an Infinite Plate with a Row of Circular Holes / 291
4.8.7 Bending of an Infinite Plate with a Single Elliptical Hole / 291
4.8.8 Bending of an Infinite Plate with a Row of Elliptical Holes / 291
4.8.9 Tube or Bar of Circular Cross Section with a Transverse Hole / 291

4.9 Shear and Torsion / 292
4.9.1 Shear Stressing of an Infinite Thin Element with Circular or Elliptical Hole, Unreinforced and Reinforced / 292
4.9.2 Shear Stressing of an Infinite Thin Element with a Round-Cornered Rectangular Hole, Unreinforced and Reinforced / 293
4.9.3 Two Circular Holes of Unequal Diameter in a Thin Element in Pure Shear / 293
4.9.4 Shear Stressing of an Infinite Thin Element with Two Circular Holes or a Row of Circular Holes / 294
4.9.5 Shear Stressing of an Infinite Thin Element with an Infinite Pattern of Circular Holes / 294
4.9.6 Twisted Infinite Plate with a Circular Hole / 294
4.9.7 Torsion of a Cylindrical Shell with a Circular Hole / 294
4.9.8 Torsion of a Tube or Bar of Circular Cross Section with a Transverse Circular Hole / 294
References / 296
Charts / 307

5 MISCELLANEOUS DESIGN ELEMENTS 439

5.1 Notation / 439
5.2 Shaft with Keyseat / 441
5.2.1 Bending / 442
5.2.2 Torsion / 442
5.2.3 Torque Transmitted Through a Key / 443
5.2.4 Combined Bending and Torsion / 443
5.2.5 Effect of Proximity of Keyseat to Shaft Shoulder Fillet / 443
5.2.6 Fatigue Failures / 444
5.3 Splined Shaft in Torsion / 445
5.4 Gear Teeth / 445
5.5 Press- or Shrink-Fitted Members / 447
5.6 Bolt and Nut / 450
5.7 Bolt Head, Turbine-Blade, or Compressor-Blade Fastening (T-Head) / 452
5.8 Lug Joint / 454
5.8.1 Lugs with $h/d < 0.5$ / 455
5.8.2 Lugs with $h/d > 0.5$ / 456
5.9 Curved Bar / 457
5.10 Helical Spring / 458
5.10.1 Round or Square Wire Compression or Tension Spring / 458
5.10.2 Rectangular Wire Compression or Tension Spring / 460
5.10.3 Helical Torsion Spring / 461

5.11 Crankshaft / 461
5.12 Crane Hook / 462
5.13 U-Shaped Member / 462
5.14 Angle and Box Sections / 463
5.15 Cylindrical Pressure Vessel with Torispherical Ends / 463
5.16 Welds / 464
5.17 Parts with Inhomogeneous Materials or Composites / 471
5.18 Parts with Defects / 471
5.19 Parts with Threads / 474
5.20 Frame Stiffeners / 475
5.21 Discontinuities with Additional Considerations / 476
5.22 Pharmaceutical Tablets with Holes / 477
5.23 Parts with Residual Stresses / 478
5.24 Surface Roughness / 479
5.25 New Approaches for Parametric Studies / 480
References / 481
Charts / 489

6 FINITE ELEMENT ANALYSIS (FEA) FOR STRESS ANALYSIS 517

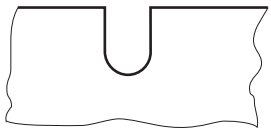
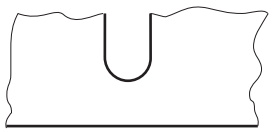
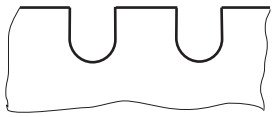
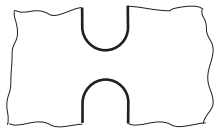
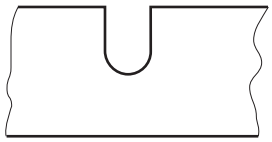
6.1 Structural Analysis Problems / 518
6.2 Types of Engineering Analysis Methods / 519
6.3 Structural Analysis Theory / 520
6.3.1 Trusses and Frame Structures / 523
6.3.1.1 Trusses / 523
6.3.1.2 Boundary Conditions (BCs) and Loads / 526
6.3.1.3 Frame Structure / 527
6.3.2 Plane Stress and Strain Problems / 530
6.3.2.1 Plane Stresses / 530
6.3.2.2 Plane Strain Problems / 535
6.3.3 Modal Analysis / 535
6.3.3.1 Two-Dimensional Truss Member in LCS / 537
6.3.3.2 Two-Dimensional Beam Member in LCS / 538
6.3.3.3 Modeling of Two-Dimensional Frame Element / 540
6.3.4 Fatigue Analysis / 542
6.3.4.1 Strain-Life Method / 543
6.3.4.2 Linear Elastic Fracture Mechanics Method / 544
6.3.4.3 Stress-Life Method / 545
6.3.4.4 Selection of Fatigue Analysis Methods / 546

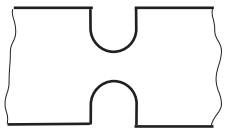
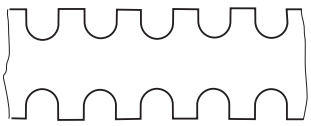
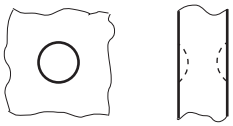
6.4 Finite Element Anlaysis (FEA) for Structural Analysis / 547
6.4.1 CAD/CAE Interface / 551
6.4.2 Materials Library / 552
6.4.3 Meshing Tool / 554
6.4.4 Analysis Types / 558
6.4.5 Tools for Boundary Conditions / 559
6.4.6 Solvers to FEA Models / 559
6.4.7 Postprocessing / 562
6.5 Planning V&V in FEA Modeling / 562
6.5.1 Sources of Errors / 563
6.5.1.1 Error Quantification / 563
6.5.1.2 System Inputs / 564
6.5.1.3 Errors of Idealization / 565
6.5.1.4 Errors of Mathematic Models / 566
6.5.1.5 Errors of Model or Analysis Type / 567
6.5.2 Verification / 567
6.5.2.1 Code Verification / 568
6.5.2.2 Calculation Verification / 571
6.5.2.3 Meshing Verification / 572
6.5.2.4 Convergence Study / 575
6.5.2.5 Benchmarking / 576
6.6 Finite Element Analysis for Verification of Structural Analysis / 577
6.7 FEA for Stress Analysis of Assembly Models / 580
6.8 Parametric Study for Stress Analysis / 582
6.9 FEA on Study of Stress Concentration Factors / 586
References / 586

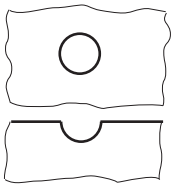
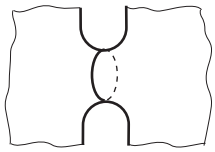
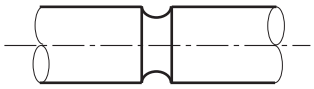
INDEX **589**

INDEX TO THE STRESS CONCENTRATION FACTORS

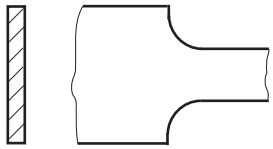
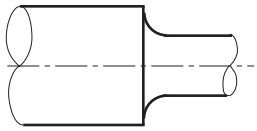
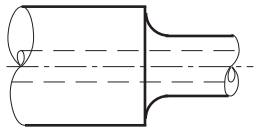
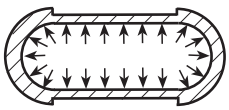
CHAPTER 2: NOTCHES AND GROOVES

Form of Stress Raiser	Load Case	Shape of Stress Raiser	Section and Equation Number	Chart Number	Page Number of Chart
  Single notch in semi-infinite thin element	Tension	U-shaped	2.3.1	2.2	82
		Hyperbolic	2.3.6	2.8	88
		Elliptical	2.3.1	2.2	82
		Flat bottom	2.3.7	2.11	91
	Bending (in-plane)	Hyperbolic	2.6.5	2.29	109
	Bending (out-of-plane)	V-shaped	2.7.1	2.36	117
		Flat bottom	2.7.1	2.36	117
		Elliptical	2.7.1	2.37	118
 Multiple notches in semi-infinite thin element	Bending (out-of-plane)	Semicircular	2.7.1	2.38	119
 Opposite notches in infinite thin element	Tension	Hyperbolic	2.3.1	2.1	81
	Bending (in-plane)	Hyperbolic	2.6.1	2.23	103
	Bending (out-of-plane)	Hyperbolic	2.7.1	2.35	116
	Shear	Hyperbolic	2.9.1	2.45	126
 Single notch in finite-width thin element	Tension	U-shaped	2.3.6	2.9	89
		Flat bottom	2.3.8	2.14	94
	Bending (in-plane)	U-shaped	2.6.5	2.30	110
		V-shaped	2.6.4	2.28	108
		Various shaped notches in impact test	2.6.5	2.31	112
		Semi-elliptical	2.6.6	2.32	113

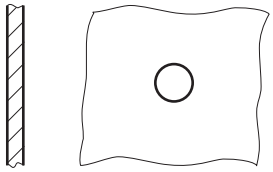
Form of Stress Raiser	Load Case	Shape of Stress Raiser	Section and Equation Number	Chart Number	Page Number of Chart
 Multiple notches on one side of finite-width thin element	Tension	Semicircular	2.3.8	2.14 2.15 2.16	94 95 96
	Bending (in-plane)	Semi-elliptical	2.6.6	2.32	113
	Bending (out-of-plane)	Semicircular	2.7.1	2.38	119
 Opposite single notches in finite-width thin element	Tension	U-shaped	2.3.3 Eq. (2.1)	2.4 2.5 2.6 2.53	84 85 86 134
		Semicircular	2.3.2	2.3	83
		V-shaped	2.3.5	2.7	87
		Flat bottom	2.3.7	2.10	90
	Bending (in-plane)	Semicircular	2.6.2	2.24	104
		U-shaped	2.6.3	2.25 2.26 2.27 2.53	105 106 107 134
		Flat bottom	2.6.7	2.33	114
	Bending (out-of-plane)	Arbitrarily shaped	2.7.2	2.39	120
 Opposite multiple notches in finite-width thin element	Tension	Semicircular	2.3.8	2.12 2.13	92 93
 Depressions in opposite sides of a thin element	Uniaxial tension	Spherical	2.4.3	2.17	97
		Cylindrical groove			

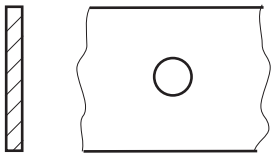
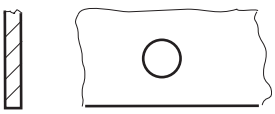
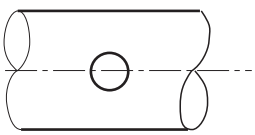
Form of Stress Raiser	Load Case	Shape of Stress Raiser	Section and Equation Number	Chart Number	Page Number of Chart
 Depression in the surface of a semi-infinite body	Uniaxial tension	Hemispherical	2.4.1		
		Hyperboloid	2.4.2		
 Groove in infinite medium	Tension	Hyperbolic	2.5.1	2.18	98
	Bending	Hyperbolic	2.8.1	2.40	121
	Torsion	Hyperbolic	2.9.2	2.46	127
 Circumferential groove in shaft of circular cross section	Tension	U-shaped	2.5.2	2.19 2.20 2.21 2.53	99 100 101 134
		Flat bottom	2.5.3	2.22 2.34	102 115
	Bending	U-shaped	2.8.2	2.41 2.42 2.43 2.53	122 123 124 134
		Flat bottom	2.6.7 2.8.3	2.34 2.44	115 125
	Tension and bending	Flat bottom	2.6.7	2.34	115
	Torsion	U-shaped	2.9.3	2.47 2.48 2.49 2.50 2.53	128 129 130 131 134
		V-shaped	2.5.4 2.9.4	2.51	132
		Flat bottom	2.9.5	2.52	133

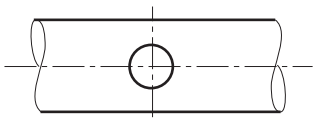
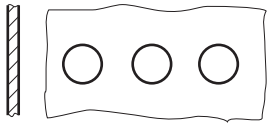
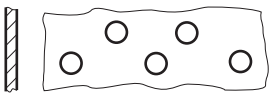
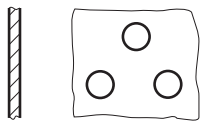
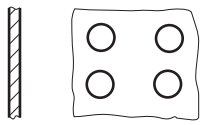
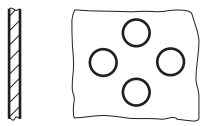
CHAPTER 3: SHOULDER FILLETS

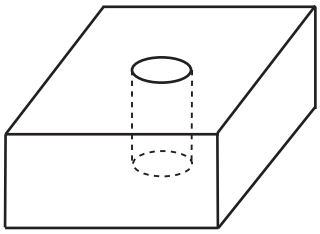
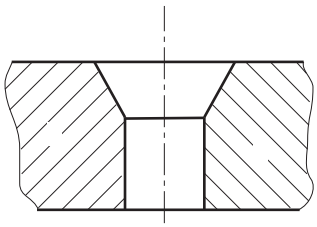
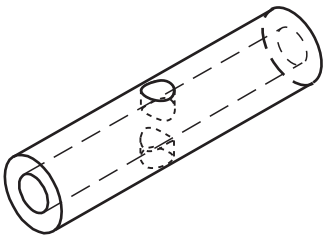
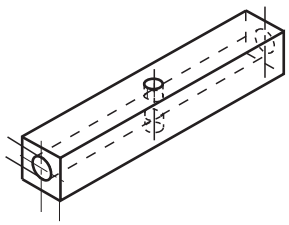
Form of Stress Raiser	Load Case	Shape of Stress Raiser	Section and Equation Number	Chart Number	Page Number of Chart
 Shoulder fillets in thin element	Tension	Single radius	3.3.1 Eq. (3.1)	3.1	151
		Tapered	3.3.5		
	Bending	Single radius	3.4.1	3.7	160
		Elliptical	3.4.3	3.9	164
		Tapered	3.3.5		
	Torsion	Tapered	3.3.5		
 Shoulder fillets in thin element	Tension	Single radius	3.3.3	3.2	152
		Trapezoidal protuberance	3.3.4	3.3	155
	Bending	Single radius	3.4.2	3.8	161
 Shoulder fillet in bar of circular cross section	Tension	Single radius	3.3.6	3.4	157
	Bending	Single radius	3.4.4	3.10 3.11	165 166
	Torsion	Single radius	3.5.1	3.12 3.13	167 168
		Compound radius	3.5.3	3.16 3.17	173 175
 Shoulder fillet in bar of circular cross section with axial hole	Tension	Single radius	3.3.7	3.5	158
	Torsion	Single radius	3.5.2	3.14 3.15	169 170
 Stepped pressure vessel	Internal pressure	Stepped ring	3.3.8	3.6	159

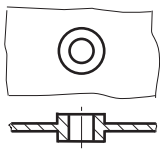
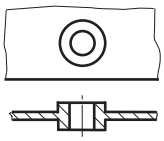
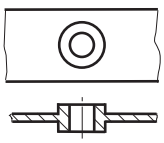
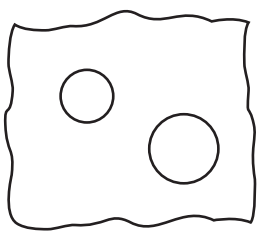
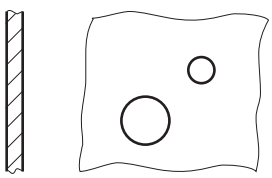
CHAPTER 4: HOLES

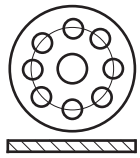
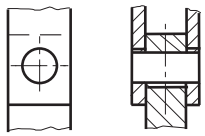
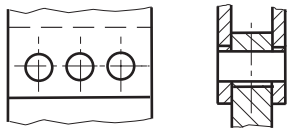
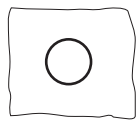
Form of Stress Raiser	Load Case	Shape of Stress Raiser	Section and Equation Number	Chart Number	Page Number of Chart
 Hole in infinite thin element	Uniaxial tension	Circular	4.3.1 Eqs. (4.9)–(4.10)		
		Elliptical	4.4.1 Eqs. (4.57) and (4.58)	4.50	334
		Elliptical hole with inclusion	4.5.12	4.50 4.75	334 366
		Circular hole with opposite semicircular lobes	4.5.2	4.60	346
		Rectangular	4.5.3 4.5.4	4.62a	348
		Equilateral triangular	4.5.6	4.65	355
		Inclined	4.5.9	4.70	361
	Internal pressure	Circular, elliptical, and other shapes	4.3.12, 4.3.19, 4.4.5 Eqs. (4.41) and (4.77)		
	Biaxial stress (in-plane)	Circular	4.3.5 Eqs. (4.17) and (4.18)		
		Rectangular	4.5.3	4.62	348
		Various shapes	4.5.1 4.5.3	4.63	352
		Equilateral triangular	4.5.6	4.65	355
		Elliptical	4.4.3 Eqs. (4.68)–(4.71)	4.54 4.55	338 339
		Inclined	4.5.9	4.69	360
	Bending (out-of-plane)	Circular	4.8.4 Eqs. (4.129) and (4.130)	4.91	382
		Elliptical	4.8.7 Eqs. (4.132) and (4.133)	4.94	385
	Shear	Circular or elliptical	4.9.1	4.97	388
		Rectangular	4.9.2	4.99	390
	Twist	Circular	4.9.6 Eq. (4.138)	4.106	398

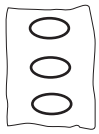
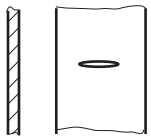
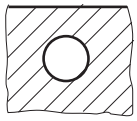
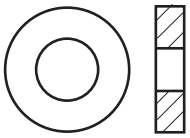
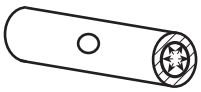
Form of Stress Raiser	Load Case	Shape of Stress Raiser	Section and Equation Number	Chart Number	Page Number of Chart
 Hole in finite-width thin element	Uniaxial tension	Circular	4.3.1 Eq. (4.9)	4.1	256
		Crack	4.7.3		
		Circular orthotropic material	4.7.2		
		Eccentrically located circular	4.3.3 Eq. (4.14)	4.3	272
		Elliptical	4.4.1, 4.4.2	4.53	337
		Elliptical orthotropic material	4.7.1		
		Circular hole with opposite semi-circular lobes	4.5.2 Eqs. (4.78) and (4.79)	4.61	347
		Slot with semicircular or semielliptical end	4.5.1	4.59	345
	Internal pressure	Various shapes	4.3.19 4.4.5		
	Bending (in-plane)	Circular in curved beam	4.8.3		
		Circular	4.8.1, 4.8.2 Eqs. (4.124)–(4.127)	4.88 4.89	379 380
		Elliptical	4.8.4	4.90	381
		Ovaloids, square	4.8.4 Eq. (4.128)		
	Bending (out-of-plane)	Circular	4.8.5 Eq. (4.129)	4.92	383
 Hole in semi-infinite thin element	Uniaxial tension	Circular	4.3.2 Eq. (4.12)	4.2	271
		Elliptical	4.4.1	4.52	336
	Internal pressure	Various shapes	4.3.19, 4.4.5		
 Hole in cylindrical shell, pipe, or bar	Tension	Circular	4.3.6	4.4	273
	Internal pressure	Circular	4.3.6 Eqs. (4.19)–(4.21)	4.5	274
	Torsion	Circular	4.9.7	4.107	399

Form of Stress Raiser	Load Case	Shape of Stress Raiser	Section and Equation Number	Chart Number	Page Number of Chart
 Transverse hole through rod or tube	Tension	Circular	4.5.7	4.66	357
	Bending	Circular	4.8.9	4.96	388
	Torsion	Circular	4.9.8	4.108	400
 Row of holes in infinite thin element	Uniaxial tension	Circular	4.3.15	4.32	314
		Elliptical	4.4.4	4.56	340
		Elliptical holes with inclusions	4.5.12	4.76	367
	Biaxial stresses (in-plane)	Circular	4.3.15	4.34	316
	Bending (out-of-plane)	Circular	4.8.6	4.93	384
		Elliptical	4.8.8	4.95	386
	Shear	Circular	4.9.4	4.102	394
 Row of holes in finite-width thin element	Uniaxial tension	Elliptical	4.4.4	4.33, 4.57	315, 341
 Double row of holes in infinite thin element	Uniaxial tension	Circular	4.3.16 Eqs. (4.46) and (4.47)	4.35 4.36	317 318
 Triangular pattern of holes in infinite thin element	Uniaxial tension	Circular	4.3.17	4.37, 4.38, 4.39	319, 320, 321
	Biaxial stresses (in-plane)	Circular	4.3.17	4.37, 4.38, 4.39, 4.41	319, 320, 321, 325
	Shear	Circular	4.9.5	4.103	395
 Square pattern of holes in infinite thin element	Uniaxial tension	Circular	4.3.17	4.40 4.43	324 327
	Biaxial stresses (in-plane)	Circular	4.3.17	4.40, 4.41, 4.42	324, 325, 326
	Shear	Circular	4.9.5	4.103 4.104	395 396
 Diamond pattern of holes in infinite thin element	Uniaxial tension	Circular	4.3.17	4.44 4.45	328 329
	Shear	Circular	4.9.5	4.105	397

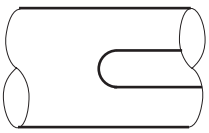
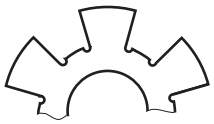
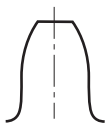
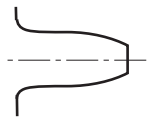
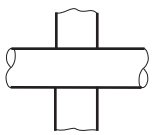
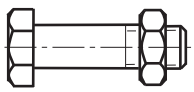
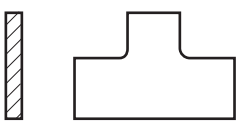
Form of Stress Raiser	Load Case	Shape of Stress Raiser	Section and Equation Number	Chart Number	Page Number of Chart
 Hole in wall of thin spherical shell	Internal pressure	Circular or elliptical	4.3.7	4.6	275
 Thick element with hole	Tension and shear	Circular	4.6		
 Countersunk hole	Tension and bending	Circular	4.6.1		
 Pressurized hollow thick cylinder with hole		Circular	4.6.7 Eq. (4.110)	4.84, 4.85	375, 376
 Pressurized hollow thick block with hole		Circular	4.6.8	4.86, 4.87	377, 378

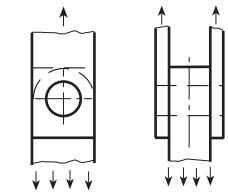
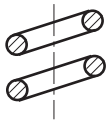
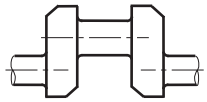
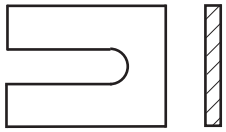
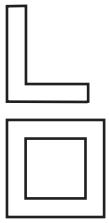
Form of Stress Raiser	Load Case	Shape of Stress Raiser	Section and Equation Number	Chart Number	Page Number of Chart
 Reinforced hole in infinite thin element	Biaxial stress (in-plane)	Circular	4.3.11	4.13, 4.14, 4.15, 4.16, 4.17, 4.18, 4.19	284, 289, 290, 291, 292, 293, 294
		Elliptical	4.4.6	4.58	342
		Square	4.5.5	4.64	353
	Shear	Elliptical	4.9.1	4.98	389
		Square	4.9.2	4.100	391
 Reinforced hole in semi-infinite thin element	Uniaxial tension	Circular	4.3.8	4.7	276
		Square	4.5.5	4.64a	353
 Reinforced hole in finite-width thin element	Uniaxial tension	Circular	4.3.9 4.3.10 Eq. (4.26)	4.8 4.9 4.10 4.11	277 280 281 282
 Hole in panel	Internal pressure	Circular	4.3.12	4.20	295
 Two holes in a finite thin element	Tension	Circular	4.3.13	4.21	296
 Two holes in infinite thin element	Uniaxial tension	Circular	4.3.13 4.3.14 Eqs. (4.42), (4.44), and (4.45)	4.22, 4.23, 4.24, 4.26, 4.27, 4.29, 4.30, 4.31	298, 299, 300, 308, 309, 311, 312, 313
	Biaxial stresses (in-plane)	Circular	4.3.13 4.3.14 Eqs. (4.43)–(4.45)	4.25 4.26 4.28	301 308 310
	Shear	Circular	4.9.3, 4.9.4	4.101	392

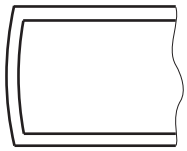
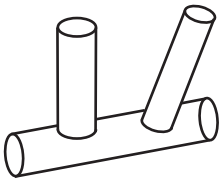
Form of Stress Raiser	Load Case	Shape of Stress Raiser	Section and Equation Number	Chart Number	Page Number of Chart
 Ring of holes in circular thin element	Radial in-plane stresses	Circular	4.3.18 Table 4.1	4.46	330
	Internal pressure	Circular	4.3.19 Table 4.2	4.47	331
 Hole in circular thin element	Internal pressure	Circular	4.3.19 Table 4.2	4.48	332
 Circular pattern of holes in circular thin element	Internal pressure	Circular	4.3.19 Table 4.2	4.49	333
 Pin joint with closely fitting pin	Tension	Circular	4.5.8 Eqs. (4.83) and (4.84)	4.67	358
 Pinned or riveted joint with multiple holes	Tension	Circular	4.5.8	4.68	359
 Cavity in infinite body	Tension	Circular cavity of elliptical cross section	4.5.11	4.71	362
		Ellipsoidal cavity of circular cross section	4.5.11	4.72	363
 Cavities in infinite panel and cylinder	Uniaxial tension or biaxial stresses	Spherical cavity	4.5.11 Eqs. (4.86)–(4.88)	4.73	364

Form of Stress Raiser	Load Case	Shape of Stress Raiser	Section and Equation Number	Chart Number	Page Number of Chart
 Row of cavities in infinite element	Tension	Ellipsoidal cavity	4.5.11	4.74	365
 Crack in thin tension element	Uniaxial tension	Narrow crack	4.4.2 Eqs. (4.62)–(4.64)	4.53	337
 Tunnel	Hydraulic pressure	Circular	4.6.2 Eqs. (4.99)	4.77 4.78	368 369
 Disk	Rotating centrifugal inertial force	Central hole	4.6.4	4.79	370
		Noncentral hole	4.6.4	4.80	371
 Ring	Diametrically opposite internal concentrated loads		4.6.5 Eq. (4.105)	4.81	372
	Diametrically opposite external concentrated loads		4.6.5 Eq. (4.106)	4.82	373
 Thick cylinder	Internal pressure	No hole in cylinder wall	4.6.6 Eqs. (4.108) and (4.109)	4.83	374
		Hole in cylinder wall	4.6.7 Eq. (4.110)	4.84	375

CHAPTER 5: MISCELLANEOUS DESIGN ELEMENTS

Form of Stress Raiser	Load Case	Shape of Stress Raiser	Section and Equation Number	Chart Number	Page Number of Chart
 Keyseat	Bending	Semicircular end	5.2.1	5.1	430
		Sled runner	5.2.1		
	Torsion	Semicircular end	5.2.2 5.2.3	5.2	431
	Combined bending and torsion	Semicircular end	5.2.4	5.3	432
 Splined shaft	Torsion		5.3	5.4	433
 Gear tooth	Bending		5.4 Eqs. (5.3) and (5.4)	5.5 5.6 5.7 5.8	434 435 436 437
 Short beam	Bending	Shoulder fillets	5.4 Eq. (5.5)	5.9	438
 Press-fitted member	Bending		5.5 Tables 5.1 and 5.2		
 Bolt and nut	Tension		5.6		
 T-head	Tension and bending	Shoulder fillets	5.7 Eqs. (5.7) and (5.8)	5.10	439

Form of Stress Raiser	Load Case	Shape of Stress Raiser	Section and Equation Number	Chart Number	Page Number of Chart
 Lug joint	Tension	Square ended	5.8	5.11 5.13	444 446
		Round ended	5.8	5.12 5.13	445 446
 Curved bar	Bending	Uniform bar	5.9 Eq. (5.11)	5.14	447
		Nonuniform: crane hook	5.12		
 Helical spring	Tension or compression	Round or square wire	5.10.1 Eqs. (5.17) and (5.19)	5.15	448
		Rectangular wire	5.10.2 Eq. (5.23)	5.16	449
	Torsional	Round or rectangular wire	5.10.3	5.17	450
 Crankshaft	Bending		5.11 Eq. (5.26)	5.18 5.19	451 452
 U-shaped member	Tension and bending		5.13 Eqs. (5.27) and (5.28)	5.20 5.21	453 454
 Angle or box sections	Torsion		5.14	5.22	455

Form of Stress Raiser	Load Case	Shape of Stress Raiser	Section and Equation Number	Chart Number	Page Number of Chart
 Cylindrical pressure vessel	Internal pressure	Torispherical ends	5.15	5.23	456
 Tubular joint	Variable	K and T joints with and without reinforcement	5.16		

PREFACE FOR THE FOURTH EDITION

Since publishing his first book on *Stress Concentration Factors* in 1953 (Peterson 1953), Rudolph Earl Peterson has become well known as an unparalleled pioneer researcher in stress analysis. The significant influence of his lifetime contribution in the field has been greatly strengthened by the publications of the book series *Peterson's Stress Concentration Factors* (Peterson 1973; Pilkey 1997; Pilkey and Pilkey 2008). These books have been published in three editions. The second and third editions were written by Walter D. Pilkey and Deborah F. Pilkey—two distinguished workers in the fields of elasticity, structural design, and stress analysis. Attributed to comprehensive and abundant information on stress analysis, these books have been widely adopted as the standard references for designing products in machinery, construction, aerospace, defense, transportation, and healthcare systems.

Peterson's Stress Concentration Factors features a comprehensive collection of cutting-edge works in stress concentration factors (SCFs), for the solids with a wide scope of geometric discontinuities, subjected to various loading conditions in different applications. However, since the publication of the third edition in 2008, many researchers have been continuously contributing to the studies of SCFs. To sustain the comprehensiveness of significant works on SCFs for readers, the new edition aims to include the newly developed contributions to stress concentrations on a wide scope of geometric discontinuities and loading conditions. Readers can still rely on the books as the unique and valuable resource in dealing with stress analysis of product designs at any level of complexity. Additionally, the new edition emphasizes the integration with computer-aided engineering (CAE) tools instead of being prepared as traditional references for

accessing engineering data, charts, and empirical formulas for manual calculations. CAE tools allow engineers to quickly and efficiently find the solutions to various engineering problems with the minimal design effort. It is appropriate that sophisticated handbooks be redesigned so that the core values of the included works can be self-guided and utilized seamlessly in the integrated process of product designs.

This fourth edition provides a comprehensive guide for stress analysis of any type of engineering design, from a simple part with a single feature and uniaxial load to any complex structure with numerous geometric discontinuities and coupled dynamic loads. While keeping the core contents of SCFs for various discontinuities and loading conditions in Chapters 2 through 4, this edition makes the extension mainly in three aspects. (1) The relevance of stress analysis in the whole product design process is discussed with a thorough introduction of the theory of elasticity, the characterization of material properties, the methods of stress analysis, the failure theories of materials, and critical activities in design processes. (2) The literatures on stress concentrations from 2007 to 2018 are surveyed to include new significant contributions of SCFs on complex geometries, composites, thermal-coupled parts, micro-level impurities and defects, as well as some artificial intelligent (AI) methods to derive parametric formulas of SCFs. (3) The significance of computer-aided engineering (CAE) in stress analysis is emphasized. The fundamentals of the FEA theory and the Solidworks Simulation package is used as an illustrative tool to show the procedure and applications of using a CAE tool for stress analysis of complex products.

The author would like to express his great appreciation for the encouragement and support from Associate Editor Kalli Schultea, Editorial Director Margaret Cummins, the Project Editor Blesy Regulas at Wiley, the Production Editor Jayalakshmi E. Thevarkandi, and the coauthor of the third edition, Deborah F. Pilkey. The author would also like to thank the gracious understanding and collaboration of his family members Rongrong Wu, Chenghao Bi, and Chengyu Bi in the completion of this version.

REFERENCES

Peterson, R. E., 1953, *Stress Concentration Design Factors*, Wiley, New York.

Peterson, R. E., 1973, *Stress Concentration Factors*, Wiley, New York.

Pilkey, W. D., 1997, *Peterson's Stress Concentration Factors* (2nd ed.), Wiley, New York.

Pilkey, W. D., and Pilkey, D. F., 2008, *Peterson's Stress Concentration Factors* (3rd ed.), Wiley, Hoboken, NJ.

PREFACE FOR THE THIRD EDITION

Computational methods, primarily the finite element method, continue to be used to calculate stress concentration factors in practice. Improvements in software, such as automated mesh generation and refinement, ease the task of these calculations. Many computational solutions have been used to check the accuracy of traditional stress concentration factors in recent years. Results of these comparisons have been incorporated throughout this third edition.

Since the previous edition, new stress concentration factors have become available, such as for orthotropic panels and cylinders, thick members, and for geometric discontinuities in tubes and hollow structures with cross bores. Recently developed stress concentration factors for countersunk holes are included in this edition. These can be useful in the study of riveted structural components.

The results of several studies of the minimum length of an element for which the stress concentration factors are valid have been incorporated in the text. These computational investigations have shown that stress concentration factors applied to very short elements can be alarmingly inaccurate.

We appreciate the support for the preparation of this new addition by the University of Virginia Center for Applied Biomechanics. The figures and charts for this edition were skillfully prepared by Wei Wei Ding. The third edition owes much to Yasmina Abdelilah, who keyed in the new material, as well as Viv Bellur and Joel Grasmeyer, who helped update the index.

The continued professional advice of our Wiley editor, Bob Argentieri, is much appreciated. Critical to this work has been the assistance of Barbara Pilkey.

The errors identified in the previous edition have been corrected. Although this edition has been carefully checked for typographic problems, it is difficult to eliminate all of them. An errata list and discussion forum is available through our web site: www.stressconcentrationfactors.com. Readers can contact Deborah Pilkey through that site. Please inform her of errors you find in this volume. Suggestions for changes and stress concentration factors for future editions are welcome.

WALTER D. PILKEY
DEBORAH F. PILKEY

PREFACE FOR THE SECOND EDITION

Rudolph Earl Peterson (1901–1982) has been *Mr. Stress Concentration* for the past half century. Only after preparing this edition of this book has it become evident how much effort he put into his two previous books: *Stress Concentration Design Factors* (1953) and *Stress Concentration Factors* (1974). These were carefully crafted treatises. Much of the material from these books has been retained intact for the present edition. Stress concentration charts not retained are identified in the text so that interested readers can refer to the earlier editions.

The present book contains some recently developed stress concentration factors, as well as most of the charts from the previous editions. Moreover, there is considerable material on how to perform computer analyses of stress concentrations and how to design to reduce stress concentration. Example calculations on the use of the stress concentration charts have been included in this edition.

One of the objectives of application of stress concentration factors is to achieve better balanced designs[1] of structures and machines. This can lead to conserving materials, cost reduction, and

[1] Balanced design is delightfully phrased in the poem, "The Deacon's Masterpiece, or the Wonderful One Hoss Shay" by Oliver Wendell Holmes (1858):

> "Fur", said the Deacon, " 't 's mighty plain
> That the weakes' place mus' stan' the strain,
> "N the way t' fix it, uz I maintain,
> Is only jest
> T' make that place uz strong the rest"

After "one hundred years to the day" the shay failed "all at once, and nothing first."

achieving lighter and more efficient apparatus. Chapter 6, with the computational formulation for design of systems with potential stress concentration problems, is intended to be used to assist in the design process.

The universal availability of general-purpose structural analysis computer software has revolutionized the field of stress concentrations. No longer are there numerous photoelastic stress concentration studies being performed. The development of new experimental stress concentration curves has slowed to a trickle. Often structural analysis is performed computationally in which the use of stress concentration factors is avoided, since a high-stress region is simply part of the computer analysis.

Graphical keys to the stress concentration charts are provided to assist the reader in locating a desired chart.

Major contributions to this revised book were made by Huiyan Wu, Weize Kang, and Uwe Schramm. Drs. Wu and Kang were instrumental throughout in developing new material and, in particular, in securing new stress concentration charts from Japanese, Chinese, and Russian stress concentration books, all of which were in the Chinese language. Dr. Schramm was a principal contributor to Chapter 6 on computational analysis and design.

Special thanks are due to Brett Matthews and Wei Wei Ding, who skillfully prepared the text and figures, respectively. Many polynomial representations of the stress concentration factors were prepared by Debbie Pilkey. Several special figures were drawn by Charles Pilkey.

WALTER D. PILKEY

CHAPTER 1

FUNDAMENTALS OF STRESS ANALYSIS

The physical world consists of various materials and civilizations have been founded on the advancement of skills and artifacts, especially tangible products that are made from natural materials. Our evolution relies greatly on the development of new products. Products are designed and made to fulfill expected *functional requirements* (FRs). For example, a conventional machine tool is designed and made to perform a certain removal process, and a fixture is added to position and secure a part when an operation such as cutting is applied.

For a tangible product, no matter what primary functions the product has, designers must ensure that the selected materials are strong enough to carry the required loads in their applications. Therefore, product design usually involves three basic tasks: (1) the understanding of the material characteristics to determine the strengths, such as *yield strengths* and *fatigue strengths*; (2) the analysis of the response of product subjected to external loads, such as by using the method of *free body diagrams* (FBDs) for internal forces and the structural analysis method for stress distribution; and (3) the determination of the weakest areas of the product, such as the use of the stress concentration factors method. The primary goal of these three tasks is to ensure that the FRs for the weakest areas of the product are within the safe zones of the material strengths. The methodologies and tools for *structural design* are used to perform these tasks.

The innovation and creativity of a new product occurs mostly at the *conceptual design* stage and the analysis and synthesis at the *detailed design* stage is most likely the routine design activities. However, such an analysis is very time-consuming and not trivial due to customized geometries, features, and dimensions of objects, as well as the complexity of loads. It is desirable to have some guides and methods that can be adopted to correlate external loads and geometric features of an object to the system behaviors directly. In this way, the effects of external loads on

Peterson's Stress Concentration Factors, Fourth Edition. Walter D. Pilkey, Deborah F. Pilkey and Zhuming Bi.
© 2020 John Wiley & Sons, Inc. Published 2020 by John Wiley & Sons, Inc.

the geometric features of objects can be quantified and utilized to optimize products. One of the classic theories in dealing with structural design is *the theory of elasticity* (Murakami 2017). In the theory of elasticity, the stress concentration factors (SCFs) method by R. E. Peterson, the author of the first version of *Peterson's Stress Concentration Factors* (Peterson 1974), is widely adopted to analyze the stresses for the prescribed geometries under given loading conditions (Hardy and Malik 1992). However, three previous versions of this book were written as handbooks containing a collection of deign formulas, experimental data, and charts for stress analysis of parts with various geometric features. While the core contents of SCFs for various discontinuities and loading conditions are presented in Chapters 2 through 4, this new edition features significant extensions in the following three chapters.

- In Chapter 1, we provide a through discussion of the relevance of stress analysis in the cycle of product design with respect to the theory of elasticity, the characteristics of material properties, the methods of stress analysis, and the failure theories of materials from the perspective of engineering design practice.
- In Chapter 5, we conduct a comprehensive survey of recent works in the field and incorporate new achievements in stress concentrations for *complex geometries*, *composites*, *thermal-coupled parts*, *micro-level impurities and defects*, as well as some *artificial intelligence* (AI) *methods* to derive parametric formulas of SCFs for acceptable estimations in a wide scope of applications.
- In Chapter 6, we expand on the introduction of the fundamentals of finite element analysis (FEA), significantly as a systematic approach for stress analysis when no formula, experimental data, or charts are available.

Note that while the previous versions of this book are prepared as a sophisticated handbook for designers to estimate stress concentrations for basic design features of machine elements, this new version aims to provide a comprehensive guide for stress analysis of any engineering designs, from a part with a single feature and uniaxial load to any level of complexity of a structure with numerous geometric discontinuities and coupled dynamic loads. To this end, a comprehensive overview on stress analysis is given in this chapter.

1.1 STRESS ANALYSIS IN PRODUCT DESIGN

Product design is the process of creating a new product, which can be tailored to meet customer's needs. *A product* is characterized as an artifact based upon its *functionalities*, *weight*, *geometry, shape*, *cost*, and upon the *holistic properties* of the integrated form. Product design is usually an iterative process with a series of design activities for designers to (1) specify functional requirements (FRs), (2) formulate design constraints, (3) define design variables and design spaces, (4) evaluate feasible alternatives against the specified requirements, and (5) optimize the solution based on the evaluation. Fig. 1.1 shows that no matter how complex a product can be, the design process may consist of two basic procedures, i.e., *top-bottom procedure* and *bottom-up*

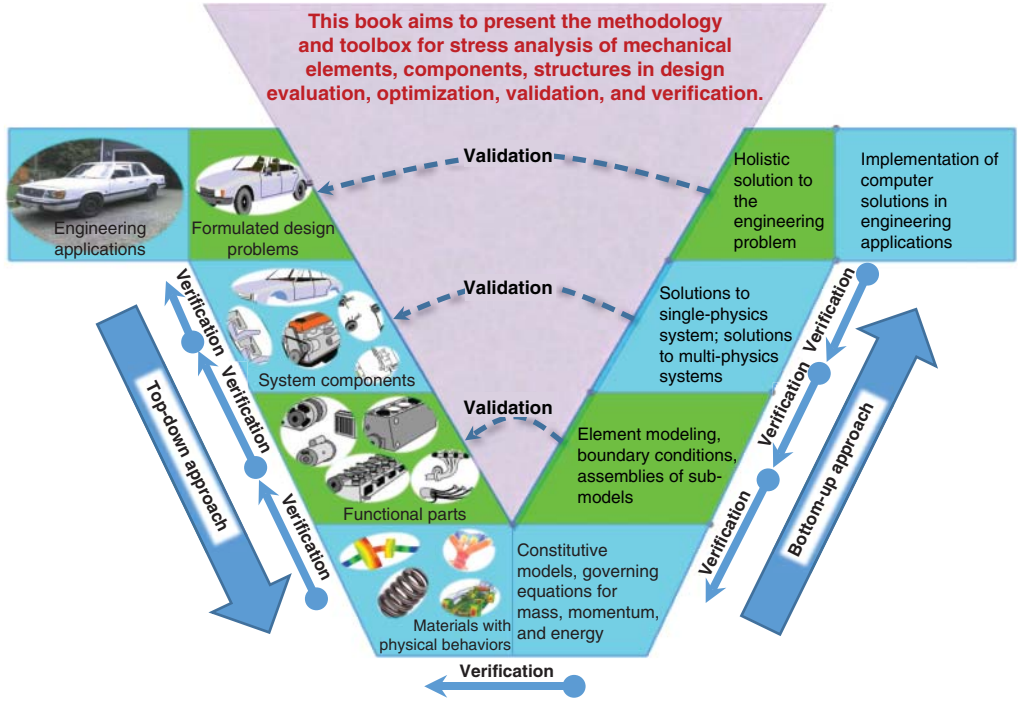


Figure 1.1 V-Model for product design and objectives of book (Bi 2018).

procedure (Bi 2018). In the top-bottom procedure, FRs at the most abstract level are decomposed into sub-FRs at lower levels until the corresponding design solution can be found for each of the sub-FRs. In the bottom-up procedure, the solutions to the sub-FRs at the lowest level are assembled *layer by layer* until the overall system solution is defined to apply to the design problem at the most abstract level. The subsolutions at any stages and domains have to be verified and validated against their expected sub-FRs. *Verification* checks whether a part or a subassembly of parts meets a set of its design specifications at design stage and *validation* ensures a part or a subassembly of parts meets the operational needs of the user.

For *a part* with a large number of design features, *an assembly* with a number of parts or components, or *a product* subjected to mixed or dynamic loading conditions, stress analysis follows a top-bottom approach and begins with one or a few of the features of a part at its most detailed level. Moreover, a stress analysis needs sufficient data of material properties; this is not a trivial task and requires a tremendous amount of time. A systematic methodology and toolbox on stress analysis is desirable, so that designers are able to evaluate stress concentrations, and identify the weakest areas efficiently. From this perspective, this new version is written as the technical guide and toolbox for stress analysis of mechanical structures at any one of the design stages as emphasized in Fig. 1.1.

1.2 SOLID OBJECTS UNDER LOADS

In this book, the methodology and tools that are discussed are used mainly for stress analysis of solid objects. Most of tangible products are made from solid materials. A mechanical product design refers to the designs of parts, components, and systems of mechanical nature, such as machine tools, fixtures, tangible structures, physical devices, and instruments. Fig. 1.2 shows some examples of common mechanical elements. In designing a mechanical system, the weakest areas of objects must be identified to determine the system capacities.

While the FRs of a mechanical product can be specified in many aspects, such as *motions*, *loads*, *tolerances*, *stiffness*, *rigidity*, and *tolerances*, the most critical requirement is to avoid *product failure*. Two main types of product failures are *static failure* and *fatigue failure*. Both failure types are related to the strengths and stresses of materials. The materials of a solid object must be sufficiently strong to carry internal and external loads during its operation. Stress analysis is essential to answer the question of whether or not the selected materials has the required strengths for the given loads.

As shown in Fig. 1.3, the stresses in a solid object are induced by external loads exerted on the object, and the stress varies from one location to another and from time to time if a dynamic load is involved. The stress distribution depends on many factors, such as the geometry and features of an object, the types and characteristic of loads, and the material properties. Stress analysis is performed to determine three types of basic relations: (1) the relations of *loads and deformation*,



(a) Shafts and axes (b) Gears (c) Bearing

(d) Threads and fasteners (e) Springs (f) Clutches and couplers

Figure 1.2 Examples of common machine elements for which stress analysis is essential in design and selection processes.

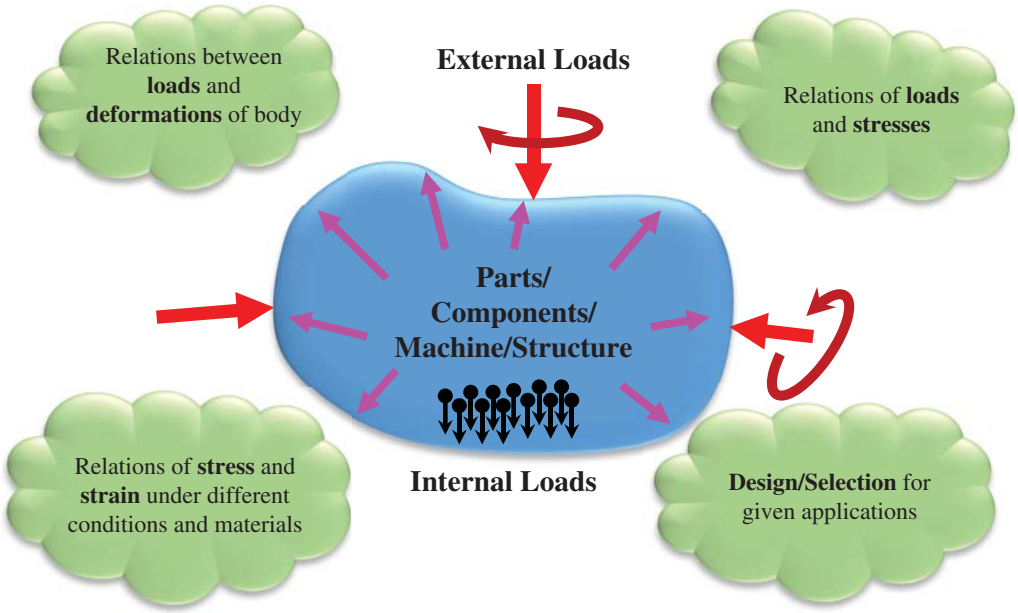


Figure 1.3 Relations in stress analysis of solids.

(2) the relations of *stresses and strains*, and (3) the relations of *loads and stresses*. In addition, design criteria to justify a material failure have to be appropriately selected to match the stresses, deformations, and deflections within the given failure criteria.

As shown in Fig. 1.4, the starting point of a stress analysis is to collect the information of solid object, which will be analyzed and designed: (1) the geometrical description of the objects, (2) the

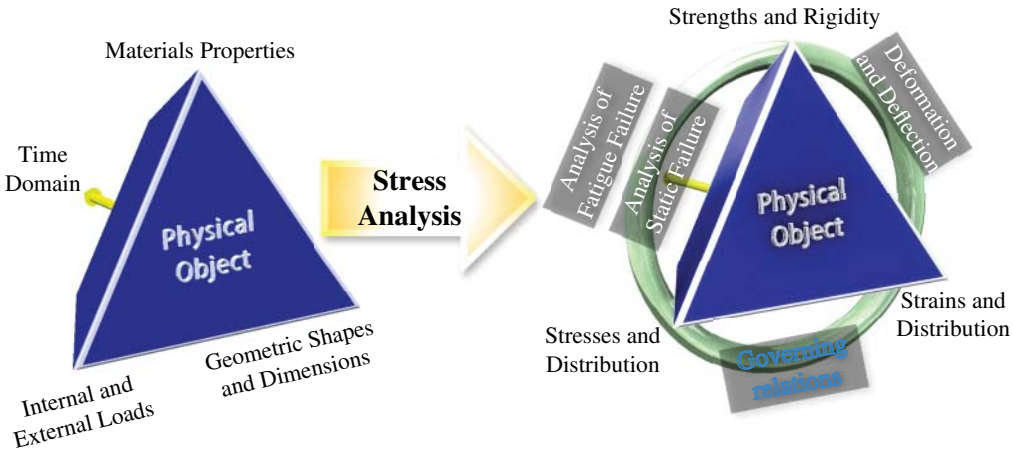


Figure 1.4 Inputs, relations, and outputs of stress analysis.

properties of the materials used for objects, (3) how the parts are joined together, if applicable; and (4) the characteristics of typical loads that will be applied. The outputs of stress analysis are *quantitative stresses*, *strains, geometric deflections,* and the optimized mechanical structures of parts. The analysis may also consider the forces varying with time, such as engine vibrations or the load of moving vehicles. In that case, the stresses and deformations will also be the functions of time and space.

1.3 TYPES OF MATERIALS

Thousands of materials are used in engineering applications, and materials can be classified based on different criteria. For example, atomic bonding forces vary in different materials, so materials are classified as *metallic*, *ceramic,* or *polymeric* based on bonding properties; moreover, combining different materials forms a *composite material*. Within each category shown in Fig. 1.5, the materials can be further classified by chemical compositions or certain mechanical or physical properties. As far as composite materials are concerned, the differences lie in the types of materials and how these materials are composed.

In the classification shown in Fig. 1.5, the basis metals are classified into *ferrous* and *nonferrous* metals. A ferrous metal contains iron as one constitutive element and a nonferrous metal is free from irons. Accordingly, a ferrous metal is magnetic in nature. Many types of metals fall into the group of nonferrous metals, and some commonly used nonferrous metals include copper, aluminum, and lead.

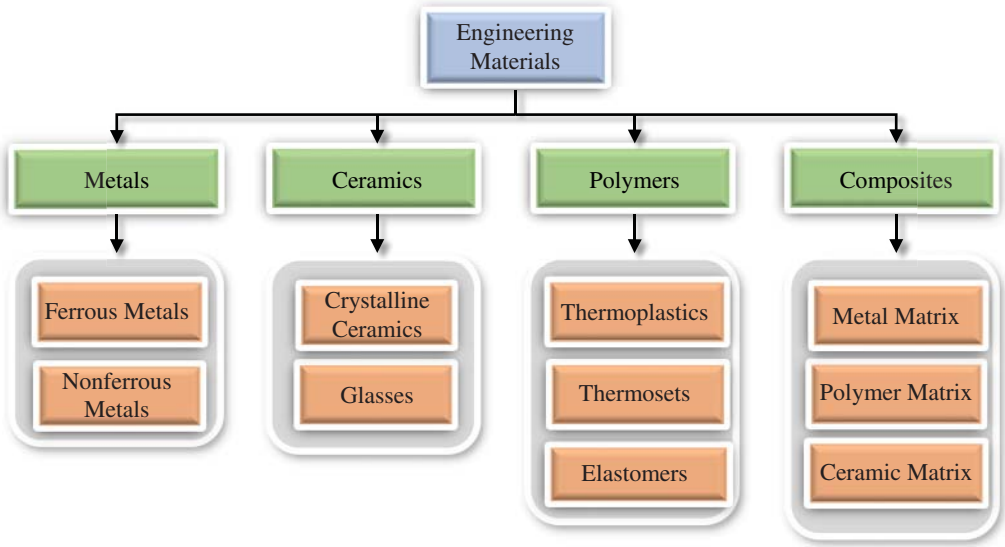


Figure 1.5 Classification of engineering materials.

Ceramic is made of *inorganic* and *nonmetallic* constituents through the processes of heating and consequent solidification. Ceramics usually have high melting points, high elastic modules, and high strengths, but limited ductility, and such materials are widely used in machining tools, such as grinding wheels and cutting chips in fine machining. Ceramics are chemically insolvent and can be utilized in some wet conditions where steel bearings might oxidize. However, using ceramics in products is not a low-effective solution. Ceramics are also vulnerable to be broken under shock loads. Depending on the level of crystalline structure, ceramics can be classified into *crystalline* ceramics and *glasses*.

Polymers are composed of recurring molecular structures as macromolecules. Polymers can be further classified as *thermoplastic*, *thermoset*, and *elastomer*. Due to the difference of molecular structures, three polymer types show significant differences in terms of their mechanical properties, such as *strength*, *toughness* and *hardness*.

A composite consists of two or more distinct materials; each of constitutive materials retains its properties. Materials are combined to create a new composite material with the properties that cannot be achieved by any of constitutive components alone. A composite material have two or more phases: *fibers*, *sheets*, or *particles* are used as reinforcing phase and are embedded in the matrix phase. The materials for the matric phase can be *metal*, *ceramic*, or *polymer*. Typically, reinforcing materials are strong but their densities are low; while the materials for the matrix are usually ductile and tough.

1.4 MATERIALS PROPERTIES AND TESTING

This book mainly concerns the elastic behaviors of materials subjected to given loads. Designers have to know the material properties to evaluate if the applied loads are within the capabilities of the selected materials. The material properties show the consistence only when design factors affecting the properties remain constants. The properties vary and are the functions of other variables, such as temperatures. If one material property is a function of a design variable, it is desirable to have a simplified linear constitutive relation for the dependent relation unless the nonlinearity must be taken into consideration. For example, if a fracture failure of material has to be modeled, the nonlinearity of the constitutive relations has to be taken into consideration.

Materials can be also classified in terms of the dependence of the material properties on the orientation of loading. The material that shows the same properties in any orientation is called as *an isotropic* material and a material that shows a difference in its properties in different orientation is call *an anisotropic* material. It should also be noted that due to numerous uncertainties, such as impurities and ingredients, the material properties are stochastically varied around their nominal values. Therefore, adding *safety factors* in product design becomes practical to deal with the uncertainties of material properties.

To compare and select materials for given applications, engineering materials are characterized to obtain their properties in some standardized ways. Table 1.1 shows typical material properties and the standardized testing methods in which the material properties are evaluated. *A critical loading condition* causing a failure of the material is of the most interest, and the corresponding stress occurring to the material is called as *a strength*. However, the material may fail in many different ways, depending on material types and loading types. One material has a number of the

TABLE 1.1 Typical Material Properties and Standardized Testing Methods

Standardized Testing Methods	Material Properties
Tensile test, bending test, torsion testing, compression test	Elasticity, rigidity, and plasticity
Brinell, Rockwell, Vickers	Hardness
Impact test	Toughness
Wöhler fatigue test	Fatigue strength

strengths if the material may fail in different ways. Therefore, to characterize a material: (1) find the relationship of external forces and deformations of object and (2) determine the stress limits that lead to a certain failure of an object.

The materials are characterized by testing specimens under different loads. Table 1.2 shows the rationales why these tests are important in engineering designs. The failure models and criteria are developed upon the quantities obtained from these tests (Gunt 2018). The failures of materials can be generally classified into *static failures*, *fatigue failures*, and *creep failures*. Any of these failure types is attributed to an exceeded stress in comparison with the corresponding strength of the said materials. To design a safe product, the standardized testing methods are used to obtain the material strengths corresponding to different failure types, so that the comparison can be fairly made in selecting materials.

1.4.1 Tensile and Compression Tests

The tensile test is the most important method in destructive material testing. Fig. 1.6 shows the typical setup of the tensile test. A standardized specimen with a known cross section is loaded uniformly with a gradually increasing force in its axial direction. The state of uniaxial stress state prevails in the specimen until the fracture commences. The *ratio of stress to strain* can be shown from the plotted load extension diagram (Gunt 2018).

The stress-strain diagram in Fig. 1.7 shows clearly that different materials may respond to a gradually increasing load in different ways; but the tensile test can at least provide five characteristic values for tensile strength S_T, yield strength S_y, proportional limit S_E, the elongation ε_F at fracture A, and the elastic modulus E.

Compression tests are less significant for testing metallic materials in contrast to tensile tests. However, when using brittle materials, such as natural stone, brick, concrete, wood, and so on, the compression test is fundamentally important. In Fig. 1.8, a standardized specimen with a known cross section is loaded uniformly with a gradually increasing force in the axial direction. A state of uniaxial stress prevails in the specimen. In Fig. 1.9, the ratio of stress to strain is plotted as the σ-ε diagram of the compression tests. The σ-ε diagram shows *the compression strength*, *the 0.2% offset yield point*, and *the compression yield stress*.

1.4.2 Hardness Tests

The module of elasticity (E) and ultimate strength (S_U) are related to the hardness. When the stresses at the contacts of two objects are investigated or the fatigue life of an object is discussed,

TABLE 1.2 Common Failure Types, Mechanisms, and Characterization Methods of Materials (Gunt 2018)

Failure Type	Failure Mechanism	Example	Characterization Methods
A *static failure* occurs suddenly. Under a normal stress, the failure leads to a partially fissured surface with matte or glossy crystalline; under a shear load, sheer lips occur at the edge of ductile fractures.	(1) Brittle fracture occurs when the maximized principal stress exceeds the ultimate tensile strength, (2) A ductile fracture occurs when the maximized shear stress the yield strength, and (3) With the presence of normal stress, a brittle fracture may occur at a reduced grain boundary cohesion.		Tensile test for ultimate tensile strength, yielding strength, fracture strength. Impact test for dynamic fracture strength.
A *fatigue failure* occurs when the material experiences an exceeded period of time subjected to repetitive or fluctuated loads. A fatigue failure is usually low-deformation fracture	The fatigue is initialized at stress-concentrated areas, such as notches or imperfections; the fatigue is accumulated and propagated to form oscillatory cracks. When the fatigue stress exceeds the fatigue strength, the remaining cross-section area fails by a forced fracture.		Wöhler fatigue test for strength and number of cycles curve (S-N curve)
A *creep failure* is progressed with time being due to various dynamic factors, such as a sustained load in dynamic processes, varying temperature, or impurities on grain boundaries.	A creep failure occurs when the size of the maximized crack exceeds the limit of creep fracture		Creep rupture test for strain-time relations (creep properties)

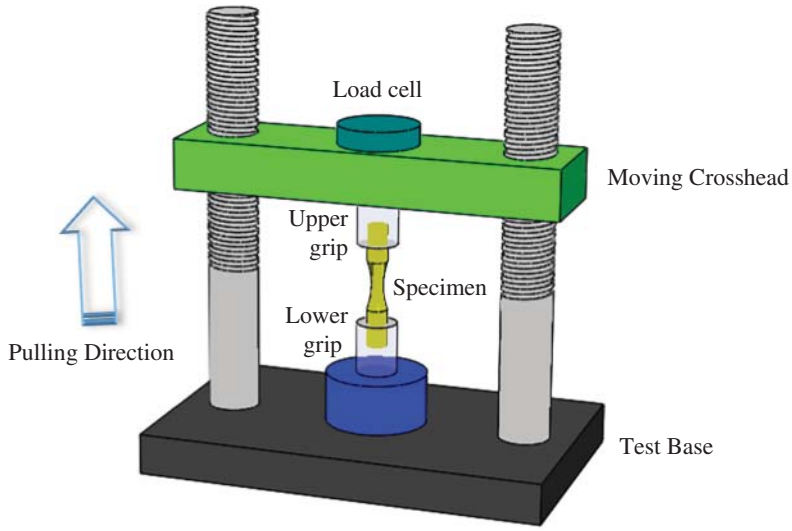
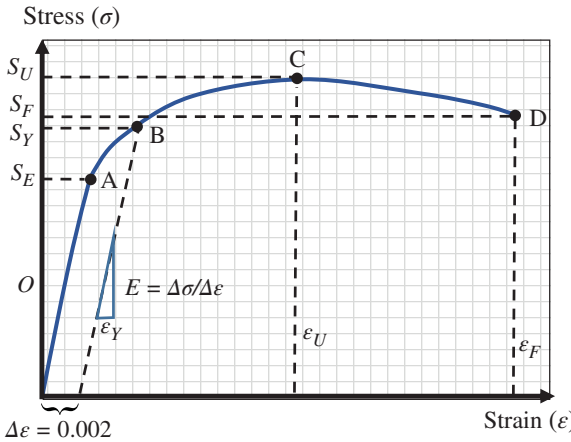


Figure 1.6 Schematic of tensile testing.



(a) Stress-strain curve from tensile test

Point A:	is the limit of elastic deformation
Point B:	is the yield point
Point C:	is the point with the maximized tensile stress
Point D:	is the point of fracture
E:	is elastic modulus
$\Delta\varepsilon = 0.002$:	is the offset strain to determine E
S_U, S_F, S_Y, and S_E:	are the stresses of ultimate tensile limit, fracture, yield, and elastic limit, respectively
ε_F, ε_U, and ε_Y:	are the strains of fracture, yield, and elastic limit, respectively

(b) Terminologies

Figure 1.7 Terminologies of stress-strain curve from tensile test.

the hardness of the material is important. Three common methods to measure thee hardness of materials are the *Brinell hardness test*, *Vickers hardness test*, and *Rockwell hardness test*.

Fig. 1.10 shows the setup of the Brinell hardness test: a hard metal sphere is used as a standardized test body; it is pressed into the workpiece by a gradually increased load at the room temperature. The surface of the lasting impression is measured optically, and the impression

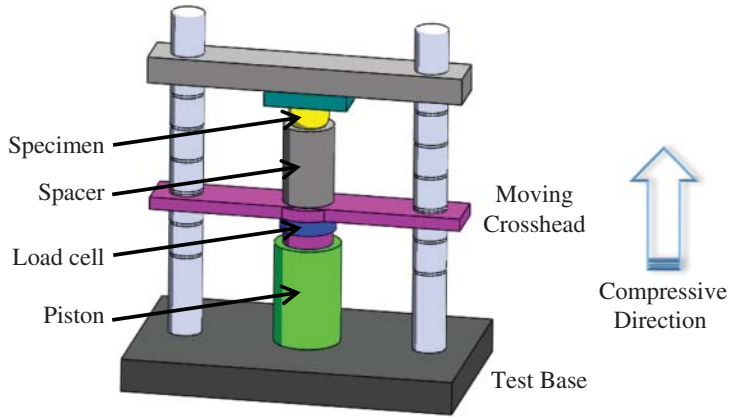
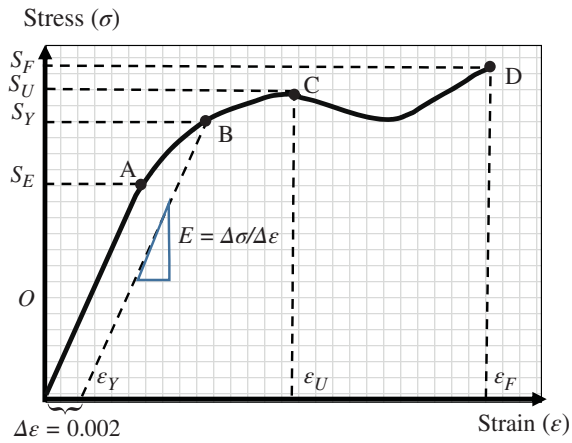


Figure 1.8 Schematic of compression testing.



(a) Stress-strain curve from compression test

Point *A*:	is the limit of elastic deformation
Point *B*:	is a reference point to determine the elastic modulus
Point *C*:	is the yield point
Point *D*:	is the point of fracture
E:	is elastic modulus
$\Delta\varepsilon = 0.002$:	is the offset strain to determine *E*
S_F, S_U, S_Y, and S_E:	are the stresses of fracture, ultimiate, yield, and elastic limit, respectively
ε_F, ε_U, and ε_Y:	are the strains of fracture, yield, and elastic limit, respectively

(b) Terminologies

Figure 1.9 Terminologies of stress-strain curve from compression test.

surface is calculated from the diameters of the impressed area and the sphere. Even with the uniaxial loading condition, the state of three-dimensional stress is developed in the specimen below the sphere. The Brinell hardness is calculated from the applied load (F) and the impression surface A_B of the spherical segment as,

$$HB = \frac{F}{g \cdot A_B} = \frac{0.102 \cdot F}{A_B} \tag{1.1}$$

where HB is the Brinell hardness, F is the applied load in Newton (N), A_B is the impression surface in mm^2, and $g = 9.81\ N/m^2$ is the gravitational acceleration to convert N into kgf.

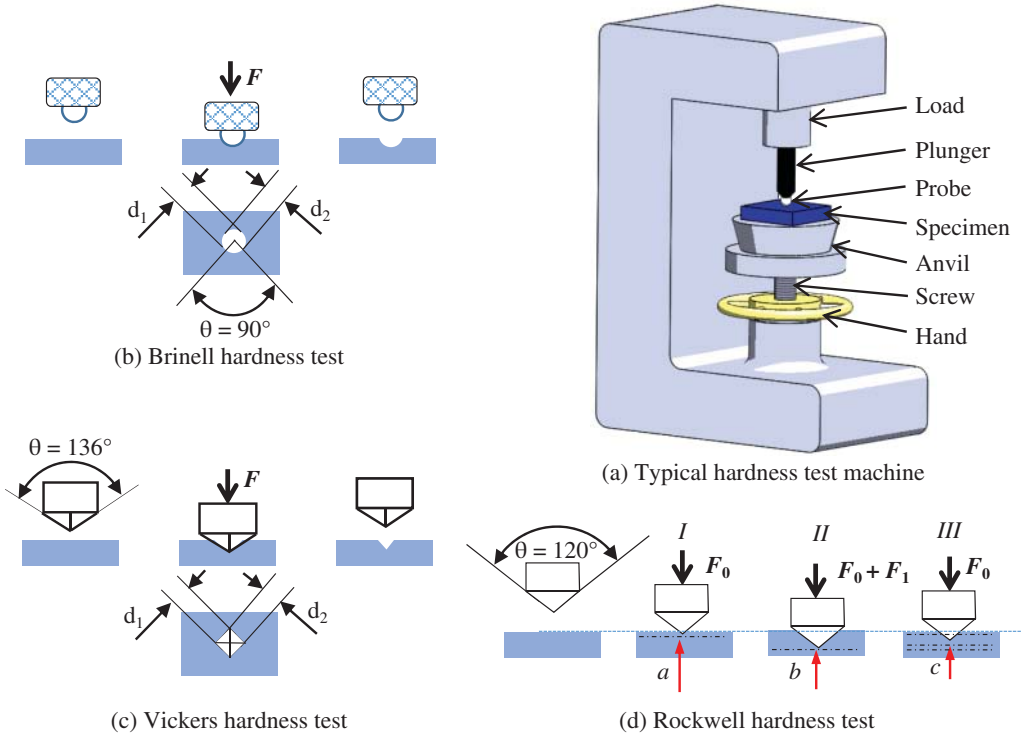


Figure 1.10 Schematic of hardness testing.

The setup of the Vickers hardness test is similar to the Brinell hardness test; while the main difference is the test body. A pyramid-shaped diamond is used as the test body in the Vickers test. The impression diagonal is determined by measuring and averaging two diagonals d_1 and d_2. The Vickers hardness is the ratio of the test load and impression surface as

$$HV = \frac{F}{g \cdot A_V} = \frac{0.102 \cdot F}{\frac{\bar{d}^2}{2 \cdot \sin^2\left(\frac{\theta}{2}\right)}} = \frac{0.204 \cdot \sin^2\left(\frac{\theta}{2}\right) \cdot F}{\bar{d}^2} \tag{1.2}$$

where HV is the Vickers hardness, F is the applied load in Newton (N), A_V is the impression surface in mm^2, $\bar{d} = \frac{d_1+d_2}{2}$ is the average diagonal distance in mm, and $\theta = 136°$ is the angle of the test body illustrated in Fig. 1.10.

In a Rockwell hardness test, the test body is a diamond cone with 120°, and the hardness is read out directly from the dial gauge. The hardness is calculated based on the measurement of the penetration depth in the specimen by the diamond cone. At phase I, a preload F_0 is applied to the test body, and the dial gauge is set to zero. At phase II, the test load is increased by F_1 and

sustained for a given duration, and the penetration depth is measured as b. At phase *III*, the test load is reduced back to F_0, and the penetration depth (c) is read again after the portion of elastic deformation is recovered. The hardness is determined based on the reading of the penetration depth (c) at phase *IV*.

1.4.3 Shear Tests

Machine elements such as screws, rivets, bolts, rivets, pins, and parallel keys are subjected to shear stresses. The shear strength determined in the shear test is important in the design of these elements; it is also useful to calculate the force required for shears and presses. Shear strengths can be measured on a shear test machine. In a shear test machine, the shear stresses are produced in the specimen by means of external shear forces until the specimen shears off. The shear strength can be determined by two different methods: the *single-shear* and the *double-shear* testing method.

Fig. 1.11 shows a setup for the application of the double-shear method. Two cross sections share the shear load, and the specimen is sheared off at these sections simultaneously. The shear strength (τ) can be simply determined by the shear force (F) divided by the total of shear areas ($2A$) when the shear fracture occurs.

Machine elements that are subjected to rotary movements are twisted. This twisting is referred to as *torsion*. The torsional stiffness is usually determined in the torsion test, which is applied for shafts, axles, wires, and springs to assess the torsional rigidity and strengths. Fig. 1.12*a* shows the setup of the torsional test: the specimen is clamped at one end and subjected to the load of a steadily increasing moment at the other end. The twisting moment causes shear stresses in the cross section of the specimen; an increase of shear stress leads to the increase of twisting and

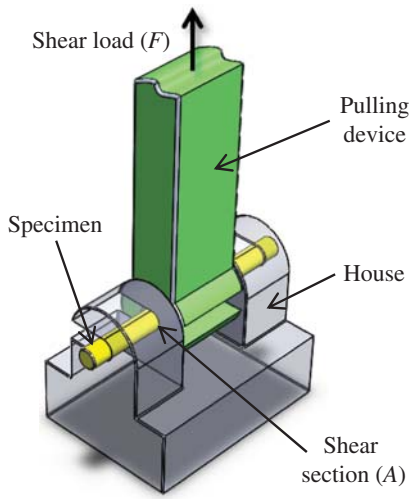


Figure 1.11 Schematic of hardness testing.

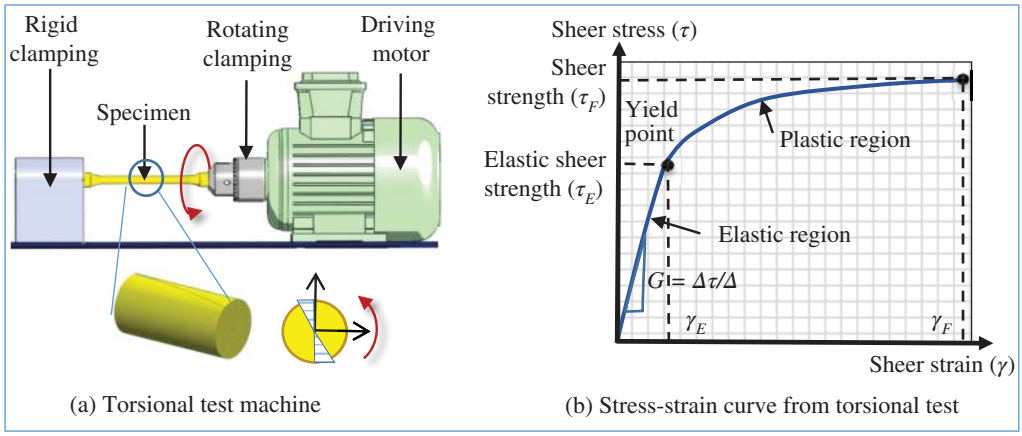


Figure 1.12 Schematic of torsional test.

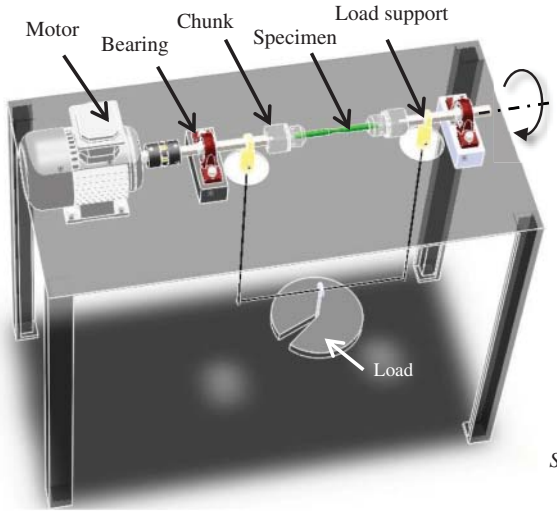
ultimately to shear fracture. Fig. 1.12*b* shows the characterized strengths from the torsional test including shear strength (τ_F), elastic shear strength (τ_E) , and the shear modulus (G).

1.4.4 Fatigue Tests

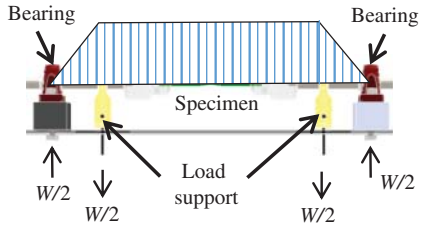
The prediction of a static failure is relatively easy in contrast to that of fatigue failure. A fatigue failure is caused by the accumulated damages from fluctuating loads. A fatigue failure is more dangerous since it is mostly invisible even before a complete fracture occurs.

A fatigue test is to determine the expected lifespan of a material subjected to a cyclic loading. The fatigue life of a material is measured as the total number of cycles that a material can survive under a fully cyclic load. If the number of cycles is specified, a fatigue test is also used to determine the maximum cyclic load that a sample can withstand for that number of cycles. All of these characteristics are extremely important to machine elements subject to fluctuating instead of steady loads.

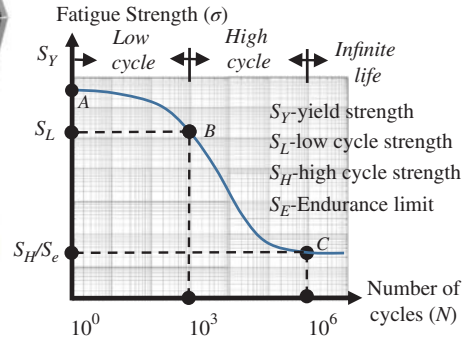
In performing a fatigue test, a specimen is loaded into a fatigue test machine, and a predetermined cyclic load is applied to cause the periodic change of stress state with a fully reversed amplitude at the area of interest. The cycle of positive and negative stresses is then repeated until the test goal is achieved. The test may be run to a predetermined number of cycles or until the sample has failed depending on the parameters of the test. Fig. 1.13*a* shows the setup of a fatigue test machine. The specimen is mounted on the shaft with an actuated rotation. The load is applied by a dead weight below the shaft, and the diagram of the bending moment on the specimen is illustrated in Fig. 1.13*b*. The bending movement causes the maximum tensile or compression stress on the surface of the specimen. Due to the continuous rotation, the state of stress at a specified location on the surface is fully reversed alternating stress (σ_a). Fig. 1.13*c* shows the result from a fatigue test is represented by an *S-N curve* for the relation of fatigue strength (S) and the number of cycles (N). The y-axis and x-axis in an S-N curve refer to the fatigue strength and the number of cycles, respectively. Special attention must be paid on the fatigue strength (S). A fatigue strength is not a constant; it is a function of the number cycles. For example, (1) if a designer is



(a) Fatigue test machine



(b) Bending moment over specimen



(c) Strength and number of cycles curve (SN curve)

Figure 1.13 Schematic of fatigue testing.

only interested in a static failure, i.e., a yield failure within one loading cycle; the yield strength S_y is the fatigue strength for 10^0; (2) if the maximum stress for a low number of cycles (10^3) is concerned, the fatigue strength is S_L; (3) if the maximum stress for a high number of cycles (10^6) is concerned, the fatigue strength is S_H. For traditional metals, if the fatigue strength is low enough to allow the material to survive for more than 10^6 cycles, such a fatigue strength is called as *endurance limit* (S_e), and an alternative stress (σ_a) whose amplitude is smaller than S_e corresponds to an *infinite fatigue life* ($> 10^6$) of the material.

The fatigue strength can be defined for the stresses subjected to different loading conditions. Fig. 1.14 shows three different loading conditions where the fatigue strengths are associated to *axial loads*, *bending loads*, and *torsional loads*, respectively.



(a) Specimen for fatigue test under tensile and compression load



(b) Specimen for fatigue test under alternative bending load



(c) Specimen for fatigue test under rotating bending load

Figure 1.14 Other fatigue tests subjected to different loading conditions.

1.4.5 Impact Tests

An impact test is suitable primarily for determining the cleavage fracture tendency or toughness property of a material. It does not provide any value of material characteristics. It does define a *notched-bar impact strength*; but this quantity does not fit directly into the calculation of material strengths. The notched-bar impact strength is helpful to select a material for a specific task where the deformation is an important criterion for the material selection. An impact test identifies quickly whether a material is brittle or tough. Note that the brittleness depends on not only the material properties, but also some external conditions, such as temperature and stress levels. Three commonly used impact tests are *Charpy tests*, *Izod tests*, and *Dynstat tests*.

Fig. 1.15 shows a typical setup of an impact tester; the key instrumentation is a pendulum hammer for an application of an impact load. In testing, the hammer falls down from a maximum height. At its lowest point, the hammer strikes the rear of a notched specimen. If the abutment penetrates or passes through the specimen, the hammer dissipates its impact energy to the specimen. The residual energy of the hammer is reduced when swinging through the lowest possible point (zero point) and the hammer decelerates. When the hammer swings through the zero point, the trailing pointer is dragged along and the applied work for the notched-bar impact is calculated and displayed on a scale. The shape of the notched-bar specimen is standardized. The notched-bar impact strength is determined from the height difference of the hammers, and the impact strength

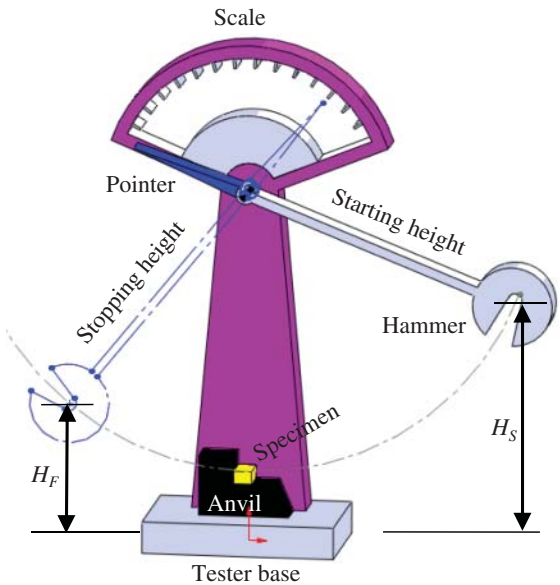


Figure 1.15 Schematic of toughness testing.

is the measure of the brittleness of the material. In the Charpy test, the test body is mounted on two sides and a pendulum strikes the center of the test body at the height of the notch. In the Izod and Dynstat tests, the test body is upright and a pendulum strikes the free end of the test body above the notch.

1.5 STATIC AND FATIGUE FAILURES

A material has its limits to carry the loads in its applications. The material may fail in different ways depending on the material characteristics and load types. Fig. 1.16 shows six main types of static failures: *yielding*, *ductile fracture*, *brittle fracture*, *shearing*, *torsional failure*, and *buckling*.

Other than static failures, any material exposes the risk of a fatigue failure. For a fatigue failure, the load exerted on an object may be small and even far below the strength of materials. The repetition of such a load might cause the fatigue failure of materials. Fatigue failures tend to be very dangerous and catastrophic. For examples, among the list of the aircraft structural failures by Wikipedia (2018) in Table 1.3, severe accidents are mostly caused by fatigues. A few of other examples of aircraft accidents caused by fatigue failures from literatures are shown in Fig. 1.17.



(a) Yielding (b) Ductile fracture (c) Brittle fracture

(d) Shearing (e) Torsional failure (f) Buckling

Figure 1.16 Six main types of materials failures.

TABLE 1.3 Some Fatigue Failures of Aircrafts (Wikipedia 2018)

Date	Accident	Cause	Fatalities	Notes
July 23, 1930	Meopham air disaster	Metal fatigue	6	The tail-plane Junkers F.13 was weakened by turbulence.
April 14, 1976	Yacimientos Petroliferos Fiscales	Metal fatigue	34	The starboard wing of the Hawker Siddeley 748 was failed outboard of engine
June 26, 1978	Helikopter Service Flight 165	Fatigue	18	The rotor blade of Sikorsky s-61 was loosened after fatigue to the knuckle joint.
October 04, 1992	EI AI Flight 1862	Corrosion in pylon fuse pin leading to metal fatigue	43	Engine 3 on Boeing 747 was broke off and knocked off engine No.4, which ripped of slats.
June 26, 1997	Helikopter Service Flight 451	Fatigue	12	The accident was caused by a fatigue crack in the spline of the Eurocopter AS 332L1. It caused the power transmission shaft to fail.
May 25, 2002	China Airlines Flight 611	Metal fatigue	225	The tail of the Boeing 747 strike led to faulty repair and the tail section was broke off and caused the aircraft to disintegrate.



(a) Southwest Airlines Accident (Durden 2018)



(b) Water bombing plane crash (McLaren 2016)



(c) Ripped off of an Aloha Airlines 737 (Drew and Mouawad 2011)



(d) Fatigue cracking of FedEx MD-10-10F (Carey 2016)



(e) The crashed Super Puma helicopter in Norway (Crisan 2016)



(f) Loss of outer CH54A main rotor (Safarian 2014)

Figure 1.17 Examples of aircraft fatigue failures.

1.6 UNCERTAINTIES, SAFETY FACTORS, AND PROBABILITIES

The materials with impurities show the variants and uncertainties of properties, and the loads applied on object involved in certain variants. Common uncertainties in a mechanical structure are (1) the uneven distribution of ingredients in the materials, such as the particles randomly distributed in composites (Fig. 1.18), (2) the effects of material processing on the properties, such as residual stresses from heat treatment or material removal processes; (3) the intensity and distribution of loading; (3) the assumptions of structural analysis models; (4) the environmental and time factors on material strengths and geometry; and (5) the effect of corrosion or wear and so on. All of these uncertainties raise the difficulties to obtain accurate values of the strengths and stresses of the materials. In design practice, uncertainties are tackled by *the deterministic method* using safety factors or *the stochastic method* using probabilities.

In a deterministic method, the safety factor is determined at the worst case; where the maximized possible load is applied on the materials with the lowest loss of function capability,

$$(n_d) = \frac{V_{\text{min, loss of function}}}{V_{\text{max, load}}} > 1 \tag{1.3}$$

where n_d is the safety factor at the worst case, $V_{\text{min, loss of function}}$ is the minimum value of a material property leading to a function loss, and $V_{\text{max, load}}$ is the maximum allowable load on object.

Alternatively, if the safety factor $n'_d = \frac{V_{\text{nominal, loss of function}}}{V_{\text{nominal, load}}}$ is defined as a ratio of nominal value $V_{\text{nominal, loss of function}}$ of the material properties and external load $V_{\text{nominal, load}}$, the allowable nominal external load can be defined by

$$V_{\text{nominal, load}} = \frac{V_{\text{nominal, loss of function}}}{n'_d} \tag{1.4}$$



Figure 1.18 Appearances of impurities in composites.

Example 1.1 Safety Factor The external load on a structure is known with an uncertainty of ±10%, and the load causing the failure of material is known within ±20%. (1) Use the deterministic method to specify the minimal safety factor to ensure the safety. (2) If a nominal load to cause the material failure is 5000 lbf, determine the allowable external load.

SOLUTION

(1) Let the nominal values of external load and the load for loss of function of materials be $V_{\text{nominal, load}}$ and $V_{\text{nominal, loss of function}}$, respectively. The uncertainty ±10% of the load leads to the range of load variants as $(0.9, 1.1) * V_{\text{norminal, load}}$, and the uncertainty ±20% of load for loss of function of materials leads to the range of its variants as $(0.8, 1.2) * V_{\text{nominal, loss of function}}$. At the worst case, $V_{\text{max, load}} = 1.1V_{\text{nominal, load}}$ and $V_{\text{min, loss of function}} = 0.8V_{\text{nominal, load}}$. Using Eq. (4.1) gets,

$$n_d = \frac{V_{\text{min, loss of function}}}{V_{\text{max, load}}} = (0.73)\frac{V_{\text{nominal, loss of function}}}{V_{\text{nominal, load}}}$$

Therefore, to ensure the safety at the worst case, the safety factor is $n'_d = \frac{V_{\text{nominal, loss of function}}}{V_{\text{nominal, load}}} > \frac{1}{0.73} = 1.38$.

The other method to deal with uncertainties is the stochastic method where the distribution of strengths and stress in materials are taken into consideration. In the stochastic method, *reliability* (R) refers to a statistical measure of the probability of the case where the materials will not fail, and *probability* (P_f) refers to the statistical measure of the probability of the case where the materials will fail. Note that R and P_f are not independent; their relations can be found as,

$$R = 1 - P_f \tag{1.5}$$

A statistical distribution of strength or stress can be described by a probability density function $f(x)$, and reliability can be calculated from the probability density function, which gives the

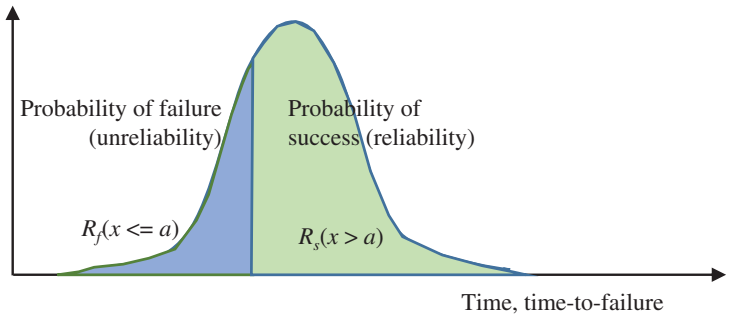


Figure 1.19 Examples of aircraft fatigue failures.

probability of an event occurring for a certain amount of time. Every reliability value has an associated time value. Thus, a time range must be specified when the reliability is evaluated based on a probability density function,

$$R(a \leq x \leq b) = \int_a^b f(x)\,dx \tag{1.6}$$

As shown in Fig. 1.19, the reliability corresponds to a system measure to perform and maintain the expected safe state of materials in normal, hostile, or uncertain application circumstances.

1.7 STRESS ANALYSIS OF MECHANICAL STRUCTURES

In engineering design, *stress analysis* is used to determine the distribution of stresses and identify critical features and locations with the highest possibility of failure. The ultimate goal of stress analysis is to ensure that the design of a structure and artifact can withstand a specified load with a given lifespan, using the minimum amount of material and satisfying other optimal criteria. Stress analysis may be performed through *classical mathematical techniques*, *analytic mathematical modeling*, *computational simulation*, *experimental testing*, or a combination of methods.

1.7.1 Procedure of Stress Analysis

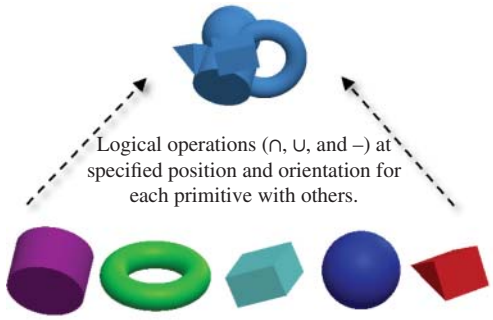
The procedure of stress analysis includes the following critical steps:

(1) Isolate objects one by one from the system, clarify the functions of every object in terms of external loads, boundary conditions and constraints,
(2) Develop the model of objects for the relations of stress distribution and exerted loads,
(3) Identify critical features and locations with the maximum stresses,
(4) Evaluate the safety of materials by comparing stresses and strengths of materials, and
(5) Optimize the design and the dimensions iteratively until all of the design constraints are met and system performances reach their optimums.

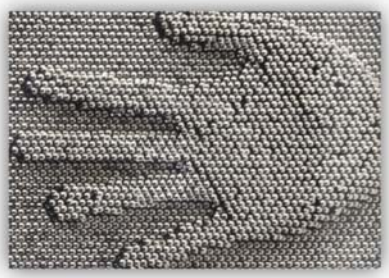
Before the stress analysis, the first step is to model and represent the geometry of objects appropriately.

1.7.2 Geometric Discontinuities of Solids

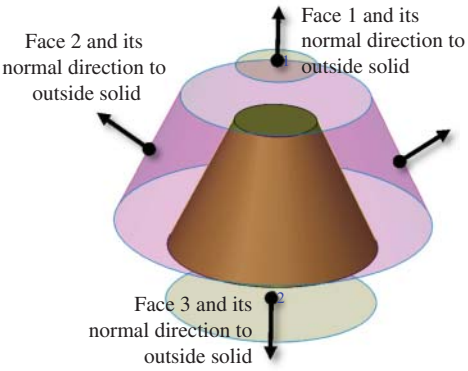
A machine element corresponds to a solid object, which has its geometry and shape with a fine volume. As shown in Figure 1.20, three common methods to represent a solid object are *constructive solid geometry* (CSG), *surface modeling*, and *spatial decomposition*. In CSG modeling, a solid volume is modelled as an assembly of primitive solids, such as cones, cylinders, and spheres. In surface modeling, a finite volume is confined by a number of boundary surfaces, and



(a) Constructive solid geometry (CSG)



(c) Spatial decomposition

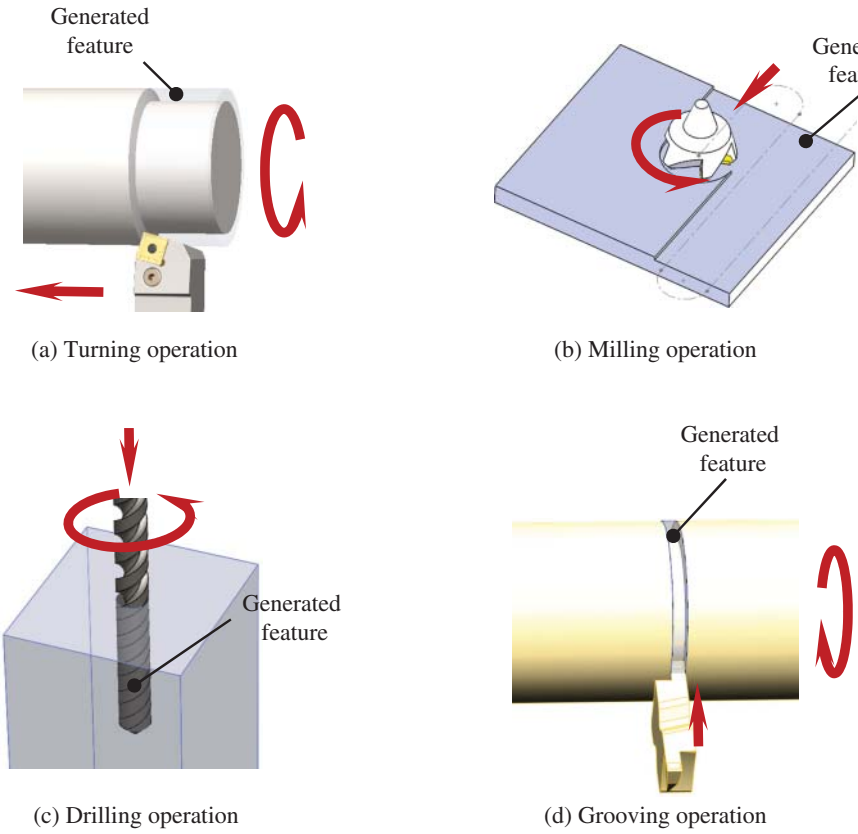


(b) Surface modeling

Figure 1.20 Three fundamental methods for solid modeling.

the direction of the normal of any position on a boundary surface specifies the inside and outside of solid. In spatial decomposition, the bounded finite volume is decomposed into multilevel cells; the state of each cell is defined as (1) "*true*" if it is completely within the solid, (2) "*false*" if it is fully beyond the solid, and (3) "*partially true*" if part of a cell is within the solid. For the state of partially true, the cell will be further decomposed until the required accuracy for the cell size is achieved.

By comparing these three modeling methods, CSG is mostly used to model products, especially for the products made from conventional machining processes. A machining process generates a primitive feature on solids. Fig. 1.21 shows a few examples of the machining processes. A turning operation in Fig. 1.21*a* generates a *revolve* feature whose dimensions are given by the feed depth and the relative position of tooling and the main motion axis. A milling operation in Fig. 1.21*b* generates an *extrusion* or *sweep* feature whose dimensions are given by geometry and path of the milling tool. The drilling operation in Fig. 1.21*c* generates an *extrusion cut* feature whose dimensions are given by the size and feed depth of the drill bit. The grooving operation in Fig. 1.21*d* generates a *revolve* feature whose dimensions are given by the tool width and the feeding distance. One machining operation generates a feature on solid object, and a sequence of machining operations generate a part with multiple features. The number of machining operations or features determines the complexity of a part.



(a) Turning operation (b) Milling operation

(c) Drilling operation (d) Grooving operation

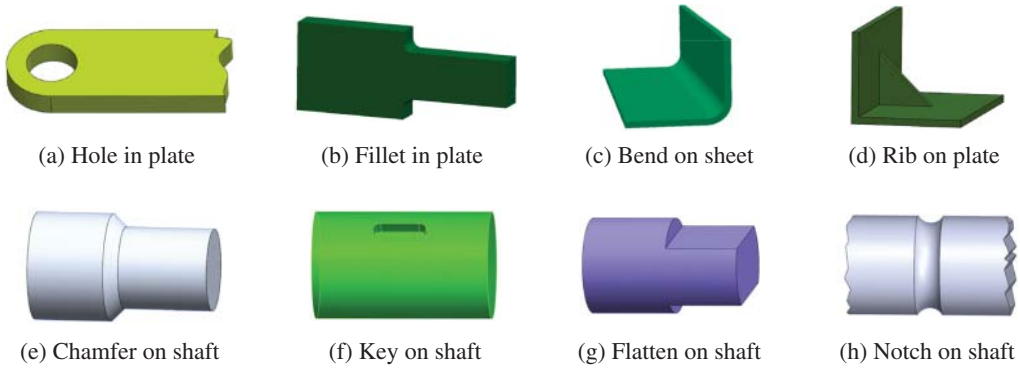
Figure 1.21 Basic features of a solid object from material removal processes.

To ensure the safe design of a product, finding the feature of a solid that shows the greatest weakness is an effective way to determine allowable loads at the critical loading condition. This is because the overall strength of object is determined by the strength at its weakest feature.

A feature with the weakest strength is always associated a geometric discontinuity of object. Fig. 1.22 shows some common geometric discontinuities over machined components. *Holes*, *fillets*, *ribs*, *bends*, *chamfers*, *keys*, *flattens*, and *notches* are all geometric discontinuities that have a discontinuity of the first-order, the second-order, or the third-order or higher of the derivative(s) of the surface model. In this book, we will discuss how these geometric discontinuities affect stress distributions on solids subjected to various loads.

1.7.3 Load Types

The response of a feature of a solid to a load differs from one load type to another. In identifying a feature with the greatest weakness, load types must be taken into consideration. In actual applications, the characteristic of loads can be very intrigue and dynamic. However, the safety design



(a) Hole in plate (b) Fillet in plate (c) Bend on sheet (d) Rib on plate

(e) Chamfer on shaft (f) Key on shaft (g) Flatten on shaft (h) Notch on shaft

Figure 1.22 Common features of geometric discontinuities.

criteria are proposed by a comparison of the stresses on an object and the strengths of materials, and materials' strengths are obtained from the standardized tests, which have been extensively discussed in Section 1.4. Therefore, it makes sense to simplify the classification of load types by corresponding the loading conditions in some commonly used and standardized tests over materials. This makes the calculated stress in an application and the strength of materials from the standardized tests more suitable for a comparison.

Fig. 1.23 shows the classification of the loads. From the perspective of *time dependence*, a load can be *static*, *sustained*, *impact*, and *cyclic*. A static load is constant along with time, a sustained load remains constant for a given period, an impact load occurs suddenly in a very short period of time, and a cyclic load varies periodically with time. From the perspective of the *load distribution*, a load can be *concentrated* at one place, or *distributed* over a boundary line or surface; a load can also be *volumetric* over the solid. From the perspective of *force characteristics*, loads can be classified as *normal load*, *shear load*, *bending load*, and *torsion load* for different types of stresses. In engineering practices, the aforementioned load types can be mixed and combined to represent complex loading conditions in various applications.

1.7.4 Stress and Representation

In structural analysis, *stress* is a physical quantity for the representation of internal forces over a unit area exerted by neighboring material particles. For example, when a beam is holding a weight, the material at any position of a cross section is pulled by the material particles next to the given position, and the stress at a certain position is quantified by the pulling force over a unit area. As shown in Fig. 1.24, corresponding to the load types in Fig. 1.23, the stresses can be classified into *tensile stress*, *compression stress*, *shear stress*, *bending stress*, *torsional stress*, and *fluctuated stress*.

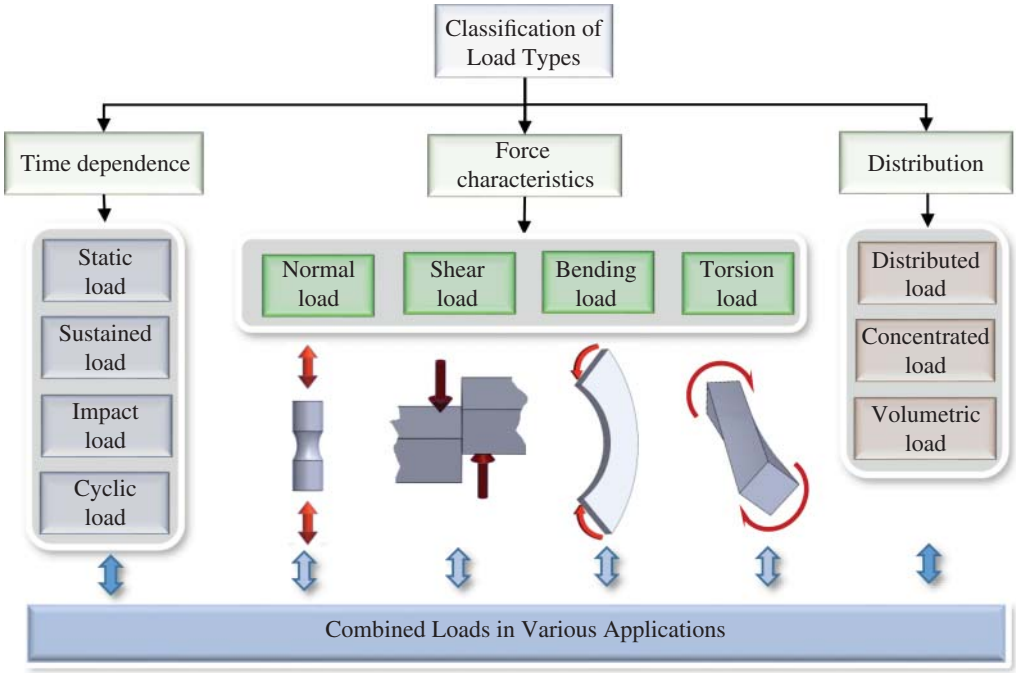


Figure 1.23 Classification of load types.

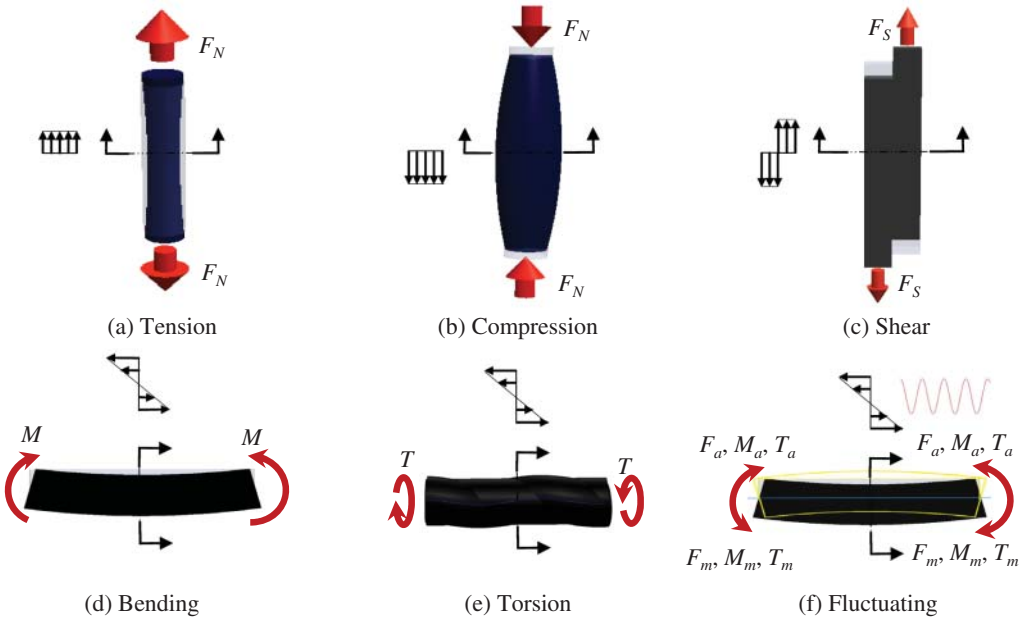


Figure 1.24 Stress types corresponding to different types of loads.

1.7.4.1 Simple Stress A *simple stress* means that the stress state can be simply defined by a scalar value while the direction of stress is known. A simple stress is commonly used in three scenarios, the *uniaxial normal stress* case in Fig. 1.24*a*, the *uniform shear stress case* in Fig. 1.24*c*, and the *isotropic normal stress case* where the level of stress/pressure is the same along any direction. Taking an example of liquid or gas at rest in a container, an infinite small cube ensures the same level of stress in any direction. Such a stress is also called as *isotropic normal*. A simple stress can be calculated from the net force and the effective area of stress as

$$\sigma = \frac{F_N}{A}; \quad \tau = \frac{F_S}{A} \tag{1.7}$$

where σ and τ are normal and shear stress, and F_N and F_s are normal and shear forces, and A is the effective area of stress.

A *cylinder stress* shows its simplicity with rotational symmetry, which commonly occurs to some machine elements, such as wheels, axles, pipes, and pillars. Often the stress patterns that occur in such parts have rotational or even cylindrical symmetry. Cylinder stresses are distributed axis symmetrically; this reduces the dimension or domain for stress analysis in solids.

1.7.4.2 General Stresses If an effective area to endure the load is given, any stress can be fully represented by a vector for its direction and magnitude. However, the reference coordinate system affects the representation of a stress vector. In addition, when the stress state is evaluated, it should be flexible to evaluate a stress component by specifying an effective area at any direction. The *Cauchy stress tensor* is widely used to represent the stress state of a point. The Cauchy stress tensor can be transformed to evaluate the stress components along any direction for the given point, including the directions for principle normal stresses or shear stresses. A Cauchy stress tensor is a second-order tensor named after Augustin-Louis Cauchy. The tensor consists of six independent components that completely define the state of stress at a point inside a material with respect to a given reference coordinate system $\{O\text{-}XYZ\}$. Note that the Cauchy stress depends on the reference coordinate system. Fig. 1.25 gives its graphical representation of nine stress components in the reference coordinate system. Accordingly, the vector tensor is expressed as

$$\boldsymbol{\sigma} = \begin{bmatrix} \sigma_x & \tau_{xy} & \tau_{xz} \\ \tau_{yx} & \sigma_y & \tau_{yz} \\ \tau_{zx} & \tau_{zy} & \sigma_z \end{bmatrix} \tag{1.8}$$

where is the $\boldsymbol{\sigma}$ Cauchy stress tensor, σ_x, σ_y, and σ_z are normal stresses along axis-X, axis-Y, and axis-Z, respectively. τ_{ij} $(i, j = x, y, z;\ i \neq j)$ is the shear stress along axis-j over a plane which is perpendicular to axis-i. In addition, one has $\tau_{ij} = \tau_{ji}$.

Once the second-order tensor $\boldsymbol{\sigma}$ is known, the first-order tensor $\boldsymbol{T}^{(\boldsymbol{n})}$ on an imaginary surface perpendicular to a unit-length direction vector $\boldsymbol{n}$ can be found as

$$\boldsymbol{T}^{(\boldsymbol{n})} = \boldsymbol{\sigma} \cdot \boldsymbol{n} \tag{1.9}$$

where $\boldsymbol{n}$ is a unit-length vector, which is normal to the imaginary surface.

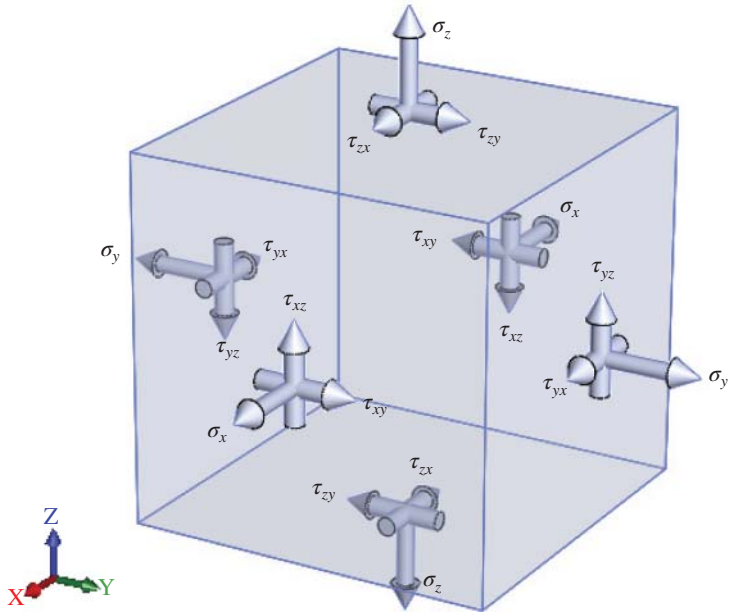


Figure 1.25 Stress equilibrium at an infinitesimal volume.

1.7.4.3 Principal Stresses and Directions A material failure is always initialized at the weakest position and direction where the stress is at its extreme in contrast to the material strength. Therefore, the Cauchy stress tensor must be converted, so that the principal stresses and the associated principal directions can be determined. The vector of principal stresses λ must be aligned with the normal unit vector $\boldsymbol{n}^p$,

$$\boldsymbol{T}^{(\boldsymbol{n}^p)} = \lambda \cdot \boldsymbol{n}^p = \boldsymbol{\sigma} \cdot \boldsymbol{n}^p \quad \text{or } (\boldsymbol{\sigma} - \lambda) \cdot \boldsymbol{n}^p = \boldsymbol{0} \tag{1.10}$$

Eqs. (1.9) and (1.10) give the conditions of a principle stress as

$$\begin{vmatrix} \sigma_x - \lambda & \tau_{xy} & \tau_{xz} \\ \tau_{yx} & \sigma_y - \lambda & \tau_{yz} \\ \tau_{zx} & \tau_{zy} & \sigma_z - \lambda \end{vmatrix} = -\lambda^3 + I_1\lambda^2 - I_2\lambda + I_3 = 0 \tag{1.11}$$

where

$$\left.\begin{aligned} I_1 &= tr(\boldsymbol{\sigma}) = \sigma_x + \sigma_y + \sigma_z \\ I_2 &= \sigma_x \cdot \sigma_y + \sigma_y \cdot \sigma_z + \sigma_x \cdot \sigma_z - \tau_{xy}^2 - \tau_{yz}^2 - \tau_{xz}^2 \\ I_3 &= \sigma_x \cdot \sigma_y \cdot \sigma_z + 2\tau_{xy} \cdot \tau_{yz} \cdot \tau_{xz} - \tau_{xy}^2 \cdot \sigma_z - \tau_{yz}^2 \cdot \sigma_x - \tau_{xz}^2 \cdot \sigma_y \end{aligned}\right\}$$

The principal stresses are the eigenvalues of Eq. (1.11). These principal stresses are unique when the stress tensor (Eq. (1.8)) is given. In other words, for whatever the reference coordinate

system {*O-XYZ*} one chooses, the solutions to Eq. (1.11) are the same. Therefore, the coefficients I_1, I_2, and I_3 in Eq. (1.11) are invariants, and they are commonly referred as *the first*, *second*, and *third stress invariants*, respectively.

Due to the symmetry of the Cauchy stress, the characteristic equation, Eq. (1.11), has three real roots λ_i $(i = 1, 2, 3)$. After three principal stresses λ_i are calculated from the characteristic equation, the maximized and minimized stresses over the principal stress directions can be found as

$$\left.\begin{aligned} \sigma_1 &= \max(\lambda_1, \lambda_2, \lambda_3) \\ \sigma_3 &= \min(\lambda_1, \lambda_2, \lambda_3) \\ \sigma_2 &= I_1 - \sigma_1 - \sigma_3 \end{aligned}\right\} \tag{1.12}$$

where σ_1 and σ_3 are the maximized and minimized stresses, respectively.

By substituting each eigenvalue $\lambda_i (i = 1, 2, 3)$ back into Eq. (1.10) respectively, a nontrivial solution of $\boldsymbol{n}_i^p$ $(i = 1, 2, 3)$ can be found. These solutions are called the *eigenvectors* of the characteristic function of Eq. (1.11. They are the principal directions associated with principal stresses, and they define the planes where the principal stresses locate. Different from the Cauchy stress, the principal stresses and principal directions are dependent only on the stress state at a point, and it is independent of the coordinate system used to determine the Cauchy stress.

A coordinate system with three principal directions $(i = 1, 2, 3)$ as the axes is called as a *principal coordinate system*. In the principal coordinate system, the Cauchy stress can be converted into a diagonal matrix as

$$\boldsymbol{\sigma}^p = \begin{bmatrix} \sigma_1 & 0 & 0 \\ 0 & \sigma_2 & 0 \\ 0 & 0 & \sigma_3 \end{bmatrix} \tag{1.13}$$

where

$$\left.\begin{aligned} I_1 &= \sigma_1 + \sigma_2 + \sigma_3 \\ I_2 &= \sigma_1 \cdot \sigma_2 + \sigma_2 \cdot \sigma_3 + \sigma_1 \cdot \sigma_3 \\ I_3 &= \sigma_1 \cdot \sigma_2 \cdot \sigma_3 \end{aligned}\right\}$$

Due to the simplicity, the *principal coordinate system* is often calculated when the stress state of a point of interest has to be analyzed.

Some design criteria are developed based on principle shear stresses instead of principle normal stresses. For example, the failures of ductile material are mostly associated with shear stresses. Note that principle normal stresses and shear stresses are dependent; one has to know how to convert from one to the other. As shown in Fig. 1.26 for the Mohr's circle, the maximum shear stress (τ_{max}) can be determined based on the principal stressed $(\sigma_1, \sigma_2, \sigma_3)$ in Eq. (1.13).

The *maximum shear stress*, or principal shear stress, is equal to one-half the difference between the largest and smallest principal stresses. It acts on a bisected plane between the directions of the largest and smallest stresses. The plane for the principal shear stress is oriented 45° from the principal stress planes.

$$\tau_{max} = \frac{1}{2} \left| \sigma_1 - \sigma_3 \right| \tag{1.14}$$

where the principal stress $\sigma_1 > \sigma_2 > \sigma_3$

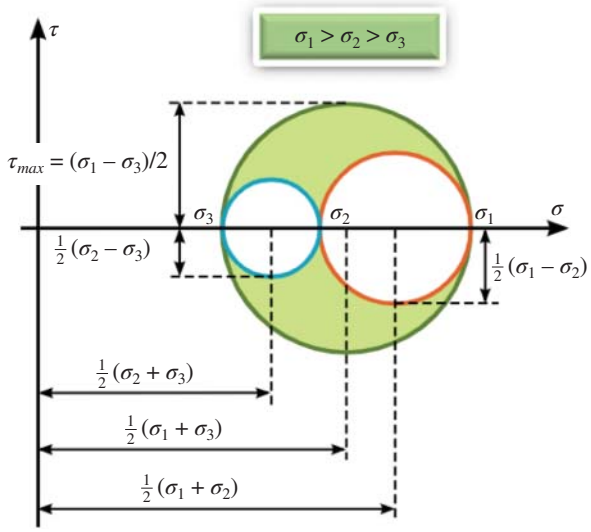


Figure 1.26 Mohr's circle for a three-dimensional stress state (Wikipedia 2018).

Eqs. (1.13) and (1.14) show that a three-dimensional stress state can be simplified and applied to two-dimensional stress states shown in Fig. 1.27. A two-dimensional stress state has three independent components, i.e., σ_x, σ_y, and τ_{xy}. Accordingly, the Mohr's circle for the relations of a two-dimensional stress state can be simplified and shown in Fig. 1.28. The principal stress in a

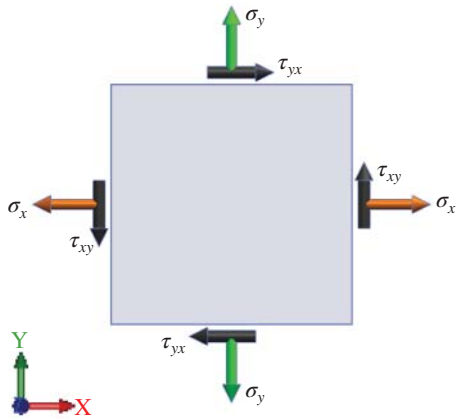


Figure 1.27 Two-dimensional stress equilibrium at an infinitesimal volume.

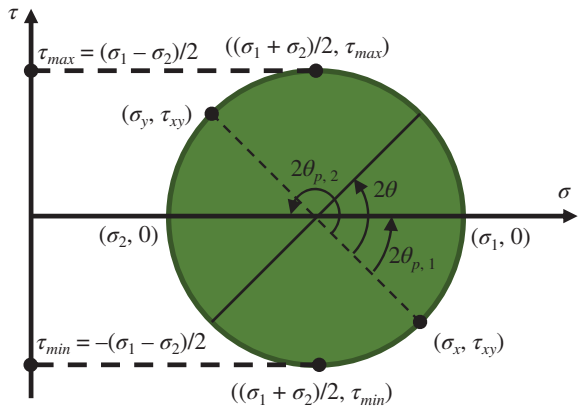


Figure 1.28 Mohr's circle for a two-dimensional stress state.

two-dimensional stress state can be found as

$$\sigma_{1,2} = \frac{\sigma_x + \sigma_y}{2} \pm \sqrt{\left(\frac{\sigma_x - \sigma_y}{2}\right)^2 + \tau_{xy}^2} \tag{1.15}$$

$$\tau_{max,min} = \pm\sqrt{\left(\frac{\sigma_x - \sigma_y}{2}\right)^2 + \tau_{xy}^2} \tag{1.16}$$

1.8 FAILURE CRITERIA OF MATERIALS

Safety is the primary functional requirement for product design. Such a functional requirement can be defined by *design criteria* or *design rules*. For safety design, a *failure criterion* is a rule or formula of failure of certain stresses or combinations of stresses in comparison with the tensile yield or ultimate strength.

In machine design, a number of the failure criteria have been proposed. One failure criterion may fit well in a certain situation, but it may not be applicable to other situations. The selection of suitable failure criteria is crucial to machine designs. The criteria of static failures subjected to static loads are discussed here, and the criteria of fatigue failures subjected to cyclic loads will be covered in Chapter 6. Fig. 1.29 provides a list of commonly used failure criteria for brittle and ductile materials, respectively. The details of these failure criteria/theories are discussed as follows.

1.8.1 Maximum Shear Stress (MSS) Theory

The maximum shear stress (MSS) *theory* states that a failure occurs when the maximum shear stress from a combination of principal stresses equals or exceeds the value obtained from the shear stress at yielding in the uniaxial tensile test.

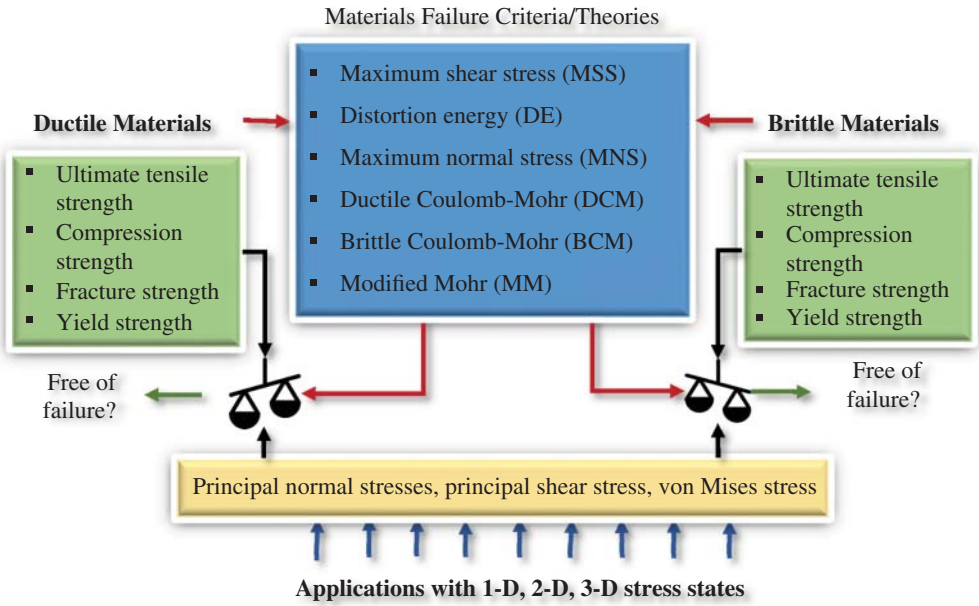


Figure 1.29 Commonly used failure theories for static loads.

In an uniaxial test, a yielding corresponds to the stress state of $\sigma_1 = S_y$, and $\sigma_2 = \sigma_3 = 0$. Therefore, the shear strength of the material is

$$S_{sy} = \frac{\sigma_1 - \sigma_3}{2} = \frac{S_y}{2} \tag{1.17}$$

where S_{sy} and S_y are shear strength and yielding strength of the material, respectively.

To apply the MSS theory, the principal stresses ($\sigma_1 \geq \sigma_2 \geq \sigma_3$) at a point are calculated and ordered, and then, the maximum shear stress τ_{max} is found as

$$\tau_{max} = \frac{\sigma_1 - \sigma_3}{2} \tag{1.18}$$

The criterion of the MSS failure is expressed as

$$\tau_{max} = \frac{\sigma_1 - \sigma_3}{2} \leq S_{sy} \quad \text{or} \quad \sigma_1 - \sigma_3 \leq S_y \tag{1.19}$$

The safety factor of the MSS theory is given as

$$N = \frac{S_{sy}}{\tau_{max}} \quad \text{or} \quad N = \frac{S_y}{\sigma_3 - \sigma_1} \tag{1.20}$$

1.8.2 Distortion Energy (DE) Theory

The *distortion energy (DE) theory* is also called the *von Mises-Hencky Theory*. It is inspired by an observation that a solid can withstand a large hydrostatic pressure without a failure. Since no distortion occurs to a solid under a uniform pressure, it is then assumed that the failure of material is related to the distortion energy. A material has a definite limited capacity to withstand the distortion energy, and such a capacity can be quantified in a standardized tensile test.

The DE theory states that a yield failure occurs when the total distortion energy from a combination of principal stresses equals or exceeds the amount of distortion energy of the material in the uniaxial tensile test when the yield strength is reached. As shown in Fig. 1.30, the strain energy U is calculated based on the history of stress σ and strain τ occurring to the material.

$$U = \frac{\sigma\varepsilon}{2} \tag{1.21}$$

For a three-dimensional stress state, Eq. (1.21) can be extended for a strain energy of a three-dimensional stress state $(\sigma_1, \sigma_2, \sigma_3)$ as

$$U = \frac{\sigma_1\varepsilon_1 + \sigma_2\varepsilon_2 + \sigma_3\varepsilon_3}{2} \tag{1.22}$$

where the principal strains ε_1, ε_2, and ε_3 are along the directions of $(\sigma_1, \sigma_2, \sigma_3)$, respectively.

The principal strains and stresses have dependent constitutive equations as

$$\left.\begin{aligned} \varepsilon_1 &= \tfrac{1}{E}\left(\sigma_1 - v\,(\sigma_2 + \sigma_3)\right) \\ \varepsilon_2 &= \tfrac{1}{E}\left(\sigma_2 - v\,(\sigma_1 + \sigma_3)\right) \\ \varepsilon_3 &= \tfrac{1}{E}\left(\sigma_3 - v\,(\sigma_1 + \sigma_2)\right) \end{aligned}\right\} \tag{1.23}$$

Substituting Eq. (1.23 into Eq. (1.22) results in the strain energy of three-dimensional stress state as

$$U = \frac{1}{2E}\left(\sigma_1^2 + \sigma_2^2 + \sigma_3^2 - 2v(\sigma_1\sigma_2 + \sigma_2\sigma_3 + \sigma_1\sigma_3)\right) \tag{1.24}$$

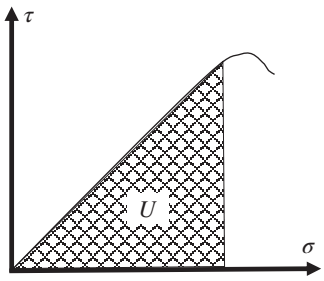


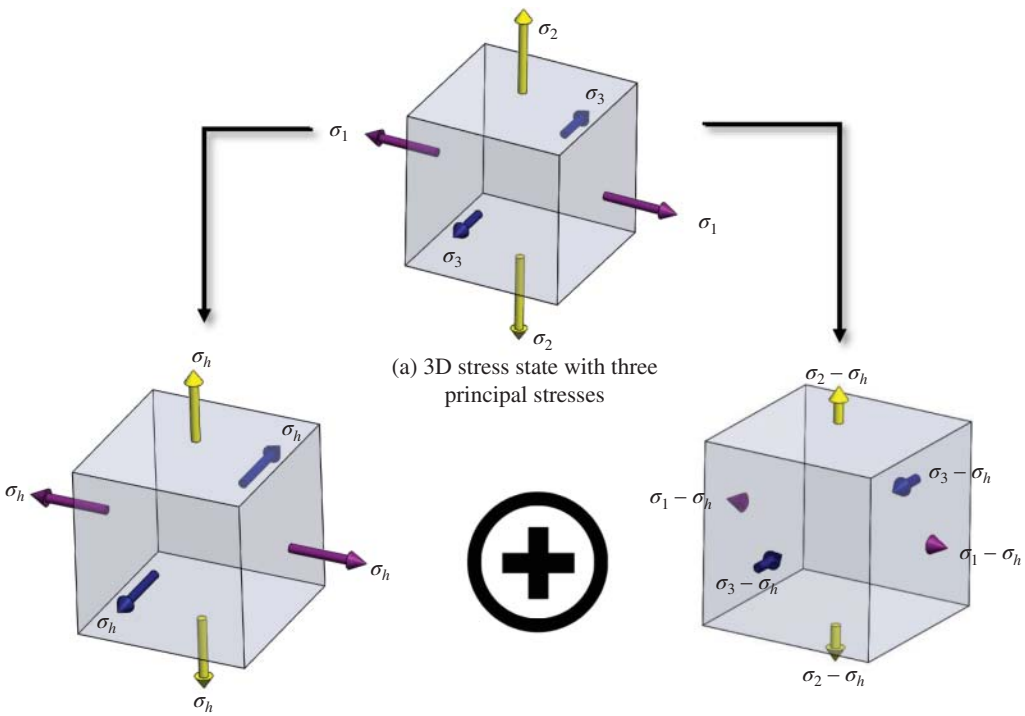
Figure 1.30 Deformed energy U from stress σ and τ.

We want to separate the distortion strain energy from the total strain energy in Eq. (1.24). This can be done by dividing the stress components into the groups of *hydro stresses* and *distortion stresses*, and evaluating the corresponding strain energy respectively. Fig. 1.31 shows such a decomposition where the hydro stresses (σ_h) and distortion stresses ($\sigma_{d,i}$ $i = 1, 2, 3$) along principal stress directions are calculated as

$$\left.\begin{aligned} \sigma_h &= \frac{\sigma_1 + \sigma_2 + \sigma_3}{3} \\ \sigma_{d,i} &= \sigma_i - \sigma_h \text{ where } i = 1, 2, 3 \end{aligned}\right\} \tag{1.25}$$

For the state of hydro stresses ($\sigma_h, \sigma_h, \sigma_h$), using Eq. (1.25) and Eq. (1.24) gives the hydro strain energy U_h as

$$U_h = \frac{3(1-2\nu)}{2E}\sigma_h^2 = \frac{(1-2\nu)}{6E}(\sigma_1 + \sigma_2 + \sigma_3)^2 \tag{1.26}$$



(a) 3D stress state with three principal stresses

(b) The part of hydro-stresses with $\sigma_h = \dfrac{\sigma_1 + \sigma_2 + \sigma_3}{3}$

(c) The part of distortion stresses $\sigma_{d,i} = \sigma_i - \sigma_h$ where$(i = 1, 2, 3)$

Figure 1.31 Decomposition of strain energy of three-dimensional stress state.

Thus, the distortion energy U_d will be the part of the total strain energy after the hydro strain energy is deducted, i.e.,

$$U_d = U - U_h = \frac{1+v}{3E}\left(\sigma_1^2 + \sigma_2^2 + \sigma_3^2 - (\sigma_1\sigma_2 + \sigma_2\sigma_3 + \sigma_1\sigma_3)\right) \tag{1.27}$$

The DE theory compares the strain energy in the application with the limit of the strain energy in the uniaxial test. When a yielding occurs in the uniaxial test, the stress state is $(S_{sy}, 0, 0)$, and the corresponding strain energy $(U_{d,test})$ can be determined by Eq. (1.24) as

$$U_{d,test} = \frac{1+v}{3E}S_{sy}^2 \tag{1.28}$$

Therefore, the DE theory can be expressed by,

$$U_d = \frac{1+v}{3E}\left(\sigma_1^2 + \sigma_2^2 + \sigma_3^2 - (\sigma_1\sigma_2 + \sigma_2\sigma_3 + \sigma_1\sigma_3)\right) \leq \frac{1+v}{3E}S_{sy}^2 = U_{d,test} \tag{1.29}$$

Eq. (1.29) is further simplified as

$$\sigma_e = \sqrt{\left(\sigma_1^2 + \sigma_2^2 + \sigma_3^2 - (\sigma_1\sigma_2 + \sigma_2\sigma_3 + \sigma_1\sigma_3)\right)} \leq S_{sy} \tag{1.30}$$

where σ_e is commonly known as von Mises effective stress.

The factor of safety N is defined in terms of σ_e and S_{sy} as

$$N = \frac{S_{sy}}{\sigma_e} = \frac{S_{sy}}{\sqrt{(\sigma_1^2 + \sigma_2^2 + \sigma_3^2 - (\sigma_1\sigma_2 + \sigma_2\sigma_3 + \sigma_1\sigma_3))}} \tag{1.31}$$

When various stresses exist at one position, it is convenient to combine all of the stresses as one effective stress (σ_e). The *von-Mises effective stress* can be referred as such as an equivalent stress.

For a stress state in three-dimensional space, the safe zones defined by MSS and DET are slightly different. *A safe zone* includes all of the stress states where the material will not fail; on the other hand, if a stress state lies outside of the safe zone, the material will fail. The boundary of a safe zone is defined by a failure design theory, such as MSS and DET. Fig. 1.32 also shows the comparison of the safe zones that MSS is more conservative than DET; while DET can predict a failure more closely.

1.8.3 Maximum Normal Stress (MNS) Theory

Brittle material allows for very limited strain, and it likely fails as a fracture before it yields. A fracture occurring to a brittle material is caused by an exceeded normal stress. A fracture failure can be described by *the maximum normal stress* (*MNS*) *theory*. The maximum normal stress theory states that a failure will occur when the magnitude of the major principal stress reaches that stress, which causes a fracture in a uniaxial test. A normal stress can be tensile or compression.

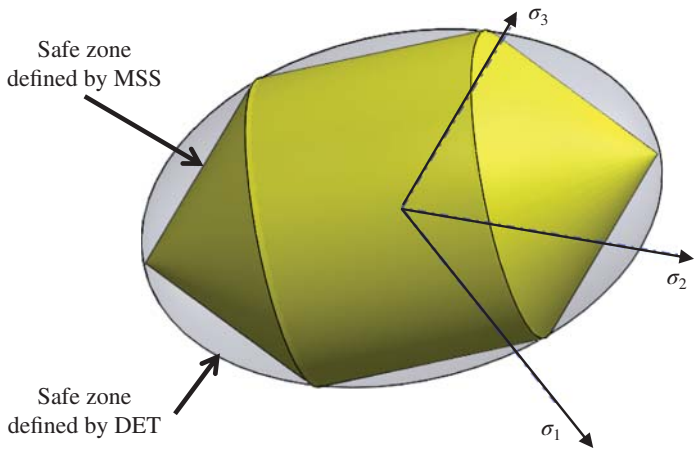


Figure 1.32 MSS and DET in three-dimensional space.

Therefore, the MNS theory applies in brittle materials for two scenarios: (1) all of the principal stresses are tensile stresses or zero, and (2) all of the principal stresses are compression stresses or zero. Fig. 1.33 shows the safe zone of the materials based on the MNS theory. Note that the MNS theory is applicable only in the first and the third quadrants of the plane formed by the axes of principal stresses σ_1 and σ_3. If the maximum tensile strength equals to the maximum compression strength (i.e., $S_{uc} = -S_{ut}$), the safe zone under compression stress state is diagonal symmetric to that of the tensile stress state. If the maximum compression strength differs from that of tensile stress (i.e., $S_{uc} \neq -S_{ut}$), the boundary lines of the safe zone subjected to compression stresses is

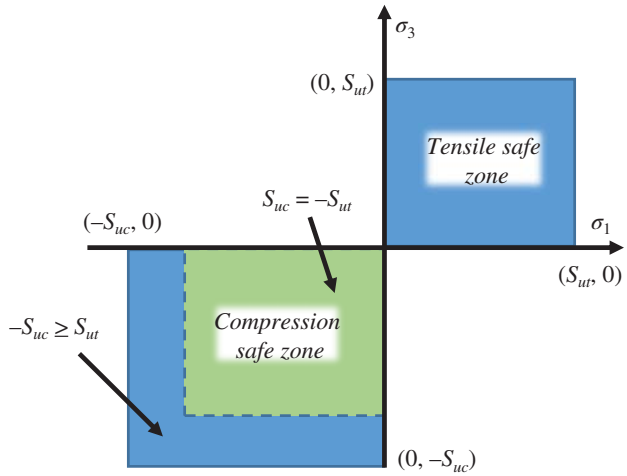


Figure 1.33 The maximum normal stress (MNS) theory.

defined by $\sigma_1 \geq -S_{uc}$ and $\sigma_3 \geq -S_{uc}$, respectively. The boundary lines of the safe zone subjected to tensile stresses is defined by $\sigma_1 <= S_{ut}$ and $\sigma_3 <= S_{ut}$, respectively. As a result, the MNS theory is mathematically expressed as

$$\left.\begin{array}{lll} \text{Compression stress:} & \sigma_3 \geq -S_{uc} & N = \left|\frac{S_{uc}}{\sigma_3}\right| \\ \text{Tensile stress:} & \sigma_1 \leq S_{ut} & N = \left|\frac{S_{ut}}{\sigma_1}\right| \end{array}\right\} \tag{1.32}$$

Many materials show the heterogeneity of material properties. The material strengths vary from one loading direction to another. Even though for the same type of normal stress, the stress direction (e.g., tensile or compression) has its impact on of the material strength. The strengths for positive (tensile) or negative (compression) stresses are different. Engineering materials, such as gray cast iron have different tensile and compressive strengths. The difference of compression and tensile strengths may be due to the presence of microscopic flaws in the materials: under a tensile load, microscopic flaws serve as nuclei to form cracks; under a compression load, these flaws are pressed together, which increases the resistance to slippage from shear stresses.

1.8.4 Ductile and Brittle Coulomb-Mohr (CM) Theory

The MNS theory is applicable to the failure criterion in the first and third quadrants. It does not account for the interdependence of normal and shear stresses in the second and fourth quadrants. The Coulomb-Mohr theory (CM) attempts to account for the interdependence by connecting opposite corners of these quadrants with diagonals. In the second and fourth quadrants, one principal stress is positive and the other one is negative. If one assumes $\sigma_1 \geq \sigma_3$ (the case in the fourth quadrant), the failure criterion of the CM theory is given as

$$\frac{\sigma_1}{S_{ut}} - \frac{\sigma_3}{S_{uc}} = \frac{1}{N} \tag{1.33}$$

The CM theory is applicable to both of ductile materials and brittle materials. When it is applied to ductile materials, it is referred as the *Ductile CM (DCM) theory*. When it is applied to brittle materials, it is referred as the *Brittle CM (BCM) theory*.

Fig. 1.34 shows the safe zone, which is symmetric about diagonal line A-A. Due to the symmetry, only the failure criteria on the right side of plane ($\sigma_1 \geq \sigma_3$) is discussed. The safe zone consists of zones I, II, and III; the envelop boundaries for three zones are found as

$$\left.\begin{array}{lll} \text{zone I:} & 0 \leq \sigma_3 \leq \sigma_1 & \frac{S_{ut}}{\sigma_1} = N \\ \text{zone II:} & \left.\begin{array}{l} 0 \leq \sigma_1 \\ \sigma_3 \leq 0 \end{array}\right\} & \frac{\sigma_1}{S_{ut}} - \frac{\sigma_3}{S_{uc}} = \frac{1}{N} \\ \text{zone III:} & \sigma_3 \leq \sigma_1 \leq 0 & \frac{-S_{uc}}{\sigma_3} = N \end{array}\right\} \tag{1.34}$$

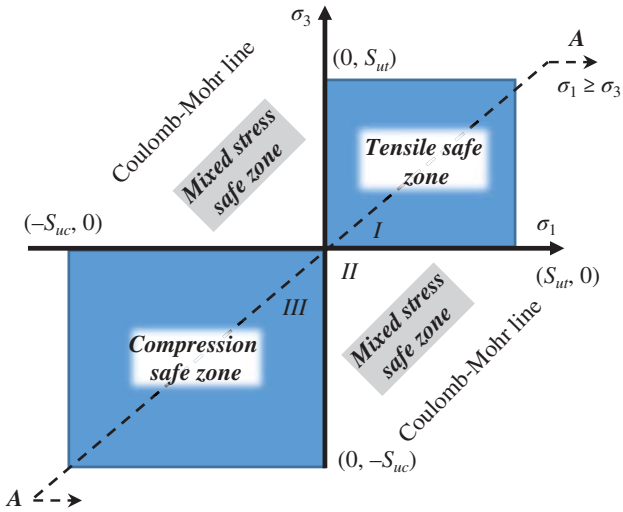


Figure 1.34 The Coulomb-Mohr (CM) theory.

1.8.5 Modified-Mohr (MM) Theory

As shown in Fig. 1.35, for some materials, such as gray cast-iron, the experimental test data about failures meets the prediction of the MNS theory in the first and third quadrants, but it does not meet the prediction of the CM theory well in the second and fourth quadrants. The *modified Mohr (MM) theory* is proposed to modify the failure criterion by the CM theory to make it fit the experimental data better in the second and fourth quadrants.

Fig. 1.35 shows the safe zone, which is symmetric about diagonal line A-A. Due to the symmetric, only the failure criteria on the right side of plane ($\sigma_1 \geq \sigma_3$) is discussed. The safe zone consists of zones I, II, and III; the envelop boundaries for three zones are found as

$$\left.\begin{array}{lll} \text{zone I:} & \left.\begin{array}{c} 0 \leq \sigma_1 \\ -S_{ut} \leq \sigma_3 \leq S_{ut} \end{array}\right\} & \dfrac{S_{ut}}{\sigma_1} = N \\ \text{zone II:} & \left.\begin{array}{c} 0 \leq \sigma_1 \\ -S_{uc} \leq \sigma_3 \leq -S_{ut} \end{array}\right\} & \dfrac{S_{uc} - S_{ut}}{S_{uc} S_{ut}} \left(\sigma_1 - \dfrac{S_{ut}\sigma_2}{S_{uc} - S_{ut}} \right) = \dfrac{1}{N} \\ \text{zone III:} & \sigma_1 \leq 0 & \dfrac{-S_{uc}}{\sigma_3} = N \end{array}\right\} \tag{1.35}$$

1.8.6 Guides for Selection of Failure Criteria

It has been discussed that a material can fail in different ways. To optimize the design of a mechanical structure, it is desirable to select an appropriate failure criterion, which matches the type of the most possible failures in applications.

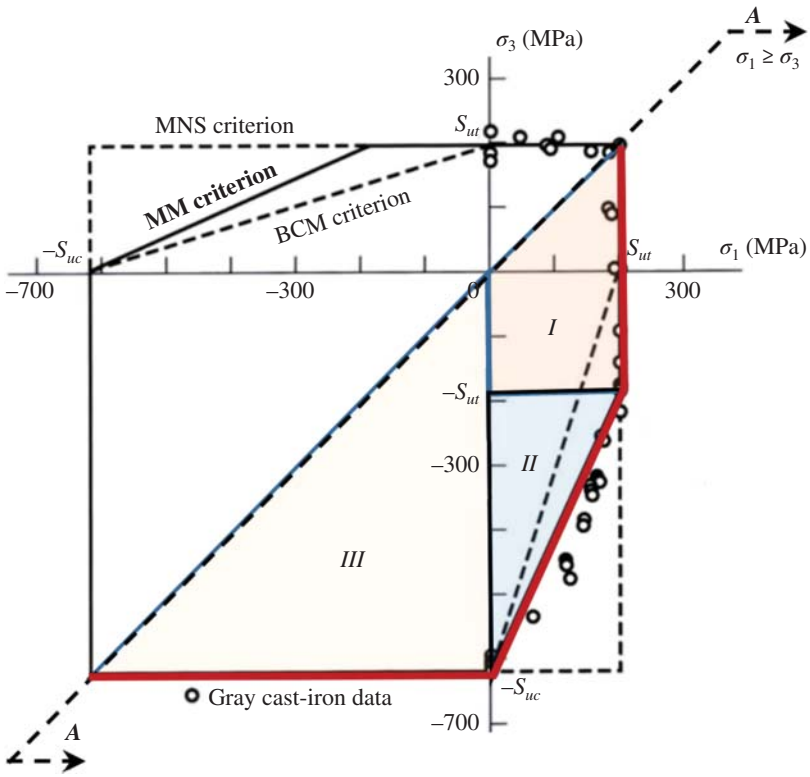


Figure 1.35 The Modified-Mohr (MM) theory.

Fig. 1.36 shows the general guide in selecting a failure criterion based on *materials*, *comparison of tensile and compressive strengths*, and *strategies* in design optimization. *First*, the strengths of materials must be known at the beginning; *second*, the principal stresses at the weakest points of object are determined from stress analysis; *finally*, the maximum stresses and material strengths are compared, based on the given failure criteria.

In Fig. 1.36, different categories of failure criteria apply to brittle and ductile materials. If a brittle material is used, the Modified Mohr (MM) theory and the Brittle Coulomb-Mohr (BCM) theory are applied for *conservative* or *aggressive* design optimization respectively. If a ductile material is used, the compressive and tensile strengths are compared, and only the Ductile Coulomb-Mohr (DCM) theory is applicable when two strengths are different. The Maximum Shear Stress (MSS) theory and Distortion Energy (DE) theory are applied for conservative or aggressive design optimization, respectively.

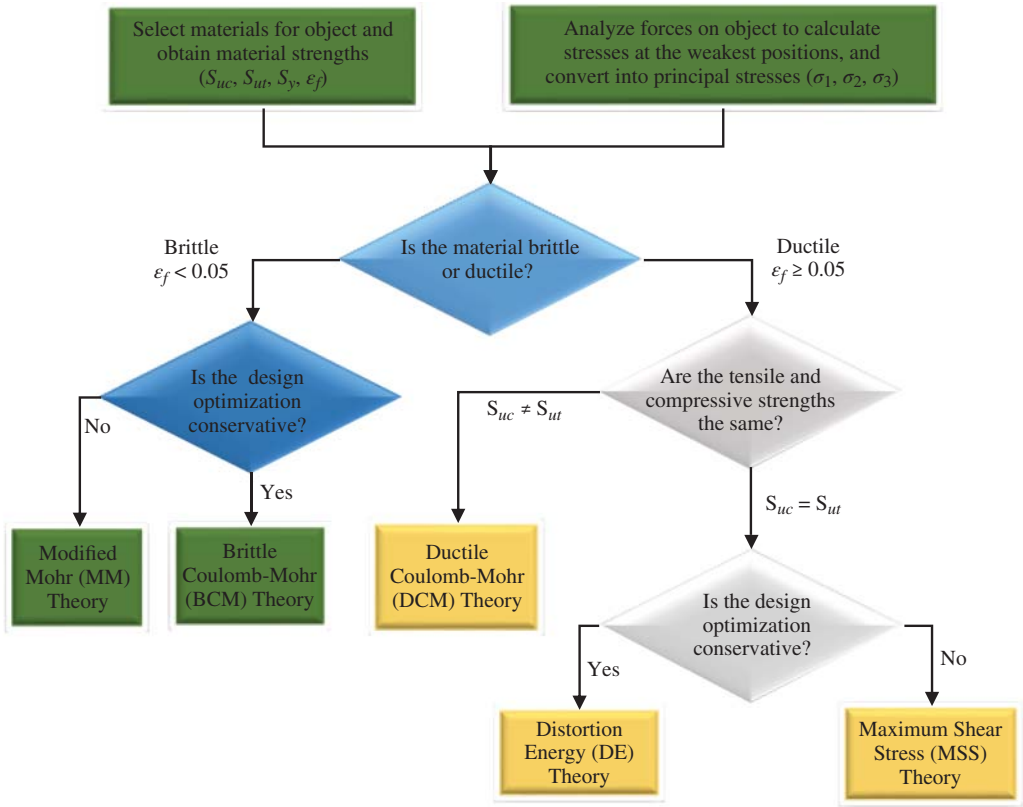


Figure 1.36 Selection guide for static failure criterion.

1.9 STRESS CONCENTRATION

A failure on an object is usually initialized at the weakest points, where either the magnitude of stress is too large in contrast to the corresponding strength or a micro crack or other damage is caused by the impurity of materials.

If an object has some geometric discontinuities, such as shoulders, grooves, holes, keyways, threads, or cracks, these discontinuities will changes simple stress distribution on well-prepared specimens in standardized material tests. Fig. 1.37 shows a few of the examples of the distribution of simple stresses. Fig. 1.38 and Fig. 1.39 show two examples that the geometric discontinuities, such as notches alter the distribution of stress in object. To make a fair comparison between the stress and strength, it is necessary to evaluate how a geometric discontinuity increases the stress at the critical area via the phenomenon of stress concentration.

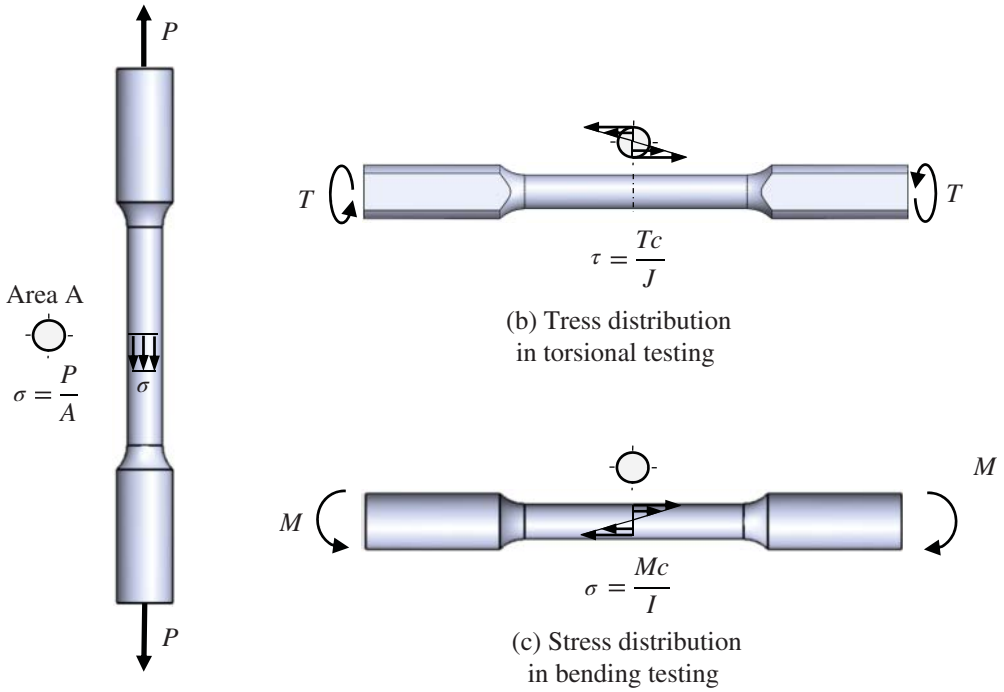


Figure 1.37 Simple stress distribution in testing of material properties.

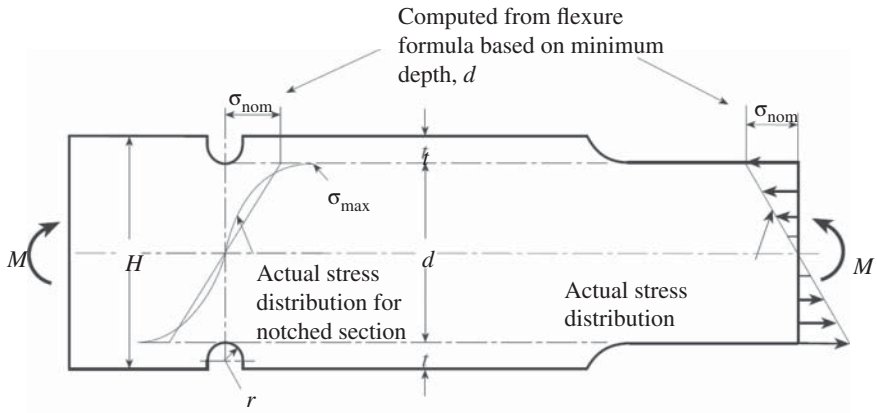
Stress concentration refers to the localized high-stresses occurring to a geometric discontinuity. Stress concentration can be measured by the *stress concentration factor* (K). Stress concentration factor (SCF) is defined as the ratio of the peak stress to a normal stress at a discontinuity as,

$$K_t = \frac{\sigma_{max}}{\sigma_{nom}} \quad \textit{for normal stress (tension or bending)} \tag{1.36}$$

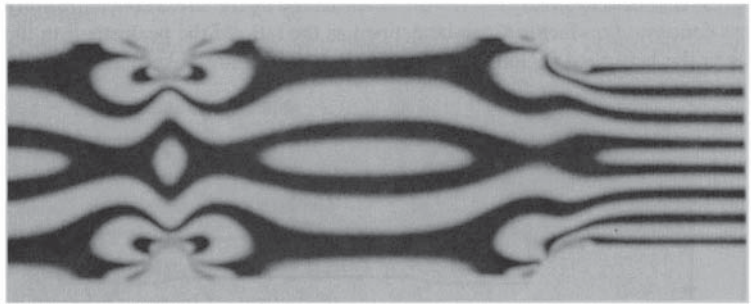
$$K_{ts} = \frac{\tau_{max}}{\tau_{nom}} \quad \textit{for shear stress (torsion)} \tag{1.37}$$

where the stresses σ_{max} and τ_{max} represent the maximum stresses to be expected in the member under the actual loads and the *nominal stresses* σ_{nom} and τ_{nom} are reference normal and shear stresses. The subscript t indicates that the SCF is a theoretical factor. That is to say, the peak stress in the body is based on the theory of elasticity, or it is derived from a laboratory stress analysis experiment. The subscript s of Eq. (1.37) is often ignored.

In the case of the theory of elasticity, a two-dimensional stress distribution of a homogeneous elastic body under known loads is a function only of the body geometry and is not dependent



(a) Bending of specimen with notched section



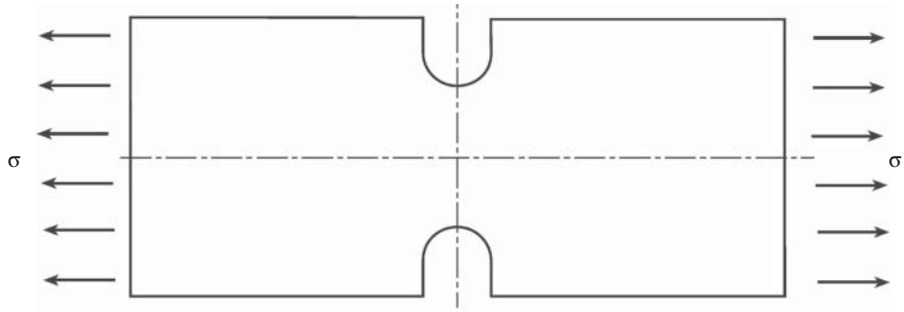
(b) Photoelastic fringe photograph

Figure 1.38 Stress concentration by a notch (Peterson 1974).

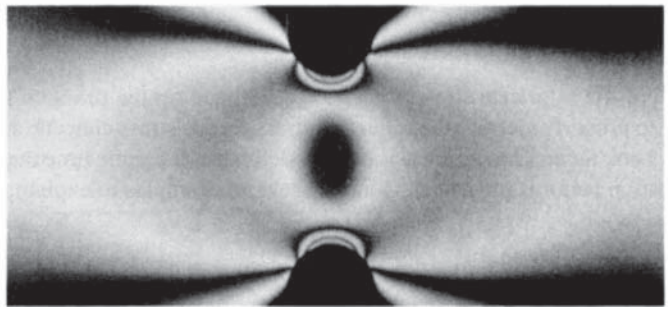
on the material properties. This book deals primarily with the elastic stress concentration factors. In the plastic range, one must consider separate stress and strain concentration factors that depend on the shape of the stress-strain curve and the stress or strain level.

Sometimes K_t is also referred to as a *form factor*. The subscript t distinguishes factors derived from theoretical or computational calculations, or experimental stress analysis methods, such as photoelasticity, or strain gage tests from factors obtained through mechanical damage tests, such as impact tests. For example, the fatigue notch factor K_f is determined using a fatigue test, which will be described in Section 1.16.

The general-purpose finite element analysis (FEA) method provides an effective alternative to substitute the stress concentration factor method for stress analysis. The fundamental of FEA as well as the procedure of using FEA stress analysis will be covered in detail in Chapter 6. In contrast to the stress concentration factor, FEA can be utilized to analyze the objects with complex geometries and loading conditions without the need of identifying the areas of stress concentration.



(a) Specimen with notched section



(b) Fringe photograph

Figure 1.39 Stress concentration of tension bar by notches (Doz Dr-ing habil K. Fethke, Universitat Rostock).

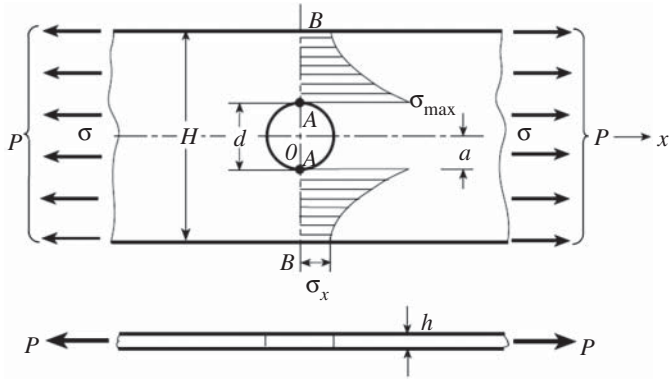
1.9.1 Selection of Nominal Stresses as Reference

SCF is dimensionless, and it is determined as a ratio of the stress at the point of interest and a reference normal stress. The reference stress σ_{nom} or τ_{nom} is determined to tailor the problem to be investigated at hand. It is very important to properly identify the reference stress for the stress concentration factor of interest. In this book, the reference stress is defined at the same time that a particular SCF is presented. Consider several examples to explain the selection of reference stresses.

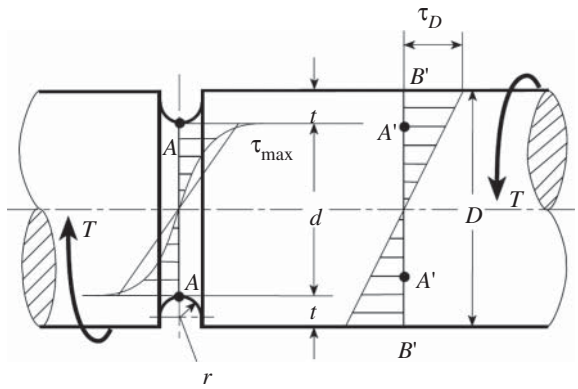
Example 1.2 Tension Bar with a Hole Uniform tension is applied to a bar with a single circular hole, as shown in Fig. 1.40*a*. The maximum stress occurs at point *A*, and the stress distribution can be shown to be as in Fig. 1.40*a*. Suppose that the thickness of the plate is *h*, the width of the plate is *H*, and the diameter of the hole is *d*. The reference stress could be defined in two ways:

(1) Use the stress in a cross section far from the circular hole as the reference stress. The area at this section is called the *gross cross-sectional area*. Thus, define as,

$$\sigma_{nom} = \sigma_g = \frac{P}{Hh} \tag{1.38}$$



(a) Tension bar with hole



(b) Torsion bar with groove

Figure 1.40 Example of determining nominal stress.

When σ_{max} is determined, the stress concentration factor K_{tg} becomes

$$K_{tg} = \frac{\sigma_{max}}{\sigma_{nom}} = \frac{\sigma_{max}}{\sigma_g} = \frac{\sigma_{max} Hh}{P} \tag{1.39}$$

(2) Use the stress based on the cross section at the hole, which is formed by removing the circular hole from the gross cross section. The corresponding area is referred to as the net cross-sectional area. If the stresses at this cross section are uniformly distributed and equal to σ_n:

$$\sigma_{nom} = \sigma_n = \frac{P}{(H-d)h} \tag{1.40}$$

With the same σ_{max}, the stress concentration factor K_{tn} based on the reference stress σ_n is determined by, namely,

$$K_{tn} = \frac{\sigma_{max}}{\sigma_{nom}} = \frac{\sigma_{max}}{\sigma_n} = \frac{\sigma_{max}(H-d)h}{P} = K_{tg}\frac{(H-d)}{H} \tag{1.41}$$

In general, K_{tg} and K_{tn} are different. Both are plotted in Chart 4.1. Observe that as d/H increases from 0 to 1, K_{tg} increases from 3 to ∞, whereas K_{tn} decreases from 3 to 2. Either K_{tn} or K_{tg} can be used in calculating the maximum stress. It would appear that K_{tg} is easier to determine as σ is immediately evident from the geometry of the bar. But the value of K_{tn} is hard to read from a stress concentration plot for $d/H > 0.5$; since the curve becomes very steep. In contrast, the value of K_{tn} is easy to read, but it is necessary to calculate the net cross-sectional area to find the maximum stress. Since the stress of interest is usually on the net cross section, K_{tn} is the more generally used factor. In addition, in a fatigue analysis, only K_{tn} can be used to calculate the stress gradient correctly. In conclusion, normally, it is more convenient to give SCFs using the reference stresses based on the net area rather than the gross area. However, if a fatigue analysis is not involved and $d/H < 0.5$, the user may choose to use K_{tn} to simplify calculations.

Example 1.3 Torsion Bar with a Groove A bar of circular cross section, with a U-shaped circumferential groove, is subject to an applied torque T. The diameter of the bar is D, the radius of the groove is r, and the depth of the groove is t. The stress distribution for the cross section at the groove is shown in Fig. 1.39*b*, with the maximum stress occurring at point A at the bottom of the groove. Among the alternatives to define the reference stress are:

(1) Use the stress at the outer surface of the bar cross section B'-B', which is far from the groove, as the reference stress. According to basic strength of materials (Pilkey 2005), the shear stress is linearly distributed along the radial direction and

$$\tau_{B'} = \tau_D = \frac{16T}{\pi D^3} = \tau_{nom} \tag{1.42}$$

(2) Consider point A' in the cross section B'-B'. The distance of A' from the central axis is same as that of point A, that is, $d = D - 2t$. If the stress at A' is taken as the reference stress, then

$$\tau_{A'} = \frac{16Td}{\pi D^4} = \tau_{nom} \tag{1.43}$$

(3) Use the surface stress of a grooveless bar of diameter $d = D - 2t$ as the reference stress. This corresponds to a bar of cross section measured at A–A of Fig. 1.39*b*. For this area $\pi d^2/4$, the maximum torsional stress taken as a reference stress would be

$$\tau_A = \frac{16T}{\pi D^3} = \tau_{nom} \tag{1.44}$$

In fact this stress based on the net area is an assumed value and never occurs at any point of interest in the bar with a U-shaped circumferential groove. However, since it is intuitively appealing and easy to calculate, it is used more often than the other two reference stresses.

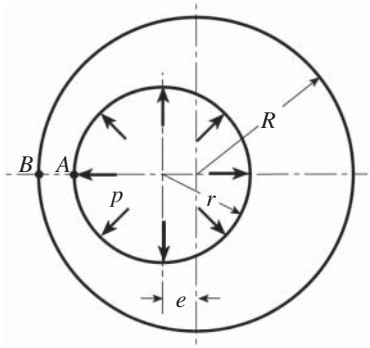


Figure 1.41 Circular cylinder with an eccentric hole.

Example 1.4 Cylinder with an Eccentric Hole A cylinder with an eccentric circular hole is subjected to internal pressure p as shown in Fig. 1.41. An elastic solution for stress is difficult to find. It is convenient to use the pressure p as the reference stress

$$\sigma_{nom} = p \tag{1.45}$$

so that

$$K_t = \frac{\sigma_{max}}{p} \tag{1.46}$$

These examples illustrate that there are many options for selecting a reference stress. In this book, the SCFs are given based on a variety of reference stresses, each of which is noted on the appropriate graph of the stress concentration factor. Sometimes, more than one SCF is plotted on a single chart. The reader should select the type of factor that appears to be the most convenient.

1.9.2 Accuracy of Stress Concentration Factors

SCFs are obtained analytically from the elasticity theory, computationally from the finite element method, and experimentally using methods such as photoelasticity or strain gages. For torsion, the membrane analogy (Pilkey and Wunderlich 1993) can be employed. When the experimental work is conducted with sufficient precision, excellent agreement is often obtained with well-established analytical stress concentration factors.

Unfortunately, the use of SCFs in analysis and design is not as a firm foundation as the theoretical basis for determining the factors. The theory of elasticity solutions are based on the formulations that include such assumptions as that the material must be *isotropic* and *homogeneous*. In reality, materials may be neither uniform nor homogeneous, and may even have defects. More data is necessary because, for the required precision in material tests, statistical procedures are often necessary. Directional effects in materials must also be carefully taken into account. It is hardly necessary to point out that the designer cannot wait for exact answers to all of these questions. As always, existing information must be reviewed and judgment used in developing

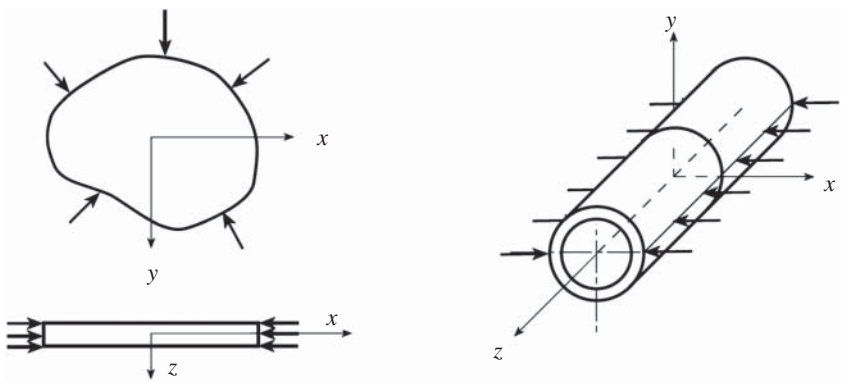
reasonable approximate procedures for design, tending toward the safe side in doubtful cases. In time, advances will take place and revisions in the use of stress concentration factors will need to be made accordingly. On the other hand, it can be said that our limited experience in using these methods has been satisfactory. It is worthwhile to note that all of the aforementioned issues can be addressed in the numerical simulation by finite element analysis (FEA), which will be discussed in Chapter 6.

1.9.3 Decay of Stress away from the Peak Stress

There are a number of theories of elasticity analytical solutions for stress concentrations, such as for an elliptical hole in a panel under tension. As can be observed in Fig. 1.39*a*, these solutions show that, typically, the stress decays approximately exponentially from the location of the peak stresses to the nominal value at a remote location, with the rate of decay higher near the peak value of stress.

1.10 STRESS CONCENTRATION AS A TWO-DIMENSIONAL PROBLEM

Consider a thin element lying in the *x*-*y* plane, loaded by in-plane forces applied in the *x*-*y* plane at the boundary (Fig. 1.42*a*). For this case the stress components σ_z, τ_{xz}, τ_{yz} can be assumed to be equal to zero. This state of stress is called *plane stress*, and the stress components σ_x, σ_y, τ_{xy} are functions of *x* and *y*. If the dimension in the *z* direction of a long cylindrical or prismatic body is very large relative to its dimensions in the *x*-*y* plane and the applied forces are perpendicular to the longitudinal direction (*z* direction) (Fig. 1.42*b*), it may be assumed that at the midsection the *z* direction strains ε_z, γ_{xz}, and γ_{yz} are equal to zero. This is called the *plane strain* state. These two-dimensional problems are referred to as *plane problems*.



(a) Plane stress (b) Plane strain

Figure 1.42 Circular cylinder with an eccentric hole.

The differential equations of equilibrium together with the compatibility equation for the stresses σ_x, σ_y, τ_{xy} in a plane elastic body are (Pilkey and Wunderlich 1993)

$$\left.\begin{aligned}\frac{\partial \sigma_x}{\partial x}+\frac{\partial \tau_{xy}}{\partial y}+\overline{p}_{Vx}=0\\ \frac{\partial \tau_{xy}}{\partial x}+\frac{\partial \sigma_y}{\partial y}+\overline{p}_{Vy}=0\end{aligned}\right\} \tag{1.47}$$

$$\left(\frac{\partial^2}{\partial x^2}+\frac{\partial^2}{\partial y^2}\right)(\sigma_x+\sigma_y)=-f(V)\left(\frac{\partial \overline{p}_{Vx}}{\partial x}+\frac{\partial \overline{p}_{Vy}}{\partial y}\right) \tag{1.48}$$

where $\overline{p}_{Vx}$ and $\overline{p}_{Vy}$ denote the components of the applied body force per unit volume in the x and y directions and $f(v)$ is a function of Poisson's ratio:

$$f(V)=\begin{cases}1+V & \textit{for plane stress}\\ \dfrac{1}{1-V} & \textit{for plane strain}\end{cases}$$

The surface conditions are

$$\left.\begin{aligned}p_x=l\sigma_x+m\tau_{xy}\\ p_y=l\tau_{xy}+m\sigma_y\end{aligned}\right\} \tag{1.49}$$

where p_x, p_y are the components of the surface force per unit area at the boundary in the x and y directions. Also, l, m are the direction cosines of the normal to the boundary. For constant body forces, $\frac{\partial \overline{p}_{Vx}}{\partial x}=\frac{\partial \overline{p}_{Vy}}{\partial y}=0$ and Eq. (1.48) becomes

$$\left(\frac{\partial^2}{\partial x^2}+\frac{\partial^2}{\partial y^2}\right)(\sigma_x+\sigma_y)=0 \tag{1.50}$$

Eqs. (1.47), (1.49), and (1.50) are usually sufficient to determine the stress distribution for two-dimensional problems with constant body forces. These equations do not contain material constants. For plane problems, if the body forces are constant, the stress distribution is a function of the body shape and loadings acting on the boundary and not of the material. This implies for plane problems that stress concentration factors are functions of the geometry and loading and not of the type of material. Of practical importance is that stress concentration factors can be found using experimental techniques, such as photoelasticty that utilize material different from the structure of interest.

1.11 STRESS CONCENTRATION AS A THREE-DIMENSIONAL PROBLEM

For three-dimensional problems, there are no simple relationships similar to Eqs. (1.47), (1.49), and (1.50) for plane problems that show the stress distribution to be a function of body shape and applied loading only. In general, the stress concentration factors will change with different

materials. For example, Poisson's ratio v is often involved in a three-dimensional stress concentration analysis. In this book most of the charts for three-dimensional stress concentration problems not only list the body shape and load but also the Poisson's ratio v for the case. The influence of Poisson's ratio on the stress concentration factors varies with the configuration. For example, in the case of a circumferential groove in a round bar under torsional load (Fig. 1.43), the stress distribution and concentration factor do not depend on Poisson's ratio. This is because the shear deformation due to torsion does not change the volume of the element, namely the cross-sectional areas remain unchanged.

As another example, consider a hyperbolic circumferential groove in a round bar under tension load P (Fig. 1.44). The stress concentration factor in the axial direction is (Neuber 1958)

$$K_{tx} = \frac{\sigma_{x,max}}{\sigma_{nom}} = \frac{1}{(a/r) + 2vC + 2}\left[\frac{a}{r}(C + v + 0.5) + (1 + v)(C + 1)\right] \tag{1.51}$$

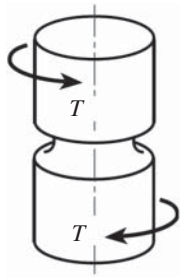


Figure 1.43 Round bar with a circumferential groove and torsional loading.

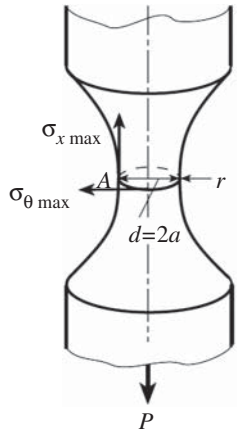


Figure 1.44 Hyperbolic circumferential groove in a round bar.

TABLE 1.4 Stress Concentration Factor as a Function of Poisson's Ratio for a Shaft in Tension with a Groove*

v	0.0	0.1	0.2	0.3	0.4	≈ 0.5
K_{tx}	3.01	2.95	2.89	2.84	2.79	2.75
$K_{t\theta}$	0.39	0.57	0.74	0.88	1.01	1.13

*The shaft has a hyperbolic circumferential groove with $a/r = 7.0$.

and in the circumferential direction is

$$K_{t\theta} = \frac{\sigma_{\theta,max}}{\sigma_{nom}} = \frac{a/r}{(a/r) + 2vC + 2}(vC + 0.5) \tag{1.52}$$

where r is the radius of curvature at the base of the groove, C is $\sqrt{\frac{a}{r} + 1}$, and the reference stress is $\sigma_{nom} = \frac{P}{\pi a^2}$. It is clear that K_{tx} and $K_{t\theta}$ are the function of v. Table 1.4 lists the stress concentration factors for different Poisson's ratios for the hyperbolic circumferential groove when $a/r = 7.0$. From this table it can be seen that as the value of v increases, K_{tx} decreases slowly whereas $K_{t\theta}$ increases relatively rapidly. When $v = 0$, $K_{tx} = 3.01$ and $K_{t\theta} = 0.39$. It is interesting that when Poisson's ratio v is equal to zero (there is no transverse contraction in the round bar), the maximum circumferential stress $\sigma_{\theta,max}$ is not equal to zero.

1.12 PLANE AND AXISYMMETRIC PROBLEMS

For a solid with axisymmetric geometry and loads with respect to its natural axis, it is convenient to use cylindrical coordinates (r, θ, x). The stress components are independent of the angle θ and $\tau_{r\theta}$, $\tau_{\theta x}$ are equal to zero. The equilibrium and compatibility equations for the axisymmetrical case are (Timoshenko and Goodier 1970)

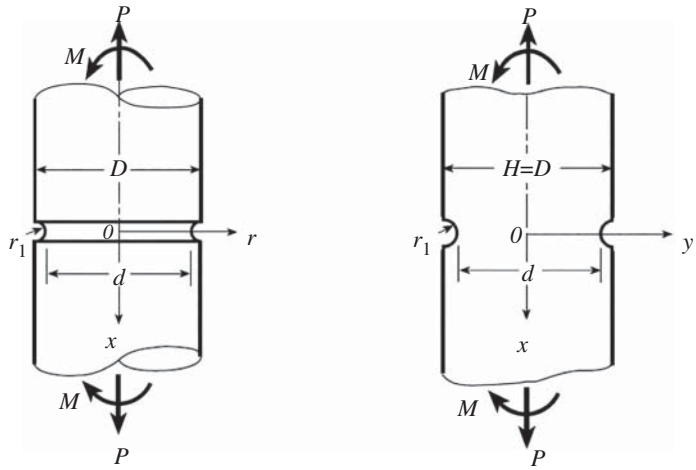
$$\left.\begin{aligned} \frac{\partial \sigma_r}{\partial r} + \frac{\partial \tau_{rx}}{\partial x} + \frac{\sigma_r - \sigma_\theta}{r} + \overline{p}_{Vr} = 0 \\ \frac{\partial \tau_{rx}}{\partial r} + \frac{\partial \sigma_r}{\partial x} + \frac{\tau_{rx}}{r} + \overline{p}_{Vx} = 0 \end{aligned}\right\} \tag{1.53}$$

$$\frac{\partial^2 \varepsilon_r}{\partial x^2} + \frac{\partial^2 \varepsilon_x}{\partial r^2} = \frac{\partial^2 \gamma_{rx}}{\partial r \partial x} \tag{1.54}$$

The strain components are

$$\varepsilon_r = \frac{\partial u}{\partial r}, \varepsilon_\theta = \frac{u}{r}, \varepsilon_x = \frac{\partial w}{\partial x}, \gamma_{rx} = \frac{\partial u}{\partial x} + \frac{\partial w}{\partial r} \tag{1.55}$$

Where u and w are the displacements in the r (radial) and x (axial) directions, respectively. The axisymmetric stress distribution in an axisymmetric solid is quite similar to the stress distribution



(a) Shaft K_{t3} (b) Shaft K_{t2}

Figure 1.45 Shaft with a circumferential groove and a plane element with the same longitudinal sectional shape.

for a two-dimensional plane element, the shape of which is the same as a longitudinal section of the axisymmetric solid (see Fig. 1.45). Strictly speaking, their stress distributions and stress concentration factors should not be equal. But under certain circumstances, their stress concentration factors are very close. To understand the relationship between plane and axisymmetric problems, consider the following cases.

Case 1. *A Shaft with a Circumferential Groove and with the Stress Raisers Far from the Central Axis of Symmetry*. Consider a shaft with a circumferential groove under tension (or bending) load, and suppose the groove is far from the central axis, $d/2 \gg r_1$, as shown in Fig. 1.45*a*. A plane element with the same longitudinal section under the same loading is shown in Fig 1.45*b*. Let K_{t3} and K_{t2} denote the stress concentration factors for the axisymmetric solid body and the corresponding plane problem, respectively. Since the groove will not affect the stress distribution in the area near the central axis, the distributions of stress components σ_x, σ_r, τ_{xr} near the groove in the axisymmetric shaft are almost the same as those of the stress components σ_x, σ_y, τ_{xr} near the notch in the plane element, so that $K_{t3} = K_{t2}$.

For the case where a small groove is a considerable distance from the central axis of the shaft, the same conclusion can be explained as follows. Set the terms with $1/r$ equal to 0 (since the groove is far from the central axis, r is very large), and note that differential Eqs. (1.53) reduces to

$$\left.\begin{aligned} \frac{\partial \sigma_r}{\partial r} + \frac{\partial \tau_{rx}}{\partial x} + \overline{p}_{Vr} = 0 \\ \frac{\partial \tau_{rx}}{\partial r} + \frac{\partial \sigma_r}{\partial x} + \overline{p}_{Vx} = 0 \end{aligned}\right\} \tag{1.56}$$

and Eq. (1.55) becomes

$$\varepsilon_r = \frac{\partial u}{\partial r}, \varepsilon_\theta = 0, \varepsilon_x = \frac{\partial w}{\partial x}, \gamma_{rx} = \frac{\partial u}{\partial x} + \frac{\partial w}{\partial r} \tag{1.57}$$

Introduce the material law

$$\varepsilon_r = \frac{1}{E}\left[\sigma_r - v(\sigma_r + \sigma_x)\right], \quad \varepsilon_\theta = 0 = \frac{1}{E}\left[\sigma_\theta - v(\sigma_x + \sigma_r)\right]$$

$$\varepsilon_x = \frac{1}{E}\left[\sigma_x - v(\sigma_r + \sigma_\theta)\right], \gamma_{rx} = \frac{1}{G}\tau_{rx}$$

into Eq. (1.54) and use Eq. (1.56). For constant body forces this leads to an equation identical (with y replaced by r) to that of Eq. (1.50). This means that the governing equations are the same. However, the stress σ_θ is not included in the governing equations and it can be derived from

$$\sigma_\theta = v(\sigma_r + \sigma_x) \tag{1.58}$$

When $v = 0$, the stress distribution of a shaft is identical to that of the plane element with the same longitudinal section.

Case 2. *General Case of an Axisymmetrical Solid with Shallow Grooves and Shoulders*. In general, for a solid of revolution with shallow grooves or shoulders under tension or bending as shown in Fig. 1.46, the stress concentration factor K_{t3} can be obtained in terms of the plane case factor K_{t2} using (Nishida 1976)

$$\left(1 + \frac{2t}{d}\right) K_{t3} - K_{t2} = \frac{t}{d}\left(1 + \sqrt{\frac{2t}{r_1}}\right) \tag{1.59}$$

Where r_1 is the radius of the groove and $t = (D - d)/2$ is the depth of the groove (or shoulder). The effective range for Eq. (1.59) is $0 \le t/d \le 7.5$. If the groove is far from the central axis, $t/d \to 0$ and $K_{t2} = K_{t3}$, which is consistent with the results discussed in Case 1.

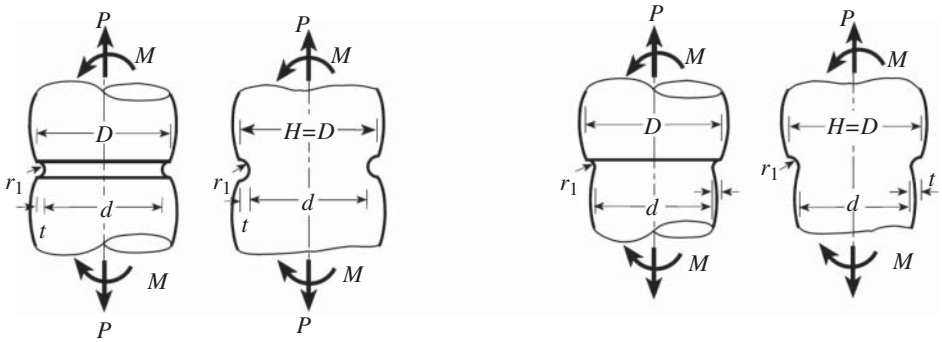


Figure 1.46 Stress concentration in shallow groove and shoulder.

Case 3. *Deep Hyperbolic Groove*. As mentioned in Section 1.11, Neuber (1958) provided formulas for bars with deep hyperbolic grooves. For the case of an axisymmetric shaft under tensile load, for which the minimum diameter of the shaft d (Fig. 1.44) is smaller than the depth of the groove, the following empirical formula is available (Nishida 1976):

$$K_{t3} = 0.75K_{t2} + 0.25 \tag{1.60}$$

Equation 1.60 is close to the theoretical value over a wide range and is useful in engineering analysis. This equation not only applies to tension loading but also to bending and shearing load. However, the error tends to be relatively high in the latter cases.

1.13 LOCAL AND NONLOCAL STRESS CONCENTRATION

If the dimensions of a stress raiser are much smaller than those of the structural member, its influence is usually limited to a localized area (or volume, for a three-dimensional case). That is, the global stress distribution of the member except for the localized area is the same as that for the member without the stress raiser. This kind of problem is referred to as *localized stress concentration*. Usually stress concentration theory deals with the *localized stress concentration* problems. The simplest way to solve these problems is to separate this localized part from the member, then to determine K_t by using the formulas and curves of a simple case with a similar raiser shape and loading. If a wide stress field is affected, the problem is called *nonlocal stress concentration* and can be quite complicated. Then a full-fledged stress analysis of the problem may be essential, probably with general-purpose structural analysis computer software.

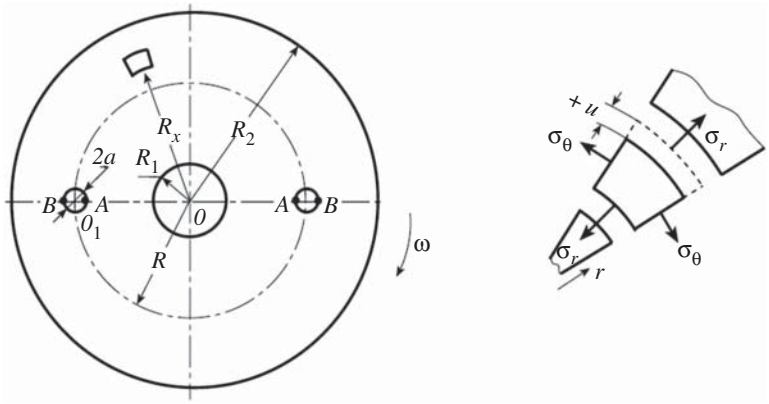
Example 1.5 Rotating Disk A disk rotating at speed ω has a central hole and two additional symmetrically located holes as shown in Fig. 1.47. Suppose that $R_1 = 0.24R_2$, a $= 0.06R_2$, $R = 0.5R_2$, $v = 0.3$. Determine the stress concentration factor near the small circle O_1.

Since $R_2 - R_1$ is more than 10 times greater than a, it can be reasoned that the existence of the small O_1 hole will not affect the general stress distribution. That is to say, the disruption in stress distribution due to circle O_1 is limited to a local area. This qualifies then as localized stress concentration.

For a rotating disk with a central hole, the theory of elasticity gives the stress components (Pilkey 2005)

$$\left.\begin{aligned} \sigma_r &= \frac{3+v}{8}\rho\omega^2\left(R_2^2 + R_1^2 - \frac{R_1^2R_2^2}{R_x^2} - R_x^2\right) \\ \sigma_\theta &= \frac{3+v}{8}\rho\omega^2\left(R_2^2 + R_1^2 + \frac{R_1^2R_2^2}{R_x^2} - \frac{1+3v}{3+v}R_x^2\right) \end{aligned}\right\} \tag{1.61}$$

Where ω is the speed of rotation (rad/s), ρ is the mass density, and R_x is the radius at which σ_r, σ_θ are to be calculated.



R_1 Radius of central hole R_2 Outer radius of the disk

R Distance between the center of the disk and the center of O_1

R_x Radius at which σ_r, σ_θ are to be calculated.

a Radius of hole O_1 r, θ Polar coordinates

Figure 1.47 Rotating disk with a central hole and two symmetrically located holes.

The O_1 hole may be treated as if it were in an infinite region and subjected to biaxial stresses σ_r, σ_θ as shown in Fig. 1.48*a*. For point A, $R_A = R - a = 0.5R_2 - 0.06R_2 = 0.44\ R_2$, and the elasticity solution of (1.61) gives

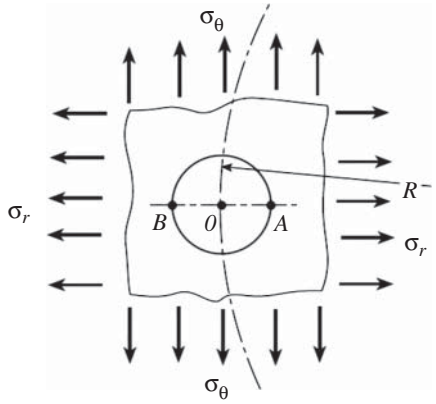
$$\left.\begin{aligned}\sigma_{rA} &= \frac{3+v}{8}\rho\omega^2 R_2^2\left(1+0.24^2-\frac{0.24^2}{0.44^2}-0.44^2\right) = 0.566\left(\frac{3+v}{8}\rho\omega^2 R_2^2\right)\\ \sigma_{\theta A} &= \frac{3+v}{8}\rho\omega^2\left(1+0.24^2+\frac{0.24^2}{0.44^2}-\frac{1+3v}{3+v}0.44^2\right) = 1.244\left(\frac{3+v}{8}\rho\omega^2 R_2^2\right)\end{aligned}\right\} \tag{1.62}$$

Substitute $\alpha = \sigma_{rA}/\sigma_{\theta A} = 0.566/1.244 = 0.455$ into the stress concentration factor formula for the case of an element with a circular hole under biaxial tensile load (Eq. 4.18) giving

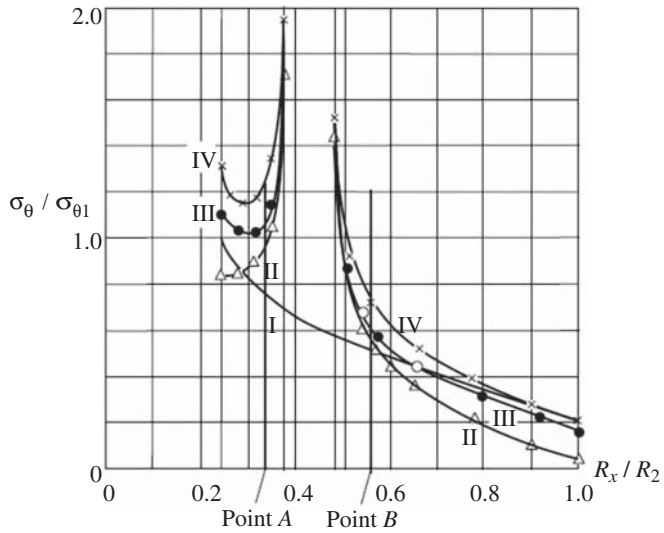
$$K_{tA} = \frac{\sigma_{A,max}}{\sigma_{\theta A}} = 3 - 0.455 = 2.545 \tag{1.63}$$

and the maximum stress at point A is

$$\sigma_{A,max} = K_{tA}\sigma_{\theta A} = 3.166\left(\frac{3+v}{8}\rho\omega^2 R_2^2\right) \tag{1.64}$$



(a) hole O_1 is treated as being subjected to biaxial stresses σ_r, σ_θ



R_x is the radius at which $\sigma_{r\max}$ is caculated

$\sigma_{\theta 1} = \sigma_\theta$ at $R_x = R_1$

(b) Results from Ku (1960). (I) No central hole; (II) approximate solution; (III) exact solution; (IV) photoelastic results (Newton 1940).

Figure 1.48 Analysis of a hollow rotating disk with two holes.

Similarly, at point B, $R_B = R + a = 0.5R_2 + 0.06R_2 = 0.56\,R_2$,

$$\left.\begin{aligned} \sigma_{rB} &= 0.56\left(\frac{3+\nu}{8}\rho\omega^2 R_2^2\right) \\ \sigma_{\theta B} &= 1.06\left(\frac{3+\nu}{8}\rho\omega^2 R_2^2\right) \end{aligned}\right\} \tag{1.65}$$

Eq. (1.65) yields $\alpha = \sigma_{rB}/\sigma_{\theta B} = 0.56/106 = 0.528$, further substitute α into the stress concentration factor formula of Eq. (4.18) gets

$$K_{tB} = 3\frac{\sigma_{B\ max}}{\sigma_{\theta B}} - 0.528 = 2.472$$

and the maximum stress at point B becomes

$$\sigma_{B\ max} = K_{tB}\sigma_{\theta B} = 2.6228\left(\frac{3+\nu}{8}\rho\omega^2 R_2^2\right) \tag{1.66}$$

To calculate the stress at the edge of the central hole, substitute $R_x = R_1 = 0.24R_2$ into σ_θ of (1.61),

$$\sigma_{\theta 1} = 2.204\left(\frac{3+\nu}{8}\rho\omega^2 R_2^2\right) \tag{1.67}$$

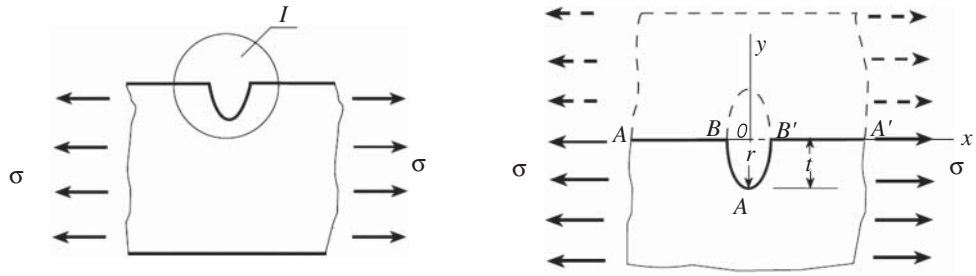
Equations (1.64) and (1.66) give the maximum stresses at points A and B of an infinite region as shown in Fig. 1.48*a*. If $\sigma_{\theta 1}$ is taken as the reference stress, the corresponding stress concentration factors are

$$\left.\begin{aligned} K_{t1A} &= \frac{\sigma_{A\ max}}{\sigma_{\theta 1}} = \frac{3.1660}{2.204} = 1.44 \\ K_{t1B} &= \frac{\sigma_{B\ max}}{\sigma_{\theta 1}} = \frac{2.6228}{2.204} = 1.19 \end{aligned}\right\} \tag{1.68}$$

This approximation of treating the hole as if it were in an infinite region and subjected to biaxial stresses is based on the assumption that the influence of circle O_1 is limited to a local area. The results are very close to the theoretical solution. Ku (1960) analyzed the case with $R_1 = 0.24R_2, R = 0.435R_2, a = 0.11R_2$. Although the circle O_1 is larger than that of this example, he still obtained reasonable approximations by treating the hole as if it were in an infinite region and subjected to biaxial stresses. The results are given in Fig. 1.48*b*, in which $\sigma_{\theta 1}$ on the central circle ($R_1 = 0.24R_2$) was taken as the reference stress. Curve II was obtained by the approximation of this example and curve III is from the theoretical solution (Howland 1930). For point A, $r/R_2 = 0.335$ and for point B, $r/R_2 = 0.545$. From Fig. 1.48*b*, it can be seen that at points A and B of the edge of hole O_1, the results from curves II and III are very close.

The method used in Example 1.5 can be summarized as follows: *First*, find the stress field in the member without the stress raiser at the position where the stress raiser occurs. This analysis provides the loading condition at this local point. *Second*, find a formula or curve from the charts in this book that applies to the loading condition and the stress raiser shape. *Finally*, use the formula or curve to evaluate the maximum stress. It should be remembered that this method is only applicable for localized stress concentration.

Consider now the concept of localized stress concentration for the study of the stress caused by notches and grooves. Begin with a thin flat element with a shallow notch under uniaxial tension load as shown in Fig. 1.49*a*. Since the notch is shallow, the bottom edge of the element is considered to be a substantial distance from the notch. It is a local stress concentration problem in the vicinity of the notch. Consider another element with an elliptic hole loaded by uniaxial stress σ as indicated in Fig. 1.49*b*. (The solution for this problem can be derived from Eq. 4.58.)



(a) Shallow groove (b) Model of I

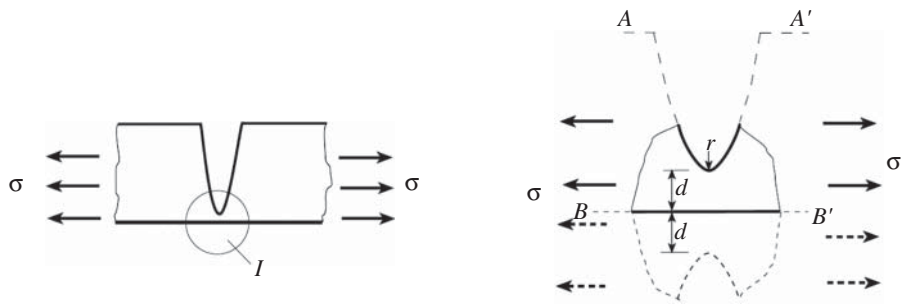
Figure 1.49 Thin flat element with a shallow notch under a uniaxial load.

Cut the second element with the symmetrical axis $A - A'$. The normal stresses on section $A - A'$ are small and can be neglected. Then the solution for an element with an elliptical hole (Eq. 4.58 with a replaced by t)

$$K_t = 1 + 2\sqrt{\frac{t}{r}} \tag{1.69}$$

can be taken as an approximate solution for an element with a shallow notch. According to this approximation, the stress concentration factor for a shallow notch is a function only of the depth t and radius of curvature r of the notch.

For a deep notch in a plane element under uniaxial tension load (Fig. 1.50*a*), the situation is quite different. For the enlarged model of Fig. 1.50*b*, the edge A-A' is considered to be a substantial distance from bottom edge B-B' and the stresses near the A-A' edge are almost zero. Such a low stress area probably can be safely neglected. The local areas that should be considered are the bottom of the groove and the straight line edge B-B' close to the groove bottom. Thus the deep notch problem, which might appear to be a nonlocal stress concentration problem, can also be considered as localized stress concentration. Furthermore the bottom part of the groove can be approximated by a hyperbola, since it is a small segment. Because of symmetry (Fig. 1.50) it is



(a) Deep groove (b) Model of I

Figure 1.50 Thin flat element with a deep notch under a uniaxial load.

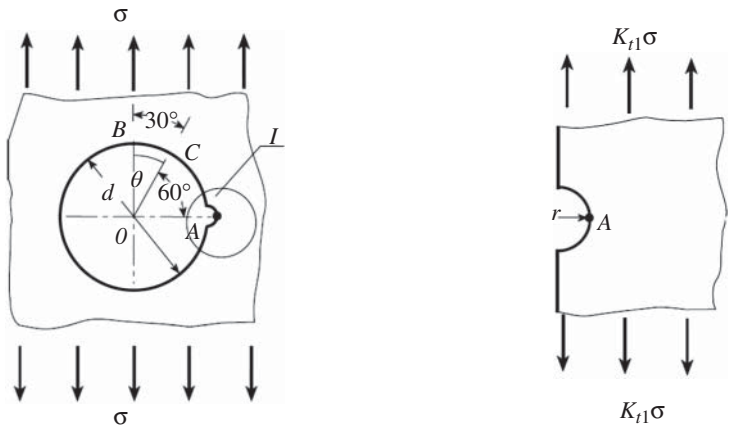
reasoned that the solution to this problem is the same as that of a plane element with two opposing hyperbola notches. The equation for the stress concentration factor is (Durelli 1982)

$$K_t = \frac{2\left(\frac{d}{r}+1\right)\sqrt{\frac{d}{r}}}{\left(\frac{d}{r}+1\right)\arctan\sqrt{\frac{d}{r}}+\sqrt{\frac{d}{r}}} \tag{1.70}$$

where d is the distance between the notch and edge B-B' (Fig. 1.50*b*). It is evident that the stress concentration factor of the deep notch is a function of the radius of curvature r of the bottom of the notch and the minimum width d of the element (Fig. 1.50). For notches of intermediate depth, refer to the Neuber method (see Eq. 2.1).

1.14 MULTIPLE STRESS CONCENTRATION

Two or more stress concentrations occurring at the same location in a structural member are said to be in a state of *multiple stress concentrations*. Multiple stress concentration problems occur often in engineering design. An example would be a uniaxially tension-loaded plane element with a circular hole, supplemented by a notch at the edge of the hole as shown in Fig. 1.51. The notch will lead to a higher stress than would occur with the hole alone. Use K_{t1} to represent the stress concentration factor of the element with a circular hole and K_{t2} to represent the stress concentration factor of a thin, flat tension element with a notch on an edge. In general, the multiple stress concentration factor of the element $K_{t1,\,2}$ cannot be deduced directly from K_{t1} and K_{t2}. The two different factors will interact with each other and produce a new stress distribution. Because of its importance in engineering design, considerable effort has been devoted



(a) Small at the edge of a circular hole

(b) Enlargement of *I*

Figure 1.51 Multiple stress concentration.

to finding solutions to the multiple stress concentration problems. Some special cases of these problems follow.

Case 1. *Geometrical Dimension of One Stress Raiser Much Smaller Than That of the Other* Assume that $d/2 \gg r$ in Fig. 1.51, where r is the radius of curvature of the notch. Notch r will not significantly influence the global stress distribution in the element with the circular hole. However, the notch can produce a local disruption in the stress field of the element with the hole. For an infinite element with a circular hole, the stress concentration factor K_{t1} is 3.0, and for the element with a semicircular notch K_{t2} is 3.06 (Chapter 2). Since the notch does not affect significantly the global stress distribution near the circular hole, the stress around the notch region is approximately $K_{t2}\sigma$. Thus the notch can be considered to be located in a tensile specimen subjected to a te $K_{t2}K_{t1}\sigma$ nsile load $K_{t1}\sigma$ (Fig. 1.51*b*). Therefore the peak stress at the tip of the notch is. It can be concluded that the multiple stress concentration factor at point A is equal to the product of K_{t1} and K_{t2},

$$K_{t1,2} = K_{t1} \cdot K_{t2} = 9.18 \tag{1.71}$$

which is close to the value displayed in Chart 4.60 for $r/d \to 0$. If the notch is relocated to point B instead of A, the multiple stress concentration factor will be different. Since at point B the stress concentration factor due to the hole is –1.0 (refer to Fig. 4.4), $K_{t1,2} = -1.0 \cdot 3.06 = -3.06$. Using the same argument, when the notch is situated at point C ($\theta = \pi/6$), $K_{t2} = 0$ (refer to Section 4.3.1 and Fig. 4.4) and $K_{t1,2} = 0 \cdot 3.06 = 0$. It is evident that the stress concentration factor can be effectively reduced by placing the notch at point C.

Consider a shaft with a circumferential groove subject to a torque T, and suppose that there is a small radial cylindrical hole at the bottom of the groove as shown in Fig. 1.52. (If there were no hole, the state of stress at the bottom of the groove would be one of pure shear, and K_{s1} for this location could be found from Chart 2.47.) The stress concentration near the small radial hole can be modeled using an infinite element with a circular hole under shearing stress. Designate the

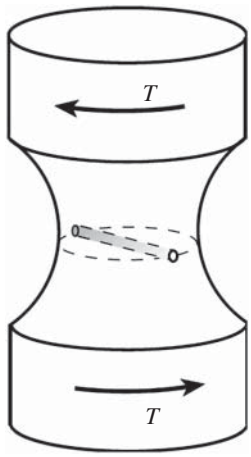


Figure 1.52 Small radial hole through a groove.

corresponding stress concentration factor as K_{s2}. (Then K_{s2} can be found from Chart 4.97, with $a = b$.) The multiple stress concentration factor at the edge of the hole is

$$K_{t1,2} = K_{s1} \cdot K_{s2} \tag{1.72}$$

Case 2. *Size of One Stress Raiser Not Much Different from the Size of the Other Stress Raiser* Under such circumstances the multiple stress concentration factor cannot be calculated as the product of the separate stress concentration factors as in Eqs. (1.71) or (1.72). In the case of Fig. 1.53, for example, the maximum stress location A_1 for stress concentration factor 1 does not coincide with the maximum stress location A_2 for stress concentration factor 2. In general, the multiple stress concentration factor adheres to the relationship (Nishida 1976)

$$max(K_{t1}, K_{t2}) < K_{t1,2} \leq K_{t1} \cdot K_{t2} \tag{1.73}$$

Some approximate formulas are available for special cases. For the three cases of Fig. 1.54—that is, a shaft with double circumferential grooves under torsion load (Fig. 1.54*a*), a semi-infinite element with double notches under tension (Fig. 1.54*b*), and an infinite element with circular and elliptical holes under tension (Fig. 1.54*c*)—an empirical formula (Nishida 1976)

$$K_{t1,2} \approx K_{t1,c} + (K_{t2e} - K_{t1,c})\sqrt{1 - \frac{1}{4}\left(\frac{d}{b}\right)^2} \tag{1.74}$$

was developed. Under the loading conditions corresponding to Fig. 1.54*a*, *b*, and *c*, as appropriate, K_{t1c} is the stress concentration factor for an infinite element with a circular hole and K_{t2e} is the stress concentration factor for an element with the elliptical notch. This approximation is quite close to the theoretical solution of the cases of Fig. 1.54*a* and *b*. For the case of Fig. 1.54*c*, the error is somewhat larger, but the approximation is still adequate.

Another effective method is to use the *equivalent ellipse* concept. To illustrate the method, consider a flat element with a hexagonal hole (Fig. 1.55*a*). An ellipse of major semiaxes *a* and

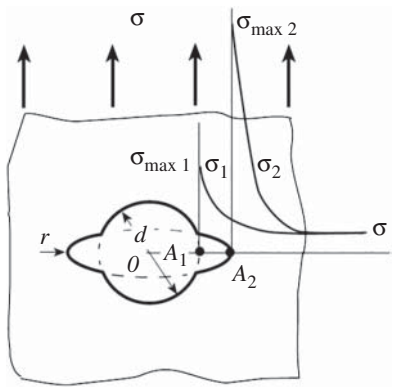
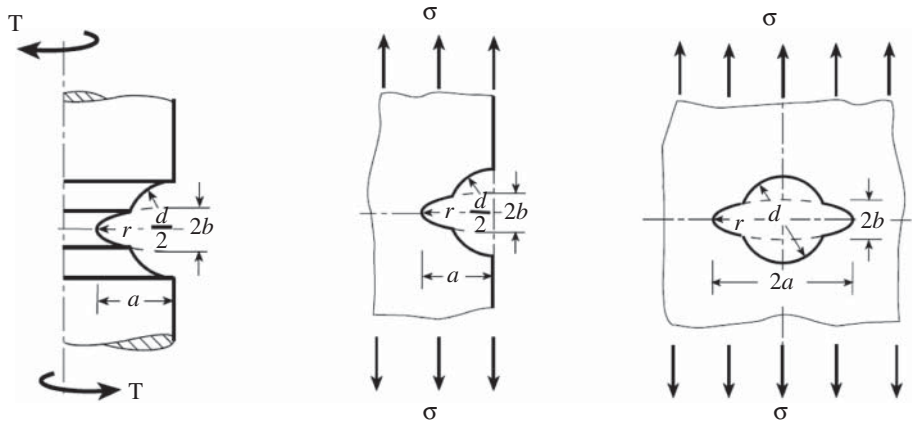


Figure 1.53 Two stress raisers of almost equal magnitude in an infinite two-dimensional element.

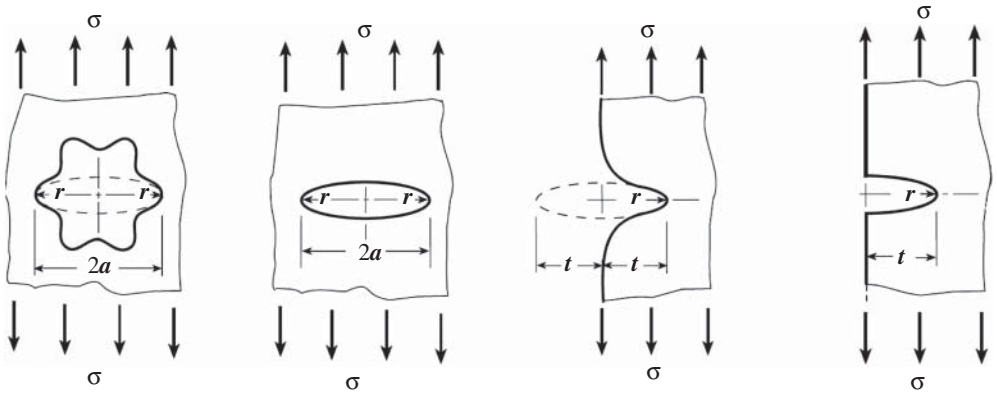


(a) Shaft with double grooves

(b) Semi-infinite element with double notches

(c) Circular hole with elliptical notches

Figure 1.54 Special cases of multiple stress concentration.



(a) Element with a hexagonal hole

(b) Element with an equivalent ellipse

(c) Semi-infinite element with a groove

(d) Semi-infinite element with the equivalent elliptic groove

Figure 1.55 Equivalent ellipses.

minimum radius of curvature r is the enveloping curve of two ends of the hexagonal hole. This ellipse is called the "equivalent ellipse" of the hexagonal hole. The stress concentration factor of a flat element with the equivalent elliptical hole (Fig. 1.55*b*) is Eq. (4.58)

$$K_t = 2\sqrt{\frac{a}{r}} + 1 \tag{1.75}$$

which is very close to the K_t for the flat element in Fig. 1.55*a*. Although this is an approximate method, the calculation is simple and the results are within an error of 10%. Similarly the stress concentration factor for a semi-infinite element with a groove under uniaxial tensile loading (Fig. 1.55*c*) can be estimated by finding K_t of the same element with the equivalent elliptical groove of Fig. 1.55*d*, for which (Nishida 1976) (Eq. 4.58)

$$K_t = 2\sqrt{\frac{t}{r}} + 1 \tag{1.76}$$

1.15 PRINCIPLE OF SUPERPOSITION FOR COMBINED LOADS

In practice, a structural member is often under the action of several types of loads, instead of being subjected to a single type of loading as represented in the graphs of this book. In such a case, evaluate the stress for each type of load separately. and superimpose the individual stresses. Since superposition presupposes a linear relationship between the applied loading and resulting response, it is necessary that the maximum stress be less than the elastic limit of the material. The following examples illustrate this procedure.

Example 1.6 Tension and Bending of a Two-Dimensional Element A notched thin element is under combined loads of tension and in-plane bending as shown in Fig. 1.56. Find the maximum stress.

For tension load P, the stress concentration factor K_{tn1} can be found from Chart 2.3 and the maximum stress is

$$\sigma_{\max 1} = K_{tn1}\sigma_{nom\ 1} \tag{1.77}$$

in which $\sigma_{nom1} = P/(dh)$. For the in-plane bending moment M, the maximum bending stress is (the stress concentration factor can be found from Chart 2.25)

$$\sigma_{\max 2} = K_{tn2}\sigma_{nom2} \tag{1.78}$$

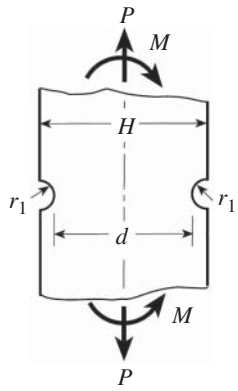


Figure 1.56 Element under tension and bending loading.

where $\sigma_{nom2} = 6M/(d^2h)$ is the stress at the base of the groove. Stresses σ_{max1} and $\sigma_{\max 2}$ are both normal stresses that occur at the same point, namely at the base of the groove. Hence, when the element is under these combined loads, the maximum stress at the notch is

$$\sigma_{\max} = \sigma_{\max 1} + \sigma_{\max 2} = K_{tn1}\sigma_{nom1} + K_{tn2}\sigma_{nom2} \tag{1.79}$$

Example 1.7 Tension, Bending, and Torsion of a Grooved Shaft A shaft of circular cross section with a circumferential groove is under the combined loads of axial force P, bending moment M, and torque T, as shown in Fig. 1.57. Calculate the maximum stresses corresponding to the various failure theories. The maximum stress is (the stress concentration factor of this shaft due to axial force P can be found from Chart 2.19)

$$\sigma_{\max 1} = K_{tn1}\frac{4P}{\pi d^2} \tag{1.80}$$

The maximum stress corresponding to the bending moment (from Chart 2.41) is

$$\sigma_{\max 2} = K_{tn2}\frac{32M}{\pi d^3} \tag{1.81}$$

The maximum torsion stress due to torque T is obtained from Chart 2.47 as

$$\tau_{\max 3} = K_{ts}\frac{16T}{\pi d^3} \tag{1.82}$$

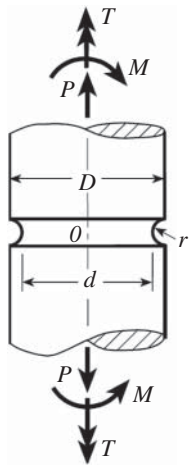


Figure 1.57 Grooved shaft subject to tension, bending, and torsion.

TABLE 1.5 The Use of Stress State in Different Failure Criteria

Failure Criterion	Applied Stress Elements	Formula
Maximum normal stress (MNS)	σ_1	$n = \dfrac{S_{ut}}{\sigma_1}$
Coulumb-Mohr theory	$\sigma_1,\ \sigma_2$	$\dfrac{\sigma_1}{\sigma_{ut}} - \dfrac{\sigma_2}{\sigma_{uc}} = \dfrac{1}{n}$
Maximum shear theory	$\sigma_1 > 0,\ \sigma_2 > 0$	$n = \dfrac{S_y}{\tau_{max}} = \dfrac{S_y}{\sigma_1 - \sigma_2}$
Distort energy theory	$\sigma_1,\ \sigma_2$	$n = \dfrac{S_y}{\sigma_{eq}} = \dfrac{S_y}{\sqrt{\sigma_1^2 - \sigma_1\sigma_2 + \sigma_1^2}}$

The maximum stresses of Eqs. (1.80)–(1.82) occur at the same location, namely at the base of the groove, and the principal stresses are calculated using the familiar formulas (Pilkey 2005)

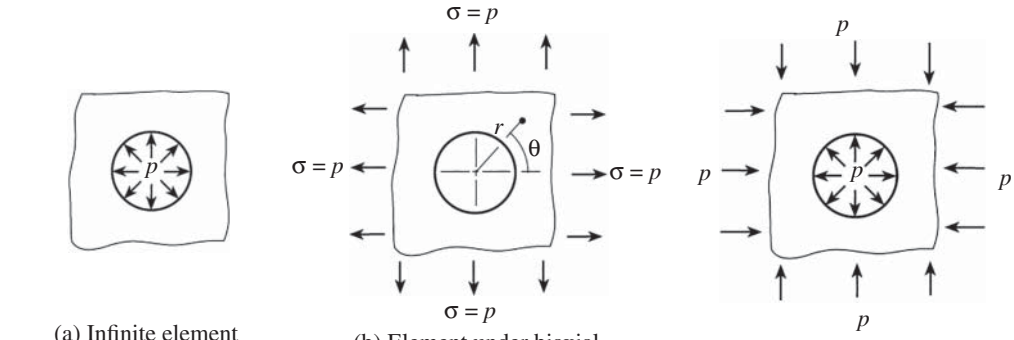
$$\sigma_1 = \frac{\sigma_{\max 1} + \sigma_{\max 2}}{2} + \frac{1}{2}\sqrt{(\sigma_{\max 1} + \sigma_{\max 2})^2 + 4\tau_{\max 3}^2} \tag{1.83}$$

$$\sigma_2 = \frac{\sigma_{\max 1} + \sigma_{\max 2}}{2} - \frac{1}{2}\sqrt{(\sigma_{\max 1} + \sigma_{\max 2})^2 + 4\tau_{\max 3}^2} \tag{1.84}$$

The various failure criteria for the base of the groove can now be formulated.

Once the state of the stress is determined, it can be used in different failure criteria in Table 1.5.

Example 1.8 Infinite Element with a Circular Hole with Internal Pressure Find the stress concentration factor for an infinite element subjected to internal pressure p on its circular hole edge as shown in Figure 1.58*a*.



(a) Infinite element subjected to internal pressure on a circular hole edge

(b) Element under biaxial tension at area remote from the hole

(c) Element under biaxial compression

Figure 1.58 (*a*) Infinite element subjected to internal pressure p on a circular hole edge; (*b*) element under biaxial tension at area remote from the hole; (*c*) element under biaxial compression.

This example can be solved by superimposing two configurations. The loads on the element can be assumed to consist of two cases: (1) biaxial tension $\sigma = p$ (Fig. 1.58*b*); (2) biaxial compression $\sigma = -p$, with pressure on the circular hole edge (Fig. 1.58*c*).

For case 1 of $\sigma = p$, the stresses at the edge of the hole are (Eq. 4.16)

$$\sigma_{r1} = 0; \quad \sigma_{\theta 1} = 2p; \quad \tau_{r\theta 1} = 0 \tag{1.85}$$

For case 2 the stresses at the edge of the hole (hydrostatic pressure) are

$$\sigma_{r2} = -p; \quad \sigma_{\theta 2} = -p; \quad \tau_{r\theta 2} = 0 \tag{1.86}$$

The stresses for both cases can be derived from the formulas of Little (1973). The total stresses at the edge of the hole can be obtained by superposition

$$\left.\begin{aligned} \sigma_r &= \sigma_{r1} + \sigma_{r2} = -p \\ \sigma_\theta &= \sigma_{\theta 1} + \sigma_{\theta 2} = p \\ \tau_{r\theta} &= \tau_{r\theta 1} + \tau_{r\theta 2} = 0 \end{aligned}\right\} \tag{1.87}$$

The maximum stress is $\sigma_{\max} = p$. If p is taken as the nominal stress (Example 1.4), the corresponding stress concentration factor can be defined as

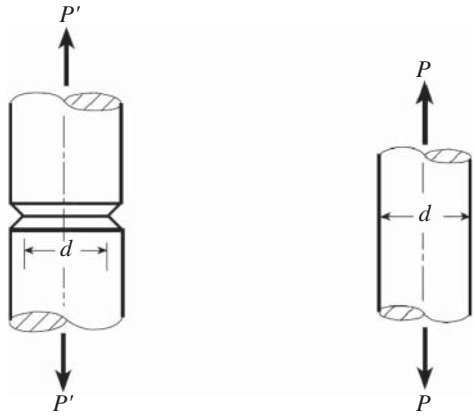
$$K_t = \frac{\sigma_{\max}}{\sigma_{nom}} = \frac{\sigma_{\max}}{p} = 1 \tag{1.88}$$

1.16 NOTCH SENSITIVITY

As noted at the beginning of this chapter, the theoretical stress concentration factors apply mainly to ideal elastic materials and depend on the geometry of the body and the loading. Sometimes a more realistic model is preferable. When the applied loads reach a certain level, plastic deformations may be involved. The actual strength of structural members may be quite different from that derived using theoretical stress concentration factors, especially for the cases of impact and alternating loads.

It is reasonable to introduce the concept of the *effective stress concentration factor* K_e. This is also referred to as the factor of stress concentration at rupture or the notch rupture strength ratio (ASTM 1994). The magnitude of K_e is obtained experimentally. For instance, K_e for a round bar with a circumferential groove subjected to a tensile load P' (Fig. 1.59*a*) is obtained as follows: (1) Prepare two sets of specimens of the actual material, the round bars of the first set having circumferential grooves, with d as the diameter at the root of the groove (Fig. 1.59*a*). The round bars of the second set are of diameter d without grooves (Fig. 1.59*b*). (2) Perform a tensile test for the two sets of specimens, the rupture load for the first set is P', while the rupture load for second set is P. (3) The effective stress concentration factor is defined as

$$K_e = \frac{P}{P'} \tag{1.89}$$



(a) With discontinuity (b) Without discontinuity

Figure 1.59 Specimens for obtaining K_e.

In general, $P' < P$ so that $K_e > 1$. The effective stress concentration factor is a function not only of geometry but also of material properties. Some characteristics of K_e for static loading of different materials are discussed briefly below.

(1) *Ductile material*. Consider a tensile loaded plane element with a V-shaped notch. The material law for the material is sketched in Fig. 1.60. If the maximum stress at the root of the notch is less than the yield strength $\sigma_{max} < \sigma_y$, the stress distributions near the notch would appear as in curves 1 and 2 in Fig. 1.60. The maximum stress value is

$$\sigma_{\max} = K_t \sigma_{nom} \tag{1.90}$$

As the $\sigma_{\max}$ exceeds σ_y, the strain at the root of the notch continues to increase but the maximum stress increases only slightly. The stress distributions on the cross section will be of the form of curves 3 and 4 in Fig. 1.60. Eq. (1.90) no longer applies to this case. As σ_{nom} continues to increase, the stress distribution at the notch becomes more uniform and the effective stress concentration factor K_e is close to unity.

(2) *Brittle material*. Most brittle materials can be treated as elastic bodies. When the applied load increases, the stress and strain retain their linear relationship until damage occurs. The effective stress concentration factor K_e is the same as K_t.

(3) *Gray cast iron*. Although gray cast irons belong to brittle materials, they contain flake graphite dispersed in the steel matrix and a number of small cavities, which produce much higher stress concentrations than would be expected from the geometry of the discontinuity. In such a case the use of the stress concentration factor K_t may result in significant error and K_e can be expected to approach unity, since the stress raiser has a smaller influence on the strength of the member than that of the small cavities and flake graphite.

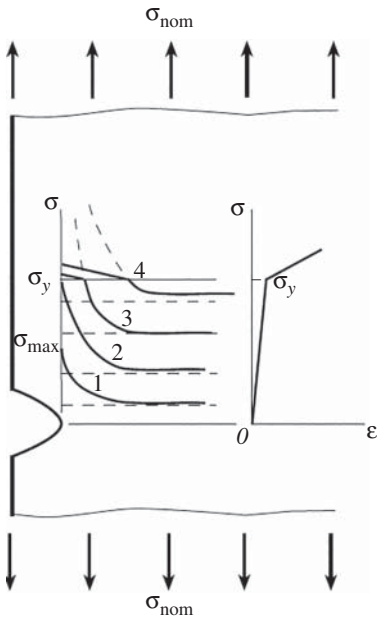


Figure 1.60 Stress distribution near a notch for a ductile material.

It can be reasoned from these three cases that the effective stress concentration factor depends on the characteristics of the material and the nature of the load, as well as the geometry of the stress raiser. Also $1 \leq K_e \leq K_t$. The maximum stress at rupture can be defined to be

$$\sigma_{\max} = K_e \sigma_{nom} \tag{1.91}$$

To express the relationship between K_e and K_t, introduce the concept of *notch sensitivity* q (Boresi et al. 1993):

$$q = \frac{K_e - 1}{K_t - 1} \tag{1.92}$$

or

$$K_e = q(K_t - 1) + 1 \tag{1.93}$$

Substitute Eq. (1.93) into Eq. (1.91):

$$\sigma_{\max} = [q(K_e - 1) + 1]\sigma_{nom} \tag{1.94}$$

If $q = 0$, then $K_e = 1$, meaning that the stress concentration does not influence the strength of the structural member. If $q = 1$, then $K_e = K_t$, implying that the theoretical stress concentration factor should be fully invoked. The notch sensitivity is a measure of the agreement between K_e and K_t.

The concepts of the effective stress concentration factor and notch sensitivity are used primarily for fatigue strength design. For fatigue loading, replace K_e in Eq. (1.89) by K_f or K_{fs}, defined as

$$K_f = \frac{\text{Fatigue limit of unnotched specimen (axial or bending)}}{\text{Fatigue limit of notched specimen (axial or bending)}} = \frac{\sigma_f}{\sigma_{nf}} \tag{1.95}$$

$$K_{fs} = \frac{\text{Fatigue limit of unnotched specimen (shear stress)}}{\text{Fatigue limit of notched specimen (shear stress)}} = \frac{\tau_f}{\tau_{nf}} \tag{1.96}$$

where K_f is the *fatigue notch factor* for normal stress and K_{fs} is the fatigue notch factor for shear stress, such as torsion. The notch sensitivities for fatigue become

$$q = \frac{K_f - 1}{K_t - 1} \tag{1.97}$$

or

$$q = \frac{K_{fs} - 1}{K_{ts} - 1} \tag{1.98}$$

where K_{ts} is defined in Eq. (1.55). The values of q vary from $q = 0$ for no notch effect ($K_{fs} = 1$) to $q = 1$ for the full theoretical effect ($K_f = K_t$).

Eqs. (1.97) and (1.98) can be rewritten in the following form for design use:

$$K_{tf} = q(K_t - 1) + 1 \tag{1.99}$$

$$K_{tsf} = q(K_{ts} - 1) + 1 \tag{1.100}$$

where K_{tf} is the *estimated* fatigue notch factor for normal stress, a calculated factor using an average q value obtained from Fig. 1.61 or a similar curve, and K_{tsf} is the *estimated* fatigue notch factor for shear stress.

If no information on q is available, as would be the case for newly developed materials, it is suggested that the full theoretical factor, K_t or K_{ts}, be used. It should be noted in this connection that if notch sensitivity is not taken into consideration at all in design ($q = 1$), the error will be on the safe side ($K_{tf} = K_t$ in Eq. (1.99)).

In plotting K_f for geometrically similar specimens, it was found that typically K_f decreased as the specimen size decreased (Peterson 1933a,b, 1943; Peterson and Wahl 1936). For this reason it is not possible to obtain reliable comparative q values for different materials by making tests of a standardized specimen of fixed dimension (Peterson 1945). Since the local stress distribution (stress gradient,[1] volume at peak stress) is more dependent on the notch radius r than on other geometrical variables (Peterson 1938; von Phillipp 1942; Neuber 1958), it was apparent that it would be more logical to plot q versus r rather than q versus d (for geometrically similar specimens the curve shapes are of course the same). Plotted q versus r curves (Peterson 1950, 1959) based on available data (Gunn 1952; Lazan and Blatherwick 1953; Templin 1954; Fralich 1959) were found to be within reasonable scatter bands. A q versus r chart for design purposes is given in Fig. 1.61; it averages the previously mentioned plots. Note that the chart is not verified for notches

[1]The stress is approximately linear in the peak stress region (Peterson 1938; Leven 1955).

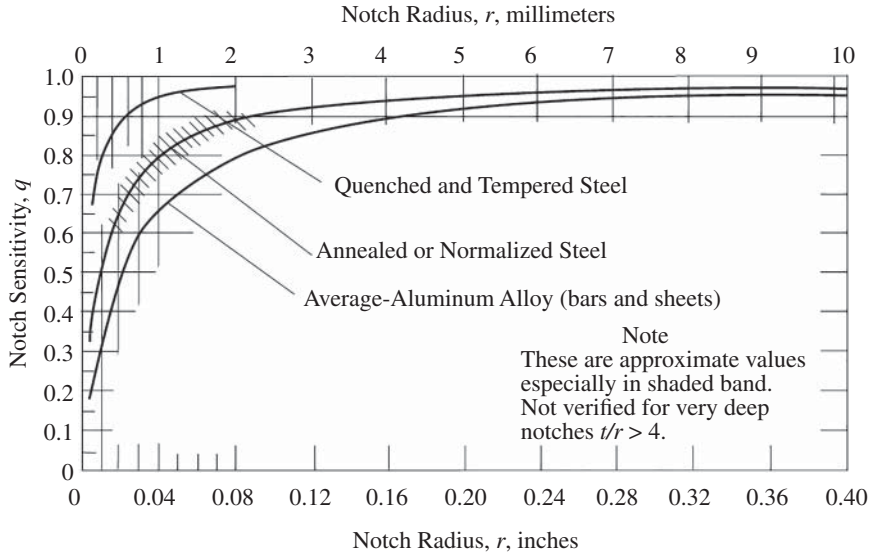


Figure 1.61 Average fatigue notch sensitivity.

having a depth greater than four times the notch radius because data is not available. Also note that the curves are to be considered as approximate (see shaded band).

Notch sensitivity values for radii approaching zero still must be studied. It is, however, well known that tiny holes and scratches do not result in a strength reduction corresponding to theoretical stress concentration factors. In fact, in steels of low tensile strength, the effect of very small holes or scratches is often quite small. However, in higher-strength steels the effect of tiny holes or scratches is more pronounced. Much more data are needed, preferably obtained from statistically planned investigations. Until better information is available, Fig. 1.61 provides reasonable values for design use.

Several expressions have been proposed for the q versus r curve. Such a formula could be useful in setting up a computer design program. Since it would be unrealistic to expect failure at a volume corresponding to the point of peak stress because of the plastic deformation (Peterson 1938), formulations for K_f are based on failure over a distance below the surface (Neuber 1958; Peterson 1974). From the K_f formulations, q versus r relations are obtained. These and other variations are found in the literature (Peterson 1945). All of the formulas yield acceptable results for design purposes. One must, however, always remember the approximate nature of the relations. In Fig. 1.61 the following simple formula (Peterson 1959) is used:[2]

$$q = \frac{1}{1 + \alpha/r} \tag{1.101}$$

where α is a material constant and r is the notch radius.

[2]The corresponding Kuhn-Hardrath formula (Kuhn and Hardrath 1952) based on Neuber relations is

$$q = \frac{1}{1 + \sqrt{\rho'/r}}$$

Either formula may be used for design purposes (Peterson 1959). The quantities α or ρ', a material constant, are determined by test data.

In Fig. 1.61, $\alpha = 0.0025$ for quenched and tempered steel, $\alpha = 0.01$ for annealed or normalized steel, $\alpha = 0.02$ for aluminum alloy sheets and bars (avg.). In Peterson (1959) more detailed values are given, including the following approximate design values for steels as a function of tensile strength:

$\sigma_{ut}/1000$	α
50	0.015
75	0.010
100	0.007
125	0.005
150	0.0035
200	0.0020
250	0.0013

where σ_{ut} is the tensile strength in pounds per square inch. In using the foregoing α values, one must keep in mind that the curves represent averages (see shaded band in Fig. 1.61).

A method has been proposed by Neuber (1968) wherein an equivalent larger radius is used to provide a lower K factor. The increment to the radius is dependent on the stress state, the kind of material, and its tensile strength. Application of this method gives results that are in reasonably good agreement with the calculations of other methods (Peterson 1953).

1.17 DESIGN RELATIONS FOR STATIC STRESS

1.17.1 Ductile Materials

Under ordinary conditions a ductile member loaded with a steadily increasing uniaxial stress does not suffer loss of strength due to the presence of a notch, since the notch sensitivity q usually lies in the range 0 to 0.1. However, if the function of the member is such that the amount of inelastic strain required for the strength to be insensitive to the notch is restricted, the value of q may approach 1.0 ($K_e = K_t$). If the member is loaded statically and is also subjected to shock loading, or if the part is to be subjected to high (Davis and Manjoine 1952) or low temperature, or if the part contains sharp discontinuities, a ductile material may behave in the manner of a brittle material, which should be studied with fracture mechanics methods. These are special cases. If there is doubt, K_t should be applied ($q = 1$). Ordinarily, for static loading of a ductile material, set $q = 0$ in Eq. (1.48), namely $\sigma_{max} = \sigma_{nom}$.[3]

Traditionally, design safety is measured by the *factor of safety n*. It is defined as the ratio of the load that would cause failure of the member to the working stress on the member. For ductile

[3]This consideration is on the basis of strength only. Stress concentration does not ordinarily reduce the strength of a notched member in a static test, but usually it does reduce total deformation to rupture. This means lower "ductility," or, expressed in a different way, less area under the stress-strain diagram (less energy expended in producing complete failure). It is often of major importance to have as much energy-absorption capacity as possible (cf. metal versus plastic for an automobile body). However, this is a consideration depending on consequence of failure, and so on, and is not within the scope of this book, which deals only with strength factors. Plastic behavior is involved in a limited way in the use of the factor L, as is discussed in this section.

material the failure is assumed to be caused by yielding and the equivalent stress σ_{eq} can be used as the working stress (the distortion energy criterion in Section 1.8.2). For axial loading (normal, or direct, stress $\sigma_1 = \sigma_{0d}$, $\sigma_2 = \sigma_3 = 0$):

$$n = \frac{\sigma_y}{\sigma_{0d}} \tag{1.102}$$

where σ_y is the yield strength and σ_{0d} is the static normal stress $= \sigma_{eq} = \sigma_1$. For bending ($\sigma_1, \sigma_{0b}, \sigma_2 = \sigma_3 = 0$),

$$n = \frac{L_b \sigma_y}{\sigma_{0b}} \tag{1.103}$$

where L_b is the limit safety factor for bending and σ_{0b} is the static bending stress.

In general, the limit safety factor L is the ratio of the load (force or moment) needed to cause complete yielding throughout the section of a bar to the load needed to cause initial yielding at the "extreme fiber" (Van den Broek 1942), assuming no stress concentration. For tension, $L = 1$; for bending of a rectangular bar, $L_b = 3/2$; for bending of a round bar, $L_b = 16/(3\pi) = 1.70$; for torsion of a round bar, $L_s = 4/3$; for a tube, it can be shown that for bending and torsion, respectively,

$$\left.\begin{aligned} L_b &= \frac{16}{3\pi}\left[\frac{1-(d_i/d_0)^3}{1-(d_i/d_0)^4}\right] \\ L_s &= \frac{4}{3}\left[\frac{1-(d_i/d_0)^3}{1-(d_i/d_0)^4}\right] \end{aligned}\right\} \tag{1.104}$$

Where d_i and d_0 are the inside and outside diameters, respectively, of the tube. These relations are plotted in Fig. 1.62.

Criteria other than complete yielding can be used. For a rectangular bar in bending, L_b values have been calculated (Steele et al. 1952), yielding to 1/4 depth $L_b = 1.22$, and yielding to 1/2 depth $L_b = 1.375$; for 0.1% inelastic strain in steel with yield point of 30,000 psi, $L_b = 1.375$. For a circular bar in bending, yielding to 1/4 depth, $L_b = 1.25$, and yielding to 1/2 depth, $L_b = 1.5$. For a tube $d_i/d_0 = 3/4$: yielding 1/4 depth, $L_b = 1.23$, and yielding 1/2 depth, $L_b = 1.34$.

All the foregoing L values are based on the assumption that the stress-strain diagram becomes horizontal after the yield point is reached, that is, the material is *elastic*, *perfectly plastic*. This is a reasonable assumption for low- or medium-carbon steel. For other stress-strain diagrams which can be represented by a sloping line or curve beyond the elastic range, a value of L closer to 1.0 should be used (Van den Broek 1942). For design L,σ_y should not exceed the tensile strength σ_{ut}.

For torsion of a round bar (shear stress), the safety factor can be determined as,

$$n = \frac{L_s \tau_y}{\tau_0} = \frac{L_s \sigma_y}{\sqrt{3}\tau_0} \tag{1.105}$$

where τ_y is the yield strength in torsion and τ_0 is the static shear stress.

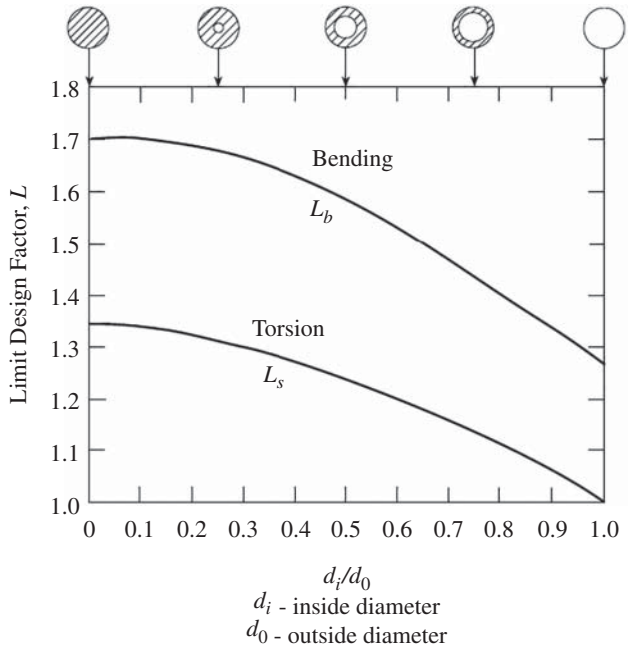


Figure 1.62 Limit safety factors for tubular members.

For combined normal (axial and bending) and shear stress the principal stresses are

$$\sigma_1 = \frac{1}{2}\left(\sigma_{0d} + \frac{\sigma_{0b}}{L_b}\right) + \frac{1}{2}\sqrt{\left[\sigma_{0d} + \frac{\sigma_{0b}}{L_b}\right]^2 + 4\left(\frac{\tau_0}{L_s}\right)^2} \tag{1.106}$$

$$\sigma_2 = \frac{1}{2}\left(\sigma_{0d} + \frac{\sigma_{0b}}{L_b}\right) - \frac{1}{2}\sqrt{\left[\sigma_{0d} + \frac{\sigma_{0b}}{L_b}\right]^2 + 4\left(\frac{\tau_0}{L_s}\right)^2} \tag{1.107}$$

where σ_{0d} is the static axial stress and σ_{0b} is the static bending stress. Since $\sigma_3 = 0$, the equilibrant von Mises theory is given by

$$\sigma_{eq} = \sqrt{\sigma_1^2 - \sigma_1\sigma_2 + \sigma_1^2}$$

so that

$$n = \frac{\sigma_y}{\sigma_{eq}} = \frac{\sigma_y}{\sqrt{\left[\sigma_{0d} + \frac{\sigma_{0b}}{L_b}\right]^2 + 3\left(\frac{\tau_0}{L_s}\right)^2}} \tag{1.108}$$

1.17.2 Brittle Materials

It is customary to apply the full K_t factor in the design of members of brittle materials. The use of the full K_t factor for cast iron may be considered, in a sense, as penalizing this material

unduly, since experiments show that the full effect is usually not obtained (Roark et al. 1938). The use of the full K_t factor may be partly justified as compensating, in a way, for the poor shock resistance of brittle materials. Since it is difficult to design rationally for shock or mishandling in transportation and installation, the larger sections obtained by the preceding rule may be a means of preventing some failures that might otherwise occur. However, notable designs of cast-iron members have been made (large paper-mill rolls, etc.) involving rather high stresses where full application of stress concentration factors would rule out this material. Such designs should be carefully made and may be viewed as exceptions to the rule. For ordinary design it seems wise to proceed cautiously in the treatment of notches in brittle materials, especially in critical load-carrying members.

The following factors of safety are based on the *maximum stress criterion* of failure of Section 1.8. For axial tension or bending (normal stress),

$$n = \frac{\sigma_{ut}}{K_t \sigma_0} \tag{1.109}$$

where σ_{ut} is the tensile ultimate strength, K_t is the stress concentration factor for normal stress, and σ_0 is the normal stress. For torsion of a round bar (shear stress),

$$n = \frac{\sigma_{ut}}{K_{ts} \sigma_0} \tag{1.110}$$

where K_{ts} is the stress concentration factor for shear stress and τ_0 is the static shear stress.

The following factors of safety are based on the failure criterion of the Modified Mohr's theory. Since the factors based on Mohr's theory are on the "safe side" compared to those based on the maximum stress criterion, they are suggested for design use. For torsion of a round bar (shear stress), the factor of safety can be found as,

$$n = \frac{\sigma_{ut}}{K_{ts} \tau_0} \left[\frac{1}{1 + \sigma_{ut}/\sigma_{uc}} \right] \tag{1.111}$$

where σ_{ut} is the tensile ultimate strength and σ_{uc} is the compressive ultimate strength. For combined normal and shear stress,

$$n = \frac{2\sigma_{ut}}{K_t \sigma_0 (1 - \sigma_{ut}/\sigma_{uc}) + (1 + \sigma_{ut}/\sigma_{uc}) \sqrt{(K_t \sigma_0)^2 + 4(K_{ts} \tau_0)^2}} \tag{1.112}$$

1.18 DESIGN RELATIONS FOR ALTERNATING STRESS

1.18.1 Ductile Materials

For alternating (completely reversed cyclic) stress, the stress concentration effects must be considered. As explained in Section 1.16, the fatigue notch factor K_f is usually less than the stress concentration factor K_t. The factor K_{tf} represents a calculated estimate of the actual fatigue notch factor K_f. Naturally, if K_f is available from tests, one uses this, but a designer is very seldom in

such a fortunate position. The expression for K_{tf} and K_{tsf}, Eqs. (1.99) and (1.100), respectively, are repeated here:

$$\left.\begin{aligned} K_{tf} &= q(K_t - 1) + 1 \\ K_{tsf} &= q(K_{ts} - 1) + 1 \end{aligned}\right\} \tag{1.113}$$

The following expressions for factors of safety, are based on the distort energy theory as discussed in Section 1.8.2:

For axial or bending loading (normal stress),

$$n = \frac{\sigma_f}{K_{tf}\sigma_a} = \frac{\sigma_f}{[q(K_t - 1) + 1]\sigma_a} \tag{1.114}$$

where σ_f is the fatigue limit (endurance limit) in axial or bending test (normal stress) and σ_a is the alternating normal stress amplitude.

For torsion of a round bar (shear stress),

$$n = \frac{\tau_f}{K_{tsf}\tau_a} = \frac{\sigma_f}{\sqrt{3}K_{ts}\tau_a} = \frac{\sigma_f}{\sqrt{3}[q(K_{ts} - 1) + 1]\tau_a} \tag{1.115}$$

where τ_f is the fatigue limit in torsion and τ_a is the alternating shear stress amplitude.

For combined normal stress and shear stress,

$$n = \frac{\sigma_f}{\sqrt{(K_{tf}\sigma_a)^2 + (K_{tsf}\tau_a)^2}} \tag{1.116}$$

By rearranging Eq. (1.68), the equation for an ellipse is obtained,

$$\frac{\sigma_a^2}{(\sigma_f/(nK_{tf}))^2} + \frac{\tau_a^2}{(\sigma_f/(n\sqrt{3}K_{tsf}))^2} = 1 \tag{1.117}$$

where $\sigma_f/(nK_{tf})$ and $\sigma_f/(n\sqrt{3}K_{tsf})$ are the major and minor semiaxes. Fatigue tests of unnotched specimens by Gough and Pollard (1935) and by Nisihara and Kawamoto (1940) are in excellent agreement with the elliptical relation. Fatigue tests of notched specimens (Gough and Clenshaw 1951) are not in as good agreement with the elliptical relation as are the unnotched, but for design purposes the elliptical relation seems reasonable for ductile materials.

1.18.2 Brittle Materials

Since our knowledge in this area is very limited, it is suggested that unmodified K_t factors be used. The Coulumb-Mohrs theory in Section 1.8, with $\sigma_{ut}/\sigma_{uc} = 1$, is suggested for design purposes for brittle materials subjected to alternating stress.

For axial or bending loading (normal stress),

$$n = \frac{\sigma_f}{K_t\sigma_a} \tag{1.118}$$

For torsion of a round bar (shear stress),

$$n = \frac{\tau_f}{K_{ts}\tau_a} = \frac{\sigma_f}{2K_{ts}\tau_a} \tag{1.119}$$

For combined normal stress and shear stress,

$$n = \frac{\sigma_f}{\sqrt{(K_t\sigma_a)^2 + (K_{ts}\tau_a)^2}} \tag{1.120}$$

1.19 DESIGN RELATIONS FOR COMBINED ALTERNATING AND STATIC STRESSES

The majority of important strength problems comprises neither simple static nor alternating cases, but involves fluctuating stress, which is a combination of both. A cyclic fluctuating stress (Fig. 1.63) having a maximum value $\sigma_{\max}$ and minimum value $\sigma_{\min}$ can be considered as having an *alternating component* of amplitude

$$\sigma_a = \frac{\sigma_{\max} - \sigma_{\min}}{2} \tag{1.121}$$

and a steady or mean component

$$\sigma_0 = \frac{\sigma_{\max} + \sigma_{\min}}{2} \tag{1.122}$$

1.19.1 Ductile Materials

In designing parts to be made of ductile materials for normal temperature use, it is the usual practice to apply the stress concentration factor to the alternating component but not to the

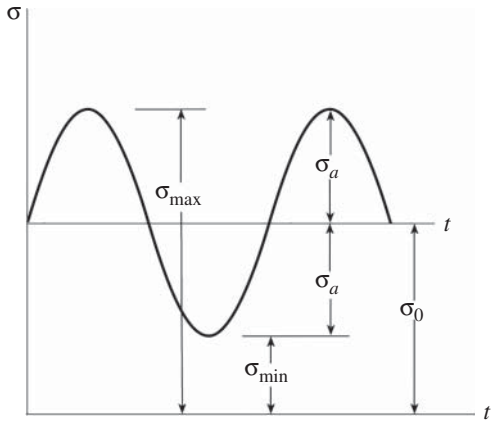


Figure 1.63 Combined alternating and steady stresses.

static component. This appears to be a reasonable procedure and is in conformity with test data (Houdremont and Bennek 1932), such as that shown in Fig. 1.64*a*. The limitations discussed in Section 1.17 still apply.

By plotting minimum and maximum limiting stresses in Fig. 1.64*a*, the relative positions of the static properties, such as yield strength and tensile strength, are clearly shown. However, one can also use a simpler representation, such as that of Fig. 1.64*b*, with the alternating component as the ordinate.

If, in Fig. 1.64*a*, the curved lines are replaced by straight lines connecting the end points σ_f and σ_f, σ_f/K_{tf} and σ_u, we have a simple approximation which is on the safe side for steel members.[4] From Fig. 1.64*b* we can obtain the following simple rule for factor of safety:

$$n = \frac{1}{(\sigma_0/\sigma_u) + (K_{tf}\sigma_a/\sigma_f)} \tag{1.123}$$

This is the same as the following Soderberg rule (Pilkey 2005), except that σ_u is used instead of σ_y. Soderberg's rule is based on the yield strength (see lines in Fig. 1.64 connecting σ_f and σ_y, σ_f/K_{tf}:

$$n = \frac{1}{(\sigma_0/\sigma_y) + (K_{tf}\sigma_a/\sigma_f)} \tag{1.124}$$

By referring to Fig. 1.64*b*, it can be shown that $n = OB/OA$. Note that in Fig. 1.64*a*, the pulsating (0 to max) condition corresponds to $\tan^{-1}2$ or 63.4°, which in Fig. 1.64*b* is 45°.

Equation (1.123) may be further modified to be in conformity with Eqs. (1.102) and (1.103), which means applying limit design for yielding, with the factors and considerations as stated in Section 1.17.1:

$$n = \frac{1}{(\sigma_{0d}/\sigma_y) + (\sigma_{0b}/L_b\sigma_y) + (K_{tf}\sigma_a/\sigma_f)} \tag{1.125}$$

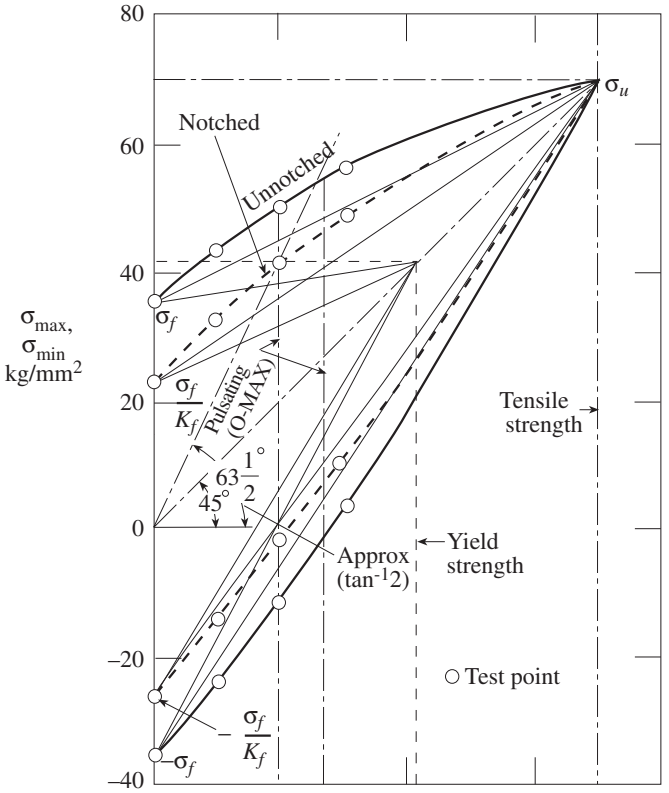
As mentioned previously $L_b\sigma_y$ must not exceed σ_u. That is, the factor of safety n from Eq. (1.125) must not exceed n from Eq. (1.124).

For torsion, the same assumptions and use of the von Mises criterion result in:

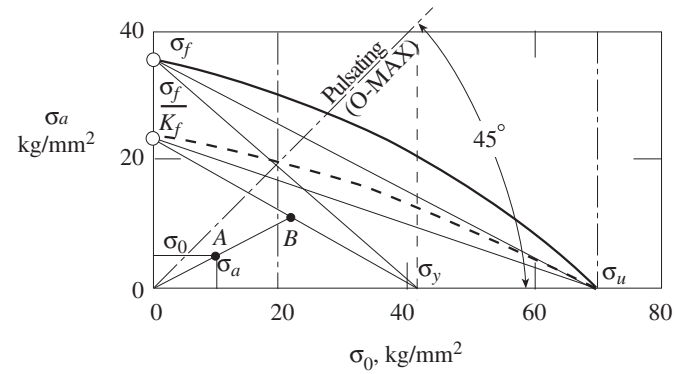
$$n = \frac{1}{\sqrt{3}[(\tau_0/L_s\sigma_y) + (K_{tsf}\tau_a/\sigma_f)]} \tag{1.126}$$

For notched specimens Eq. (1.126) represents a design relation, being on the safe edge of test data (Smith 1942). It is interesting to note that, for unnotched torsion specimens, static torsion (up to a maximum stress equal to the yield strength in torsion) does not lower the limiting alternating torsional range. It is apparent that further research is needed in the torsion region; however, since

[4]For steel members, a cubic relation (Peterson 1952; Nichols 1969) fits available data fairly well, $\sigma_a = [\sigma_f/(7K_{tf})]\left\{8 - \left[\frac{\sigma_m}{\sigma_u} + 1\right]^3\right\}$. This is the equation for the lower full curve of Figure 1.64*b*. For certain aluminum alloys, the σ_a, σ_m curve has a shape (Lazan and Blatherwick 1952) that is concave slightly below the σ_f/K_f, σ_u line at the upper end and is above the line at the lower end.



(a) Limiting minimum and maximum values



(b) Limiting alternating and steady components

Figure 1.64 Limiting values of combined alternating and steady stresses for plain and notched specimens (data from Schenck, 0.7% C steel, Houdremont and Bennek 1932).

notch effects are involved in design (almost without exception), the use of Eq. (1.126) is indicated. Even in the absence of stress concentration, Eq. (1.126) would be on the "safe side," though by a large margin for relatively large values of statically applied torque.

For a combination of *static* (*steady) and alternating normal stresses plus static and alternating shear stresses* (alternating components in phase) the following relation, derived by Soderberg (1930), is based on expressing the shear stress on an arbitrary plane in terms of static and alternating components, assuming failure is governed by the maximum shear theory and a "straight-line" relation similar to Eq. (1.124) and finding the plane that gives a minimum factor of safety n (Peterson 1953):

$$n = \frac{1}{\sqrt{[\sigma_0/\sigma_y + (K_t\sigma_a/\sigma_f)]^2 + 4[\tau_0/\sigma_y + (K_{ts}\tau_a/\sigma_f)]^2}} \tag{1.127}$$

The following modifications are made to correspond to the end conditions represented by Eqs. (1.102), (1.103), (1.105), (1.114), and (1.115). Then Eq. (1.127) becomes

$$n = \frac{1}{\sqrt{[\sigma_{0d}/\sigma_y + \sigma_{0b}/(L_b\sigma_y) + (K_{tf}\sigma_a/\sigma_f)]^2 + 3[\tau_0/(L_s\sigma_y) + (K_{tsf}\tau_a/\sigma_f)]^2}} \tag{1.128}$$

For steady stress only, Eq. (1.128) reduces to Eq. (1.108).

For alternating stress only, Eq. (1.128) reduces to Eq. (1.116).

For normal stress only, Eq. (1.128) reduces to Eq. (1.125).

For torsion only, Eq. (1.128) reduces to Eq. (1.126).

In tests by Ono (1921, 1929) and by Lea and Budgen (1926) the alternating bending fatigue strength was found not to be affected by the addition of a static (steady) torque (less than the yield torque). Other tests reported in a discussion by Davies (1935) indicate a lowering of the bending fatigue strength by the addition of static torque. Hohenemser and Prager (1933) found that a static tension lowered the alternating torsional fatigue strength; Gough and Clenshaw (1951) found that steady bending lowered the torsional fatigue strength of plain specimens but that the effect was smaller for specimens involving stress concentration. Further experimental work is needed in this area of special combined stress combinations, especially in the region involving the additional effect of stress concentration. In the meantime, while it appears that use of Eq. (1.128) may be overly "safe" in certain cases of alternating bending plus steady torque, it is believed that Eq. (1.128) provides a reasonable general design rule.

1.19.2 Brittle Materials

A "straight-line" simplification similar to that of Fig. 1.64 and Eq. (1.123) can be made for brittle material, except that the stress concentration effect is considered to apply also to the static (steady) component.

$$n = \frac{1}{K_t[(\sigma_0/\sigma_{ut}) + (\sigma_a/\sigma_f)]} \tag{1.129}$$

As previously mentioned, unmodified K_t factors are used for the brittle material cases.

For *combined shear and normal stresses*, data is very limited. For combined alternating bending and static torsion, Ono (1921) reported a decrease of the bending fatigue strength of cast iron as steady torsion was added. By use of the Soderberg method (Soderberg 1930) and basing failure on the normal stress criterion (Peterson 1953), we obtain

$$n = \frac{2}{K_t\left(\frac{\sigma_0}{\sigma_{ut}} + \frac{\sigma_a}{\sigma_f}\right) + \sqrt{K_t^2\left(\frac{\sigma_0}{\sigma_{ut}} + \frac{\sigma_a}{\sigma_f}\right)^2 + 4K_{ts}^2\left(\frac{\tau_0}{\sigma_{ut}} + \frac{\tau_a}{\sigma_f}\right)^2}} \tag{1.130}$$

A rigorous formula for combining Mohr's theory components of Eqs. (1.64) and (1.72) does not seem to be available. The following approximation, which satisfies Eqs. (1.61), (1.63), (1.70), and (1.71), may be of use in design, in the absence of a more exact formula.

$$n = \frac{2}{K_t\left(\frac{\sigma_0}{\sigma_{ut}} + \frac{\sigma_a}{\sigma_f}\right)\left(1 - \frac{\sigma_{ut}}{\sigma_{uc}}\right) + \left(1 + \frac{\sigma_{ut}}{\sigma_{uc}}\right)\sqrt{K_t^2\left(\frac{\sigma_0}{\sigma_{ut}} + \frac{\sigma_a}{\sigma_f}\right)^2 + 4K_{ts}^2\left(\frac{\tau_0}{\sigma_{ut}} + \frac{\tau_a}{\sigma_f}\right)^2}} \tag{1.131}$$

For steady stress only, Eq. (1.131) reduces to Eq. (1.112).
For alternating stress only, with $\sigma_{ut}/\sigma_{uc} = 1$, Eq. (1.131) reduces to Eq. (1.120).
For normal stress only, Eq. (1.131) reduces to Eq. (1.129).
For torsion only, Eq. (1.131) reduces to

$$n = \frac{1}{K_{ts}\left(\frac{\tau_0}{\sigma_{ut}} + \frac{\tau_a}{\sigma_f}\right)\left(1 + \frac{\sigma_{ut}}{\sigma_{uc}}\right)} \tag{1.132}$$

This in turn can be reduced to the component cases of Eqs. (1.111) and (1.119).

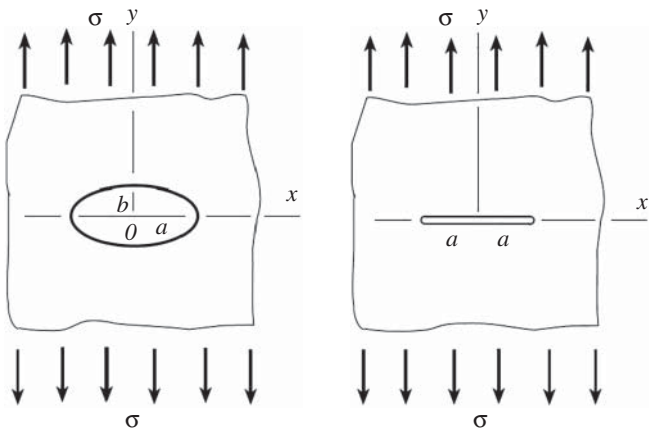
1.20 LIMITED NUMBER OF CYCLES OF ALTERNATING STRESS

In *Stress Concentration Safety Factors* (1953), Peterson presented formulas for a limited number of cycles (upper branch of the S-N diagram). These relations were based on an average of available test data and therefore apply to polished test specimens 0.2 to 0.3 in. diameter. If the member being designed is not too far from this size range, the formulas may be useful as a rough guide, but otherwise they are questionable, since the number of cycles required for a crack to propagate to rupture of a member depends on the size of the member.

Fatigue failure consists of three stages: *crack initiation, crack propagation,* and *rupture*. Crack initiation is thought not to be strongly dependent on size, although from statistical considerations of the number of "weak spots," one would expect some effect. So much progress has been made in the understanding of crack propagation under cyclic stress, that it is believed that reasonable estimates can be made for a number of problems.

1.21 STRESS CONCENTRATION FACTORS AND STRESS INTENSITY FACTORS

Consider an elliptical hole of major axis $2a$ and minor axis $2b$ in a plane element (Fig. 1.65*a*). If $b \to 0$ (or $a \gg b$), the elliptical hole becomes a crack of length $2a$ (Fig. 1.65*b*). The *stress intensity factor K* represents the strength of the elastic stress fields surrounding the crack tip (Pilkey 2005). It would appear that there might be a relationship between the stress concentration factor and the stress intensity factor. Creager and Paris (1967) analyzed the stress distribution around the tip of a crack of length $2a$ using the coordinates shown in Fig. 1.66. The origin O of



(a) Elliptic hole (b) Crack

Figure 1.65 Elliptic hole model of a crack as b → 0 .

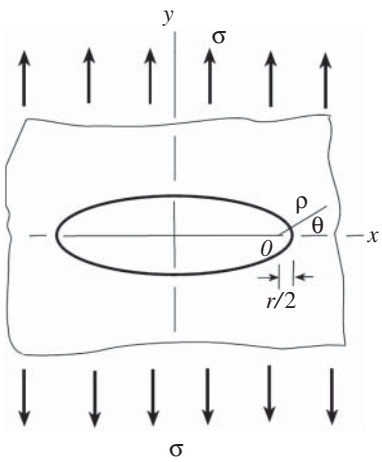


Figure 1.66 Coordinate system for stress at the tip of an ellipse.

the coordinates is set a distance of $r/2$ from the tip, in which r is the radius of curvature of the tip. The stress σ_y in the y direction near the tip can be expanded as a power series in terms of the radial distance. Discarding all terms higher than second order, the approximation for mode I fracture (Pilkey 2005, Sec. 7.2) becomes

$$\sigma_y = \sigma + \frac{K_I}{\sqrt{2\pi\rho}} \frac{r}{2\rho} \cos\frac{3\theta}{2} + \frac{K_I}{\sqrt{2\pi\rho}} \cos\frac{\theta}{2} \left(1 + \sin\frac{\theta}{2} \sin\frac{3\theta}{2}\right) \tag{1.133}$$

where σ is the tensile stress remote from the crack, (ρ, θ) are the polar coordinates of the crack tip with origin O (Fig. 1.66), K_I is the mode I stress intensity factor of the case in Fig. 1.65b. The maximum longitudinal stress occurs at the tip of the crack, that is, at $\rho = r/2,\ \theta = 0$. Substituting this condition into Eq. (1.133) gives

$$\sigma_{max} = \sigma + \frac{2K_I}{\sqrt{\pi r}} \tag{1.134}$$

However, the stress intensity factor can be written as (Pilkey 2005)

$$K_I = C\sigma\sqrt{\pi a} \tag{1.135}$$

where C is a constant that depends on the shape and the size of the crack and the specimen. Substituting Eq. (1.135) into Eq. (1.134), the maximum stress is

$$\sigma_{max} = \sigma + 2C\sigma\sqrt{\frac{a}{r}} \tag{1.136}$$

With σ as the reference stress, the stress concentration factor at the tip of the crack for a two-dimensional element subjected to uniaxial tension is

$$K_t = \frac{\sigma_{max}}{\sigma_{nom}} = 1 + 2C\sqrt{\frac{a}{r}} \tag{1.137}$$

Eq. (1.137) gives an approximate relationship between the stress concentration factor and the stress intensity factor. Due to the rapid development of fracture mechanics, a large number of crack configurations have been analyzed, and the corresponding results can be found in various handbooks. These results may be used to estimate the stress concentration factor for many cases. For instance, for a crack of length $2a$ in an infinite element under uniaxial tension, the factor C is equal to 1, so the corresponding stress concentration factor is

$$K_t = \frac{\sigma_{max}}{\sigma_{nom}} = 1 + 2\sqrt{\frac{a}{r}} \tag{1.138}$$

Eq. (1.138) is the same as found in Chapter 4 (Eq. 4.58) for the case of a single elliptical hole in an infinite element in uniaxial tension. It is not difficult to apply Eq. (1.137) to other cases.

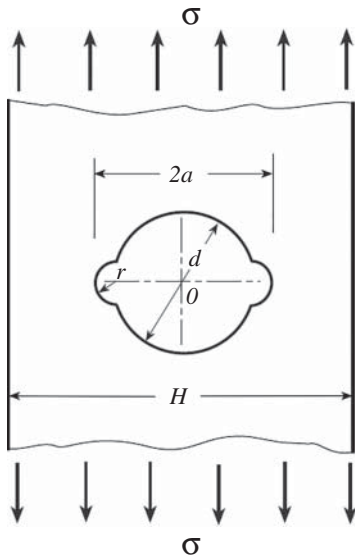


Figure 1.67 Element with a circular hole with two opposing semicircular lobes.

Example 1.9 Element with a Circular Hole with Opposing Semicircular Lobes Find the stress concentration factor of an element with a hole of diameter d and opposing semicircular lobes of radius r as shown in Fig. 1.67, which is under uniaxial tensile stress σ. Use known stress intensity factors. Suppose that $a/H = 0.1, r/d = 0.1$.

For this problem, choose the stress intensity factor for the case of radial cracks emanating from a circular hole in a rectangular panel as shown in Fig. 1.68. From Sih (1973) it is found that $C = 1.0249$ when $a/H = 0.1$. The crack length is $a = d/2 + r$ and $r/d = 0.1$, so

$$\frac{a}{r} = \frac{\frac{d}{2} + r}{r} = 1 + \frac{d}{2r} = 1 + \frac{1}{2 \times 0.1} = 6 \tag{1.139}$$

Substitute $C = 1.0249$ and $a/r = 6$ into Eq. (1.138),

$$K_t = 1 + 2 \times 1.0249 \times \sqrt{6} = 6.02 \tag{1.140}$$

The stress concentration factor for this case also can be found from Chart 4.61. Corresponding to $a/H = 0.1,\ r/d = 0.1$, the stress concentration factor based on the net area is

$$K_{tn} = 4.80 \tag{1.141}$$

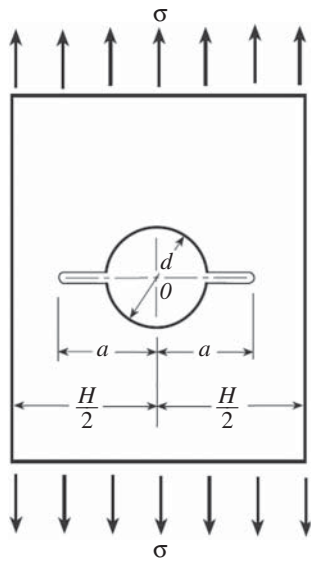


Figure 1.68 Element with a circular hole and a pair of equal length cracks.

The stress concentration factor based on the gross area is (Example 1.1)

$$K_t = \frac{K_{tn}}{1 - \frac{d}{h}} = \frac{4.80}{1 - 0.2} = 6.00 \tag{1.142}$$

The results of Eqs. (1.140) and (1.142) are very close.
Further results are listed below. It would appear that this kind of approximation is reasonable.

H	r/d	K_t From Eq. (1.137)	K_{tg} From Chart 4.61	% Difference
0.2	0.05	7.67	7.12	7.6
0.2	0.25	4.49	4.6	−2.4
0.4	0.1	6.02	6.00	0.33
0.6	0.1	6.2	6.00	0.3
0.6	0.25	4.67	4.7	−0.6

Shin et al. (1994) compared the use of Eq. (1.137) with the stress concentration factors obtained from handbooks and the finite element method. The conclusion is that in the range of practical engineering geometries where the notch tip is not too close to the boundary line of the element, the discrepancy is normally within 10%. Table 1.6 provides a comparison for a case in which two identical parallel ellipses in an infinite element are not aligned in the axial loading direction (Fig. 1.69).

TABLE 1.6 Stress Concentration Factors for the Configurations of Fig. 1.67

a/l	a/r	e/f	C	K_t	K_t From Eq. (1.89)	Discrepancy (90%)
0.34	87.1	0.556	0.9	17.84	17.80	−0.2
0.34	49	0.556	0.9	13.38	13.60	1.6
0.34	25	0.556	0.9	9.67	10.00	3.4
0.34	8.87	0.556	0.9	6.24	6.36	1.9
0.114	0.113	1.8	1.01	1.78	1.68	−6.0

Sources: Values for C from Shin et al. (1994); values for K_t from Murakami (1987).

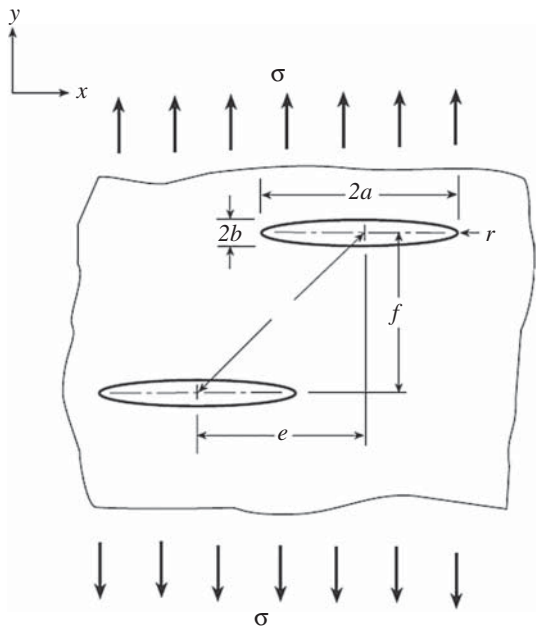


Figure 1.69 Infinite element with two identical ellipses that are not aligned in the direction.

1.22 SELECTION OF SAFETY FACTORS

A safety factor defines maximum allowable external load on a specific material when the uncertainties of materials, stresses, and loads are taken into consideration. However, when uncertainties are unknown, a safety factor must be specified appropriately to trade off the functionalities and costs of products. A safety factor is selected based on the level of uncertainties on both of materials and application environment, and Table 1.7 gives the guides of selecting the value of safety factor for the designs of machine elements in various applications.

TABLE 1.7 Guides for Selection of Safety Factors of Machine Elements in Different Applications

Recommended Safety Factor n_d	Applicable Scenarios
1.25–1.5	**Exceptionally reliable materials** used under **controllable conditions** and subjected to loads and stresses that can be determined **with certainty**: used almost invariably where low weight is a particularly important consideration.
1.5–2	**Well-known materials**, under reasonably constant environmental conditions, subjected to loads and stresses that can be determined readily.
2–2.5	**Average materials** operated in ordinary environments and subjected to loads and stresses that can be determined.
2.5–3	**Less tried or for brittle materials** under average conditions of environment, load, and stress.
3–4	**Untried materials** used under average conditions of environment, load, and stress or used with better known materials that are to be used in uncertain environments or subjected to uncertain stresses.
1.25–4	Repeated loads: the factors established in items 1–6 are acceptable but must be applied to the **endurance limit** rather than the yield strength of the material.
2–4	Impact forces: the factors given in items 3–6 are acceptable, but **an impact factor** should be included.
2.5–8	Brittle materials: where the ultimate strength is used as the theoretical maximum, the factors presented in items 1–6 should be approximately **doubled**.

TABLE 1.8 A List of Commonly Used Design Factors in Determining Safety Factor

No.	Design Factor	No.	Design Factor	No.	Design Factor
1	Functionalities*	10	Cost	18	Control
2	Strength/stress*	11	Friction	19	Surface*
3	Deflections/stiffness*	12	Weight	20	Lubrication
4	Wear*	13	Life*	21	Marketability
5	Corrosion	14	Noise	22	Maintenance
6	Safety*	15	Styling	22	Volume*
7	Reliability*	16	Shape*	23	Liability
8	Manufacturability	17	Size*	24	Recycling capability
9	Utility*				

** Highlighted design factors are related to stress analysis.*

Other than the functionalities of a product, other design considerations must also be taken into account in determining the value of a safety factor. Table 1.8 shows the priority list of commonly used design factors, which affect the determination of the safety factors, and the highlighted design factors are related to stress analysis.

REFERENCES

ASTM, 1994, *Annual Book of ASTM Standards*, Vol. 03.01, American Society for Testing and Materials, Philadelphia, PA.

Bi, Z. M., 2018, *Finite Element Analysis Application: A Systematic and Practical Approach*, Academic Press of Elsevier, ISBN: 9780128103999.

Boresi, A. P., Schmidt, R. J., and Sidebottom, O. M., 1993, *Advanced Mechanics of Materials*, 5th ed., Wiley, New York.

Carey, B., 2016, NTSB: corrosion, fatigue cracking behind 2016 FedEx landing accident, http://atwonline.com/safety/ntsb-corrosion-fatigue-cracking-behind-2016-fedex-landing-accident.

Creager, M., and Paris, P. C., 1967, Elastic field equations for blunt cracks with reference to stress corrosion cracking, *Int. J. Fract. Mech*., Vol. 3, pp. 247–252.

Crisan, M., 2016, "Metal fatigue" fault in Norway crash helicopter, https://www.bbc.com/news/uk-scotland-north-east-orkney-shetland-36428236.

Davis, E. A., and Manjoine, M. J., 1952, Effect of notch geometry on rupture strength at elevated temperature, *Proc. ASTM*, Vol. 52.

Draffin, J. O., and Collins, W. L., 1938, Effect of size and type of specimens on the torsional properties of cast iron, *Proc. ASTM*, Vol. 38, p. 235.

Drew, C., and Mouawad, J., 2011, Scrutiny lags as jetlinears show the effects of age, https://www.nytimes.com/2011/04/18/business/18plane.html.

Durden, T., 2018, Fatal Southwest Airlines accident blamed on "metal fatigue" inside exploded engine: NTSB, https://www.zerohedge.com/news/2018-04-18/ntsb-says-fatal-southwest-airlines-crash-caused-metal-fatigue-inside-engine.

Durelli, A. J., 1982, *Stress Concentrations*, U.M. Project SF-CARS, School of Engineering, University of Maryland, Office of Naval Research, Washington, DC.

Fralich, R. W., 1959, Experimental investigation of effects of random loading on the fatigue life of notched cantilever beam specimens of 7075-T6 aluminum alloy, *NASA Memo 4-12-59L*, National Aeronautics and Space Administration, Washington, DC.

Gough, H. J., and Clenshaw, W. J., 1951, Some experiments on the resistance of metals to fatigue under combined stresses, *ARC R&M 2522*, Aeronautical Research Council, London.

Gough, H. J., and Pollard, H. V., 1935, Strength of materials under combined alternating stress, *Proc. Inst. Mech. Eng. London*, Vol. 131, p. 1, Vol. 132, p. 549.

Gunn, N. J. R, 1952, *Fatigue properties at low temperature on transverse and longitudinal notched specimens of DTD363A aluminum alloy, Tech. Note Met*. 163, Royal Aircraft Establishment, Farnborough, England.

Gunt, 2018, *Mechanical testing methods*, https://www.gunt.de/images/download/Mechanical-materials-testing-methods-basic-knowledge_english.pdf.

Hardy, S. J., Malik, N. H., 1992, A survey of post-Peterson Stress Concentration Factor Data, *Int. J Fatigue*, Vol. 14, No. 3, pp. 147–153.

Hohenemser, K., and Prager, W., 1933, Zur Frage der Ermüdungsfestigkeit bei mehrachsigen Spannungsuständen, *Metall*, Vol. 12, p. 342.

Houdremont, R., and Bennek, H., 1932, Federstähle, *Stahl Eisen*, Vol. 52, p. 660.

Howland, R. C. J., 1930, On the stresses in the neighborhood of a circular hole in a strip under tension, *Trans. R. Soc. London Ser. A*, Vol. 229, p. 67.

Ku, T.-C., 1960, Stress concentration in a rotating disk with a central hole and two additional symmetrically located holes, *J. Appl. Mech*., Vol. 27, Ser. E, No. 2, pp. 345–360.

Kuhn, P., and Hardrath, H. F., 1952, An engineering method for estimating notch-size effect in fatigue tests of steel, *NACA Tech. Note 2805*, National Advisory Committee on Aeronautics, Washington, DC.

Lazan, B. J., and Blatherwick, A. A., 1952, Fatigue properties of aluminum alloys at various direct stress ratios, *WADC TR 52-306 Part I*, Wright-Patterson Air Force Base, Dayton, OH.

Lazan, B. J., and Blatherwick, A. A., 1953, Strength properties of rolled aluminum alloys under various combinations of alternating and mean axial stresses, *Proc. ASTM*, Vol. 53, p. 856.

Lea, F. C., and Budgen, H. P., 1926, Combined torsional and repeated bending stresses, *Engineering London*, Vol. 122, p. 242.

Leven, M. M., 1955, Quantitative three-dimensional photoelasticity, *Proc. SESA*, Vol. 12, No. 2, p. 167.

Little, R. W., 1973, *Elasticity*, Prentice-Hall, Englewood Cliffs, NJ, p. 160.

McLaren, N, 2016, Undetected stress fatigue crack caused wing to break off in water bombing plane crash that killed pilot David Black, http://www.abc.net.au/news/2016-02-16/south-coast-dromader-crash-final-report-released/7170920.

Murakami, Y., 1987, *Stress Intensity Factor Handbook*, Pergamon Press, Elmsford, NY.

Murakami, Y., 2017, Theory of Elasticity and Stress Concentration, Wiley, New York, ISBN: 9781119274063 |DOI:10.1002/9781119274063, 2017.

Neuber, H., 1958, *Kerbspannungslehre*, 2nd ed. (in German), Springer-Verlag, Berlin; translation, 1961, *Theory of Notch Stresses*, Office of Technical Services, U.S. Department of Commerce, Washington, DC, 1961, p. 207.

Neuber, H., 1968, Theoretical determination of fatigue strength at stress concentration, *Rep. AFML-TR-68-20*, Air Force Materials Laboratory, Wright-Patterson Air Force Base, Dayton, OH.

Newton, R. E., 1940, A photoelastic study of stresses in rotating disks, *J. Appl. Mech.*, Vol. 7, p. 57.

Nichols, R. W., Ed., 1969, *A Manual of Pressure Vessel Technology*, Elsevier, London, Chap. 3.

Nishida, M., 1976, *Stress Concentration*, Mori Kita Press, Tokyo (in Japanese).

Nisihara, T., and Kawamoto, A., 1940, The strength of metals under combined alternating stresses, *Trans. Soc. Mech. Eng. Jpn*., Vol. 6, No. 24, p. S-2.

Ono, A., 1921, Fatigue of steel under combined bending and torsion, *Mem. Coll. Eng. Kyushu Imp. Univ.*, Vol. 2, No. 2.

Ono, A., 1929, Some results of fatigue tests of metals, *J. Soc. Mech. Eng. Jpn*., Vol. 32, p. 331.

Peterson, R. E., 1933a, Stress concentration phenomena in fatigue of metals, *Trans. ASME Appl. Mech. Sect*., Vol. 55, p. 157.

Peterson, R. E., 1933b, Model testing as applied to strength of materials, *Trans. ASME Appl. Mech. Sect*., Vol. 55, p. 79.

Peterson, R. E., 1938, Methods of correlating data from fatigue tests of stress concentration specimens, *Stephen Timoshenko Anniversary Volume*, Macmillan, New York, p. 179.

Peterson, R. E., 1943, Application of stress concentration factors in design, *Proc. Soc. Exp. Stress Anal*., Vol. 1, No. 1, p. 118.

Peterson, R. E., 1945, Relation between life testing and conventional tests of materials, *ASTA Bull*., p. 13.

Peterson, R. E., 1950, Relation between stress analysis and fatigue of metals, *Proc. Soc. Exp. Stress Anal*., Vol. 11, No. 2, p. 199.

Peterson, R. E., 1952, Brittle fracture and fatigue in machinery, in *Fatigue and Fracture of Metals*, Wiley, New York, p. 74.

Peterson, R. E., 1953, *Stress Concentration Design Factors*, Wiley, New York.

Peterson, R. E., 1959, Analytical approach to stress concentration effect in aircraft materials, *Tech. Rep. 59-507*, U.S. Air Force–WADC Symposium on Fatigue of Metals, Dayton, OH, p. 273.

Peterson, R. E., 1974, *Stress Concentration Factors*, Wiley, New York.

Peterson, R. E., and Wahl, A. M., 1936, Two and three dimensional cases of stress concentration and comparison with fatigue tests, *Trans. ASME Appl. Mech. Sect*., Vol. 57, p. A-15.

Pilkey, W. D., 2005, *Formulas for Stress, Strain, and Structural Matrices*, 2nd ed., Wiley, Hoboken, NJ.

Pilkey, W. D., and Wunderlich, W., 1993, *Mechanics of Structures: Variational and Computational Methods*, CRC Press, Boca Raton, FL.

Roark, R. J., Hartenberg, R. S., and Williams, R. Z., 1938, The influence of form and scale on strength, *Univ. Wisc. Exp. Stn. Bull*. 84.

Safarian, P., 2014, Fatigue and damage tolerance requirements of civil aviation, Davies, V. C., 1935, Discussion based on theses of S. K. Nimhanmimie and W. J. Huitt (Battersea Polytechnic), *Proc. Inst. Mech. Eng. London*, Vol. 131, p. 66.

Shin, C. S., Man, K. C., and Wang, C. M., 1994, A practical method to estimate the stress concentration of notches, *Int. J. Fatigue*, Vol. 16, No. 4, pp. 242–256.

Sih, G. C., 1973, *Handbook of Stress Intensity Factors*, Lehigh University, Bethlehem, PA.

Smith, J. O., 1942, The effect of range of stress on the fatigue strength of metals, *Univ. Ill. Exp. Stn. Bull*. 334.

Soderberg, C. R., 1930, Working stress, *Trans. ASME*, Vol. 52, Pt. 1, p. APM 52–2.

Steele, M. C., Liu, C. K., and Smith, J. O., 1952, Critical review and interpretation of the literature on plastic (inelastic) behavior of engineering metallic materials, research report, Department of Theoretical and Applied Mechanics, University of Illinois, Urbana, IL.

Templin, R. L., 1954, Fatigue of aluminum, *Proc. ASTM*, Vol. 54, p. 641.

Timoshenko, S., and Goodier, J. N., 1970, *Theory of Elasticity*, McGraw-Hill, New York.

Van den Broek, J. A., 1942, *Theory of Limit Design*, Wiley, New York.

Von Phillipp, H. A., 1942, Einfluss von Querschittsgrösse und Querschittsform auf die Dauerfestigkeit bei ungleichmässig verteilten Spannungen, *Forschung*, Vol. 13, p. 99.

Sources of Stress Concentration Factors

Neuber, H., 1958, *Theory of Notch Stresses*, 2nd ed., Springer-Verlag, Berlin; translation, 1961, Office of Technical Services, U.S. Department of Commerce, Washington, DC.

Nishida, M., 1976, *Stress Concentration*, Mori Kita Press, Tokyo (in Japanese).

Pilkey, W. D., 2005, *Formulas for Stress, Strain, and Structural Matrices*, 2nd ed., Wiley, Hoboken, NJ.

Wikipedia, 2018, *Mohr's circle*, https://en.wikipedia.org/wiki/Mohr%27s_circle.

CHAPTER 2

NOTCHES AND GROOVES

2.1 NOTATION

Definition:

Panel. A thin flat element with in-plane loading. This is a sheet that is sometimes called as membrane.

Symbols:

SCF = Stress Concentration Factor

a = width of a notch or semimajor axis of an ellipse

b = distance between notch centers or semiminor axis of an ellipse

c = distance between notch centers

d = minimum diameter (for three-dimensional) or minimum width (for two-dimensional) of member

D = diameter of member

h_o = minimum thickness of a thin element

h = thickness of a thin element

H = height or width of member

K_t = stress concentration factor (SCF)

K_{tg} = stress concentration factor (SCF) with the nominal stress based on gross area

K_{tn} = stress concentration factor (SCF) with the nominal stress based on net area

Peterson's Stress Concentration Factors, Fourth Edition. Walter D. Pilkey, Deborah F. Pilkey and Zhuming Bi.
© 2020 John Wiley & Sons, Inc. Published 2020 by John Wiley & Sons, Inc.

L = length of member
m = bending moment per unit length
M = bending moment
P = total applied in-plane force
r = radius of a notch, notch bottom radius
t = depth of a notch
T = torque
α = open angle of notch
ν = Poisson's ratio
σ = normal stress
τ = shear stress

2.2 STRESS CONCENTRATION FACTORS

A U-shaped notch or circumferential groove is a geometrical shape of considerable interest in engineering. It occurs in some machine elements such as in turbine rotors between blade rows and at seals. Other examples are found in a variety of shafts shown in Fig. 2.1, such as a shoulder relief groove or a retainer for a spring washer.

The round-bottomed V-shaped notch or circumferential groove, and to a lesser extent the U-shaped notch, are conventional contour shapes for the investigation of stress concentration in the areas of fatigue, creep-rupture, and brittle fracture. In addition, a threaded part may be considered as a member with multiple grooves.

As mentioned in Chapter 1, two basic K_t factors may be defined: i.e., (1) K_{tg} which is based on the larger (gross) section of width H and (2) K_{tn} which is based on the smaller (net) section

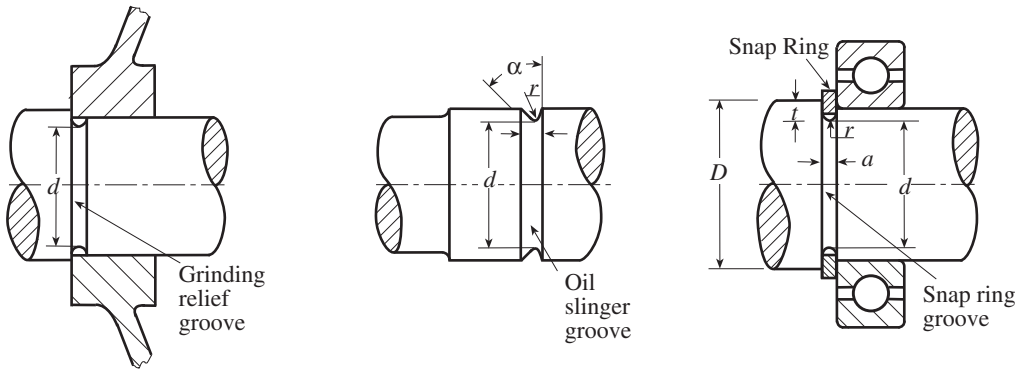


Figure 2.1 Examples of grooved shafts.

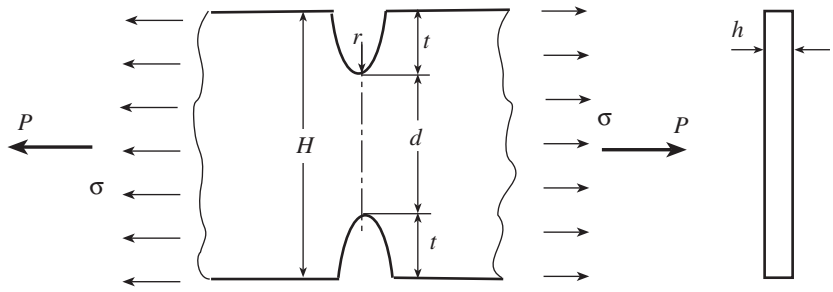


Figure 2.2 Bar with opposite notches.

of width d (Fig. 2.2). For tension, $K_{tg} = \sigma_{\max}/\sigma$, where $\sigma = P/hH$ and $K_{tn} = \sigma_{\max}/\sigma_{\text{nom}}$, and $\sigma_{\text{nom}} = P/hd$. Since design calculations are usually based on the critical section (width d) where $\sigma_{\max}$ is located, K_{tn} is the generally used factor. Unless otherwise specified, K_t refers to K_{tn} in this chapter.

Neuber (1958) finds the theoretical stress concentration factors for the deep hyperbolic notch (Fig. 2.3*a*) and the shallow elliptical notch (Fig. 2.3*b*) in infinitely wide members under tension, bending, and shear. These results will be given in this chapter. For finite width members, Neuber introduces the following ingenious simple relation for notches with arbitrary shapes:

$$K_{tn} = 1 + \sqrt{\frac{(K_{te} - 1)^2(K_{th} - 1)^2}{(K_{te} - 1)^2 + (K_{th} - 1)^2}} \tag{2.1}$$

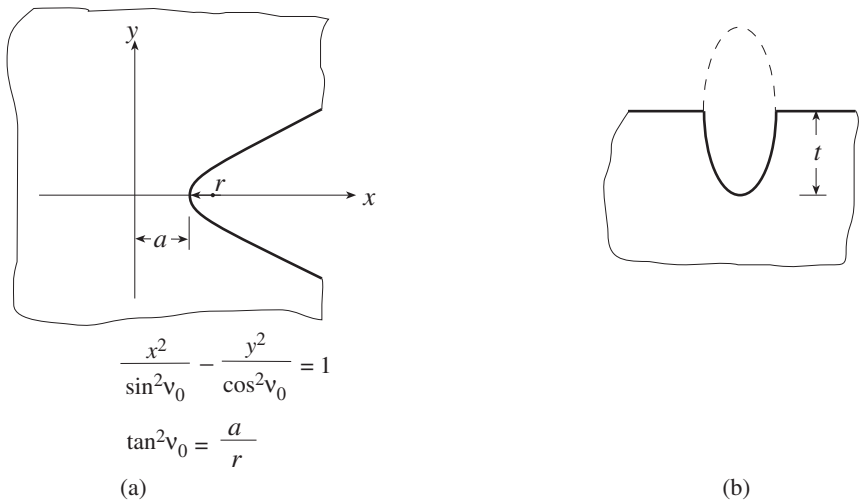


Figure 2.3 Notches: (*a*) deep hyperbolic; (*b*) shallow elliptical.

where K_{te} is the SCF for a shallow elliptical notch (with the same t/r as for the notch in the finite width member) in a semi-infinitely wide member, K_{th} is the SCF for a deep hyperbolic notch (with the same r/d as for the notch in the finite width member) in an infinitely wide member, t is the notch depth, r is the notch radius (minimum contour radius), d is a minimum diameter (three-dimensional) or minimum width (two-dimensional) of the member.

Here, a flat bar with opposite notches of arbitrary shape is considered as an example, and its design parameters are notch depth t, notch radius r, and a minimum bar width d. If K_{te} is the SCF of a shallow elliptical notch of Chart 2.2 with the same t/r and K_{th} is the SCF of a deep hyperbolic notch of Chart 2.1 with the same r/d, then K_{tn} of Eq. (2.1) is an estimation of the SCF of the flat bar with opposite notches.

Equation (2.1) is not exact enough; since recent investigations have provided more accurate values for the parameter ranges covered by the investigations, the results from these intigations will be presented in the following sections. If the actual member has a notch or groove that is either very deep or shallow, the Neuber approximation will be close. However, for a value of d/H in the region of $1/2$, the Neuber K_t can be as much as 12% below the actual SCF, and it is on the unsafe side from a design standpoint. More accurate values are desirable over the most used ranges of parameters. These form the basis of some of the charts presented here. However, when a value for an extreme condition such as a very small or large r/d is sought, the Neuber method seems the only analyical formulae to predict a SCF. Some charts covering the extreme ranges are also included in this book.

Another use of the charts of Neuber factors is in designing a test piece for the maximum K_t, which will be discussed in detail in Section 2.10.

In this chapter, the K_t factors of the flat members are covered, a flat member has two-dimensional states of stress (plane stresses) when the thichness is small; two-dimensional states apply strictly well to very thin sheets, and ideally to where $h/r \to 0$, where $h =$ element thickness and $r =$ notch radius. As h/r increases, a state of plane strain is approached, in which case the stress at the notch surface at the middle of the element thickness increases and the stress at the element surface decreases. As the beginning of Chapter 4, some guidance has been provided as the introductory remarks.

In general, the K_t factor for a notch can be lowered by use of a reinforcing bead (Suzuki 1967).

2.3 NOTCHES IN TENSION

2.3.1 Opposite Deep Hyperbolic Notches in an Infinite Thin Element; Shallow Elliptical, Semicircular, U-Shaped, or Keyhole-Shaped Notches in Semi-Infinite Thin Elements; Equivalent Elliptical Notch

Chart 2.1 gives the K_{tn} values for the deep ($d/H \to 0$) hyperbolic notch in an infinite thin element (Neuber 1958; Peterson 1953). Chart 2.2 provides the K_{tg} values for an elliptical or U-shaped notch in a semi-infinite thin element (Seika 1960; Bowie 1966; Barrata and Neal 1970). For a higher t/r value, the value of K_{tg} for the U-notch is up to 1% higher than for the elliptical notch. For practical purposes, the solid curve of Chart 2.2 covers both cases.

Many researchers have studied the semicircular notch ($t/r = 1$) in a semi-infinite thin element. Ling (1967) summarizes the K_t factors from different researchers:

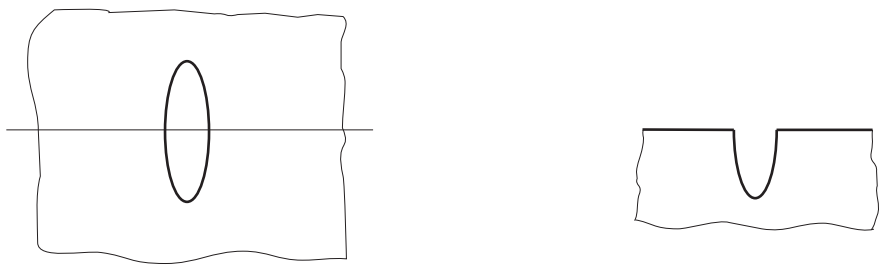
1936	Maunsell	3.05
1940	Isibasi	3.06
1941	Weinel	3.063
1948	Ling	3.065
1965	Yeung	3.06
1965	Mitchell	3.08

Similar to the "equivalent elliptical hole" in an infinite panel (see Section 4.5.1), an "equivalent elliptical notch" in a semi-infinite thin element may be defined as an elliptical notch that has the same t/r and envelops the notch geometry under consideration. All type of notches, U-shaped, and keyholes (circular hole connected to edge by saw cut) have very nearly the same K_t as the equivalent elliptical notch. Note that the "equivalent elliptical notch" applies for tension, and it is not applicable for shear.

SCFS have been approximated by splitting a thin element with a central hole axially through the middle of the hole shown in Fig. 2.4, and K_t is used for the hole to represent the resulting notches. From Eq. (1.138) the stress concentration factor for an elliptical hole in a thin element is

$$K_t = 1 + 2\sqrt{\frac{t}{r}} \tag{2.2}$$

where t is the semiaxis that is perpendicular to the tensile loading. Chart 2.2 shows this K_t also. The factors for the U-shaped slot (Isida 1955) are practically the same. A comparison of the curves for notches and holes in Chart 2.2 shows that the preceding approximation can be in error by as much as 10% for the larger values of t/r.



(a) (b)

Figure 2.4 Equivalent notch from splitting a thin element with a hole: (*a*) thin element with a hole; (*b*) half of thin element with a notch.

2.3.2 Opposite Single Semicircular Notches in a Finite-Width Thin Element

For a finite-width thin element with opposite semicircular notches subjected to tensile loading, Chart 2.3 gives K_{tg} and K_{tn} factors (Isida 1953; Ling 1968; Appl and Koerner 1968; Hooke 1968) where the difference of K_{tg} and K_{tn} are illustrated.

Here, a bar of constant width H and a constant force P is considered. As notches are cut deeper (increasing $2r/H$), K_{tn} decreases, reflecting a decreasing of stress concentration, which is defined by a ratio of the peak stress and average stress across d. This continues until $2r/H \to 1$, in effect a uniform stress tension specimen. The K_{tg} increases as $2r/H$ increases, reflecting the increase in $\sigma_{\max}$ owing to the loss of section. Slot (1972) finds that with $2r/H = 1/2$ in a strip of length $1.5H$, a good agreement is obtained with the stress distribution for σ applied at infinity.

2.3.3 Opposite Single U-Shaped Notches in a Finite-Width Thin Element

Strain gage tests (Kikukawa 1962), photoelastic tests (Flynn and Roll 1966), and mathematical analysis (Appl and Koerner 1969) provide the consistent data for the opposite U-shaped notches in a flat bar (two-dimensional case) in Chart 2.4. The cureve in Chart provides an important check of the mathematical results (Isida 1953; Ling 1968) for the semicircular notch (Chart 2.3), a special case of the U-notch. There is an excellent agreement for the values of $H/d \leq 2$. The photoelastic results (Wilson and White 1973) for $H/d = 1.05$ are also in a good agreement.

Barrata (1972) has compared empirical formulas for K_{tn} with the experimentally determined values, and he concludes that the following two formulas can predict SCFs satisfactorily.

Barrata and Neal (1970):

$$K_{tn} = \left(0.780 + 2.243\sqrt{\frac{t}{r}}\right)\left[0.993 + 0.180\left(\frac{2t}{H}\right) - 1.060\left(\frac{2t}{H}\right)^2 + 1.710\left(\frac{2t}{H}\right)^3\right]\left(1 - \frac{2t}{H}\right) \tag{2.3}$$

Heywood (1952):

$$K_{tn} = 1 + \left[\frac{t/r}{1.55(H/d) - 1.3}\right]^n \qquad n = \frac{H/d - 1 + 0.5\sqrt{t/r}}{H/d - 1 + \sqrt{t/r}} \tag{2.4}$$

with t the depth of a notch, $t = (H - d)/2$.

Referring to Chart 2.4, Eq. (2.3) gives the values; which are in good agreement with the solid curves for $r/d < 0.25$. Eq. (2.4) is in better agreement for $r/d > 0.25$. For the dashed curves (not the dot-dash curve for semicircular notches), Eq. (2.3) gives a lower value as r/d increases. The tests on which the formulas are based do not include the parameter values corresponding to the dashed curves, which are uncertain owing to their determination by interpolation of r/d curves having H/d as abscissae. In the absence of better basic data, the dashed curves, representing higher values, should be used for design.

In Chart 2.4, the values of r/d are from 0 to 0.3, and the values of H/d are from 1 to 2, which cover the most widely used parameter ranges. There is considerable evidence (Kikukawa 1962; Flynn and Roll 1966; Appl and Koerner 1969) that for greater values of r/d and H/d, the K_t versus H/d curve for a given r/d does not flatten out but reaches a peak value and then decreases slowly toward a somewhat lower K_t value as $H/d \to \infty$. The effect is small and is not shown in Chart 2.4.

In Chart 2.4, the range of parameters corresponds to the investigations of Kikukawa (1962), Flynn and Roll (1967), and Appl and Koerner (1969). For smaller and larger r/d values, the Neuber values (Eq. 2.1, Charts 2.5 and 2.6), although approximation, are the only wide-range values available and are useful for certain problems. The largest errors are at the midregion of d/H. For shallow or deep notches, the error becomes progressively smaller. Some specific photoelastic tests (Liebowitz et al. 1967) with $d/H \approx 0.85$ and r/H varying from ≈ 0.001 to 0.02 gave a higher K_{tn} value than does Chart 2.5.

2.3.4 Finite-Width Correction Factors for Opposite Narrow Single Elliptical Notches in a Finite-Width Thin Element

For a very narrow elliptical notch approaching a crack, the "finite-width correction" formulas have been proposed by Westergaard (1939), Irwin (1958), Bowie (1963), Dixon (1962), Brown and Strawley (1966), and Koiter (1965). The plots for opposite narrow edge notches are given by Peterson (1974).

The formula (Brown and Strawley 1966; Barrata and Neal 1970), which is based on Bowie's results for opposite narrow elliptical notches in a finite-width thin element (Fig. 2.2), is satisfactory for the values of $2t/H < 0.5$:

$$\frac{K_{tg}}{K_{t\infty}} = 0.993 + 0.180\left(\frac{2t}{H}\right) - 0.160\left(\frac{2t}{H}\right)^2 + 1.710\left(\frac{2t}{H}\right)^3 \tag{2.5}$$

where t is the crack length and $K_{t\infty}$ is K_t for $H = \infty$.

The following formula by Koiter (1965) covers the entire $2t/H$ range. For the lower $2t/H$ range, Eq. (2.5) shows a good agreement. For the mid-$2t/H$ range, Eq. (2.5) generates a somewhat lower value.

$$\frac{K_{tg}}{K_{t\infty}} = \left[1 - 0.50\left(\frac{2t}{H}\right) - 0.0134\left(\frac{2t}{H}\right)^2 + 0.081\left(\frac{2t}{H}\right)^3\right]\left[1 - \frac{2t}{H}\right]^{-1/2} \tag{2.6}$$

The gross area factor K_{tg} is related to the net area factor K_{tn} as

$$\frac{K_{tn}}{K_{t\infty}} = \frac{K_{tg}}{K_{t\infty}}\left(1 - \frac{2t}{H}\right) \tag{2.7}$$

2.3.5 Opposite Single V-Shaped Notches in a Finite-Width Thin Element

The $K_{t\alpha}$ factors have been obtained by Appl and Koerner (1969) for the flat tension bar with opposite V notches as a function of the V angle, α (Chart 2.7). The Leven-Frocht (1953) method of

relating $K_{t\alpha}$ to the K_{tu} of a corresponding U notch as used in Chart 2.7, shows that for $H/d = 1.66$, the angle has little effect up to 90°. For $H/d = 3$, it has little effect up to 60°. In comparing these results with Chart 2.28 where the highest value of H/d is 1.82, the agreement is good even though the two cases are different [symmetrical notches, in tension (Chart 2.7); notch on one side, in bending (Chart 2.28)].

2.3.6 Single Notch on One Side of a Thin Element

Neuber (1958) estimates the K_{tn} values for a semi-infinite thin element with a deep hyperbolic notch, and the tension loading is applied along a midline through the minimum section (Chart 2.8). Chart 2.9 presents the curves of K_{tn} based on photoelastic tests (Cole and Brown 1958). Corresponding Neuber K_{tn} factors obtained from Chart 2.8 and Eq. (2.1) are lower than the K_{tn} factors of Chart 2.9 about an average of 18%.

The curve for the semicircular notch is obtained by noting that for this case $r = H - d$ or $H/d = 1 + r/d$ and that $K_{tn} = 3.065$ at $r/d \to 0$.

2.3.7 Notches with Flat Bottoms

Chart 2.10 gives the stress concentration factors K_{tn} for opposing notches in finite-width thin elements, with flat bottoms (Hetényi and Liu 1956; Neuber 1958; Sobey 1965). Finite element analyses have given SCFs, which are up to 10% higher than the experimental results in Chart 2.10 (ESDU 1989).

Chart 2.11 provides the SCFs for a rectangular notch on the edge of a wide (semi-infinite) flat panel in tension (Rubenchik 1975; ESDU 1981). The maximum stress $\sigma_{\max}$ occurs at points A of the figure in Chart 2.11. When $a = 2r$, the notch base is semicircular, and two points A coincide at the base of the notch.

2.3.8 Multiple Notches in a Thin Element

It has long been recognized that a single notch represents a higher degree of stress concentration than a series of closely spaced notches of the same kind as the single notch. Considered from the standpoint of flow analogy, a smoother flow is obtained in Fig. 2.5*b* and *c*, than in Fig. 2.5*a*.

For the infinite row of semicircular edge notches, Atsumi (1958) obtains the SCF as a function of notch spacing and the relative width of a bar, which is summarized in Charts 2.12 and 2.13. For an infinite notch spacing, the K_{tn} factors are in agreement with the single-notch factors of Isida (1953) and Ling (1968) in Chart 2.3.

For a specific case with $r/H = 1/4$ and $b/a = 3$ by Slot (1972), a good agreement is obtained with the corresponding value by Atsumi (1958).

An analysis (Weber 1942) of a semi-infinite panel with an edge of wave form of depth t and minimum radius r gives $K_{tn} = 2.13$ for $t/r = 1$ and $b/a = 2$, which is in agreement with Chart 2.12.

Stress concentration factors K_{tn} are available for the case of an infinite row of circular holes in a panel stressed in tension in the direction of the row (Weber 1942; Schulz 1941, 1943–1945). If we consider the panel as split along the axis of the holes, the K_{tn} values should be nearly the

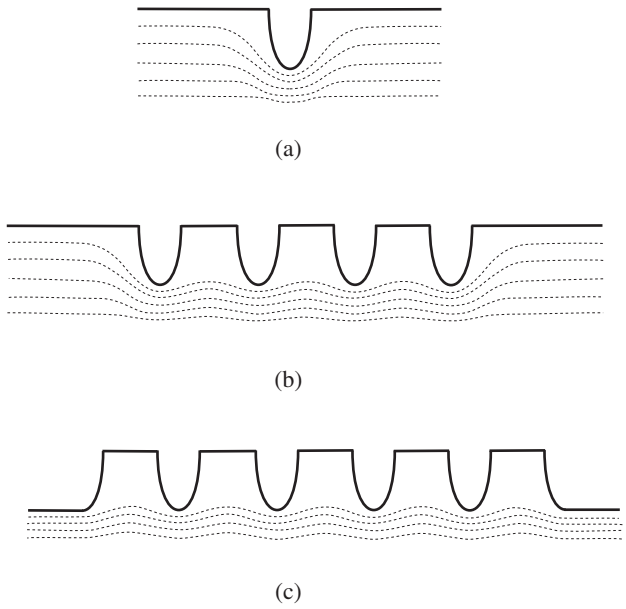


Figure 2.5 Multiple notches.

same (for the single hole, $K_{tn} = 3$; for the single notch, $K_{tn} = 3.065$). The K_{tn} curve for the holes as a function of b/a fits well (slightly below) the top curve of Chart 2.12.

For a finite number of multiple notches (Fig. 2.5*b*), the stress concentration of the intermediate notches is considerably reduced. The maximum stress concentration occurs at the end notches (Charts 2.14 and 2.15; Durelli et al. 1952), and this is also reduced (as compared to a single notch) but to a lesser degree than for the intermediate notches. Sometimes a member can be designed as in Fig. 2.5*c*, resulting in a reduction of stress concentration as compared to Fig. 2.5*b*.

Chart 2.13 includes the SCFs for two pairs of notches (Atsumi 1967) in a square pattern ($b/H = 1$).

Hetényi (1943) and Durelli et al. (1952) perform the photoelastic tests for various numbers (up to six) of semicircular notches. The results (Charts 2.14, 2.15, and 2.16) are consistent with the SCFs for the infinite row by the mathematical model by Atsumi (1958). Chart 2.16 provides, for comparison, K_{tg} for a groove that corresponds to a lower K_{tg} limit for any number of semicircular notches with overall edge dimension c.

For the Aero thread shape (semicircular notches with $b/a = 1.33$), two-dimensional photoelastic tests (Hetényi 1943) of six notches give K_t values of 1.94 for the intermediate notch and 2.36 for the end notch. For the Whitworth thread shape (V notch with rounded bottom), the corresponding photoelastic tests (Hetényi 1943) gave K_t values of 3.35 and 4.43, respectively.

Fatigue tests (Moore 1926) of threaded specimens and specimens having a single groove of the same dimensions have shown considerably higher strength for the threaded specimens.

2.3.9 Analytical Solutions for Stress Concentration Factors for Notched Bars

Gray et al. (1995) derive the closed-form expressions of the SCFs for thin bars in tension or bending with notches in terms of the depth of the notch, the end radius, and the width of the bar. They replace the shape of the notch as an equivalent ellipse or hyperbola. The closed-form relations are based on finite element analyses. Noda et al. (1995) provide the formulas for the SCFs for single-side and opposite notches under tension.

2.4 DEPRESSIONS IN TENSION

2.4.1 Hemispherical Depression (Pit) in the Surface of a Semi-Infinite Body

For a semi-infinite body with a hemispherical depression under equal biaxial stress (Fig. 2.6), Eubanks (1954) finds that K_t is 2.23 for Poisson's ratio $\nu = 1/4$. This is about 7% higher than for the corresponding case of a spherical cavity ($K_t = 2.09$ for $\nu = 1/4$) from Chart 4.73. Moreover, the semicircular edge notch in tension ($K_t = 3.065$) in Chart 2.2 is about 2% higher than the circular hole in tension ($K_t = 3$) in Chart 4.1 and Eq. (4.18).

2.4.2 Hyperboloid Depression (Pit) in the Surface of a Finite-Thickness Element

The hyperboloid depression simulates the type of pit caused by meteoroid impact of an aluminum panel (Denardo 1968). For equal biaxial stress (Fig. 2.7), the values of K_t in the range of 3.4 to

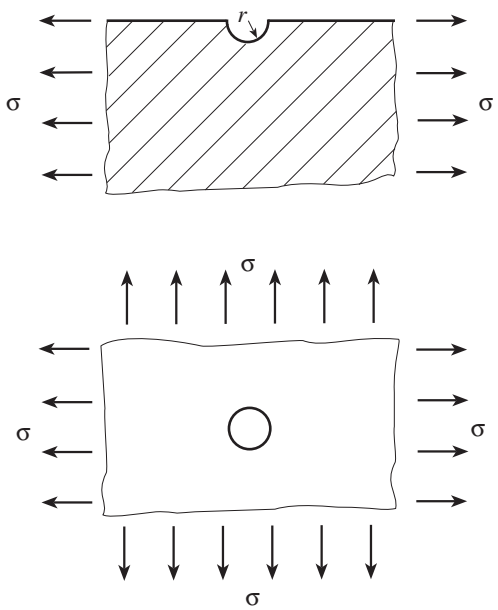


Figure 2.6 Semi-infinite body with a hemispherical depression under equal biaxial stress.

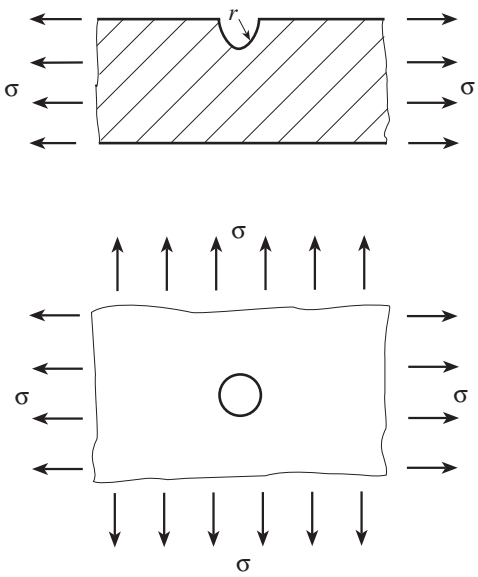


Figure 2.7 Hyperbolical depression in the surface of a finite thickness panel under equal biaxial stress.

3.8 are obtained for individual specific geometries by Reed and Wilcox (1970). They find that the K_t values are higher than for the complete penetration in the form of a circular hole ($K_t = 2$; see Eq. 4.17).

2.4.3 Opposite Shallow Spherical Depressions (Dimples) in a Thin Element

The geometry of opposite dimples in a thin element has been suggested for a test piece in which a crack at the thinnest location can progress only into a region of lower stress (Cowper 1962). Dimpling is often used to remove a small surface defect. If the depth is small relative to the thickness (h_o/h approaching 1.0 in Chart 2.17), the stress increase is small. The $K_{tg} = \sigma_{\max}/\sigma$ values are shown for uniaxial stressing in Chart 2.17. These values also apply for equal biaxial stressing.

The calculated values of Chart 2.17 are for a shallow spherical depression having a diameter greater than four or five times the thickness of the element. In terms of the variables given in Chart 2.17, the spherical radius is

$$r = \frac{1}{4}\left[\frac{d^2}{(h - h_o)} + (h - h_o)\right] \tag{2.8}$$

for $d \geq 5h$, $r/h_o > 25$. For such a relatively large radius, the stress increase for a thin section ($h_o/h \to 0$) is due to the thinness of section rather than stress concentration per se (i.e., stress gradient is not steep).

For comparison, a groove with the same sectional contour as the dimple is used. K_{tg} is shown by the dashed line on Chart 2.17, the K_{tg} values are calculated from the K_{tn} values of Chart 2.6. Note that in Chart 2.6, the K_{tn} values for $r/d = 25$ represent a stress concentration of about 1%. The K_{tg} factors therefore essentially represent the loss of the section.

The removal of a surface defect in a thick section by means of creating a relatively shallow spherical depression results in a negligible stress concentration, on the order of 1%.

2.5 GROOVES IN TENSION

2.5.1 Deep Hyperbolic Groove in an Infinite Member (Circular Net Section)

The exact K_t values for the Neuber's solution (Peterson 1953; Neuber 1958) are given in Chart 2.18 for a deep hyperbolic groove in an infinite member. Note that Poisson's ratio has only a relatively small effect.

2.5.2 U-Shaped Circumferential Groove in a Bar of Circular Cross Section

The K_{tn} values for a bar of circular cross section with a U groove (Chart 2.19) are obtained by multiplying the K_{tn} of Chart 2.4 by the ratio of the corresponding Neuber three-dimensional K_{tn} (Chart 2.18) over two-dimensional K_{tn} values (Chart 2.1). This is an approximation. However, after the comparison with the bending and torsion cases, the results seem reasonable.

The maximum stress occurs at the bottom of the groove. Cheng (1970) has obtained $K_{tn} = 1.85$ for $r/d = 0.209$ and $D/d = 1.505$ by the photoelastic test. The corresponding K_{tn} from Chart 2.19 is 1.92 agrees fairly well with Cheng's value evevn though he believes to be somewhat low. The finite element studies by ESDU (1989) have confirmed the stress concentration values in Chart 2.19 and Chart 2.22.

The K_{tn} factors approximated by the Neuber (1958) formula are given in Chart 2.20 for smaller r/d values and in Chart 2.21 for larger r/d values (e.g., test specimens).

2.5.3 Flat-Bottom Grooves

Chart 2.22 gives the K_{tn} factors for the flat-bottom grooves under a tension based on the Neuber formula (Peterson 1953; ESDU 1981).

2.5.4 Closed-Form Solutions for Grooves in Bars of Circular Cross Section

There are a variety of studies leading to analytical equations for SCFs for grooves in the bars with a circular cross section. In Nisitani and Noda (1984), a solution technique is proposed to calculate SCFs for V-shaped grooves under tension, torsion, or bending. For several cases, the resulting factors are shown to be reasonably close to the results available previously. A variety of SCFs charts are included in their publications.

Noda et al. (1995) provide the formulas for V-shaped grooves for bars subjected to tension, torsion, and bending. Noda and Takase (1999) extend the formulas to cover grooves of any shape in bars under tension and bending.

2.6 BENDING OF THIN BEAMS WITH NOTCHES

2.6.1 Opposite Deep Hyperbolic Notches in an Infinite Thin Element

The exact K_{tn} values of Neuber's solution (Peterson 1953; Neuber 1958) are presented in Chart 2.23 for infinite thin elements subjected to in-plane moments with opposite deep hyperbolic notches.

2.6.2 Opposite Semicircular Notches in a Flat Beam

Chart 2.24 provides the K_{tn} values determined mathematically (Isida 1953; Ling 1967) for a thin beam element with opposite semicircular notches. Slot (1972) finds that with $r/H = 1/4$ of a strip with the length of $1.5H$, a good agreement is obtained with the stress distribution for M applied at infinity.

Troyani et al. (2004) show computationally that for very short bars, the stress concentration factors are larger than the results from the conventional methods. More specifically, they find that for $L/H < 0.5$ (see Fig. 2.8 for the definitions of L and H), the use of the SCFs in Chart 2.25 can significantly underestimate values obtained from the theory of elasticity.

2.6.3 Opposite U-Shaped Notches in a Flat Beam

Chart 2.25 gives the stress concentration factor K_{tn} for opposite U-shaped notches in a finite-width thin beam element. These curves are obtained by increasing the photoelastic K_{tn} values (Frocht 1935), which in tension are known to be low, to agree with the semicircular notch mathematical values of Chart 2.24, which are assumed to be accurate. The photoelastic tests by Wilson and White (1973) and the numerical results by Kitagawa and Nakade (1970) are in a good agreement. The K_{tn} values are approximated and extended for the values of r/d in Charts 2.26 and 2.27.

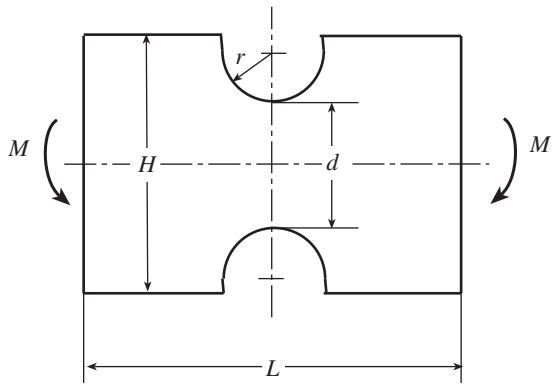


Figure 2.8 Bending of a flat beam with opposite U-shaped notches.

2.6.4 V-Shaped Notches in a Flat Beam Element

The effect of notch angle on the SCFs is presented in Chart 2.28 for a bar in bending with a V-shaped notch on one side (Leven and Frocht 1953). The K_{tn} value is for a U notch. $K_{t\alpha}$ is for a notch with inclined sides having an included angle α but with all other dimensions the same as for the corresponding U notch case. The curves of Chart 2.28 are based on the data from the specimens covering a H/d range up to 1.82. Any effect of H/d up to this value is sufficiently small that single α curves are adequate. For larger H/d values, the α curves may be lower (see Chart 2.7).

2.6.5 Notch on One Side of a Thin Beam

Chart 2.29 provides K_{tn} for bending of a semi-infinite thin element with a deep hyperbolic notch (Neuber 1958). In Chart 2.30*a*, K_{tn} curves are given based on the photoelastic tests by Leven and Frocht (1953). Corresponding Neuber K_{tn} factors in Chart 2.29 and Eq. (2.1) are on the average 6% higher than the K_{tn} factors in Chart 2.30*a*.

The curve for the semicircular notch is obtained by noting that for this case $H/d = 1 + r/d$ and that $K_{tn} = 3.065$ at $r/d \to 0$.

In Chart 2.30*b*, the finite-width correction factors are given for a bar with a notch on one side. The full curve represents a crack (Wilson 1970) and the dashed curve represents a semicircular notch (Leven and Frocht 1953). The correction factor for the crack is the ratio of the stress-intensity factors. In the small-radius with a narrow-notch limit, the ratio is valid for the stress concentration (Irwin 1960; Paris and Sih 1965). Note that the end points of the curves are 1.0 at $t/H = 0$ and $1/K_{t\infty}$ at $t/H = 1$. The $1/K_{t\infty}$ values at $t/H = 1$ for elliptical notches are obtained from $K_{t\infty}$ of Chart 2.2. These $1/K_t$ values at $t/H = 1$ are useful in sketching in approximate values for elliptical notches.

If $K_{tg}/K_{t\infty}$ (not shown in Chart 2.30*b*) is plotted, the curves start at 1.0 at $t/H = 0$, dip below 1.0, reach a minimum in the $t/H = 0.10$ to 0.15 range, and then turn upward to go to infinity at $t/H = 1.0$. This means that for bending, the effect of the nominal stress gradient is to cause $\sigma_{\max}$ to decrease slightly as the notch is cut into the surface, but beyond a depth of $t/H = 0.25$ to 0.3, the maximum stress is greater than for the infinitely deep bar. The same effect, only of slight magnitude, is obtained by Isida (1953) for the bending case of a bar with opposite semicircular notches (Chart 2.24; K_{tg} not shown). In tension, since there is no nominal stress gradient, this effect is not obtained.

Chart 2.31 gives the K_{tn} factors for various impact specimens.

2.6.6 Single or Multiple Notches with Semicircular or Semielliptical Notch Bottoms

From the work on propellant grains, it is known (Tsao et al. 1965) "that the stress concentration factor for an optimized semielliptic notch is significantly lower than that for the more easily formed semicircular notch." The photoelastic tests (Tsao et al. 1965; Nishioka and Hisamitsu 1962; Ching et al. 1968) are made on the beams in bending, with variations of beam and notch depth, notch spacing, and semielliptical notch bottom shape. The ratio of beam depth

to notch depth H/t (notch on one side only) is varied from 2 to 10. Chart 2.32 provides the results for $H/t = 5$.

For the single notch with $t/a = 2.666$, the ratio of K_{tn} for the semicircular bottom to the K_{tn} for the optimum semielliptical bottom, $a/b = 2.4$, is 1.25, as shown in Chart 2.32. In other words, a stress is considerably reduced by 20% by using a semielliptical notch bottom instead of a semicircular notch bottom. As can be found from Chart 2.32, the stress can be further reduced by using multiple notches.

Although these results are for a specific case of a beam in bending, it is reasonable to expect that, in general, a considerable stress reduction can be obtained by use of the semielliptic notch bottom. The optimum a/b of the semiellipse varies from 1.8 to greater than 3, with the single notch and the wider spaced multiple notches averaging at about 2 and the closer spaced notches increasing toward 3 and greater.

Other uses of the elliptical contour are found in Chart 4.59 for the slot end, where the optimum a/b is about 3, and in Chart 3.9, for the shoulder fillet.

2.6.7 Notches with Flat Bottoms

Chart 2.33 offers the stress concentration factors K_{tn} for thin beams with opposite notches with flat bottoms (Neuber 1958; Sobey 1965). For a shaft with flat-bottom grooves in bending and/or tension, the stress concentration factors K_{tn} are given in Chart 2.34 (Rubenchik 1975; ESDU 1981).

2.6.8 Closed-Form Solutions for Stress Concentration Factors for Notched Beams

As mentioned in Section 2.3.9, Gray et al. (1995) contain the analytical expressions of SCFs for thin-walled bars with in-plane bending. Also, Noda et al. (1995) present the formulas of SCFs for thin-walled bars with single-side and opposite V-shaped notches under tension and in-plane and out-of-plane bending, as well as U-shaped notches with out-of-plane bending.

2.7 BENDING OF PLATES WITH NOTCHES

2.7.1 Various Edge Notches in an Infinite Plate in Transverse Bending

Stress concentration factors K_{tn} for opposite deep hyperbolic notches in a thin plate (Lee 1940; Neuber 1958) are given in Chart 2.35. The factors are obtained for transverse bending.

The bending of a semi-infinite plate with a V-shaped notch or a rectangular notch with rounded corners (Shioya 1959) is covered in Chart 2.36. At $r/t = 1$, both curves have the same K_{tn} value (semicircular notch). Note that the curve for the rectangular notch has a minimum K_{tn} at about $r/t = 1/2$.

Chart 2.37 gives the K_{tn} factors for the elliptical notch (Shioya 1960). For comparison, the corresponding curve for the tension case from Chart 2.2 is shown. This reveals that the tension K_{tn} factors are considerably higher.

Chart 2.38 gives the K_t factors for an infinite row of semicircular notches as a function of the notch spacing (Shioya 1963). As the notch spacing increases, the K_t value for the single notch is approached asymptotically.

2.7.2 Notches in a Finite-Width Plate in Transverse Bending

The SCFs are approximated by the Neuber method (Peterson 1953; Neuber 1958) which makes use of the exact values for the deep hyperbolic notch (Lee 1940) and the shallow elliptical notch (Shioya 1960) in infinitely wide members. The second-power relation is used to modified the SCFs for finite-width members with the correct end conditions, and Chart 2.39 shows the results for the thin plate.

No direct results are available for intermediate thicknesses. Assume that the tension case represents the maximum values for a thick plate in bending, Chart 2.4 can be used for $t/h \to 0$. For the thin plate ($t/h \to \infty$), Chart 2.39 can be used as discussed in the preceding paragraph for intermediate thickness ratios. Chart 4.92 provides some guidance for the use of the values in Chart 4.94 for the region of $b/a = 1$.

2.8 BENDING OF SOLIDS WITH GROOVES

2.8.1 Deep Hyperbolic Groove in an Infinite Member

In Chart 2.40, stress concentration factors K_{tn} for Neuber's exact solution (Peterson 1953; Neuber 1958) are given for the bending of an infinite three-dimensional solid with a deep hyperbolic groove. The net section on the groove plane is circular.

2.8.2 U-Shaped Circumferential Groove in a Bar of Circular Cross Section

The K_{tn} values of Chart 2.41 for a U-shaped circumferential groove in a bar of circular cross section are obtained by the method used in the tension case (see Section 2.5.2). K_{tn} factors for small r/d values are approximated in Chart 2.42 and for large r/d values (e.g., test specimens), in Chart 2.43. Using finite element analyses, the SCFs of Chart 2.41 (and Chart 2.44) have been shown to be reasonably accurate (ESDU 1989).

Example 2.1 Design of a Shaft with a Circumferential Groove Suppose that we wish to estimate the bending fatigue strength of the shaft shown in Fig. 2.9 for two materials: an axle steel (normalized 0.40% C), and a heat-treated 3.5% nickel steel. These materials have the fatigue strengths of 30,000 and 70,000 lb/in.^{2}, respectively, when tested in the conventional manner, with no stress concentration effects, in a rotating beam machine.

Firstly, K_{tn} is to be determined. From Fig. 2.9, $d = 1.378 - (2)0.0625 = 1.253$ in. and $r = 0.03125$ in. Then, $D/d = 1.10$ and $r/d = 0.025$; Chart 2.41 shows that the corresponding SCF is $K_{tn} = 2.90$.

Fig. 1.31 shows a q value of 0.76 for the axle steel and 0.93 for the heat-treated alloy steel for $r = 0.03125$ in..

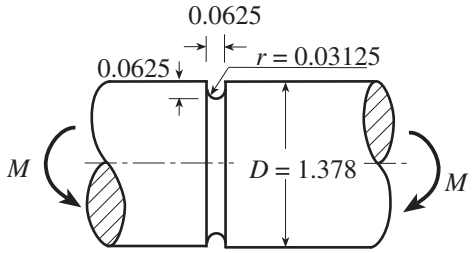


Figure 2.9 Grooved shaft.

Substituting in Eq. (1.99), for axle steel,

$$K_{tf} = 1 + 0.76(2.90 - 1) = 2.44$$

$$\sigma_{tf} = \frac{30{,}000}{2.44} = 12{,}300 \text{ lb/in.}^2$$

for heat-treated alloy steel,

$$K_{tf} = 1 + 0.93(2.90 - 1) = 2.77$$

$$\sigma_{tf} = \frac{70{,}000}{2.77} = 25{,}200 \text{ lb/in.}^2$$

This shows that the strength values of 12,000 and 25,000 lb/in^2 can be expected under the fatigue conditions for the shaft of Fig. 2.9 when the shaft is made of normalized axle steel and quenched-and-tempered alloy steel (as specified), respectively. These are not working stresses, since a safety factor must be applied that depends on type of service, consequences of failure, and other factors. Different safety factors are used throughout industry depending on service and experience. The strength of a member, however, is not, in the same sense, a matter of opinion or judgment and should be estimated in accordance with the best methods available. Naturally, a test of the member is desirable whenever possible. In any event, an initial calculation is made, and this should be done carefully and include all known factors.

2.8.3 Flat-Bottom Grooves in Bars of Circular Cross Section

Chart 2.24 presents the SCFs for a bar of circular cross section with flat-bottom grooves (Peterson 1953; Sobey 1965; ESDU 1981).

2.8.4 Closed-Form Solutions for Grooves in Bars of Circular Cross Section

The work of Nisitani and Noda (1984), Noda et al. (1995), and Noda and Takase (1999) discussed in Section 2.5.4 contains the closed-form formulas for various-shaped grooves for bars under bending.

2.9 DIRECT SHEAR AND TORSION

2.9.1 Deep Hyperbolic Notches in an Infinite Thin Element in Direct Shear

Chart 2.45 gives the SCFs by Neuber (1958) where shearing forces are applied to an infinite thin element with deep hyperbolic notches. These forces are parallel to the notch axis[1] as shown in Chart 2.45.

The location of $\sigma_{\max}$ is at

$$x = \frac{r}{\sqrt{1 + (2r/d)}} \tag{2.9}$$

The location of $\tau_{\max}$ along the line corresponding to the minimum section is at

$$y = \frac{d}{2}\sqrt{\frac{(d/2r) - 2}{d/2r}} \tag{2.10}$$

At the location of $\sigma_{\max}$, $K_{ts} = \tau_{\max}/\tau_{\text{nom}} = (\sigma_{\max}/2)/\tau_{\text{nom}} = K_t/2$, is greater than the K_{ts} value for the minimum section shown in Chart 2.45.

For combined shear and bending, Neuber (1958) shows that for large d/r values, it is a good approximation to add the two K_t factors (Charts 2.35 and 2.45); even though the maxima do not occur at the same location along the notch surface. The case of a twisted sheet with hyperbolic notches has been analyzed by Lee (1940).

2.9.2 Deep Hyperbolic Groove in an Infinite Member

Chart 2.46 presents the SCFs K_{ts} based on Neuber's exact solution (Peterson 1953; Neuber 1958) for the torsion of an infinite three-dimensional solid with a deep hyperbolic groove. The net section is circular in the groove plane.

2.9.3 U-Shaped Circumferential Groove in a Bar of Circular Cross Section Subject to Torsion

Chart 2.47, for a U-shaped circumferential groove in a bar of circular cross section, is based on electric analog results (Rushton 1967), using a technique that has also provided results in agreement with the exact values for the hyperbolic notch in the parameter range of present interest. The mathematical results for semicircular grooves (Hamada and Kitagawa 1968; Matthews and Hooke 1971) are in reasonably good agreement with Chart 2.47. The K_{ts} values of Chart 2.47 are somewhat higher (average 4.5%) than the photoelastic values of Leven (1955). However, the photoelastic values are not in agreement with the values by Okubo (1952, 1953).

[1] For equilibrium, the shear force couple $2bV$ must be counterbalanced by an equal couple symmetrically applied remotely from the notch (Neuber 1958). To avoid possible confusion with the combined shear and bending case, the countercouple is not shown in Chart 2.45.

Chart 2.48 shows a leveling of the K_{ts} curve at a D/d value of about 2 or less for high r/d values. The K_{ts} factors beyond the r/d range of Chart 2.47 are approximated for small r/d values in Chart 2.49 and for large r/d values (e.g., test specimens) in Chart 2.50.

Example 2.2 Analysis of a Circular Shaft with a U-Shaped Groove The circular shaft of Fig. 2.10 has a U-shaped groove, with $t = 10.5$ mm deep. The radius of the groove root is $r = 7$ mm, and the bar diameter away from the notch is $D = 70$ mm. The shaft is subjected to a bending moment of $M = 1.0$ kN · m and a torque of $T = 2.5$ kN · m. Find the maximum shear stress and the equivalent stress at the root of the notch.

The minimum radius of this shaft is

$$d = D - 2t = 70 - 2 \times 10.5 = 49 \text{ mm} \tag{1}$$

Then

$$\frac{r}{d} = \frac{7}{49} = 0.143 \quad \text{and} \quad \frac{D}{d} = \frac{70}{49} = 1.43 \tag{2}$$

From Chart 2.41, the SCF for bending is to be approximately

$$K_{tn} = 1.82 \tag{3}$$

Similarly from Chart 2.48, the SCF for torsion is

$$K_{ts} = 1.46 \tag{4}$$

As indicated in Chart 2.41, σ_{nom} is found as

$$\sigma_{\text{nom}} = \frac{32M}{\pi d^3} = \frac{32 \times 1.0 \times 10^3}{\pi \times (0.049)^3} = 86.58 \text{ MPa} \tag{5}$$

Thus the maximum tensile stress at the root of the groove is

$$\sigma_{\max} = K_{tn}\sigma_{\text{nom}} = 1.82 \times 86.58 = 157.6 \text{ MPa} \tag{6}$$

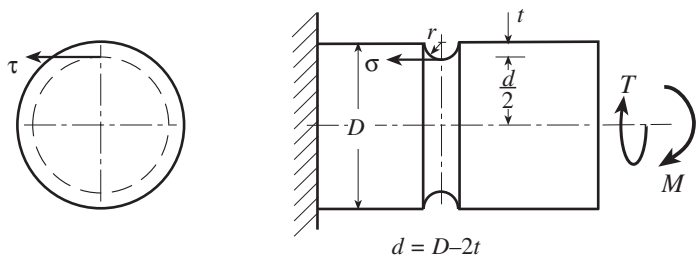


Figure 2.10 Shaft, with circumferential U-shaped groove, subject to torsion and bending.

In the case of torsion, the shear stress τ_{nom} is found to be

$$\tau_{\text{nom}} = \frac{16T}{\pi d^3} = \frac{16 \times 2.5 \times 10^3}{\pi \times 0.049^3} = 108.2 \text{ MPa} \tag{7}$$

so that the maximum torsional shear stress at the bottom of the groove is

$$\tau_{\max} = K_{ts}\tau_{\text{nom}} = 1.46 \times 108.2 = 158.0 \text{ MPa} \tag{8}$$

The principal stresses are found to be (Pilkey 2005)

$$\begin{aligned}
\sigma_1 &= \frac{1}{2}\sigma_{\max} + \frac{1}{2}\sqrt{\sigma_{\max}^2 + 4\tau_{\max}^2} \\
&= \frac{1}{2} \times 157.6 + \frac{1}{2}\sqrt{157.6^2 + 4 \times 158.0^2} \\
&= 78.8 + 176.6 = 255.4 \text{ MPa} \\
\sigma_2 &= \frac{1}{2}\sigma_{\max} - \frac{1}{2}\sqrt{\sigma_{\max}^2 + 4\tau_{\max}^2} = 78.8 - 176.6 = -97.8 \text{ MPa}
\end{aligned} \tag{9}$$

Thus the corresponding maximum shear stress is

$$\frac{\sigma_1 - \sigma_2}{2} = 176.6 \text{ MPa} \tag{10}$$

which, of course, differs from the maximum torsional shear stress of (8).

Finally, the equivalent stress (Eq. 1.35) becomes

$$\begin{aligned}
\sigma_{\text{eq}} &= \sqrt{\sigma_1^2 - \sigma_1\sigma_2 + \sigma_2^2} \\
&= \sqrt{255.4^2 - 255.4 \times (-97.8) + (-97.8)^2} \\
&= 315.9 \text{ MPa}
\end{aligned}$$

2.9.4 V-Shaped Circumferential Groove in a Bar of Circular Cross Section Under Torsion

Chart 2.51 shows the $K_{ts\alpha}$ factors for the V groove (Rushton 1967), with variable angle α, using the style of Charts 2.7 and 2.28. For $\alpha \leq 90°$, the curves are nearly independent of r/d. For $\alpha = 135°$, separate curves are needed for $r/d = 0.005$, 0.015, and 0.05. The effect of the V angle may be compared with Charts 2.7 and 2.28.

2.9.5 Shaft in Torsion with Grooves with Flat Bottoms

The Chart 2.52 gives the K_{ts} factors for flat-bottom notches in a shaft of circular cross section under tension.

2.9.6 Closed-Form Formulas for Grooves in Bars of Circular Cross Section Under Torsion

As mentioned in Section 2.5.4, Noda et al. (1995) provide the closed-form expressions for V-shaped grooves under torsion as well as for tension and bending.

2.10 TEST SPECIMEN DESIGN FOR MAXIMUM K_t FOR A GIVEN r/D OR r/H

The test piece is assumed to have a given outside diameter (or width), D (or H).[2] For a particular notch bottom radius, r, it is shown that the notch depth (the d/D or r/H ratio) gives the maximum K_t.[3]

From the curves of Charts 2.5, 2.20, 2.26, 2.42, and 2.49, the maximum K_t values are plotted in Chart 2.53 with r/H and d/H as variables for two-dimensional problems and r/D and d/D for three-dimensional. Although these values are approximate, in that the Neuber approximation is involved (as detailed in the introductory remarks at the beginning of this chapter), the maximum region is quite flat. Therefore, K_t is not highly sensitive to variations in d/D or d/H in the maximum region.

From Chart 2.53, it can be seen that a rough guide to obtain the maximum K_t in a specimen in the most used r/D or r/H range is to make the smaller diameter, or width, about three-fourths of the larger diameter, or width (assuming that one is working with a given r and D or H).

Another specimen design problem occurs when r and d are given. The smaller diameter d may, in some cases, be determined by the testing machine capacity. In this case, K_t increases with an increase of D/d until reaches a "knee" at a D/d value which depends on the r/d value (see Chart 2.48). For the smaller r/d values, a value of $d/D = 1/2$ where the "knee" is reached would be indicated, and for the larger r/d values, the value of $d/D = 3/4$ would be appropriate.

REFERENCES

Appl, F. J., and Koerner, D. R., 1968, Numerical analysis of plane elasticity problems, *Proc. Am. Soc. Civ. Eng*., Vol. 94, p. 743.

Appl, F. J., and Koerner, D. R., 1969, Stress concentration factors for U-shaped, hyperbolic, and rounded V-shaped notches, *ASME Pap. 69-DE-2*, Engineering Society Library, United Engineering Center, New York.

Atsumi, A., 1958, Stress concentration in a strip under tension and containing an infinite row of semicircular notches, *Q. J. Mech. Appl. Math*., Vol. 11, Pt. 4, p. 478.

Atsumi, A., 1967, Stress concentrations in a strip under tension and containing two pairs of semicircular notches placed on the edges symmetrically, *Trans. ASME Appl. Mech. Sect*., Vol. 89, p. 565.

Barrata, F. I., 1972, Comparison of various formulae and experimental stress-concentration factors for symmetrical U-notched plates, *J. Strain Anal*., Vol. 7, p. 84.

[2]The width D frequently depends on the available bar size.

[3]The minimum notch bottom radius is often dictated by the ability of the shop to produce accurate, smooth, small radius.

Barrata, F, I., and Neal, D. M., 1970, Stress concentration factors in U-shaped and semi-elliptical shaped edge notches, *J. Strain Anal*., Vol. 5, p. 121.

Bowie, O. L., 1963, Rectangular tensile sheet with symmetric edge cracks, *AMRA TR 63-22*, Army Materials and Mechanics Research Center, Watertown, MA.

Bowie, O. L., 1966, Analysis of edge notches in a semi-infinite region, *AMRA TR 66-07*, Army Materials and Mechanics Research Center, Watertown, MA.

Brown, W. F., and Strawley, J. E., 1966, Plane strain crack toughness testing of high strength metallic materials, *STP 410*, American Society for Testing and Materials, Philadelphia, PA, p. 11.

Cheng, Y. F., 1970, Stress at notch root of shafts under axially symmetric loading, *Exp. Mech*., Vol. 10, p. 534.

Ching, A., Okubo, S., and Tsao, C. H., 1968, Stress concentration factors for multiple semi-elliptical notches in beams under pure bending, *Exp. Mech*., Vol. 8, p. 19N.

Cole, A. G., and Brown, A. F. C., 1958, Photoelastic determination of stress concentration factors caused by a single U-notch on one side of a plate in tension, *J. R. Aeronaut. Soc*., Vol. 62, p. 597.

Cowper, G. R., 1962, Stress concentrations around shallow spherical depressions in a flat plate, *Aeronaut. Rep. LR-340*, National Research Laboratories, Ottawa, Ontario, Canada.

Denardo, B. P., 1968, Projectile shape effects on hypervelocity impact craters in aluminum, *NASA TN D-4953*, National Aeronautics and Space Administration, Washington, DC.

Dixon, J. R., 1962, Stress distribution around edge slits in a plate loaded in tension: the effect of finite width of plate, *J. R. Aeronaut. Soc*., Vol. 66, p. 320.

Durelli, A. J., Lake, R. L., and Phillips, E., 1952, Stress concentrations produced by multiple semi-circular notches in infinite plates under uniaxial state of stress, *Proc. Soc. Exp. Stress Anal*., Vol. 10, No. 1, p. 53.

ESDU 1981, 1989, *Stress Concentrations*, Engineering Science Data Unit, London.

Eubanks, R. A., 1954, Stress concentration due to a hemispherical pit at a free surface, *Trans. ASME Appl. Mech. Sect*., Vol. 76, p. 57.

Flynn, P. D., and Roll, A, A., 1966, Re-examination of stresses in a tension bar with symmetrical U-shaped grooves, *Proc. Soc. Exp. Stress Anal*., Vol. 23, Pt. 1, p. 93.

Flynn, P. D., and Roll, A. A., 1967, A comparison of stress concentration factors in hyperbolic and U-shaped grooves, *Proc. Soc. Exp. Stress Anal*., Vol. 24, Pt. 1, p. 272.

Frocht, M. M., 1935, Factors of stress concentration photoelasticity determined, *Trans. ASME Appl. Mech. Sect*., Vol. 57, p. A-67.

Gray, T. G. F., Tournery, F., Spence, J., and Brennan, D., 1995, Closed-form functions for elastic stress concentration factors in notched bars, *J. Strain Anal*., Vol. 30, p. 143.

Grayley, M. E., 1979, Estimation of the stress concentration factors at rectangular circumferential grooves in shafts under torsion, *ESDU Memo. 33*, Engineering Science Data Unit, London.

Hamada, M., and Kitagawa, H., 1968, Elastic torsion of circumferentially grooved shafts, *Bull. Jpn. Soc. Mech. Eng*., Vol. 11, p. 605.

Hetényi, M., 1943, The distribution of stress in threaded connections, *Proc. Soc. Exp. Stress Anal*., Vol. 1, No. 1, p. 147.

Hetényi, M. and Liu, T. D., 1956, Method for calculating stress concentration factors, *J. Appl. Mech*., Vol. 23.

Heywood, R. B., 1952, *Designing by Photoelasticity*, Chapman & Hall, London, p. 163.

Hooke, C. J., 1968, Numerical solution of plane elastostatic problems by point matching, *J. Strain Anal*., Vol. 3, p. 109.

Irwin, G. R., 1958, Fracture, in *Encyclopedia of Physics*, Vol. 6, Springer-Verlag, Berlin, p. 565.

Irwin, G. R., 1960, Fracture mechanics, in *Structural Mechanics*, Pergamon Press, Elmsford, NY.

Isida, M., 1953, On the tension of the strip with semi-circular notches, *Trans. Jpn. Soc. Mech. Eng*., Vol. 19, p. 5.

Isida, M., 1955, On the tension of a strip with a central elliptic hole, *Trans. Jpn. Soc. Mech. Eng*., Vol. 21.

Kikukawa, M., 1962, Factors of stress concentration for notched bars under tension and bending, *Proc. 10th International Congress on Applied Mechanics*, Elsevier, New York, p. 337.

Kitagawa, H., and Nakade, K., 1970, Stress concentrations in notched strip subjected to in-plane bending, *Technol. Rep. of Osaka Univ*., Vol. 20, p. 751.

Koiter, W. T., 1965, Note on the stress intensity factors for sheet strips with crack under tensile loads, *Rep. 314*, Laboratory of Engineering Mechanics, Technological University, Delft, The Netherlands.

Lee, G. H., 1940, The influence of hyperbolic notches on the transverse flexure of elastic plates, *Trans. ASME Appl. Mech. Sect*., Vol. 62, p. A-53.

Leven, M. M,, 1955, Quantitative three-dimensional photoelasticity, *Proc. SESA*, Vol. 12, No. 2, p. 167.

Leven, M. M., and Frocht, M. M., 1953, Stress concentration factors for a single notch in a flat plate in pure and central bending, *Proc. SESA*, Vol. 11, No. 2, p. 179.

Ling, C.-B., 1967, On stress concentration at semicircular notch, *Trans. ASME Appl. Mech. Sect*., Vol. 89, p. 522.

Ling, C.-B., 1968, On stress concentration factor in a notched strip, *Trans. ASME Appl. Mech. Sect*., Vol. 90, p. 833.

Matthews, G. J., and Hooke, C. J., 1971, Solution of axisymmetric torsion problems by point matching, *J. Strain Anal*., Vol. 6, p. 124.

Moore, R. R., 1926, Effect of grooves, threads and corrosion upon the fatigue of metals, *Proc. ASTM*, Vol. 26, Pt. 2, p. 255.

Neuber, H., 1958, *Kerbspannungslehre*, 2nd ed., Springer-Verlag, Berlin; translation, 1961, *Theory of Notch Stresses*, Office of Technical Services, U.S. Department of Commerce, Washington, DC.

Nishioka, K. and Hisamitsu, N., 1962, On the stress concentration in multiple notches, *Trans. ASME Appl. Mech. Sect*., Vol. 84, p. 575.

Nisitani, H., and Noda, N., 1984, Stress concentration of a cylindrical bar with a V-shaped circumferential groove under torsion, tension or bending, *Eng. Fract. Mech*., Vol. 20, p. 743.

Noda, N., and Takase, Y., 1999, Stress concentration formulas useful for any shape of notch in a round test specimen under tension and under bending, *Fatigue Fract. Eng. Mater. Struct*., Vol. 22, p. 1071.

Noda, N., Sera, M., and Takase, Y., 1995, Stress concentration factors for round and flat test specimens with notches, *Int. J. Fatigue*, Vol. 17, p. 163.

Okubo, H., 1952, Approximate approach for torsion problem of a shaft with a circumferential notch, *Trans. ASME Appl. Mech. Sect*., Vol. 54, p. 436.

Okubo, H., 1953, Determination of surface stress by means of electroplating, *J. Appl. Phys*., Vol. 24, p. 1130.

Paris, P. C., and Sih, G. C., 1965, Stress analysis of cracks, *ASTM Spec. Tech. Publ. 381*, American Society for Testing and Materials, Philadelphia, PA, p. 34.

Peterson, R. E., 1953, *Stress Concentration Design Factors*, Wiley, New York.

Peterson, R. E., 1974, *Stress Concentration Factors*, Wiley, New York.

Pilkey, W. D., 2005, *Formulas for Stress, Strain, and Structural Matrices*, 2nd ed.,Wiley, New York.

Reed, R. E., and Wilcox, P. R., 1970, Stress concentration due to a hyperboloid cavity in a thin plate, *NASA TN D-5955*, National Aeronautics and Space Administration, Washington, DC.

Rubenchik, V. Y., 1975, Stress concentration close to grooves, *Vestn. Mashin*., Vol. 55, No. 12, pp. 26–28.

Rushton, K. R., 1964, Elastic stress concentrations for the torsion of hollow shouldered shafts determined by an electrical analogue, *Aeronaut. Q*., Vol. 15, p. 83.

Rushton, K. R., 1967, Stress concentrations arising in the torsion of grooved shafts, *J. Mech. Sci*., Vol. 9, p. 697.

Schulz, K. J., 1941, Over den Spannungstoestand in doorborde Platen (On the state of stress in perforated plates), Doctoral thesis, Technische Hochschule, Delft, The Netherlands.

Schulz, K. J., 1942, On the state of stress in perforated strips and plates, *Proc. Koninklÿke Nederlandsche Akadamie van Wetenschappen* (Netherlands Royal Academy of Science), Amsterdam, Vol. 45, pp. 233, 341, 457, 524.

Schulz, K. J., 1943–1945, On the state of stress in perforated strips and plates, *Proc. Koninklÿke Nederlandsche Akadamie van Wetenschappen* (Netherlands Royal Academy of Science), Amsterdam, Vol. 46–48, pp. 282, 292.

Seika, M., 1960, Stresses in a semi-infinite plate containing a U-type notch under uniform tension, *Ing.-Arch*., Vol. 27, p. 20.

Shioya, S., 1959, The effect of square and triangular notches with fillets on the transverse flexure of semi-infinite plates, *Z. Angew. Math. Mech*., Vol. 39, p. 300.

Shioya, S., 1960, On the transverse flexure of a semi-infinite plate with an elliptic notch, *Ing.-Arch*., Vol. 29, p. 93.

Shioya, S., 1963, The effect of an infinite row of semi-circular notches on the transverse flexure of a semi-infinite plate, *Ing.-Arch*., Vol. 32, p. 143.

Slot, T., 1972, *Stress Analysis of Thick Perforated Plates*, Technomic Publishing Co., Westport, CT.

Sobey, A. J., 1965, Stress concentration factors for round rectangular holes in infinite sheets, *ARC R&M 3407*, Aeronautical Research Council, London.

Suzuki, S. I., 1967, Stress analysis of a semi-infinite plate containing a reinforced notch under uniform tension, *Int. J. Solids Struct*., Vol. 3, p. 649.

Troyani, N., Hernández, S. I., Villarroel, G., Pollonais, Y., and Gomes, C., 2004, Theoretical stress concentration factors for short flat bars with opposite U-shaped notches subjected to in-plane bending, *Int. J. Fatigue*, Vol. 26, pp. 1303–1310.

Tsao, C. H., Ching, A., and Okubo, S., 1965, Stress concentration factors for semi-elliptical notches in beams under pure bending, *Exp. Mech*., Vol. 5, p. 19A.

Weber, C., 1942, Halbebene mit periodisch gewelltem Rand, *Z. Angew. Math. Mech*., Vol. 22, p. 29.

Westergaard, H. M., 1939, Bearing pressures and cracks, *Trans. ASME Appl. Mech. Sect*., Vol. 61, p. A-49.

Wilson, I. H., and White, D. J., 1973, Stress concentration factors for shoulder fillets and grooves in Plates, *J. Strain Anal*., Vol. 8, p. 43.

Wilson, W. K., 1970, Stress intensity factors for deep cracks in bending and compact tension specimens, in *Engineering Fracture Mechanics*, Vol. 2, Pergamon Press, London.

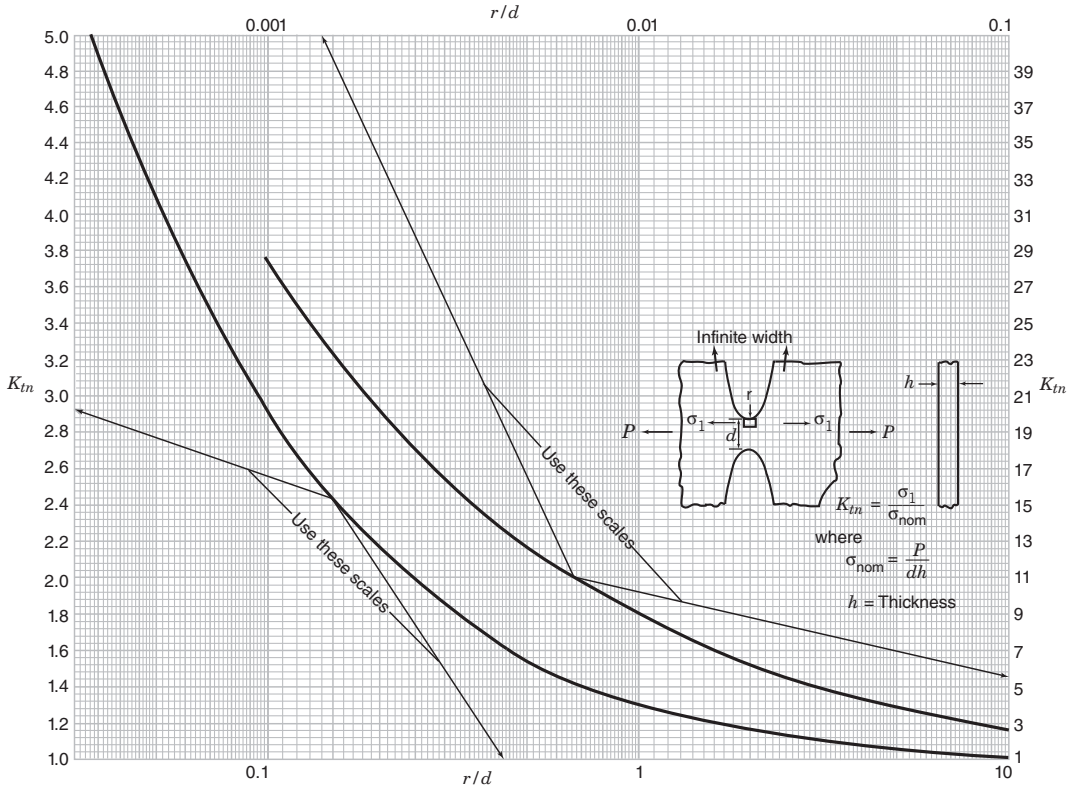


Chart 2.1 Stress concentration factors K_{tn} for opposite deep hyperbolic notches in an infinitely wide thin element in tension (Neuber 1958).

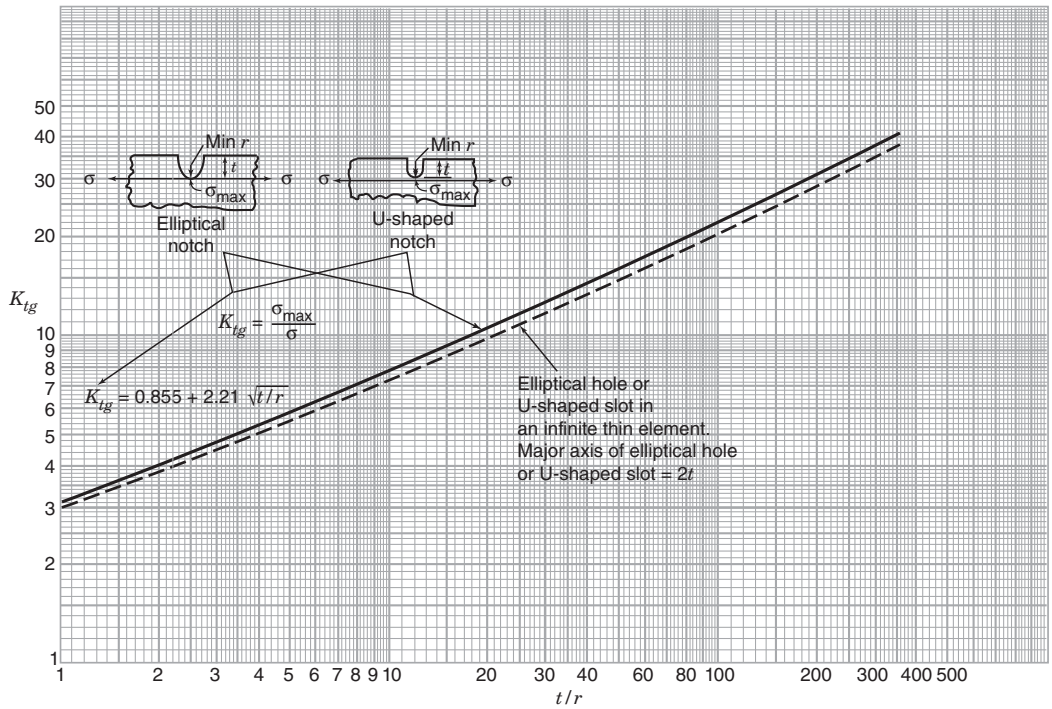


Chart 2.2 Stress concentration factors K_{tg} for an elliptical or U-shaped notch in a semi-infinite thin element in tension (Seika 1960; Bowie 1966; Baratta and Neal 1970).

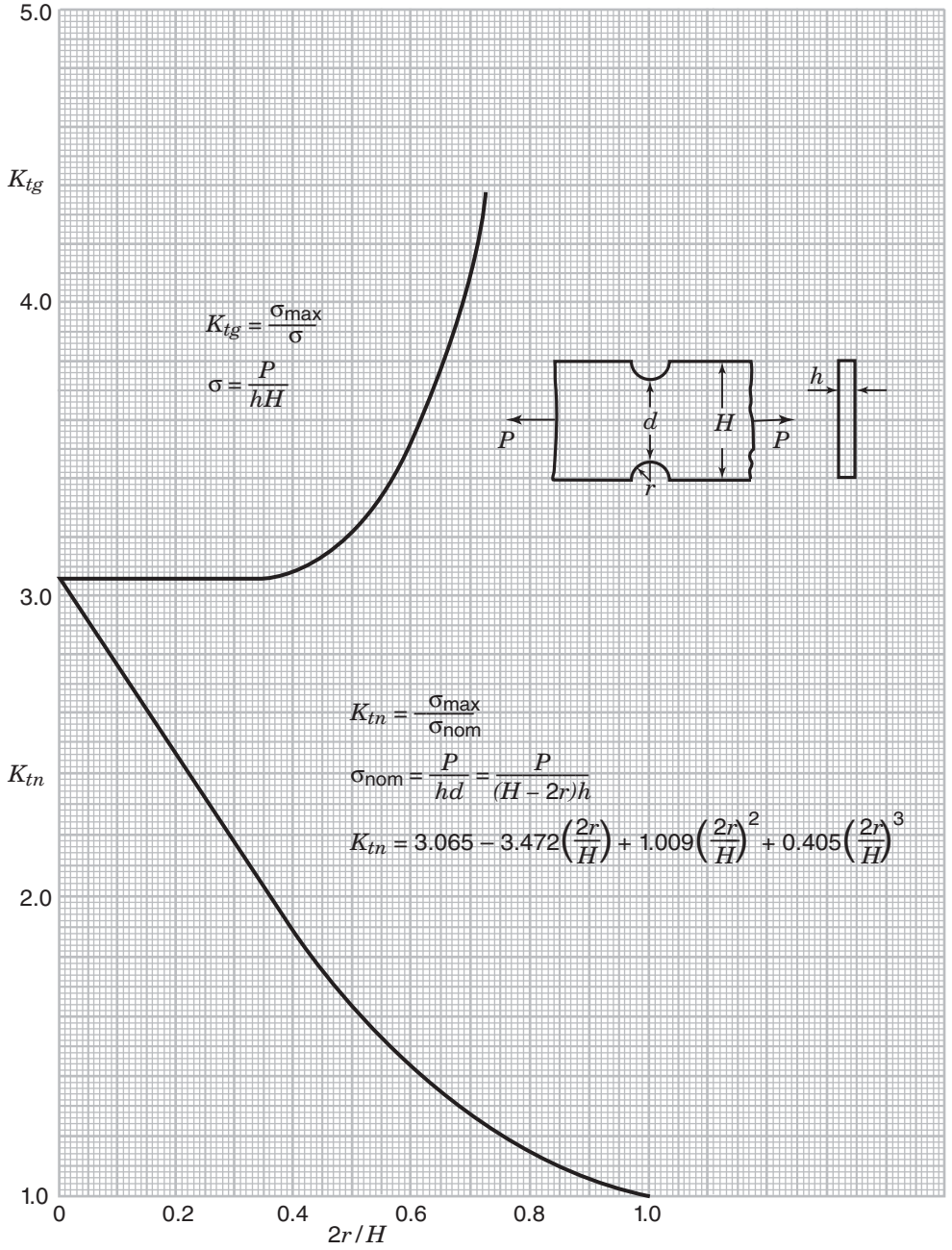


Chart 2.3 Stress concentration factors K_{tg} and K_{tn} for a tension strip with opposite semicircular edge notches (Isida 1953; Ling 1968).

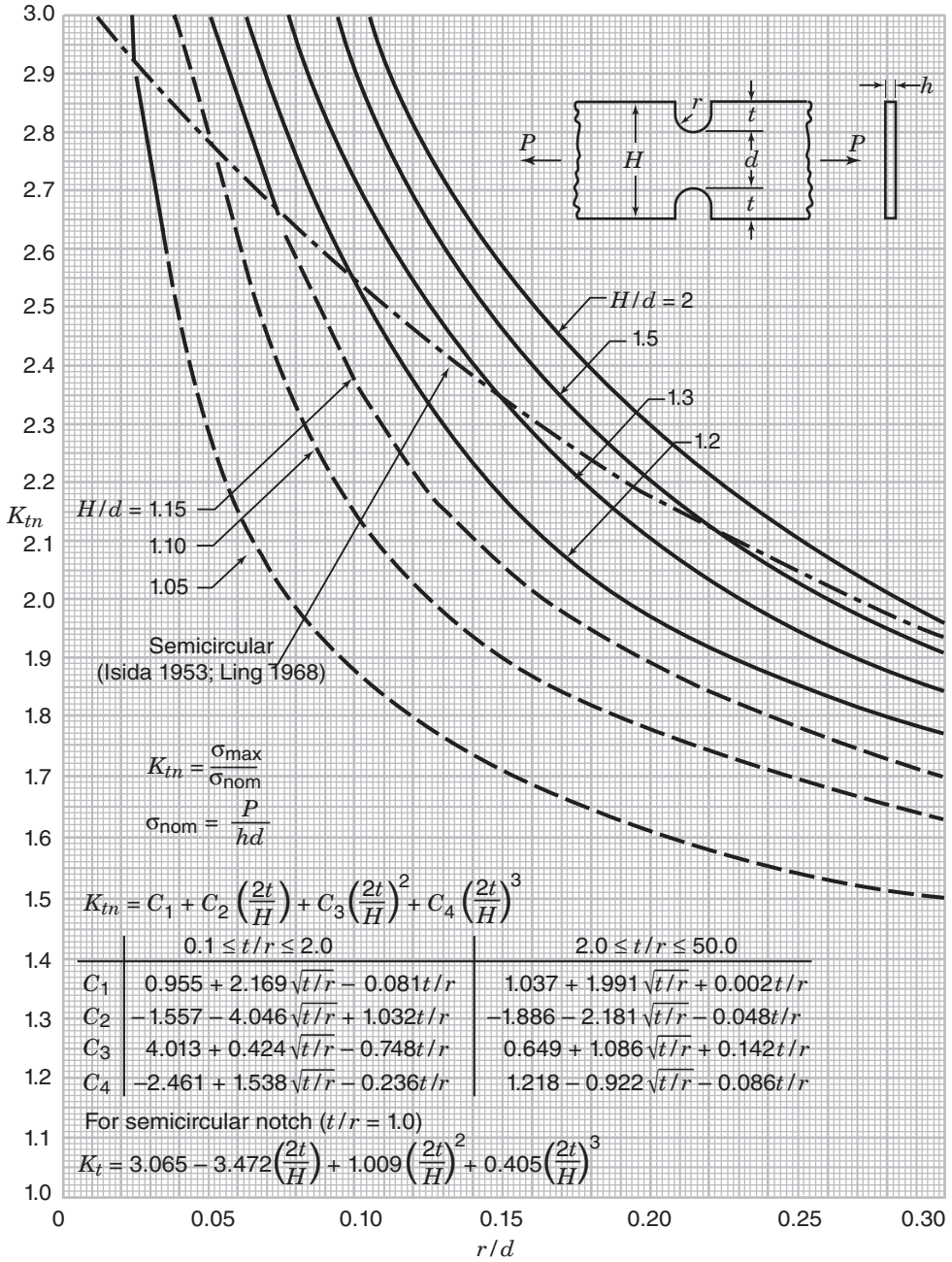


Chart 2.4 Stress concentration factors K_{tn} for a flat tension bar with opposite U-shaped notches (from data of Isida 1953; Flynn and Roll 1966; Ling 1968; Appl and Koerner 1969).

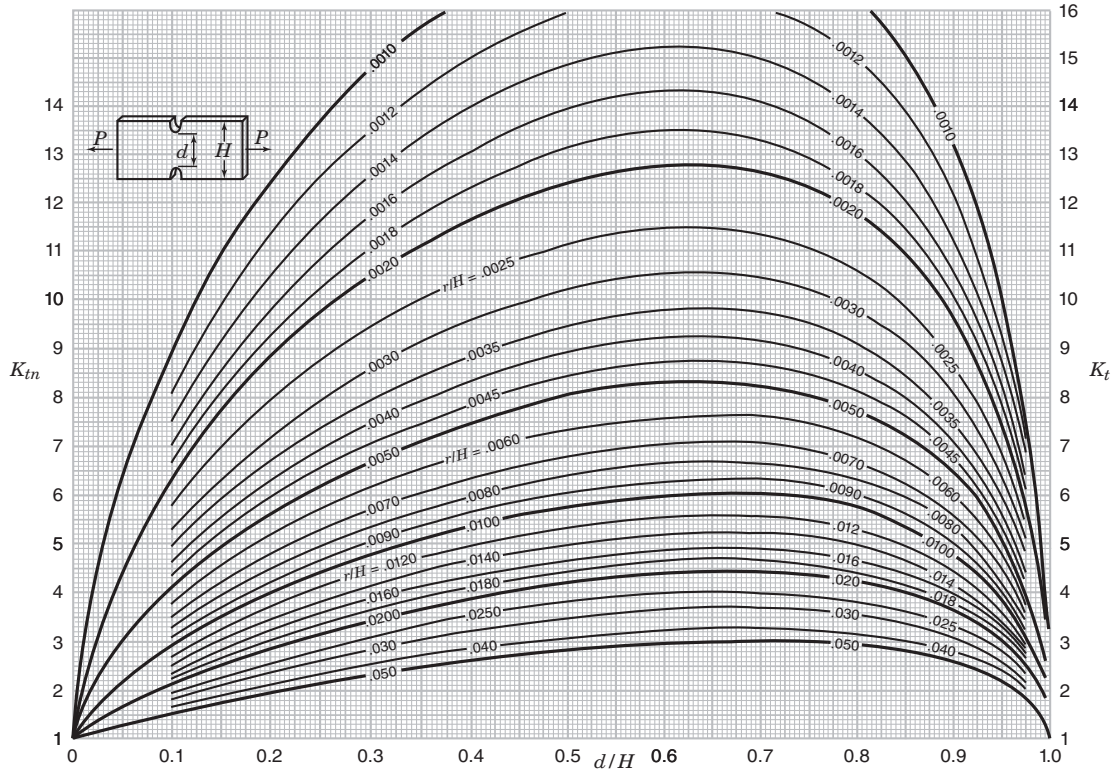


Chart 2.5 Stress concentration factors K_{tn} for a flat tension bar with opposite U-shaped notches (calculated using Neuber 1958 theory, Eq. 2.1), r/H from 0.001 to 0.05.

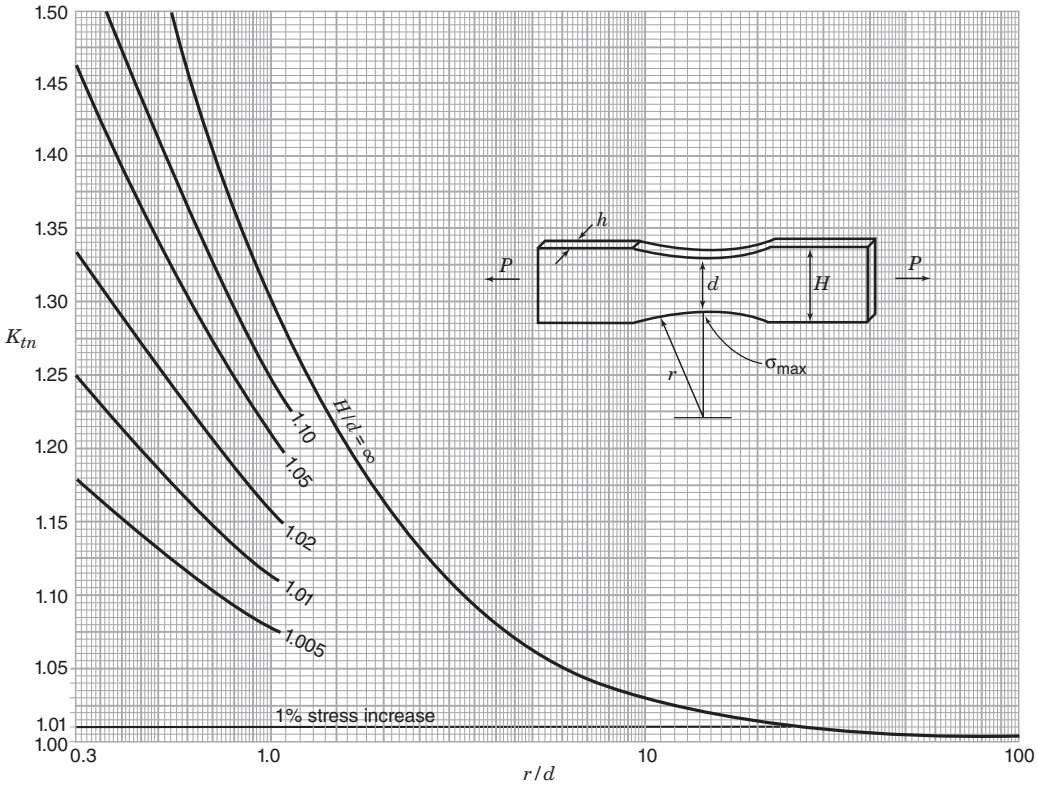


Chart 2.6 Stress concentration factors K_m for a flat test specimen with opposite shallow U-shaped notches in tension (calculated using Neuber 1958 theory, Eq. 2.1).

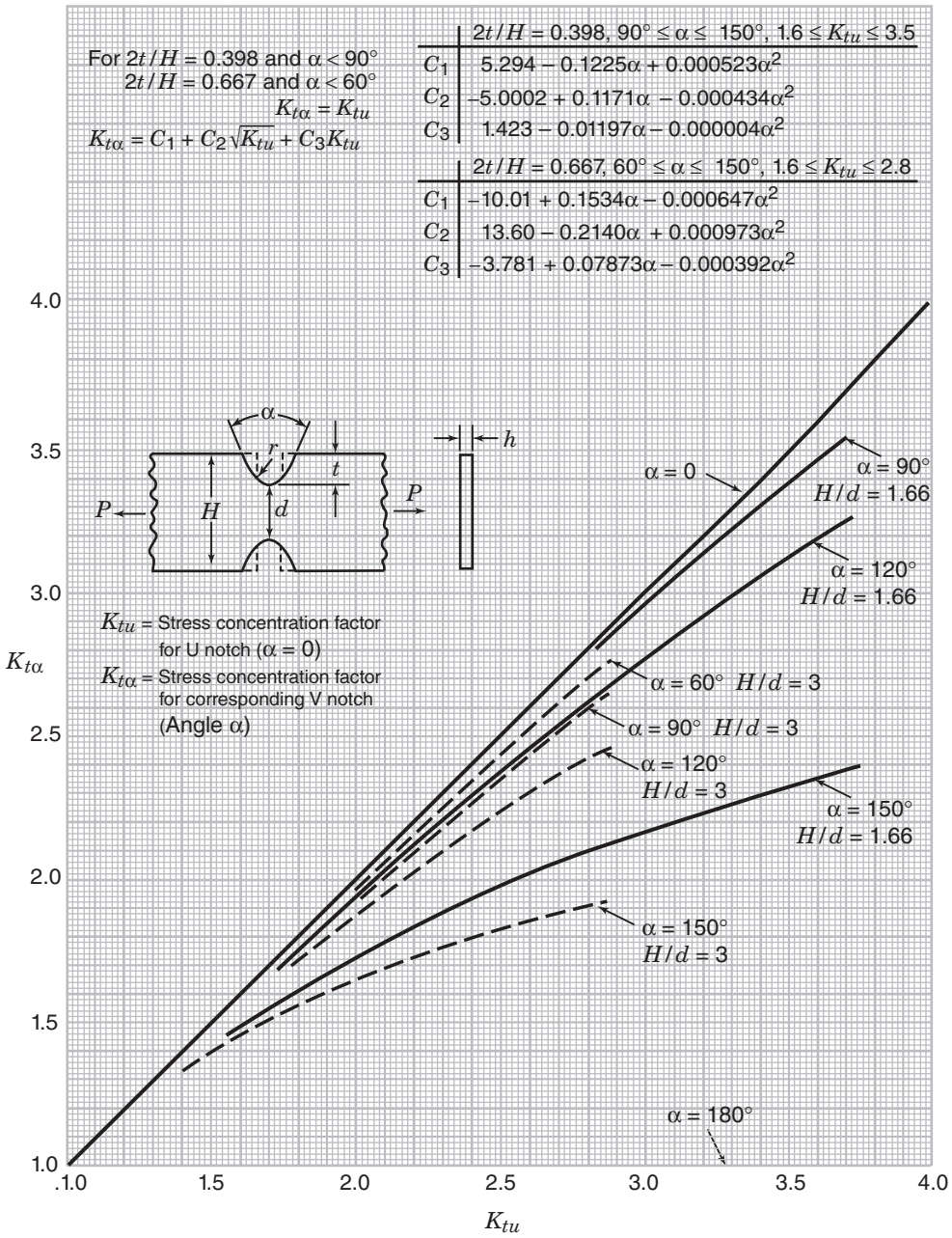


Chart 2.7 Stress concentration factors $K_{t\alpha}$ for a flat tension bar with opposite V-shaped notches (from data of Appl and Koerner 1969).

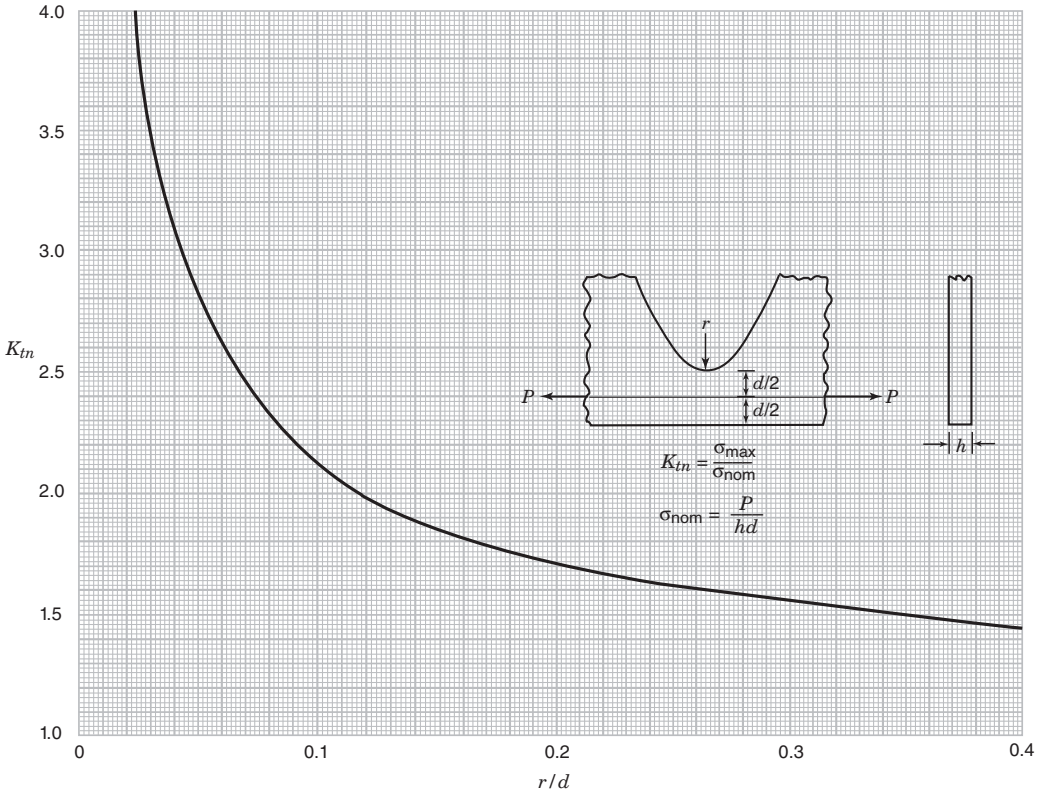


Chart 2.8 Stress concentration factors K_{tn} for tension loading of a semi-infinite thin element with a deep hyperbolic notch. tension loading in line with middle of minimum section (approximate values; Neuber 1958).

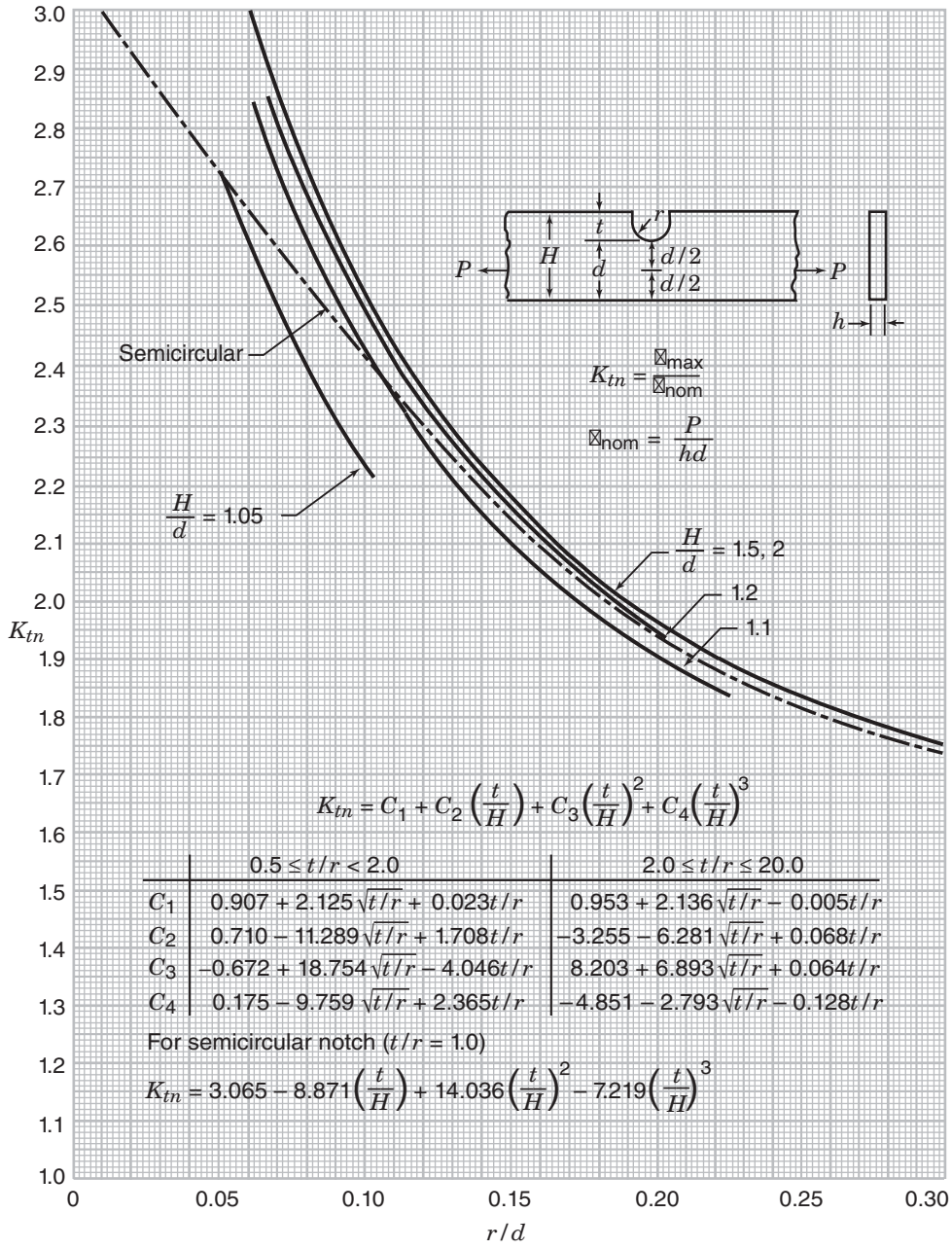


Chart 2.9 Stress concentration factors K_{tn} for a flat tension bar with a U-shaped notch at one side (from photoelastic data of Cole and Brown 1958). Tension loading in line with middle of minimum section.

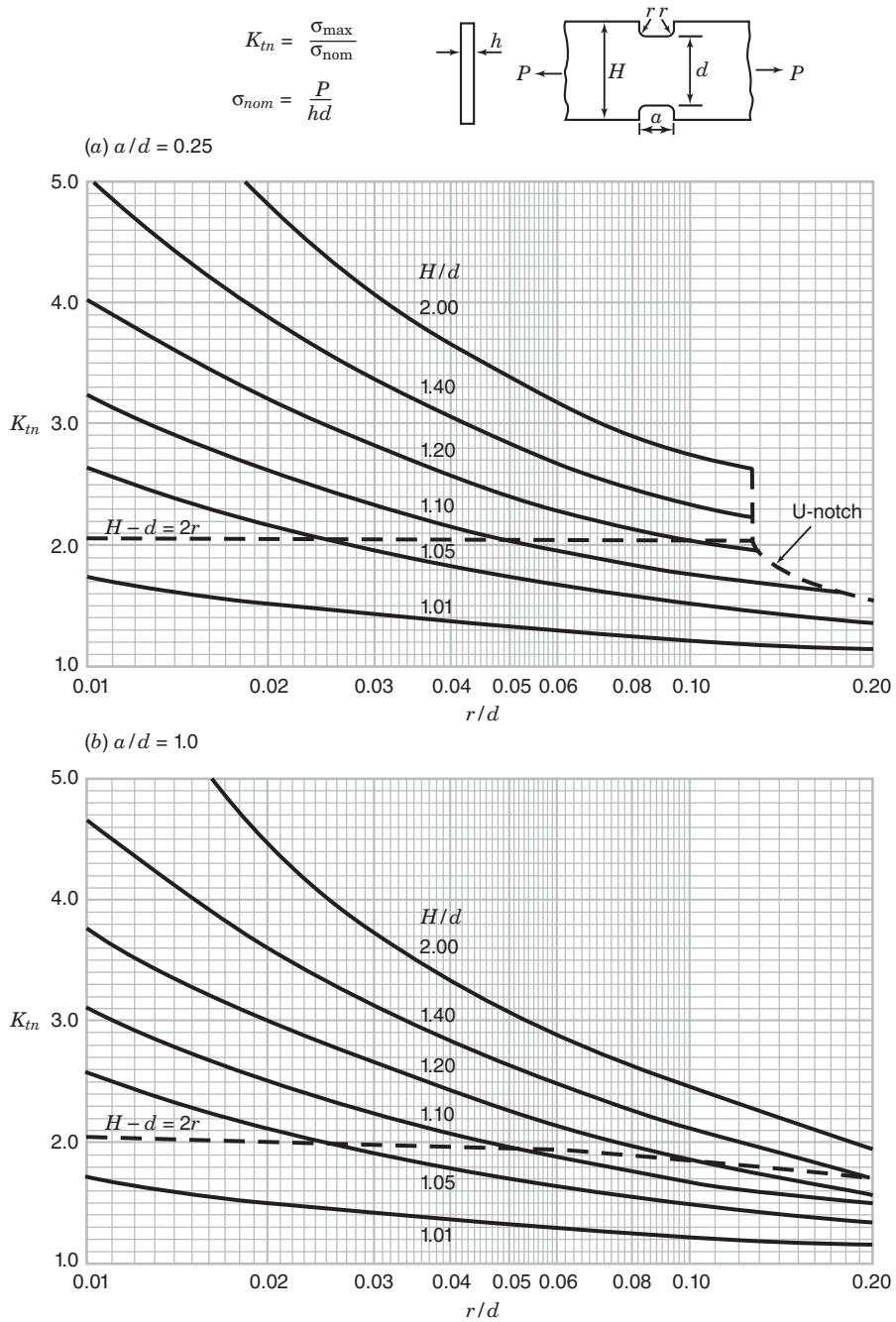


Chart 2.10 Stress concentration factors K_{tn} for opposing notches with flat bottoms in finite-width flat elements in tension (Hetényi and Liu 1956; Neuber 1958; Sobey 1965; ESDU 1981): (*a*) $a/d = 0.25$; (*b*) $a/d = 1.0$.

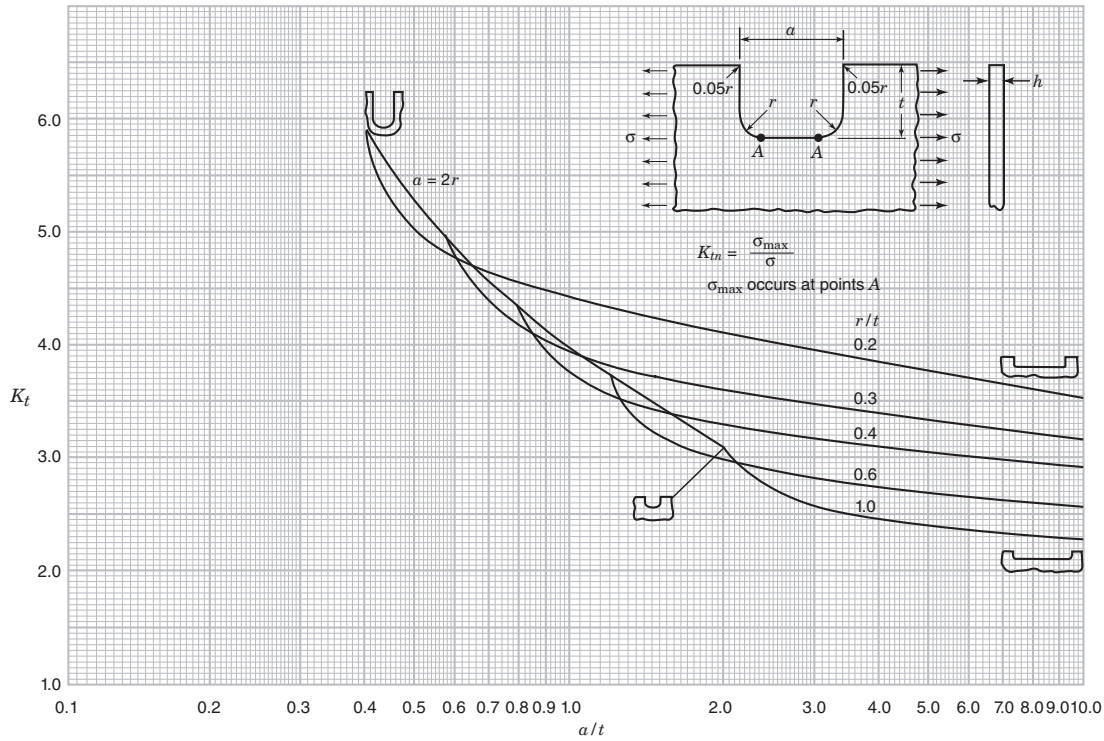


Chart 2.11 Stress concentration factors K_t for notches with flat bottoms in semi-infinite flat elements in tension (Rubenchik 1975; ESDU 1981).

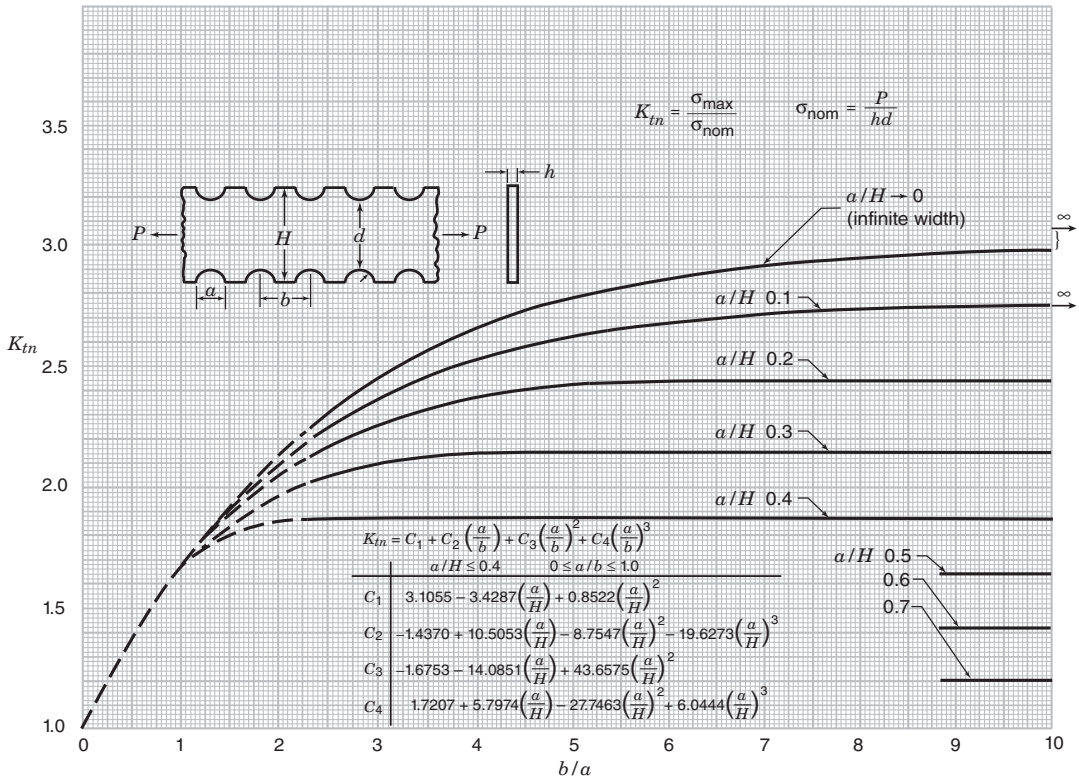


Chart 2.12 Stress concentration factors K_{tn} for a tension bar with infinite rows of semicircular edge notches (from data of Atsumi 1958).

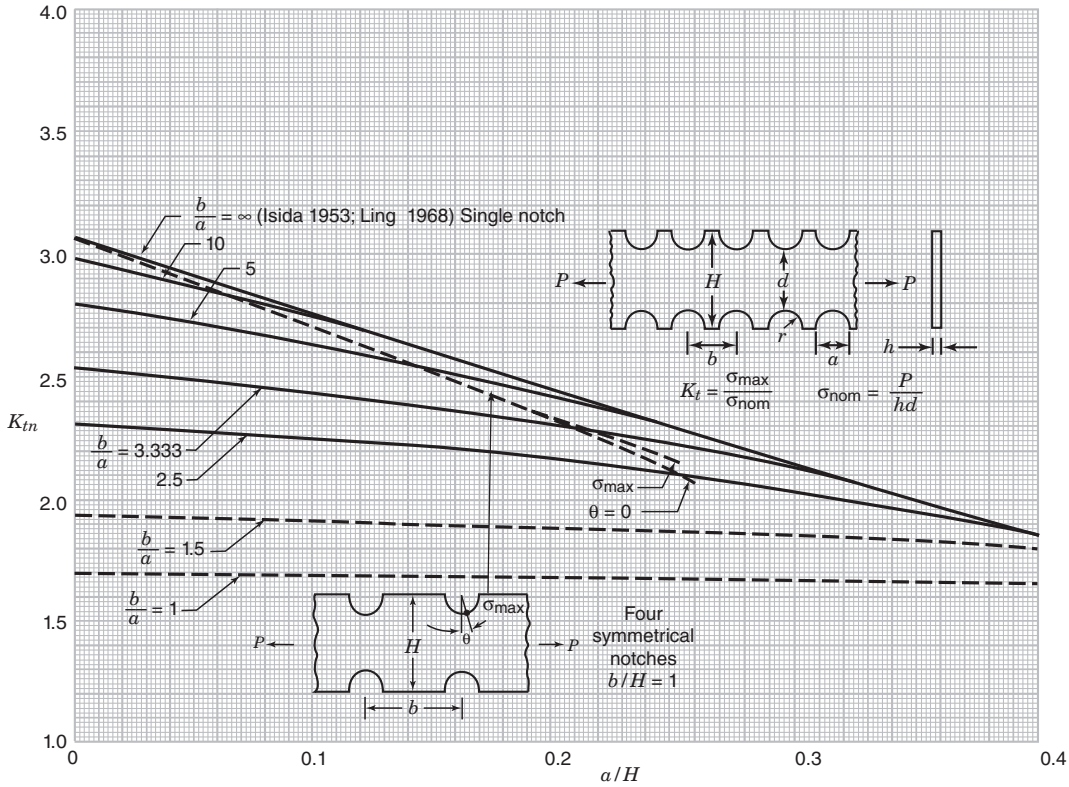


Chart 2.13 Stress concentration factors K_{tn} for a tension bar with infinite rows of semicircular edge notches (from data of Atsumi 1958).

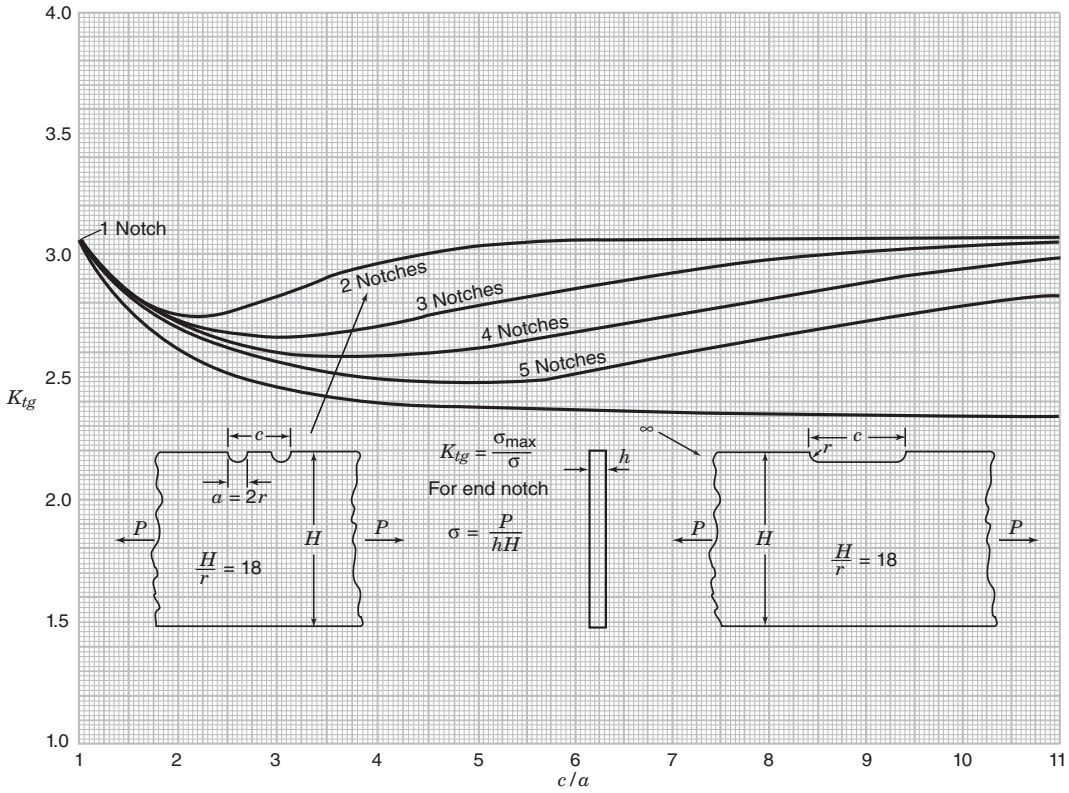


Chart 2.14 Stress concentration factors K_{tg} for tension case of a flat bar with semicircular and flat-bottom notches, $H/r = 18$ (photoelastic tests by Durelli et al. 1952).

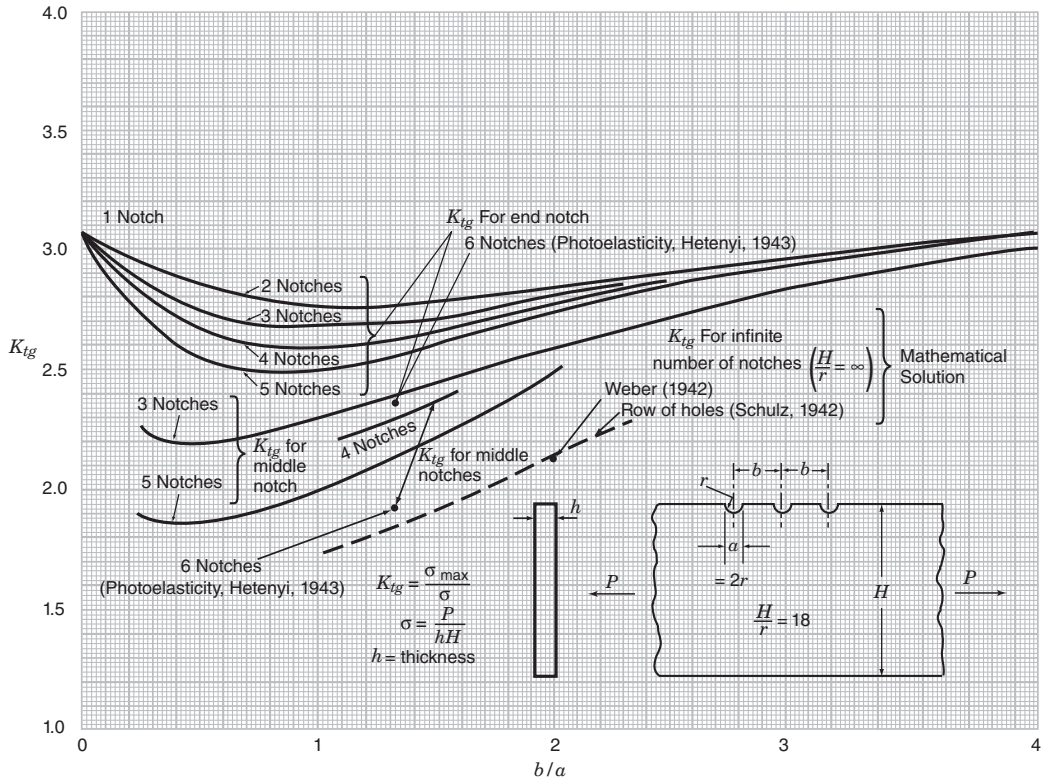


Chart 2.15 Stress concentration factors K_{tg} for tension case of a flat bar with semicircular notches, $H/r = 18$ (photoelastic tests by Durelli et al. 1952).

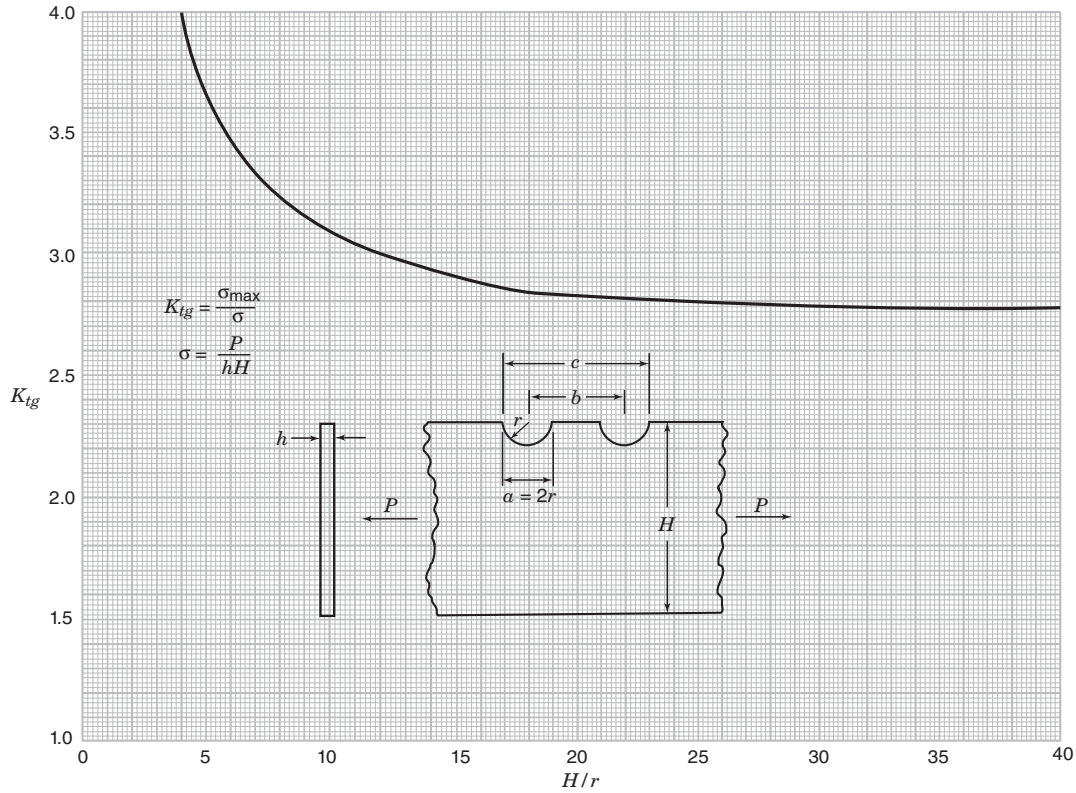


Chart 2.16 Stress concentration factors K_{tg} for tension case of a flat bar with two semicircular notches, $b/a = 2$, $c/a = 3$ (from photoelastic tests by Durelli et al. 1952).

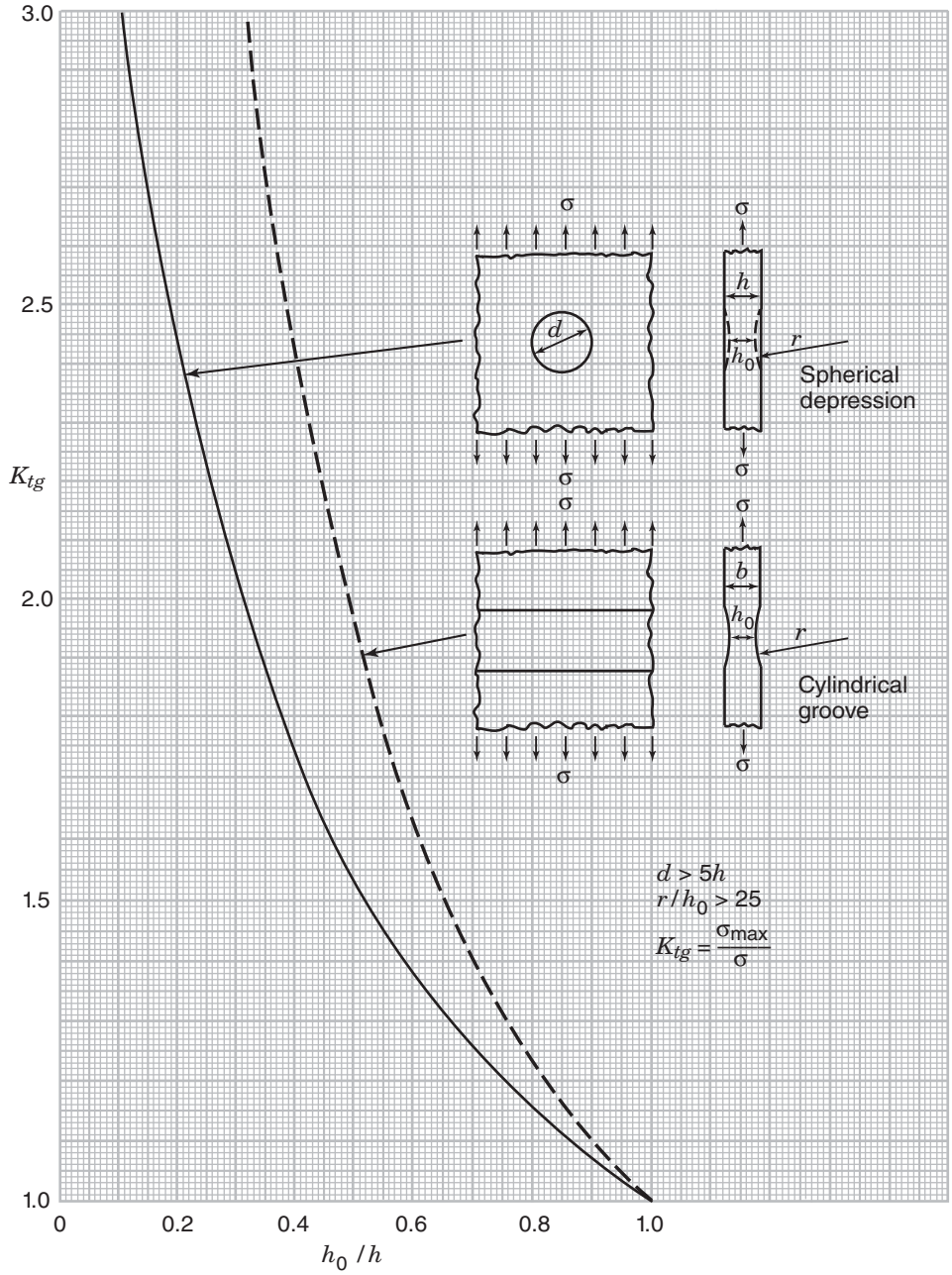


Chart 2.17 Stress concentration factors K_{tg} for a uniaxially stressed infinite thin element with opposite shallow depressions (dimples) (Cowper 1962).

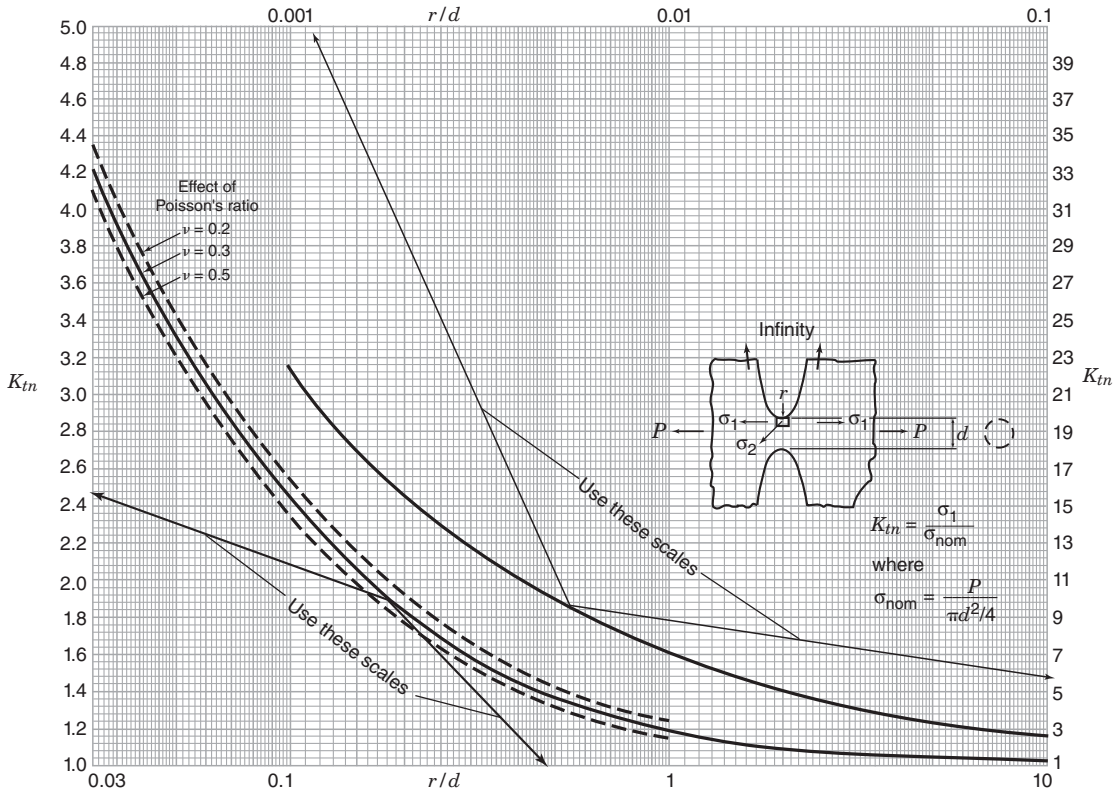


Chart 2.18 Stress concentration factors K_{tn} for a deep hyperbolic groove in an infinitely wide member with a circular net section, three-dimensional case, in tension (Neuber 1958 solution).

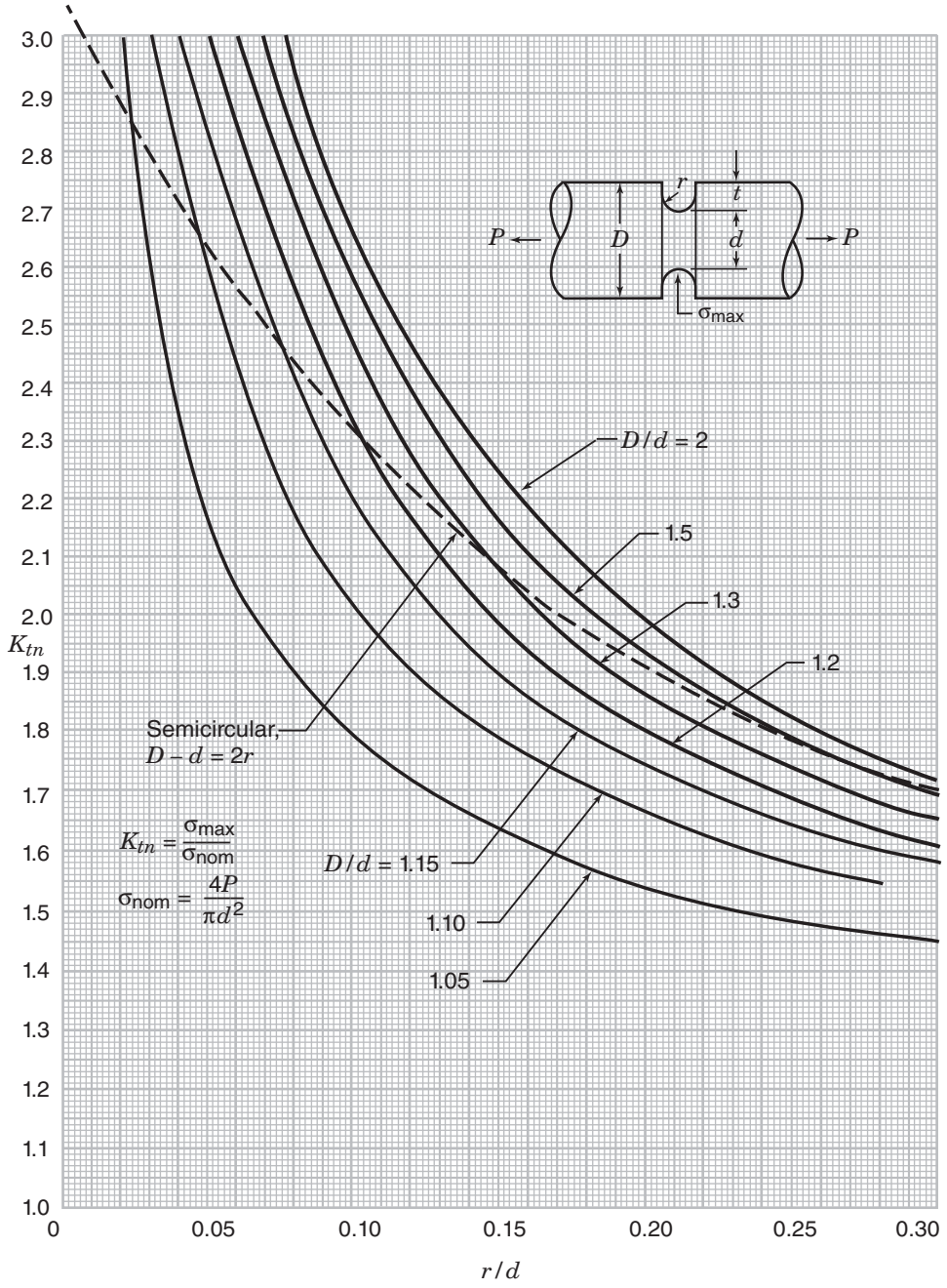


Chart 2.19 Stress concentration factors K_{tn} for a tension bar of circular cross section with a U-shaped groove. Values are approximate.

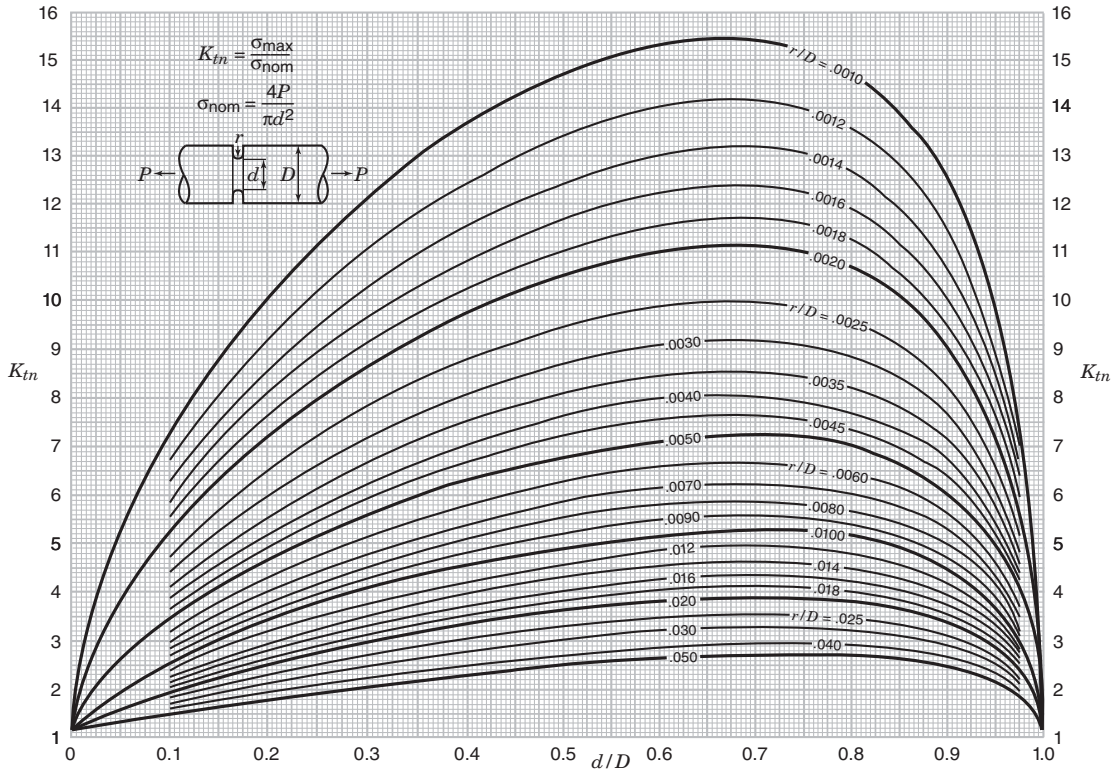


Chart 2.20 Stress concentration factors K_{tn} for a grooved shaft in tension with a U-shaped groove, r/d from 0.001 to 0.05 (from Neuber 1958 formulas).

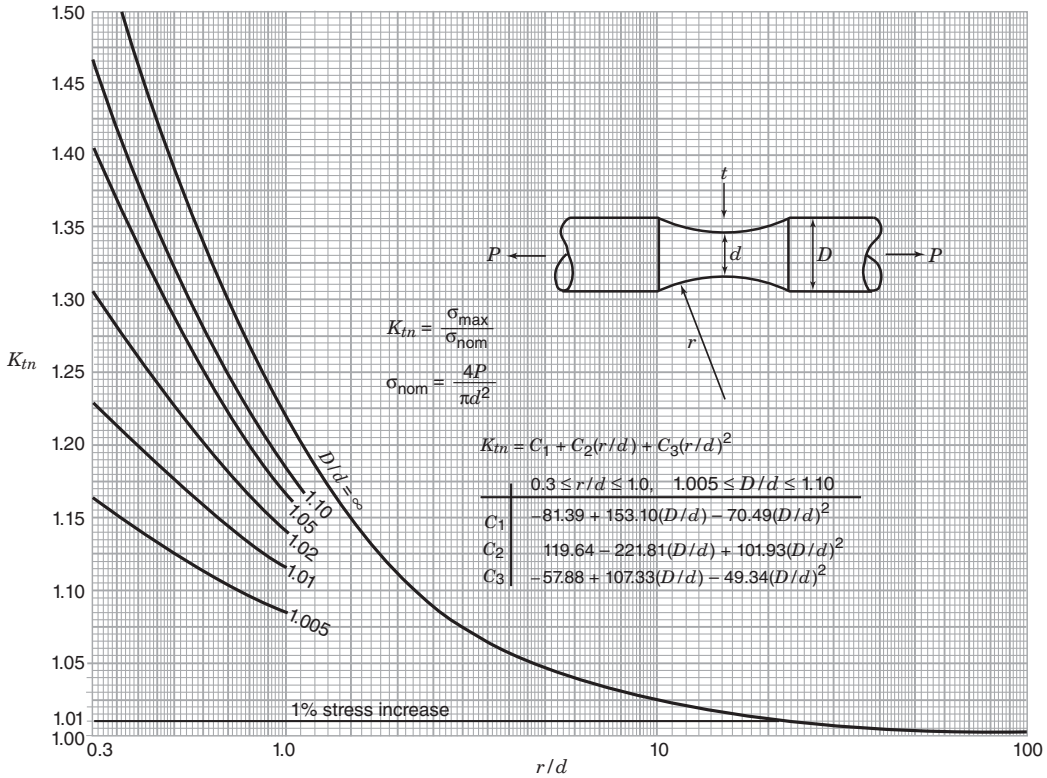


Chart 2.21 Stress concentration factors K_{tn} for a test specimen of circular cross section in tension with a U-shaped groove (curves represent calculated values using Neuber 1958 theory).

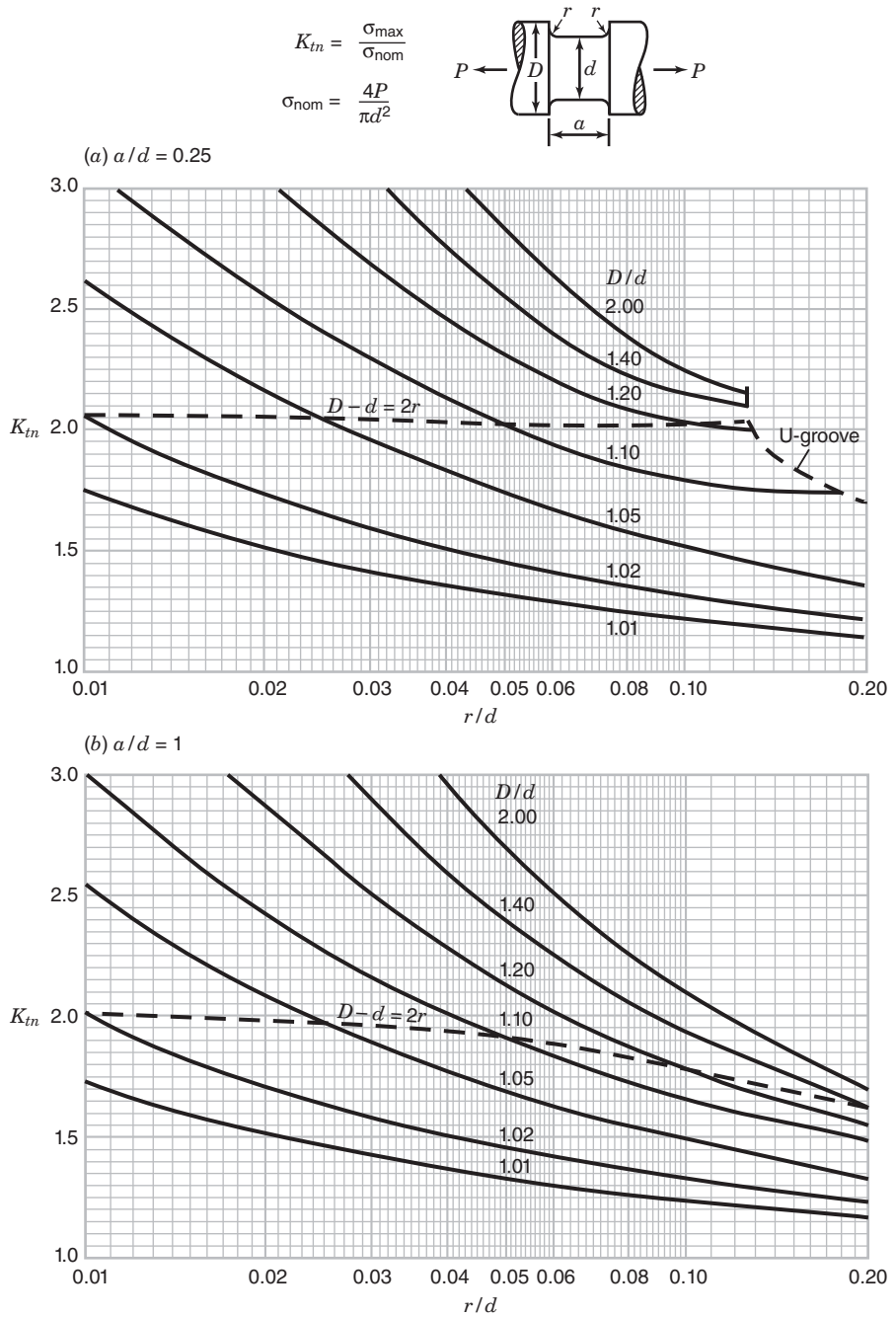


Chart 2.22 Stress concentration factors K_{tn} for flat-bottom grooves in tension (Neuber 1958 formulas; ESDU 1981): (*a*) $a/d = 0.25$; (*b*) $a/d = 1$.

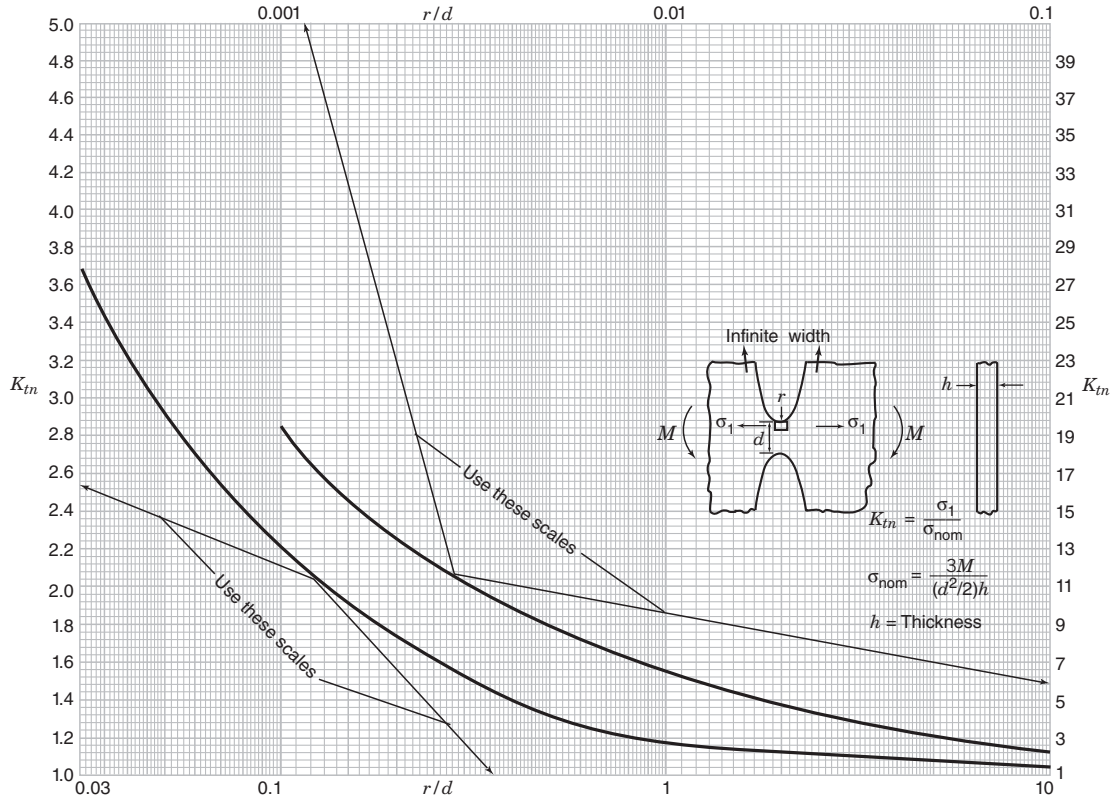


Chart 2.23 Stress concentration factors K_{tn} for opposite deep hyperbolic notches in an infinitely wide thin element, two-dimensional case, subject to in-plane moments (Neuber 1958 solution).

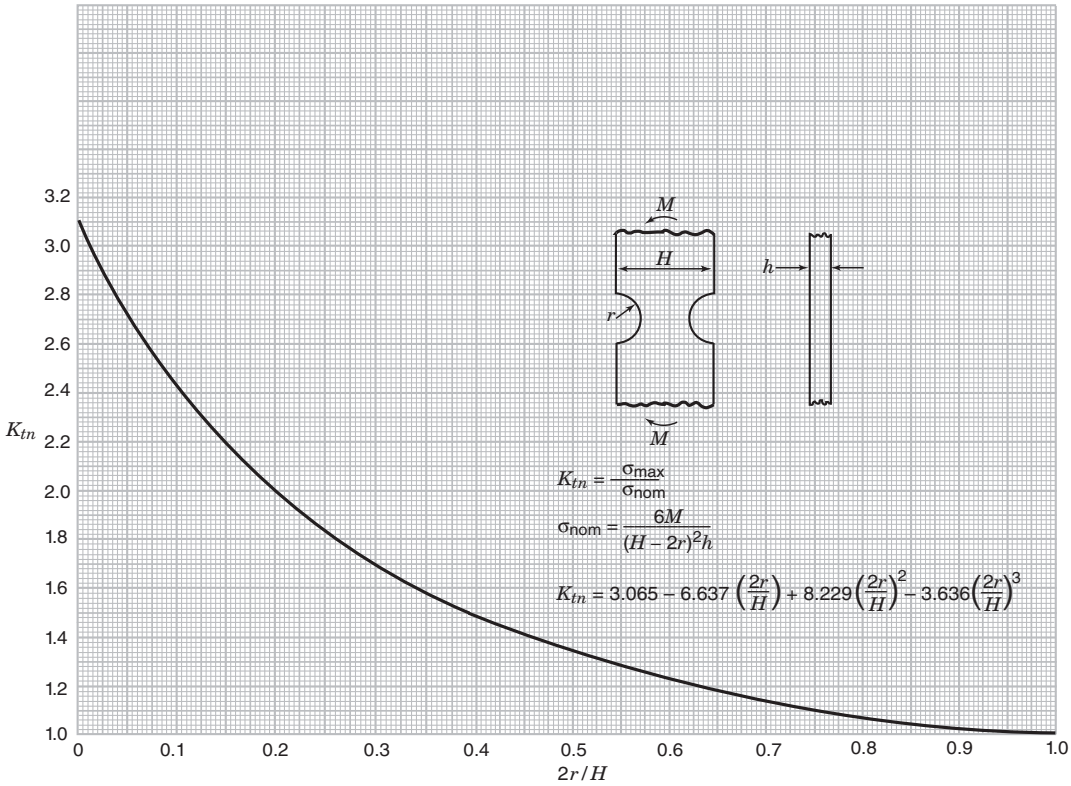


Chart 2.24 Stress concentration factors K_{tn} for bending of a flat beam with semicircular edge notches (Isida 1953; Ling 1967).

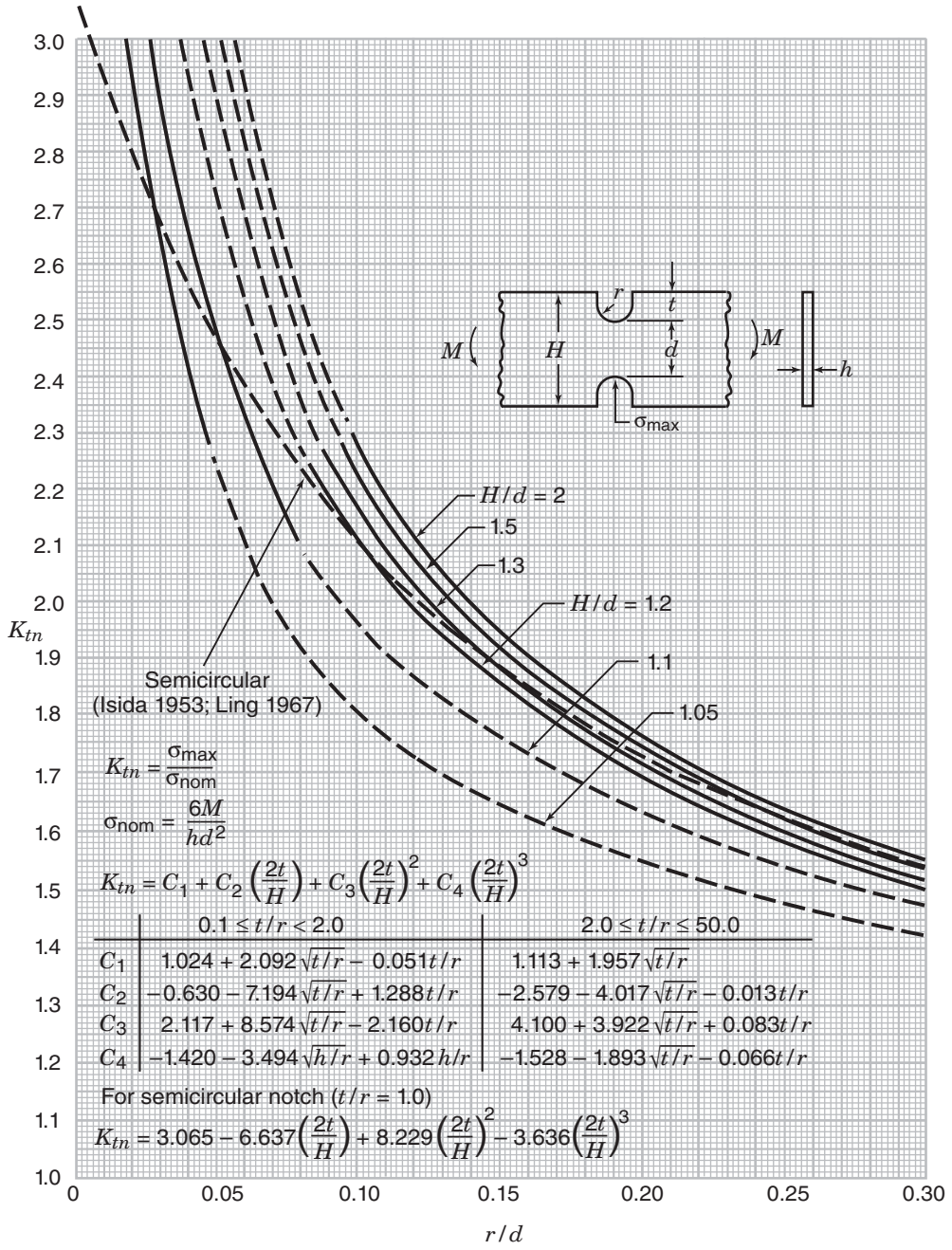


Chart 2.25 Stress concentration factors K_{tn} for bending of a flat beam with opposite U notches (from data of Frocht 1935; Isida 1953; Ling 1967).

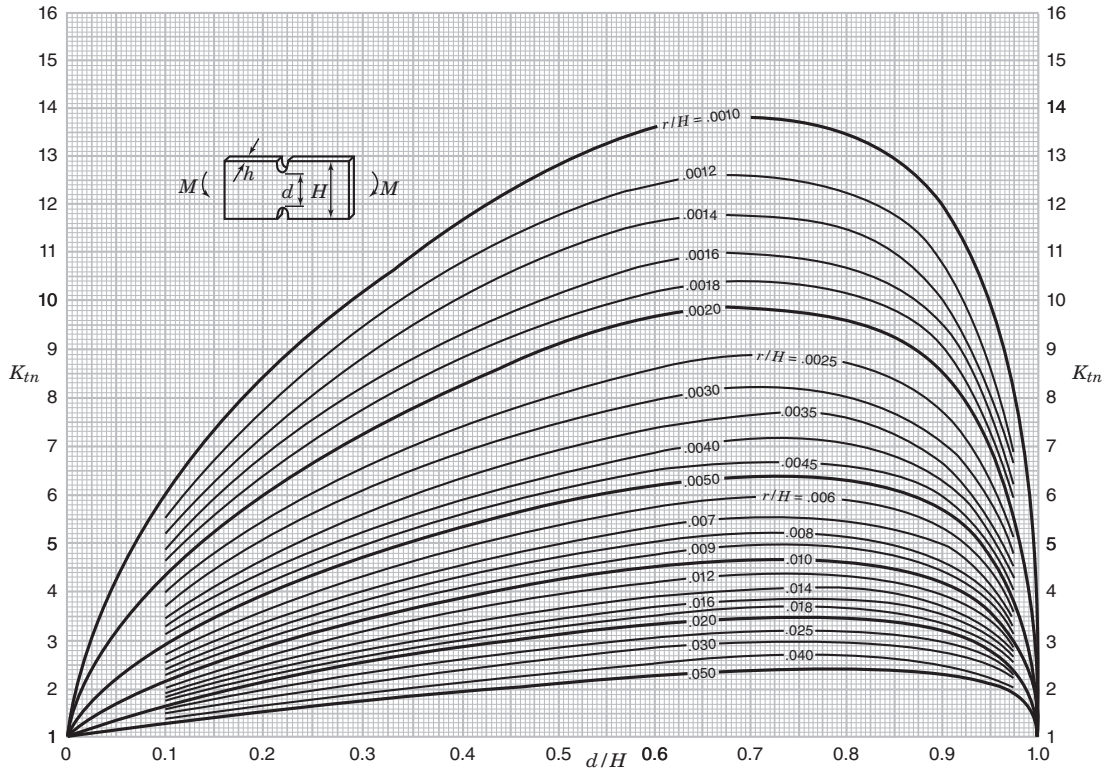


Chart 2.26 Stress concentration factors K_{tn} for bending of flat beam with opposite U notches, r/H from 0.001 to 0.05 (from Neuber 1958 formulas).

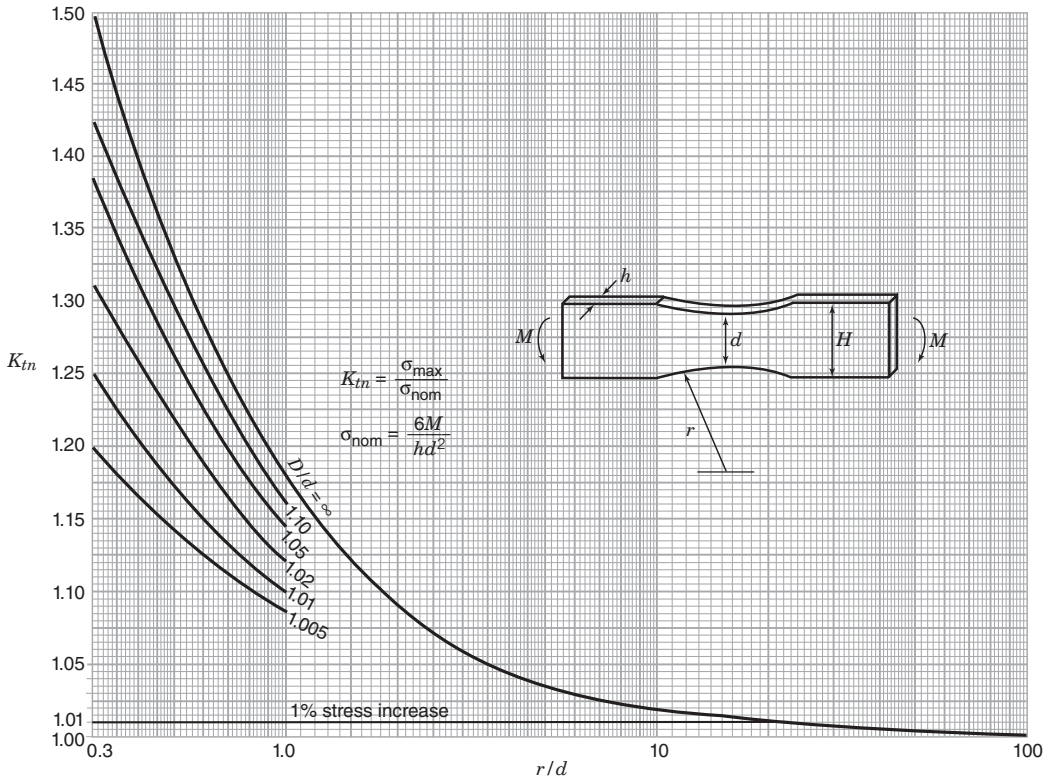


Chart 2.27 Stress concentration factors K_{tn} for bending of a flat beam with opposite shallow U notches (curves represent calculated values using Neuber 1958 theory).

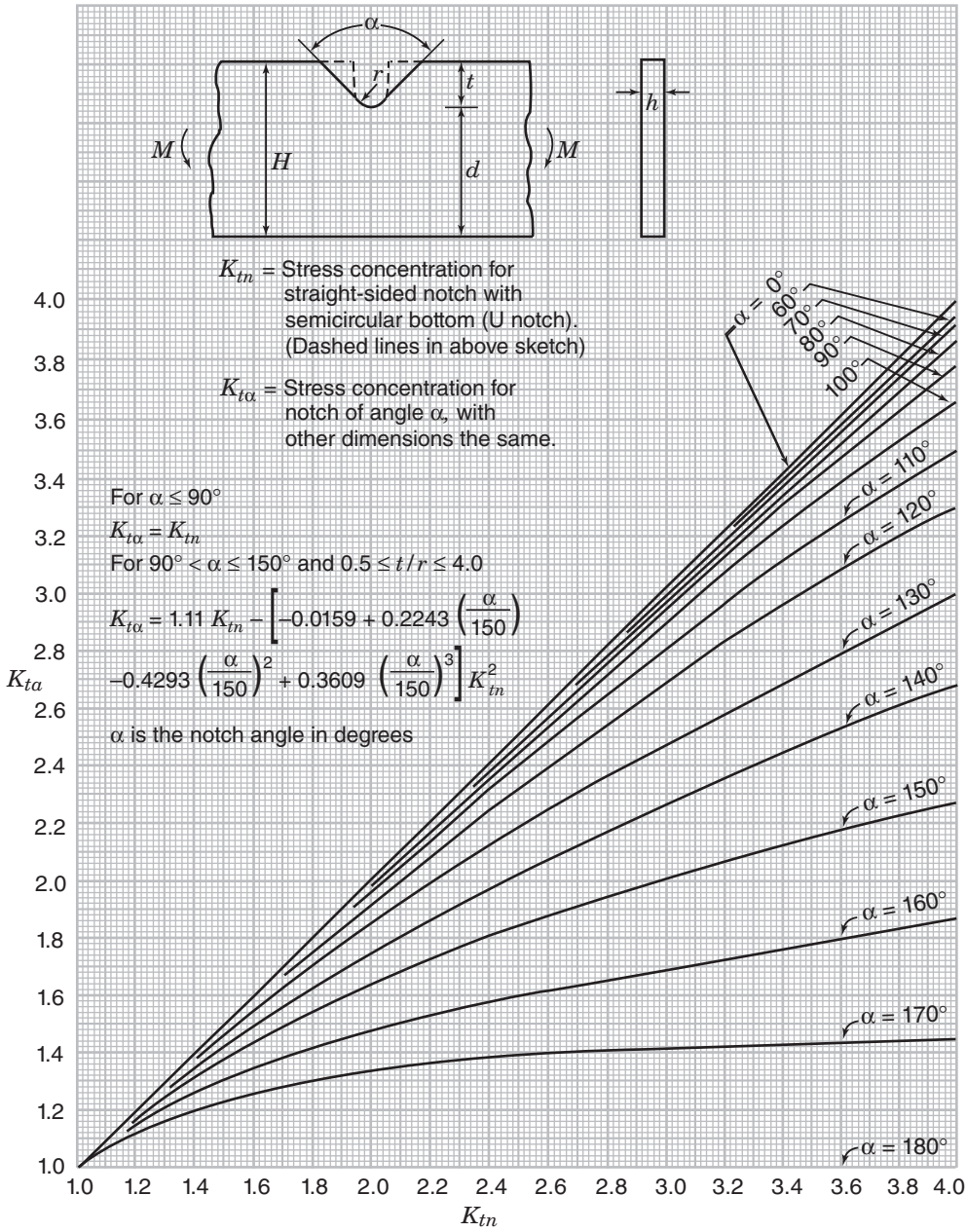


Chart 2.28 Effect of notch angle on stress concentration factors for a thin beam element in bending with a V-shaped notch on one side (Leven and Frocht 1953).

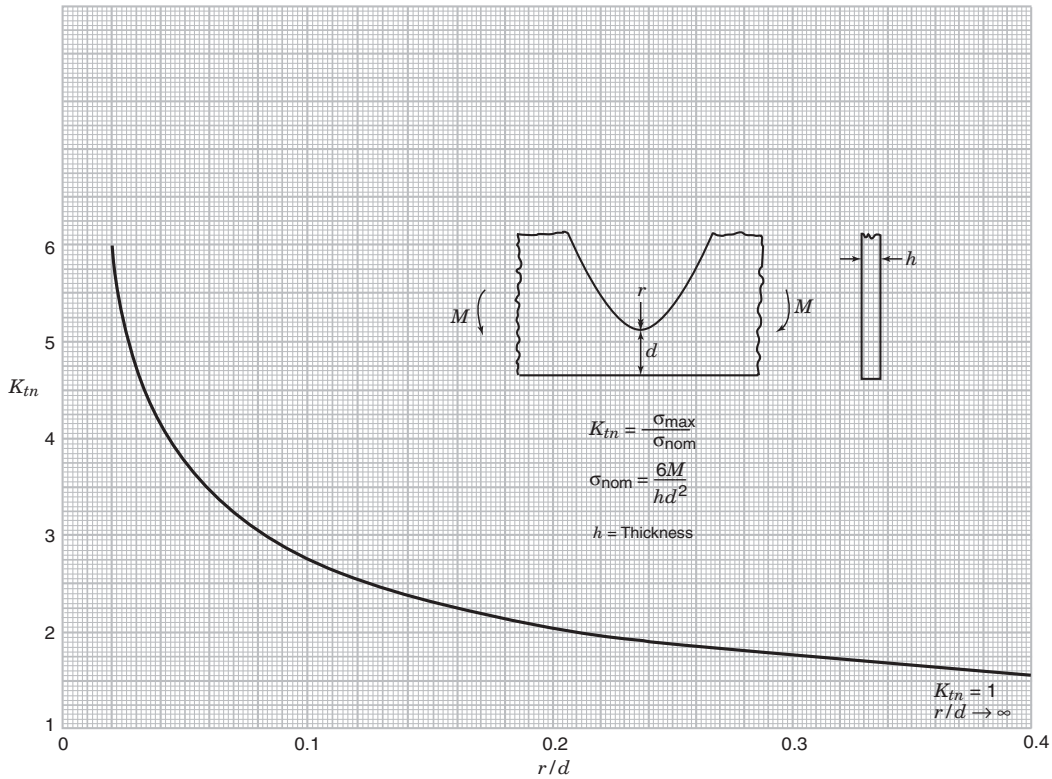


Chart 2.29 Stress concentration factors K_m for bending of a semi-infinite thin element with a deep hyperbolic notch (Neuber 1958).

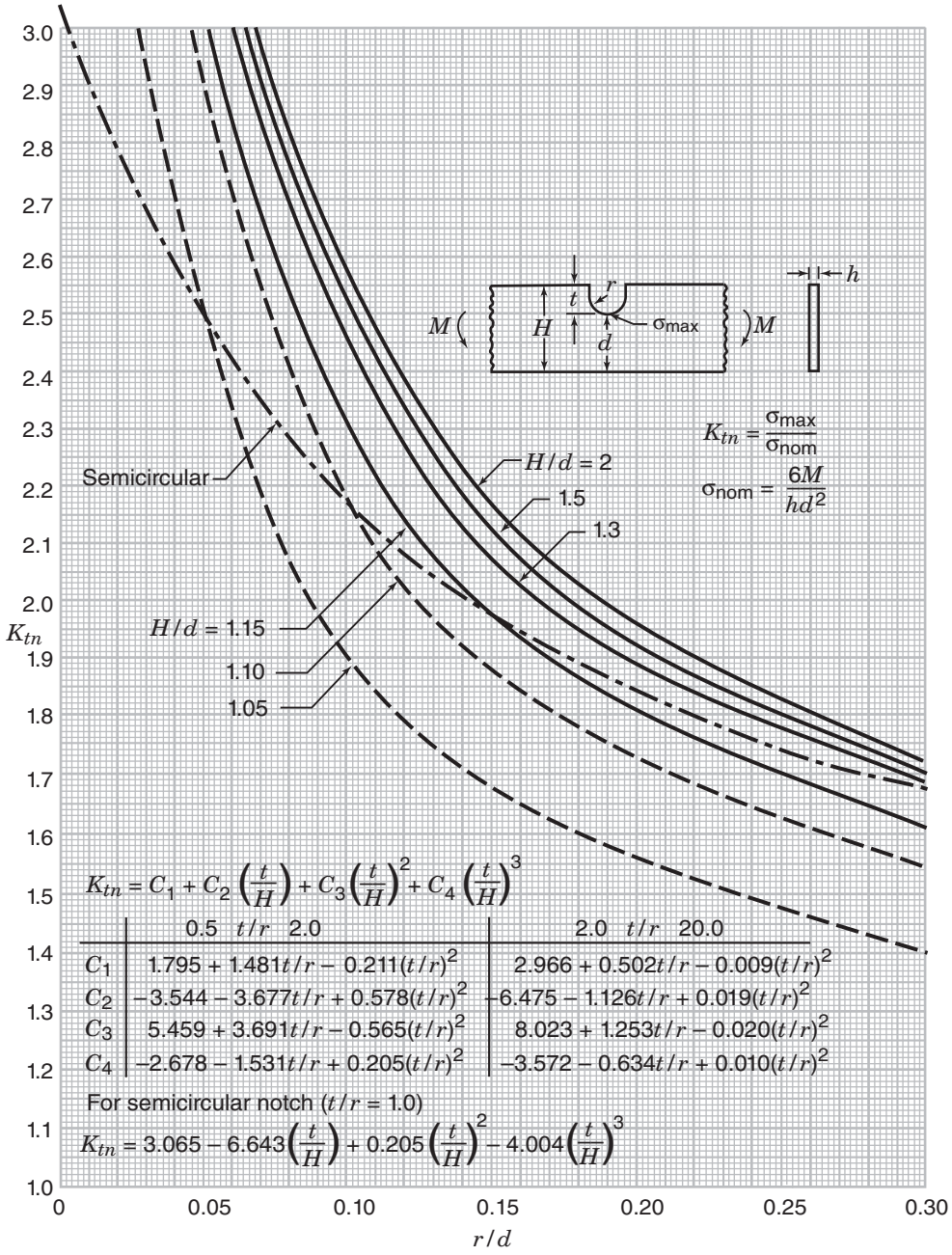


Chart 2.30*a* Bending of a thin beam element with a notch on one side (Leven and Frocht 1953): stress concentration factors K_{tn} for a U-shaped notch.

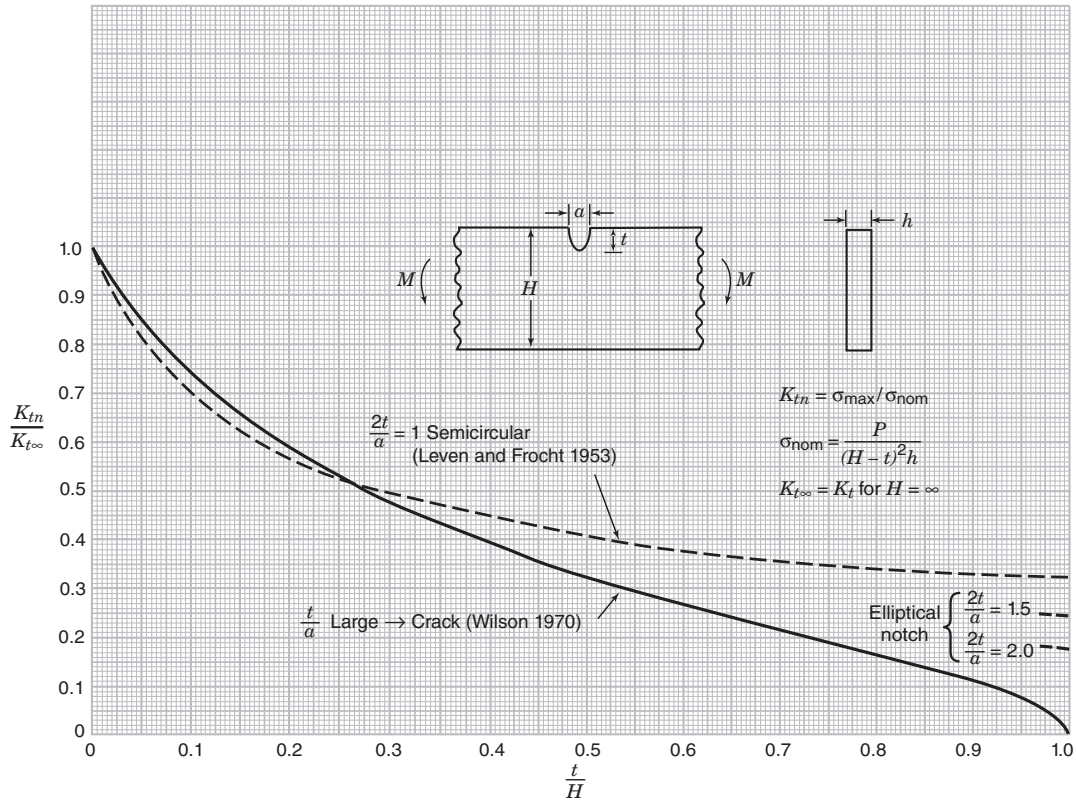


Chart 2.30*b* Bending of a thin beam element with a notch on one side (Leven and Frocht 1953): finite-width concentration factors for cracks (Wilson 1970).

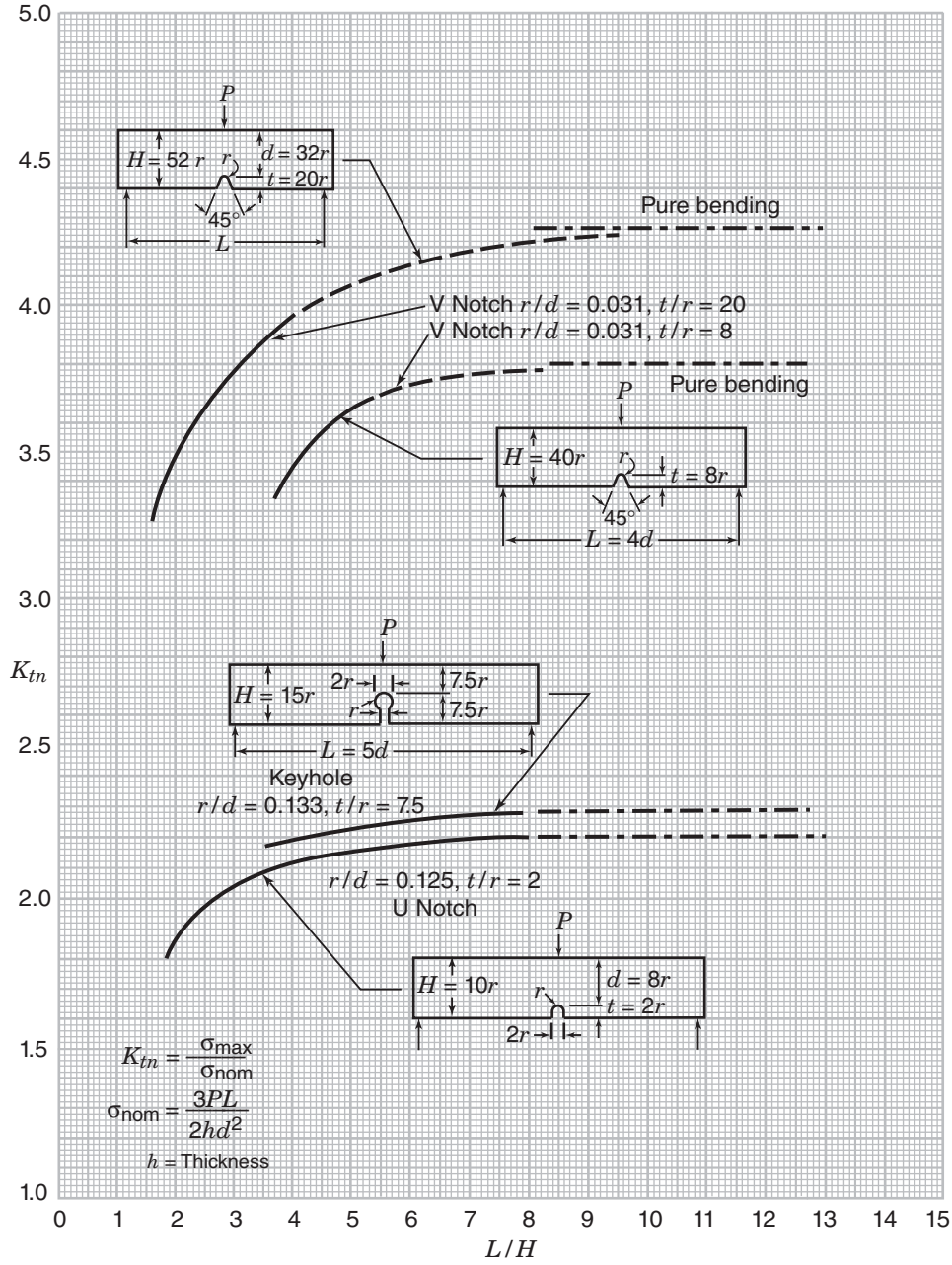


Chart 2.31 Effect of span on stress concentration factors for various impact test pieces (Leven and Frocht 1953).

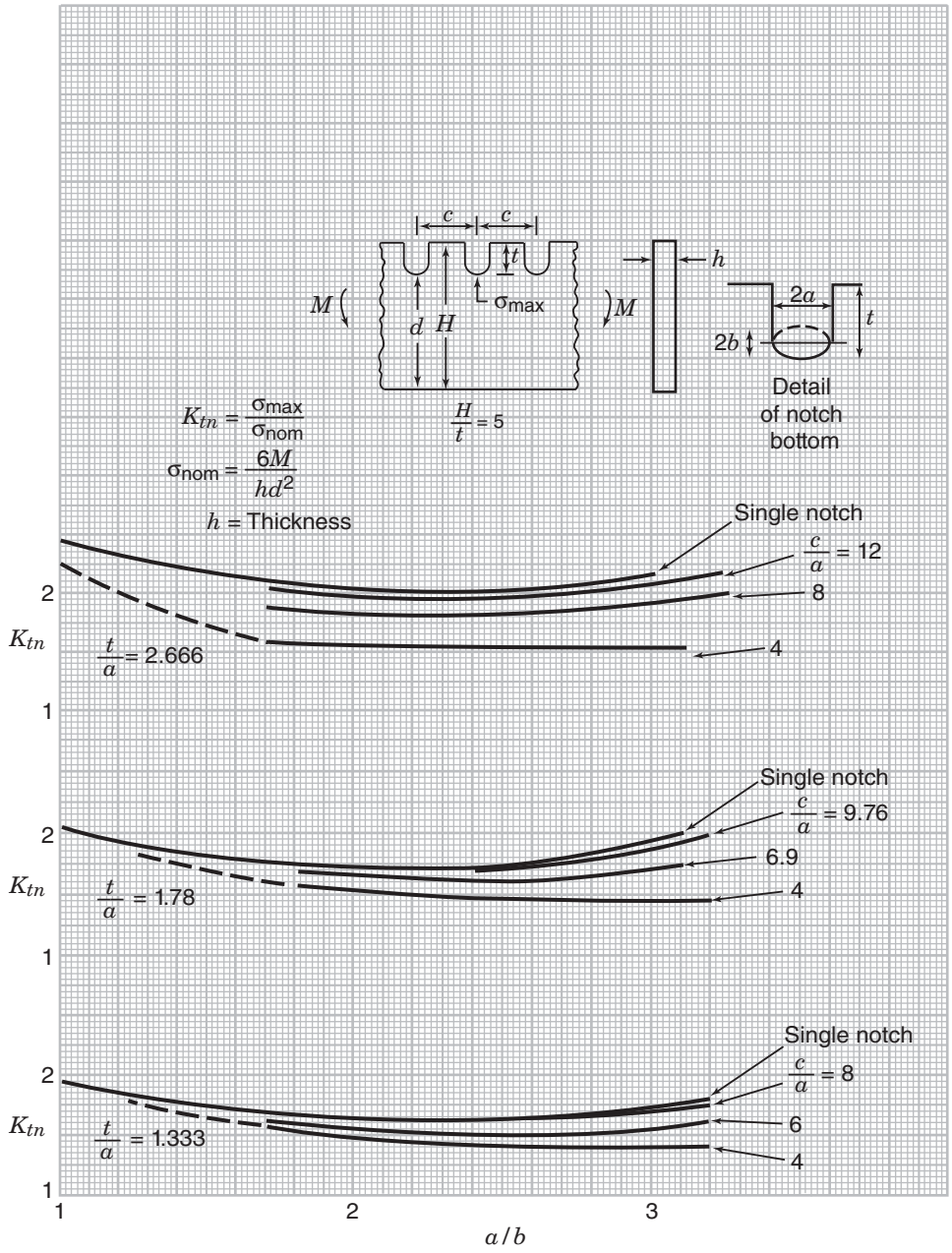


Chart 2.32 Stress concentration factors K_{tn} for bending of a thin beam having single or multiple notches with a semielliptical bottom (Ching et al. 1968).

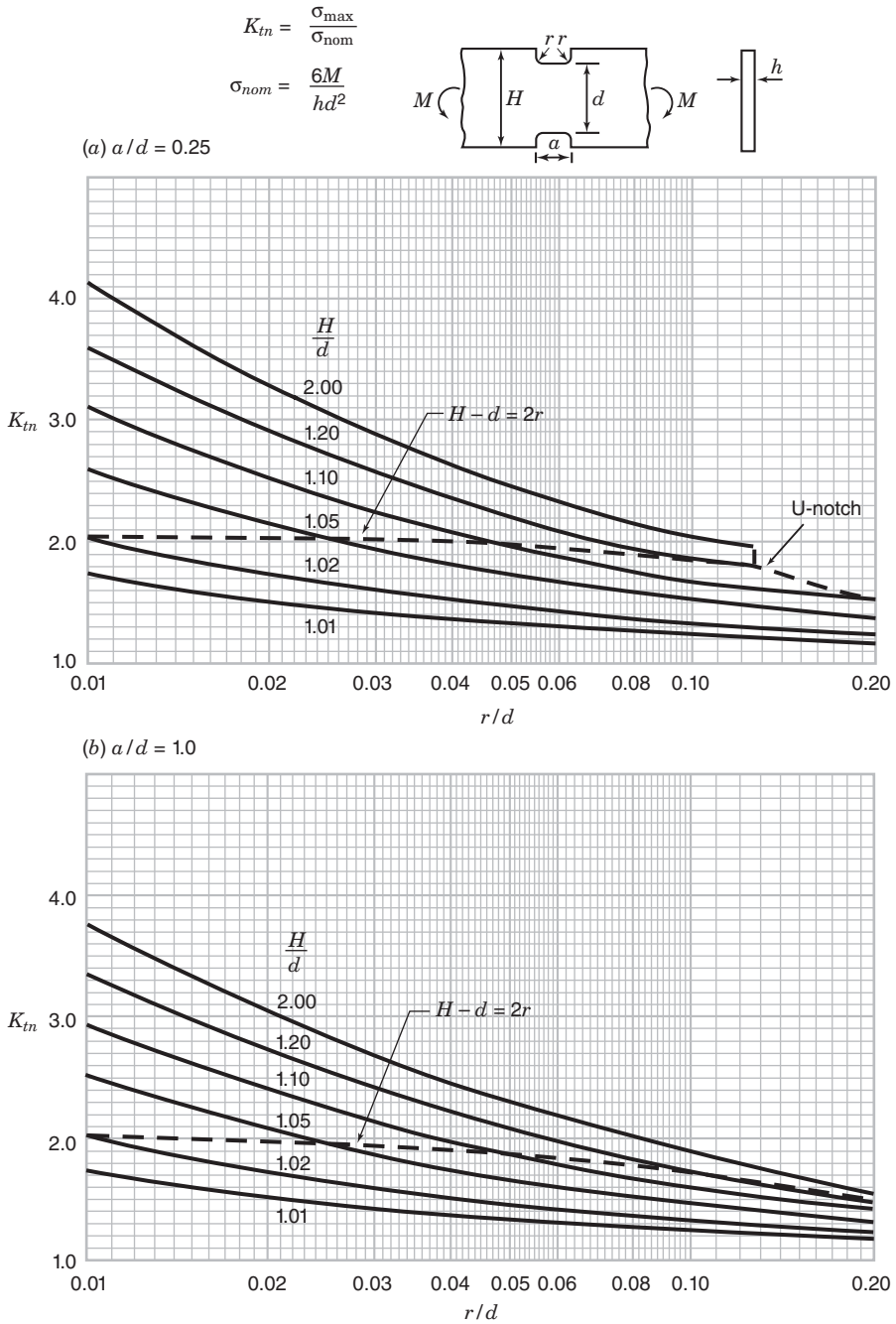
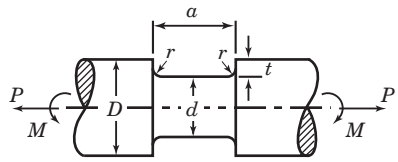


Chart 2.33 Stress concentration factors K_{tn} for thin beam in bending with opposite notches with flat bottoms (Neuber 1958; Sobey 1965; ESDU 1981): (*a*) $a/d = 0.25$; (*b*) $a/d = 1.0$.

$$K_{tn} = \frac{\sigma_{max}}{\sigma_{nom}}$$

$$\sigma_{nom} = \frac{4P}{\pi d^2} + \frac{32M}{\pi d^3}$$



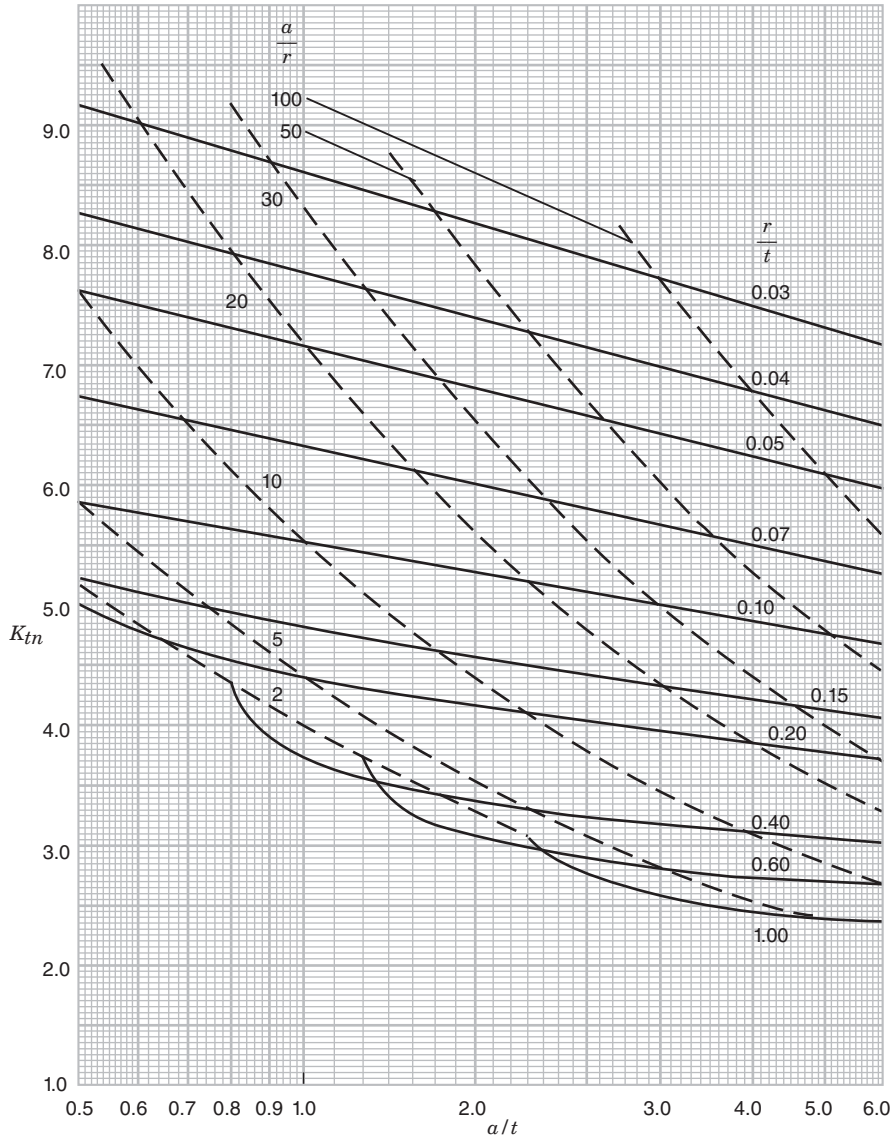


Chart 2.34 Stress concentration factors K_{tn} for a shaft in bending and/or tension with flat-bottom groove (Rubenchik 1975; ESDU 1981).

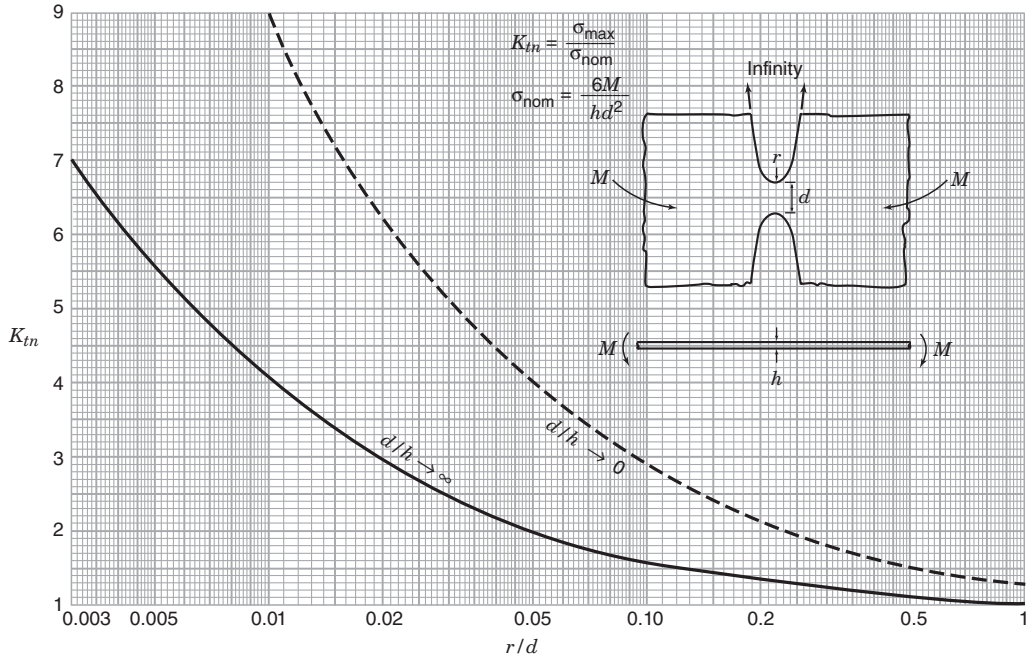


Chart 2.35 Stress concentration factors K_{tn} for a deep hyperbolic notch in an infinitely wide thin plate in transverse bending, $\nu = 0.3$ (Lee 1940; Neuber 1958).

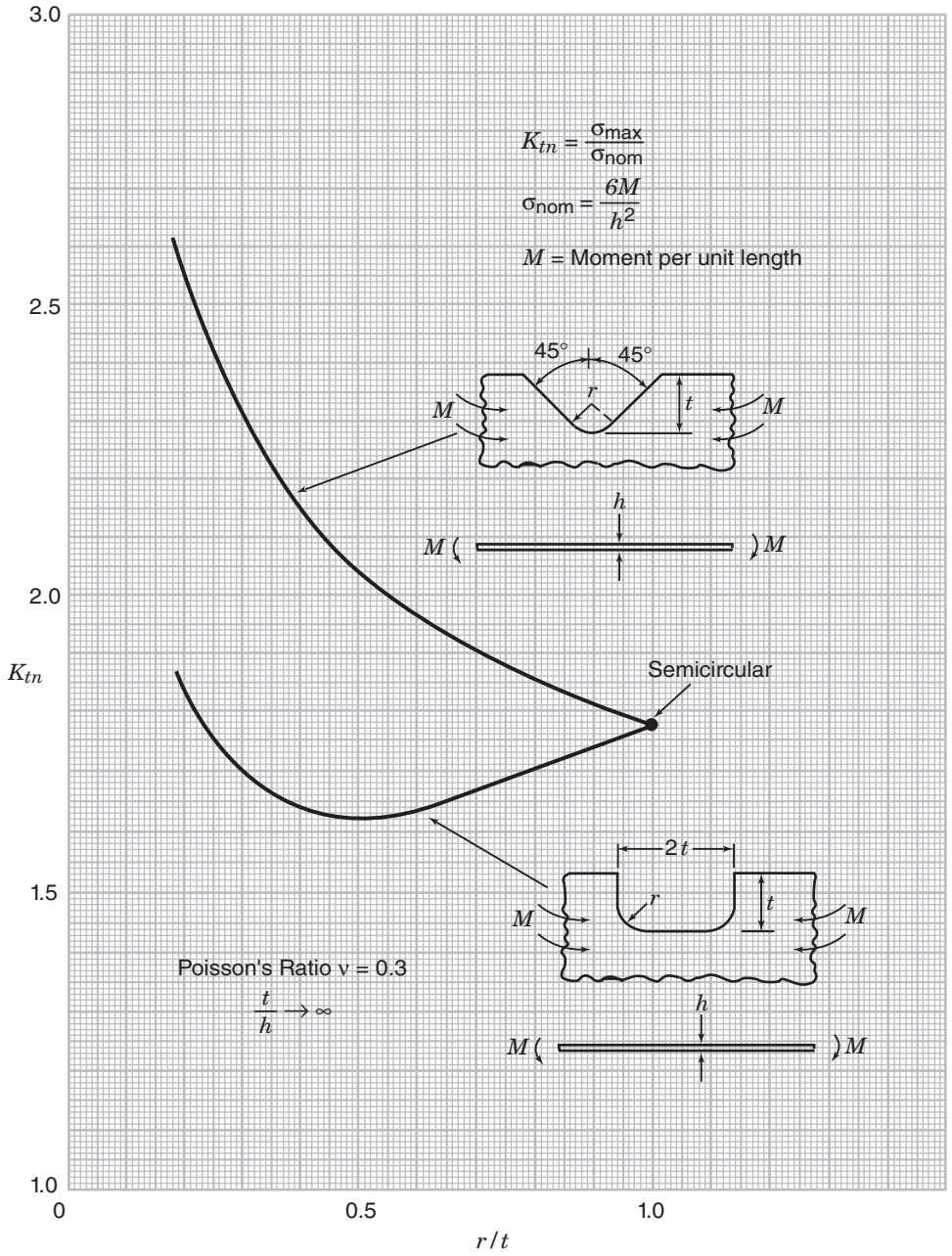


Chart 2.36 Stress concentration factors K_{tn} for rounded triangular or rectangular notches in semi-infinite plate in transverse bending (Shioya 1959).

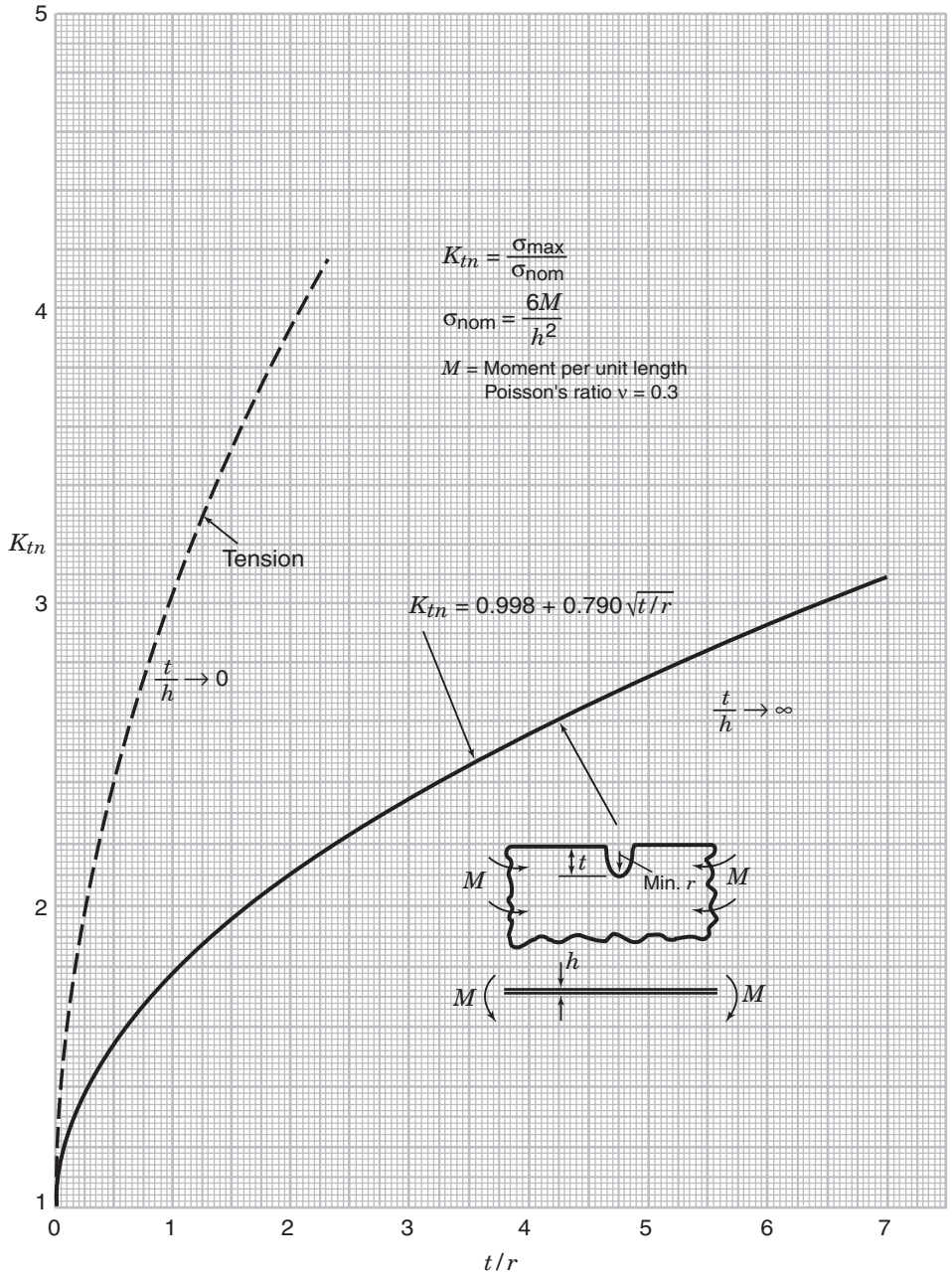


Chart 2.37 Stress concentration factors K_{tn} for an elliptical notch in a semi-infinite plate in transverse bending (from data of Shioya 1960).

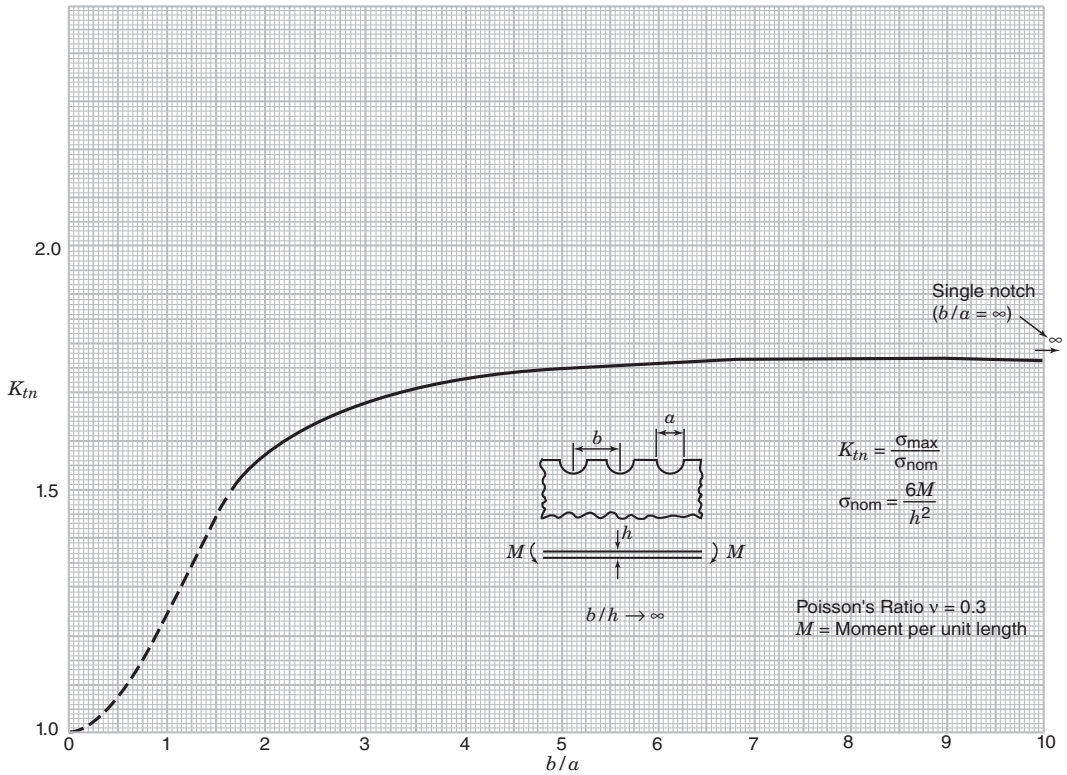


Chart 2.38 Stress concentration factors K_{tn} for infinite row of semicircular notches in a semi-infinite plate in transverse bending (from data of Shioya 1963).

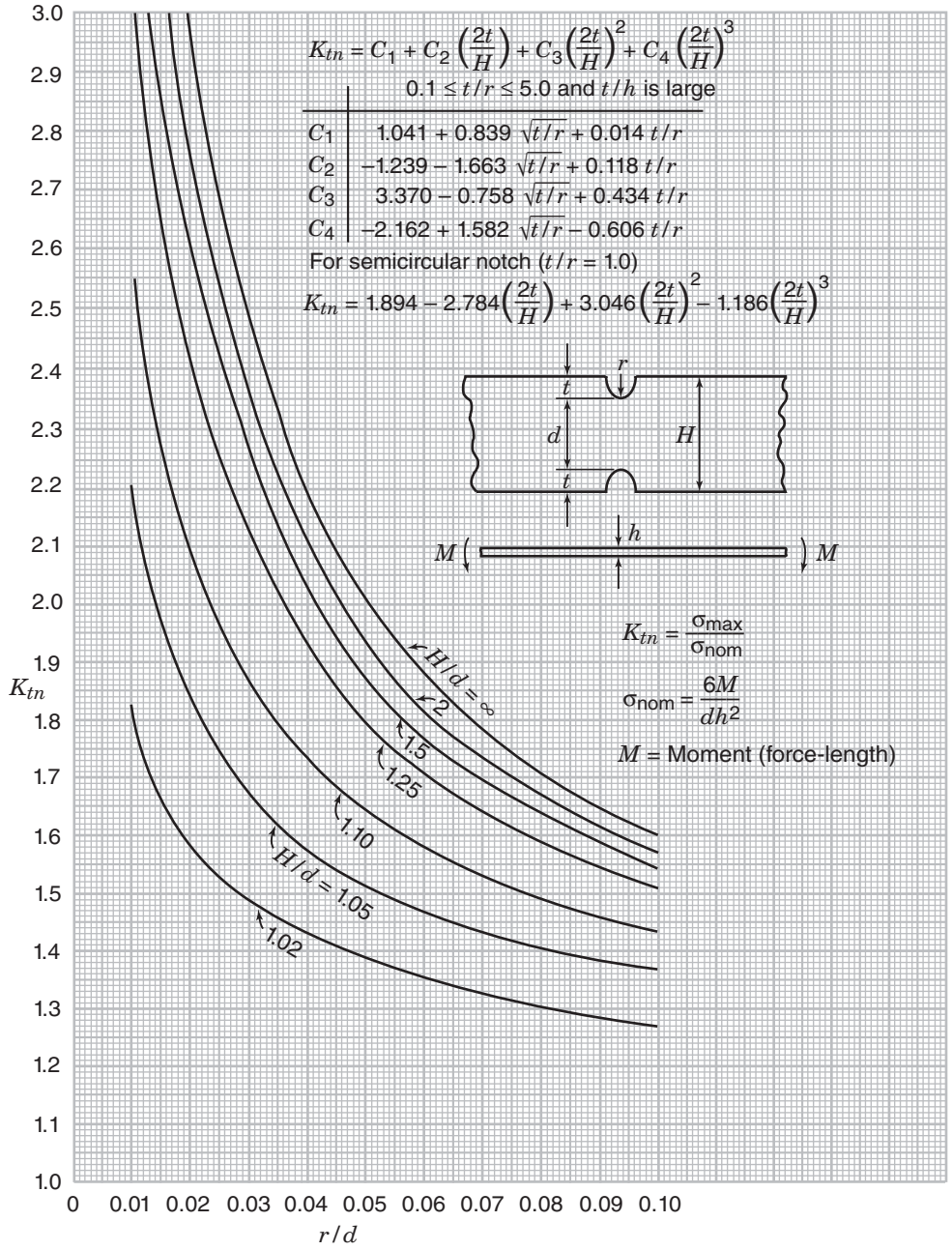


Chart 2.39 Stress concentration factors K_{tn} for a thin notched plate in transverse bending, t/h large (based on mathematical analyses of Lee 1940; Neuber 1958; Shioya 1960).

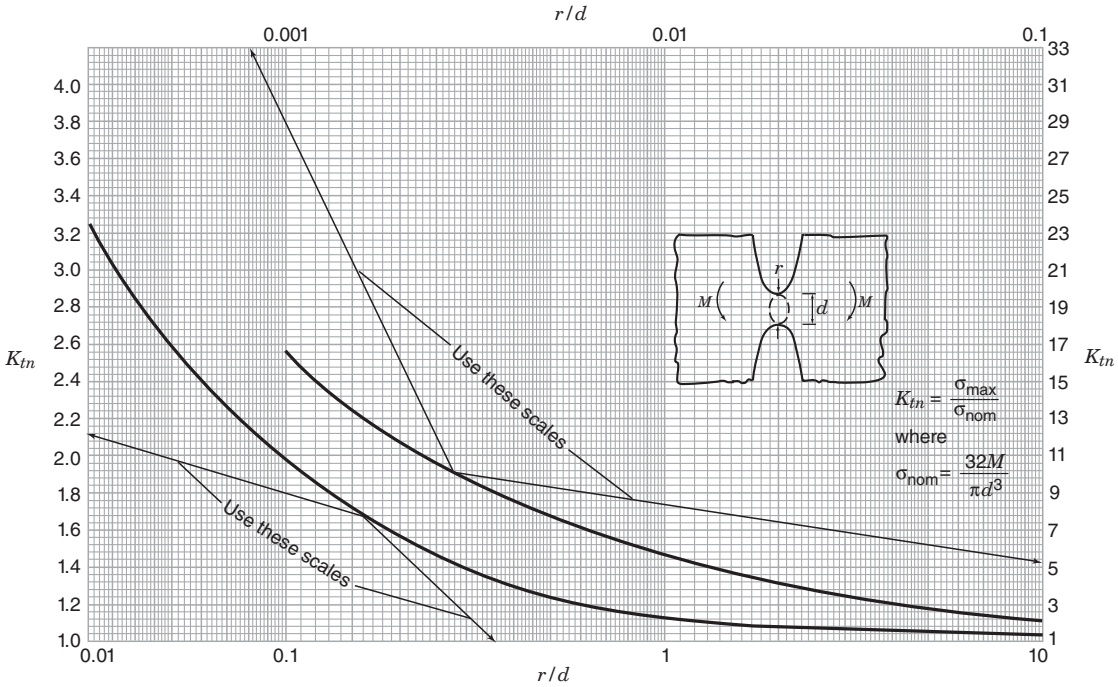


Chart 2.40 Stress concentration factors K_{tn} for a deep hyperbolic groove in an infinite-member, three-dimensional case, subject to moments (Neuber 1958 solution). The net cross section is circular.

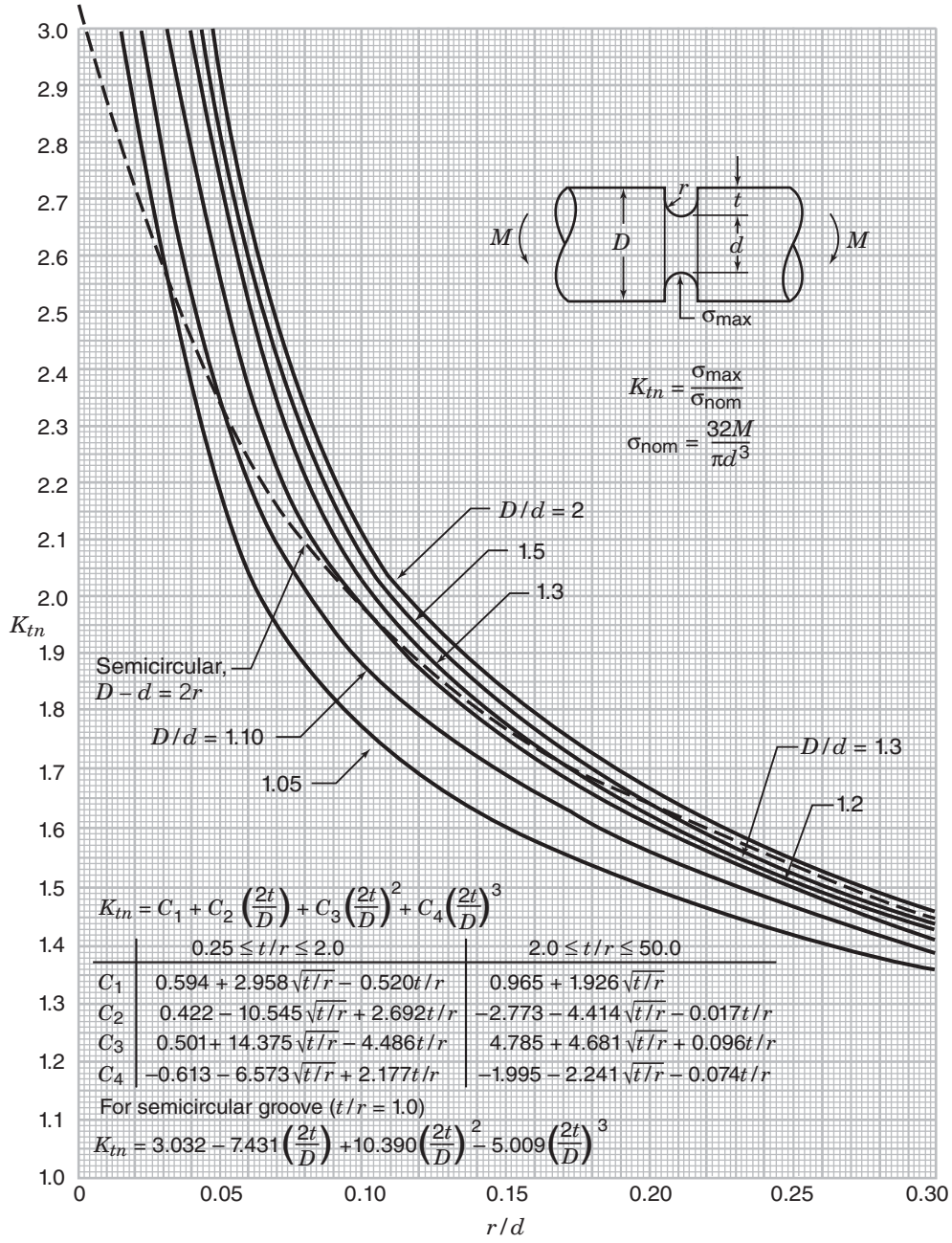


Chart 2.41 Stress concentration factors K_{tn} for bending of a bar of circular cross section with a U-shaped groove. K_t values are approximate.

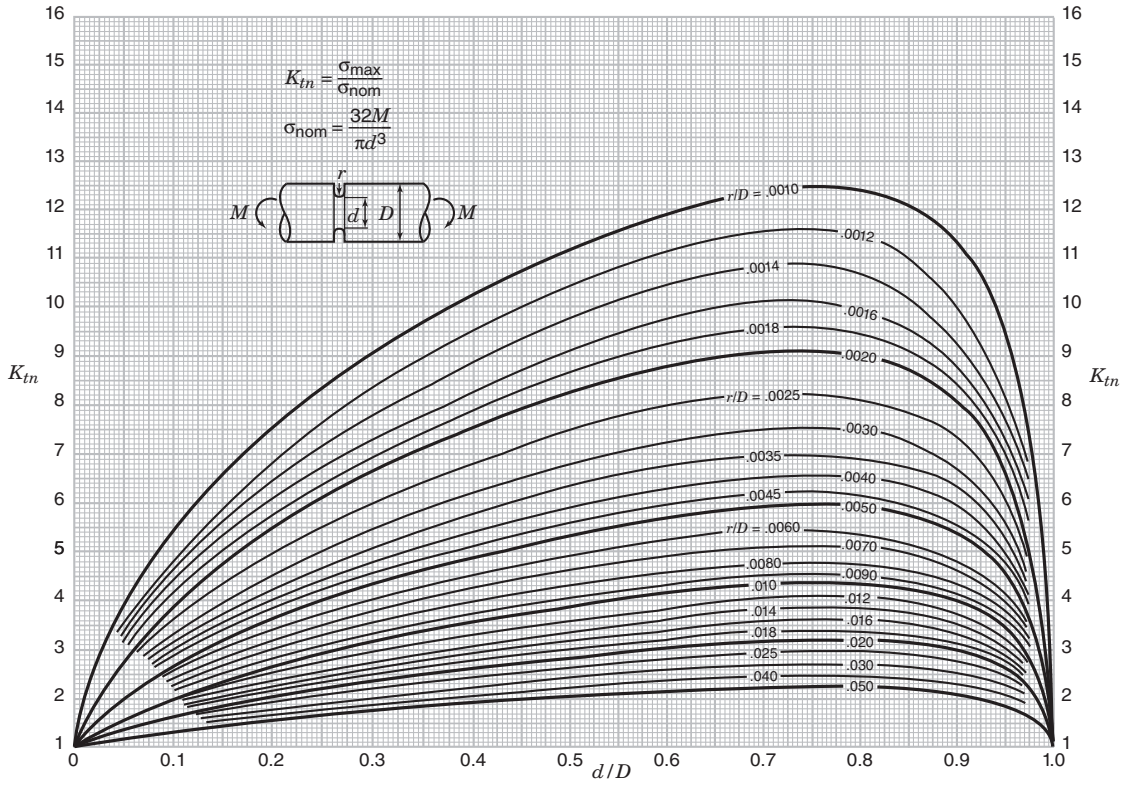


Chart 2.42 Stress concentration factors K_{tn} for a U-shaped grooved shaft of circular cross section in bending, r/D from 0.001 to 0.050 (from Neuber 1958 formulas).

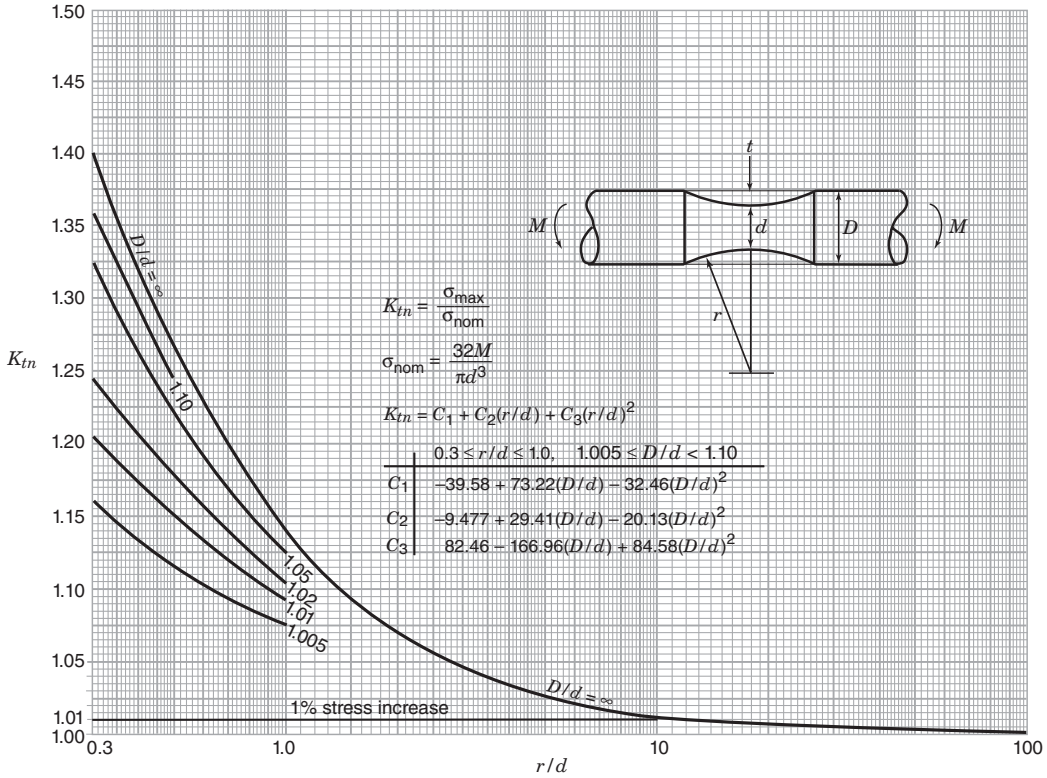


Chart 2.43 Stress concentration factors K_{tn} for bending of a bar of circular cross section with a shallow U-shaped groove (curves represent calculated values using Neuber 1958 theory).

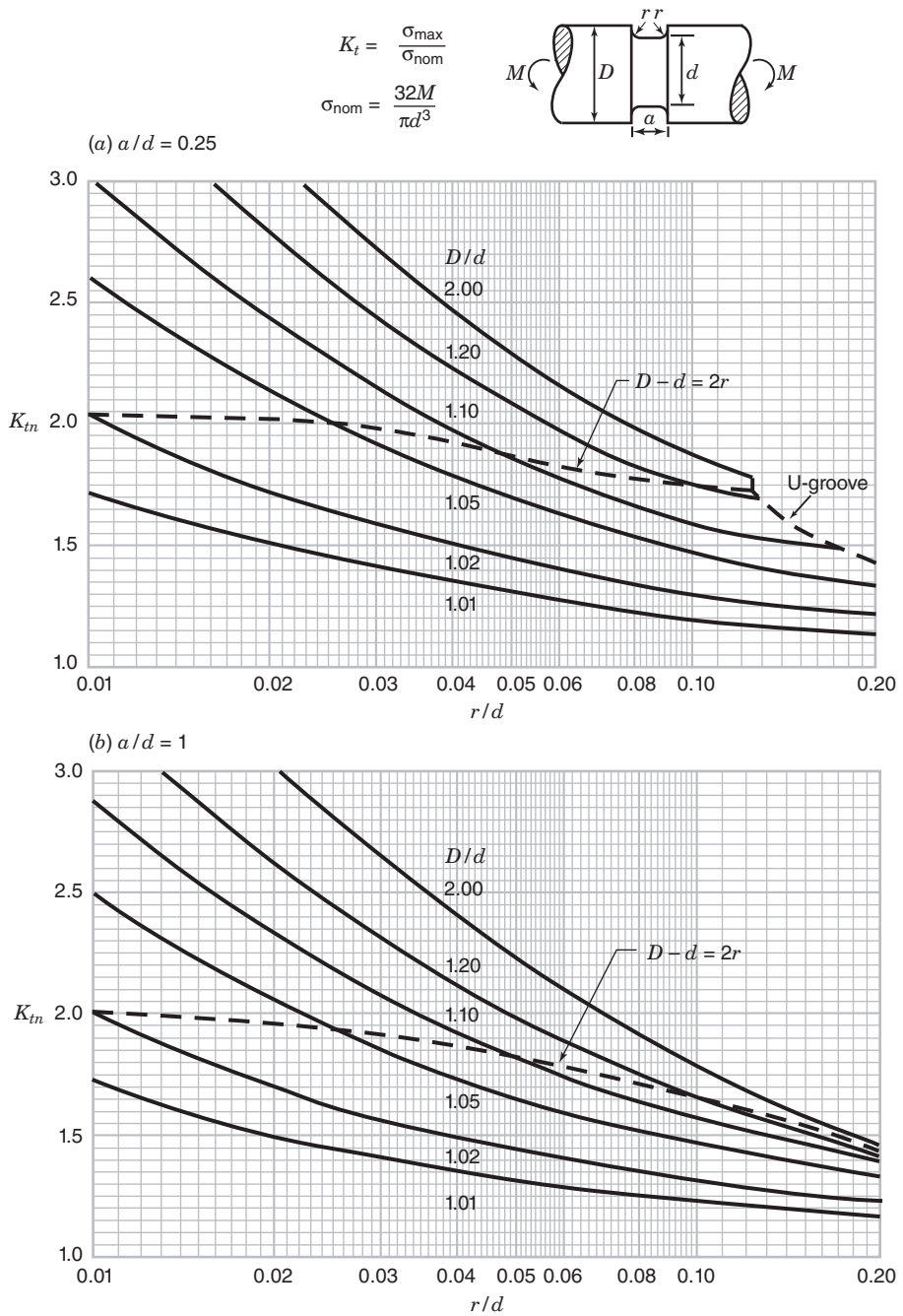


Chart 2.44 Stress concentration factors K_{tn} for bending of a bar of circular cross section with flat-bottom grooves (from Peterson 1953; ESDU 1981): (*a*) $a/d = 0.25$; (*b*) $a/d = 1.0$.

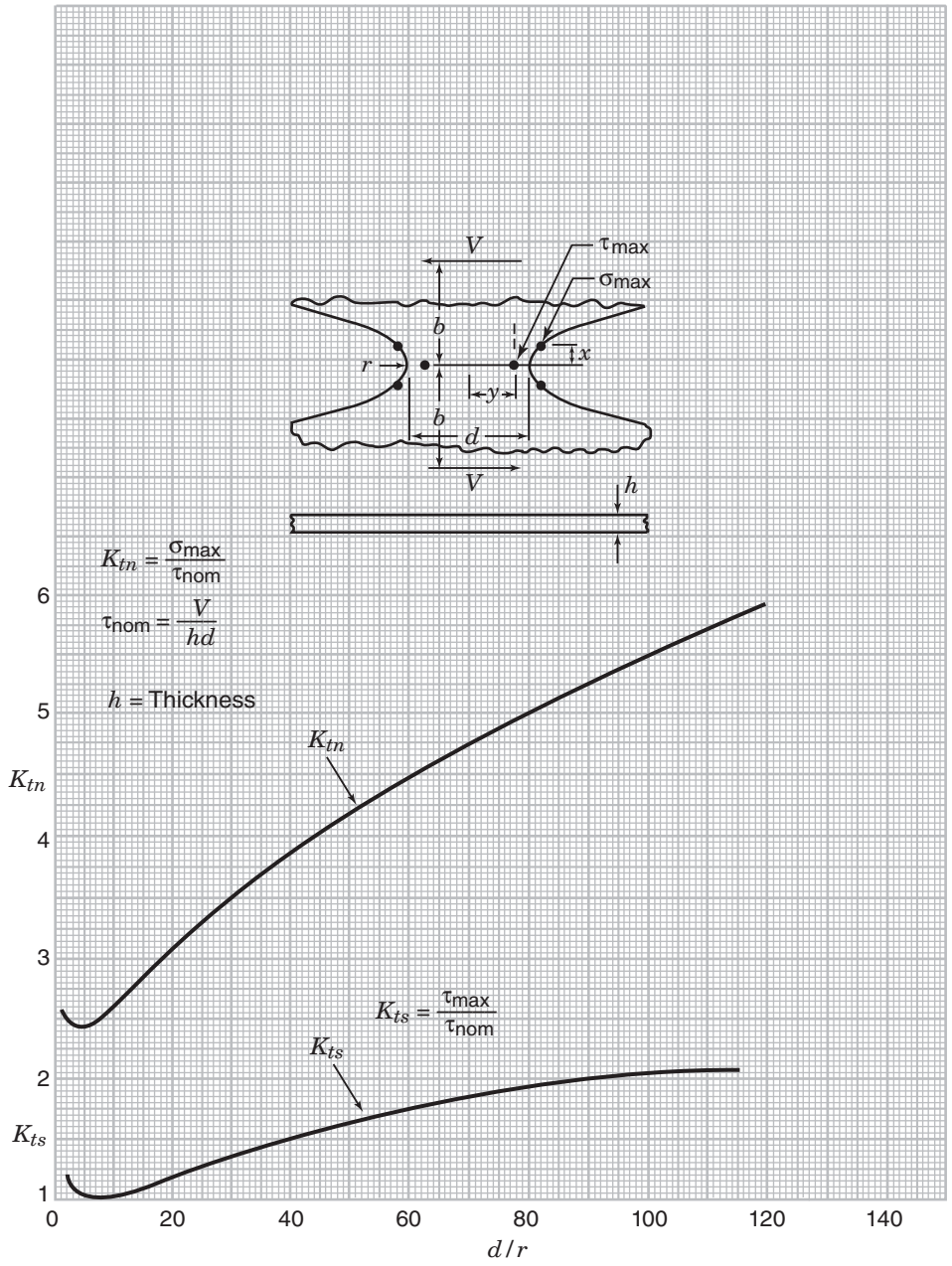


Chart 2.45 Stress concentration factors K_{tn} and K_{ts} for opposite deep hyperbolic notches in an infinite thin element in shear (Neuber 1958).

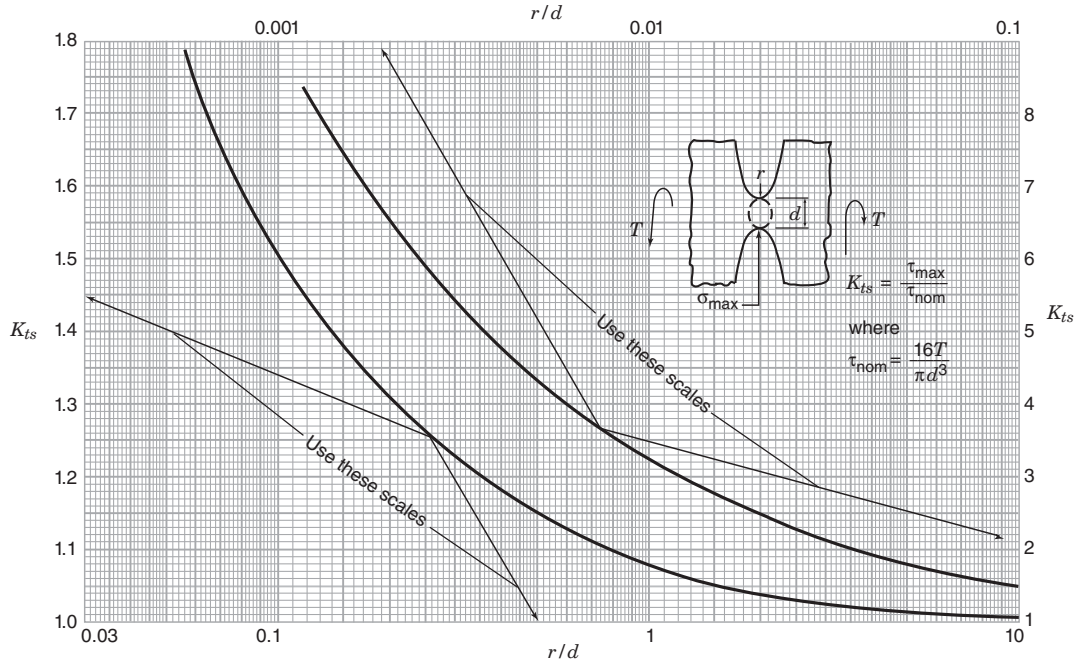


Chart 2.46 Stress concentration factors K_{ts} for a deep hyperbolic groove in an infinite member, torsion (Neuber 1958 solution). The net cross section is circular.

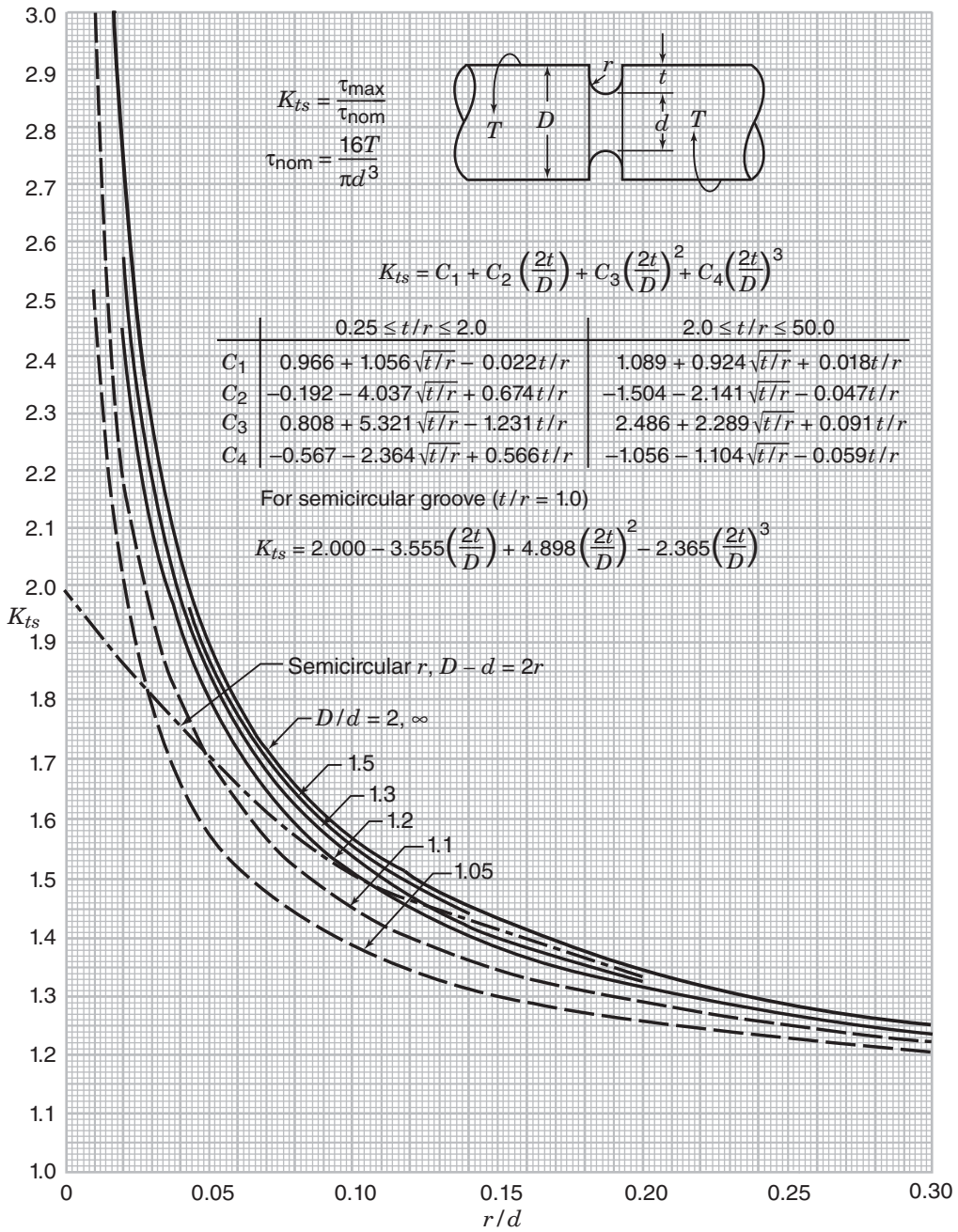


Chart 2.47 Stress concentration factors K_{ts} for torsion of a bar of circular cross section with a U-shaped groove (from electrical analog data of Rushton 1967).

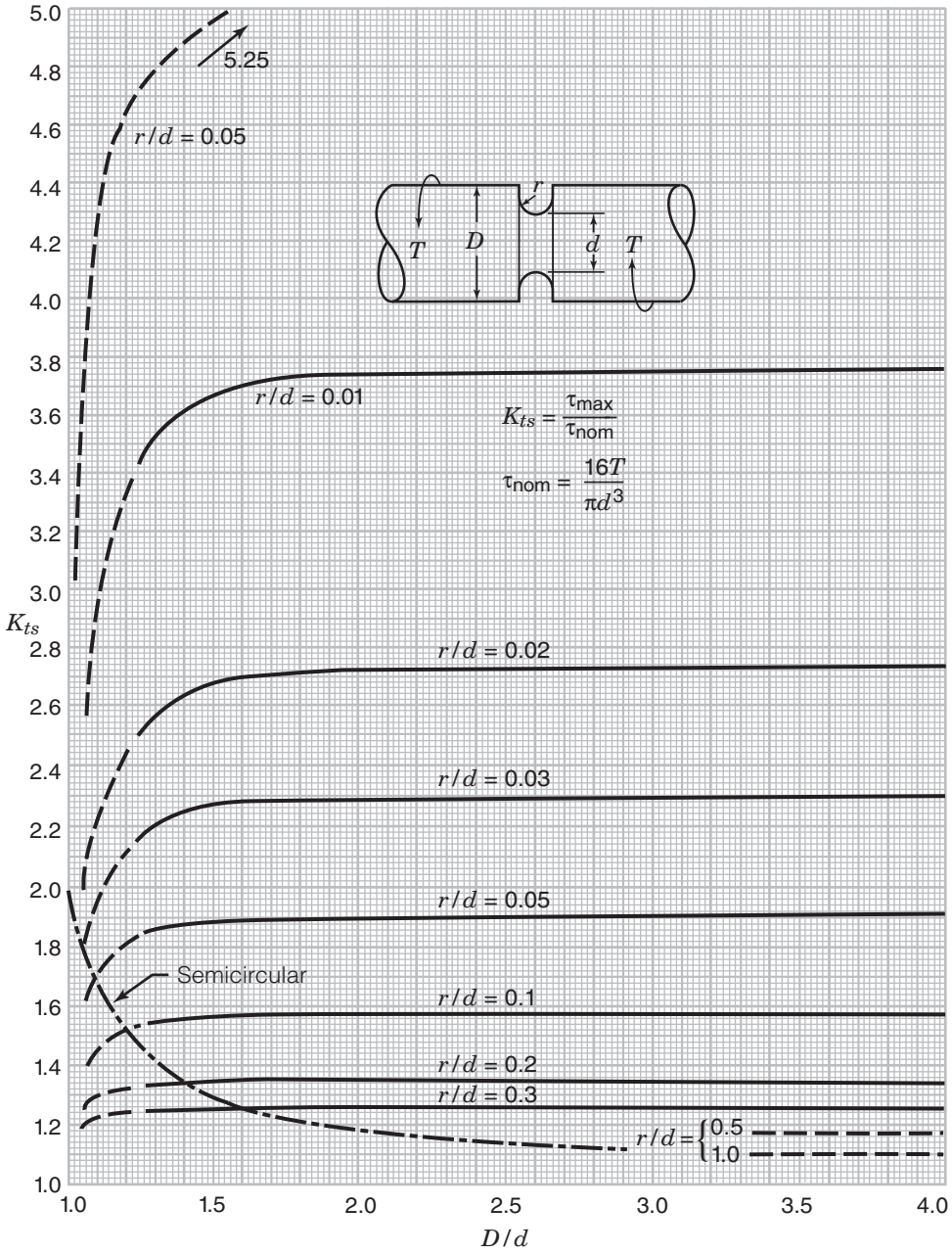


Chart 2.48 Stress concentration factors K_{ts} for torsion of a bar of circular cross section with a U-shaped groove (from electrical analog data of Rushton 1967).

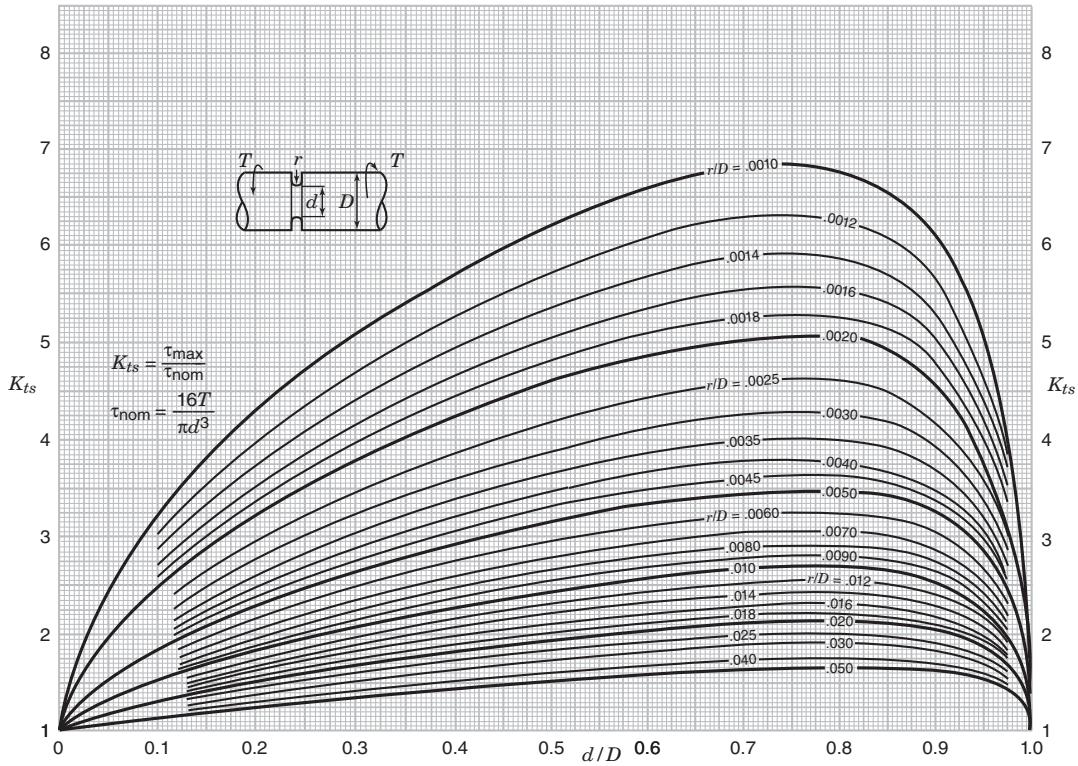


Chart 2.49 Stress concentration factors K_{ts} for a U-shaped grooved shaft of circular cross section in torsion, r/D from 0.001 to 0.050 (from Neuber 1958 formulas).

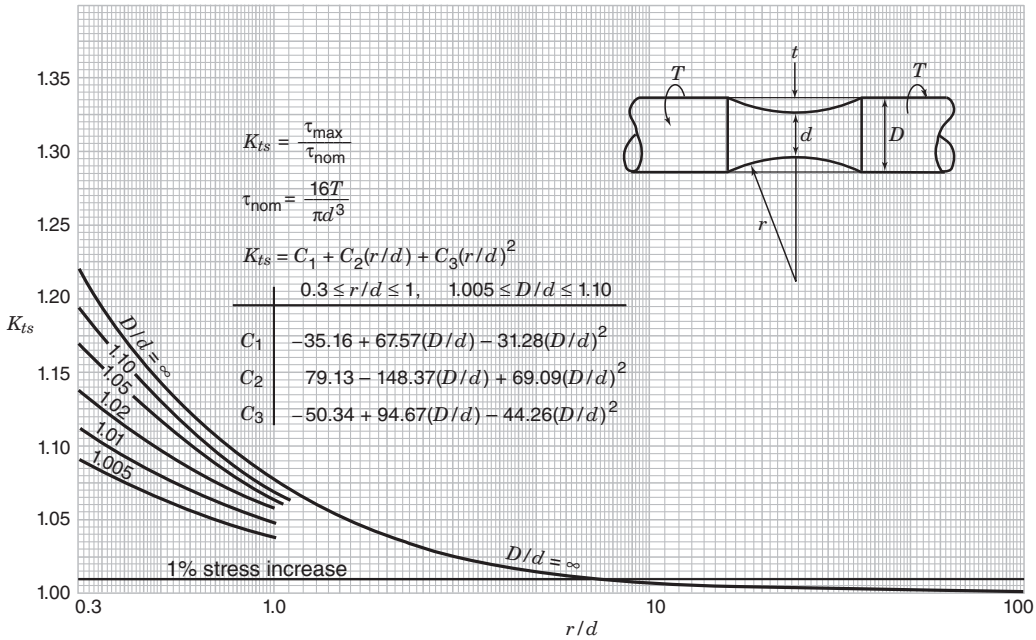


Chart 2.50 Stress concentration factors K_{ts} for the torsion of a bar of circular cross section with a shallow U-shaped groove (curves represent calculated values using Neuber 1958 theory).

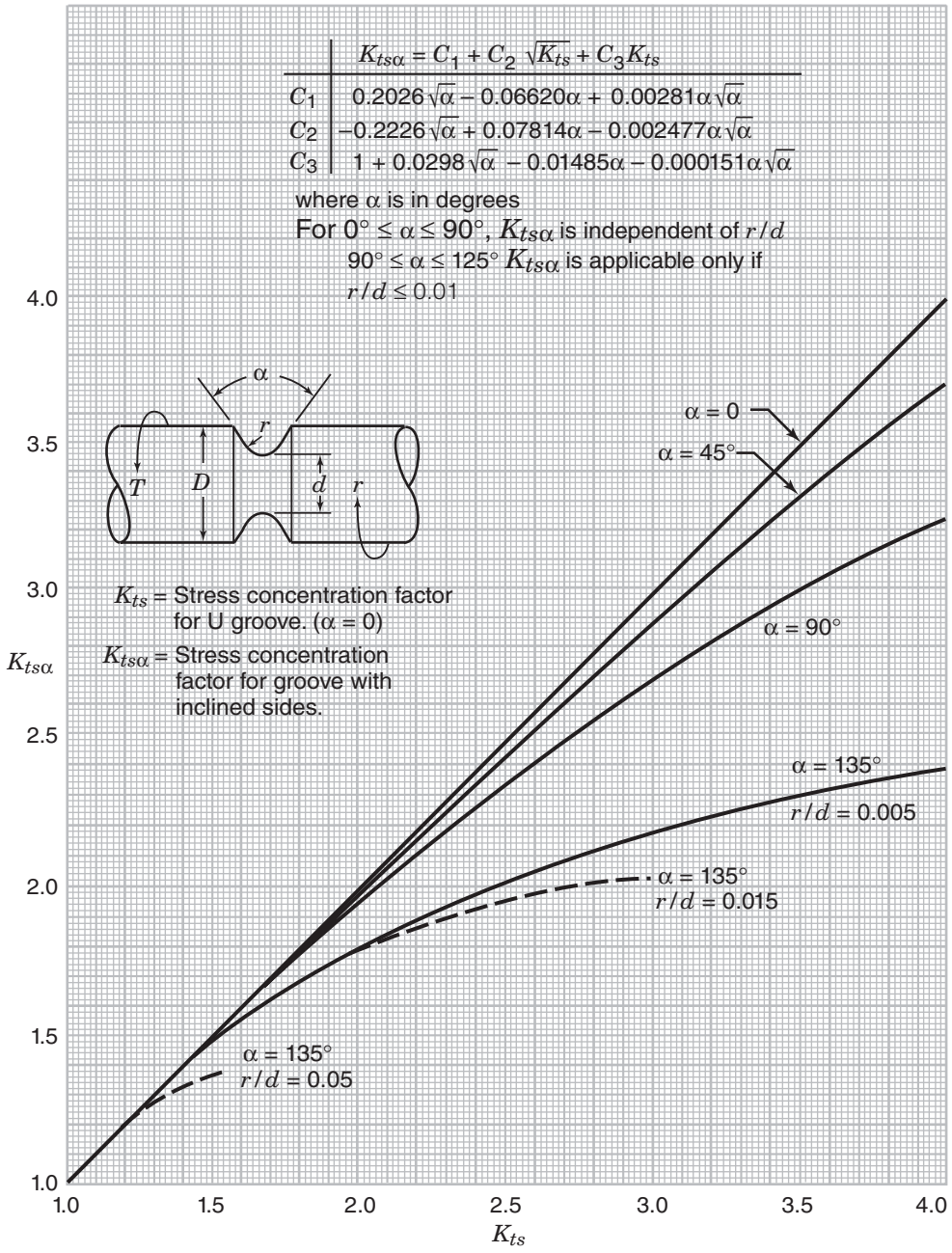


Chart 2.51 Stress concentration factors $K_{ts\alpha}$ for torsion of a bar of circular cross section with a V groove (Rushton 1967).

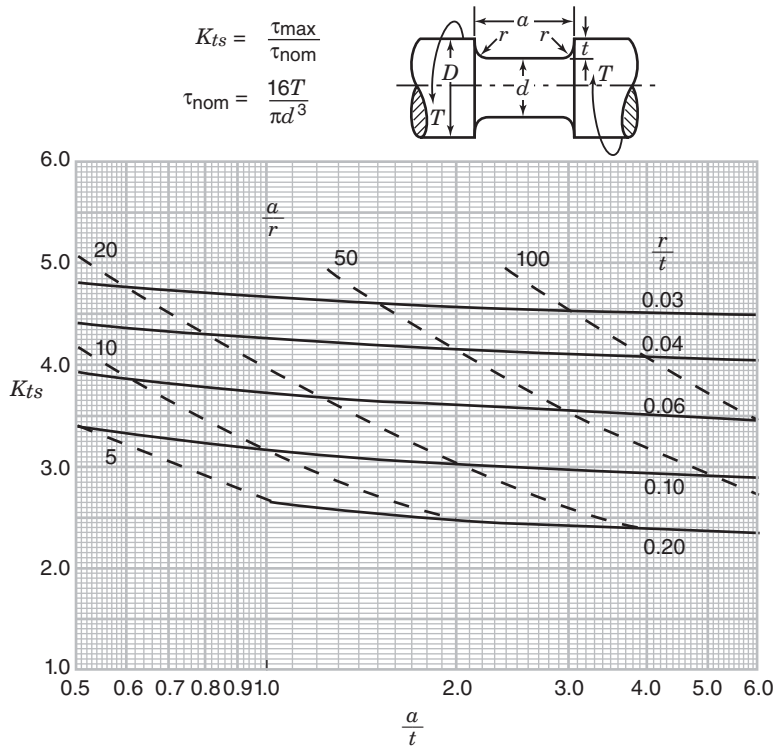


Chart 2.52 Stress concentration factors K_{ts} for a shaft in torsion with flat-bottom groove (Rubenchik 1975; Grayley 1979; ESDU 1981).

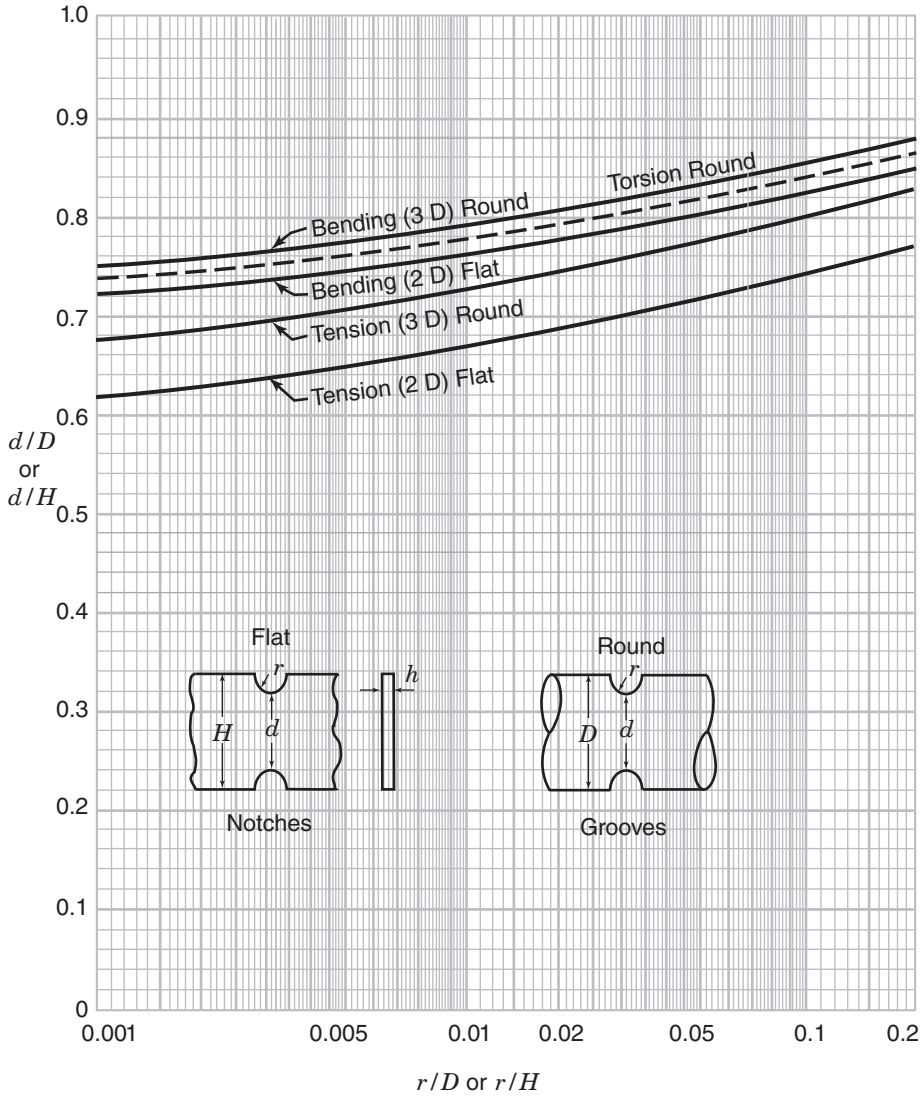


Chart 2.53 Approximate geometric relations for maximum stress concentration for notched and grooved specimens (based on Neuber 1958 relations).

CHAPTER 3

SHOULDER FILLETS

The shoulder fillets shown in Fig. 3.1 are representative of the most common types of stress concentrations that are encountered in machine design practice. Shafts, axles, spindles, rotors, and so forth, usually involve a number of diameters connected by shoulders with rounded fillets replacing the sharp corners that were often used in former years.

3.1 NOTATION

Definition:

Panel. A thin flat element with in-plane loading

Symbols:

SCF = stress concentration factor
a = semimajor axis of an ellipse
b = semiminor axis of an ellipse
d = smaller diameter of circular bar; smaller width of thin flat element
d_f = middle diameter or width of streamline fillet
d_i = diameter of central (axial) hole
D = larger diameter of circular bar
h = thickness of a thin flat element
H = larger width (depth) of thin flat element

Peterson's Stress Concentration Factors, Fourth Edition. Walter D. Pilkey, Deborah F. Pilkey and Zhuming Bi.
© 2020 John Wiley & Sons, Inc. Published 2020 by John Wiley & Sons, Inc.

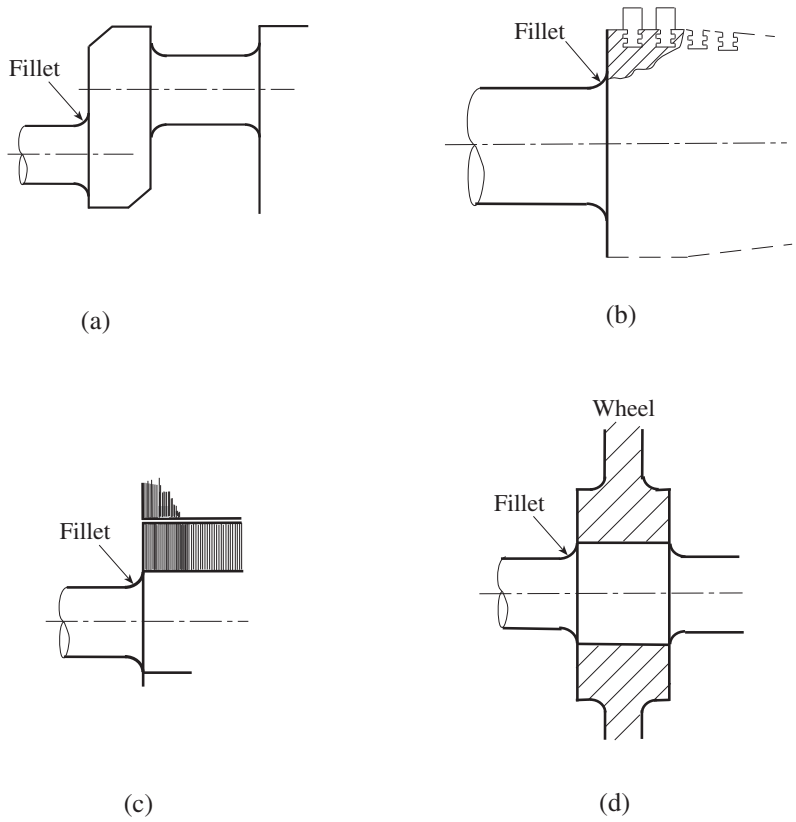


Figure 3.1 Examples of filleted members: (*a*) engine crankshaft; (*b*) turbine rotor; (*c*) motor shaft; (*d*) railway axle.

H_x = depth of equivalent wide shoulder element
K_t = stress concentration factor
K_{ts} = stress concentration factor for shear (torsion)
K_{tI}, K_{tII} = stress concentration factors at I, II
L = length or shoulder width
L_x = axial length of fillet
L_y = radial height of fillet
M = bending moment
P = applied tension force
r = fillet radius
r_1 = fillet radius at end of compound fillet that merges into shoulder fillet
r_2 = fillet radius at end of compound fillet that merges into shaft

t = fillet height
T = torque
θ = angle
σ = stress
σ_{nom} = nominal stress
σ_{max} = maximum stress
τ_{max} = maximum shear stress
τ_{nom} = nominal shear stress
ϕ = location of maximum stress measured from the center of the fillet radius

3.2 STRESS CONCENTRATION FACTORS

Unless otherwise specified, the stress concentration factor K_t is based on the smaller width or diameter, d. In the case of tension load in Fig. 3.2, the SCF is defined as $K_t = \sigma_{max}/\sigma_{nom}$, where $\sigma_{nom} = P/hd$ for a thin flat element of thickness h and $\sigma_{nom} = 4P/\pi d^2$ for a circular bar.

The majority of SCFs for the fillets under tension and bending are from photoelastic tests, and the rest are found from finite element analyses. For torsion, the SCFs for the fillets are from a mathematical analysis. Peterson (1953) gives a method to approximate the K_t values for smaller r/d values where r is the fillet radius. The charts in this book are extended well into the small r/d range, owing to the use of recently published results.

The K_t factors for the thin flat members in this chapter are for two-dimensional states of stress (plane stress) and apply only to very thin panels or, more strictly, to where $h/r \to 0$. As h/r increases, a state of plane strain is approached. As the stress at the fillet surface at the middle of the panel thickness increases, the stress at the panel surface decreases.

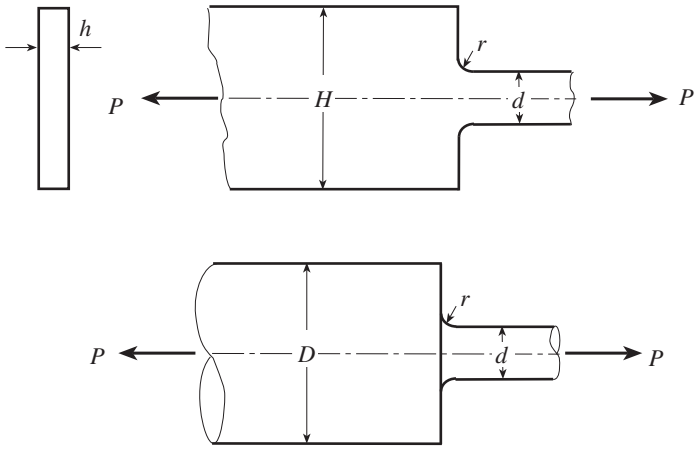


Figure 3.2 Fillets in a thin element and a circular bar.

Some cases of SCFs in Chapter 5 on miscellaneous design elements are related to fillets.

3.3 TENSION (AXIAL LOADING)

3.3.1 Opposite Shoulder Fillets in a Flat Bar

Chart 3.1 presents the SCFs for a stepped flat tension bar. These curves are the modifications of the K_t factors determined through the photoelastic tests (Frocht 1935). However, these values have been found to be too low, owing probably to the small size of the models and to possible edge effects. The curves in the r/d range of 0.03 to 0.3 have been obtained as follows:

$$K_t(\text{Chart 3.1}) = K_t\ (\text{Fig.57, Peterson 1953}) \times \left[\frac{K_t\ (\text{Chart 2.4})}{K_t\ (\text{notch, Frocht 1935})}\right] \tag{3.1}$$

The r/d range is extended to lower values by the photoelastic tests (Wilson and White 1973). The data fit well with the above results from Eq. (3.1) for $H/d > 1.1$.

Other photoelastic tests (Fessler et al. 1969) give the K_t values that agree reasonably well with the $H/d = 1.5$ and two curves of Chart 3.1.

3.3.2 Effect of Length of Element

The SCFs of Chart 3.1 are for the elements of an unspecified length. Troyani et al. (2003) use the standard finite element software to compute SCFs of the model of Fig. 3.3 of various lengths L. It has shown, for example, that for a very short element with $L/H = 0.5$, the SCFs are higher than those given in Chart 3.1 by an average of 5% for $H/d = 1.05$ and 90% for $H/d = 2.0$.

3.3.3 Effect of Shoulder Geometry in a Flat Member

The factors of Chart 3.1 are for the case where the large width H extends back from the shoulder a relatively great distance. Frequently, one encounters a case in design where this shoulder width L (Fig. 3.4) is relatively narrow.

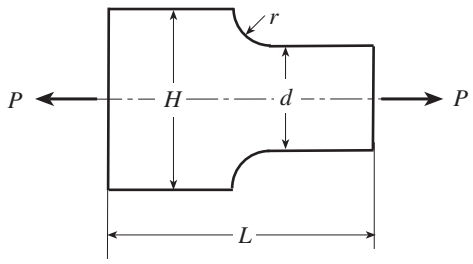


Figure 3.3 Element of length L.

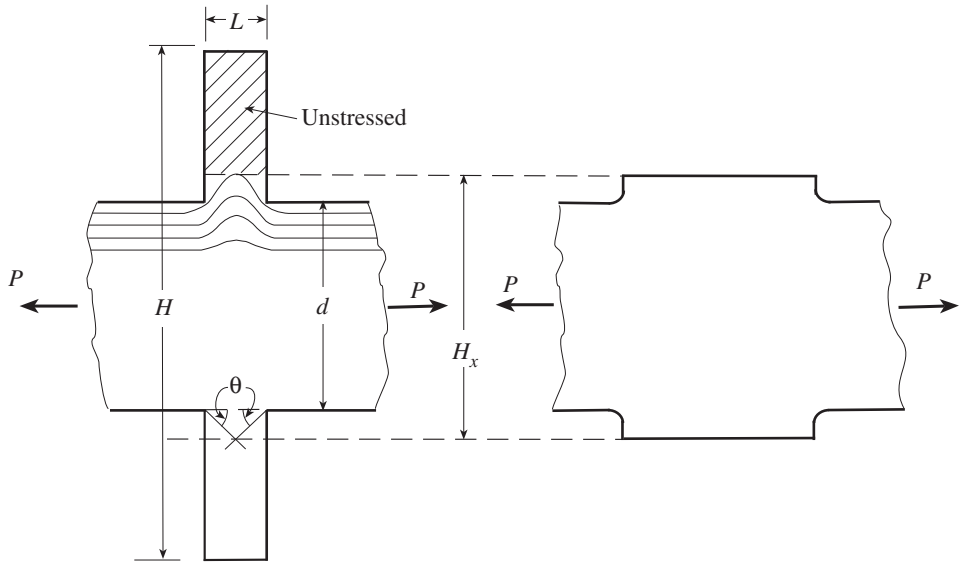


Figure 3.4 Effect of a narrow shoulder.

In one of the early investigations in the photoelasticity field, Baud (1928) note that in the case of a narrow shoulder, the outer part is unstressed, and thus he proposes the formula of

$$H_x = d + 0.3L \tag{3.2}$$

where H_x is the depth of a wide shoulder member that has the same K_t factor shown in Fig. 3.4.

The same result can be obtained graphically by drawing the intersecting lines at an angle θ of 17° (Fig. 3.4). Sometimes, a larger angle θ up to 30° is used. The rule introduced by Baud (1934) has proven useful for a rough approximation.

Although the K_t factors for bending of flat elements with narrow shoulders (Section 3.4.2) are published (Leven and Hartman) in 1951, it is not until 1968 that the tension case was systematically investigated (Kumagai and Shimada) (Chart 3.2). Referring to Charts 3.2*c* and *d*, note that at $L/d = 0$, a cusp remains. Also $K_t = 1$ at $L/d = -2r/d$ (see the dashed lines in Charts 3.2*c* and *d* for extrapolation to $K_t = 1$). The extrapolation formula gives the exact L/d value for $K_t = 1$ for $H/d = 1.8$ (Chart 3.2*c*) when $r/d \leq 0.4$, and for $H/d = 5$ (Chart 3.2*d*) when $r/d \leq 2$. Kumagai and Shimada (1968) state that their results are consistent with previous data (Spangenberg 1960; Scheutzel and Gross 1966) obtained for different geometries. Kumagai and Schimada (1968) develop the empirical formulas to cover their results.

Round bar values are not available. It is suggested that Eq. (1.15) be used.

3.3.4 Effect of a Trapezoidal Protuberance on the Edge of a Flat Bar

Sometimes, a weld bead can be adequately approximated as a trapezoidal protuberance, and Chart 3.3 shows the geometrical configuration in the sketch. A finite difference method is used to find

the SCFs (Derecho and Munse 1968). The resulting K_t factors for $\theta = 30^\circ$ and 60° are given in Chart 3.3. The dashed curve corresponds to a protuberance height where the radius is exactly tangent to the angular side. That is, below the dashed curve, there are no straight sides, only segments of a circle as seen in the sketch of Chart 3.3.

A comparison (Derecho and Munse 1968) of K_t factors with corresponding (large L/t) factors, obtained from Figs. 36 and 62 of Peterson (1953) for filleted members with angle correction, shows the latter to be around 7% higher on the average, with the variations from 2% to 15%. Peterson (1953) provide a similar comparison using the increased K_t fillet values in Chart 3.1, and it show that these values (corrected for angle) are about 17% higher (varying between 14% and 22%) than the Derecho and Munse values.

Strain gage measurements (Derecho and Munse 1968) lead to the results that K_t factors are 32%, 23%, and 31% higher, with one value (for the lowest K_t) is 2.3% lower than the computed values. They comment: "the above comparisons suggest that the values [in Chart 3.3] … may be slightly lower than they should be. It may be noted here that had a further refinement of the spacing been possible in the previously discussed finite-difference solution, slightly higher values of the stress concentration factor could have been obtained." It is possible that the factors may be more than slightly lower.

A typical weld bead would correspond to a geometry of small t/L, with H/d near 1.0. For example, referring to Chart 3.3*a* for $t/L = 0.1$ and $r/L = 0.1$, K_t= 1.55 is surprisingly low. Even if the K_t is increased by 17% on the safe side in design, a SCF value of $K_t = 1.8$ is still relatively low.

3.3.5 Fillet of Noncircular Contour in a Flat Stepped Bar

Circular fillets are usually used for simplicity in drafting and machining. The circular fillet does not correspond to minimum stress concentration.

The variable radius fillet is often found in old machinery (using many cast-iron parts) where the designer or builder apparently produced the result intuitively. Sometimes, the variable radius fillet can be approximated by a fillet with two radii, resulting in the compound fillet illustrated in Fig. 3.5.

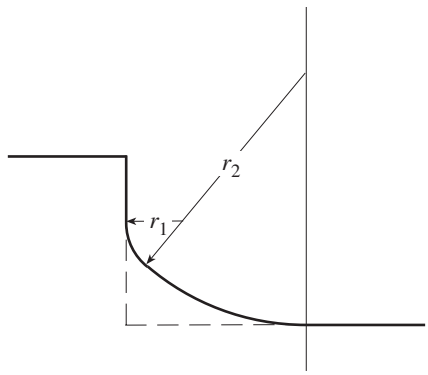


Figure 3.5 Compound fillet.

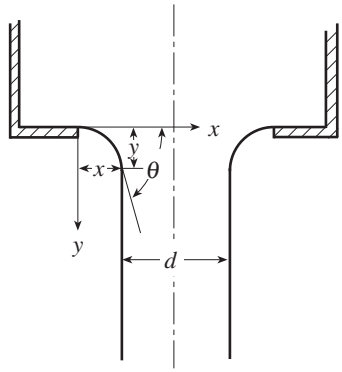


Figure 3.6 Ideal frictionless liquid flow from an opening in the bottom of a tank.

Baud (1934) proposes a fillet form with the same contour as that gives mathematically for an ideal, frictionless liquid flowing by gravity from an opening in the bottom of a tank (Fig. 3.6):

$$x = 2\frac{d}{\pi}\sin^2\frac{\theta}{2} \tag{3.3}$$

$$y = \frac{d}{\pi}\left[\log\tan\left(\frac{\theta}{2}+\frac{\pi}{4}\right) - \sin\theta\right] \tag{3.4}$$

Baud notes that in this case, the liquid at the boundary has a constant velocity and he reasons that the same boundary may also be the contour of constant stress for a tension member.

By the means of a photoelastic test in tension, Baud observes that no appreciable stress concentration occurs with the fillet of a streamline form.

For bending and torsion, Thum and Bautz (1934) apply the correction in accordance with the cube of the diameter and obtain a shorter fillet than for tension. This correction leads to Table 3.1. Thum and Bautz also demonstrate by the means of fatigue tests in bending and in torsion that, with fillets having the proportions of Table 3.1, no appreciable stress concentration effect is observed.

To reduce the length of the streamline fillet, Deutler and Harvers (Lurenbaum 1937) suggest a special elliptical form based on theoretical considerations of Föppl (Timoshenko and Goodier 1970).

Grodzinski (1941) discusses the fillets of parabolic form. He also gives a simple graphical method, which may be used to make a template or a pattern for a cast part (Fig. 3.8). Dimensions a and b are usually dictated by space or design considerations. Firstly, divide each distance into the same number of parts and number the divisions in the order shown; secondly, connect the points having the same numbers by straight lines; finally, this results in an envelope of gradually increasing radius as shown in Fig. 3.8.

For heavy shafts or rolls, Morgenbrod (1939) suggests a tapered fillet with radii at the ends and the included angle of the tapered portion being between 15° and 20° (Fig. 3.9). This is similar to the basis of the tapered cantilever fatigue specimen of McAdam (1923), which has been shown by Peterson (1930) to have a stress variation of less than 1% over a 2 in. length, with a nominal diameter of 1 in. This conical surface is tangent to the constant-stress cubic solid of revolution.

TABLE 3.1 Proportions for a Streamline Fillet[a]

y/d	d_f/d for Tension	d_f/d for Bending or Torsion	y/d	d_f/d for Tension	d_f/d for Bending or Torsion
0.0	1.636	1.475	0.3	1.187	1.052
0.002	1.610	1.420	0.4	1.134	1.035
0.005	1.594	1.377	0.5	1.096	1.026
0.01	1.572	1.336	0.6	1.070	1.021
0.02	1.537	1.287	0.7	1.051	1.018
0.04	1.483	1.230	0.8	1.037	1.015
0.06	1.440	1.193	0.9	1.027	1.012
0.08	1.405	1.166	1.0	1.019	1.010
0.10	1.374	1.145	1.3	1.007	1.005
0.15	1.310	1.107	1.6	1.004	1.003
0.2	1.260	1.082	∞	1.000	1.000

[a]See Fig. 3.7 for notation.

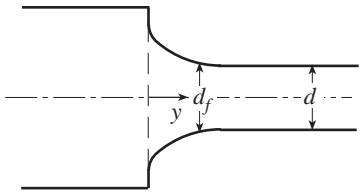


Figure 3.7 Notation for Table 3.1

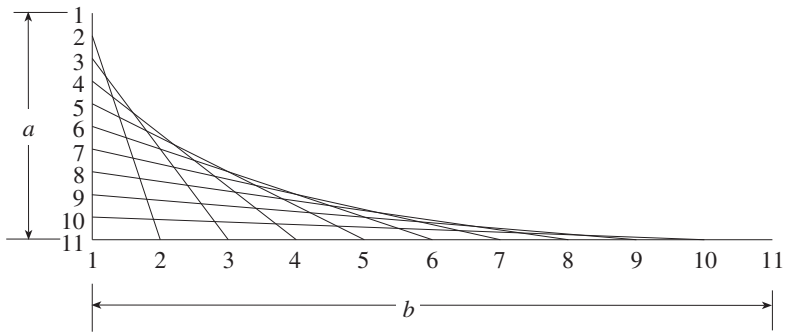


Figure 3.8 Construction of special fillet (Grodzinski 1941).

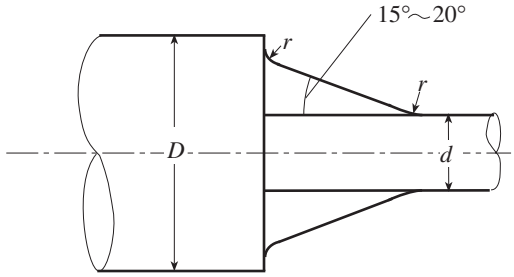


Figure 3.9 Tapered fillet suggested by Morgenbrod (1939).

The photoelastic tests have provided the SCFs for a range of useful elliptical fillets under bending (Section 3.4.3). The degree of improvement obtained may be useful to a case of tension load. Clock (1952) approximates an elliptical fillet by using an equivalent segment of a circle and provides corresponding K_t values.

Heywood (1969) provides an excellent treatment of optimum transition shapes. His discussion includes some interesting observations about the shapes found in nature such as tree trunks and branches, thorns, and animal bones.

3.3.6 Stepped Bar of Circular Cross Section with a Circumferential Shoulder Fillet

In this section, a stepped bar of circular cross section with a circumferential shoulder fillet is considered. The K_t values for this case (Chart 3.4) was obtained by ratioing the K_t values of Chart 3.1 in accordance with the three- to two-dimensional notch values, as explained in Section 2.5.2. Chart 3.4 is labeled as "approximate" in view of the procedure.

For the d/D values that are considered valid for comparison (0.6, 0.7, 0.9), the photoelastic results for round bars (Allison 1962) are somewhat lower than the values of Chart 3.4. The photoelastic tests (Fessler et al. 1969) give the K_t values for $D/d = 1.5$ that are in good agreement with Chart 3.4.

Although the stress concentration values in Chart 3.4 seem to be confirmed by finite element analyses in ESDU (1989), Tipton et al. (1996) contend on the basis of finite element analyses that the SCF curves of Chart 3.4 can underestimate the stresses by as much as 40%. For $0.002 \leq r/d \leq 0.3$ and $1.01 \leq D/d \leq 6.0$ they suggest that the equation

$$K_t = 0.493 + 0.48\left(\frac{D}{d}\right)^{-2.43} + \left(\frac{r}{d}\right)^{-0.48}\sqrt{\frac{3.43 - 3.41(D/d)^2 + 0.0232(D/d)^4}{1 - 8.85(D/d)^2 - 0.078(D/d)^4}} \tag{3.5}$$

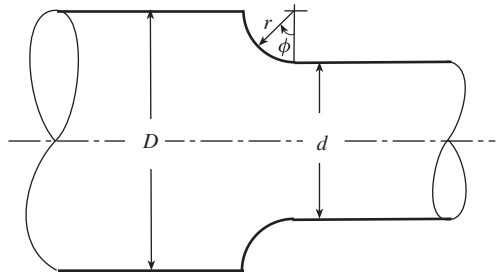


Figure 3.10 Location of ϕ maximum stress in the fillet.

provides better values than the SCFs in Chart 3.4. Eq. (3.5) is obtained by curve fitting based on finite element results. The location of ϕ (of Fig. 3.10) of the maximum stress in the fillet is found to be a function of the geometry. For the same ranges of r/d and D/d they find

$$\phi \text{ (degrees)} = 4 - 2.84\left(\frac{D}{d}\right)^{-8.47} + \left[\frac{-11.27 + 11.14(D/d)}{1 - 1.27(D/d)}\right] \ln \frac{r}{d} + \left[-0.44 + 0.9\left(\frac{D}{d}\right)^{-3.17}\right] \left(\ln \frac{r}{d}\right)^2 \tag{3.6}$$

For this case of tensile loading, the formula of Eq. (3.5) corresponds closely for a variety of cases with the finite element analyses of Gooyer and Overbeeke (1991).

3.3.7 Tubes

Chart 3.5 gives the stress concentration factors K_t are given for thin-walled tubes with fillets. The data is based on the work of Lee and Ades (1956). In Chart 3.5, K_t is shown versus t/r for various values of t/h for a tube subject to tension. The plot holds only when $\left(d_i/h + d_i/t\right) > 28$. For $d_i < 28ht/(t + h)$, K_t will be smaller.

For solid shafts ($d_i = 0$), K_t is reduced as t/h increases. The location of $\sigma_{\max}$ is in the fillet near the smaller tube.

3.3.8 Stepped Pressure Vessel Wall with Shoulder Fillets

Chart 3.6 is for a pressure vessel with a stepped wall and shoulder fillets. The K_t curve is based on the calculations by Griffin and Thurman (1967). A direct comparison (Griffin and Kellogg 1967) with a specific photoelastic test by Leven (1965) shows a good agreement. The strain gage results of Heifetz and Berman (1967) are in reasonably good agreement with Chart 3.6. Lower values have been obtained in the finite element analysis of Gwaltney et al. (1971).

For comparison, the model Chart 3.1 can be split in half axially. The corresponding K_t curves have the same shape as in Chart 3.6, but they are somewhat higher. The cases are not strictly comparable and, furthermore, Chart 3.1 is approximated.

3.4 BENDING

3.4.1 Opposite Shoulder Fillets in a Flat Bar

Chart 3.7 shows the stress concentration factors for the in-plane bending of a thin element with opposing shoulder fillets. The photoelastic values by Leven and Hartman (1951) cover the r/d range from 0.03 to 0.3, whereas the photoelastic tests of Wilson and White (1973) cover r/d values in the 0.003 to 0.03 range. These results blend together reasonably well and form the basis of Chart 3.7.

3.4.2 Effect of Shoulder Geometry in a Flat Thin Member

In Chart 3.8, the K_t factors are given for various shoulder parameters for a fillet bar in bending (Leven and Hartman 1951). For $L/H = 0$, a cusp remains. For $H/d = 1.25$ (Chart 3.8*a*) and $r/d \leq 1/8$, $K_t = 1$ when $L/H = -1.6r/d$. For $H/d = 2$ (Chart 3.8*b*) and $r/d \leq 1/2$, $K_t = 1$ when $L/H = -r/d$. For $H/d = 3$ (Chart 3.8*c*) and $r/d \leq 1$, $K_t = 1$ when $L/H = -(2/3)(r/d)$. The dashed lines in Chart 3.8 show the extrapolation to $K_t = 1$. Only limited information is available for the bars with a circular cross section. It is suggested that the designer obtains an adjusted value by ratioing in accordance with the corresponding Neuber three- to two-dimensional notch values (Peterson 1953, p. 61), or Eq. (1.15).

3.4.3 Elliptical Shoulder Fillet in a Flat Member

The photoelastic tests by Berkey (1944) provide the K_t factors for the flat element with in-plane bending (Chart 3.9). The corresponding factors for a round shaft should be somewhat lower. An estimate can be made by comparing the corresponding Neuber three- to two-dimensional notch factors, as discussed in Section 2.5.2.

3.4.4 Stepped Bar of Circular Cross Section with a Circumferential Shoulder Fillet

Leven and Hartman (1951) conduct the photoelastic tests on the stepped bars of circular cross section in the r/d range of 0.03 to 0.3. Using the plane bending tests by Wilson and White (1973), reasonable extensions of curves have been made in the r/d range below 0.03. The results are presented in Chart 3.10.

In comparison with the photoelastic tests on other round bars (Allison 1961a,b) for the d/D ratios considered valid for comparison, there is a reasonably good agreement for $d/D = 0.6, 0.8$. However, for $d/D = 0.9$ the results are lower.

In the design of machinery shafts, where bending and torsion are the primary loadings of concern, small steps (D/d near 1.0) are often used. Since for this region, Chart 3.10 is not very suitable. Chart 3.11 is provided where the curves go to $K_t = 1.0$ at $D/d = 1.0$.

Tipton et al. (1996) perform a finite element analysis and show that for $r/d < 0.05$, the SCF of Charts 3.10 and 3.11 can underestimate the maximum stress between 3 and 21%. The smaller the ratio r/d is, the greater the possible error is. The potential underestimation of Charts 3.4, 3.10, and

3.11 is identified previously by Gooyer and Overbeeke (1991) and Hardy and Malik (1992). In the finite element analyses, Tipton et al. (1996) calculate the elastic stress concentration factor K_t as $K_t = \sigma_1/\sigma_{\text{nom}}$, where σ_1 is the maximum principal stress and $\sigma_{\text{nom}} = 32M/\pi d^3$, as in Charts 3.10 and 3.11 for bending. For tension, they use $\sigma_{\text{nom}} = 4P/\pi d^2$. For the geometric limits $0.002 \leq r/d \leq 0.3$ and $1.01 \leq D/d \leq 6.0$, they find that the stress concentration factor K_t for bending can be represented as

$$K_t = 0.632 + 0.377\left(\frac{D}{d}\right)^{-4.4} + \left(\frac{r}{d}\right)^{-0.5}\sqrt{\frac{-0.14 - 0.363(D/d)^2 + 0.503(D/d)^4}{1 - 2.39(D/d)^2 + 3.368(D/d)^4}} \tag{3.7}$$

The location of the maximum stress in the fillet is shown as ϕ in Fig. 3.10 and is determined to be given by

$$\phi \text{ (degrees)} = 0.4 + \left(\frac{D}{d}\right)^{0.06} + \left[-6.95 + 7.3\left(\frac{D}{d}\right)^{-6.7}\right]\ln\frac{r}{d} + \left[-0.31 + 1.15\left(\frac{D}{d}\right)^{-1} - 3.19\left(\frac{D}{d}\right)^{-2} + 2.76\left(\frac{D}{d}\right)^{-3}\right]\left(\ln\frac{r}{d}\right)^2 \tag{3.8}$$

3.5 TORSION

3.5.1 Stepped Bar of Circular Cross Section with a Circumferential Shoulder Fillet

Investigations of the filleted shaft in torsion have been made by use of photoelasticity (Allison 1961a,b; Fessler et al. 1969), with strain gages (Weigand 1943), by the use of the electrical analog (Jacobsen 1925; Rushton 1964), and numerical computations by Matthews and Hooke (1971). The computational approach, using a numerical technique based on the elasticity equations and the point-matching method for satisfying boundary conditions approximately, is believed to be of the satisfactory accuracy. Currently, most computational stress concentration studies are performed in general purpose structural analysis software. Matthews and Hooke provide the K_{ts} values (Chart 3.12) lower than those used previously by Peterson (1953). In the lower r/d range, it provides higher values than the results from Rushton's electrical analog.

An empirical relation (Fessler et al. 1969) based on the published data including two photoelastic tests by the authors is in a satisfactory agreement with the values of Chart 3.12 in the area covered by their tests. Also in agreement are the results of a finite element study (ESDU 1989).

In design of machinery shafts, where bending and torsion are the main cases of interest, small steps (D/d near 1.0) are often used. For this region, Chart 3.12 is not very suitable, and Chart 3.13 has been provided, wherein the curves go to $K_{ts} = 1.0$ at $D/d = 1.0$.

3.5.2 Stepped Bar of Circular Cross Section with a Circumferential Shoulder Fillet and a Central Axial Hole

Central (axial) holes are used in the large forgings for inspection purposes and in the shafts for cooling or fluid transmission purposes.

For a hollow shaft, a reasonable design procedure is to find the ratios of SCFs from Chart 3.14 that have been obtained from the electrical analog values (Rushton 1964) and then, using the K_{ts} values om Charts 3.12 and 3.13, to find the K_{ts} factors of the hollow shaft. Chart 3.14 provides the ratios of the K_{ts} values for the hollow shaft to the K_{tso} values for the solid shaft in Charts 3.12 and 3.13. These ratios, $(K_{ts} - 1)/(K_{tso} - 1)$, are plotted against the ratio d_i/d. Chart 3.15 gives K_{ts} for hollow shafts, plotted, in contrast to the preceding table, versus r/d. Both Charts 3.14 and 3.15 are based on the data from Rushton (1964). The SCFs in Chart 3.15 are nearly duplicated in ESDU (1989) using finite element analyses.

The strength/width ratio of the small-diameter portion of the shaft increases with an increase of hollowness ratio. However, this is usually not of substantial benefit in practical designs due to a larger weight of the large-diameter portion of shaft. An exception may occur when the diameters are close together ($D/d = 1.2$ or less).

3.5.3 Compound Fillet

For a shouldered shaft in torsion, the SCF can be controlled by adjusting the size of a single radius fillet. Specifically, the SCF is reduced by increasing the radius of the fillet. However, an increase in radius may not be possible due to practical constraints on the axial length (L_x) and radial height (L_y) as shown in Fig. 3.11. Occasionally, the lowest single radius fillet SCF K_{ts} (e.g., from Charts 3.12 and 3.13) that fits within the restrictions on L_y and L_x can be improved up to about 20% by using a double radius fillet.

For a double radius fillet, two distinct maximum stress concentrations occur. The first one is on the circumferential line *II*, which is located close to where radii r_1 and r_2 are tangential to each other. The second one occurs where r_2 is first parallel to d on the circumferential line *I*. For the cases that satisfy the constraints on L_y and L_x, the lowest maximum shear stress occurs to the largest fillet for which K_{tI} equals K_{tII}. Care should be taken to ensure that the two fillets fit well at their intersection. Small changes in r_1 can lead to corresponding changes in the shear stress at *II* due to stress concentration.

For $K_{tI} = K_{tII}$, Chart 3.16 provides plots of r_2/d versus L_x/d and L_y/d for $r_2/r_1 = 3$ and 6 (Battenbo and Baines 1974; ESDU 1981). The corresponding reduction in $K_{tI}/K_t = K_{tII}/K_t$ versus r_2/r_1 is given in Chart 3.17.

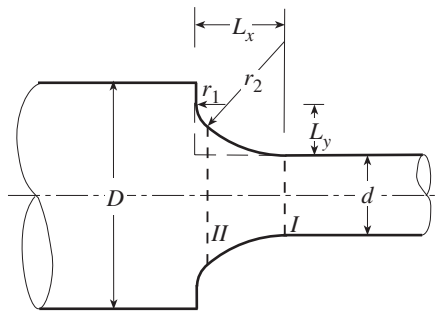


Figure 3.11 Double radius fillet.

Example 3.1 Design of a Fillet for a Shaft in Torsion Suppose that a fillet with a SCF values less than 1.26 is to be chosen for a shaft in torsion. In the notation of Fig. 3.11, $d = 4$ in., $D = 8$ in. There is a spacing washer carrying the maximum allowable 45° chamfer of 0.5 in. to accommodate the fillet.

For a single radius (r) fillet, let $r = L_y$ and calculate

$$\frac{D}{d} = \frac{8}{4} = 2, \quad \frac{r}{d} = \frac{0.5}{4} = 0.125$$

From Chart 3.12, $K_t = 1.35$. This value exceeds the desired $K_t = 1.26$.

If a double radius fillet is employed, then for a SCF with a value less than 1.26,

$$\frac{K_{tI}}{K_t} = \frac{K_{tII}}{K_t} = \frac{1.26}{1.35} = 0.93$$

Both L_x and L_y must be less than 0.5 in. For a double radius fillet, $L_x > L_y$, so that $L_y = 0.5$ in. is the active constraint. From the upper curve in Chart 3.17, $r_2/r_1 = 3$ can satisfy this constraint. Use $L_x = 0.5$ in. in Chart 3.16*a*, and observe that for $L_y/d = 0.5/4 = 0.125$

$$\frac{r_2}{d} = 0.19$$

for which L_x/d is 0.08. Finally, the double radius fillet would have the properties

$$r_2 = 0.19 \times 4 = 0.76 \text{ in.}$$

$$L_y = 0.08 \times 4 = 0.32 \text{ in.}$$

$$r_1 = 0.76/3 = 0.2533 \text{ in.}$$

3.6 METHODS OF REDUCING STRESS CONCENTRATION AT A SHOULDER

One of the problems occurring in the design of shafting, rotors, and other relevant parts, is how to reduce the concentrated stresses at a shoulder fillet (Fig. 3.12*a*) while maintaining the positioning line I–I and dimensions D and d. This can be done in a number of ways, and some of which are illustrated in Fig. 3.12*b*, *c*, *d*, *e*, and *f*. By cutting into the shoulder, a larger fillet radius can be obtained (Fig. 3.12*b*) without developing interference with the fitted member. A ring insert could be used as at Fig. 3.12*c*, but this needs an additional part. A similar result could be obtained as shown in Fig. 3.12*d* except that a smooth fillet surface is more difficult to realize.

Sometimes, the methods of Fig. 3.12*b*, *c*, and *d* are not helpful because the shoulder height $(D - d)/2$ is too small. A relief groove (Fig. 3.12*e*, *f*) may be used provided that this does not conflict with the location of a seal or other shaft requirements. Fatigue tests (Oschatz 1933; Thum and Bruder 1938) show a considerable gain in strength due to relief grooving.

It should be noted that in the case that there is also a combined stress concentration and fretting corrosion problem at the bearing fit (see Section 5.5), the gain due to fillet improvement

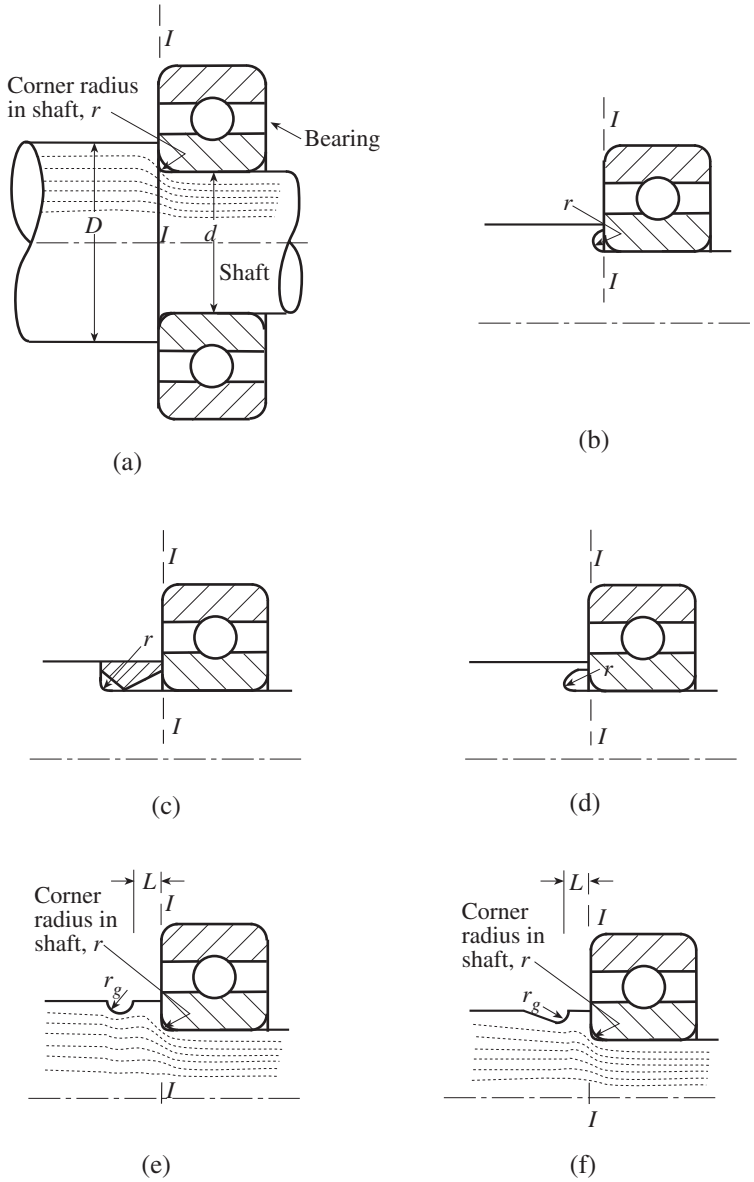


Figure 3.12 Techniques for reducing stress concentration in stepped shaft with bearing: (*a*) with corner radius only; (*b*) undercut; (*c*) inserted ring; (*d*) undercut to simulate a ring; (*e*) relief groove; (*f*) relief groove.

might be limited by failure at the fitted surface. However, the fatigue tests by Thum and Bruder (1938) show that for the tested specific proportions, the strength is increased by the use of relief grooves.

REFERENCES

Allison, I. M., 1961a, The elastic stress concentration factors in shouldered shafts, *Aeronaut. Q.*, Vol. 12, p. 189.

Allison, I. M., 1961b, The elastic concentration factors in shouldered shafts: II, Shafts subjected to bending, *Aeronaut. Q.*, Vol. 12, p. 219.

Allison, I. M., 1962, The elastic concentration factors in shouldered shafts: III, Shafts subjected to axial load, *Aeronaut. Q.*, Vol. 13, p. 129.

Appl, F. J., and Koerner, D. R., 1969, Stress concentration factors for U-shaped, hyperbolic and rounded V-shaped notches, *ASME Pap. 69-DE-2*, American Society of Mechanical Engineers, New York.

Battenbo, H., and Baines, B. H., 1974, Numerical stress concentrations for stepped shafts in torsion with circular and stepped fillets, *J. Strain Anal.*, Vol. 2, pp. 90–101.

Baud, R. V., 1928, Study of stresses by means of polarized light and transparencies, *Proc. Eng. Soc. West. Pa.*, Vol. 44, p. 199.

Baud, R. V., 1934, Beiträge zur Kenntnis der Spannungsverteilung in Prismatischen und Keilförmigen Konstruktionselementen mit Querschnittsübergängen, *Eidg. Materialprüf. Ber.,* Vol. 83, Zurich; see also *Prod. Eng.*, 1934, Vol. 5, p. 133.

Berkey, D. C., 1944, Reducing stress concentration with elliptical fillets, *Proc. Soc. Exp. Stress Anal.*, Vol. 1, No. 2, p. 56.

Clock, L. S., 1952, Reducing stress concentration with an elliptical fillet, *Des. News*, May 15.

Derecho, A. T., and Munse, W. H., 1968, Stress concentration at external notches in members subjected to axial loading, *Univ. Ill. Eng. Exp. Stn. Bull. 494*.

ESDU, 1981, 1989, *Stress Concentrations*, Engineering Science Data Unit, London.

Fessler, H., Rogers, C. C., and Stanley, P., 1969, Shouldered plates and shafts in tension and torsion, *J. Strain Anal.*, Vol. 4, p. 169.

Frocht, M. M., 1935, Factors of stress concentration photoelastically determined, *Trans. ASME Appl. Mech. Sect.*, Vol. 57, p. A-67.

Gooyer, L.E., and Overbeeke, J. L., 1991, The stress distributions in shoulder shafts under axisymmetric loading, *J. Strain Anal.*, Vol. 26, No. 3, pp. 181–184.

Griffin, D. S., and Kellogg, R. B., 1967, A numerical solution for axially symmetrical and plane elasticity problems, *Int. J. Solids Struct.*, Vol. 3, p. 781.

Griffin, D. S., and Thurman, A. L., 1967, Comparison of DUZ solution with experimental results for uniaxially and biaxially loaded fillets and grooves," *WAPD TM-654*, Clearinghouse for Scientific and Technical Information, Springfield, VA.

Grodzinski, P., 1941, Investigation on shaft fillets, *Engineering* (*London*), *Vol.* 152, p. 321.

Gwaltney, R. C., Corum, J. M., and Greenstreet, W. L., 1971, Effect of fillets on stress concentration in cylindrical shells with step changes in outside diameter, *Trans. ASME J. Eng. Ind.*, Vol. 93, p. 986.

Hardy, S. J., and Malik, N. H., 1992, A survey of post-Peterson Stress concentration factor data, *Int. J. Fatigue*, Vol. 14, p.149.

Heifetz, J. H., and Berman, I., 1967, Measurements of stress concentration factors in the external fillets of a cylindrical pressure vessel, *Exp. Mech.*, Vol. 7, p. 518.

Heywood, R. B., 1969, *Photoelasticity for Designers*, Pergamon Press, Elmsford, NY, Chap. 11.

Jacobsen, L. S., 1925, Torsional stress concentrations in shafts of circular cross section and variable diameter, *Trans. ASME Appl. Mech. Sect*., Vol. 47, p. 619.

Kumagai, K., and Shimada, H., 1968, The stress concentration produced by a projection under tensile load, *Bull. Jpn. Soc. Mech. Eng.*, Vol. 11, p. 739.

Lee, L. H. N., and Ades, C. S., 1956, Stress concentration factors for circular fillets in stepped walled cylinders subject to axial tension, *Proc. Soc. Exp. Stress Anal.*, Vol. 14, No. 1.

Leven, M. M., 1965, Stress distribution in a cylinder with an external circumferential fillet subjected to internal pressure, *Res. Memo.* 65-9D7-520-M1, Westinghouse Research Laboratories, Pittsburgh, PA.

Leven, M. M., and Hartman, J. B., 1951, Factors of stress concentration for flat bars with centrally enlarged section, *Proc. SESA*, Vol. 19, No. 1, p. 53.

Lurenbaum, K., 1937, *Ges. Vortrage der Hauptvers. der Lilienthal Gesell*., p. 296.

Matthews, G. J., and Hooke, C. J., 1971, Solution of axisymmetric torsion problems by point matching, *J. Strain Anal.*, Vol. 6, p. 124.

McAdam, D. J., 1923, Endurance properties of steel, *Proc. ASTM*, Vol. 23, Pt. II, p. 68.

Morgenbrod, W., 1939, Die Gestaltfestigkeit von Wälzen und Achsen mit Hohlkehlen, *Stahl Eisen*, Vol. 59, p. 511.

Oschatz, H., 1933, Gesetzmässigkeiten des Dauerbruches und Wege zur Steigerung der Dauerhaltbarkeit, *Mitt. Materialprüfungsanst. Tech. Hochsch. Darmstadt*, Vol. 2.

Peterson, R. E., 1930, Fatigue tests of small specimens with particular reference to size effect, *Proc. Am. Soc. Steel Treatment*, Vol. 18, p. 1041.

Peterson, R. E., 1953, *Stress Concentration Design Factors*, Wiley, New York.

Rushton, K. R., 1964, Elastic stress concentration for the torsion of hollow shouldered shafts determined by an electrical analogue, *Aeronaut. Q.*, Vol. 15, p. 83.

Scheutzel, B., and Gross, D., 1966, *Konstruktion*, Vol. 18, p. 284.

Spangenberg, D., 1960, *Konstruktion*, Vol. 12, p. 278.

Thum, A., and Bautz, W., 1934, Der Entlastungsübergang: Günstigste Ausbildung des Überganges an abgesetzten Wellen u. dg., *Forsch. Ingwes*., Vol. 6, p. 269.

Thum, A., and Bruder, E., 1938, Dauerbruchgefahr an Hohlkehlen von Wellen und Achsen und ihre Minderung, *Deutsche Kraftfahrtforschung im Auftrag des Reichs-Verkehrsministeriums*, No. 11, VDI Verlag, Berlin.

Timoshenko, S., and Goodier, J. N., 1970, *Theory of Elasticity*, 3rd ed., McGraw-Hill, New York, p. 398.

Tipton, S. M., Sorem, J. R., and Rolovic, R. D., 1996, Updated stress concentration factors for filleted shafts in bending and tension, *J. Mech. Des.*, Vol. 118, p. 321.

Troyani, N., Marin, A., Garcia, H., Rodriguez, F., and Rodriguez, S., 2003, Theoretical stress concentration factors for short shouldered plates subjected to uniform tension, *J. Strain Anal. Eng. Des.*, Vol. 38, pp. 103–113.

Weigand, A., 1943, Ermittlung der Formziffer der auf Verdrehung beanspruchten abgesetzen Welle mit Hilfe von Feindehnungsmessungen, *Luftfahrt Forsch*., Vol. 20, p. 217.

Wilson, I. H., and White, D. J., 1973, Stress concentration factors for shoulder fillets and grooves in plates, *J. Strain Anal.*, Vol. 8, p. 43.

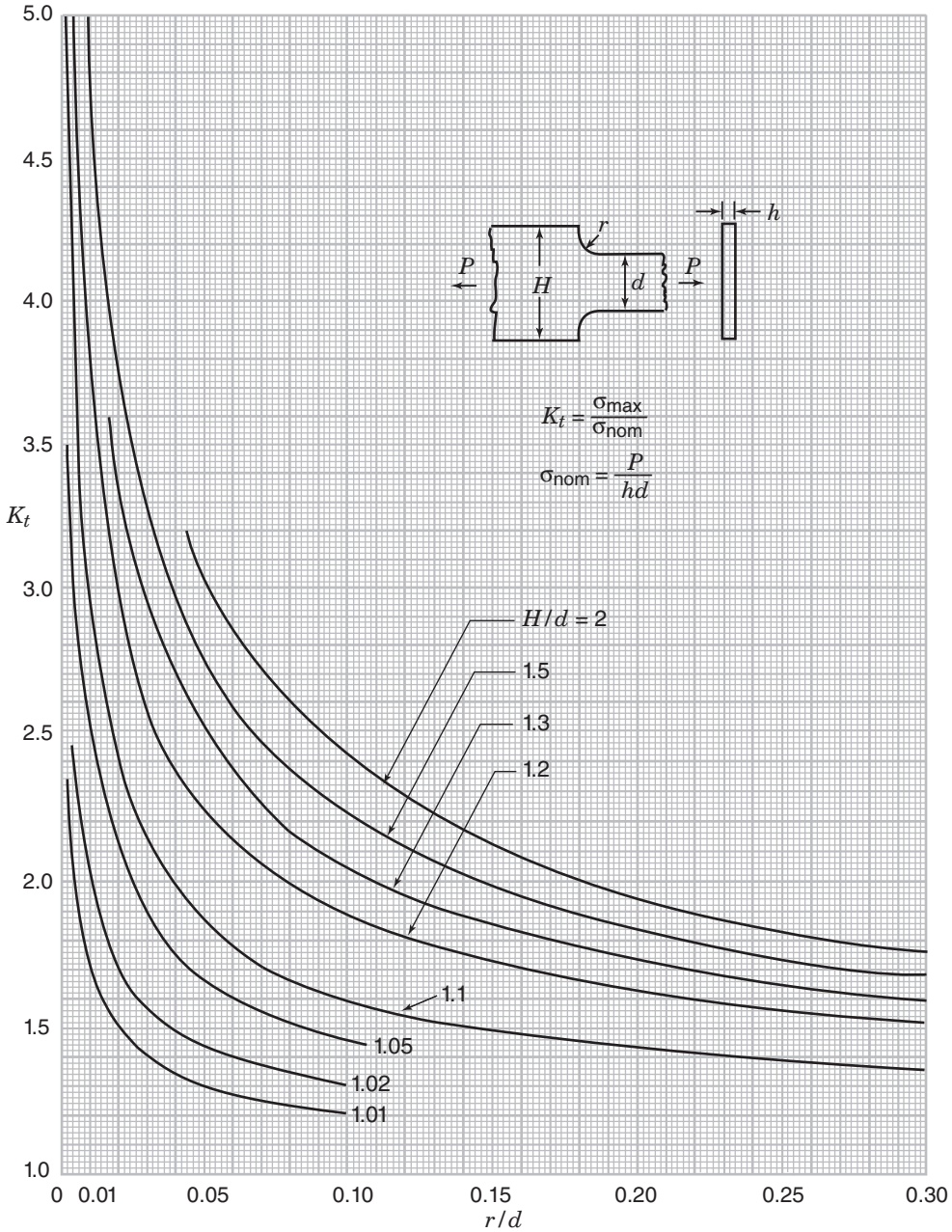


Chart 3.1 Stress concentration factors K_t for a stepped flat tension bar with shoulder fillets (based on data of Frocht 1935; Appl and Koerner 1969; Wilson and White 1973).

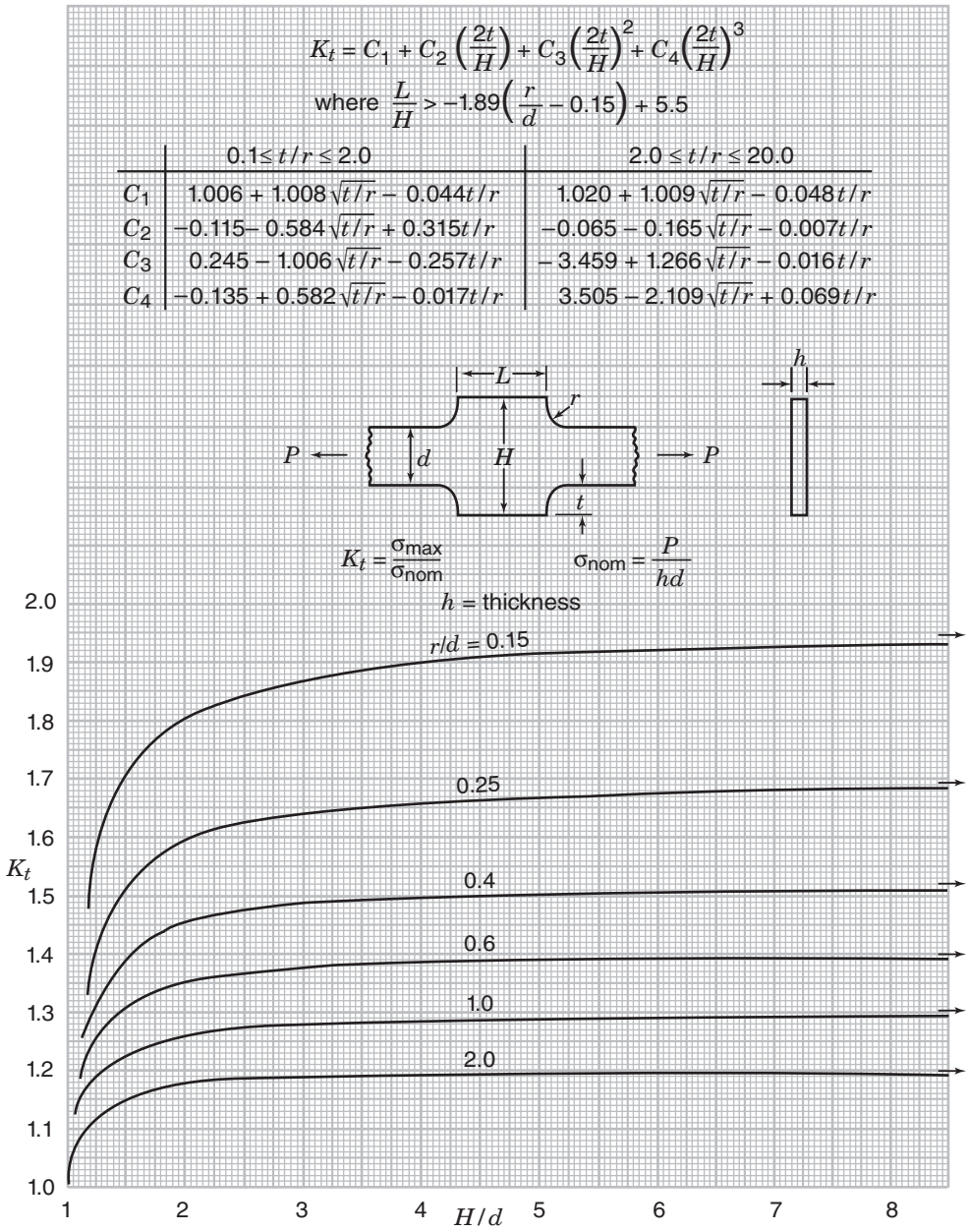


Chart 3.2*a* Stress concentration factors K_t for a stepped flat tension bar with shoulder fillets (Kumagai and Shimada, 1968): $L/d = 1.5$.

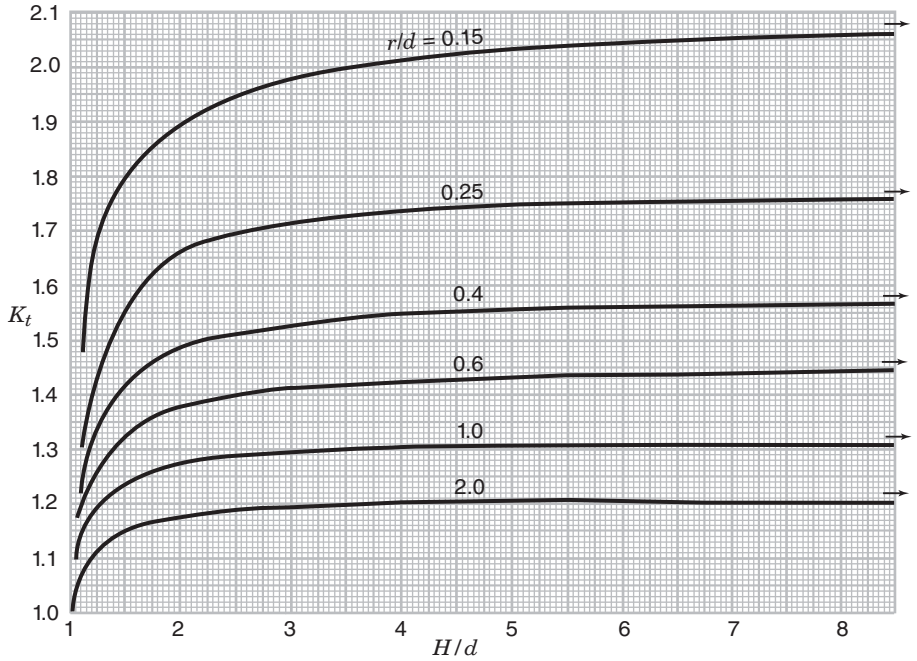


Chart 3.2*b* Stress concentration factors K_t for a stepped flat tension bar with shoulder fillets (Kumagai and Shimada, 1968): $L/d = 3.5$.

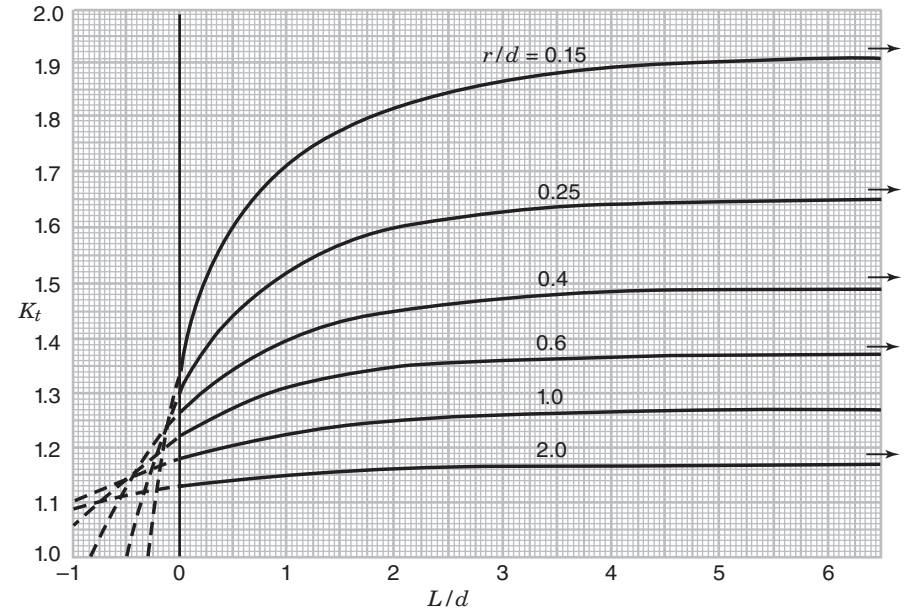


Chart 3.2*c* Stress concentration factors K_t for a stepped flat tension bar with shoulder fillets (Kumagai and Shimada, 1968): $H/d = 1.8$.

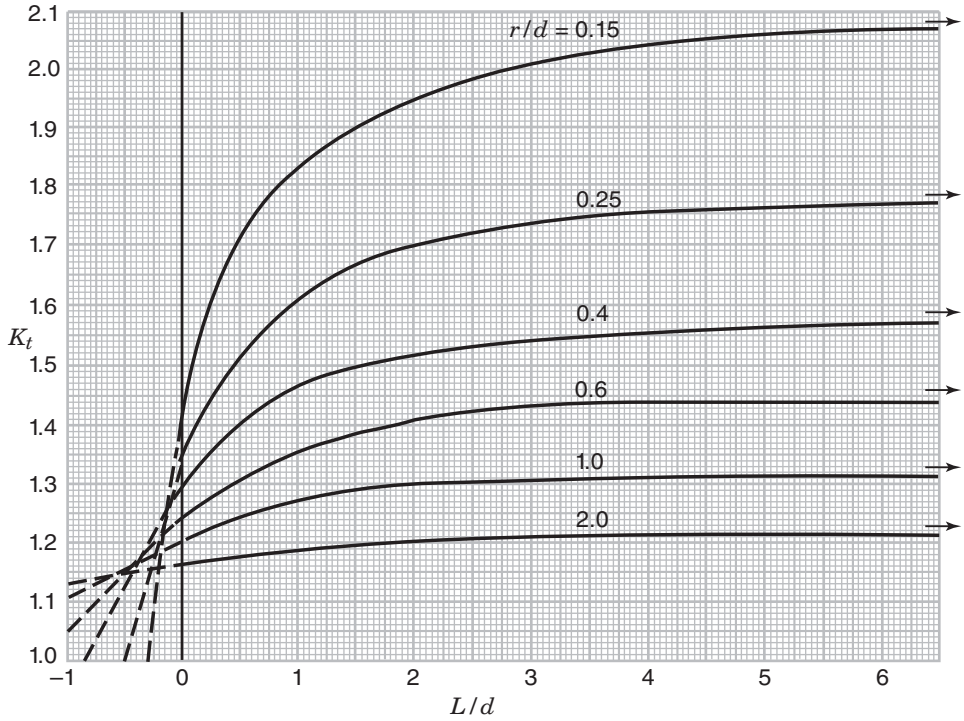


Chart 3.2*d* Stress concentration factors K_t for a stepped flat tension bar with shoulder fillets (Kumagai and Shimada, 1968): $H/d = 5$.

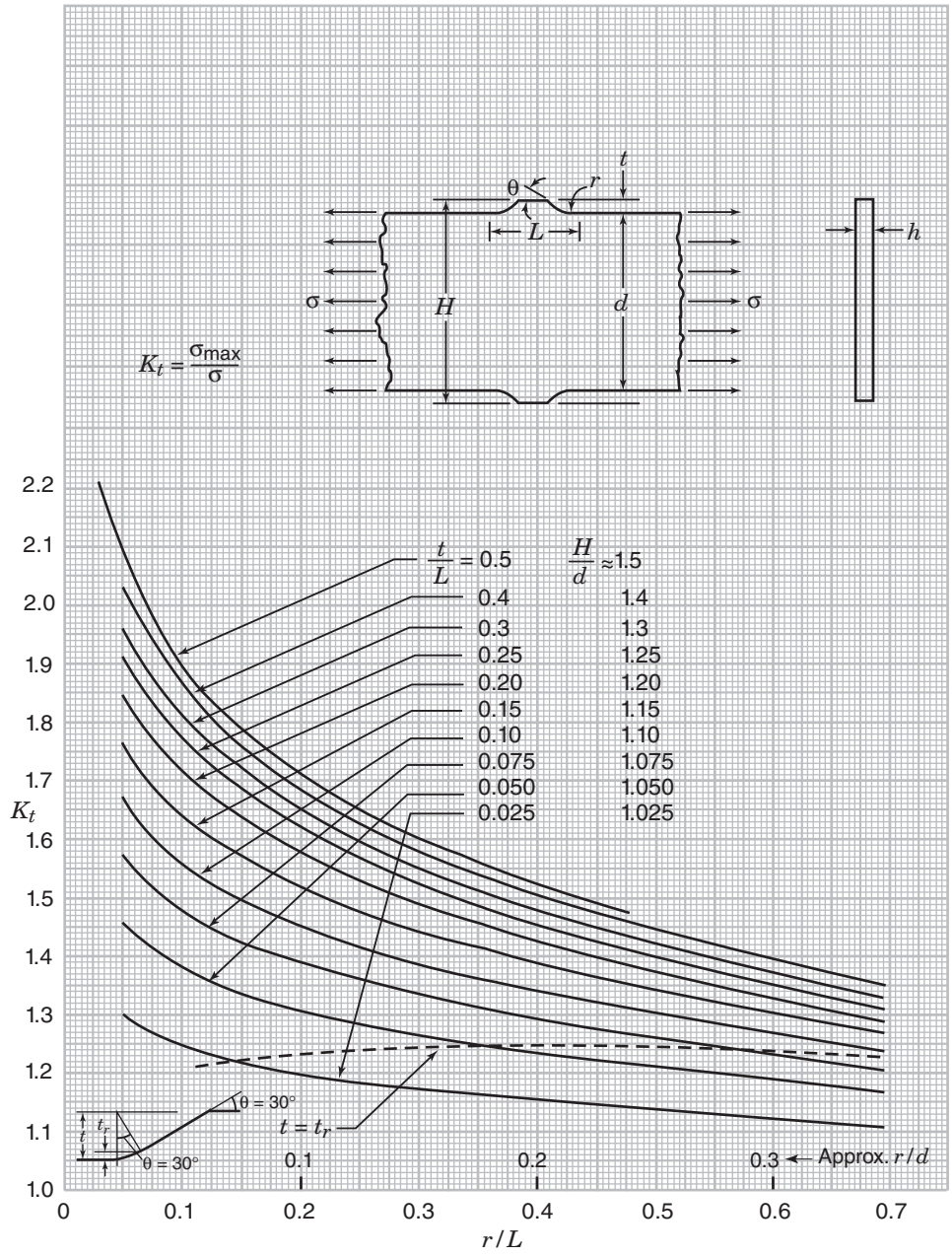


Chart 3.3*a* Stress concentration factors K_t for a trapezoidal protuberance on a tension member $L/(d/2) = 1.05$ (Derecho and Munse 1968): $\theta = 30^\circ$.

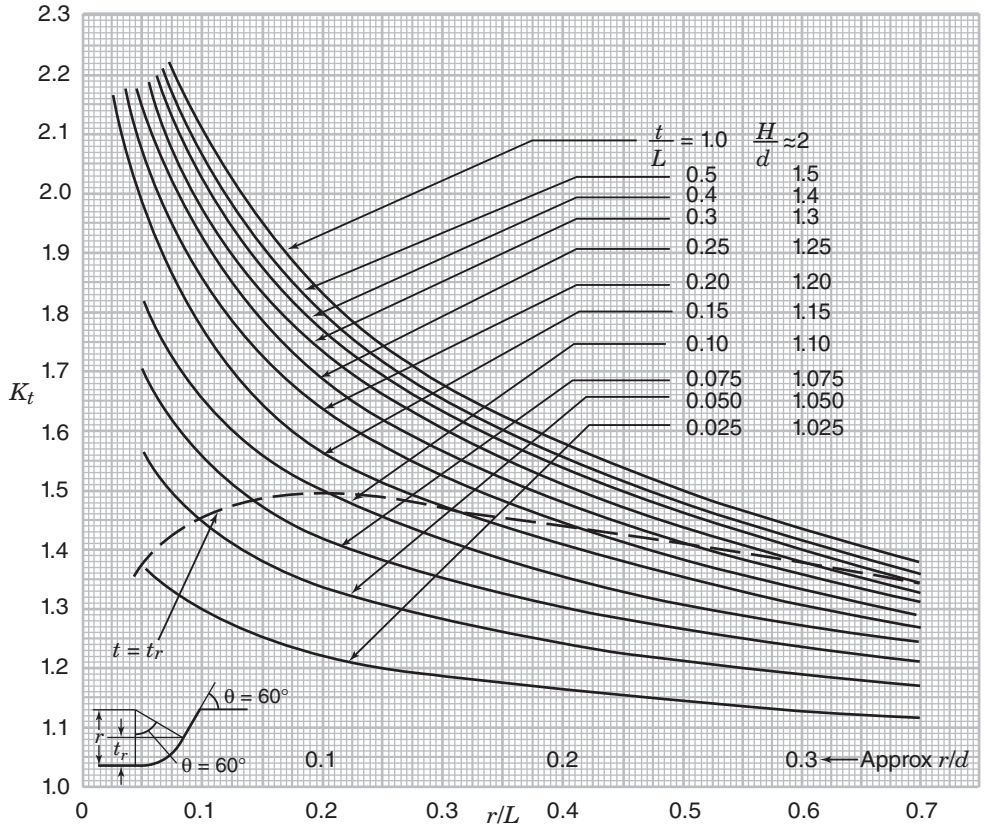


Chart 3.3*b* Stress concentration factors K_t for a trapezoidal protuberance on a tension member $L/(d/2) = 1.05$ (Derecho and Munse 1968): $\theta = 60^\circ$.

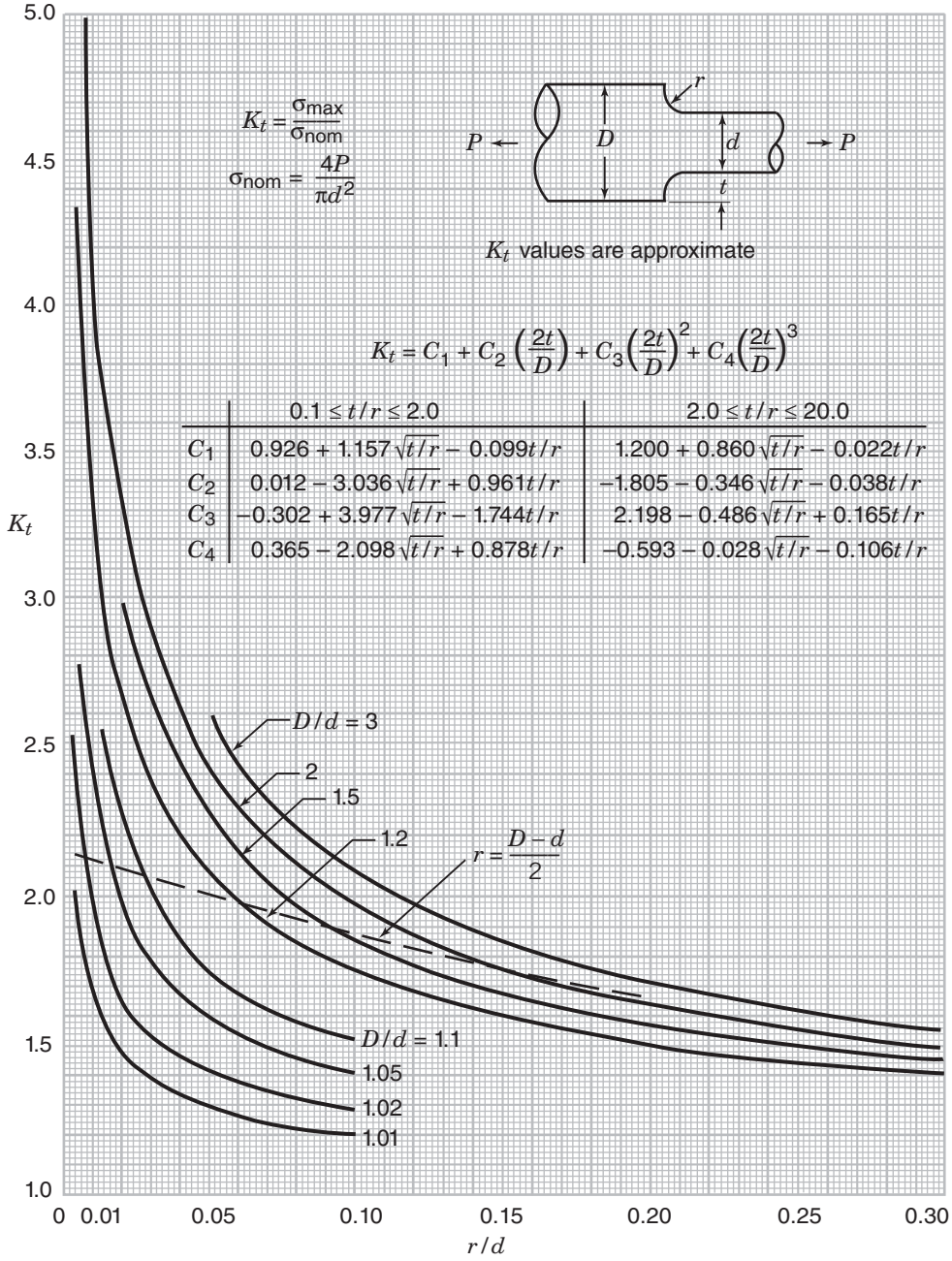


Chart 3.4 Stress concentration factors K_t for a stepped tension bar of circular cross section with shoulder fillet.

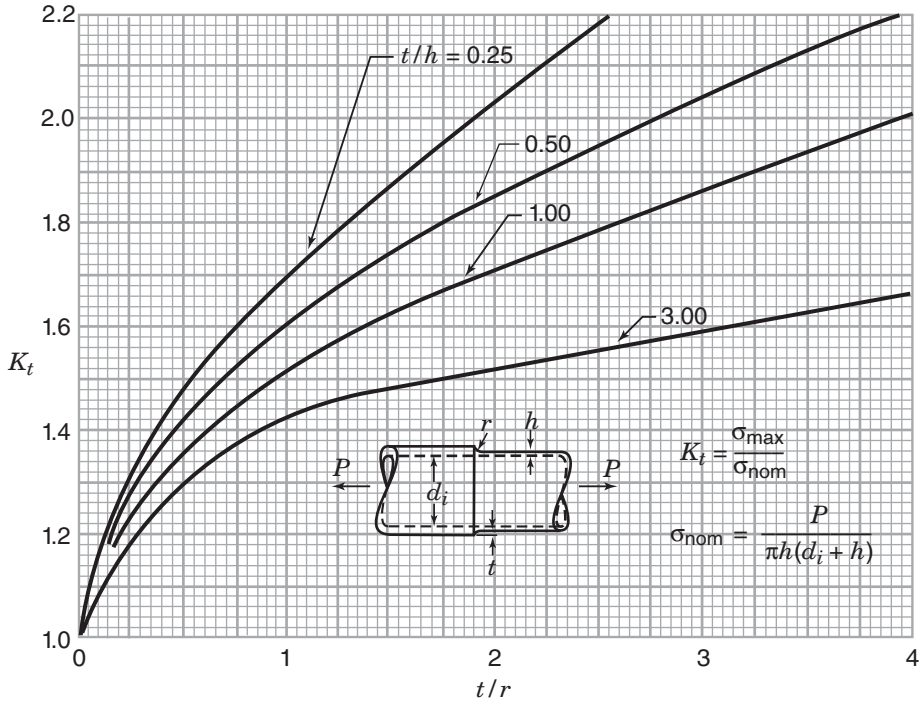


Chart 3.5 Stress concentration factors K_t for a tube in tension with fillet (Lee and Ades 1956; ESDU 1981): $(d_i/h + d_i/t) > 28$.

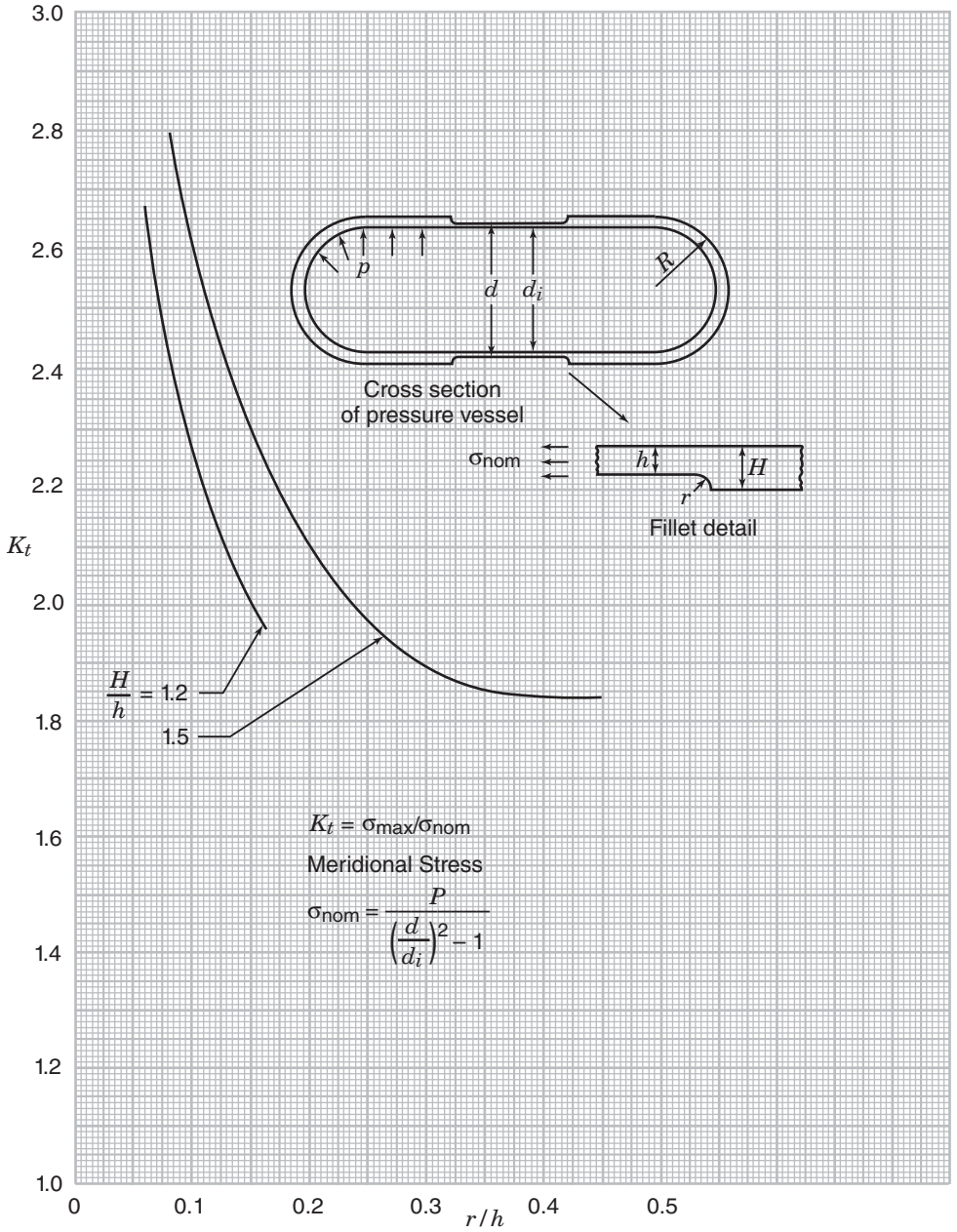


Chart 3.6 Stress concentration factors K_t for a stepped pressure vessel wall with a shoulder fillet $R/H \approx 10$ (Griffin and Thurman 1967).

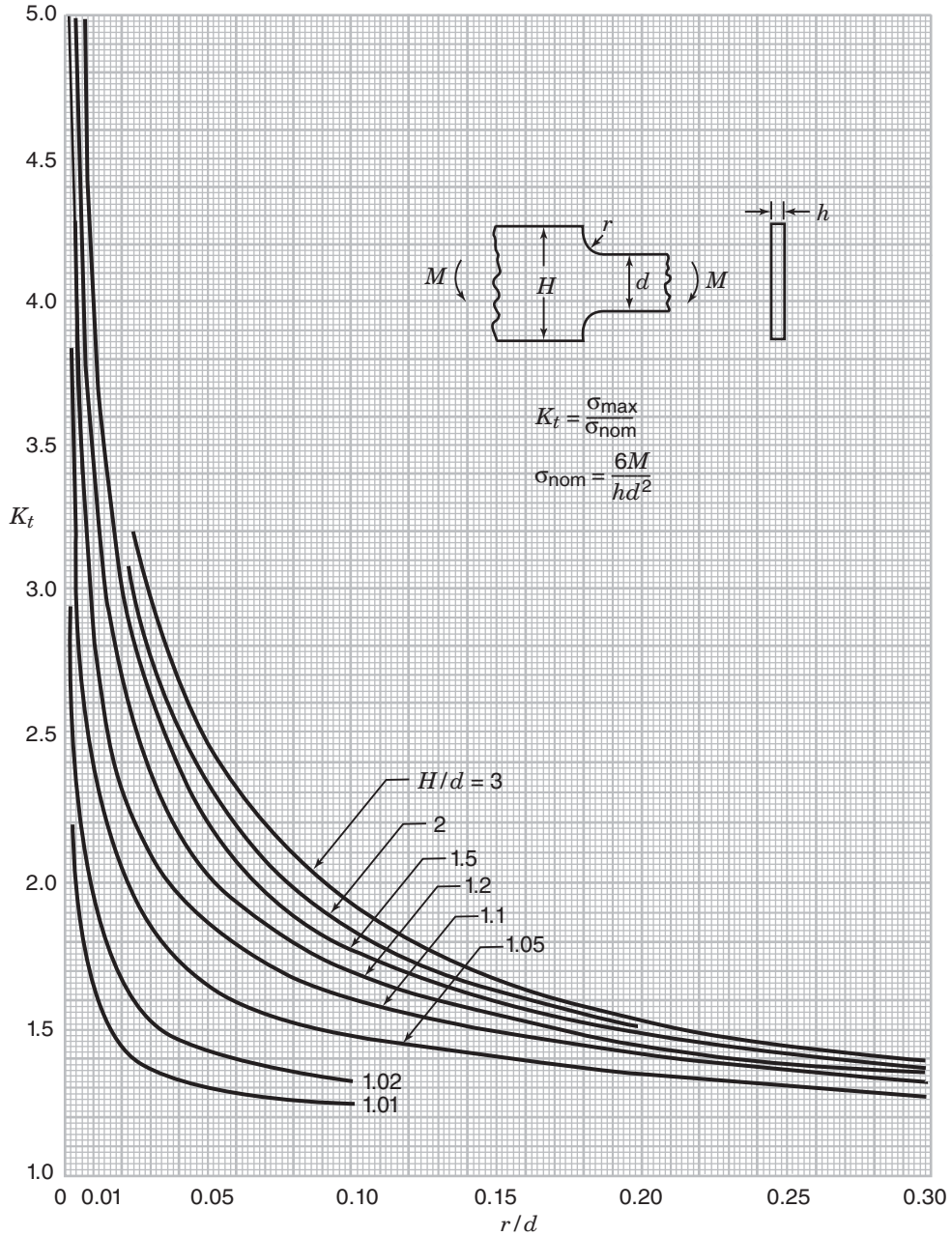


Chart 3.7 Stress concentration factors K_t for bending of a stepped flat bar with shoulder fillets (based on photoelastic tests of Leven and Hartman 1951; Wilson and White 1973).

$$K_t = C_1 + C_2\left(\frac{2t}{H}\right) + C_3\left(\frac{2t}{H}\right)^2 + C_4\left(\frac{2t}{H}\right)^3$$

where $\frac{L}{H} > -2.05\left(\frac{r}{d} - 0.025\right) + 2.0$

	$0.1 \le t/r \le 2.0$	$2.0 \le t/r \le 20.0$
C_1	$1.006 + 0.967\sqrt{t/r} + 0.013t/r$	$1.058 + 1.002\sqrt{t/r} - 0.038t/r$
C_2	$-0.270 - 2.372\sqrt{t/r} + 0.708t/r$	$-3.652 + 1.639\sqrt{t/r} - 0.436t/r$
C_3	$0.662 + 1.157\sqrt{t/r} - 0.908t/r$	$6.170 - 5.687\sqrt{t/r} + 1.175t/r$
C_4	$-0.405 + 0.249\sqrt{t/r} - 0.200t/r$	$-2.558 + 3.046\sqrt{t/r} - 0.701t/r$

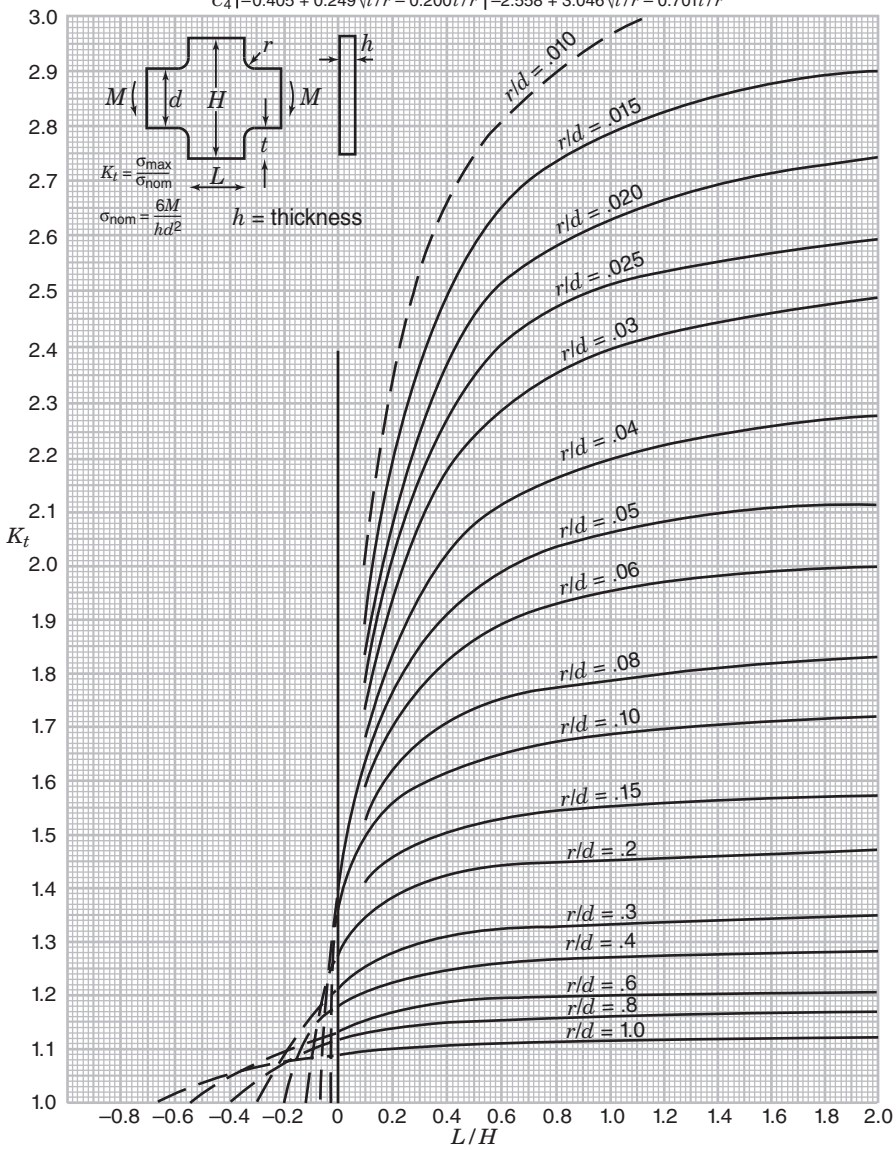


Chart 3.8*a* Effect of shoulder width L on stress concentration factors K_t for filleted bars in bending (based on photoelastic data by Leven and Hartman 1951): $H/d = 1.25$.

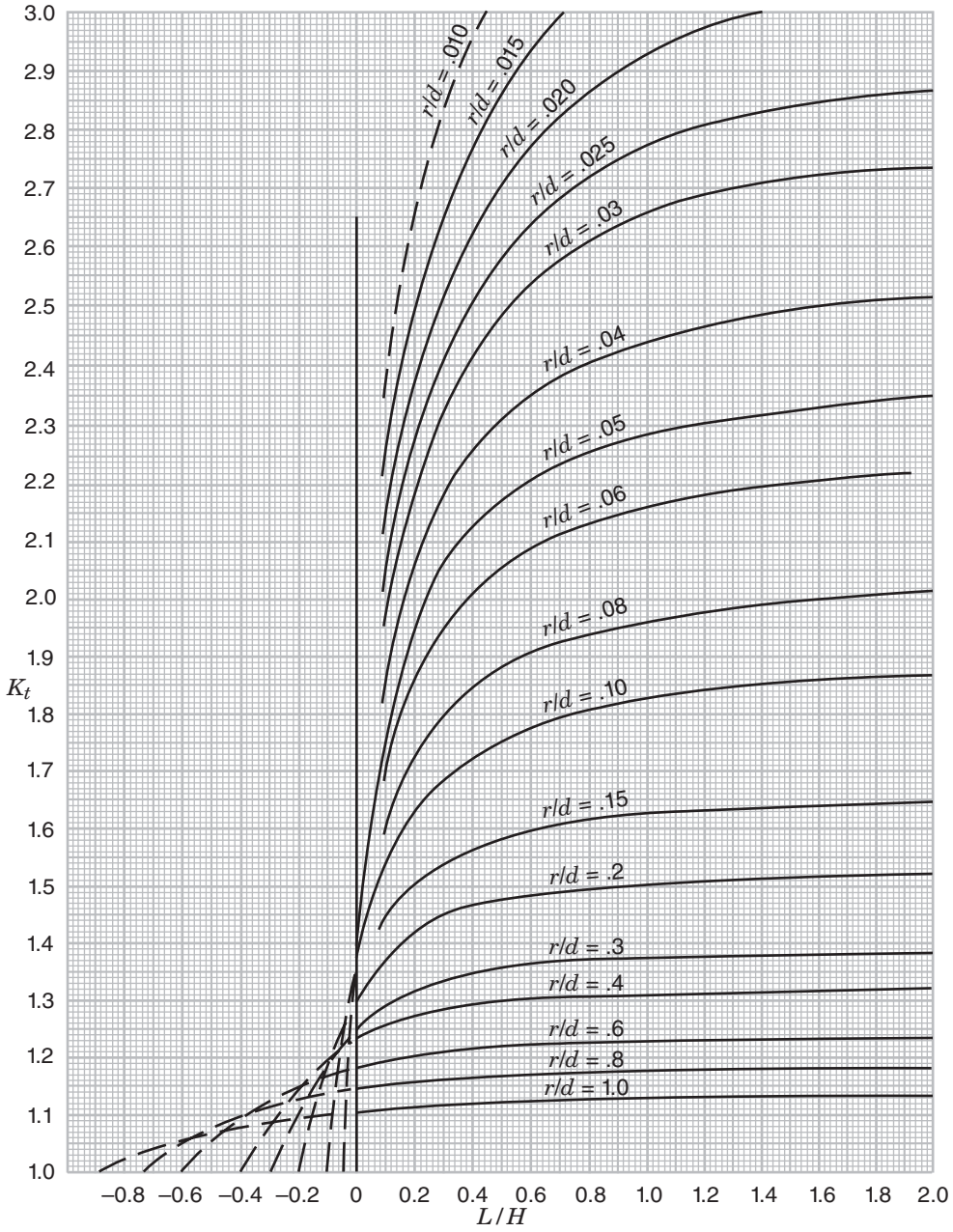


Chart 3.8*b* Effect of shoulder width L on stress concentration factors K_t for filleted bars in bending (based on photoelastic data by Leven and Hartman 1951): $H/d = 2$.

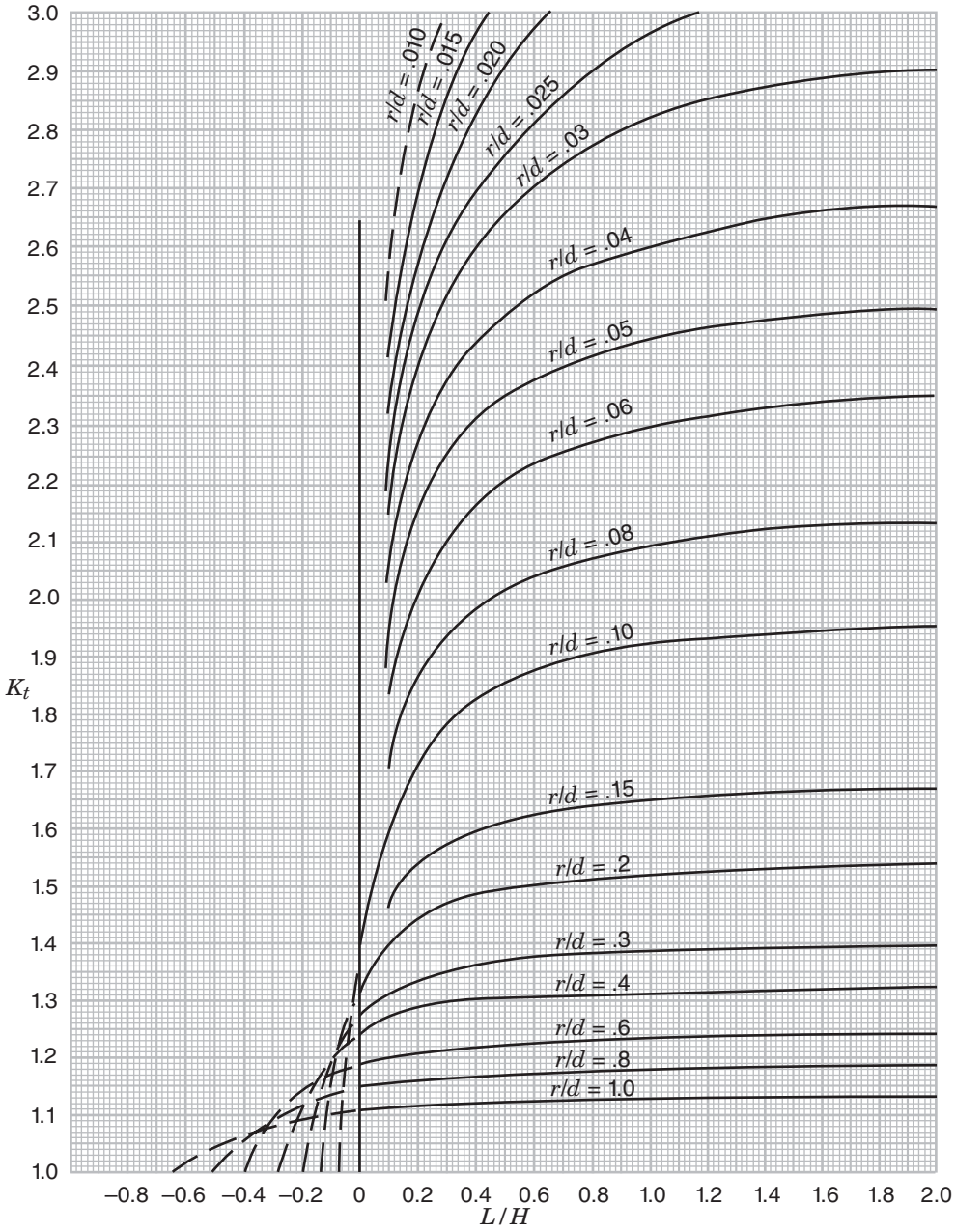


Chart 3.8*c* Effect of shoulder width L on stress concentration factors K_t for filleted bars in bending (based on photoelastic data by Leven and Hartman 1951): $H/d = 3$.

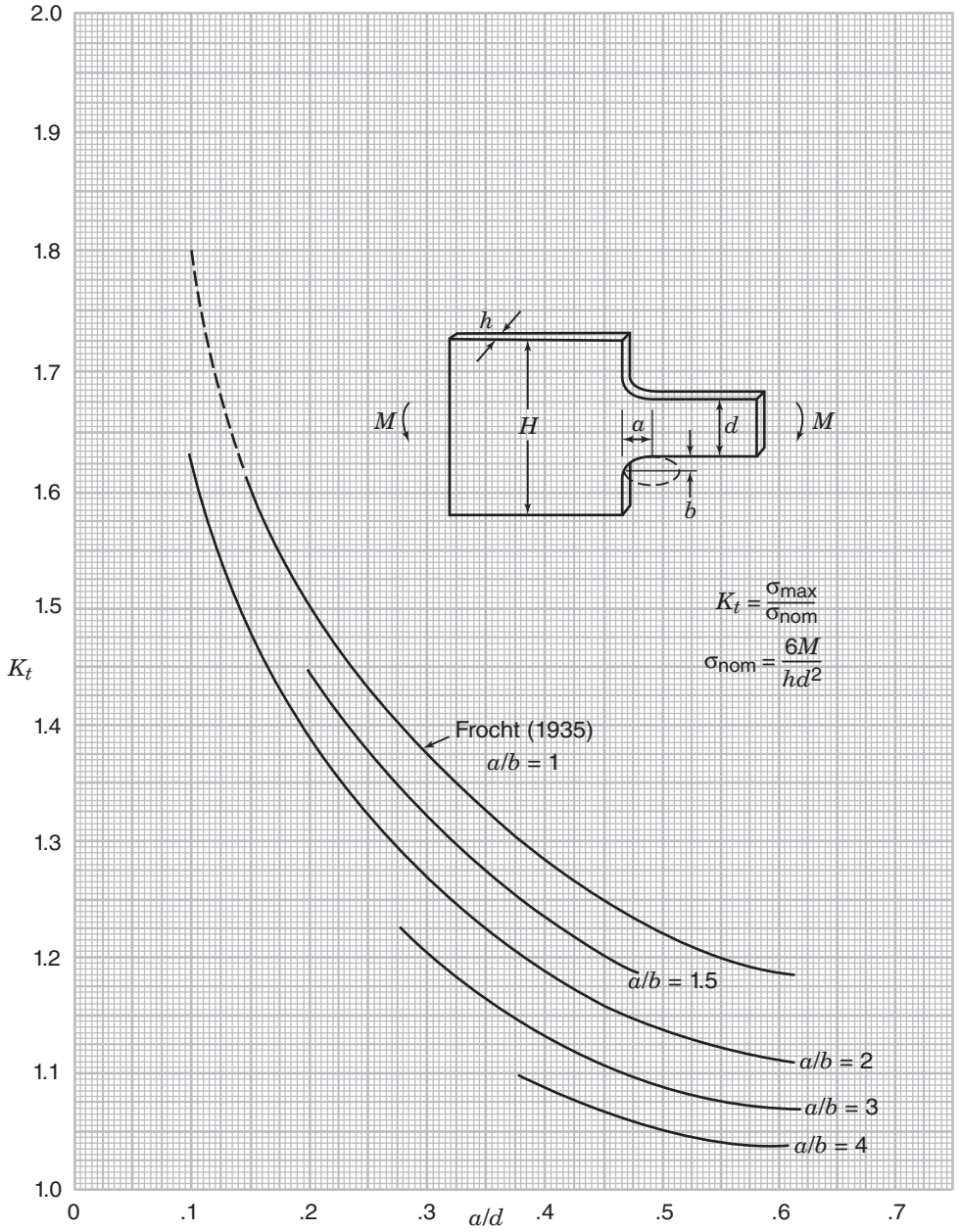


Chart 3.9 Stress concentration factors K_t for the bending case of a flat bar with an elliptical fillet, $H/d \approx 3$ (photoelastic tests of Berkey 1944).

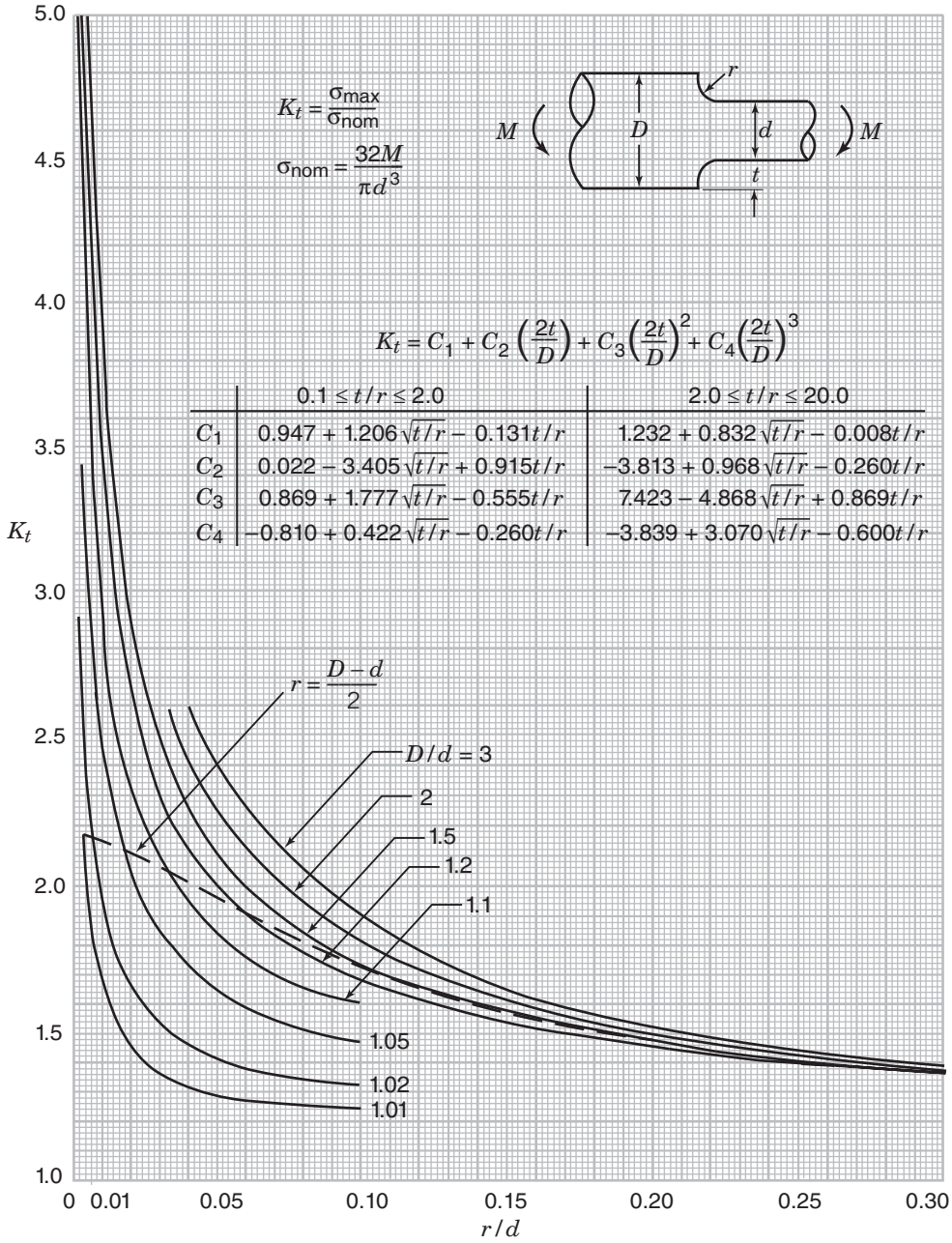


Chart 3.10 Stress concentration factors K_t for bending of a stepped bar of circular cross section with a shoulder fillet (based on photoelastic tests of Leven and Hartman 1951; Wilson and White 1973).

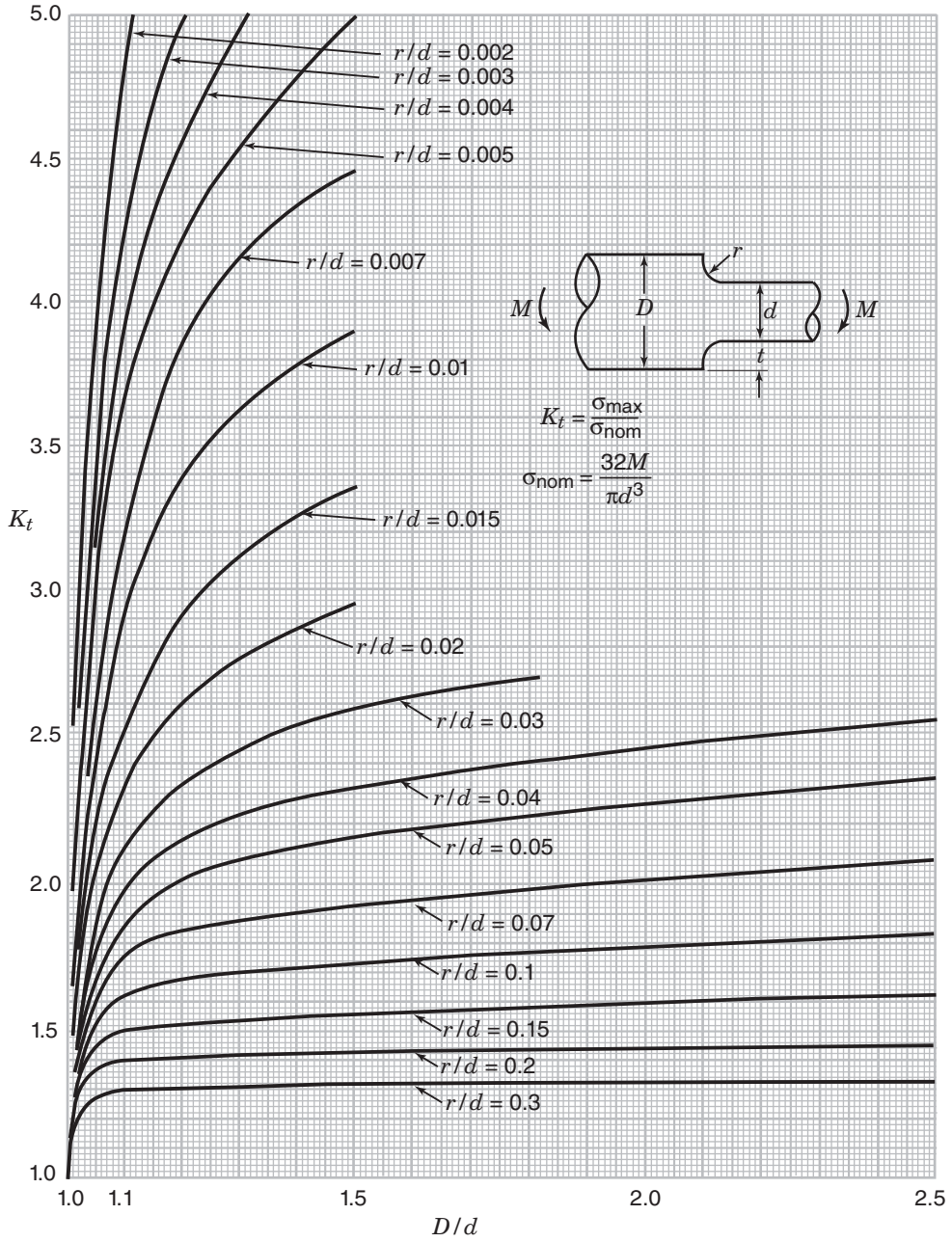


Chart 3.11 Stress concentration factors K_t for bending of a stepped bar of circular cross section with a shoulder fillet (based on photoelastic tests of Leven and Hartman 1951; Wilson and White 1973). This chart serves to supplement Chart 3.10.

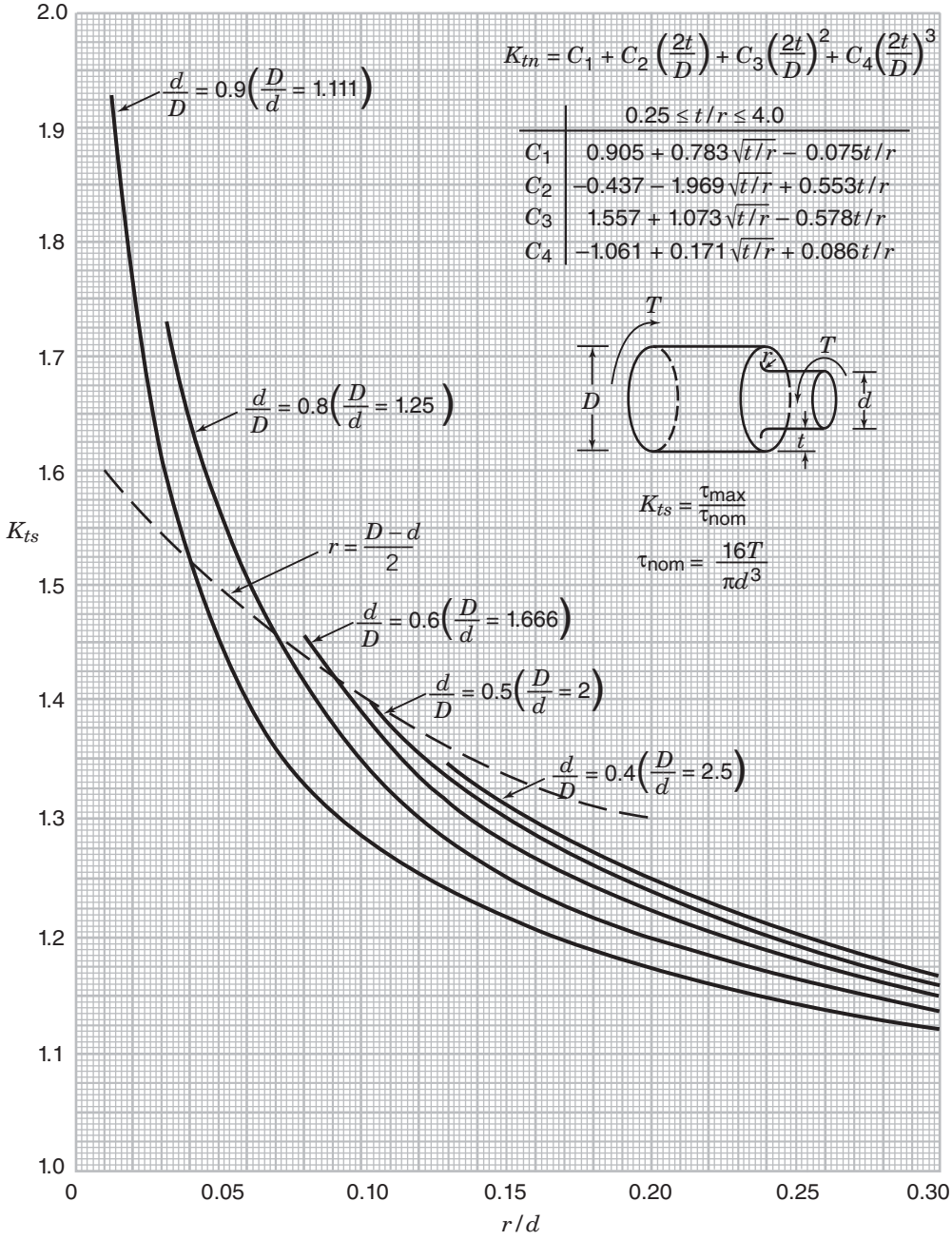


Chart 3.12 Stress concentration factors K_{ts} for torsion of a shaft with a shoulder fillet (data from Matthews and Hooke 1971).

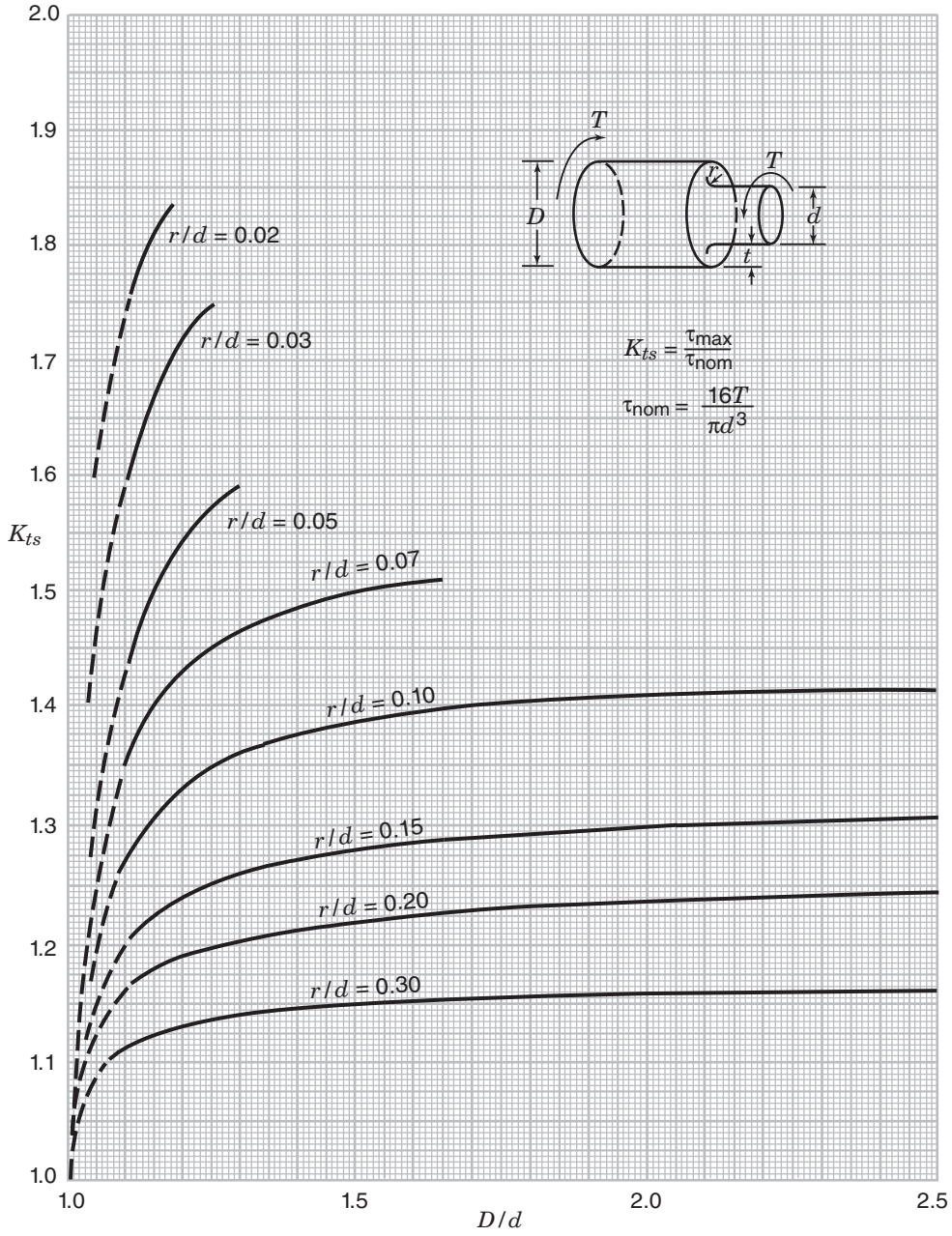


Chart 3.13 Stress concentration factors K_{ts} for torsion of a shaft with a shoulder fillet (data from Matthews and Hooke 1971). This chart serves to supplement Chart 3.12.

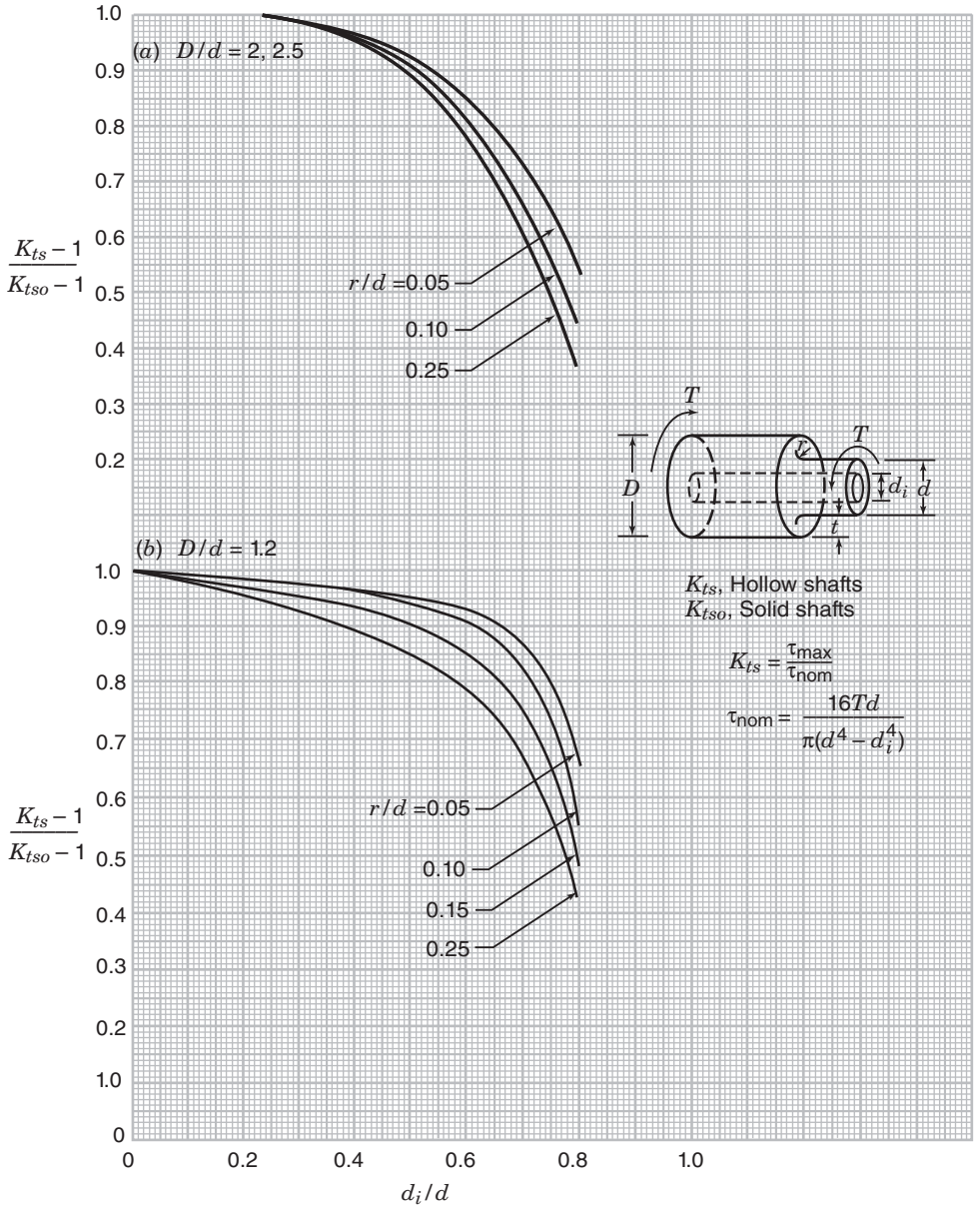


Chart 3.14 Effect of axial hole on stress concentration factors of a torsion shaft with a shoulder fillet (from data of Rushton 1964): (*a*) $D/d = 2, 2.5$; (*b*) $D/d = 1.2$.

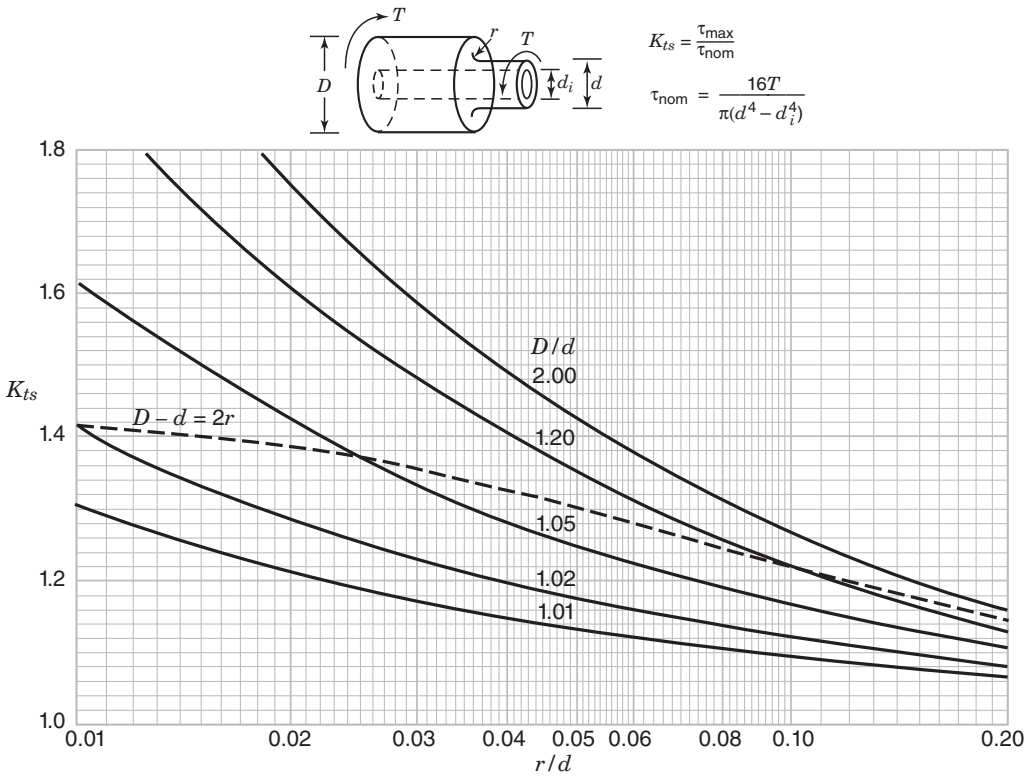


Chart 3.15*a* Stress concentration factors of a torsion tube with a shoulder fillet (Rushton 1964; ESDU 1981): $d_i/d = 0.515$.

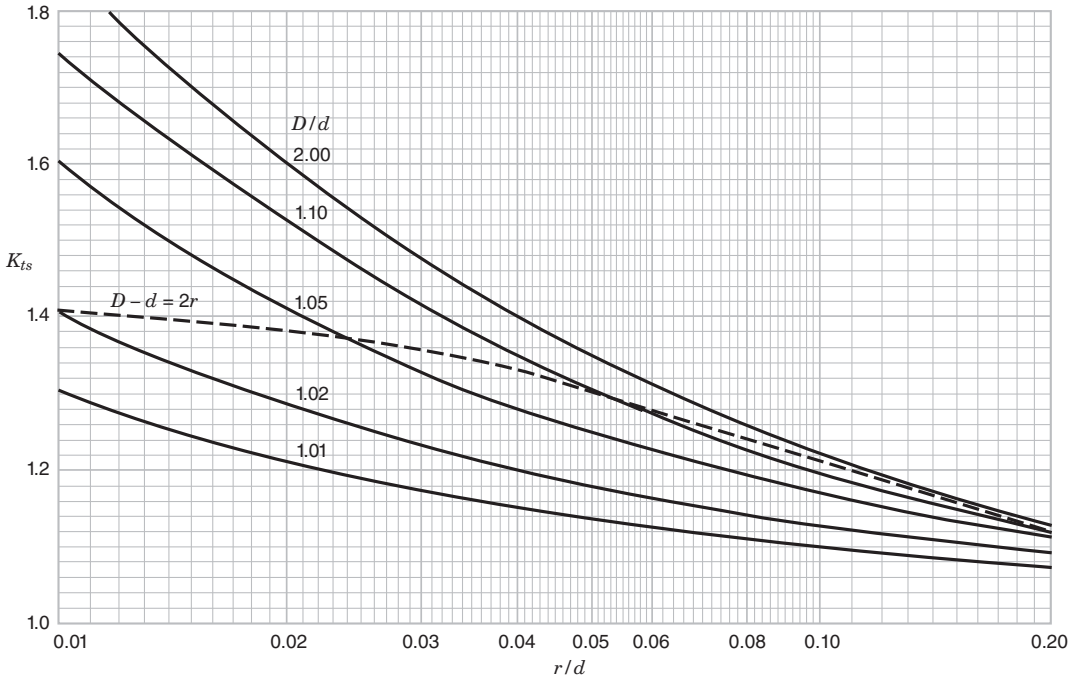


Chart 3.15*b* Stress concentration factors of a torsion tube with a shoulder fillet (Rushton 1964; ESDU 1981): $d_i/d = 0.669$.

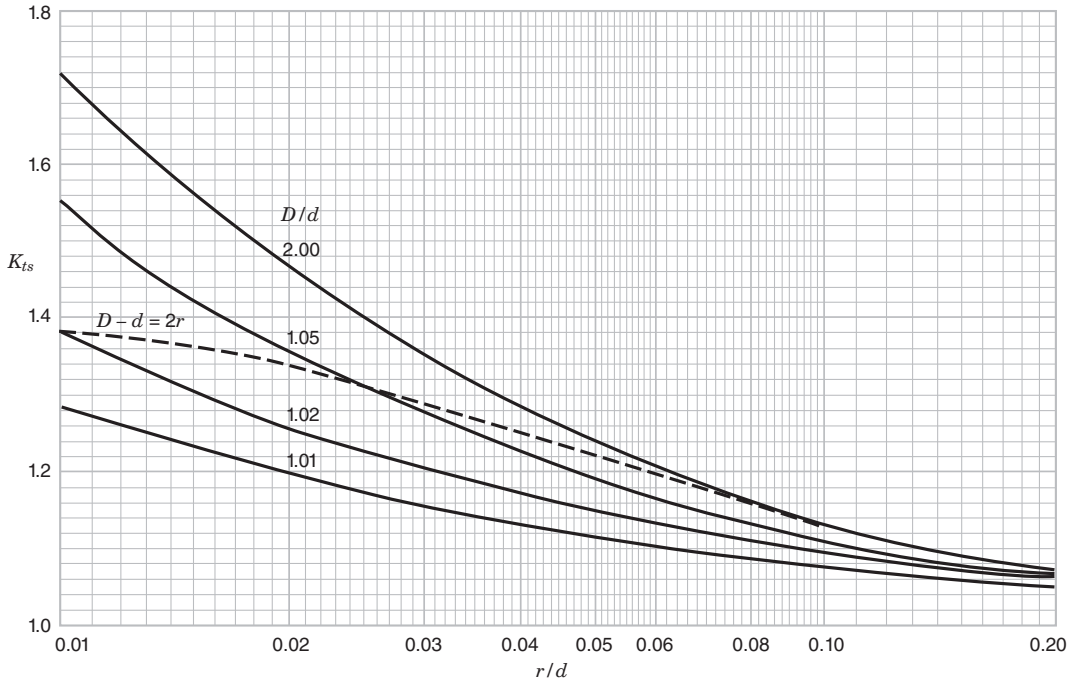


Chart 3.15*c* Stress concentration factors of a torsion tube with a shoulder fillet (Rushton 1964; ESDU 1981): $d_i/d = 0.796$.

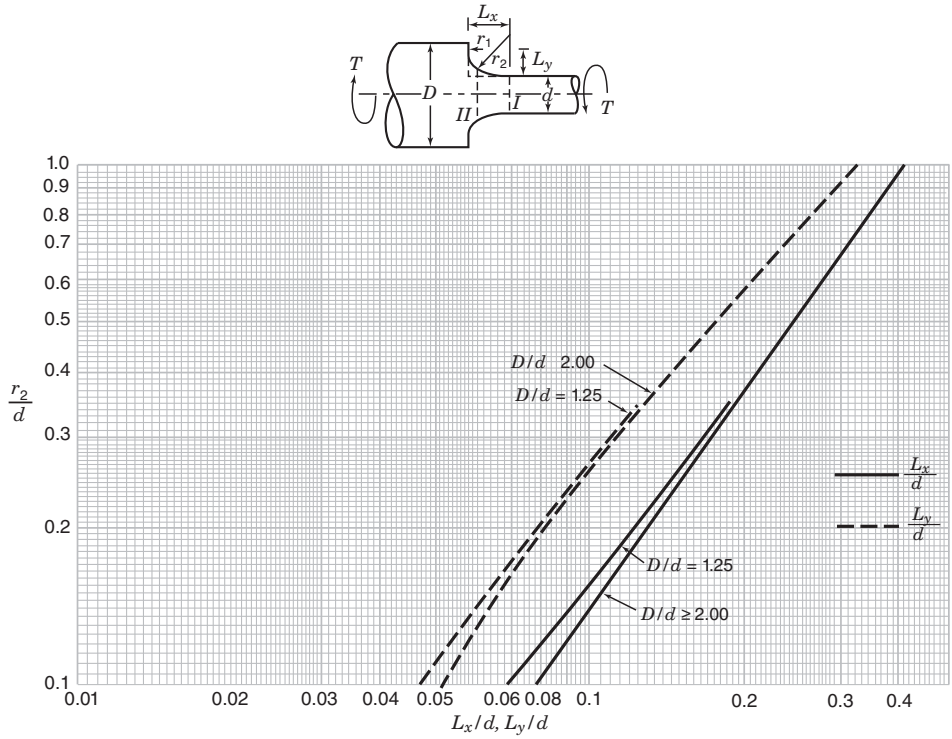


Chart 3.16*a* Radius of compound fillet for shoulder shaft in torsion, $K_{tI} = K_{tII}$ (Battenbo and Baines 1974; ESDU 1981): $r_2/r_1 = 3$.

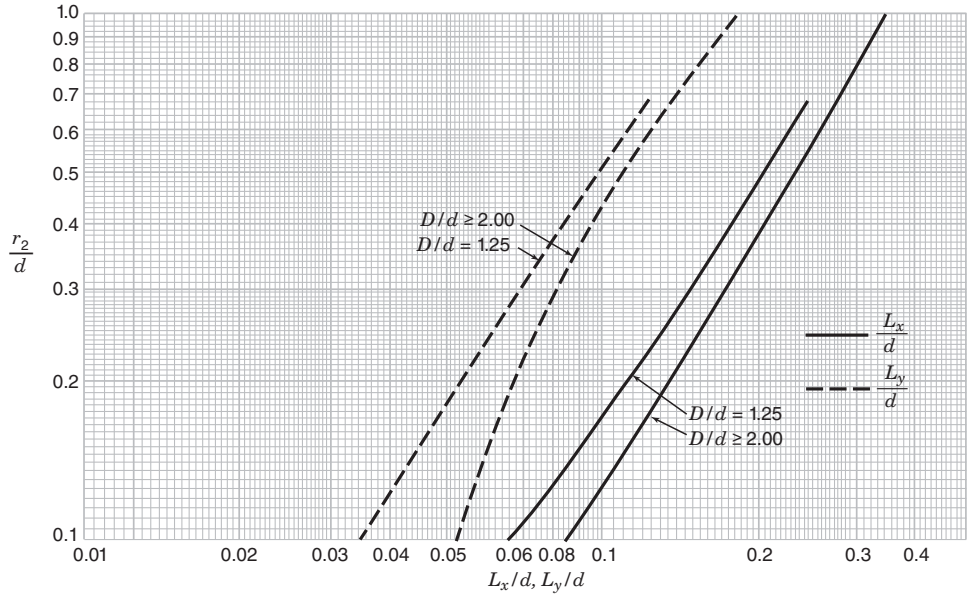


Chart 3.16*b* Radius of compound fillet for shoulder shaft in torsion, $K_{tI} = K_{tII}$ (Battenbo and Baines 1974; ESDU 1981): $r_2/r_1 = 6$.

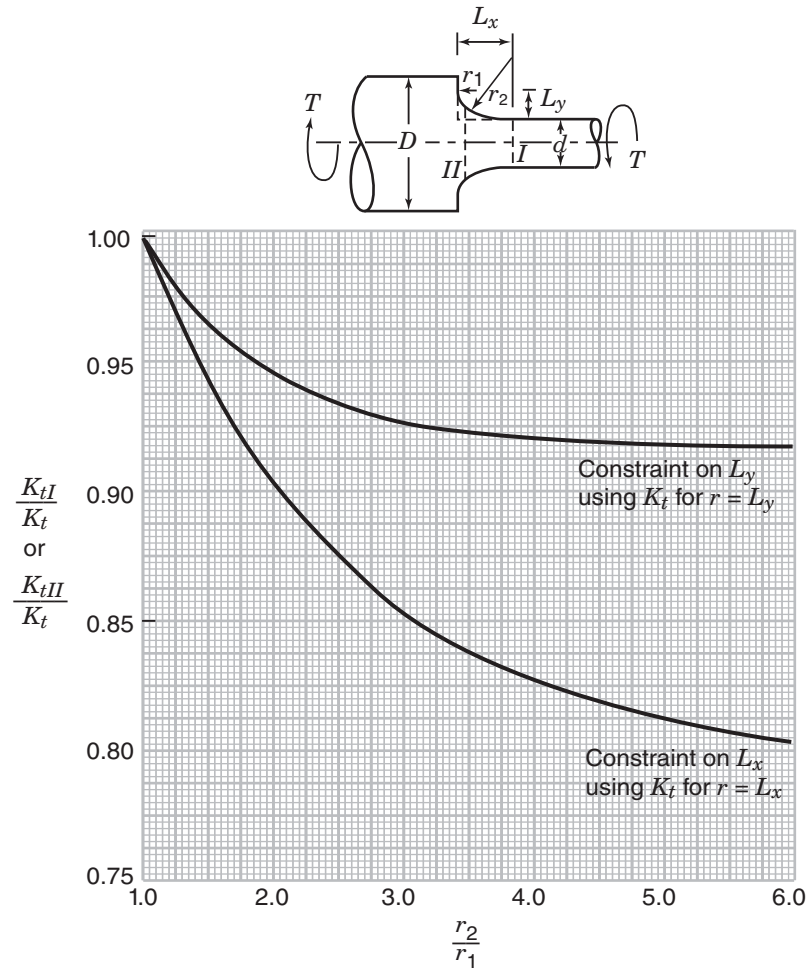


Chart 3.17 Maximum possible reduction in stress concentration, $K_{tI} = K_{tII}$ (Battenbo and Baines 1974; ESDU 1981).

CHAPTER 4

HOLES

Fig. 4.1 shows some structural members with transverse holes. In this chapter, the formulas and figures of the stress concentration factors (SCFs) are arranged according to the loading (tension, torsion, bending, etc.), the shape of the hole (circular, elliptical, rectangular, etc.), single and multiple holes, two- and three-dimensional cases. In addition to "empty holes," various-shaped inclusions are treated.

4.1 NOTATION

Definitions:

Panel. A thin flat element with in-plane loading. This is a plane sheet that is sometimes referred to as a *membrane* or *diaphragm*.

Plate. A thin flat element with transverse loading. This element is characterized by transverse displacements (i.e., deflections).

Symbols:

SCF = stress concentration factor
a = radius of hole
a = major axis of ellipse
a = half crack length
A = area (or point)

Peterson's Stress Concentration Factors, Fourth Edition. Walter D. Pilkey, Deborah F. Pilkey and Zhuming Bi.
© 2020 John Wiley & Sons, Inc. Published 2020 by John Wiley & Sons, Inc.

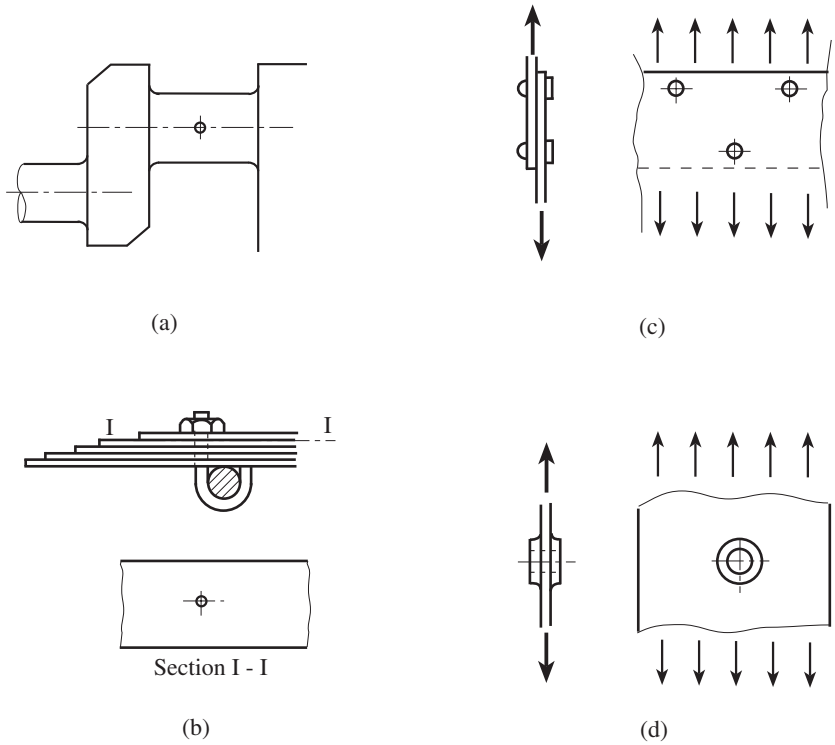


Figure 4.1 Examples of parts with transverse holes: (*a*) oil hole in crankshaft (bending and torsion); (*b*) clamped leaf spring (bending); (*c*) riveted flat elements; (*d*) hole with reinforcing bead.

A_r = effective cross-sectional area of reinforcement
b = minor axis of ellipse
c = distance from center of hole to the nearest edge of element
C_A = reinforcement efficiency factor
C_s = shape factor
d = diameter of hole
D = outer diameter of reinforcement surrounding a hole
e = distance from center of hole to the furthest edge of the element
E = modulus of elasticity
E' = modulus of elasticity of inclusion material
h = thickness
h_r = thickness of reinforcement
h_t = total thickness, including reinforcement $\left(h_t = h + h_r \text{ or } h + 2h_r\right)$
H = height or width of element

K_t = theoretical stress concentration factor for normal stress
K_{te} = stress concentration factor at edge of the hole based on von Mises stress
K_{tf} = estimated fatigue notch factor for normal stress
K_{tg} = stress concentration factor with the nominal stress based on gross area
K_{tn} = stress concentration factor with the nominal stress based on net area
l = pitch, spacing between notches or holes
L = length of element
p = pressure
P = load
q = notch sensitivity factor
r = radius of hole, arc, notch
r, θ = polar coordinates
r, θ, x = cylindrical coordinates
R = radius of thin cylinder or sphere
s = distance between the edges of two adjacent holes
x, y, z = rectangular coordinates
α = material constant for evaluating notch sensitivity factor
ν = Poisson's ratio
σ = normal stress, typically the normal stress on gross section
σ_n = normal stress based on net area
σ_{eq} = equivalent stress
$\sigma_{\max}$ = maximum normal stress or maximum equivalent stress
σ = nominal or reference normal stress
σ_{tf} = estimated fatigue strength
σ_1, σ_2 = biaxial in-plane normal stresses
$\sigma_1, \sigma_2, \sigma_3$ = principal stresses
τ = shear stress

4.2 STRESS CONCENTRATION FACTORS

As discussed in Section 1.21, the stress concentration factor (SCF) is defined as the ratio of the peak stress in the body to a reference stress. Usually the SCF is K_{tg}, for which the reference stress is based on the gross cross-sectional area, or K_{tn}, for which the reference stress is based on the net cross-sectional area. For a two-dimensional element with a single hole (Fig. 1.40*a*), the formulas for these stress concentration factors are

$$K_{tg} = \frac{\sigma_{\max}}{\sigma} \tag{4.1}$$

where K_{tg} is the SCF based on gross stress, $\sigma_{\max}$ is the maximum stress, at the edge of the hole, σ is the stress on gross section far from the hole, and

$$K_{tn} = \frac{\sigma_{\max}}{\sigma_n} \tag{4.2}$$

where K_{tn} is the SCF based on net (nominal) stress and σ_n is the net stress $\sigma/(1 - d/H)$, with d the hole diameter and H the width of element (Fig. 1.4*a*). From the foregoing,

$$K_{tn} = K_{tg}\left(1 - \frac{d}{H}\right) = K_{tg}\frac{\sigma}{\sigma_n} \tag{4.3}$$

or

$$K_{tg} = \frac{\sigma_n}{\sigma}K_{tn} = \frac{\sigma_n}{\sigma} \cdot \frac{\sigma_{\max}}{\sigma_n} \tag{4.4}$$

The significance of K_{tg} and K_{tn} can be seen by referring to Chart 4.1. The factor K_{tg} takes into account the two effects: (1) the increased stress due to loss of section (term σ_n/σ in Eq. 4.4); and (2) the increased stress due to geometry (term $\sigma_{\max}/\sigma_n$). As the element becomes narrower (the hole becomes larger), $d/H \to 1$, $K_{tg} \to \infty$. However, K_{tn} takes account of only one effect, i.e., the increased stress due to geometry. As the hole becomes larger, $d/H \to 1$, the element becomes in the limit a uniform tension member, with $K_{tn} = 1$. Either Eq. (4.1) or (4.2) can be used to evaluate $\sigma_{\max}$. Usually the simplest procedure is to use K_{tg}. If the stress gradient is of concern as in certain fatigue problems, the proper factor to use is K_{tn}. See Section 1.9 for more discussion on the use of K_{tg} and K_{tn}.

Example 4.1 Fatigue Stress of an Element with a Square Pattern of Holes Consider a thin, infinite element with four holes arranged in a square pattern subjected to uniaxial tension with $s/l = 0.1$ (Fig. 4.2). From Chart 4.2, it can be found that $K_{tg} = 10.8$ and $K_{tn} = (s/l)K_{tg} = 1.08$, the difference being that K_{tg} takes account of the loss of section. The material is low carbon steel and the hole diameter is 0.048 in. Assuming a fatigue strength (specimen without stress concentration) $\sigma_f = 30{,}000$ lb/in.^{2}, we want to find the estimated fatigue strength of the member with holes.

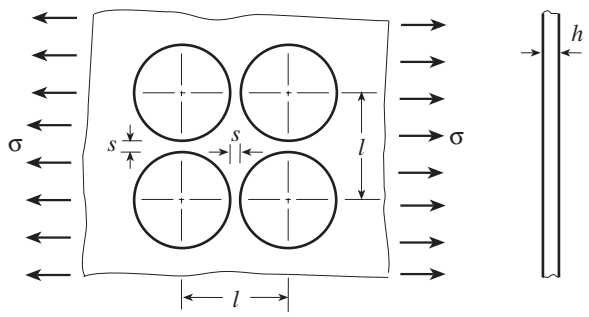


Figure 4.2 Thin infinite element with four holes.

From Eq. (1.96) expressed in terms of estimated values, the estimated fatigue stress σ_{tf} of the member with holes is given by

$$\sigma_{tf} = \frac{\sigma_f}{K_{tf}} \tag{1}$$

where K_{tf} is the estimated fatigue notch factor of the member with holes. From Eq. (1.99),

$$K_{tf} = q(K_t - 1) + 1 \tag{2}$$

where K_t is the theoretical stress concentration factor of the member and q is the notch sensitivity of the member and from Eq. (1.101),

$$q = \frac{1}{1 + \alpha/r} \tag{3}$$

where α is a material constant and r is the notch radius.

For annealed or normalized steel, it is found that $\alpha = 0.01$ (Section 1.16) and for a hole of radius $r = 0.024$, the notch sensitivity is given by

$$q = \frac{1}{1 + 0.01/0.024} \approx 0.7 \tag{4}$$

If the factor K_{tn} is used as K_t,

$$K_{tf} = q(K_{tn} - 1) + 1 = 0.7(1.08 - 1) + 1 = 1.056 \tag{5}$$

Using the obtained K_{tf}, σtf can be found as,

$$\sigma_{tf} = \frac{\sigma_f}{K_{tf}} = \frac{30{,}000}{1.056} = 28{,}400 \text{ lb/in.}^2 \tag{6}$$

This means that if the effect of stress concentration is considered, the estimated fatigue stress on the net section is 28,400 lb/in.^{2}

Since $s/l = 0.1$, the area of the gross section $(l \times h)$ is 10 times that of the net section $(s \times h) = (s/l)(l \times h) = 0.1(l \times h)$. Due to the fact that the total applied loading remains unchanged, the estimated fatigue stress applied on the gross section should be 2,840 lb/in.^{2}

If the estimation is obtained by use of the factor K_{tg},

$$K'_{tf} = q(K_{tg} - 1) + 1 = 0.7(10.8 - 1) + 1 = 7.86 \tag{7}$$

$$\sigma'_{tgf} = \frac{\sigma_f}{K'_{tf}} = \frac{30{,}000}{7.86} = 3{,}820 \text{ lb/in.}^2 \tag{8}$$

Thus, if K_{tg} is used, the estimated fatigue stress on the gross section is 3820 lb/in.^{2}, and the corresponding estimated fatigue stress on the net section is

$$\sigma'_{tf} = \frac{\sigma'_{tgf}}{s/l} = 38{,}200 \text{ lb/in.}^2 \tag{9}$$

The result of Eq. (9) is erroneous, since it means that the fatigue limit of a specimen with holes (σ'_{tf}) is larger than the fatigue limit of a specimen without holes (σ_f). When q is applied, it is necessary to use K_{tn}. Note that 28,400 lb/in.^{2} is close to the full fatigue strength of 30,000 lb/in.^{2} This is because an element between two adjacent holes is like a tension specimen, with a small stress concentration due to the relatively large holes.

4.3 CIRCULAR HOLES WITH IN-PLANE STRESSES

4.3.1 Single Circular Hole in an Infinite Thin Element in Uniaxial Tension

A fundamental case of stress concentration is the stress distribution around a circular hole in an infinite thin element (panel) subjected to uniaxial in-plane tension (Fig. 4.3). In polar coordinates, Timoshenko and Goodier (1970) treated it as a plane stress problem, with the applied stress σ in the theory of elasticity.

$$\begin{aligned}
\sigma_r &= \frac{1}{2}\sigma\left(1 - \frac{a^2}{r^2}\right) + \frac{1}{2}\sigma\left(1 - \frac{4a^2}{r^2} + \frac{3a^4}{r^4}\right)\cos 2\theta \\
\sigma_\theta &= \frac{1}{2}\sigma\left(1 + \frac{a^2}{r^2}\right) - \frac{1}{2}\sigma\left(1 + \frac{3a^4}{r^4}\right)\cos 2\theta \\
\tau_{r\theta} &= -\frac{1}{2}\sigma\left(1 + \frac{2a^2}{r^2} - \frac{3a^4}{r^4}\right)\sin 2\theta
\end{aligned} \tag{4.5}$$

where a is the radius of the hole, r and θ are the polar coordinates of a point in the element as shown in Fig. 4.3. At the edge of the hole with $r = a$,

$$\begin{aligned}
\sigma_r &= 0 \\
\sigma_\theta &= \sigma(1 - 2\cos 2\theta) \\
\tau_{r\theta} &= 0
\end{aligned} \tag{4.6}$$

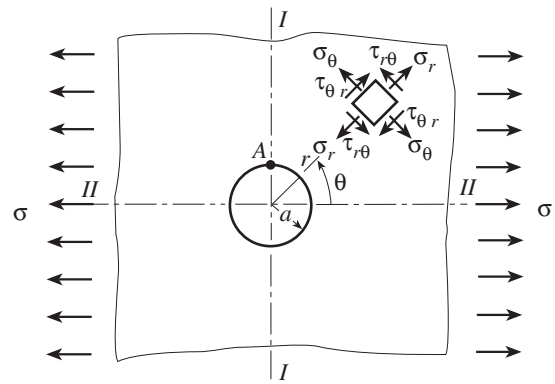


Figure 4.3 Infinite thin element with hole under tensile load.

At point A, $\theta = \pi/2$ (or $3\pi/2$) and

$$\sigma_{\theta A} = 3\sigma$$

This is the maximum stress around the circle, so the SCF for this case is 3. The hole in a panel is such a commonly referenced case that often other SCFs are compared to the "standard" of 3. The value of $K_{tA} = 3$ is shown in Chart 4.1 for a panel of infinite width, that is, for large H.

The distribution of σ_θ at the edge of the hole is shown in Fig. 4.4. At point B, with $\theta = 0$, Eq. (4.6) gives

$$\sigma_{\theta B} = -\sigma$$

When $\theta = \pm\pi/6$ (or $\pm 5\pi/6$)

$$\sigma_\theta = 0$$

Consider section I–I, which passes through the center of the hole and point A, as shown in Fig. 4.3. For the points on section I–I, $\theta = \pi/2$ (or $3\pi/2$) and Eq. (4.5) becomes

$$\begin{aligned} \sigma_r &= \frac{3}{2}\sigma\left(\frac{a^2}{r^2} - \frac{a^4}{r^4}\right) \\ \sigma_\theta &= \frac{1}{2}\sigma\left(2 + \frac{a^2}{r^2} + \frac{3a^4}{r^4}\right) \\ \tau_{r\theta} &= 0 \end{aligned} \tag{4.7}$$

From Eq. (4.7), it can be observed that on cross section I–I, when $r = a$, $\sigma_\theta = 3\sigma$, and as r increases, σ_θ decreases. Eventually, when r is large enough, $\sigma_\theta = \sigma$, and the stress distribution recovers to a uniform state. Also, it follows from Eq. (4.7) that the stress concentration caused by a single hole is localized. When, for example, $r = 5.0a$, σ_θ decreases to 1.02σ. Thus, after $5a$ distance from the center, the stress is very close to a uniform distribution.

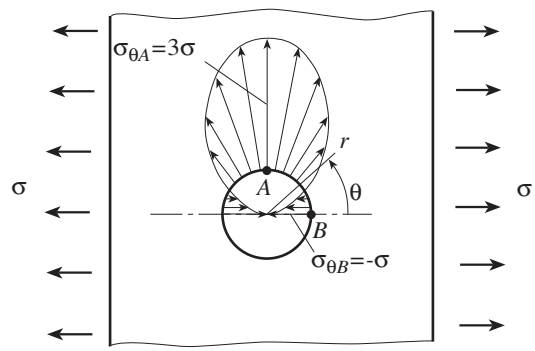


Figure 4.4 Circumferential stress distribution on the edge of a circular hole in an infinite thin element.

The stress distribution over cross section $II-II$ of Fig. 4.3 can be obtained using similar reasoning. Thus, from Eq. (4.5) with $\theta = 0$ (or $\theta = \pi$),

$$\begin{aligned} \sigma_r &= \frac{1}{2}\sigma\left(2 - \frac{5a^2}{r^2} + \frac{3a^4}{r^4}\right) \\ \sigma_\theta &= \frac{1}{2}\sigma\left(\frac{a^2}{r^2} - \frac{3a^4}{r^4}\right) \\ \tau_{r\theta} &= 0 \end{aligned} \tag{4.8}$$

Fig. 4.5 shows the σ_θ distribution on section $I-I$ and the σ_r distribution over section $II-II$. Note that on cross section $II-II$, $\sigma_r \leq \sigma$, although it finally reaches σ. The stress gradient on section $II-II$ is less than that on section $I-I$. For example, on section $II-II$ when $r = 11.0a$, $\sigma_r = 0.98\sigma$ or $\sigma - \sigma_r = 2\%$. In contrast, on section $I-I$, when $r = 5.0a$, σ_θ reaches σ within the 2% deviation.

For the tension case of a finite-width thin element with a circular hole, K_t values are given in Chart 4.1 for $d/H \leq 0.5$ (Howland 1929–1930, 1935). The photoelastic values by Wahl and Beeuwkes (1934) and the analytical results (Isida 1953; Christiansen 1968) are in good agreement. For a row of holes in the longitudinal direction with a hole-to-hole center distance/hole diameter of 3, and with $d/H = 1/2$, Slot (1972) obtained good agreement with the Howland K_t value (Chart 4.1) for the single hole with $d/H = 1/2$.

In a photoelastic test (Coker and Filon 1931), it is noted that as d/H approaches the unity, the stress σ_θ on the outside edges of the panel approaches ∞, which corresponds to $K_{tn} = 2$.

Many researchers also indicate that $K_{tn} = 2$ for $d/H \to 1$ (Wahl and Beeuwkes 1934; Heywood 1952; Koiter 1957). Wahl and Beeuwkes observe that when the hole diameter so closely approaches the width of the panel, the minimum section between the edge of the element and the hole becomes an infinitely thin filament. For any finite deformation, they note that "this filament may move inward toward the center of the hole sufficiently to allow for a uniform stress

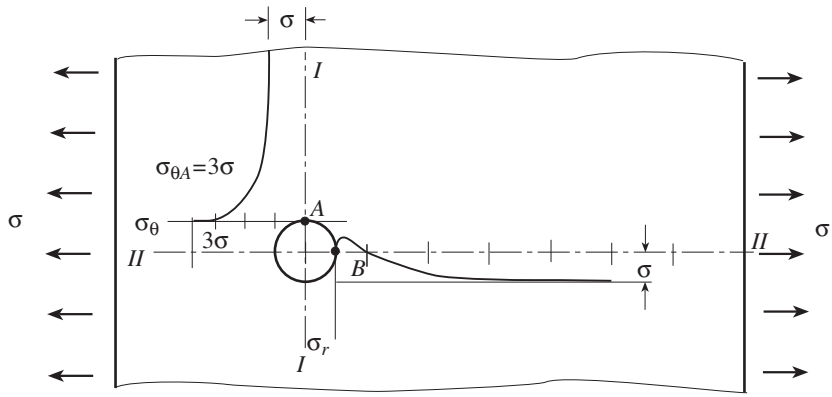


Figure 4.5 Distribution of σ_θ on section $I-I$ and σ_r on section $II-II$.

distribution, thus giving $K_{tn} = 1$. For infinitely small deformations relative to the thickness of this filament, however, K_{tn} may still be equal to 2." They find with a steel model test that the curve does not drop down to the unity as fast as would appear from certain photoelastic tests (Hennig 1933). Since the inward movement varies with σ and E, the K_{tn} would not drop to 1.0 as rapidly as with a plastic model. The case of $d/H \to 1$, does not have much significance from a design standpoint. The further discussion is provided in Belie and Appl (1972).

An empirical formula for K_{tn} is proposed to cover the entire d/H range (Heywood 1952),

$$K_{tn} = 2 + \left(1 - \frac{d}{H}\right)^3 \tag{4.9}$$

The formula is in a good agreement with the results of Howland for $d/H < 0.3$ (Heywood 1952) and is only about 1.5% lower at $d/H = 1/2$ ($K_{tn} = 2.125$ versus $K_{tn} = 2.16$ for Howland). The Heywood's formula of Eq. (4.9) is satisfactory for many design applications; since in most cases, d/H is less than 1/3. Note that the formula gives $K_{tn} = 2$ as $d/H \to 1$, which seems reasonable.

The Heywood's formula, when expressed as K_{tg}, becomes

$$K_{tg} = \frac{2 + (1 - d/H)^3}{1 - (d/H)} \tag{4.10}$$

4.3.2 Single Circular Hole in a Semi-Infinite Element in Uniaxial Tension

The SCFs for a circular hole near the edge of a semi-infinite element in tension are shown in Chart 4.2 (Udoguti 1947; Mindlin 1948; Isida 1955a). The load carried by the section between the hole and the edge of the panel is (Mindlin 1948)

$$P = \sigma ch\sqrt{1 - (a/c)^2} \tag{4.11}$$

where σ is the stress applied to semi-infinite panel, c is the distance from center of hole to edge of panel, a is the radius of hole, and h is the thickness of panel.

In Chart 4.2, the upper curve gives values of $K_{tg} = \sigma_B/\sigma$, where σ_B is the maximum stress at the edge of the hole nearest the edge of the thin tensile element. Although the K_{tg} may be used directly in design, it is thought desirable to also compute K_{tn} based on the load carried by the minimum net section. The K_{tn} factor will be comparable with the SCFs for other cases (Example 4.1). Based on the actual load carried by the minimum net section (Eq. 4.11), the average stress on the net section $A{-}B$ is

$$\sigma_{\text{net A–B}} = \frac{\sigma ch\sqrt{1 - (a/c)^2}}{(c - a)h} = \frac{\sigma\sqrt{1 - (a/c)^2}}{1 - a/c}$$

$$K_{tn} = \frac{\sigma_B}{\sigma_{\text{net A–B}}} = \frac{\sigma_B(1 - a/c)}{\sigma\sqrt{1 - (a/c)^2}} \tag{4.12}$$

The symbols σ, c, a, h have the same meaning as those in Eq. (4.11).

4.3.3 Single Circular Hole in a Finite-Width Element in Uniaxial Tension

The case of a tension bar of finite width having an eccentrically located hole has been solved analytically by Sjöström (1950). The semi-infinite strip values are in an agreement with Chart 4.2. Also the special case of the centrally located hole is in agreement with the Howland solution in Chart 4.1. The results of the Sjöström analysis are given as the values of $K_{tg} = \sigma_{\max}/\sigma$ in the upper part of Chart 4.3. These values may be used directly in design. An attempt will be made in the following to arrive at the approximated K_{tn} factors based on the net section. When the hole is centrally located ($e/c = 1$ in Chart 4.3), the load carried by section $A{-}B$ is σch. As e/c is increased to infinity, the load carried by section $A{-}B$ is, from Eq. (4.11), $\sigma ch\sqrt{1-(a/c)^2}$. Assuming a linear relation between the foregoing end conditions, that is, $e/c = 1$ and $e/c = \infty$, results in the following expression for the load carried by section $A{-}B$:

$$P_{\text{A–B}} = \frac{\sigma ch\sqrt{1-(a/c)^2}}{1-(c/e)(1-\sqrt{1-(a/c)^2})} \tag{4.13}$$

The stress on the net section $A{-}B$ is

$$\sigma_{net\,\text{A–B}} = \frac{\sigma ch\sqrt{1-(a/c)^2}}{h(c-a)[1-(c/e)(1-\sqrt{1-(a/c)^2})]}$$

so that

$$K_{tn} = \frac{\sigma_{\max}}{\sigma_{\text{net}}} = \frac{\sigma_{\max}(1-a/c)}{\sigma\sqrt{1-(a/c)^2}}[1-(c/e)(1-\sqrt{1-(a/c)^2})] \tag{4.14}$$

It is seen from the lower part of Chart 4.3 that this relation brings all the K_{tn} curves rather closely together. For all practical purposes, then, the curve for the centrally located hole ($e/c = 1$) is, under the assumptions of Chart 4.3, a reasonable approximation for all eccentricities.

4.3.4 Effect of Length of Element

Many of the elements are considered with an infinite length. Troyani et al. (2002) study the effect of the length of an element on SCFs in Fig. 4.6. To do so, they perform finite element

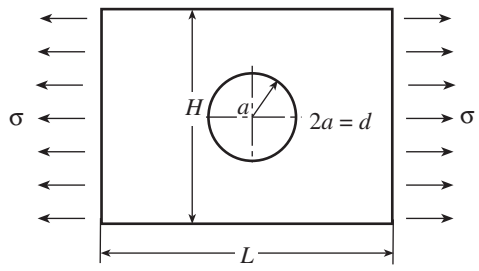


Figure 4.6 Effect of length of an element (Troyani et al. 2002).

analyses of thin elements of varying lengths in uniaxial tension. They find that if the length of the element is less than its width, the SCF available for an element of infinite length is of questionable accuracy. The SCF for several lengths are compared with the SCFs of Chart 4.1 for an infinite-length element.

4.3.5 Single Circular Hole in an Infinite Thin Element under Biaxial In-Plane Stresses

If a thin infinite element is subjected to biaxial in-plane tensile stresses σ_1 and σ_2 as shown in Fig. 4.7, the SCF may be derived by superposition. Eq. (4.5) is the solution for the uniaxial problem of Fig. 4.3. At the edge of the hole for the biaxial case of Fig. 4.7, the stresses caused by σ_1 are calculated by setting $r = a$, $\sigma = \sigma_1$, $\theta = \theta + \pi/2$ in Eq. (4.6):

$$\begin{aligned} \sigma_r &= 0 \\ \sigma_\theta &= \sigma_1(1 + 2\cos 2\theta) \\ \tau_{r\theta} &= 0 \end{aligned} \tag{4.15}$$

Superimpose Eq. (4.15) and Eq. (4.6) with σ replaced by σ_2, which represents the stresses under uniaxial tension σ_2:

$$\begin{aligned} \sigma_r &= 0 \\ \sigma_\theta &= (\sigma_2 + \sigma_1) - 2(\sigma_2 - \sigma_1)\cos 2\theta \\ \tau_{r\theta} &= 0 \end{aligned} \tag{4.16}$$

Let $\sigma_2/\sigma_1 = \alpha$ so that

$$\sigma_\theta = \sigma_1(1 + \alpha) + 2\sigma_1(1 - \alpha)\cos 2\theta$$

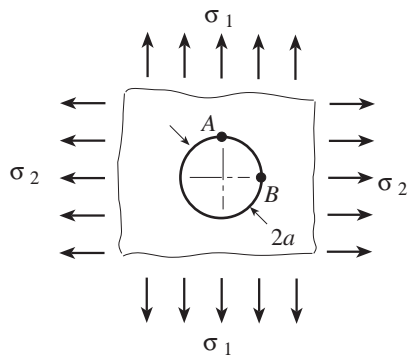


Figure 4.7 Infinite thin element under biaxial tensile in-plane loading.

Assume that $\alpha \leq 1$. Then

$$\sigma_{\theta\max} = \sigma_{\theta B} = \sigma_1(3 - \alpha)$$
$$\sigma_{\theta\min} = \sigma_{\theta A} = \sigma_1(3\alpha - 1)$$

If σ_1 is taken as the reference stress, the stress concentration factors at points A and B are

$$K_{tA} = \frac{\sigma_{\theta\min}}{\sigma_1} = 3\alpha - 1 \tag{4.17}$$
$$K_{tB} = \frac{\sigma_{\theta\max}}{\sigma_1} = 3 - \alpha \tag{4.18}$$

It is interesting to note that if σ_1 and σ_2 are both of the same sign (positive or negative), the stress concentration factor is less than 3, which is the stress concentration factor caused by uniaxial stress. For equal biaxial stresses, $\sigma_1 = \sigma_2$, the stresses at A and B are $\sigma_A = \sigma_B = 2\sigma_1$ or $K_t = 2$ ($h_r/h = 0, D/d = 1$ in Chart 4.13*a*). When σ_1 and σ_2 have the same magnitude but are of opposite sign (the state of pure shear), $K_t = 4$ ($K_{tA} = -4$, $K_{tB} = 4$). This is equivalent to shear stresses $\tau = \sigma_1$ at 45° ($a/b = 1$ in Chart 4.97).

4.3.6 Single Circular Hole in a Cylindrical Shell with Tension or Internal Pressure

Considerable analytical work has been done on the stresses in a cylindrical shell having a circular hole (Lekkerkerker 1964; Eringen et al. 1965; Van Dyke 1965). The SCFs are given in Chart 4.4 for tension and in Chart 4.5 for internal pressure. In both charts, the factors for membrane (tension) and for total stresses (membrane plus bending) are given. The torsion case is given in Section 4.9.7 and Chart 4.107.

For pressure loading, the analysis assumes that the force representing the total pressure corresponding to the area of the hole is carried as a perpendicular shear force distributed around the edge of the hole. This is shown schematically in Chart 4.5. Results are given as a function of dimensionless parameter β:

$$\beta = \frac{\sqrt[4]{3(1 - \nu^2)}}{2}\left(\frac{a}{\sqrt{Rh}}\right) \tag{4.19a}$$

where R is the mean radius of shell, h is the thickness of shell, a is the radius of hole, and ν is Poisson's ratio. In Charts 4.4 and 4.5 and Fig. 4.8, where $\nu = 1/3$,

$$\beta = 0.639\frac{a}{\sqrt{Rh}} \tag{4.19b}$$

The analysis assumes a shallow, thin shell. *Shallowness* means a small curvature effect over the circumferential coordinate of the hole, which means a small a/R. *Thinness* of course implies a small h/R. The region of validity is shown in Fig. 4.8.

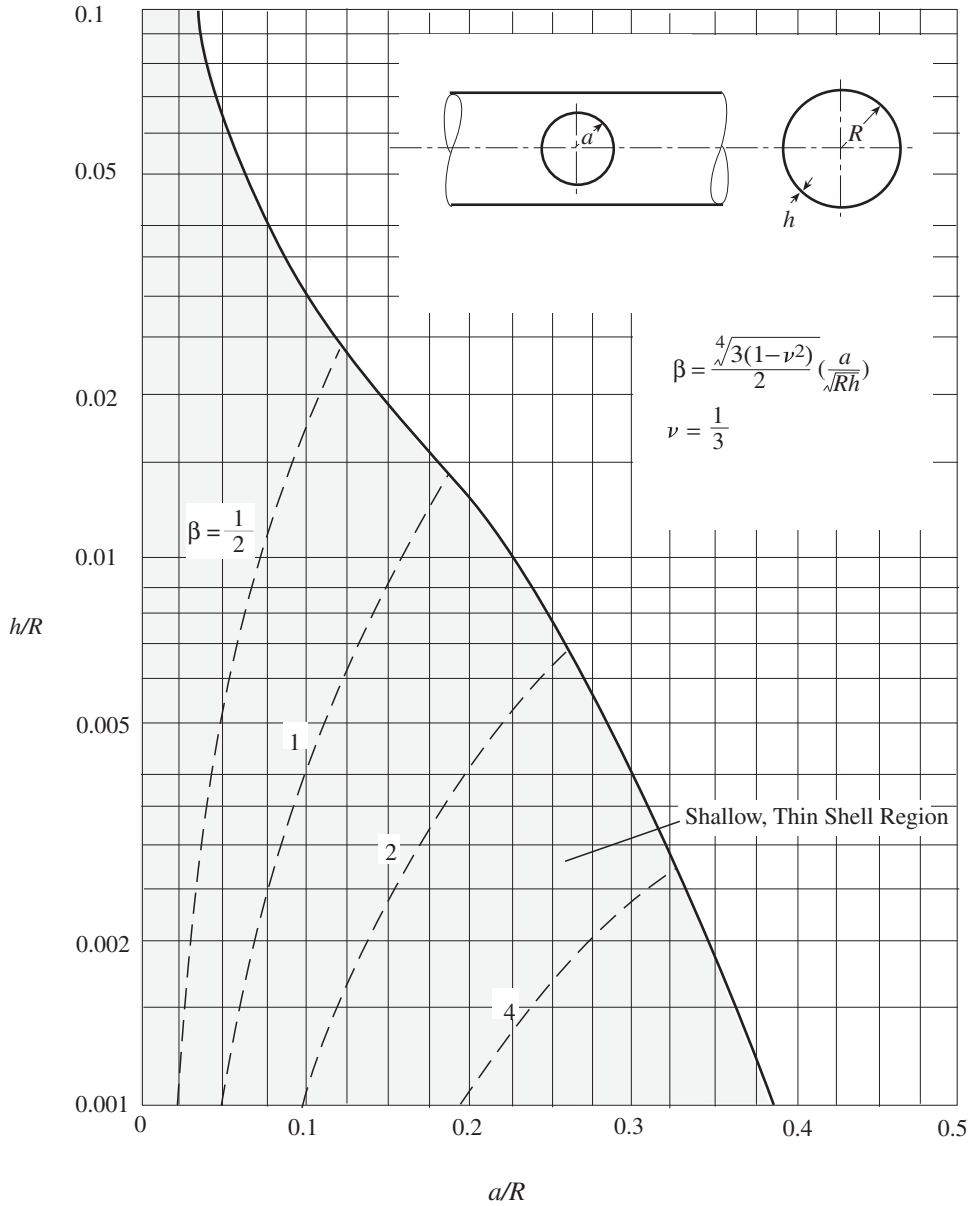


Figure 4.8 Region of validity of shallow, thin shell theory (Van Dyke 1965).

The physical significance of β can be evaluated by rearranging Eq. (4.19*b*):

$$\beta = 0.639 \frac{(a/R)}{\sqrt{h/R}} \tag{4.19c}$$

For example, by solving Eq. (4.19*c*) for h, a 10-in.-diameter cylinder with a 1-in. hole would have a thickness of 0.082 in. for $\beta = 1/2$, a thickness of 0.02 in. for $\beta = 1$, a thickness of 0.005 in. for $\beta = 2$, and a thickness of 0.0013 in. for $\beta = 4$. Although $\beta = 4$ represents a very thin shell, large values of β often occur in aerospace structures. Lind (1968) gives a formula for the pressurized shell where β is large compared to unity.

The K_t factors in Charts 4.4 and 4.5 are quite large for the larger values of β, corresponding to very thin shells. Referring to Fig. 4.8, one has,

β	h/R
4	< 0.003
2	< 0.007
1	< 0.015
1/2	< 0.025

In the region of $\beta = 1/2$, the K_t factors are not unusually large. A study of the effect of element length on SCFs in Troyani et al. (2005) shows that for lengths L less than the mean cylinder diameter, the SCFs in Chart 4.4 may be significantly lower than those obtained with a finite element code.

The theoretical results (Lekkerkerker 1964; Eringen et al. 1965; Van Dyke 1965) are, with one exception, in a good agreement. Experiments have been made by Houghton and Rothwell (1962) and by Lekkerkerker (1964). The comparisons by Van Dyke (1965) show reasonably good agreement for pressure loading (Houghton and Rothwell 1962). A poor agreement is obtained for the tension loading (Houghton and Rothwell 1962). Referring to tests on tubular members (Jessop et al. 1959), the results for $d_i/D = 0.9$ are in a good agreement for tension loadings (Chart 4.66). The photoelastic tests (Durelli et al. 1967) are made for the pressurized loading. Strain gage results (Pierce and Chou 1973) have been obtained for values of β up to 2 and agree reasonably well with Chart 4.4.

The analytical expressions for the SCFs in cylinders with a circular hole subject to uniaxial tension and internal pressure are provided in Savin (1961) and are discussed in Wu and Mu (2003). For a cylinder with $a/R \ll \sqrt{h/R}$ with axial tensile loading along the cylinder axial direction,

$$K_t = \begin{cases} 3 + \left[3(1-\nu^2)\right]^{1/2} \dfrac{\pi a^2}{4Rh} & \text{at } A(\theta = \pi/2) \\ -\left\{1 + [3(1-\nu^2)]^{1/2}\right\} \left(\dfrac{\pi a^2}{4Rh}\right) & \text{at } B(\theta = 0^\circ) \end{cases} \tag{4.20}$$

where A and B are as shown in Chart 4.1, θ is defined in Chart 4.5, and ν is Poisson's ratio.

For a cylinder with $a/R \ll \sqrt{h/R}$ subject to internal pressure p,

$$K_t = \begin{cases} \dfrac{\sigma_{\theta=0}}{\sigma_{\text{axial}}} = 1 - \left[3(1-\nu^2)\right]^{1/2} \dfrac{\pi a^2}{4Rh} & \text{at } \theta = 0 \\ \dfrac{\sigma_{\theta=\pi/2}}{\sigma_{\text{hoop}}} = \dfrac{5}{2}\left\{1 + [3(1-\nu^2)]^{1/2} \dfrac{9\pi a^2}{20Rh}\right\} & \text{at } \theta = \pi/2 \end{cases} \tag{4.21}$$

where σ_{axial} and σ_{hoop} are equal to $pR/2h$ and pR/h, respectively.

The case of two circular holes has been analyzed by Hanzawa et al. (1972) and Hamada et al. (1972). It is found that the interference effect is similar to that in an infinite thin element, although the SCFs are higher for the shell. The membrane and bending stresses for the single hole (Hamada et al. 1972) are in a good agreement with the results by Van Dyke (1965) on which Charts 4.4 and 4.5 are based.

The SCFs have been obtained for the special case of a pressurized ribbed shell with a reinforced circular hole interrupting a rib (Durelli et al. 1971). The stresses around an elliptical hole in a cylindrical shell in tension have been determined by Murthy (1969), Murthy and Rao (1970), and Tingleff (1971).

4.3.7 Circular or Elliptical Hole in a Spherical Shell with Internal Pressure

In this section, the holes in the wall of a thin spherical shell subject to internal pressure are considered. Chart 4.6 based on the K_t factors determined analytically (Leckie et al. 1967) covers the openings varying from a circle to an ellipse with $b/a = 2$. Referring to Chart 4.6, the K_t values for the four b/a values in an infinite flat element biaxially stressed are shown along the left-hand edge of the chart. The curves show the increase due to bending and shell curvature in relation to the flat element values. The experimental results (Leckie et al. 1967) are in a good agreement. Application to the case of an oblique nozzle is discussed by Leckie et al. (1967).

4.3.8 Reinforced Hole Near the Edge of a Semi-Infinite Element in Uniaxial Tension

Assume a semi-infinite thin element is subjected to uniaxial tension. A circular hole with integral reinforcement of the same material is located near the edge of the element. Chart 4.7 shows the SCFs (Mansfield 1955; Wittrick 1959a; Davies 1963; ESDU 1981). High stresses would be expected to occur at points A and B. In the chart, the values of K_{tgA} and K_{tgB} are plotted versus $A_e/(2ah)$ for a series of values of c/a. The quantity A_e is called the effective cross-sectional area of reinforcement,

$$A_e = C_A A_r \tag{4.22}$$

where A_r is the cross-sectional area of the reinforcement (constant around hole), C_A is the reinforcement efficiency factor. Some values of C_A are given in Chart 4.7.

For point A, which is at the element edge, the gross stress concentration factor is defined as the ratio of the maximum stress acting along the edge and the tensile stress σ:

$$K_{tgA} = \frac{\sigma_{\max}}{\sigma} \tag{4.23}$$

where $\sigma_{\max}$ is the maximum stress at point A along the edge.

At the junction (B) of the element and the reinforcement, the three-dimensional stress fields are complicated. It is reasonable to use the equivalent stress σ_{eq} (Section 1.8) at B as the basis to define the stress concentration factor. Define the gross stress concentration factor K_{tgB} as

$$K_{tgB} = \frac{\sigma_{\text{eq}}}{\sigma} \tag{4.24}$$

As shown in Chart 4.7, the two points B are symmetrically located with respect to the minimum cross section I–I. For $A_e/(2ah) < 0.1$, the two points B coincide for any value of c/a. If $A_e/(2ah) > 0.1$, the two points B move further away as either c/a or $A_e/(2ah)$ increases. Similarly, the two edge stress points A are also symmetrical relative to the minimum cross section I–I and spread apart with an increase in c/a. For $c/a = 1.2$, the distance between two points A is equal to a. When $c/a = 5$, the distance is $6a$.

If the distance between element edges of a finite-width element and the center of the hole is greater than $4a$ and the reference stress is based on the gross cross section, the data from Chart 4.7 will provide a reasonable approximation.

The value of C_A depends on the geometry of the reinforcement and the manner in which it is mounted. If the reinforcement is symmetrical about the mid-plane of the thin element. If the reinforcement is connected to the thin element without defect, then the change in stress across the junction can be ignored and the reinforcement efficiency factor is equal to 1 ($C_A = 1$ and $A_e = A_r$). If the reinforcement is nonsymmetric and lies only to one side of the element, the following approximation is available:

$$C_A = 1 - \frac{A_r \bar{y}^2}{I} \tag{4.25}$$

where $\bar{y}$ is the distance of the centroid of the reinforcement from the mid-plane of the element (e.g., see Fig. 4.9), I is the moment of inertia of the reinforcement about the mid-plane of the element. If the reinforcement is not symmetric, bending stress will be induced in the element. The data in Chart 4.7 ignore the effect of this bending.

Example 4.2 ***L Section Reinforcement*** Find the maximum stresses in a thin element with a 4.1-in.-radius hole, whose center is 5.5 in. from the element's edge. The thickness of the element is 0.04 in. The hole is reinforced with an L section as shown in Fig. 4.9. A uniaxial in-plane tension stress of $\sigma = 6900\,\text{lb/in.}^2$ is applied to the thin element. For the reinforcement, with the dimensions of Fig. 4.9, $A_r = 0.0550\,\text{in.}^2$, $\bar{y} = 0.0927$ in., and $I = 0.000928\,\text{in.}^4$, where A_r is the cross-sectional area of the L-section reinforcement, $\bar{y}$ is the distance of the centroid of the reinforcement from the mid-plane of the element, and I is the moment of inertia of the reinforcement about the mid-plane of the element (Fig. 4.9).

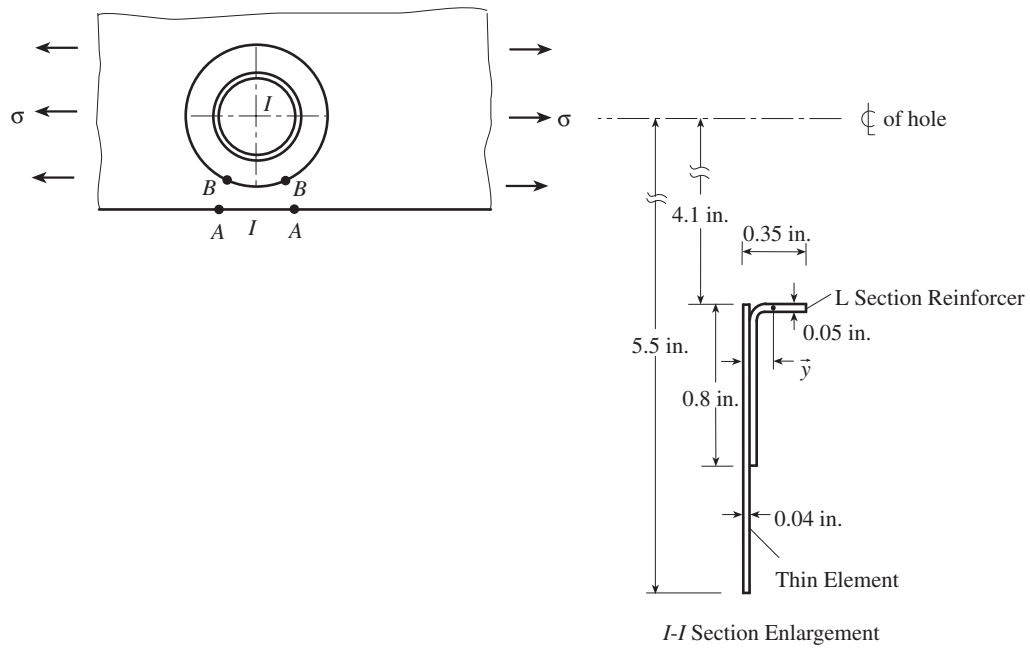


Figure 4.9 Hole with *L*-section reinforcement.

Firstly, the reinforcement efficiency factor C_A is calculated using Eq. (4.25),

$$C_A = 1 - \frac{A_r \bar{y}^2}{I} = 1 - \frac{0.0550 \cdot 0.0927^2}{0.000928} = 0.490 \tag{1}$$

Secondly, the effective cross-sectional area is given by (Eq. 4.22)

$$A_e = C_A A_r = 0.490 \cdot 0.0550 = 0.0270 \text{ in.}^2 \tag{2}$$

Finally,

$$\frac{A_e}{2ah} = \frac{0.0270}{2 \cdot 4.1 \cdot 0.04} = 0.0822 \quad \text{and} \quad \frac{c}{a} = \frac{5.5}{4.1} = 1.34 \tag{3}$$

From the curves of Chart 4.7 for $A_e/(2ah) = 0.0822$, when $c/a = 1.3$, $K_{tgB} = 2.92$, $K_{tgA} = 2.40$, and when $c/a = 1.5$, $K_{tgB} = 2.65$, $K_{tgA} = 1.98$, the stress concentration factors at $c/a = 1.34$ can be derived by interpolation,

$$K_{tgB} = 2.92 + \frac{2.65 - 2.92}{1.5 - 1.3} \cdot (1.34 - 1.3) = 2.86 \tag{4}$$

$$K_{tgA} = 2.40 + \frac{1.98 - 2.40}{1.5 - 1.3} \cdot (1.34 - 1.3) = 2.32 \tag{5}$$

The stresses at point A and B are (Eqs. 4.23 and 4.24),

$$\sigma_A = 2.32 \cdot 6900 = 16{,}008 \text{ lb/in.}^2 \tag{6}$$

$$\sigma_B = 2.86 \cdot 6900 = 19{,}734 \text{ lb/in.}^2 \tag{7}$$

where σ_B is the equivalent stress at point B.

4.3.9 Symmetrically Reinforced Hole in a Finite-Width Element in Uniaxial Tension

For a symmetrically reinforced hole in a thin element of prescribed width, the experimental results of interest for design application are the photoelastic test values of Seika and Ishii (1964, 1967). These tests use an element 6 mm thick, with a hole 30 mm in diameter and symmetrically cemented into the hole. It has a stiffening ring of various thicknesses containing various diameters d of the central hole. The width of the element is also varied. A constant in all tests was D/h = diameter of ring/thickness of element = 5.

Chart 4.8 presents $K_{tg} = \sigma_{\max}/\sigma$ values, where σ = gross stress, for various width ratios H/D = width of element/diameter of ring. In all cases, $\sigma_{\max}$ is located on the hole surface at 90° to the applied uniaxial tension. Only in the case of $H/D = 4$, the effect of fillet radius is investigated (Chart 4.8*c*).

For $H/D = 4$ and $D/h = 5$, Chart 4.9 shows the net stress concentration factor defined as,

$$P = \sigma A = \sigma_{\text{net}} A_{\text{net}}$$

where P is the total applied force

$$\begin{aligned} K_{tn} &= \frac{\sigma_{\max}}{\sigma_{\text{net}}} = \frac{\sigma_{\max} A_{\text{net}}}{\sigma A} = \frac{K_{tg} A_{\text{net}}}{A} \\ &= K_{tg} \frac{(H-D)h + (D-d)h_t + (4-\pi)r^2}{Hh} \\ &= K_{tg} \frac{[(H/d)-1] + [1-(d/D)](h_t/h) + (4-\pi)r^2/(Dh)}{H/D} \end{aligned} \tag{4.26}$$

where d is the diameter of the hole, D is the outside diameter of the reinforcement, H is the width of the element, h is the thickness of the element, h_t is the thickness of the reinforcement, and r is the fillet radius at the junction of the element and the reinforcement.

Note from Chart 4.9, the K_{tn} values are grouped closer together than the K_{tg} values of Chart 4.8*c*. and also note that the minimum K_{tn} occurs at $h_t/h \approx 3$ when $r > 0$. Thus for efficient section use, the h_t/h should be set at about 3.

The $H/D = 4$ values are particularly useful since they can be used without serious error for thee wide-element problems. This can be demonstrated by using Eq. (4.26) to replot the K_{tn} curve

in terms of d/H (diameter of hole/width of element) and extrapolating it for $d/H = 0$, equivalent to an infinite element in Chart 4.10.

Not from Chart 4.8*c* that the lowest K_{tg} factor achieved by the reinforcements used in this series of tests is approximately 1.1, with $h_t/h \geq 4$, $d/D = 0.3$, and $r/h = 0.83$. By decreasing d/D, that is, by increasing D relative to d, the K_{tg} factor can be brought to 1.0.

For a wide element without reinforcement, $K_{tg} = 3$; to reduce this to 1, it is evident that h_t/h should be 3 or somewhat greater. The solution is approximated based on the curved bar theory by Timoshenko (1924), and a comparison curve is shown in Chart 4.8*c*.

4.3.10 Nonsymmetrically Reinforced Hole in a Finite-Width Element in Uniaxial Tension

Chart 4.11 shows the SCFs for an asymmetrically reinforced hole in a finite-width element in tension. The photoelastic tests are made with $d/h = 1.833$ (Lingaiah et al. 1966). Except for one series of tests, the volume of the reinforcement (V_R) is made equal to the volume of the hole (V_H). In Chart 4.11, the effect of varying the ring height (and corresponding ring diameter) is shown for various d/H ratios. A minimum K_t value is reached at about $h_t/h = 1.45$ and $D/d = 1.8$.

A shape factor is defined as

$$C_s = \frac{D/2}{h_t - h} \tag{4.27}$$

For the photoelastic tests with $d/h = 1.833$ and $V_R/V_H = 1$, the shape factor C_s is chosen to be 3.666 which is shown in Fig. 4.10. If one wishes to lower K_t by increasing V_R/V_H, the shape factor $C_s = 3.666$ should be maintained as an interim procedure.

In Chart 4.12, where the abscissa scale is d/H, the extrapolation is shown to $d/H = 0$. This provides the intermediate values for relatively wide elements.

The curves shown are for a zero fillet radius. A fillet radius r of 0.7 of the element thickness h reduces K_{tn} approximately 12%. For small radii, the reduction is approximately linearly proportional to the radius. Thus, for example, for $r/h = 0.35$, the reduction is approximately 6%.

4.3.11 Symmetrically Reinforced Circular Hole in a Biaxially Stressed Wide, Thin Element

Pressure vessels, turbine casings, deep sea vessels, aerospace devices, and other structures subjected to pressure require the perforation of the shell by holes to accommodate control

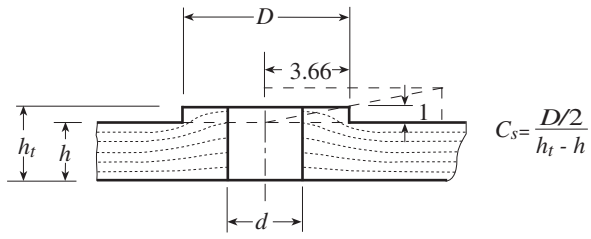


Figure 4.10 Shape factor for a nonsymmetric reinforced circular hole.

mechanisms, windows, and the accesses to personnel. Although these designs involve complicating factors such as vessel curvature and closure details, some guidance can be obtained from the work on flat elements, especially for small openings, including those for leads and rods.

The state of stress in a pressurized thin spherical shell is biaxial, $\sigma_1 = \sigma_2$. For a circular hole in a biaxially stressed thin element with $\sigma_1 = \sigma_2$, from Eqs. (4.17) or (4.18), $K_t = 2$. The stress state in a pressurized cylindrical shell is $\sigma_2 = \sigma_1/2$, where σ_1 is the hoop stress and σ_2 is the longitudinal (axial) stress. For the corresponding flat panel, $K_t = 2.5$ (Eq. 4.18, with $\alpha = \sigma_2/\sigma_1 = 1/2$). By proper reinforcement design, these factors can be reduced to 1, with a resultant large gain in strength. It has long been the practice to reinforce holes, but design information for achieving a specific K value, and in an optimum way, is not available.

The reinforcement considered here is a ring type of rectangular cross section, symmetrically disposed on both sides of the panel (Chart 4.13). The results are for flat elements and applicable for pressure vessels only when the diameter of the hole is small compared to the vessel diameter. The data should be useful in optimization over a fairly wide practical range.

A considerable number of theoretical analyses are available (Gurney 1938; Beskin 1944; Levy et al. 1948; Reissner and Morduchow 1949; Wells 1950; Mansfield 1953; Hicks 1957; Wittrick 1959a; Savin 1961; Houghton and Rothwell 1961; Davies 1967). In most of these analyses, it assumes that the edge of the hole, in an infinite sheet, is reinforced by a "compact" rim (one whose round or square cross-sectional dimensions are small compared to the diameter of the hole). Some of the analyses (Gurney 1938; Beskin 1944; Davies 1967) do not assume a compact rim. Most analyses are concerned with stresses in the sheet. Where the rim stresses are considered, they are assumed to be uniformly distributed in the thickness direction.

The curves in Chart 4.13 provide the SCFs for circular holes with symmetrical reinforcement. This chart is based on the theoretical (analytical) derivation of Gurney (1938). The maximum stresses occur at the hole edge and at the element to reinforcement junction. Because of the complexity of the stress fields at the junction of the element and the reinforcement, the von Mises stress of Section 1.8 is used as the basis to define the SCFs. Suppose that σ_1 and σ_2 represent the principal stresses in the element remote from the hole and reinforcement. The corresponding von Mises (equivalent) stress is given by (Eq. 1.35)

$$\sigma_{\text{eq}} = \sqrt{\sigma_1^2 - \sigma_1\sigma_2 + \sigma_2^2} \tag{4.28}$$

The SCFs based on σ_{eq} are defined as

$$K_{ted} = \frac{\sigma_{\max d}}{\sigma_{\text{eq}}} \tag{4.29}$$

$$K_{teD} = \frac{\sigma_{\max D}}{\sigma_{\text{eq}}} \tag{4.30}$$

where K_{ted} is the SCF at the edge of the hole, and K_{teD} is the stress concentration factor at the junction of the element and reinforcement.

The plots of K_{ted} and K_{teD} versus h_r/h for various values of D/d are provided in Chart 4.13. For these curves, $\nu = 0.25$ and $h_r < (D - d)$. The highest equivalent stress occurs at the edge of

a hole for the case of low values of h_r/h. For high values of h_r/h, the highest stress is located at the junction of the element and the reinforcement.

If the reinforcement and the element have different Young's moduli, which introduces a modulus-weighted h_r/h (Pilkey 2005), that is, multiply h_r/h by E_r/E for use in entering the charts. The quantities E_r and E are the Young's moduli of the reinforcement and the element materials, respectively.

Example 4.3 Reinforced Circular Thin Element with In-Plane Loading A 10-mm-thick element has a 150-mm-diameter hole. It is reinforced symmetrically about the mid-plane of the element with two 20-mm-thick circular rings of 300-mm outer diameter and 150-mm inner diameter. The stresses $\sigma_x = 200\ \text{MN/m}^2$, $\sigma_y = 100\ \text{MN/m}^2$, and $\tau_{xy} = 74.83\ \text{MN/m}^2$ are applied on this element as shown in Fig. 4.11. Find the equivalent stress at the edge of the hole and at the junction of the reinforcement and the element.

For this element

$$\frac{h_r}{h} = \frac{2 \cdot 20}{10} = 4, \frac{D}{d} = \frac{300}{150} = 2 \tag{1}$$

If there were no hole, the principal stresses would be calculated as

$$\sigma_1 = \frac{1}{2}(200 + 100) + \frac{1}{2}\sqrt{(200 - 100)^2 + 4 \cdot 74.83^2} = 240\ \text{MN/m}^2 \tag{2}$$

$$\sigma_2 = \frac{1}{2}(200 + 100) - \frac{1}{2}\sqrt{(200 - 100)^2 + 4 \cdot 74.83^2} = 60\ \text{MN/m}^2 \tag{3}$$

The ratio of the principal stresses is $\sigma_2/\sigma_1 = 60/240 = 0.25$, and from Eq. (4.28), the corresponding equivalent stress is

$$\sigma_{\text{eq}} = \sqrt{240^2 - 240 \cdot 60 + 60^2} = 216.33\ \text{MN/m}^2 \tag{4}$$

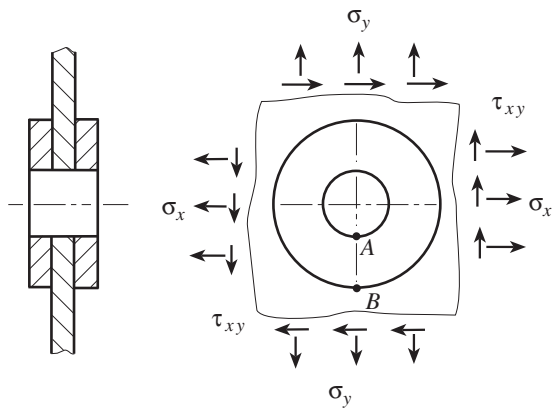


Figure 4.11 Symmetrically reinforced circular hole in an infinite in-plane loaded thin element.

The SCFs for this case cannot be obtained from the curves in Chart 4.13 directly. First, read the SCFs for $D/d = 2$ and $h_r/h = 4$ in Chart 4.13 to find

	$\sigma_2 = \sigma_1$	$\sigma_2 = \sigma_1/2$	$\sigma_2 = 0$	$\sigma_2 = -\sigma_1/2$	$\sigma_2 = -\sigma_1$
$K_{teB} = K_{teD}$	1.13	1.33	1.63	1.74	1.76
$K_{teA} = K_{ted}$	0.69	1.09	1.20	1.09	0.97

Use the table values and the Lagrangian 5-point interpolation method (Kelly 1967) to find, for $\sigma_2/\sigma_1 = 0.25$,

$$\begin{aligned} K_{teA} &= 1.18 \\ K_{teB} &= 1.49 \end{aligned} \tag{5}$$

with the equivalent stresses

$$\begin{aligned} \sigma_{\text{eq}B} &= 1.49 \cdot 216.33 = 322.33 \text{ MN/m}^2 \\ \sigma_{\text{eq}A} &= 1.18 \cdot 216.33 = 255.27 \text{ MN/m}^2 \end{aligned} \tag{6}$$

The results of strain gage tests made at NASA by Kaufman et al. (1962) on in-plane loaded flat elements with noncompact reinforced circular holes can be used for design purposes. The diameter of the holes is eight times the thickness of the element. The connection between the panel and the reinforcement included no fillet. The actual case, using a fillet, would in some instances be more favorable. They find that the degree of agreement with the theoretical results of Beskin (1944) varies considerably with the variation of reinforcement parameters. Since in these strain gage tests, the width of the element is 16 times the hole diameter, it can be assumed that for practical purposes, an invariant condition corresponding to an infinite element has been attained. Since no correction has been made for the section removal by the hole, $K_{tg} = \sigma_{\max}/\sigma_1$ is used.

Charts 4.14 to 4.17 are based on the strain gage results of Kaufman and are developed in a form more suitable for the types of problem encountered in turbine and pressure vessel design. These show the SCFs for given D/d and h_t/h. These charts involve in the interpolation in regions of sparse data. For this reason, the charts are labeled as approximated stress concentration values. Further interpolation can be used to obtain K_{tg} values between the curves.

In Charts 4.14 to 4.19, the stress concentration factor $K_{tg} = \sigma_{\max}/\sigma_1$ has been used instead of $K_{te} = \sigma_{\max}/\sigma_{\text{eq}}$. The former is perhaps more suitable where the designer wishes to obtain $\sigma_{\max}$ as simply and directly as possible. For $\sigma_1 = \sigma_2$, the two factors are the same. For $\sigma_2 = \sigma_1/2$, $K_{te} = (2/\sqrt{3})K_{tg} = 1.157K_{tg}$.

In Charts 4.14 to 4.17, it assumes that as D/d is increased, an invariant condition is approached where $h_t/h = 2/K_{tg}$ for $\sigma_1 = \sigma_2$; $h_t/h = 2.5/K_{tg}$ for $\sigma_2 = \sigma_1/2$. It further assumes that for relatively small values of D/d less than 1.7, the constant values of K_{tg} are reached as h_t/h is increased; that is, the outermost part of the reinforcement in the thickness direction becomes stress free (dead photoelastically) (Fig. 4.12).

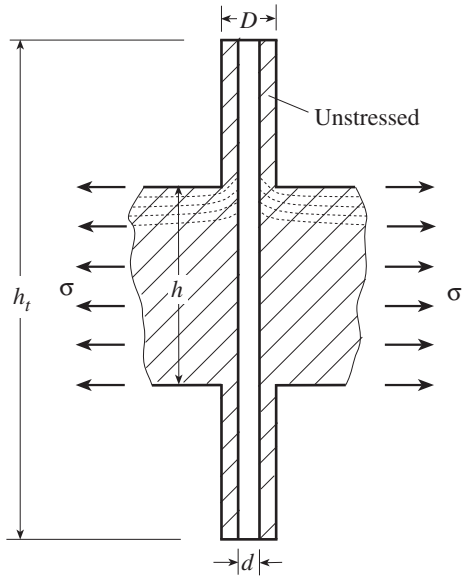


Figure 4.12 Effect of narrow reinforcement.

Charts 4.14 to 4.17 are plotted in terms of two ratios defining the reinforcement proportions D/d and h_t/h. When these ratios are not much greater than 1.0, the stress in the rim of the reinforcement exceeds the stress in the element. The basis for this conclusion can be observed in the charts. To the left of and below the dashed line $K_{tg} \approx 1$, K_{tg} is greater than 1, so the maximum stress in the rim is higher than in the element. When the ratios are large, the reverse is true. Also note in Charts 4.14 to 4.17, the crossover, or limit, the line (dotted line denoted $K_{tg} \approx 1$) divides the plot ing two regions. Beyond the line (toward the upper right), the maximum stress in the reinforcement is approximately equal to the applied nominal stress, $K_{tg} = 1$. In the other direction (toward the lower left), the maximum stress is in the rim, with K_{tg} increasing from approximately 1 at the crossover line to a maximum (2 for $\sigma_1 = \sigma_2$ and 2.5 for $\sigma_2 = \sigma_1/2$) at the origin. It is useful to consider that the left-hand and lower straight line edges of the diagrams (Charts 4.14 to 4.17) also represent the above maximum conditions. Then, one can readily interpolate an intermediate curve, as for $K_{tg} = 1.9$ in Charts 4.14 and 4.15 or $K_{tg} = 2.3$ in Charts 4.16 and 4.17.

The reinforcement variables D/d and h_t/h can be used to form two dimensionless ratios:

$A/(hd)$ = cross-sectional area of added reinforcement material/cross-sectional area of the hole,

$$\frac{A}{hd} = \frac{(D-d)(h_t-h)}{hd} = \left(\frac{D}{d} - 1\right)\left(\frac{h_t}{h} - 1\right) \tag{4.31}$$

V_R/V_H = volume of added reinforcement material/volume of hole,

$$\frac{V_R}{V_H} = \frac{(\pi/4)(D^2 - d^2)(h_t - h)}{(\pi/4)d^2h} = \left[\left(\frac{D}{d}\right)^2 - 1\right]\left(\frac{h_t}{h} - 1\right) \tag{4.32}$$

The ratio $F = A/(hd)$ is used in pressure vessel design in the form (ASME 1974),

$$A = Fhd \tag{4.33}$$

where $F \geq 1$. Then Eq. (4.33) becomes

$$\frac{A}{dh} \geq 1 \tag{4.34}$$

Although for certain specified conditions (ASME 1974), F may be less than 1, usually $F = 1$. The ratio V_R/V_H is useful in arriving at optimum designs where the weight is considered (aerospace devices, deep sea vehicles, etc.).

In Charts 4.14 and 4.16, a family of A/hd curves has been drawn, and in Charts 4.15 and 4.17, a family of V_R/V_H curves has been drawn, each pair for $\sigma_1 = \sigma_2$ and $\sigma_2 = \sigma_1/2$ stress states. Note that there are the locations of tangency between the $A/(hd)$ or V_R/V_H curves and the K_{tg} curves. These locations represent optimum design conditions, that is, for any given value of K_{tg}, such a location is the minimum cross-sectional area or the weight of reinforcement. The dot-dash curves, labeled "locus of minimum," provide the full range of optimum conditions. For example, for $K_{tg} = 1.5$ in Chart 4.15, the minimum V_R/V_H occurs at the point where the dashed line ($K_{tg} = 1.5$) and the solid line (V_R/V_H) are tangent. This occurs at $(D/d, h_t/h) = (1.55,1.38)$. The corresponding value of V_R/V_H is $1/2$. Any other point corresponds to larger K_{tg} or V_R/V_H. It is clear that K_{tg} does not depend solely on the reinforcement area A (as assumed in a number of analyses) but also on the shape (rectangular cross-sectional proportions) of the reinforcement.

In Charts 4.18 and 4.19, the K_{tg} values corresponding to the dot-dash locus curves are presented in terms of $A/(hd)$ and V_R/V_H. Note that the largest gains in reducing K_{tg} are made at relatively small reinforcements and that to reduce K_{tg} from, say, 1.2 to 1.0 requires a relatively large volume of material.

The pressure vessel codes (ASME 1974) formula (Eq. 4.34) may be compared with the values of Charts 4.14 and 4.16, which are for symmetrical reinforcements of a circular hole in a flat element. For $\sigma_1 = \sigma_2$ (Chart 4.14), a value of K_{tg} of approximately 1 is attained at $A/(hd) = 1.6$. For $\sigma_2 = \sigma_1/2$ (Chart 4.16), a value of K_{tg} of approximately 1 is attained at A/hd a bit higher than 3.

It must be borne in mind that the tests (Kaufman et al. 1962) are for $d/h = 8$. For pressure vessels, d/h may be less than 8, and for aircraft windows, d/h is greater than 8. If d/h is greater than 8, the stress distribution would not be expected to change markedly; furthermore, the change would be toward a more favorable distribution.

However, for a markedly smaller d/h ratio, the optimal proportions corresponding to $d/h = 8$ are not satisfactory. To illustrate, Fig. 4.13*a* shows the approximately optimum proportions $h_t/h = 3$, $D/d = 1.8$ from Chart 4.14 where $d/h = 8$. If we now consider a case where $d/h = 4$ (Fig. 4.13*b*), we see that the previous proportions ($h_t/h = 3$, $D/d = 1.8$) are unsatisfactory for spreading the stress in the thickness direction. As an interim procedure, for $\sigma_1 = \sigma_2$,

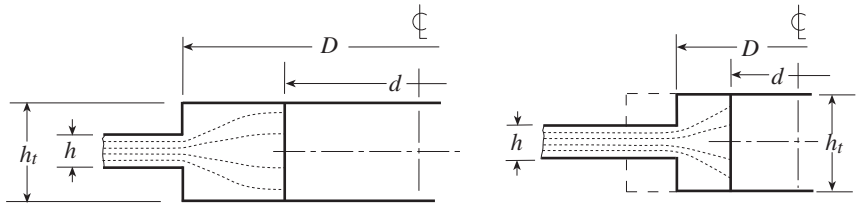


Figure 4.13 Effects of different d/h ratios: (*a*) $d/h = 8$; (*b*) $d/h = 4$.

it is suggested that the optimum h_t/h value be found from Chart 4.14 or 4.16 and then D/d is determined in such a way that the same reinforcement shape factor $[(D-d)/2]/[(h_t-h)/2]$ is maintained. For $\sigma_1 = \sigma_2$, the stress pattern is symmetrical, with the principal stresses in radial and tangential (circular) directions.

From Chart 4.14, for $\sigma_1 = \sigma_2$, the optimum proportions for $K_{tg} \approx 1$ are approximately $D/d = 1.8$ and $h_t/h = 3$. The reinforcement shape factor is

$$C_1 = \frac{(D-d)/2}{(h_t-h)/2} = \frac{[(D/d)-1]d}{[(h_t/h)-1]h} \tag{4.35}$$

For $D/d = 1.8$, $h_t/h = 3$, and $d/h = 8$, the shape factor C_1 is equal to 3.2.

On the basis of Charts 4.14 to 4.17, for $\sigma_1 = \sigma_2$, the suggested tentative reinforcement proportions for d/h values less than 8 are,

$$\frac{h_t}{h} = 3 \tag{4.36}$$

$$\frac{D}{d} = \frac{C_1[(h_t/h)-1]}{d/h} + 1 \tag{4.37}$$

Substitute $h_t/h = 3$ into Eq. (4.37) and retaining the shape factor of $C_1 = 3.2$ yield,

$$\frac{D}{d} = \frac{6.4}{d/h} + 1 \tag{4.38}$$

For $d/h = 4$, Eq. (4.38) reduces to $D/d = 2.6$ as shown by the dashed line in Fig. 4.13*b*.

For $\sigma_2 = \sigma_1/2$ and $d/h < 8$, it is suggested as an interim procedure that the shape factor $C_s = (D/2)/(h_t - h)$ of Eq. (4.27) for $d/h = 8$ be maintained for the smaller values of d/h (see Eq. 4.27, uniaxial tension):

$$C_s = \frac{D/2}{h_t - h} = \frac{D/d}{2[(h_t/h)-1]}\left(\frac{d}{H}\right) \tag{4.39}$$

For $D/d = 1.75$, $h_t/h = 5$, and $d/h = 8$, $C_s = 1.75$. For d/h less than 8 and $h_t/h = 5$, D/d can be obtained from Eq. (4.39) as,

$$\frac{D}{d} = \frac{2C_s[(h_t/h)-1]}{d/h} = \frac{14}{d/h} \tag{4.40}$$

The foregoing formulas are based on $K_{tg} \approx 1$. If a higher value of K_{tg} is used, for example, to obtain a more favorable V_R/V_H ratio (i.e., less weight), the same procedure may be followed to obtain the corresponding shape factors.

Example 4.4 Weight Optimization Through Adjustment of K_{tg} Consider an example of a design trade-off. Suppose for $\sigma_2 = \sigma_1/2$, the rather high reinforcement thickness ratio of $h_t/h = 5$ is reduced to $h_t/h = 4$. Chart 4.16 shows that the K_{tg} factor increases from about 1.0 to only 1.17. Also from Chart 4.19, the volume of reinforcement material is reduced 33% (V_R/V_H of 8.4 to 5.55).

The general formula for this example based on Eq. (4.39), for $h_t/h = 4$ and $d/h < 8$ is

$$\frac{D}{d} = \frac{2C_s[(h_t/h) - 1]}{d/h} = \frac{10.5}{d/h} \tag{1}$$

Similarly for $\sigma_1 = \sigma_2$, if we accept $K_{tg} = 1.1$ instead of 1.0, we see from the locus of minimum $A/(hd)$, Chart 4.14, that $h_t/h = 2.2$ and $D/d = 1.78$. From Chart 4.19, the volume of reinforcement material is reduced 41% (V_R/V_H of 4.4 to 2.6).

The general formula for this example, based on Eq. (4.37), for d/h values less than 8 is

$$\frac{h_t}{h} = 2.2 \tag{2}$$

$$\frac{D}{d} = \frac{6.25}{d/h} + 1 \tag{3}$$

The foregoing procedure may add more weight than is necessary for cases where $d/h < 8$, but from a stress standpoint, the procedure would be on the safe side. The same procedure applied to d/h values larger than 8 would go in the direction of lighter, more "compact" reinforcements. However, owing to the planar extent of the stress distribution around the hole, it is not recommended to extend the procedure to relatively thin sheets, $d/h > 50$, such as in an airplane structure. Consult Gurney (1938), Beskin (1944), Levy et al. (1948), Reissner and Morduchow (1949), Wells (1950), Mansfield (1953), Hicks (1957), Wittrick (1959*a*,*b*), Savin (1961), Houghton and Rothwell (1961), and Davies (1967).

Where the weight is important, some further reinforcements may be worth considering. Due to the nature of stress-flow lines, the outer corner region is unstressed (Fig. 4.14*a*). An ideal contour would be similar to Fig. 4.14*b*.

Kaufman et al. (1962) study a reinforcement of triangular cross section as shown Fig. 4.14*c*. The angular edge at *A* may not be practical, since a lid or other member often is used. A compromise shape may be considered (Fig. 4.14*d*). Dhir and Brock (1970) present the results for a shape like Fig. 4.14*d* and point out the large savings of weight that is attained.

The studies of a "neutral hole," that is, a hole that does not create stress concentration (Mansfield 1953), and of a variation of sheet thickness that results in uniform hoop stress for a circular hole in a biaxial stressed sheet (Mansfield 1970) are worthy of further consideration for certain design applications (i.e., molded parts).

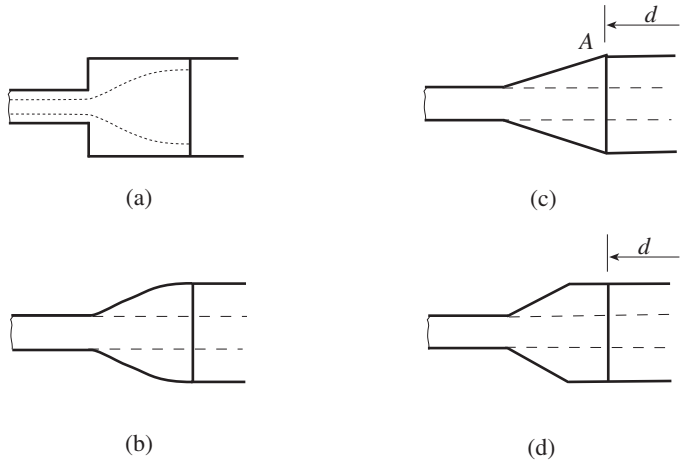


Figure 4.14 Reinforcement shape optimal design based on weight.

4.3.12 Circular Hole with Internal Pressure

As illustrated in Example 1.8, the SCF of an infinite element with a circular hole with internal pressure (Fig. 4.15) may be obtained through superposition of the solutions for the cases of Fig. 1.58*b* and *c*. At the edge of the hole, this superposition provides

$$\begin{aligned} \sigma_r &= \sigma_{r1} + \sigma_{r2} = -p \\ \sigma_\theta &= \sigma_{\theta 1} + \sigma_{\theta 2} = p \\ \tau_{r\theta} &= \tau_{r\theta 1} + \tau_{r\theta 2} = 0 \end{aligned} \tag{4.41}$$

so that the corresponding SCF is $K_t = \sigma_\theta / p = 1$.

The case of a square panel with a pressurized central circular hole could be useful as a cross section of a construction conduit. The $K_t = \sigma_{\max}/p$ factors (Durelli and Kobayashi 1958; Riley et al. 1959) are given in Chart 4.20. Note that for the thinner walls ($a/e > 0.67$), the maximum stress occurs on the outside edge at the thinnest section (point *A*).

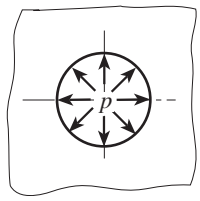


Figure 4.15 Infinite element with a hole with internal pressure.

For the thicker wall ($a/e < 0.67$), the maximum stress occurs on the hole edge at the diagonal location (point B). As a matter of interest the K_t based on the Lamè solution (Timoshenko and Goodier 1970) is shown, although for $a/e > 0.67$. These are not the maximum values. A check at a/e values of $1/4$ and $1/2$ with theoretical factors (Sekiya 1955) shows a good agreement.

An analysis (Davies 1965) covering a wide a/e range is in a good agreement with Chart 4.20. By plotting $(K_t - 1)(1 - a/e)/(a/e)$ versus a/e, the linear relations are obtained for small and large a/e values. The extrapolation is made to $(K_t - 1)(1 - a/e)/(a/e) = 2$ at $a/e \to 1$, as indicated by an analysis by Koiter (1957) and to 0 for $a/e \to 0$.

The upper curve (maximum) values of Chart 4.20 are in a reasonably good agreement with other recently calculated values (Slot 1972). For a pressurized circular hole near a corner of a large square panel (Durelli and Kobayashi 1958), the maximum K_t values are quite close to the values for the square panel with a central hole.

For the hexagonal panel with a pressurized central circular hole (Slot 1972), the K_t values are somewhat lower than the corresponding values of the upper curve of Chart 4.20, with $2a$ defined as the width across the sides of the hexagon. For other cases involving a pressurized hole, see Sections 4.3.19 and 4.4.5.

For an eccentrically located hole in a circular panel, see the SCFS in Table 4.2 (Section 4.3.19) and Charts 4.48 and 4.49.

4.3.13 Two Circular Holes of Equal Diameter in a Thin Element in Uniaxial Tension or Biaxial In-Plane Stresses

The SCFs for the case of two equal holes in a thin element subjected to uniaxial tension σ are considered here. Assume first the case where the holes lie along a line that is perpendicular to the direction of stress σ shown in Fig. 4.16, from the conclusions for a single hole (Section 4.3.3), the stress concentration at point B will be rather high if the distance between the two holes is relatively small. Chart 4.21a shows this characteristic for a finite-width panel.

The SCFs for an infinite thin element are provided in Chart 4.21b. In this case, when $l > 6a$, the influence between the two holes will be weak. Then it is reasonable to adopt the results for a single hole with $K_t = 3$.

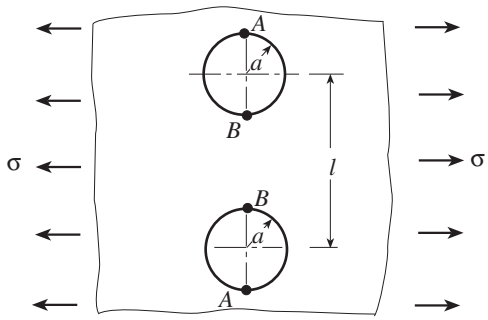


Figure 4.16 Two circular holes of equal diameter, aligned on a line perpendicular to the direction of stress σ.

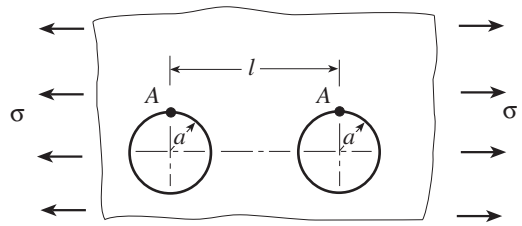


Figure 4.17 Two circular holes of equal diameter, aligned along σ.

If the holes lie along a line that is parallel to the stress σ shown in Fig. 4.17, the situation is different. As discussed in Section 4.3.1, for a single hole, the maximum stress occurs at point A and decreases very rapidly in the direction parallel to σ (Fig. 4.4). For two holes, there is some influence between the two locations A if l is small. The stress distribution for σ_θ tends to become uniform more rapidly than in the case of a single hole. The SCF is less than 3. However, as l increases, the influence between the two holes decreases, so K_t increases. At the location $l = 10a$, $K_t = 2.98$, which is quite close to the SCF of the single-hole case and is consistent with the distribution of Fig. 4.4. Several SCFs for two equal circular holes are presented in Charts 4.21 to 4.25.

Assume that section $B{-}B$ of Chart 4.21b carries a load corresponding to the distance between center lines, one has,

$$K_{tnB} = \frac{\sigma_{\max B}(1 - d/l)}{\sigma} \tag{4.42}$$

This corresponds to the light K_{tnB} lines of Charts 4.21b and 4.24. It should be noted that near $l/d = 1$, the factor becomes low in value (less than 1 for the biaxial case). If the same basis is used as for Eq. (4.11) (i.e., actual load carried by minimum section), the heavy K_{tnB} curves of Charts 4.21b and 4.24 are obtained. In this case,

$$K_{tnB} = \frac{\sigma_{\max B}(1 - d/l)}{\sigma\sqrt{1 - (d/l)^2}} \tag{4.43}$$

Note that K_{tnB} in Charts 4.21b and 4.24 approaches 1.0 as l/d approaches 1.0, the element tending to become, in effect, a uniformly stressed tension member. A photoelastic test by North (1965) of a panel with two holes having $l/d = 1.055$ and uniaxially stressed transverse to the axis of the holes shows nearly uniform stress in the ligament.

In Chart 4.22, $\sigma_{\max}$ is located at $\theta = 90^\circ$ for $l/d = 0$, $\theta = 84.4^\circ$ for $l/d = 1$, and θ approaches 90° as l/d increases. In Chart 4.23, $\sigma_{\max}$ for $\alpha = 0^\circ$ is the same as in Chart 4.22 ($\theta = 84.4^\circ$ for $l/d = 1.055$, $\theta = 89.8^\circ$ for $l/d = 6$); $\sigma_{\max}$ for $\alpha = 45^\circ$ is located at $\theta = 171.8^\circ$ at $l/d = 1.055$ and decreases toward 135° with increasing values of l/d; $\sigma_{\max}$ for $\alpha = 90^\circ$ is located at $\theta = 180^\circ$.

The numerical determination of K_t (Christiansen 1968) for a biaxially stressed plate with two circular holes with $l/d = 2$ is in a good agreement with the corresponding values of Ling (1948a) and Haddon (1967). For the more general case of a biaxially stressed plate in which the center line of two holes is inclined 0°, 15°, 30°, 45°, 60°, 75°, 90°, to the stress direction, the SCFs are

given in Chart 4.25 (Haddon 1967). These curves represent the relation between K_t and a/l for various values of the principal stress ratio σ_1/σ_2. It is assumed that the σ_1 and σ_2 are uniform in the area far from the holes. If the minimum distance between an element edge and the center of either hole is greater than $4a$, these curves can be used without significant error. There are discontinuities in the slopes of some of the curves in Chart 4.25, which correspond to sudden changes in the positions of the maximum (or minimum) stress.

Example 4.5 Flat Element with Two Equal-Sized Holes Under Biaxial Stresses Assume that a thin flat element with two 0.5-in. radius holes is subjected to uniformly distributed stresses $\sigma_x = 3180$ psi, $\sigma_y = -1020$ psi, $\tau_{xy} = 3637$ psi, along the straight edges far from the holes as shown in Fig. 4.18*a*. If the distance between the centers of the holes is 1.15 in., find the maximum stresses at the edges of the holes.

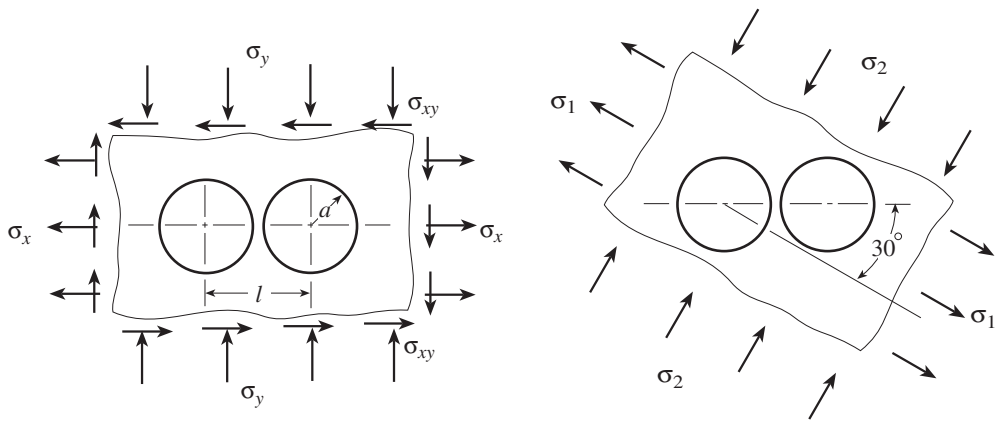
For an area far from the holes, the resolution of the applied stresses gives the principal stresses as,

$$\sigma_1 = \frac{1}{2}(\sigma_x + \sigma_y) + \frac{1}{2}\sqrt{(\sigma_x - \sigma_y)^2 + 4\tau_{xy}^2} = 5280 \text{ psi} \tag{1}$$

$$\sigma_2 = \frac{1}{2}(\sigma_x + \sigma_y) - \frac{1}{2}\sqrt{(\sigma_x - \sigma_y)^2 + 4\tau_{xy}^2} = -3120 \text{ psi} \tag{2}$$

The angle θ_1 between σ_x and the principal stress σ_1 is given by (Pilkey 2005) as,

$$\tan 2\theta_1 = \frac{2\tau_{xy}}{\sigma_x - \sigma_y} = 1.732 \tag{3}$$



$l = 1.15$ in. $a = 0.5$ in.

(a) (b)

Figure 4.18 Two holes in an infinite panel subject to combined stresses.

or

$$\theta_1 = 30^\circ \tag{4}$$

Now, the next step is to find the maximum stress of a flat element under biaxial tensile stresses σ_1 and σ_2, where σ_1 forms a 30° angle with the line connecting the hole centers (Fig. 4.18*b*). Chart 4.25 applies to this case, so,

$$\frac{\sigma_2}{\sigma_1} = \frac{-3120}{5280} = -0.591 \tag{5}$$

$$\frac{a}{l} = \frac{0.5}{1.15} = 0.435 \tag{6}$$

It can be found from Chart 4.25*c* that when the abscissa value $a/l = 0.435$, $K_t = 4.12$ and -5.18 for $\sigma_2/\sigma_1 = -0.5$, and $K_t = 4.45$ and -6.30 for $\sigma_2/\sigma_1 = -0.75$. The SCFs for $\sigma_2/\sigma_1 = -0.591$ is found through the interpolation as,

$$K_t = 4.24 \quad \text{and} \quad -5.58 \tag{7}$$

The extreme stresses at the edges of the holes are

$$\sigma_{\max} = \begin{cases} 4.24 \cdot 5280 = 22{,}390 \text{ psi} & \text{(tension)} \\ -5.58 \cdot 5280 = -29{,}500 \text{ psi} & \text{(compression)} \end{cases} \tag{8}$$

where $\sigma_1 = 5280$ psi is the nominal stress.

Example 4.6 Two Equal-Sized Holes Lying at an Angle in a Flat Element Under Biaxial Stresses Figure 4.19*a* shows a segment of a flat thin element containing two holes of 10-mm diameter; find the extreme stresses near the holes.

The principal stresses are (Pilkey 2005),

$$\sigma_{1,2} = \frac{1}{2}(\sigma_x + \sigma_y) \pm \frac{1}{2}\sqrt{(\sigma_x - \sigma_y)^2 + 4\tau_{xy}^2} = -38.2, 28.2 \text{ MPa} \tag{1}$$

and they occur at (see Fig. 4.19*b*),

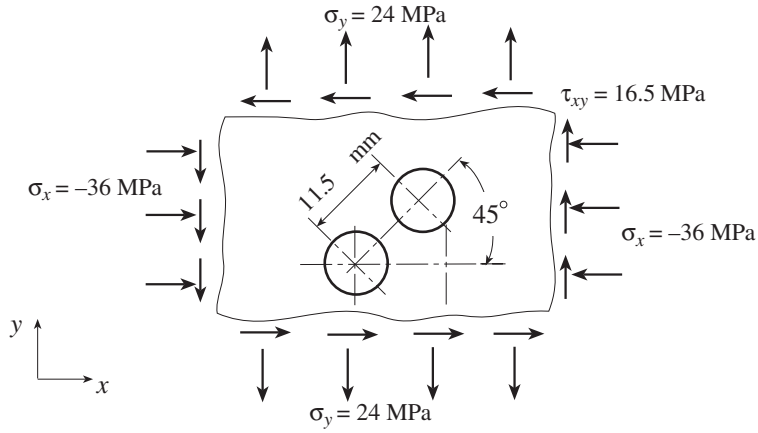
$$\theta = \frac{1}{2}\tan^{-1}\frac{2\tau_{xy}}{\sigma_x - \sigma_y} = -14.4^\circ \tag{2}$$

Use Chart 4.25 to find the extreme stresses at,

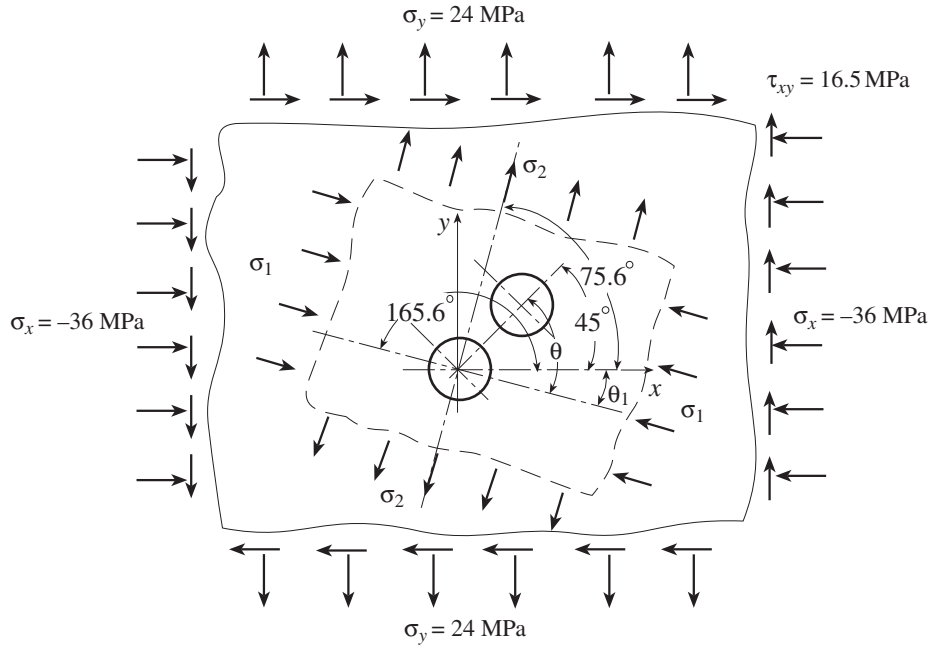
$$\theta = 45^\circ + 14.4^\circ = 59.4^\circ \tag{3}$$

Since Chart 4.25 applies only for angles $\theta = 0$, 15°, 30°, 45°, 60°, 75°, and 90°, the SCFs for $\theta = 60^\circ$ can be considered to be adequate approximations. Alternatively, use the linear interpolation. This leads to, for $a/l = 5/11.5 = 0.435$ and $\sigma_2/\sigma_1 = 56.5/(-80.5) = -0.702$,

$$K_t = 6.9 \quad \text{and} \quad -3.7 \tag{4}$$



(a)



(b)

Figure 4.19 Two holes lying at an angle, subject to combined stresses.

Thus

$$\sigma_{\max} = \sigma_1 K_t = \begin{cases} -80.5 \times 6.9 = -263.9 \text{ MPa} \\ -80.5 \times (-3.7) = 141.5 \text{ MPa} \end{cases} \tag{5}$$

are the extreme stresses occurring at each hole boundary.

4.3.14 Two Circular Holes of Unequal Diameter in a Thin Element in Uniaxial Tension or Biaxial In-Plane Stresses

The SCFs are developed for two circular holes of unequal diameters in panels in uniaxial and biaxial tension. The values for K_{tg} for a uniaxial tension in an infinite element are obtained by Haddon (1967). His geometrical notation is used in Charts 4.26 and 4.27, since this is convenient in deriving expressions for K_{tn}.

For Chart 4.26, to obtain K_{tn} exactly, one must know the exact loading of the ligament between the holes in tension and bending and the relative magnitudes of these loadings. For two equal holes, the loading is tensile, but its relative magnitude is not known. In the absence of this information, two methods were proposed to determine if reasonable K_{tn} values could be obtained.

Procedure A. Arbitrarily assumes (Chart 4.26) that the unit thickness load carried by s is $\sigma(b + a + s)$, then

$$\sigma_{\text{net}} s = \sigma(b + a + s)$$

$$K_{tn} = \frac{\sigma_{\max}}{\sigma_{\text{net}}} = \frac{K_{tg} \cdot s}{b + a + s} \tag{4.44}$$

Procedure B. Based on Eq. (4.11), assume that the unit thickness load carried by s is made up of two parts: $\sigma c_1 \sqrt{1 - (b/c_1)^2}$ from the region of the larger hole, carried over distance $c_R = bs/(b + a)$; $\sigma c_2 \sqrt{1 - (b/c_2)^2}$ from the region of the smaller hole, carried over distance $c_a = as/(b + a)$. In the foregoing $c_1 = b + c_b$; $c_2 = a + c_a$. For either the smaller or larger hole,

$$K_{tn} = \frac{K_{tg}}{\left(1 + \frac{(b/a)+1}{s/a}\right)\sqrt{1 - \left(\frac{(b/a)+1}{(b/a)+1+(s/a)}\right)^2}} \tag{4.45}$$

Referring to Chart 4.26, procedure A is not satisfactory in that K_{tn} for equal holes is less than 1 for the values of s/a below 1. As s/a approaches 0, for two equal holes, the ligament becomes essentially a tension specimen, so one would expect a condition of uniform stress ($K_{tn} = 1$) to be approached. Procedure B is not satisfactory below $s/a = 1/2$, but it does provide K_{tn} values greater than 1. For s/a greater than $1/2$, this curve has a reasonable shape, assuming that $K_{tn} = 1$ at $s/a = 0$.

In Chart 4.27, $\sigma_{\max}$ denotes the maximum tension stress. For $b/a = 5$, $\sigma_{\max}$ is located at $\theta = 77.8^\circ$ at $s/a = 0.1$ and increases to 87.5° at $s/a = 10$. Also $\sigma_{\max}$ for $b/a = 10$ is located at $\theta = 134.7^\circ$ at $s/a = 0.1$, 90.3° at $s/a = 1$, 77.8° at $s/a = 4$, and 84.7° at $s/a = 10$. The $\sigma_{\max}$ locations for $b/a = 1$ are given in the discussion of Chart 4.23. Since $s/a = 2[(l/d) - 1]$ for $b/a = 1$, $\theta = 84.4^\circ$ at $s/a = 0.1$, and 89.8° at $s/a = 10$. The highest compression stress occurs at $\theta = 100^\circ$.

For biaxial tension, $\sigma_1 = \sigma_2$, the K_{tg} values have been obtained by Salerno and Mahoney (1968) in Chart 4.28. The maximum stress occurs at the ligament side of the larger hole.

Charts 4.29 to 4.31 provide more curves for different b/a values and loadings, which are also based on Haddon (1967). These charts can be useful in considering SCFs of neighboring cavities of different sizes. In these charts, the stress concentration factors K_{tgb} (for the larger hole) and K_{tga} (for the smaller hole) are plotted against a/c. In the case of Chart 4.30, there are two sets of curves for the smaller hole, which corresponds to different locations on the boundary of the hole. The stress at point A is negative and the stresses at points B or C are positive, when the element is under uniaxial tension load. Equation (4.45) can be used to evaluate K_{tn}, if necessary.

Example 4.7 Thin Tension Element with Two Unequal Circular Holes A uniaxial fluctuating stress of $\sigma_{\max} = 24\ \text{MN/m}^2$ and $\sigma_{\min} = -62\ \text{MN/m}^2$ is applied to a thin element as shown in Fig. 4.20. It is given that $b = 98$ mm, $a = 9.8$ mm, and that the centers of the two circles are 110.25 mm apart. Find the range of stresses occurring at the edge of the holes.

The geometric ratios are found to be $b/a = 98/9.8 = 10$ and $a/c = 9.8/(110.25 - 98) = 0.8$. From Chart 4.30, the SCFs are found to be $K_{tgb} = 3.0$ at point D, $K_{tga} = 0.6$ at point B, and -4.0 at point A. When $\sigma_{\min} = -62\ \text{MN/m}^2$ is applied to the element, the stresses corresponding to points A, B, and D are

$$\begin{aligned} -4.0 \times (-62) &= 248\ \text{MN/m}^2 \quad \text{at A} \\ 0.6 \times (-62) &= -37.2\ \text{MN/m}^2 \quad \text{at B} \\ 3.0 \times (-62) &= -186\ \text{MN/m}^2 \quad \text{at C} \end{aligned} \tag{1}$$

When $\sigma_{\max} = 24\ \text{MN/m}^2$ is applied, the stresses corresponding to points A, B, and D are found to be

$$\begin{aligned} -4.0 \times 24 &= -96\ \text{MN/m}^2 \quad \text{at A} \\ 0.6 \times 24 &= 14.4\ \text{MN/m}^2 \quad \text{at B} \\ 3.0 \times 24 &= 72\ \text{MN/m}^2 \quad \text{at C} \end{aligned} \tag{2}$$

The critical stress, which varies between -96 and $248\ \text{MN/m}^2$, is at point A.

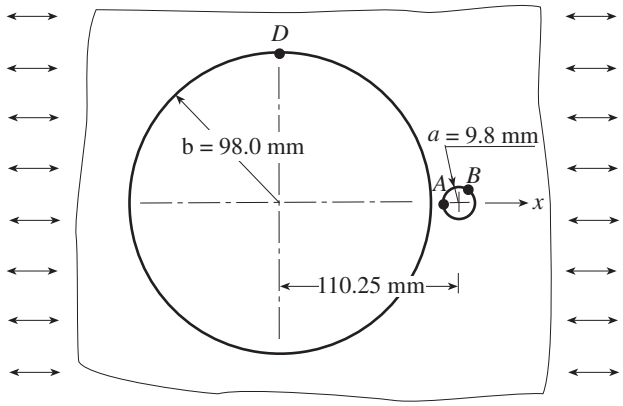


Figure 4.20 Thin element with two circular holes of unequal diameters.

4.3.15 Single Row of Equally Distributed Circular Holes in an Element in Tension

For a single row of holes in an infinite panel, Schulz (1941) develop the curves as functions of d/l (Charts 4.32 and 4.33), where l is the distance between the centers of the two adjoining holes and d is the diameter of the holes. Meijers (1967) the SCFs calculated by Meijers (1967) are in agreement with the Schulz values. Slot (1972) find that when the height of an element is larger than $3d$ (Chart 4.32), the stress distribution agrees well with the case of an element with infinite height.

For the cases of the element stressed parallel to the axis of the holes (Chart 4.33), when $l/d = 1$, the half element is equivalent to having an infinite row of edge notches. This portion of the curve (between $l/d = 0$ and 1) is in agreement with the work of Atsumi (1958) on edge notches.

For a row of holes in the axial direction with $l/d = 3$, and with $d/H = 1/2$, Slot obtains a good agreement with the Howland K_t value (Chart 4.1) for the single hole with $a/H = 1/2$. A specific K_t value obtained by Slot for $l/d = 2$ and $d/H = 1/3$ is in a good agreement with the Schulz curves (Chart 4.33).

The biaxially stressed case (Chart 4.34), from the work of Hütter (1942), represents an approximation in the midregion of d/l. Hütter's values for the uniaxial case with perpendicular stressing are inaccurate in the mid-region.

For a finite-width panel (strip), Schulz (1942–1945) provides the K_t values for the dashed curves of Chart 4.33. The K_t factors for $d/l = 0$ are the Howland (1929–1930, 1935) values. The K_t factors for the strip are in an agreement with the Nisitani (1968) values of Chart 4.57 ($a/b = 1$).

The K_t factors for a single row of holes in an infinite plate in transverse bending are given in Chart 4.95, in shear in Chart 4.102.

4.3.16 Double Row of Circular Holes in a Thin Element in Uniaxial Tension

A double row of staggered circular holes are considered here. This configuration is used in riveted and bolted joints. The K_{tg} values of Schulz (1941) are presented in Chart 4.35. Comparable values of Meijers (1967) are in agreement.

Chart 4.35 shows that as θ increases, the two rows grow farther apart. At $\theta = 90^\circ$, the K_{tg} values are the same as for a single row (Chart 4.32). For $\theta = 0^\circ$, a single row occurs with an intermediate hole in the span l. The curves 0° and 90° are basically the same, except that as a consequence of the nomenclature of Chart 4.35, l/d for $\theta = 0^\circ$ is twice l/d for $\theta = 90^\circ$ for the same K_{tg}. The type of plot used in Chart 4.35 makes it possible to obtain K_{tg} for intermediate values of θ by drawing θ versus l/d curves for various values of K_{tg}. In this way, the important case of $\theta = 60^\circ$ shown dashed on Chart 4.35 is obtained. For $\theta < 60^\circ$, $\sigma_{\max}$ occurs at points A, and for $\theta > 60^\circ$, $\sigma_{\max}$ occurs at points B. At $\theta = 60^\circ$, both points A and B are the maximum stress points.

In obtaining K_{tn} based on a net section, two relations are needed since for a given l/d, the area of the net sections A–A and B–B depends on θ (Chart 4.36). For $\theta < 60^\circ$, A–A is the minimum section and the following formula is used,

$$K_{tnA} = \frac{\sigma_{\max}}{\sigma}\left(1 - 2\frac{d}{l}\cos\theta\right) \tag{4.46}$$

For $\theta > 60^\circ$, $B{-}B$ is the minimum section and the formula is based on the net section in the row,

$$K_{tnB} = \frac{\sigma_{\max}}{\sigma}\left(1 - \frac{d}{l}\right) \tag{4.47}$$

At 60°, these formulas give the same result. The K_{tn} values in accordance with Eqs. (4.46) and (4.47) are given in Chart 4.36.

4.3.17 Symmetrical Pattern of Circular Holes in a Thin Element in Uniaxial Tension or Biaxial In-Plane Stresses

Symmetrical triangular or square patterns of circular holes are used in heat exchanger and nuclear vessel design (O'Donnell and Langer 1962). The notation used in these fields will be employed here. Several charts here give the SCFs versus the ligament efficiency. *Ligament efficiency* is defined as the minimum distance (s) of solid material between two adjacent holes divided by the distance (l) between the centers of the same holes; that is, ligament efficiency $= s/l$. It is assumed here that the hole patterns are repeated throughout the panel.

For the triangular pattern of Chart 4.37, Horvay (1952) obtains a solution for long and slender ligaments subjected to tension and shear (Chart 4.38). Horvay considers the results as not valid for s/l greater than 0.2. The photoelastic tests (Sampson 1960; Leven 1963, 1964) are made over the s/l range used in design. The computed values (Goldberg and Jabbour 1965; Meijers 1967; Grigolyuk and Fil'shtinskii 1970) are in a good agreement but differ slightly in certain ranges. When this occurs, the computed values (Meijers 1967) are used in Charts 4.37 and 4.41. Subsequent computed values (Slot 1972) are in a good agreement with the values of Meijers (1967).

A variety of SCFs for several locations on the boundaries of the holes are given in Chart 4.39 (Nishida 1976) for a thin element with a triangular hole pattern.

For the square pattern, Bailey and Hicks (1960), with the confirmation by Hulbert and Niedenfuhr (1965) and O'Donnell (1967), have obtained the solutions for applied biaxial fields oriented in the square and diagonal directions (Charts 4.40, 4.41). The photoelastic tests by Nuno et al. (1964) are in an excellent agreement with the mathematical results found by Bailey and Hicks (1960) for the square direction of loading. However, as pointed out by O'Donnell (1966), these SCFs are lower than those by Bailey and Hicks (1960) for intermediate values of s/l for the diagonal direction of loading. The validations by Leven (1967) of the diagonal case shows an agreement with the previous photoelastic tests (Nuno et al. 1964) and this lead to a recheck of the mathematical solution of this case. This is done by Hulbert under the PVRC sponsorship at the instigation of O'Donnell. The corrected results are given in O'Donnell (1967), which is essentially in his publication (O'Donnell 1966) with the Hulbert correction. Later the confirmatory results are obtained by Meijers (1967). Subsequently, computed values (Grigolyuk and Fil'shtinskii 1970; Slot 1972) are in a good agreement with those of Meijers (1967).

The $\sigma_2 = -\sigma_1$ state of stress (Sampson 1960; Bailey and Hicks 1960; O'Donnell 1966 and 1967) shown in Chart 4.41 corresponds to shear stress $\tau = \sigma_1$ at 45°. For instance, the SCF of a cylindrical shell with a symmetrical pattern of holes under shear loading can be found from Chart 4.103.

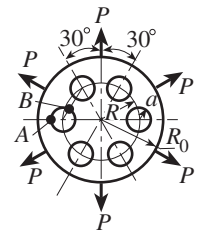
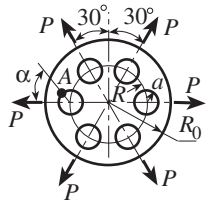
The $\sigma_2 = \sigma_1/2$ state of stress, Chart 4.40, corresponds to the case of a thin cylindrical shell with a square pattern of holes under the loading of inner pressure.

The values of the stress concentration factors K_{tg} are obtained for uniaxial tension and for various states of biaxiality of stress (Chart 4.42) by superposition. Chart 4.42 is approximate. Note that the lines are not straight, but they are nearly straight, so that the curved lines drawn should not be significantly in error. For uniaxial tension, Charts 4.43 to 4.45, are for rectangular and diamond patterns (Meijers 1967).

4.3.18 Radially Stressed Circular Element with a Ring of Circular Holes, with or without a Central Circular Hole

For the case of six holes in a circular element loaded by six external radial forces, the maximum K_{tg} values are given for four specific cases shown in Table 4.1. K_{tg} is defined as $R_0\,\sigma_{\max}/P$ for an element of unit thickness. A good agreement is obtained for the maximum K_{tg}

TABLE 4.1 Maximum K_{tg} for Circular Holes in Circular Element Loaded Externally with Concentrated Radial Forces

Pattern	Spacing	Maximum K_{tg}	Location	References
1 	$R/R_0 = 0.65$ $a/R_0 = 0.2$	4.745	A	Hulbert 1965 Buivol 1960
	$R/R_0 = 0.7$ $a/R_0 = 0.25$	5.754	B	
2 	$R/R_0 = 0.65$ $a/R_0 = 0.2$	9.909	A $\alpha = 50°$	Hulbert 1965 Buivol 1960, 1962
	$R/R_0 = 0.6$ $a/R_0 = 0.2$	7.459	A $\alpha = 50°$	

values of Hulbert (1965) and the corresponding experimental and numerical values by Buivol (1960, 1962).

For the case of a circular element with radial edge loading and with a central hole and a ring of four or six holes, the maximum K_t values (Kraus 1963) are shown in Chart 4.46 as a function of a/R_0 for two cases: (1) all holes of equal size ($a = R_i$) and (2) the central hole $1/4$ of outside diameter of the element ($R_i/R_0 = 1/4$). Kraus points out that with the assumption of axial stresses and strains, the results apply to both plane stress and plane strain.

For the case of an annulus flange ($R = 0.9R_0$), the maximum K_t values (Kraus et al. 1966) are shown in Chart 4.47 as a function of hole size and the number of holes. K_t is defined as $\sigma_{\max}$ divided by σ_{nom}, the average tensile stress on the net radial section through a hole. K_t factors are given for other values of R_i/R_0 and R/R_0 (Kraus et al. 1966).

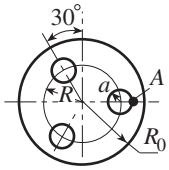
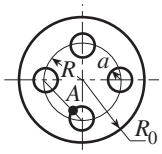
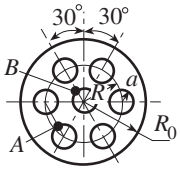
4.3.19 Thin Element with Circular Holes with Internal Pressure

As stated in Section 4.3.12, the SCF of an infinite element with a circular hole with internal pressure can be obtained through superposition. This state of stress can be separated into two cases. One case is equal biaxial tension, and the other is equal biaxial compression with the internal pressure p. For the second case, since every point in the infinite element is in a state of equal biaxial compressive stress, $(-p)$, the SCF is equal to $K_{t2} = \sigma_{\max}/p = -p/p = -1$. For the first case when there are multiple holes, the stress concentration factor K_{t1} depends on the number of holes, the geometry of the holes, and the distribution of the holes. Thus, from superposition, the stress concentration factor K_t for elements with holes is $K_t = K_{t1} + K_{t2} = K_{t1} - 1$. That is, the SCF for an element with circular holes with internal pressure can be obtained by subtracting 1 from the SCF for the same element with the same holes, but under external equal biaxial tension with stress of magnitude equal to the internal pressure p.

For two holes in an infinite thin element with internal pressure only, the K_t factors are found by subtracting 1.0 from the biaxial K_{tg} values of Charts 4.24, 4.25 (with $\sigma_1 = \sigma_2$), and 4.28. For an infinite row of circular holes with internal pressure, the K_t can be obtained by subtracting 1.0 from the K_t of Chart 4.34. For different patterns of holes with internal pressure, the K_t can be obtained in the same way from Charts 4.37 (with $\sigma_1 = \sigma_2$), 4.39*b*, and 4.40 (with $\sigma_1 = \sigma_2$). This method can be used for any pattern of holes in an infinite thin element. That is, as long as the K_t for equal biaxial tension state of stress is known, the K_t for the internal pressure only can be found by subtracting 1.0 from the K_t for the equal biaxial tension case. The maximum K_t values for specific spacings of hole patterns in circular panels are given in Table 4.2. Some other hole patterns in an infinite panel are discussed in Peterson (1974).

For the $a/R_0 = 0.5$ case of the single hole eccentrically located in a circular panel (Hulbert 1965), a sufficient number of eccentricities are calculated to permit Chart 4.48 to be prepared. For a circular ring of three or four holes in a circular panel, Kraus (1962) obtains the K_t factors for variable hole size (Chart 4.49). With the general finite element codes available, it is relatively straightforward to compute stress concentration factors for a variety of cases.

TABLE 4.2 Maximum K_t for Circular Holes in Circular Element Loaded with Internal Pressure Only

Pattern	Spacing	Maximum K_t	Location	References
1 	$a/R_0 = 0.5$	See Chart 4.48	See Chart 4.48	Hulbert 1965 Timoshenko and Goodier 1970
2 	$R/R_0 = 0.5$ $a/R_0 = 0.2$	See Chart 4.49	See Chart 4.49	Savin 1961 Kraus 1963
3 	$R/R_0 = 0.5$ $a/R_0 = 0.2$	See Chart 4.49	See Chart 4.49	Savin 1961 Kraus 1963
	$R/R_0 = 0.5$ $a/R_0 = 0.25$	2.45	A	Hulbert 1965
4 	$R/R_0 = 0.6$ $a/R_0 = 0.2$	2.278 Pressure in all holes	A	Hulbert 1965
		1.521 Pressure in center hole only	B	

4.4 ELLIPTICAL HOLES IN TENSION

Assume that an elliptical hole has a major axis $2a$ and minor axis $2b$ and the elliptical coordinates are used (Fig. 4.21*a*),

$$x = \sqrt{a^2 - b^2}\cosh\alpha\cos\beta$$
$$y = \sqrt{a^2 - b^2}\sinh\alpha\sin\beta \tag{4.48}$$

Let $\tanh\alpha_0 = b/a$ so that

$$\cosh\alpha_0 = \frac{a}{\sqrt{a^2 - b^2}}$$
$$\sinh\alpha_0 = \frac{b}{\sqrt{a^2 - b^2}} \tag{4.49}$$

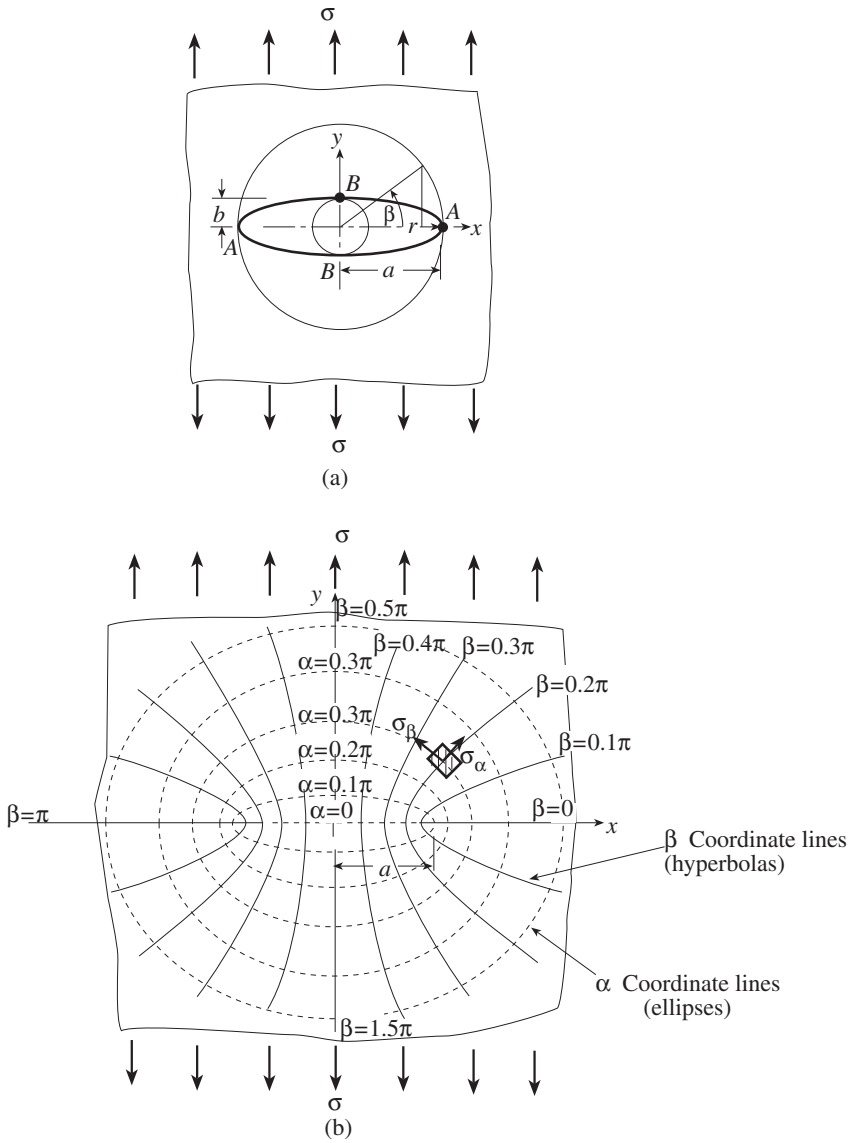


Figure 4.21 Elliptical hole in uniaxial tension: (*a*) notation; (*b*) elliptical coordinates and stress components (*c*) decay pattern for σ_y stress with distance $(x - a)$ away from the hole; (*d*) stress applied in direction perpendicular to the minor axis of the ellipse.

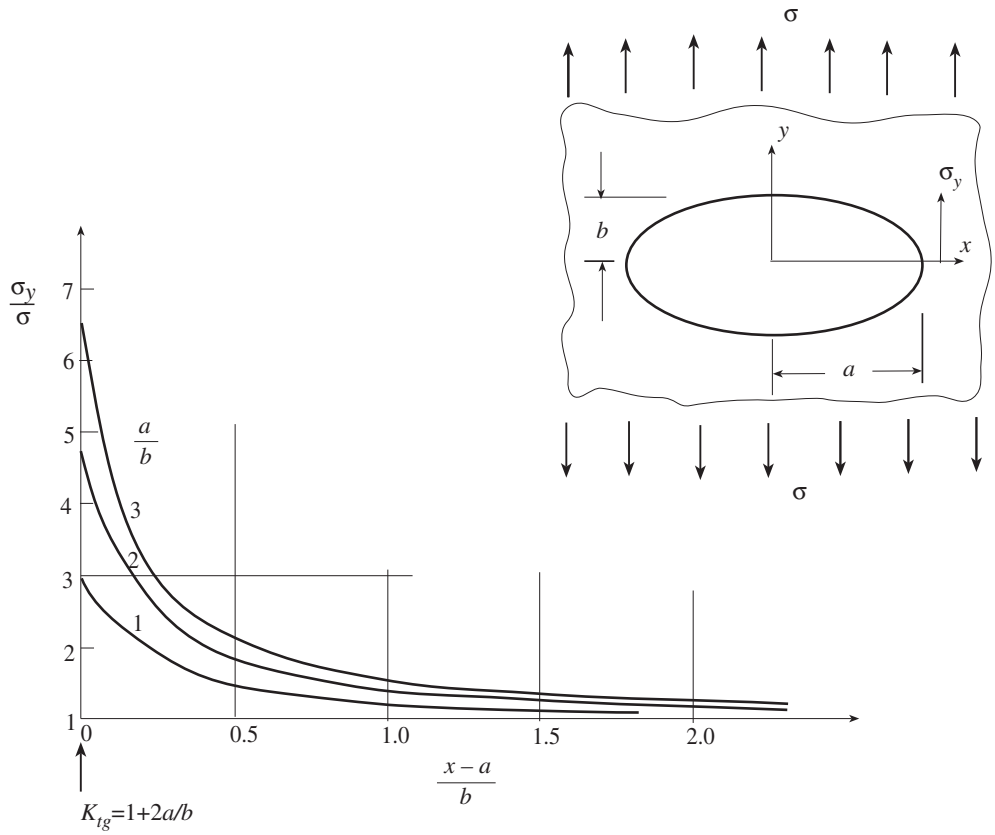


Figure 4.21 (*continued*) Elliptical hole in uniaxial tension: (*a*) notation; (*b*) elliptical coordinates and stress components (*c*) decay pattern for σ_y stress with distance $(x - a)$ away from the hole; (*d*) stress applied in direction perpendicular to the minor axis of the ellipse.

and Eq. (4.48) becomes

$$x = a \cdot \cos\beta$$
$$y = b \cdot \sin\beta \tag{4.50}$$

or

$$\frac{x^2}{a^2} + \frac{y^2}{b^2} = 1$$

This represents all the points on the elliptical hole of major axis $2a$ and minor axis $2b$. As α changes, Eq. (4.48) represents a series of ellipses which are plotted with the dashed lines in Fig. 4.21*b*. As $\alpha \to 0$, $b \to 0$, and the equation for the ellipse becomes

$$x = a \cdot \cos\beta$$
$$y = 0 \tag{4.51}$$

This corresponds to a crack (i.e., an ellipse of zero height, $b = 0$) and of length $2a$.

For $\beta = \pi/6$, Eq. (4.48) represents a hyperbola

$$x = \frac{\sqrt{3}}{2}\sqrt{a^2 - b^2}\cosh\alpha$$
$$y = \frac{1}{2}\sqrt{a^2 - b^2}\sinh\alpha \tag{4.52}$$

or

$$\frac{x^2}{\frac{3}{4}(a^2 - b^2)} - \frac{y^2}{\frac{1}{4}(a^2 - b^2)} = 1$$

As β changes from 0 to 2π, Eq. (4.48) represents a series of hyperbolas orthogonal to the ellipses in Fig. 4.21*b*. The elliptical coordinates (α, β) can represent any point in a two-dimensional plane. The coordinate directions are the directions of the tangential lines of the ellipses and of hyperbolas, which pass through that point.

4.4.1 Single Elliptical Hole in Infinite- and Finite-Width Thin Elements in Uniaxial Tension

Define the stress components in elliptic coordinates as σ_α and σ_β as shown in Fig. 4.21*b*, the elastic stress distribution of the case of an elliptical hole in an infinite-width thin element in uniaxial tension is determined by Inglis (1913) and Kolosoff (1910). At the edge of the elliptical hole, the sum of the stress components σ_α and σ_β is given by the formula (Inglis 1913),

$$(\sigma_\alpha + \sigma_\beta)_{\alpha_0} = \sigma\frac{\sinh 2\alpha_0 - 1 + e^{2\alpha_0}\cos 2\beta}{\cosh 2\alpha_0 - \cos 2\beta} \tag{4.53}$$

Since the stress σ_α is equal to zero at the edge of the hole ($\alpha = \alpha_0$), Eq. (4.53) becomes,

$$(\sigma_\beta)_{\alpha_0} = \sigma\frac{\sinh 2\alpha_0 - 1 + e^{2\alpha_0}\cos 2\beta}{\cosh 2\alpha_0 - \cos 2\beta} \tag{4.54}$$

The maximum value of $(\sigma_\beta)_{\alpha_0}$ occurs at $\beta = 0, \pi$, namely at the ends of the major axis of the ellipse (point A, Fig. 4.21a),

$$(\sigma_\beta)_{\alpha_0,\beta=0} = \sigma \frac{\sinh 2\alpha_0 - 1 + e^{2\alpha_0}}{\cosh 2\alpha_0 - 1} = \sigma(1 + 2\coth \alpha_0) = \sigma\left(1 + \frac{2a}{b}\right) \tag{4.55}$$

From Eq. (4.54) at point B, Fig. 4.21a,

$$(\sigma_\beta)_{\alpha_0,\beta=\pi/2} = \sigma \frac{\sinh 2\alpha_0 - 1 - e^{2\alpha_0}}{\cosh 2\alpha_0 + 1} = \sigma \frac{-(\cosh 2\alpha_0 + 1)}{\cosh 2\alpha_0 + 1} = -\sigma \tag{4.56}$$

The SCF for this infinite-width case is

$$K_{tg} = \frac{(\sigma_\beta)_{\alpha_0,\beta=0}}{\sigma} = \frac{\sigma[1 + (2a/b)]}{\sigma} = 1 + \frac{2a}{b} \tag{4.57}$$

or

$$K_{tg} = 1 + 2\sqrt{\frac{a}{r}} \tag{4.58}$$

where r is the radius of curvature of the ellipse at point A (Fig. 4.21a).

If $b = a$, then $K_{tg} = 3$, and Eq. (4.57) is consistent with the case of a circular hole. Chart 4.50 is a plot of K_{tg} of Eq. (4.57). The decay of the stress as a function of the distance $(x - a)$ away from the elliptical hole is shown in Fig. 4.21c for the holes of several ratios a/b (ESDU 1985).

When the uniaxial tensile stress σ is in the direction perpendicular to the minor axis of an elliptical hole as shown in Fig. 4.21d, the stress at the edge of the hole can be obtained from a transformation of Eq. (4.54). Fig. 4.21d shows that this case is equivalent to the configuration of Fig. 4.21a if the coordinate system x', y' (Fig. 4.21d) is introduced. In the new coordinates, the semimajor axis is $a' = b$, the semiminor axis is $b' = a$, and the elliptical coordinate is $\beta' = \beta + (\pi/2)$.

In the x', y' coordinates, substitution of Eq. (4.49) into Eq. (4.54) leads to

$$(\sigma_{\beta'})_{\alpha_0'} = \sigma \frac{\frac{2a'b'}{a'^2 - b'^2} - 1 + \frac{a'+b'}{a'-b'}\cos 2\beta'}{\frac{a'^2+b'^2}{a'^2-b'^2} - \cos 2\beta'} \tag{4.59}$$

The transformation of Eq. (4.59) into the coordinate system x, y gives

$$\begin{aligned}(\sigma_\beta)_{\alpha_0} &= \sigma \frac{-\frac{2ab}{a^2-b^2} - 1 - \frac{a+b}{a-b}\cos(\pi + 2\beta)}{-\frac{a^2+b^2}{a^2-b^2} - \cos(\pi + 2\beta)} \\ &= \sigma \frac{\frac{2ab}{a^2-b^2} + 1 - \frac{a+b}{a-b}\cos 2\beta}{\frac{a^2+b^2}{a^2-b^2} - \cos 2\beta}\end{aligned} \tag{4.60}$$

Substitution of Eq. (4.49) into Eq. (4.60) leads to

$$(\sigma_\beta)_{\alpha_0} = \sigma \frac{\sinh 2\alpha_0 + 1 - e^{2\alpha_0} \cos 2\beta}{\cosh 2\alpha_0 - \cos 2\beta} \tag{4.61}$$

For an elliptical hole in a finite-width tension panel, the stress concentration values K_t of Isida (1953, 1955a, b) are presented in Chart 4.51. The SCFs for an elliptical hole near the edge of a finite-width panel are provided in Chart 4.51, while those for a semi-infinite panel (Isida 1955a) are given in Chart 4.52.

4.4.2 Width Correction Factor for a Cracklike Central Slit in a Tension Panel

For the very narrow ellipse approaching a crack (Chart 4.53), a number of "finite-width correction" formulas have been proposed including those by Dixon (1960), Westergaard (1939), Irwin (1958), Brown and Srawley (1966), Fedderson (1965), and Koiter (1965). The correction factors have also been calculated by Isida (1965).

The Brown-Srawley formula for $a/H < 0.3$,

$$\begin{aligned} \frac{K_{tg}}{K_{t\infty}} &= 1 - 0.2 \cdot \frac{a}{H} + \left(\frac{2a}{H}\right)^2 \\ \frac{K_{tn}}{K_{t\infty}} &= \frac{K_{tg}}{K_{t\infty}} \left(1 - \frac{2a}{H}\right) \end{aligned} \tag{4.62}$$

where $K_{t\infty}$ is equal to K_t for an infinitely wide panel.

The Fedderson formula,

$$\frac{K_{tg}}{K_{t\infty}} = \left(\sec \pi \frac{a}{H}\right)^{1/2} \tag{4.63}$$

The Koiter formula,

$$\frac{K_{tg}}{K_{t\infty}} = \left[1 - 0.5 \cdot \frac{2a}{H} + 0.326\left(\frac{2a}{H}\right)^2\right] \left[1 - \frac{2a}{H}\right]^{-1/2} \tag{4.64}$$

Eqs. (4.62) to (4.64) represent the ratios of stress-intensity factors. In the small-radius, narrow-slit limit, the ratios are valid for stress concentration (Irwin 1960; Paris and Sih 1965).

Eq. (4.64) covers the entire a/H range from 0 to 0.5 (Chart 4.53), with correct end conditions. Eq. (4.62) is in a good agreement for $a/H < 0.3$. Eq. (4.63) is in a good agreement (Rooke 1970; generally less than 1% difference; at $a/H = 0.45$, less than 2%). Isida values are within 1% difference (Rooke 1970) for $a/H < 0.4$.

The photoelastic tests (Dixon 1960; Papirno 1962) of tension members with a transverse slit connecting two small holes are in a reasonable agreement with the foregoing, taking into consideration the accuracy limits of the photoelastic test.

Chart 4.53 also provides the SCFs for circular and elliptical holes. These SCFs have been corrected by Isida (1966) for an eccentrically located crack in a tension strip.

4.4.3 Single Elliptical Hole in an Infinite, Thin Element Biaxially Stressed

If the element is subjected to biaxial tension σ_1 and σ_2 shown in Fig. 4.22*a*, the solution can be obtained by superposition of Eqs. (4.54) and (4.61),

$$(\sigma_\beta)_{\alpha_0} = \frac{(\sigma_1 + \sigma_2)\sinh 2\alpha_0 + (\sigma_2 - \sigma_1)(1 - e^{2\alpha_0}\cos 2\beta)}{\cosh 2\alpha_0 - \cos 2\beta} \tag{4.65}$$

The decay of the σ_y and σ_x stresses away from the edges of the ellipse is shown in Fig. 4.22*b* for several values of the ratio a/b (EDSU 1985).

If the element is subjected to biaxial tension σ_1 and σ_2, while the major axis is inclined an angle θ as shown in Fig. 4.23, the stress distribution at the edge of the elliptic hole, where $\alpha = \alpha_0$, is (Inglis 1913)

$$(\sigma_\beta)_{\alpha_0} = \frac{(\sigma_1 + \sigma_2)\sinh 2\alpha_0 + (\sigma_2 - \sigma_1)[\cos 2\theta - e^{2\alpha_0}\cos 2(\beta - \theta)]}{\cosh 2\alpha_0 - \cos 2\beta} \tag{4.66}$$

Eq. (4.66) is a generalized formula for the stress calculation on the edge of an elliptical hole in an infinite element subject to uniaxial, biaxial, and shear stress states. For example, assume the

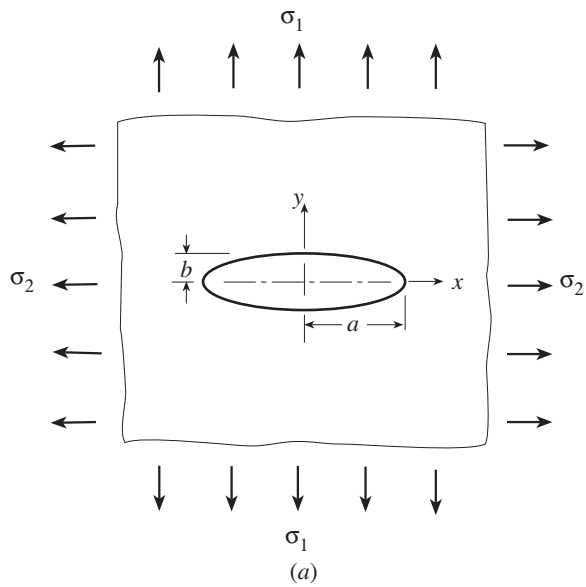
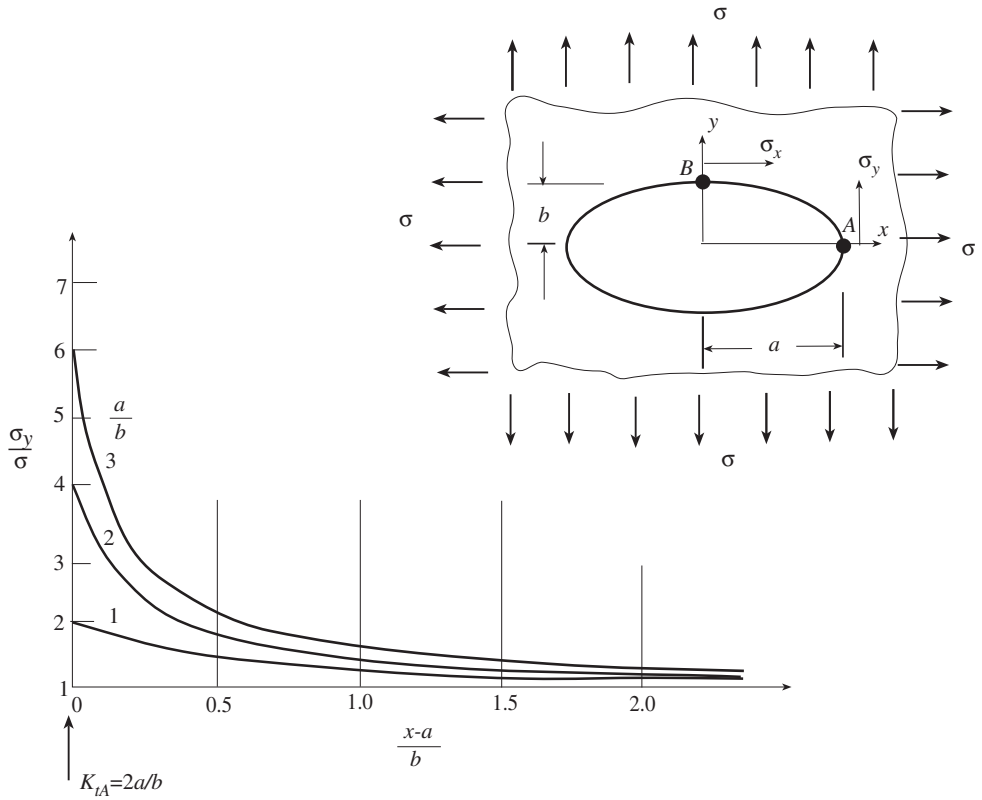
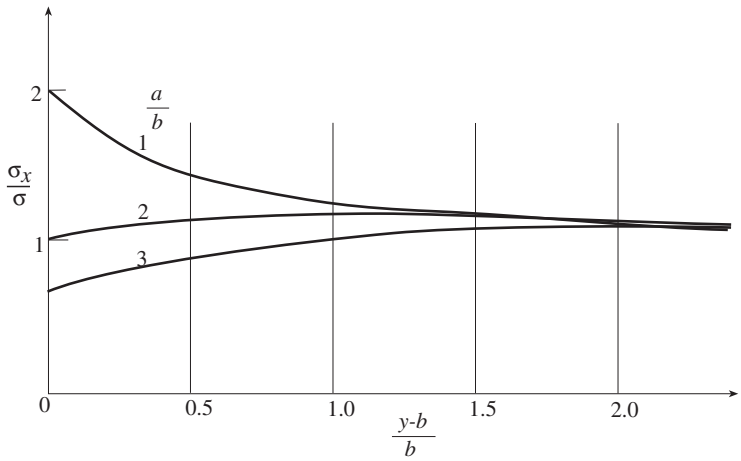


Figure 4.22 Elliptical hole in biaxial tension. (*a*) notation. (*b*) decay patterns for σ_y and σ_x stresses as a function of the distance away from the elliptical hole.





(*b*)

Figure 4.22 (*continued*) Elliptical hole in biaxial tension. (*a*) notation. (*b*) decay patterns for σ_y and σ_x stresses as a function of the distance away from the elliptical hole.

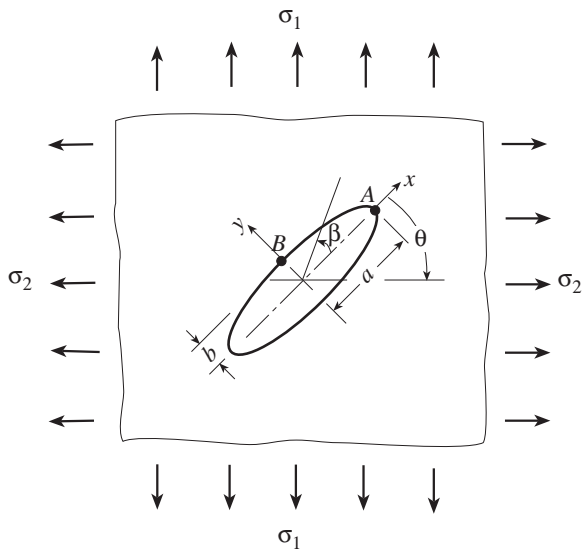


Figure 4.23 Biaxial tension of an obliquely oriented elliptical hole.

stress state of the infinite element is σ_x, σ_y, and τ_{xy} in Fig. 4.24. The two principal stresses σ_1 and σ_2 and the incline angle θ are found (Pilkey 2005) as

$$\sigma_1 = \frac{\sigma_x + \sigma_y}{2} + \sqrt{\left(\frac{\sigma_x - \sigma_y}{2}\right)^2 + \tau_{xy}^2}$$

$$\sigma_2 = \frac{\sigma_x + \sigma_y}{2} - \sqrt{\left(\frac{\sigma_x - \sigma_y}{2}\right)^2 + \tau_{xy}^2} \tag{4.67}$$

$$\tan 2\theta = \frac{2\tau_{xy}}{\sigma_x - \sigma_y}$$

The substitution of σ_1, σ_2, and θ into Eq. (4.66) leads to the stress distribution along the edge of the elliptical hole. Furthermore, the maximum stress along the edge can be found and the stress concentration factor is calculated.

Example 4.8 Pure Shear Stress State around an Elliptical Hole Consider an infinite plane element, with an elliptical hole, that is subjected to uniform shear stress τ. The direction of τ is parallel to the major and minor axes of the ellipse as shown in Fig. 4.25*a*. Find the stress concentration factor.

This two-dimensional element is in a state of stress of pure shear. The principal stresses are $\sigma_1 = \tau$ and $\sigma_2 = -\tau$. The angle between the principal direction and the shear stress τ is $\pi/4$ (Pilkey 2005). This problem then becomes to calculate the SCF of an element with an elliptical

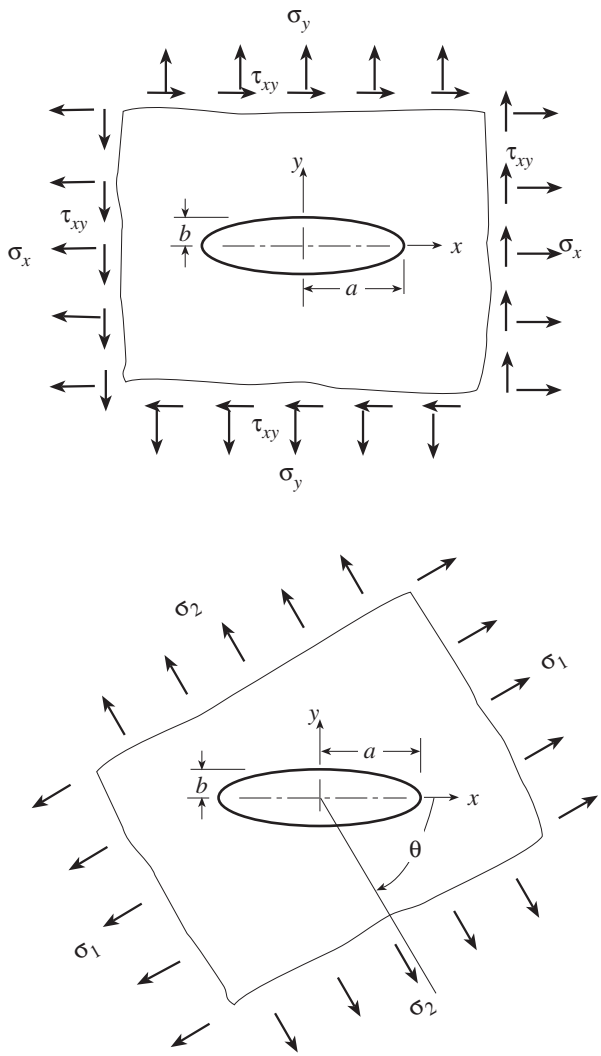
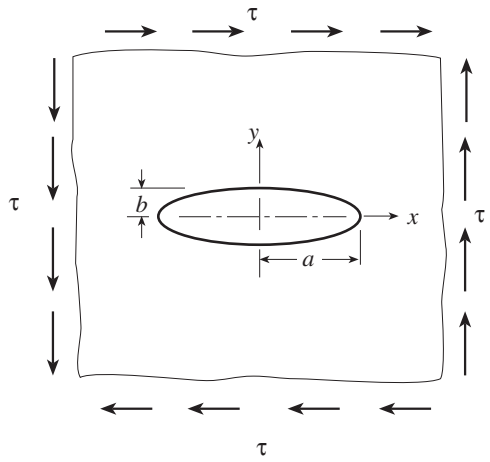


Figure 4.24 Single elliptical hole in an infinite thin element subject to arbitrary stress states.

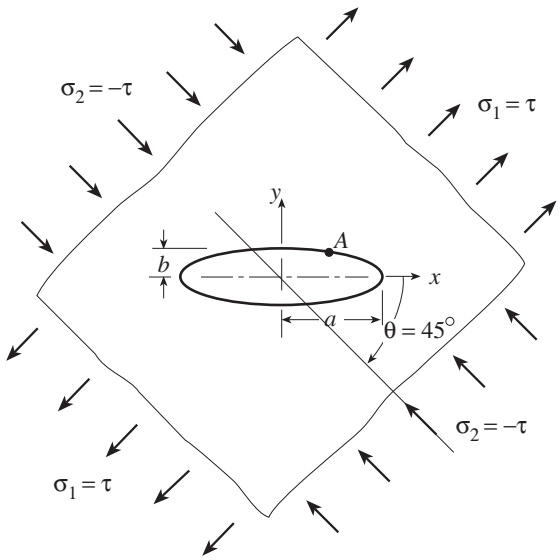
hole under biaxial tension, with the direction of σ_2 inclined at an angle of $-\pi/4$ to the major axis $2a$ as shown in Fig 4.25*b*.

Substitute $\sigma_1 = \tau$, $\sigma_2 = -\tau$ and $\theta = \pi/4$ into Eq. (4.66) to get

$$(\sigma_\beta)_{\alpha_0} = \frac{2\tau e^{2\alpha_0} \sin 2\beta}{\cosh 2\alpha_0 - \cos 2\beta} \tag{1}$$



(a)



(b)

Figure 4.25 Elliptical hole in pure shear.

From Eq. (4.49),

$$e^{2\alpha_0} = \frac{a+b}{a-b}, \quad \cosh 2\alpha_0 = \frac{a^2+b^2}{a^2-b^2},$$
$$\sinh 2\alpha_0 = \frac{2ab}{a^2-b^2} \tag{2}$$

Substitute (2) into (1):

$$(\sigma_\beta)_{\alpha_0} = \frac{2\tau(a+b)^2 \sin 2\beta}{a^2+b^2-(a^2-b^2)\cos 2\beta} \tag{3}$$

Differentiate (3) with respect to β, and set the result equal to 0. The extreme stresses occur when

$$\cos 2\beta = \frac{a^2-b^2}{a^2+b^2} \tag{4}$$

and

$$\sin 2\beta = \pm\frac{2ab}{a^2+b^2} \tag{5}$$

The maximum stress occurs at point A, which corresponds to (4) and $\sin 2\beta = 2ab/(a^2+b^2)$, so

$$\sigma_{\beta\max} = \frac{\tau(a+b)^2}{ab} \tag{6}$$

If the stress τ is used as a reference stress, the corresponding stress concentration factor is

$$K_t = \frac{(a+b)^2}{ab} \tag{7}$$

Example 4.9 Biaxial Tension Around an Elliptical Hole Suppose that an element is subjected to tensile stresses σ_1, σ_2 and the direction of σ_2 forms an angle θ with the major axis of the hole as shown in Fig. 4.23.; find the SCF at the perimeter of the hole for (1): $\theta = 0$ and (2): $\sigma_1 = 0, \theta = \pi/6$.

Eq. (4.67) applies to these two cases:

$$(\sigma_\beta)_{\alpha_0} = \frac{(\sigma_1+\sigma_2)\sinh 2\alpha_0 + (\sigma_2-\sigma_1)[\cos 2\theta - e^{2\alpha_0}\cos 2(\beta-\theta)]}{\cosh 2\alpha_0 - \cos 2\beta} \tag{1}$$

Set the derivative of $(\sigma_\beta)_{\alpha_0}$ with respect to β equal to zero. Then, the condition for the maximum stress is

$$(\sigma_2-\sigma_1)[\sin 2\theta(1-\cos 2\beta\cdot\cosh 2\alpha_0) - \cos 2\theta\cdot\sin 2\beta\cdot\sinh 2\alpha_0]$$
$$= (\sigma_1+\sigma_2)e^{-2\alpha_0}\sinh 2\alpha_0\cdot\sin 2\beta \tag{2}$$

For case 1, $\theta = 0$ and (2) reduces to

$$(\sigma_2 - \sigma_1) \cdot \sin 2\beta = (\sigma_1 + \sigma_2)e^{-2\alpha_0} \sin 2\beta \tag{3}$$

It is evident that only $\beta = 0, \pi/2$, which correspond to points A and B of Fig. 4.23, satisfy Eq. (3). Thus, the extreme values are

$$\sigma_A = \frac{(\sigma_1 + \sigma_2)\sinh 2\alpha_0 + (\sigma_2 - \sigma_1)(1 - e^{2\alpha_0})}{\cosh 2\alpha_0 - 1} \tag{4}$$

$$\sigma_B = \frac{(\sigma_1 + \sigma_2)\sinh 2\alpha_0 + (\sigma_2 - \sigma_1)(1 + e^{2\alpha_0})}{\cosh 2\alpha_0 + 1} \tag{5}$$

Substitute Eq. (4.49) into (4) and (5),

$$\sigma_A = \left(1 + \frac{2a}{b}\right)\sigma_1 - \sigma_2 \tag{6}$$

$$\sigma_B = \left(1 + \frac{2b}{a}\right)\sigma_2 - \sigma_1 \tag{7}$$

Taking σ_2 as the reference stress, the stress concentration factors are

$$K_{tgA} = \left(1 + \frac{2a}{b}\right)\frac{\sigma_1}{\sigma_2} - 1 \tag{8}$$

$$K_{tgB} = \left(1 + \frac{2b}{a}\right) - \frac{\sigma_1}{\sigma_2} \tag{9}$$

For case 2, using the same reasoning and setting $\sigma_1 = 0$, $\theta = \pi/6$, $n = b/a$, Eqs. (1) and (2) become

$$(\sigma_\beta)_{\alpha_0} = \sigma_2 \frac{2n + \frac{1}{2}(1 - n^2) - \frac{1}{2}(1 + n)^2(\cos 2\beta - \sqrt{3}\sin 2\beta)}{1 + n^2 - (1 - n^2)\cos 2\beta} \tag{10}$$

$$\frac{\sqrt{3}}{2}(1 - \cos 2\beta) - \frac{\sqrt{3}}{2}n^2(1 + \cos 2\beta) = \frac{n(3 - n)}{1 + n}\sin 2\beta \tag{11}$$

From Eq. (11), it is seen that if $a = b$, the extreme stress points occur at $\beta = -\pi/6, \pi/3$ and the maximum stress point corresponds to $\beta = \pi/3$:

$$\sigma_{\beta\max} = \frac{2 - \frac{1}{2} \cdot 2^2\left(-\frac{1}{2} - \frac{3}{2}\right)}{2}\sigma_2 = 3\sigma_2 \tag{12}$$

so that

$$K_t = 3 \tag{13}$$

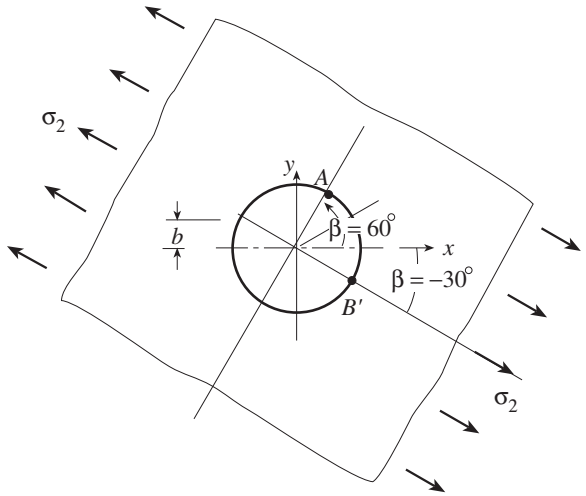


Figure 4.26 Maximum stress location for uniaxial stress.

This is the same result as for a circular hole, with the maximum stress point located at A (Fig. 4.26). For an elliptical hole with $b = a/3$, the maximum stress occurs when $\cos 2\beta = 0.8$, that is, $\beta = 161.17^\circ$ or $\beta = 341.17^\circ$.

$$K_t = 3.309 \tag{14}$$

The SCFs corresponding to different b/a values are tabulated in the table below. It is seen that as the value of b/a decreases, the maximum stress point gradually reaches the tip of the elliptical hole.

b/a	1	0.9	0.8	0.7	0.6	0.5	0.4	0.3	0.1
β	0.33π	0.32π	0.29π	0.27π	0.23π	0.19π	0.14π	0.09π	0.02π
K_t	3.00	2.91	2.83	2.79	2.78	2.76	3.04	3.50	8.16

In Chart 4.54, the stress σ_1 is perpendicular to the a dimension of the ellipse, regardless of whether a is larger or smaller than b. The abscissa scale (σ_2/σ_1) goes from –1 to +1. In other words, σ_2 is numerically equal to or less than σ_1.

The usual SCFs based on normal stresses with σ_1 as the reference stress are taken from Eqs. (6) and (7) of Example 4.9 as

$$K_{tA} = \frac{\sigma_A}{\sigma_1} = 1 + \frac{2a}{b} - \frac{\sigma_2}{\sigma_1} \tag{4.68}$$

$$K_{tB} = \frac{\sigma_B}{\sigma_1} = \frac{\sigma_2}{\sigma_1}\left(1 + \frac{2}{a/b}\right) - 1 \tag{4.69}$$

These factors are shown in Chart 4.54.

For $\sigma_1 = \sigma_2$

$$K_{tA} = \frac{2a}{b} \tag{4.70}$$

$$K_{tB} = \frac{2}{a/b} \tag{4.71}$$

Setting Eq. (4.68) equal to Eq. (4.69), the stresses at A and B are equal when

$$\frac{\sigma_2}{\sigma_1} = \frac{a}{b} \tag{4.72}$$

The tangential stress is uniform around the ellipse for the condition of Eq. (4.72). Equation. (4.72) is shown by a dot-dash curve on Chart 4.54. This condition occurs only for σ_2/σ_1 between 0 and 1, with the minor axis perpendicular to the major stress σ_1. Eq. (4.72) provides a means of design optimization for elliptical openings. For example, for $\sigma_2 = \sigma_1/2$, $\sigma_A = \sigma_B$ for $a/b = 1/2$, with $K_t = 1.5$. Keeping $\sigma_2 = \sigma_1/2$ constant, note that if a/b is *decreased*, K_{tA} becomes less than 1.5 but K_{tB} becomes greater than 1.5. For example, for $a/b = 1/4$, $K_{tA} = 1$, $K_{tB} = 3.5$. If a/b is increased, K_{tB} becomes less than 1.5, but K_{tA} becomes greater than 1.5. For example, for $a/b = 1$ (circular opening), $K_{tA} = 2.5$, $K_{tB} = 0.5$.

One usually thinks of a circular hole as having the lowest stress concentration, but it actually depends on the stress system. We see that for, $\sigma_2 = \sigma_1/2$ the maximum stress for a circular hole (Eq. 4.18) greatly exceeds that for the optimum ellipse ($a/b = 1/2$) by a factor of $2.5/1.5 = 1.666$.

An airplane cabin is basically a cylinder with $\sigma_2 = \sigma_1/2$ where $\sigma_1 =$ hoop stress, $\sigma_2 =$ axial stress. This indicates that a favorable shape for a window would be an ellipse of height 2 and width 1. The 2 to 1 factor is for a single hole in an infinite sheet. It is worth to note that there are other modifying factors, the proximity of adjacent windows, the stiffness of the structures, and so on. A round opening, which is often used, does not seem to be the most favorable design from a stress standpoint, although other considerations may enter.

It is sometimes said that what has a pleasing appearance often turns out to be technically correct. This is not always true when the following case is considered. In the foregoing consideration of airplane windows, a stylist would no doubt wish to orient elliptical windows with the long axis in the horizontal direction to give a "streamline" effect, as was done with the decorative "portholes" in the hood of one of the automobiles of the past. The horizontal arrangement would be most unfavorable from a stress standpoint, where $K_{tA} = 4.5$ as against 1.5 oriented vertically.

The SCF based on the maximum shear stress (Chart 4.54) is defined as

$$K_{ts} = \frac{\sigma_{\max}/2}{\tau_{\max}}$$

where, from Eq. (1.18),

$$\tau_{\max} = \frac{\sigma_1 - \sigma_2}{2} \quad \text{or} \quad \frac{\sigma_1 - \sigma_3}{2} \quad \text{or} \quad \frac{\sigma_2 - \sigma_3}{2}$$

In a sheet, with $\sigma_3 = 0$,

$$\tau_{\max} = \frac{\sigma_1 - \sigma_2}{2} \quad \text{or} \quad \frac{\sigma_1}{2} \quad \text{or} \quad \frac{\sigma_2}{2}$$

For $0 \le (\sigma_2/\sigma_1) \le 1$,

$$K_{ts} = \frac{\sigma_{\max}/2}{\sigma_1/2} = K_t \tag{4.73}$$

For $-1 \le (\sigma_2/\sigma_1) \le 0$,

$$K_{ts} = \frac{\sigma_{\max}/2}{(\sigma_1 - \sigma_2)/2} = \frac{K_t}{1 - (\sigma_2/\sigma_1)} \tag{4.74}$$

Since σ_2 is negative, the denominator is greater than σ_1, resulting in a lower numerical value of K_{ts} as compared to K_t, as seen in Chart 4.54. For $\sigma_2 = -\sigma_1$, $K_{ts} = K_t/2$.

The SCF based on equivalent stress is defined as

$$K_{te} = \frac{\sigma_{\max}}{\sigma_{\text{eq}}}$$

$$\sigma_{\text{eq}} = \frac{1}{\sqrt{2}}\sqrt{(\sigma_1 - \sigma_2)^2 + (\sigma_1 - \sigma_3)^2 + (\sigma_2 - \sigma_3)^2}$$

For $\sigma_3 = 0$,

$$\sigma_{\text{eq}} = \frac{1}{\sqrt{2}}\sqrt{(\sigma_1 - \sigma_2)^2 + \sigma_1^2 + \sigma_2^2}$$

$$= \sigma_1\sqrt{1 - (\sigma_2/\sigma_1) + (\sigma_2/\sigma_1)^2} \tag{4.75}$$

$$K_{te} = \frac{K_t}{\sqrt{1 - (\sigma_2/\sigma_1) + (\sigma_2/\sigma_1)^2}} \tag{4.76}$$

K_{te} values are shown in Chart 4.55.

For obtaining $\sigma_{\max}$, the simplest factor K_t is adequate. For mechanics of materials problems, the latter two factors, which are associated with failure theory, are useful.

The condition $\sigma_2/\sigma_1 = -1$ is equivalent to pure shear oriented 45° to the ellipse axes. This case and the case where the shear stresses are parallel to the ellipse axes are discussed in Section 4.9.1 and Chart 4.97. Jones and Hozos (1971) provide some values for biaxial stressing of a finite panel with an elliptical hole.

The stresses around an elliptical hole in a cylindrical shell in tension are studied by Murthy (1969), Murthy and Rao (1970), and Tingleff (1971). The values for an elliptical hole in a pressurized spherical shell are presented in Chart 4.6.

4.4.4 Infinite Row of Elliptical Holes in Infinite- and Finite-Width Thin Elements in Uniaxial Tension

Nisitani (1968) provides the SCFs for an infinite row of elliptical holes in an infinite panel (Chart 4.56). This chart covers a row of holes in the stress direction as well as a row perpendicular to the stress direction. The ordinate values are plotted as K_t/K_{t0}, where $K_{t0} = K_t$ for the single hole (Eq. 4.58). The results are in an agreement with the results by Schulz (1941) for circular holes. The effect of finite width is shown in Chart 4.57 (Nisitani 1968). The quantity K_{t0} is the SCF for a single hole in a finite-width element (Chart 4.51). Nisitani concludes that the interference effect of multi-holes K_t/K_{t0}, where K_t is for multi-holes and K_{t0} is for a single hole, is proportional to the square of the major semiaxis of the ellipse over the distance between the centers of the holes, a^2/c.

4.4.5 Elliptical Hole with Internal Pressure

As mentioned in Section 4.3.19 on the thin element with circular holes with internal pressure, the SCFs of an infinite element with circular holes with internal pressure can be found through superposition. This is true for elliptical holes as well. For elliptical holes with internal pressure in an infinite element, as stated in Section 4.3.19, K_t can be found by subtracting 1.0 from the case of Section 4.4.3, Eq. (8), Example 4.9, for $\sigma_1/\sigma_2 = 1$. Thus

$$K_t = \frac{2a}{b} - 1 \tag{4.77}$$

4.4.6 Elliptical Holes with Bead Reinforcement in an Infinite Thin Element under Uniaxial and Biaxial Stresses

In Chart 4.58, the values of K_t for reinforced elliptical holes are plotted against $A_r/[(a+b)h]$ for various values of a/b subjected to uniaxial and biaxial loading conditions (Wittrick 1959a,b; Houghton and Rothwell 1961; ESDU 1981). Here, A_r is the cross-sectional area of the bead reinforcement. The care must be taken in attempting to superimpose the maximum equivalent stresses for different loadings. These stresses are not directly additive if the location of the maximum stresses are different for different loading conditions. The stresses in the panel at its junction with the reinforcement are given here. The chart is based on $\nu = 0.33$.

4.5 VARIOUS CONFIGURATIONS WITH IN-PLANE STRESSES

4.5.1 Thin Element with an Ovaloid; Two Holes Connected by a Slit under Tension; Equivalent Ellipse

The "equivalent ellipse" concept (Cox 1953; Sobey 1963; Hirano, 1950) is useful for the ovaloid (slot with semicircular ends, Fig. 4.27*a*) and other openings such as two holes connected by a slit (Fig. 4.27*b*). If such a shape is enveloped (Fig. 4.27) by an ellipse (same major axis a and

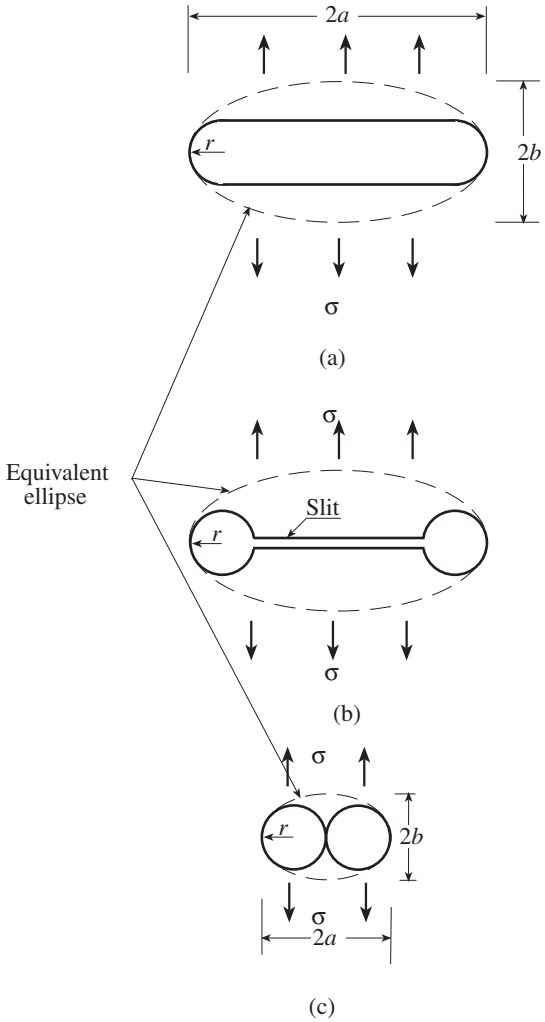


Figure 4.27 Equivalent ellipses: (*a*) ovaloid; (*b*) two holes connected by a slit; (*c*) two tangential circular holes.

minimum radius r), the K_t values for the shape and the equivalent ellipse may be nearly the same. In the case of the ovaloid, the K_t for the ellipse is within 2% of the correct value. The K_t for the ellipse can be calculated using Eq. (4.57).

Another comparison is provided by two tangential circular holes (Fig. 4.27*c*) of Chart 4.21*b*, where $K_t = 3.869$ for $l/d = 1$. This compares closely with the "equivalent ellipse" value of $K_t = 3.828$ found from Eq. (4.57). The cusps resulting from the enveloping ellipse are, in effect, stress-free ("dead" photoelastically). A similar stress free region occurs for two holes connected

by a slit. The round-cornered square hole oriented 45° to the applied uniaxial stress (Isida 1960), not completely enveloped by the ellipse, is approximated by an "equivalent ellipse."

The previously published values for a slot with semicircular ends (Frocht and Leven 1951) are low compared with the K_t values for the elliptical hole (Chart 4.51) and for a circular hole (Chart 4.1). It is suggested that the values for the equivalent ellipse be used. It has been shown that since the equivalent ellipse applies for tension, it is not applicable for shear (Cox 1953).

A photoelastic investigation (Durelli et al. 1968) of a slot of constant $a/b = 3.24$ finds the optimum elliptical slot end as a function of a/H, where H is the panel width. The optimum shape was an ellipse of a/b about 3 (Chart 4.59), and this results in a reduction of K_{tn}, from the value for the semicircular end of about 22% at $a/H = 0.3$ to about 30% for $a/H = 0.1$ with an average reduction of 26%. The authors state that the results may prove useful in the design of solid propellant grains. Although the numerical conclusions apply only to $a/b = 3.24$, it is clear that the same method of optimization may be useful in other design configurations with the possibility of significant stress reductions.

4.5.2 Circular Hole with Opposite Semicircular Lobes in a Thin Element in Tension

Thin tensile elements with circular holes with opposite semicircular lobes have been used for fatigue tests of sheet materials, since the stress concentrator can be readily produced with minimum variation from piece to piece (Gassner and Horstmann 1961; Schulz 1964). The mathematical results (Mitchell 1966) for an infinitely wide panel are shown in Chart 4.60 and are compared with an ellipse of the same overall width and minimum radius (equivalent ellipse).

For a finite-width panel (Chart 4.61) representative of a test piece, Mitchell (1966) develop an empirical formula,

$$K_t = K_{t\infty}\left[1 - \frac{2a}{H} + 4\left(\frac{6}{K_{t\infty}} - 1\right)\left(\frac{a}{H}\right)^2 + 8\left(1 - \frac{4}{K_{t\infty}}\right)\left(\frac{a}{H}\right)^3\right] \tag{4.78}$$

where $K_{t\infty} = K_t$ for infinitely wide panel (see Chart 4.60), a is the half width of hole plus lobes, and H is the width of the panel.

(1) For $H = \infty$, $a/H = 0$, $K_t = K_{t\infty}$.

(2) For $r/d \to 0$, $K_{t\infty}$ is obtained by multiplying K_t for the hole, 3.0, by K_t for the semicircular notch (Ling 1967), 3.065, resulting in $K_{t\infty} = 9.195$. The Mitchell (1966) value is $3(3.08) = 9.24$.

(3) For r/d greater than about 0.75, the middle hole is entirely swallowed up by the lobes. The resulting geometry, with middle opposite cusps, is the same as in Chart 4.21*b* ($l/d < 2/3$).

(4) For $r/d \to \infty$, a circle is obtained, $K_{t\infty} = 3$. Eq. (4.78) reduces to the Heywood formula (Heywood 1952).

$$K_t = 2 + \left(1 - \frac{a}{H}\right)^3 \tag{4.79}$$

The photoelastic tests by Cheng (1968) confirm the accuracy of the Mitchell formula.

Miyao (1970) has solved the case for one lobe. The K_t values are lower, varying from 0% at $r/d \to 0$ to about 10% at $r/d = 0.5$ (ovaloid, see Chart 4.62). Miyao also gives K_t values for the biaxial tension.

4.5.3 Infinite Thin Element with a Rectangular Hole with Rounded Corners Subject to Uniaxial or Biaxial Stress

The rectangular opening with rounded corners is often found in structures, such as ship hatch openings and airplane windows. Mathematical results, with specific data obtained by computer, have been published (Heller et al. 1958; Sobey 1963; Heller 1969). For uniaxial tension, K_t is given in Chart 4.62*a*, where the stress σ_1 is perpendicular to the *a* dimension. The top dashed curve of Chart 4.62*a* is for the ovaloid (slot with semicircular ends). In Section 4.5.1, it is noted that for uniaxial tension and for the same a/r, the ovaloid and the equivalent ellipse are the same for all practical purposes (Eq. 4.57). In the published results (Sobey 1963; ESDU 1970) for the rectangular hole, the ovaloid values are close to the elliptical values. The latter are used in Chart 4.62*a* to give the ovaloid curve a smoother shape. All of Charts 4.62 show clearly the minimum K_t as a function of r/a.

In Chart 4.62, it is noted that for $a/b > 1$, either the ovaloid represents the minimum K_t (see Chart 4.62*c*) or the rectangular hole with a particular (optimum) radius (r/a between 0 and 1) represents the minimum K_t (Charts 4.62*a*, *b*, and *d*).

A possible design problem is to select a shape of opening having a minimum K_t within rectangular limits *a* and *b*. In Chart 4.63 the following shapes are compared: ellipse, ovaloid, rectangle with rounded corners (for radius giving minimum K_t).

For the uniaxial case (top three dashed curves of Chart 4.63), the ovaloid has a lower K_t than the ellipse when $a/b > 1$ and a higher value when $a/b < 1$. The K_t for the optimum rectangle is lower than (or equal to) the K_t for the ovaloid. It is lower than the K_t for the ellipse when $a/b > 0.85$, higher when $a/b < 0.85$.

One might think that a circular opening in a tension panel would have a lower maximum stress than a round-cornered square opening having a width equal to the circle diameter. From Charts 4.62*a* and 4.63, it can be seen that *a square opening with corner radii of about a third of the width has a lower maximum stress than a circular opening of the same width*. The photoelastic studies show similar conclusions hold for notches and shoulder fillets. These remarks apply to the uniaxial tension case but not for a biaxial case with $\sigma_1 = \sigma_2$. For $\sigma_2 = \sigma_1/2$, the optimum opening has only a slightly lower K_t.

The solid line curves of Chart 4.63, representing $\sigma_2 = \sigma_1/2$, the stress state of a cylindrical shell under pressure, show that the ovaloid and optimum rectangle are fairly comparable and that their K_t values are lower than the ellipse for $a/b > 1$ and $a/b < 0.38$, greater for $a/b > 0.38$ and $a/b < 1$.

Note that for $a/b = 1/2$, K_t reaches the *low value of 1.5* for the ellipse. It is to be noted here that the ellipse is in this case superior to the ovaloid, $K_t = 1.5$ as compared to $K_t = 2.08$.

For the equal biaxial state, which is found in a pressurized spherical shell, the dot-dash curves of Chart 4.63 show that the ovaloid is the optimum opening in this case and gives a lower K_t than the ellipse (except of course at $a/b = 1$, where both become circles).

For a round-cornered square hole oriented 45° to the applied tension, Hirano (1950) has shown that the "equivalent ellipse" concept (see Section 4.5.1) is applicable.

4.5.4 Finite-Width Tension Thin Element with Round-Cornered Square Hole

In comparing the K_t values of Isida (1960) (for the finite-width strip) with Chart 4.62*a*, it appears that the satisfactory agreement is obtained only for small values of a/H, the half-hole width/element width. As a/H increases, K_t increases approximately as,

$K_{tg}/K_{t\infty} \approx 1.01, 1.03, 1.05, 1.09, 1.13$, for $a/H = 0.05, 0.1, 0.15, 0.2$, and 0.25, respectively.

4.5.5 Square Holes with Rounded Corners and Bead Reinforcement in an Infinite Panel under Uniaxial and Biaxial Stresses

The stress concentration factor K_t for reinforced square holes is given as a function of A_r for various values of r/a for the uniaxial and biaxial loading stress in Chart 4.64 (Sobey 1968; ESDU 1981). A_r is the cross-sectional area of the reinforcement. The curves are based on $v = 0.33$.

A care must be taken in attempting to superimpose the maximum equivalent stresses for different loadings. These stresses are not directly additive if the location of the maximum stresses differ for different loading conditions. The stresses in the panel at its junction with the reinforcement are given here.

4.5.6 Round-Cornered Equilateral Triangular Hole in an Infinite Thin Element Under Various States of Tension

The triangular hole with rounded corners has been used in some vehicle window designs as well as in certain architectural designs. The stress distribution around a triangular hole with rounded corners has been studied by Savin (1961).

The K_t values for $\sigma_2 = 0$ (σ_1 only), $\sigma_2 = \sigma_1/2$, and $\sigma_2 = \sigma_1$ in Chart 4.65*a* are determined by Wittrick (1963) by a complex variable method using a polynomial transformation function for mapping the contour. The corner radius is not constant. The radius r is the minimum radius, positioned symmetrically at the corners of the triangle. For $\sigma_2 = \sigma_1/2$, the equivalent SCF (von Mises) is $K_{te} = (2/\sqrt{3})K_t = 1.157K_t$. For $\sigma_2 = \sigma_1$ and $\sigma_2 = 0$, $K_{te} = K_t$. In Chart 4.65*b*, the K_t factors of Chart 4.65*a* are replotted as a function of σ_2/σ_1.

4.5.7 Uniaxially Stressed Tube or Bar of Circular Cross Section with a Transverse Circular Hole

The transverse (diametral) hole through a tube or bar of circular cross section occurs in engineering practice in lubricant and coolant ducts in shafts, in connectors for control or transmission rods, and in various types of tubular framework. The stress concentration factors K_{tg} and K_{tn} are shown in Chart 4.66. The results of Leven (1955) and of Thum and Kirmser (1943) for the solid shaft are in a close agreement. The solid round bar curves of Chart 4.66 represent both sets of data. The K_{tg} curves are checked with finite element analyses by ESDU (1989).

The results for the tubes are from British data (Jessop et al. 1959; ESDU 1965), and the SCFs are defined as,

$$K_{tg} = \frac{\sigma_{\max}}{\sigma_{\text{gross}}} = \frac{\sigma_{\max}}{P/A_{\text{tube}}} = \frac{\sigma_{\max}}{P/[(\pi/4)(D^2 - d_i^2)]} \tag{4.80}$$

$$K_{tn} = \frac{\sigma_{\max}}{\sigma_{\text{net}}} = \frac{\sigma_{\max}}{P/A_{\text{net}}} = K_{tg}\frac{A_{\text{net}}}{A_{\text{tube}}} \tag{4.81}$$

where the ratio $A_{\text{net}}/A_{\text{tube}}$ has been determined mathematically (Peterson 1968). The formulas will not be repeated here, although specific values can be obtained by dividing the Chart 4.66 values of K_{tn} by K_{tg}.

If the hole is sufficiently small relative to the shaft diameter, the hole may be considered to be of rectangular cross section. Then

$$\frac{A_{\text{net}}}{A_{\text{tube}}} = 1 - \frac{4\pi(d/D)[1 - (d_i/D)]}{1 - (d_i/D)^2} \tag{4.82}$$

It can be seen from the bottom curves of Chart 4.66 that the error due to this approximation is small below $d/D = 0.3$.

Thum and Kirmser (1943) find that the maximum stress do not occur on the surface of the shaft but at a small distance inside the hole on the surface of the hole. This is later corroborated by other investigators (Leven 1955; Jessop et al. 1959). The $\sigma_{\max}$ value used in developing Chart 4.66 is the maximum stress inside the hole.

4.5.8 Round Pin Joint in Tension

The case of a pinned joint in an infinite thin element has been solved mathematically by Bickley (1928). The finite-width case has been solved by Knight (1935), where the element width is equal to twice the hole diameter d and by Theocaris (1956) for $d/H = 0.2$ to 0.5. The experimental results (strain gage or photoelastic) have been obtained by Coker and Filon (1931), Schaechterle (1934), Frocht and Hill (1940), Jessop et al. (1958), and Cox and Brown (1964).

Two methods have been used in defining K_{tn}.

(1) The nominal stress is based on net section,

$$\sigma_{nd} = \frac{P}{(H - d)h}$$
$$K_{tnd} = \frac{\sigma_{\max}}{\sigma_{nd}} = \sigma_{\max}\frac{(H - d)h}{P} \tag{4.83}$$

(2) The nominal stress is based on bearing area,

$$\sigma_{nb} = \frac{P}{dh}$$
$$K_{tnb} = \frac{\sigma_{\max}}{\sigma_{nb}} = \frac{\sigma_{\max} dh}{P} \tag{4.84}$$

Note that

$$\frac{K_{tnd}}{K_{tnb}} = \frac{1}{d/H} - 1 \tag{4.85}$$

In Chart 4.67, the K_{tnb} curve corresponds to the Theocaris (1956) data for $d/H = 0.2$ to 0.5. The values of Frocht and Hill (1940) and Cox and Brown (1964) are in a good agreement with Chart 4.67, although it is slightly lower. From $d/H = 0.5$ to 0.75, the foregoing 0.2–0.5 curve is extended to be consistent with the Frocht and Hill values. The resulting curve is for joints where c/H is 1.0 or greater. For $c/H = 0.5$, the K_{tn} values are somewhat higher.

From Eq. (4.85), $K_{tnd} = K_{tnb}$ at $d/H = 1/2$. It seems more logical to use the lower (solid line) branches of the curves in Chart 4.67, since in practice, d/H is usually less than $1/4$. This means that Eq. (4.84), based on the bearing area, is generally used.

Chart 4.67 is for closely fitting pins. The K_t factors are increased by clearance in the pin fit. For example, at $d/H = 0.15$, K_{tnb} values (Cox and Brown 1964) of approximately 1.1, 1.3, and 1.8 are obtained for clearances of 0.7%, 1.3%, and 2.7%, respectively. (For an in-depth discussion of lug-clevis joint systems, see Chapter 5.) The effect of interference fits is to reduce the stress concentration factor.

A joint with an infinite row of pins has been analyzed (Mori 1972). It is assumed that the element is thin (two-dimensional case), that there are no friction effects, and that the pressure on the hole wall is distributed as a cosine function over half of the hole. The SCFs (Chart 4.68) have been recalculated based on Mori's work to be related to $\sigma_{\text{nom}} = P/d$ rather than to the mean peripheral pressure in order to be defined in the same way as in Chart 4.67. It is seen from Chart 4.68 that decreasing e/d from a value of 1.0 results in a progressively increasing stress concentration factor. Also, as in Chart 4.67, increasing d/l or d/H results in a progressively increasing stress concentration factor. The end pins in a row carry a relatively greater share of the load. The exact distribution depends on the elastic constants and the joint geometry (Mitchell and Rosenthal 1949).

4.5.9 Inclined Round Hole in an Infinite Panel Subjected to Various States of Tension

The inclined round hole is found in oblique nozzles and control rods in nuclear and other pressure vessels.

The curve for uniaxial stressing and $\nu = 0.5$. The second curve from the top of Chart 4.69 (which is for an inclination of 45°), is based on the photoelastic tests of Leven (1970), Daniel (1970), and McKenzie and White (1968) and the strain gage tests of Ellyin (1970a). The K_t factors (McKenzie and White 1968; Ellyin 1970b; Leven 1970) adjusted to the same K_t definition (to be explained in the next paragraph) for $h/b \sim 1$ are in a good agreement [K_t of Daniel (1970) is for $h/b = 4.8$]. Theoretical K_t factors (Ellyin 1970b) are considerably higher than the experimental factors as the angle of inclination increases. However, the theoretical curves are used in estimating the effect of Poisson's ratio and in estimating the effect of the state of stress. As $h/b \to 0$, the $K_{t\infty}$ values are for the corresponding ellipse (Chart 4.50). For a large h/b, the $K_{t\infty}$ values at the midsection are for a circular hole ($a/b = 1$ in Chart 4.51). This result is a consequence of the flow lines in the middle region of a thick panel taking a direction perpendicular to

the axis of the hole. For uniaxial stress σ_2, the midsection $K_{t\infty}$ is the maximum value. For uniaxial stress σ_1, the surface $K_{t\infty}$ is the maximum value.

For design use, it is desirable to start with a factor corresponding to infinite width and then have a method of correcting this to the a/H ratio involved in any particular design (a = semimajor width of surface hole; H = width of panel). This can be done, for design purposes, in the following way, for any inclination the surface ellipse has a corresponding a/b ratio. In Chart 4.53, K_{tn}, K_{tg}, and $K_{t\infty}$ are obtained for the a/H ratio of interest ($K_{t\infty}$ is the value at $a/H \to 0$). The ratios of these values are used to adjust the experimental values to $K_{t\infty}$ in Charts 4.69 and 4.70. In design, the same ratio method is used in going from $K_{t\infty}$ to the K_t corresponding to the actual a/H ratio.

In Chart 4.70, the effect of inclination angle θ is given. The $K_{t\infty}$ curve is based on the photoelastic K_{tg} values of McKenzie and White (1968) adjusted to $K_{t\infty}$ as described above. The curve is for $h/b = 1.066$ corresponding to the flat peak region of Chart 4.69. The effect of Poisson's ratio is estimated in the Ellyin's work.

For uniaxial stress σ_1 in panels, the maximum stress is located at A in Chart 4.69. An attempt to reduce this stress by rounding the edge of the hole with a contour radius $r = b$ produced the surprising result (Daniel 1970) of increasing the maximum stress (for $h/b = 4.8$, 30% higher for $\theta = 45°$, 50% higher for $\theta = 60°$). The maximum stress is located at the point of tangency of the contour radius with a line perpendicular to the panel surfaces. The stress increase has been explained (Daniel 1970) by the stress concentration due to the egg-shaped cross section in the horizontal plane. For $\theta = 75.5°$ and $h/b = 1.066$, it is found (McKenzie and White 1968) that for $r/b < 2/9$, a small decrease in stress is obtained by rounding the corner, but above $r/b = 2/9$, the stress is increased rapidly, which is consistent with the b result (Daniel 1970).

The strain gage tests are made by Ellyin and Izmiroglu (1973) on 45° and 60° oblique holes in 1 in.-thick steel panels subjected to tension. The effects of rounding the corner A (Chart 4.69) and of blunting the corner with a cut perpendicular to the panel surface are evaluated in most of the tests $h/b \approx 0.8$. For $\theta = 45°$, the SCFs are obtained in the region $r/h < 0.2$. However, for $h/b > 0.2$, the maximum stress is increased by rounding.

It is difficult to compare the various investigations of panels with an oblique hole having a rounded corner because of large variations in h/b. Also the effect depends on r/h and h/b. Leven (1970) has obtained a 25% maximum stress reduction in an 45° oblique nozzle in a pressure vessel model by blunting the acute nozzle corner with a cut perpendicular to the vessel axis. From the perspective of flow lines, it appears that the stress lines are not as concentrated for the vertical cut as for the "equivalent" radius.

4.5.10 Pressure Vessel Nozzle (Reinforced Cylindrical Opening)

A nozzle in pressure vessel and nuclear reactor technology denotes an integral tubular opening in the pressure vessel wall (see Fig. 4.28). The extensive strain gage (Hardenberg and Zamrik 1964) and photoelastic tests (WRC 1966; Seika et al. 1971) are made for various geometric reinforcement contours aiming to reduce stress concentration. Figure 4.28 is an example of a resulting "balanced" design (Leven 1966). The SCFs for oblique nozzles (nonperpendicular intersection) are also available (WRC 1970).

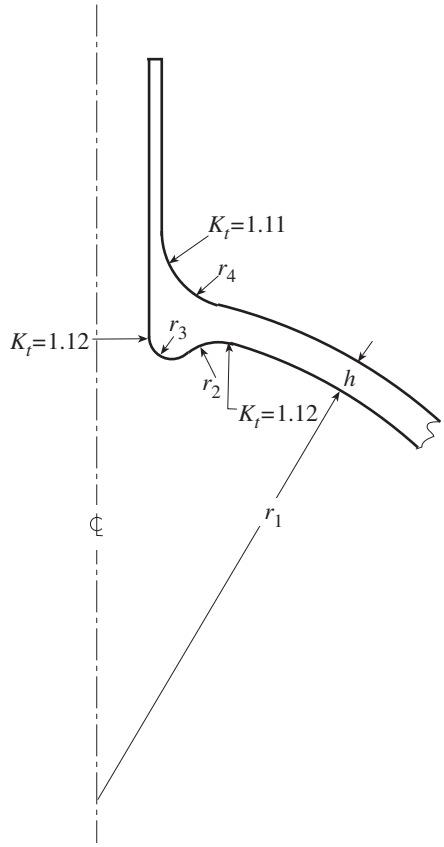


Figure 4.28 Half section of "balanced" design of nozzle in spherical vessel (Leven 1966).

4.5.11 Spherical or Ellipsoidal Cavities

The SCFs for the cavities are useful in evaluating the effects of porosity in materials (Peterson 1965). The stress distribution around a cavity having the shape of an ellipsoid of revolution has been obtained by Neuber (1958) for various types of stressing. The case of tension in the direction of the axis of revolution is shown in Chart 4.71. Note that the effect of Poisson's ratio v is relatively small. It is seen that high K_t factors are obtained as the ellipsoid becomes thinner and approaches the condition of a disk-shaped transverse crack.

The case of stressing perpendicular to the axis has been solved for an internal cavity having the shape of an elongated ellipsoid of revolution (Sadowsky and Sternberg 1947). From Chart 4.72, it is seen that for a circularly cylindrical hole ($a = \infty, b/a \to 0$) that the value of $K_t = 3$ is obtained and that this reduces to $K_t = 2.05$ for the spherical cavity ($b/a = 1$). If an elliptical shape $a/b = 3$ and ($a/r = 9$) is considered, from Eq. (4.57) and Chart 4.71, it is found that for a cylindrical hole of elliptical cross section, $K_t = 7$. For a circular cavity of elliptical cross section (Chart 4.71),

$K_t = 4.6$. For an ellipsoid of revolution (Chart 4.72), $K_t = 2.69$. The order of the factors quoted above seems reasonable if one considers the course streamlines must take in going around the shapes under consideration.

Sternberg and Sadowsky (1952) study the "interference" effect of two spherical cavities in an infinite body subjected to hydrostatic tension. With a space of one diameter between the cavities, the factor is increased less than 5%, $K_t = 1.57$, as compared to infinite spacing (single cavity), $K_t = 1.50$. This compares with approximately 20% for the analogous plane problem of circular holes in biaxially stressed panels of Chart 4.24.

In Chart 4.73, the stress concentration factors K_{tg} and K_{tn} are given for tension of a circular cylinder with a central spherical cavity (Ling 1959). The value for the infinite body is (Timoshenko and Goodier 1970),

$$K_t = \frac{27 - 15\nu}{14 - 10\nu} \tag{4.86}$$

where ν is Poisson's ratio. For $\nu = 0.3$, $K_t = 2.045$.

For a large spherical cavity in a round tension bar, Ling shows that $K_t = 1$ for $d/D \to 1$. Koiter (1957) obtains the following for $d/D \to 1$,

$$K_t = (6 - 4\nu)\frac{1 + \nu}{5 - 4\nu^2} \tag{4.87}$$

In Chart 4.73, a curve for K_{tg} is given for a biaxially stressed moderately thick element with a central spherical cavity (Ling 1959). For an infinite thickness (Timoshenko and Goodier 1970),

$$K_{tg} = \frac{12}{7 - 5\nu} \tag{4.88}$$

This value corresponds to the pole position on the spherical surface perpendicular to the plane of the applied stress.

The curve for the flat element of Chart 4.73 is calculated for $\nu = 1/4$. The value for $d/h = 0$ and $\nu = 0.3$ is also shown.

The effect of spacing for a row of "disk-shaped" ellipsoidal cavities (Nisitani 1968) is shown in Chart 4.74 in terms of K_t/K_{t0}, where $K_{t0} = K_t$ for the single cavity (Chart 4.71). These results are for Poisson's ratio 0.3. Nisitani (1968) concludes that the interference effect is proportional to the cube of the ratio of the major semiwidth of the cavity over the distance between the centers of the cavities. In the case of holes in thin elements (Section 4.4.4), the proportionality is as the square of the ratio.

4.5.12 Spherical or Ellipsoidal Inclusions

The evaluation of the effect of inclusions on the strength of materials, especially in fatigue and brittle fracture, is an important consideration in engineering technology. The stresses around an inclusion have been analyzed by considering that the hole or cavity is filled with a material having a different modulus of elasticity, E', and that adhesion between the two materials is perfect.

Donnell (1941) has obtained relations for cylindrical inclusions of elliptical cross section in a panel for E'/E varying from 0 (hole) to ∞ (rigid inclusion). Donnell finds that for Poisson's

ratio $v = 0.25$ to 0.3, the plane stress and plane strain values are sufficiently close for him to use a formulation giving a value between the two cases (approximation differs from exact values 1.5% or less). Edwards (1951) extended the work of Goodier (1933) and Donnell (1941) to cover the case of the inclusion having the shape of an ellipsoid of revolution.

The curves for E'/E for $1/4$, $1/3$, and $1/2$ are shown in Charts 4.50 and 4.72. These ratios are in the range of interest in considering the effect of silicate inclusions in steel. It is seen that the hole or cavity represents a more critical condition than a corresponding inclusion of the type mentioned.

For a rigid spherical inclusion, $E'/E = \infty$, in an infinite member, Goodier (1933) obtains the following relations for uniaxial tension.

For the maximum adhesion (radial) stress at the axial (pole) position,

$$K_t = \frac{2}{1+v} + \frac{1}{4-5v} \tag{4.89}$$

For $v = 0.3$, $K_t = 1.94$.

For the tangential stress at the equator (position perpendicular to the applied stress),

$$K_t = \frac{v}{1+v} - \frac{5v}{8-10v} \tag{4.90}$$

For $v = 0.3$, $K_t = -0.69$.

For $v = 0.2$, $K_t = 0$. For $v > 0.2$, K_t is negative—that is, the tangential stress is compressive. The same results are obtained (Chu and Conway 1970) by using a different method.

The case of a rigid circular cylindrical inclusion may be useful in the design of plastic members and concrete structures reinforced with steel wires or rods. Goodier (1933) has obtained the following plane strain relation for a circular cylindrical inclusion with $E'/E = \infty$,

$$K_t = \frac{1}{2}\left(3 - 2v + \frac{1}{3-4v}\right) \tag{4.91}$$

For $v = 0.3$, $K_t = 1.478$.

The studies have been made of the stresses in an infinite body containing a circular cylindrical inclusion of length one and two times the diameter d, with a corner radius r and with the cylinder axis in line with the applied tension (Chu and Conway 1970). The results may provide some guidance for a design condition where a reinforcing rod ends within a concrete member. For a length/diameter ratio of 2 and a corner radius/diameter ratio of $1/4$, the following K_{ta} values are obtained ($K_{ta} = \sigma_a/\sigma$ = maximum normal stress/applied stress): $K_{ta} = 2.33$ for $E'/E = \infty$, $K_{ta} = 1.85$ for $E'/E = 8$, $K_{ta} = 1.63$ for $E'/E = 6$.

For a length/diameter ratio = 1, K_{ta} does not vary greatly with corner radius/diameter ratio varying from 0.1 to 0.5 (spherical, $K_{ta} = 1.94$). Below $r/d = 0.1$, K_{ta} rises rapidly ($K_{ta} = 2.85$ at $r/d = 0.05$). Defining $K_{tb} = \tau_{\max}/\sigma$ for the bond shear stress, the following values are obtained: $K_{tb} = 2.35$ at $r/d = 0.05$, $K_{tb} = 1.3$ at $r/d = 1/4$, $K_{tb} = 1.05$ at $r/d = 1/2$ (spherical).

Donnell (1941) obtains the following relations for a rigid elliptical cylindrical inclusion.

Pole position A, Chart 4.75,

$$K_{tA} = \frac{\sigma_{\max A}}{\sigma} = \frac{3}{16}\left(1 - \frac{b}{a}\right) \tag{4.92}$$

Midposition B,

$$K_{tB} = \frac{\sigma_{\max B}}{\sigma} = \frac{3}{16}\left(5 + 3\frac{a}{b}\right) \tag{4.93}$$

These stresses are radial (normal to the ellipse), adhesive tension at A and compression at B. The tangential stresses are the one-third of the foregoing values.

It is seen that for the elliptical inclusion with its major axis in the tension direction, a failure would start at the pole by a rupture of bond, with the crack progressing perpendicular to the applied stress. For the inclusion with its major axis perpendicular to the applied tensile stress, it is seen that for a/b less than about 0.15, the compressive stress at the end of the ellipse will cause a plastic deformation; but that cracking would eventually occur at position A by the rupture of bond, followed by progressive cracking perpendicular to the applied tensile stress.

Nisitani (1968) has obtained the exact values for the plane stress and plane strain radial stresses for the pole position A, Chart 4.75, of the rigid elliptical cylindrical inclusion,

$$K_t = \frac{(\gamma + 1)[(\gamma + 1)(a/b) + (\gamma + 3)]}{8\gamma} \tag{4.94}$$

where $\gamma = 3 - 4\nu$ for plane strain, $\gamma = (3 - \nu)/(1 + \nu)$ for plane stress, a is the ellipse half-width parallel to applied stress, b is the ellipse half-width perpendicular to applied stress, and ν is Poisson's ratio. For plane strain,

$$K_t = \frac{(1 - \nu)[2(1 - \nu)(a/b) + 3 - 2\nu]}{3 - 4\nu} \tag{4.95}$$

Eq. (4.95) reduces to Eq. (4.89) for the circular cylindrical inclusion. As stated, Eqs. (4.94) and (4.95) are sufficiently close to Eq. (4.92) so that a single curve can be used in Chart 4.75. A related case of a panel having a circular hole with a bonded cylindrical insert ($r_i/r_o = 0.8$) having a modulus of elasticity 11.5 times the modulus of elasticity of the panel has been studied by a combined photoelasticity and Moiré analysis (Durelli and Riley 1965).

The effect of spacing on a row of rigid elliptical inclusions (Nisitani 1968) is shown in Chart 4.76 as a ratio of the K_t for the row and the K_{t0} for the single inclusion (Chart 4.75). Shioya (1971) has obtained the K_t factors for an infinite tension panel with two circular inclusions.

4.6 HOLES IN THICK ELEMENTS

Although a few of the elements treated in this chapter can be thick, most are thin panels. In this section, several thick elements with holes will be presented.

As shown in Section 4.3.1, the stress concentration factor K_t for the hole in a plane thin element with uniaxial tension is 3. In an element of arbitrary thickness in uniaxial tension with a

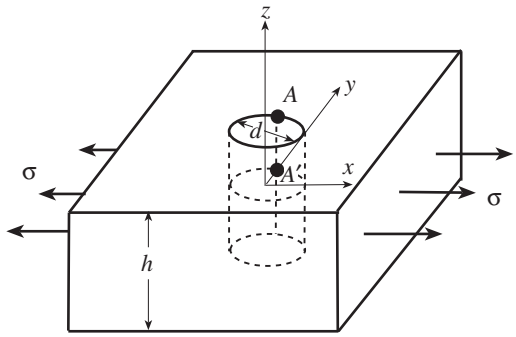


Figure 4.29 Element with a transverse hole.

transverse circular hole (Fig. 4.29), the maximum stress varies on the surface of the hole across the thickness of the element. Sternberg and Sadowsky (1949) show with a three-dimensional analysis that this stress is lower at the surface (point A) and somewhat higher in the interior (point A'). In particular, it is found that the stress distribution on the surface of the hole depends on the thickness to diameter ratio (h/d), where d is the diameter of the hole, as well as on the distance z from the mid-thickness.

In the Sternberg and Sadowsky work, it was shown that for an element of thickness $0.75d$ subjected to uniaxial tension, with Poisson's ratio $\nu = 0.3$, the maximum stress at the surface is 7% less than the two-dimensional stress concentration factor of 3.0, whereas the stress at midplane is less than 3% higher. A finite element analysis by Young and Lee (1993) confirms this trend, although the SCFs from finite element analysis are about 5% higher than the values calculated theoretically. Further insight into the theoretical solution for the stress concentration of a thick element with a circular hole in tension is given in Folias and Wang (1990). Sternberg and Sadowsky put forth "the general assertion that factors of stress concentration based on two-dimensional analysis sensibly apply to elements of arbitrary thickness ratio."

In the analysis by Youngdahl and Sternberg (1966) on an infinitely thick solid (semi-infinite body, mathematically) subjected to shear (or biaxial stress $\sigma_2 = -\sigma_1$) and with $\nu = 0.3$, the maximum stress at the surface of the hole is found to be 23% lower than the value normally utilized for a thin element (Eqs. 4.17 and 4.18), and the corresponding stress at a depth of the hole radius is 3% higher.

Chen and Archer (1989) derive the expressions for the SCFs of a thick plate subject to bending with a circular hole. They show that the thick plate theory leads to the results close to those that have been obtained with the theory of elasticity. Bending of flat thin members is considered in Section 4.8.

In summarizing the foregoing discussion of stress variation in the thickness direction of elements with a hole, it can be said that the usual two-dimensional SCFs are sufficiently accurate for the design application of the elements with arbitrary thickness. This is of interest in the mechanics of materials and failure analysis, since a failure would be expected to start down the hole rather than at the surface, in the absence of other factors, such as those due to processing or manufacturing.

4.6.1 Countersunk Holes

Countersunk-rivet connections are common in joining structural components. This often occurs with aircraft structures where aerodynamically smooth surfaces can be important.

The notation for a countersunk hole model is shown in Fig. 4.30, where

h = thickness of element
d = diameter of hole
e = edge distance
b = straight-shank length
θ_c = countersunk angle

The SCFs for countersunk holes are studied experimentally and computationally in Whaley (1965), Cheng (1978), Young and Lee (1993), Shivakumar and Newman (1995), and Shivakumar et al. (2006). The loadings can be tension, bending, and a combination of loads to simulate riveted joints.

Through a sequence of finite element simulations, Young and Lee (1993) find that the maximum stress occurs at the root of the countersunk of the hole, 90° from the applied tensile loading. It is also shown that there is no significant influence on K_t of a variation in countersunk angle θ_c between 90° and 100°, which is a common range in practice. The critical parameters are found to be the straight-shank length and the edge distance. Some countersunk K_t trends in terms of these parameters are provided in Table 4.3. For edge distances of less than $2d$, a substantial increase in K_t can be expected. The curves useful for calculating K_t are developed. For a thin element, the traditional K_t can be used for $e > 2.5d$ and for edge distances in the range $1 \leq (e/d) > 2.5$,

$$K_t\Big|_{\text{straight-shank hole}} = 14.21 - 14.96\frac{e}{d} + 7.06\left(\frac{e}{d}\right)^2 - 1.13\left(\frac{e}{d}\right)^3 \tag{4.96}$$

For a countersunk hole of similar e and h/d,

$$K_t\Big|_{\text{countersunk hole}} = \left(0.72\frac{h-b}{h} + 1\right) K_t\Big|_{\text{straight-shank hole}} \tag{4.97}$$

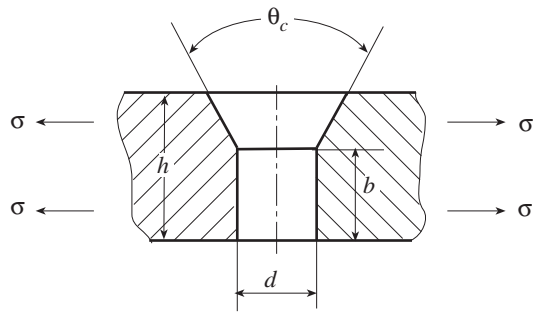


Figure 4.30 Notation for a countersunk hole.

TABLE 4.3 Countersunk Stress Concentration Factors

Countersunk Depth $\frac{h-b}{h}$ (%)	Average Increase in K_t over Straight-shank Hole K_t (%)	Typical K_t for $e > 2.5d$
25	8	3.5
50	27	4.0
75	64	4.5

Based on further finite element analyses, Shivakumar et al. (2006) propose and refine the versions of Eqs. (4.96) and (4.97).

Example 4.10 Stress Concentration in a Countersunk Hole in an Element Subjected to Tension Find the K_t for a hole of diameter $d = 7$ mm in an element of thickness $h = 7$ mm, with countersunk angle $\theta_c = 100°$ and countersunk depth of 25%, that is, $(h - b)/h = 0.25$. The edge distance is $e = 2d$.

From Eq. (4.96) with $e/d = 2$,

$$K_t\Big|_{\text{straight-shank hole}} = 14.21 - 14.96(2) + 7.06(2)^2 - 1.13(2)^3 = 3.49 \tag{1}$$

Finally, from Eq. (4.97),

$$K_t\Big|_{\text{countersunk hole}} = \left(0.72\frac{h-b}{h} + 1\right) K_t\Big|_{\text{straight-shank hole}} = (0.72 \cdot 0.25 + 1)3.49 = 4.12 \tag{2}$$

4.6.2 Cylindrical Tunnel

Mindlin (1939) has solved the following cases of an indefinitely long cylindrical tunnel: (1) hydrostatic pressure, $-cw$, at the tunnel location before the tunnel is formed (c = distance from the surface to the center of the tunnel, w = weight per unit volume of material); (2) material restrained from lateral displacement; (3) no lateral stress.

The results for case 1 are shown in Chart 4.77 in dimensionless form, $\sigma_{\max}/2wr$ versus c/r, where r is the radius of the tunnel. It is seen that the minimum value of the peripheral stress $\sigma_{\max}$ is reached at values of $c/r = 1.2$, 1.25, and 1.35 for $v = 0$, 1/4, and 1/2, respectively. For smaller values of c/r, the increased stress is due to the thinness of the "arch" over the hole, whereas for larger values of c/r, the increased stress is due to the increased pressure created by the material above.

An arbitrary SCF may be defined as $K_t = \sigma_{\max}/p = \sigma_{\max}/(-cw)$, where p = hydrostatic pressure, equal to $-cw$. Chart 4.77 may be converted to K_t as shown in Chart 4.78 by dividing $\sigma_{\max}/2wr$ ordinates of Chart 4.77 by $c/2r$, half of the abscissa values of Chart Chart 4.77. It is seen from Chart 4.78 that for a large value of c/r, K_t approaches 2, the well-known K_t for a hole in a hydrostatic or biaxial stress field.

For a deep tunnel with a large c/r (Mindlin 1939),

$$\sigma_{\max} = -2cw - rw\left[\frac{3-4v}{2(1-v)}\right] \tag{4.98}$$

By writing (rw) as $(r/c)(cw)$, we can factor out $(-cw)$ to obtain,

$$K_t = \frac{\sigma_{\max}}{-cw} = 2 + \frac{1}{c/r}\left[\frac{3-4v}{2(1-v)}\right] \tag{4.99}$$

The second term arises from the weight of the material removed from the hole. As c/r becomes large, this term becomes negligible and K_t approaches 2 as indicated in Chart 4.78. The solutions for various tunnel shapes (circular, elliptical, rounded square) at depths not influenced by the surface have been obtained with and without a rigid liner (Yu 1952).

4.6.3 Intersecting Cylindrical Holes

The intersecting cylindrical holes (Riley 1964) are in the form of a cross (+), a tee (T), or a round-cornered ell (L) with the plane containing the hole axes perpendicular to the applied uniaxial stress (Fig. 4.31). This case is of interest in tunnel design and in various geometrical arrangements of fluid ducting in machinery.

Three-dimensional photoelastic tests by Riley are made of an axially compressed cylinder with these intersecting cylindrical hole forms located with the hole axes in a midplane perpendicular to the applied uniaxial stress. The cylinder is 8 in. in diameter, and all holes are 1.5 in. in diameter. The maximum nominal stress concentration factor K_{tn} (see Chart 4.66 for a definition of K_{tn}) for the three intersection forms is found to be 3.6, corresponding to the maximum tangential stress at the intersection of the holes at the plane containing the hole axes.

The K_{tn} value of 3.6, based on nominal stress, applies only for the tested cylinder. A more useful value is an estimated $K_{t\infty}$ in an infinite body. We attempt to obtain this value as follows.

Firstly, it is observed that K_{tn} for the cylindrical hole away from the intersection is 2.3. The gross (applied) SCF is $K_{tg} = K_{tn}/(A_{\text{net}}/A) = 2.3/(0.665) = 3.46$ for the T intersection (A = cross-sectional area of cylinder, A_{net} = cross-sectional area in plane of hole axes). Referring to Chart 4.1, it is seen that for $d/H = 1 - 0.665 = 0.335$, the same values of $K_{tn} = 2.3$ and $K_{tg} = 3.46$ are obtained and that the $K_{t\infty}$ value for the infinite width, $d/H \to 0$, is 3. The agreement is not as close for the cross and L geometries, as there is about 6% deviation.

Secondly, we start with $K_{tn} = 3.6$ and make the assumption that $K_{t\infty}/K_{tn}$ is the same as in Chart 4.1 for the same d/H. $K_{t\infty} = 3.6(3/2.3) = 4.7$. This estimate is more useful generally than the specific test geometry value $K_{tn} = 3.6$.

Riley (1964) points out that the stresses are highly localized at the intersection, decreasing to the value of the cylindrical hole within an axial distance equal to the hole diameter. Also noted is the small value of the axial stresses.

The experimental determination of the maximum stress at the very steep stress gradient at the sharp corner is difficult. It may be that the value just given is too low. For example, $K_{t\infty}$ for the intersection of a small hole into a large one would theoretically[1] be 9.

[1]The situation with respect to multiplying of stress concentration factors is somewhat similar to the case discussed in Section 4.5.2 and illustrated in Chart 4.60.

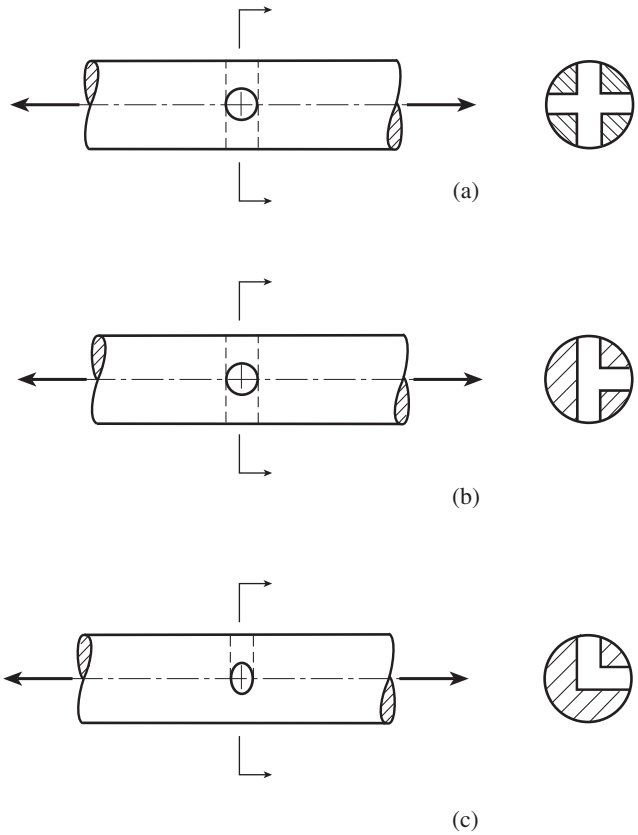


Figure 4.31 Intersecting holes in cylinder: (*a*) cross hole; (*b*) T hole; (*c*) round-cornered L hole.

It seems that a rounded corner at the intersection (in the plane of the hole axes) would be beneficial in reducing K_t. This would be a practical expedient in the case of a tunnel or a cast metal part, but it does not seem to be practically attainable in the case where the holes have been drilled. An investigation of three-dimensional photoelastic models with the varied corner radius would be of interest. There have been several studies of pressurized systems with intersecting cylinders. In particular, pressurized hollow thick cylinders and square blocks with crossbores in the side walls are discussed in later sections.

4.6.4 Rotating Disk with a Hole

For a rotating disk with a central hole, the maximum stress is tangential (circumferential) occurring at the edge of the hole (Robinson 1944; Timoshenko 1956; Pilkey 2005),

$$\sigma_{\max} = \frac{\gamma\Omega^2}{g}\left(\frac{3+\nu}{4}\right)\left[R_2^2 + \left(\frac{1-\nu}{3+\nu}\right)R_1^2\right] \tag{4.100}$$

where γ is the weight per unit volume, Ω is the angular velocity of rotation (rad/s), g is the gravitational acceleration, v is Poisson's ratio, R_1 is the hole radius, R_2 is the outer radius of the disk. Note that for a thin ring, $R_1/R_2 = 1$, $\sigma_{\max} = (\gamma\Omega^2/g)R_2^2$.

The K_t factor can be defined in several ways, depending on the choice of nominal stress:

(1) σ_{Na} is the stress at the center of a disk without a hole. At radius $(R_1 + R_2)/2$ where both the radial and tangential stress reach the same maximum value,

$$\sigma_{Na} = \frac{\gamma\Omega^2}{g}\left(\frac{3+v}{8}\right)R_2^2 \tag{4.101}$$

The use of this nominal stress results in the top curve of Chart 4.79. This curve gives a reasonable result for a small hole; for example, for $R_1/R_2 \to 0$, $K_{ta} = 2$. However, as R_1/R_2 approaches 1.0 (thin ring), the higher factor is not realistic.

(2) σ_{Nb} is the average tangential stress:

$$\sigma_{Nb} = \frac{\gamma\Omega^2}{3g}\left(1 + \frac{R_1}{R_2} + \frac{R_1^2}{R_2^2}\right)R_2^2 \tag{4.102}$$

The use of this nominal stress results in a more reasonable relationship, giving $K_t = 1$ for the thin ring. However, for a small hole, Eq. (4.101) appears preferable.

(3) The curve of σ_{Nb} is adjusted to fit linearly the end conditions at $R_1/R_2 = 0$ and at $R_1/R_2 = 1.0$ and σ_{Nb} becomes

$$\sigma_{Nc} = \frac{\gamma\Omega^2}{3g}\left(1 + \frac{R_1}{R_2} + \frac{R_1^2}{R_2^2}\right)\left[3\left(\frac{3+v}{8}\right)\left(1 - \frac{R_1}{R_2}\right) + \frac{R_1}{R_2}\right]R_2^2 \tag{4.103}$$

For a small central hole, Eq. (4.101) will be satisfactory for most purposes. For larger holes and in cases where notch sensitivity (Section 1.9) is involved, Eq. (4.103) is suggested.

For a rotating disk with a noncentral hole, photoelastic results are available for variable radial locations for two sizes of hole (Barnhart et al. 1951). Here, the nominal stress σ_N is taken as the tangential stress in a solid disk at a point corresponding to the outermost point (marked A, Chart 4.80) of the hole. Since the holes in this case are small relative to the disk diameter, this is a reasonable procedure.

$$\sigma_{Nc} = \frac{\gamma\Omega^2}{g}\left(\frac{3+v}{8}\right)\left[1 - \left(\frac{1+3v}{3+v}\right)\left(\frac{R_A}{R_2}\right)^2\right]R_2^2 \tag{4.104}$$

The same investigation (Barnhart et al. 1951) covers the cases of a disk with six to ten noncentral holes located on a common circle, as well as a central hole. Heténi (1939a,b) investigates the special cases of a rotating disk containing a central hole plus two or eight symmetrically disposed noncentral holes.

The similar investigations (Leist and Weber 1956; Green et al. 1964; Fessler and Thorpe 1967a,b) are made for a disk with a large number of symmetrical noncentral holes, such as is used in gas turbine disks. The optimum number of holes is found (Fessler and Thorpe 1967a) for various geometrical ratios. Reinforcement bosses do not reduce the peak stresses by a significant amount (Fessler and Thorp 1967b), but the use of a tapered disk does lower the peak stresses at the noncentral holes.

4.6.5 Ring or Hollow Roller

The case of a ring subjected to concentrated loads acting along a diametral line (Chart 4.81) has been solved mathematically for $R_1/R_2 = 1/2$ by Timoshenko (1922) and for $R_1/R_2 = 1/3$ by Billevicz (1931). An approximate theoretical solution is given by Case (1925). The photoelastic investigations are made by Horger and Buckwalter (1940) and Leven (1952). The values shown in Charts 4.81 and 4.82 represent the average of the photoelastic data and mathematical results, all of which are in a good agreement. For $K_t = \sigma_{\max}/\sigma_{\text{nom}}$, the maximum tensile stress is used for $\sigma_{\max}$, and for σ_{nom} the basic bending and tensile components as given by Timoshenko (1956) for a thin ring are used.

For the ring loaded internally (Chart 4.81),

$$K_t = \frac{\sigma_{\max A}[2h(R_2 - R_1)]}{P\left[1 + \frac{3(R_2+R_1)(1-2/\pi)}{R_2-R_1}\right]} \tag{4.105}$$

For the ring loaded externally (Chart 4.82),

$$K_t = \frac{\sigma_{\max B}[\pi h(R_2 - R_1)^2]}{3P(R_2 + R_1)} \tag{4.106}$$

The case of a round-cornered square hole in a cylinder subjected to opposite concentrated loads has been analyzed by Seika (1958).

4.6.6 Pressurized Cylinder

The Lamé solution (Pilkey 2005) for the circumferential (tangential or hoop) stress in a cylinder with internal pressure p is

$$\sigma_{\max} = \frac{p(R_1^2 + R_2^2)}{(R_2^2 - R_1^2)} = p\frac{(R_2/R_1)^2 + 1}{(R_2/R_1)^2 - 1} = p\frac{(R_1/R_2)^2 + 1}{1 - (R_1/R_2)^2} \tag{4.107}$$

where p is the pressure, R_1 is the inside radius, and R_2 is the outside radius. The two K_t relations of Chart 4.83 are

$$\begin{aligned} K_{t1} &= \frac{\sigma_{\max}}{\sigma_{\text{nom}}} = \frac{\sigma_{\max}}{\sigma_{av}} \\ K_{t1} &= \frac{(R_1/R_2)^2 + 1}{(R_1/R_2)^2 + R_1/R_2} \end{aligned} \tag{4.108}$$

and

$$K_{t2} = \frac{\sigma_{\max}}{p}$$
$$K_{t2} = \frac{(R_1/R_2)^2 + 1}{1 - (R_1/R_2)^2} \tag{4.109}$$

At $R_1/R_2 = 1/2$, the K_t factors are equal, $K_t = 1.666$. The branches of the curves below $K_t = 1.666$ are regarded as more meaningful when applied to analysis of mechanics of materials problems.

4.6.7 Pressurized Hollow Thick Cylinder with a Circular Hole in the Cylinder Wall

The pressurized thick cylinders with wall holes are encountered frequently in the high-pressure equipment industry. Crossbores in the side walls of pressure vessels can cause significant stress concentrations that can lower the ability to withstand fatigue loading. Consider crossbores that are circular in cross section (Fig. 4.32).

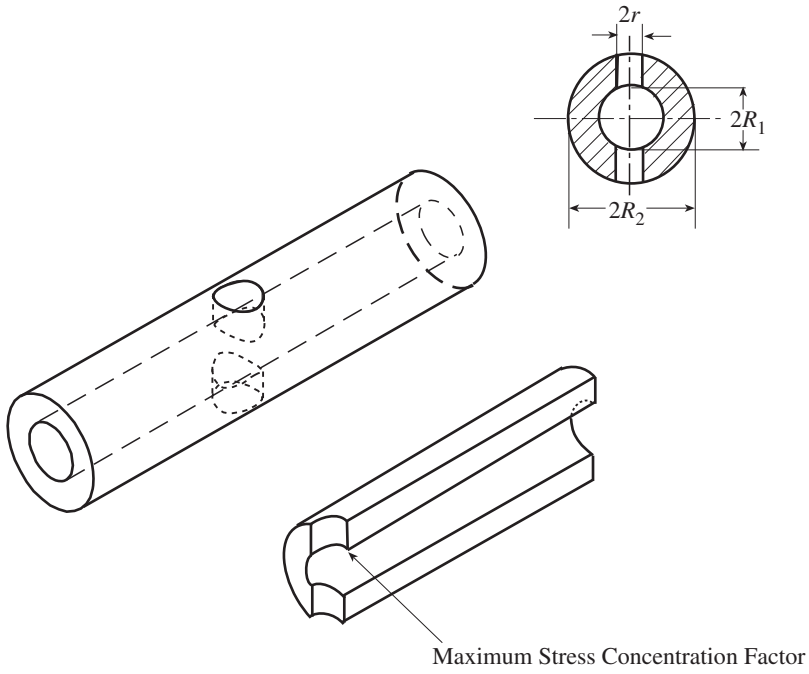


Figure 4.32 Pressurized thick cylinder with a circular crosshole.

The maximum Lamé circumferential (hoop) stress in a thick cylinder with internal pressure p is given by Eq. (4.107). The hoop stress concentration factor is the ratio of the maximum stress at the surface of the hole in the cylinder at the intersection of the crossbore to the maximum Lamé hoop stress at the hole of a cylinder without a crossbore. That is,

$$K_t = \frac{\sigma_{\max}}{\sigma_{\text{Lamé hoop}}} = \frac{\sigma_{\max}}{p\left[\frac{(R_2/R_1)^2+1}{(R_2/R_1)^2-1}\right]} \tag{4.110}$$

The stress concentration factors of Chart 4.84 are generated using finite elements (Dixon et al. 2002) for closed-end thick cylinders. They compare, in depth, the finite element results with the existing literature. For example, it is found that the photoelastic studies of Gerdeen (1972) show somewhat different trends than displayed in Chart 4.84, as do the photoelastic results of Yamamoto and Terada (2000) and the work of Lapsley and MacKensie (1997). Gerdeen also gives the K_t factors for a press-fitted cylinder on an unpressurized cylinder with a sidehole or with a crosshole.

Strain gage measurements (Gerdeen and Smith 1972) on pressurized thick-walled cylinders with well-rounded crossholes result in minimum K_t factors (1.0 to 1.1) when the holes are of equal diameter (K_t defined by Eq. 4.110). The fatigue failures in compressor heads have been reduced by making the holes of equal diameter and using larger intersection radii.

The shear stress concentration can occur at the surface of the intersection of the crossbore and the hole of the primary cylinder. Chart 4.85 gives the shear SCFs calculated using a finite element analysis (Dixon et al. 2002).

4.6.8 Pressurized Hollow Thick Square Block with a Circular Hole in the Wall

The stress concentration in the stress fields are caused by a crossbore in a closed-end, thick-walled, long hollow block with a square cross section (Fig. 4.33). Finite element solutions for hoop stress concentration factors, as described in Dixon et al. (2002), where pressure is applied to all internal surfaces, are given in Chart 4.86 with the notation as shown in Fig. 4.33, where the location of the SCF is identified. Chart 4.87 provides the shear SCFs. For $R_2/R_1 \leq 2$, the SCFs for blocks are slightly greater than those for cylinders (Charts 4.86 and 4.87). For $R_2/R_1 > 2$, the SCFs for blocks and cylinders with crossbores are virtually the same.

Badr (2006) develop a hoop stress concentration factors for elliptic crossbores in blocks with rectangular cross sections and showed that the hoop stress concentration factors at the crossbore intersections are smaller for elliptic crossbores than for circular crossbores.

4.6.9 Other Configurations

The photoelastic tests led to the SCFs for star-shaped holes in an element under external pressure (Fourney and Parmerter 1961, 1963, 1966). Other photoelastic tests are applied to a tension panel with nuclear reactor hole patterns (Mondina and Falco 1972). These results are treated in Peterson (1974).

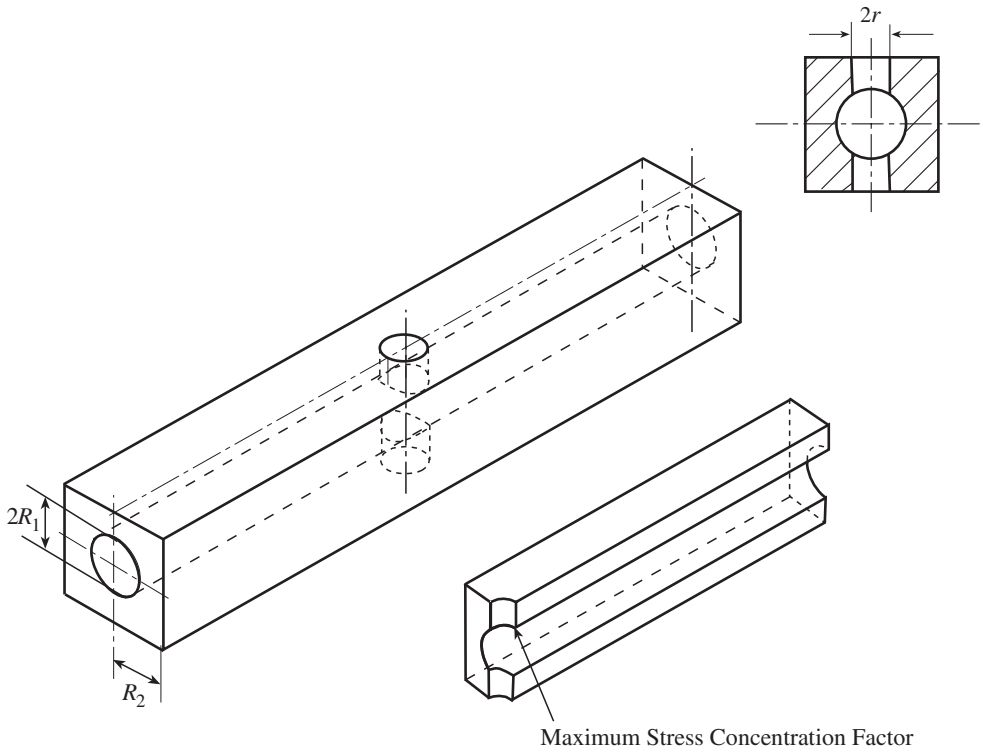


Figure 4.33 Pressurized hollow thick square block with a circular hole in the wall.

4.7 ORTHOTROPIC THIN MEMBERS

4.7.1 Orthotropic Panel with an Elliptical Hole

Tan (1994) derived several formulas for the SCF for an orthotropic panel subject to uniaxial tension with an elliptical hole (Fig. 4.34). A viable approximate expression valid for the range $0 \le b/a \le 1$ is

$$\frac{K_{t\infty}}{K_{tg}} = \frac{\lambda^2}{(1-\lambda)^2} + \frac{1-2\lambda}{(1-\lambda)^2}\sqrt{1+(\lambda^2-1)(2a/H)^2} - \frac{\lambda^2(2a/H)^2}{(1-\lambda)\sqrt{1+(\lambda^2-1)(2a/H)^2}}$$
$$+\frac{\lambda^7}{2}\left(\frac{2a}{H}\right)^6\left(K_{t\infty}-1-\frac{2}{\lambda}\right)\left\{\left[1+(\lambda^2-1)\left(\frac{2a}{H}\right)^2\right]^{-5/2}\right.$$
$$\left.-\left(\frac{2a}{H}\right)^2\left[1+(\lambda^2-1)\left(\frac{2a}{H}\right)^2\right]^{-7/2}\right\} \tag{4.111}$$

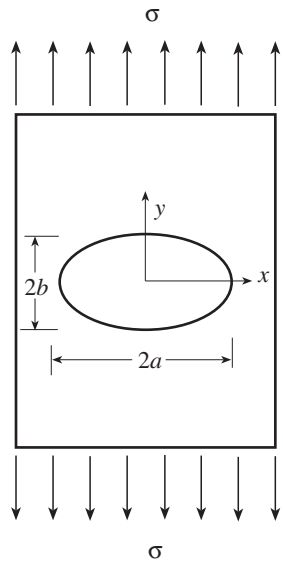


Figure 4.34 Finite-width panel subjected to tension with a central elliptical hole.

where $\lambda = b/a$ and $K_{t\infty}$ is the SCF for a panel of infinite width. For a laminate panel, Tan gives

$$K_{t\infty} = 1 + \frac{1}{\lambda}\sqrt{\frac{2}{A_{66}}\left(\sqrt{A_{11}A_{22}} - A_{12} + \frac{A_{11}A_{22} - A_{12}^2}{2A_{66}}\right)} \tag{4.112}$$

where A_{ij} denotes the effective laminate in-plane stiffnesses with 1 and 2 parallel and perpendicular to the loading directions, respectively. Consult a reference such as Tan (1994) or Barbero (1998) on laminated composites for details on the definitions of A_{ij}.

In terms of the familiar material constants, Eq. (4.112) can be expressed as

$$K_{t\infty} = 1 + \frac{1}{\lambda}\sqrt{2\left(\sqrt{\frac{E_x}{E_y}} - \nu_{xy} + \frac{E_x}{2G_{xy}}\right)} \tag{4.113}$$

where E_x and E_y are Young's moduli in the x and y directions and G_{xy} and ν_{xy} are the shear modulus and Poisson's ratio in the x, y plane. The equivalent moduli of Eq. (4.113) of the laminate are given in the literature (Barbero 1998) in terms of A_{ij}. If the laminate is quasi-isotropic, $E_x = E_y = E$, $G_{xy} = G$, and $\nu_{xy} = \nu$.

The approximate K_{tn} can be obtained from the relationship between the net and gross concentration factors

$$K_{tn} = K_{tg}\left(1 - \frac{2a}{H}\right) \tag{4.114}$$

4.7.2 Orthotropic Panel with a Circular Hole

For a circular hole, with $\lambda = b/a = 1$, Eq. (4.111) reduces to

$$\frac{K_{t\infty}}{K_{tg}} = \frac{2 - (2a/H)^2 - (2a/H)^4}{2} + \frac{(2a/H)^6(K_{t\infty} - 3)[1 - (2a/H)^2]}{2} \tag{4.115}$$

with $2a = d$, Eq. (4.114) corresponds to Eq. (4.3).

4.7.3 Orthotropic Panel with a Crack

To represent a crack, let $\lambda = b/a = 0$. Then Eq. (4.111) reduces to

$$\frac{K_{t\infty}}{K_{tg}} = \sqrt{1 - \left(\frac{2a}{H}\right)^2} \tag{4.116}$$

which is independent of the material properties. Equation (4.116) is the same as the formula derived by Dixon (1960) for a crack in a panel loaded in tension.

4.7.4 Isotropic Panel with an Elliptical Hole

For an isotropic panel with an elliptical opening and uniaxial tension, Eq. (4.57) gives $K_{t\infty} = 1 + 2\lambda$ for an infinite-width panel. Substitution of this expression into Eq. (4.111) gives

$$\begin{aligned}\frac{K_{t\infty}}{K_{tg}} = {} & \frac{\lambda^2}{(1-\lambda)^2} + \frac{1 - 2\lambda}{(1-\lambda)^2}\sqrt{1 + (\lambda^2 - 1)\left(\frac{2a}{H}\right)^2} \\ & - \frac{\lambda^2}{1-\lambda}\left(\frac{2a}{H}\right)^2\left[1 + (\lambda^2 - 1)\left(\frac{2a}{H}\right)^2\right]^{-1/2}\end{aligned} \tag{4.117}$$

4.7.5 Isotropic Panel with a Circular Hole

For a circular hole ($\lambda = b/a = 1$), from Eq. (4.117),

$$\frac{K_{t\infty}}{K_{tg}} = \frac{2 - (2a/H)^2 - (2a/H)^4}{2} \tag{4.118}$$

The net stress concentration factor K_{tn} is obtained using Eq. (4.114). Equation (4.117) applies to an isotropic panel with a crack.

4.7.6 More Accurate Theory for $a/b < 4$

Tan (1994) shows that the SCFs above are more accurate for $a/b \geq 4$ than for $a/b < 4$. An improved $K_{t\infty}/K_{tg}$ for an ellipse with $a/b < 4$ is shown to be

$$\begin{aligned}\frac{K_{t\infty}}{K_{tg}} &= \frac{\lambda^2}{(1-\lambda)^2} + \frac{1-2\lambda}{(1-\lambda)^2}\sqrt{1+(\lambda^2-1)\left(\frac{2a}{H}M\right)^2} \\ &\quad -\frac{\lambda^2}{1-\lambda}\left(\frac{2a}{H}M\right)^2\left[1+(\lambda^2-1)\left(\frac{2a}{H}M\right)^2\right]^{-1/2} \\ &\quad +\frac{\lambda^7}{2}\left(\frac{2a}{H}M\right)^6\left(K_{t\infty}-1-\frac{2}{\lambda}\right)\left\{\left[1+(\lambda^2-1)\left(\frac{2a}{H}M\right)^2\right]^{-5/2}\right. \\ &\quad \left.-\left(\frac{2a}{H}M\right)^2\left[1+(\lambda^2-1)\left(\frac{2a}{H}M\right)^2\right]^{-7/2}\right\} \end{aligned} \tag{4.119}$$

where M is a magnification factor given by

$$M^2 = \frac{\sqrt{1-8\left[\frac{3(1-2a/H)}{2+(1-2a/H)^3}-1\right]}-1}{2(2a/H)^2} \tag{4.120}$$

For a circular hole with $\lambda = b/a = 1$, Eq. (4.119) reduces to

$$\frac{K_{t\infty}}{K_{tg}} = \frac{3(1-2a/H)}{2+(1-2a/H)^3} + \frac{1}{2}\left(\frac{2a}{H}M\right)^6(K_{t\infty}-3)\left[1-\left(\frac{2a}{H}M\right)^2\right] \tag{4.121}$$

For an isotropic panel, the more accurate theory for $a/b < 4$ becomes

$$\begin{aligned}\frac{K_{t\infty}}{K_{tg}} &= \frac{\lambda^2}{(1-\lambda)^2} + \frac{1-2\lambda}{(1-\lambda)^2}\sqrt{1+(\lambda^2-1)\left(\frac{2a}{H}M\right)^2} \\ &\quad -\frac{\lambda^2}{1-\lambda}\left(\frac{2a}{H}M\right)^2\left[1+(\lambda^2-1)\left(\frac{2a}{H}M\right)^2\right]^{-1/2}\end{aligned} \tag{4.122}$$

For a circular hole when $\lambda = b/a = 1$, Eq. (4.122) simplifies to

$$\frac{K_{t\infty}}{K_{tg}} = \frac{3(1-2a/H)}{2+(1-2a/H)^3} \tag{4.123}$$

which corresponds to the Heywood formula of Eqs. (4.9) and (4.10).

4.8 BENDING

Several bending problems for beams and plates are to be considered in Fig. 4.35. For plate bending, two cases are of particular interest: (1) simple bending with $M_1 = M, M_2 = 0$ or in normalized form $M_1 = 1, M_2 = 0$; and (2) cylindrical bending with $M_1 = M, M_2 = \nu M$, or $M_1 = 1, M_2 = \nu$.

The plate bending moments M_1, M_2, and M are uniformly distributed with dimensions of moment per unit length. The cylindrical bending case removes the anticlastic bending resulting from the Poisson's ratio effect. At the beginning of application of bending, the simple condition occurs. As the deflection increases, the anticlastic effect is not realized, except for a slight curling at the edges. In the region of the hole, it is reasonable to assume that the cylindrical bending condition exists. For design problems the cylindrical bending case is generally more applicable than the simple bending case.

It seems that for transverse bending, rounding or chamfering of the hole edge would reduce the stress concentration factor.

For $M_1 = M_2$, isotropic transverse bending, K_t is independent of d/h, the diameter of a hole over the thickness of a plate. This case corresponds to in-plane biaxial tension of a thin element with a hole.

4.8.1 Bending of a Beam with a Central Hole

An effective method of weight reduction for a beam in bending is to remove material near the neutral axis, often in the form of a circular hole or a row of circular holes. Howland and Stevenson (1933) have obtained the K_{tg} values mathematically for a single hole represented by the curve of Chart 4.88,

$$K_{tg} = \frac{\sigma_{\max}}{6M/(H^2 h)} \tag{4.124}$$

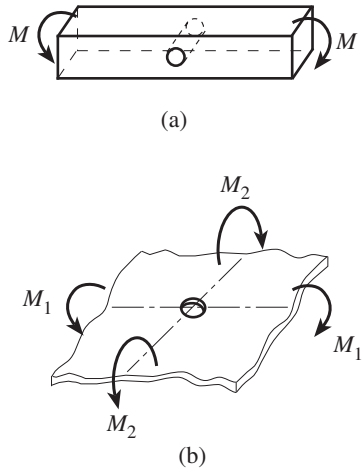


Figure 4.35 Transverse bending of beam and plate: (*a*) beam; (*b*) plate.

For a beam M is the net moment on a cross section. The units of M for a beam are force · length. The symbols are defined in Chart 4.88. The stress concentration factor K_{tg} is the ratio of $\sigma_{\max}$ to σ at the beam edge distant axially from the hole. The photoelastic tests by Ryan and Fischer (1938) and by Frocht and Leven (1951) are in a good agreement with Howland and Stevenson's mathematical results.

The factor K_{tn} is based on the section modulus of the net section. The distance from the neutral axis is taken as $d/2$, so that σ_{nom} is at the edge of the hole.

$$K_{tn} = \frac{\sigma_{\max}}{6Md/[(H^3 - d^3)h]} \tag{4.125}$$

Another form of K_{tn} has been used where σ_{nom} is at the edge of the beam.

$$K'_{tn} = \frac{\sigma_{\max}}{6MH/[(H^3 - d^3)h]} \tag{4.126}$$

The factor K'_{tn} of Eq. (4.126) and Chart 4.88 appears to be a linear function of d/H. Also K'_{tn} is equal to $2d/H$, prompting Heywood (1952) to comment that this configuration has the "curious result that the stress concentration factor is independent of the relative size of the hole, and forms the only known case of a notch showing such independency."

Note from Chart 4.88 that the hole does not weaken the beam for $d/H <\sim 0.45$. For design purposes, $K_{tg} = 1$ for $d/H <\sim 0.45$.

On the outer edge, the stress has peaks at A, A. However, this stress is less than at B, except at and to the left of a transition zone in the region of C where $K_t = 1$ is approached. The angle $\alpha = 30°$ is found to be independent of $d/(H - d)$ over the investigated range.

4.8.2 Bending of a Beam with a Circular Hole Displaced from the Center Line

The K_{tg} factor, as defined by Eq. (4.124), has been obtained by Isida (1952) for the case of an eccentrically located hole and is shown in Chart 4.89. At line $C-C$, $K_{tgB} = K_{tgA}$, corresponding to the maximum stress at B and A, respectively (see the sketch in Chart 4.89). Above $C-C$, K_{tgB} is the greater of the two stresses. Below $C-C$, K_{tgA} is the greater, approaching $K_{tg} = 1$ or no effect of the hole.

At $c/e = 1$, the hole is central, with factors as given in the preceding subsection (Chart 4.88). For $a/c \to 0$, K_{tg} is 3 multiplied by the ratio of the distance from the center line to the edge, in terms of c/e:

$$K_{tg} = 3\frac{1 - c/e}{1 + c/e} \tag{4.127}$$

The calculated values of Isida (1952) are in agreement with the photoelastic results of Nishida (1952).

4.8.3 Curved Beams with Circular Holes

Paloto et al. (2003) provide the SCFs for flat curved elements under bending loads with circular holes near the edges. They show the influence of the curvature on the stress concentration factors. They developed both stress concentration factor curves and analytical expressions.

4.8.4 Bending of a Beam with an Elliptical Hole; Slot with Semicircular Ends (Ovaloid); or Round-Cornered Square Hole

The K_{tn} factors for an ellipse as defined by Eq. (4.126) are obtained by Isida (1953). These factors have been recalculated for K_{tg} of Eq. (4.98), and for K_{tn} of Eq. (4.99), and are presented in Chart 4.90. The photoelastic values of Frocht and Leven (1951) for a slot with semicircular ends are in reasonably good agreement when compared with an ellipse having the same a/r.

Note in Chart 4.90 that the hole does not weaken the beam for a/H values less than at points C, D, and E for $a/r = 4$, 2, and 1, respectively. For design, use $K_t = 1$ to the left of the intersection points.

On the outer edge, the stress has peaks at A, A. But this stress is less than at B, except at and to the left of a transition zone in the region of C, D, and E, where $K_t = 1$ is approached. In the photoelastic tests (Frocht and Leven 1951), the angles $\alpha = 35^\circ$, 32.5°, and 30° for $a/r = 4$, 2, and 1, respectively, are found to be independent of the $a/(H - 2a)$ over the investigated range.

For the shapes approximating ovaloids and round-cornered square holes (parallel and at 45°), K'_{tg} factors are obtained (Joseph and Brock 1950) for central holes that are small compared to the beam depth

$$K'_{tg} = \frac{\sigma_{\max}}{12Ma/(H^3 h)} \tag{4.128}$$

4.8.5 Bending of an Infinite- and a Finite-Width Plate with a Single Circular Hole

For simple bending ($M_1 = 1$, $M_2 = 0$) of an infinite plate with a circular hole, Reissner (1945) obtains K_t as a function of d/h as shown in Chart 4.91.

For $d/h \to 0$, $K_t = 3$.

For $d/h \to \infty$,

$$K_t = \frac{5 + 3\nu}{3 + \nu} \tag{4.129}$$

giving $K_t = 1.788$ when $\nu = 0.3$.

For cylindrical bending ($M = 1$, $M_2 = \nu$) of an infinite plate, $K_t = 2.7$ as $d/h \to 0$.

For $d/h \to \infty$, Goodier (1936) obtains

$$K_t = (5 - \nu)\frac{1 + \nu}{3 + \nu} \tag{4.130}$$

or $K_t = 1.852$ for $\nu = 0.3$.

For design problems, the cylindrical bending case is usually more applicable. For $M_1 = M_2$ under isotropic bending, K_t is independent of d/h, and the case corresponds to biaxial tension of a panel with a hole.

For a finite width plate and various d/h values, K_t is given in Chart 4.92, based on Charts 4.1 and 4.91 with the K_{tn} gradient at $d/H = 0$ equal to

$$\frac{\Delta K_{tn}}{\Delta(d/H)} = -K_{tn} \tag{4.131}$$

The photoelastic tests (Goodier and Lee 1941; Drucker 1942) and strain gage measurements (Dumont 1939) are in a reasonably good agreement with Chart 4.92.

4.8.6 Bending of an Infinite Plate with a Row of Circular Holes

For an infinite plate with a row of circular holes, Tamate (1957) has obtained K_t values for simple bending ($M_1 = 1, M_2 = 0$) and for cylindrical bending ($M_1 = 1, M_2 = v$) with M_1 bending in the x and y directions (Chart 4.93). For design problems, the cylindrical bending case is usually more applicable. The K_t value for $d/l \to 0$ corresponds to the single hole (Chart 4.91). The dashed curve is for two holes (Tamate 1958) in a plate subjected to simple bending ($M_1 = 1, M_2 = 0$).

For bending about the x direction, nominal stresses are used in Chart 4.93, resulting in the K_{tn} curves that decrease as d/l increases. On the other hand, the K_{tg} value of $\sigma_{\max}/\sigma$ increases as d/l increases. The two factors are related by $K_{tg} = K_{tn}/(1 - d/l)$.

4.8.7 Bending of an Infinite Plate with a Single Elliptical Hole

The SCFs for the bending of an infinite plate with an elliptical hole (Neuber 1958; Nisitani 1968) are given in Chart 4.94.

For simple bending ($M_1 = 1, M_2 = 0$),

$$K_t = 1 + \frac{2(1 + v)(a/b)}{3 + v} \tag{4.132}$$

where a is the half width of ellipse perpendicular to M_1 bending direction (Chart 4.94), b is the half width of ellipse perpendicular to half width, a, and v is Poisson's ratio.

For cylindrical bending (Goodier 1936; Nisitani 1968) ($M_1 = 1, M_2 = v$),

$$K_t = \frac{(1 + v)[2(a/b) + 3 - v]}{3 + v} \tag{4.133}$$

For design problems, the cylindrical bending case is usually more applicable. For $M_1 = M_2$ subjected to isotropic bending, K_t is independent of a/h, and the case corresponds to in-plane biaxial tension of a thin element with a hole.

4.8.8 Bending of an Infinite Plate with a Row of Elliptical Holes

Chart 4.95 presents the effect of spacing (Nisitani 1968) for a row of elliptical holes in an infinite plate under bending. The stress concentration factor K_t values are given as a ratio of the single hole value (Chart 4.94). The ratios are so close for simple and cylindrical bending that these cases can be represented by a single set of curves (Chart 4.95). For bending about the y axis, a row of edge notches is obtained for $a/c \geq 0.5$. For bending about the x axis, the nominal stress is used, resulting in K_{tn} curves that decrease as a/c increases. Factor K_{tg} values, $\sigma_{\max}/\sigma$, increase as a/c increases, where $K_{tg} = K_{tn}/(1 - 2a/c)$.

4.8.9 Tube or Bar of Circular Cross Section with a Transverse Hole

The K_t relations for tubes or bars of circular cross section with a transverse (diametral) circular hole are presented in Chart 4.96. The curve for the solid shaft is based on blending the data of

Thum and Kirmser (1943) and the British data (Jessop et al. 1959; ESDU 1965). There is some uncertainty regarding the exact position of the dashed portion of the curve. A finite element study (ESDU 1989) verifies the accuracy of the solid line curves.

The photoelastic test by Fessler and Roberts (1961) is in a good agreement with Chart 4.96. The factors are defined as

$$K_{tg} = \frac{\sigma_{\max}}{\sigma_{\text{gross}}} = \frac{\sigma_{\max}}{M/Z_{\text{tube}}} = \frac{\sigma_{\max}}{MD/(2I_{\text{tube}})}$$
$$= \frac{\sigma_{\max}}{32MD/[\pi(D^4 - d_i^4)]} \tag{4.134}$$

$$K_{tn} = \frac{\sigma_{\max}}{\sigma_{\text{net}}} = \frac{\sigma_{\max}}{M/Z_{\text{net}}} = \frac{\sigma_{\max}}{Mc/I_{\text{net}}} \tag{4.135}$$

where $c = \sqrt{(D/2)^2 - (d/2)^2}$ and

$$K_{tn} = K_{tg}\frac{Z_{\text{net}}}{Z_{\text{tube}}} \tag{4.136}$$

The quantities Z_{tube} and Z_{net} are the gross and net section moduli ($\sigma = M/Z$). Other symbols are defined in Chart 4.96.

Thum and Kirmser (1943) find that the maximum stress do not occur on the surface of the shaft but at a small distance inside the hole on the surface of the hole. The $\sigma_{\max}$ value used in developing Chart 4.96 is the maximum stress inside the hole. No factors are given for the somewhat lower stress at the shaft surface. If these factors are of interest, Thum and Kirmser's work should be examined.

The ratio $Z_{\text{net}}/Z_{\text{tube}}$ has been determined mathematically (Peterson 1968), although the formulas will not be repeated here. Specific values can be obtained by dividing the Chart 4.96 values of K_{tn} by K_{tg}. If the hole is sufficiently small relative to the shaft diameter, the hole may be considered to be of square cross section with edge length d:

$$\frac{Z_{\text{net}}}{Z_{\text{tube}}} = 1 - \frac{(16/3\pi)(d/D)[1 - (d_i/D)^3]}{1 - (d_i/D)^4} \tag{4.137}$$

It can be seen from the bottom curves of Chart 4.96 that the error due to this approximation is small below $d/D = 0.2$.

4.9 SHEAR AND TORSION

4.9.1 Shear Stressing of an Infinite Thin Element with Circular or Elliptical Hole, Unreinforced and Reinforced

By the superposition of σ_1 and $\sigma_2 = -\sigma_1$ uniaxial stress distributions, the shear case $\tau = \sigma_1$ is obtained. For the circular hole, $K_t = \sigma_{\max}/\tau = 4$ is obtained from Eq. (4.69) for $a/b = 1, \sigma_2/\sigma_1 = -1$. This is also found in Chart 4.97, which treats an elliptical hole in an infinite panel subject to shear stress, at $a/b = 1$. Further $K_{ts} = \tau_{\max}/\tau = (\sigma_{\max}/2)/\tau = 2$.

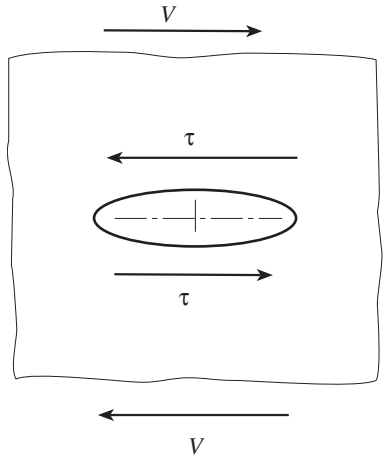


Figure 4.36 Elliptical hole subject to shear force.

For the elliptical hole, Chart 4.97 shows K_t for shear stress orientations in line with the ellipse axes (Godfrey 1959) and at 45° to the axes. The 45° case corresponds to $\sigma_2 = -\sigma_1 = \tau$, as obtained from Eq. (4.66).

The case of shearing forces parallel to the major axis of the elliptical hole, with the shearing force couple counterbalanced by a symmetrical remotely located opposite couple (Fig. 4.36), is solved by Neuber (1958). The Neuber's K_t factors are higher than the parallel shear factors in Chart 4.97. For example, for a circle the "shearing force" K_t factor (Neuber 1958) is 6 as compared to 4 in Chart 4.97.

For symmetrically reinforced elliptical holes, Chart 4.98 provides SCFs for pure shear stresses. The quantity A_r is the cross-sectional area of the reinforcement.

4.9.2 Shear Stressing of an Infinite Thin Element with a Round-Cornered Rectangular Hole, Unreinforced and Reinforced

In Chart 4.99, $K_t = \sigma_{\max}/\tau$ is given for shear stresses in line with the round-cornered rectangular hole axes (Sobey 1963; ESDU 1970). In Chart 4.62*d*, $\sigma_2 = -\sigma_1$ is equivalent to shear stress τ at 45° to the hole axes (Heller et al. 1958; Heller 1969).

For symmetrically reinforced square holes, the K_t is shown in Chart 4.100 (Sobey 1968; ESDU 1981). The stress is based on the von Mises stress. The maximum stresses occur at the corner.

4.9.3 Two Circular Holes of Unequal Diameter in a Thin Element in Pure Shear

The SCFs are developed for two circular holes in panels in pure shear. The values for K_{tg} are obtained by Haddon (1967). Charts 4.101*a* and 4.101*b* show the K_{tg} curves. These charts are useful in considering SCFs of neighboring cavities of different sizes. Two sets of curves are provided for the larger hole and the smaller hole, respectively.

4.9.4 Shear Stressing of an Infinite Thin Element with Two Circular Holes or a Row of Circular Holes

For an infinite thin element with a row of circular holes, Chart 4.102 presents $K_t = \sigma_{\max}/\tau$ for shear stresses in line with the hole axis (Meijers 1967; Barrett et al. 1971). The location of $\sigma_{\max}$ varies from $\theta = 0^\circ$ for $l/d \to 1$ to $\theta = 45^\circ$ for $l/d \to \infty$.

4.9.5 Shear Stressing of an Infinite Thin Element with an Infinite Pattern of Circular Holes

In Chart 4.103 for infinite thin elements, $K_t = \sigma_{\max}/\tau$ is given for square and equilateral triangular patterns of circular holes for shear stressing in line with the pattern axis (Sampson 1960; Bailey and Hicks 1960; O'Donnell 1967; Meijers 1967). Subsequent computed values (Hooke 1968; Grigolyuk and Fil'shtinskii 1970) are in a good agreement with Meijers's results. Note that $\sigma_2 = -\sigma_1$ is equivalent to shear stressing τ at 45° to the pattern axis in Chart 4.41.

In Charts 4.104 and 4.105, $K_t = \sigma_{\max}/\tau$ is given for rectangular and diamond (triangular, not limited to equilateral) patterns (Meijers 1967), respectively.

4.9.6 Twisted Infinite Plate with a Circular Hole

In Chart 4.106, $M_x = 1$, $M_y = -1$ corresponds to a twisted plate (Reissner 1945). $K_t = \sigma_{\max}/\sigma$, where σ is due to bending moment M_x. For $h/d \to \infty$ ($d/h \to 0$), $K_t = 4$. For $d/h \to \infty$,

$$K_t = 1 + \frac{1 + 3\nu}{3 + \nu} \tag{4.138}$$

giving $K_t = 1.575$ for $\nu = 0.3$.

4.9.7 Torsion of a Cylindrical Shell with a Circular Hole

Some SCFs for the torsion of a cylindrical shell with a circular hole are given in Chart 4.107. (For a discussion of the parameters, see Section 4.3.4.) The K_t factors (Van Dyke 1965) of Chart 4.107 are compared with experimental results (Houghton and Rothwell 1962; Lekkerkerker 1964), with a reasonably good agreement.

4.9.8 Torsion of a Tube or Bar of Circular Cross Section with a Transverse Circular Hole

For the torsion of a tube or bar of solid circular cross section with a circular hole through the tube or bar, the SCFs of Chart 4.108 are based on the photoelastic tests by Jessop et al. (1959) and ESDU (1965) and the strain gage tests by Thum and Kirmser (1943). The SCFs for K_{tg} are checked with finite element analyses by ESDU (1989). The factors are defined as,

$$K_{tg} = \frac{\sigma_{\max}}{\tau_{\text{gross}}} = \frac{\sigma_{\max}}{TD/(2J_{\text{tube}})} = \frac{\sigma_{\max}}{16TD/[\pi(D^4 - d_i^4)]} \tag{4.139}$$

$$K_{tn} = \frac{\sigma_{\max}}{\tau_{\text{net}}} = \frac{\sigma_{\max}}{TD/(2J_{\text{net}})} = K_{tg}\frac{J_{\text{net}}}{J_{\text{tube}}} \tag{4.140}$$

Other symbols are defined in Chart 4.108. The quantities J_{tube} and J_{net} are the gross and net polar moments of inertia, or in some cases the torsional constants.

Thum and Kirmser (1943) find that the maximum stress do not occur on the surface of the shaft but at a small distance inside the hole on the surface of the hole. This has been corroborated by later investigators (Leven 1955; Jessop et al. 1959). In the chart here, $\sigma_{\max}$ denotes the maximum stress inside the hole. No stress concentration factors are given for the somewhat lower stress at the shaft surface. If they are of interest, they can be found in Leven and in Jessop et al. The case of $d/D = 0$ represents a flat panel, that is, a tube with an infinite radius of curvature. Chart 4.108 gives a stress concentration factor of 4 for the flat panel in shear with a circular hole.

The $J_{\text{net}}/J_{\text{tube}}$ ratios have been determined mathematically (Peterson 1968). Although the formulas and charts will not be repeated here, the specific values can be obtained by dividing the Chart 4.108 values of K_{tn} by K_{tg}. If the hole is sufficiently small relative to the shaft diameter, the hole may be considered to be of square cross section with edge length d, giving

$$\frac{J_{\text{net}}}{J_{\text{tube}}} = 1 - \frac{(8/3\pi)(d/D)\{[1 - (d_i/D)^3] + (d/D)^2[1 - (d_i/D)]\}}{1 - (d_i/D)^4} \tag{4.141}$$

The bottom curves of Chart 4.108 show that the error due to the foregoing approximation is small, below $d/D = 0.2$.

The maximum stress $\sigma_{\max}$ is uniaxial and the maximum shear stress $\tau_{\max} = \sigma_{\max}/2$ occurs at 45° from the tangential direction of $\sigma_{\max}$. The maximum shear SCF can be defined as

$$K_{tsg} = \frac{K_{tg}}{2} \tag{4.142}$$

$$K_{tsn} = \frac{K_{tn}}{2} \tag{4.143}$$

If in Chart 4.108, the ordinate values are divided by 2, the maximum shear SCFs will be represented.

Another SCF can be defined based on the equivalent stress of the applied system. The applied shear stress τ corresponds to principal stresses σ and $-\sigma$, 45° from the shear stress directions. The equivalent stress $\sigma_{\text{eq}} = \sqrt{3}\sigma$. The equivalent stress concentration factors are

$$K_{teg} = \frac{\sigma_{\max}}{\sigma_{\text{eq}}} = \frac{K_{tg}}{\sqrt{3}} \tag{4.144}$$

$$K_{ten} = \frac{K_{tn}}{\sqrt{3}} \tag{4.145}$$

Referring to Chart 4.108, the ordinate values divided by $\sqrt{3}$ give the corresponding K_{te} factors.

The SCFs from Eqs. (4.142) to (4.145) are useful in mechanics of materials problems where one wishes to determine the initial plastic condition. The case of a torsion cylinder with a central spherical cavity has been analyzed by Ling (1952).

ESDU (1989) provides a formula for the maximum stress when a transverse hole passes through a tube or rod subjected to simultaneous torsion, tension, and bending,

$$\sigma_{\max} = \frac{1}{3}(K_{\text{ten}}\sigma_{\text{nomten}} + K_{\text{bend}}\sigma_{\text{nombend}}) \times \left\{ 1 + 2\left[1 + \frac{9}{4}\left(\frac{K_{\text{tor}}\sigma_{\text{nomtor}}}{K_{\text{ten}}\sigma_{\text{nomten}} + K_{\text{bend}}\sigma_{\text{nombend}}} \right)^2 \right]^{1/2} \right\} \tag{4.146}$$

where the subscripts *ten*, *bend*, and *tor* refer to the gross SCFs of Charts 4.66, 4.87, and 4.99, respectively.

$$\sigma_{\text{nomten}} = \frac{4P}{\pi(D^2 - d_i^2)}$$

$$\sigma_{\text{nombend}} = \sigma_{\text{gross}} = \frac{32MD}{\pi(D^4 - d_i^4)}$$

$$\tau_{\text{nomtor}} = \tau_{\text{gross}} = \frac{16TD}{\pi(D^4 - d_i^4)}$$

If only tension and bending are present,

$$\sigma_{\max} = K_{\text{ten}}\sigma_{\text{nomten}} + K_{\text{bend}}\sigma_{\text{nombend}} \tag{4.147}$$

The location of the maximum stress is a function of the relative magnitude of the tension, bending, or torsion loadings.

REFERENCES

ASME, 1974, *ASME Boiler and Pressure Vessel Code: Pressure Vessels*, Section VIII, American Society of Mechanical Engineers, New York, p. 30.

Atsumi, A., 1958, Stress concentration in a strip under tension and containing an infinite row of semicircular notches, *Q. J. Mech. Appl. Math*., Vol. 11, p. 478.

Atsumi, A., 1960, Stresses in a circular cylinder having an infinite row of spherical cavities under tension, *Trans. ASME Appl. Mech. Sect*., Vol. 82, p. 87.

Badr, E.A., 2006, Stress concentration factors for pressurized elliptic crossbores in blocks, *Int. J. Pressure Vessels Piping*, Vol. 83, p. 442.

Bailey, R., and Hicks, R., 1960, Behavior of perforated plates under plane stress, *J. Mech. Eng. Sci*., Vol. 2, p. 143.

Barbero, E. J., 1998, *Introduction to Composite Materials Design*, Taylor & Francis, Philadelphia, PA.

Barnhart, K. E., Hale, A. L., and Meriam, J. L., 1951, Stresses in rotating disks due to noncentral holes, *Proc. Soc. Exp. Stress Anal*., Vol. 9, No. 1, p. 35.

Barrett, R. F., Seth, P. R., and Patel, G. C., 1971, Effect of two circular holes in a plate subjected to pure shear stress, *Trans. ASME Appl. Mech. Sect*., Vol. 93, p. 528.

Belie, R. G., and Appl., F. J., 1972, Stress concentration in tensile strips with large circular holes, *Exp. Mech*., Vol. 12, p. 190; discussion, 1973, Vol. 13, p. 255.

Beskin, L., 1944, Strengthening of circular holes in plates under edge forces, *Trans. ASME Appl. Mech. Sect*., Vol. 66, p. A-140.

Bickley, W. G., 1928, Distribution of stress round a circular hole in a plate, *Philos. Trans. R. Soc. (London) Ser. A*, Vol. 227, p. 383.

Billevicz, V., 1931, Analysis of stress in circular rings, Ph.D. dissertation, University of Michigan, Ann Arbor, MI.

Brown, W. F, and Srawley, S. R., 1966, *Plane Strain Crack Toughness Testing of High Strength Metallic Materials*, American Society for Testing and Materials, Philadelphia, PA.

Buivol, V. N., 1960, Experimental investigations of the stressed state of multiple connected plates, *Prikl. Mekh*., Vol. 3, p. 328 (in Ukranian).

Buivol, V. N., 1962, Action of concentrated forces on a plate with holes, *Prikl. Mekh*., Vol. 8, No. 1, p. 42 (in Ukranian).

Chen, P. S., and Archer, R. R., 1989, Stress concentration factors due to the bending of a thick plate with circular hole, *Ing. Arch*., Vol. 59, p. 401.

Cheng, Y. F., 1968, A photoelastic study of stress concentration factors at a doubly-symmetric hole in finite strips under tension, *Trans. ASME Appl. Mech. Sect*., Vol. 90, p. 188.

Cheng, Y. F., 1978, Stress concentration factors for a countersunk hole in a flat bar in tension and transverse bending, *Trans. ASME Appl. Mech. Sect*., Vol. 45, p. 929.

Christiansen, S., 1968, Numerical determination of stresses in a finite or infinite plate with several holes of arbitrary form, *Z. Angew. Math. Mech*., Vol. 48, p. T131.

Chu, W. L., and Conway, D. H., 1970, A numerical method for computing the stresses around an axisymmetrical inclusion, *Int. J. Mech. Sci*., Vol. 12, p. 575.

Coker, E. G., and Filon, L. N. G., 1931, *A Treatise on Photoelasticity*, Cambridge University Press, Cambridge, p. 486.

Cox, H. L., 1953, Four studies in the theory of stress concentration, *Rep. 2704*, Aeronautical Research Council, London.

Cox, H. L., and Brown, A. F. C., 1964, Stresses round pins in holes, *Aeronaut. Q*., Vol. 15, p. 357.

Daniel, I. M., 1970, Photoelastic analysis of stresses around oblique holes, *Exp. Mech*., Vol. 10, p. 467.

Davies, G. A. O., 1963, Stresses around a reinforced circular hole near a reinforced straight edge, *Aeronaut. Q*., Vol. 14, pp. 374–386.

Davies, G. A. O., 1965, Stresses in a square plate having a central circular hole, *J. R. Aeronaut. Soc*., Vol. 69, p. 410.

Davies, G. A. O., 1967, Plate-reinforced holes, *Aeronaut. Q*., Vol. 18, p. 43.

Dhir, S. K., and Brock, J. S., 1970, A new method of reinforcing a hole effecting large weight savings, *Int. J. Solids Struct*., Vol. 6, p. 259.

Dixon, J. R., 1960, Stress distribution around a central crack in a plate loaded in tension: Effect on finite width of plate, *J. R. Aeronaut. Soc*., Vol. 64, p. 141.

Dixon, R. D., Peters, D. T., and Keltjens, J. G. M, 2002, Stress concentration factors of cross-bores in thick walled cylinders and square blocks, *J. Pressure Vessel Technol*., Vol. 436, p. 31; see also Vol. 126, No. 2, pp. 184–187 (2004).

Donnell, L. H., 1941, Stress concentrations due to elliptical discontinuities in plates under edge forces, *Van Karman Anniversary Volume*, California Institute of Technology, Pasadena, CA, p. 293.

Drucker, D. C., 1942, The photoelastic analysis of transverse bending of plates in the standard transmission polariscope, *Trans. ASME Appl. Mech. Sect*., Vol. 64, p. A-161.

Dumont, C., 1939, Stress concentration around an open circular hole in a plate subjected to bending normal to the plane of the plate, *NACA Tech. Note 740*, National Advisory Committee on Aeronautics, Washington, DC.

Durelli, A. J., and Kobayashi, A. S., 1958, Stress distribution around hydrostatically loaded circular holes in the neighborhood of corners, *Trans. ASME Appl. Mech. Sect*., Vol. 80, p. 178.

Durelli, A. J., and Riley, W. F., 1965, *Introduction to Photomechanics*, Prentice-Hall, Englewood Cliffs, NJ, p. 233.

Durelli, A. J., del Rio, C. J., Parks, V. J., and Feng, H., 1967, Stresses in a pressurized cylinder with a hole, *Proc. ASCE*, Vol. 93, p. 383.

Durelli, A. J., Parks, V. J., and Uribe, S., 1968, Optimization of a slot end configuration in a finite plate subjected to uniformly distributed load, *Trans. ASME Appl. Mech. Sect*., Vol. 90, p. 403.

Durelli, A. J., Parks, V. J., Chandrashekhara, K., and Norgard, J. S., 1971, Stresses in a pressurized ribbed cylindrical shell with a reinforced circular hole interrupting a rib, *Trans. ASME J. Eng. Ind*., Vol. 93, p. 897.

Edwards, R. H., 1951, Stress concentrations around spheroidal inclusions and cavities, *Trans. ASME Appl. Mech. Sect*., Vol. 75, p. 19.

Ellyin, F., 1970a, Experimental study of oblique circular cylindrical apertures in plates, *Exp. Mech*., Vol. 10, p. 195.

Ellyin, F., 1970b, Elastic stresses near a skewed hole in a flat plate and applications to oblique nozzle attachments in shells, *WRC Bull. 153*, Welding Research Council, New York, p. 32.

Ellyin, F., and Izmiroglu, U. M., 1973, Effect of corner shape on elastic stress and strain concentration in plates with an oblique hole, *Trans. ASME J. Eng. Ind*., Vol. 95, p. 151.

Eringen, A. C., Naghdi, A. K., and Thiel, C. C., 1965, State of stress in a circular cylindrical shell with a circular hole, *WRC Bull. 102*, Welding Research Council, New York.

ESDU, 1965, 1970, 1981, 1985, 1989, *Stress Concentrations*, Engineering Science Data Unit, London.

Fedderson, C. E., 1966, Discussion of plain strain crack toughness testing, *ASTM Spec. Tech. Publ. 410*, American Society for Testing and Materials, Philadelphia, PA, p. 77.

Fessler, H., and Roberts, E. A., 1961, Bending stresses in a shaft with a transverse hole, in *Selected Papers on Stress Analysis*, Stress Analysis Conference, Delft, The Netherlands, 1959, Reinhold Publishing, New York, p. 45.

Fessler, H., and Thorpe, T. E., 1967a, Optimization of stress concentrations at holes in rotating discs, *J. Strain Anal*., Vol. 2, p. 152.

Fessler, H., and Thorpe, T. E., 1967b, Reinforcement of noncentral holes in rotating discs, *J. Strain Anal*., Vol. 2, p. 317.

Folias, E. S., and Wang, J. J., 1990, On the three-dimensional stress field around a circular hole in a plate of arbitrary thickness, *Comp. Mech*., Vol. 6, p. 376.

Fourney, M. E., and Parmerter, R. R., 1961, Stress concentrations for internally perforated star grains, *NAVWEPS Rep. 7758*, Bureau of Naval Weapons.

Fourney, M. E., and Parmerter, R. R., 1963, Photoelastic design data for pressure stresses in slotted rocket grains, *J. AIAA*, Vol. 1, p. 697.

Fourney, M. E., and Parmerter, R. R., 1966, Parametric study of rocket grain configurations by photoelastic analysis, *AFSC Rep. AFRPL-TR-66-52*.

Frocht, M. M., and Hill, H. N., 1940, Stress concentration factors around a central circular hole in a plate loaded through a pin in the hole, *Trans. ASME Appl. Mech. Sect*., Vol. 62, p. A-5.

Frocht, M. M., and Leven, M. M., 1951, Factors of stress concentration for slotted bars in tension and bending, *Trans. ASME Appl. Mech. Sect*., Vol. 73, p. 107.

Gassner, E., and Horstmann, K. F., 1961, The effect of ground to air to ground cycle on the life of transport aircraft wings which are subject to gust loads, *RAE Transl. 933*.

Gerdeen, J. C., 1972, Analysis of stress concentration in thick cylinders with sideholes and crossholes, *Trans. ASME J. Eng. Ind*., Vol. 94, Ser. B, p. 815.

Gerdeen, J. C., and Smith, R. E., 1972, Experimental determination of stress concentration factors in thick-walled cylinders with crossholes and sideholes, *Exp. Mech*., Vol. 12, p. 530.

Godfrey, D. E. R., 1959, *Theoretical Elasticity and Plasticity for Engineers*, Thames & Hudson, London, p, 109.

Goldberg, J. E., and Jabbour, K. N., 1965, Stresses and displacements in perforated plates, *Nucl. Struct. Eng*., Vol. 2, p. 360.

Goodier, J. N., 1933, Concentration of stress around spherical and cylindrical inclusions and flaws, *Trans. ASME Appl. Mech. Sect*., Vol. 55, p. A-39.

Goodier, J. N., 1936, Influence of circular and elliptical holes on transverse flexure of elastic plates, *Phil. Mag*., Vol. 22, p. 69.

Goodier, J. N., and Lee, G. H., 1941, An extension of the photoelastic method of stress measurement to plates in transverse bending, *Trans. ASME Appl. Mech. Sect*., Vol. 63, p. A-27.

Green, W. A., Hooper, G. T. J., and Hetherington, R., 1964, Stress distributions in rotating discs with non-central holes, *Aeronaut. Q*., Vol. 15, p. 107.

Grigolyuk, E. I., and Fil'shtinskii, L. A., 1970, *Perforirorannye Plastiny i Obolocki* (Perforated Plates and Shells), Nauka Publishing House, Moscow.

Gurney, C., 1938, An analysis of the stresses in a flat plate with reinforced circular hole under edge forces, *ARC R&M 1834*, Aeronautical Research Council, London.

Haddon, R. A. W., 1967, Stresses in an infinite plate with two unequal circular holes, *Q. J. Mech. Appl. Math*., Vol. 20, pp. 277–291.

Hamada, M., Yokoya, K., Hamamoto, M., and Masuda, T., 1972, Stress concentration of a cylindrical shell with one or two circular holes, *Bull. Jpn. Soc. Mech. Eng*., Vol. 15, p. 907.

Hanzawa, H., Kishida, M., Murai, M., and Takashina, K., 1972, Stresses in a circular cylindrical shell having two circular cutouts, *Bull. Jpn. Soc. Mech. Eng*., Vol. 15, p. 787.

Hardenberg, D. E., and Zamrik, S. Y., 1964, Effects of external loadings on large outlets in a cylindrical pressure vessel, *WRC Bull. 96*, Welding Research Council, New York.

Heller, S. R., 1969, Stress concentration factors for a rectangular opening with rounded comers in a biaxially loaded plate, *J. Ship Res*., Vol. 13, p. 178.

Heller, S. R., Brock, J. S., and Bart, R., 1958, The stresses around a rectangular opening with rounded corners in a uniformly loaded plate, *Proc. 3rd U.S. Natl. Congr. Appl. Mech*., American Society of Mechanical Engineers, Philadelphia, PA, p. 357.

Hennig, A., 1933, Polarisationsoptische Spannungsuntersuchungen am gelochten Zugstab und am Nietloch, *Forsch. Gebiete Ing., VDI*, Vol. 4, p. 53.

Hetényi, M., 1939a, The application of hardening resins in three-dimensional photoelastic studies, *J. Appl. Phys*., Vol. 10, p. 295.

Hetényi, M., 1939b, Some applications of photoelasticity in turbine-generator design, *Trans. ASME Appl. Mech. Sect*., Vol. 61, p. A-151.

Heywood, R. B., 1952, *Designing by Photoelasticity*, Chapman & Hall, London.

Hicks, R., 1957, Reinforced elliptical holes in stressed plates, *J. R. Aeronaut. Soc*., Vol. 61, p. 688.

Hirano, F., 1950, Study of shape coefficients of two-dimensional elastic bodies, *Trans. Jpn. Soc. Mech. Eng*., Vol. 16, No. 55, p. 52 (in Japanese).

Hooke, C. J., 1968, Numerical solution of plane elastostatic problems by point matching, *J. Strain Anal*., Vol. 3, p. 109.

Horger, O. J., and Buckwalter, T. V., 1940, Photoelasticity as applied to design problems, *Iron Age*, Vol. 145, Pt. II, No. 21, p. 42.

Horvay, G., 1952, The plane-stress problem of perforated plates, *Trans. ASME Appl. Mech. Sect*., Vol. 74, p. 355.

Houghton, D. S., and Rothwell, A., 1961, The analysis of reinforced circular and elliptical cutouts under various loading conditions, *Rep. 151*, College of Aeronautics, Cranfield, England.

Houghton, D. S., and Rothwell A., 1962, The effect of curvature on the stress concentration around holes in shells, *Rep. 156*, College of Aeronautics, Cranfield, England.

Howland, R. C. J., 1929–1930, On the stresses in the neighborhood of a circular hole in a strip under tension, *Philos. Trans. R. Soc. (London) Ser. A*, Vol. 229, p. 67.

Howland, R. C. J., 1935, Stresses in a plate containing an infinite row of holes, *Proc. R. Soc. (London) Ser. A*, Vol. 148, p. 471.

Howland, R. C. J., and Stevenson, A. C., 1933, Biharmonic analysis in a perforated strip, *Philos. Trans. R. Soc. A (London) Ser. A*, Vol. 232, p. 155.

Hulbert, L. E., 1965, The numerical solution of two-dimensional problems of the theory of elasticity, *Eng. Exp. Stn. Bull. 198*, Ohio State University, Columbus, OH.

Hulbert, L. E., and Niedenfuhr, F. W., 1965, Accurate calculation of stress distributions in multiholed plates, *Trans. ASME Ind. Sect*., Vol. 87, p. 331.

Hütter, A., 1942, Die Spannungsspitzen in gelochten Blechscheiben und Streifen, *Z. Angew. Math. Mech*., Vol. 22, p. 322.

Inglis, C.E., 1913, Stresses in a plate due to the presence of cracks and sharp corners, *Engineering (London)*, Vol. 95, p. 415.

Irwin, G. R., 1958, Fracture, in *Encyclopedia of Physics*, Vol. 6, Springer-Verlag, Berlin.

Irwin, G. R., 1960, Fracture mechanics, in *Structural Mechanics*, Pergamon Press, Elmsford, NY.

Isida, M., 1952, On the bending of an infinite strip with an eccentric circular hole, *Proc. 2nd Jpn. Congr. Appl. Mech*., p. 57.

Isida, M., 1953, Form factors of a strip with an elliptic hole in tension and bending, *Sci. Pap. Faculty Engr. Tokushima Univ*., Vol. 4, p. 70.

Isida, M., 1955a, On the tension of a semi-infinite plate with an elliptic hole, *Sci. Pap. Faculty of Engr. Tokushima Univ*., Vol. 5, p. 75 (in Japanese).

Isida, M., 1955b, On the tension of a strip with a central elliptic hole, *Trans. Jpn. Soc. Mech. Eng*., Vol. 21, p. 514.

Isida, M., 1960, On the tension of an infinite strip containing a square hole with rounded corners, *Bull. Jpn. Soc. Mech. Eng*., Vol. 3, p. 254.

Isida, M., 1965, Crack tip intensity factors for the tension of an eccentrically cracked strip, report, Department of Mechanics, Lehigh University, Bethlehem, PA.

Isida, M., 1966, Stress intensity factors for the tension of an eccentrically cracked strip, *Trans. ASME Appl. Mech. Sect*., Vol. 88, p. 674.

Jessop, H. T., Snell, C., and Holister, G. S., 1958, Photoelastic investigation of plates with single interference-fit pins with load applied (a) to pin only and (b) to pin and plate simultaneously, *Aeronaut. Q*., Vol. 9, p. 147.

Jessop, H. T., Snell, C., and Allison, I. M., 1959, The stress concentration factors in cylindrical tubes with transverse cylindrical holes, *Aeronaut. Q*., Vol. 10, p. 326.

Jones, N., and Hozos, D., 1971, A study of the stress around elliptical holes in flat plates, *Trans. ASME J. Eng. Ind*., Vol. 93, p. 688.

Joseph, J. A., and Brock, J. S., 1950, The stresses around a small opening in a beam subjected to pure bending, *Trans. ASME Appl. Mech. Sect*., Vol. 72, p. 353.

Kaufman, A., Bizon, P. T., and Morgan, W. C., 1962, Investigation of circular reinforcements of rectangular cross-section around central holes in flat sheets under biaxial loads in the elastic range, *NASA TN D-1195*, National Aeronautics and Space Administration, Washington, DC.

Kelly, L. G., 1967, *Handbook of Numerical Methods and Applications*, Addison-Wesley, Reading, MA.

Knight, R. C., 1935, Action of a rivet in a plate of finite breadth, *Philos. Mag., Ser. 7*, Vol. 19, p. 517.

Koiter, W. T., 1957, An elementary solution of two stress concentration problems in the neighborhood of a hole, *Q. Appl. Math*., Vol. 15, p. 303.

Koiter, W. T., 1965, Note on the stress intensity factors for sheet strips with crack under tensile loads, report, Laboratory of Engineering Mechanics, Technological University, Delft, The Netherlands.

Kolosoff, G., 1910, Dissertation, St. Petersburg, Russia.

Kraus, H., 1962, Pressure in multibore bodies, *Int. J. Mech. Sci*., Vol. 4, p. 187.

Kraus, H., 1963, Stress concentration factors for perforated annular bodies loaded in their plane, unpublished report, Pratt and Whitney Co., East Hartford, CT.

Kraus, H., Rotondo, P., Haddon, W. D., 1966, Analysis of radially deformed perforated flanges, *Trans. ASME Appl. Mech. Sect*., Vol. 88, p. 172.

Lapsley C., and Mackensie, D., 1997, Residual stress at radial cross-bores, in *Pressure Vessel Technology*, Vol. 344, *High Pressure Technology*, American Society of Mechanical Engineers, p. 51.

Leckie, F. A., Paine, D. J., and Penny, R. K., 1967, Elliptical discontinuities in spherical shells, *J. Strain Anal*., Vol. 2, p. 34.

Leist, K., and Weber, J., 1956, Optical stress distributions in rotating discs with eccentric holes, *Rep. 57*, Institute for Jet Propulsion, German Research Institute for Aeronautics, Aachen, Germany.

Lekkerkerker, J. G., 1964, Stress concentration around circular holes in cylindrical shells, *Proc. 11th International Congress on Applied Mechanics*, Springer-Verlag, Berlin, p. 283.

Leven, M. M., 1938, 1952, unpublished data obtained at Carnegie Institute of Technology and Westinghouse Research Laboratories.

Leven, M. M., 1955, Quantitative three-dimensional photoelasticity, *Proc. SESA*, Vol. 12, p. 157.

Leven, M. M., 1963, Effective elastic constants in plane stressed perforated plates of low ligament efficiency, *Res. Rep. 63-917-520-R1*, Westinghouse Research Laboratories, Pittsburgh, PA.

Leven, M. M., 1964, Stress distribution in a perforated plate of 10% ligament efficiency subjected to equal biaxial stress, *Res. Rep. 64-917-520-R1*, Westinghouse Research Laboratories, Pittsburgh, PA.

Leven, M. M., 1966, Photoelastic determination of the stresses in reinforced openings in pressure vessels, *WRC Bull. 113*, Welding Research Council, New York, p. 25.

Leven, M. M., 1967, Photoelastic analysis of a plate perforated with a square pattern of penetrations, *Res. Memo. 67-1D7-TAADS-MI*, Westinghouse Research Laboratories, Pittsburgh, PA.

Leven, M. M., 1970, Photoelastic determination of the stresses at oblique openings in plates and shells, *WRC Bull. 153*, Welding Research Council, New York, p. 52.

Levy, S., McPherson, A. E., and Smith, F. C., 1948, Reinforcement of a small circular hole in a plane sheet under tension, *Trans. ASME Appl. Mech. Sect*., Vol. 70, p. 160.

Lind, N. C., 1968, Stress concentration of holes in pressurized cylindrical shells, *AIAA J*., Vol. 6, p. 1397.

Ling, C.-B., 1948a, On the stresses in a plate containing two circular holes, *J. Appl. Phys*., Vol. 19, p. 77.

Ling, C.-B., 1948b, The stresses in a plate containing an overlapped circular hole, *J. Appl. Phys*., Vol. 19, p. 405.

Ling, C.-B., 1952, Torsion of a circular cylinder having a spherical cavity, *Q. Appl. Math*., Vol. 10, p. 149.

Ling, C.-B., 1959, Stresses in a stretched slab having a spherical cavity, *Trans. ASME Appl. Mech. Sect*., Vol. 81, p. 235.

Ling, C.-B., 1967, On stress concentration at semicircular notch, *Trans. ASME Appl. Mech. Sect*., Vol. 89, p. 522.

Lingaiah, K., North, W. P. T., and Mantle, J. B., 1966, Photoelastic analysis of an asymmetrically reinforced circular cutout in a flat plate subjected to uniform unidirectional stress, *Proc. SESA*, Vol. 23, No. 2, p. 617.

Mansfield, E. H., 1953, Neutral holes in plane sheet-reinforced holes which are elastically equivalent to the uncut sheet, *Q. J. Mech. Appl. Math*., Vol. 6, p. 370.

Mansfield, E. H., 1955, Stress considerations in the design of pressurized shells, *ARC CP 217*, Aeronautical Research Council, London.

Mansfield, E. H., 1970, Analysis of a class of variable thickness reinforcement around a circular hole in a flat sheet, *Aeronaut. Q*., Vol. 21, p. 303.

McKenzie, H. W., and White, D. J., 1968, Stress concentration caused by an oblique round hole in a flat plate under uniaxial tension, *J. Strain Anal*., Vol. 3, p. 98.

Meijers, P., 1967, Doubly-periodic stress distributions in perforated plates, Dissertation, Technische Hochschule, Delft, The Netherlands.

Mindlin, R. D., 1939, Stress distribution around a tunnel, *Proc. ASCE*, Vol. 65, p. 619.

Mindlin, R. D., 1948, Stress distribution around a hole near the edge of a plate in tension, *Proc. SESA*, Vol. 5, pp. 56–68.

Mitchell, L. H., 1966, Stress concentration factors at a doubly-symmetric hole, *Aeronaut. Q*., Vol. 17, p. 177.

Mitchell, W. D., and Rosenthal, D., 1949, Influence of elastic constants on the partition of load between rivets, *Proc. SESA*, Vol. 7, No. 2, p. 17.

Miyamoto, H., 1957, On the problem of the theory of elasticity for a region containing more than two spherical cavities, *Trans. Jpn. Soc. Mech. Eng.*, Vol. 23, p. 437.

Miyao, K., 1970, Stresses in a plate containing a circular hole with a notch, *Bull. Jpn. Soc. Mech. Eng*., Vol. 13, p. 483.

Mondina, A., and Falco, H., 1972, Experimental stress analysis on models of PWR internals, *Dis. Macch. Palermo*, Vol. 3, p. 77.

Mori, A., 1972, Stress distributions in a semi-infinite plate with a row of circular holes, *Bull. Jpn. Soc. Mech. Eng*., Vol. 15, p. 899.

Murthy, M. V. V., 1969, Stresses around an elliptic hole in a cylindrical shell, *Trans. ASME Appl. Mech. Sect*., Vol. 91, p. 39.

Murthy, M. V. V., and Rao, M. N. B., 1970, Stresses in a cylindrical shell weakened by an elliptic hole with major perpendicular to shell axis, *Trans. ASME Appl. Mech. Sect*., Vol. 92, p. 539.

Neuber, H., 1958, *Kerbspannungslehre*, 2nd ed., Springer-Verlag, Berlin; translation, 1961, *Theory of Notch Stresses*, Office of Technical Services, U.S. Department of Commerce, Washington, DC.

Nishida, M., 1976, *Stress Concentration*, Morikita Shuppan, Tokyo (in Japanese).

Nisitani, H., 1968, Method of approximate calculation for interference of notch effect and its application, *Bull. Jpn. Soc. Mech. Eng*., Vol. 11, p. 725.

North, W. E., 1965, A photoelastic study of the interaction effect of two neighboring holes in a plate under tension, M.S. thesis, University of Pittsburgh, Pittsburgh, PA.

Nuno, H., Fujie, T., and Ohkuma, K., 1964, Experimental study on the elastic properties of perforated plates with circular holes in square patterns, *MAPI Lab. Res. Rep. 74*, Mitsubishi Atomic Power Industries Laboratory, Ohmiya, Japan.

O'Donnell, W. J., 1966, A study of perforated plates with square penetration patterns, *WAPD-T-1957*, Bettis Atomic Power Laboratory, Pittsburgh, PA.

O'Donnell, W. J., 1967, A study of perforated plates with square penetration patterns, *WRC Bull. 124*, Welding Research Council, New York.

O'Donnell, W. J., and Langer, B. P., 1962, Design of perforated plates, *Trans. ASME Ind. Sect*., Vol. 84, p. 307.

Paloto, J. C., Santos, R. D., and Domínguez, P., 2003, Stress concentration factors for a circular hole in curved beams under bending loads, *Strain*, Vol. 39, p. 27.

Papirno, R., 1962, Stress concentrations in tensile strips with central notches of varying end radii, *J. R. Aeronaut. Soc*., Vol. 66, p. 323.

Paris, P. C., and Sih, G. C., 1965, Stress analysis of cracks, *ASTM Spec. Tech. Publ*., American Society for Testing and Materials, Philadelphia, PA, p. 34.

Peterson, R. E., 1965, The interaction effect of neighboring holes or cavities, with particular reference to pressure vessels and rocket cases, *Trans. ASME Basic Eng. Sect*., Vol. 87, p. 879.

Peterson, R. E., 1968, Stress concentration factors for a round bar with a transverse hole, *Rep. 68-1D7-TAEUGR8*, Westinghouse Research Laboratories, Pittsburgh, PA.

Peterson, R. E., 1974, *Stress Concentration Factors*, Wiley, New York.

Pierce, D. N., and Chou, S. I., 1973, Stress state around an elliptic hole in a circular cylindrical shell subjected to axial loads, presented at the SESA Meeting, Los Angeles, CA.

Pilkey, W. D., 2005, *Formulas for Stress, Strain, and Structural Matrices*, 2nd ed., Wiley, Hoboken, NJ.

Reissner, E., 1945, The effect of transverse shear deformation on the bending of elastic plates, *Trans. ASME Appl. Mech. Sect*., Vol. 67, p. A-69.

Reissner, H., and Morduchow, M., 1949, Reinforced circular cutouts in plane sheets, *NACA TN 1852*, National Advisory Committee on Aeronautics, Washington, DC.

Riley, W. F., 1964, Stresses at tunnel intersections, *Proc. ASCE J. Eng. Mech. Div*., Vol. 90, p. 167.

Riley, W. F., Durelli, A. J., and Theocaris, P. S., 1959, Further stress studies on a square plate with a pressurized central circular hole, *Proc. 4th Annual Conference on Solid Mechanics*, University of Texas, Austin, TX.

Robinson, E. L., 1944, Bursting tests of steam-turbine disk wheels, *Trans. ASME Appl. Mech. Sect*., Vol. 66, p. 380.

Rooke, D. P., 1970, Width corrections in fracture mechanics, *Eng. Fracture Mech*., Vol. 1, pp. 727–728.

Ryan, J. J., and Fischer, L. J., 1938, Photoelastic analysis of stress concentration for beams in pure bending with central hole, *J. Franklin Inst*., Vol. 225, p. 513.

Sadowsky, M. A., and Sternberg, E., 1947, Stress concentration around an ellipsoidal cavity in an infinite body under arbitrary plane stress perpendicular to the axis of revolution of cavity, *Trans. ASME Appl. Mech. Sect*., Vol. 69, p. A-191.

Salerno, V. L., and Mahoney, J. B., 1968, Stress solution for an infinite plate containing two arbitrary circular holes under equal biaxial stresses, *Trans. ASME Ind. Sect*., Vol. 90, p. 656.

Sampson, R. C., 1960, Photoelastic analysis of stresses in perforated material subject to tension or bending, *Bettis Tech. Rev. WAP-BT-18*, Bettis Atomic Power Laboratory, Pittsburgh, PA.

Savin, G. N., 1961, *Stress Concentration Around Holes*, Pergamon Press, Elmsford, NY.

Schaechterle, K., 1934, On the fatique strength of riveted and welded joints and the design of dynamically stressed structural members based on conclusions drawn from fatigue tests, *Int. Assoc. Bridge Struct. Eng*., Vol. 2, p. 312.

Schulz, K. J., 1941, Over den Spannungstoestand in doorborde Platen (On the state of stress in perforated plates), doctoral dissertation, Technische Hochschule, Delft, The Netherlands.

Schulz, K. J., 1942–1945, On the state of stress in perforated strips and plates, *Proc. Koninklÿke Nederlandsche Akadamie van Wetenschappen* (Netherlands Royal Academy of Science), Amsterdam, Vol. 45 (1942), p. 233, 341, 457, 524; Vol. 46–48 (1943–1945), pp. 282, 292.

These papers were summarized by C. B. Biezeno, Survey of papers on elasticity published in Holland, 1940–1946, *Adv. Appl. Mech*., Vol. 1, Academic Press, New York (1948), p. 105. Biezeno comments, "The calculations are performed only for a strip with one row of holes, though an extensive program of further investigation was projected, which unfortunately could not be executed; the Jewish author, who lived in Holland, was arrested and marched off to Germany or Poland, which meant his destruction."

Seika, M., 1958, The stresses in a thick cylinder having a square hole under concentrated loading, *Trans. ASME Appl. Mech. Sect*., Vol. 80, p. 571.

Seika, M., and Amano, A., 1967, The maximum stress in a wide plate with a reinforced circular hole under uniaxial tension: Effects of a boss with fillet, *Trans. ASME Appl. Mech. Sect*., Vol. 89, p. 232.

Seika, M., and Ishii, M., 1964, Photoelastic investigation of the maximum stress in a plate with a reinforced circular hole under uniaxial tension, *Trans. ASME Appl. Mech. Sect*., Vol. 86, p. 701.

Seika, M., Isogimi, K., and Inoue, K., 1971, Photoelastic study of stresses in a cylindrical pressure vessel with a nozzle, *Bull. Jpn. Soc. Mech. Eng*., Vol. 14, p. 1036.

Sekiya, T., 1955, An approximate solution in the problems of elastic plates with an arbitrary external form and a circular hole, *Proc. 5th Jpn. Natl. Congr. Appl. Mech*., p. 95.

Shioya, S., 1971, On the tension of an infinite thin plate containing a pair of circular inclusions, *Bull. Jpn. Soc. Mech. Eng*., Vol. 14, p. 117.

Shivakumar, K. N., and Newman, J. C., 1992, Stress concentrations for straight-shank and countersunk holes in plates subjected to tension, bending, and pin loading, *NASA Tech. Rep. 3192*, National Aeronautics and Space Administration, Washington, DC.

Shivakumar, K. N., and Newman, J. C., 1995, Stress concentration equations for straight-shank and countersunk holes in plates, *Trans. ASME Appl. Mech. Sect*., Vol. 62, p. 248.

Shivakumar, K.N., Bhargava, A., and Hamoush, S., 2006, An equation for stress concentration factors in countersunk holes, *Comp. Mater. Continua*, Vol. 3, p. 97.

Sjöström, S., 1950, On the stresses at the edge of an eccentically located circular hole in a strip under tension, *Rep. 36*, Aeronautical Research Institute, Stockholm, Sweden.

Slot, T., 1972, *Stress Analysis of Thick Perforated Plates*, Technomic Publishing, Westport, CT.

Sobey, A. J., 1963, Stress concentration factors for rounded rectangular holes in infinite sheets, *ARC R&M 3407*, H.M. Stationery Office, London.

Sobey, A. J., 1968, Stress concentration factors for reinforced rounded-square holes in sheets, *ARC R&M 3546*, H.M. Stationery Office, London.

Sternberg, E., and Sadowsky, M. A., 1949, Three-dimensional solution for the stress concentration around a circular hole in a plate of arbitrary thickness, *Trans. ASME Appl. Mech. Sect*., Vol. 71, p. 27.

Sternberg, E., and Sadowsky, M. A., 1952, On the axisymmetric problem of the theory of elasticity for an infinite region containing two spherical cavities, *Trans. ASME Appl. Mech. Sect*., Vol. 76, p. 19.

Tamate, O., 1957, Einfluss einer unendichen Reihe gleicher Kreislöcher auf die Durchbiegung einer dünnen Platte, *Z. Angew. Math. Mech*., Vol. 37, p. 431.

Tamate, O., 1958, Transverse flexure of a thin plate containing two holes, *Trans. ASME Appl. Mech. Sect*., Vol. 80, p. 1.

Theocaris, P. S., 1956, The stress distribution in a strip loaded in tension by means of a central pin, *Trans. ASME Appl. Mech. Sect*., Vol. 78, p. 482.

Thum, A., and Kirmser, W., 1943, Überlagerte Wechselbeanspruchungen, ihre Erzeugung und ihr Einfluss auf die Dauerbarkeit und Spannungsausbildung quergebohrter Wellen, *VDI-Forschungsheft 419*, Vol. 14(b), p. 1.

Timoshenko, S., 1922, On the distribution of stresses in a circular ring compressed by two forces along a diameter, *Philos. Mag*., Vol. 44, p. 1014.

Timoshenko, S., 1924, On stresses in a plate with a circular hole, *J. Franklin Inst*., Vol. 197, p. 505.

Timoshenko, S., 1956, *Strength of Materials, Pt. II*, 3rd ed., Van Nostrand, Princeton, NJ, p. 208.

Timoshenko, S., and Goodier, J. N., 1970, *Theory of Elasticity*, 3rd ed., McGraw-Hill, New York, p. 398.

Tingleff, O., 1971, Stress concentration in a cylindrical shell with an elliptical cutout, *AIAA J*., Vol. 9, p. 2289.

Troyani, N., Gomes, C., and Sterlacci, G., 2002, Theoretical stress concentration factors for short rectangular plates with centered circular holes, *Trans. ASME J. Mech. Des*., Vol. 124, p. 126.

Troyani, N., Jaimes, N., Sterlacci, G., and Gomes, C., 2005, Stress concentration effects in short cylindrical vessels with holes subjected to tension: a complete account, *J. Pressure Vessel Technol*., Vol. 127, p. 184.

Udoguti, T., 1947, Solutions of some plane elasticity problems by using dipole coordinates: Part I, *Trans. Jpn. Soc. Mech. Eng*., Vol. 13, p. 17 (in Japanese).

Van Dyke, P., 1965, Stresses about a circular hole in a cylindrical shell, *AIAA J*., Vol. 3, p. 1733.

Wahl, A. W., and Beeuwkes, R., 1934, Stress concentration produced by holes and notches, *Trans. ASME Appl. Mech. Sect*., Vol. 56, p. 617.

Wells, A. A., 1950, On the plane stress distribution in an infinite plate with rim-stiffened elliptical opening, *Q. J. Mech. Appl. Math*., Vol. 2, p. 23.

Westergaard, H. M., 1939, Bearing pressure and cracks, *Trans. ASME Appl. Mech. Sect*., Vol. 61, p. A-49.

Whaley, R. E., 1965, Stress concentration factors for countersunk holes, *Exp. Mech*., Vol. 5, p. 257.

Wittrick, W. H., 1959a, The stress around reinforced elliptical holes in plane sheet, *Rep. ARL SM267*, Aeronautics Research Laboratory, Australia.

Wittrick, W. H., 1959b, Stress around reinforced elliptical holes, with applications to pressure cabin windows, *Aeronaut. Q*., Vol. 10, p. 373–400.

Wittrick, W. H., 1963, Stress concentrations for uniformly reinforced equilateral triangular holes with rounded comers, *Aeronaut. Q*., Vol. 14, p. 254.

WRC, 1966, *WRC Bull. 113*, Welding Research Council.

WRC, 1970, *WRC Bull. 113*, Welding Research Council.

Wu, H. C., and Mu, B., 2003, On stress concentrations for isotropic/orthotropic plates and cylinders with a circular hole, *Composites Pt. B*, Vol. 34, p.127.

Yamamoto, K., and Terada, S., 2000, Stress concentrations factors for cross bores in KHK standard, *Rep. HPI-ASME-004*, High Pressure Institute of Japan.

Young, J. B., and Lee, K. K., 1993, Stress concentration factors in countersunk holes, *Aeronaut. J*., Vol. 97, p. 267.

Youngdahl, C. K., and Sternberg, E., 1966, Three-dimensional stress concentration around a cylindrical hole in a semi-infinite elastic body, *Trans. ASME Appl. Mech. Sect*., Vol. 88, p. 855.

Yu, Y. Y., 1952, Gravitational stresses on deep tunnels, *Trans. ASME Appl. Mech. Sect*., Vol. 74, p. 537.

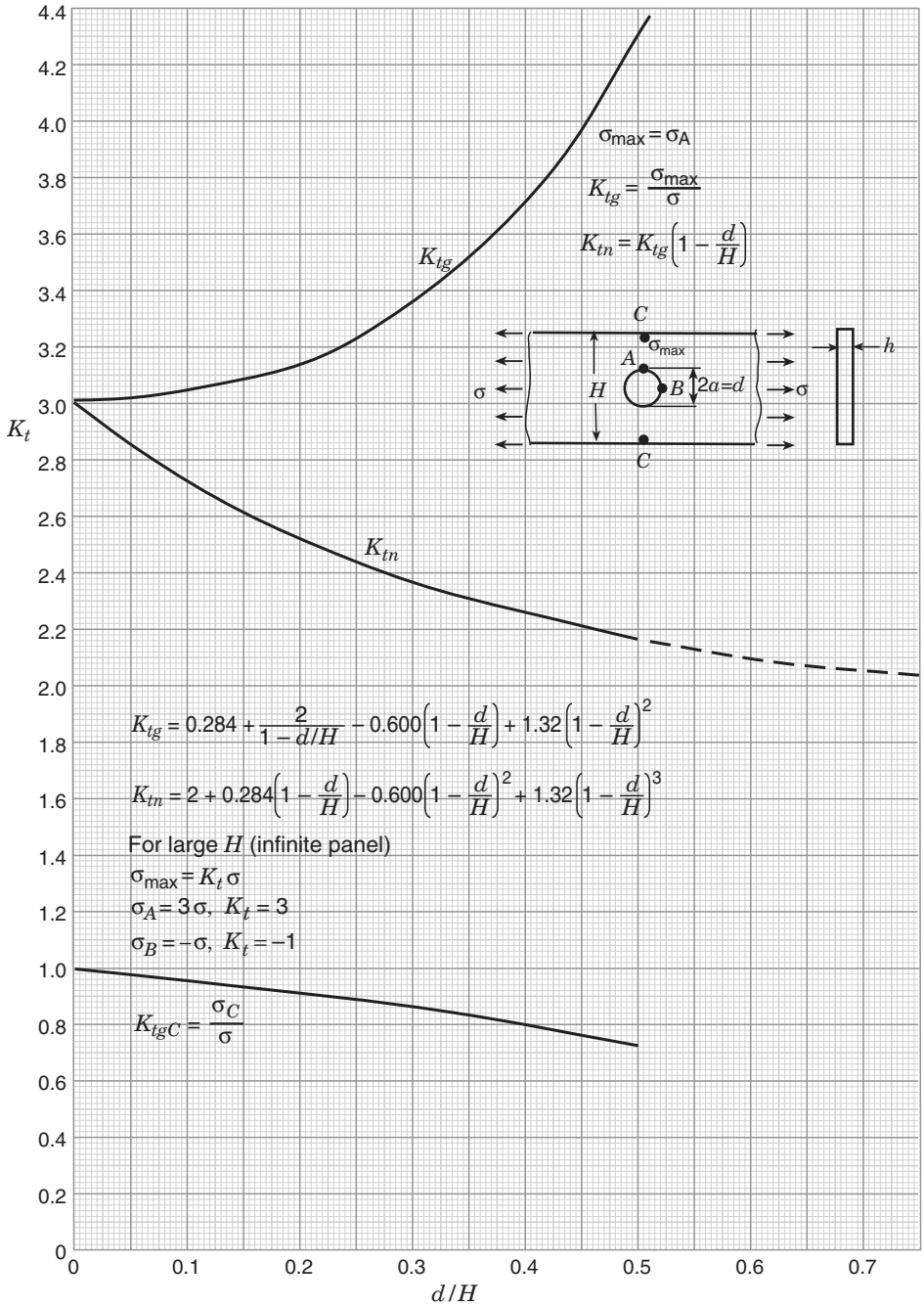


Chart 4.1 Stress concentration factors K_{tg} and K_{tn} for the tension of a finite-width thin element with a circular hole (Howland 1929–1930).

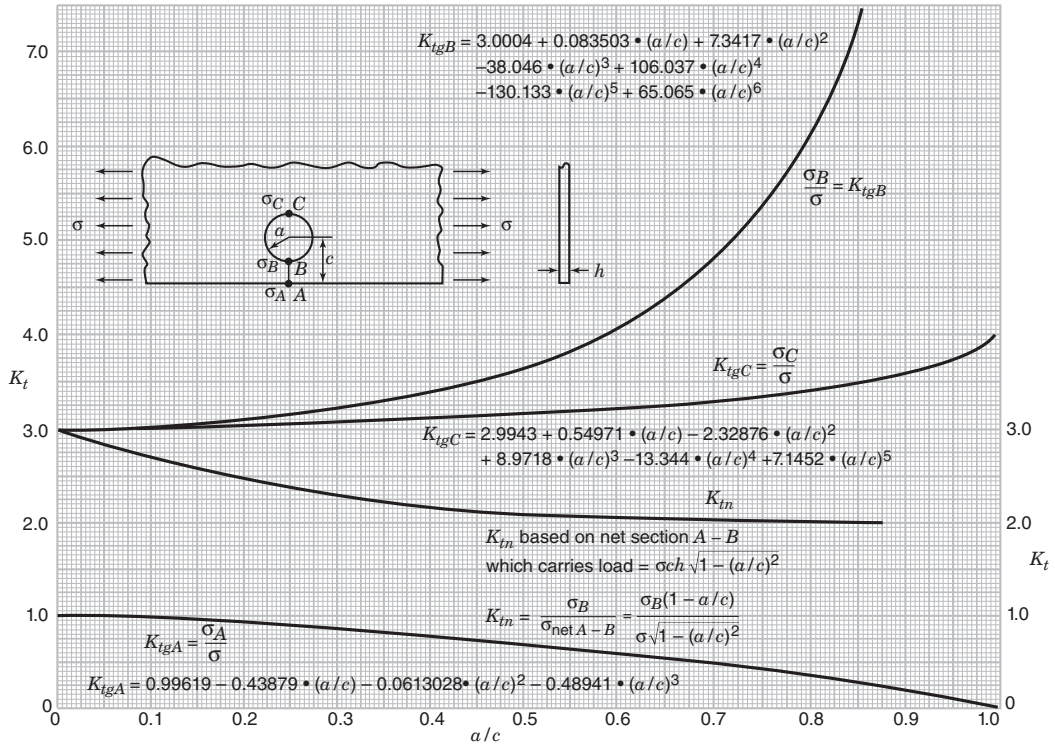


Chart 4.2 Stress concentration factors for the tension of a thin semi-infinite element with a circular hole near the edge (Udoguti 1947; Mindlin 1948; Isida 1955a).

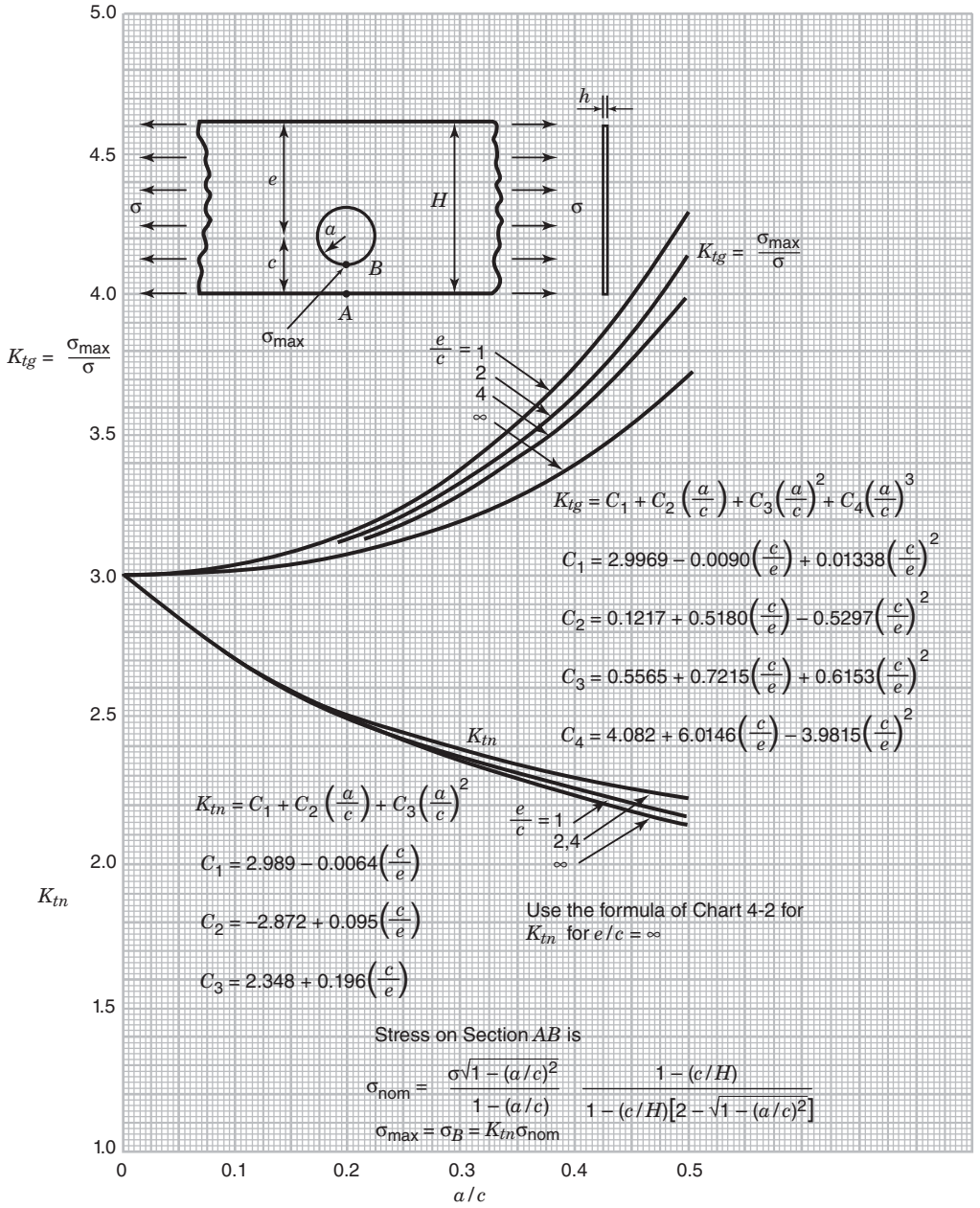


Chart 4.3 Stress concentration factors for the tension of a finite-width element having an eccentrically located circular hole (based on mathematical analysis of Sjöström 1950). $e/c = \infty$ corresponds to Chart 4.2.

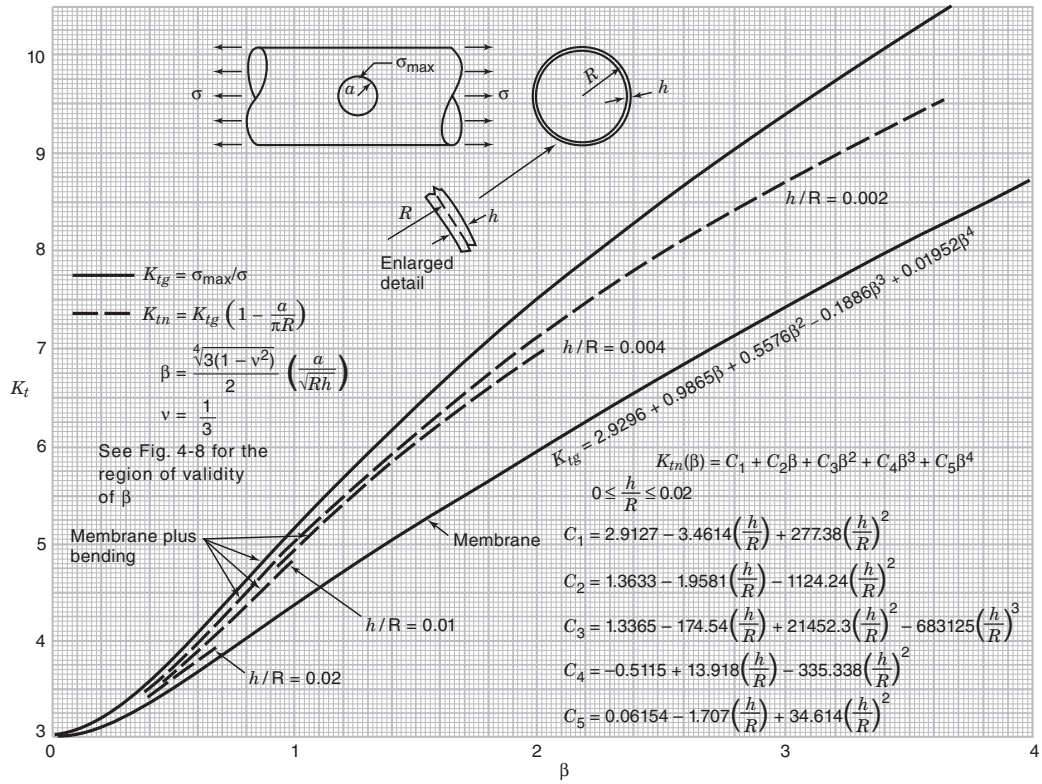


Chart 4.4 Stress concentration factors for a circular hole in a cylindrical shell in tension (based on data of Van Dyke 1965).

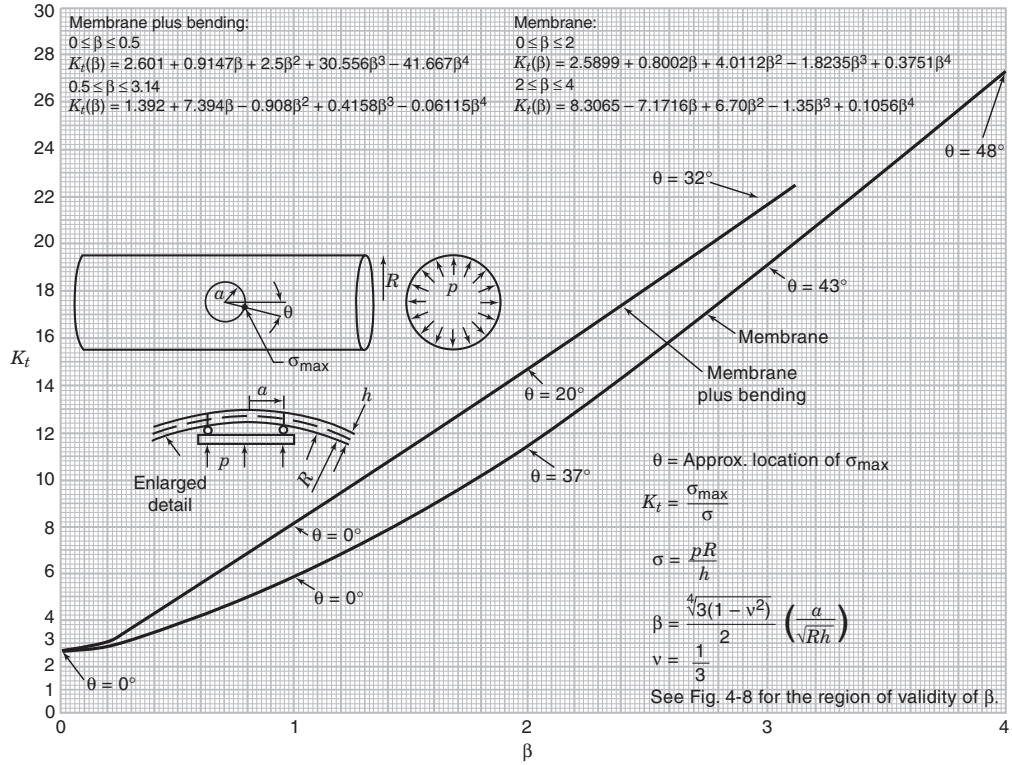


Chart 4.5 Stress concentration factors for a circular hole in a cylindrical shell with internal pressure (based on data of Van Dyke 1965).

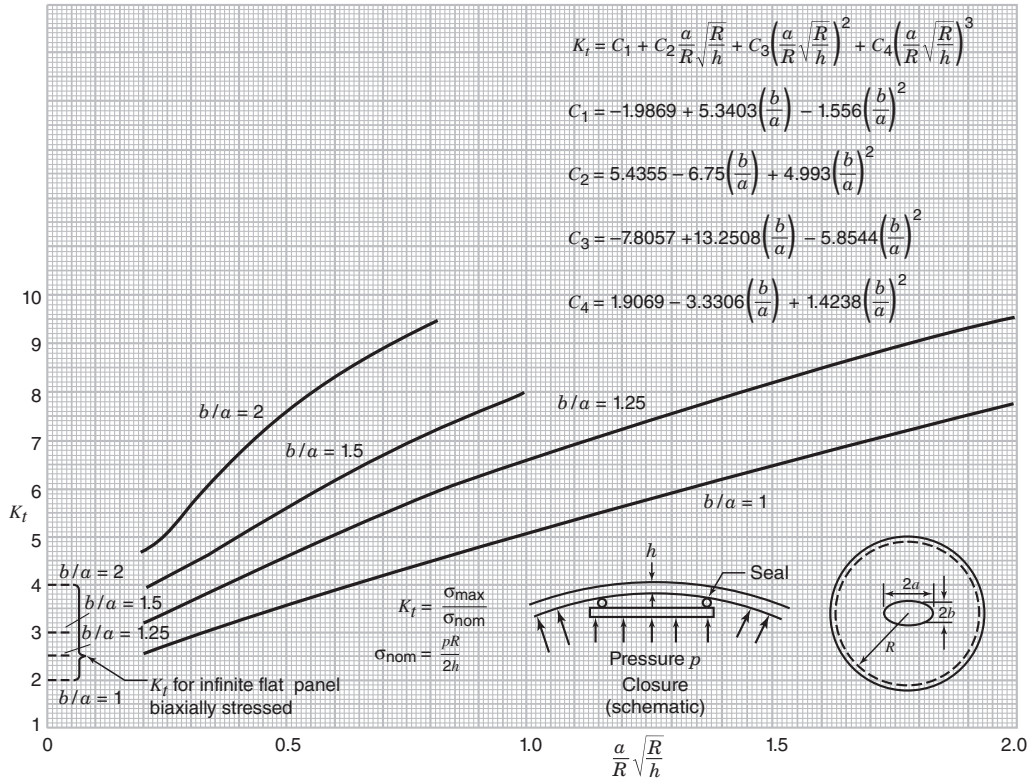


Chart 4.6 Stress concentration factors for a pressurized spherical shell with elliptical hole (Leckie et al. 1967).

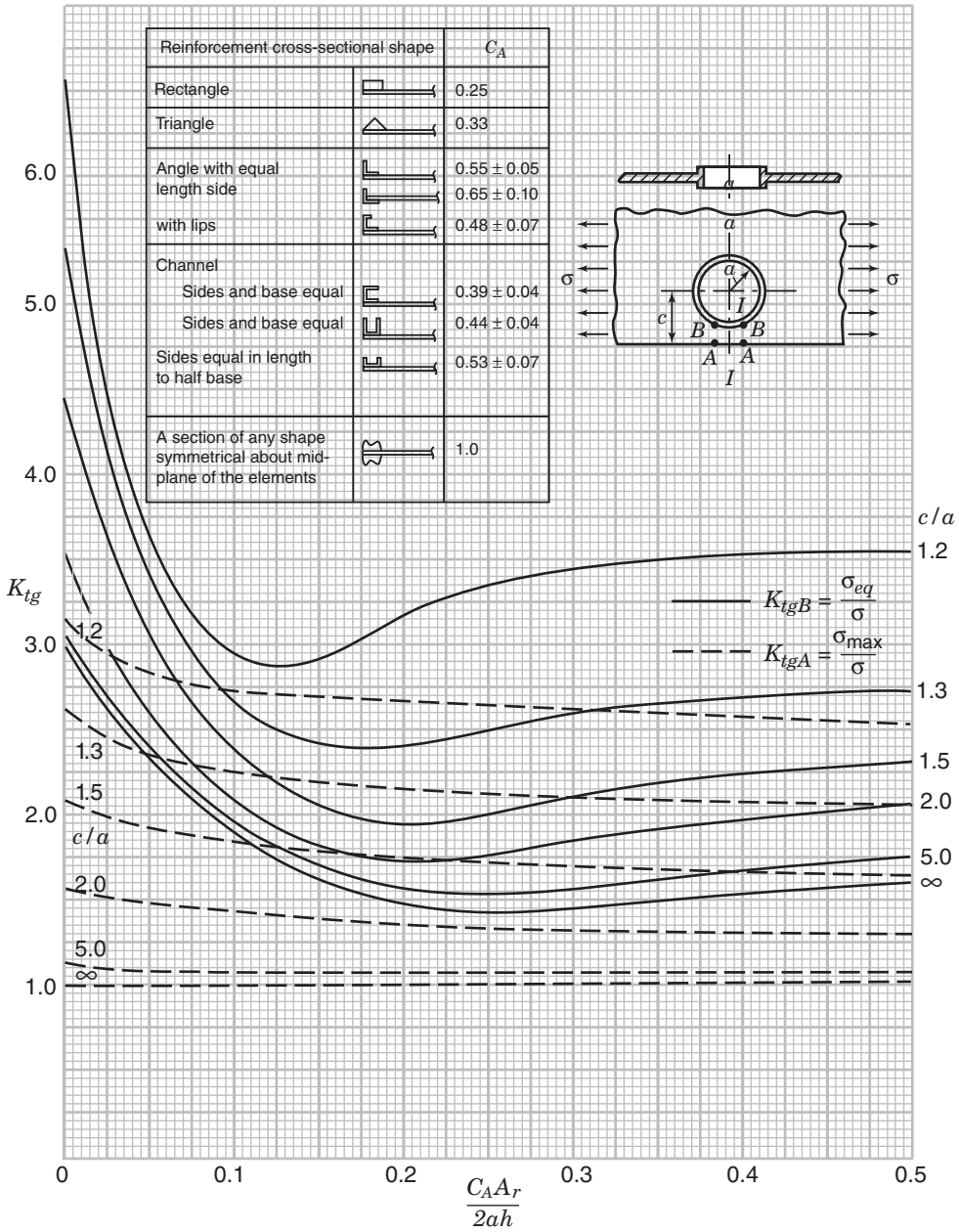


Chart 4.7 Stress concentration factors for various shaped reinforcements of a circular hole near the edge of a semi-infinite element in tension (data from Mindlin 1948; Mansfield 1955; Wittrick 1959; Davies 1963; ESDU 1981).

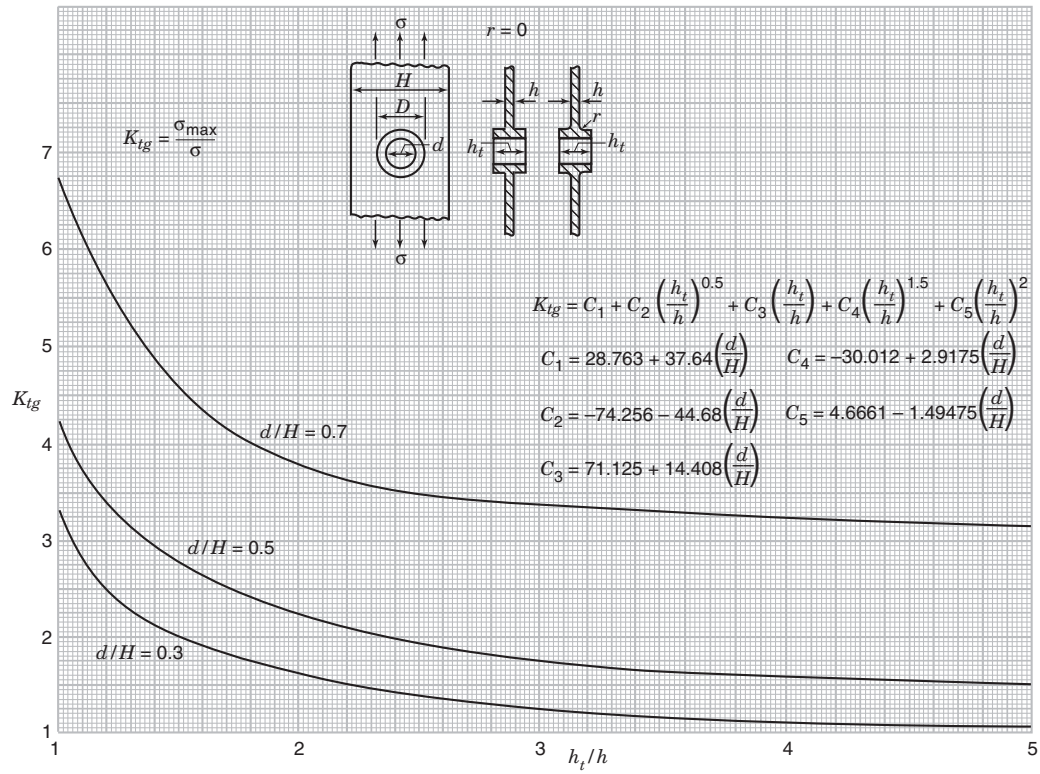


Chart 4.8*a* Stress concentration factors K_{tg} for a reinforced circular hole in a thin element in tension (Seika and Amano 1967): $H/D = 1$, $D/h = 5.0$, $r = 0$.

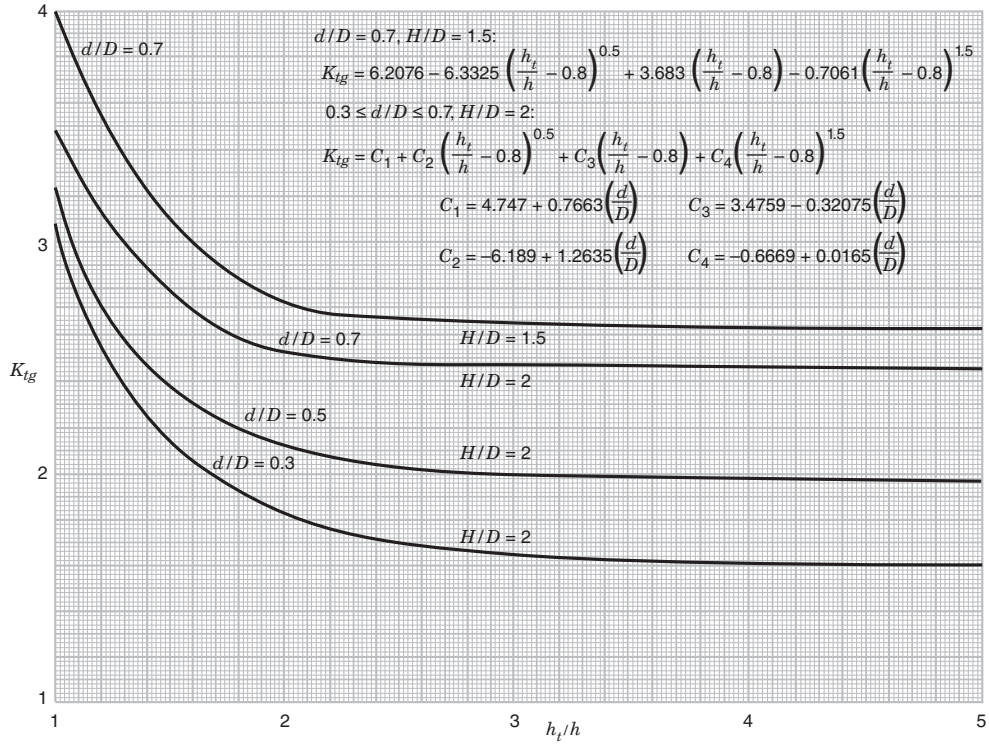


Chart 4.8*b* Stress concentration factors K_{tg} for a reinforced circular hole in a thin element in tension (Seika and Amano 1967): $H/D = 4.0$, $D/h = 5.0$.

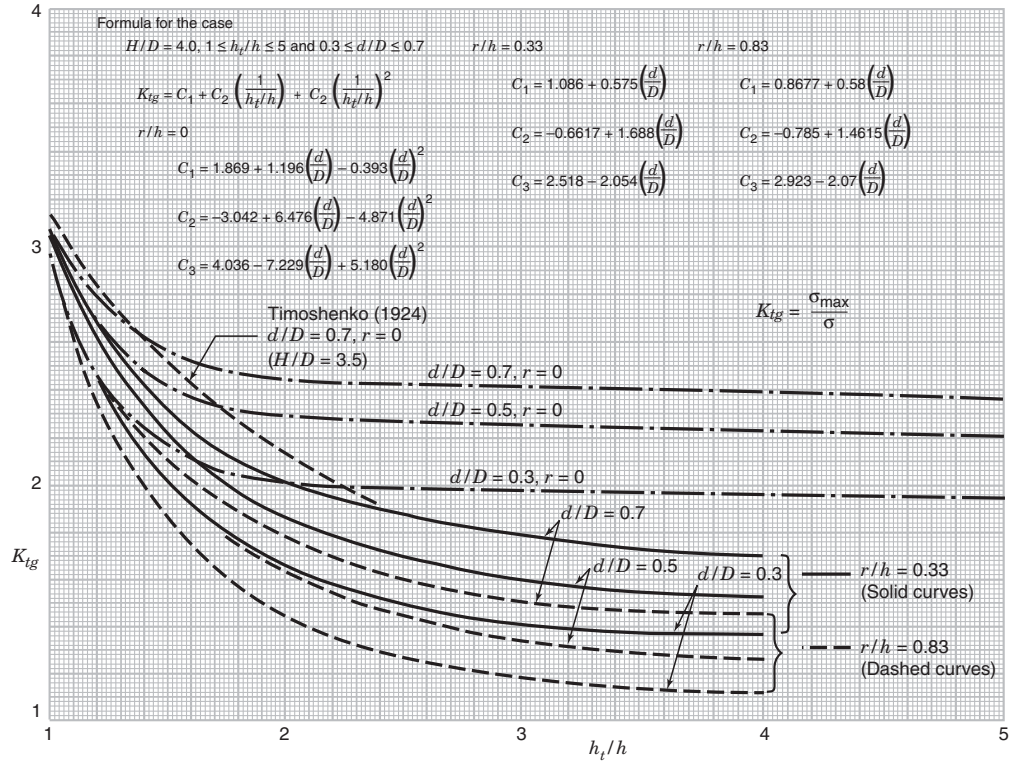


Chart 4.8*c* Stress concentration factors K_{tg} for a reinforced circular hole in a thin element in tension (Seika and Amano 1967): $H/D = 4$ (except in one case with $H/D = 3.5$), $D/h = 5.0$, $r = 0, 0.33, 0.83$.

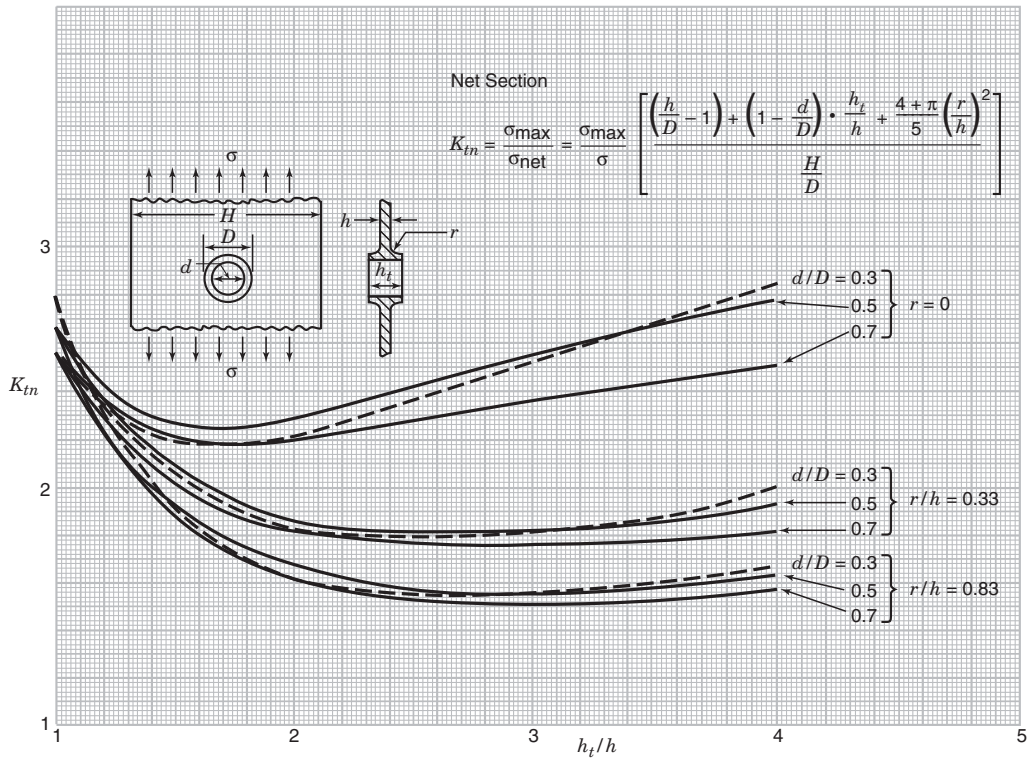


Chart 4.9 Stress concentration factors K_{tn} for a reinforced circular hole in a thin element in tension, $H/D = 4.0$, $D/h = 5.0$ (Seika and Ishii 1964; Seika and Amano 1967).

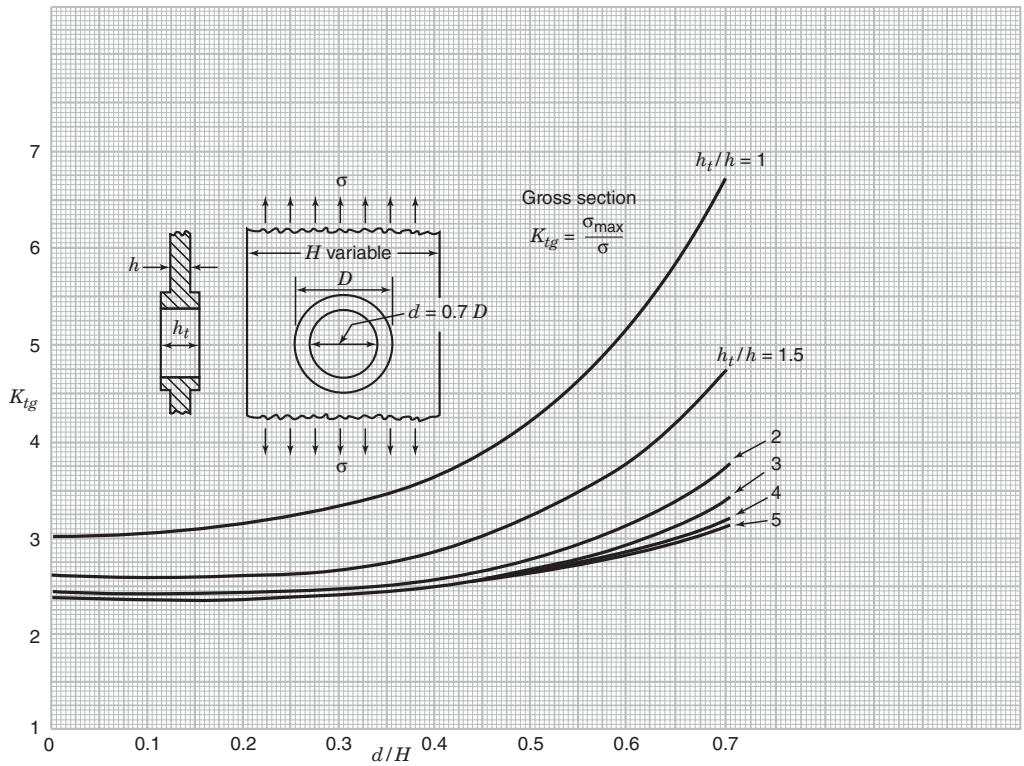


Chart 4.10 Stress concentration factors K_{tg} for a reinforced circular hole in a thin element in tension, $d/D = 0.7$, $D/h = 5.0$ (Seika and Ishii 1964).

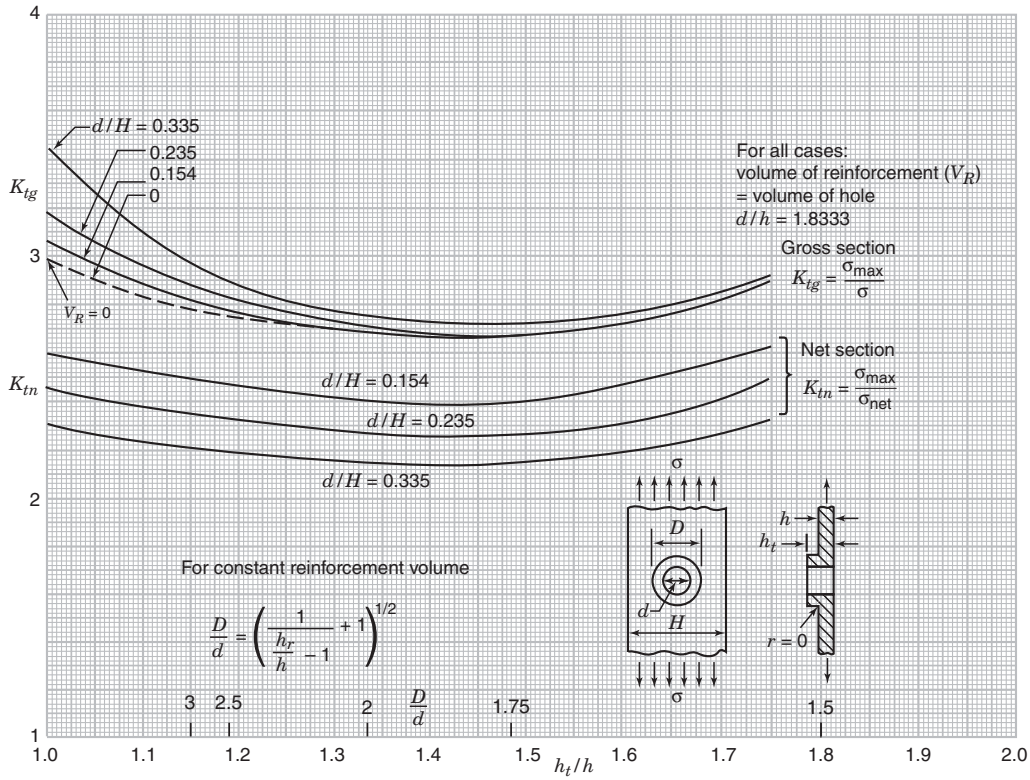


Chart 4.11 Stress concentration factors for a uniaxially stressed thin element with a reinforced circular hole on one side (from photoelastic tests of Lingaiah et al. 1966).

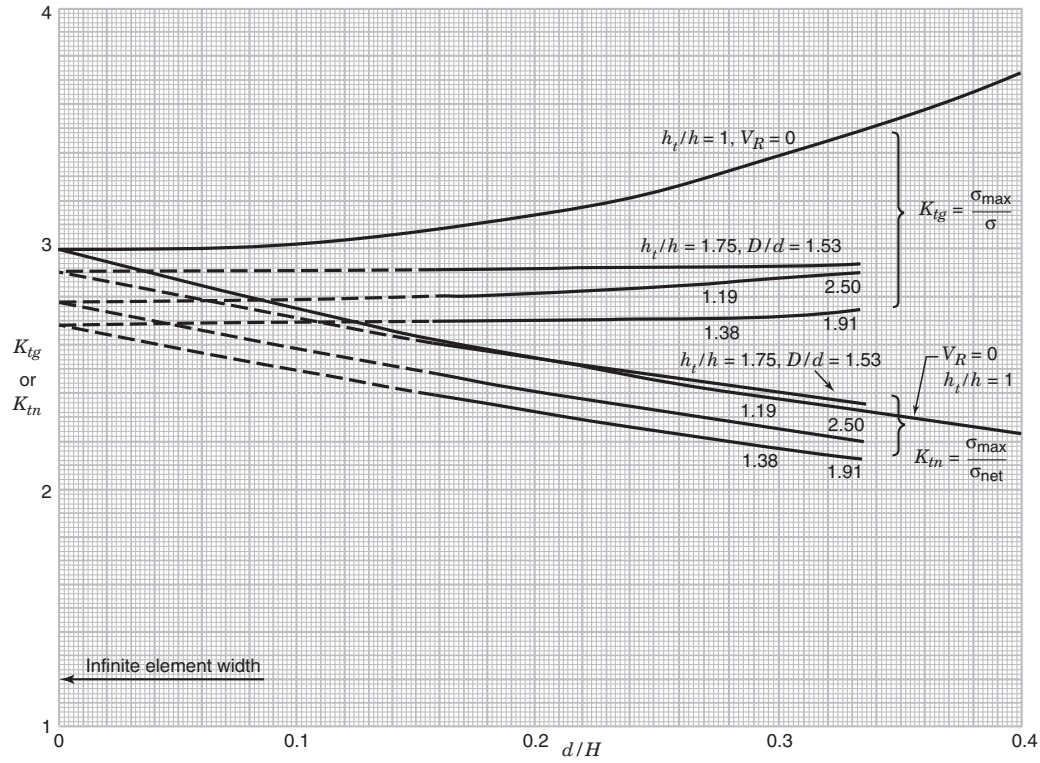
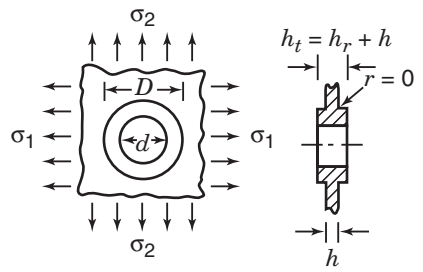


Chart 4.12 Extrapolation of K_{tg} and K_{tn} values of Chart 4.11 to an element of infinite width (from photoelastic tests of Lingaiah et al. 1966).



h_r < (D – d)
ν = 0.25

At edge of hole:

$$- - - \quad K_{ted} = \frac{\sigma_{\max d}}{\sigma_{eq}}$$

In panel at edge of reinforcement:

$$\text{———} \quad K_{teD} = \frac{\sigma_{\max D}}{\sigma_{eq}}$$

$$\sigma_{eq} = (\sigma_1^2 - \sigma_1\sigma_2 + \sigma_2^2)^{1/2}$$

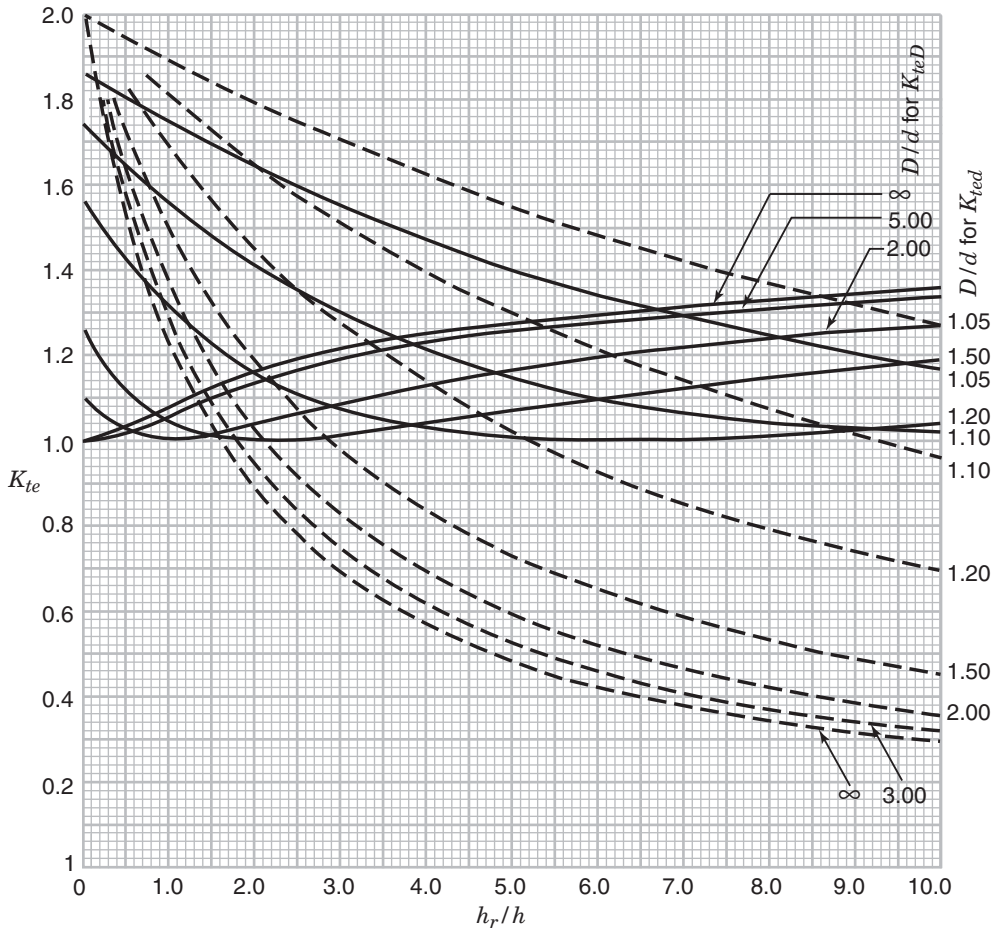


Chart 4.13*a* Analytical stress concentration factors for a symmetrically reinforced circular hole in a thin element with in-plane biaxial normal stresses, σ_1 and σ_2 (Gurney 1938; ESDU 1981): equal biaxial stresses, $\sigma_2 = \sigma_1$, $\sigma_{eq} = \sigma_1 = \sigma_2$.

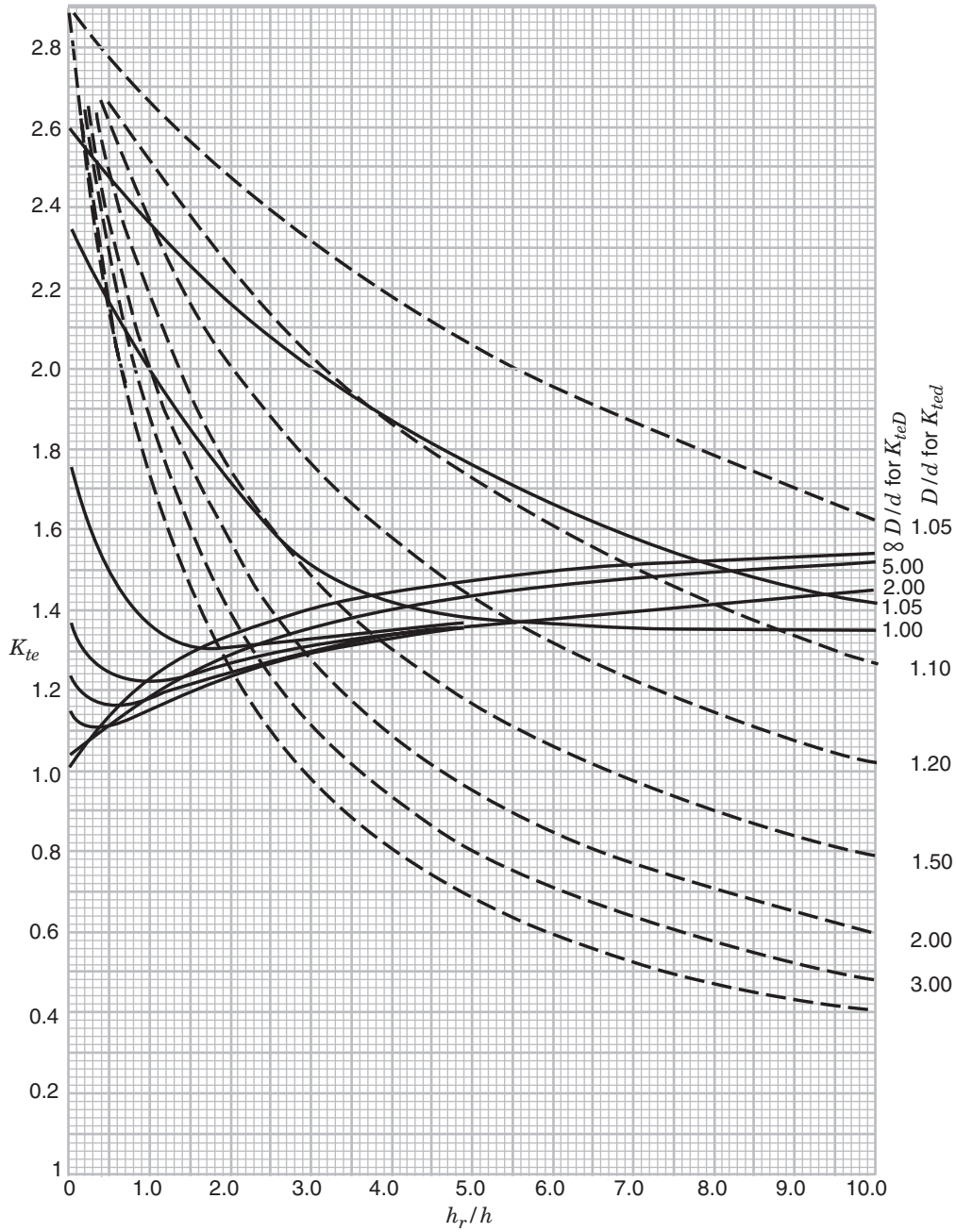


Chart 4.13*b* Analytical stress concentration factors for a symmetrically reinforced circular hole in a thin element with in-plane biaxial normal stresses, σ_1 and σ_2 (Gurney 1938; ESDU 1981): unequal biaxial stresses, $\sigma_2 = \frac{1}{2}\sigma_1$, $\sigma_{eq} = (\sqrt{3}/2)\sigma_1$.

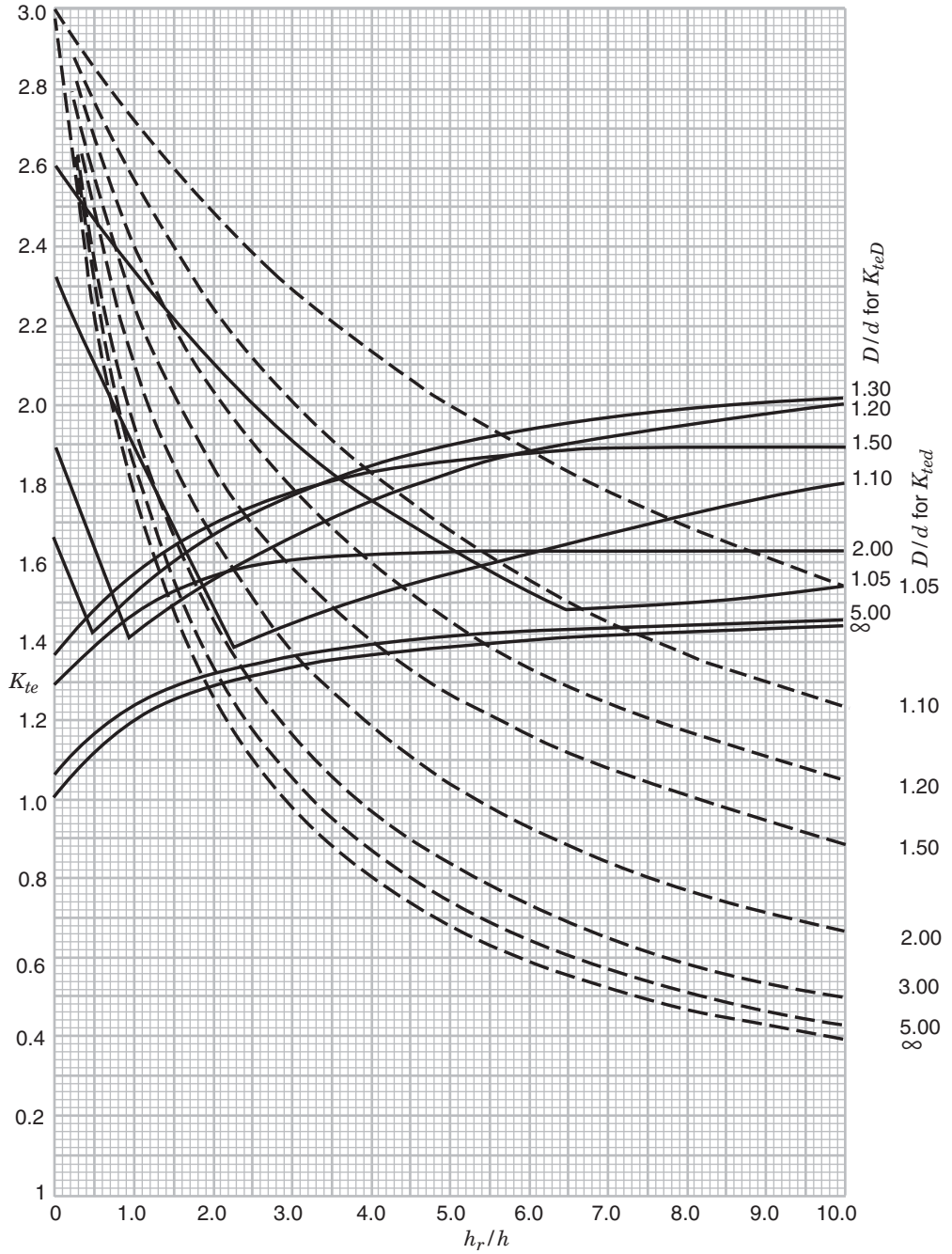


Chart 4.13*c* Analytical stress concentration factors for a symmetrically reinforced circular hole in a thin element with in-plane biaxial normal stresses, σ_1 and σ_2 (Gurney 1938; ESDU 1981): uniaxial stress, $\sigma_2 = 0$, $\sigma_1 = \sigma$, $\sigma_{eq} = \sigma$.

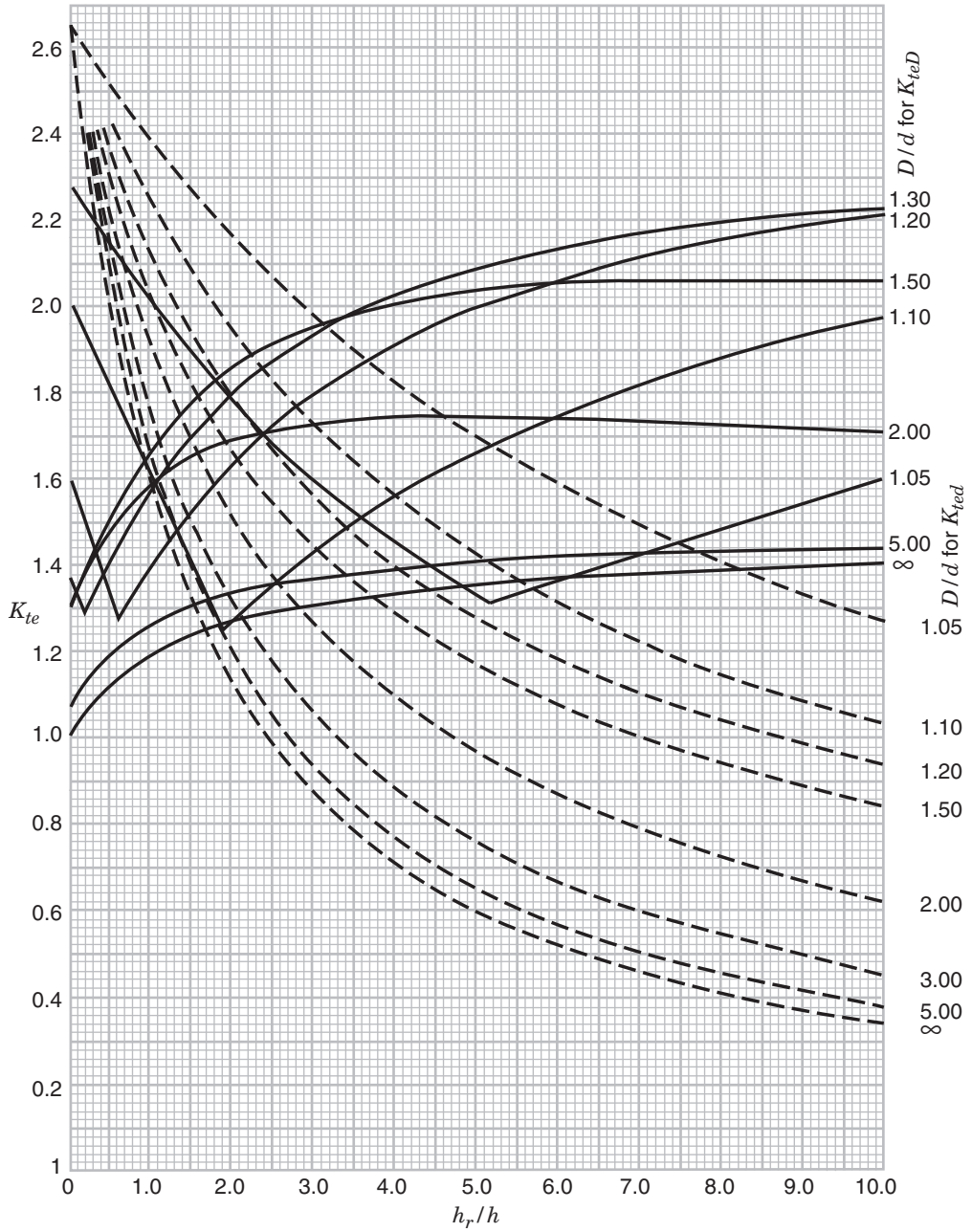


Chart 4.13*d* Analytical stress concentration factors for a symmetrically reinforced circular hole in a thin element with in-plane biaxial normal stresses, σ_1 and σ_2 (Gurney 1938; ESDU 1981): unequal tensile and compressive biaxial stresses, $\sigma_2 = -\frac{1}{2}\sigma_1$, $\sigma_{eq} = -(\sqrt{7}/2)\sigma_1$.

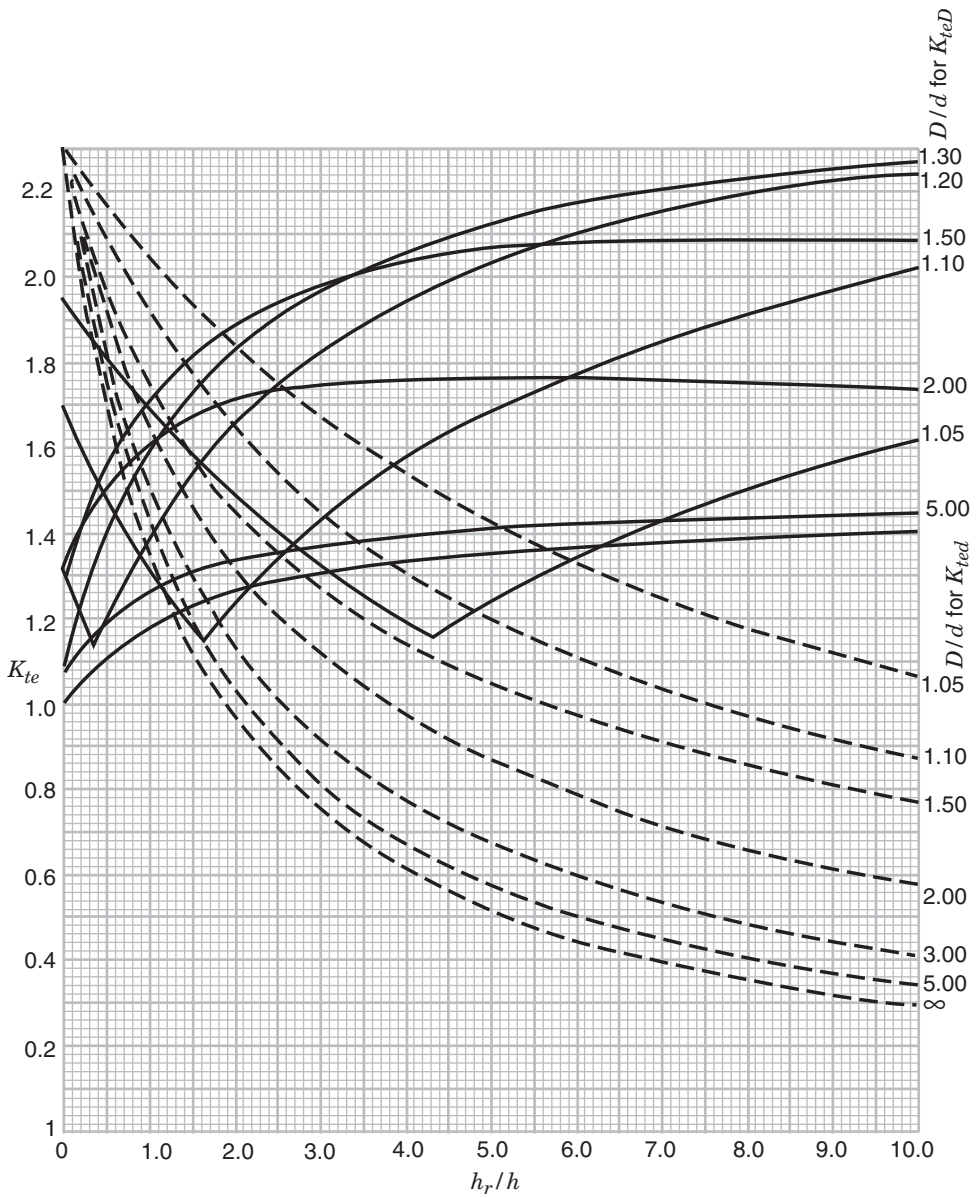


Chart 4.13*e* Analytical stress concentration factors for a symmetrically reinforced circular hole in a thin element with in-plane biaxial normal stresses, σ_1 and σ_2 (Gurney 1938; ESDU 1981): pure shear, equal tensile and compressive biaxial stresses, $\sigma_2 = -\sigma_1$, $\sigma_{eq} = \sqrt{3}\sigma_1$.

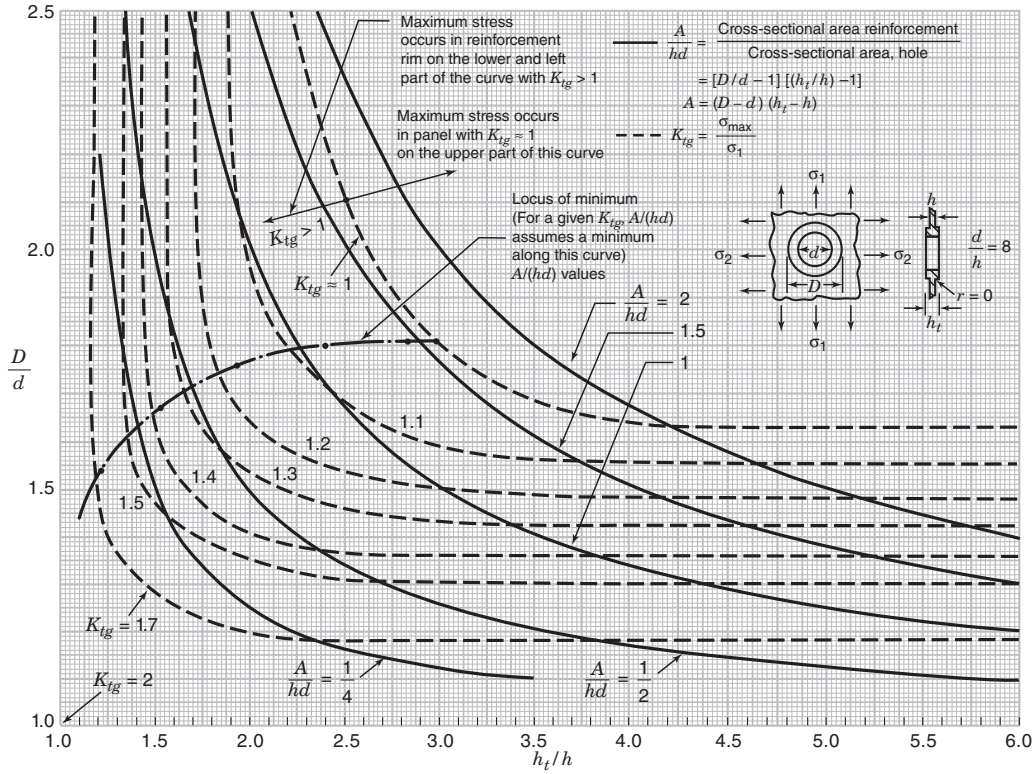


Chart 4.14 Area ratios and experimental stress concentration factors K_{tg} for a symmetrically reinforced circular hole in a panel with equal biaxial normal stresses, $\sigma_1 = \sigma_2$ (approximate results based on strain gage tests by Kaufman et al. 1962).

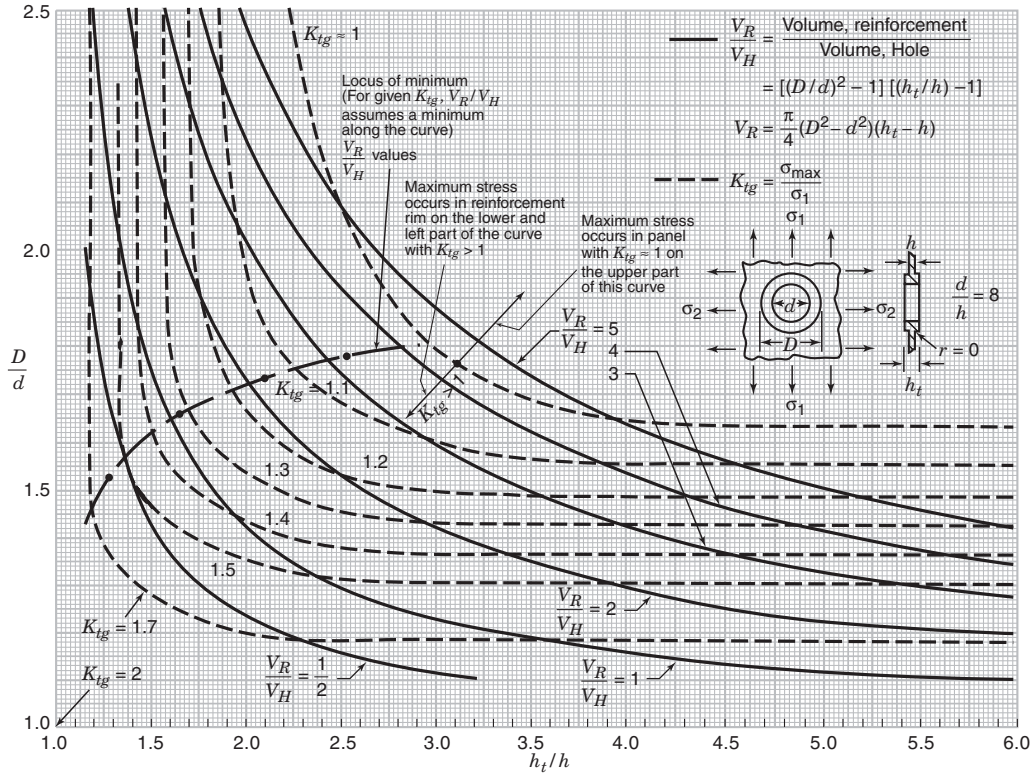


Chart 4.15 Volume ratios and experimental stress concentration factors K_{tg} for a symmetrically reinforced circular hole in a panel with equal biaxial normal stresses, $\sigma_1 = \sigma_2$ (approximate results based on strain gage tests by Kaufman et al. 1962).

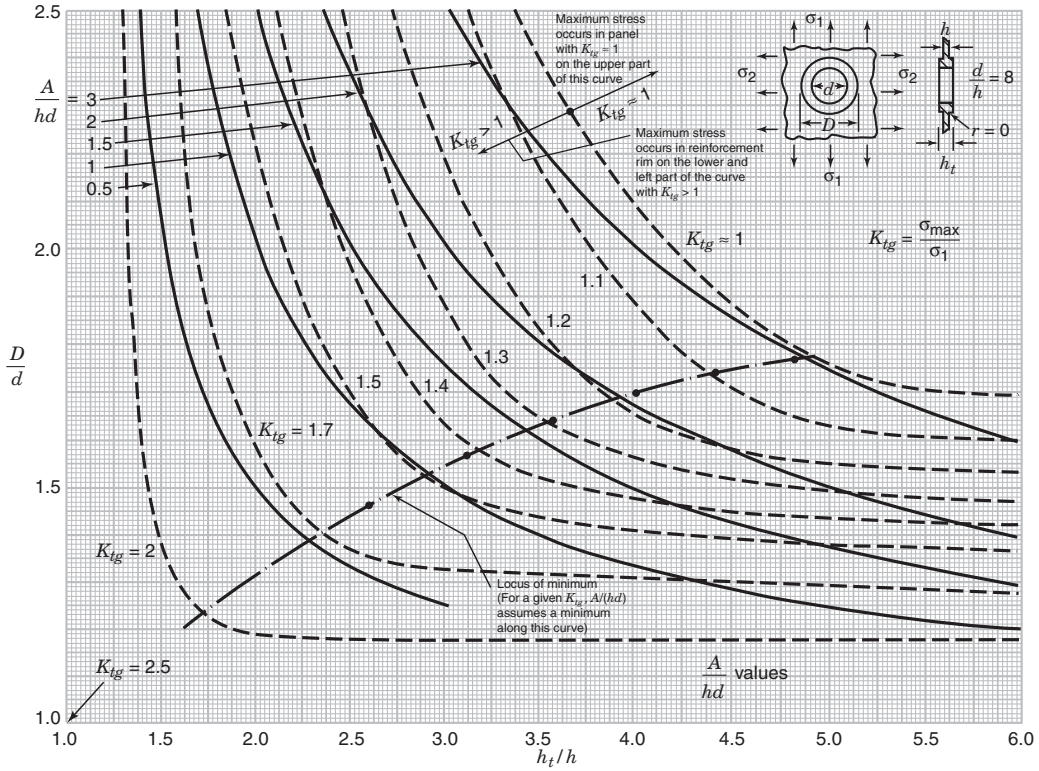


Chart 4.16 Area ratios and experimental stress concentration factors K_{tg} for a symmetrically reinforced circular hole in a panel with unequal biaxial normal stresses, $\sigma_2 = \sigma_1/2$ (approximate results based on strain gage tests by Kaufman et al. 1962).

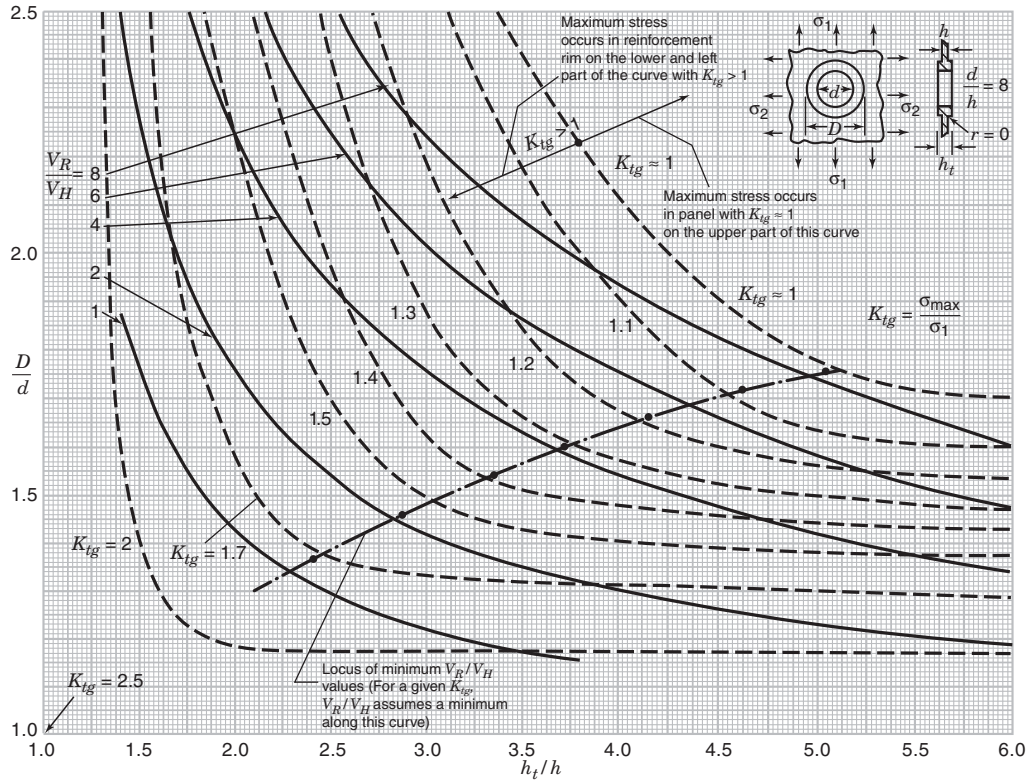


Chart 4.17 Volume ratios and experimental stress concentration factors K_{tg} for a symmetrically reinforced circular hole in a panel with unequal biaxial normal stresses, $\sigma_2 = \sigma_1/2$ (approximate results based on strain gage tests by Kaufman et al. 1962).

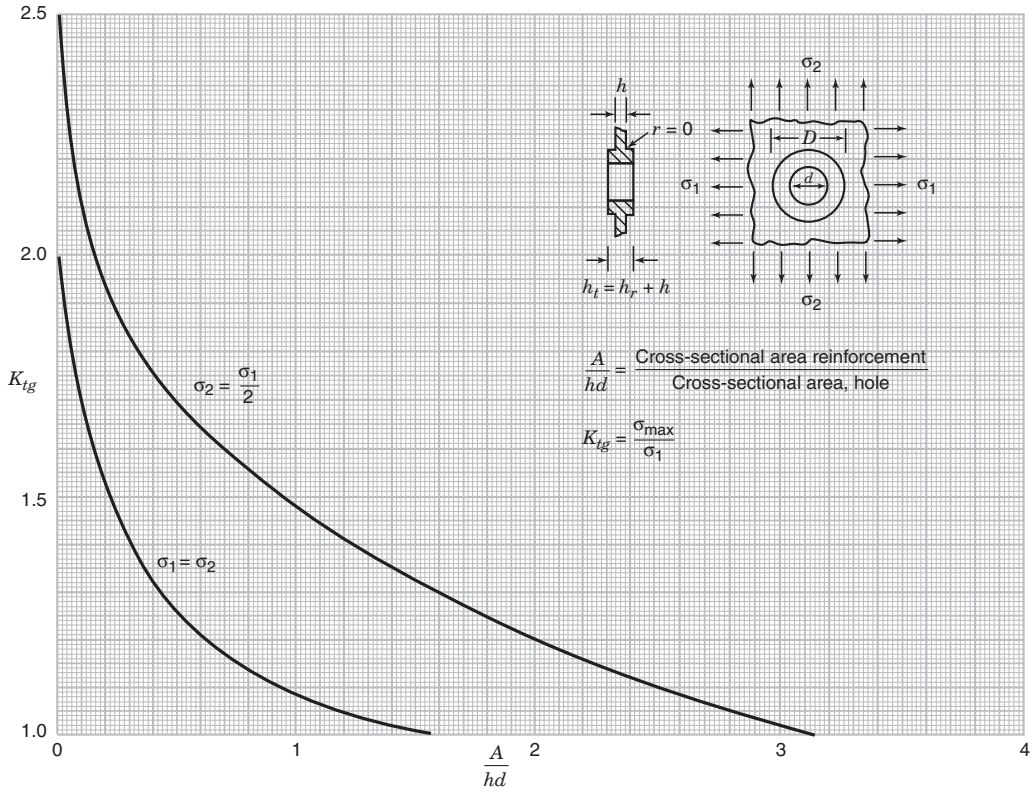


Chart 4.18 Approximate minimum values of K_{tg} versus area ratios for a symmetrically reinforced circular hole in a panel with biaxial normal stresses (based on strain gage tests by Kaufman et al. 1962).

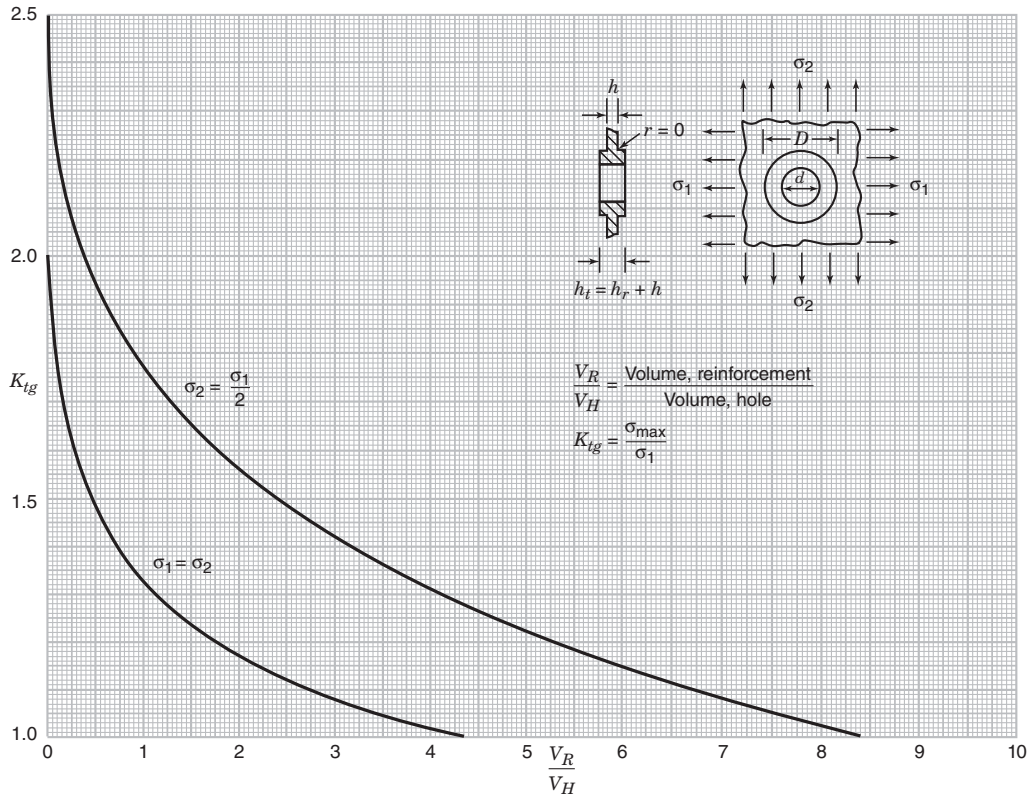


Chart 4.19 Approximate minimum values of K_{tg} versus volume ratios for a symmetrically reinforced circular hole in a panel with biaxial normal stresses (based on strain gage tests by Kaufman et al. 1962).

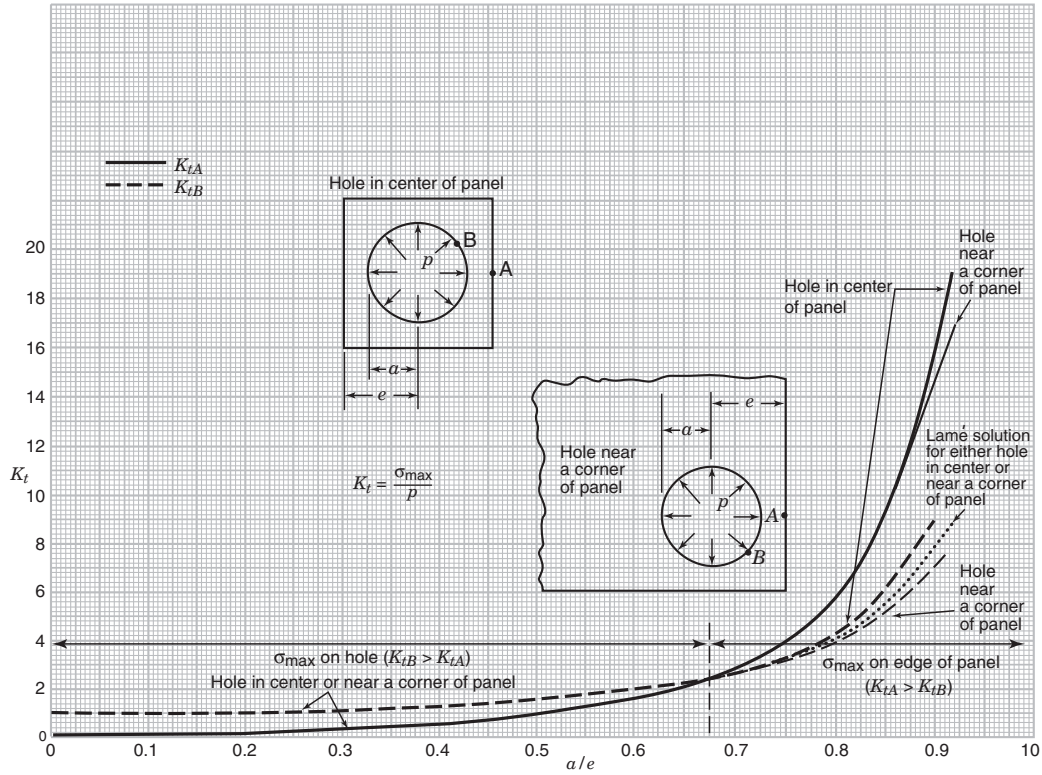


Chart 4.20 Stress concentration factors K_t for a square panel with a pressurized circular hole (Durelli and Kobayashi 1958; Riley et al. 1959).

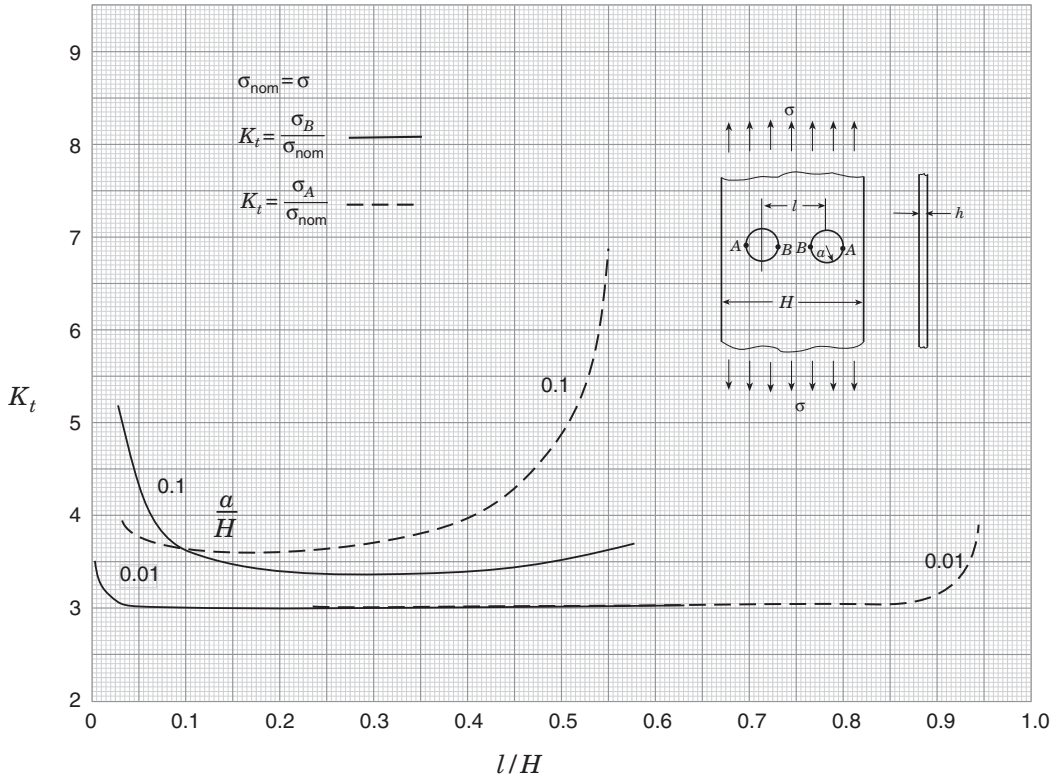


Chart 4.21*a* Stress concentration factors for the tension of a finite-width panel with two circular holes (ESDU 1985).

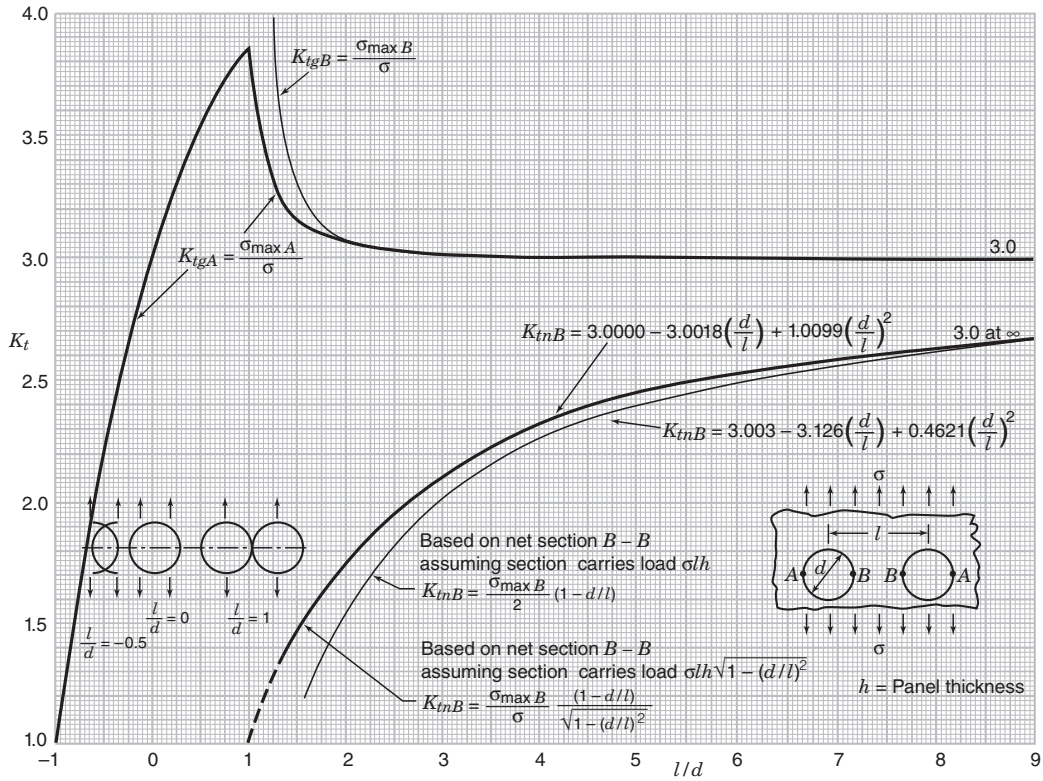


Chart 4.21*b* Stress concentration factors K_{tg} and K_{tn} for tension case of an infinite panel with two circular holes (based on mathematical analyses of Ling 1948a,b and Haddon 1967). Tension perpendicular to the line of holes.

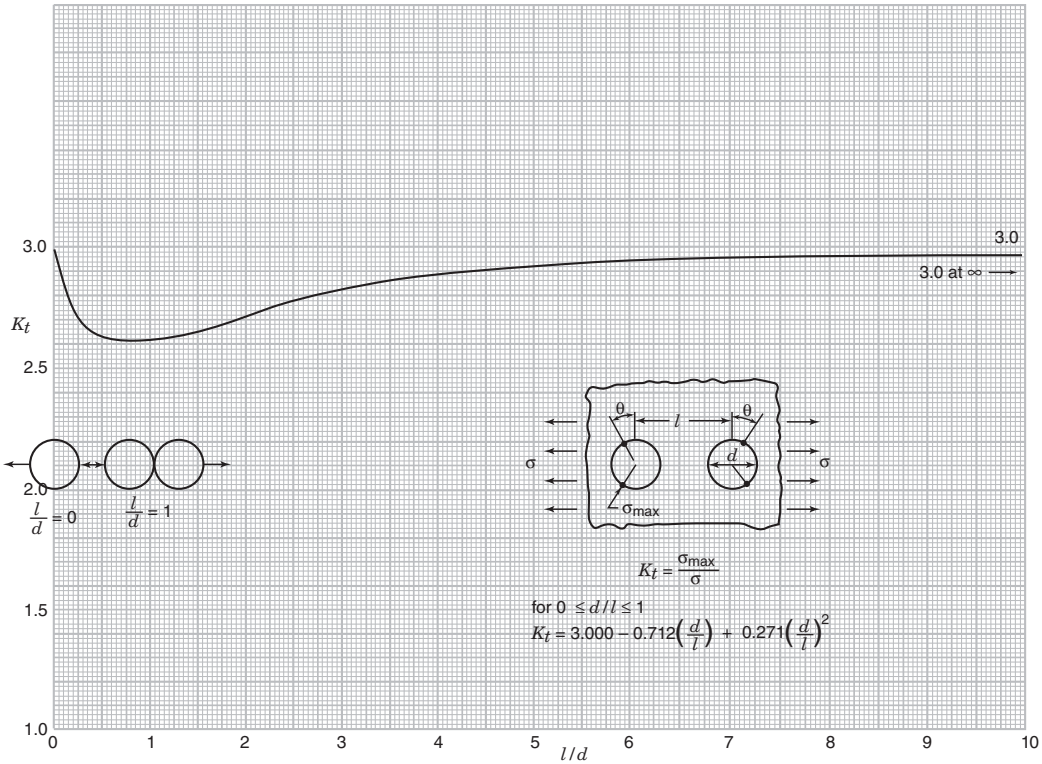


Chart 4.22 Stress concentration factors K_t for uniaxial tension case of an infinite panel with two circular holes (based on mathematical analysis of Ling 1948a,b and Haddon 1967). Tension parallel to the line of holes.

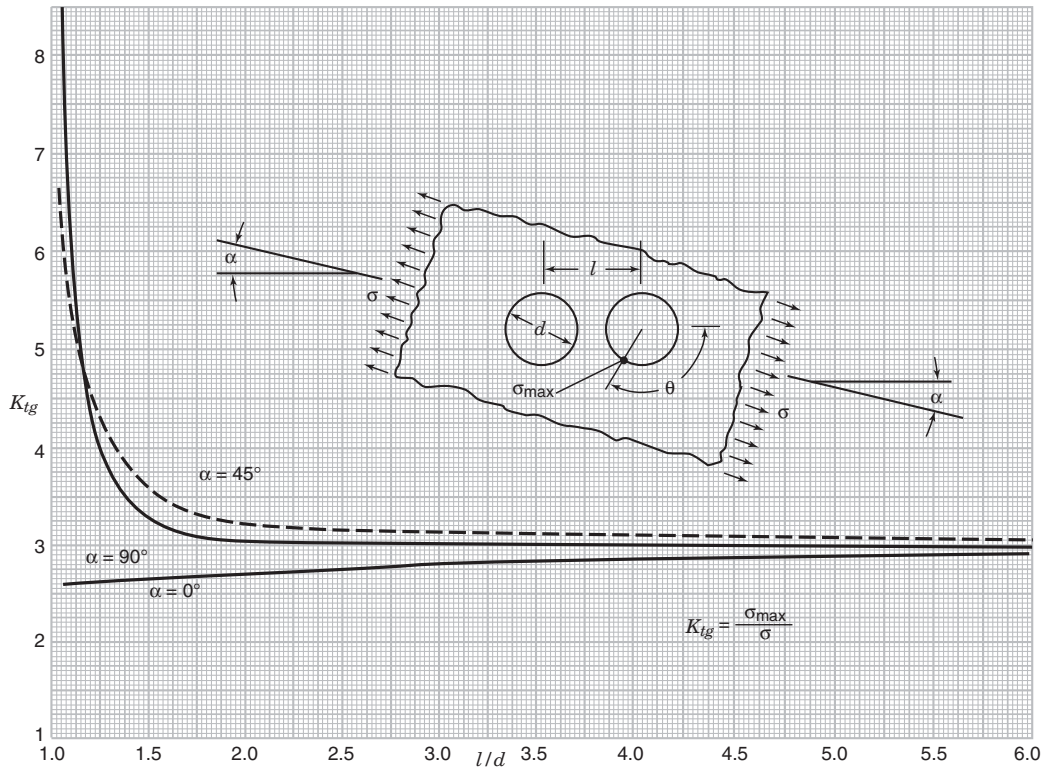


Chart 4.23 Stress concentration factors K_{tg} for tension case of an infinite panel with two circular holes (from mathematical analysis of Haddon 1967). Tension at various angles.

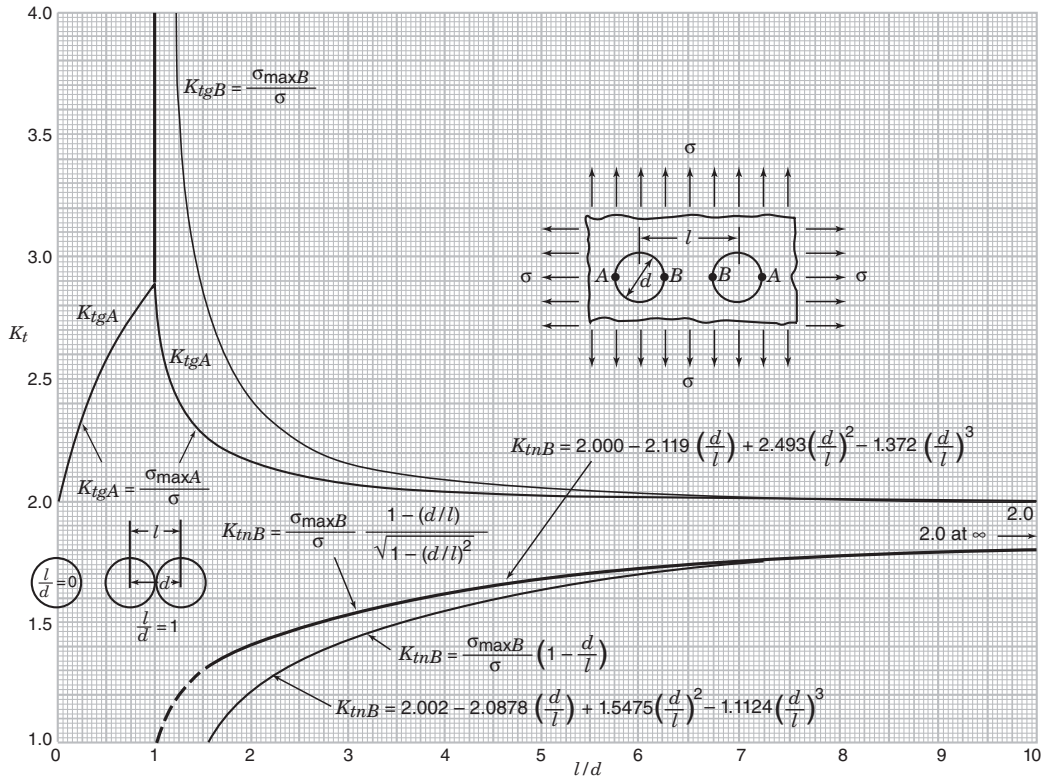
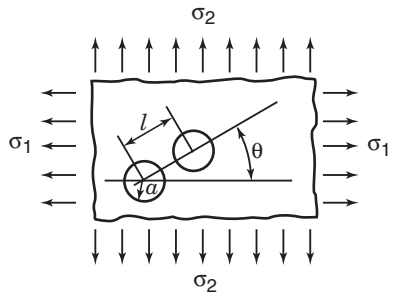


Chart 4.24 Stress concentration factors K_{tg} and K_{tn} for equal biaxial tension case of an infinite panel with two circular holes (based on mathematical analyses of Ling 1948a,b and Haddon 1967).



$$K_{tg} = \frac{\sigma_{max}}{\sigma_1}$$

σ_{max} = Maximum normal stress at the boundary of the holes

σ_1, σ_2 are positive in tension, negative in compression.

$|\sigma_1| \geq |\sigma_2|$

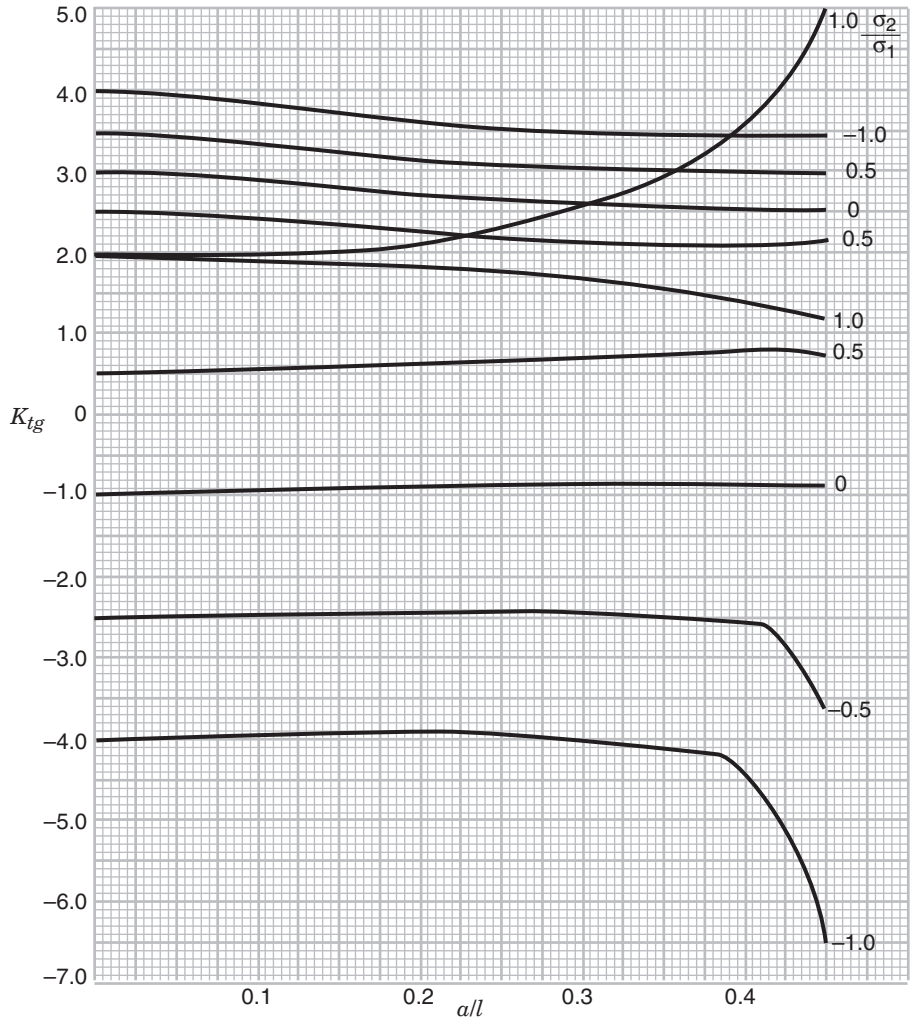


Chart 4.25*a* Stress concentration factors K_{tg} for a panel with two holes under biaxial stresses (Haddon 1967; ESDU 1981): $\theta = 0°$.

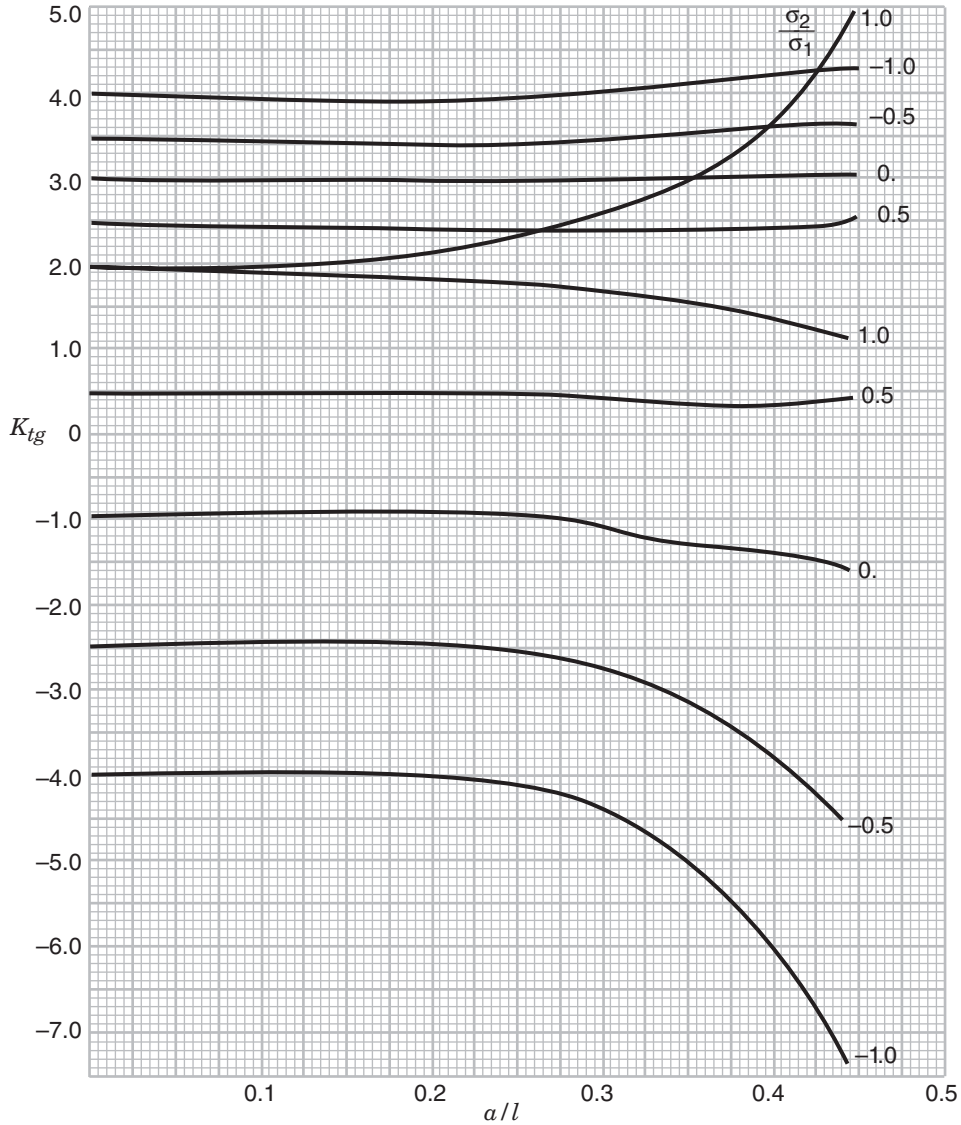


Chart 4.25*b* Stress concentration factors K_{tg} for a panel with two holes under biaxial stresses (Haddon 1967; ESDU 1981): $\theta = 15^{\circ}$.

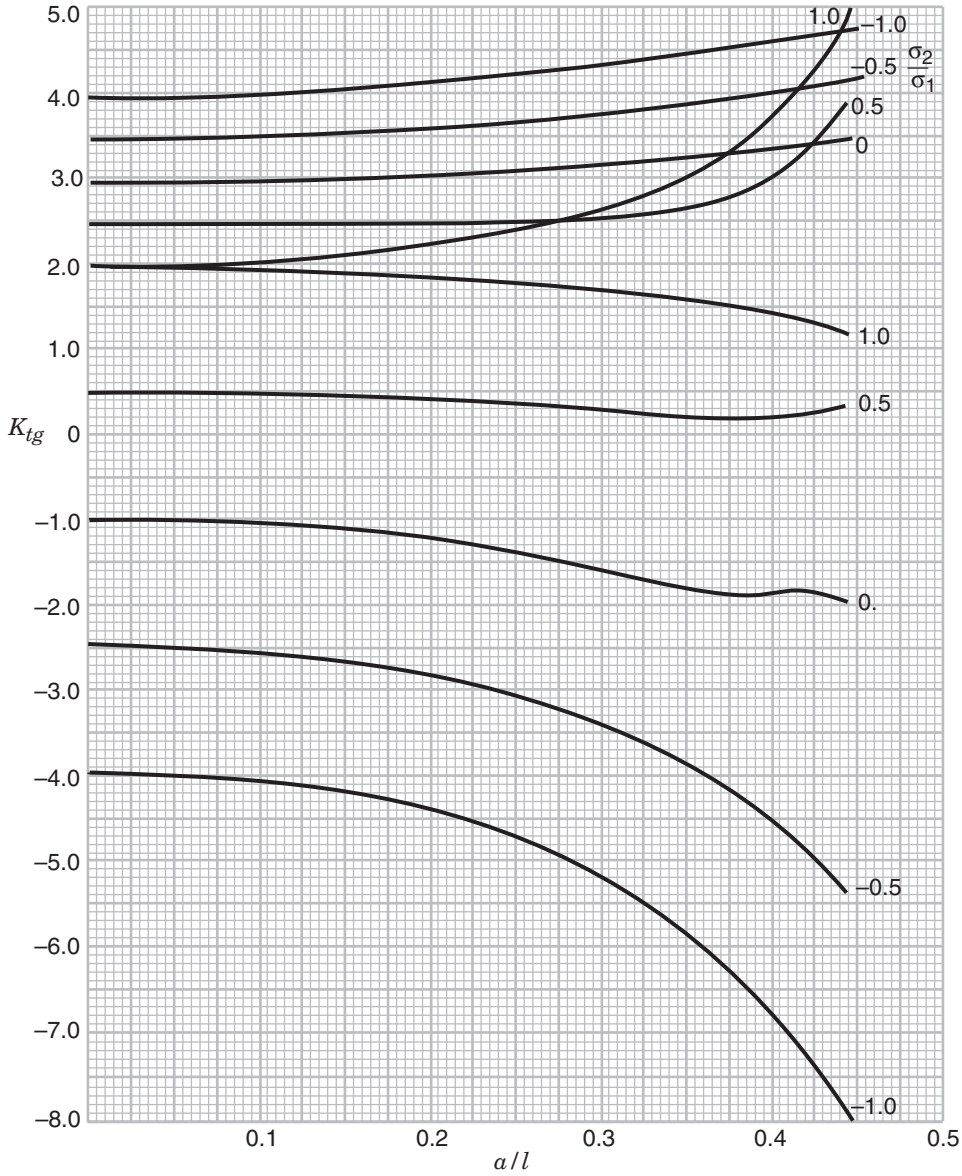


Chart 4.25*c* Stress concentration factors K_{tg} for a panel with two holes under biaxial stresses (Haddon 1967; ESDU 1981): $\theta = 30^{\circ}$.

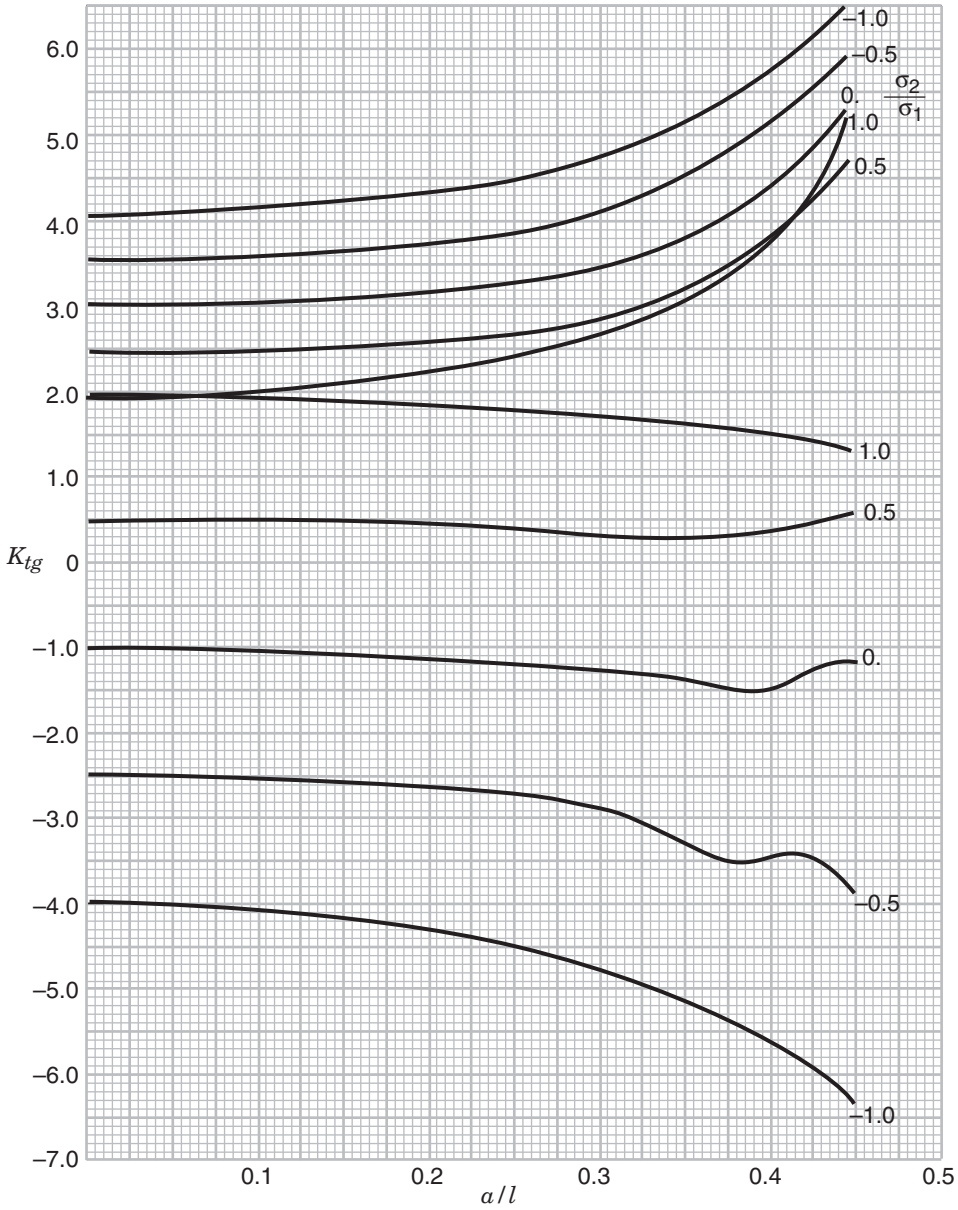


Chart 4.25*d* Stress concentration factors K_{tg} for a panel with two holes under biaxial stresses (Haddon 1967; ESDU 1981): $\theta = 45^{\circ}$.

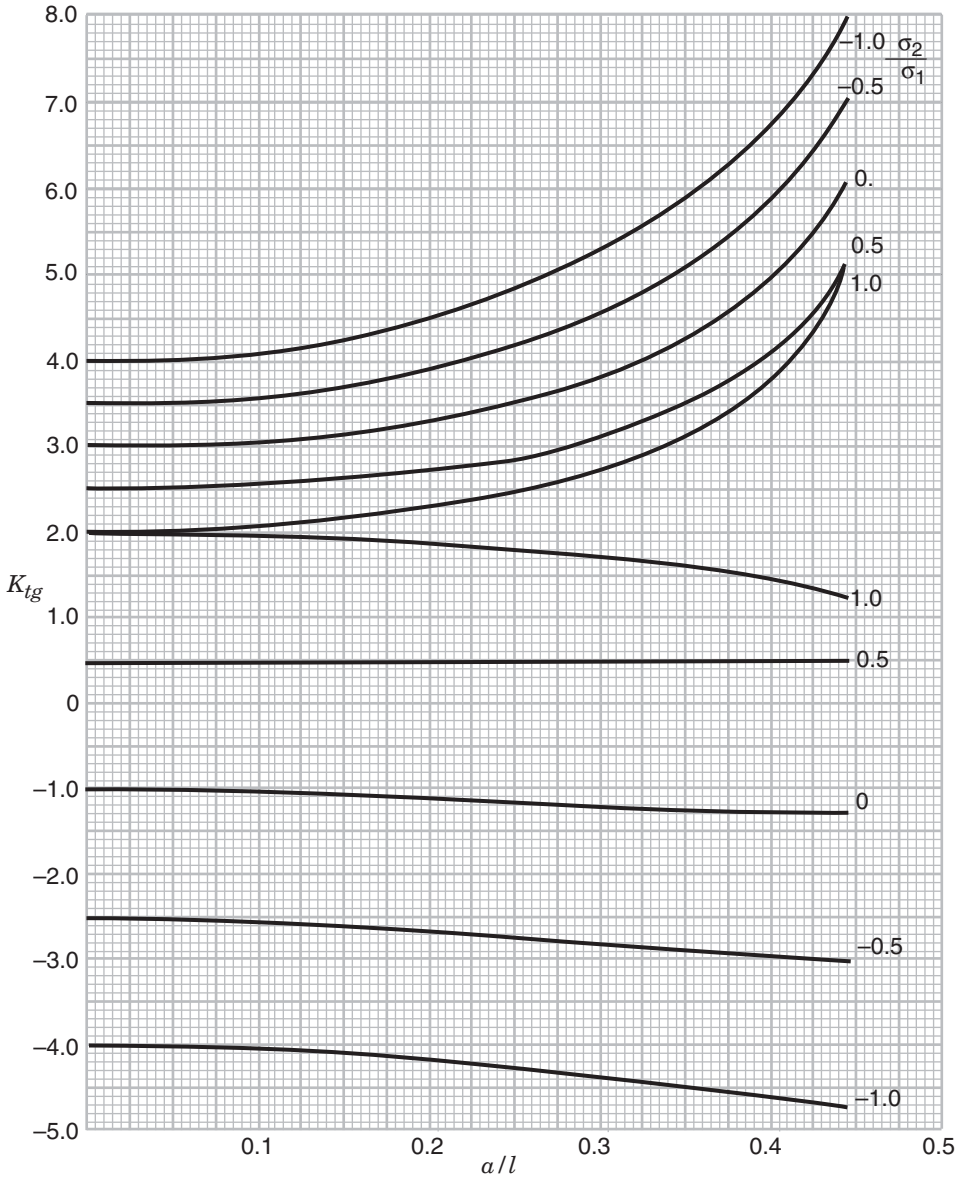


Chart 4.25*e* Stress concentration factors K_{tg} for a panel with two holes under biaxial stresses (Haddon 1967; ESDU 1981): $\theta = 60^{\circ}$.

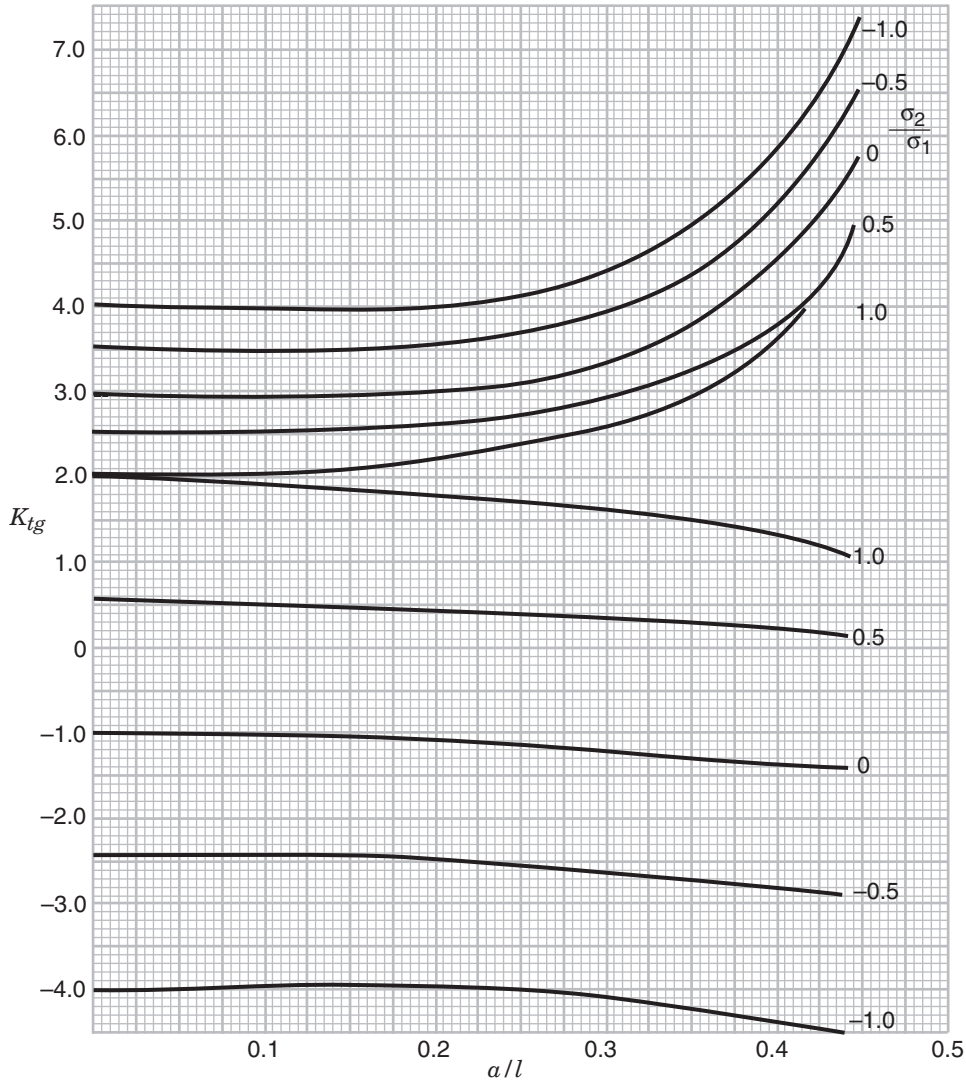


Chart 4.25*f* Stress concentration factors K_{tg} for a panel with two holes under biaxial stresses (Haddon 1967; ESDU 1981): $\theta = 75^\circ$.

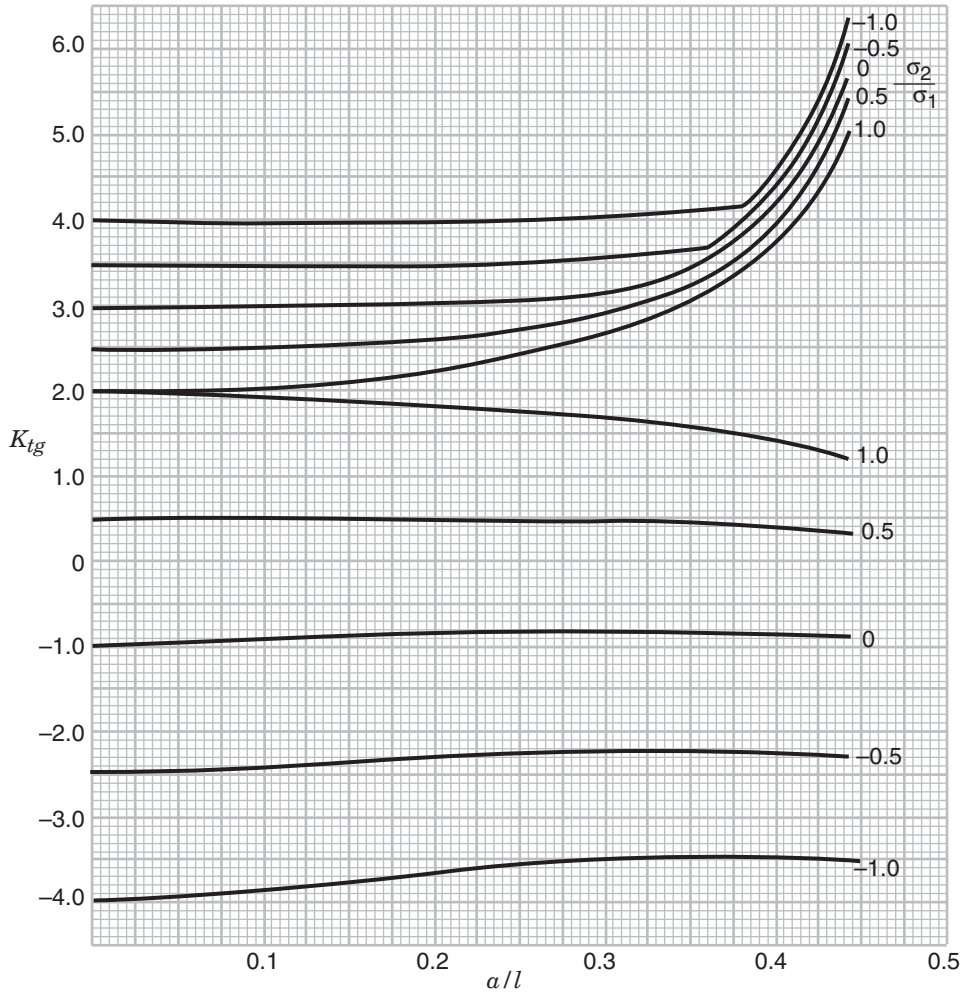


Chart 4.25*g* Stress concentration factors K_{tg} for a panel with two holes under biaxial stresses (Haddon 1967; ESDU 1981): $\theta = 90^\circ$.

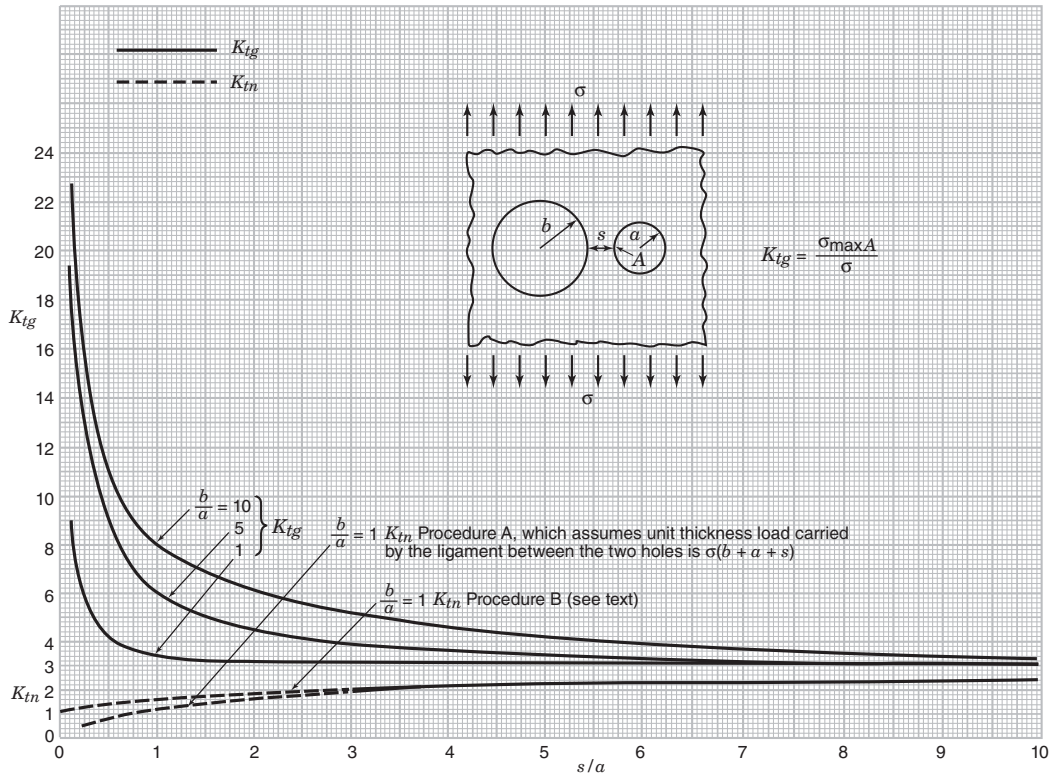


Chart 4.26 Stress concentration factors K_{tg} and K_{tn} for tension in an infinite thin element with two circular holes of unequal diameter (from mathematical analysis of Haddon 1967). Tension perpendicular to the line of holes.

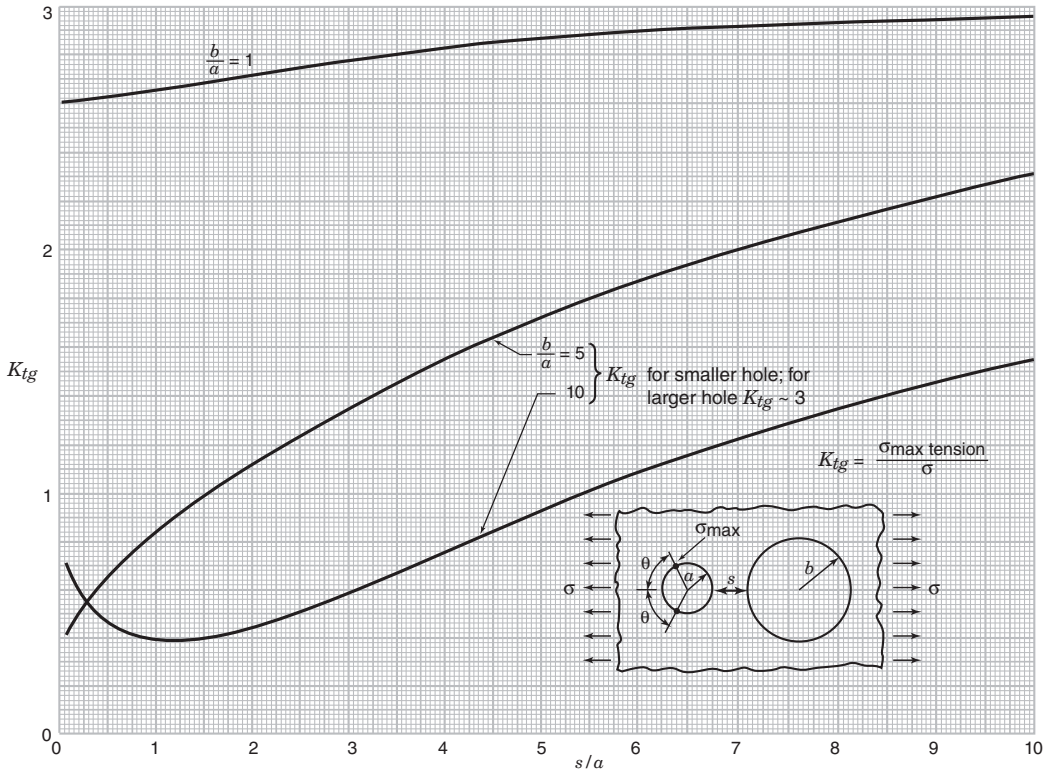


Chart 4.27 Stress concentration factors K_{tg} for tension in an infinite thin element with two circular holes of unequal diameter (from mathematical analysis of Haddon 1967). Tension parallel to the line of holes.

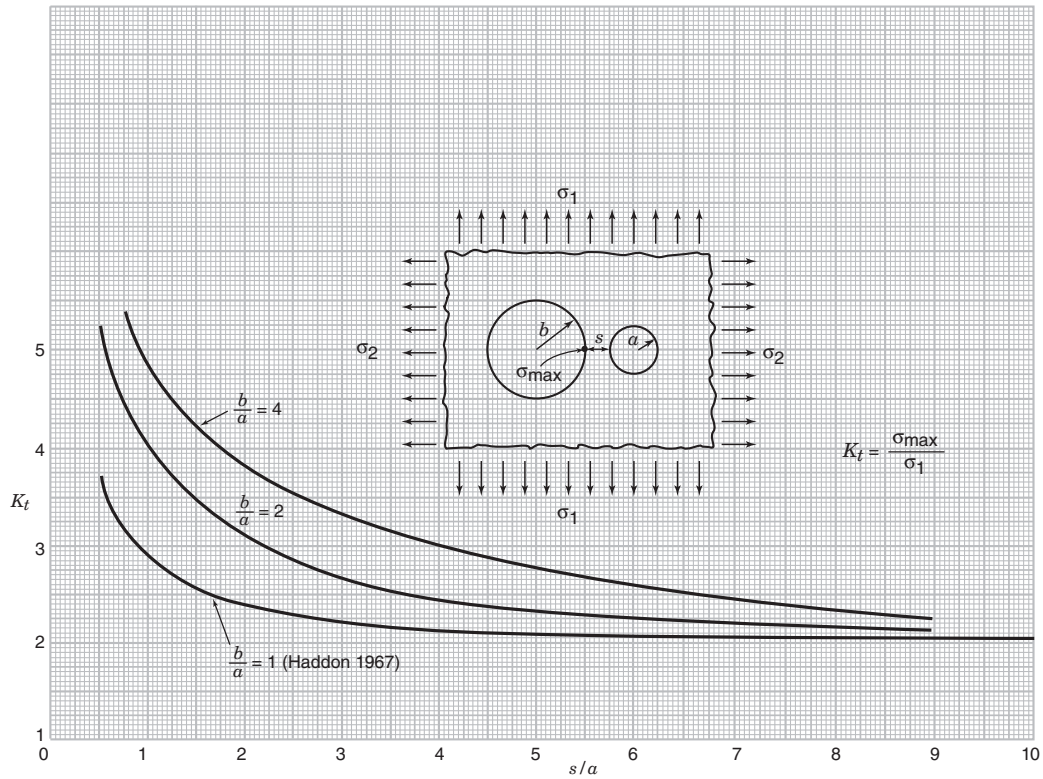


Chart 4.28 Stress concentration factors K_t for biaxial tension in infinite thin element with two circular holes of unequal diameter, $\sigma_1 = \sigma_2$ (Haddon 1967; Salerno and Mahoney 1968).

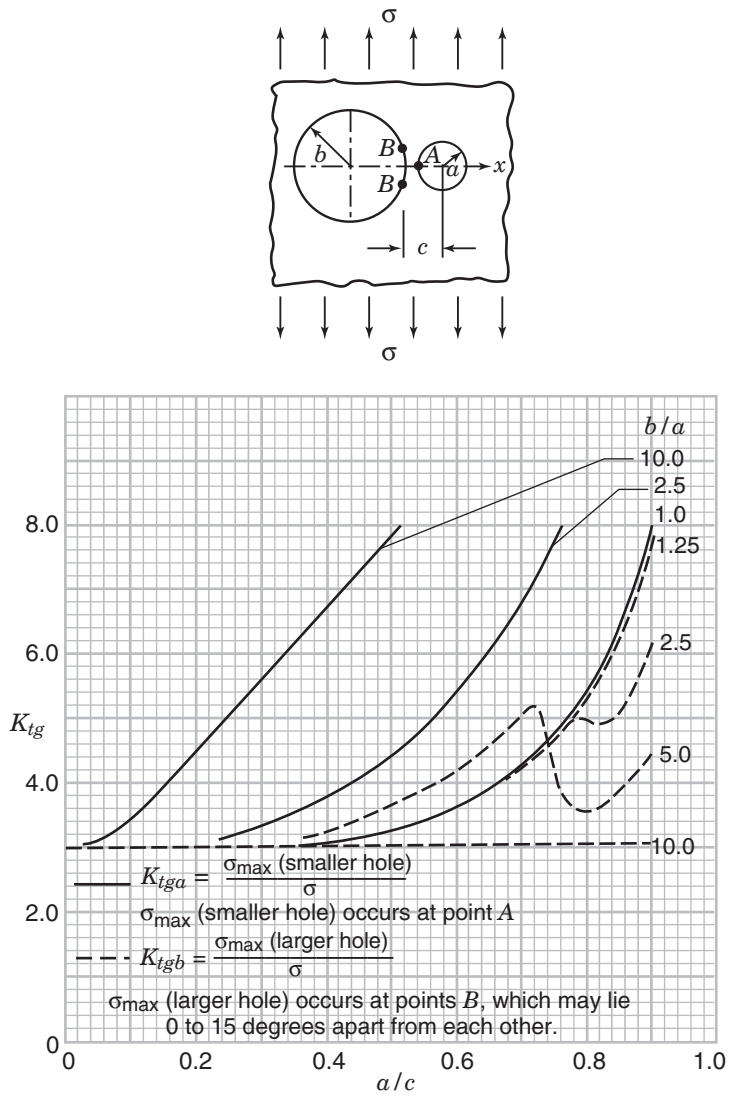


Chart 4.29 Stress concentration factors K_{tg} for tension in infinite thin element with two circular holes of unequal diameter (from mathematical analysis of Haddon 1967; ESDU 1981). Tension perpendicular to the line of holes.

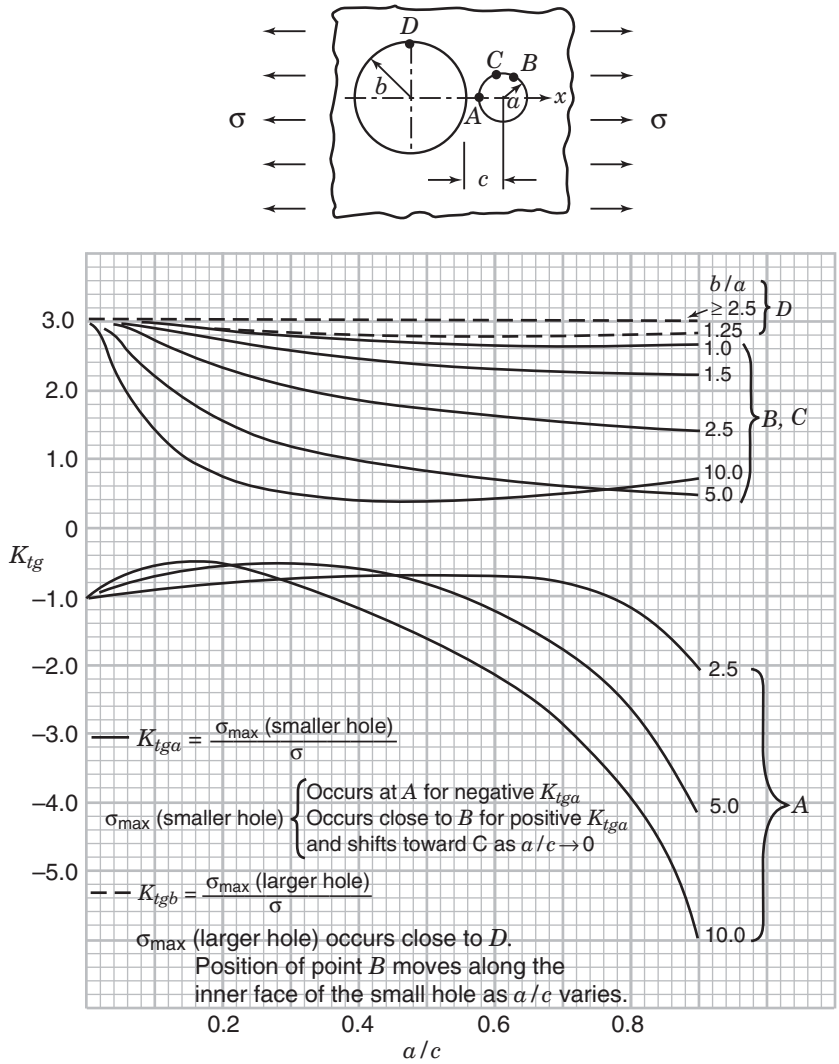
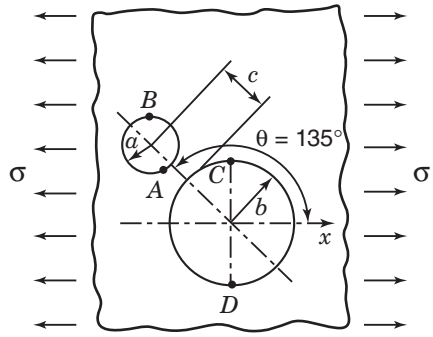


Chart 4.30 Stress concentration factors K_{tg} for tension in infinite thin element with two circular holes of unequal diameter (from mathematical analysis of Haddon 1967; ESDU 1981). Tension parallel to the line of holes.



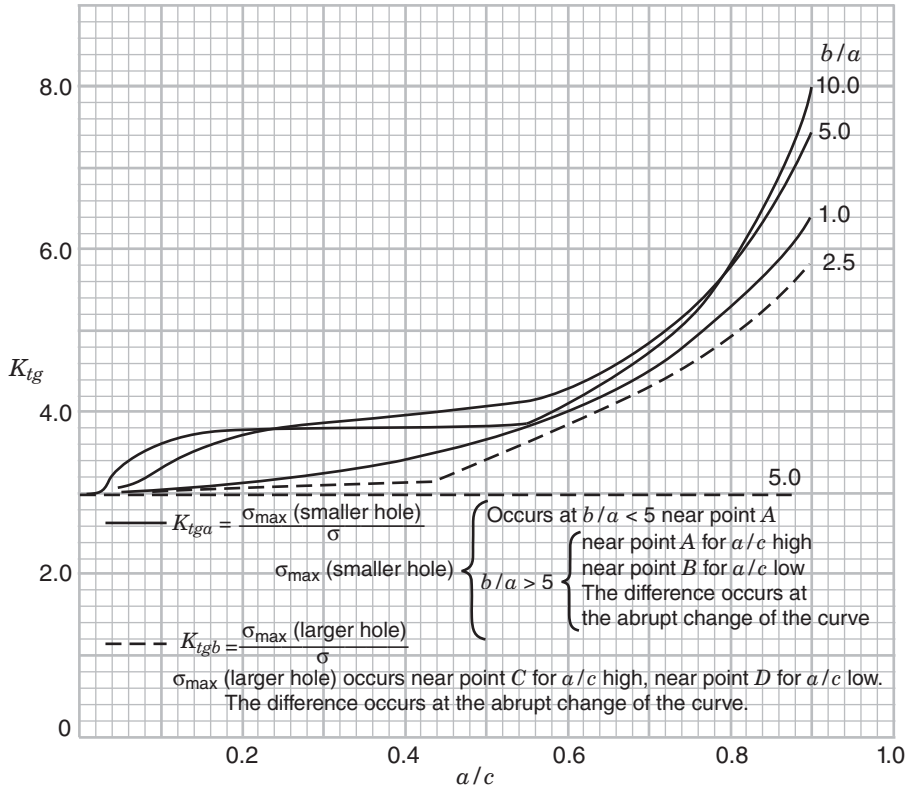


Chart 4.31 Stress concentration factors K_{tg} for tension in infinite thin element with two circular holes of unequal diameter (from mathematical analysis of Haddon 1967; ESDU 1981). Holes aligned diagonal to the loading.

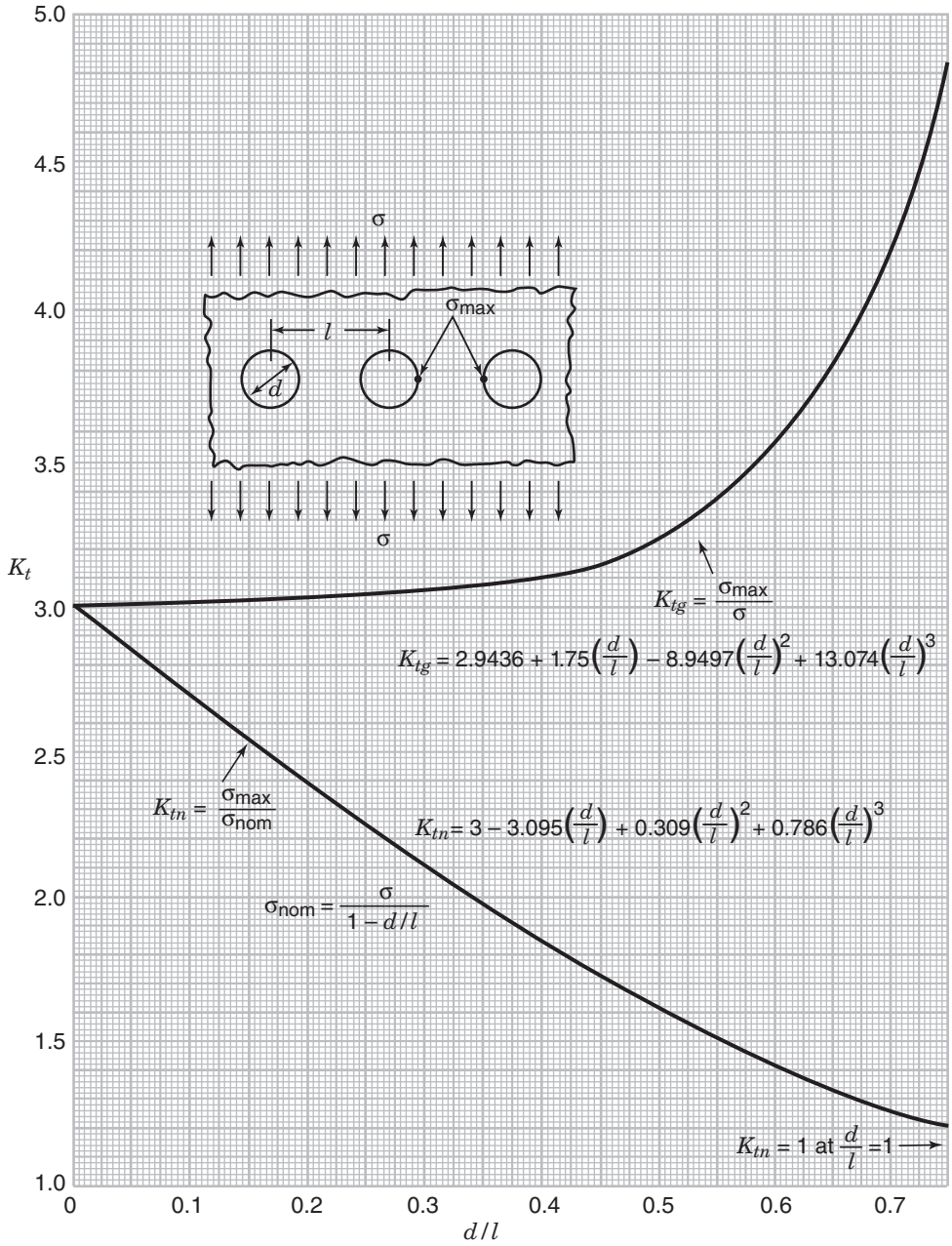


Chart 4.32 Stress concentration factors K_{tg} and K_{tn} for uniaxial tension of an infinite thin element with an infinite row of circular holes (Schulz 1941). Stress perpendicular to the axis of the holes.

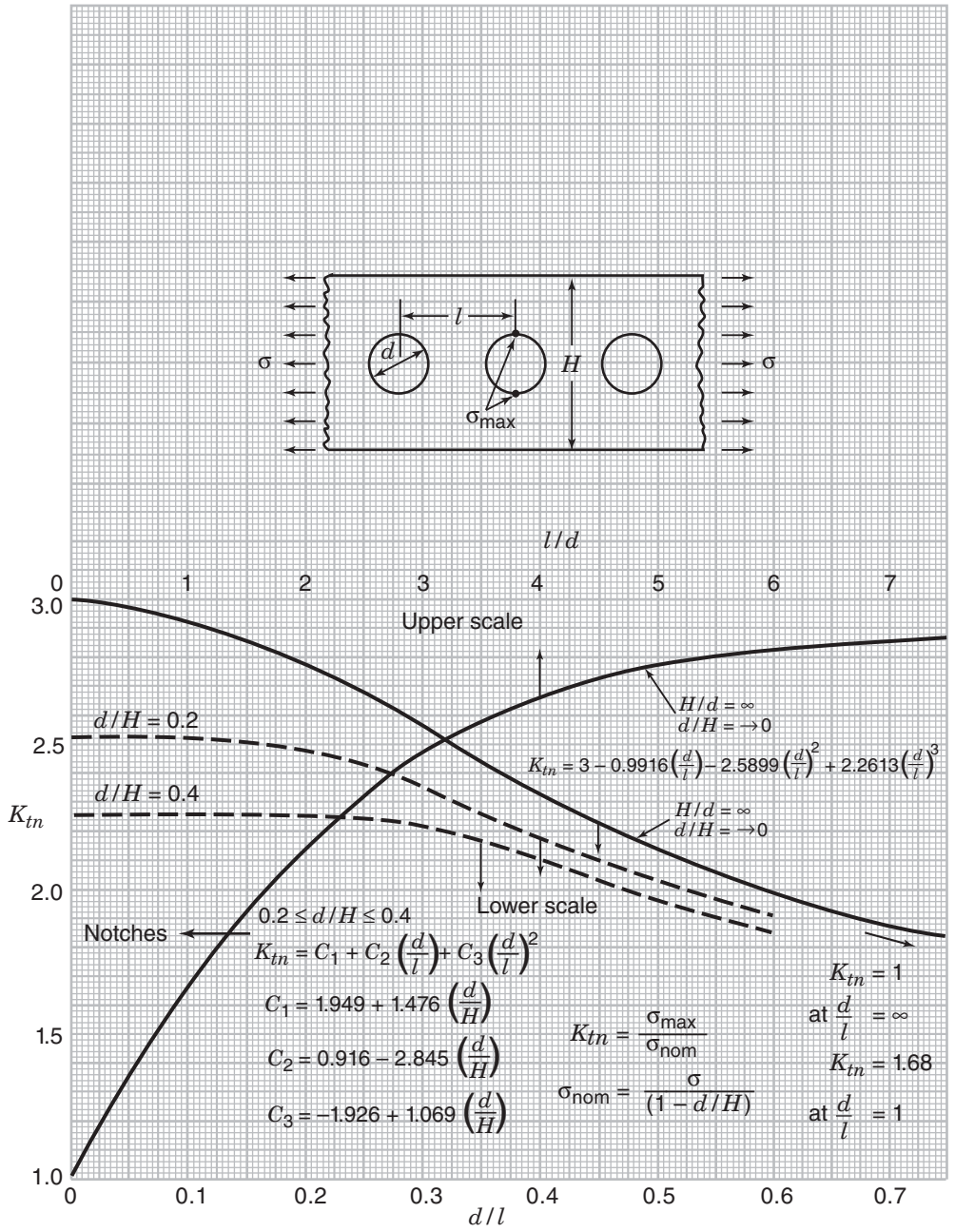


Chart 4.33 Stress concentration factors K_{tn} for uniaxial tension of a finite-width thin element with an infinite row of circular holes (Schulz 1941). Stress parallel to the axis of the holes.

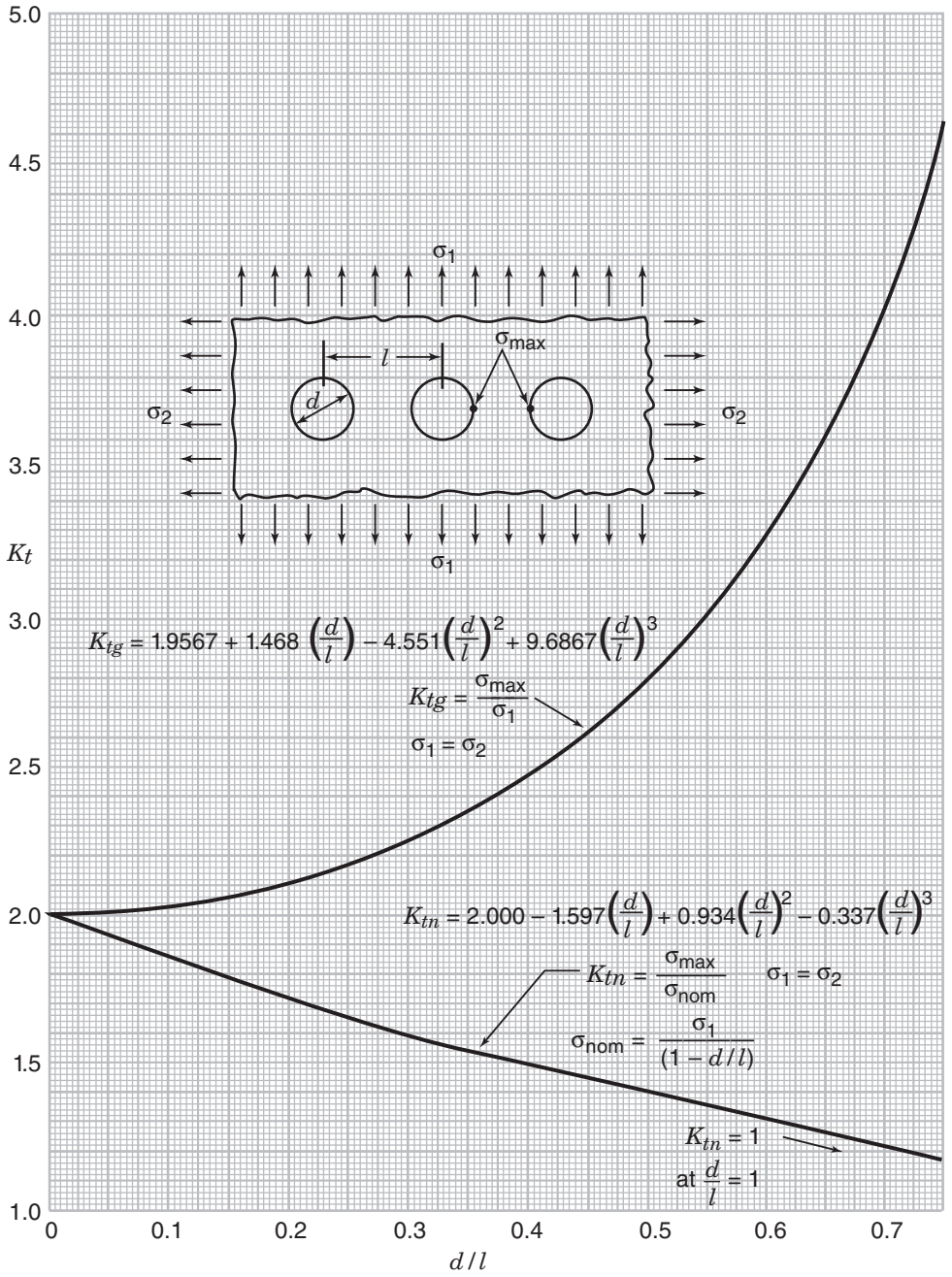


Chart 4.34 Stress concentration factors K_{tg} and K_{tn} for a biaxially stressed infinite thin element with an infinite row of circular holes, $\sigma_1 = \sigma_2$ (Hütter 1942).

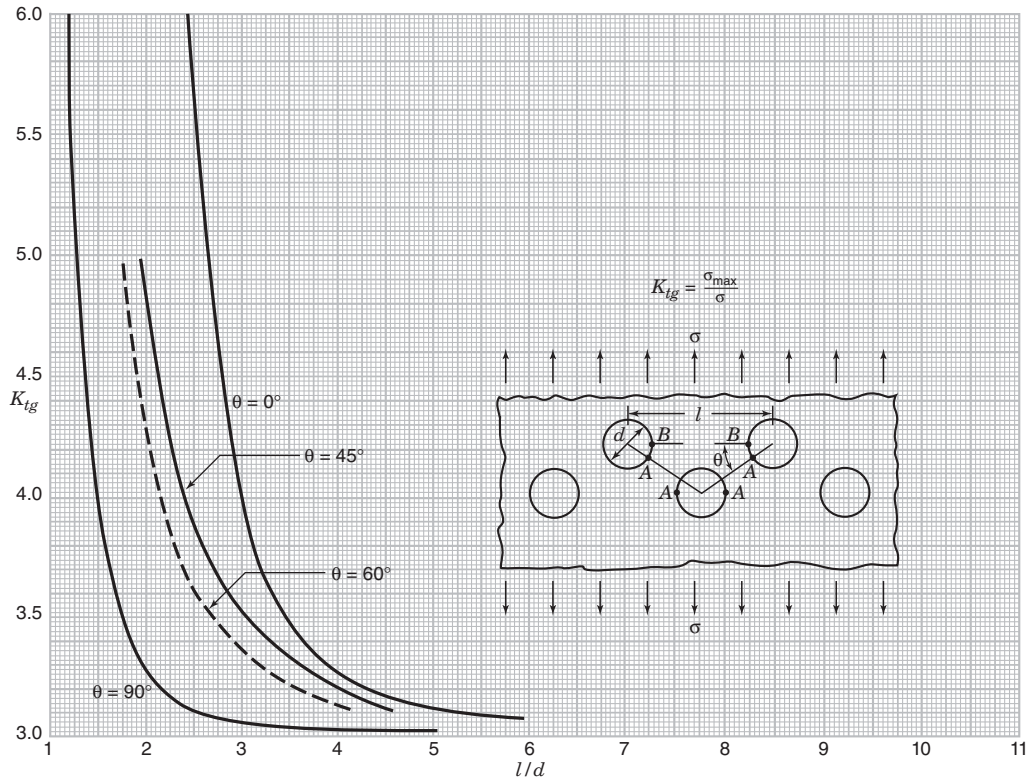


Chart 4.35 Stress concentration factors K_{tg} for a double row of holes in a thin element in uniaxial tension (Schulz 1941). Stress applied perpendicular to the axis of the holes.

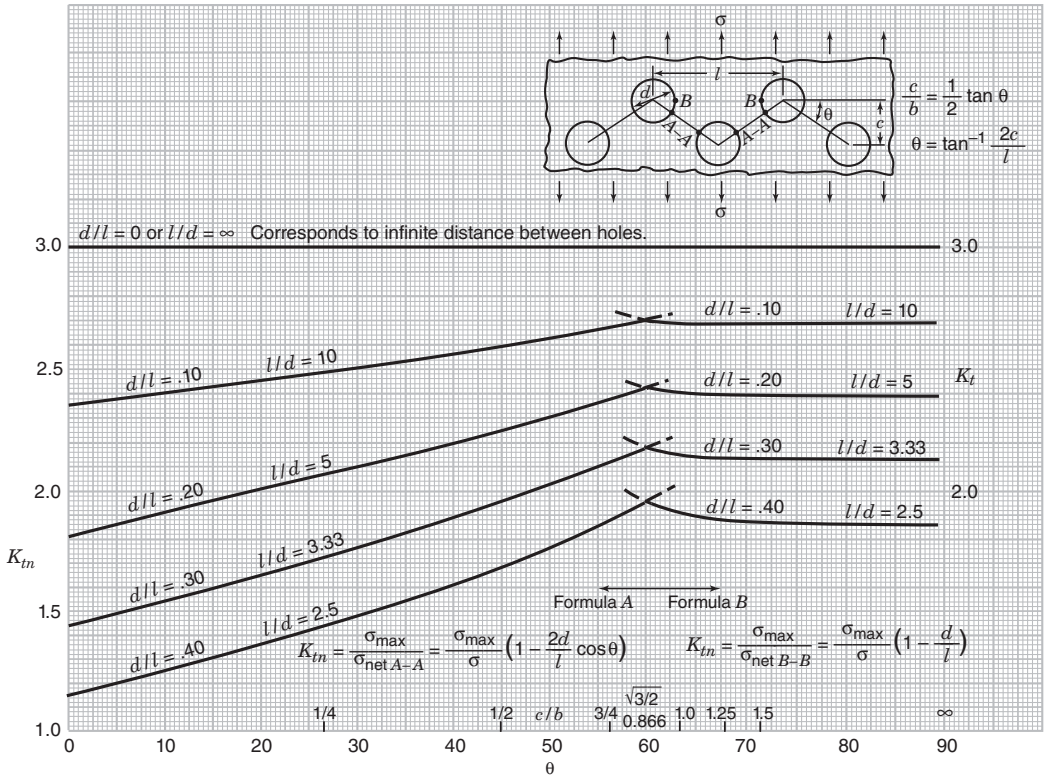


Chart 4.36 Stress concentration factors K_{tn} for a double row of holes in a thin element in uniaxial tension (based on mathematical analysis of Schulz 1941). Stress applied perpendicular to the axes of the holes.

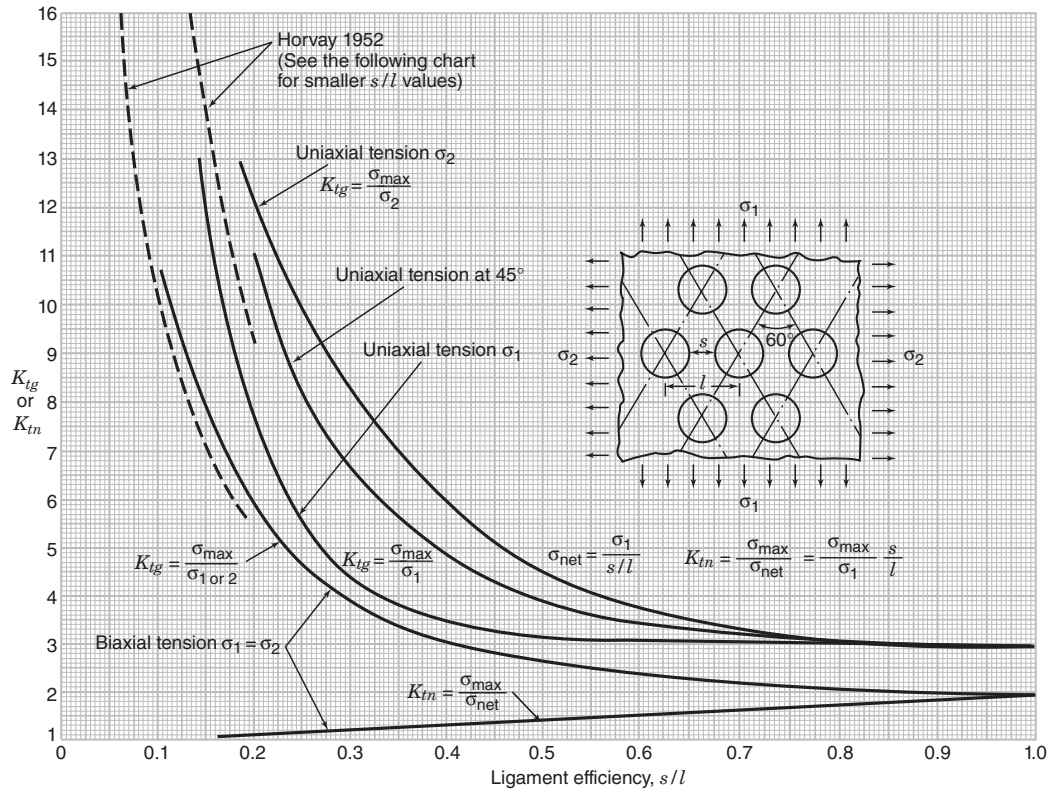


Chart 4.37 Stress concentration factors K_{tg} and K_{tn} for a triangular pattern of holes in a thin element subject to uniaxial and biaxial stresses (Sampson 1960; Meijers 1967). The pattern is repeated throughout the element.

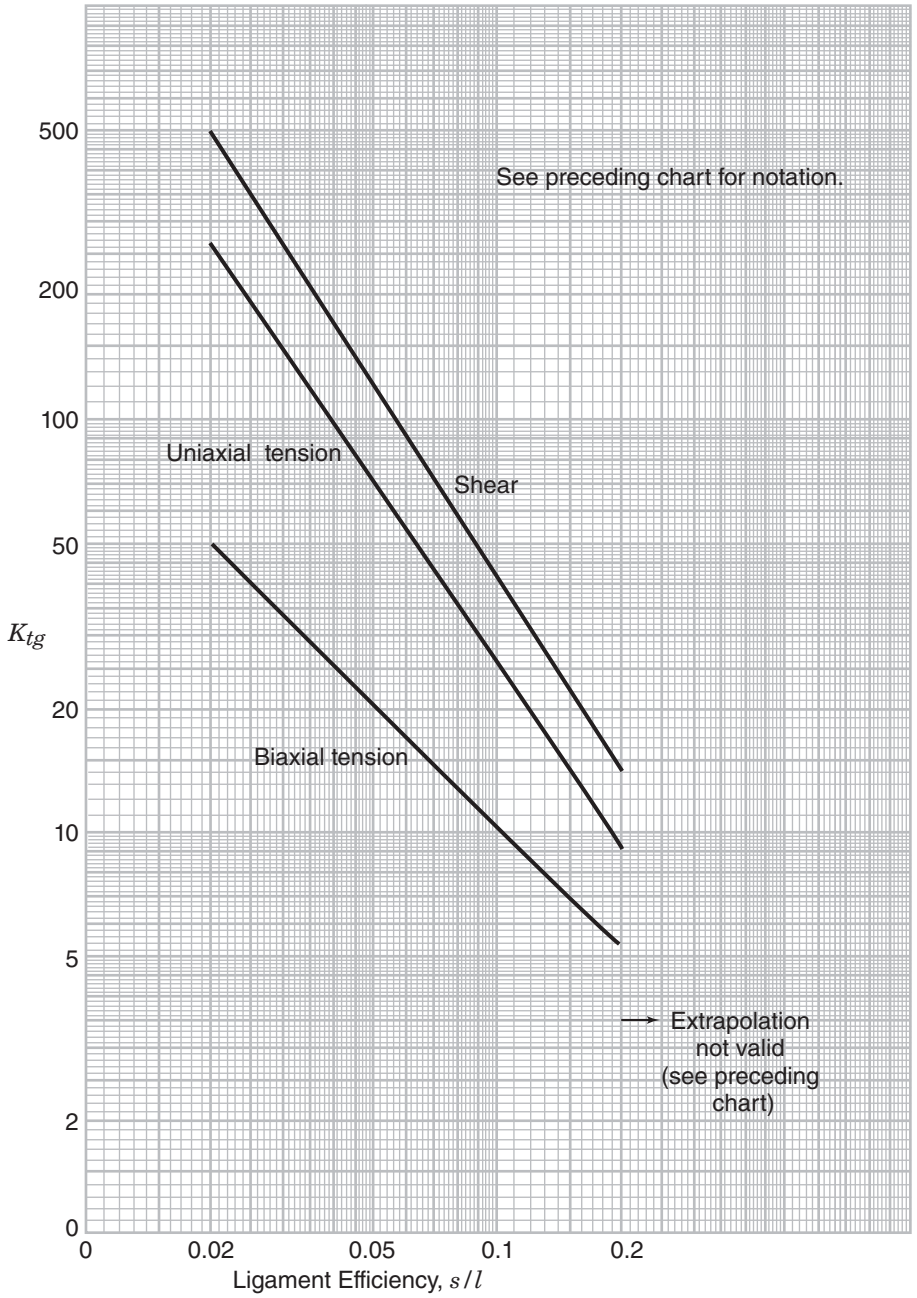


Chart 4.38 Stress concentration factors K_{tg} for the triangular pattern of holes of Chart 4.37 for low values of ligament efficiency (Horvay 1952).

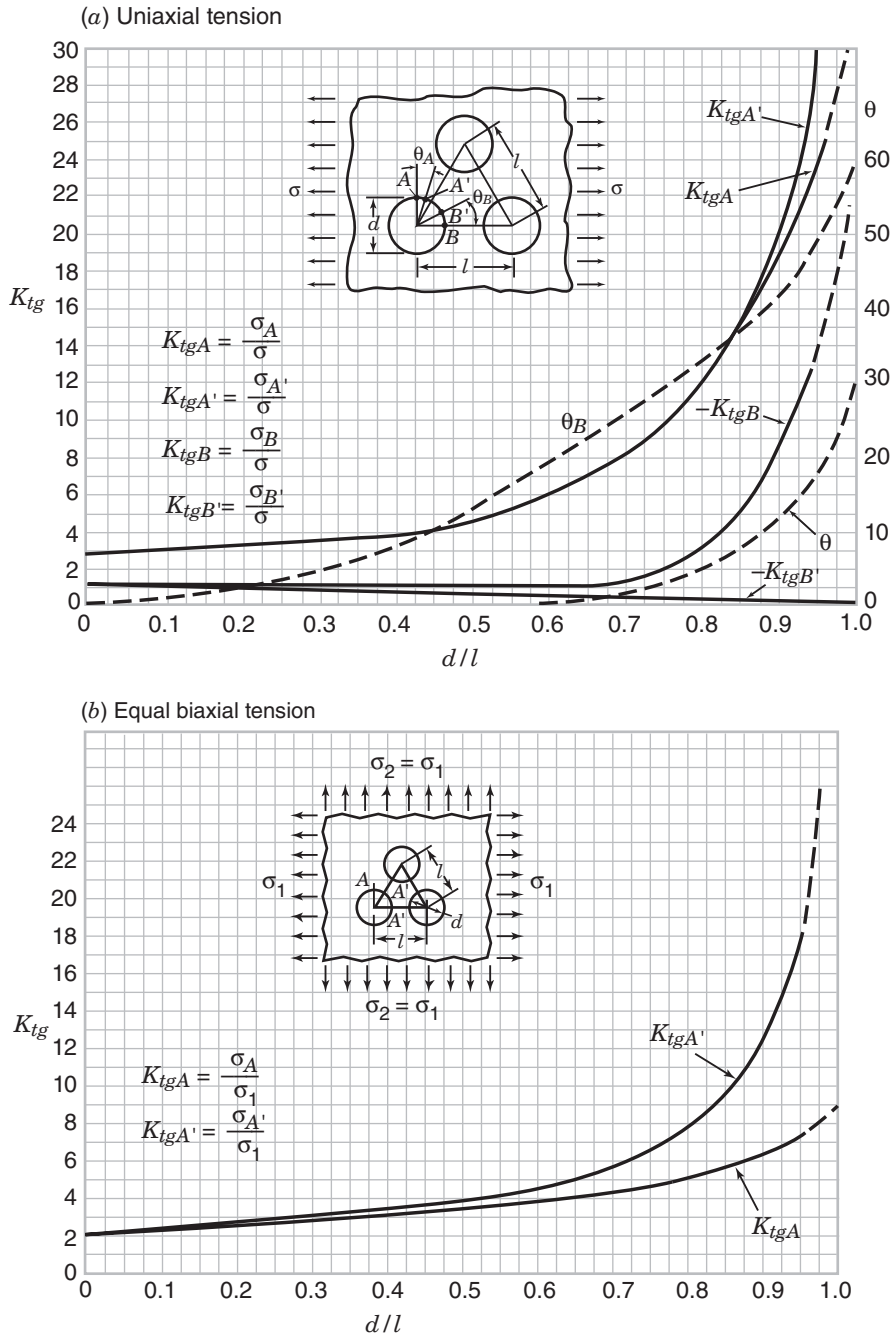


Chart 4.39*a,b* Stress concentration factors K_{tg} for particular locations on the holes, for a triangular pattern of holes in a thin element subject to uniaxial and biaxial stresses (Nishida 1976). The pattern is repeated throughout the element: (*a*) uniaxial tension; (*b*) equal biaxial tension.

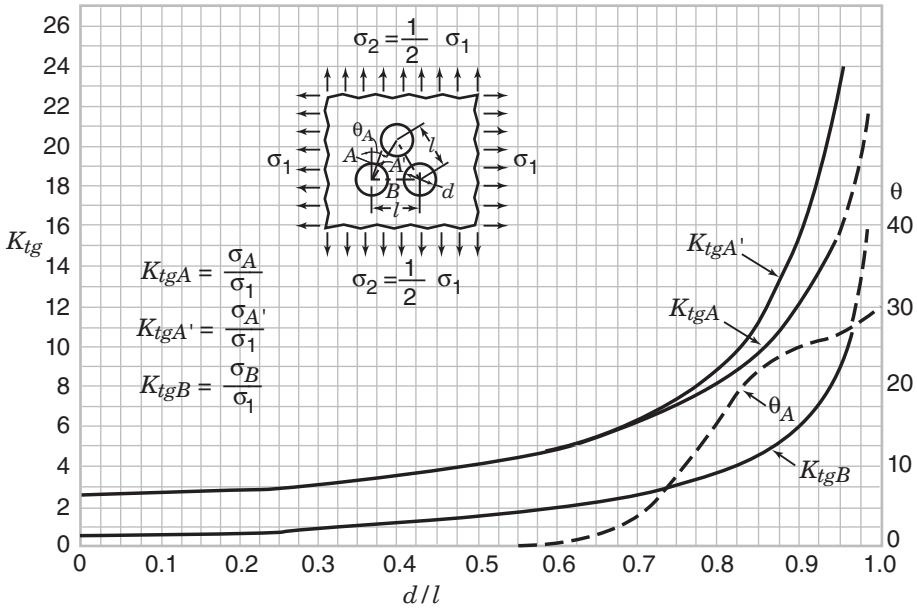


Chart 4.39*c* Stress concentration factors K_{tg} for particular locations on the holes, for a triangular pattern of holes in a thin element subject to uniaxial and biaxial stresses (Nishida 1976): biaxial tension with $\sigma_2 = \sigma_1/2$.

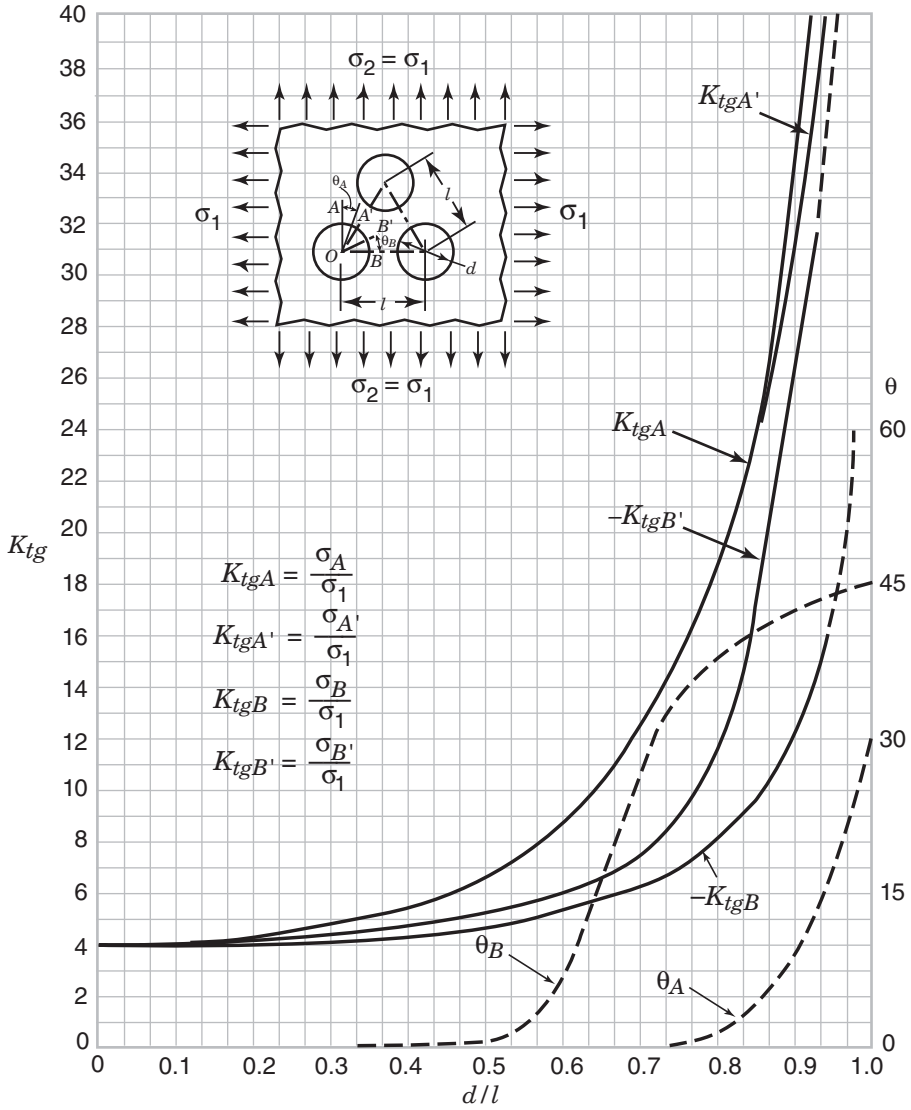


Chart 4.39*d* Stress concentration factors K_{tg} for particular locations on the holes, for a triangular pattern of holes in a thin element subject to uniaxial and biaxial stresses (Nishida 1976): Pure shear, biaxial stresses with $\sigma_2 = -\sigma_1$.

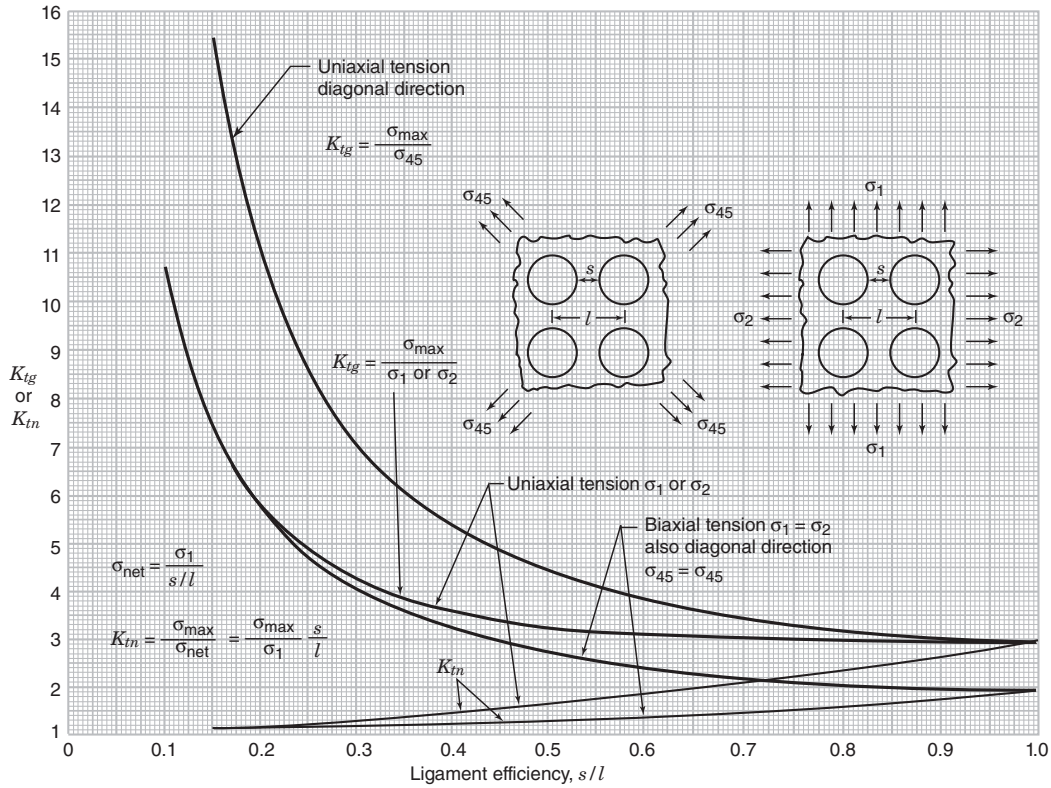


Chart 4.40 Stress concentration factors K_{tg} and K_{tn} for a square pattern of holes in a thin element subject to uniaxial and biaxial stresses (Bailey and Hicks 1960; Hulbert 1965; Meijers 1967). The pattern is repeated throughout the element.

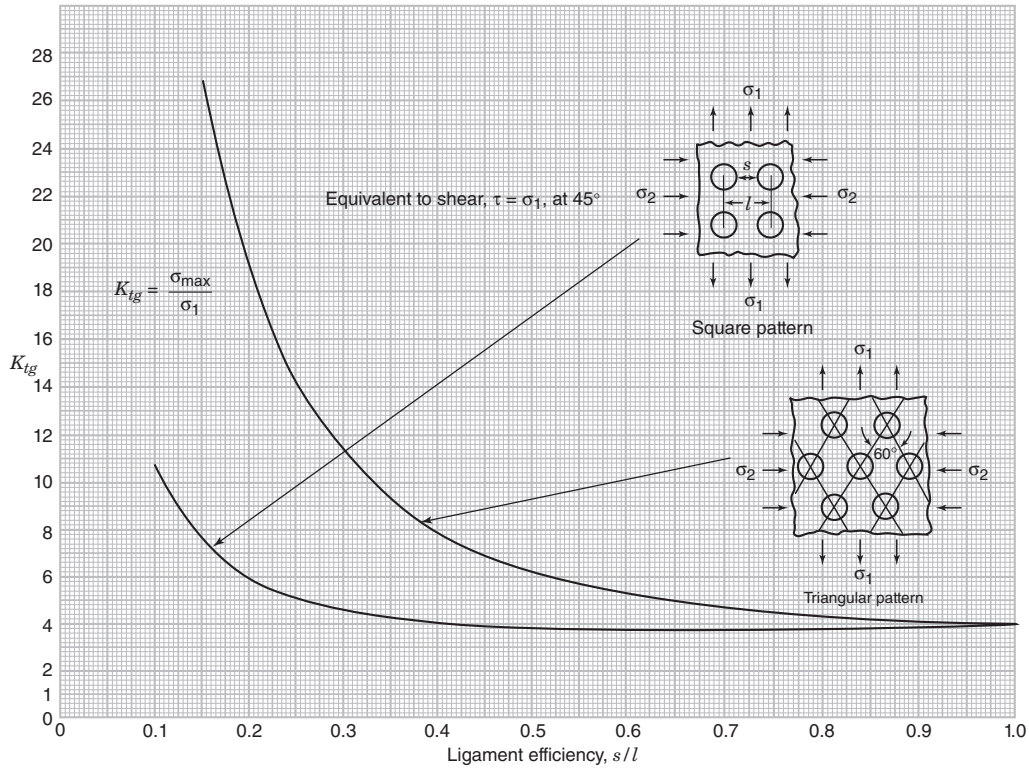


Chart 4.41 Stress concentration factors K_{tg} for patterns of holes in a thin element subject to biaxial stresses. Pure shear $\sigma_2 = -\sigma_1$ (Sampson 1960; Bailey and Hicks 1960; Hulbert and Niedenfuhr 1965; Meijers 1967). The pattern is repeated throughout the element.

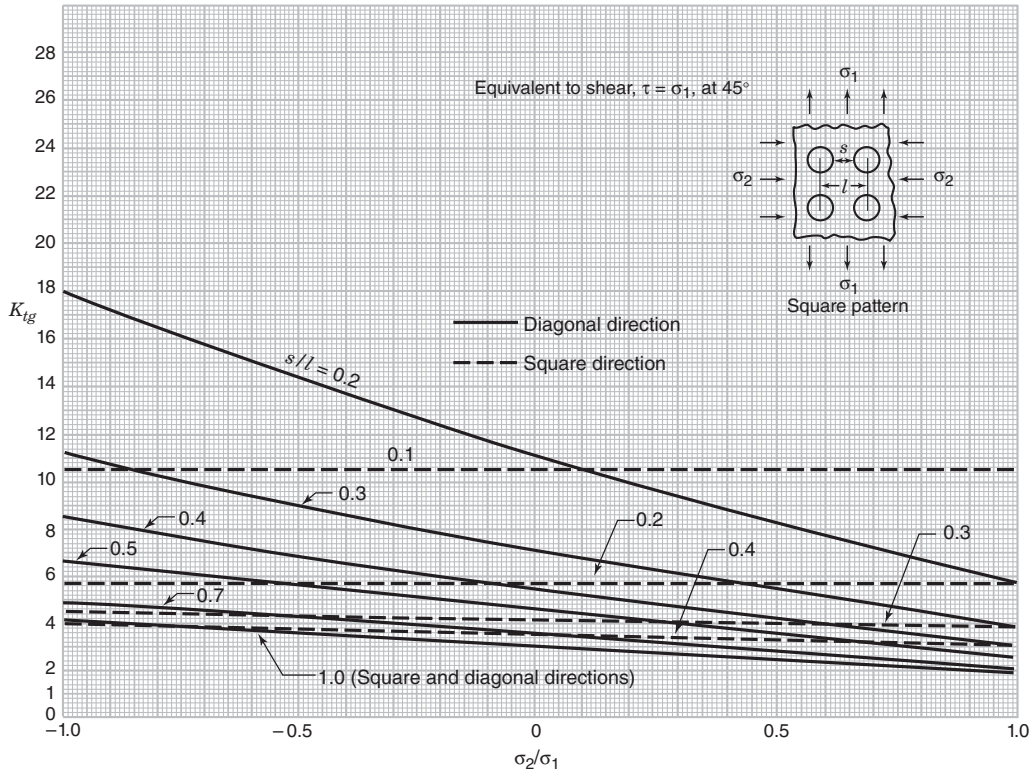


Chart 4.42 Stress concentration factors K_{tg} versus σ_2/σ_1 for a square pattern of holes in a thin element subject to biaxial stresses (Sampson 1960; Bailey and Hicks 1960; Hulbert 1965; Meijers 1967). The pattern is repeated throughout the element.

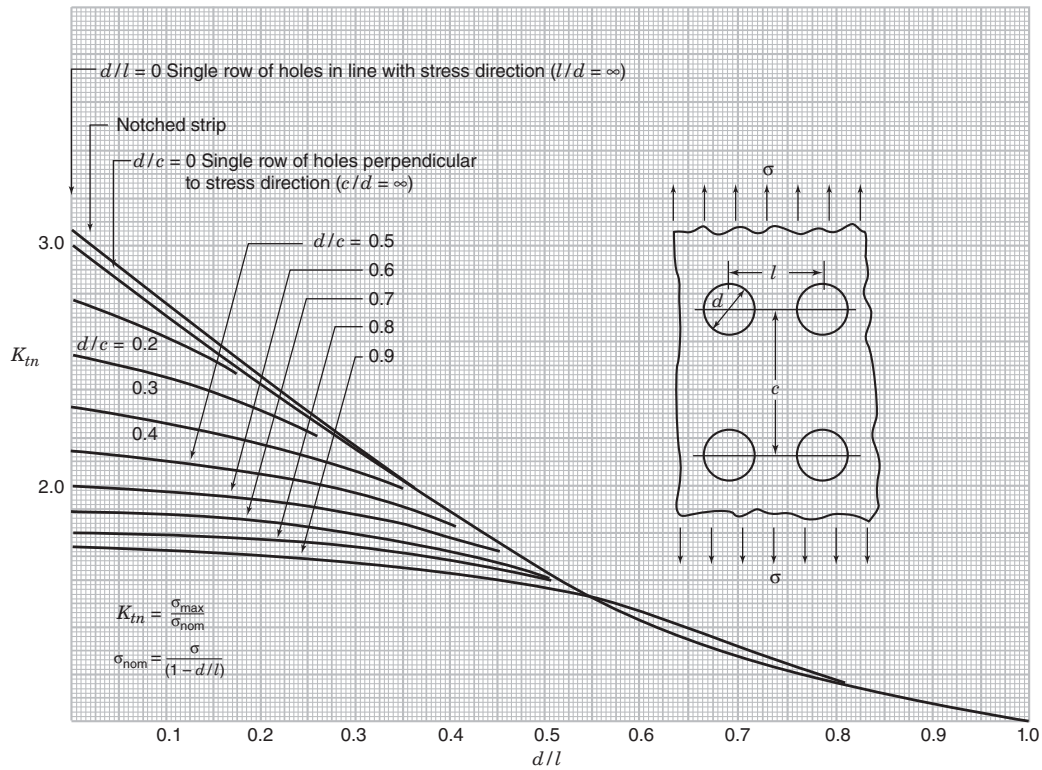


Chart 4.43 Stress concentration factors K_{tn} for a rectangular pattern of holes in a thin element subject to uniaxial stresses (Meijers 1967). The pattern is repeated throughout the element.

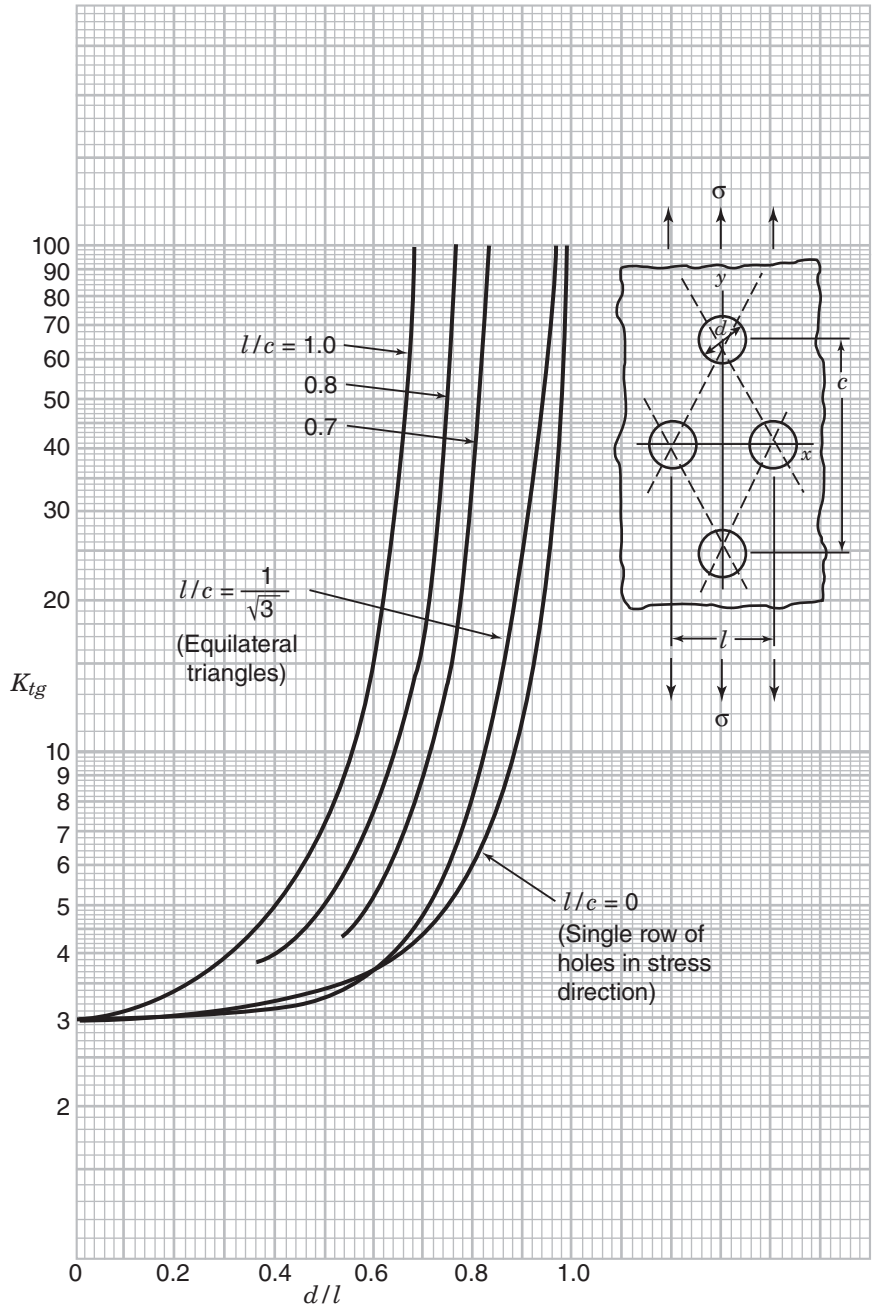


Chart 4.44 Stress concentration factors K_{tg} for a diamond pattern of holes in a thin element subject to uniaxial stresses in the y direction (Meijers 1967). The pattern is repeated throughout the element.

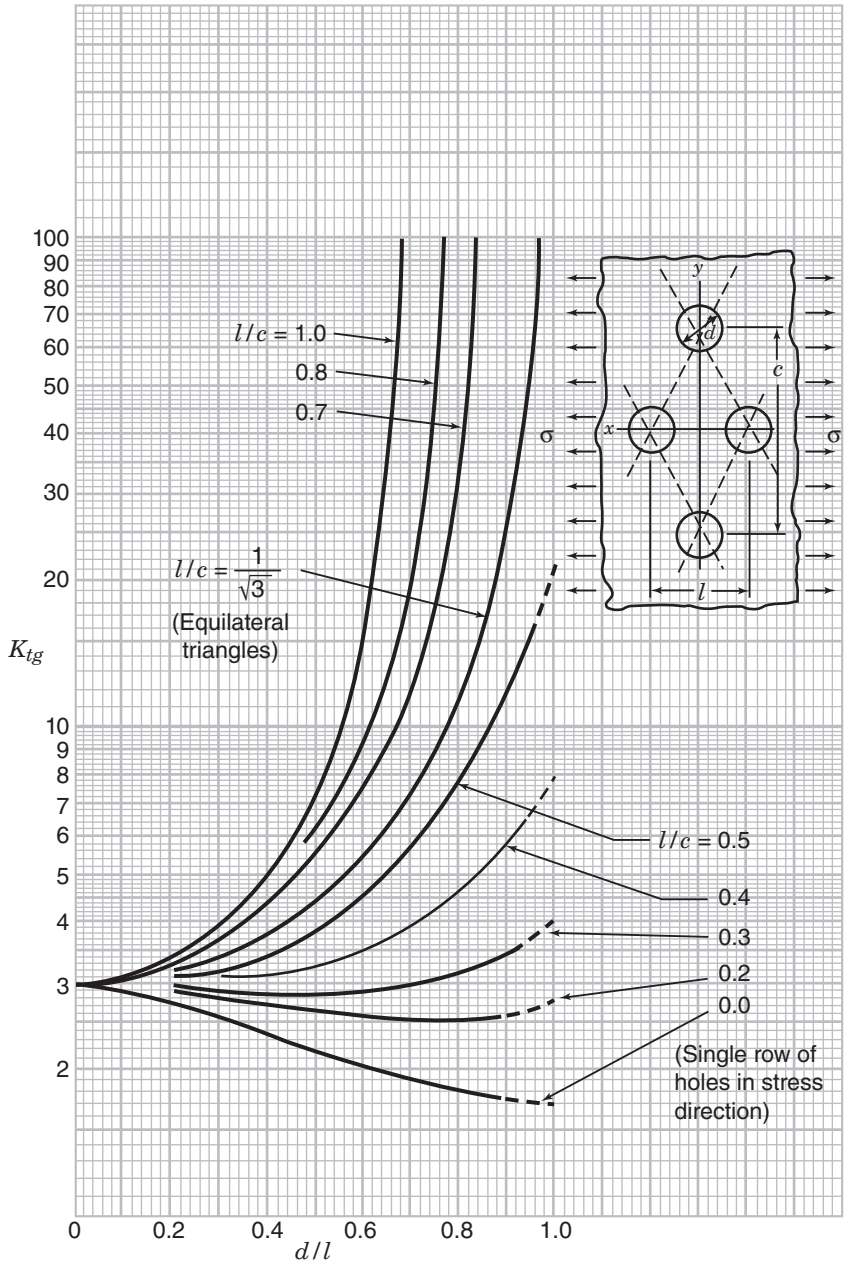


Chart 4.45 Stress concentration factors K_{tg} for a diamond pattern of holes in a thin element subject to uniaxial stresses in the x direction (Meijers, 1967). The pattern is repeated throughout the element.

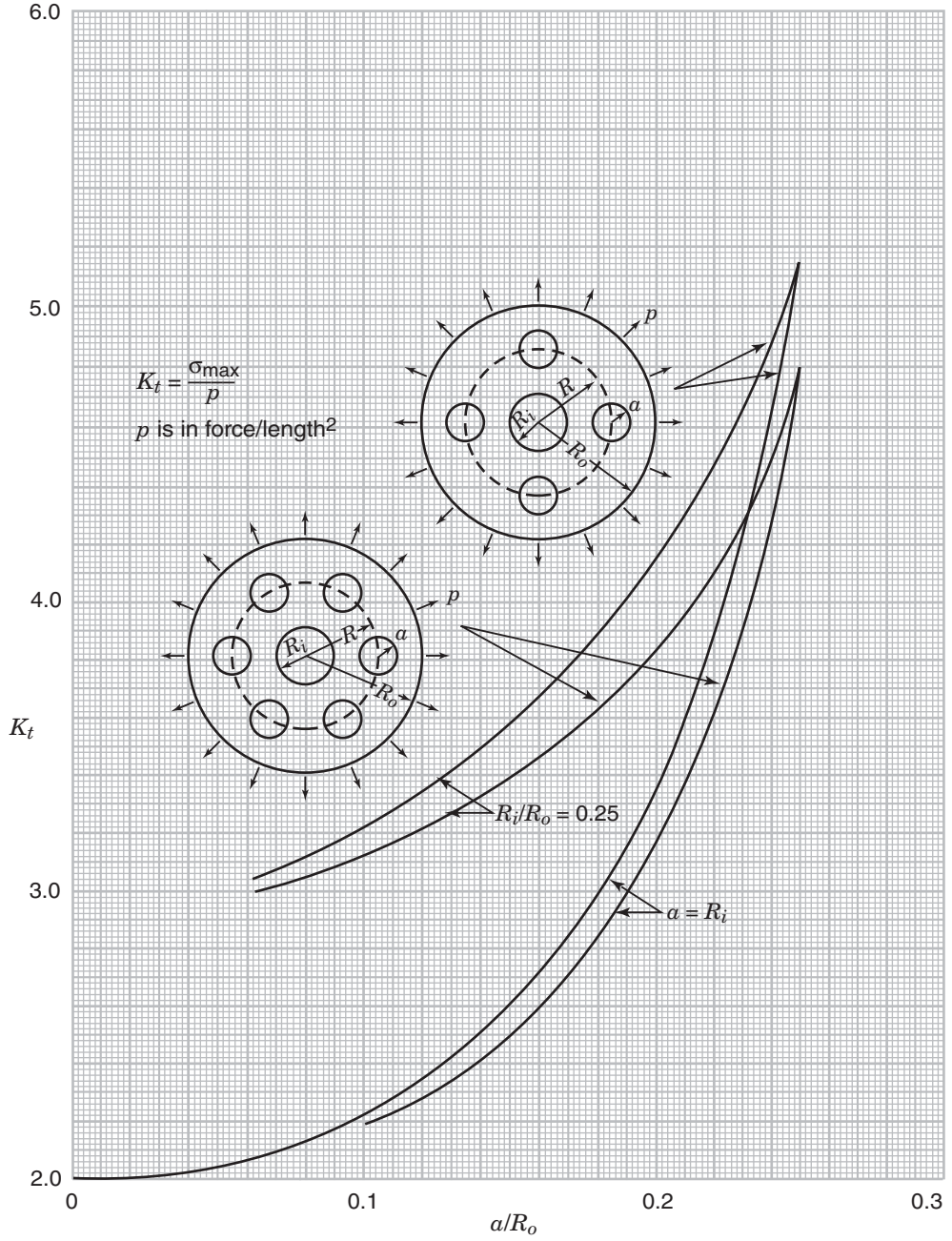


Chart 4.46 Stress concentration factors K_t for a radially stressed circular element, with a central circular hole and a ring of four or six noncentral circular holes, $R/R_0 = 0.625$ (Kraus 1963).

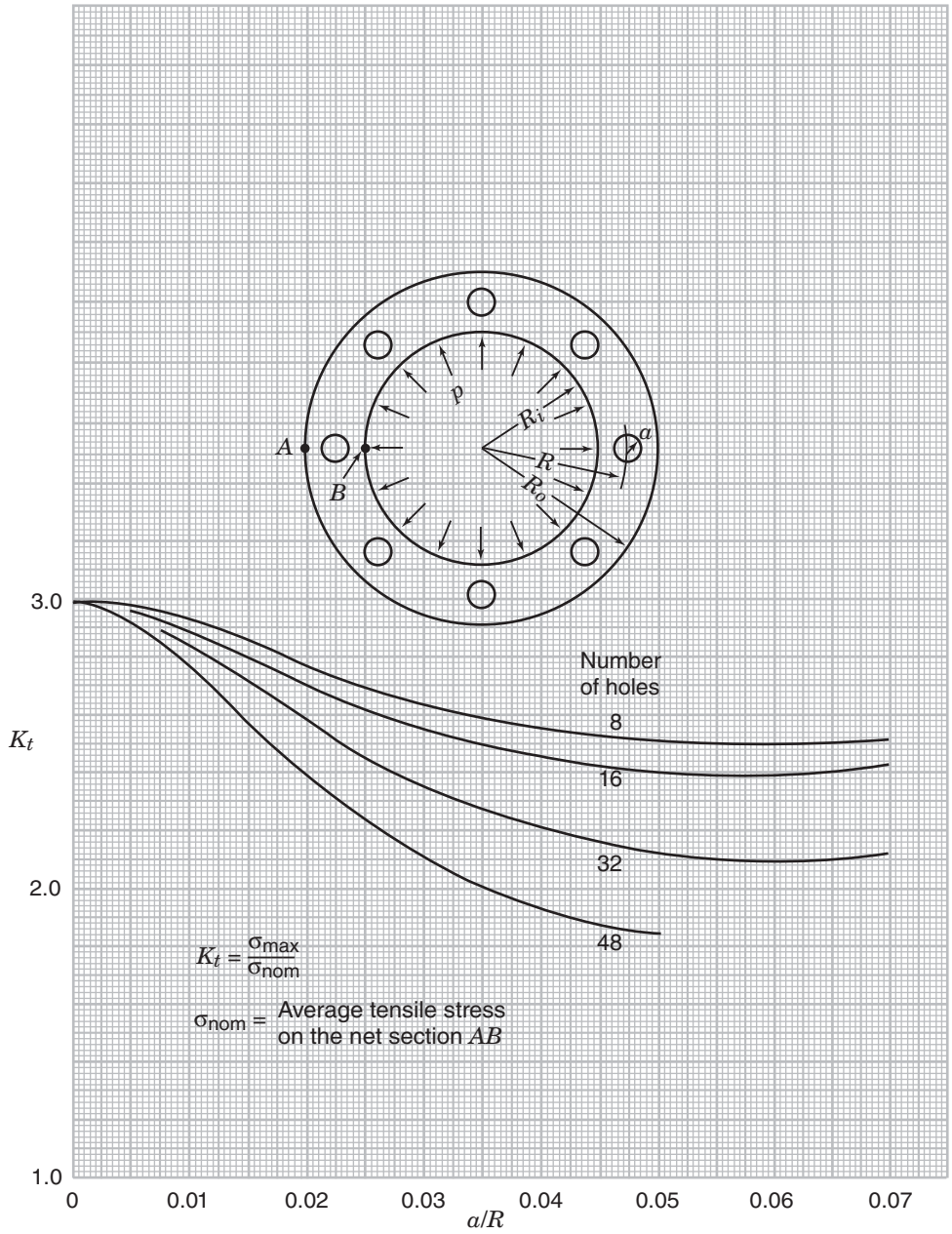


Chart 4.47 Stress concentration factors K_t for a perforated flange with internal pressure, $R_i/R_0 = 0.8$, $R/R_0 = 0.9$ (Kraus et al. 1966).

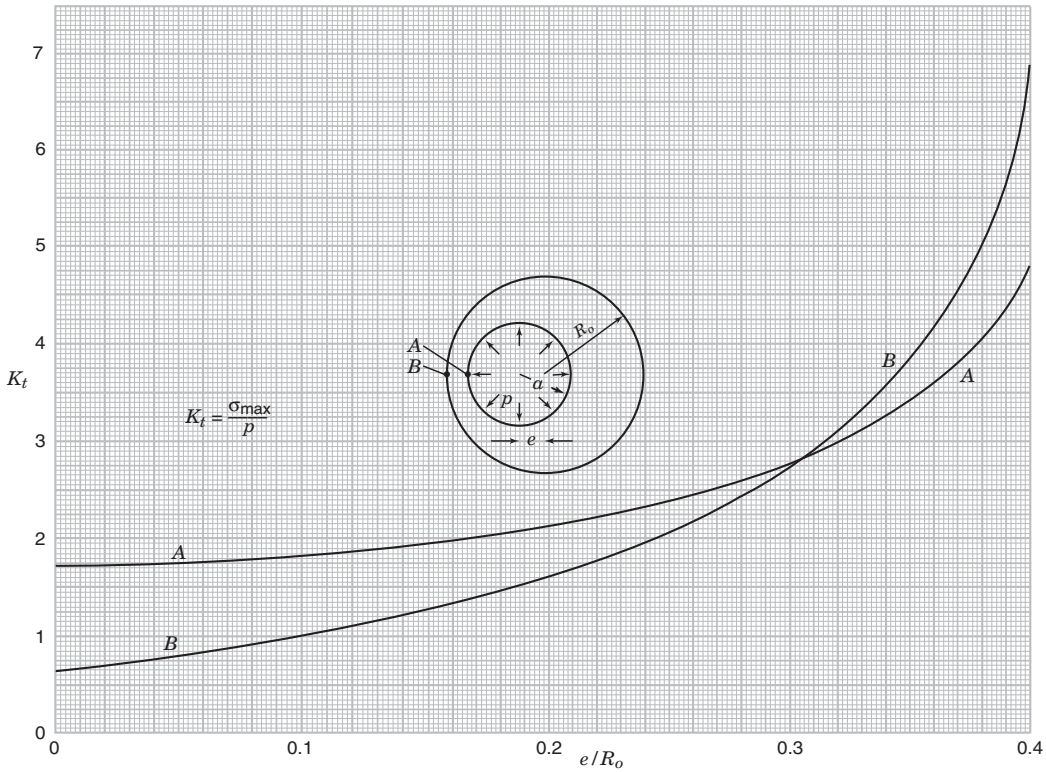


Chart 4.48 Stress concentration factors K_t for a circular thin element with an eccentric circular hole with internal pressure, $a/R_0 = 0.5$ (Savin 1961; Hulbert 1965).

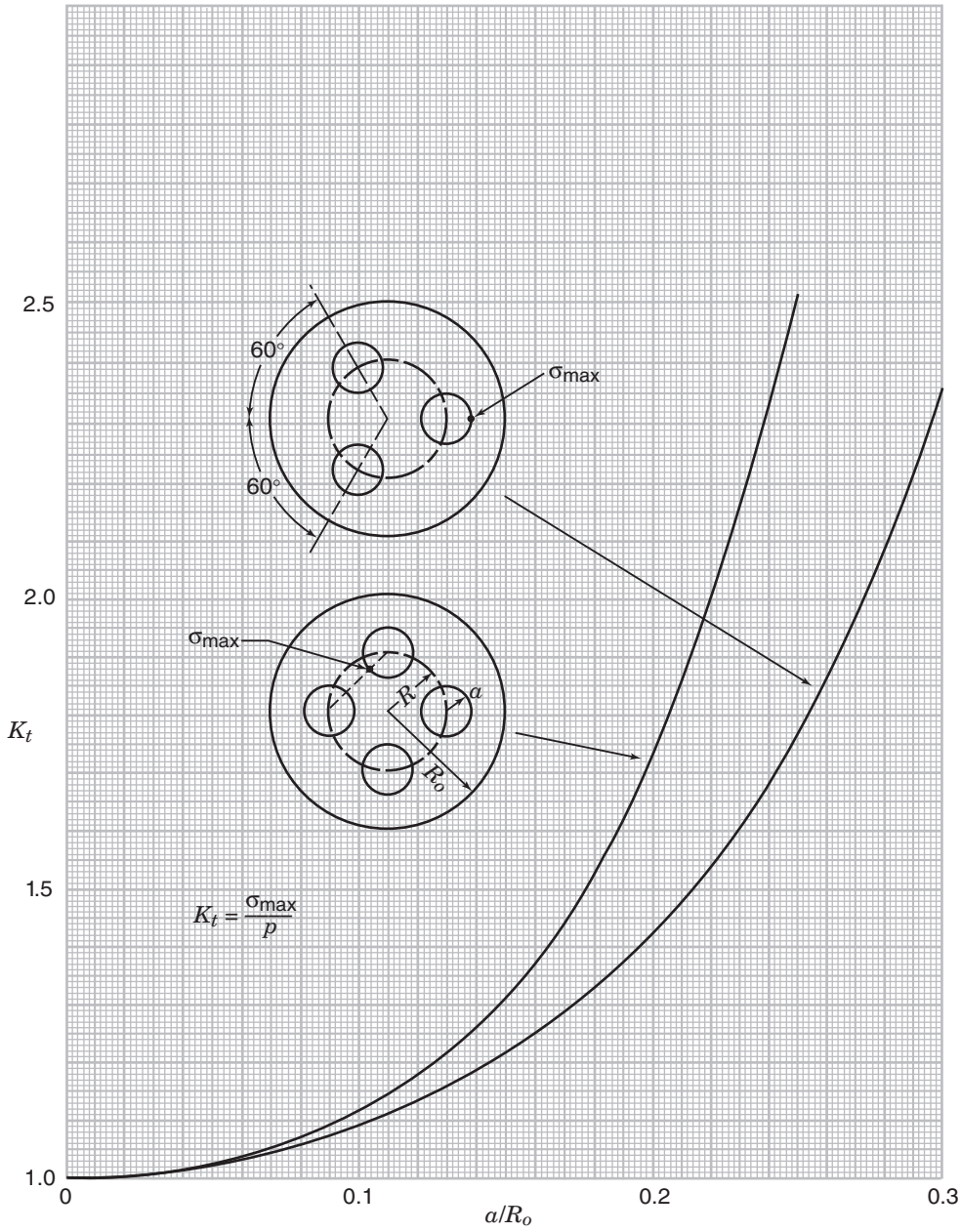


Chart 4.49 Stress concentration factors K_t for a circular thin element with a circular pattern of three or four holes with internal pressure in each hole, $R/R_0 = 0.5$ (Kraus 1962).

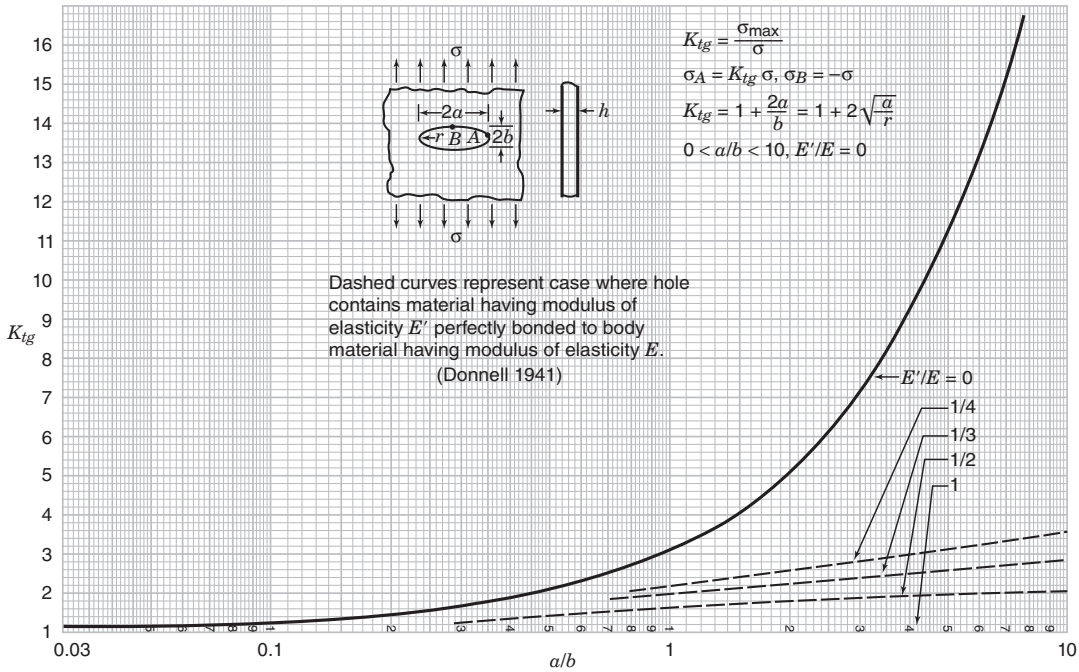


Chart 4.50 Stress concentration factors K_{tg} for an elliptical hole in an infinite panel in tension (Kolosoff 1910; Inglis, 1913).

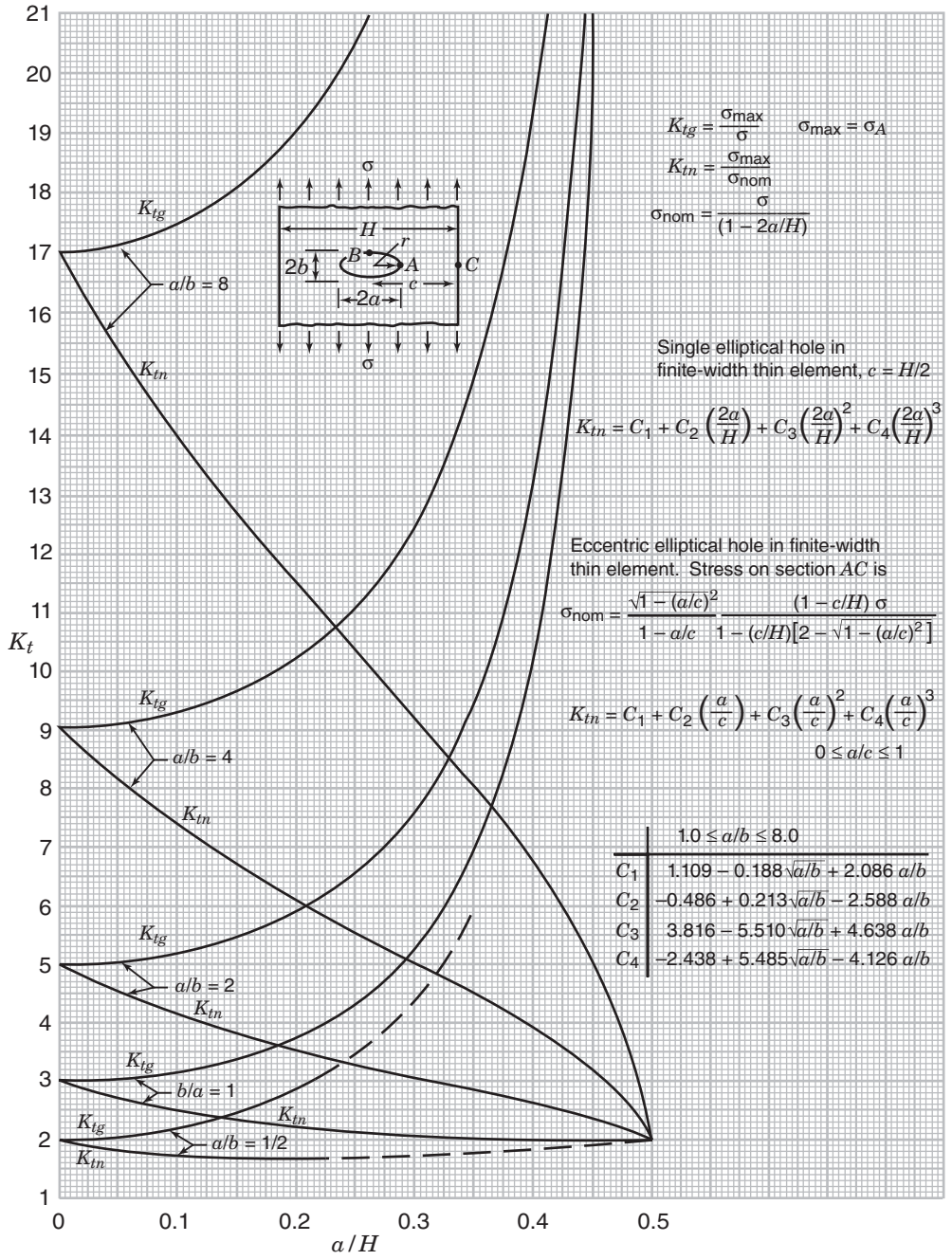


Chart 4.51 Stress concentration factors K_{tg} and K_{tn} of an elliptical hole in a finite-width thin element in uniaxial tension (Isida 1953, 1955b).

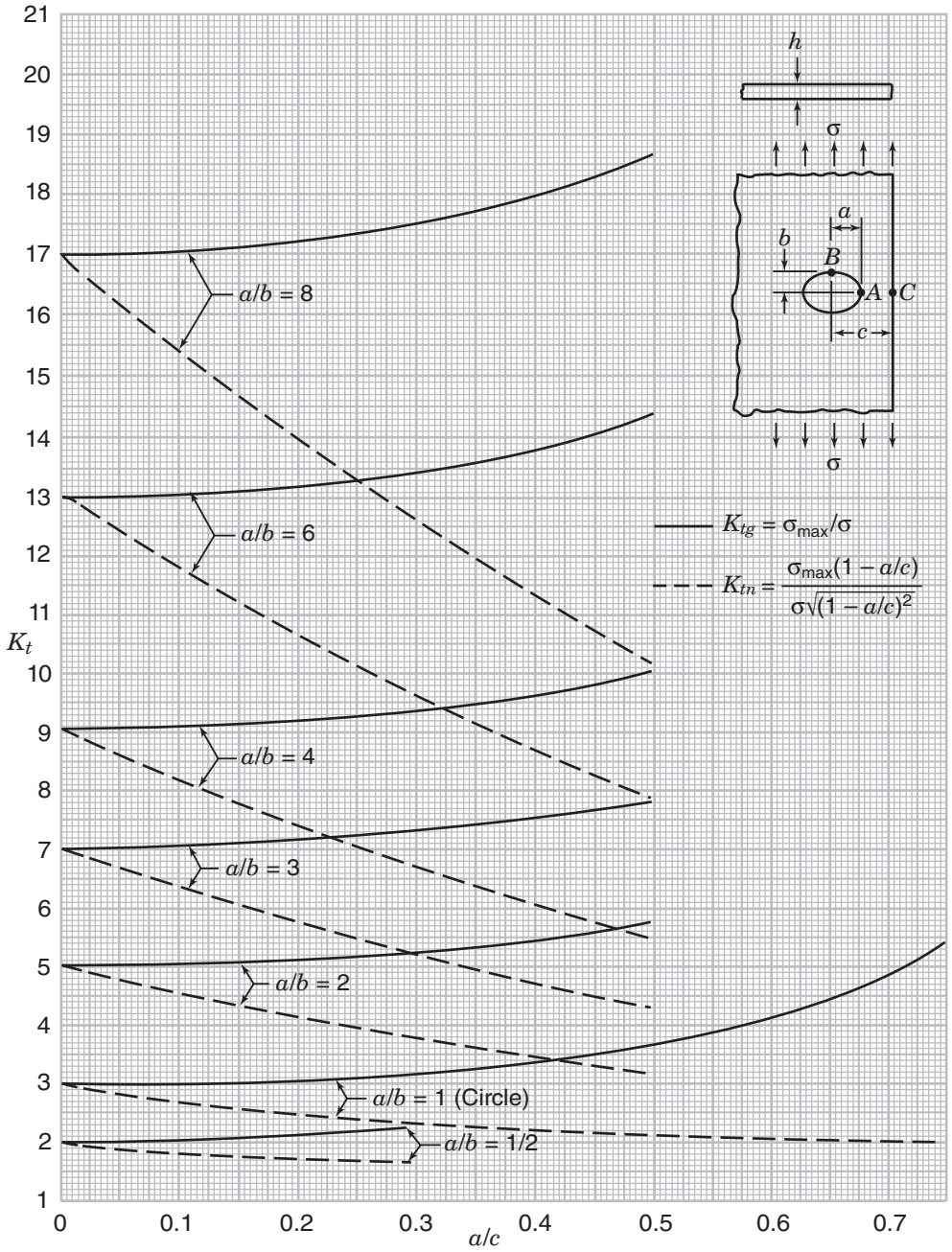


Chart 4.52 Stress concentration factors K_t for a semi-infinite tension panel with an elliptical hole near the edge (Isida 1955a).

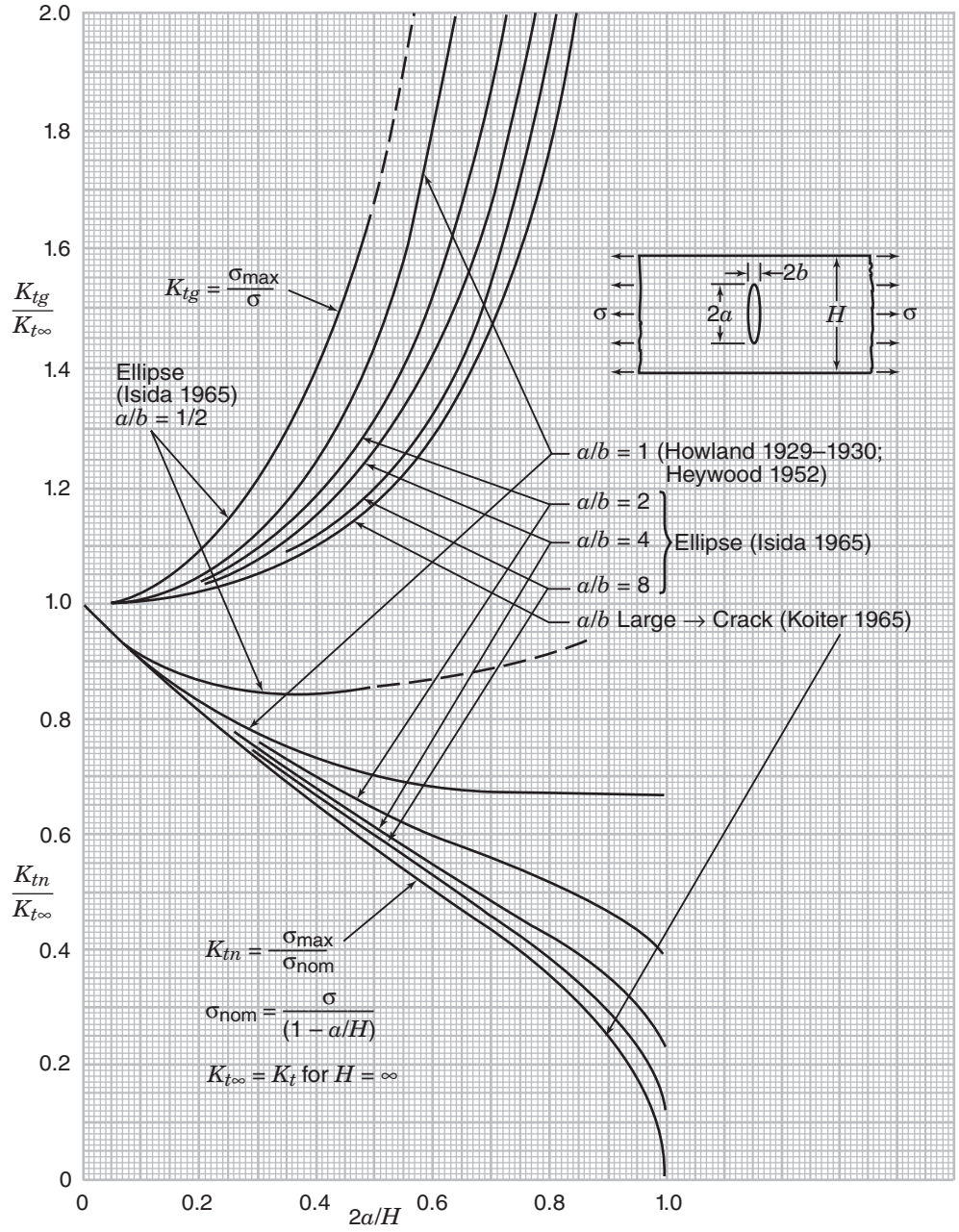


Chart 4.53 Finite-width correction factor $K_t/K_{t\infty}$ for a tension strip with a central opening.

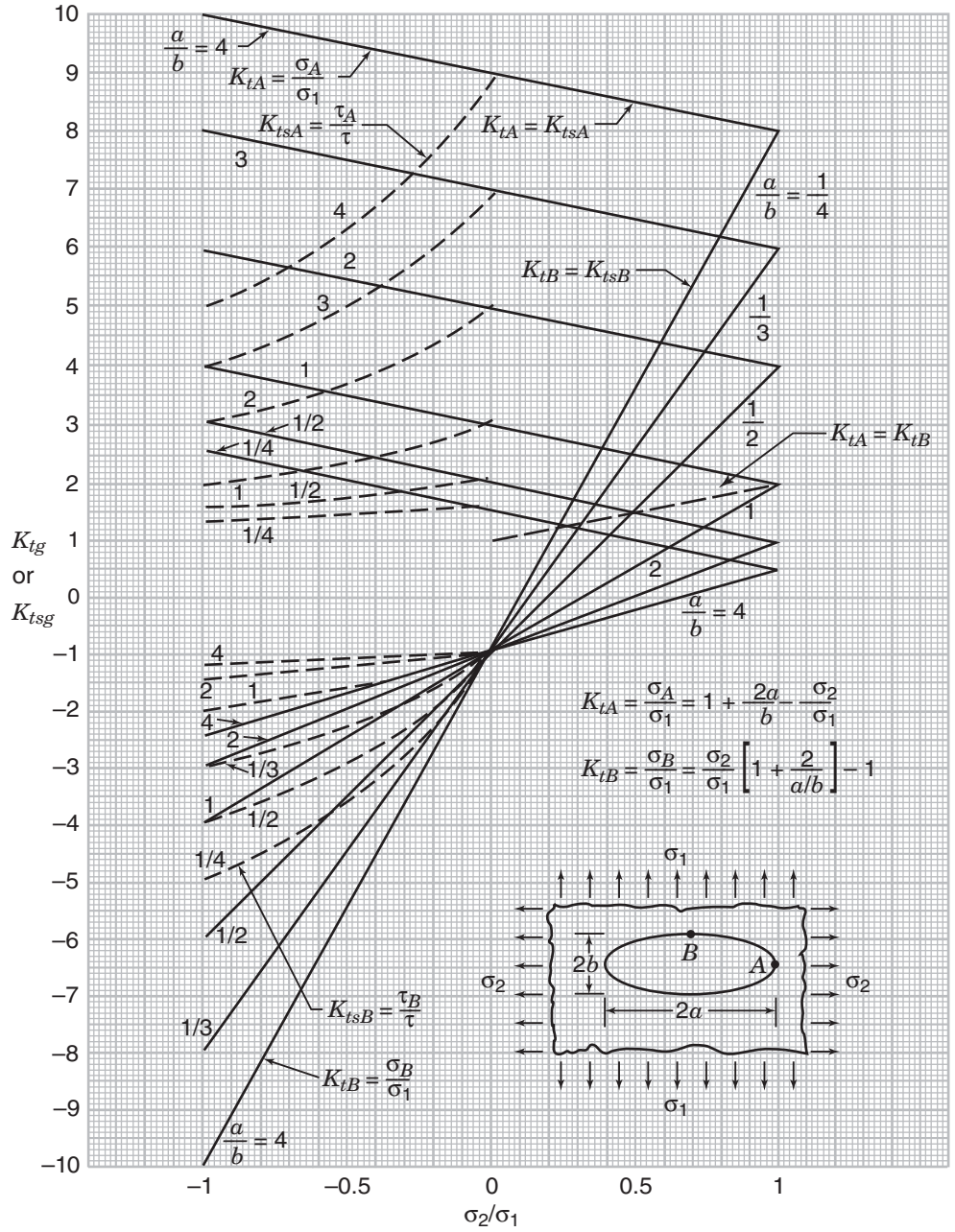


Chart 4.54 Stress concentration factors K_t and K_{ts} for an elliptical hole in a biaxially stressed panel.

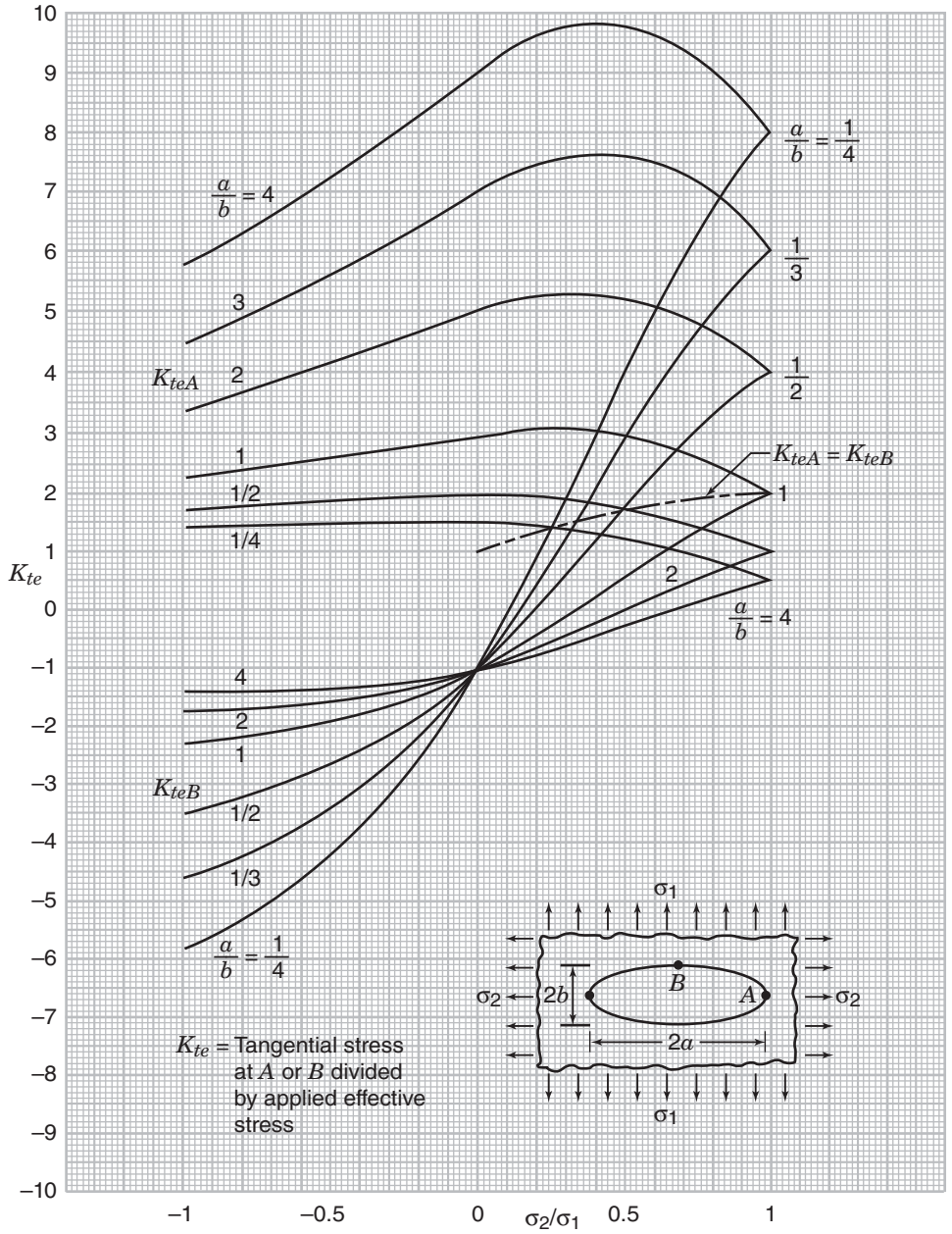


Chart 4.55 Stress concentration factors K_{te} for an elliptical hole in a biaxially stressed panel.

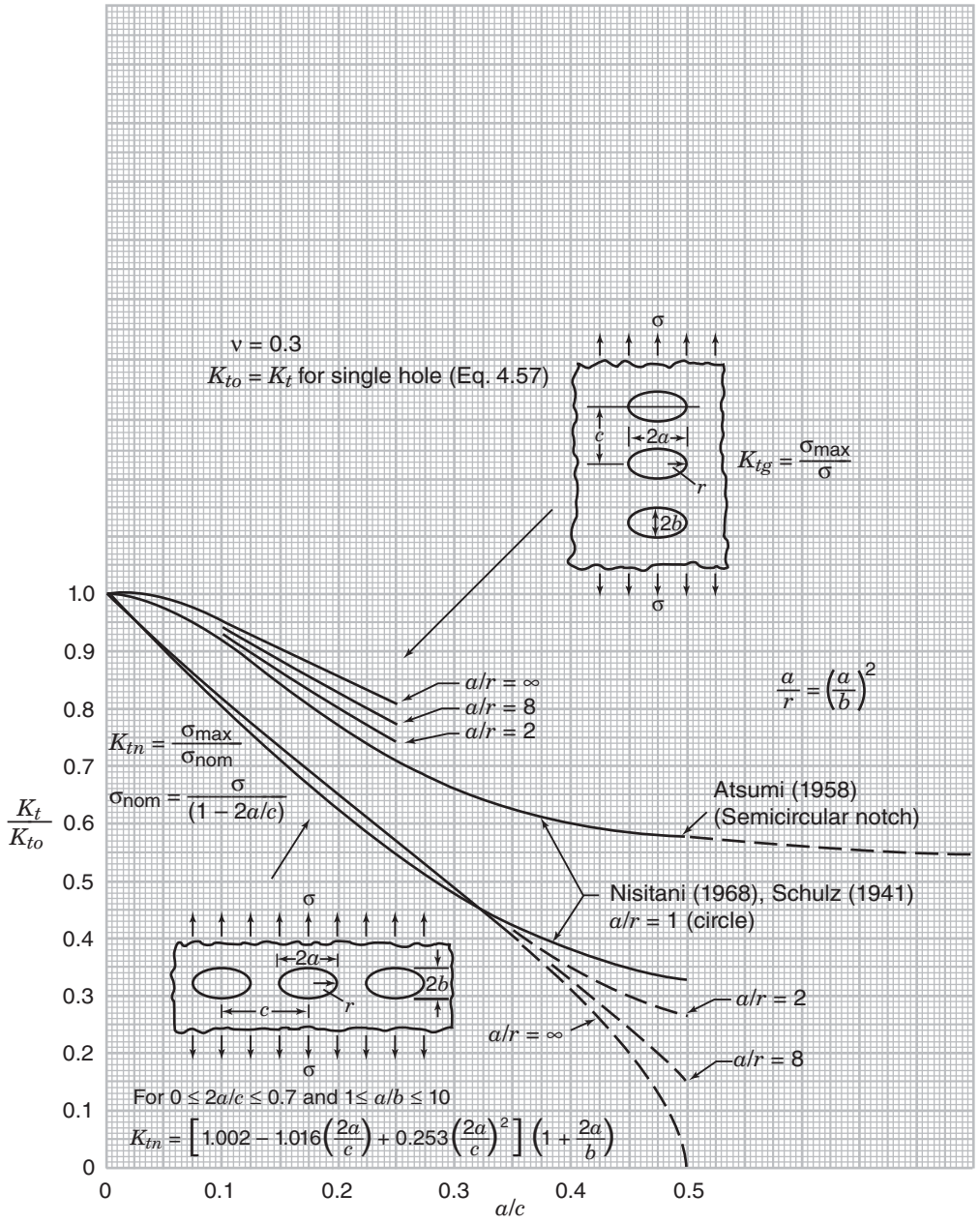


Chart 4.56 Effect of spacing on the stress concentration factor of an infinite row of elliptical holes in an infinite tension member (Schulz 1941; Nisitani 1968).

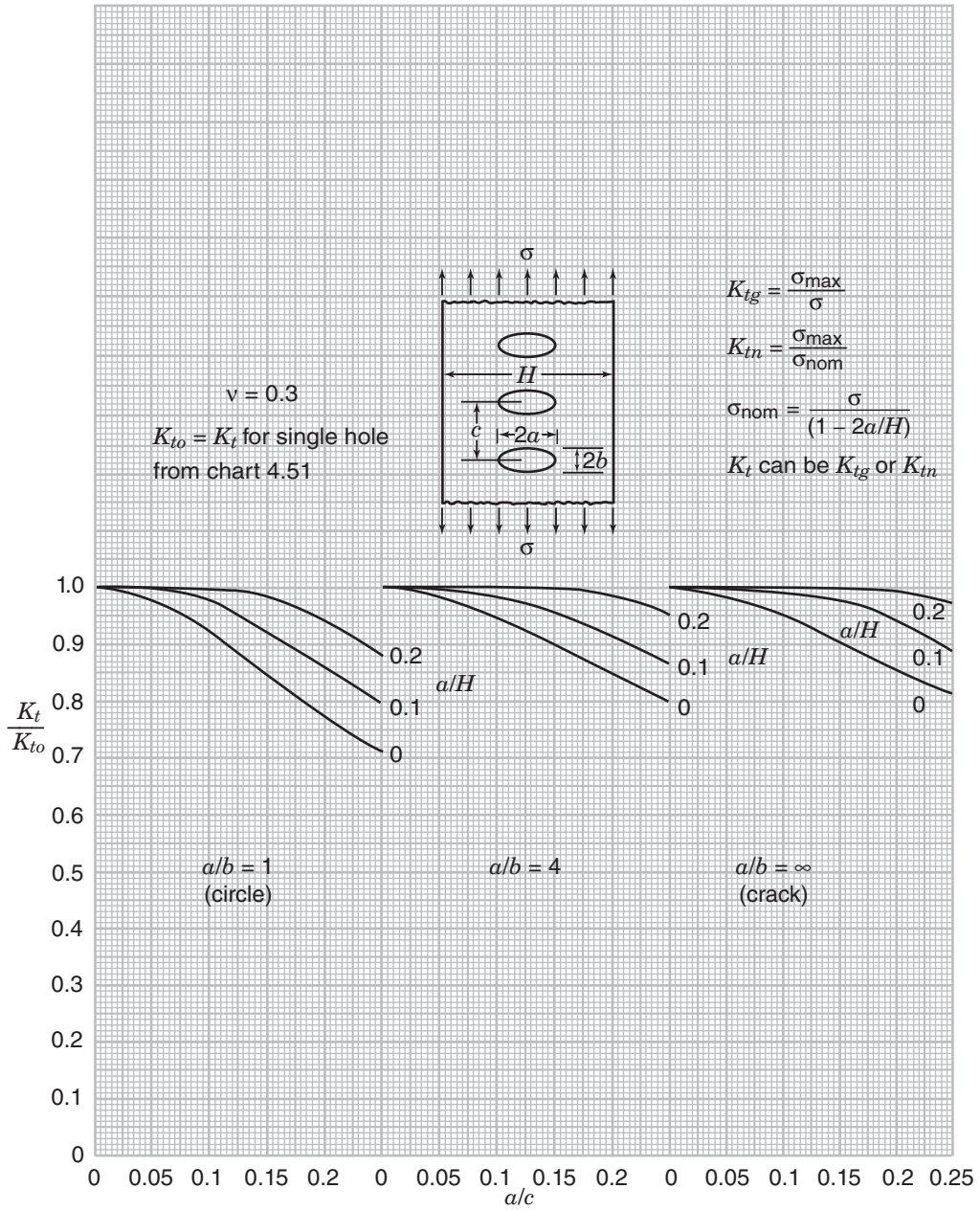


Chart 4.57 Effect of spacing on the stress concentration factor of an infinite row of elliptical holes in a finite-width thin element in tension (Nisitani 1968).

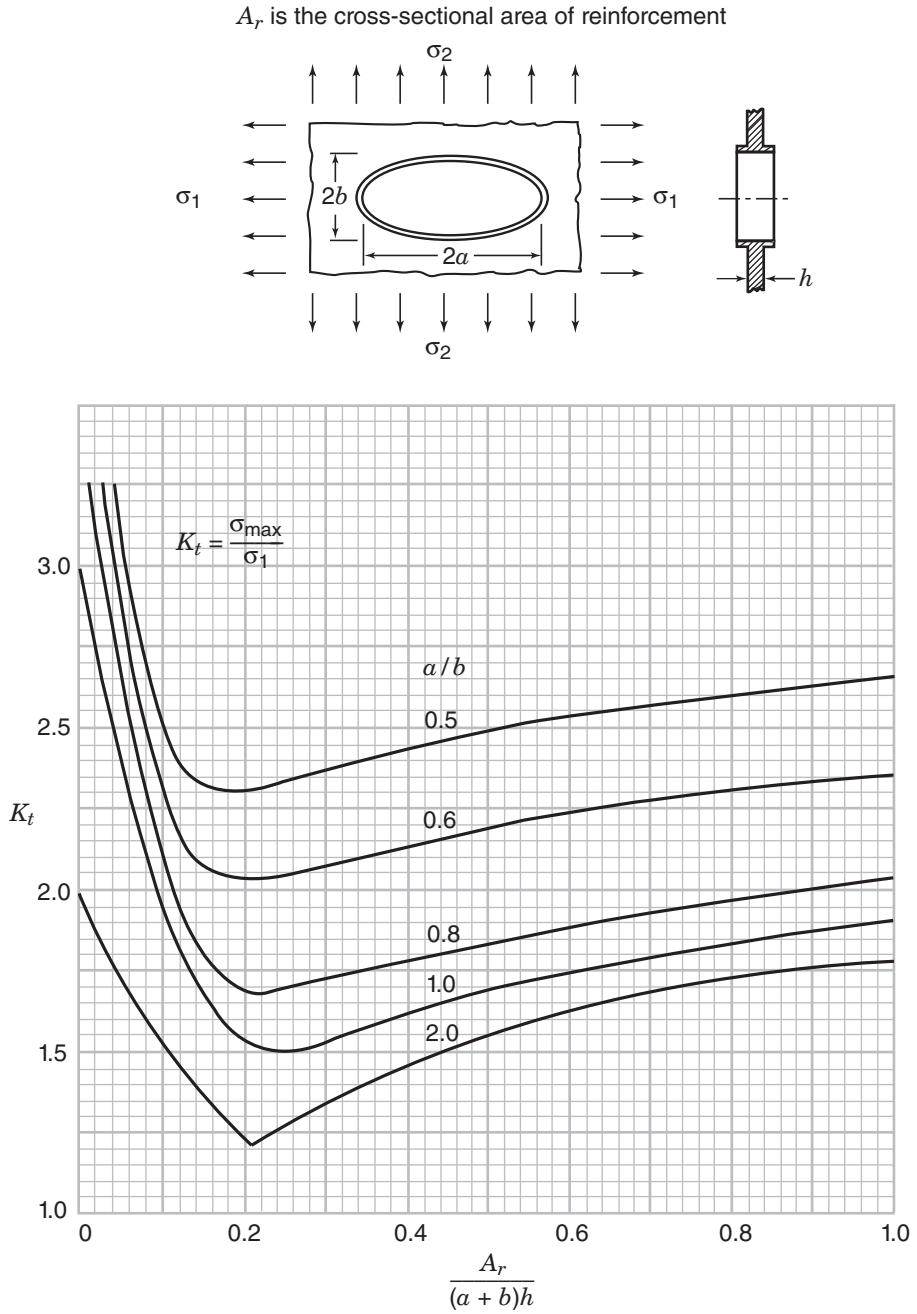


Chart 4.58*a* Stress concentration factors K_t of elliptical holes with bead reinforcement in an infinite panel under uniaxial and biaxial stresses (Wittrick 1959a,b; Houghton and Rothwell 1961; ESDU 1981): $\sigma_2 = 0$.

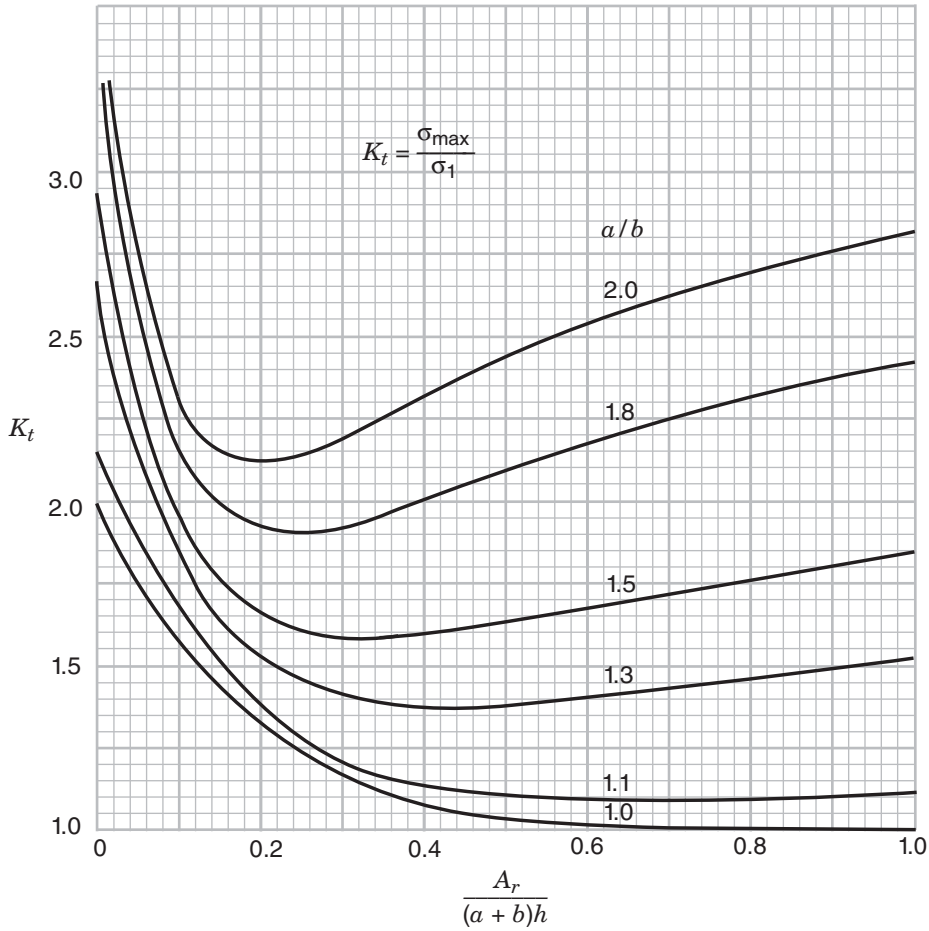


Chart 4.58*b* Stress concentration factors K_t of elliptical holes with bead reinforcement in an infinite panel under uniaxial and biaxial stresses (Wittrick 1959a,b; Houghton and Rothwell 1961; ESDU 1981): $\sigma_2 = \sigma_1$.

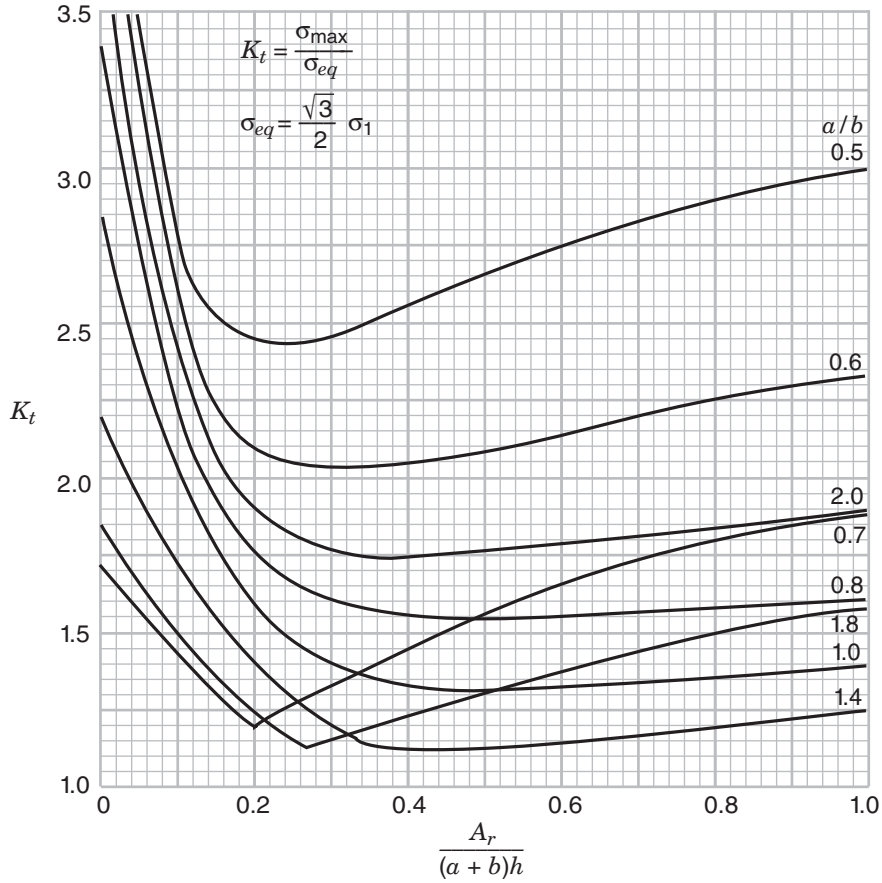


Chart 4.58*c* Stress concentration factors K_t of elliptical holes with bead reinforcement in an infinite panel under uniaxial and biaxial stresses (Wittrick 1959a,b; Houghton and Rothwell 1961; ESDU 1981): $\sigma_2 = \sigma_1/2$.

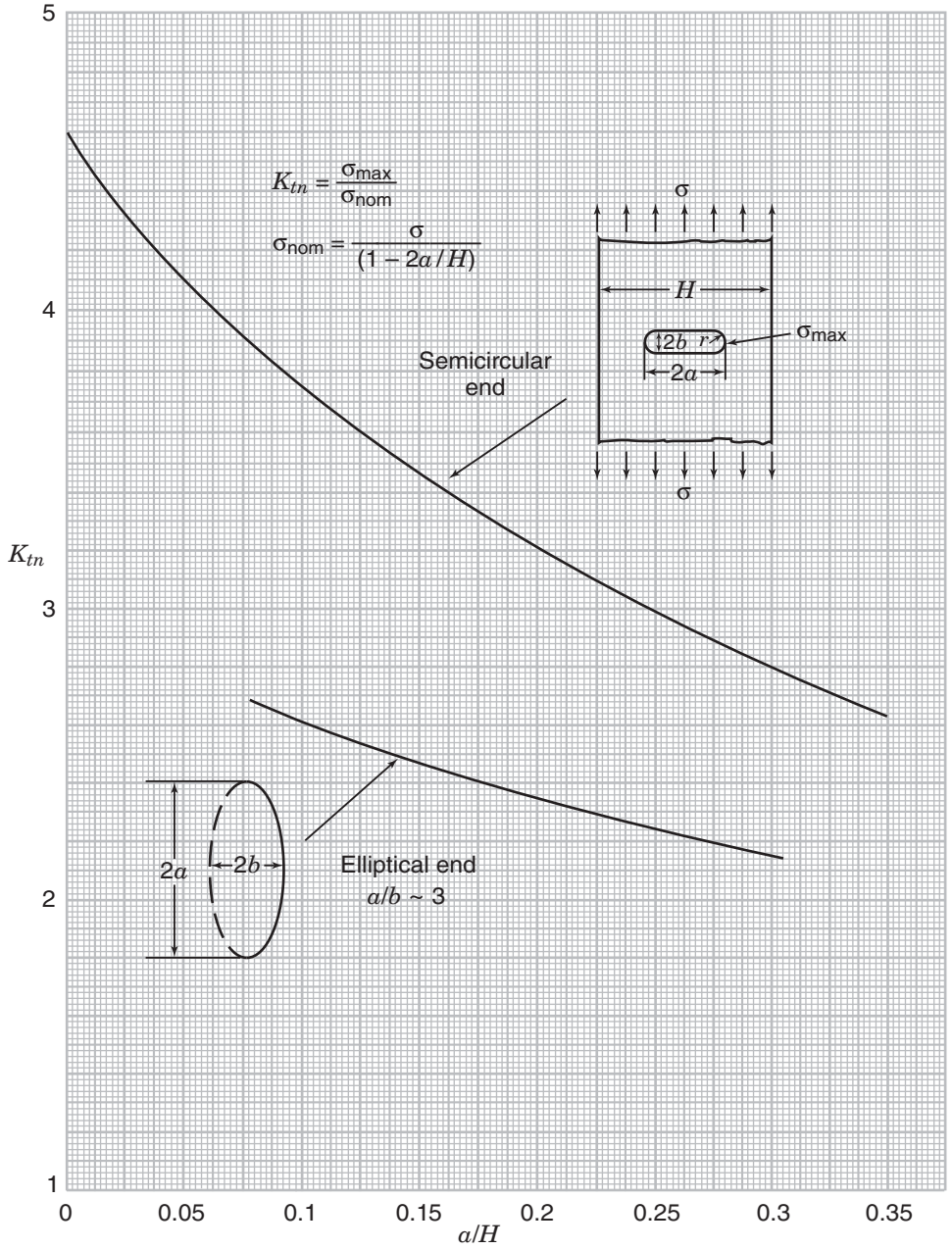


Chart 4.59 Optimization of slot end, $a/b = 3.24$ (Durelli et al. 1968).

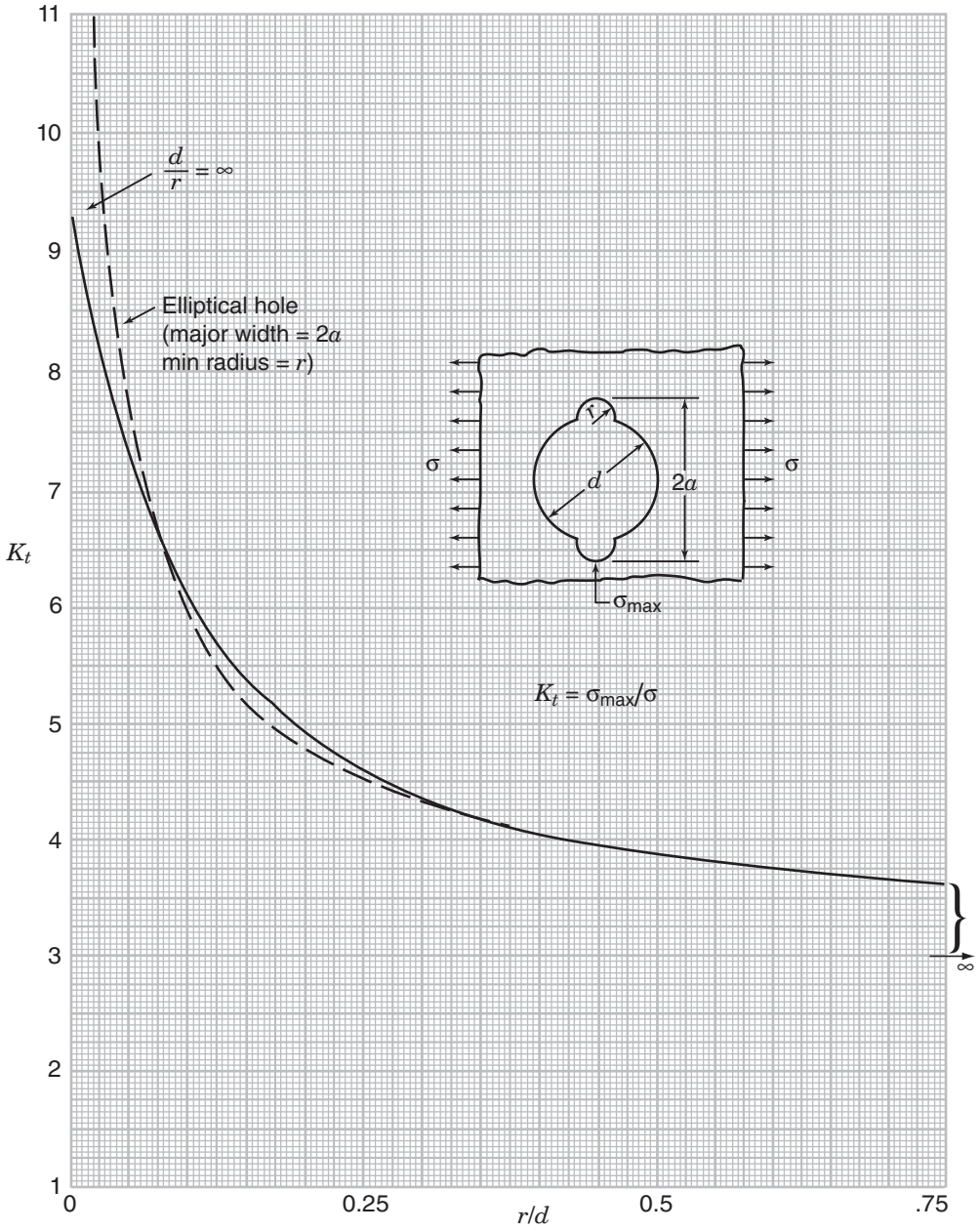


Chart 4.60 Stress concentration factor K_t for an infinitely wide tension element with a circular hole with opposite semicircular lobes (from data of Mitchell 1966).

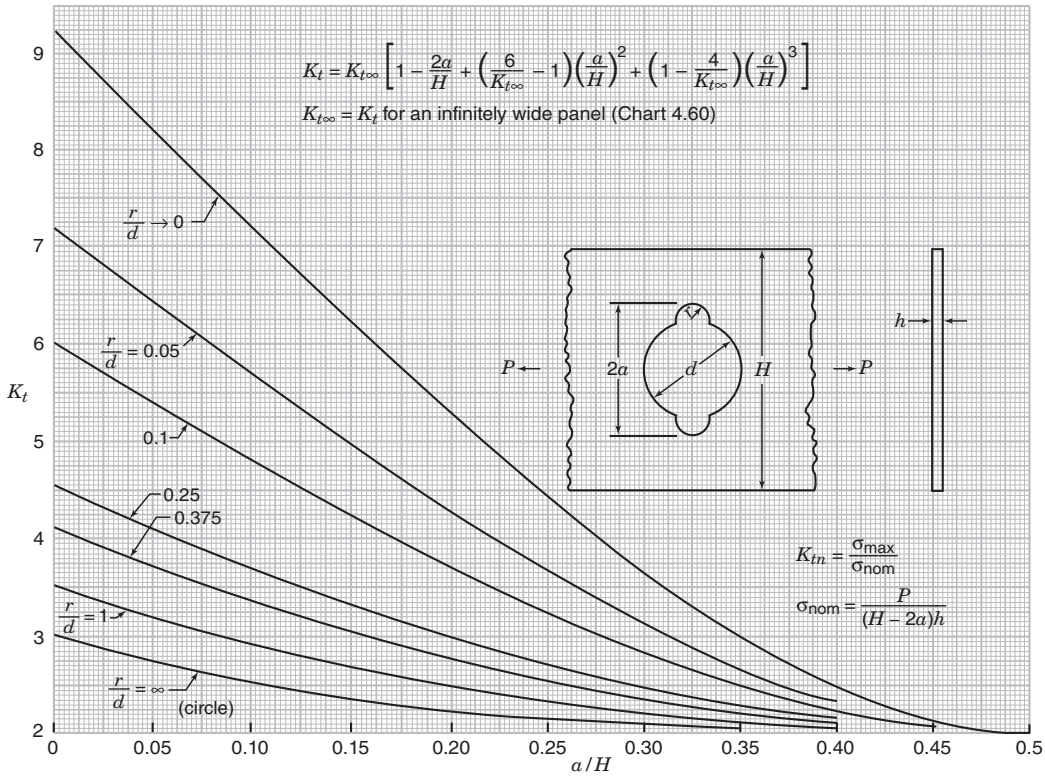


Chart 4.61 Stress concentration factors K_t for a finite-width tension thin element with a circular hole with opposite semicircular lobes (Mitchell 1966 formula).

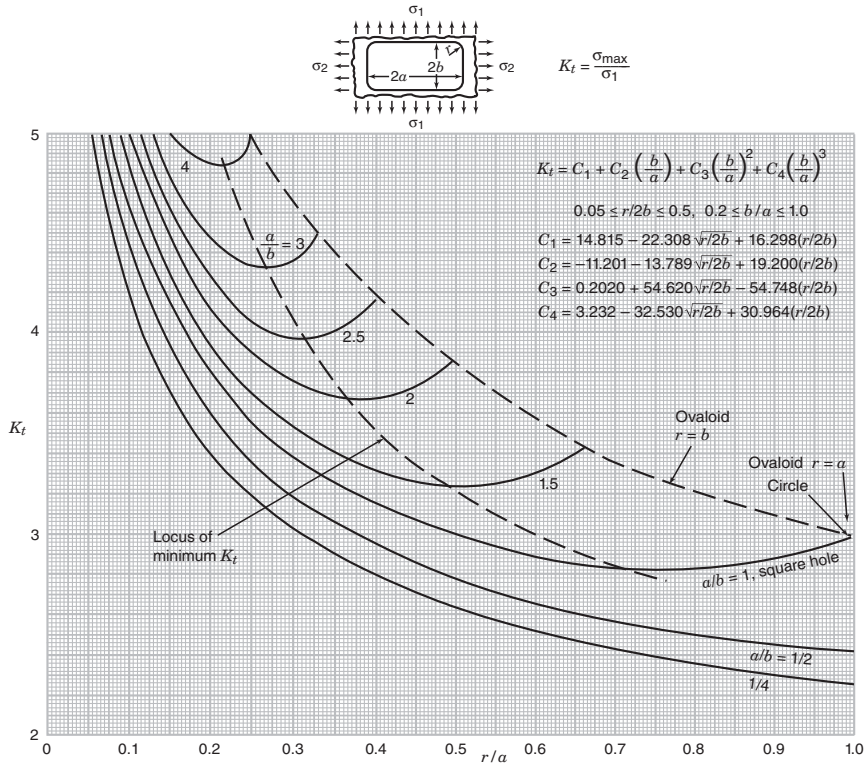


Chart 4.62*a* Stress concentration factors K_t for a rectangular hole with rounded corners in an infinitely wide thin element (Sobey 1963; ESDU 1970): uniaxial tension, $\sigma_2 = 0$.

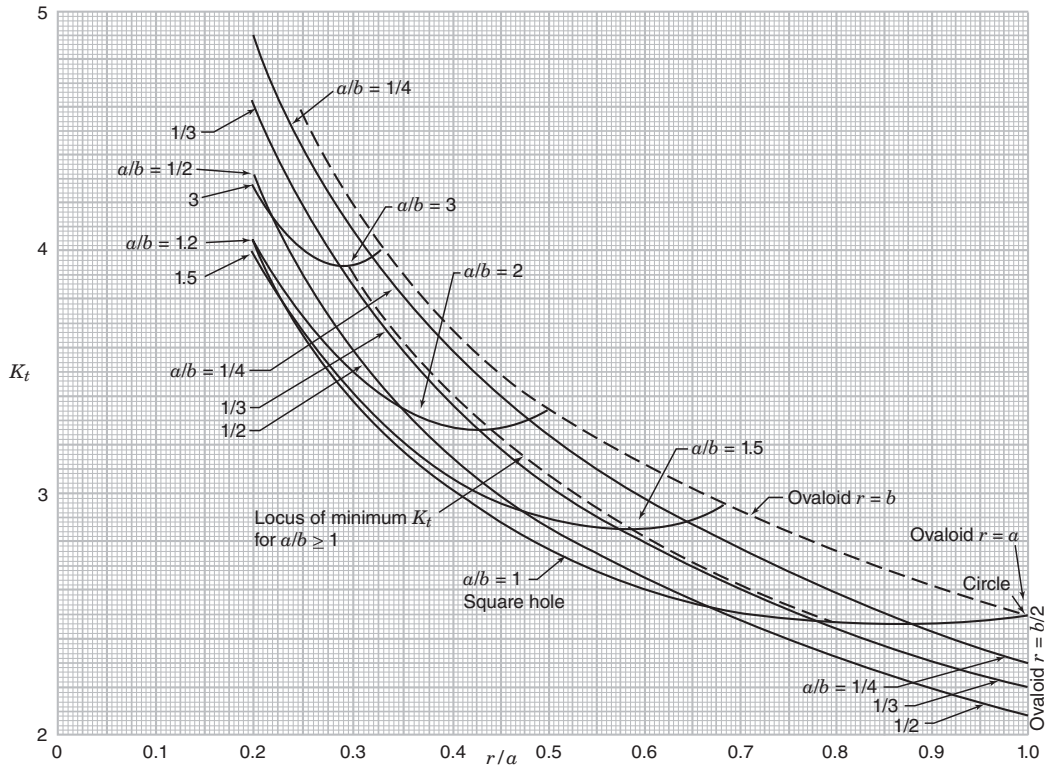


Chart 4.62*b* Stress concentration factors K_t for a rectangular hole with rounded corners in an infinitely wide thin element (Sobey 1963; ESDU 1970): unequal biaxial tension, $\sigma_2 = \sigma_1/2$.

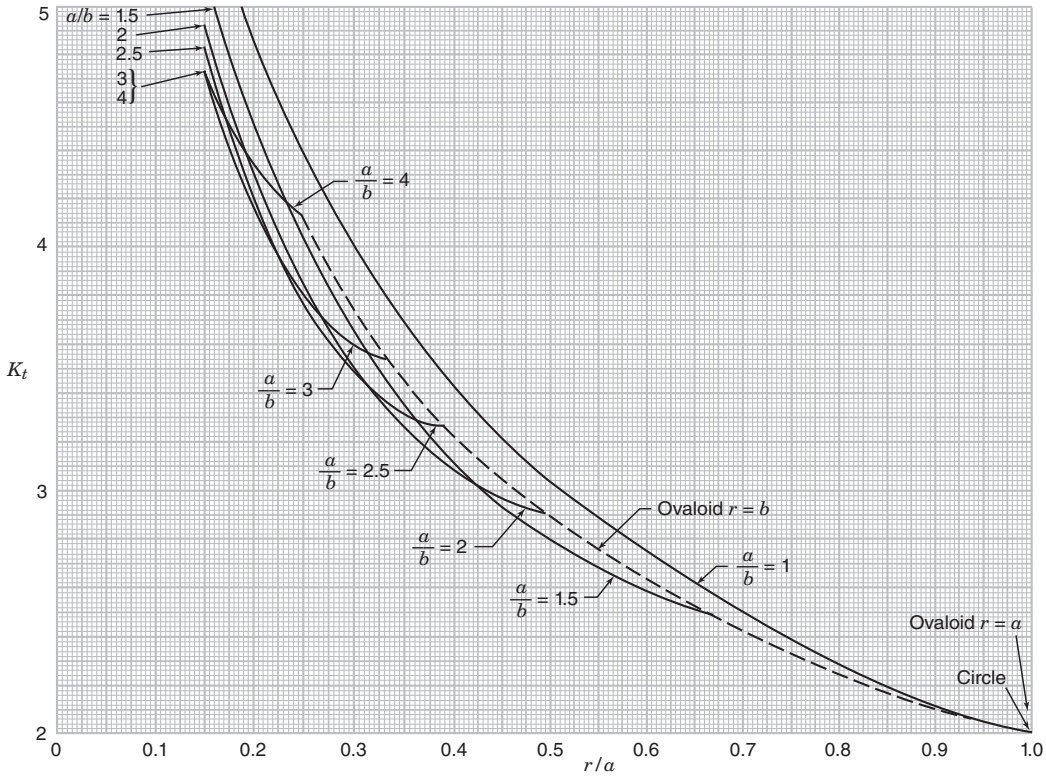


Chart 4.62*c* Stress concentration factors K_t for a rectangular hole with rounded corners in an infinitely wide thin element (Sobey 1963; ESDU 1970): equal biaxial tension, $\sigma_1 = \sigma_2$.

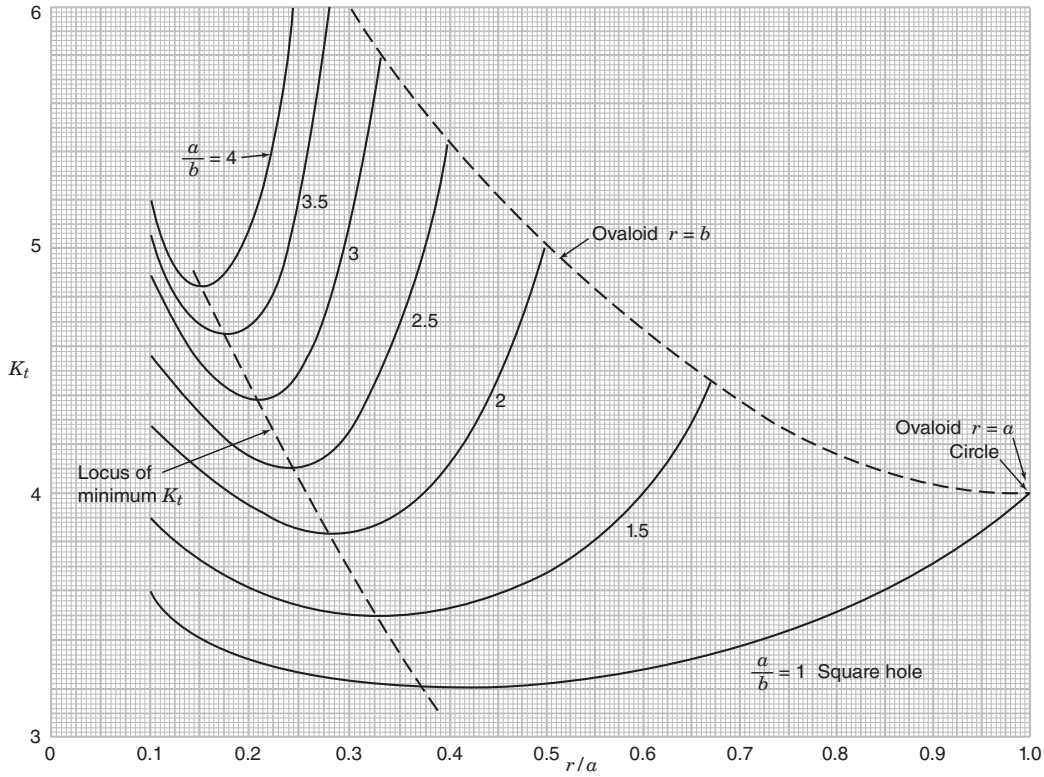


Chart 4.62*d* Stress concentration factors K_t for a rectangular hole with rounded corners in an infinitely wide thin element (Sobey 1963; ESDU 1970): unequal biaxial tension, $\sigma_1 = -\sigma_2$. Equivalent to shear, $\tau = \sigma_1$, at 45°.

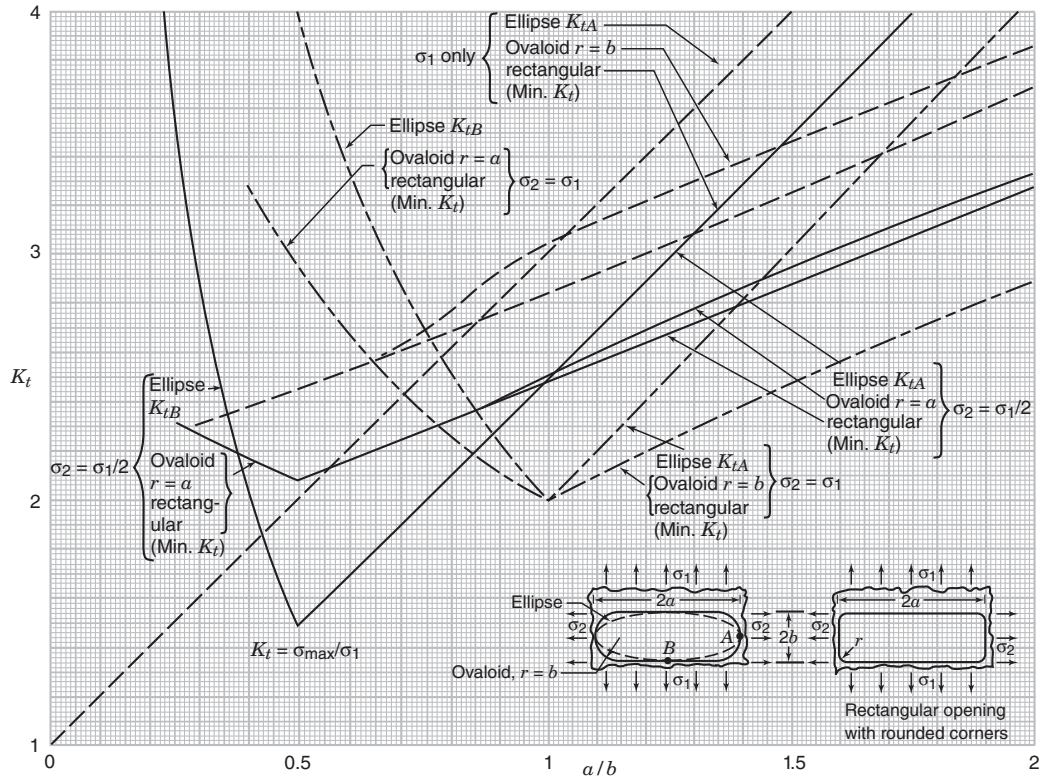


Chart 4.63 Comparison of stress concentration factors of various-shaped holes.

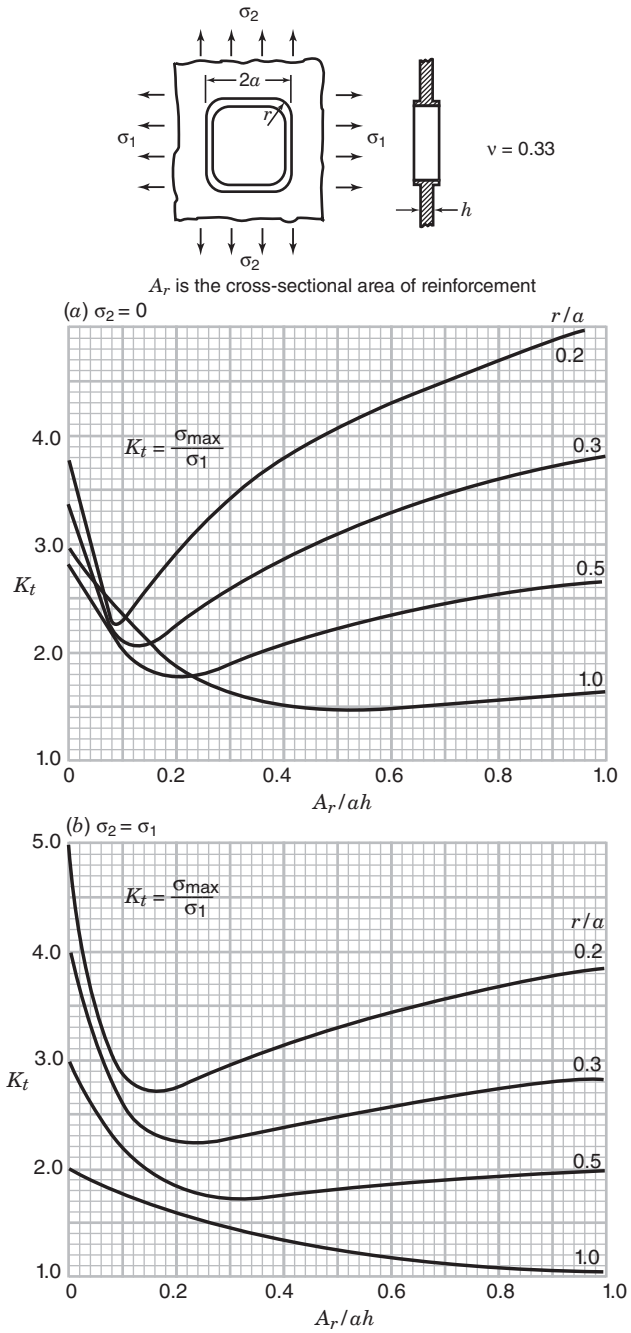


Chart 4.64*a,b* Stress concentration factors of round-cornered square holes with bead reinforcement in an infinite panel under uniaxial or biaxial stresses (Sobey 1968; ESDU 1981): (*a*) $\sigma_2 = 0$; (*b*) $\sigma_2 = \sigma_1$.

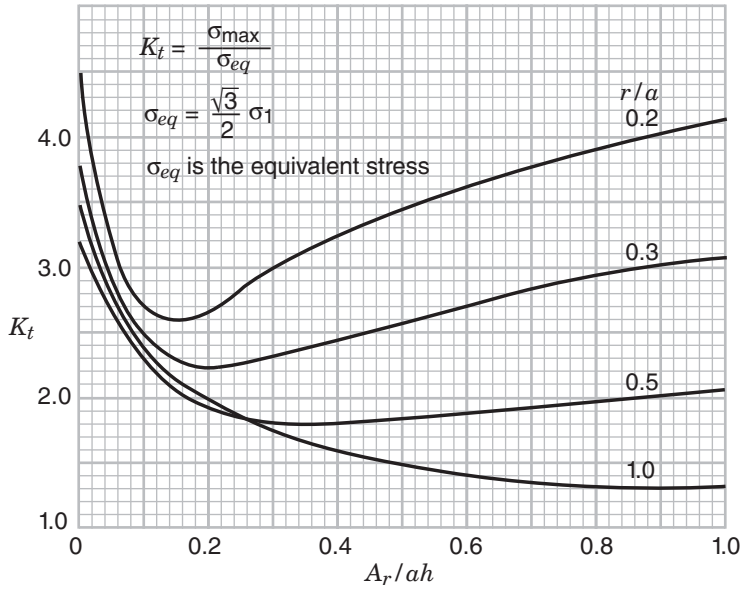


Chart 4.64*c* Stress concentration factors of round-cornered square holes with bead reinforcement in an infinite panel under uniaxial or biaxial stresses (Sobey 1968; ESDU 1981): $\sigma_2 = \sigma_1/2$.

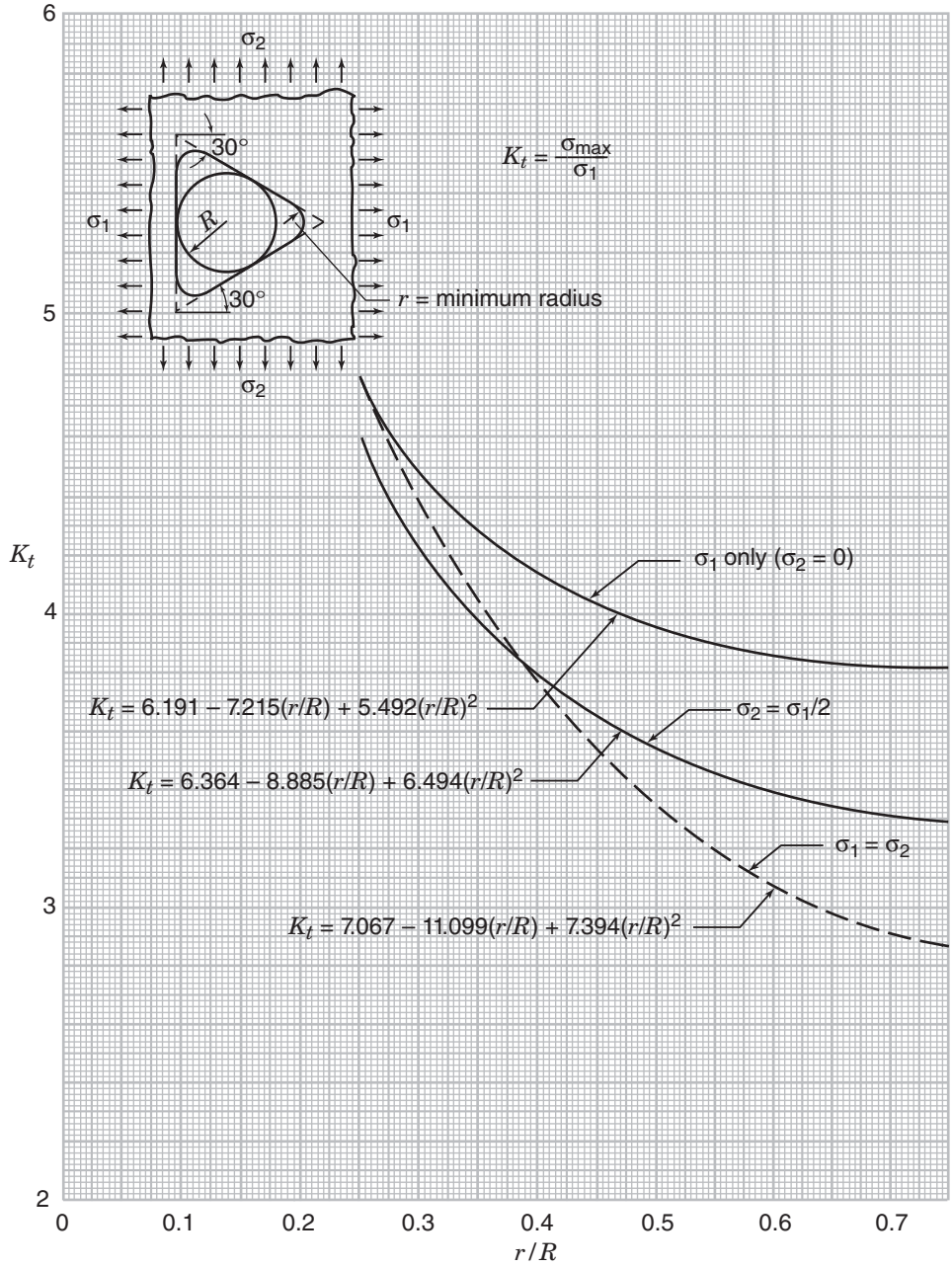


Chart 4.65*a* Stress concentration factors K_t for an equilateral triangular hole with rounded corners in an infinite thin element (Wittrick 1963): K_t as a function of r/R.

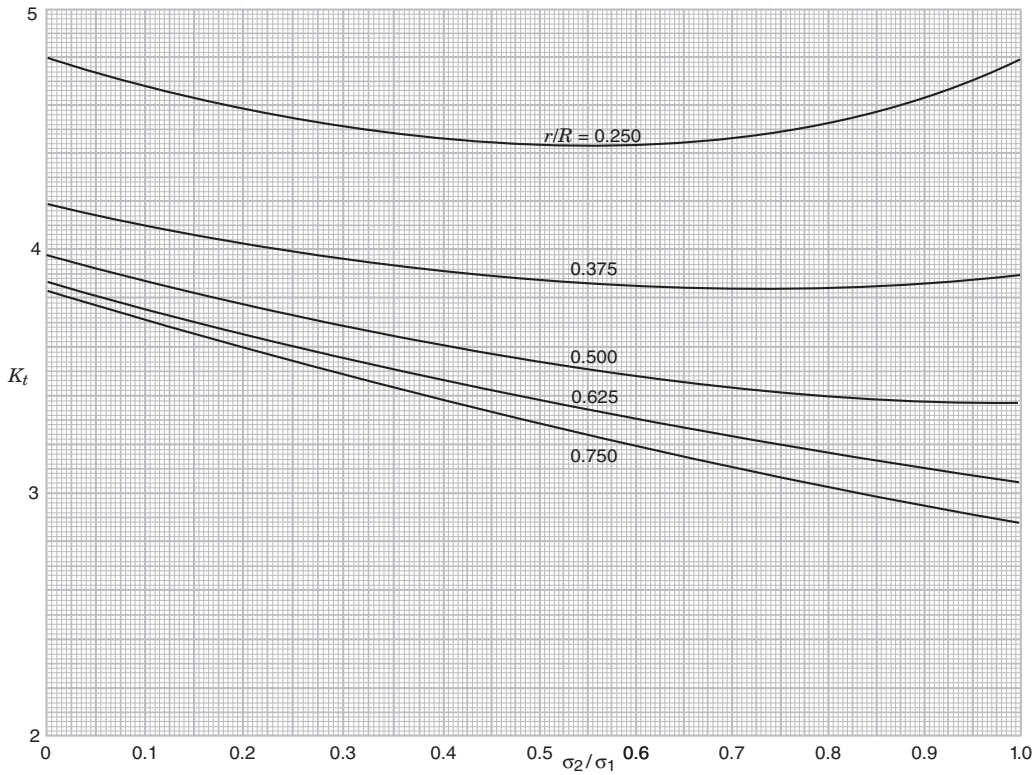


Chart 4.65*b* Stress concentration factors K_t for an equilateral triangular hole with rounded corners in an infinite thin element (Wittrick 1963): K_t as a function of σ_2/σ_1.

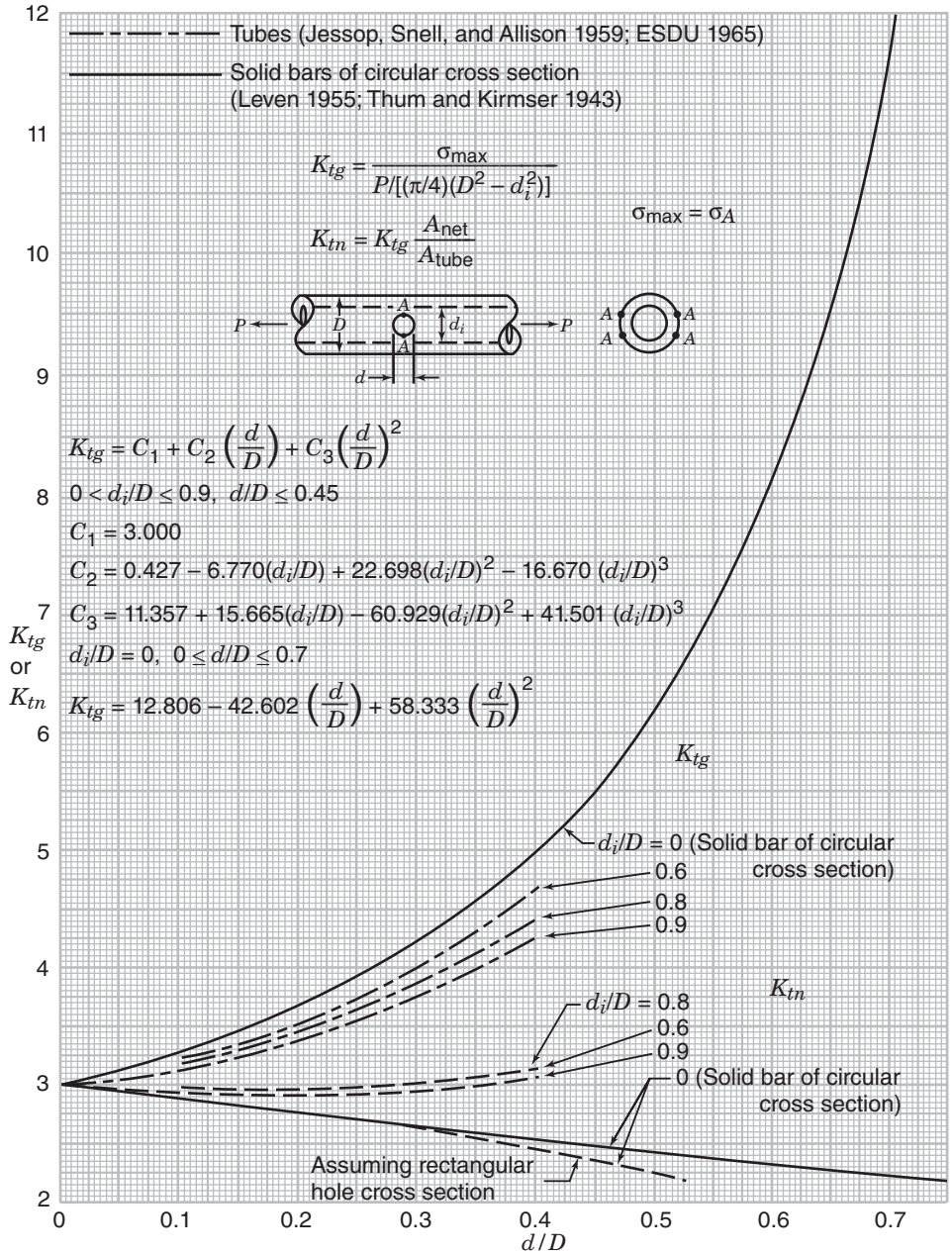


Chart 4.66 Stress concentration factors K_{tg} and K_{tn} for tension of a bar of circular cross section or tube with a transverse hole. Tubes (Jessop et al. 1959; ESDU 1965); Solid bars of circular cross section (Thum and Kirmser 1943; Leven 1955).

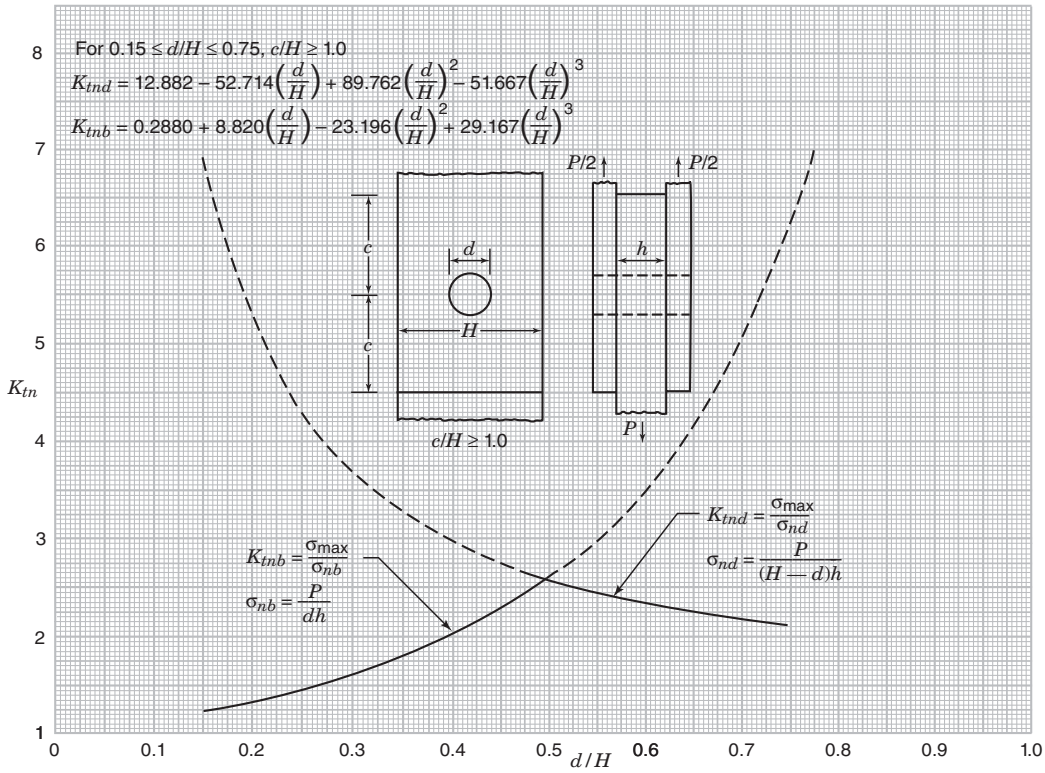


Chart 4.67 Stress concentration factors K_{tn} for a pin joint with a closely fitting pin (Frocht and Hill 1951; Theocaris 1956).

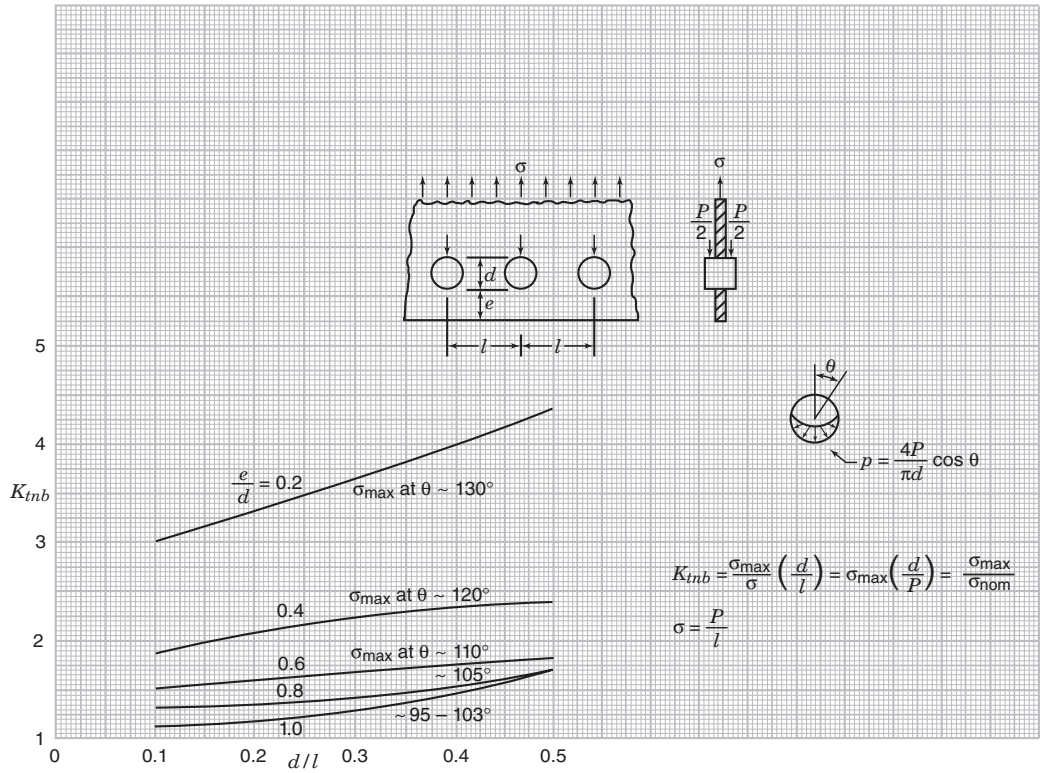


Chart 4.68 Stress concentration factors K_m for a pinned or riveted joint with multiple holes (from data of Mori 1972).

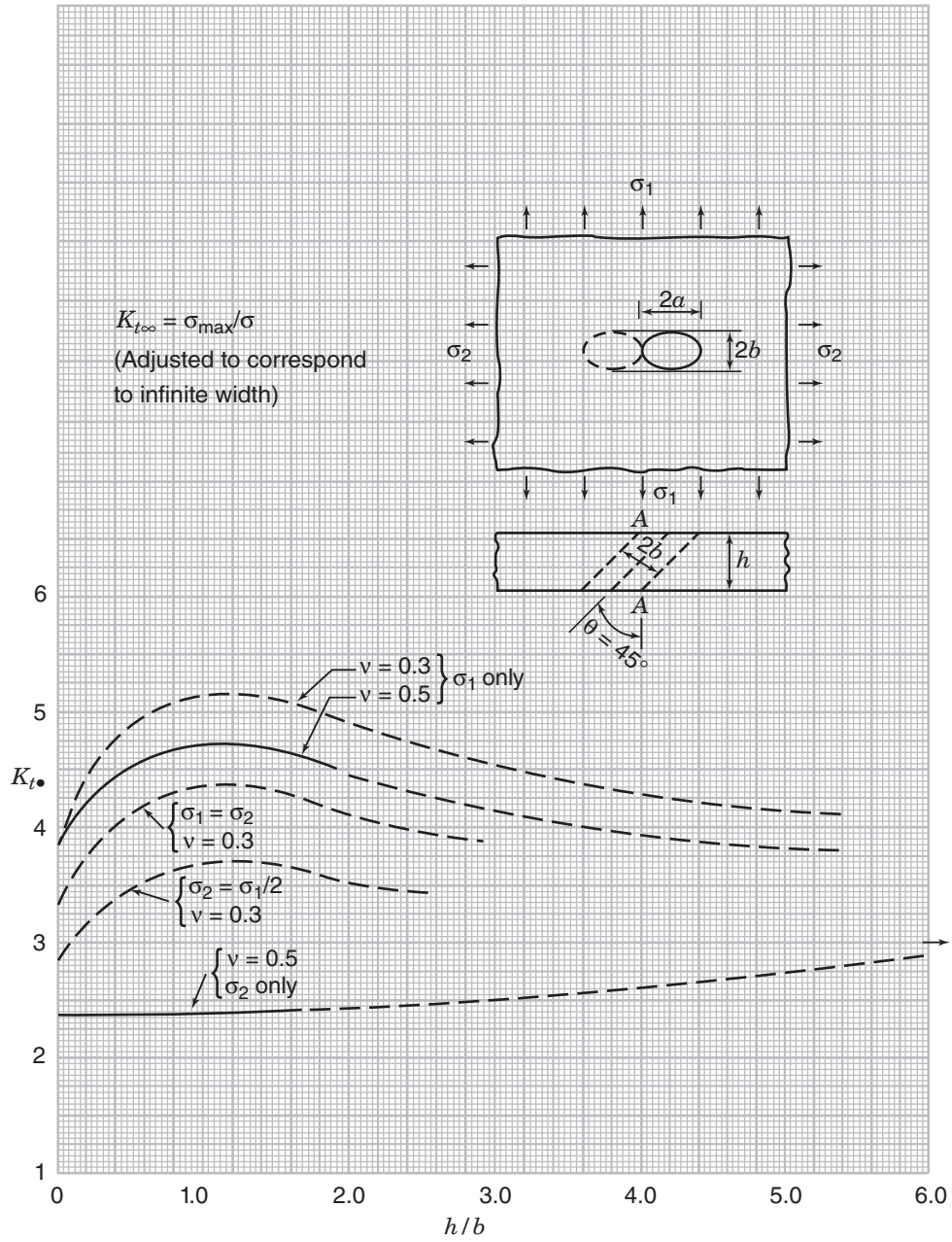


Chart 4.69 Stress concentration factors $K_{t\infty}$ for a circular hole inclined 45° from the perpendicular to the surface of an infinite panel subjected to various states of tension (based on McKenzie and White 1968; Leven 1970; Daniel 1970; Ellyin 1970).

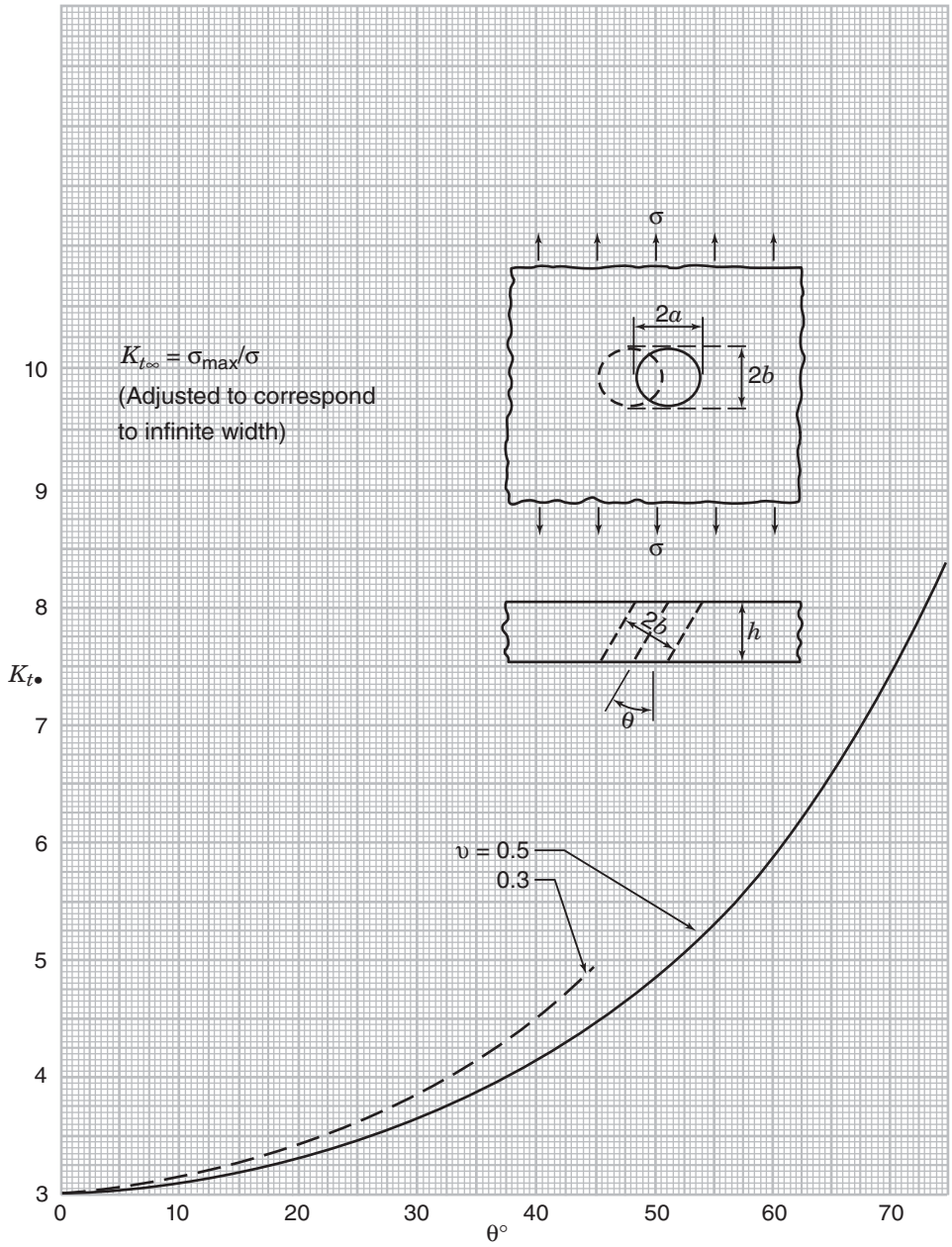


Chart 4.70 Stress concentration factors $K_{t\infty}$ for a circular hole inclined $\theta°$ from the perpendicular to the surface of an infinite panel subjected to tension, $h/b = 1.066$ (based on McKenzie and White 1968; Ellyin 1970).

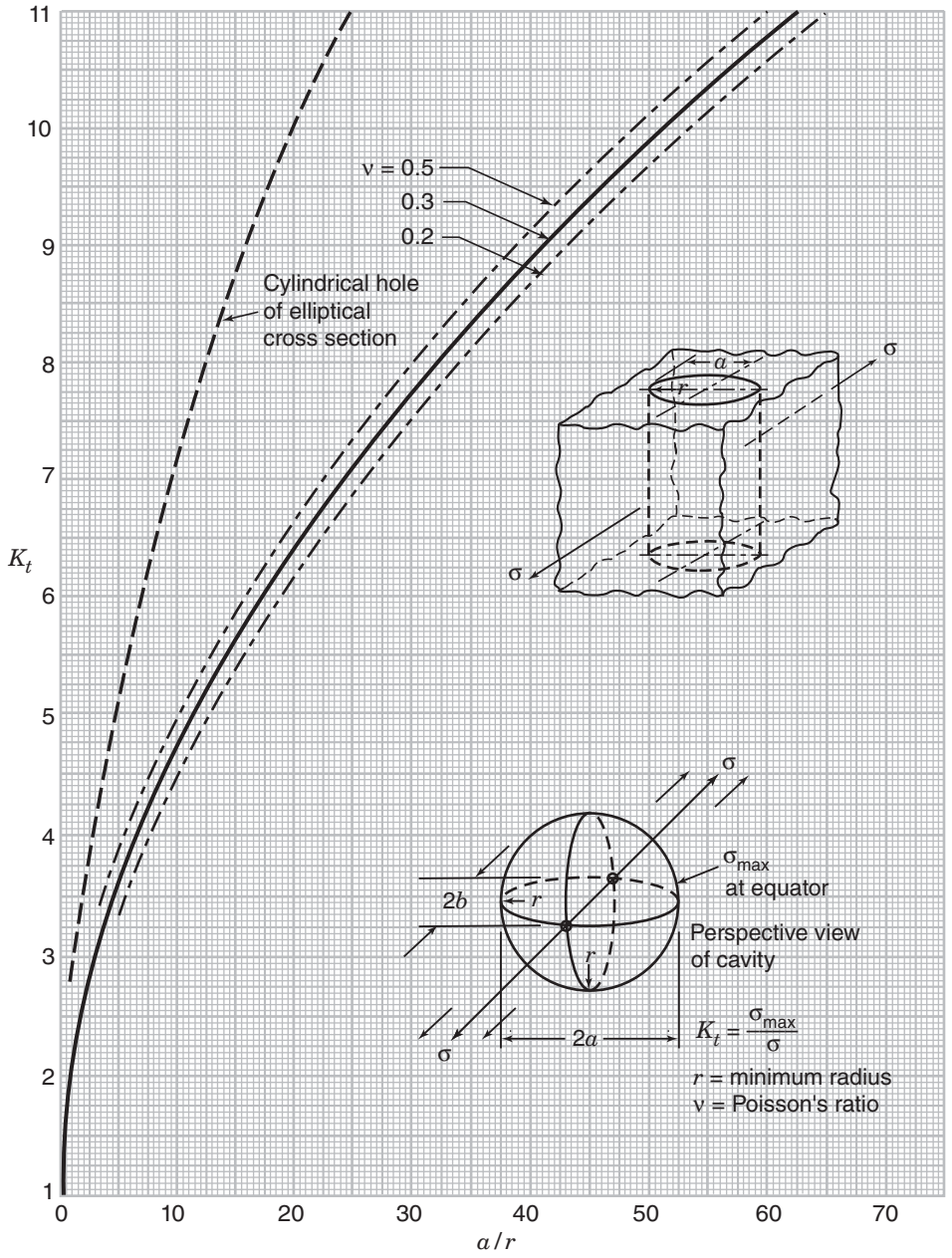


Chart 4.71 Stress concentration factors K_t for a circular cavity of elliptical cross section in an infinite body in tension (Neuber 1958).

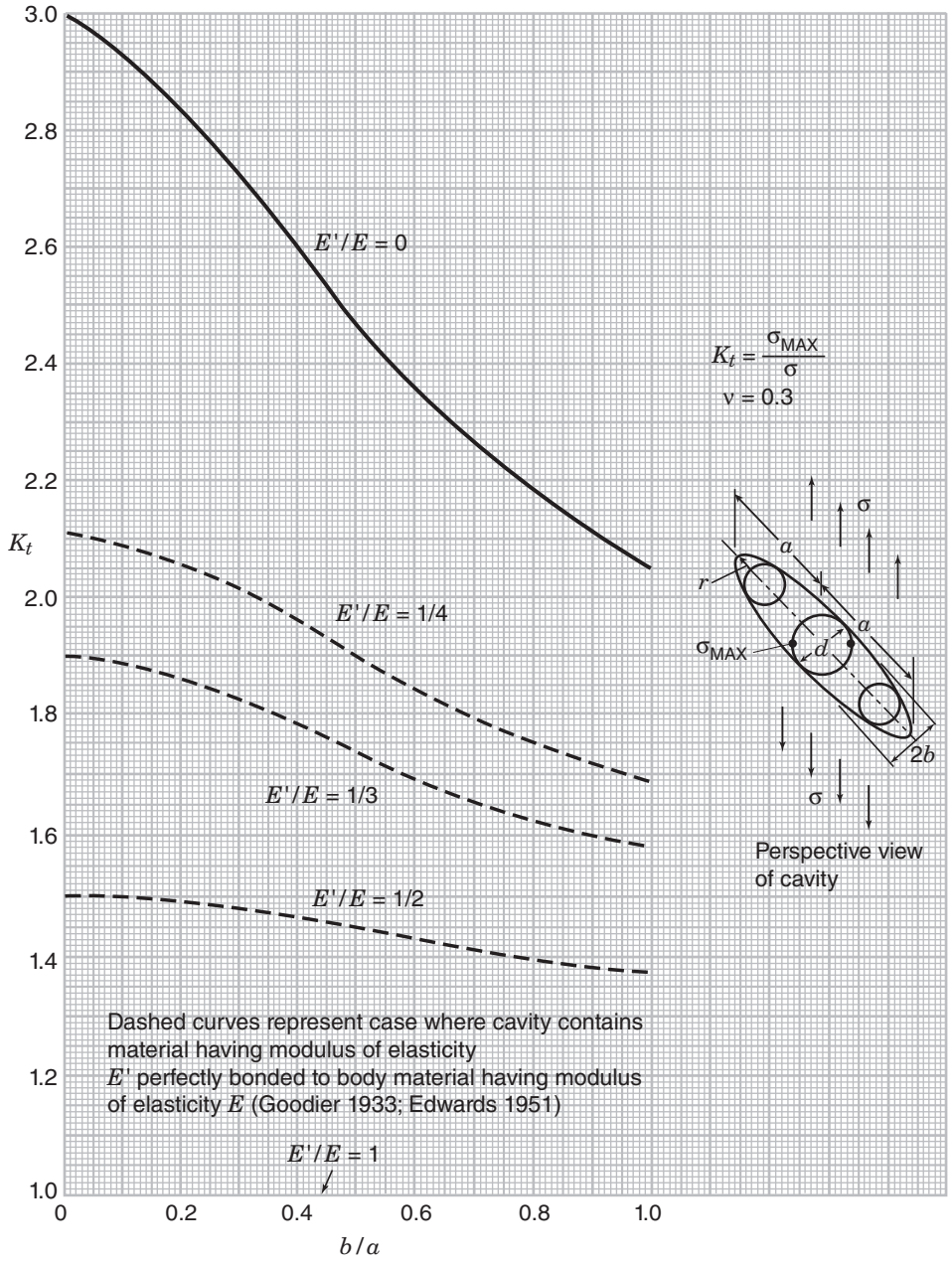


Chart 4.72 Stress concentration factors K_t for an ellipsoidal cavity of circular cross section in an infinite body in tension (mathematical analysis of Sadowsky and Sternberg 1947).

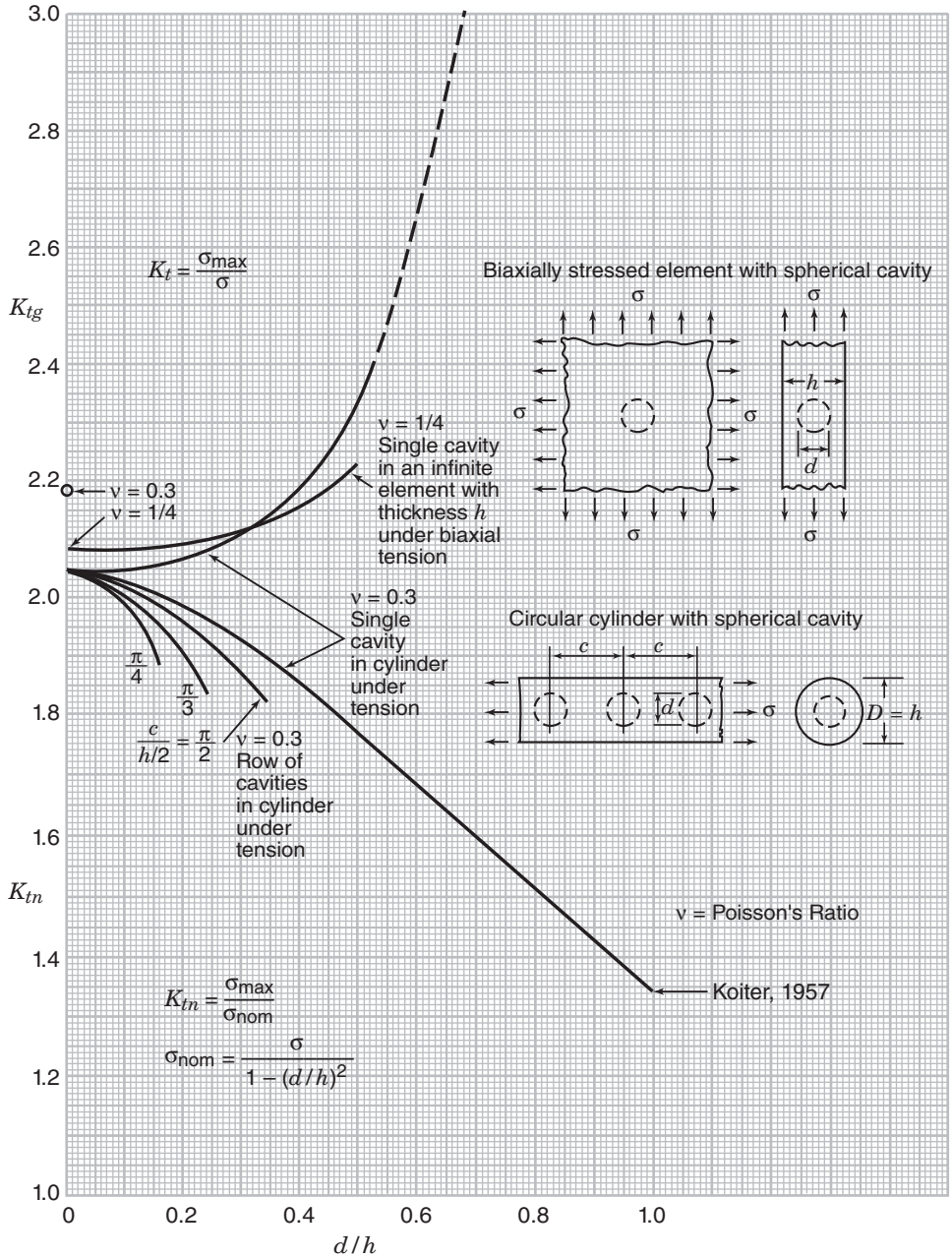


Chart 4.73 Stress concentration factors K_{tg} and K_{tn} for spherical cavities in finite-width flat elements and cylinders (Ling 1959; Atsumi 1960).

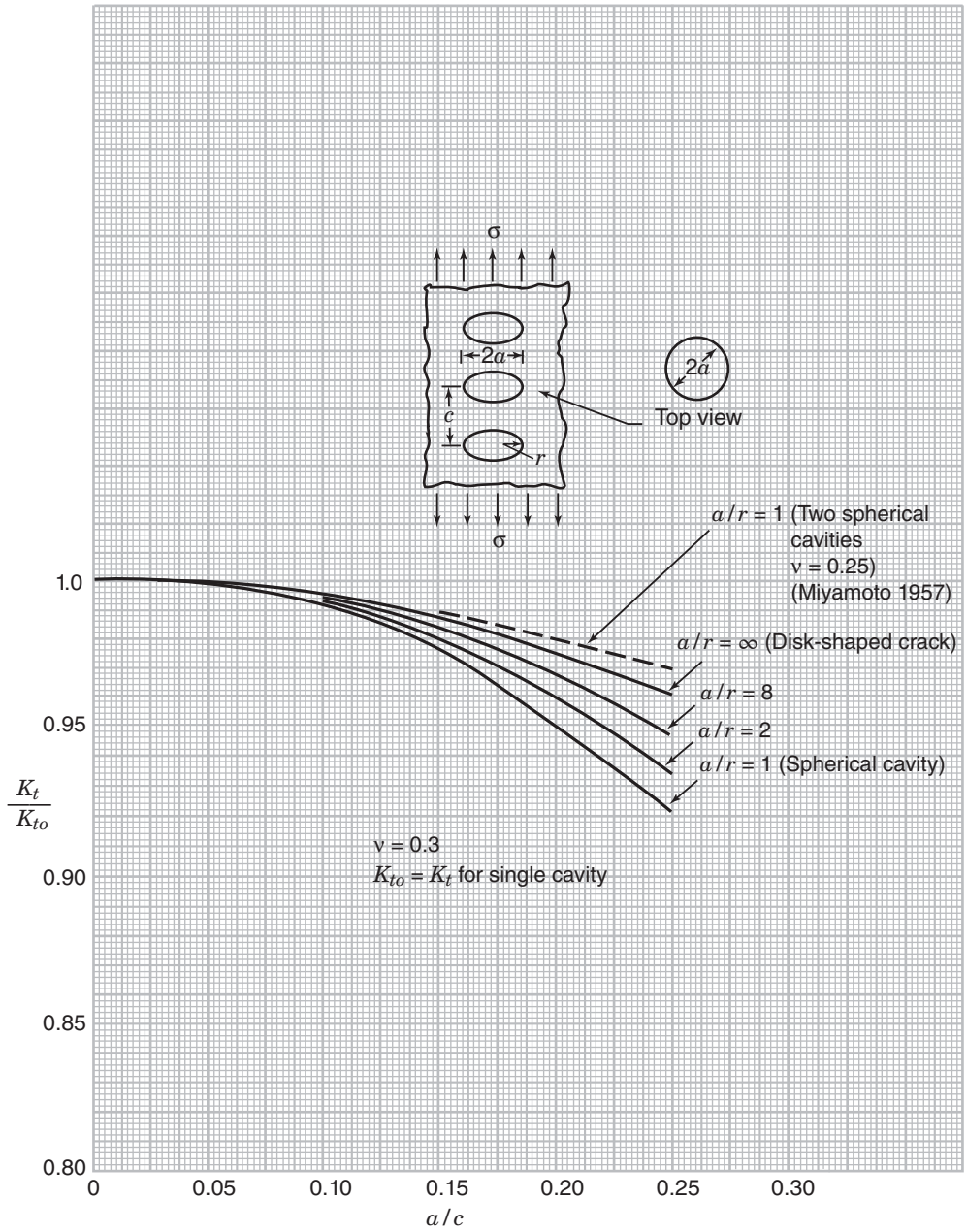


Chart 4.74 Effect of spacing on the stress concentration factor of an infinite row of ellipsoidal cavities in an infinite tension member (Miyamoto 1957).

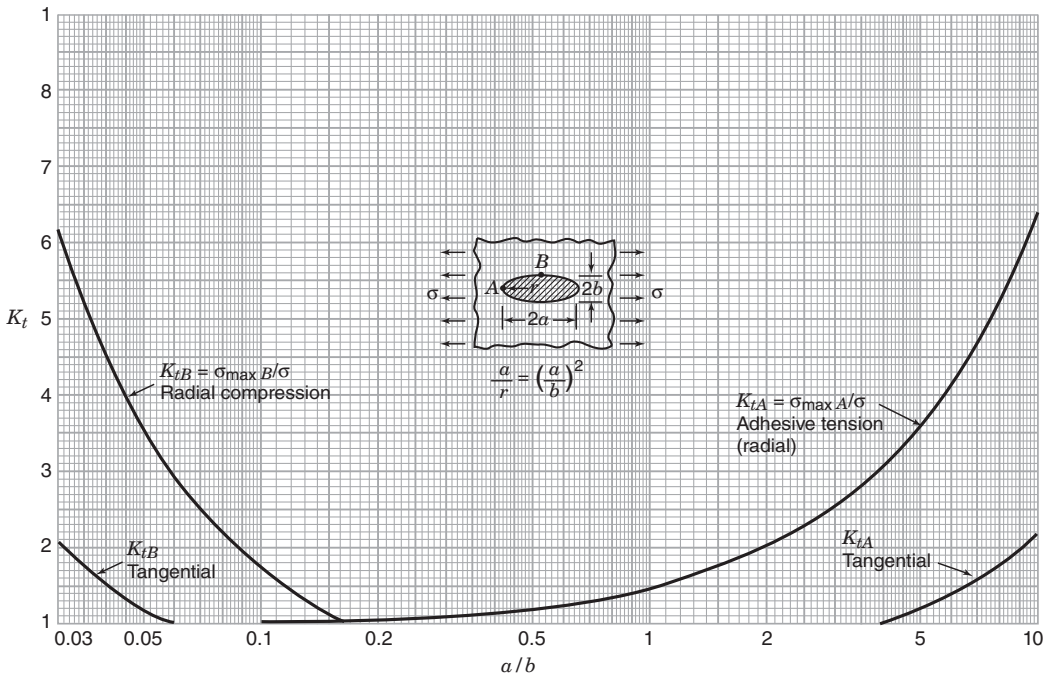


Chart 4.75 Stress concentration factors K_t for an infinite member in tension having a rigid elliptical cylindrical inclusion (Goodier 1933; Donnell 1941; Nisitani 1968).

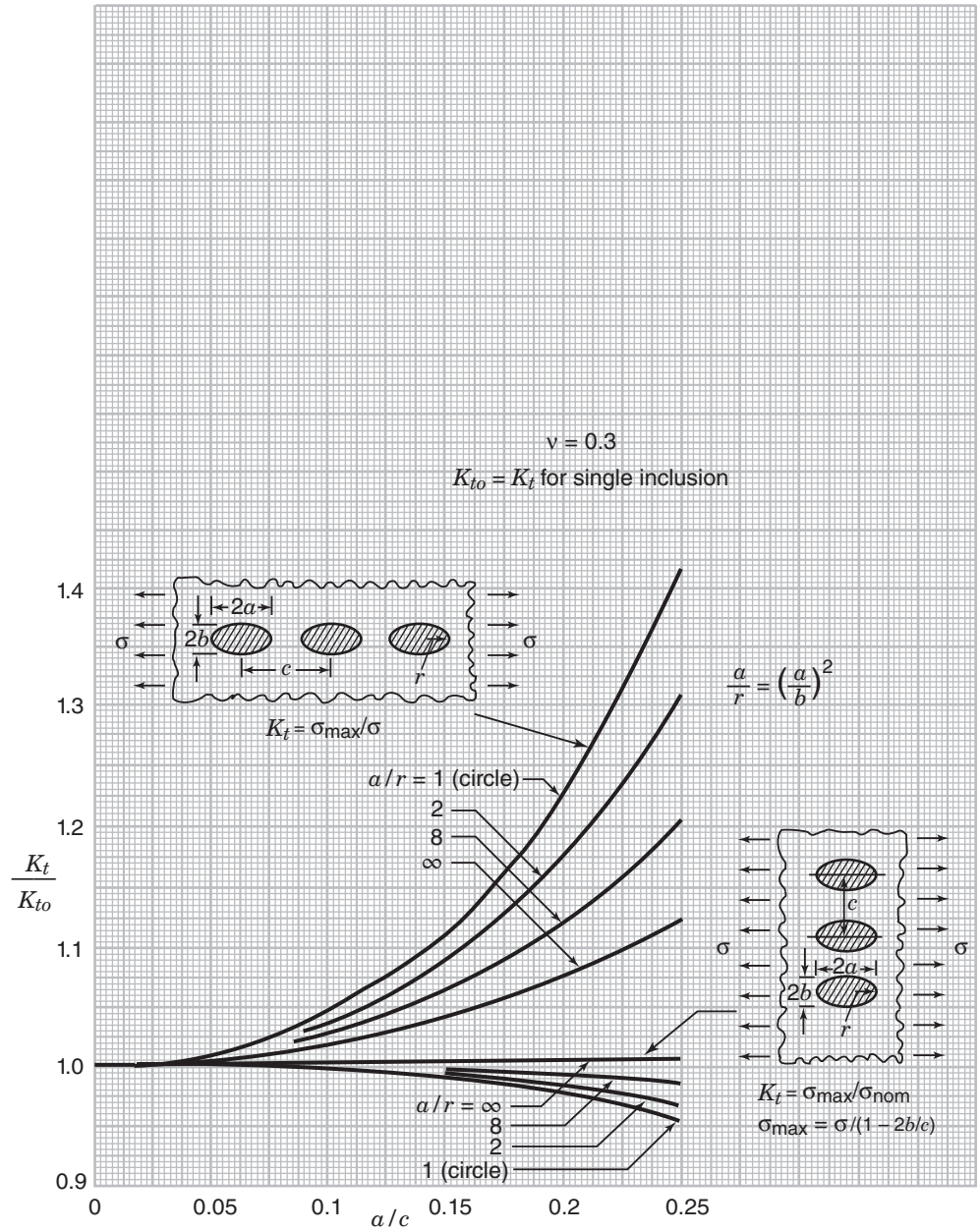


Chart 4.76 Effect of spacing on the stress concentration factor of an infinite tension panel with an infinite row of rigid cylindrical inclusions (Nisitani 1968).

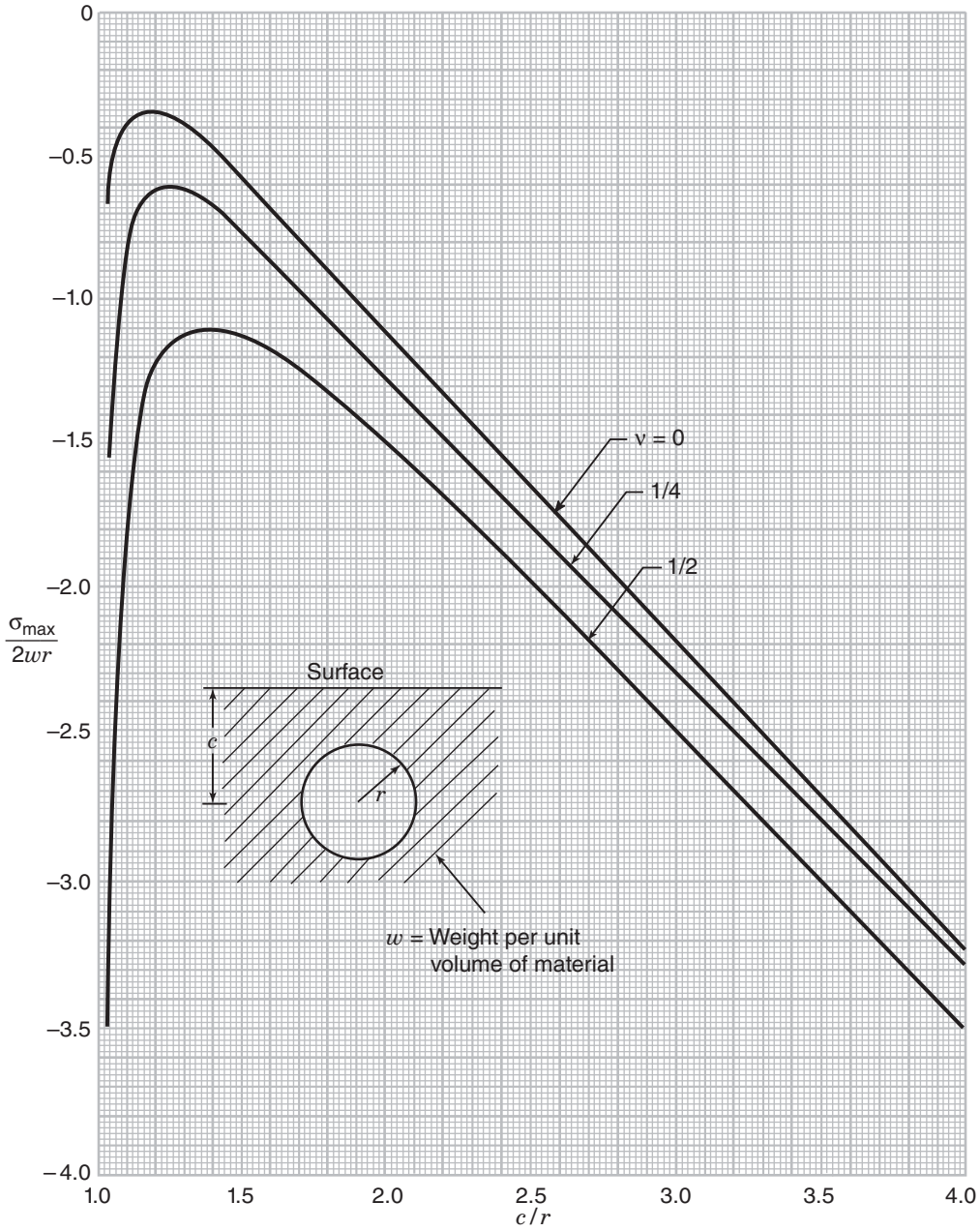


Chart 4.77 Maximum peripheral stress in a cylindrical tunnel subjected to hydrostatic pressure due to the weight of the material (Mindlin 1939).

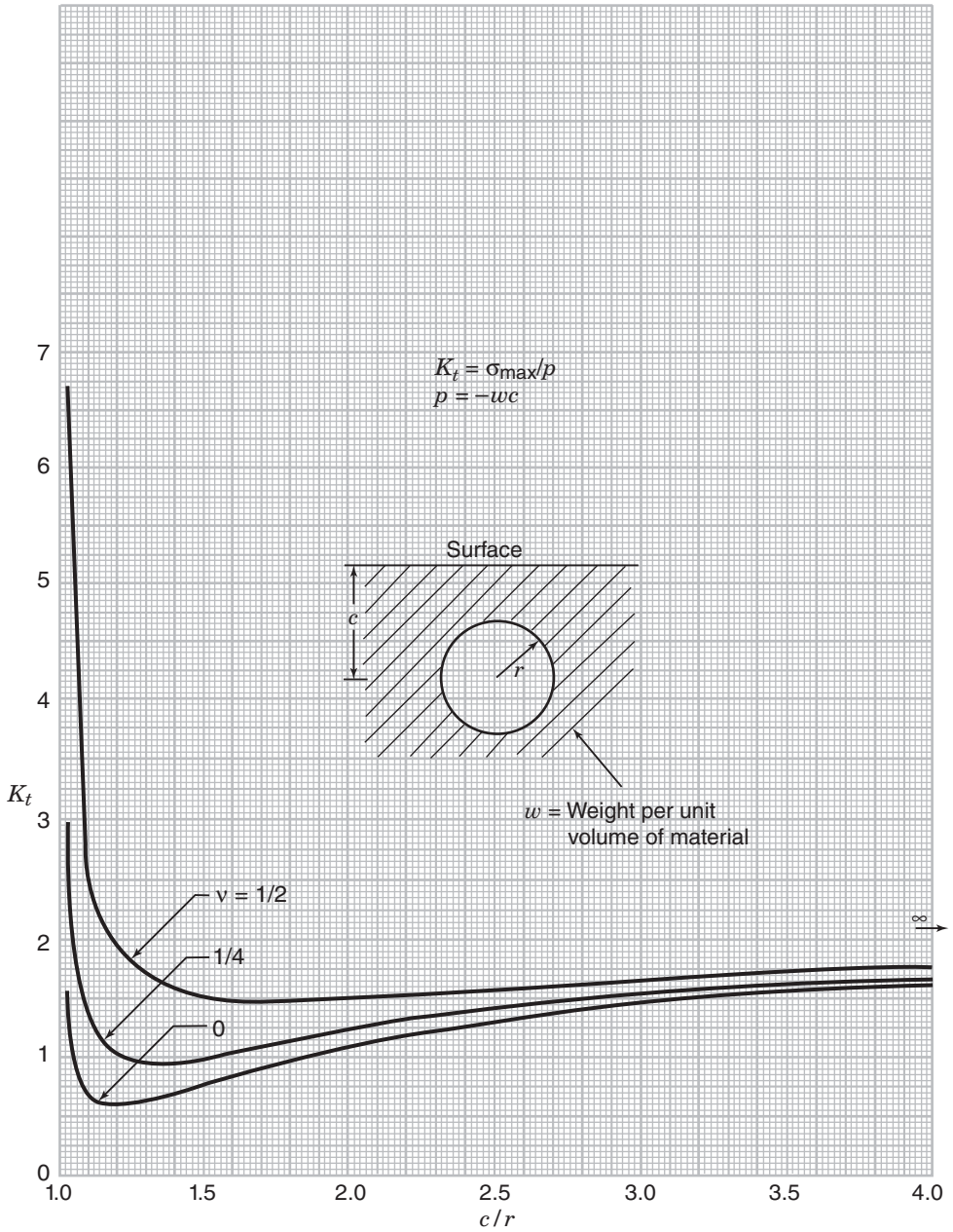


Chart 4.78 Stress concentration factors K_t for a cylindrical tunnel subjected to hydrostatic pressure due to the weight of the material (based on Chart 4.77).

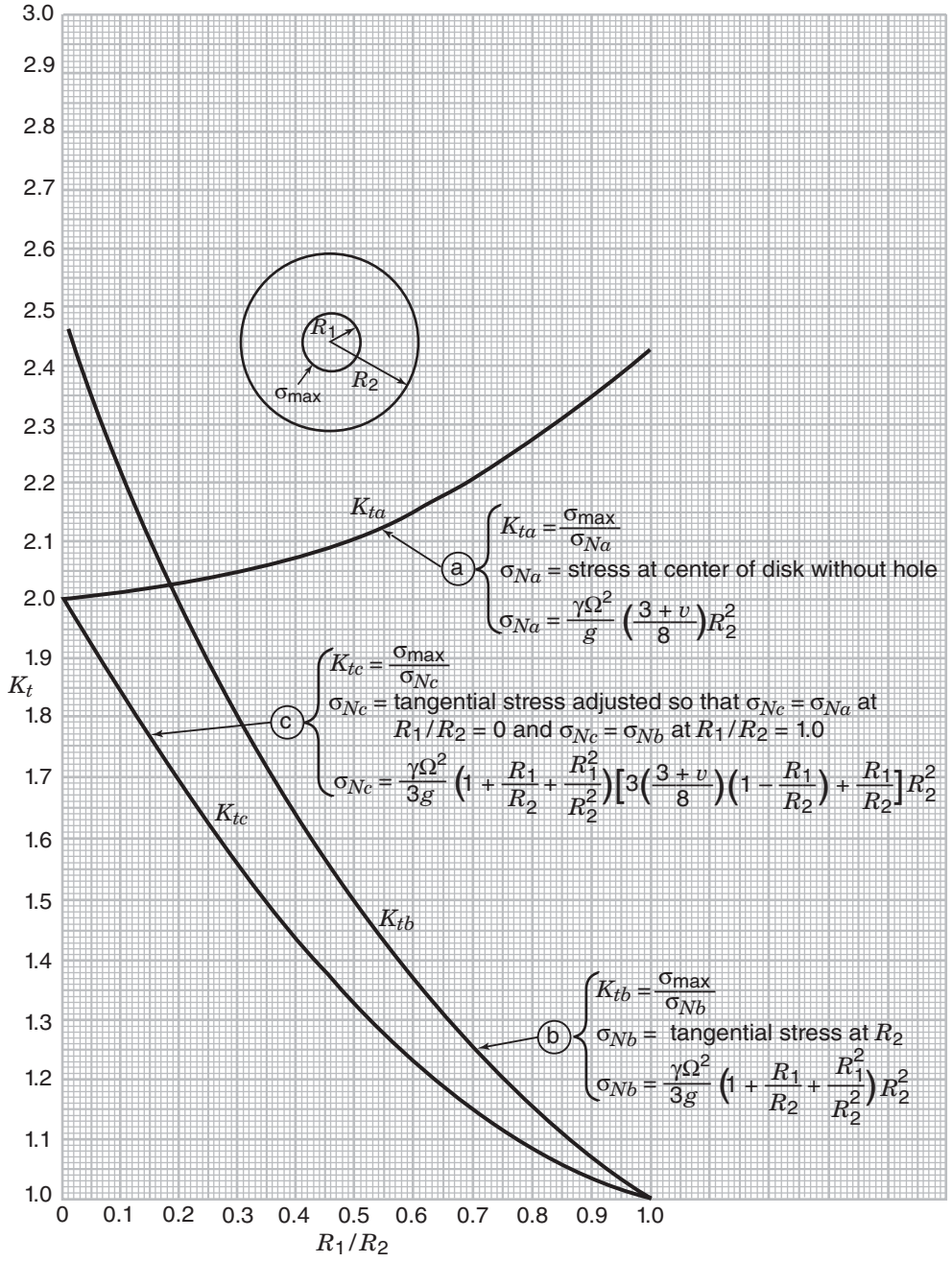


Chart 4.79 Stress concentration factors K_t for a rotating disk with a central hole.

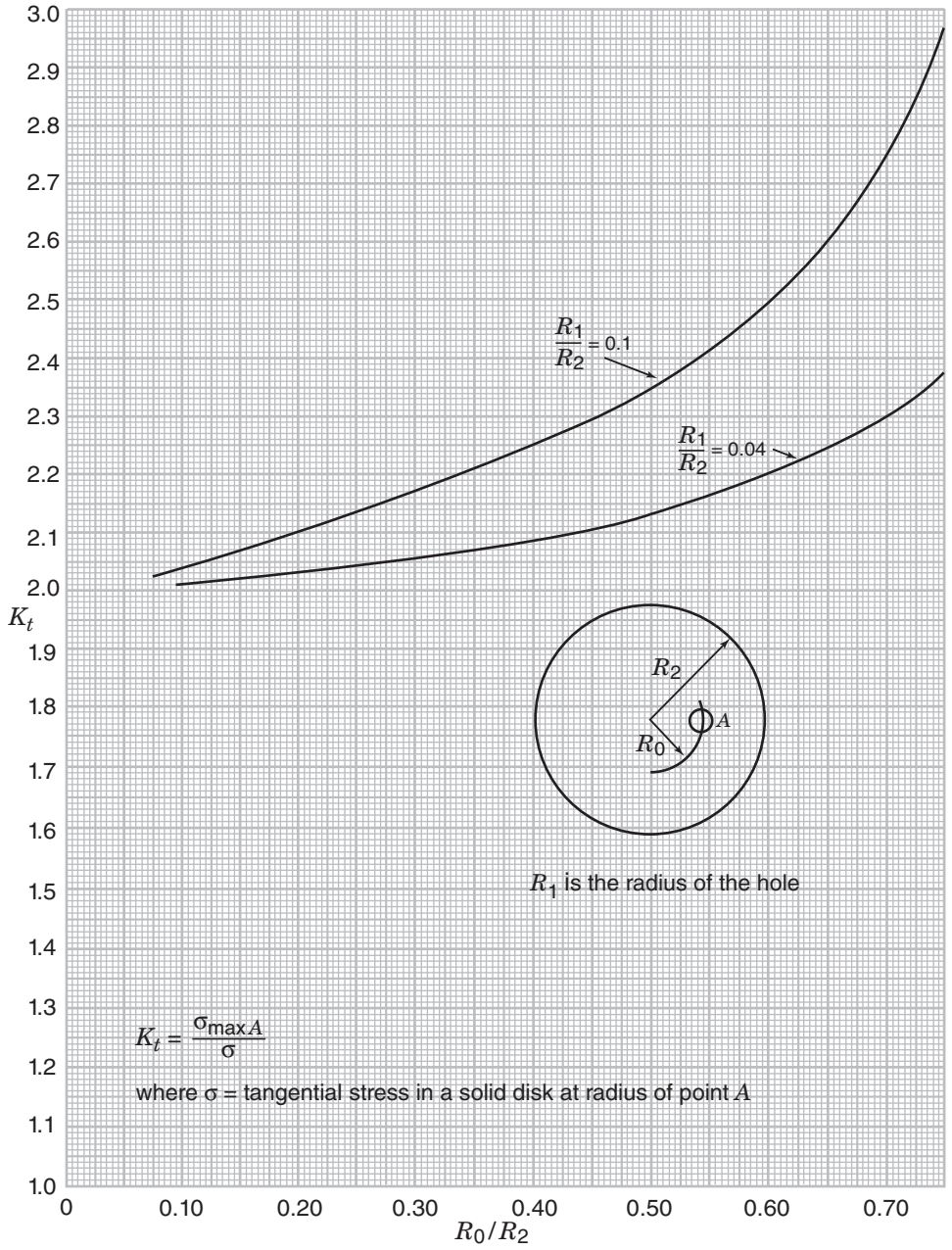


Chart 4.80 Stress concentration factors K_t for a rotating disk with a noncentral hole (photoelastic tests of Barnhart et al. 1951).

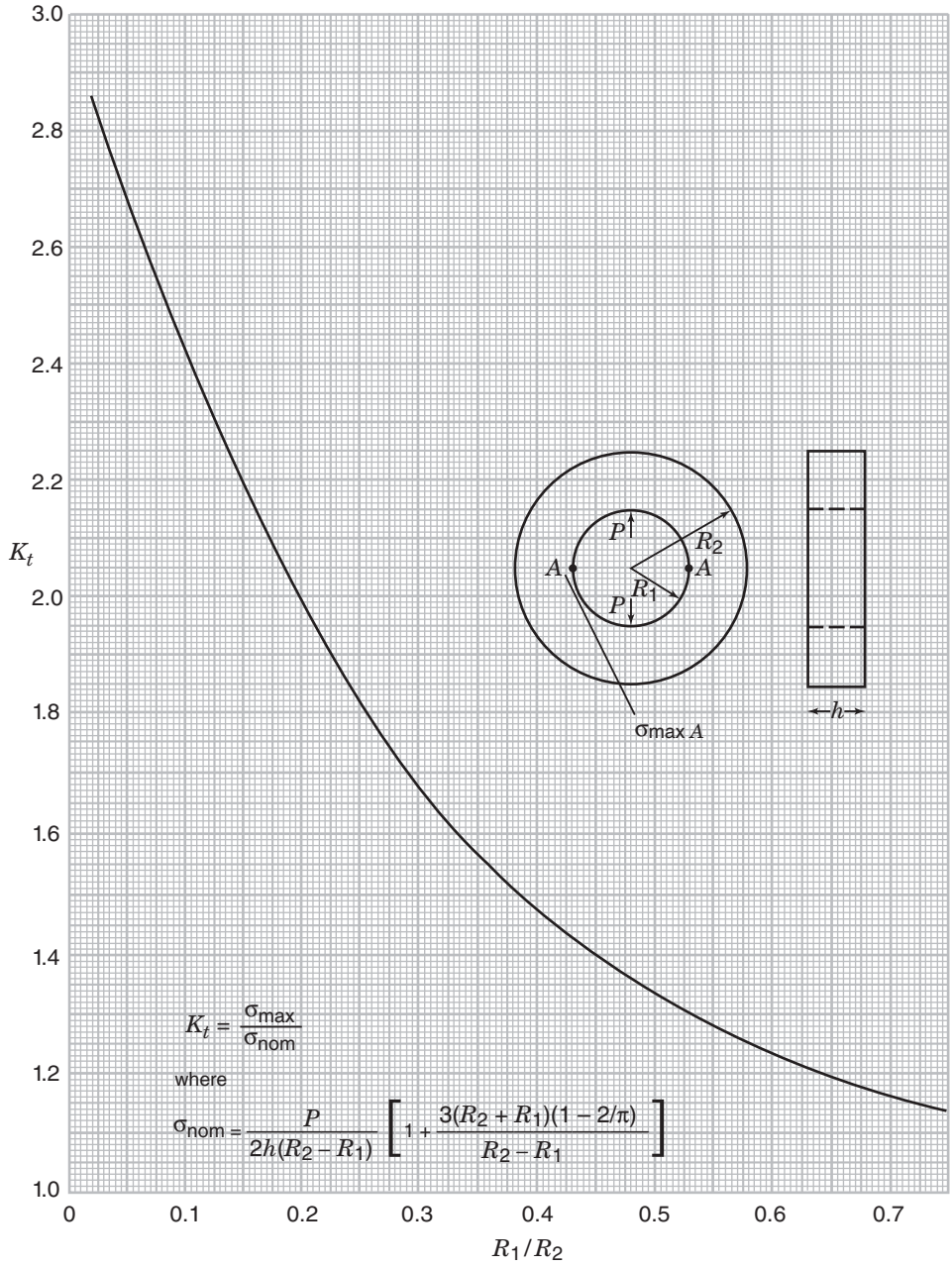


Chart 4.81 Stress concentration factors K_t for a ring or hollow roller subjected to diametrically opposite internal concentrated loads (Timoshenko 1922; Horger and Buckwalter 1940; Leven 1952).

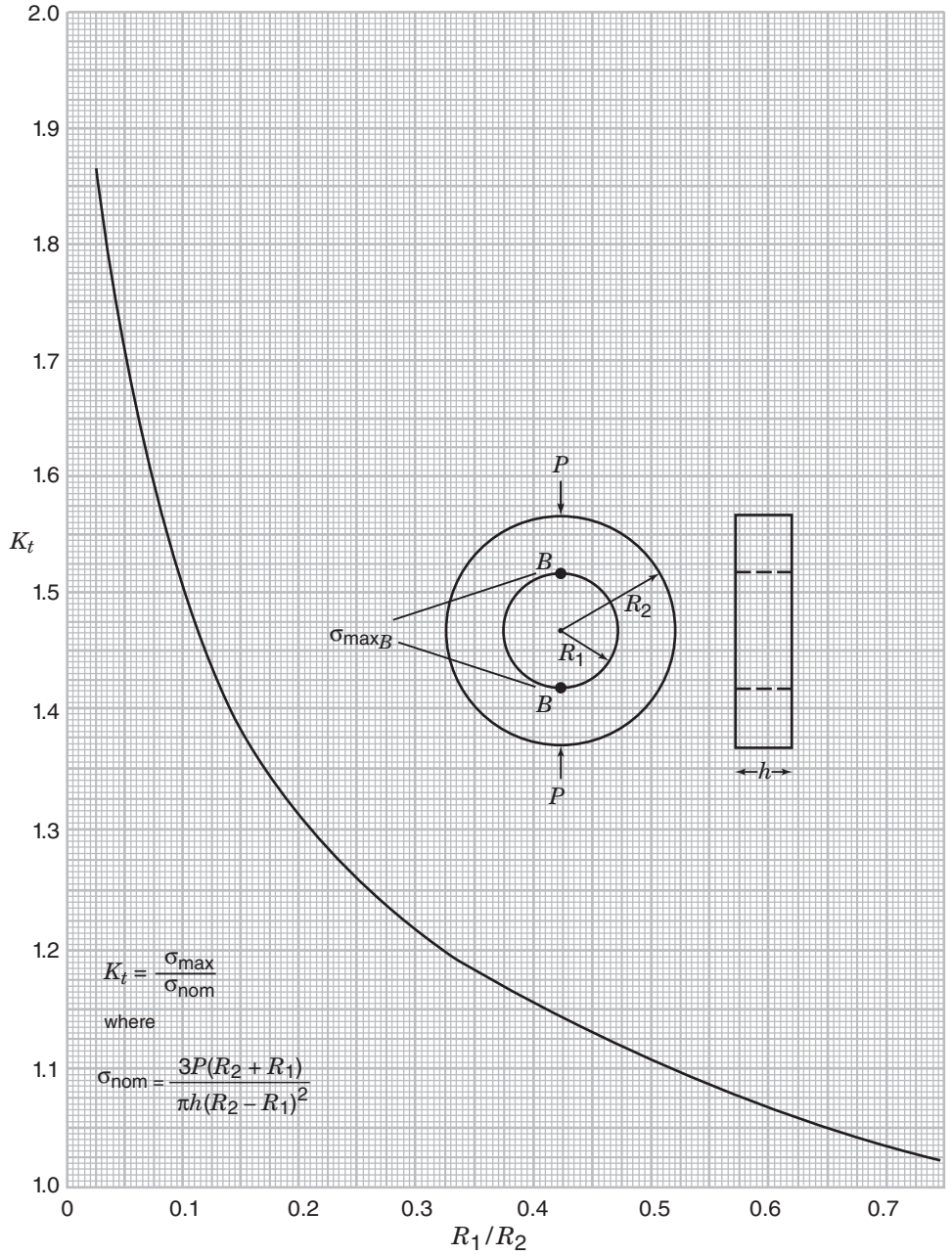


Chart 4.82 Stress concentration factors K_t for a ring or hollow roller compressed by diametrically opposite external concentrated loads (Timoshenko 1922; Horger and Buckwalter 1940; Leven 1952).

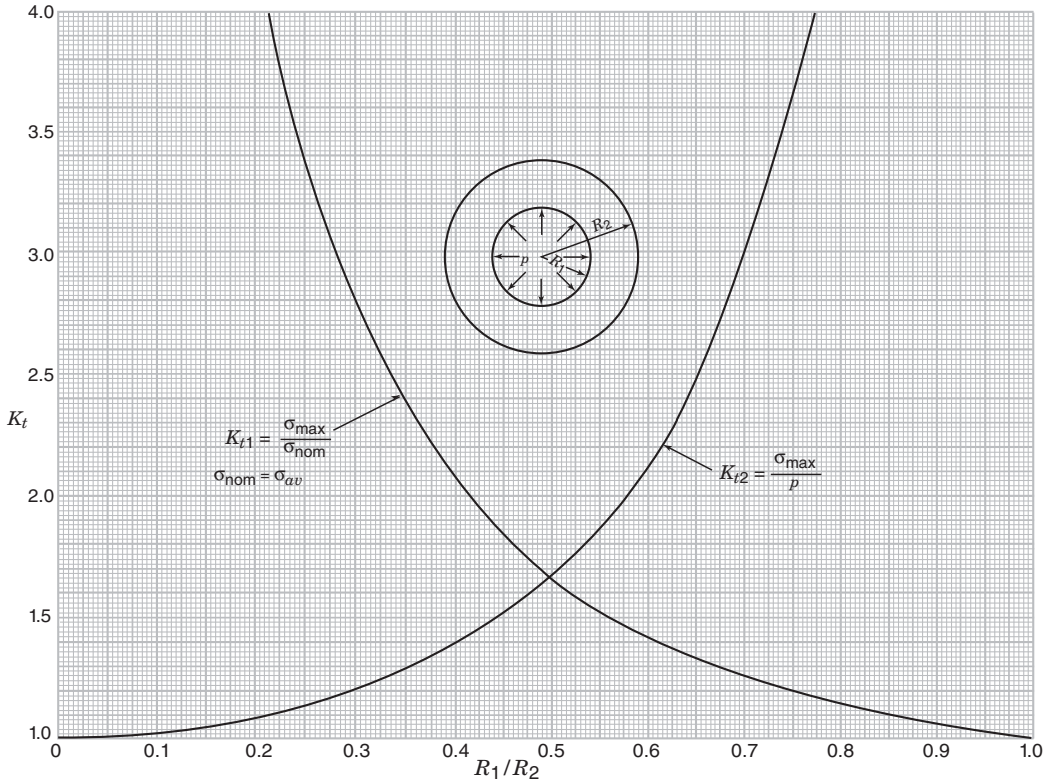


Chart 4.83 Stress concentration factors K_t for a cylinder subject to internal pressure (based on Lamé solution, Pilkey 2005).

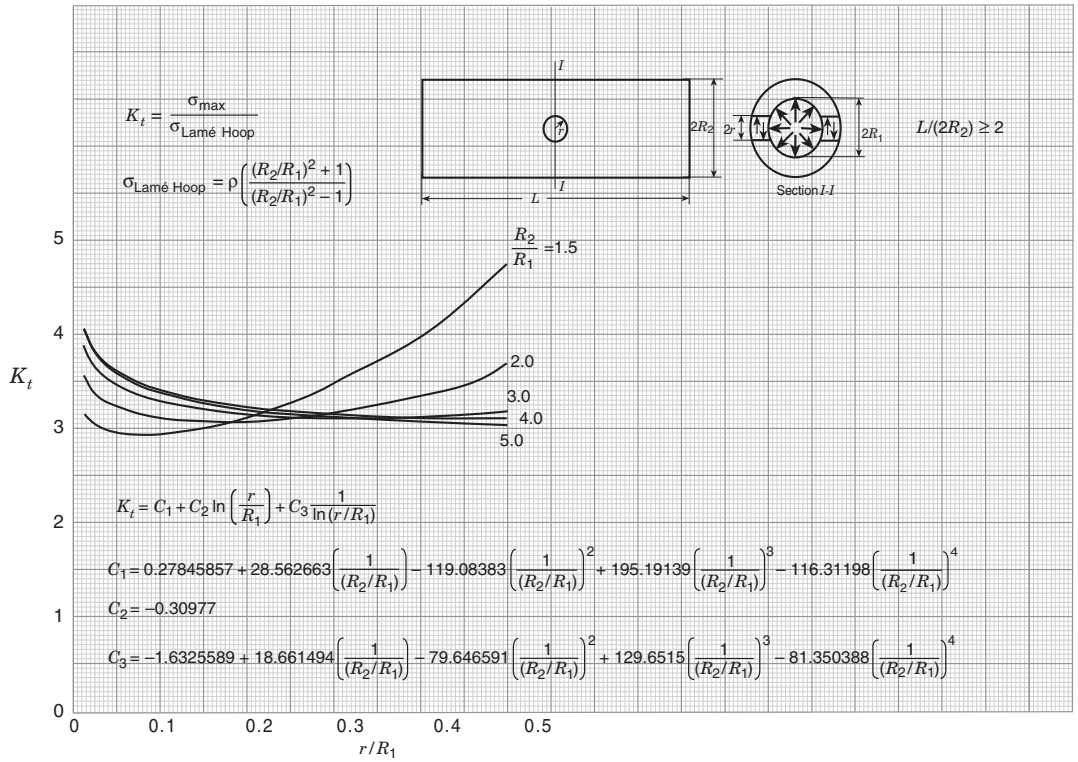


Chart 4.84 Hoop stress concentration factors k_t for a pressurized thick cylinder with a circular hole in the cylinder wall (based on finite element analyses of Dixon, Peters, and Keltjens 2002).

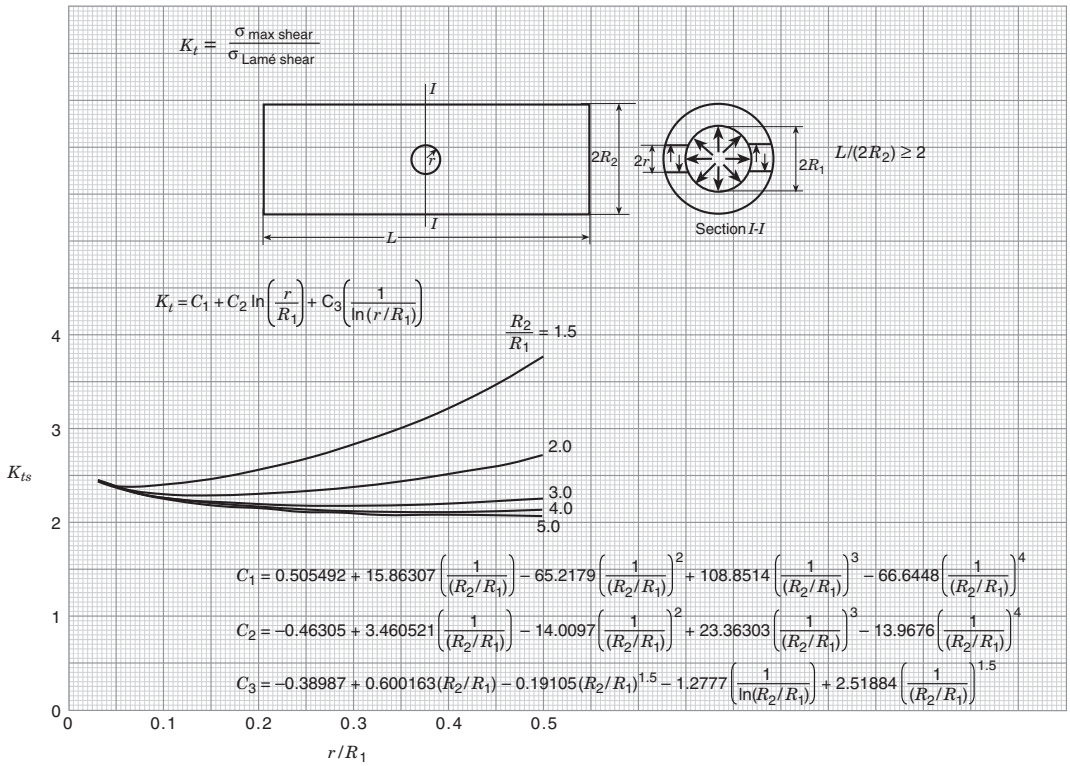


Chart 4.85 Shear stress concentration factors K_t for a pressurized thick cylinder with a circular hole in the cylinder wall (based on finite element analyses of Dixon, Peters, and Keltjens 2002).

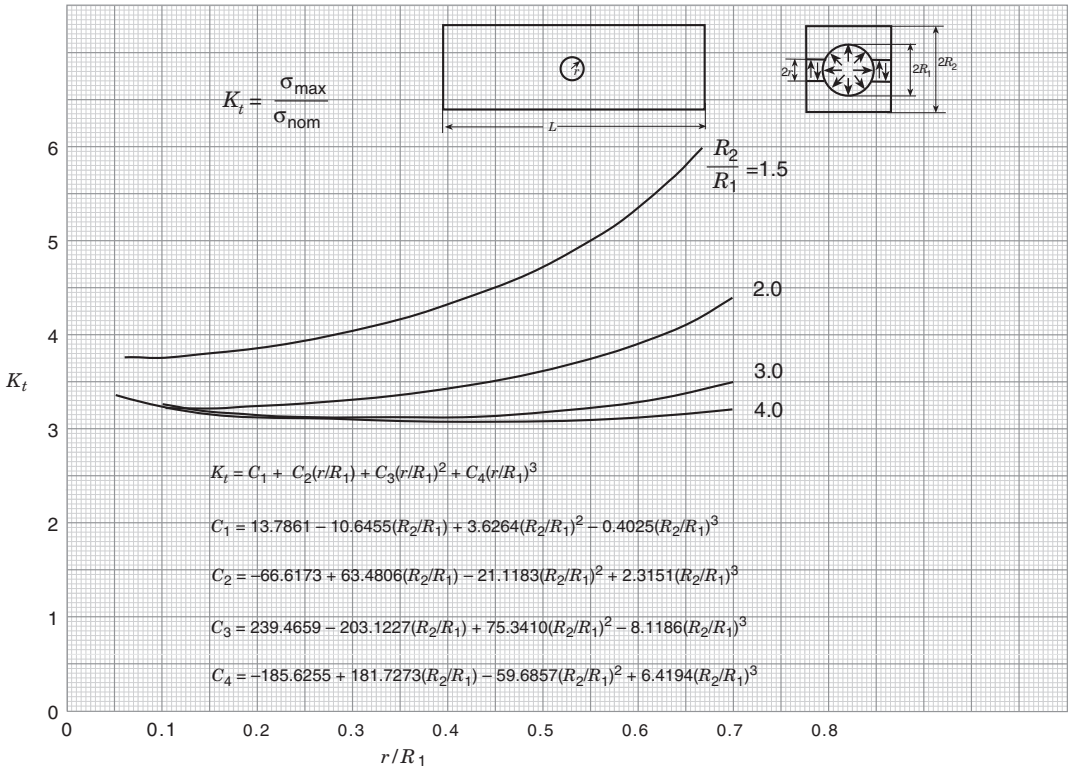


Chart 4.86 Hoop stress concentration factors K_t for a pressurized block with a circular crossbore in the block wall (based on finite element analyses of Dixon, Peters, and Keltjens 2002).

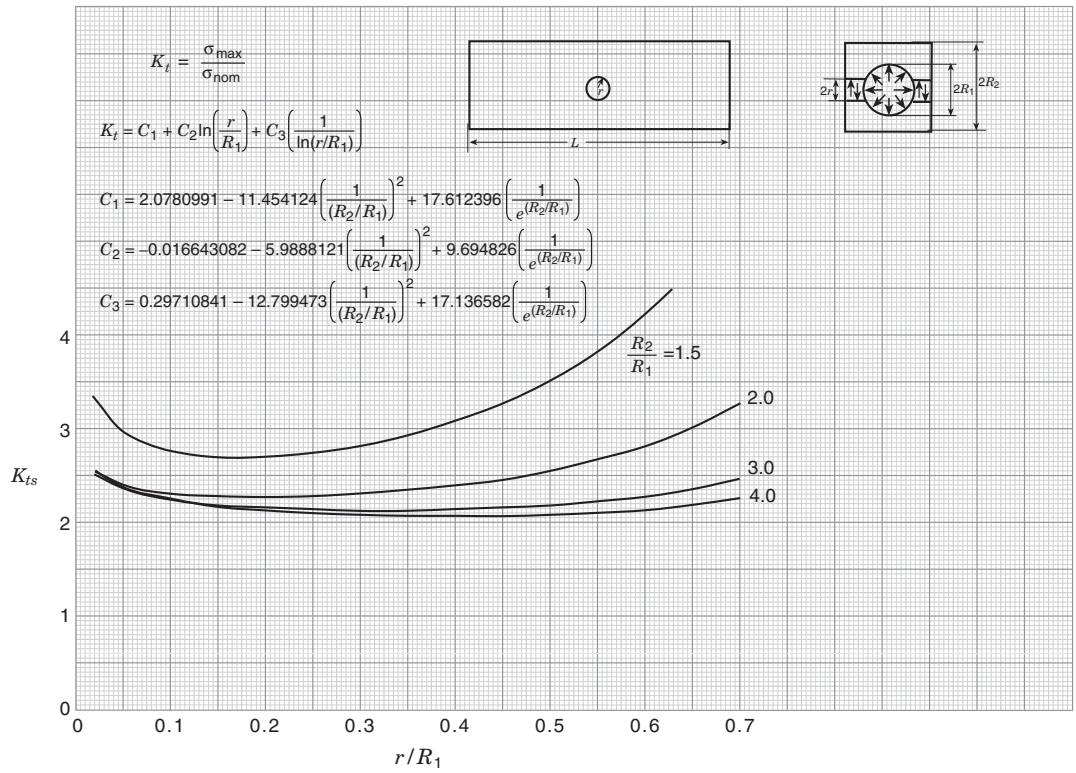


Chart 4.87 Shear stress concentration factors K_t for a pressurized block with a circular crossbore in the block wall (based on finite element analyses of Dixon, Peters, and Keltjens 2002).

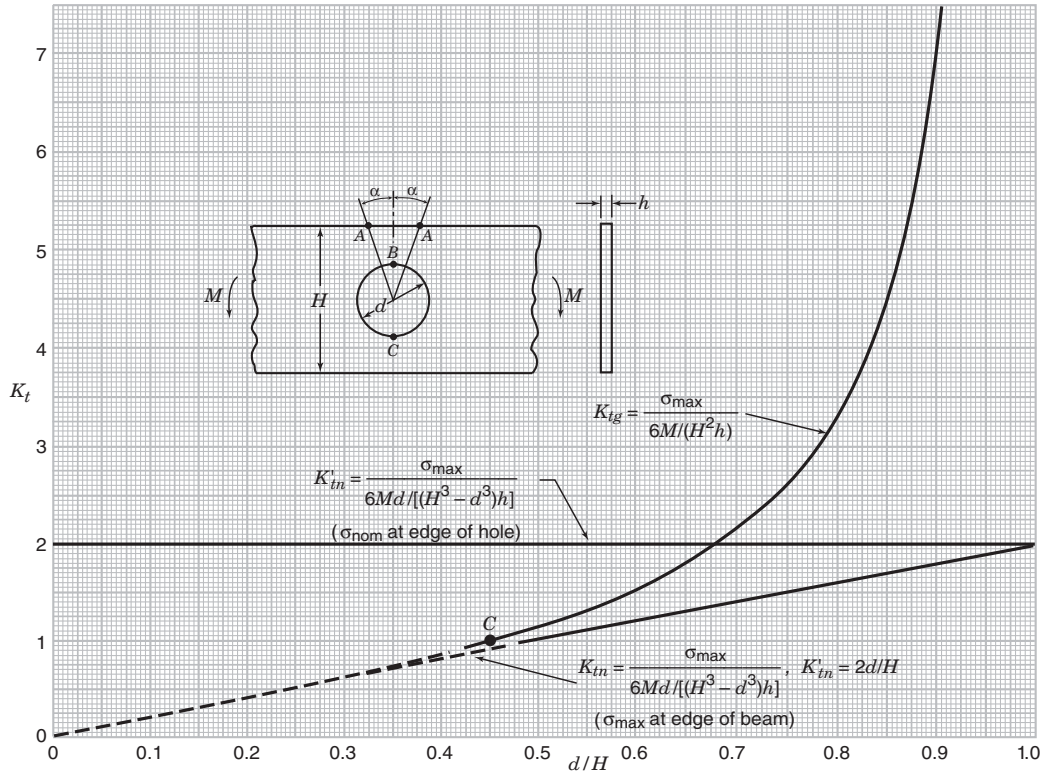


Chart 4.88 Stress concentration factors K_t for in-plane bending of a thin beam with a central circular hole (Howland and Stevenson 1933; Heywood 1952).

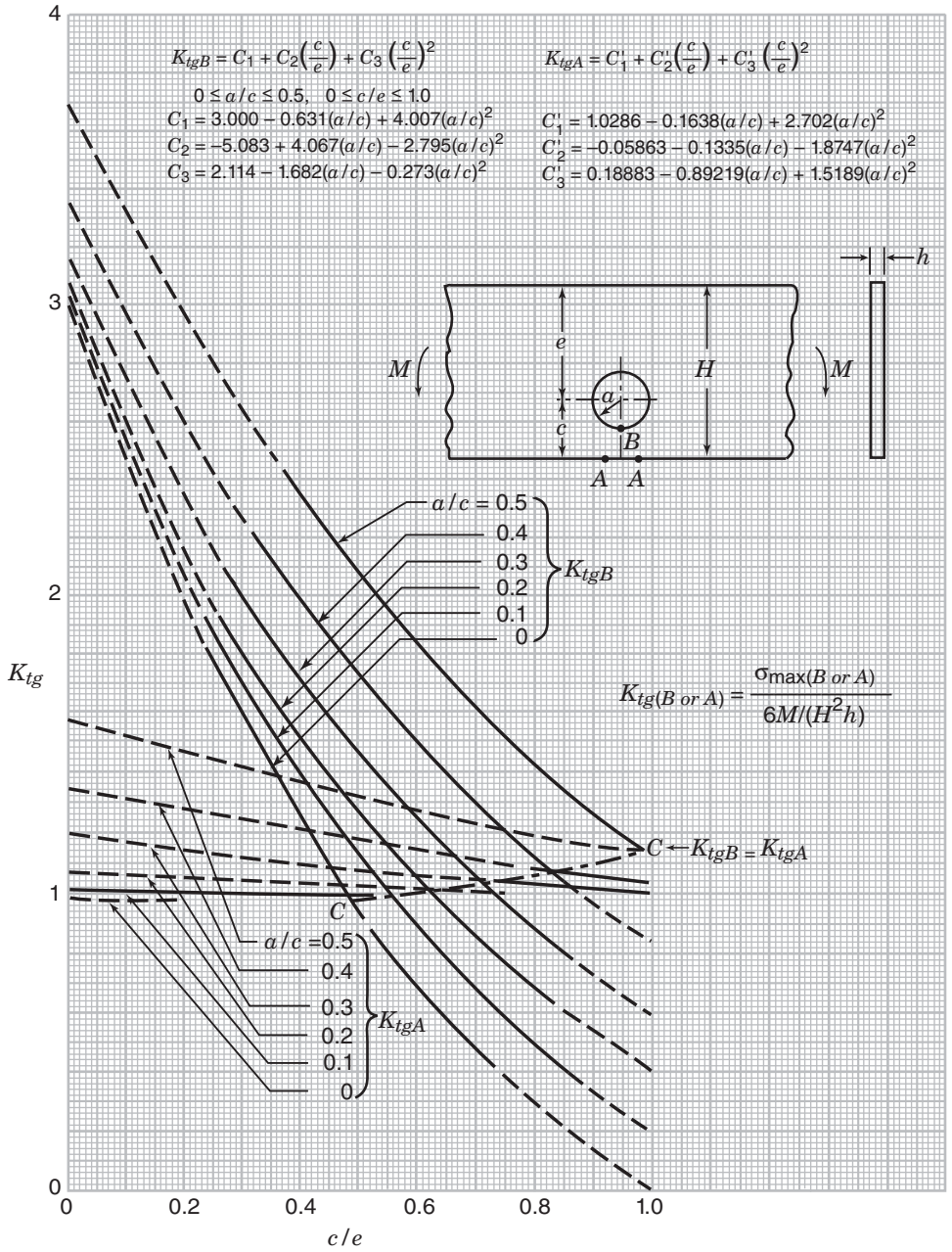


Chart 4.89 Stress concentration factors K_{tg} for bending of a thin beam with a circular hole displaced from the center line (Isida 1952).

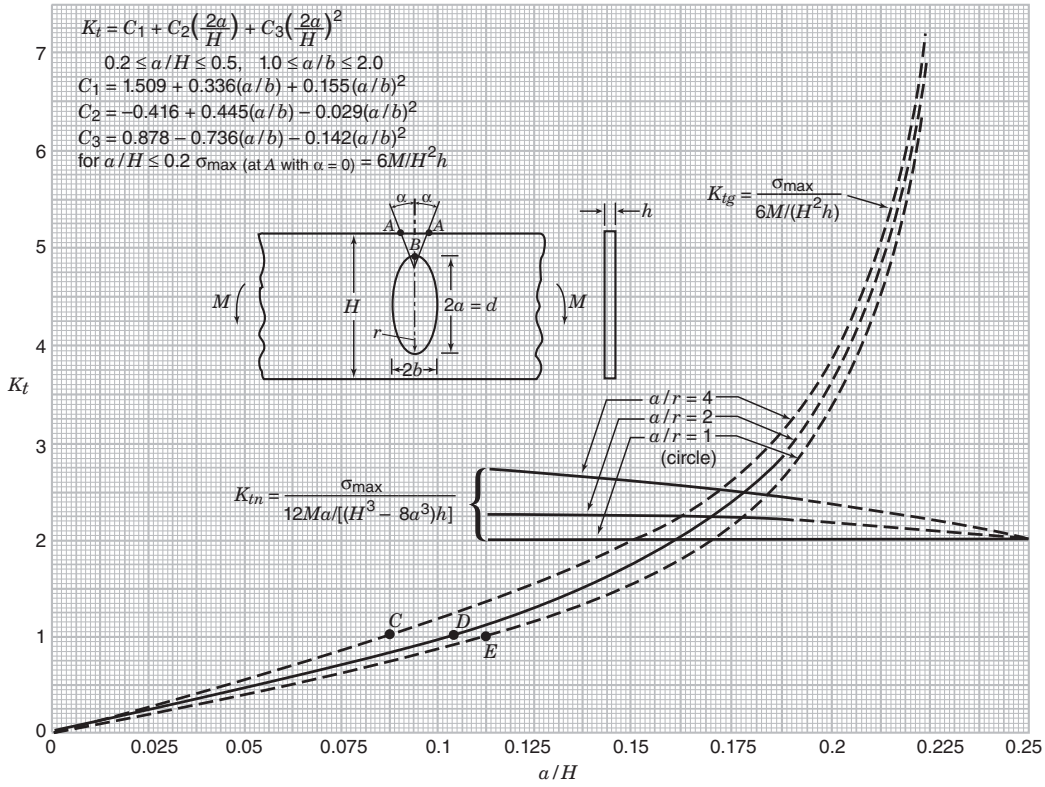


Chart 4.90 Stress concentration factors K_{tg} and K_{tn} for bending of a beam with a central elliptical hole (from data of Isida 1953).

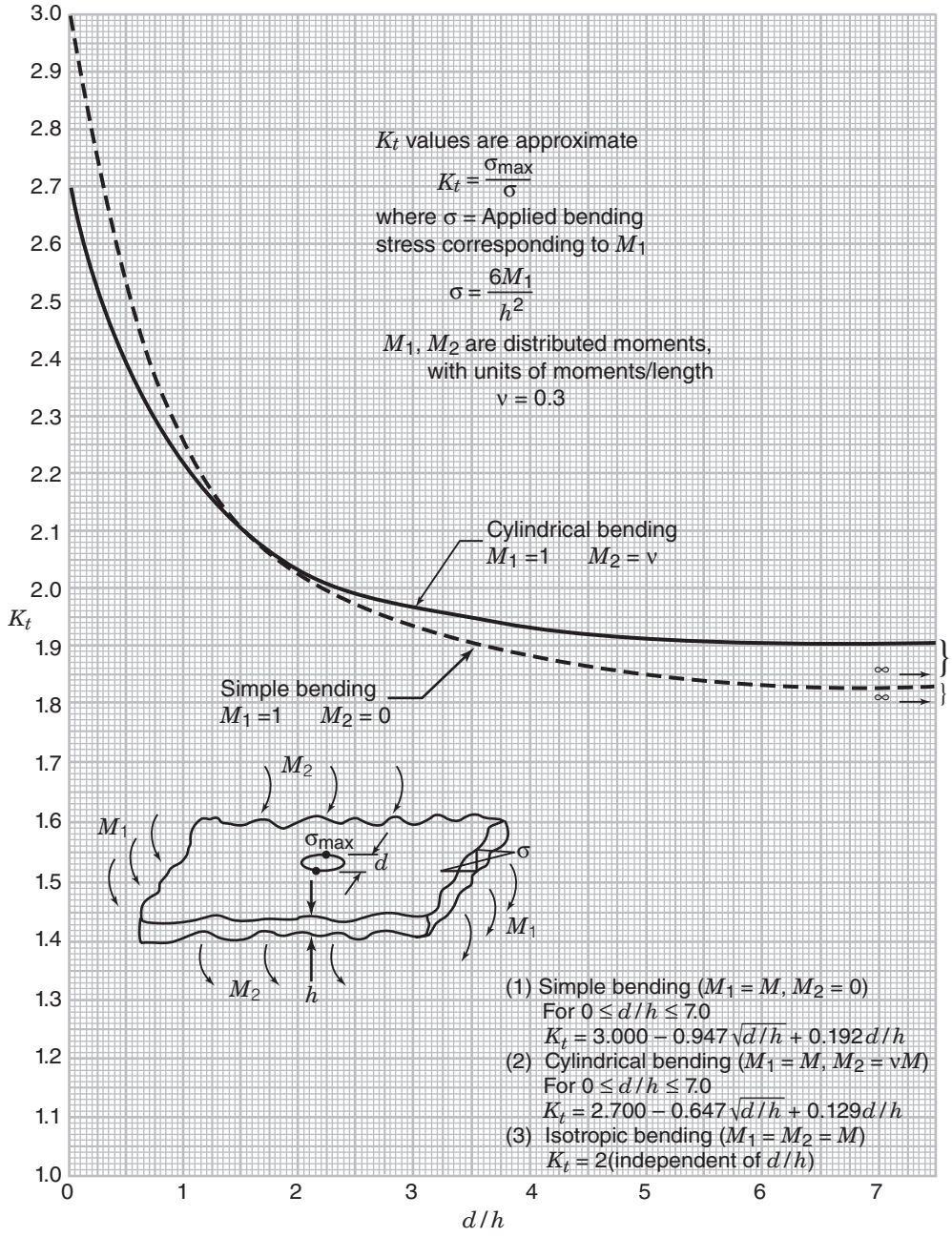


Chart 4.91 Stress concentration factors K_t for bending of an infinite plate with a circular hole (Goodier 1936; Reissner 1945).

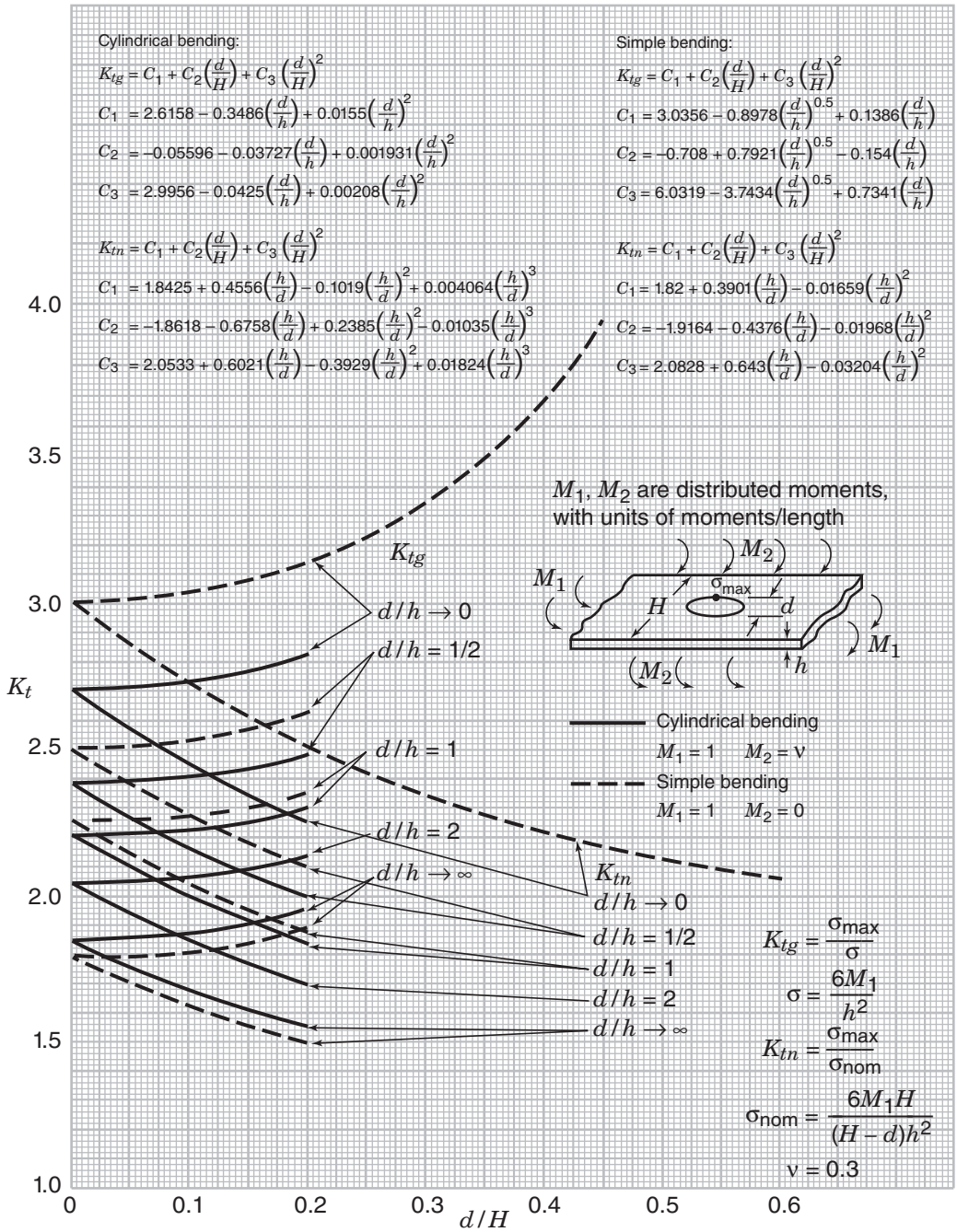


Chart 4.92 Stress concentration factors K_{tg} and K_{tn} for bending of a finite-width plate with a circular hole.

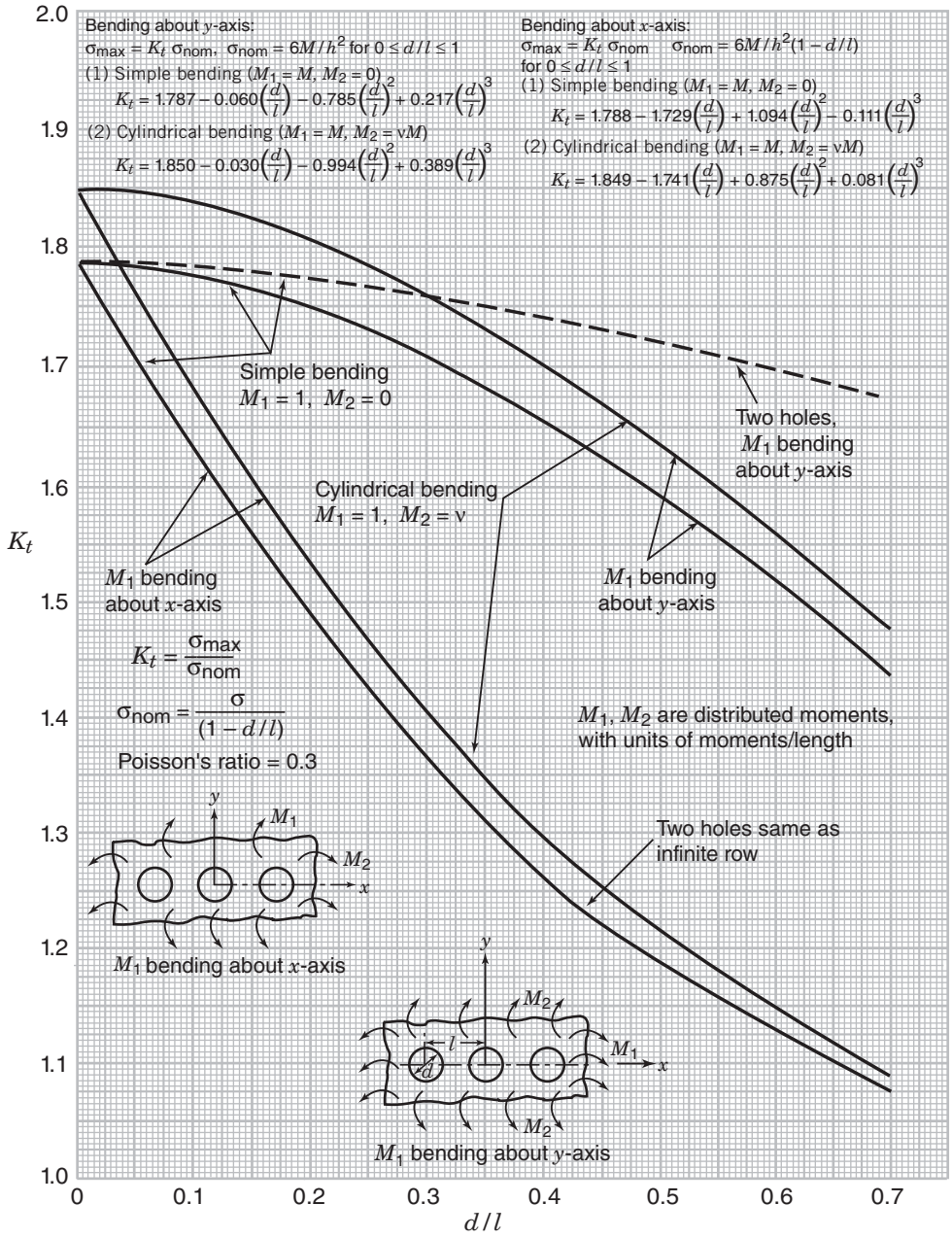


Chart 4.93 Stress concentration factors for an infinite row of circular holes in an infinite plate in bending (Tamate 1957, 1958).

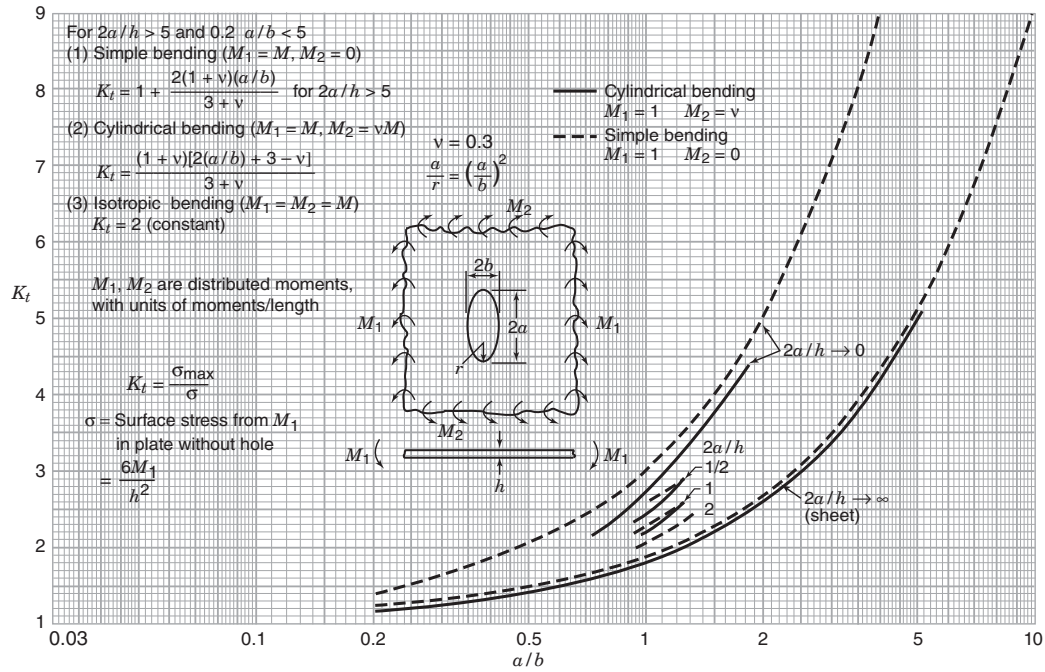


Chart 4.94 Stress concentration factors K_t for bending of an infinite plate having an elliptical hole (Neuber 1958; Nisitani 1968).

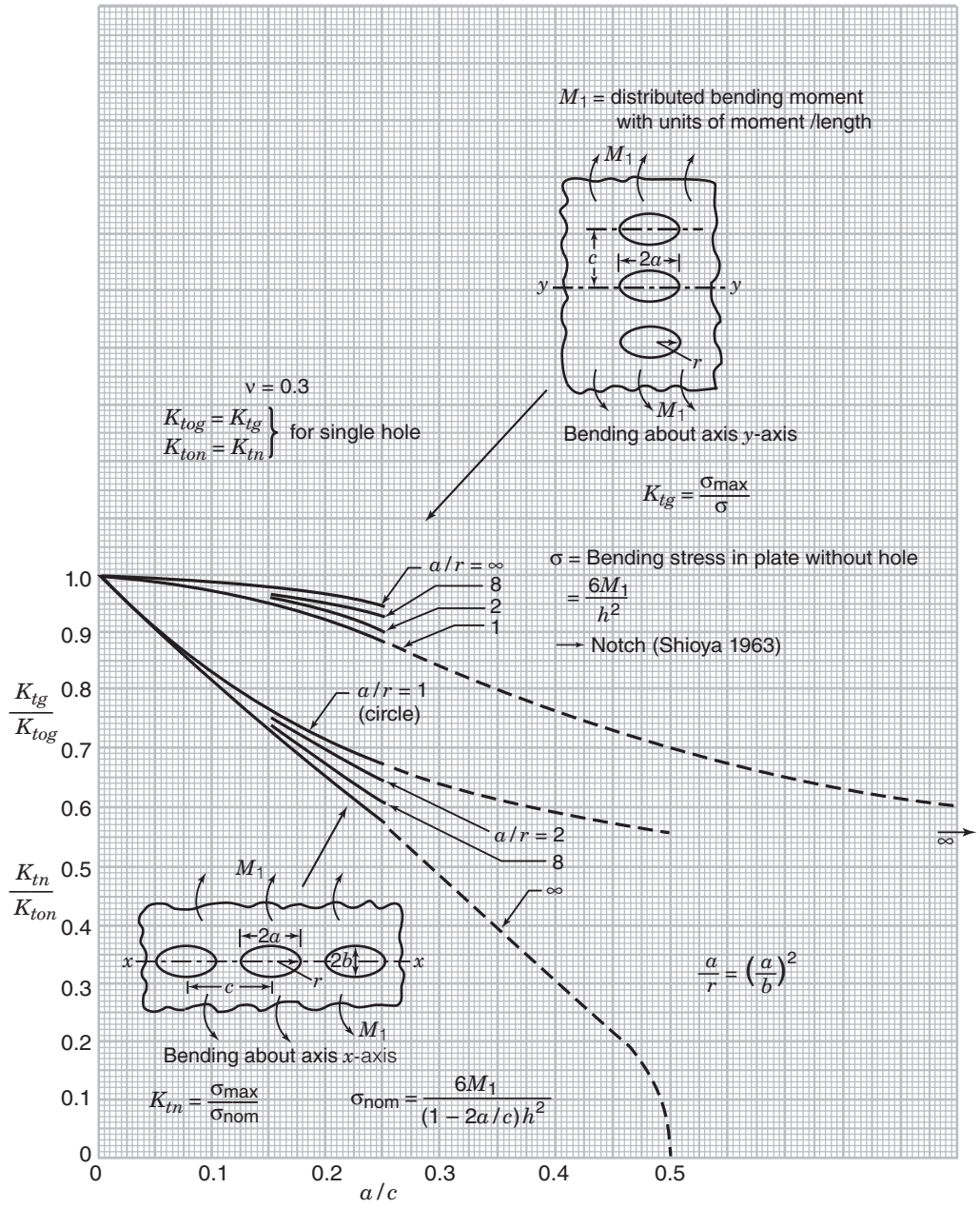


Chart 4.95 Effects of spacing on the stress concentration factors of an infinite row of elliptical holes in an infinite plate in bending (Tamate 1958; Nisitani 1968).

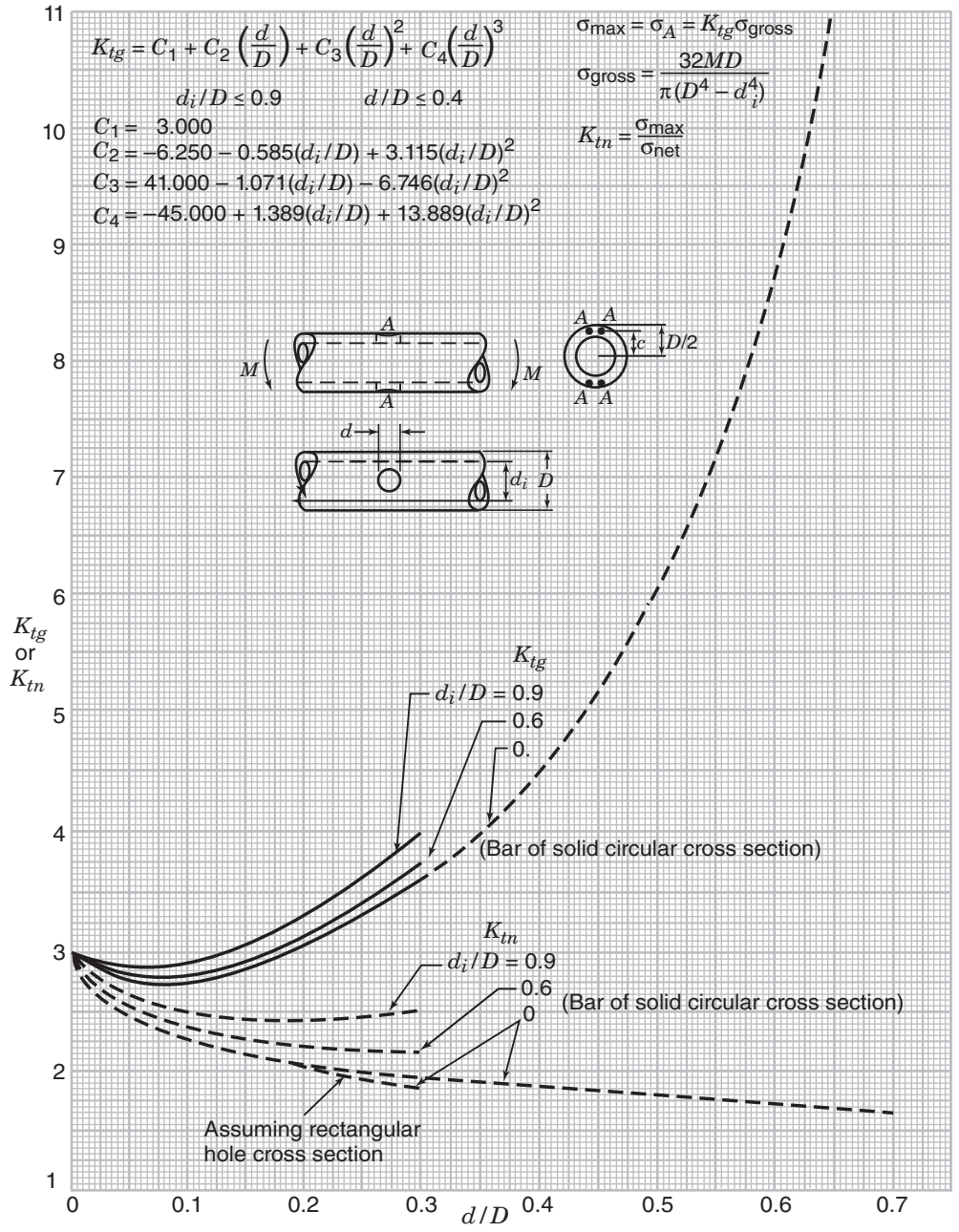


Chart 4.96 Stress concentration factors K_{tg} and K_{tn} for bending of a bar of solid circular cross section or tube with a transverse hole (Jessop et al. 1959; ESDU 1965); bar of solid circular cross section (Thum and Kirmser 1943).

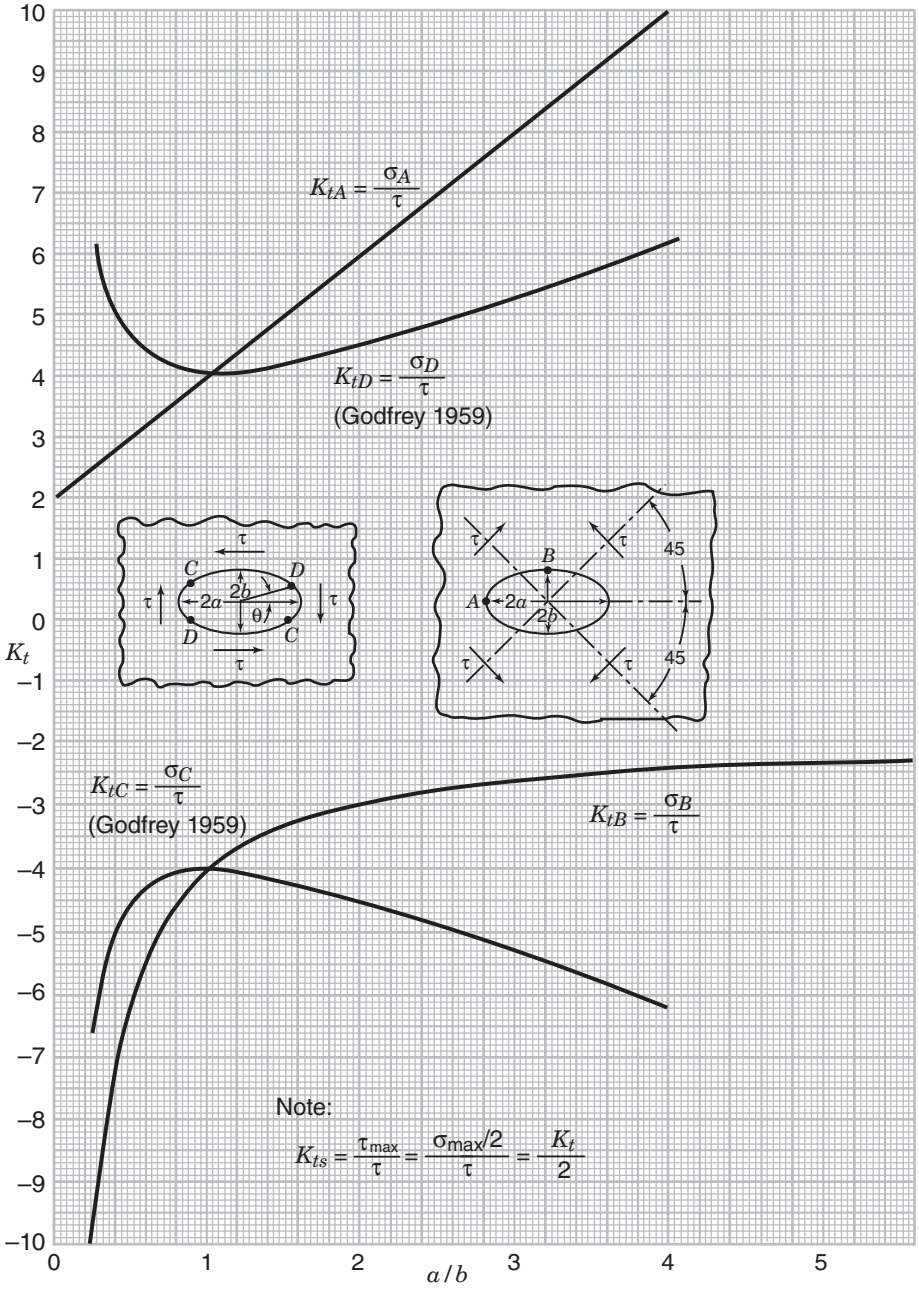


Chart 4.97 Stress concentration factors for an elliptical hole in an infinite thin element subjected to shear stress.

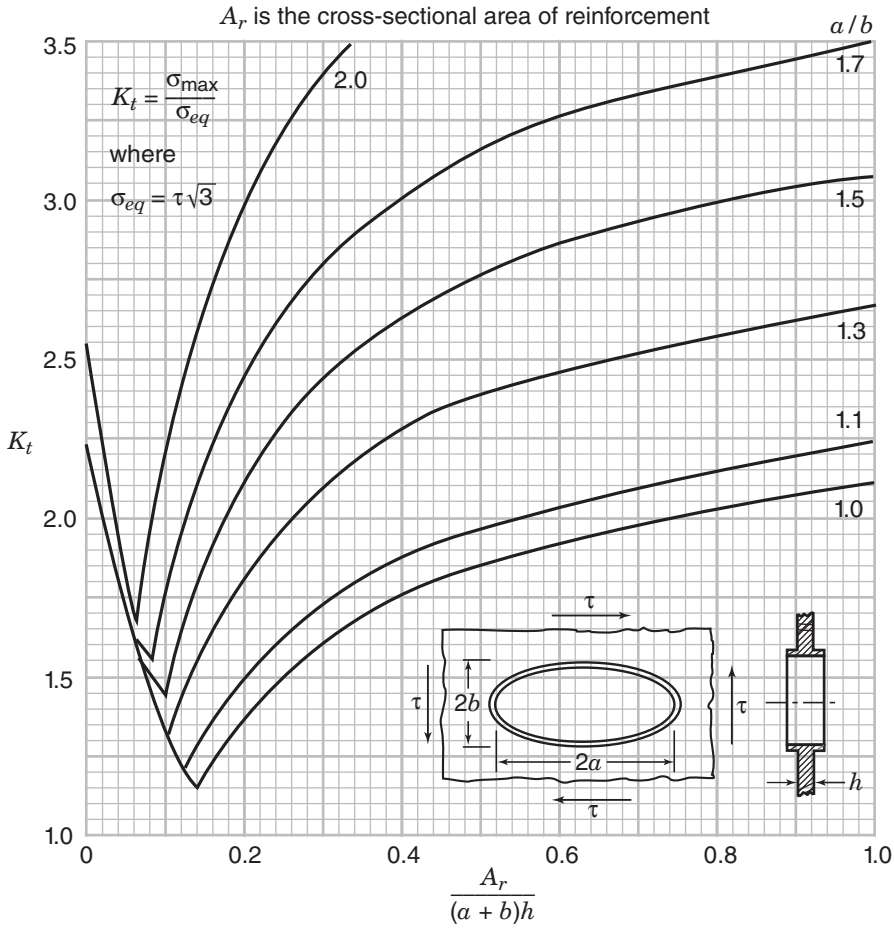


Chart 4.98 Stress concentration factors K_t for elliptical holes with symmetrical reinforcement in an infinite thin element subjected to shear stress (Wittrick 1959a,b; Houghton and Rothwell 1961; ESDU 1981).

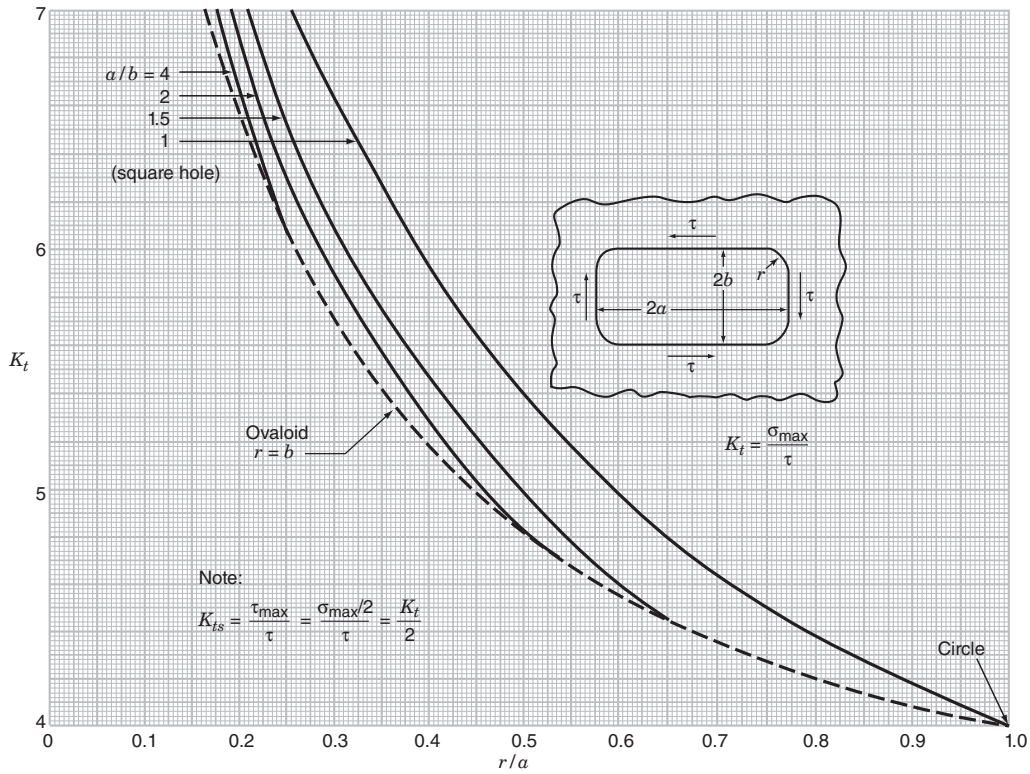
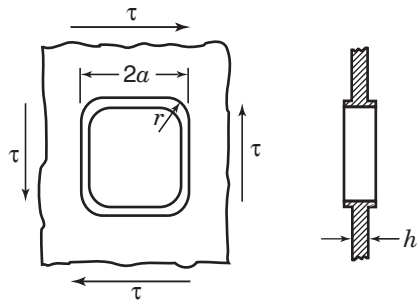


Chart 4.99 Stress concentration factors K_t for a rectangular hole with rounded corners in an infinitely wide thin element subjected to shear stress (Sobey 1963; ESDU 1970).



$$K_t = \frac{\sigma_{max}}{\sigma_{eq}}$$

$$\sigma_{eq} = \tau\sqrt{3}$$

A_r is the cross-sectional area of reinforcement

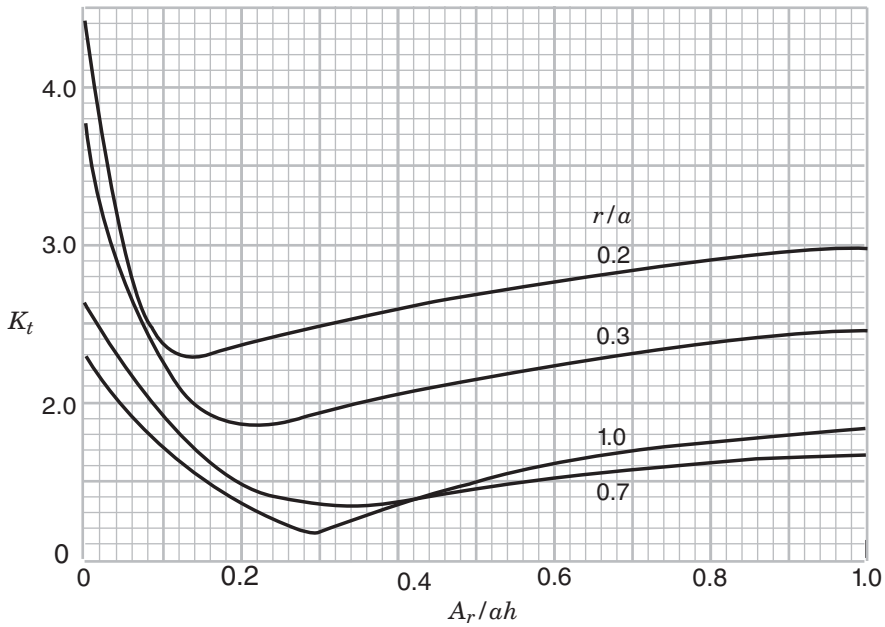
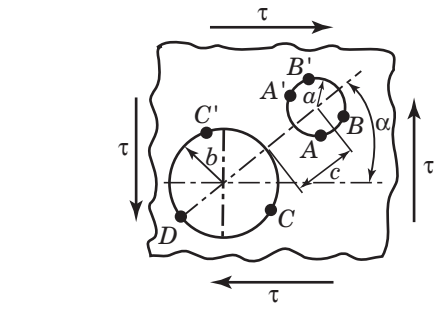


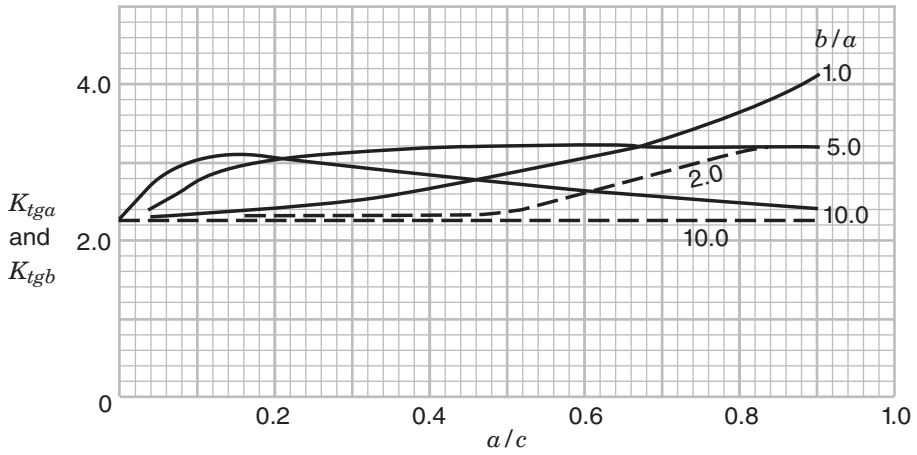
Chart 4.100 Stress concentration factor K_t for square holes with symmetrical reinforcement in an infinite thin element subject to pure shear stress (Sobey 1968; ESDU 1981).



$$K_{tga} = \frac{\sigma_{max}\ \text{(smaller hole)}}{\sigma_{nom}}$$

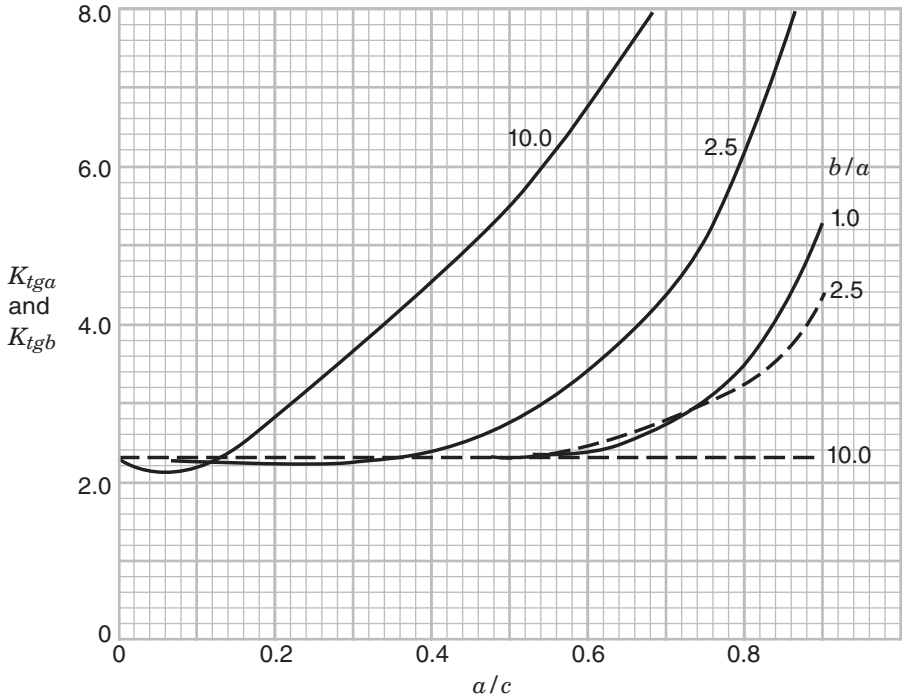
$$K_{tgb} = \frac{\sigma_{max}\ \text{(larger hole)}}{\sigma_{nom}}$$

$$\sigma_{nom} = \tau\sqrt{3}$$



σ_{max} (smaller hole) is located close to A when a/c is high; σ_{max} shifts close to point B at a/c low.
σ_{max} (larger hole) is located close to point C.
Stresses at points A', B' and C' are equal in magnitude, but opposite in sign to those at A, B, and C.

Chart 4.101*a* Stress concentration factors K_{tg} for pure shear in an infinite thin element with two circular holes of unequal diameter (Haddon 1967; ESDU 1981): $\alpha = 0°$.



σ_{max} (smaller hole) is located close to A for all values of b/a and a/c.
σ_{max} (larger hole) is located between the points B and C when $a/c > 0.6$,
at points B and D when $a/c < 0.6$.

Chart 4.101*b* Stress concentration factors K_{tg} for pure shear in an infinite thin element with two circular holes of unequal diameter (Haddon 1967; ESDU 1981): $\alpha = 135^\circ$.

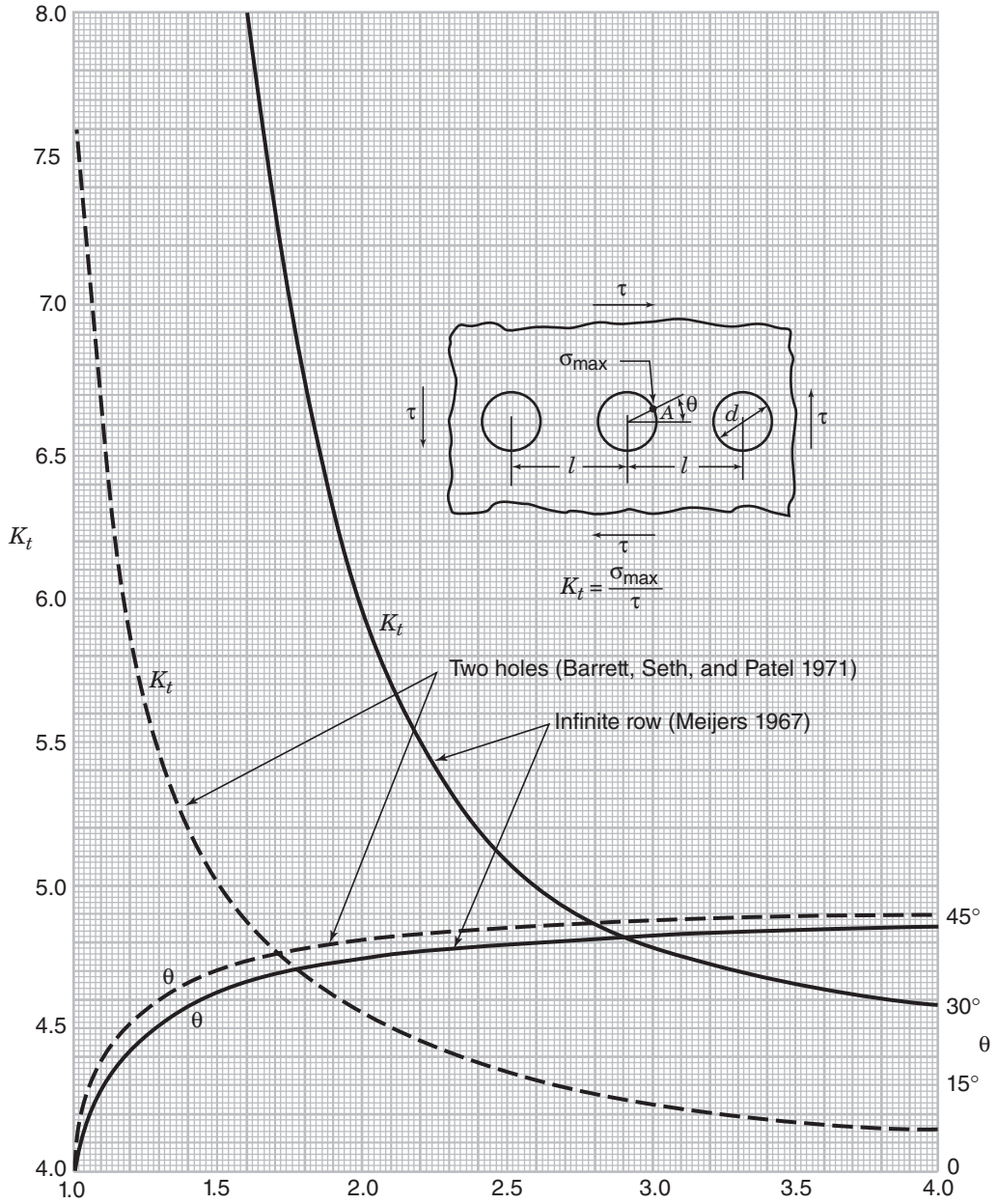


Chart 4.102 Stress concentration factors K_t for single row of circular holes in an infinite thin element subjected to shear stress.

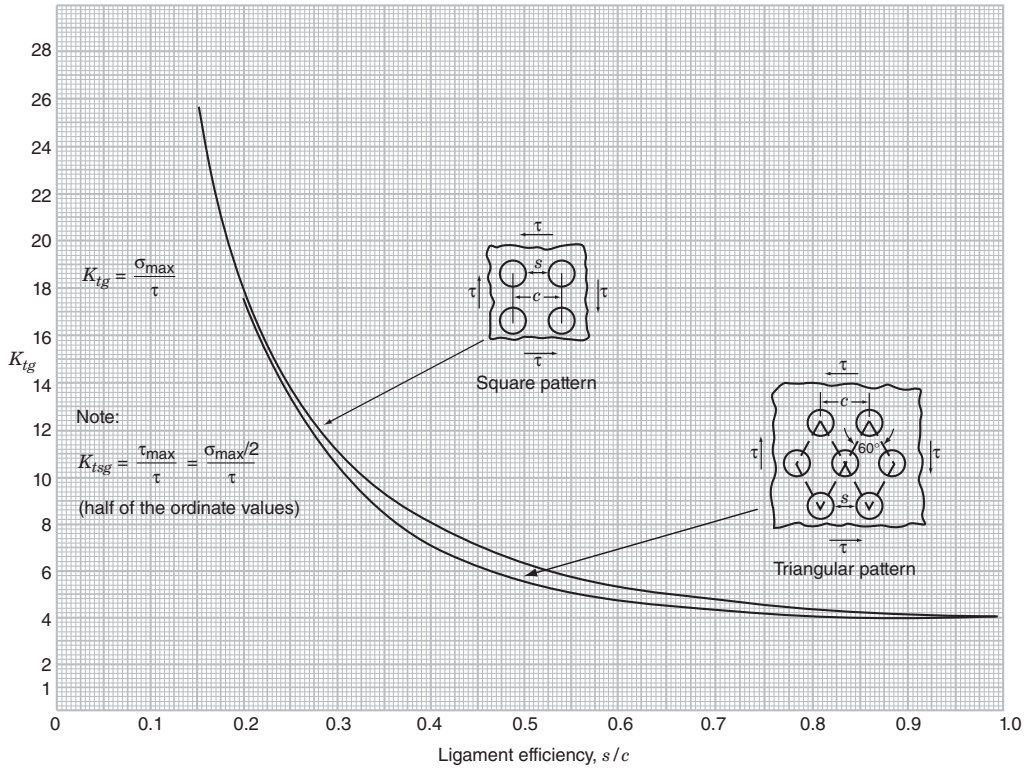


Chart 4.103 Stress concentration factors K_{tg} for an infinite pattern of holes in a thin element subjected to shear stress (Sampson 1960; Bailey and Hicks 1960; Hulbert and Niedenfuhr 1965; Meijers 1967).

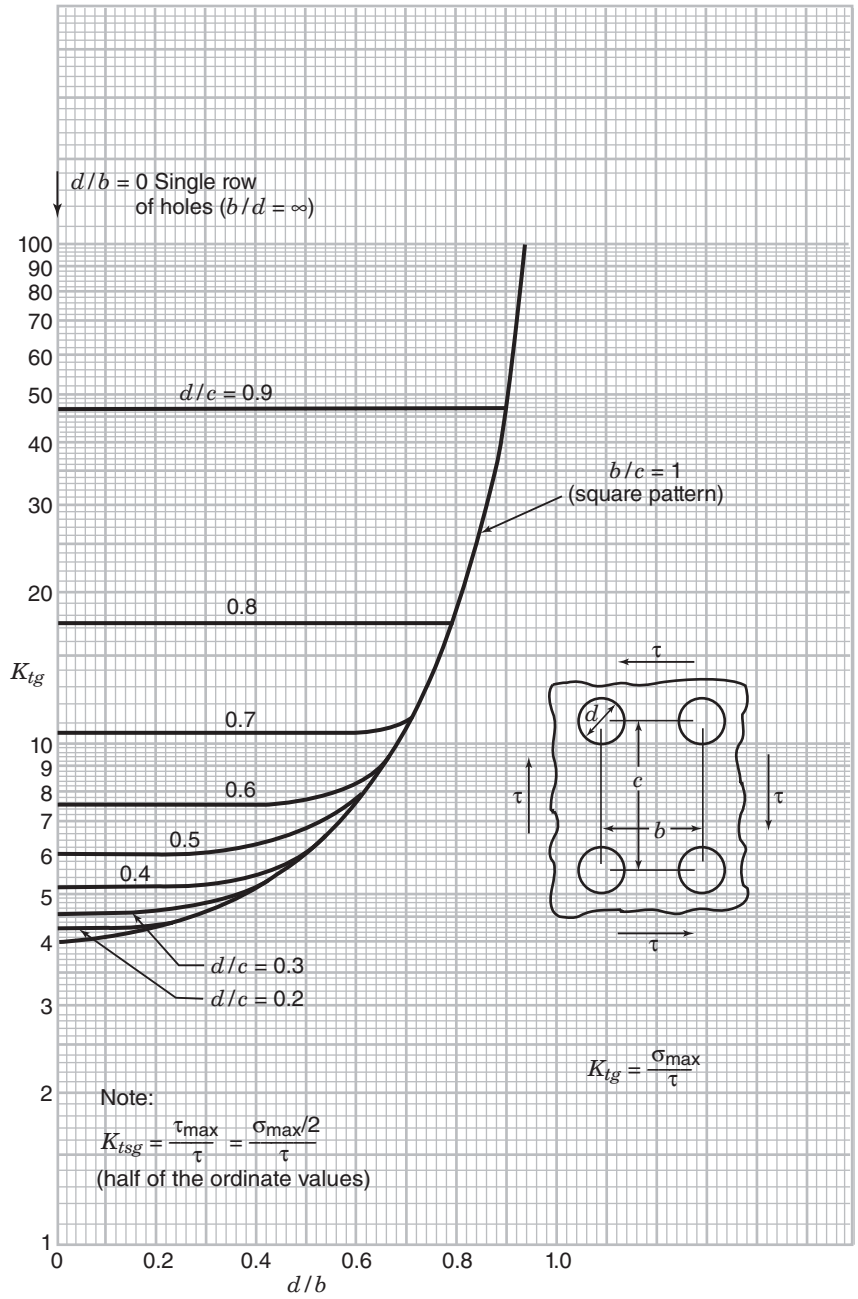


Chart 4.104 Stress concentration factors K_{tg} for an infinite rectangular pattern of holes in a thin element subjected to shear stress (Meijers 1967).

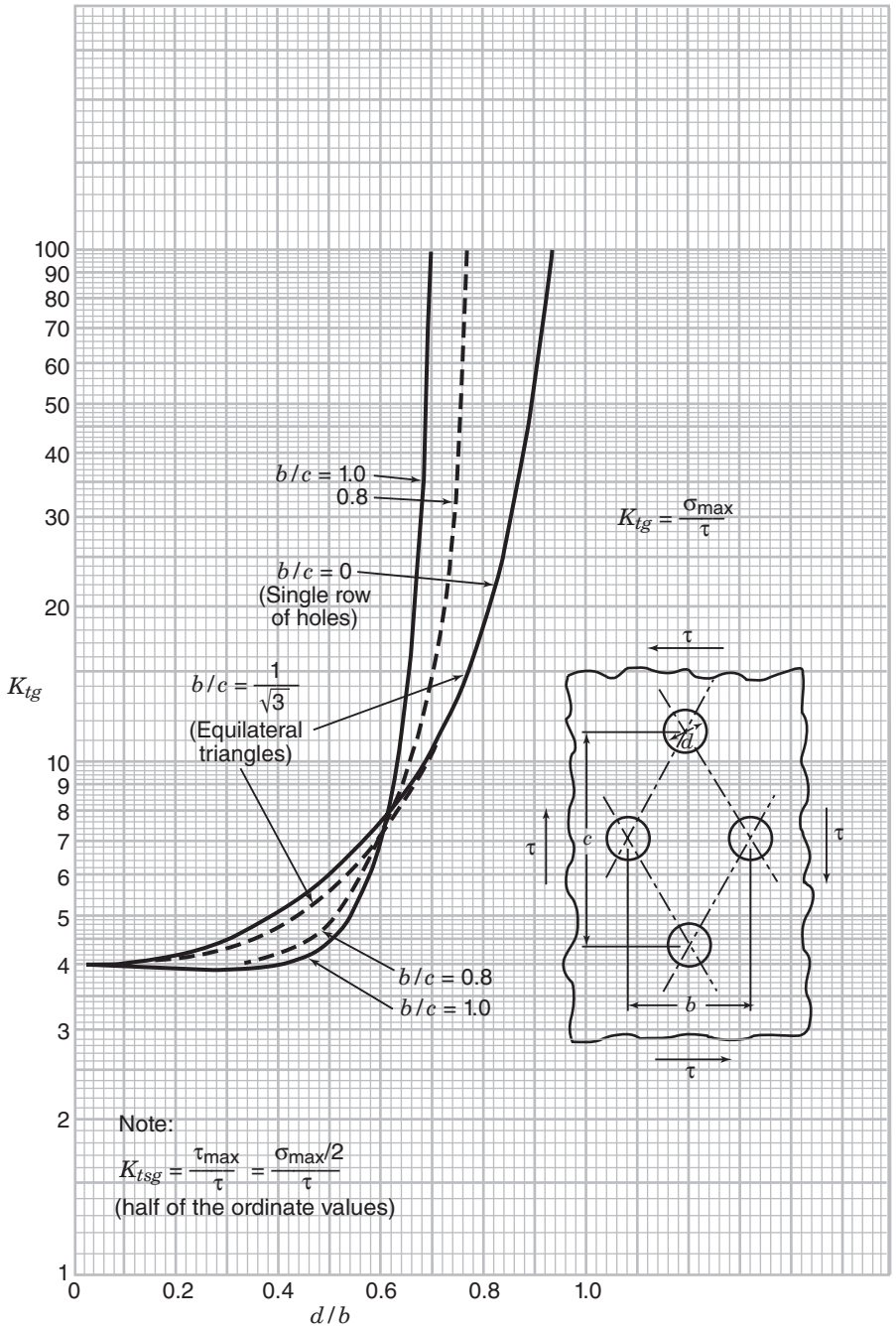


Chart 4.105 Stress concentration factors K_{tg} for an infinite diamond pattern of holes in a thin element subjected to shear stress (Meijers 1967).

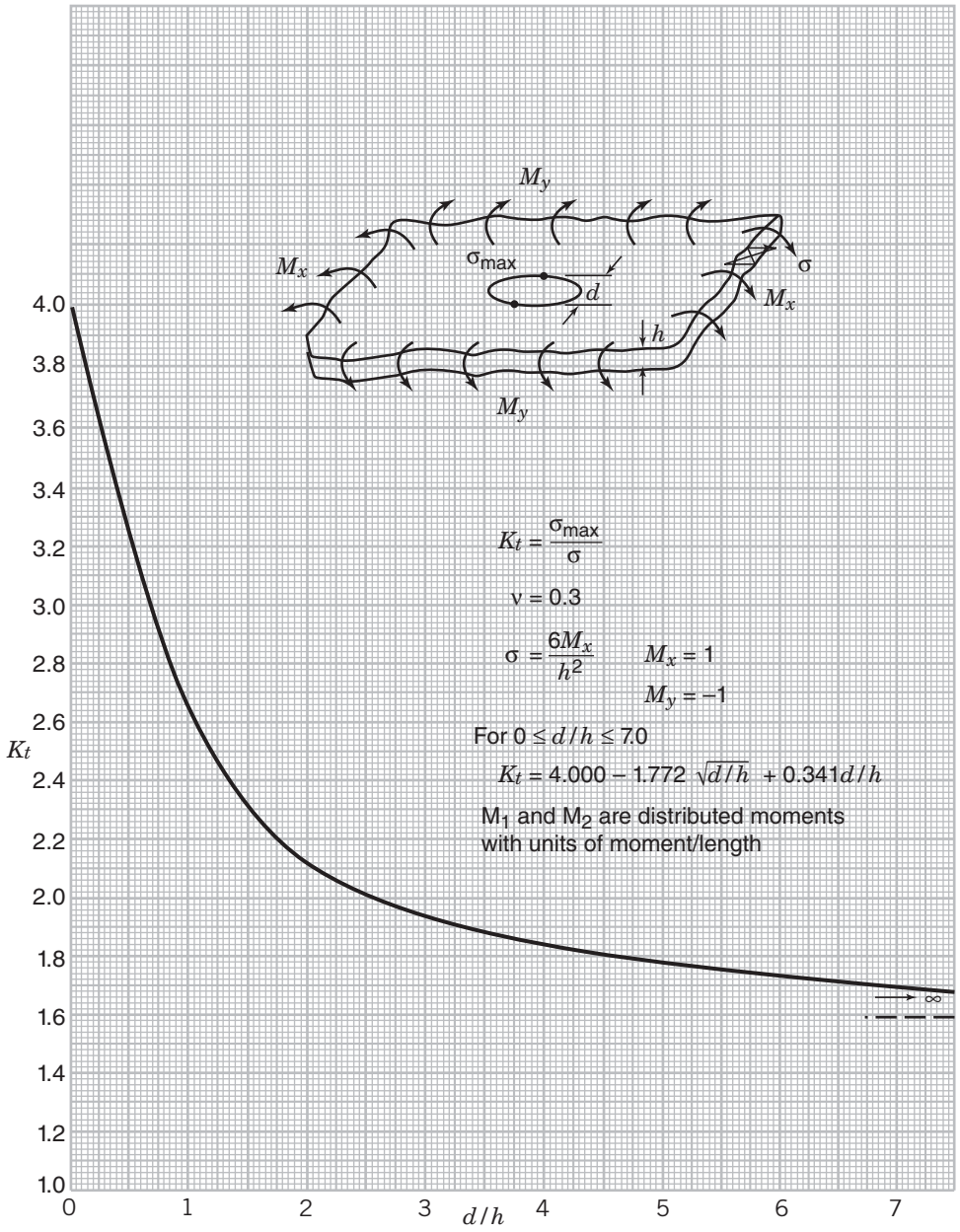


Chart 4.106 Stress concentration factors K_t for a twisted plate with a circular hole (Reissner 1945).

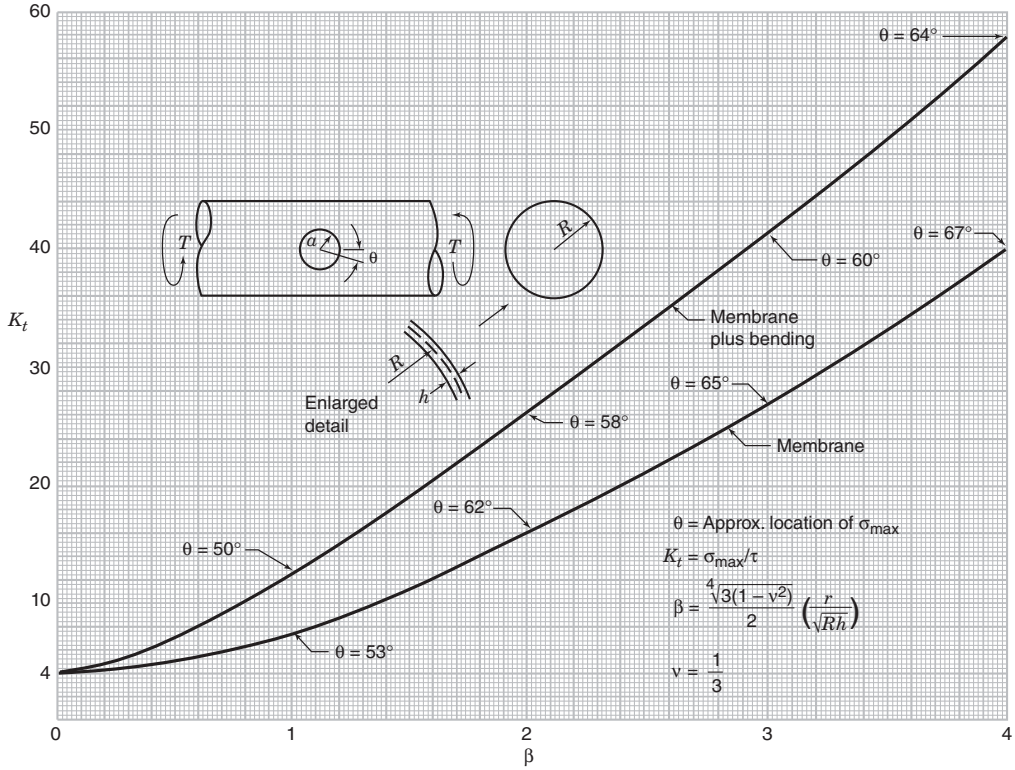


Chart 4.107 Stress concentration factors for a circular hole in a cylindrical shell stressed in torsion (based on data of Van Dyke 1965).

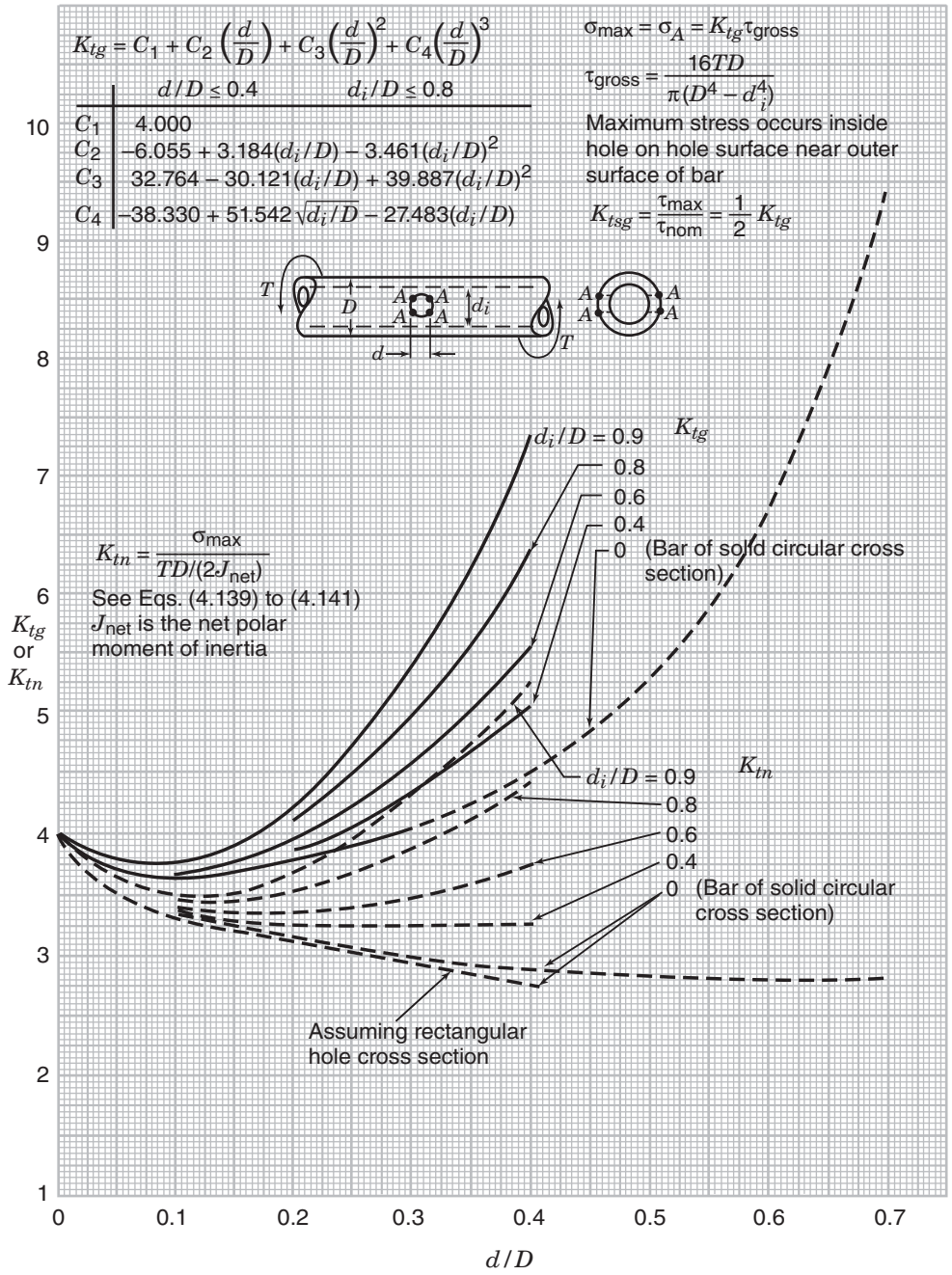


Chart 4.108 Stress concentration factors K_{tg} and K_{tn} for torsion of a tube or bar of circular cross section with a transverse hole (Jessop et al. 1959; ESDU 1965; bar of circular cross section Thum and Kirmser 1943).

CHAPTER 5

MISCELLANEOUS DESIGN ELEMENTS

This chapter provides stress concentration factors for various elements used in machine design. These include shafts with keyseats, splined shafts, gear teeth, shrink-fitted members, bolts and nuts, lug joints, curved bars, hooks, rotating disks, and rollers. In addition, this chapter discusses the recent works on stress concentration factors of machine elements that are complex geometries and cannot be simply classified into certain types of machine elements due to the diversity of geometric parameters, material properties, and loading conditions.

5.1 NOTATION

Symbols:

SCF = stress concentration factor

FEA = Finite Element Analysis

a = wire diameter

b = keyseat width; tooth length; width of cross section

c = distance from center of hole to lug end for a lug-pin fit; distance from centroidal axis to outer fiber of a beam cross section; spring index

d = shaft diameter; diameter of hole; mean coil diameter

Peterson's Stress Concentration Factors, Fourth Edition. Walter D. Pilkey, Deborah F. Pilkey and Zhuming Bi.
© 2020 John Wiley & Sons, Inc. Published 2020 by John Wiley & Sons, Inc.

D = larger shaft diameter

e = pin-to-hole clearance as a percentage of d, the hole diameter; gear contact position height

E_{lug} = moduli of elasticity of lug

E_{pin} = moduli of elasticity of pin

h = thickness

I = moment of inertia of beam cross section

K_t = stress concentration factor

K_{te} = stress concentration factor for axially loaded lugs at a pin-to-hole clearance of e% of the pin hole ($h/d < 0.5$)

K'_{te} = stress concentration factor for axially loaded lugs at a pin-to-hole clearance of e% of the pin hole ($h/d > 0.5$)

K_f = fatigue notch factor

l = length

L = length (see Chart 5.10)

m = thickness of bolt head

M = bending moment

N = number of teeth

p = pressure

P = axial load

P_d = diametral pitch

r = radius

r_f = minimum radius

r_s = shaft shoulder fillet radius

r_t = tip radius

R_1 = inner radius of cylinder

R_2 = outer radius of cylinder

t = keyseat depth; width of tooth

T = torque

w = gear tooth horizontal load

w_n = gear tooth normal load

W = width of lug

η_e = correction factor for the stress concentration factor of lug-pin fits

v = Poisson's ratio

σ = stress

σ_{nom} = nominal stress

σ_{max} = maximum stress

5.2 SHAFT WITH KEYSEAT

The U.S. standard keyseat (keyway) (ANSI 1967) has an average[1] value of $b/d = 1/4$ and $t/d = 1/8$ for a shaft diameter up to 6.5 in. (Fig. 5.1). For a shaft diameter above 6.5 in., the average value is $b/d = 1/4$ and $t/d = 0.09$. The suggested proportions of fillet radius are $r/d = 1/48 = 0.0208$ for a shaft diameter up to 6.5 in. and $r/d = 0.0156$ for a shaft diameter above 6.5 in.

In design of a keyed shaft, one must also take into consideration the shape of the end of the keyseat. Fig. 5.2 shows two types of keyseat ends, i.e., end-milled keyseats and sled-runner keyseats. An end-milled keyseat is more widely used due to its compactness and longitudinal positioning of key. However, a sled-runner keyseat has a low stress concentration factor (SCF) in bending.

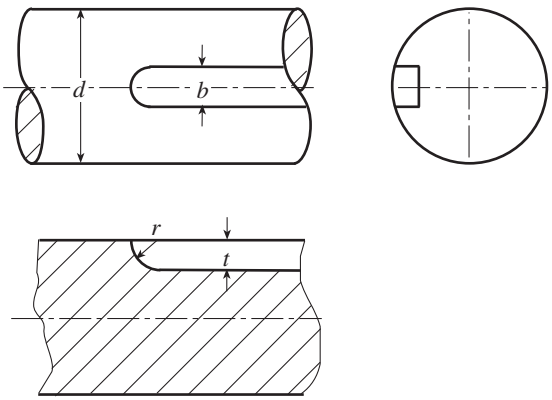


Figure 5.1 Keyseat.

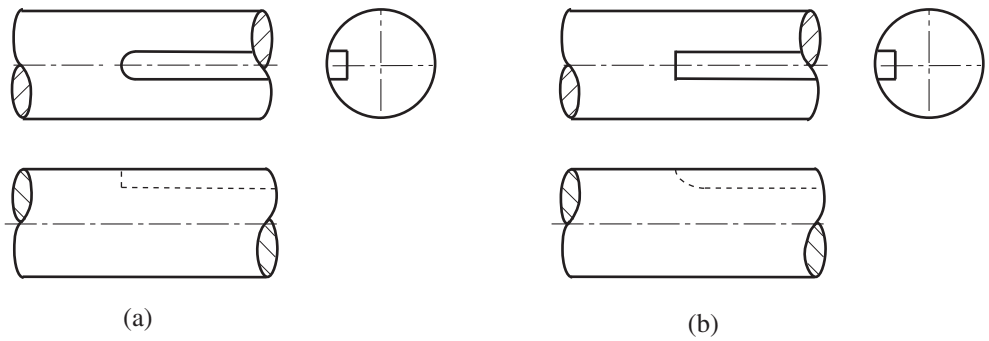


Figure 5.2 Types of keyseat ends: (a) end-milled keyseat (also, referred to as semicircular or profiled end); (b) sled-runner keyseat.

[1]The keyseat width, depth, and fillet radius are in the multiples of 1/32 in.. Each size applies to a range of shaft diameters.

5.2.1 Bending

Hetényi (1939a,b) makes a comparison of the surface stresses for the two types of keyseats in bending ($b/d = 0.313$, $t/d = 0.156$) photoelastically and finds the SCFs of two keyseats are $K_t = 1.79$ (semicircular end) and $K_t = 1.38$ (sled-runner), respectively. Perterson (1932) performs the fatigue tests to obtain K_f factors (fatigue notch factors) for two keysesats and turns out the same ratio as that of two K_t values.

Fessler et al. (1969a,b) provide a comprehensive photoelastic investigation on British standard end-milled keyseats. Corresponding to the U.S. standard in Chart 5.1, the British value $K_{tA} = 1.6$ has been used for the surface in both cases $b/d = 1/4$. It appears that the surface factor is not significantly affected by the moderate change of depth ratio of keyseat (Fessler et al. 1969a,b). The maximum stress occurs at an angle less than 10° from the point of tangency shown as location A in Chart 5.1. Note that K_{tA} is independent of r/d.

For K_t at location B of the fillet in Chart 5.1, the British K_t values for bending have been adjusted for the keyseat depth in the U.S. standard. The ratio of $t/d = 1/8 = 0.125$ in the United States corresponds to the ratio of $t/d = 1/12 = 0.0833$ in British for the extrapolations in Chart 3.1. Also note that the maximum fillet stress is located at the end of the keyway, about 15° up on the fillet.

The foregoing discussion refers to the shafts with a diameter less than 6.5 in and the ratio of $t/d = 0.125$. For a shaft with a large diameter and $t/d = 0.09$, it seems that the K_t factor would not differ significantly when the values of t/d and r/d are changed. Therefore, it is suggested that for design, the K_t values for $t/d = 0.125$ and $r/d = 0.0208$ be used for the shafts with any diameters.

5.2.2 Torsion

For the surface at the semicircular keyseat end, Leven (1949) and Fessler et al. (1969a,b) obtain the SCF of $K_{tA} = \sigma_{\max}/\tau \approx 3.4$. The maximum normal stress, tangential to the semicircle, occurs at 50° from the axial direction, which is independent of r/d. The maximum shear stress is at 45° to the maximum normal stress; the corresponding shear SCF is a half of the normal SCF, i.e., $K_{tsa} = \tau_{\max}/\tau \approx 1.7$. For the SCF K_{ts} in the fillet of the straight part of a U.S. standard keyseat, Leven (1949) obtains it from a mathematical model and validates K_{ts} photoelastically. The maximum shear stresses at B (Chart 5.2) are in the longitudinal and perpendicular directions. The maximum normal stresses are of the same magnitude and are at 45° to the direction of the shear stress. Therefore, $K_{tsB} = \tau_{\max}/\tau$ is equal to $K_{tB} = \sigma_{\max}/\sigma = \sigma_{\max}/\tau$, where $\tau = 16T/\pi d^3$.

Nisida (1963) makes the photoelastic test of specimen with a keyseat that has the same depth ratio ($t/d = 1/8$) but a large width ratio ($b/d = 0.3$). K_t factors show a good agreement when the keyseat shape changes. Griffith and Taylor (1917–1918) and Okubo (1950a) obtain the results of the SCFs for the cases with other geometrical proportions. For a semicircular groove (Timoshenko and Goodier 1970), K_t is 2 for $r/d \to 0$ and K_t would be estimated as 2.1 for $r/d = 0.125$. This fits quite well with an extension of Leven's curve. The photoelastic results of Fessler et al. (1969a,b) are in a reasonable agreement with Leven's values at $r/d = 0.0052$ and 0.0104; however, for the case of $r/d = 1/48 = 0.0208$, the K_t value from Fessler et al. (1969a,b) seems low in comparison with the previously mentioned results and the extension to $r/d = 0.125$.

The K_t values in the straight part of the fillet of a semicircular keyseat end from Fessler et al. (1969a,b) appear to be lower than, or about the same as, that from the Leven's curve for the straight part.

5.2.3 Torque Transmitted Through a Key

Solakian and Karelitz (1932) and Gibson and Gilet (1938) investigate the stresses in keyseats when a torque is transmitted through a key by two-dimensional photoelasticity. However, the results are inapplicable to design since the stresses vary along the length direction of keyseat.

The upper dashed curve of Chart 5.2 is an estimation of K_t of the fillet when the torque is transmitted by a key with a length of $2.5d$. The dashed curve is obtained by using the ratio of K_t values with and without a key. It is determined by an "electroplating method" with the keyseats of different cross-sectional proportions (Okubo et al. 1968). In their tests with a key, the friction of the shaft is minimized. In a design application, the degree of press-fit pressure is an important factor.

5.2.4 Combined Bending and Torsion

The investigation by Fessler et al. (1969a,b) leads to the chart used to obtain K_t of a shaft subjected to the combined bending and torsion. The shaft uses the British keyseat proportions ($b/d = 0.25$, $t/d = 1/12 = 0.0833$) for $r/d = 1/48 = 0.0208$. The nominal stress for the chart is defined as

$$\sigma_{\text{nom}} = \frac{16M}{\pi d^3}\left[1 + \sqrt{1 + \left(\frac{T^2}{M^2}\right)}\right] \tag{5.1}$$

Chart 5.3 provides a rough estimation of K_t for the keyseats in the U.S. standard. It is based on the use of straight lines to approximate the results of the British chart. Note that $K_t = \sigma_{\max}/\sigma_{\text{nom}}$ and $K_{ts} = \tau_{\max}/\sigma_{\text{nom}}$, and the value of σ_{nom} is calculated in Eq. (5.1).

Chart 5.3 is for $r/d = 1/48 = 0.0208$. If r/d decreases, the middle two lines are moved upward in accordance with the values of Charts 5.1 and 5.2; however, the top and bottom lines remain fixed.

5.2.5 Effect of Proximity of Keyseat to Shaft Shoulder Fillet

The photoelastic tests by Fessler et al. (1969a,b) are made of the shafts with $D/d = 1.5$ (large diameter/small diameter) in the British keyseat proportions ($b/d = 0.25$, $t/d = 0.0833$, $r/d = 0.0208$). With the keyseat end located at the position where the shaft shoulder fillet begins shown in Fig. 5.3*a*, the maximum stress of the keyseat fillet is not affected by varying the fillet of the shaft shoulder r_s/d in a range from 0.021 to 0.083, where r_s is the radius of the shaft shoulder fillet. In torsion, the maximum surface stress on the semicircular keyseat end terminating at the beginning of the shoulder fillet is increased about 10% over the corresponding stress of a straight shaft with a keyseat. The increase ceases to zero as the keyseat end is moved a distance of $d/10$ away from the beginning of the shaft shoulder filler radius as shown in Fig. 5.3*b*.

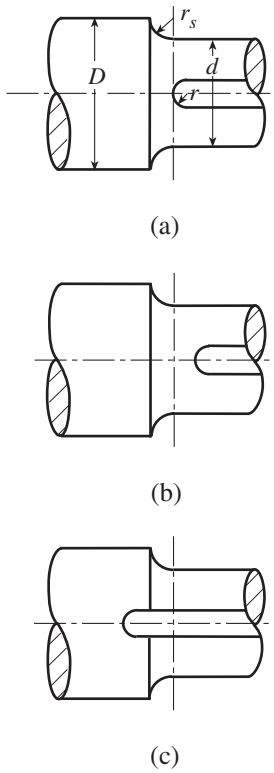


Figure 5.3 Location of end of keyseat with respect to shaft shoulder: (a) keyseat end at beginning of shoulder fillet; (b) keyseat end away from shoulder fillet; (c) keyseat end cut into shoulder.

For a keyseat cut into the shaft shoulder as shown in Fig. 5.3*c*, the effect is to reduce K_t for bending (fillet and surface) and for torsion (surface). For torsion (fillet), K_t is also reduced except the case when the end of the keyway is located at an axial distance of $0.07d$ to $0.25d$ from the beginning of the fillet.

5.2.6 Fatigue Failures

A designer may be interested in using the foregoing K_t factors for keyseats to determine fatigue lives of machine elements. Despite the fact that the problem of determining a fatigue fail is a complex one, some comments may be helpful.

For keyways, a fatigue is often initiated by shear stress; however, the crack is propagated by normal stress. Referring to Charts 5.1 to 5.3, two critical locations are involved: (1) a keyseat fillet with a small radius and (2) the surface of the shaft at a semicircular keyway end with a large radius, which is three or more times of the fillet radius. Both the initiation and fracture of cracks are the functions of the stress gradient, which is mainly related to the "notch" radius. This radius

must be taken into consideration when the fatigue life of a part is analyzed. In certain instances, a fillet with a nonpropagating crack should have a small radius.

For the pure torsion ($M/T = 0$) in Chart 5.3, it is expected that the crack would be initialized by shear stress in the fillet; but the stress gradient is so steep that an initial failure at the surface is also possible. The direction of final crack will be determined by the normal stresses over surface associated with the maximum K_{tA}. For the pure bending ($T/M = 0$), a failure will more likely occur primarily at the surface. This is supported by the fatigue tests (Peterson 1932) and the service failures discussed in (Peterson 1950). In certain instances, a torsional fatigue starts at the fillet and develops into a peeling type of failure. This particular type may be influenced by the key and possibly by a fillet radius of a keyseat smaller than the standard value. However, due to numerous design factors such as differing geometries, press-fit and key conditions, and the ratios of steady and alternating bending and torsional stress components, the prediction of crack initialization and fractures of keyseats is challenging.

5.3 SPLINED SHAFT IN TORSION

In a three-dimensional photoelastic study on a particular eight-tooth spline by Yoshitake (1962), the tooth fillet radius is varied in three tests, and the relational curve of K_{ts} with respect to r/d is shown in Chart 5.4. A test of an involute spline with a full fillet radius gives a K_{ts} value of 2.8. Note that the data in Chart 5.4 is for an open spline and there is no mating member.

In the case of a test with a mating pair, the fitted length is slightly greater than the outside diameter of the spline. The maximum longitudinal bending stress of a tooth occurs at the end of the tooth and is about the same numerically as the maximum torsion stress.

Okubo (1950b) analyzes mathematically on the torsion and corresponding strain of a shaft with n longitudinal semicircular grooves. For the case of a shaft with a single groove, Timoshenko and Goodier (1970) find that when $r/d \to 0$, $K_{ts} = 2$.

5.4 GEAR TEETH

A gear tooth can be modeled with a short cantilever beam, and the maximum stress occurs at the fillet of the root of the tooth. Due to the combination of tangent and radical loads, the stresses on the two sides of tooth are not symmetric. A fracture or fatigue failure occurs to the tension side. The photoelastic tests by Dolan and Broghamer (1942) generate Charts 5.5 and 5.6 where the SCFs of tooth are given for the practice of gear design. The notation of gear is illustrated in Fig. 5.4.

A fillet of tooth is often generated by a hob or cutter, and its radius is not constant (Michalec 1966). A hobbing tool has a number of straight-sided teeth (see the sketch of Chart 5.7) with a tip radius r_t. This radius has been standardized for full-depth teeth (Baumeister 1967), i.e., $r_t = 0.209/P_d$ for 14.5° pressure angle and $r_t = 0.235/P_d$ for a 20° pressure angle. For stub teeth, r_t has not been standardized; but it is recommended to set $r_t = 0.3/P_d$. In Charts 5.5 and 5.6, the full curves are approximated by the interpolation of the data points from the photoelastic tests for

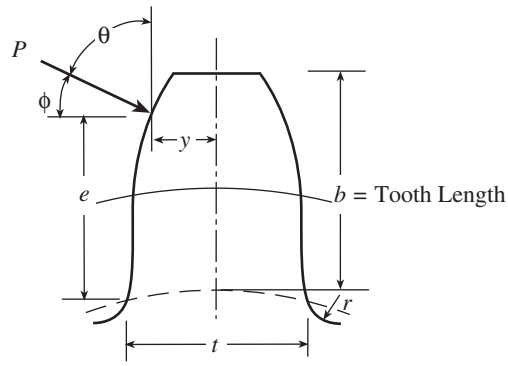


Figure 5.4 Gear notation.

these r_t values. The tool radius r_t generates a gear tooth fillet of variable radius. The minimum radius is denoted r_f. Candee (1941) gives the formulae to calculate r_f from r_t as:

$$r_f = \frac{(b - r_t)^2}{N/(2P_d) + (b - r_t)} + r_t \tag{5.2}$$

where b is the dedendum, N is the number of teeth, and P_d is the diametric pitch, which can be calculated as the number of teeth divided by the pitch diameter.

The dedendum $b = 1.157/P_d$ for full-depth teeth and $1/P_d$ for stub teeth. Equation (5.2) is shown graphically in Chart 5.7. The curve for 20° stub teeth is shown dashed; since r_t is not standardized and there is uncertainty regarding application of Eq. (5.2).

Dolan and Broghamer (1942) develop the following empirical relations for the stress concentration factor of the fillet on the tension side:

For 14.5° pressure angle,

$$K_t = 0.22 + \frac{1}{(r_f/t)^{0.2}(e/t)^{0.4}} \tag{5.3}$$

For 20° pressure angle,

$$K_t = 0.18 + \frac{1}{(r_f/t)^{0.15}(e/t)^{0.45}} \tag{5.4}$$

In certain instances, a grinder with a specific form is used to generate a semicircular fillet radius between two teeth. Chart 5.8 is constructed to evaluate the effect of the fillet radius based on Eqs. (5.3) and (5.4). Note that the lowest K_t factors occur when the load is applied at the tip of the tooth. However, owing to an increased moment arm, the maximum fillet stress occurs at this position – neglecting load division (Baud and Peterson 1929). However, only extremely accurate gearing may count on this beneficial effect reliably (Peterson 1930). Considering then the lowest curves ($e/t = 1$), it should be noted that the value of r_f/t for the standardized teeth lies within the range of (0.1, 0.2), which depends on the number of teeth. Setting a semicircular fillet with

$r_t/t \approx 0.3$ does not decrease the value of K_t significantly. Although the decrease of K_t intuitively seems beneficial, this gain needs to be weighed against other economic and technical factors such as the decreased effective rim of a pinion with a small number of teeth (DeGregorio 1968). This is especially true when a keyway is present.

In addition to their photoelastic tests of gear teeth, Dolan and Broghamer (1942) test the straight-sided short cantilever beams with different loads and fillet radius, and the results are given in Chart 5.9, and the empirical formula for K_t at the tension side is derived as:

$$K_t = 1.25 \left[\frac{1}{(r/t')^{0.2}(e/t)^{0.3}} \right] \tag{5.5}$$

The stress concentration factor K_t on the compression side is also shown in Chart 5.9. Since the compressive side is not critical region, the empirical formulae is not derived.

To present the effect of the fillet radius of teeth, Chart 5.8 shows that it is preferable to use Eqs. (5.3) and (5.4) due to the combination of tangent and radical loads. Chart 5.9 also includes the information of SCFs of longer beams for the case of large e/t by Weibel (1934) and Riggs and Frocht (1938).

The results of SCFs of gear teeth by Dolan and Broghamer (1942) are confirmed by the subsequent photoelastic investigation by Jacobson (1955). In addition, Aida and Terauchi (1962) propose the following analytical solution for the tensile maximum stress at the gear fillet:

$$\sigma_{\max} = \left(1 + 0.08\frac{t}{r}\right)(0.66\sigma_{Nb} + 0.40\sqrt{\sigma_{Nb}^2 + 36\tau_N^2} + 1.15\sigma_{Nc}) \tag{5.6}$$

where

$$\sigma_{Nb} = \frac{6Pe\sin\theta}{bt^2} \qquad \text{(see Fig. 5.4)}$$

$$\sigma_{Nc} = -\frac{P\cos\theta}{bt} - \frac{6Py\cos\theta}{bt^2}$$

$$\tau_N = \frac{P\sin\theta}{bt}$$

Some other photoelastic tests result in a satisfactory check of the foregoing analytical results, which are in good agreement with the results of Dolan and Broghamer (1942).

5.5 PRESS- OR SHRINK-FITTED MEMBERS

Gears, pulleys, wheels, and similar elements are often assembled on a shaft by means of a press fit or shrink fit. Peterson and Wahl (1935) do the photoelastic tests on the flat models shown in Fig. 5.5. The testing condition is $\sigma_{\text{nom}}/p = 1.36$, where σ_{nom} is the nominal bending stress in the shaft and p is the average normal pressure exerted by the member on the shaft. These lead to the SCF of $K_t = 1.95$ for the plain member and $K_t = 1.34$ for the grooved member.

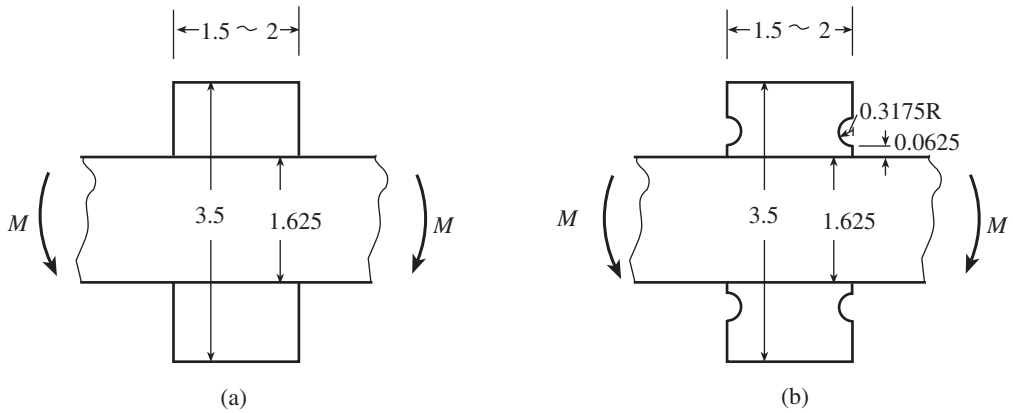


Figure 5.5 Press-fit models, with dimensions in inches: (a) plain member; (b) grooved member.

Fatigue tests of the "three-dimensional" case are made for a collar pressed[2] on a 1.625-in.-diameter medium-carbon (0.42% C) steel shaft. The proportions are the same as for the previously mentioned photoelastic models. The fatigue tests yield the bending "fatigue-notch factors" of $K_f = 2.0$ for the plain member and $K_f = 1.7$ for the grooved member. Note that the factors for the plain member seem to be in good agreement; however, this is not significant since the fatigue result is due to a combination of stress concentration and "fretting corrosion" (Tomlinson 1927; Tomlinson et al. 1939; ASTM 1952; Nishioka et al. 1968). The "fretting corrosion" produces a weakening effect over and above the concentrated stress. Note that the fatigue factor for the grooved member is higher than the stress concentration factor. This is no doubt due to the fretting corrosion, which becomes relatively more prominent for lower-stress condition cases. The fretting corrosion effect varies considerably with the combination of materials. Table 5.1 gives some fatigue results (Horger and Maulbetsch 1936).

The similar test is made in Germany (Thum and Bruder 1938), and the results are reported in Table 5.2. The reaction in testing is applied through the inner race, somewhat lower values of are obtained. Some tests are made with relief grooves as shown in Section 3.6 and the results give lower values of K_f.

Another favorable construction (Horger and Buckwalter 1940; White and Humpherson 1969), as shown in Fig. 5.6, is to enlarge the shaft at the fit and to round out the shoulders; in such a way, the critical region A (Fig. 5.6*a*) is relieved as at B (Fig. 5.6*b*). Even though the photoelastic tests (Horger and Buckwalter 1940) have no quantitative information, it is clear that if the shoulder is ample, a failure will occur in the fillet. In such a case, the design can be rationalized in accordance with Chapter 3.

As noted previously, K_f factors are a function of size. K_f is increased toward a limiting value when the geometrically similar size is increased. For the diameter of 50-mm ($\approx 2 - in.$),

[2]The calculated radial pressure in this case is 16,000 lb/in.^{2} ($\sigma_{nom}/p = 1$). However, the tests (Thum and Wunderlich 1933; Peterson and Wahl 1935) indicate that over a wide range of pressures, this variable does not affect K_f, except for the case of very light pressure, which results in a lower K_f.

TABLE 5.1 Stress Concentration Factors for Press-Fit Shafts of 2-in. Diameter

Roller-Bearing Inner Race of Case Hardened Cr–Ni–Mo Steel Pressed on the Shaft	K_f
1. No external reaction through collar	
a. 0.45% C axle steel shaft	2.3
2. External reaction through collar	
a. 0.45% C axle steel shaft	2.9
b. Cr–Ni–Mo steel, heat-treated to 310 Brinell	3.9
c. 2.6% Ni steel, 57,000 psi fatigue limit	3.3–3.8
d. Same, heat treated to 253 Brinell	3.0

TABLE 5.2 Stress Concentration Factors for Press-Fit Shafts of 0.66-in. Diameter[a]

Reaction Not Carried by the Inner Race
1. 0.36% C axle steel shaft
a. Press-fit and shoulder fillet ($r = 0.04$ in., $D/d = 1.3$))
b. Same, shoulder fillet only (no inner race present)
c. Press-fit only (no shoulder)
2. 1.5% Ni–0.5% Cr steel shaft (236 Brinell)
a. Press-fit and shoulder fillet ($r = 0.04$ in., $D/d = 1.3$)
b. Same, shoulder fillet (no inner race)

[a] d, Diameter of shaft; D, outer diameter of ring.

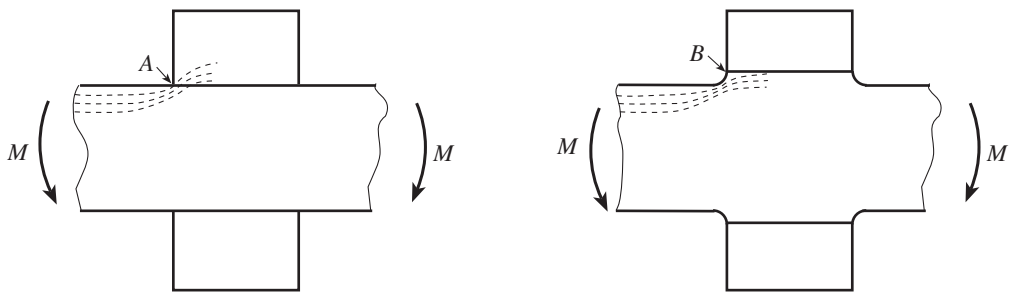


Figure 5.6 Shoulder design for fitted member, with schematic stress "flow lines": (*a*) plain shaft; (*b*) shaft with shoulder.

$K_f = 2.8$ is obtained for 0.39% C axle steel (Nishioka and Komatsu 1967). For the models with a diameter of $3\frac{1}{2}$ to 5 in., K_f values of the order of 3 to 4 are obtained for turbine rotor alloy steels (Coyle and Watson 1963–1964). For 7- to $9\frac{1}{2}$-in. wheel fit models (Horger 1953, 1956; AAR 1950), K_f values of the order 4 to 5 are obtained for a variety of axle steels, based on the fatigue limit of conventional specimens. Nonpropagating cracks are found, in some instances at about half of the fatigue limit of the press-fitted member. The photoelastic tests of a press-fitted ring on a shaft with six lands or spokes by Adelfio and DiBenedetto (1970) give the K_t factors on the order of 2 to 4.

The situation with regard to press fits is complicated; since the stress concentration and fretting corrosion exist simultaneously. The mechanism of how the fretting corrosion affecting the stress concentration is not well understood.

5.6 BOLT AND NUT

Martinaglia (1942) estimates that the probabilities of the bolt failures are distributed in the following scenarios as: (1) 15% under the head, (2) 20% at the end of the thread, and (3) 65% in the thread at the nut face. By using a reduced bolt shank shown in Fig. 2.5*c* as compared to Fig. 2.5*b*, the situation with regard to the fatigue failures of group *b* type can be improved (Staedel 1933; Wiegand 1933). With a reduced shank, a larger fillet radius can be provided under the head (see Section 5.7), thereby improving the design with regard to group *a* type failure.

In regards to group *c* type of the failure in the threads at the nut face, Hetényi (1943) investigates various bolt-and-nut combinations by means of three-dimensional photoelastic tests. For the Whitworth threads with a root radius of 0.1373 pitch (Baumeister 1967), the testing results are shown in Fig. 5.7 that $K_{tg} = 3.85$ for bolt and nut with standard proportions; $K_{tg} = 3.00$ for nut

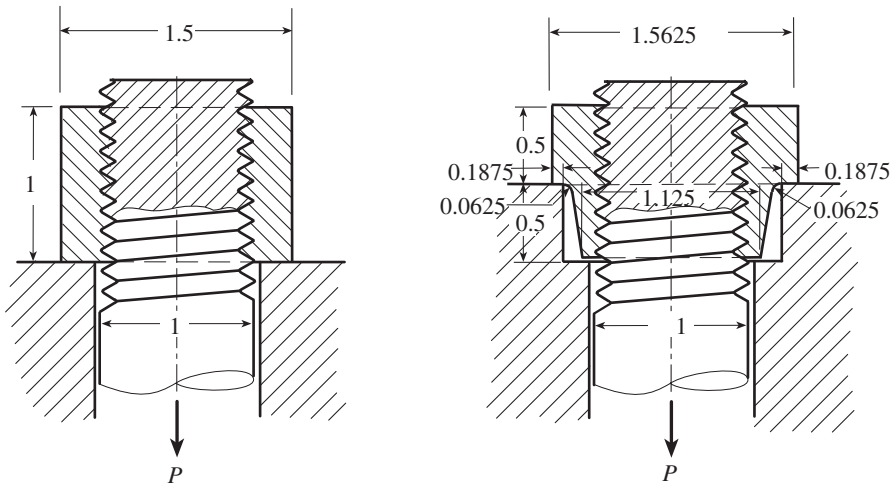


Figure 5.7 Nut designs tested photoelastically, with dimensions in inches (Hetényi 1943).

having lip based on the full body (shank) nominal stress. If the SCFs are calculated for the area at the thread bottom (which is more realistic from a stress concentration standpoint, since this corresponds to the location of the maximum stress), then $K_{tn} = 2.7$ for the standard nut, and $K_{tn} = 2.1$ for the tapered nut.

The later tests by Brown and Hickson (1952–1953) using a Fosterite model twice as large and thinner slices, result in $K_{tg} = 9$ for the standard nut based on the body diameter (see authors' closure) (Brown and Hickson 1952–1953). This corresponds to $K_{tn} = 6.7$ for the standard nut based on the root diameter. This compares with the value of 2.7 by Hetényi (1943). The value of $K_{tn} = 6.7$ should be used in design where fatigue or embrittling is involved, with a correction for notch sensitivity (Fig. 1.31).

As discussed by Brown and Hickson (1952–1953), Taylor reports a fatigue SCF of $K_{fn} = 7$ for a 3-in.-diameter bolt with a root contour radius/root diameter; which is half of that of the photoelastic model of Brown and Hickson. He estimates that if his fatigue test would be made on a bolt of the same geometry as the photoelastic model, the K_{fn} value might be as low as 4.2.

For a root radius of 0.023 in., a notch sensitivity factor q is estimated as 0.67 from Fig. 1.31 for "mild steel." The photoelastic $K_{tn} = 6.7$ would then correspond to $K_{fn} = 4.8$. Although this is in a fair agreement with the estimation by Taylor, the basis of such an estimation involves in some uncertainties.

A photoelastic investigation by Marino and Riley (1964) on buttress threads shows that by modifying the thread-root contour radius, the maximum stress is reduced by 22%.

In a nut designed with a lip (Fig. 5.8*b*), the peak stress is relieved by the lip being stressed in the same direction as the bolt. The fatigue test by Wiegand (1933) shows that the lip design to be about 30% stronger than the standard nut design (Fig. 5.8*a*), which is generally agreed with the photoelastic tests by Hetényi (1943).

In the arrangement shown in Fig. 5.8*c*, the transmitted load is not reversed. The fatigue test by Wiegand (1933) shows that a fatigue strength is more than double that of the standard bolt-and-nut combination (Fig. 5.8*a*).

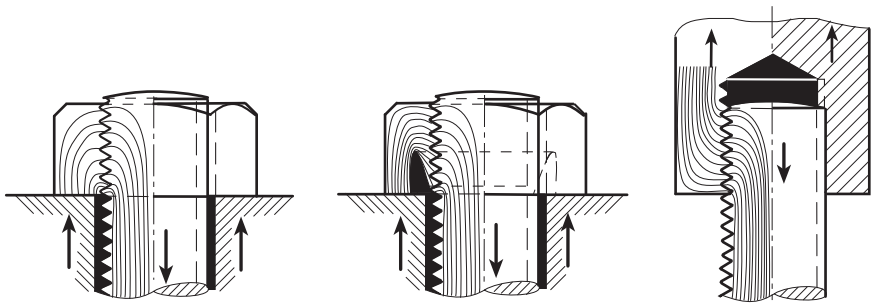


Figure 5.8 Nut designs fatigue tested (Wiegand 1933).

Using the material of a lower modulus of elasticity for a nut is helpful in reducing the peak stress in the bolt threads. The fatigue tests (Wiegand 1933; Kaufmann and Jäniche 1940) have shown the gains in strength of 35% to 60% depending on materials.

Other methods to reduce K_t of a bolt-and-nut combination include the uses of tapered threads and differential thread spacing; however, these methods are not as practical.

5.7 BOLT HEAD, TURBINE-BLADE, OR COMPRESSOR-BLADE FASTENING (T-HEAD)

A vital difference between the case of a bar with shoulder fillets (Fig. 5.9*a*) and the T-head case (Fig. 5.9*b*) is the manner of loading. Another difference in the above cases is that the dimension of L in Fig. 5.9*b*, is seldom greater than d. As L is decreased, the bending of the overhanging portion becomes more prominent.

Chart 5.10 presents the $\sigma_{\max}/\sigma$ values as determined photoelastically by Hetényi (1939b). In this case, σ is simply determined as P/A, i.e., the load divided by the shank cross-sectional area. Therefore, the value of $\sigma_{\max}/\sigma$ expresses the stress concentration in the simplest form in design.

However, it is also useful to consider a modified procedure for K_t, so that when the comparisons are made between different kinds of fatigue tests, the resulting values of notch sensitivity will have a more comparable meaning, as explained in the introduction of Chapter 4. For this purpose, two kinds of K_t factors are considered: (1) K_{tA} based on tension and (2)K_{tB} based on bending.

For tension:

$$K_{tA} = \frac{\sigma_{\max}}{\sigma} \tag{5.7}$$

where

$$\sigma = \sigma_{\text{nom } A} = \frac{P}{hd}$$

For bending:

$$K_{tB} = \frac{\sigma_{\max}}{\sigma_{\text{nom } B}}$$

where

$$\sigma_{\text{nom } B} = \frac{M}{I/c} = \frac{Pl}{2}\left(\frac{6}{hL^2}\right) = \frac{3}{4}\frac{Pd}{hL^2}\left(\frac{H}{d} - 1\right) \tag{5.8}$$

with $l = (H - d)/4$. Thus

$$K_{tB} = \frac{\sigma_{\max}}{\sigma[3(H/d - 1)/4(L/d)^2]} \tag{5.9}$$

Note that for $K_{tA} = K_{tB}$,

$$\frac{(H/d - 1)}{(L/d)^2} = \frac{4}{3} \quad \text{or} \quad \frac{ld}{L^2} = \frac{1}{3} \tag{5.10}$$

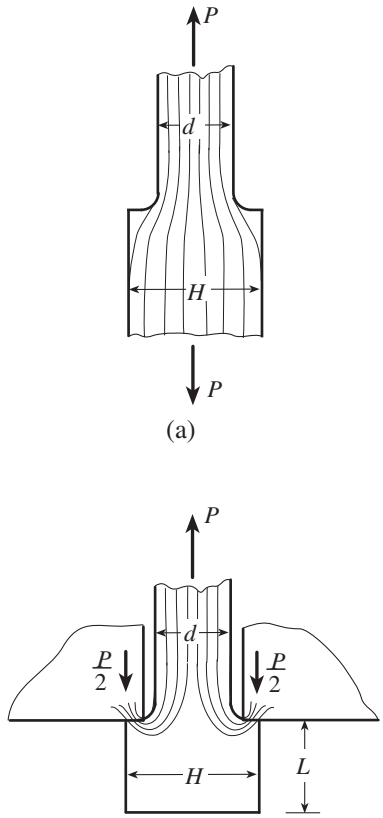


Figure 5.9 Transmittal of load (schematic): (a) stepped tension bar; (b) T-head.

In Chart 5.10*f*, the values of K_{tA} and K_{tB} are plotted with ld/L^2 as the abscissa variable. For $(ld/L^2) > 1/3$, K_{tB} is used; for $(ld/L^2) < 1/3$, K_{tA} is used. This procedure is similar to that used for the pinned joint (Section 5.8, and earlier Section 4.5.8) and, as in that case, not only extremely high factors can be avoided, but also a safer basis for extrapolation can be provided (in this case to smaller L/d values).

In Charts 5.10*a* and 5.10*d*, the dashed line represents the equal values of K_{tA} and K_{tB} from Eqs. (5.7) and (5.9). Below this line, the $\sigma_{\max}/\sigma$ values are the same as K_{tA}. Above the dashed line, all of the $\sigma_{\max}/\sigma$ values are higher, usually much higher, than the corresponding K_{tB} values, which in magnitude are all lower than the values represented by the dashed line (i.e., the dashed line represents maximum K_{tA} and K_{tB} values as shown by the peaks in Chart 5.10*f*).

The effect of moving concentrated reactions closer to the fillet is shown in Chart 5.10*e*. The sharply increasing K_t values are due to a proximity effect (Heténi 1939b); since the nominal bending is decreasing while the nominal tension remains the same.

The T-head factors may be applied directly in the case of a T-shaped blade fastening of rectangular cross section. In the case of the head of a round bolt, the lower factors are found from Chapters 2 and 3. However, the ratios will not be directly comparable to those of Chapter 3, since the part of the T-head factor is due to proximity effect. To be on the safe side, it is recommended to use the unmodified T-head factors for bolt heads.

Steam-turbine blade fastenings are often made as a "double T-head." In gas-turbine blades, multiple projections are used in the "fir-tree" type of fastening. Some photoelastic data has been obtained for multiple projections (Durelli and Riley 1965; Heywood 1969).

5.8 LUG JOINT

In this section, the SCFs at the perimeter of a hole in a lug with a pin are discussed (Frocht and Hill 1940; Theocaris 1956; Cox and Brown 1964; Meek 1967; Gregory 1968; Whitehead et al. 1978; ESDU 1981). The notation of a lug joint is illustrated in Fig. 5.10.

The pin-to-hole clearance as a percentage of the hole diameter d is designated as e. Thus, from Fig. 5.11, $e = \delta/d$. The quantity K_{te} is the SCF at $e\%$ clearance. Thus $K_{t0.2}$ refers to a 0.2% clearance between the hole and the pin. K_{t100} is used for the limiting case of point (line) loading. In this case, the load P is applied uniformly across the thickness of the lug at location C of Fig. 5.10. When h/d (the ratio of lug thickness to hole diameter) < 0.5, the stress concentration factor is designated as K_{te}. For $h/d > 0.5$, K'_{te} is used.

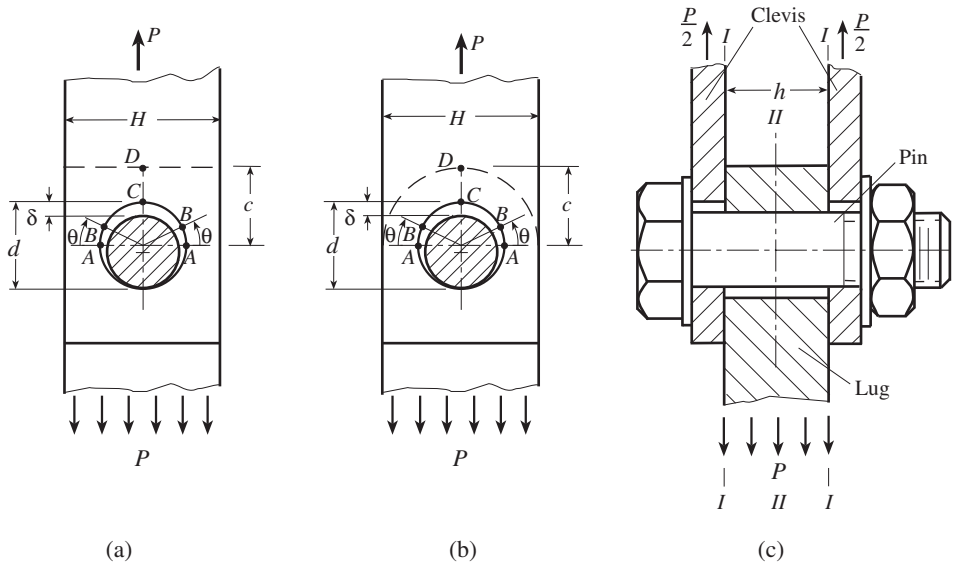


Figure 5.10 Lugs with pins: (a) square-ended lug; (b) round-ended lug; (c) section through lug assembly center line.

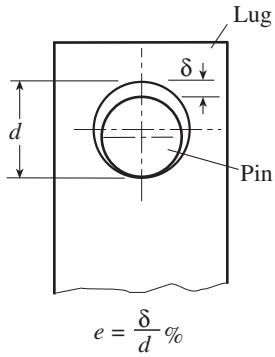


Figure 5.11 Clearance of a lug-pin fit.

The SCF is influenced by the lug geometry as well as the clearance of the pin in the hole. For perfectly fitting pins, $\sigma_{\max}$ occurs at the point labeled with A in Fig. 5.10. If there is a clearance between the pin and the hole, $\sigma_{\max}$ increases in value and occurs at point B, for which $10^\circ < \theta < 35^\circ$.

The bending stresses occur along the $C - D$ section if $c - d/2$ is quite small. Then $\sigma_{\max}$ will occur at point D. However, this scenario is not discussed further here.

Charts 5.11 and 5.12 give the SCFs K_{te} for square-ended and round-ended lugs (ESDU 1981). Each of these charts provides a curve for the limiting condition $c/H = \infty$. In practice, this limit applies for the values of $c/H > 1.5$.

The studies by ESDU (1981) show that if $h/d < 0.5$ for a lug, K_{te} is not significantly affected if the pin and lug are made of different materials. More specifically, there is no significant effect if the ratio of the elastic moduli $E_{\text{pin}}/E_{\text{lug}}$ is between 1 and 3. Interested readers can refer to Section 5.8.2 for further discussion of the effect of different materials, especially for the case of $h/d > 0.5$.

5.8.1 Lugs with $h/d < 0.5$

For precisely manufactured pins and lug-holes, as might be the case for laboratory instrumentation, e tends to be less than 0.1%. The curves of SCFs for square-ended lugs for such a case are given in Chart 5.11. The solid curves of K_{te} in Chart 5.11 are for pin clearances in square-ended lugs of 0.2% of d. The upper limit K_{t100} curve in Chart 5.12 is a reasonable limit of the estimation for the square-ended lugs.

For round-ended lugs, Chart 5.12 gives the curves of $K_{t0.2}$ and K_{t100}. The experiments by ESDU (1981) confirmed that the SCFs in these curves are reasonable approximations.

The K_{te} for any lug-hole, pin clearance percent e can be obtained from $K_{t0.2}$ and K_{t100} by defining a correction factor f as $f = (K_{te} - K_{t0.2})/(K_{t100} - K_{t0.2})$, f is plotted in Chart 5.12 (ESDU 1981). Accordingly, $K_{te} = K_{t0.2} + f(K_{t100} - K_{t0.2})$. Surface finish variations and geometric imperfections can affect stress concentration factors. Therefore, the value of f should be treated as an approximation especially for the case of $e < 0.1$.

5.8.2 Lugs with $h/d > 0.5$

The stress concentration factors K'_{te} for pin and hole joints with $h/d > 0.5$ can be obtained from Chart 5.13. In using Chart 5.13, K_{te} values are taken from Charts 5.11 and 5.12 as needed. Chart 5.13 gives the relation of the ratio K'_{te}/K_{te} versus h/d (ESDU 1981); it applies for small clearances between pin and hole. The curves are actually prepared for square-ended lugs with $d/H = 0.45$ and $c/H = 0.67$. However, they also provide reasonable estimations for square- and round-ended lugs with $0.3 \leq d/H \leq 0.6$. The upper curve in Chart 5.13 applies to $E_{\text{pin}} = E_{\text{lug}}$, where E is the modulus of elasticity. The lower curve, for $E_{\text{pin}}/E_{\text{lug}} = 3.0$, is based on a single data point of $h/d = 2.24$. As h/d increases, the bending occurring to pin increases, and loading at the hole ends (sections I–I in Fig. 5.10*c*) also increases. This is accompanied by a decrease in loading at the center of the hole region (sections II–II in Fig. 5.10*c*).

If there is a no negligible clearance between the sides of the lug and the loading fork (faces I–I of Fig. 5.10*c*), the bending on pin may increase; it implies an increase of K'_{te}/K_{te} over the pin shown in Chart 5.13. The smoothed corners of the lug hole may have a similar effect. Stress concentrations can be increased if loading on the fork is not symmetric.

Example 5.1 Pin and Hole Joint. Determine the peak stress concentration factor for the lug shown in Fig. 5.12. The pin is nominally of the diameter of 65 mm; while it varies within $65 - 0.02$ to $65 - 0.16$ mm. The hole diameter is also nominally of the diameter of 65 mm and varies within $65 + 0.10$ to $65 + 0.20$ mm.

The upper bound for the clearance is $0.20 + 0.16 = 0.36$ mm, giving

$$e = \frac{0.36}{65} \times 100 = 0.55\% \tag{1}$$

From the dimensions in Fig. 5.12,

$$\frac{d}{H} = \frac{65}{(2 \times 65)} = 0.5 \tag{2}$$

$$\frac{c}{H} = \frac{80}{(2 \times 65)} = 0.62 \tag{3}$$

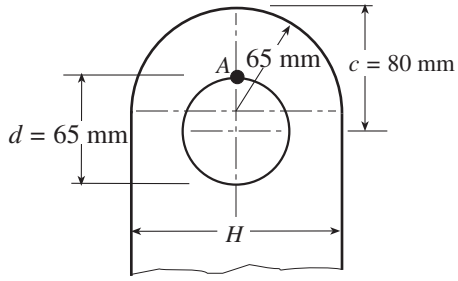


Figure 5.12 Lug of Example 5.1.

Chart 5.12 for round-ended lugs shows the values of $K_{t0.2}$ and K_{t100} for being 2.68 and 3.61, respectively. Let K_{te} be $e = 0.55\%$ in Chart 5.12, the correction factor f for $e = 0.55$ is 0.23. Then

$$\begin{aligned} K_{te} &= K_{t0.2} + f(K_{t100} - K_{t0.2}) \\ &= 2.68 + 0.23(3.61 - 2.68) = 2.89 \end{aligned} \tag{4}$$

This is the maximum stress concentration factor for the lug, and the corresponding maximum stress occurs at point A of Fig. 5.12.

The lower bound for the clearance is $0.10 + 0.02 = 0.12$ mm, so $e = (0.12/65)100 = 0.18\%$. From Chart 5.12, the correction factor f is -0.02 for $\mathrm{e} = 0.18$. Thus $K_{te} = K_{t0.2} + f(K_{t100} - K_{t0.2}) = 2.68 - 0.02(3.61 - 2.68) = 2.66$.

5.9 CURVED BAR

A curved bar subjected to bending will have a higher stress on the inside edge as shown in Fig. 5.13. Stress analysis on curved bars is covered by Timoshenko (1956). The formulas for typical cross sections (Pilkey 2005) and a graphical method for a general cross section are given by Wilson and Quereau (1928). In Chart 5.14, the values of K_t are given for five cross sections.

The following formula by Wilson and Quereau (1928) works reasonably well for ordinary cross sections except triangular cross sections:

$$K_t = 1.00 + B\left(\frac{I}{bc^2}\right)\left(\frac{1}{r-c} + \frac{1}{r}\right) \tag{5.11}$$

where I is the moment of inertia of the cross section, b is the maximum breadth of the section, c is the distance from the centroidal axis to the inside edge, r is the radius of curvature, and $B = 1.05$ for the circular or elliptical cross section and 0.5 for other cross sections.

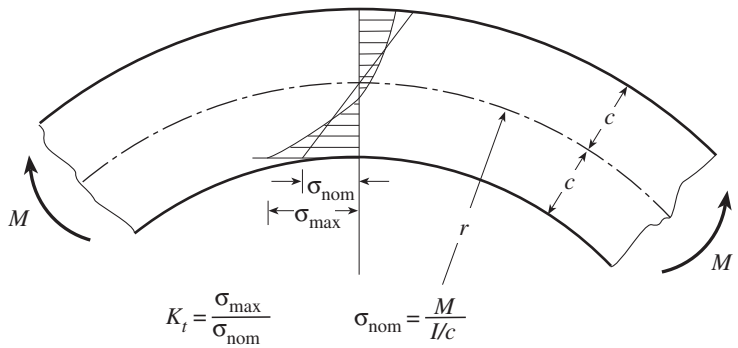


Figure 5.13 Stress concentration in curved bar subjected to bending.

In regards to notch sensitivity, the q versus r curves in Fig. 1.31 do not apply to a curved bar unless the stress gradient concept is adopted (Peterson 1938).

5.10 HELICAL SPRING

5.10.1 Round or Square Wire Compression or Tension Spring

A helical spring may be regarded as a curved bar subjected to a twisting moment and a direct shear load (Wahl 1963). The final paragraph in the preceding section applies to helical springs.

For a round wire helical compression or tension spring with a small pitch angle, the *Wahl factor*, C_w, is used in the design as a correction factor for taking into account curvature and direct shear stress in Chart 5.15 (Wahl 1963).

For round wire,

$$C_w = \frac{\tau_{\max}}{\tau} = \frac{4c-1}{4c-4} + \frac{0.615}{c} \tag{5.12}$$

$$\tau = \frac{T(a/2)}{J} = \frac{P(d/2)}{\pi a^3/16} = \frac{8Pd}{\pi a^3} = \frac{8Pc}{\pi a^2} \tag{5.13}$$

where T is the torque, P is the axial load, c is the spring index d/a, d is the mean coil diameter, a is the wire diameter, and J is the polar moment of inertia.

For a spring with square wire in Fig. 5.14 (Göhner 1932), the shape correction factor α is $\alpha = 0.416$ for $b = h = a$. Here a is the width and depth of the square wire, $1/\alpha = 2.404$ and

$$C_w = \frac{\tau_{\max}}{\tau} \tag{5.14}$$

$$\tau_{\max} = \tau\left(1 + \frac{1.2}{c} + \frac{0.56}{c^2} + \frac{0.5}{c^3}\right) \tag{5.15}$$

$$\tau = \frac{Pd}{\alpha a^3} = \frac{2.404Pd}{a^3} = \frac{2.404Pc}{a^2} \tag{5.16}$$

The corresponding SCFs may be useful for mechanics of materials problems, and they are obtained by taking the nominal shear stress τ_{nom} as the sum of the torsional stress τ of Eq. (5.13) and the direct shear stress $\tau = 4P/\pi a^2$ for a round wire. In the case of the wire of square cross section, τ_{nom} is the sum of the torsional stress of Eq. (5.16) and the direct shear stress $\tau = P/a^2$.

For round wire,

$$\begin{aligned} K_{ts} &= \frac{\tau_{\max}}{\tau_{\text{nom}}} \\ &= \frac{(8Pd/\pi a^3)[(4c-1)/(4c-4)] + 4.92P/\pi a^2}{8Pd/\pi a^3 + 4P/\pi a^2} \\ &= \frac{2c[(4c-1)/(4c-4)] + 1.23}{2c+1} \end{aligned} \tag{5.17}$$

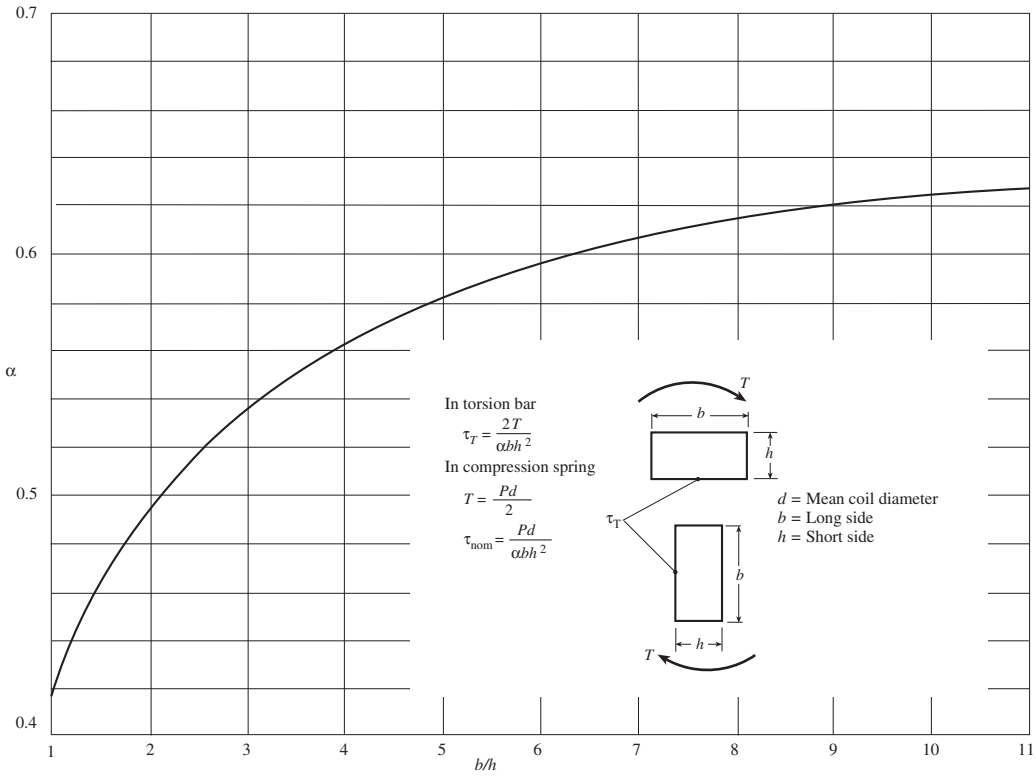


Figure 5.14 Factor α for a torsion bar of rectangular cross section.

$$\tau_{\max} = K_{ts}\left[\frac{4P}{\pi a^2}(2c+1)\right] \tag{5.18}$$

For square wire,

$$\begin{aligned} K_{ts} &= \frac{\tau_{\max}}{\tau_{\text{nom}}} \\ &= \frac{(2.404Pd/a^3)(1+1.2/c+0.56/c^2+0.5/c^3)}{2.404Pd/a^3+P/a^2} \\ &= \frac{2.404c(1+1.2/c+0.56/c^2+0.5/c^3)}{2.404c+1} \end{aligned} \tag{5.19}$$

$$\tau_{\max} = K_{ts}\left[\frac{P}{a^2}(2.404c+1)\right] \tag{5.20}$$

Chart 5.15 gives the values of C_w and K_{ts} where K_{ts} is lower than the correction factor C_w. For design calculations, it is recommended that the simpler Wahl factor be used. The same value of $\tau_{\max}$ will be obtained whether one uses C_w or K_{ts}.

The effect of the pitch angle is determined by Ancker and Goodier (1958). The effect of a pitch angle up to 10° is small, but a pitch angle at 20° can increase the stress sufficiently to make a correction of stress.

5.10.2 Rectangular Wire Compression or Tension Spring

For a wire of rectangular cross section, the results of Liesecke (1933) are converted into SCFs in the following way: the nominal stress is taken as the maximum stress in a straight torsion bar of the corresponding rectangular cross section plus the direct shear stress:

$$\tau_{\text{nom}} = \frac{Pd}{\alpha bh^2} + \frac{P}{bh} \tag{5.21}$$

where the shape correction factor α is given in Fig. 5.14, b is the long side of rectangular cross section, h is the short side of rectangular cross section, and d is the mean coil diameter.

According to Liesecke (1933),

$$\tau_{\max} = \frac{\beta Pd}{bh\sqrt{bh}} \tag{5.22}$$

where b is the side of rectangle perpendicular to axis of spring, h is the side of rectangle parallel to axis of spring, and β is the Liesecke factor,

$$K_{ts} = \frac{\tau_{\max}}{\tau_{\text{nom}}} \tag{5.23}$$

where K_{ts} is given in Chart 5.16 and α is given in Fig. 5.14.

5.10.3 Helical Torsion Spring

Torque is applied in a plane perpendicular to the axis of the spring in Chart 5.17 (Wahl 1963):

$$K_t = \frac{\sigma_{\max}}{\sigma_{\text{nom}}}$$

For a circular wire with a diameter of $a = h$,

$$\sigma_{\text{nom}} = \frac{32Pl}{\pi a^3} \tag{5.24}$$

For a rectangular wire,

$$\sigma_{\text{nom}} = \frac{6Pl}{bh^2} \tag{5.25}$$

where Pl is the moment (torque; see Chart 5.17), b is the side of rectangle perpendicular to axis of spring, and h is the side of rectangle parallel to the axis of spring.

The effect of pitch angle has been studied by Ancker and Goodier (1958). The correction is small for a pitch angle less than 15°.

5.11 CRANKSHAFT

The maximum stresses in the fillets of the pin and journal of a series of crankshafts in bending are determined by strain gauges (Arai 1965). There were 178 tests made where design parameters were varied systematically in a comprehensive manner. The SCF is defined as $\sigma_{\max}/\sigma_{\text{nom}}$, where $\sigma_{\text{nom}} = M(d/2)/I = M/(\pi d^3/32)$. The strains are measured in the fillet in the axial plane. The smaller circumferential strain in the fillet is not measured.

K_t values are found to be in a good agreement whether or not the moment is uniform or applied by means of concentrated loads at the middle of the bearing areas. The K_t values for the pin and journal fillets are sufficiently close so that an average value over the fillet can be used.

From the standpoint of stress concentration, the most important design variables are the web thickness ratio t/d and the fillet radius ratio r/d. Chart 5.18 and 5.19 give the notation and stress concentration factors, respectively.

K_t is found to be relatively insensitive to the changes in the web width ratio b/d, and the crank "throw" as expressed[3] by s/d over the practical ranges of these parameters. It is also found that K_t is not affected by the cutting of the corners of the web.

Arai points out that as the web thickness t increases to the extreme, K_t should agree with that of a straight stepped shaft. He refers to Fig. 65 of Peterson (1953) and an extended t/d value of 1 to 2. This is an enormous extrapolation in Chart 5.18. It seems that smooth curves can be drawn to the shaft values; however, this does not constitute a verification.

[3]When the inside of the crankpin and the outside of the journal are in line, $s = 0$ (see Chart 5.18). When the crankpin is closer, s is positive (as shown in the sketch). When the crankpin's inner surface is farther away than $d/2$, s is negative.

Referring to the sketch in Chart 5.18, sometimes it is beneficial to recess the fillet fully or partially. It is found that as δ is increased, K_t is increased. However, the designer should examine such an increase against the possibility of using a larger fillet radius, an increase of the bearing area, or a decrease of the shaft length.

An empirical formula is developed by Arai to cover the entire range of tests:

$$K_t = 4.84C_1 \cdot C_2 \cdot C_3 \cdot C_4 \cdot C_5 \tag{5.26}$$

where

$$\begin{aligned}
C_1 &= 0.420 + 0.160\sqrt{[1/(r/d)] - 6.864} \\
C_2 &= 1 + 81\{0.769 - [0.407 - (s/d)]^2\}(\delta/r)(r/d)^2 \\
C_3 &= 0.285[2.2 - (b/d)]^2 + 0.785 \\
C_4 &= 0.444/(t/d)^{1.4} \\
C_5 &= 1 - [(s/d) + 0.1]^2/[4(t/d) - 0.7]
\end{aligned}$$

No literature has been found on the SCFs of crankshafts in torsion loading.

5.12 CRANE HOOK

A crane hook is another case of curved bars. Pilkey (2005) develops a generally applicable procedure for tensile and bending stresses in crane hooks. Wahl (1946) provides a simple numerical method, which is used to obtain the value of K_t as 1.56 in a typical example of a crane hook with an approximately trapezoidal cross section.

5.13 U-SHAPED MEMBER

The case of a U-shaped member subjected to a spreading type of loading has been investigated photoelastically (Mantle and Dolan 1948), and the results are included in Charts 5.20 and 5.21.

The location of the maximum stress depends on the proportions of the U member and the position of the load. For variable back depth d, for $b = r$, and for the loads applied at the distance of L with one to three times of r from the center of curvature (Chart 5.20), the maximum stress occurs at position B for a small value of d, and it occurs at position A for a large value of d. The K_t values are defined by Mantle and Dolan (1948) as:

For position A,

$$K_{tA} = \frac{\sigma_{\max} - P/a_A}{M_A c_A / I_A} = \frac{\sigma_{\max} - P/hd}{6P(L + r + d/2)/hd^2} \tag{5.27}$$

where d is the back depth (Chart 5.20), b is the arm width ($= r$), c_A is the distance of the centroid of the cross section $A - A'$ to the inside edge of the U-shaped member, a_A is the area of the cross

section $A - A'$, M_A is the bending moment at the cross section $A - A'$, I_A is the moment of inertia of the cross section $A - A'$, h is the thickness, r is the inside radius ($= b$), and L is the distance from line of application of load to center of curvature.

For position B,

$$K_{tB} = \frac{\sigma_{\max}}{M_B c_B / I_B} = \frac{\sigma_{\max}}{P(L + l)c_B I_B} \tag{5.28}$$

where I_B is the moment of inertia of the cross section $B - B'$, c_B is the distance from the centroid of the cross section $B - B'$ to the inside edge of the U-shaped member, l is the horizontal distance from the center of curvature to the centroid of the cross section $B - B'$, and M_B is the bending moment at the cross section $B - B'$. In the case of position B, the angle θ (Chart 5.20) is found to be close to 20°.

Where the outside dimensions are constant, $b = d$ and r varies, causing b and d to vary correspondingly (Chart 5.21), the maximum stress occurs at position A, except for a large value of r/d. Chart 5..21 gives the values of K_t for a condition where the line of load application remains the same.

5.14 ANGLE AND BOX SECTIONS

A great deal of effort has been put on beam sections in torsion (Lyse and Johnston 1935; Pilkey 2005). Chart 5.22 shows the mathematical results by Huth (1950) for angle and box sections. For box sections, the values given are valid only when a is large in comparison to h, 15 to 20 times as great. The bending of angle sections can be approximated based on the results on knee frames (Richart et al. 1938). Pilkey (2005) provides the formulas of stresses for numerous other cross-sectional shapes.

5.15 CYLINDRICAL PRESSURE VESSEL WITH TORISPHERICAL ENDS

Chart 5.23 is for a cylindrical pressure vessel with torispherical caps based on the photoelastic data by Fessler and Stanley (1965). The maximum stresses used in the K_t factors are in the longitudinal (meridional) direction. The nominal stress used in Chart 5.23 is $pd/4h$, which is the stress in the longitudinal direction in a closed cylinder subjected to pressure p referring to the notation in Chart 5.28. Although the K_t factors for the knuckle are for $h/d = 0.05$ (or adjusted to that value), Fessler and Stanley (1965) find that K_t increases very slowly with an increase of thickness.

Referring to Chart 5.28, the maximum K_t is at the crown above lines *ABC* and *CDE*. Between lines *ABC* and *FC*, the maximum K_t is at the knuckle. Below line *FE*, the maximum stress is the hoop stress in the straight cylindrical portion.

Design recommendations by ASME (1971) are given in Chart 5.23. These include r_i/D not less than 0.06, R_i/D not greater than 1.0, and r_i/h not less than 3.0. Finally, Fessler and Stanley (1966) given a critical evaluation of stress analyses in pressure vessels with torispherical ends.

5.16 WELDS

Many structures, such as offshore structures, are constructed with tubular members. Wave forces on offshore structures lead to variable loading on the structures and create the need for fatigue design of the joints. Although there have been experimental studies, most of these SCFs have been generated using finite elements. Numerous works have been reported on the SCFs of tubular joints. Saini et al. (2016) provide a review of existing works on the SCFs of tubular and non-tubular joints for design of offshore installations, and they discuss existing works based on the classifications of joint types in Fig. 5.15 (Saini et al. 2016).

Pang et al. (2009) use the experimental method to determine the SCFs of toes and roots of dragline tubular joints subjected to tension or compression forces in the main chord. Ye et al. (2012) present the experimental study to determine the SCFs and the stochastic characteristics for a typical welded steel bridge T-joint. Yang et al. (2015) investigate the SCFs for tubular N-joints with negative large eccentricity under compressive loads in vertical braces.. Gho and Gao (2004) use the MARC software to investigate SCFs for completely overlapped tubular K(N)-joints under

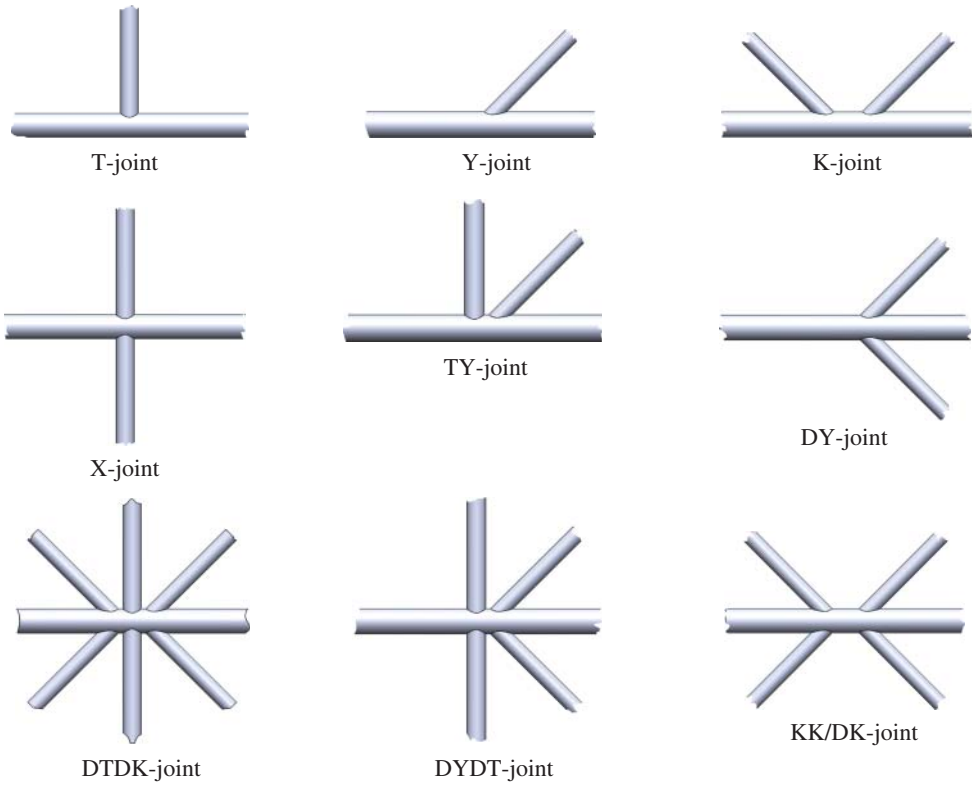


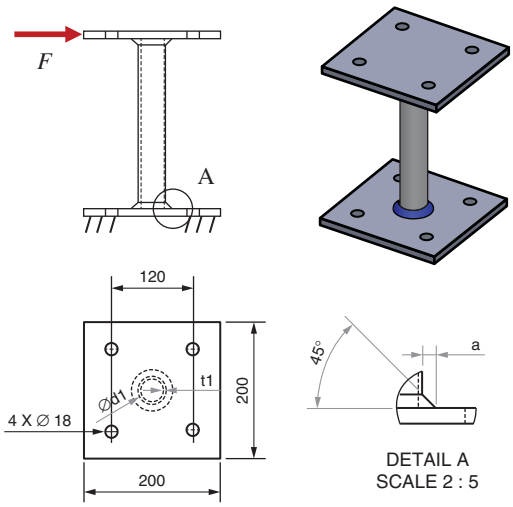
Figure 5.15 Classification of joint types by Saini et al (2016).

lap brace axial compression. They create 192 FEA models of joints in the parametric study, and find that the wall thickness ratio of brace and chord is most crucial to SCFs, and the maximum SCF occurs on the brace saddle near the lap brace. In addition, they find that the gap on the brace surface between the outer surfaces of the chord and the lap brace affects the SCFs greatly. Gho et al. (2003) runs a full-scale experimental test on a uniplanar overlapping K-joint to validate analytical results and compare with existing parametric formulas. Gho and Gao (2004) and Gao et al. (2007) propose the parametric equations to calculate the SCFs for completely overlapped tubular joints subjected to an in-plane bending load. The equations are developed based on the results from 5184 simulation models. It is found that the maximum SCF occurs at the crown heel of lap brace in the bending plane.

A few of referenced parametric formulas for solving stress concentrations in tubular members are originated from Kuang et al. (1975), Wordsworth (1981), Wordsworth and Smedley (1978), and Efthymiou and Durkin (1985). Morgan and Lee (1997, 1998) propose the formulas of the SCFs for tubular K-joints subjected to balanced axial loading and out-of-plane bending, respectively. Smedley and Fisher (1991) gives a comprehensive summary of the parametric solutions for simple tubular joints. They assess available methodologies in determining SCFs in tubular joints and derive the parametric equations to reduce the anomalies in existing methods. Fung et al. (2002) study the tubular T-joints reinforced with gussets ("doubler" plates) and perform a parametric study by varying geometric parameters such as wall thickness and diameter. The reinforced and unreinforced tubular T-joints are compared to prove that the SCFs in reinforced T-joints are lower. Nie et al. (2017) suggest using an additional bugle plate to stiffen the joints of chord and braces. Such stiffened joints are called bulge formed joints, and they develop parametric equations to calculate SCFs of the joints subjected to balanced axial loads. Woghiren and Brennan (2009) investigate the SCFs of KK joints with multiplanar stiffeners in the structure. Choo et al. (2005) and van der Vegte et al. (2005) find the significant strength enhancements for reinforced T-joints by finite element studies. Morgan and Lee (1998) use the finite element analysis (FEA) method to perform a parametric study on the SCFs of tubular K-joints. Dijkstra et al. (1988) provides some favorable results comparing finite element basic load cases such as axial load on the braces and in-plane bending moment with the experiments and the parametric formulas for T-joints and K-T joints. Brennan et al. (2000) create the FEA models for 80 weld toe T-butt plates subjected to tensional and bending loads, and the design variables include weldments angles and attachment widths, and weld root radii. They represent the SCFs in a parametric form, and they extend the developed equations to calculate the SCFs of skewed T-joints.

Romeijn et al. (1993) provide the guidelines in using FEA to model weld shapes, boundary conditions, extrapolations, and torsional brace moments. Later, Romeijin and Wardenier (1994) use the FEA method for the parametric studies on uniplanar and multiplanar welded tubular joints to address the relationships of stress and strain concentration factors. Lee and Bownes (2002) use the T-butt solutions to calculate the stress intensity factors for the tubular joints. They find that all of the design variables for weld angle, weld toe grinding, bend angle, and chord wall thickness affect the fatigue life of welds, and their results are validated by an experimental fatigue database.

Krscanski and Turkalj (2012) indicate that many major factors affecting the fatigue life of products are at the component level; they model the T-joints with welded fillets. T-joints in the



(a) T-joint notation

T-joint	plate	d_i x t_i
1	200 mm x 200 mm x 10 mm	ϕ48.3 mm x 3.2 mm
2		ϕ42.4 mm x 2.6 mm
3		ϕ42.4 mm x 2.0 mm

(b) Dimensions of three types

SCF	$K_{f,\ FEA}$	$K_{f,\ notspot}$	$K_{f,\ exp}$
1	1.47-1.58	1.61-1.73	0.9-1
2	1.63-1.64	1.67-1.67	1.4-1.5
3	1.63-1.64	1.71-1.71	1.3-1.4

(c) Fatigue stress concentration factors (SCF)

Figure 5.16 Stress concentration factors of T-joints. (Mashiri and Zhao 2006; Krscanski and Turkalj 2012)

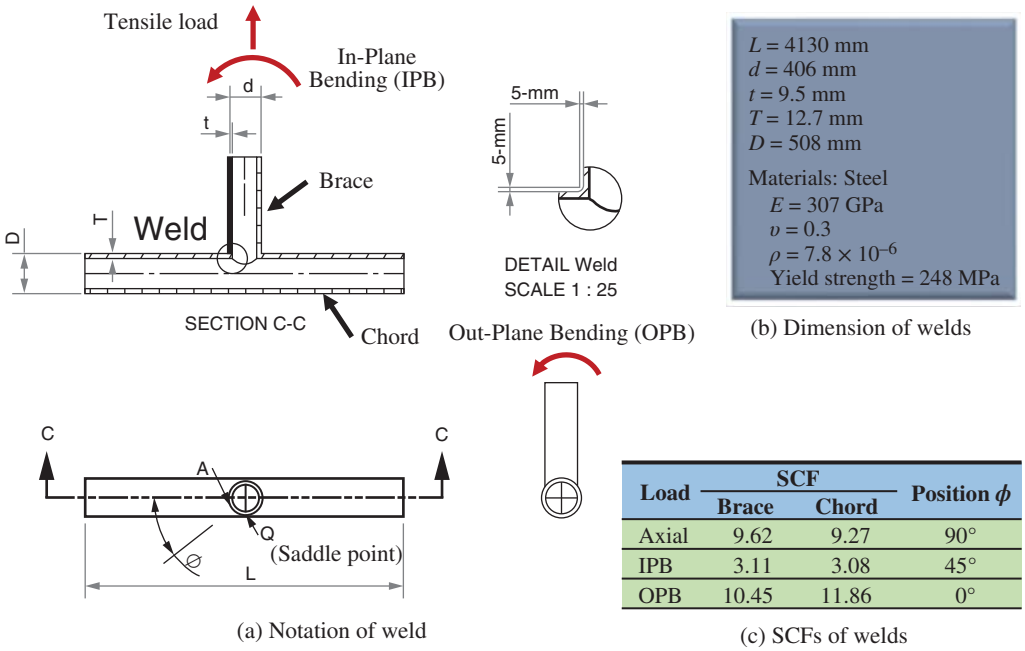
discussion consist of circular hollow section (CHS) and a plate. They find that stresses are much higher than the interpolated from the experimental data. Fig. 5.16*a* shows the notation of the T-joint they have investigated, and Fig. 5.16*c* gives the comparison of the results from FEA and experiments for the dimensions of T-joints specified in Fig. 5.16b.

N'Diaye et al. (2009) used FEA to predict the location of hot-spot stresses in the welds subjected to the combined axial, in-plane bending, out-plane bending, and dynamic loads. They find that the hot-spot stresses (HSS) occur to the crown and saddle points. When a dynamic load is applied, the SCFs decrease on the brace and chord members but increase considerably in the notch. The conclusion is drawn from the simulation of the model shown in Fig. 5.17a subjected to the combination of axial load, in-plane bending, and out-plane bending. Fig. 5.17b gives the dimensions and material properties, and Fig. 5.17c shows the maximum SCFs in the brace and chord members and the positions where the maximum SCFs occur.

Ahmadia et al. (2012) create 118 FEA models to investigate the effect of geometrical parameters on the SCFs along the weld toe of the intersection between the outer brace and the chord on the chord-side. Note that the chord is internally ring-stiffened and the K-joint and it is subjected to balanced axial loads as shown in Fig. 5.18. A nonlinear regression analysis is applied on the FEA results to obtain the following equations of SCFs occurring to the critical areas specified in Fig. 5.18c (Ahmadia et al. 2012):

Toe (out brace, compression):

$$\left.\begin{aligned} SCF &= 0.675\tau^{0.895}\gamma^{0.465}\beta^{0.345}\eta^{-0.477}\theta^{0.189}(1 - 0.538\,\eta\tau - 0.137\,\eta\gamma + 5.385\,\eta\beta + 1.322\,\eta\theta) \\ R^2 &= 0.987 \end{aligned}\right\} \tag{5.29}$$



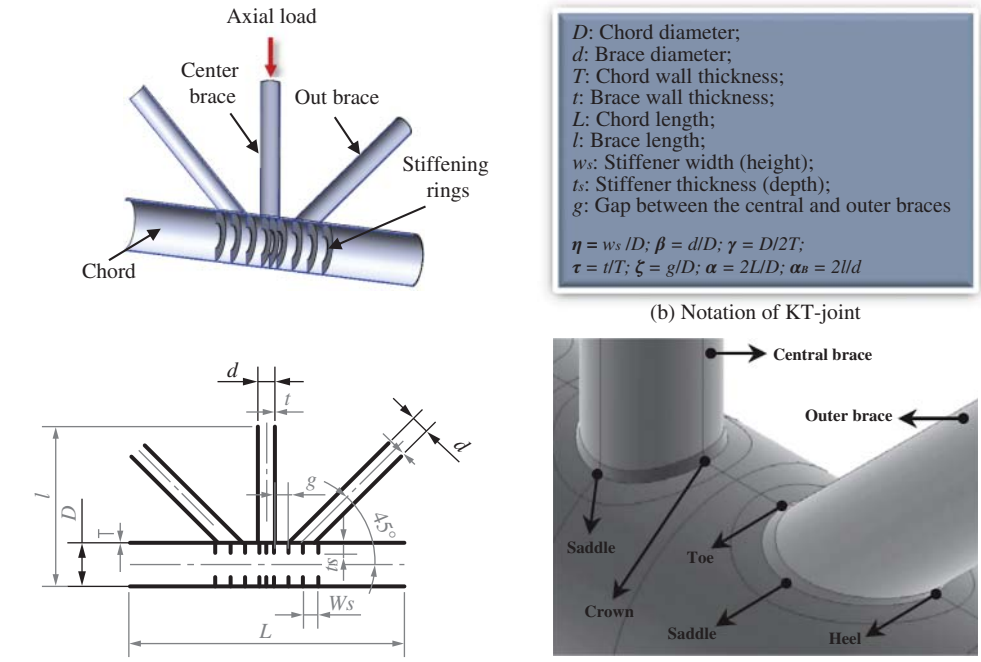
(a) Notation of weld

(b) Dimension of welds

Load	SCF		Position ϕ
	Brace	Chord	
Axial	9.62	9.27	90°
IPB	3.11	3.08	45°
OPB	10.45	11.86	0°

(c) SCFs of welds

Figure 5.17 Geometry and SCFs of weld subjected to a combined load. (N'Diaye et al. 2009)



(a) Geometry and dimensions

(b) Notation of KT-joint

(c) Enlarged critical areas of joints

Figure 5.18 Stiffened KT-joint subjected to balanced axial loading. (Ahmadia et al. 2012)

Saddle (out brace, compression):

$$\left.\begin{array}{l} SCF = 0.060\tau^{0.569}\gamma^{0.925}\beta^{0.367}\eta^{-0.908}\theta^{1.669} \\ R^2 = 0.944 \end{array}\right\} \tag{5.30}$$

Heel (out brace, compression):

$$\left.\begin{array}{l} SCF = 0072\tau^{0.660}\gamma^{0.828}\beta^{0.690}\eta^{-0.807}\theta^{1.094}(1 + 2.902\ \eta\tau - 0.255\ \eta\gamma - 4.230\ \eta\beta + 6.242\ \eta\theta) \\ R^2 = 0.969 \end{array}\right\} \tag{5.31}$$

Toe (out brace, tensile):

$$\left.\begin{array}{l} SCF = 0.131\tau^{0.951}\gamma^{0.505}\beta^{0.186}\eta^{-0.792}\theta^{0.725}(1 - 8.463\ \eta\tau + 0.13749\ \eta\gamma + 4.117\ \eta\beta \\ \qquad +2.994\ \eta\theta) \\ R^2 = 0.965 \end{array}\right\} \tag{5.32}$$

Saddle (out brace, tensile):

$$\left.\begin{array}{l} SCF = 0.032\tau^{1.143}\gamma^{0.446}\beta^{-1.168}\eta^{-0.916}\theta^{1.714}(1 - 14.411\ \eta\tau + 0.178\ \eta\gamma + 59.634\ \eta\beta \\ \qquad -10.621\ \eta\theta) \\ R^2 = 0.915 \end{array}\right\} \tag{5.33}$$

Heel (out brace, tensile):

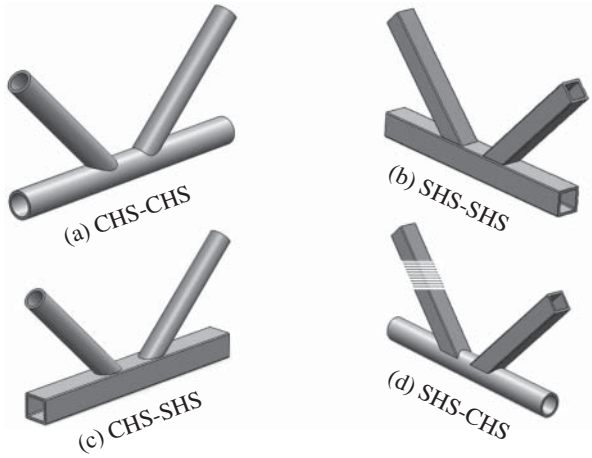
$$SCF = 2.00 \tag{5.34}$$

Note that the unit of θ in the above equations is in radians, and R^2 is adopted to make the correction when the details of complex nature of the problem are available (Ahmadia et al. 2012).

The same method is applied to determine the SCFs of the same type of KJ-joints subjected to the in-plane bending loads (Ahmadi et al. 2016). In another publication of their works, the SCFs of the similar welds called DKT joints are discussed (Ahmaid et al. 2011).

K-joints can be formed differently depending on the geometric shapes of braces and chords. Chen et al. (2017) investigate the SCFs of four different K-joints consisting of circular chord and square braces as shown in Fig. 5.19. In addition, three design variables under considerations are β for the ratio of brace side length and chord diameter, 2γ for the ratio of chord diameter to chord thickness, and τ for the ratio of brace thickness and chord thicknesses. However, their conclusions seem suspicious since SCFs of toe points in all of five specimens are below 0.4. In other words, it does not make practical sense to investigate SCFs on the toe points of K-joints subjected to the axial loading conditions that they propose.

As shown Fig. 5.20, Cheng et al. (2015) investigate the impact of the joining orientations on the SCFs and fatigue resistance. Subjected to the out-the-plane bending, the predicted fatigue lives of structural members are longer than those from the other prediction formulas, which show that the formulas for the conventional joints can be used to estimate the fatigue lives of square bird-beak



CHS – Circular Hollow Section SHS – Square Hollow Section

Figure 5.19 Different K-joints consisting of circular chord and square braces. (Chen et al. 2017)

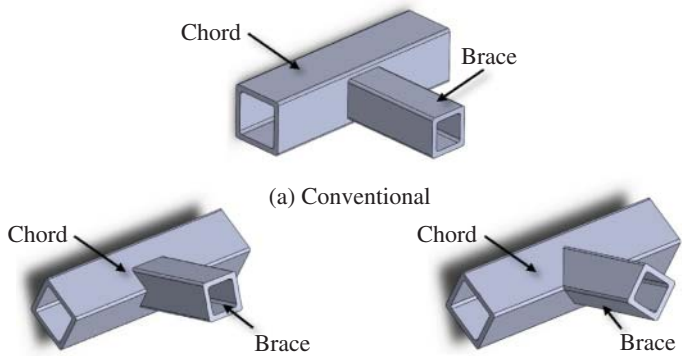


Figure 5.20 Square bird-beak T-joints with square hollow section. Cheng et al. (2015)

joints if the hot spot stress ranges have been properly determined. Tong et al. (2015) propose the formulae to calculate SCFs of T-joints with diamond bird beak square hollow sections subjected to axial and bending loads in both of brace and chord.

Feng and Young (2013) investigate the SCFs of tubular X-joints of square hollow sections with cold-formed stainless steel. The materials under investigation include duplex and high strength austenitic and normal strength stainless steel (AISI 304). They find that the design formulae by Zhao et al. (2001) for carbon steel tubular X-joints are nonconservative, and they propose new design formulae for the calculation of SCFs instead. Fig. 5.21 shows the representation of an

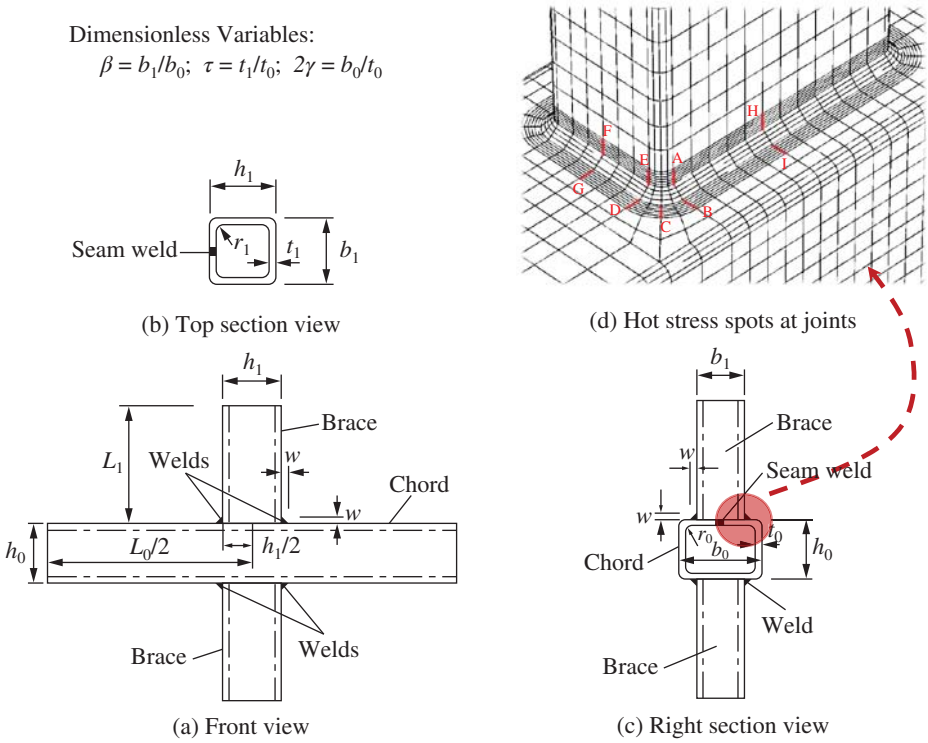


Figure 5.21 Description of X-joint and hot stress spots (Feng and Young 2013)

X-joint with the specified hot stress spots (*A*-*I*), and the following equation is proposed to calculate SCFs on these spots,

$$SCF = (a + b \cdot \beta + c \cdot \beta^2 + d \cdot (2\gamma))(2\gamma)^{(e+f\cdot\beta+g\cdot\beta^2)} \cdot \tau^h \tag{5.35}$$

where the definitions of the dimensionless variables are given in Fig. 5.21 and the corresponding coefficients are given in Table 5.3.

TABLE 5.3 Coefficients for SCFs of X-joints of cold-formed steel with square hollow sections (Feng and Young 2013)

Hot Stress Spots		*a*	*b*	*c*	*d*	*e*	*f*	*g*	*h*
Brace	A/E/F	0.725	–2.000	2.000	–0.0025	0.270	4.350	–4.200	0.250
	H	1.700	–5.000	5.000	–0.0015	–0.250	4.480	–4.200	0.500
Chord	B/I	0.191	–1.276	1.856	–0.0002	4.288	–3.800	–0.155	0.800
	C	0.015	0.250	–0.250	–0.0002	1.500	0.788	–0.950	0.500
	D/G	0.075	–0.300	0.540	0.0003	1.200	1.800	–2.700	0.300

5.17 PARTS WITH INHOMOGENEOUS MATERIALS OR COMPOSITES

With the same geometry, loading, and type of discontinuities, the composite materials demonstrate different stress distribution from that of homogeneous materials. The homogeneity of the materials affects SCFs. Kubair and Bhanu-Chandar (2008) investigate the impact of the inhomogeneity on stress distribution for a composite plate with circular hole. The design variables of inhomogeneous materials are the intrinsic inhomogeneity length scale, the modulus ratio and the power-law index of functional graded materials. Their results show that the SCF is reduced when the modulus of elasticity progressively is increased away from the hole; while the angular position with the maximum tensile stress is not affected. The order of the significance of the impact on the SCF is the power-law index, the variation of inhomogeneity length scale, and finally, the modulus ratio.

Functionally graded materials are widely used in thermal barrier coatings of gas turbine engines, rocket nozzles, and smart structures. Enab (2014) draws the similar result that the SCFs in functional graded plates have been reduced considerably in the plate with elliptic holes subjected to biaxial loadings. Zappalorto and Carraro (2015) present an engineering formula to calculate SCFs of orthotropic notched platform under tensile loads; the SCF of composite is a function of the elastic modules and SCFs of the corresponding isotropic materials.

Kumar et al. (2016) investigate the stress concentration of orthotropic laminates with a circular hole subjected to uniaxial loads. The simulations in Ansys APDL shows that the SCF depends on the orientation of fibers as well as material properties for orthotropic laminates. The SCF increases when the ratio of axial Young's modules is increased (E_y/E_x) and the Poisson ratio (μ_{xy}) is decreased.

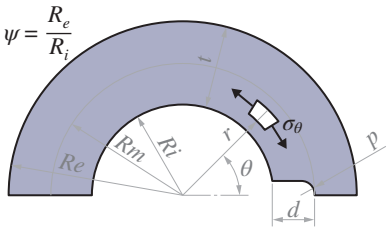
5.18 PARTS WITH DEFECTS

Teran et al. (2013) propose a methodology to evaluate the SCFs in the grinded regions of T–butt welded connections subjected to a bending load; the grinding operation is performed to remove cracking materials at the weld toe of the connections.

de Carvalho (2005) evaluates the SCFs for a pressurized cylinder with a radial U-notch along its length. The design variables include a dimensionless ψ for the ration of the external to internal radii, the length of the U notch, and the thickness of the vessel. Fig. 5.22*a* shows the geometry and dimensions of the vessels, and Fig. 5.22*b* provides the calculated SCFs for different values of ψ and (d/t).

Carbon steel pipes for nuclear power plants are designed to withstand many hypothetical accidents. In the operation, the pipes with flaws are detected and assessed for continued plant operation. One type of flaw is a blunt flaw of local wall thinning caused by erosion or corrosion. Kim and Son (2004) discuss the impact of defect geometries on the SCFs of pipes with wall thinning shown in Fig. 5.23. The considered loading condition is a combination of internal pressure and bending over the structure.

Existing works in mechanical components mainly care the planar flaws such as pores in welds due to lack of fusion, undercuts, and groove-shaped localized corrosion. Furthermore, volumetric flaws such as porosity, cavities, solid inclusions should be modeled as two-dimensional or



(a) Geometry with U-notch

ψ	K_t
1.26	$K_t^{1.26} = 1.81 + 18.84\left(\frac{d}{t}\right) - 17.24\left(\frac{d}{t}\right)^2 + 57.68\left(\frac{d}{t}\right)^3 - 20.83\left(\frac{d}{t}\right)^4$
1.52	$K_t^{1.52} = 2.35 + 29.31\left(\frac{d}{t}\right) - 28.87\left(\frac{d}{t}\right)^2 + 58.06\left(\frac{d}{t}\right)^3 - 20.83\left(\frac{d}{t}\right)^4$
2.00	$K_t^{2.00} = 3.40 + 33.10\left(\frac{d}{t}\right) - 13.07\left(\frac{d}{t}\right)^2 - 17.87\left(\frac{d}{t}\right)^3 - 45.83\left(\frac{d}{t}\right)^4$
3.00	$K_t^{3.00} = 4.81 + 48.45\left(\frac{d}{t}\right) - 106.1\left(\frac{d}{t}\right)^2 + 176.76\left(\frac{d}{t}\right)^3 - 87.5\left(\frac{d}{t}\right)^4$

(b) SCFs for different dimensions

Figure 5.22 SCFs of circular vessel with a radial U notch (de Carvalho 2005).

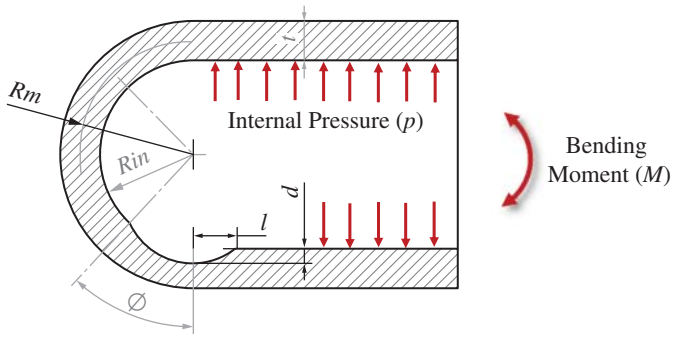


Figure 5.23 A pipe with local wall thinning, subject to internal pressure p and bending moment M (Kim and Song 2004).

three-dimensional flaws, so that the fracture mechanics concept be used to evaluate the safety of mechanical design. Impurities and the inclusions cause the stress concentration of the composites subjected to external loads. Chen (2016) investigates the type of impurities represented by cracks where the material properties of cracks are different from that of the matrix. The cracks are modeled as embedded inclusions with elliptic shapes, and the maximum SCFs occur at the crown points. The obtained SCFs are used to determine the stress intensity factors of cracks. Livieri and Segala (2016) derive the equations to estimate stress intensity factors along the whole borders of embedded elliptical cracks in cylindrical and spherical vessels subjected to uniform internal pressure.

Pachound et al. (2017a,b) indicate that when high-strength steels are used in pressure tunnels and shafts, the joints by welds are subjected to the risk of hydrogen induced cold cracking in base materials. They observe that the longitudinal butt welds are critical regions when the products are loaded transversely, and they develop parametric equations for stress intensity factors. These equations show that the weld profile has a significant influence on stress intensity for semielliptical surface cracks; while an embedded elliptical crack has ignorable influence on stress intensity within the range of relative crack depth in their study.

Bihar et al. (2015) develop an empirical method for the calculation of SCFs for a pair of equally sized spherical cavities embedded in a large continuum in a three-dimensional space. The data

of SCFs can be used to evaluate the effect of the pores on the material strength and the probable location of the pores that will initiate a fatigue crack. The casting with two pores is modeled in Fig. 5.24, and the design variables include the inter-cavity distance and the orientation of the intercavity axis with respect to the loading direction on the SCFs. Table 5.4 provides the SCFs for the given values of these parameters. Bidhar et al. (2015a,b) further extend their investigation of the SCFs for the castings with unequal-size cavities.

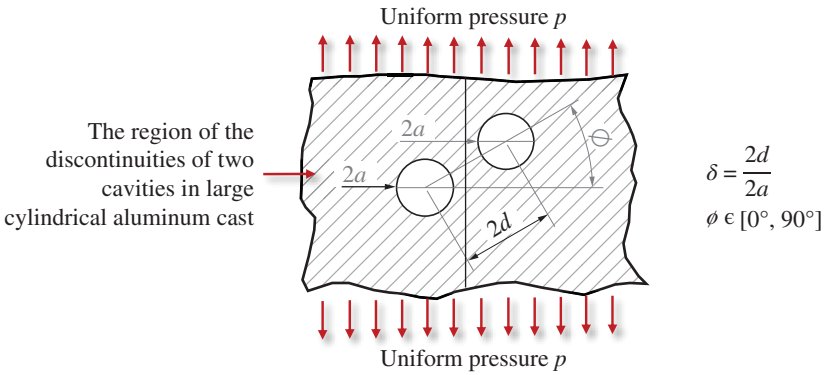


Figure 5.24 Layout of a pair of identical spherical cavities in an infinite continuum (Bidhar et al. 2015a,b).

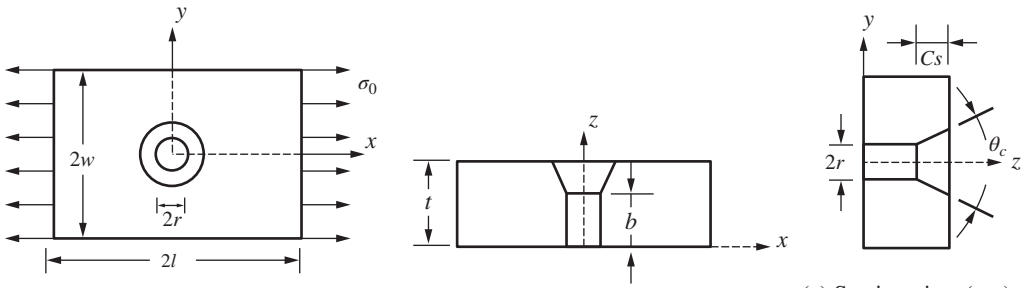
TABLE 5.4 SCFs of Aluminum Cast with Due Spherical Cavities (Bidhar et al. 2015a,b)

	Orientation Angle ϕ							
δ	*0°*	*20°*	*30°*	*40°*	*45°*	*50°*	*60°*	*90°*
1.0050	9.1372	7.8650	6.5419	5.0536	4.2170	3.3519	2.1802	1.9882
1.0100	6.9827	6.0289	5.2504	4.0170	2.3793	2.7346	2.1582	1.9261
1.0200	5.3557	4.7115	4.1727	3.2804	2.8561	2.3143	2.1069	1.9386
1.0400	4.1166	3.7903	3.3866	2.7145	2.3672	2.1450	2.0688	1.9051
1.0600	3.5608	3.3912	2.9996	2.4793	2.2161	2.1423	2.0872	1.9288
1.1000	3.0223	2.9421	2.7129	2.3183	2.1165	2.1395	2.0775	1.9163
1.2000	2.4312	2.4553	2.4599	2.1815	2.1110	2.1083	2.0937	1.9421
1.3000	2.4025	2.3023	2.4918	2.1382	2.1067	2.1089	2.0866	1.9414
1.4000	2.1445	2.3721	2.3736	2.1394	2.1458	2.0945	2.0821	1.9627
2.0000	2.1584	2.1580	2.1580	2.1580	2.1580	2.1580	2.1580	2.1580

Parameters and modeling conditions:
The radius of cylinder (D) is at least 40 times of the radius (a) of the cavities.
Two cavities have an equal radius of a.
The central distance of two cavities is defined as $2d$.
The dimensionless distance δ is defined as $\delta = 2d/2a$.
The tensile load is set as uniform pressure of $\sigma_0 = 10$ MPa, the materials is set as aluminum alloy with a Young's modules of 76 GPa and a Poisson's ratio of 0.3.

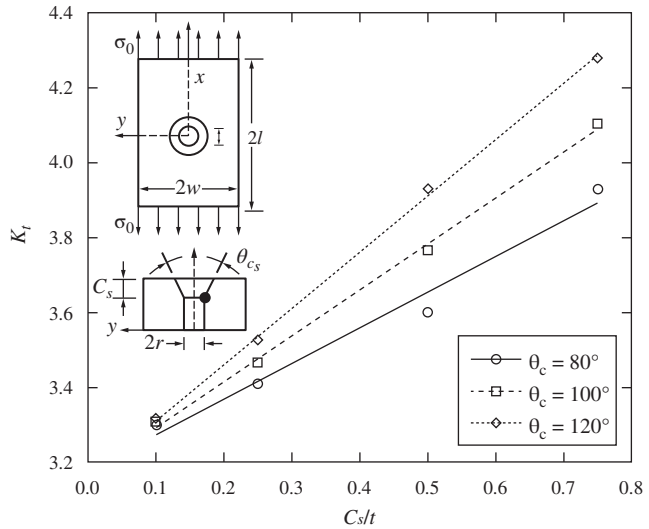
5.19 PARTS WITH THREADS

Joining is a common process in structural engineering and the quality of joints affects the strength of the assembled structure greatly. Riveting is often used to join thin components such as plates and shells; while rivets normally produce the discontinuities through the thickness of joined objects in the form of countersunk holes. Darwish et al. (2012) modify the equations of SCFs for the plates with centered countersunk holes shown in Fig. 5.25, and the plot for SCF prediction is shown in Fig. 5.26.



(a) Front view (x-y) (b) Section view (x-z) (c) Section view (y-z)

Figure 5.25 Configuration of countersunk hole (Darwish et al. 2012).



$$K_h = 3 + \frac{1 + \left(\frac{r}{w}\right)^{1.4}}{1 - \left(\frac{r}{w}\right)^{0.5}}$$

$$K_{ss} = 1 + \frac{0.3\left(\frac{t}{r}\right)}{5 + \left(\frac{t}{r}\right)^2}$$

$$K_{Cs} = 1 + \left(\frac{r}{w}\right)^{1.8}\left(\frac{t}{r}\right)\left(\frac{C_s}{t}\right) + 0.28\left(\frac{t}{r}\right)^{0.1}\left(\frac{C_s}{t}\right) + 0.1\left(\frac{t}{r}\right)^{1.5}\left(\frac{C_s}{t}\right)^2$$

$$K_{\theta c} = 1 + m(\theta_c - 100°)$$

$$K_t = K_h \times K_{SS} \times K_{Cs} \times K_{\theta c}$$

Figure 5.26 SCF of countersunk hole (Darwish et al. 2012).

Pipe drill tools are used in oil wells and they consist of joined pipes, which transfer the applied torque from motors to the bit at the well bottom. To form a drill string, these pipes are connected by means of the threaded connections. Considerable stresses are expected in the tool joint teeth subjected to axial loading. Shahani and Sharifi (2009) use the FEA method to analyze the threaded tool joints, and load types under consideration include tension, compression, pure preload, and a combination of above.

5.20 FRAME STIFFENERS

Stress analysis on the connections of the side shells and the stiffeners of web frames are critical to ship structures. Inspired by the limitation of existing procedures in calculating SCFs, Parunov et al. (2013) propose a new procedure for extrapolating stresses to the weld toes based on the FEA simulation; note that the total SCF at a critical position is the sum of the SCFs under the axial load and bending loads, which are calculated, respectively. Fig. 5.27 shows the details of stiffener supports under their investigation.

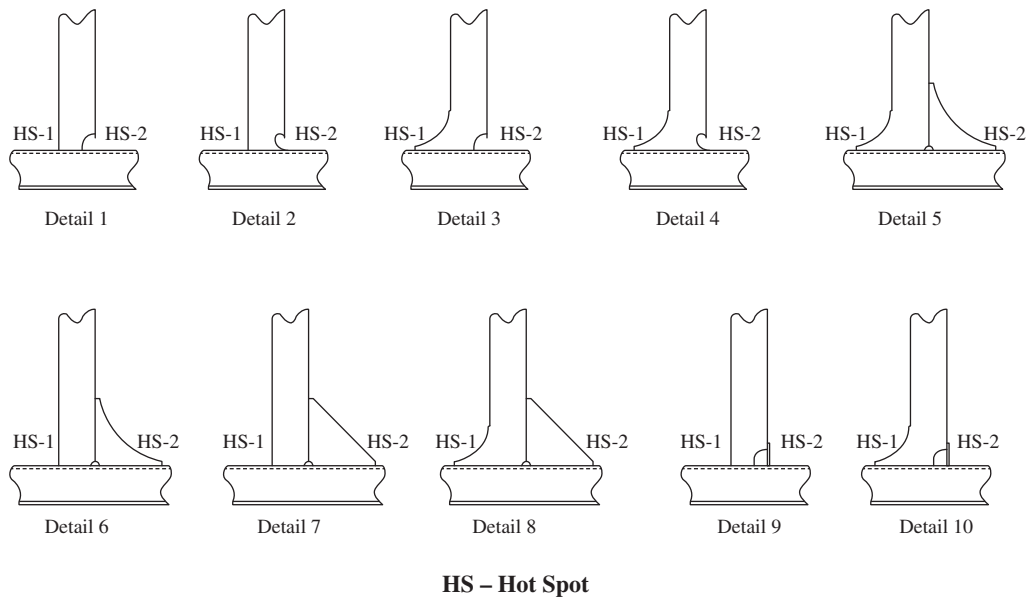


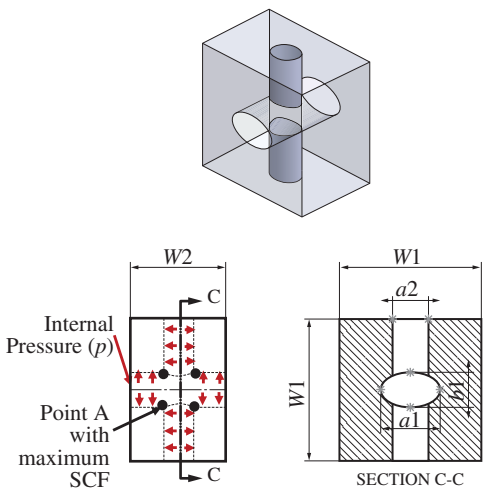
Figure 5.27 Details of stiffen supports in ship structures (Parunov et al. 2013).

5.21 DISCONTINUITIES WITH ADDITIONAL CONSIDERATIONS

Badr (2006) indicated that many engineering components such as valves, pipe connections and fluid ends have cross-bores; he uses FEA to investigate the SCFs for a block with cross-bores shown in Fig. 5.28*a*, and he finds that the maximum tensile stress occurs at the point on the intersections of two bores shown as point A. The corresponding relation of the SCF and geometric parameters are given in Fig. 5.28*b*.

In some applications, grooved or cracked components cannot be replaced economically or practically due to high replacement cost or the practical restrictions. Such circumstances bring the necessity to assess the reliability of products with defected parts. Sunil et al. (2017) investigate the impact of different types of geometric discontinuities on the fatigue lives of the Al6061T6 alloy parts from the perspective of SCFs. They show the results that under uniform axial loads, the elliptical grooved specimen deform plastically with the SCF of 1.4 absorbing a large magnitude of energy; while the V-groove specimen with SCF of 1.73 fails in a brittle manner with relatively negligible deflection.

The SCFs in Chapters 2 to 4 are developed by taking some major design variables; while some variables to be ignored might affect SCFs considerably. When the charts and formulas of the SCFs are used, one has to be cautious to check if the assumptions for these SCFs are violated. Troyani et al. (2004) discuss the cases of rectangular plate with opposite U-shaped notches subjected to in-plane bending. Theoretical SCFs are available; but they do not take into consideration the length as a design variable. As shown in Fig. 5.29, Troyani et al. (2004) use the finite element analysis to find that there exists a threshold value called a transition length. If the actual length of the plate is smaller than a transition length, the theoretical SCFs will not be valid anymore; the actual SCFs are significantly large.



(a) Geometry of block with cross-bores

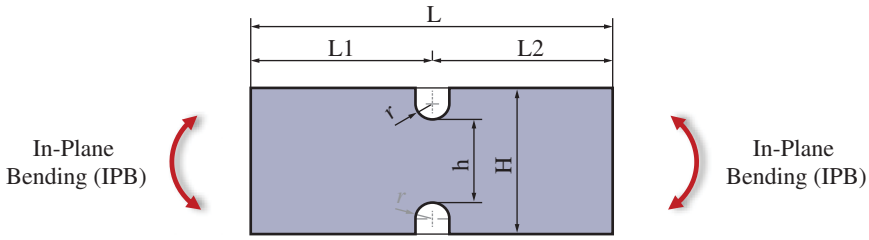
$$K = c_0 + c_1\left(\frac{a_2}{a_1}\right)^2 + c_2\left(\frac{a_2}{a_1}\right)^2 \theta + c_3\theta^2 + c_4\theta^4$$

$$\theta = cos^{-1}\frac{b_1}{a_1}$$

w_1/a_1	c_0	c_1	c_2	c_3	c_4
1.5	7.721	18.300	–12.517	–3.927	0.737
1.75	7.829	8.029	–1.373	–2.478	0.087
2	7.178	6.671	–3.523	–3.391	0.856
2.5	6.481	6.169	–2.701	–4.275	1.891
3	5.564	2.444	–0.875	–1.342	–0.056
5	5.300	2.295	–0.368	–1.433	–0.060

(b) SCFs and correction coefficients

Figure 5.28 SCFs of the block with cross-bores subjected to uniform international pressure p (Badr 2006).



(a) Notation of plate subjected to in-plane bending

L/H	*H/h* = 1.2		*H/h* = 1.5		*H/h* = 2.0	
	Corrected SCF	Error (%)	Corrected SCF	Error (%)	Corrected SCF	Error (%)
>1.0	2.10	-	2.22	-	2.24	-
1.0	2.11	0.4	2.23	0.45	2.24	0
0.8	2.14	1.9	2.28	2.70	2.24	0
0.6	2.26	7.6	2.46	10.8	2.27	1.34
0.4	2.62	24.8	3.11	40.0	2.91	29.9

(b) Notation of plate subjected to in-plane bending

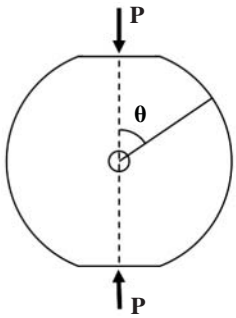
Figure 5.29 SCFs of bended plate affected lengths (Troyani et al. 2004).

In Bahai's work (Bahai 2001) the SCFs of the threaded connections are discussed, and the considered loads include internal preloads, external axial load, and external bending load. The SCF is a function of tooth and coupling geometry and as well as the types and combination of loads.

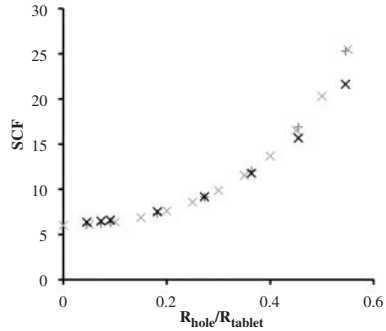
Concrete-filled steel tubes (CFSTs) have the advantages of high strength, high ductility, high stiffness, and full usage of construction materials to gain better fatigue resistance subjected to dynamic loads from waves, wind, and current. Chen et al. (2010) study the SCFs of concrete-filled tubular T-joints subject to both axial loading and in-plane bending. The comparative study with hollow steel tubular T-joint specimens shows the concrete filling effectively reduces the peak stress concentration factors. Tong et al. (2017) conduct experiments and FEA simulations and present the formulae of the SCFs of welds, which are used to join a brace with a circular hollow section (CHS) and a chord with concrete-filled square hollow (CFSHS).

5.22 PHARMACEUTICAL TABLETS WITH HOLES

Mechanical strength is also an important property for medical products, such as pharmaceutical tablets. The design criterion called the Brittle Fracture Index (BFI) is directly related to SCF. Croquelois et al. (2017) observe that existing literatures have contradictory results about the SCF for a disc with a hole subjected to diametrical compression, and they use the numerical simulation to obtain the correct values of SCF as 6, which is shown in Fig. 5.30. It is also applicable for the case of the flattened disc geometry. It is interesting to note that this value of SCF is nearly independent of the hole size if the ratio between the hole and the table diameters is lower than 0.1.



(a) Mode of a compression of tablet with a hole



(b) SCF verse R_{hole}/R_{tablet}

Material properties:	(1) E = 4.4 GPa, υ = 0.25 for spray-dried lactose monohydrate (SDLac) (2) E = 3.7 GPa, υ = 0.23 for anhydrous calcium phosphate (aCP)
Loading conditions:	P = 10 N, displacement = 0.01 mm
Tablet dimensions:	Diameter 11 mm, thickness 3 mm
Ratio of hole and external diameters:	0.045 ~ 0.55
FEA model:	2D shell model in Abaqus 6.13

Figure 5.30 SCF of tablet subjected to diametric compression (Croquelois et al. 2017a,b).

Zappalorto et al. (2011) investigate the impact of different notches on the SCFs of the round bars under torsional loading, and they are able to develop the closed-form relations to correlate generalized stress intensity factors of notch geometry to that of typical parabolic, semielliptic, and hyperbolic notches.

5.23 PARTS WITH RESIDUAL STRESSES

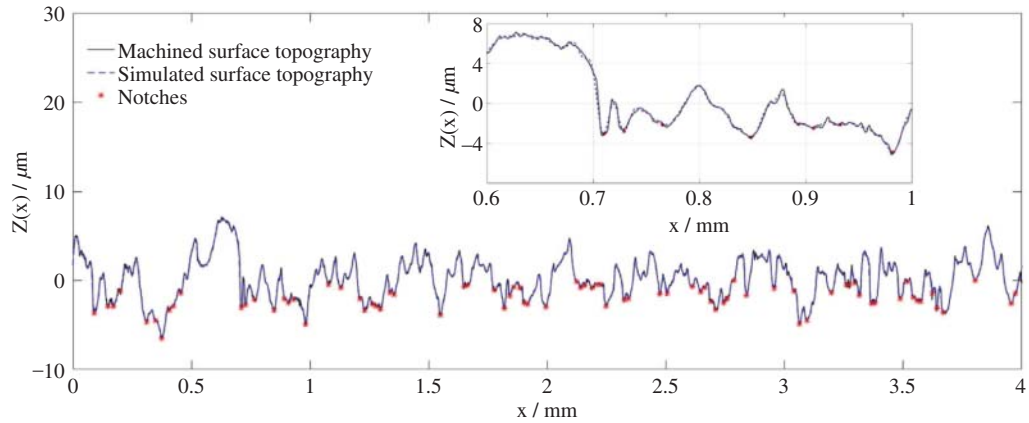
Cao et al. (2013) develop an FEA model to look into the impact of welding temperature on residual stress of K-joints. The nonlinearity of material properties is modeled, and the annealing treatment after the welding process is also considered. The stresses are evaluated under an axial load in two conditions, i.e., (1) with welding residual stress and (2) without welding residual stress. It is found that the difference of the SCFs from two models is less than 10%. It also shows that the residual stress led by welding exceeds the yield stress of the material; but an annealing treatment can reduce welding residual stress greatly.

Jiang and Zhao (2012) also investigate the impact of thermal residual stress on the SCFs. They conduct a comparative study on the joints welded at ambient temperature and preheating temperature of 100 °C, and they examine the differences of stresses at the toes of welds. The conclusion is that the impact of residual stresses depends on the level of stress caused by bending: the greater the bending stress is, the lower the impact of residual stress. They suggest using the residual stress factor to evaluate the thermal impact by welding.

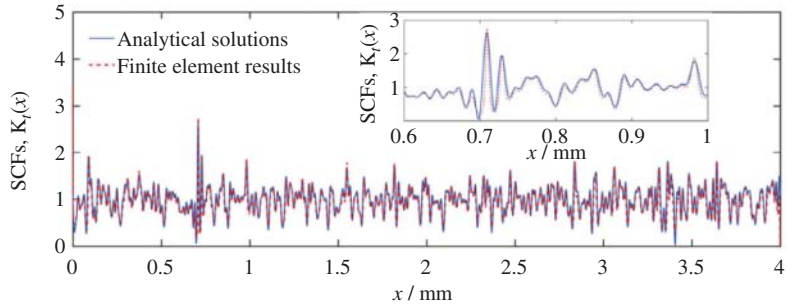
Steam turbine engines in thermal power plants are subjected to frequent startups and load changes. These dynamic loads cause an unsteady temperature distribution with respect to time. Thermal-induced stresses shorten the operating lives of turbine engines. It is necessary to have accurate knowledge of transient thermal stresses at critical positions that are susceptible to failure. Choi et al. (2012) investigate thermal induced SCFs for the inner surface of the casing and valve, which account for geometric variations. FEA models are developed to determine SCFs for the casings and valves, and obtained SCFs are used to estimate the total strain range and assess the low-cycle fatigue life based on the life assessment procedure in Korea.

5.24 SURFACE ROUGHNESS

Surface topography affects the stress distribution. As shown in Fig. 5.31, surface topography can be viewed as geometrical discontinuities at micro-levels. Cheng et al. (2017a, b) represent surface roughness by the means of the Fourier transform, and use the first-order boundary perturbation



(a) Representation of surface roughness (Cheng et al. 2017a)



(b) SCFs of surface topography from FEA and analytical models by Cheng et al. (2017a)

Figure 5.31 Surface topography viewed as geometric discontinuities (Cheng et al. 2017a,b).

approach to derive the stress distribution of specimen with machined surface topography. Further, they use the point method (PM) and line method (LM) in the theory of critical distance (TCD) to derive analytical models of fatigue notch factors for the surfaces with roughness. A finite element analysis (FEA) model is developed to represent surface roughness on sides and give the displacement load at two ends. This FEA model is used to verify the proposed analytical models. The comparison shows a discrepancy of less than 15% for the highest 10 values of SCFs for three machined surface topologies.

In Medina and Hinderliter (2014), surface topology is characterized as the Gaussian distribution of heights and auto correlation length (ACL). They combine the Gao's first-order perturbation method, the Hilbert transform, and an energy conservation principal and relate these methods to the Parseval theorem. The root-mean-square (RMS) value of K_t results in a function of the ratio RMS-roughness to ACL. Medina and Hinderliter (2014) derive the following equation to calculate the SCF for slightly roughened random surfaces:

$$K_t^{RMS} = 1 + 2\sqrt{2}\frac{RMS}{ACL} \tag{5.36}$$

where K_t^{RMS} is the root-mean-square value of the direction of the SCF, ACL is auto correction length, and RMS is the root-mean-square.

A welding process in assembly may create micro-structural heterogeneous zones characterized as macroscopic geometrical discontinuities. These zones are often the origins of stress concentration where the fatigue cracks can be initiated and propagated. Farida et al. (2011) indicate that it is important to study the stress distributions in these zones, and they model the welds with one or two pores subjected to uniaxial tensile stress. Their results include only the information of stress distributions without SCFs.

5.25 NEW APPROACHES FOR PARAMETRIC STUDIES

Parametric equations for the SCF calculation from numerical simulations have their limitations in the scope of applications due to the assumptions made in simulation models. Taking an example of butt-welded joints, SCF formulas need to take into consideration of geometrical stiffness associated with single-V and double-V configurations. Dabiri et al. (2017) develop an artificial neural network (ANN) model trained with a large number of numerical models of butt welds; the new model is developed for a wide range of local weld parameters under axial tension and bending loads. It is able to yield accurate estimations of SCFs for butt-welds and maintained consistency in their prediction in all of the SCF ranges. Wang et al. (2016) adopt Extreme Learning Machine (ELM) to predict fatigue SCFs. The input parameters include tensile strength, yield strength; fatigue strength, theoretical stress concentration factor, notch root radius, samples size and notch fatigue limit, and the outputs are the values of fatigue SCFs. The ELM-based algorithm can be trained through randomly generated parameters of hidden neurons.

Medina (2015) developed analytical equations that can generate the SCFs for a number of shallow irregularities on the surface for the plane of stress condition to the first-order approximation.

With a shallow shape and for any first-order Holder-continuous surface $f(x)$, a number of SCFs for various loads can be generated from,

$$K_t(x) = 1 - 2 \cdot H(f'(x)) \tag{5.37}$$

where $H()$ is the Hibert transform and $f(x)$ is the spatial derivative of $f(x)$ with respect to x, and $f(x)$ describes the surface profile along x.

For an example, by considering a semielliptical notch with a and b for the depth and half-width of the notch, the profile is described as,

$$f(x) = -a\sqrt{1 - \left(\frac{x}{b}\right)^2} * \prod_{2b}(x) \tag{5.38}$$

where $\prod_{2b}(x)$ is the rectangular pulse function as,

$$f(x) = -a\sqrt{1 - \left(\frac{x}{b}\right)^2} * \prod_{2b}(x) = \begin{cases} 1, & |x| < b \\ 0, & elsewhere \end{cases} \tag{5.39}$$

Using Eq. (5.37) and applying the Hibert transform followed by differentiation get,

$$K_t(x) = 1 - 2 \times \begin{cases} -\dfrac{a}{b}, & |x| < b \\ -\dfrac{a}{b} + \dfrac{ax}{b^2\sqrt{\left(\frac{x}{b}\right)^2 - 1}}, & x > b \\ -\dfrac{a}{b} - \dfrac{ax}{b^2\sqrt{\left(\frac{x}{b}\right)^2 - 1}}, & x < -b \end{cases} \tag{5.40}$$

Eq. (5.40) shows the maximum SCF within the notch is $K_t(x) = 1 + 2\frac{a}{b}$, corresponding to $|x| < b$.

In Lee et al. (2011), the Lagrangian interpolation method is integrated with FEA-based simulations to develop the model for the calculation of SCFs of tubular joints. They argue that the Lagrangian interpolation generates more accurate results than that from the parametric regression method.

REFERENCES

Adelfio, B., and DiBenedetto, F., 1970, Forzamento su Appoggio Discontinue (Shrink-fitted ring over discontinous support), *Dis. Macch.*, Palermo, Vol. 3, p. 21.

Ahmadia, H., Lotfollahi-Yaghina, M. A., Yong-Bob, S., and Aminfara, M. H., 2012, Parametric study and formulation of outer-brace geometric stress concentration factors in internally ring-stiffened tubular KT-joints of offshore structures, *Applied Ocean Research*, Vol. 38, pp. 74–91.

Ahmadi, H., Yeganeh, A., Mohammadi, A. H., and Zavvar, E., 2016, Probabilistic analysis of stress concentration factors in tubular KT-joints reinforced with internal ring stiffeners under in-plane bend loads, *Thin-Wallet Structures*, Vol. 99, pp. 58–75.

Aida, T., and Terauchi, Y., 1962, On the bending stress in a spur gear, *Bull Jpn. Soc. Mech. Eng.*, Vol. 5, p. 161.

Ancker, C. J., and Goodier, J. N., 1958, Pitch and curvature corrections for helical springs, *Trans. ASME Appl. Mech. Sect.*, Vol. 80, pp. 466, 471, 484.

ANSI, 1967, Keys and keyseats, *U.S. Standard ANSI B17.1*, American Society of Mechanical Engineers, New York; reaffirmed 1973 and 1987.

Arai, J., 1965, The bending stress concentration factor of a solid crankshaft, *Bull. Jpn. Soc. Mech. Eng.*, Vol. 8, p. 322.

ASME, 1971, *Boiler and Pressure Vessel Code: Pressure Vessels*, Section VIII, American Society of Mechanical Engineers, New York, pp. 18, 27.

AAR, 1950, Passenger car axle tests, *4th Prog. Rep.*, Association of American Railroads, Washington, DC, p. 26.

ASTM, 1952, Symposium on fretting corrosion, *STP 144*, American Society for Testing and Materials, Philadelphia, PA.

Badr, E. A., 2006, Stress concentration factors for pressurized elliptic crossbores in blocks, *International Journal of Pressure Vessels and Piping*, Vol. 83, pp. 442–446.

Bahai, H., 2001, A parametric model for axial and bending stress concentration factors in API drillstring threaded connectors, *International Journal of Pressure Vessels and Piping*, Vol. 78, pp. 495–505.

Baud, R. V., and Peterson, R. E., 1929, Load and stress cycles in gear teeth, *Mech. Eng.*, Vol. 51, p. 653.

Baumeister, T., Ed., 1967, *Marks' Standard Handbook for Mechanical Engineers*, McGraw-Hill, New York, pp. 8, 20, 21, 133.

Bidhar, S., Kuwazuru, O., Shiihara, Y., Utsunomiya, T., Hangai, Y., Nomura, M., Watanabe, I., and Yoshikawa, N., 2015a, Empirical formulation of stress concentration factor around an arbitrary-sized spherical dual-cavity system and its application to aluminum die-castings, *Applied Mathematical Modelling*, Vol. 39, pp. 5707–5723.

Bidhar, S., Kuwazuru, O., Shiihara, Y., Hangai, Y., Utsunomiya, T., Watanabe, I., and Yoshikawa, N., 2015b, Practical application of empirical formulation of the stress concentration facto around equally sized due spherical cavities to aluminum die cast, *Applied Mathematical Modelling*, Vol. 39, pp. 881–893.

Brennan, F. P., Peleties, P., and Hellier, A. K., 2000, Predicting weld toe stress concentration factors for T and skewed T-joint plate connections, *International Journal of Fatigue*, Vol. 22, No. 7, pp. 573–584.

Brown, A. F. C., and Hickson, V. M., 1952–1953, A photoelastic study of stresses in screw threads, *Proc. IME*, Vol. 1B, p. 605; discussion, p. 608.

Candee, A. H., 1941, *Geometrical Determination of Tooth Factor*, American Gear Manufacturers Association, Pittsburgh, PA.

Cao, Y. Meng, Z., Zhang, S., and Tian, H., 2013, FEM study on the stress concentration factors of K-joints with welding residual stress, *Applied Ocean Research*, Vol. 43, pp. 195–205.

Chen, J., Chen, J., and Jin, W.-L., 2010, Experiment investigation of stress concentration factor of concrete-filled tubular T joints, *Journal of Constructional Steel Research*, Vol. 66, pp. 1510–1515.

Chen, Y. Z., 2016, Evaluation of stress intensity factors from stress concentration factors for a crack embedded in dissimilar elliptic inclusion, *Theoretical and Applied Fracture Mechanics*, Vol. 84, pp. 177–182.

Chen, Y., Wan, J., Hu, K., Yang, J., and Chen, X., 2017, Stress concentration factors of circular chord and square braces K-joints under axial loading, *Thin-Walled Structures*, Vol. 113, pp. 287–298.

Cheng, B., Qian, Q., and Zhao, X.-L., 2015, Stress concentration factors and fatigue behavior of square bird-beak SHS T-joints under out-of-plane bending, *Engineering Structure*, Vol. 99, pp. 677–684.

Cheng, Z., Liao, R., Lu, W., and Wang, D., 2017a, Fatigue notch factors prediction of rough specimen by the theory of critical distance, *International Journal of Fatigue*, Vol. 104, pp. 195–205.

Cheng, Z., Liao, R., and Lu, W., 2017b, Surface stress concentration factor via Fourier representation and its application for machined surfaces, *International Journal of Solids and Structures*, Vols. 113–114, pp. 108–117.

Choi, W., Fujiyama, K., Kim, B., and Song, G., 2012, Development of thermal stress concentration factors for life assessment of turbine castings, *International Journal of Pressure Vessels and Piping*, Vol. 98, pp. 1–7.

Choo, Y. S., van der Vegte, G. J., Zettlemoyer, N., Li, B. H., and Liew, J. Y. R., 2005, Static strength of T-joints reinforced with doubler or collar plates: I, Experimental investigations, *J. Struct. Eng.*, Vol. 131, p. 119.

Cox, H. L., and Brown, A. F. C., 1964, Stresses around pins in holes, *Aeronaut. Q.*, Vol. XV, Pt. 4, pp. 357–372.

Coyle, M. B., and Watson, S. J., 1963–1964, Fatigue strength of turbine shafts with shrunk-on discs, *Proc. Inst. Mech. Eng. (London)*, Vol. 178, p. 147.

Croquelois, B., Girardot, J., Kopp, J. B., Cazautets, C., Tchoreloff, P., and Mazel, V., 2017, Breaking pharmaceutical tablets with a hole: reevaluation of the stress concentration factor and influence of the hole size, *Powder Technology*, Vol. 317, pp. 126–132.

Dabiri, M., Ghafouri, M., Raftar, H. R. Rohani, and Bjork, T., 2017, Utilizing artificial neural networks for stress concentration factor calculation in butt welds, *Journal of Constructional Steel Research*, Vol. 138, pp. 488–498.

Darwish, F., Gharaibeh, M., and Tashtoush, G., 2012, A modified equation for the stress concentration factor in countersunk holes, *European Journal of Mechanics A/Solids*, Vol. 36, pp. 94–103.

de Carvalho, E. A., 2005, Stress concentration factors for an internally pressurized circular vessel containing a radial U notch, *International Journal of Pressure Vessels and Piping*, Vol. 82, pp. 517–521.

DeGregorio, G., 1968, Ricerca sul Forzamento delle Corone Dentate (Research on shrunk-on gear rings), *Tech. Ital. Triesta*, Vol. 33, p. 1.

Dijkstra, O. D., Puthli, R. S., and Snijder, H. H., 1988, Stress concentration factors in T and K-T tubular joints using finite element analysis, *J. Energy Resour. Technol.*, Vol. 110, p. 246.

Dolan, T. J., and Broghamer, E. L., 1942, A photoelastic study of stresses in gear tooth fillets, *Univ. Illinois Exp. Stn. Bull.* 335.

Durelli, A. J., and Riley, W. F., 1965, *Introduction to Photomechanics*, Prentice-Hall, Englewood Cliffs, NJ, p. 220.

Efthymiou, M., and Durkin, S., 1985, Stress concentrations in T/Y and gap overlap K-joints, in *Behaviour of Offshore Structures*, Elsevier, Amsterdam, The Netherlands, p. 429.

Enab, T. A., 2014, Stress concentration analysis in functional graded plates with elliptic holes under biaxial loading, *Ain Shams Engineering Journal*, Vol. 5, pp. 839–850.

ESDU, 1981, *Stress Concentrations*, Engineering Sciences Data Unit, London.

Farida, B., Boualem, S., Amin, M. M. E., and Benali, B., 2011, 3-D finite element analysis of stress concentration factor in spot-welded joints of steel: the effect of process-induced porosity, *Computational Materials Science*, Vol. 50, pp. 1450–1459.

Feng, R., and Young, B., 2013, Stress concentration factors of cold formed stainless steel tubular X-joints, *Journal of Constructional Steel Research*, Vol. 91, pp. 26–41.

Fessler, H., and Stanley, P., 1965, Stresses in torispherical drumheads: a photoelastic investigation, *J. Strain Anal.*, Vol. l, p. 69.

Fessler, H., and Stanley, P., 1966, Stresses in torispherical drumheads: a critical evaluation, *J. Strain Anal.*, Vol. l, p. 89.

Fessler, H., Rogers, C. C., and Stanley, P., 1969a, Stresses at end-milled keyways in plain shafts subjected to tension, bending and torsion, *J. Strain Anal.*, Vol. 4, p. 180.

Fessler, H., Rogers, C. C., and Stanley, P., 1969b, Stresses at keyway ends near shoulders, *J. Strain Anal.*, Vol. 4, p. 267.

Frocht, M. M., and Hill, H. N., 1940, Stress-concentration factors around a central circular hole in a plate loaded through pin in the hole, *Trans. ASME Appl. Mech. Sect.*, Vol. 62, pp. A5–A9.

Fung, T. C., Soh, C. K., Chan, T. K., and Erni, 2002, Stress concentration factors of doubler plate reinforced tubular T joints, *J. Struct. Eng*., Vol. 128, p. 1399.

Gao, F., Shao, Y. B., and Gho, W. M., 2007, Stress and strain concentration factors of completely overlapped tubular joints under lap brace IPB load, *Journal of Constructional Steel Research*, Vol. 63, pp. 305–316.

Gho, W. M., Fung, T. C., and Soh, C. K., 2003, Stress and strain concentration factors of completely overlapped tubular K(N) joints, *J. Struct. Eng.*, Vol. 129, p. 21.

Gho, W.-M., and Gao, F., 2004, Parametric equations for stress concentration factors in completely overlapped tubular K(N)-joints, *Journal of Constructional Steel Research*, Vol. 60, pp. 1761–1782.

Gibson, W. H., and Gilet, P. M., 1938, Transmission of torque by keys and keyways, *J. Inst. Eng. Austr*., Vol. 10, p. 393.

Göhner, O., 1932, Die Berechnung Zylindrischer Schraubenfedern, *Z. Ver. Dtsch. Ing.*, Vol. 76, p. 269.

Gregory, R. D., 1968, Stress concentration around a loaded bolt in an axially loaded bar, *Proc. Camb. Philos. Soc., No.* 64, pp. 1215–1326.

Griffith, G. I., and Taylor, A. A., 1917–1918, Use of soap films in solving torsion problems, *Tech. Rep. Br. Adv. Comm. Aeronaut*., Vol. 3, p. 910.

Hetényi, M., 1939a, The application of hardening resins in three-dimensional photoelastic studies, *J. Appl. Phys.*, Vol. 10, p. 295.

Hetényi, M., 1939b, Some applications of photoelasticity in turbine-generator design, *Trans. ASME Appl. Mech. Sect*., Vol. 61, p. A-151.

Hetényi, M., 1943, The distribution of stress in threaded connections, *Proc. Soc. Exp. Stress Anal.*, Vol. 1, No. 1, p. 147.

Heywood, R. B., 1969, *Photoelasticity for Designers*, Pergamon Press, Elmsford, NY, p. 326.

Horger, O. J., 1953, Press fitted assembly, *in ASME Metals Engineering Handbook: Design*, McGraw-Hill, New York, p. 178.

Horger, O. J., 1956, Fatigue of large shafts by fretting corrosion, *Proc. International Conference on Fatigue*, Institute of Mechanical Engineers, London, p. 352.

Horger, O. J., and Buckwalter, T. V., 1940, Photoelasticity as applied to design problems, *Iron Age*, Vol. 145, Pt. II, No. 21, p. 42.

Horger, O. J., and Maulbetsch, J. L., 1936, Increasing the fatigue strength of press-fitted axle assemblies by rolling, *Trans. ASME Appl. Mech. Sect*., Vol. 58, p. A-91.

Huth, J. H., 1950, Torsional stress concentration in angle and square tube fillets, *Trans. ASME Appl. Mech. Sect*., Vol. 72, p. 388.

Jacobson, M. A., 1955, Bending stresses in spur gear teeth: proposed new design factors based on a photoelastic investigation, *Proc. Inst. Mech. Eng.*, Vol. 169, p. 587.

Jiang, J., and Zhao, M., 2012, Influence of residual stress on stress concentration factor for high strength steel welded joints, *Journal of Constructional Steel Research*, Vol. 72, pp. 20–28.

Kaufmann, F., and Jäniche, W., 1940, Beitrag zur Dauerhaltbarkeit von Schraubenverbindungen, *Tech. Mitt. Krupp Forschungsber*., Vol. 3, p. 147.

Kim, Y.-J., and Son, B.-G., 2004, Finite element based stress concentration factors for pipes with local wall thinning, *International Journal of Pressure Vessels and Piping*, Vol. 81, pp. 897–906.

Krscanski, S., and Turkalj, G., 2012, FEM stress concentration factors for fillet welded CHS-plate T-joint, *Engineering Review*, Vol. 32, No. 3, pp. 147–155.

Kumar, A., Agrawal, A., Ghadai, R., and Kalita, K., 2016, Analysis of stress concentration in orthotropic laminates, *Procidia Technology*, Vol. 23, pp. 156–162.

Kuang, J. G., Potvin, A. B., and Leick, R. D., 1975, Stress concentrations in tubular joints, *Proc. Offshore Technological Conference 0TC2205*, Houston, TX, p. 593.

Kubair, S. V., and Bhanu-Chandar, B., 2008, Stress concentration factor due to a circular hole in functionally graded panels under uniaxial tension, *International Journal of Mechanical Sciences*, Vol. 50, pp. 732–742.

N'Diaye, A., Hariri, S., Pluvinage, G., and Azari, Z., 2009, Stress concentration factor analysis for welded, notched T-joints under combined axial, bending, and dynamic loads, *International Journal of Fatigue*, Vol. 31, pp. 367–374.

Lee, C. K., Chiew, S. P., Lie, S. T., and Sopha, T., 2011, Stress concentration factor predication by the mult-dimensional Lagrangian interpolation method, *Engineering Fracture Mechanics*, Vol. 78, pp. 1008–1028.

Lee, M. M. K., and Bownes, D., 2002, Fatigue life prediction of offshore tubular joints using fracture mechanics, *Fatigue Fract. Eng. Mater. Struct.*, Vol. 25, p. 1025.

Leven, M. M., 1949, Stresses in keyways by photoelastic methods and comparison with numerical solution, *Proc Soc. Exp. Stress Anal.*, Vol. 7, No. 2, p. 141.

Liesecke, G., 1933, Berechnung Zylindrischer Schraubenfedern mit Rechteckigem Drahtquerschnitt, *Z. VDI*, Vol. 77, pp. 425, 892.

Livieri, P., and Segala, F., 2016, Stress intensity factors for embedded elliptical cracks in cylindrical and spherical vessels. *Theoretical and Applied Fracture Mechanics*, Vol. 86, pp. 260–266.

Lyse, I., and Johnston, B. G., 1935, Structural beams in torsion, *Lehigh Univ. Pub*., Vol. 9, p. 477.

Mantle, J. B., and Dolan, T. J., 1948, A photoelastic study of stresses in U-shaped members, *Proc. Soc. Exp. Stress Anal.*, Vol. 6, No. 1, p. 66.

Marino, R, L., and Riley, W. F., 1964, Optimizing thread-root contours using photoelastic methods, *Exp. Mech.*, Vol. 4, p. 1.

Martinaglia, L., 1942, Schraubenverbindungen, *Schweiz. Bauztg*., Vol. 119, p. 107.

Mashiri, F. R., and Zhao, X.-L., 2006, Thin circular hollow section-to-plate T-joints: stress concentration factors and fatigue failure under in-plane bending, *Thin Walled Structures*, Vol. 44, pp. 159–169.

Medina, H., and Hinderliter, B., 2014, The stress concentration factor for slightly roughened random surfaces: analytical solution, *International Journal of Solids and Structures*, Vol. 51, p. 2012–2018.

Meek, R. M. G., 1967, Effect of pin bending on the stress distribution in thick plates loaded through pins, *NEL Rep.* 311.

Michalec, G. W., 1966, *Precision Gearing: Theory and Practice*, Wiley, New York, p. 466.

Morgan, M. R., and Lee, M. M. K., 1997, New parametric equations for stress concentration factors in tubular K-joints under balanced axial loading, *International Journal of Fatigue*, Vol. 19, No. 4, pp. 309–317.

Morgan, M. R., and Lee, M. M. K., 1998, Parametric equations for distributions of stress concentration factors in tubular K-joints under out-of-plane moment loading, *International Journal of Fatigue*, Vol. 20, No. 6, pp. 449–461.

Nie, F., Zhang, Q., Qin, X., and Sun, Y., 2017, Stress concentration factors (SCFs) of bulge formed K-joints under balanced axial loads, *Applied Ocean Research*, Vol. 69, pp. 53–64.

Nishioka, K., and Komatsu, H., 1967, Researches on increasing the fatigue strength of press-fitted shaft assembly, *Bull. Jpn. Soc. Mech. Eng.*, Vol. 10, p. 880.

Nishioka, K., Nishimura, S., and Hirakawa, K., 1968, Fundamental investigations of fretting fatigue, *Bull. Jpn. Soc. Mech. Eng*., Vol. 11, p. 437; 1969, Vol. 12, pp. 180, 397, 408.

Nisida, M., 1963, New photoelastic methods for torsion problems, in *Symposium on Photoelasticity*, M. M. Frocht, Ed., Pergamon Press, Elmsford, NY, p. 109.

Okubo, H., 1950a, On the torsion of a shaft with keyways, *Q. J. Mech. Appl. Math.*, Vol. 3, p. 162.

Okubo, H., 1950b, Torsion of a circular shaft with a number of longitudinal notches, *Trans. ASME, Appl. Mech. Sect*., Vol. 72, p. 359.

Okubo, H., Hosono, K., and Sakaki, K., 1968, The stress concentration in keyways when torque is transmitted through keys, *Exp. Mech.*, Vol. 8, p. 375.

Pachound, A. J., Manso, P. A., and Schleiss, A. J., 2017a, Stress intensity factors for axial semielliptical surface cracks and embedded elliptical cracks at longitudinal butt welded joints of steel-lined pressure tunnels and shafts considering weld shape, *Engineering Fracture Mechanics*, Vol. 179, pp. 93–119.

Pachound, A. J., Manso, P. A., and Schleiss, A. J., 2017b, New parametric equation to estimate notch stress concentration factors at butt welded joints modeling the weld profile with splines, *Engineering Failure Analysis*, Vol. 72, pp. 11–24.

Pang, N. L., Zhao, X. L., Mashiri, F. R., and Dayawansa, P., 2009, Full-size testing to determine stress concentration factors of dragline tubular joints, *Engineering Structures*, Vol. 31, pp. 43–56.

Parunov, J., Corak, M., and Gilja, I., 2013, Calculated and prescribed stress concentration factors of ship side longitudinal connections, *Engineering Structures*, Vol. 52, pp. 629–641.

Peterson, R. E., 1930, Load and deflection cycles in gear teeth, *Proc. 3rd International Applications of Mechanics Congress*, Stockholm, Sweden, p. 382.

Peterson, R. E., 1932, Fatigue of shafts having keyways, *Proc. ASTM* , Vol. 32, Pt. 2, p. 413.

Peterson, R. E., 1938, Methods of correlating data from fatigue tests of stress concentration specimens, *Stephen Timoshenko Anniversary Volume*, Macmillan, New York, p. 179.

Peterson, R. E., 1950, Interpretation of service fractures, in *Handbook of Experimental Stress Analysis*, M. Hetényi, Ed., Wiley, New York, pp. 603, 608, 613.

Peterson, R. E., 1953, *Stress Concentration Design Factors*, Wiley, New York.

Peterson, R. E., and Wahl, A. M., 1935, Fatigue of shafts at fitted members, with a related photoelastic analysis, *Trans. ASME Appl. Mech. Sect*., Vol. 57, p. A-l.

Pilkey, W. D., 2005, *Formulas for Stress, Strain, and Structural Matrices*, 2nd ed., Wiley, Hoboken, NJ.

Richart, F. E., Olson, T. A., and Dolan, T. J., 1938, Tests of reinforced concrete knee frames and bakelite models, *Univ. Ill. Exp. Stn. Bull.* 307.

Riggs, N. C., and Frocht, M. M., 1938, *Strength of Materials*, Ronald Press, New York, p. 389.

Romeijn, A., and Wardenier, J. 1994, Stress and strain concentration factors of welded tubular joints caused by chord loading, *Proc. 6th International Symposium on Tubular Structures*, Melbourne, Australia, p. 643.

Romeijn, A., Puthli, R. S., and Wardenier, J., 1993, Guidelines on the numerical determination of stress concentration factors of tubular joints, *Proc. 5th International Symposium on Tubular Structures*, Nottingham, England, p. 625.

Saini, D. S., Karmakar, D., and Ray-Chaudhuri, S., 2016, A review of stress concentration factors in tubular and non-tubular joints for design of offshore installations, *Journal of Ocean Engineering and Science*, Vol. 1, pp. 186–202.

Shahani, A. R., and Sharifi, S. M. H., 2009, Contact stress analysis and calculation of stress concentration factors at the tool joint of a drill pipe, *Materials and Design*, Vol. 30, pp. 3615–3621.

Smedley, P., and Fisher, P. 1991, Stress concentration factors for simple tubular joints, *Proc. 1st International Offshore and Polar Engineering Conference*, Edinburgh, Scotland, p. 475.

Solakian, A. G., and Karelitz, G. B., 1932, Photoelastic studies of shearing stresses in keys and keyways, *Trans. ASME Appl. Mech. Sect*., Vol. 54, p. 97.

Staedel, W., 1933, Dauerfestigkeit von Schrauben, *Mitt. Materialprüfungsanst. Tech. Hochsch. Darmstadt*, No. 4, VDI Verlag, Berlin.

Sunil, K. S., Neelakantha, C. L., Prem, K. N., and Saviraj, A. S., 2017, Effect of geometric discontinuity on stress concentration factor of Al6061T6 alloy under bending load, *Materials Today: Proceedings*, Vol. 4, pp. 11039–11043.

Teran, G., Albiter, A. and Cuamatzi-Melendez, R., 2013, Parametric evaluation of the stress concentration factors in T-butt welded connections, *Engineering Structures*, Vol. 56, pp. 2484–1495.

Theocaris, P. S., 1956, The stress distribution in a strip loaded in tension by means of a central pin, *Trans. ASME*, Vol. 78, pp. 85–90.

Thum, A., and Bruder, E., 1938, Dauerbruchgefahr an Hohlkehlen von Wellen und Achsen und ihre Minderung, *Deutsche Kraftfahrtforsch. Auftrag Reichs-Verkehrsministeriums*, No. 11, VDI Verlag, Berlin.

Thum, A., and Wunderlich, F., 1933, Der Einfluss von Einspannund Kantandgriffsstellen auf die Dauerhaltbarkeit der Konstruktionen, *Z. VDI*, Vol. 77, p. 851.

Timoshenko, S., and Goodier, J. N., 1970, *Theory of Elasticity*, 3rd ed., McGraw Hill, New York, p. 398.

Tomlinson, G. A., 1927, The rusting of steel surface on contact, *Proc. R. Soc. (London) A*, Vol. 115, p. 472.

Tomlinson, G. A., Thorpe, P. L., and Gough, H. J., 1939, An investigation of the fretting corrosion of closely fitting surfaces, *Proc. Inst. Mech. Eng. (London)*, Vol. 141, p. 223.

Tong, L. W., Xu, G. W., Yang, D. L., Mashiri, F. R., and Zhao, X. L., 2017, Stress concentration factors in CHS-CFSHS T-joint: experiments, FE analysis and formulae, *Engineering Structures*, Vol. 151, pp. 406–421.

Tong, L., Xu, G., Liu, Y., Yan, D., and Zhao, X.-L., 2015, Finite element analysis and formulae for stress concentration factors of diamond bird-beak SHS T-joints, *Thin-Walled Structures*, Vol. 86, pp. 108–120.

Troyani, N., Hernandez, S. I., Villarroel, G., Pollonais, Y., and Gomes, C., 2004, Theoretical stress concentration factors for short flat bars with opposite U-shaped notches subjected to in-plane bending, *International Journal of Fatigue*, Vol. 26, pp. 1303–1310.

Van der Vegte, G. J., Choo, Y. S., Liang, J. X., Zettlemoyer, N., and Liew, J. Y. R., 2005, Static strength of T-joints reinforced with doubler or collar plates: Part II, Numerical simulations, *J. Struct. Eng.*, Vol. 131, p. 129.

Wahl, A. M., 1946, Calculation of stresses in crane hooks, *Trans. ASME Appl. Mech. Sect*., Vol. 68, p. A-239.

Wahl, A. M., 1963, *Mechanical Springs*, 2nd ed., McGraw-Hill, New York.

Wang, B., Zhao, W., Du, Y., Zhang, G., and Yang, Y., 2016, Prediction of fatigue stress concentration factor using extreme learning machine, *Computational Materials Science*, Vol. 125, pp. 136–145.

Weibel, E. E., 1934, Studies in photoelastic stress determination, *Trans. ASME Appl. Mech. Sect*., Vol. 56, p. 637.

White, D. J., and Humpherson, J., 1969, Finite-element analysis of stresses in shafts due to interference-fit hubs, *J. Strain Anal.*, Vol. 4, p. 105.

Whitehead, R. S., Abbey, A. J., and Glen-Bott, M. G., 1978, Analytical determination of stress intensity factors for attachment lugs, *Rep. SON(P) 199*, British Aerospace, Aircraft Group, Warton Division, Warton, England.

Wiegand, H., 1933, Über die Dauerfestigkeit von Schraubenwerkstoffen und Schraubenverbindungen, Thesis, Technische Hochshule Darmstadt; Also published as No. 14 (1934), *Wissenschaftliche Veröffentlichungen der Firma*, Bauer & Schaurte A.G., Neuss, Germany.

Wilson, B. J., and Quereau, J. F., 1928, A simple method of determining stress in curved flexural members, *Univ. Ill. Exp. Stn. Circ.* 16.

Woghiren, C. O., and Brennan, F. P., 2009, Weld toe stress concentrations in multi-planar stiffened tubular KK joints, *International Journal of Fatigue*, Vol. 31, pp. 164–172.

Wordsworth, A. C., 1981. Stress concentration factors at K and KT tubular joints, *Proc. Fatigue in Offshore Structure Steels*, London, 56.

Wordsworth, A.C., and Smedley, G. C., 1978, Stress concentration at unstiffened tubular joints, *IX/P31-(1–7)*, European Offshore Steels Research Seminar, Cambridge, England.

Yang, J., Chen, Y., and Hu, K., 2015, Stress concentration factors of negative large eccentricity tubular N-joints under axial compressive loading in vertical brace, *Thin-walled structures*, Vol. 96, pp. 359–371.

Ye, X. W., Ni, Y. Q., and Ko, J. M., 2012, Experimental evaluation of stress concentration factor of welded steel bridge T-joints, *Journal of Constructional Steel Research*, Vol. 70, pp. 78–85.

Yoshitake, H., 1962, Photoelastic stress analysis of the spline shaft, *Bull. Jpn. Soc. Mech. Eng.*, Vol. 5, p. 195.

Young, W. C., and Budynas, R. G., 2002, *Roark's Formulas for Stress and Strain*, 7th ed., McGraw-Hill, New York.

Zappalorto, M., Berto, F., and Lazzarin, P., 2011, Practical expression for the notch stress concentration factors of round bar under torsion, *International Journal of Fatigue*, Vol. 3, pp. 382–295.

Zappalorto, M., and Carraro, P. A., 2015, An engineering formula for the stress concentration factor of orthotropic composite plates, *Composites: Part B*, Vol. 68, pp. 51–58.

Zhao, X. L., Herion, S., Packer, J. A., Puthli, R. S., Sedlacek, G., and Wardenier, J., 2001, *Design guide for circular and rectangular hollow section welded joints under fatigue loading*. Berlin, Germany: Comité International pour le Développement et l'Étude de la Construction Tubulaire (CIDECT), Verlag TÜV Rheinland; 2001.

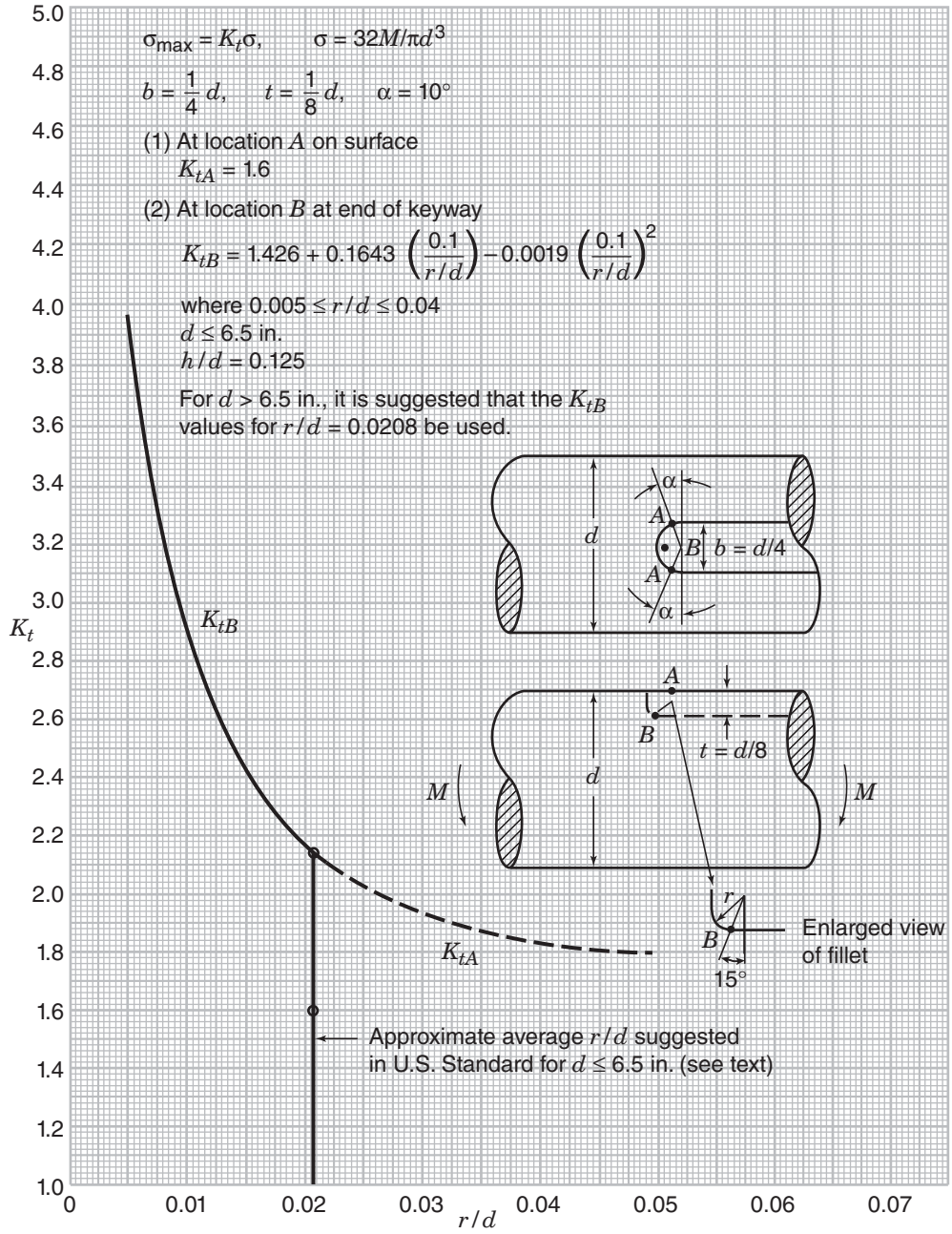


Chart 5.1 Stress concentration factors K_t for bending of a shaft of circular cross section with a semicircular end keyseat (based on data of Fessler et al. 1969a,b).

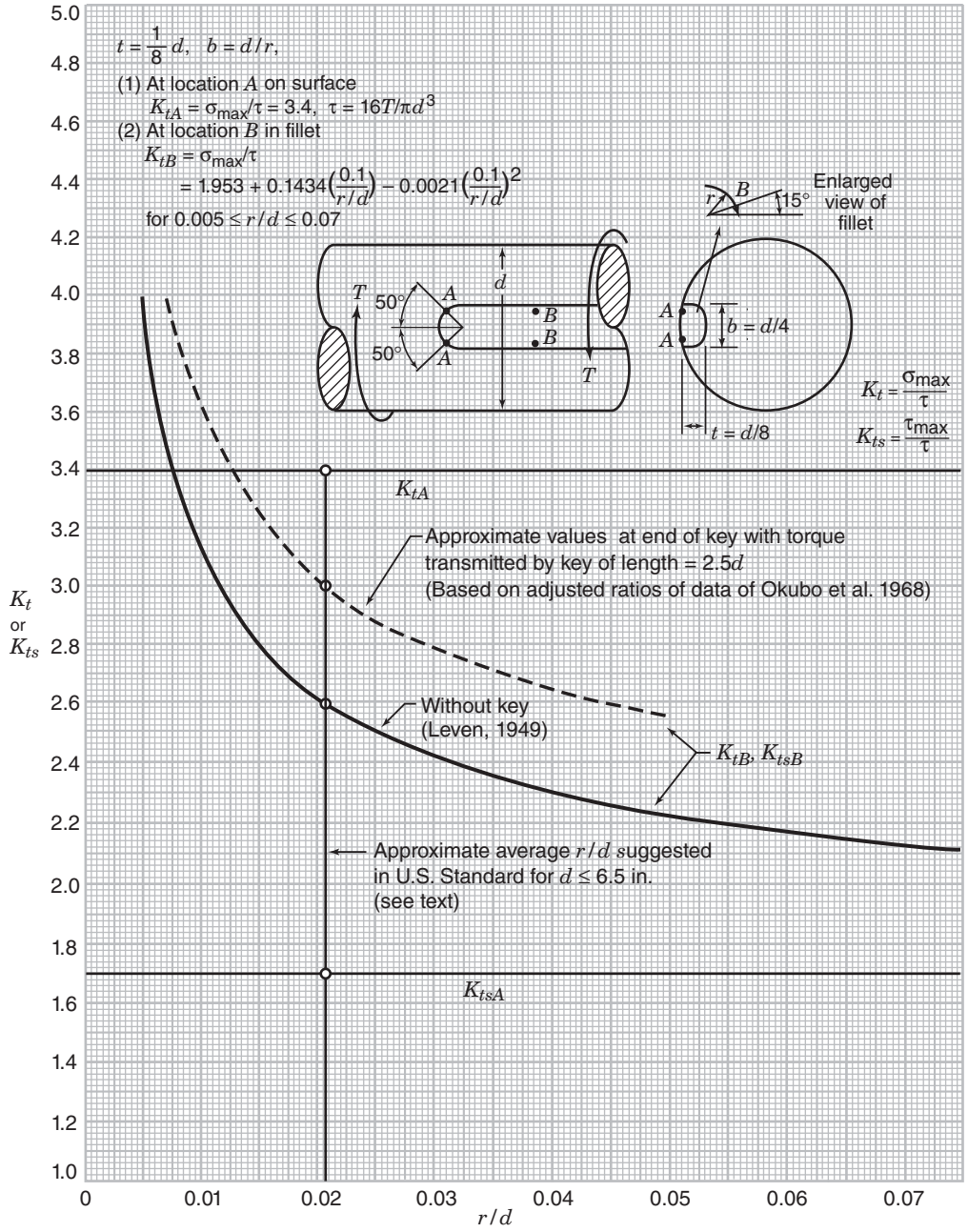


Chart 5.2 Stress concentration factors K_t, K_{ts} for a torsion shaft with a semicircular end keyseat (Leven 1949; Okubo et al. 1968).

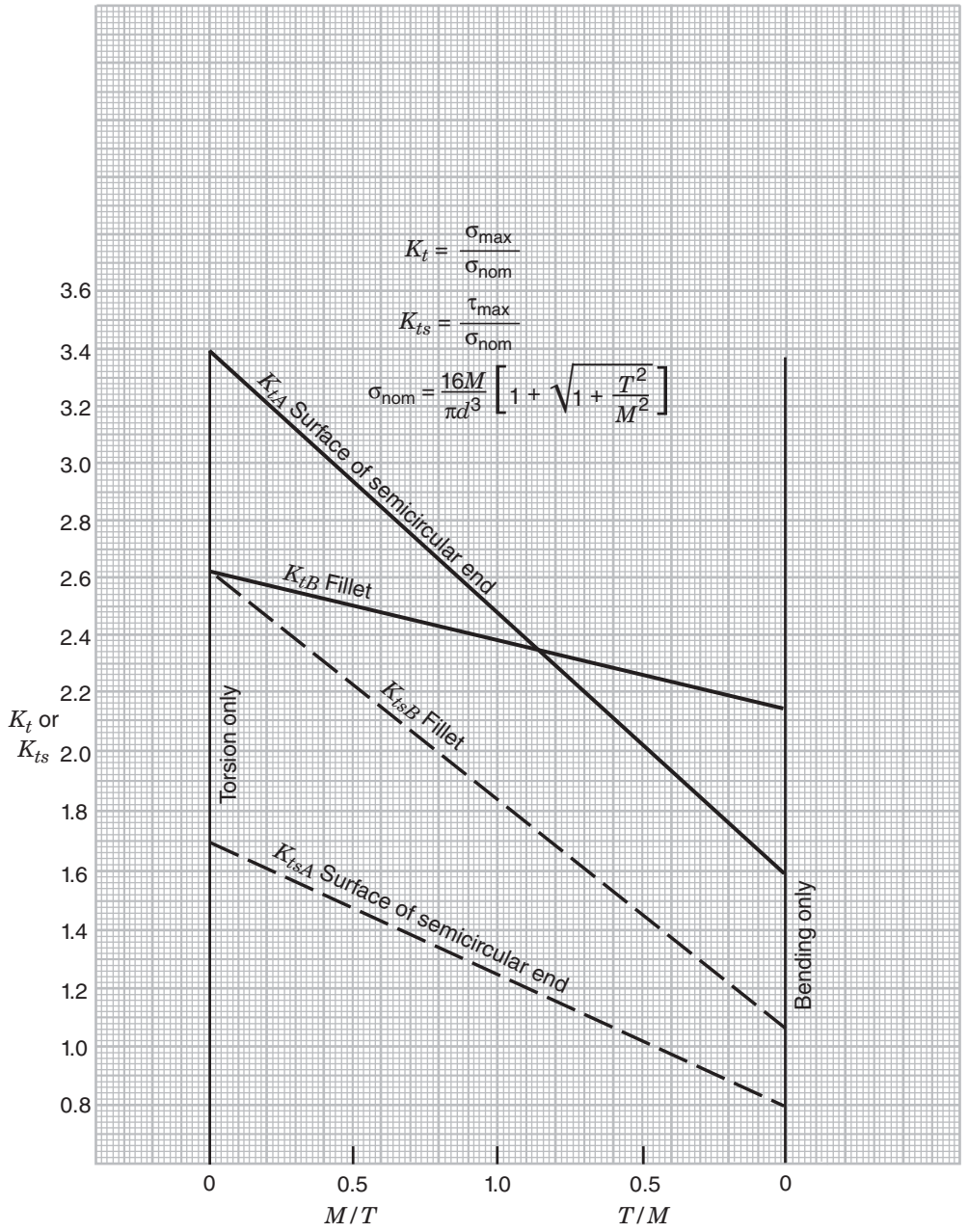


Chart 5.3 Stress concentration factors K_t and K_{ts} for combined bending and torsion of a shaft with a semicircular end keyseat. $b/d = 1/4$, $t/d = 1/8$, $r/d = 1/48 = 0.0208$ (approximate values based on method of Fessler et al. 1969a,b).

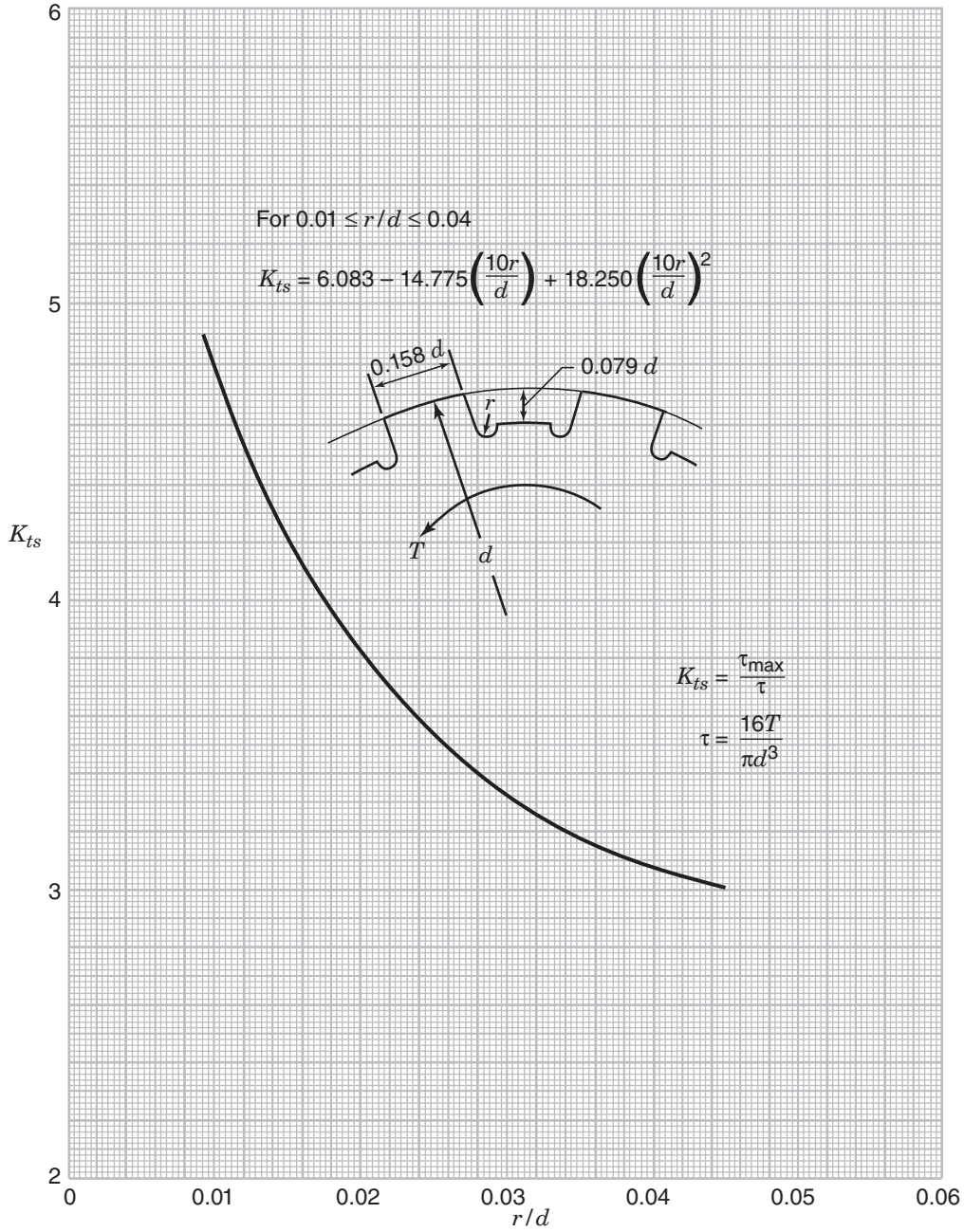


Chart 5.4 Stress concentration factors K_{ts} for torsion of a splined shaft without a mating member (photoelastic tests of Yoshitake et al. 1962). Number of teeth = 8.

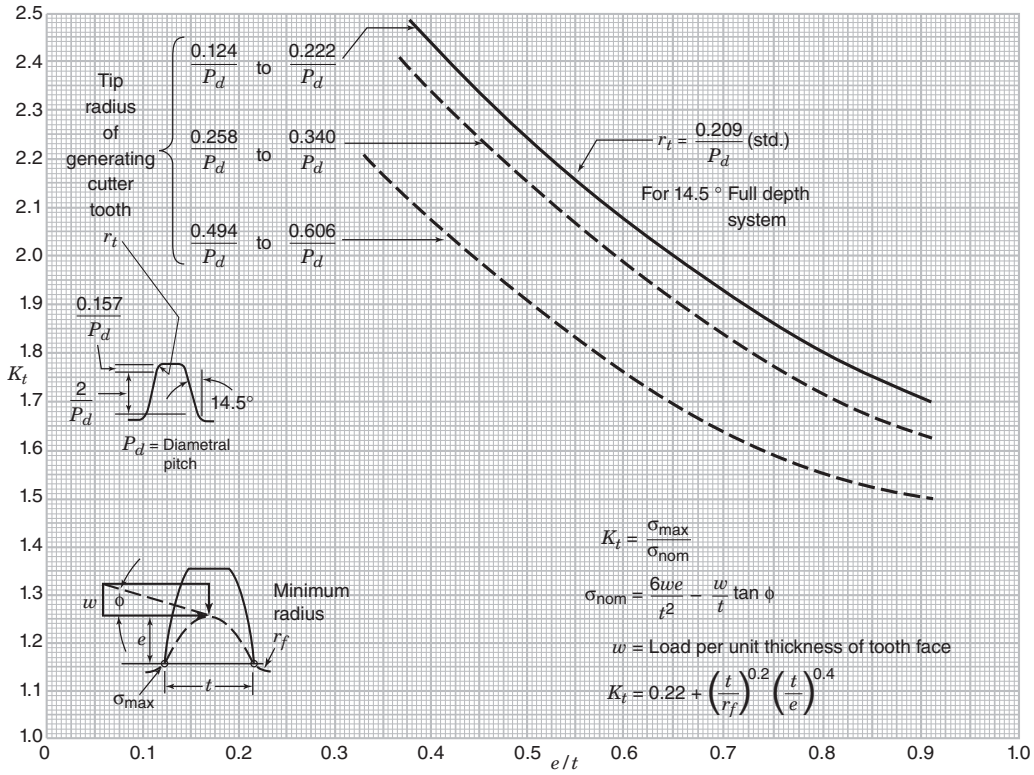


Chart 5.5 Stress concentration factors K_t for the tension side of a gear tooth fillet with a 14.5° pressure angle (from photoelastic data of Dolan and Broghamer 1942).

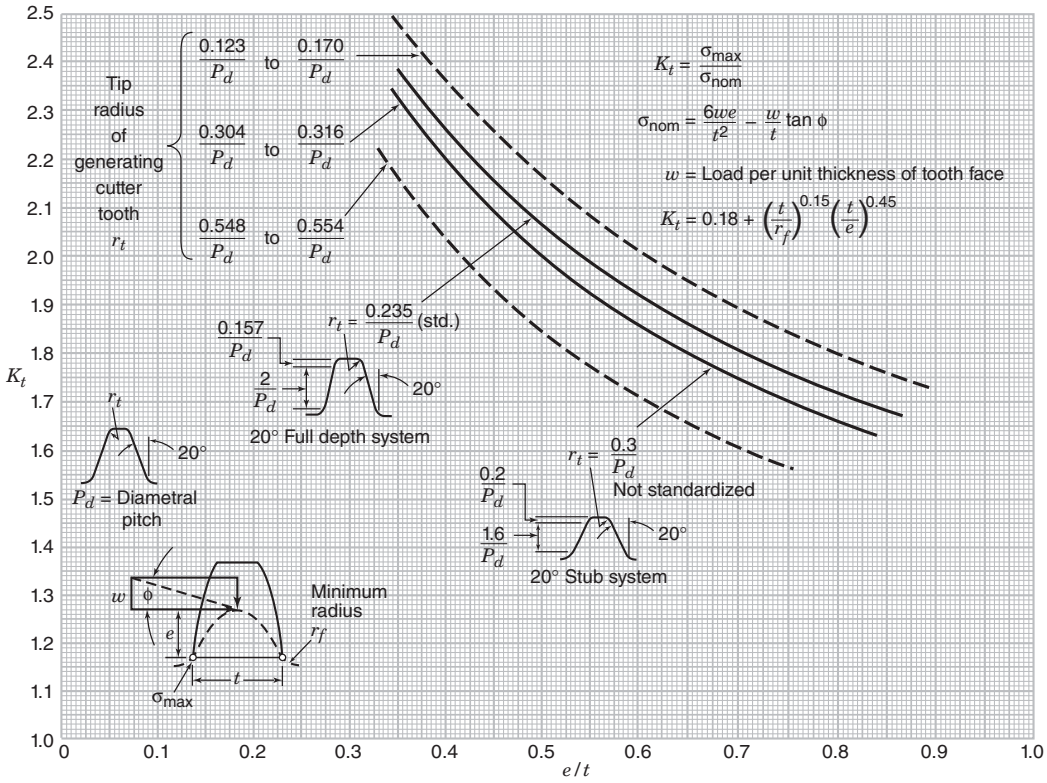


Chart 5.6 Stress concentration factors K_t for the tension side of a gear tooth fillet, 20° pressure angle (from photoelastic data of Dolan and Broghamer 1942).

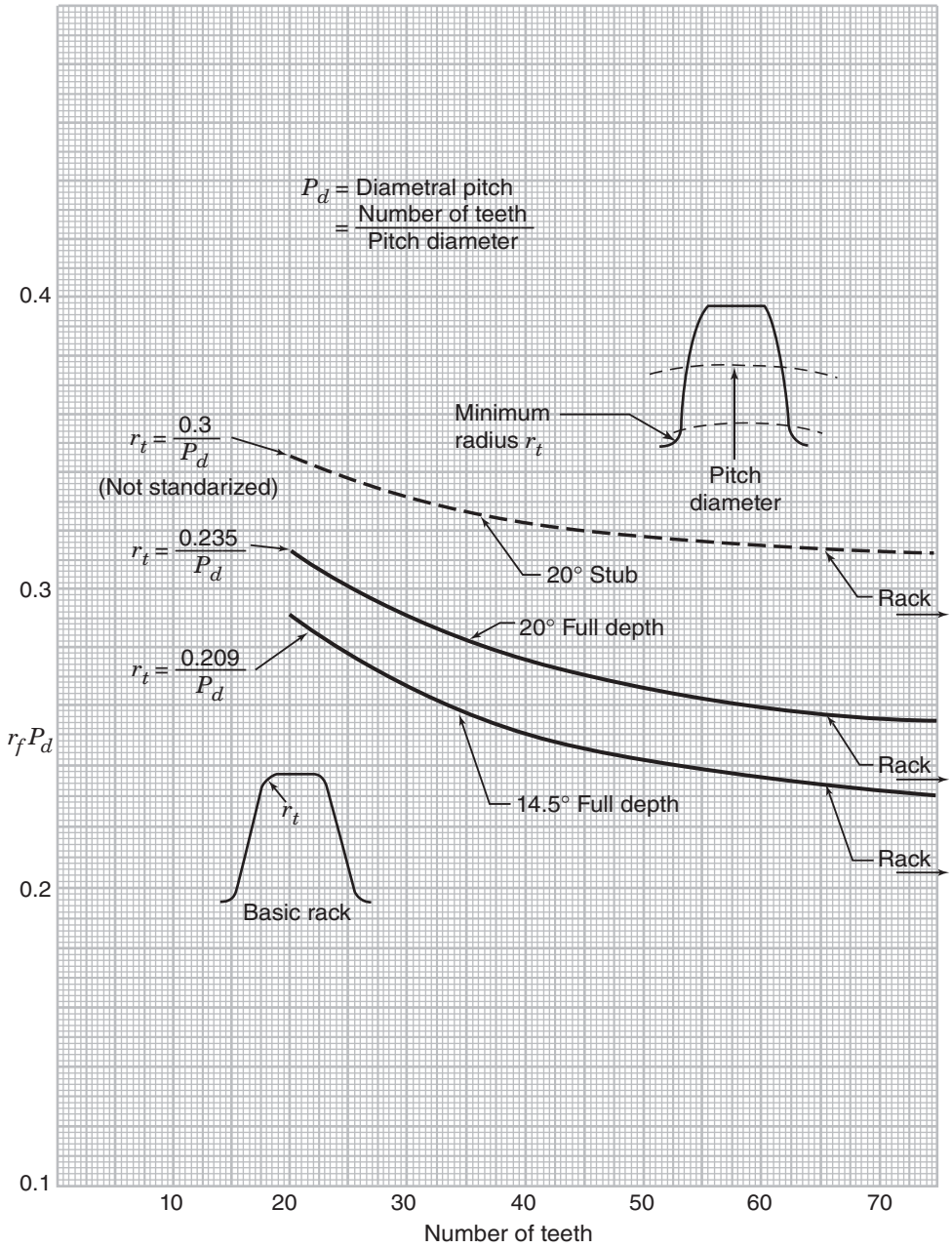


Chart 5.7 Minimum fillet radius r_f of gear tooth generated by a basic rack (formula of Candee 1941).

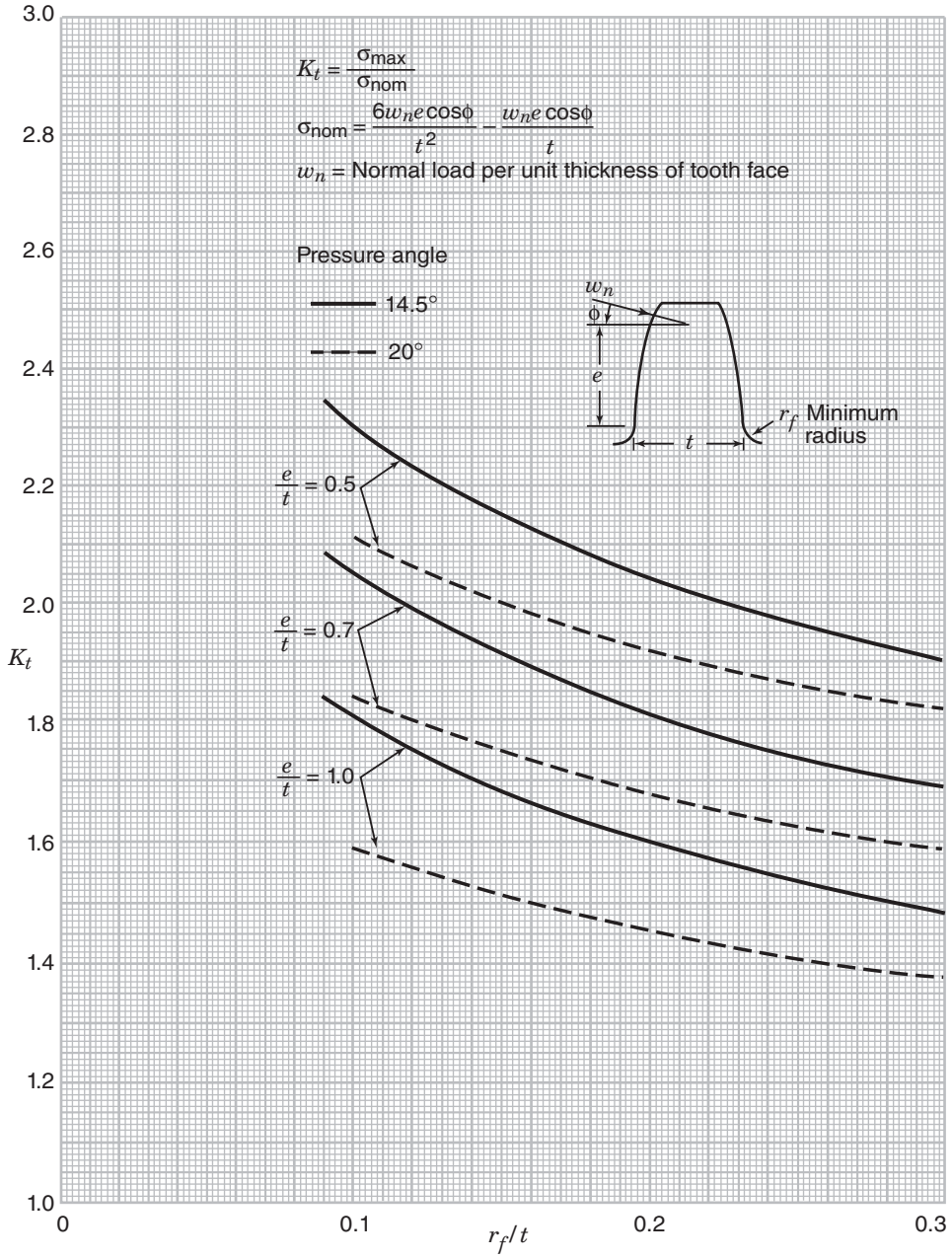


Chart 5.8 Stress concentration factors K_t for the tension side of a gear tooth fillet (empirical formula of Dolan and Broghamer 1942).

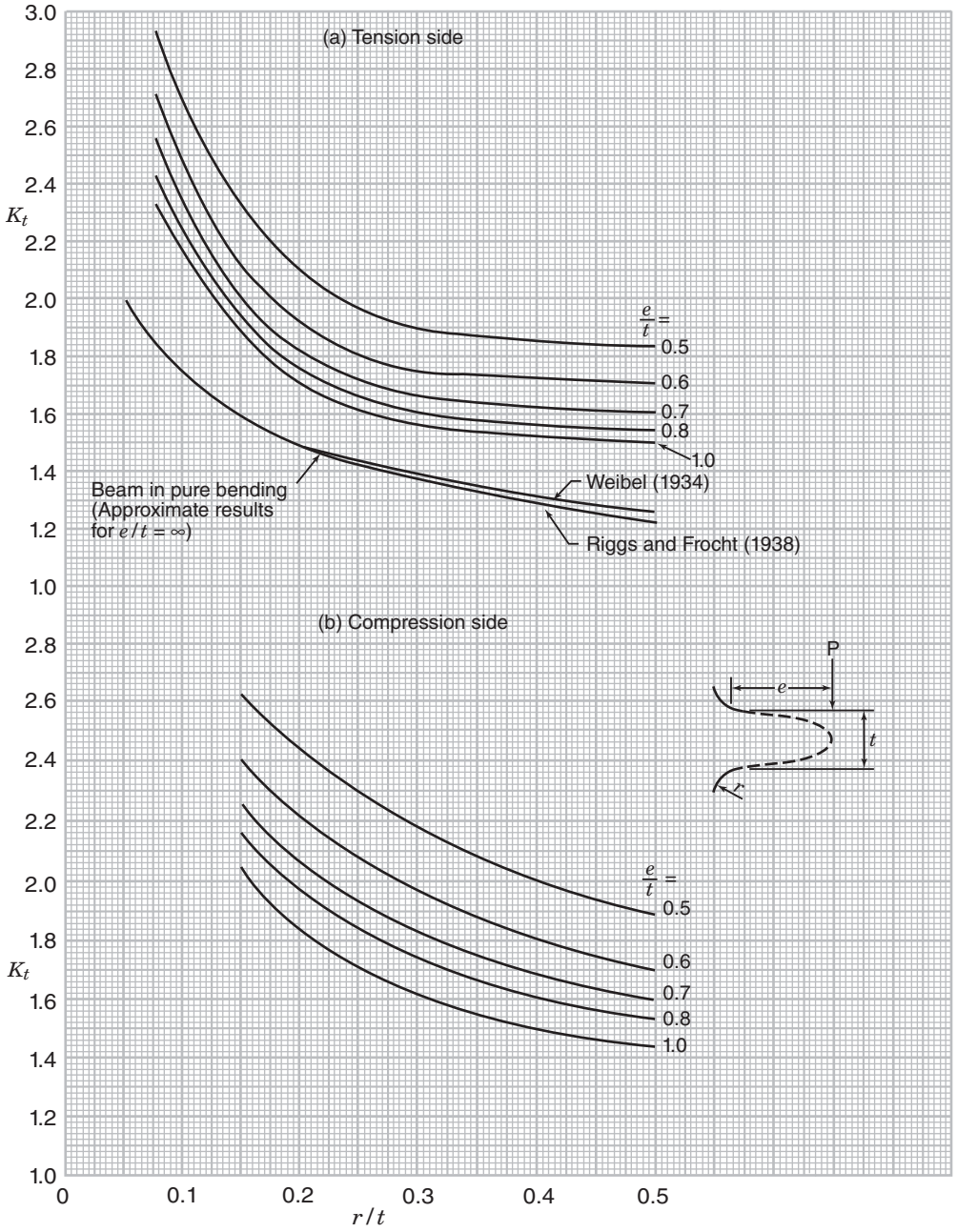


Chart 5.9 Stress concentration factors K_t for bending of a short beam with a shoulder fillet (photoelastic tests of Dolan and Broghamer 1942): (*a*) tension side; (*b*) compression side.

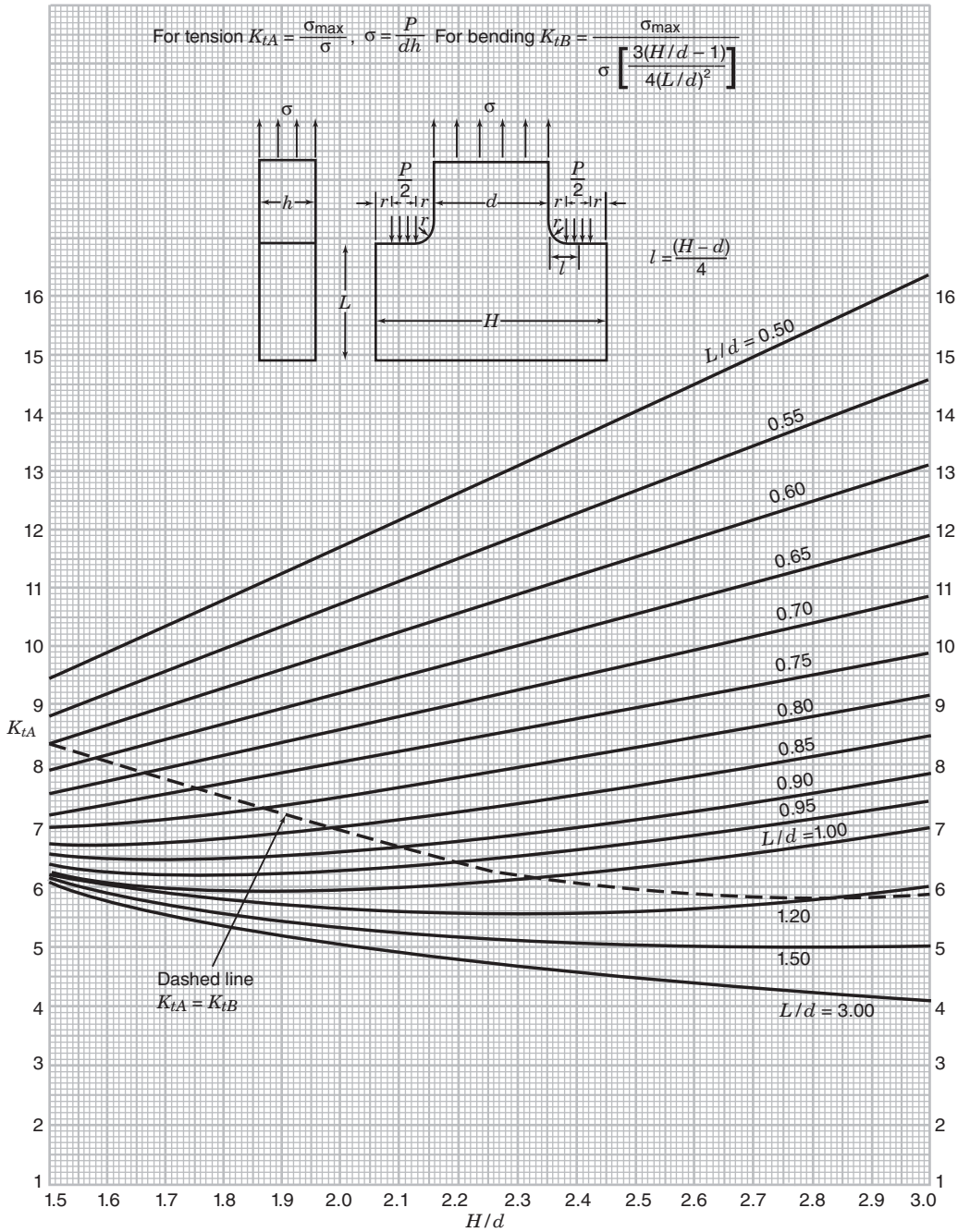


Chart 5.10*a* Stress concentration factors for a T-head (photoelastic tests of Hetényi 1939b, 1943): $r/d = 0.05$.

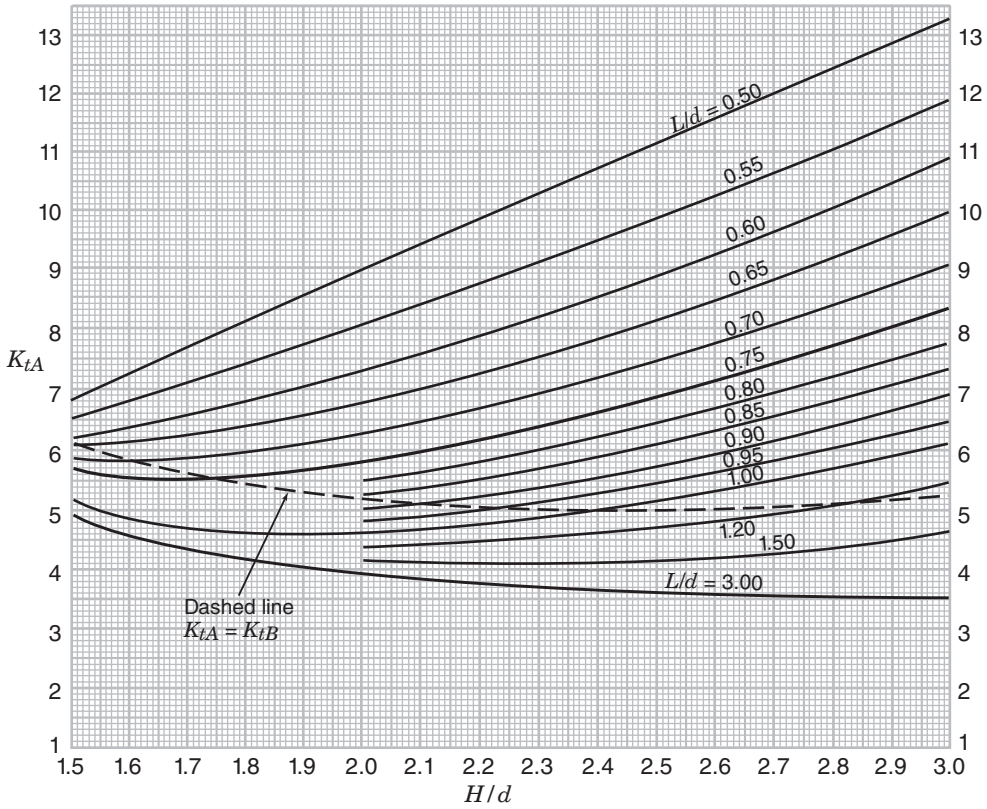


Chart 5.10*b* Stress concentration factors for a T-head (photoelastic tests of Hetényi 1939b, 1943): $r/d = 0.075$.

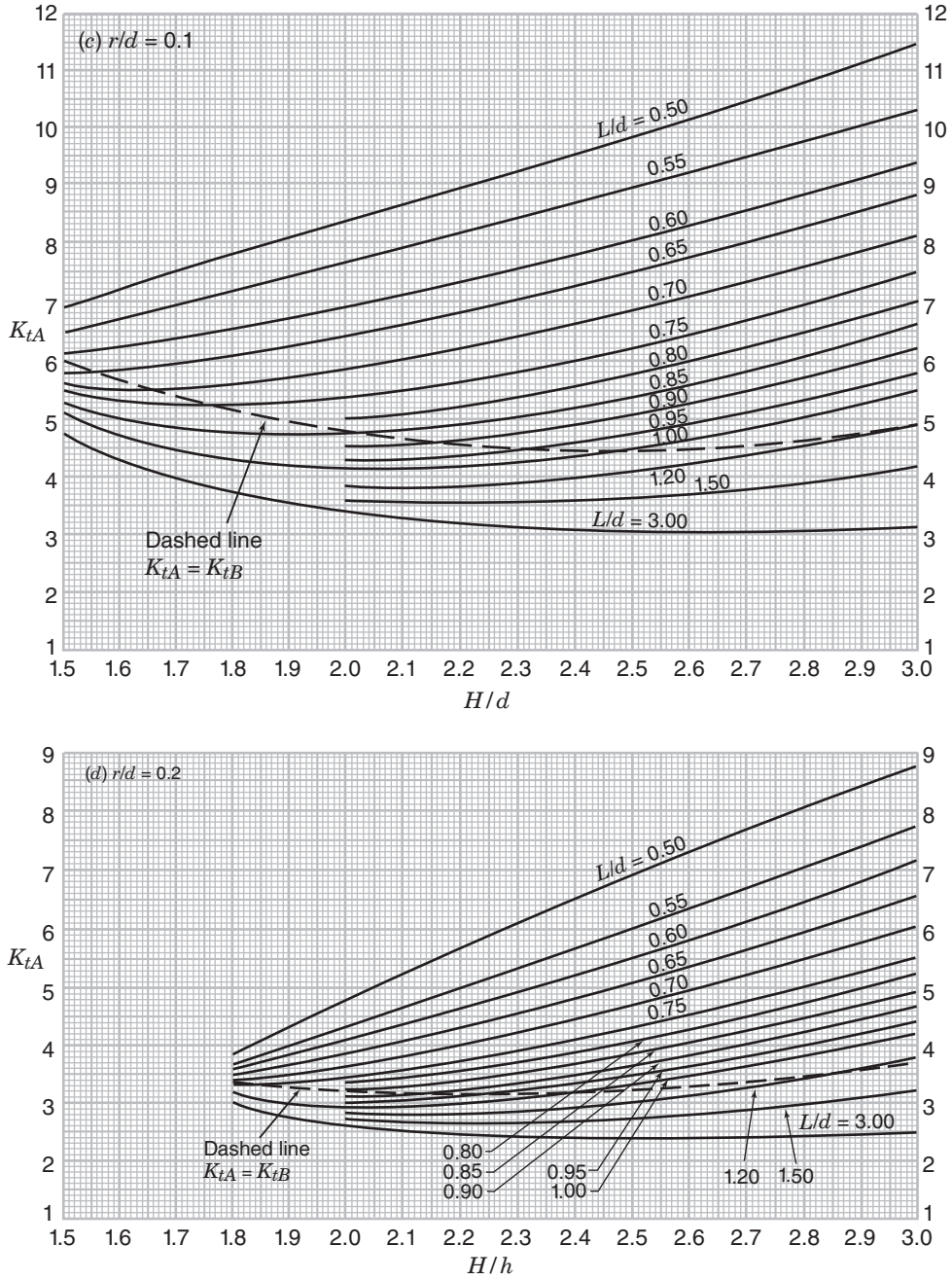
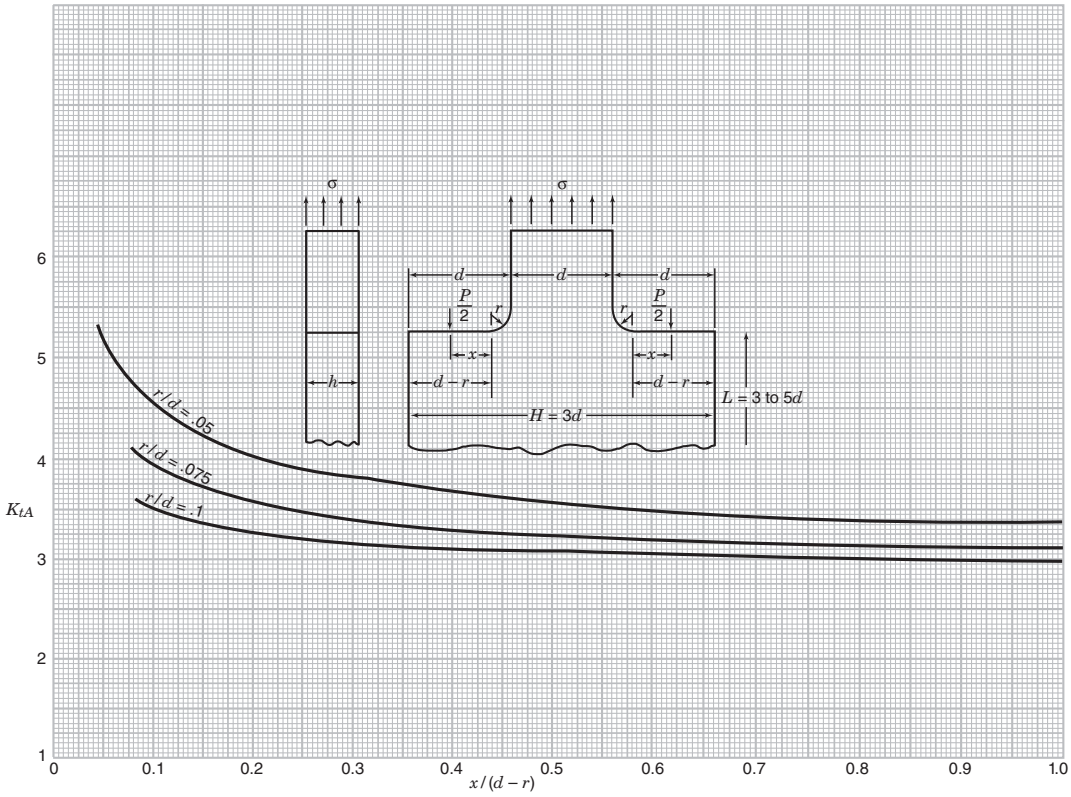


Chart 5.10*c,d* Stress concentration factors for a T-head (photoelastic tests of Hetényi 1939b, 1943): (*c*) $r/d = 0.1$; (*d*) $r/d = 0.2$.



501

Chart 5.10*e* Stress concentration factors for a T-head (photoelastic tests of Hetényi 1939b, 1943): Variable location of concentrated reaction $P/2$.

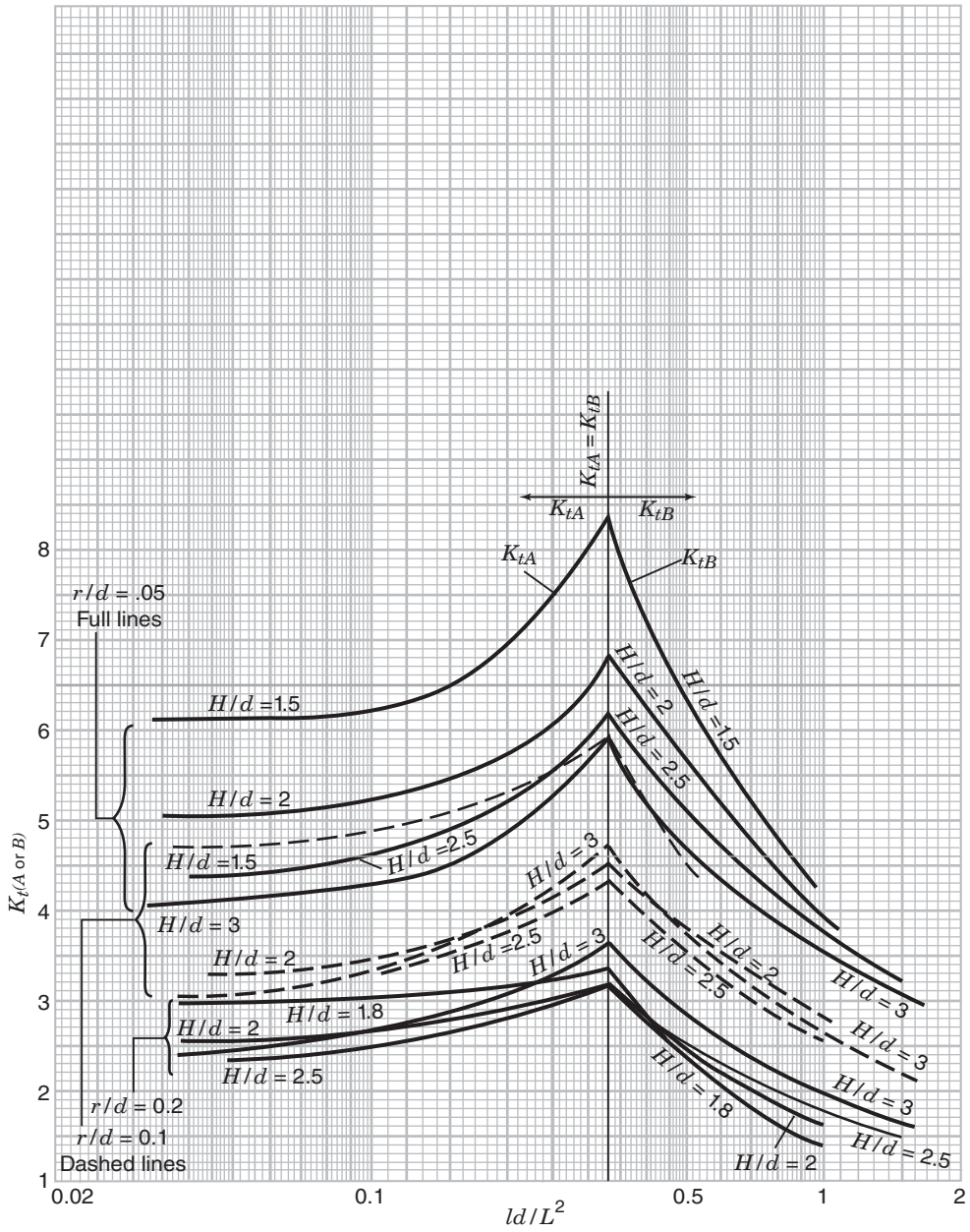


Chart 5.10*f* Stress concentration factors for a T-Head (photoelastic tests of Hetényi 1939b, 1943): K_{tA} and K_{tB} versus ld/L^2.

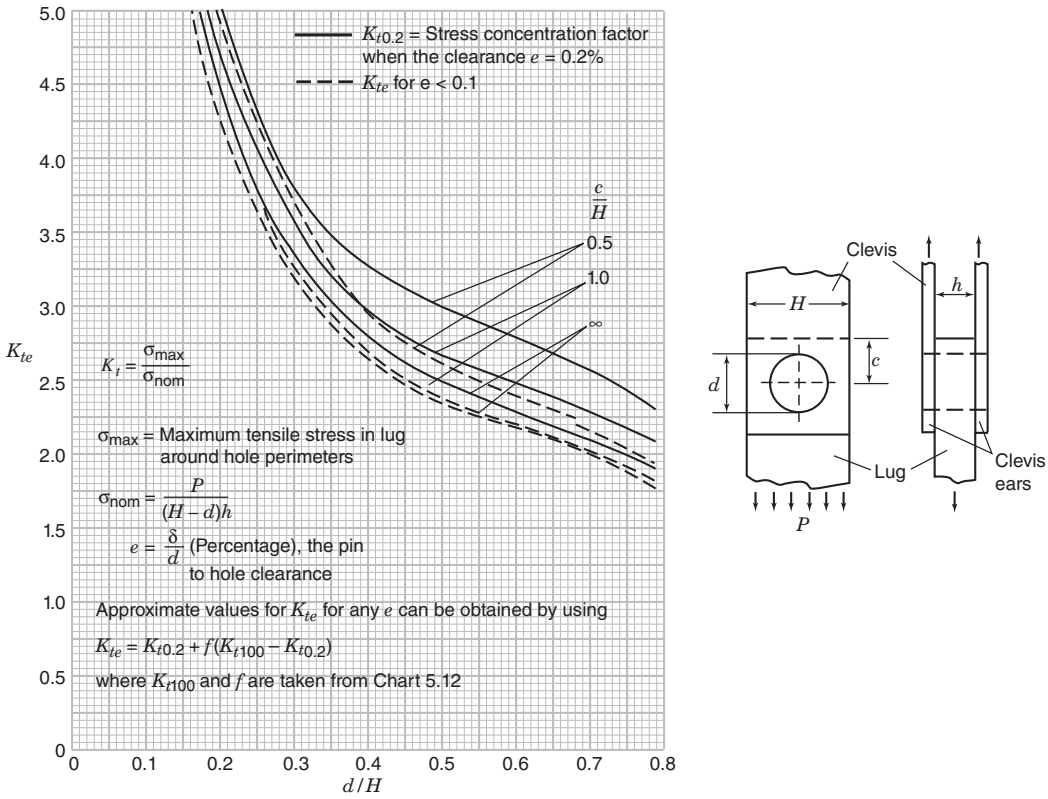


Chart 5.11 Stress concentration factors K_{te} for square-ended lugs, $h/d < 0.5$ (Whitehead et al. 1978; ESDU 1981).

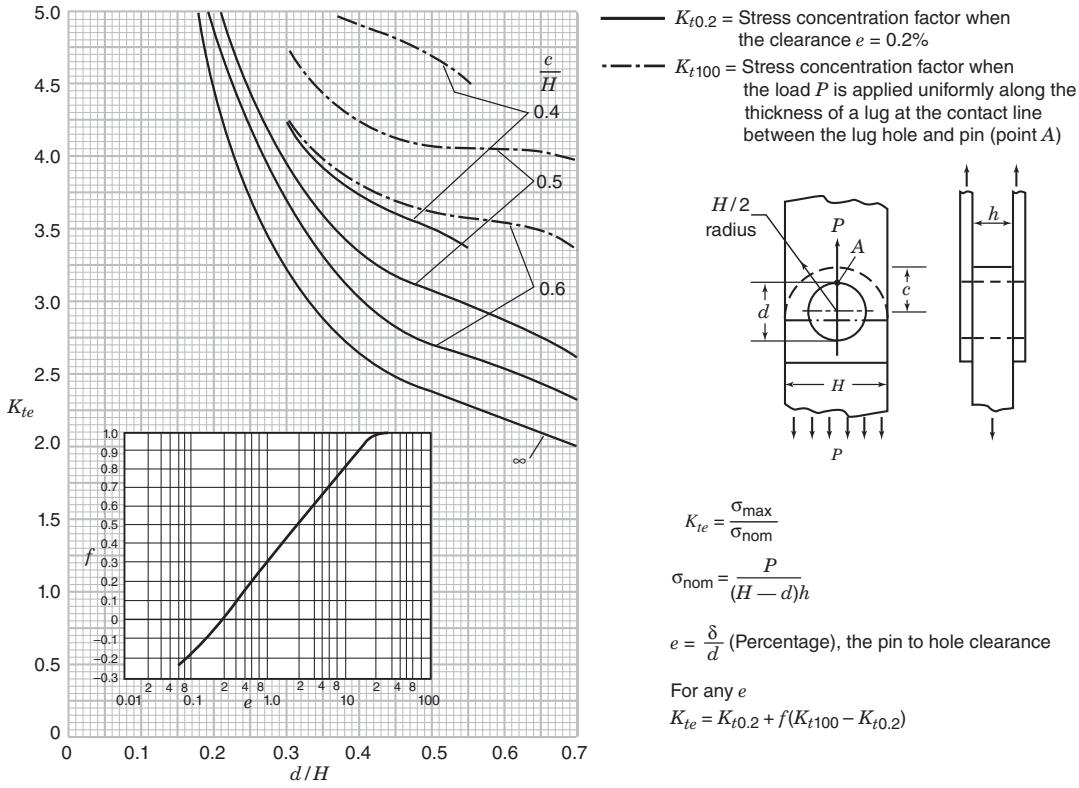


Chart 5.12 Stress concentration factors K_{te} for round-ended lugs, $h/d < 0.5$ (Whitehead et al. 1978; ESDU 1981).

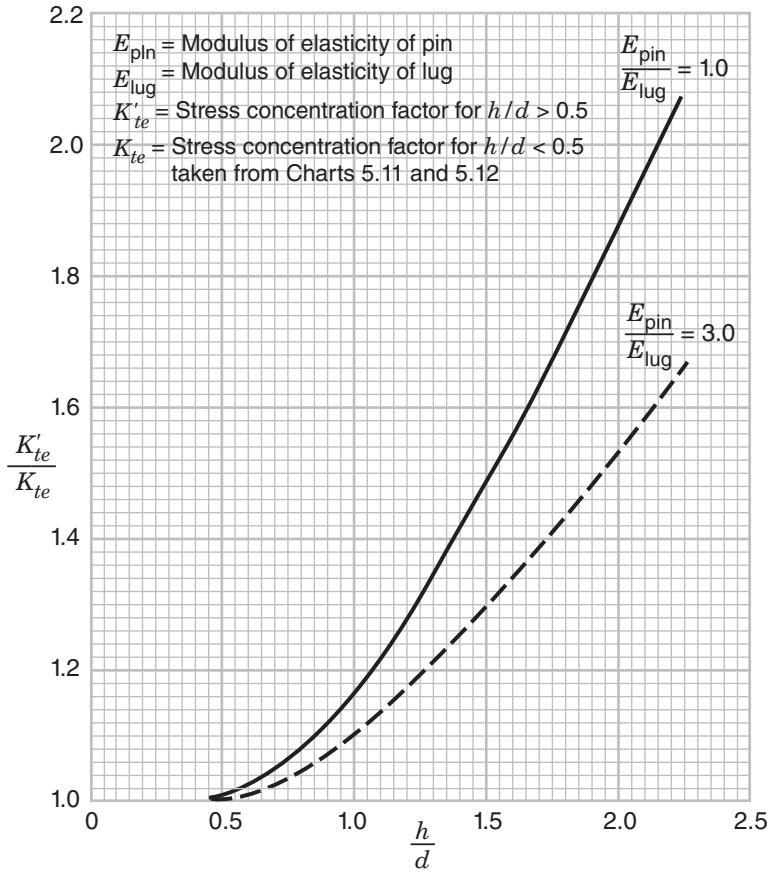


Chart 5.13 Stress concentration factors K'_{te} for thick lugs. Square or round ended lugs with $h/d > 0.5$ and $0.3 \leq d/H \leq 0.6$ (Whitehead et al. 1978; ESDU 1981).

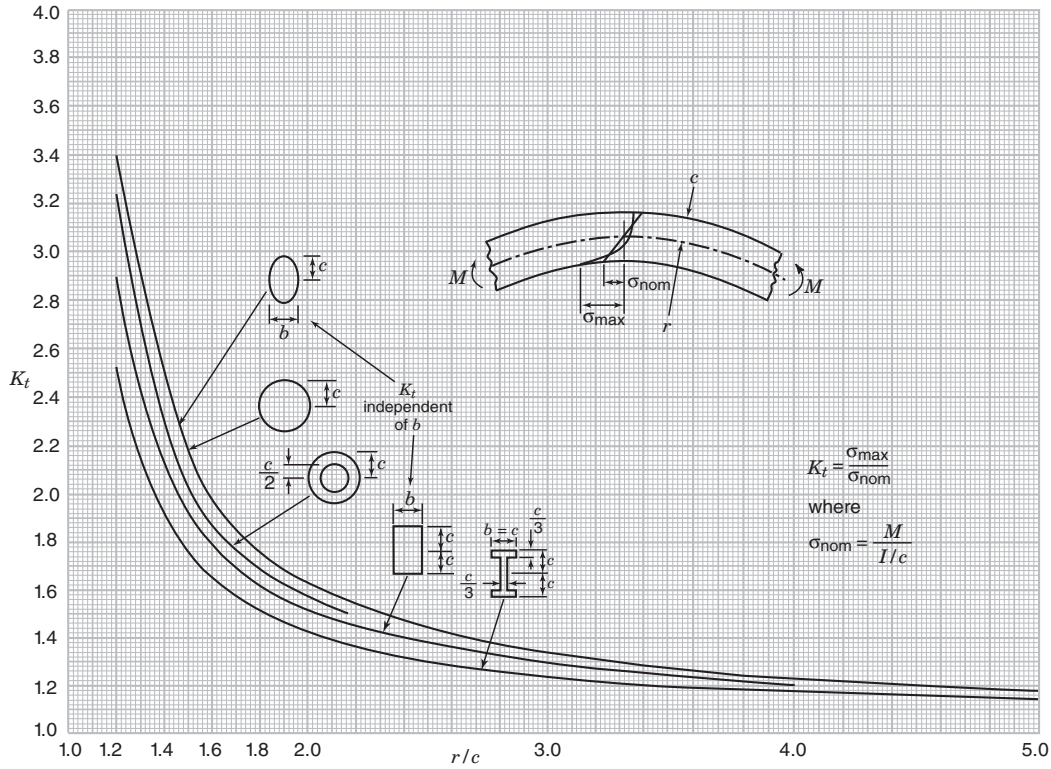


Chart 5.14 Stress concentration factors K_t for a curved bar in bending.

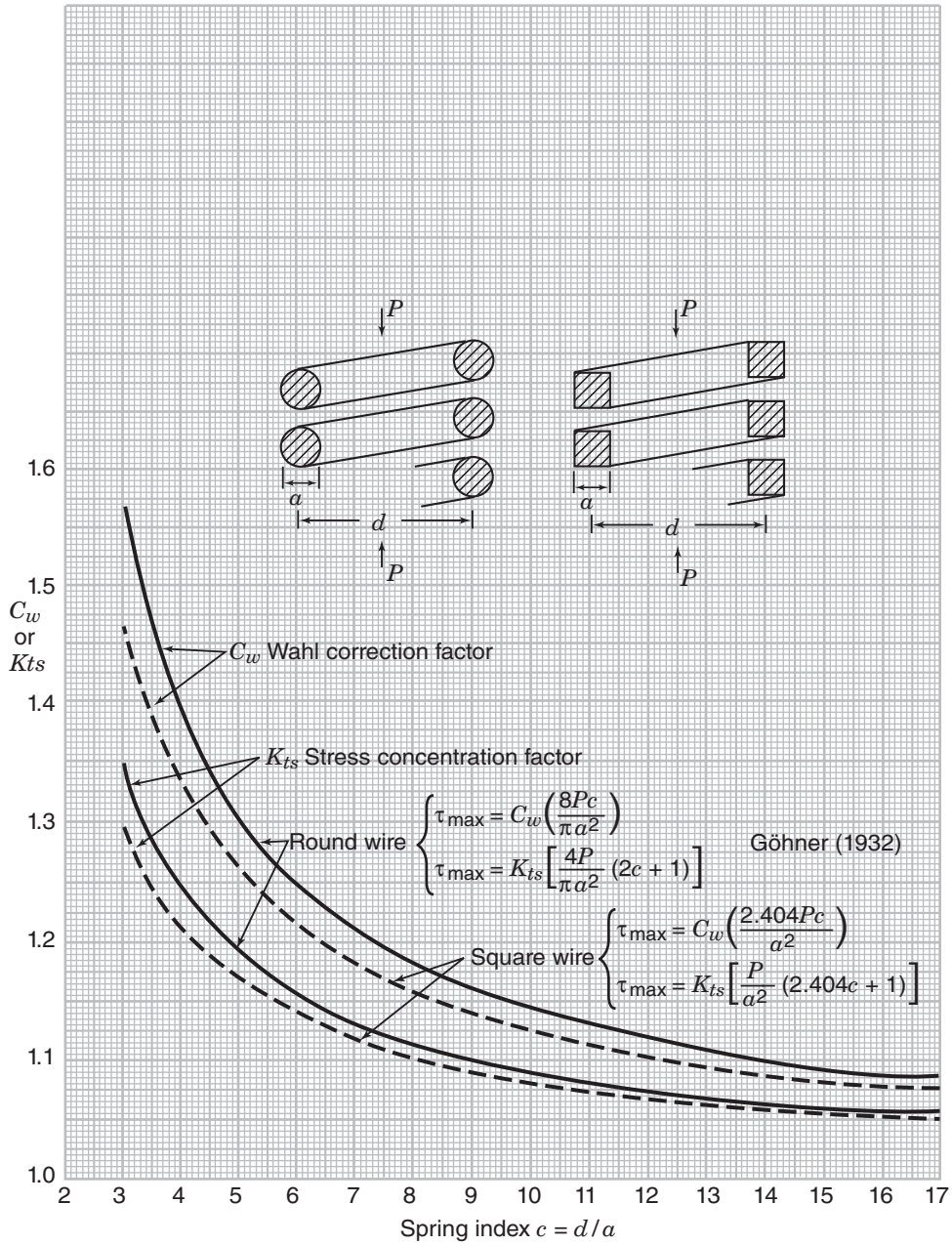


Chart 5.15 Stress factors C_w and K_{ts} for helical compression or tension springs of round or square wire (from mathematical relations of Wahl 1963).

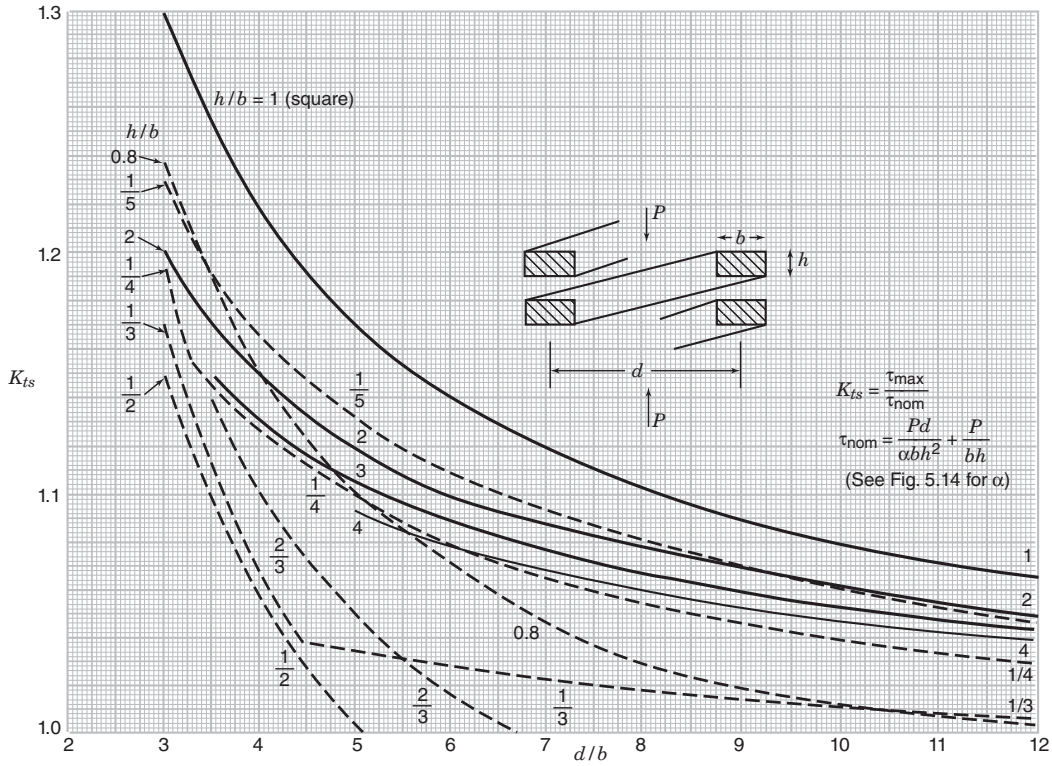


Chart 5.16 Stress concentration factors K_{ts} for a helical compression or tension spring of rectangular wire cross section (based on Liesecke 1933).

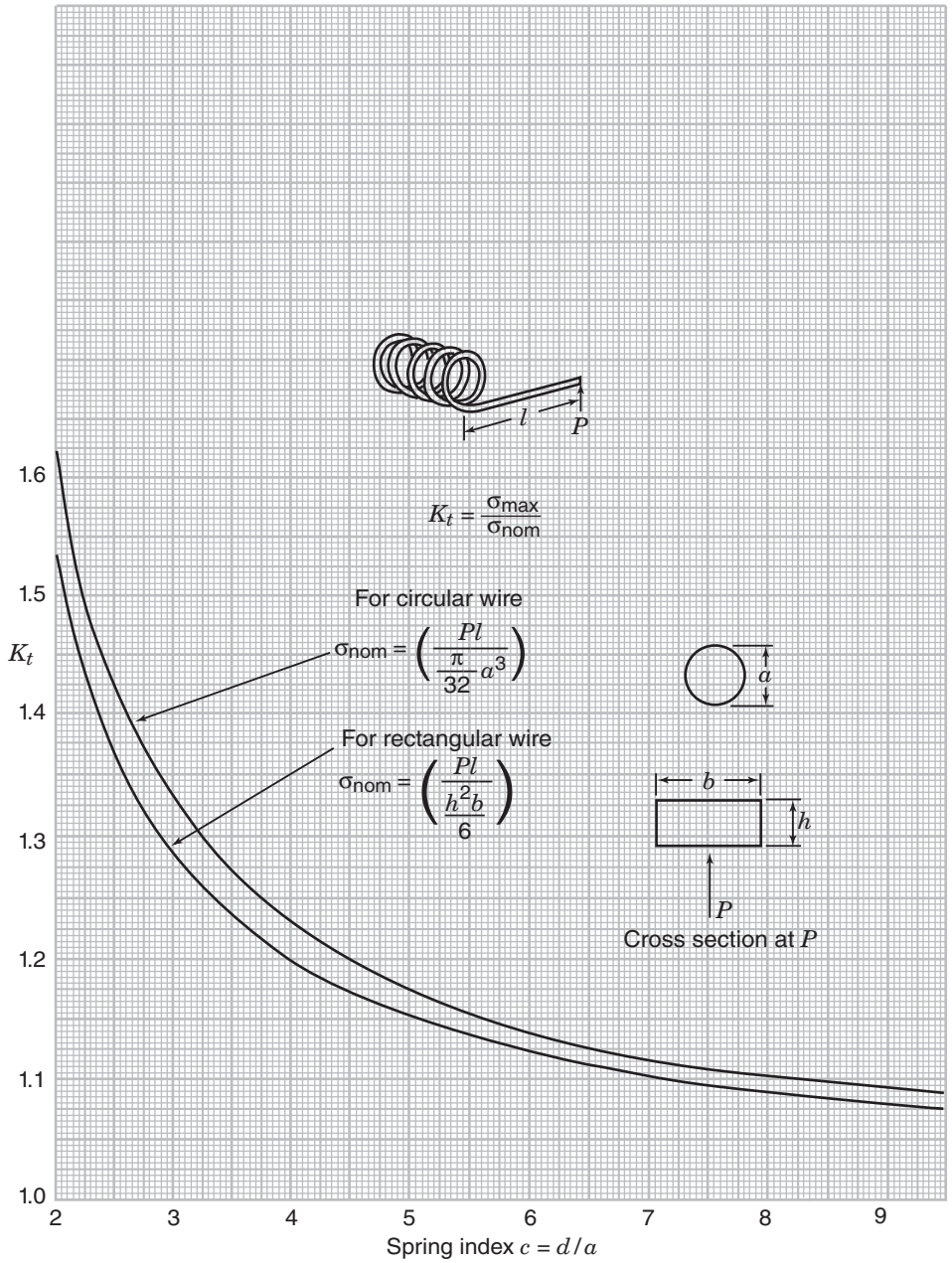


Chart 5.17 Stress concentration factors K_t for a helical torsion spring (Wahl 1963).

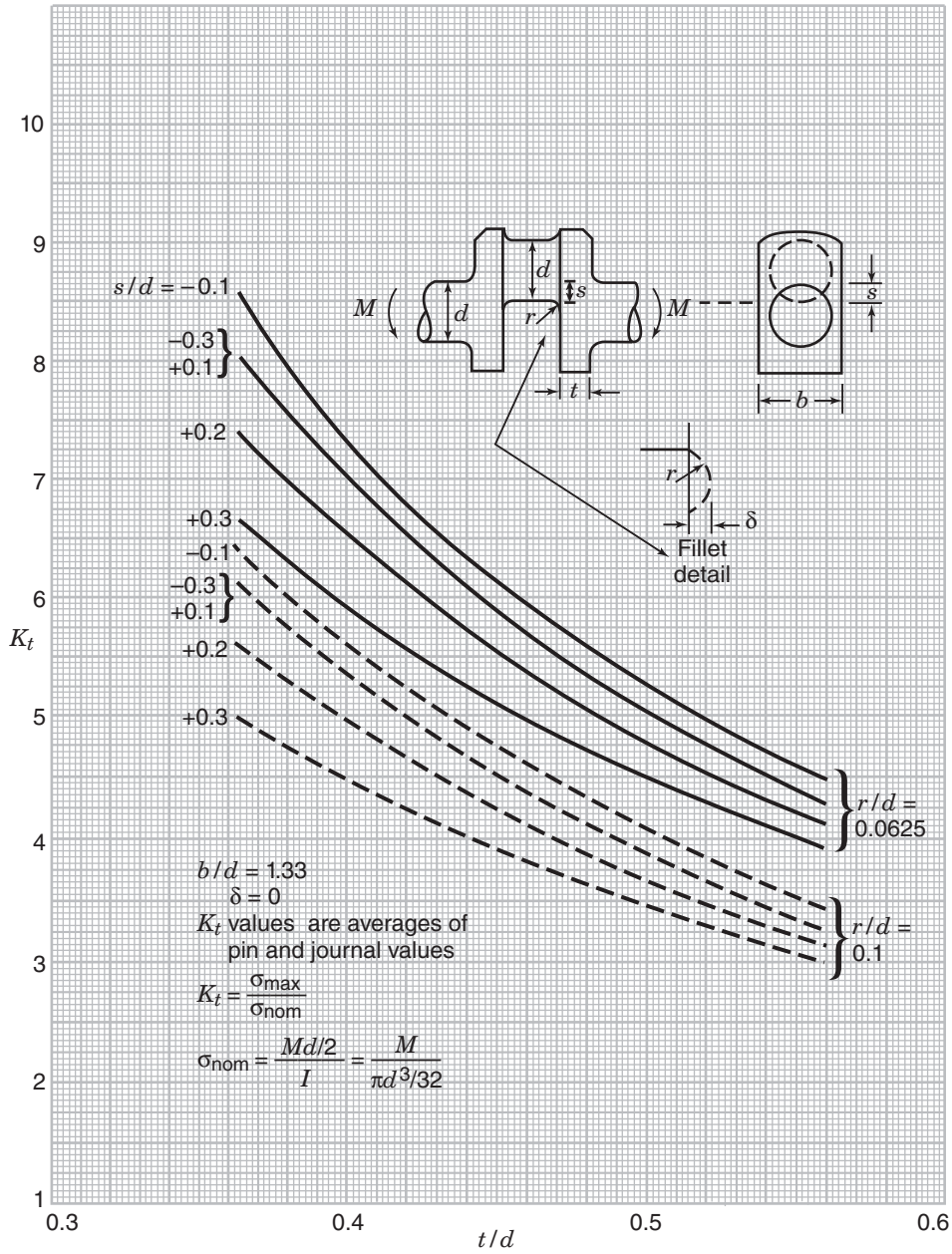


Chart 5.18 Stress concentration factors K_t for a crankshaft in bending (from strain gage values of Arai 1965).

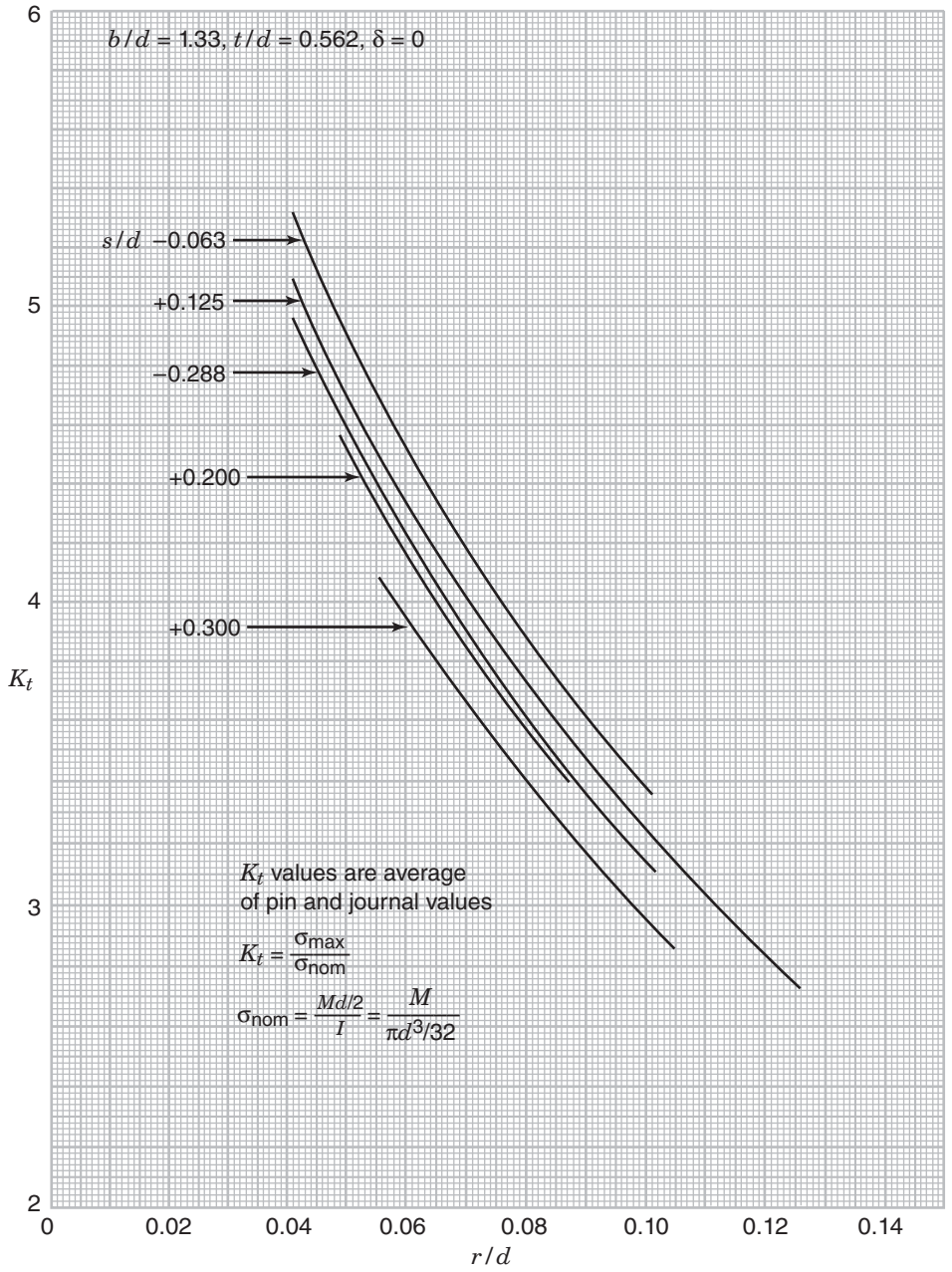


Chart 5.19 Stress concentration factors K_t for a crankshaft in bending (strain gage values of Arai 1965). See Chart 5.18 for notation.

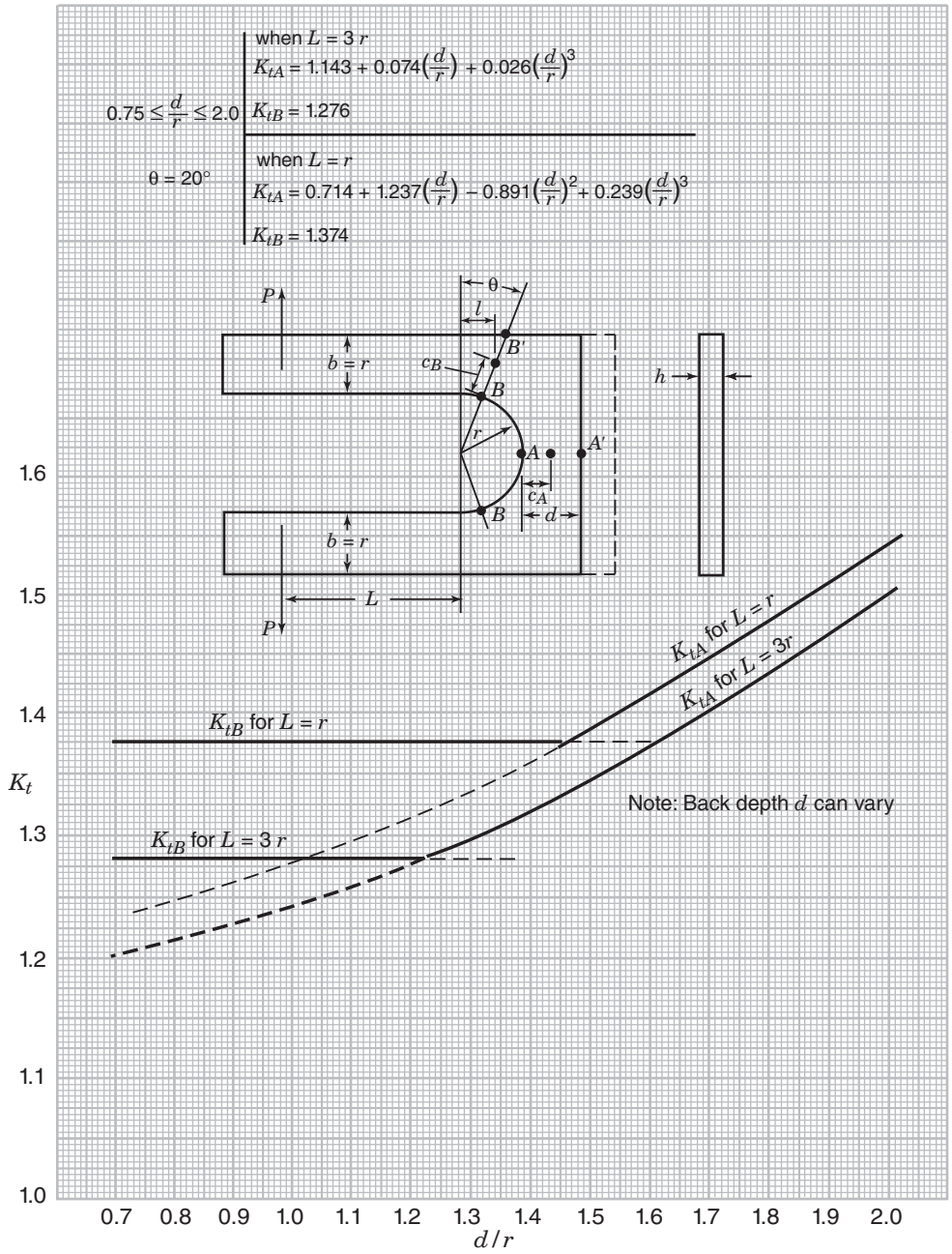


Chart 5.20 Stress concentration factors K_t for a U-shaped member (based on photoelastic tests of Mantle and Dolan 1948).

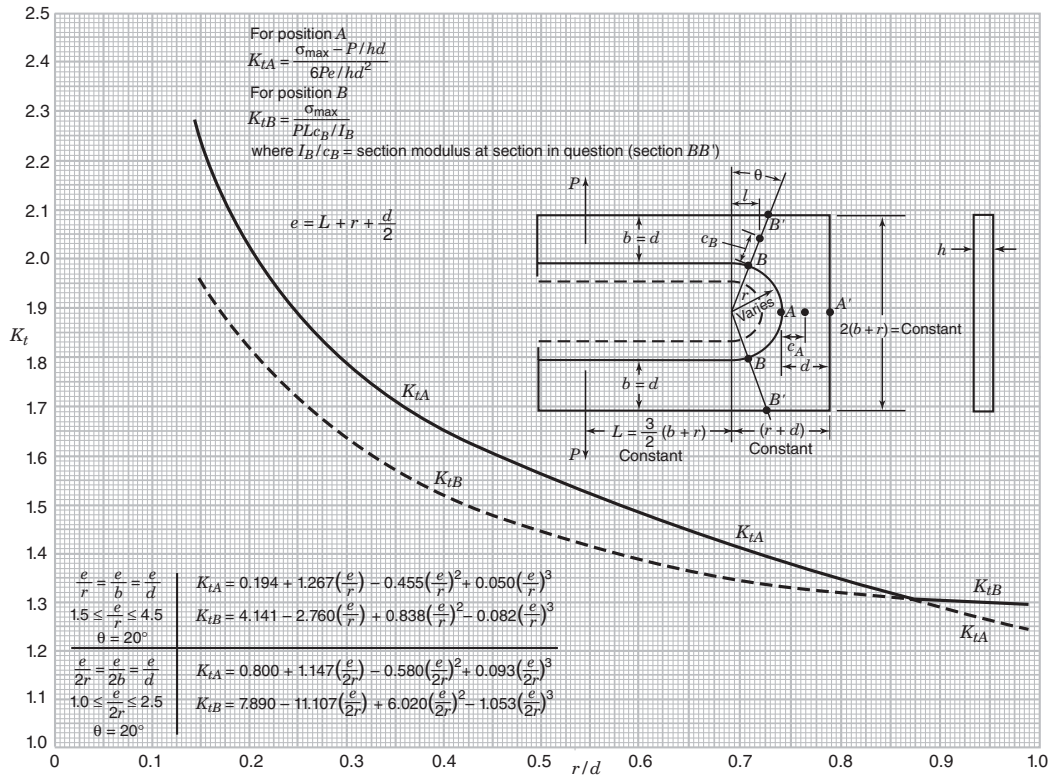


Chart 5.21 Stress concentration factors K_t for a U-shaped member (based on photoelastic tests of Mantle and Dolan 1948).

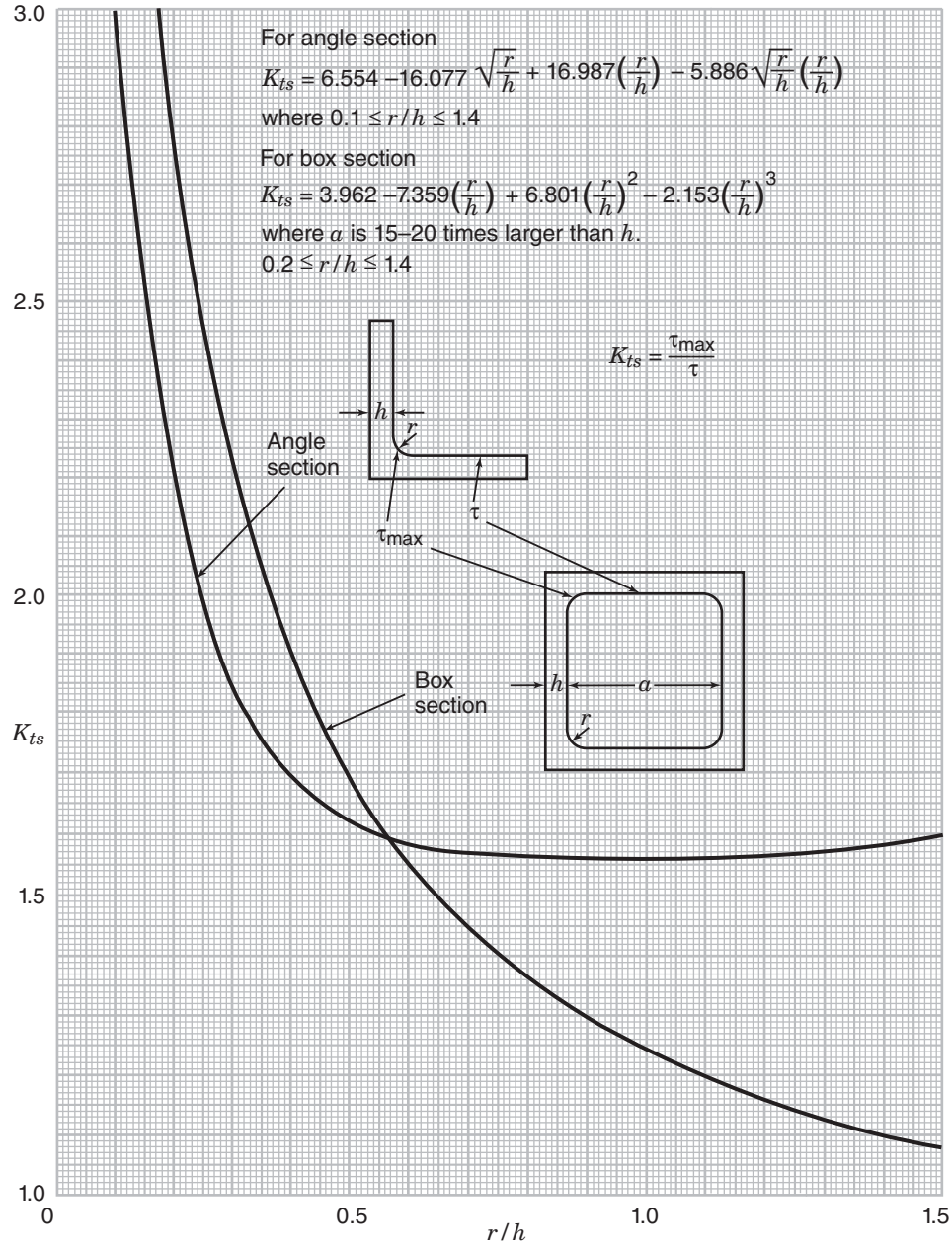


Chart 5.22 Stress concentration factors K_{ts} for angle or box sections in torsion (mathematical determination by Huth 1950).

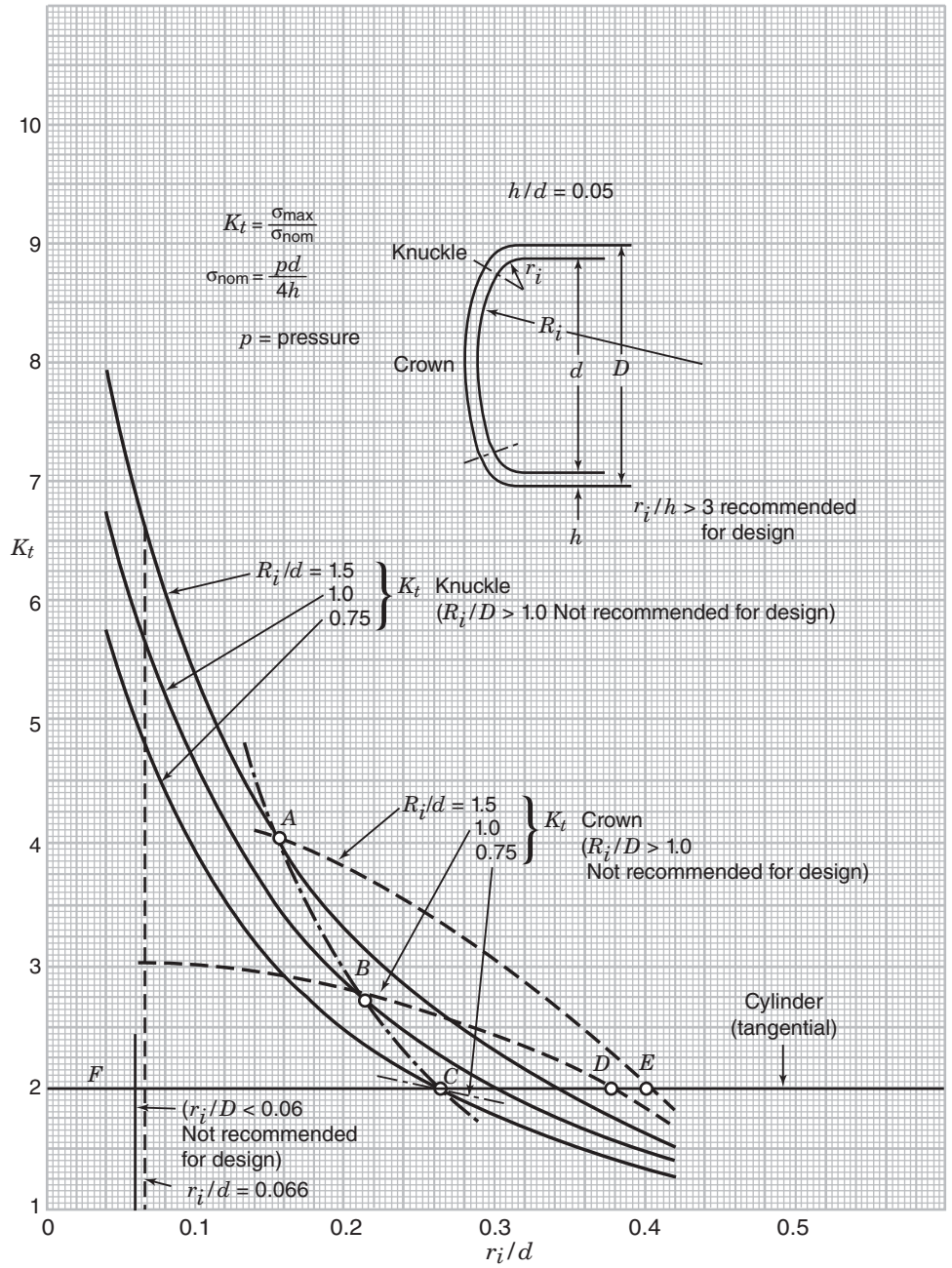


Chart 5.23 Stress concentration factors K_t for a cylindrical pressure vessel with torispherical ends (from data of Fessler and Stanley 1965).

CHAPTER 6

FINITE ELEMENT ANALYSIS (FEA) FOR STRESS ANALYSIS

Stress analysis is essential to ensure the safety of mechanical structure. In the preceding chapters, the method of stress concentration factors (SCFs) has been introduced to identify the weakest feature, which determines the overall strength of a structure. However, this method has its limitations due to the following reasons:

(1) The stress concentration can be determined only when the types of discontinuities and the load type are specified.
(2) The experimental conditions where SCFs are determined are different from those of analyzed objects in applications.
(3) The only SCFs that are available are intended for simple discontinuities and single load type or simple combinations of loads. It is infeasible to obtain SCFs for an infinite number of the possible combinations of multiple discontinuities and load types.
(4) Not all of the features with the stress concentration can be clearly defined as geometric discontinuities.
(5) When the loads are complex and the object has a number of features, it is impractical to analyze and combine SCFs for the areas of interest.

Therefore, a generic method is desirable to analyze stresses on an arbitrary object subjected to arbitrary loading conditions.

The finite element analysis (FEA) method is a default tool for stress analysis for complex objects to address all of the aforementioned issues. In this chapter, the structural analysis problem

Peterson's Stress Concentration Factors, Fourth Edition. Walter D. Pilkey, Deborah F. Pilkey and Zhuming Bi.
© 2020 John Wiley & Sons, Inc. Published 2020 by John Wiley & Sons, Inc.

is formulated, the basics of FEA theory is reviewed, the general procedure of using FEA for structural analysis is presented, and a number of case studies are presented to illustrate how FEA is applied for stress analysis.

6.1 STRUCTURAL ANALYSIS PROBLEMS

Structural analysis is to determine the effects of loads on solid objects. Structural analysis is required for any structures or objects that withstand different loads, such as machines, tools, vehicles, buildings, bridges, and instruments. Structural analysis aims to compute stress distribution and the deformation of solids, as well as other associated quantities, such as safety factors, reaction forces, displacements, and stability. Structural analysis is used to verify if an object meets the given functional requirements (FRs), such as the strengths, accuracy, and cost. Therefore, structural analysis is essential to the majority of engineering designs.

As shown in Fig. 6.1, since structural design is essential to the design of any product, structural design problems are highly diversified in terms of *time-dependence of loads*, *materials properties*

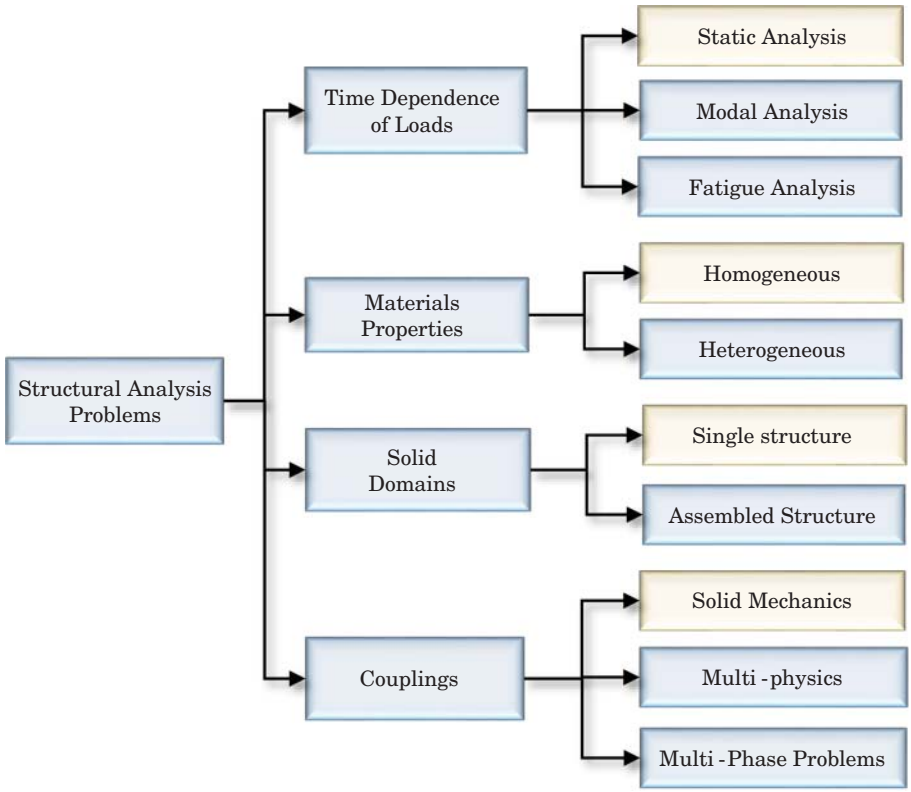


Figure 6.1 Classification of structural analysis problems (Bi 2018).

of solids, *the characteristics of solid domains*, and *coupling of disciplinary behaviors*. The method of SCFs introduced in the precedent chapters is suitable only to the manual calculations for the simplest design cases at every aspect.

6.2 TYPES OF ENGINEERING ANALYSIS METHODS

Generic engineering tools are desirable to solve diversified structural problems with arbitrary complexity of loads, geometries, materials properties, couplings, and the combination of these factors. As shown in Fig. 6.2, generic engineering tools can be classified into *graphic, experimental*, and *computational* methods.

- Graphic methods used to be popular before computers were invented, They helped to gain basic understandings of design problems but are obviously limited to small-scale problems.
- Even today, experimental methods are still widely adopted by companies in practice to engineering problems due to high reliability and acceptability of experimental results. However, experimental methods show their limitations in several aspects: (1) experiments need physical products ready to be tested, which are not always available at any design stage; (2) experiments usually require testing devices and the instrumentations for measurement; and (3) if a product or system involves a large number of design variables, it is impractical to investigate the performances of all systems for any combination of design variables.

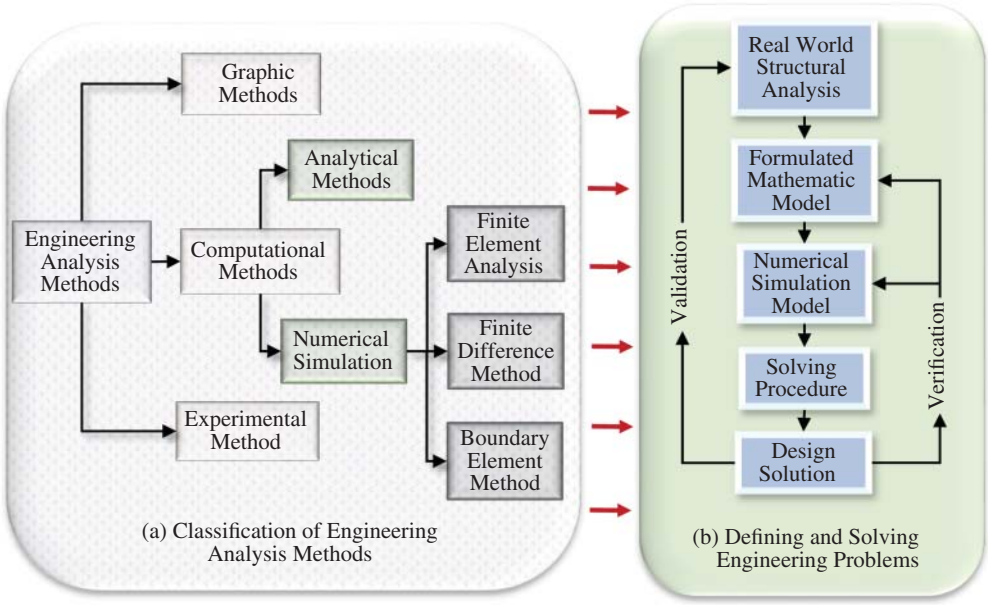


Figure 6.2 Types of design analysis methods for engineering solutions.

- Computational methods can be *analytical* or *numerical,* and engineering problems are solved by computers. Analytical methods derive *exact* solutions directly for the formulated mathematic models of solids with simple geometry and boundaries. Numerical methods, on the other hand, are the most widely used to find *approximate* solutions to simple or complex engineering problems. In contrast to graphic or experimental methods, computational methods are playing more critical roles in engineering design in the sense that (1) modern products or systems are too complicated for graphic or experimental methods to find complete solutions. (2) In general, a computational method is capable of obtaining engineering solutions in more cost-effective ways at the shortened time. (3) A computational method is performed on virtual models of products; even before a product or system is prototyped, the computational tool can predict system performance for a number of application scenarios. It can shorten the cycle-time of product development greatly. (4) Modern CAD tools have been evolved as very powerful with great capabilities in solving a wide scope of engineering problems without sophisticated training.

Fig. 6.2 shows the numerical methods can be further subcategorized into *finite element methods* (FEA), *finite difference methods*, and *boundary element methods*. These methods show their commonalities in sense that (1) all of methods are generic, which can be applied in various engineering problems. (2) In the solving process, the *divide and conquer* strategy is adopted to deal with the variety and complexity of engineering problems. However, different numerical methods show their uniqueness of the strategies in dealing with the derivatives or integral terms of mathematic models. For example, an FEA method differs from a finite difference method in the approximation of the derivatives in a mathematical model. FEA and finite difference method use different mathematic methods (*approximated integration* or *finite difference*) to deal with the terms of the derivatives in mathematic models. An FEA differs from a boundary element method in the ways of the discretization for a continuous domain. FEA treads solids as its domains, and the *elements* and *nodes* of a model are in solids. A boundary element method treads boundary surfaces as its domains, and the elements and nodes of a model are on boundary surfaces.

6.3 STRUCTURAL ANALYSIS THEORY

A mechanical system is subjected to different types of loads, such as force, pressure, heat, temperature, or constraints at supports. A number of critical tasks in a structural analysis include (1) to model and analyze the response of system to given loads, (2) identify critical areas of loading conditions, (3) evaluate corresponding stresses, and (4) determine whether or not the obtained stresses at critical areas exceed the strength of selected materials.

As shown in Fig. 6.3, external forces applied in a continuous domain can be classified as *volume force*, such as a weight caused by gravity, a *surface force*, such as a drag force by pressure, and a *concentrated load*, such as a point load on beam. Any one of external loads will affect the stress distribution over the domain. For any position with an infinitesimal volume, its stress state can be described as

$$\boldsymbol{\sigma} = \begin{bmatrix} \sigma_x & \sigma_y & \sigma_z & \tau_{xy} & \tau_{xz} & \tau_{yz} \end{bmatrix}^T \tag{6.1}$$

where σ_x, σ_y, and σ_z are the components of normal stresses and τ_{xy}, τ_{xz}, τ_{yz} are the components of shear stresses over x-y, x-z, and y-z planes, respectively.

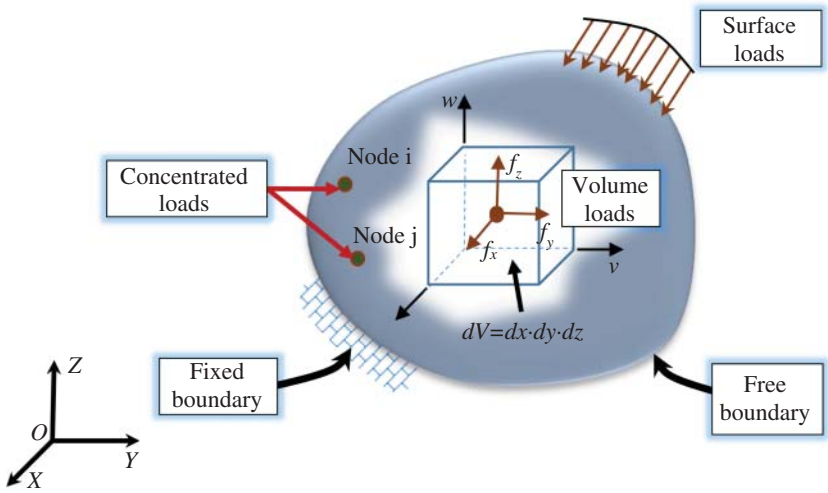


Figure 6.3 Description of structural analysis.

Fig. 6.4 shows the force equilibrium at an infinitesimal volume ($dx \times dy \times dz$). The force with six components in the stress state of Eq. (6.1) are balanced by the body force. Three equations are needed to describe the force equilibrium along the x-, y-, and z- axis, respectively.

Take an example of the stress equilibrium over the Y-Z plane,

$$\left.\begin{aligned}\sum F_y = &\left(\sigma_y + \frac{\partial \sigma_y}{\partial y}dy\right)dxdz - \sigma_y dxdz + \left(\tau_{xy} + \frac{\partial \tau_{xy}}{\partial x}dx\right)dydz - \tau_{xy}dxdz \\ &+ \left(\tau_{zy} + \frac{\partial \tau_{zy}}{\partial z}dz\right)dxdy - \tau_{zy}dxdy - f_y dxdydz = 0\end{aligned}\right\} \tag{6.2}$$

Eq. (6.2) can be further simplified as

$$\frac{\partial \tau_{xy}}{\partial x} + \frac{\partial \sigma_y}{\partial y} + \frac{\partial \tau_{yz}}{\partial z} + f_y = 0 \tag{6.3}$$

Since the selection of X, Y, and Z is arbitrary, the same force equilibrium condition applies to X-Z plane and X-Y plane. As a result, the conditions of the force equilibrium on three planes are

$$\left.\begin{aligned}\frac{\partial \sigma_x}{\partial x} + \frac{\partial \tau_{xy}}{\partial y} + \frac{\partial \tau_{xz}}{\partial z} + f_x = 0 \\ \frac{\partial \tau_{xy}}{\partial x} + \frac{\partial \sigma_y}{\partial y} + \frac{\partial \tau_{yz}}{\partial z} + f_y = 0 \\ \frac{\partial \tau_{xz}}{\partial z} + \frac{\partial \tau_{yz}}{\partial y} + \frac{\partial \sigma_z}{\partial z} + f_z = 0\end{aligned}\right\} \tag{6.4}$$

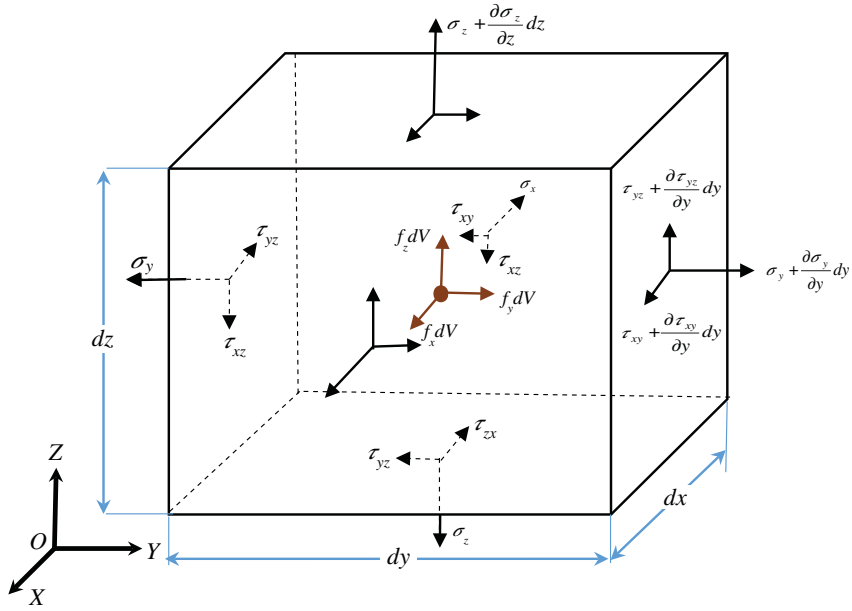


Figure 6.4 Stress equilibrium at an infinitesimal volume.

Note that external forces turn into the distributed stress over object, and the response of the materials is quantified by the strain state $\varepsilon = \begin{bmatrix} \varepsilon_x & \varepsilon_y & \varepsilon_z & \gamma_{xy} & \gamma_{zy} & \gamma_{xz} \end{bmatrix}^T$ as

$$\left.\begin{aligned} \varepsilon_x &= \frac{1}{2}\left(\sigma_x - v(\sigma_y + \sigma_z)\right) \\ \varepsilon_y &= \frac{1}{2}\left(\sigma_y - v(\sigma_y + \sigma_z)\right) \\ \varepsilon_z &= \frac{1}{2}\left(\sigma_z - v(\sigma_x + \sigma_y)\right) \\ \gamma_{xy} &= \frac{\tau_{xy}}{G}, \gamma_{yz} = \frac{\tau_{yz}}{G}, \gamma_{xz} = \frac{\tau_{xz}}{G} \end{aligned}\right\} \tag{6.5}$$

where E is the elastic or Young's modulus, v is Poisson's ratio, and G is shear modulus or modules of rigidity. Shear modulus G depends on elastic modulus E by the relation of

$$G = \frac{E}{2(1+v)} \tag{6.6}$$

Alternatively, Eq. (6.5) can also be reformatted to determine the state of stresses based on the given strains as

$$\{\sigma\} = [\boldsymbol{D}]\{\varepsilon\} \tag{6.7}$$

where $[\boldsymbol{D}]$ is the matrix form of the Hooke's law in a three-dimensional space, i.e.,

$$[\boldsymbol{D}] = \frac{E}{(1+v)(1-2v)} \begin{bmatrix} 1-v & v & v & 0 & 0 & 0 \\ v & 1-v & v & 0 & 0 & 0 \\ v & v & 1-v & 0 & 0 & 0 \\ 0 & 0 & 0 & \frac{1}{2}-v & 0 & 0 \\ 0 & 0 & 0 & 0 & \frac{1}{2}-v & 0 \\ 0 & 0 & 0 & 0 & 0 & \frac{1}{2}-v \end{bmatrix} \tag{6.8}$$

Depending on the type of design problems, the stress and strain relations can be simplified if not all of the directions have nonzero stresses. In the following, the physical behaviors for a few of classic mechanical design problems are discussed.

6.3.1 Trusses and Frame Structures

6.3.1.1 Trusses A mechanical structure is often needed to support loads in a large space. To fully utilize materials, a set of spatially structured members are assembled to replace bulk bodies. Fig. 6.5 shows some examples of the applications of truss structures in construction, factory, and transportation. The majority of components in these applications are *trusses*, which can be idealized as binary elements in a system model. In design a truss structure, the number,



Figure 6.5 Truss-structure examples with distributed loads in large space (Bi 2018).

types, materials, configurations, and cross-section areas of trusses are optimized to maximize the material utilization and the capability of structure.

Mathematically, a truss structure consists of a number of *joints*, connected by two-force binary members. Each truss member in the structure consists of two *nodes* and carries either a *compressive* or *tensile* force. A joint allows a free rotation of two members without a relative displacement at the junction. To facilitate structural analysis, it is assumed that external loads are concentrated and applied on the joints.

Fig. 6.6 shows that the behavior of a linear truss member is represented by the displacements on node i and node j as u_i and u_j. In the one-dimensional local coordinate system (LCS) whose axis is aligned with the neutral axis of truss, the solid domain of the element is $x \in (0, L)$. To calculate the displacement $u(x)$ at any position x, the interpolation in the element can be performed using the shape functions of two nodes as

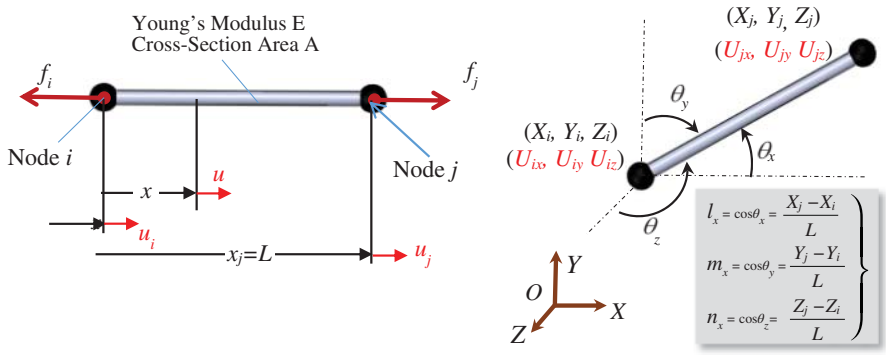
$$u(x) = \begin{bmatrix} S_i(x) & S_i(x) \end{bmatrix} \begin{Bmatrix} u_i \\ u_j \end{Bmatrix} \quad \text{and} \quad \frac{du(x)}{dx} = \begin{bmatrix} S_i'(x) & S_j'(x) \end{bmatrix} \begin{Bmatrix} u_i \\ u_j \end{Bmatrix} \tag{6.9}$$

where $S_i(x)$ and $S_j(x)$ are the shape functions associated with node i and j as

$$S_i(x) = \frac{l - x}{l}, S_j(x) = \frac{x}{l}$$

Assume that a truss member has a length of L and a uniform cross-section area of A with the elasticity modulus of E, the potential energy of the truss member can be evaluated as

$$\Pi = \int_V \frac{1}{2} E \frac{d\boldsymbol{u}}{dx} dV - (f_i \cdot u_i + f_j \cdot u_j) = \frac{EA}{2} \int_V \frac{d\boldsymbol{u}}{dx} dx - (f_i \cdot u_i + f_j \cdot u_j) \tag{6.10}$$



(a) Local coordinate system (LCS) (b) Global coordinate system (GCS)

Figure 6.6 A one-dimensional truss element in LCS and GCS.

Using the condition for the minimal potential energy $\frac{\partial \Pi}{\partial u_i} = \frac{\partial \Pi}{\partial u_j} = 0$ yields,

$$\begin{bmatrix} k_e & -k_e \\ -k_e & k_e \end{bmatrix} \begin{Bmatrix} u_i \\ u_j \end{Bmatrix} = \begin{Bmatrix} f_i \\ f_j \end{Bmatrix} \tag{6.11}$$

where $k_e = \frac{EA}{L}$ is the equivalent stiffness coefficient.

As shown in Fig. 6.6, even though a truss member only has its displacement along the axial direction in its LCS; a truss member can be an arbitrary position in a two- or three-dimensional space. Therefore, the coordination transformation must be performed to transform an element model from LCS to a global coordinate system (GCS). To this end, Eq. (6.11) is expanded to model the relations of forces and the displacements of nodes in GCS as,

$$\left[\boldsymbol{K}_{L,e}\right]\{u\} = \begin{bmatrix} k_e & 0 & 0 & -k_e & 0 & 0 \\ 0 & 0 & 0 & 0 & 0 & 0 \\ 0 & 0 & 0 & 0 & 0 & 0 \\ -k_e & 0 & 0 & k_e & 0 & 0 \\ 0 & 0 & 0 & 0 & 0 & 0 \\ 0 & 0 & 0 & 0 & 0 & 0 \end{bmatrix} \begin{Bmatrix} u_i \\ 0 \\ 0 \\ u_j \\ 0 \\ 0 \end{Bmatrix} = \begin{Bmatrix} f_i \\ 0 \\ 0 \\ f_j \\ 0 \\ 0 \end{Bmatrix} \tag{6.12}$$

where $[\boldsymbol{K}_{L,e}]$ is the three-dimensional stiffness matrix of a truss element with respect to GCS.

Similarly, the nodal displacements need to be transformed from LCS to GCS as,

$$\begin{Bmatrix} U_{ix} \\ U_{iy} \\ U_{iz} \end{Bmatrix} = [T] \cdot \begin{Bmatrix} u_i \\ 0 \\ 0 \end{Bmatrix}, \begin{Bmatrix} U_{jx} \\ U_{jy} \\ U_{jz} \end{Bmatrix} = [T] \cdot \begin{Bmatrix} u_j \\ 0 \\ 0 \end{Bmatrix} \tag{6.13}$$

where

$[\boldsymbol{T}] = \begin{bmatrix} l_x & l_y & l_z \\ m_x & m_y & m_z \\ n_x & n_y & n_z \end{bmatrix}$ and

$\begin{Bmatrix} l_x \\ m_x \\ n_x \end{Bmatrix}, \begin{Bmatrix} l_y \\ m_y \\ n_y \end{Bmatrix}, \begin{Bmatrix} l_z \\ m_z \\ n_z \end{Bmatrix}$ are the vectors of directional cosines of the axes x, y, z of LCS expressed in GCS.

Note that the x-axis must be selected to be aligned with the axial direction of a truss member; while the directions of y- and z- axes can be arbitrary as long as the perpendicular relations of x- with y- and z- are satisfied.

The coordinate transformation from GCS to LCS can be obtained by reformatting Eq. (6.13) as

$$\begin{Bmatrix} u_i & 0 & 0 & u_j & 0 & 0 \end{Bmatrix}^T = \left[T_{global\_local}\right] \begin{Bmatrix} U_{ix} & U_{iy} & U_{iz} & U_{jx} & U_{jy} & U_{jz} \end{Bmatrix}^T \tag{6.14}$$

where

$$\left[T_{global\_local}\right] = \begin{bmatrix} l_x & m_x & n_x & 0 & 0 & 0 \\ l_y & m_y & m_y & 0 & 0 & 0 \\ l_z & m_z & n_z & 0 & 0 & 0 \\ 0 & 0 & 0 & l_x & m_x & n_x \\ 0 & 0 & 0 & l_y & m_y & n_y \\ 0 & 0 & 0 & l_z & m_y & n_z \end{bmatrix} \tag{6.15}$$

Substituting Eq. (6.15) into Eq. (6.12) gets

$$[K_{G,e}] \cdot \begin{Bmatrix} U_{ix} \\ U_{iy} \\ U_{iz} \\ U_{jx} \\ U_{jy} \\ U_{jz} \end{Bmatrix} = \begin{Bmatrix} F_{ix} \\ F_{iy} \\ F_{iz} \\ F_{jx} \\ F_{jy} \\ F_{jz} \end{Bmatrix} \tag{6.16}$$

where

$$\begin{aligned} [K_{G,e}] &= [T]' \cdot [K_{L,e}] \cdot [T] \\ &= \begin{bmatrix} l_x & l_y & l_z & 0 & 0 & 0 \\ m_x & m_y & m_z & 0 & 0 & 0 \\ n_x & n_y & n_z & 0 & 0 & 0 \\ 0 & 0 & 0 & l_x & l_y & l_z \\ 0 & 0 & 0 & m_x & m_y & m_z \\ 0 & 0 & 0 & n_x & n_y & n_z \end{bmatrix} \cdot \begin{bmatrix} k_e & 0 & 0 & -k_e & 0 & 0 \\ 0 & 0 & 0 & 0 & 0 & 0 \\ 0 & 0 & 0 & 0 & 0 & 0 \\ -k_e & 0 & 0 & k_e & 0 & 0 \\ 0 & 0 & 0 & 0 & 0 & 0 \\ 0 & 0 & 0 & 0 & 0 & 0 \end{bmatrix} \cdot \begin{bmatrix} l_x & m_x & n_x & 0 & 0 & 0 \\ l_y & m_y & m_y & 0 & 0 & 0 \\ l_z & m_z & n_z & 0 & 0 & 0 \\ 0 & 0 & 0 & l_x & m_x & n_x \\ 0 & 0 & 0 & l_y & m_y & n_y \\ 0 & 0 & 0 & l_z & m_y & n_z \end{bmatrix} \\ &= k_e \begin{bmatrix} l_x^2 & l_x m_x & l_x n_x & -l_x^2 & -l_x m_x & -l_x n_x \\ l_x m_x & m_x^2 & m_x n_x & -l_x m_x & -m_x^2 & -m_x n_x \\ l_x n_x & m_x n_x & n_x^2 & -l_x n_x & -l_x m_x & -n_x^2 \\ -l_x^2 & -l_x m_x & -l_x n_x & l_x^2 & l_x m_x & l_x n_x \\ -l_x m_x & -m_x^2 & -m_x n_x & l_x m_x & m_x^2 & m_x n_x \\ -l_x n_x & -m_x n_x & -n_x^2 & l_x n_x & l_x m_x & n_x^2 \end{bmatrix} \end{aligned}$$

Note that the deviated stiffness matrix relates only to the directional cosines of local x-axis where the deformation occurs.

6.3.1.2 Boundary Conditions (BCs) and Loads Truss members are two-force members. Since a junction of two members does not restrain any rotation, each node in a truss element has three translational degrees of freedom (DoF). Fig. 6.7 shows the types of the boundary conditions

(BCs) on nodes. The constraints imposed on a node can be one-, two- or three-DoF. In the case of Fig. 6.7*d*, the constrained displacement is not aligned with any axis of a coordinate system. A new reference plane has to be created, so that the boundary condition of a roller can be defined to restrain the motion perpendicular to that reference plane.

Only nodal forces are applicable to a truss structure. Therefore, external loads on trusses must be converted to equivalent nodal forces. Taking an example of the gravity force, the equivalent nodal loads must be determined based on the force or moment equilibrium or energy conservation of truss members.

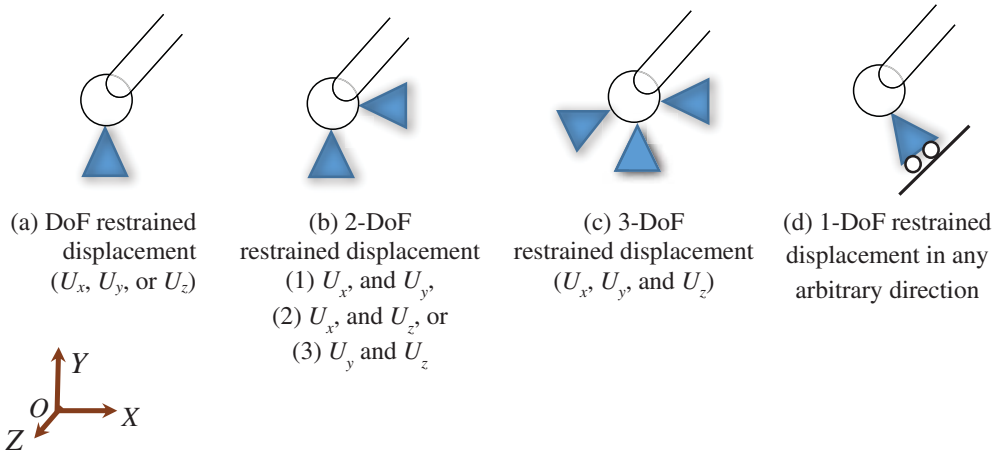
6.3.1.3 Frame Structure The resistance to rotational displacements is not taken into account in the mathematical model of a truss structure; it is applicable only to the scenarios where the impact of rotational restraints is ignorable. However, a truss structure may be assembled by *riveting*, *fastening*, *welding*, or *mechanical joints* in the real-world applications (Fig. 6.8), the element types, such as bending or frame members have to be used to represent a real-world structure appropriately. Fig. 6.9 shows a three-dimensional frame member with six DOFs. Each node has three translational and three rotational displacements.

The vector for the displacements of a three-dimensional frame is given as

$$\{\boldsymbol{u}\} = \{u_i, v_i, w_i, \theta_{ix}, \theta_{iy}, \theta_{iz}, u_j, v_j, w_j, \theta_{jx}, \theta_{jy}, \theta_{jz}\}^T \tag{6.17}$$

The coordinate transformation from GCS to LCS can be obtained by reformatting Eq. (6.13) as

$$\begin{aligned}&\{u_i, v_i, w_i, \theta_{ix}, \theta_{iy}, \theta_{iz}, u_j, v_j, w_j, \theta_{jx}, \theta_{jy}, \theta_{jz}\}^T \\ &\quad = [T_{global\_local}]_{12\times12}\{U_i, V_i, W_i, \theta_{iX}, \theta_{iY}, \theta_{iZ}, V_i, V_j, W_j, \theta_{jX}, \theta_{jY}, \theta_{jZ}\}^T\end{aligned} \tag{6.18}$$



(a) DoF restrained displacement (U_x, U_y, or U_z)

(b) 2-DoF restrained displacement (1) U_x, and U_y, (2) U_x, and U_z, or (3) U_y and U_z

(c) 3-DoF restrained displacement (U_x, U_y, and U_z)

(d) 1-DoF restrained displacement in any arbitrary direction

Figure 6.7 Types of boundary conditions for truss structure.



(a) Restraints on rotations and translations

(b) Restraints on translations

Figure 6.8 Various joints in truss, beam, and frame structures (Bi 2018).

where $U_i, V_i, W_i, \theta_{iX}, \theta_{iY}, \theta_{iZ}$, and $V_i, V_j, W_j, \theta_{jX}, \theta_{jY}, \theta_{jZ}$ are the displacements at node i and node j in GCS, respectively, and $[T_{global\_local}]_{12\times12}$ is the coordinate transformation as

$$[T_{global\_local}]_{12\times12} = \begin{bmatrix} l_x & m_x & n_x & 0 & 0 & 0 & 0 & 0 & 0 & 0 & 0 & 0 \\ l_y & m_y & n_y & 0 & 0 & 0 & 0 & 0 & 0 & 0 & 0 & 0 \\ l_z & m_z & n_z & 0 & 0 & 0 & 0 & 0 & 0 & 0 & 0 & 0 \\ 0 & 0 & 0 & l_x & m_x & n_x & 0 & 0 & 0 & 0 & 0 & 0 \\ 0 & 0 & 0 & l_y & m_y & n_y & 0 & 0 & 0 & 0 & 0 & 0 \\ 0 & 0 & 0 & l_z & m_z & n_z & 0 & 0 & 0 & 0 & 0 & 0 \\ 0 & 0 & 0 & 0 & 0 & 0 & l_x & m_x & n_x & 0 & 0 & 0 \\ 0 & 0 & 0 & 0 & 0 & 0 & l_y & m_y & n_y & 0 & 0 & 0 \\ 0 & 0 & 0 & 0 & 0 & 0 & l_z & m_z & n_z & 0 & 0 & 0 \\ 0 & 0 & 0 & 0 & 0 & 0 & 0 & 0 & 0 & l_x & m_x & n_x \\ 0 & 0 & 0 & 0 & 0 & 0 & 0 & 0 & 0 & l_y & m_y & n_y \\ 0 & 0 & 0 & 0 & 0 & 0 & 0 & 0 & 0 & l_z & m_z & n_z \end{bmatrix} \tag{6.19}$$

where $\{l_x \quad m_x \quad n_x\}^T$, $\{l_y \quad m_y \quad n_y\}^T$ and $\{l_z \quad m_z \quad n_z\}^T$ are the vectors of the directional cosines of the axes x, y, z of LCS expressed in GCS.

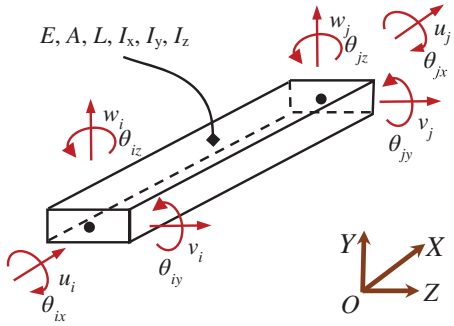


Figure 6.9 Description of three-dimensional frame element.

The minimized potential energy method can be used to determine the stiffness matrix $[K]_{L,frame}$ for the relation of displacements and loads in LCS, and the result is found as (Gavin 2012, what-when-how 2018)

$$[K]_{L,frame} = \begin{bmatrix} \frac{EA}{L} & 0 & 0 & 0 & 0 & 0 & -\frac{EA}{L} & 0 & 0 & 0 & 0 & 0 \\ & \frac{12EI_z}{L^3} & 0 & 0 & 0 & \frac{6EI_z}{L^2} & 0 & -\frac{12EI_z}{L^3} & 0 & 0 & 0 & \frac{12EI_z}{L^3} \\ & & \frac{12EI_y}{L^3} & 0 & -\frac{6EI_y}{L^2} & 0 & 0 & 0 & -\frac{12EI_y}{L^3} & 0 & -\frac{6EI_y}{L^2} & 0 \\ & & & \frac{GJ}{L} & 0 & 0 & 0 & 0 & 0 & -\frac{GJ}{L} & 0 & 0 \\ & & & & \frac{4EI_y}{L} & 0 & 0 & 0 & \frac{6EI_y}{L^2} & 0 & \frac{2EI_y}{L} & 0 \\ & & & & & \frac{4EI_z}{L} & 0 & -\frac{6EI_z}{L^2} & 0 & 0 & 0 & \frac{2EI_z}{L} \\ & & & & & & \frac{EA}{L} & 0 & 0 & 0 & 0 & 0 \\ & & & & & & & \frac{12EI_z}{L^3} & 0 & 0 & 0 & -\frac{6EI_z}{L^2} \\ & & & & & & & & \frac{12EI_y}{L^3} & 0 & \frac{6EI_y}{L^2} & 0 \\ & & & & & & & & & \frac{GJ}{L} & 0 & 0 \\ & & & & & & & & & & \frac{4EI_y}{L} & 0 \\ & & & & & & & & & & & \frac{4EI_z}{L} \end{bmatrix}$$

Symmetric to upper triangular matrix

Accordingly, the model of a three-dimensional frame element can be obtained as

$$\begin{aligned}&[K]_{G,frame} \cdot \{U_i, V_i, W_i, \theta_{iX}, \theta_{iY}, \theta_{iZ}, V_i, V_j, W_j, \theta_{jX}, \theta_{jY}, \theta_{jZ}\}^T \\ &= \{F_{iX}, F_{iY}, F_{iZ}, T_{iX}, T_{iY}, T_{iZ}, F_{jX}, F_{jY}, F_{jiZ}, T_{jX}, T_{jY}, T_{jZ}\}^T\end{aligned} \tag{6.20}$$

where $[K]_{G,frame} = \left[T_{global_{local}}\right]^T_{12\times12} \cdot [K]_{L,frame} \cdot \left[T_{global_{local}}\right]_{12\times12}$ is the stiffness matrix of frame element in GCS, and $F_{iX}, F_{iY}, F_{iZ}, T_{iX}, T_{iY}, T_{iZ}$ and $F_{jX}, F_{jY}, F_{jiZ}, T_{jX}, T_{jY}, T_{jZ}$ are the forces applied on node i and node j, respectively.

6.3.2 Plane Stress and Strain Problems

Many problems in a structural analysis can be solved satisfactorily by a two-dimensional simulation model. Two general types in the plane theory of elasticity are *plane stress* and *plane strain*. Both of them are defined by specifying certain restraints on stress or strain fields. An object is said to be in a plane stress state if the stress vector is zero across a plane. If such a case occurs to the entire domain of a structure, for example of a thin plate, the structural analysis of the object can be simplified considerably by representing the stress state as a two-dimensional tensor.

6.3.2.1 Plane Stresses Fig. 6.10 gives some examples of the applications where the products or parts can be analyzed by a plane stress model.



Figure 6.10 Examples of plane-stress applications (Bi 2018).

Under a plane stress state, all of the stresses occur on the same plane. Assume that all of stresses occur on X-Y plane, i.e., $\sigma_z = 0$, and $\tau_{xz} = \tau_{yz} = 0$, Eqs. (6.7) and (6.8) can be simplified as,

$$\{\boldsymbol{\sigma}\} = \begin{Bmatrix} \sigma_x \\ \sigma_y \\ \tau_{xy} \end{Bmatrix} = [\boldsymbol{D}]\varepsilon = \frac{E}{1-\upsilon^2} \begin{bmatrix} 1 & \upsilon & 0 \\ \upsilon & 1 & 0 \\ 0 & 0 & \frac{1-\upsilon}{2} \end{bmatrix} \begin{Bmatrix} \varepsilon_x \\ \varepsilon_y \\ \gamma_{xy} \end{Bmatrix} \tag{6.21}$$

where $[\boldsymbol{D}]$ is a symmetric matrix, i.e., $[D] = [D]^T$.

The principle of the minimized potential energy is applied to formulate element models about nodal displacements. The potential energy of an element consists of the strain energy of materials and the work made by external loads. Assume that external loads are applied on nodes, the potential energy of an element can be evaluated as,

$$\Pi = \Lambda - \sum_{i=1}^{n} F_i \cdot U_i \tag{6.22}$$

where Π is the total potential energy, Λ is the strain energy, n is the degrees of freedom of element, F_i is an external load over the *i-th* degree of freedom, and U_i is the displacement on the *i-th* degree of freedom.

The total strain energy of element can be evaluated as,

$$\Lambda = \int_V \frac{1}{2}[\boldsymbol{\sigma}]^T[\varepsilon]dV = \int_V \frac{1}{2}[\varepsilon]^T[D]^T[\varepsilon]dV = \int_V \frac{1}{2}[\varepsilon]^T[D]\,[\varepsilon]dV \tag{6.23}$$

In an FEA model, the behavior of a continuous domain is collectively represented by state variables of nodes. An element model describes the relations of external forces and state values on nodes. An element model depends on the number of nodes, DoF on each node, geometric shape, and the governing equations of physical behaviors. In this section, we discuss two basic types of two-dimensional plane elements, i.e., *linear triangle element* and *rectangle element*.

Fig. 6.11 shows a linear triangle element in a GCS. It consists of three nodes (i, j, and k),

whose coordinates in GCS are given as (X_i, Y_i), (X_j, Y_j), and (X_k, Y_k), respectively. The element behavior is represented by the displacements on three nodes, namely, (U_{ix}, U_{iy}), (U_{jx}, U_{jy}), and (U_{kx}, U_{ky}). To derive the model of a triangle element in Fig. 6.11, the interpolation is performed, so that the displacement (u, v) in an arbitrary position (X, Y) can be derived from the displacements at nodes using shape functions.

$$\begin{Bmatrix} u \\ v \end{Bmatrix} = \begin{bmatrix} S_i & 0 & S_j & 0 & S_k & 0 \\ 0 & S_i & 0 & S_j & 0 & S_k \end{bmatrix} \begin{Bmatrix} U_{ix} \\ U_{iy} \\ U_{jx} \\ U_{jy} \\ U_{kx} \\ U_{ky} \end{Bmatrix} \tag{6.24}$$

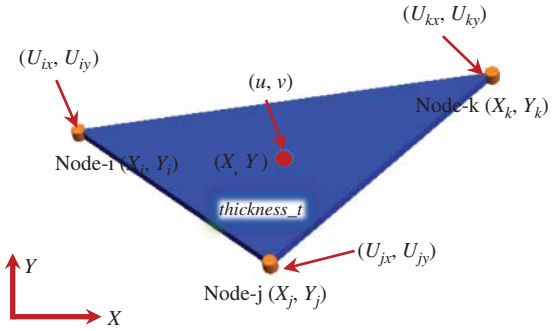


Figure 6.11 Triangular element with plane stress.

where the shape functions of a triangular element are given as (Bi 2018)

$$\left.\begin{aligned} S_i(x,y) &= \frac{|\Delta_i|}{|\Delta|} = \frac{\alpha_i + \beta_i \cdot x + \delta_i \cdot y}{|\Delta|} \\ S_j(x,y) &= \frac{|\Delta_j|}{|\Delta|} = \frac{\alpha_j + \beta_j \cdot x + \delta_j \cdot y}{|\Delta|} \\ S_k(x,y) &= \frac{|\Delta_k|}{|\Delta|} = \frac{\alpha_k + \beta_k \cdot x + \delta_k \cdot y}{|\Delta|} \end{aligned}\right\} \tag{6.25}$$

where

$$\left.\begin{aligned} |\Delta| &= \begin{vmatrix} 1 & x_i & y_i \\ 1 & x_j & y_j \\ 1 & x_k & y_k \end{vmatrix} \\ \alpha_i &= x_j y_k - x_k y_j, \quad \alpha_j = x_k y_i - x_i y_k, \quad \alpha_k = x_i y_j - x_j y_i \\ \beta_i &= y_j - y_k, \quad \beta_j = y_k - y_i, \quad \beta_k = y_i - y_j \\ \delta_i &= x_k - x_j, \quad \delta_j = x_i - x_k, \quad \delta_k = x_j - x_i \end{aligned}\right\} \tag{6.26}$$

and (x_i, y_i), (x_j, y_j), (x_k, y_k) are the coordinates of nodes i, j, k in Fig. 6.11.

The plane-strain can be derived from Eq. (6.24) as

$$\begin{Bmatrix} \varepsilon_x \\ \varepsilon_y \\ \gamma_{xy} \end{Bmatrix} = \begin{Bmatrix} \dfrac{\partial u}{\partial x} \\ \dfrac{\partial v}{\partial y} \\ \dfrac{\partial u}{\partial y} + \dfrac{\partial v}{\partial x} \end{Bmatrix} = \begin{bmatrix} \dfrac{\partial S_i}{\partial x} & 0 & \dfrac{\partial S_j}{\partial x} & 0 & \dfrac{\partial S_k}{\partial x} & 0 \\ 0 & \dfrac{\partial S_i}{\partial y} & 0 & \dfrac{\partial S_j}{\partial y} & 0 & \dfrac{\partial S_k}{\partial y} \\ \dfrac{\partial S_i}{\partial y} & \dfrac{\partial S_i}{\partial x} & \dfrac{\partial S_j}{\partial y} & \dfrac{\partial S_j}{\partial x} & \dfrac{\partial S_k}{\partial y} & \dfrac{\partial S_k}{\partial x} \end{bmatrix} \begin{Bmatrix} U_{ix} \\ U_{iy} \\ U_{jx} \\ U_{jy} \\ U_{kx} \\ U_{ky} \end{Bmatrix} \tag{6.27}$$

Substituting Eq. (6.24) and using (6.25) into Eq. (6.27) yields

$$\{\varepsilon\} = [\boldsymbol{B}] \cdot \{\boldsymbol{U}\} \tag{6.28}$$

Expanding Eq. (6.23) by substituting Eq. (6.28) yields its matrix form as

$$\Lambda = \frac{1}{2} \int_V \{\boldsymbol{U}\}^T [\boldsymbol{B}]^T [D][\boldsymbol{B}]\{\boldsymbol{U}\} dV \tag{6.29}$$

where $\{\varepsilon\} = \begin{Bmatrix} \varepsilon_x \\ \varepsilon_y \\ \gamma_{xy} \end{Bmatrix}$ is the vector of two-dimensional strain,

$[\boldsymbol{B}] = \frac{1}{2A} \begin{bmatrix} \beta_i & 0 & \beta_j & 0 & \beta_k & 0 \\ 0 & \delta_i & 0 & \delta_j & 0 & \delta_k \\ \delta_i & \beta_i & \delta_j & \beta_j & \delta_k & \beta_k \end{bmatrix}$ is the matrix for the strain-displacement relation,

$(\beta_i, \beta_j, \beta_k, \delta_i, \delta_j, \delta_k)$ are the coefficients defined in Eq. (6.26), and

A is the area of the triangle element.

For the triangle element, applying the principle of minimum potential energy $\frac{\partial \boldsymbol{\Lambda}}{\partial \boldsymbol{U}} = \{\boldsymbol{F}\}$ in Eq. (6.29) gets

$$(A \cdot t)[\boldsymbol{B}]^T [\boldsymbol{D}][\boldsymbol{B}] \cdot \{\boldsymbol{U}\} = \{\boldsymbol{F}\} \tag{6.30}$$

where A and t are the area and thickness of the triangle element, $[\boldsymbol{D}]$ and $[\boldsymbol{B}]$ are the matrices of constants defined in Eqs. (6.21) and (6.29), and $\{\boldsymbol{U}\}$ and $\{\boldsymbol{F}\}$ are the vectors of state variables and loads of element, respectively.

Note that if the distributed load is applied on an edge of a triangle element, it should also be included as a part of the external load in Eq. (6.30).

Fig. 6.12 shows a rectangle element in GCS. It consists of four nodes (i, j, m and n), whose coordinates are given as (X_i, Y_i), (X_j, Y_j), (X_m, Y_m) and (X_n, Y_n), respectively. The element behavior is represented by displacements on four nodes, namely, (U_{ix}, U_{iy}), (U_{jx}, U_{jy}), (U_{mx}, U_{my}) and (U_{nx}, U_{ny}). To derive the model of a rectangle element in Fig. 6.12, the interpolation is performed, so that the displacement (u, v) in an arbitrary position (X, Y) can be derived from the displacements at nodes using shape functions.

$$\begin{Bmatrix} u \\ v \end{Bmatrix} = \begin{bmatrix} S_i & 0 & S_j & 0 & S_m & 0 & S_n & 0 \\ 0 & S_i & 0 & S_j & 0 & S_m & 0 & S_n \end{bmatrix} \begin{Bmatrix} U_{ix} \\ U_{iy} \\ U_{jx} \\ U_{jy} \\ U_{mx} \\ U_{my} \\ U_{nx} \\ U_{ny} \end{Bmatrix} \tag{6.31}$$

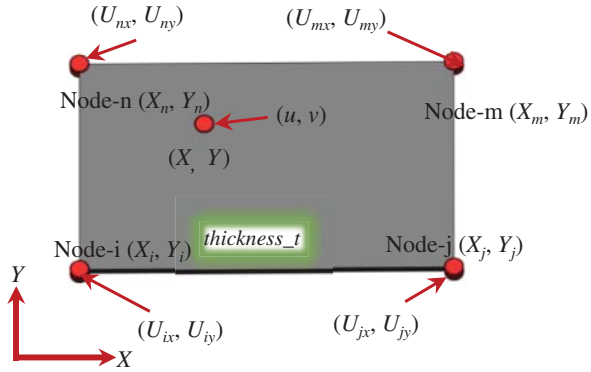


Figure 6.12 Rectangle element with plane stress.

where the shape functions of a rectangle element are given as (Bi 2018)

$$\left.\begin{aligned} S_i(x,y) &= \left(\frac{l-x}{l}\right)\left(\frac{w-y}{w}\right) \\ S_j(x,y) &= \frac{x}{l}\left(\frac{w-y}{w}\right) \\ S_m(x,y) &= \frac{x}{l}\frac{y}{w} \\ S_n(x,y) &= \left(\frac{l-x}{l}\right)\frac{y}{w} \end{aligned}\right\} \tag{6.32}$$

Where l and w are the length and width of a rectangle element, respectively.
The model for the plane-strain state can be derived from Eq. (6.31) as

$$\begin{Bmatrix} \varepsilon_x \\ \varepsilon_y \\ \gamma_{xy} \end{Bmatrix} = \begin{Bmatrix} \dfrac{\partial u}{\partial x} \\ \dfrac{\partial v}{\partial y} \\ \dfrac{\partial u}{\partial y} + \dfrac{\partial v}{\partial x} \end{Bmatrix} = \begin{bmatrix} \dfrac{\partial S_i}{\partial x} & 0 & \dfrac{\partial S_j}{\partial x} & 0 & \dfrac{\partial S_m}{\partial x} & 0 & \dfrac{\partial S_n}{\partial x} & 0 \\ 0 & \dfrac{\partial S_i}{\partial y} & 0 & \dfrac{\partial S_j}{\partial y} & 0 & \dfrac{\partial S_m}{\partial y} & 0 & \dfrac{\partial S_n}{\partial y} \\ \dfrac{\partial S_i}{\partial y} & \dfrac{\partial S_i}{\partial x} & \dfrac{\partial S_j}{\partial y} & \dfrac{\partial S_j}{\partial x} & \dfrac{\partial S_m}{\partial y} & \dfrac{\partial S_m}{\partial x} & \dfrac{\partial S_n}{\partial y} & \dfrac{\partial S_n}{\partial x} \end{bmatrix} \begin{Bmatrix} U_{ix} \\ U_{iy} \\ U_{jx} \\ U_{jy} \\ U_{mx} \\ U_{my} \\ U_{nx} \\ U_{ny} \end{Bmatrix} \tag{6.33}$$

Substituting Eq. (6.31) and using (6.32) into Eq. (6.33) gets

$$\{\varepsilon\} = [\boldsymbol{B}] \cdot \{\boldsymbol{U}\} \tag{6.34}$$

Using the Eq. (6.33) for the strains in Eq. (6.34) yields

$$\Lambda = \frac{1}{2}\int_V \{\boldsymbol{U}\}^T[\boldsymbol{B}]^T[D][\boldsymbol{B}]\{\boldsymbol{U}\}dV \tag{6.35}$$

where $[\boldsymbol{B}] = \begin{bmatrix} \frac{-(w-y)}{lw} & 0 & \frac{(w-y)}{lw} & 0 & \frac{y}{lw} & 0 & -\frac{y}{lw} & 0 \\ 0 & \frac{-(l-x)}{lw} & 0 & \frac{-x}{lw} & 0 & \frac{x}{lw} & 0 & \frac{(l-x)}{lw} \\ \frac{-(l-x)}{lw} & \frac{-(w-y)}{lw} & \frac{-x}{lw} & \frac{(w-y)}{lw} & \frac{x}{lw} & \frac{y}{lw} & \frac{(l-x)}{lw} & -\frac{y}{lw} \end{bmatrix}$

For a rectangle element, applying the principle of minimum potential energy $\frac{\partial \Lambda}{\partial U} = \{\boldsymbol{F}\}$ in Eq. (6.29) gets

$$\left[\int_A [\boldsymbol{B}]^T[\boldsymbol{D}][\boldsymbol{B}]tdA\right] \cdot \{\boldsymbol{U}\} = \{\boldsymbol{F}\} \tag{6.36}$$

where $[\boldsymbol{D}]$ and $[\boldsymbol{B}]$ are the matrices defined in Eqs. (6.21) and (6.35), and $\{\boldsymbol{U}\}$ and $\{\boldsymbol{F}\}$ are the vectors of field variables and loads of element, respectively.

Note that if the distributed load is applied on an edge of a rectangle element, it should also be included as a part of the external load in Eq. (6.36).

6.3.2.2 Plane Strain Problems If the dimensions in one direction (z-axis) are extremely large compared to those in the other two directions (x- and y- axes), the deformation in z-axis is restrained. Therefore, the corresponding principal strain (ε_z) is zero. Even though all of three principal stresses are nonzero components, the principal stress in z-axis depends on the principal stresses in x- and y- axes, which will not be included in the plain strain model. Fig. 6.13 gives some examples of applications where a structure or product can be analyzed by a plane-strain model.

As shown in Fig. 6.14, the plane-strain state corresponds to the case where $\varepsilon_z = 0$, and $\gamma_{xz} = \gamma_{yz} = 0$. Therefore, Eq. (6.7) can be simplified as

$$\{\boldsymbol{\sigma}\} = \begin{Bmatrix} \sigma_x \\ \sigma_y \\ \tau_{xy} \end{Bmatrix} = [\boldsymbol{D}]\{\varepsilon\} = \frac{E}{(1+\upsilon)(1-2\upsilon)} \begin{bmatrix} 1-\upsilon & \upsilon & 0 \\ \upsilon & 1-\upsilon & 0 \\ 0 & 0 & \frac{1-\upsilon}{2} \end{bmatrix} \begin{Bmatrix} \varepsilon_x \\ \varepsilon_y \\ \gamma_{xy} \end{Bmatrix} \tag{6.37}$$

The plane-strain model is similar to a plan-stress model except for the constitutive model $[\boldsymbol{D}]$. The models for triangular and rectangle elements are derived in Eqs. (6.30) and (6.36) and are applicable to plane-strain elements as well; however, the constitutive model $[\boldsymbol{D}]$ is defined in Eq. (6.37).

6.3.3 Modal Analysis

Modal analysis concerns the dynamic response of a structure subjected to vibrational excitations. The goal of modal analysis is to determine the natural frequencies and corresponding mode shapes of an object or structure subjected to boundary conditions. The mathematical model for



Figure 6.13 Examples of plane strain parts.

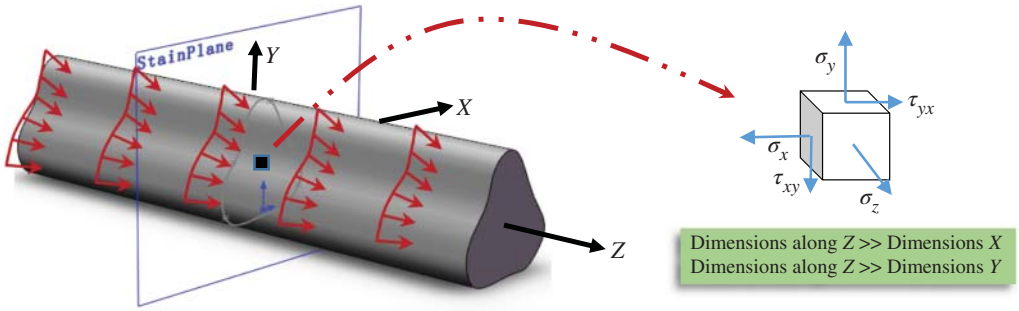


Figure 6.14 Stress state in a plane-strain model (Bi 2018).

a modal analysis is called an eigenvalue system, and the solution to such a model is represented by eigenvalues and eigenvectors, which correspond to the natural frequencies and mode shapes, respectively. Fig. 6.15 shows a number of engineering design problems where modal analyses are essential to ensure the safe applications of structures or systems. Most of these applications involve dynamic loads or excitations whose frequencies must be away from any of natural frequencies of products.

In this section, two-dimensional frame elements are used as an example to develop element models for modal analysis. A node in a two-dimensional frame element may have loads



Figure 6.15 Examples of products where modal analyses are needed (Bi 2018).

and displacements along x-, and y- axes, and a rotational displacement around z-axis. We assume that small deformations are applied in the element; in other words, the model of a two-dimensional frame can be treated as a combined model from one-dimensional axial member and two-dimensional beam member.

6.3.3.1 Two-Dimensional Truss Member in LCS Two-dimensional truss member is its LCS, and can be described in Fig. 6.16. If the linear approximation is used, it includes two nodes (i and j).

The interpolations in two-dimensional truss member for *displacements* and *velocities* are performed separately as

$$u_x = [\boldsymbol{S}]\{\boldsymbol{u}\} = \begin{bmatrix} \frac{L-x}{L} & \frac{x}{L} \end{bmatrix} \begin{Bmatrix} u_{ix} \\ u_{jx} \end{Bmatrix} \tag{6.38}$$

$$\dot{u}_x = [\boldsymbol{S}]\{\dot{\boldsymbol{u}}\} = \begin{bmatrix} \frac{L-x}{L} & \frac{x}{L} \end{bmatrix} \begin{Bmatrix} \dot{u}_{ix} \\ \dot{u}_{jx} \end{Bmatrix} \tag{6.39}$$

Assume that a system includes potential energy Λ, kinematic energy T, and the work done by external force, the application of the potential minimum energy principle yields the Lagrange's equation as,

$$\frac{d}{dt}\left(\frac{\partial T}{\partial \dot{q}_i}\right) - \frac{\partial T}{\partial q_i} + \frac{\partial \Lambda}{\partial q_i} = Q_i \quad (n = 1, 2 \cdots n) \tag{6.40}$$

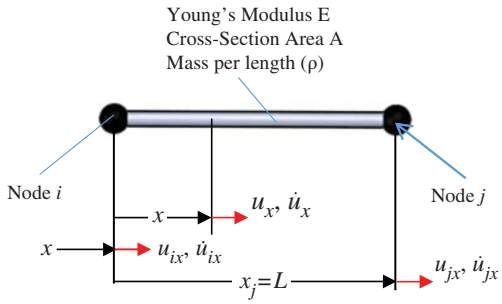


Figure 6.16 Two-dimensional truss member in LCS for modal analysis.

where

t is time variable,
T is kinetic energy of system and
q_i is an independent DoF of system ($i = 1, 2, \ldots n$)
$\dot{q}_i$ is the velocity along a DoF of system ($i = 1, 2, \ldots n$)
Λ is the potential energy of system
Q_i is the external load along one DoF ($i = 1, 2, \ldots n$)

A truss member has two displacements (u_{ix}, u_{jx}) and corresponding velocities $(\dot{u}_{ix}, \dot{u}_{jx})$. The potential and kinetic energies are evaluated respectively as,

$$\Lambda = \int_V \frac{1}{2} E \left(\frac{du}{dx}\right)^2 dV = \frac{EA}{2} \int_L \{\boldsymbol{u}\}^T \left[\frac{\partial \{\boldsymbol{S}\}}{\partial x}\right]^T \left[\frac{\partial \{\boldsymbol{S}\}}{\partial x}\right] \{\boldsymbol{u}\} dl \tag{6.41}$$

$$T = \int_V \frac{1}{2} \rho (\dot{u})^2 dV = \frac{\rho A}{2} \int_L \{\dot{\boldsymbol{u}}\}^T [\boldsymbol{S}]^T [\boldsymbol{S}] \{\dot{\boldsymbol{u}}\} dl \tag{6.42}$$

Substituting Eqs. (6.41) and (6.42) into Eq. (6.40) gets,

$$[\boldsymbol{M}]^{(L,e)} \{\ddot{\boldsymbol{u}}\} + [\boldsymbol{K}]^{(L,e)} \{\boldsymbol{u}\} = \{\boldsymbol{f}\} \tag{6.43}$$

where

$[\boldsymbol{M}]$ is the mass matrix for a two-dimensional axial member: $[\boldsymbol{M}]^{(L,e)} = \frac{\rho AL}{6} \begin{bmatrix} 2 & 1 \\ 1 & 2 \end{bmatrix}$

$[\boldsymbol{K}]$ is the stiffness matrix for a two-dimensional axial member: $[\boldsymbol{K}]^{(L,e)} = \frac{EA}{L} \begin{bmatrix} 1 & -1 \\ -1 & 1 \end{bmatrix}$

$\{\boldsymbol{f}\}$: is the vector of external loads.

6.3.3.2 Two-Dimensional Beam Member in LCS A two-dimensional beam member is its LCS and can be described in Fig. 6.17. Each node in a beam member consists of

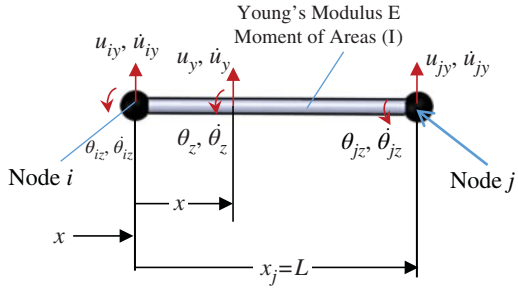


Figure 6.17 Two-dimensional beam element in LCS for modal analysis.

two displacements, i.e., y-axis displacement (u_y) and z-axis rotational displacement (θ_z). Correspondingly, the velocities on these two displacement directions are defined.

The interpolations in a two-dimensional beam member for displacements and velocities are performed separately as,

$$u = [\boldsymbol{S}]\{\boldsymbol{u}\} = \left[1 - \frac{3x^2}{L^2} + \frac{2x^3}{L^3} \quad x - \frac{2x^2}{L} + \frac{x^3}{L^2} \quad \frac{3x^2}{L^2} - \frac{2x^3}{L^3} \quad -\frac{x^2}{L} + \frac{x^3}{L^2}\right] \begin{Bmatrix} u_{iy} \\ \theta_{iz} \\ u_{jy} \\ \theta_{jz} \end{Bmatrix} \tag{6.44}$$

$$\dot{u} = [\boldsymbol{S}]\{\dot{\boldsymbol{u}}\} = \left[1 - \frac{3x^2}{L^2} + \frac{2x^3}{L^3} \quad x - \frac{2x^2}{L} + \frac{x^3}{L^2} \quad \frac{3x^2}{L^2} - \frac{2x^3}{L^3} \quad -\frac{x^2}{L} + \frac{x^3}{L^2}\right] \begin{Bmatrix} \dot{u}_{iy} \\ \dot{\theta}_{iz} \\ \dot{u}_{jy} \\ \dot{\theta}_{jz} \end{Bmatrix} \tag{6.45}$$

The strain of a beam member can be found from Eq. (6.44) as

$$\{\varepsilon\} = -y\frac{\partial^2 u}{\partial x^2} = -y\left[\frac{\partial^2 \boldsymbol{S}}{\partial x^2}\right]\{\boldsymbol{u}\}$$

$$= -y\left[-\frac{6}{L^2} + \frac{12x}{L^3} \quad -\frac{4}{L} + \frac{6x}{L^2} \quad \frac{6}{L^2} - \frac{12x}{L^3} \quad -\frac{2}{L} + \frac{6x}{L^2}\right] \begin{Bmatrix} u_{iy} \\ \theta_{iz} \\ u_{jy} \\ \theta_{jz} \end{Bmatrix} \tag{6.46}$$

The strain energy of a beam number is calculated as

$$\Lambda = \int_V \frac{1}{2} E\left(-y\frac{d^2 u}{dx^2}\right)^2 dV = \frac{EI}{2}\int_L \{\boldsymbol{u}\}^T \left[\frac{\partial^2 \{\boldsymbol{S}\}}{\partial x^2}\right]^T \left[\frac{\partial^2 \{\boldsymbol{S}\}}{\partial x^2}\right]\{\boldsymbol{u}\} dl \tag{6.47}$$

And the kinetic energy is calculated as,

$$T = \int_V \frac{1}{2}\rho(\dot{u})^2 dV = \frac{\rho A}{2}\int_L \{\dot{\boldsymbol{u}}\}^T [\boldsymbol{S}]^T [\boldsymbol{S}]\{\dot{\boldsymbol{u}}\} dl \tag{6.48}$$

Thus, substituting Eqs. (6.47) and (6.48) into Eq. (6.40) to obtain the conditions for the minimized potential energy as

$$[\boldsymbol{M}]^{(L,e)}\{\ddot{\boldsymbol{u}}\} + [\boldsymbol{K}]^{(L,e)}\{\boldsymbol{u}\} = \{\boldsymbol{f}\} \tag{6.49}$$

where

$[\boldsymbol{M}]^{(L,e)}$ is the mass matrix for a two-dimensional beam element

$$[\boldsymbol{M}]^{(L,e)} = \frac{\rho AL}{420}\begin{bmatrix} 156 & 22L & 54 & -13L \\ 22L & 4L^2 & 13L & -3L^2 \\ 54 & 13L & 156 & -22L \\ -13L & -3L^2 & -22L & 4L^2 \end{bmatrix}$$

$[\boldsymbol{K}]^{(L,e)}$ is the stiffness matrix for a two-dimensional beam element

$$[\boldsymbol{K}]^{(L,e)} = \frac{EI}{L^3}\begin{bmatrix} 12 & 6L & -12 & 6L \\ 6L & 4L^2 & -6L & 2L^2 \\ -12 & -6L & -12 & -6L \\ 6L & 2L^2 & -6L & 4L^2 \end{bmatrix}$$

6.3.3.3 Modeling of Two-Dimensional Frame Element As shown in Fig. 6.18, a two-dimensional beam member consists of x- and y- displacements and z- rotational displacement. Under the assumption of the small deformation where the deformations under a variety of loads can be summed linearly. Accordingly, the mass matrix and stiffness matrix is obtained by assembling Eqs. (6.43) and (6.49) as,

$$[\boldsymbol{M}]^{(L,e)}\{\ddot{\boldsymbol{u}}\} + [\boldsymbol{K}]^{(L,e)}\{\boldsymbol{u}\} = \{\boldsymbol{f}\} \tag{6.50}$$

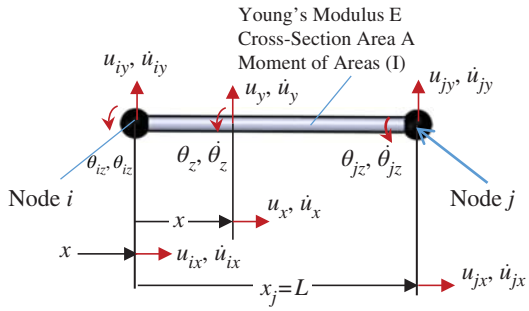


Figure 6.18 Two-dimensional frame member in LCS for modal analysis.

where

$[\boldsymbol{M}]^{(L,e)}$: is the mass matrix for a two-dimensional frame element:

$$[\boldsymbol{M}]^{(L,e)} = \frac{\rho AL}{420}\begin{bmatrix} 140 & 0 & & 70 & 0 & 0 \\ 0 & 156 & 22L & 0 & 54 & -13L \\ 0 & 22L & 4L^2 & 0 & 13L & -3L^2 \\ 70 & 0 & 0 & 140 & 0 & 0 \\ 0 & 54 & 13L & 0 & 156 & -22L \\ 0 & -13L & -3L^2 & 0 & -22L & 4L^2 \end{bmatrix}$$

$[\boldsymbol{K}]^{(L,e)}$ is the stiffness matrix of a two-dimensional frame element:

$$[\boldsymbol{K}]^{(L,e)} = \begin{bmatrix} \frac{EA}{L} & 0 & 0 & -\frac{EA}{L} & 0 & 0 \\ 0 & \frac{12EI}{L^3} & \frac{6EI}{L^2} & 0 & -\frac{12EI}{L^3} & \frac{6EI}{L^2} \\ 0 & \frac{6EI}{L^2} & \frac{4EI}{L} & 0 & -\frac{6EI}{L^2} & \frac{2EI}{L} \\ -\frac{EA}{L} & 0 & 0 & \frac{EA}{L} & 0 & 0 \\ 0 & -\frac{12EI}{L^3} & -\frac{6EI}{L^2} & 0 & \frac{12EI}{L^3} & -\frac{6EI}{L^2} \\ 0 & \frac{6EI}{L^2} & \frac{2EI}{L} & 0 & -\frac{6EI}{L^2} & \frac{4EI}{L} \end{bmatrix}$$

For a two-dimensional structure consisting of frame members, all of the element models in their LCSs have to be transformed into the corresponding ones in GCS, so that they can be assembled into a system model. In the coordinate transformation, let

$$\{\ddot{\boldsymbol{U}}\} = [T]\{\ddot{\boldsymbol{u}}\}, \quad \{\boldsymbol{U}\} = [T]\{\boldsymbol{u}\} \quad \{\boldsymbol{F}\} = [T]\{\boldsymbol{f}\} \tag{6.51}$$

where the coordinate transformation T from LCS to GCS is

$$[T] = \begin{bmatrix} \cos\theta & \sin\theta & 0 & 0 & 0 & 0 \\ -\sin\theta & \cos\theta & 0 & 0 & 0 & 0 \\ 0 & 0 & 1 & 0 & 0 & 0 \\ 0 & 0 & 0 & \cos\theta & \sin\theta & 0 \\ 0 & 0 & 0 & -\sin\theta & \cos\theta & 0 \\ 0 & 0 & 0 & 0 & 0 & 1 \end{bmatrix}$$

Substituting Eq. (6.51) into Eq. (6.50) gets the model of a two-dimensional frame element in GCS as,

$$[\boldsymbol{M}]^{(G,E)}\{\ddot{\boldsymbol{U}}\} + [\boldsymbol{K}]^{(G,E)}\{\boldsymbol{U}\} = \{\boldsymbol{F}\} \tag{6.52}$$

where

$[\boldsymbol{M}]^{(\mathrm{G,e})}$: is the mass matrix for two-dimensional frame element in GLS: $[\boldsymbol{M}]^{(G,e)} = [T]^T[\boldsymbol{M}]^{(L,e)}[T]$

$[\boldsymbol{K}]^{(\mathrm{G,e})}$ is the stiffness matrix of a two-dimensional frame element in GLS: $[\boldsymbol{K}]^{(G,e)} = [T]^T[\boldsymbol{K}]^{(L,e)}[T]$

$[\boldsymbol{F}]^{(\mathrm{G,e})}$ is the load of a two-dimensional frame element in GLS: $\{\boldsymbol{F}\} = [T]\{\boldsymbol{f}\}$

For a two-dimensional structure consisting of two-dimensional frame elements, the assembled system model in GLS becomes,

$$[\boldsymbol{M}]^{(G)}\{\ddot{\boldsymbol{U}}\}^{(G)} + [\boldsymbol{K}]^{(G)}\{\boldsymbol{U}\}^{(G)} = \{\boldsymbol{F}\}^{(G)} \tag{6.53}$$

where $[\boldsymbol{M}]^{(G)}$, $[\boldsymbol{K}]^{(G)}$ are the mass matrix and stiffness matrix of the two-dimensional frame structure, respectively; and $\{\boldsymbol{U}\}^{(G)}$, $\{\boldsymbol{F}\}^{(G)}$ are the vectors of displacements and loads in the structure,

In modal analysis, the harmonic solution of Eq. (6.53) is concerned, and the solution is assumed as,

$$\left.\begin{aligned}\{\boldsymbol{U}\}^{(G)} &= \{\boldsymbol{X}\}\cdot\sin(\omega t+\phi)\\ \{\boldsymbol{F}\}^{(G)} &= \boldsymbol{0}\end{aligned}\right\} \tag{6.54}$$

Substituting Eq. (6.54) into Eq. (6.53) gives,

$$(\omega^2[\boldsymbol{M}]^{(G)} - [\boldsymbol{K}]^{(G)})\{\boldsymbol{X}\}\sin(\omega t+\phi) = 0 \tag{6.55}$$

Eq. (6.55) specifies the conditions of natural frequencies as,

$$|\omega^2[\boldsymbol{M}]^{(G)} - [\boldsymbol{K}]^{(G)}| = 0 \tag{6.56}$$

where $|\bullet|$ is the determinate of a matrix.

6.3.4 Fatigue Analysis

Fatigue is a phenomenon of materials where the accumulative damage occurs by repetitive loads. Structures and systems in many applications are subjected to dynamic and repetitive loads, which induce fluctuating or cyclic stresses. Invisible damage on the materials caused by such loads is accumulated until it leads to a structural fracture. Fatigue causes over 90% of all mechanical service failures (ASM International 2008).

Fig. 6.19 shows a few applications where fatigue analysis must be performed in the designs of mechanical structures or components. In these applications, the magnitude of stress that causes fatigue damage could be much less than the ultimate strength of material. However, the frequency of a repetitive load is very high, and the product is generally required to run safely for a long time. This implies that the materials must endure a repetitive load with a large number of loading cycles. Taking the example of a car engine, if an average reciprocating speed is 4000 revolutions per minute (RPM) and a 400-hour duration test is performed, the expected fatigue life is 9.6×10^7 cycles (Shariyat et al. 2016). By any means, the experimental solution to a fatigue analysis usually takes a long time. In addition, a fatigue test often involves a high cost for the development of a testing platform and instrumentation. Moreover, it is impractical to test a large number of application scenarios for products. Therefore, FEA-based simulations have been widely adopted for the fatigue analysis of mechanical designs.



Figure 6.19 Examples of products where modal analysis needed (Bi 2018).

Fatigue refers to the weakening of a material caused by cyclic loads on the material. Fatigue is the progressive and localized structure damage under a dynamic load. The progress of fatigue can be divided into three stages; i.e., *crack initiation*, *crack growth*, and *fracture*. The fatigue behavior of material not only relates to the properties of material, but also relates to many other factors, such as the application environment, characteristics of loads, temperature, and surface conditions (Nanninga, 2008). The methods to analyze the fatigue life of a machine element have been discussed extensively (Hamrock et al., 1999; Budynas and Nisbett, 2015), and three major methods are *the strain-life method*, *the linear-elastic fracture mechanics method*, and *the stress-life method*.

6.3.4.1 Strain-Life Method The strain-life method is the best approach yet advanced to explain the nature of fatigue failure (Budynas and Nisbett, 2015). However, it was based on some idealizations and assumptions, which brings the uncertainties in predicting fatigue damages. A fatigue failure is assumed to begin at a local discontinuity (e.g., corner, notch, crack, or other stress concentration). When the stress at the discontinuity exceeds the elastic limit, the plastic strain occurs, and a fatigue fracture corresponds to an accumulation of cyclic plastic strains. Correspondingly, the total strain at the critical area can be quantified as

$$\frac{\Delta\varepsilon}{2} = \frac{\sigma'_F}{E}(2N)^b + \varepsilon'_F(2N)^c \tag{6.57}$$

where

$\Delta\varepsilon$	is the total strain,
E	is the elastic modulus of material,
N	is the number of reversals of cyclic loading,
b and c	are the slope of the elastic and plastic strain lines, respectively,
σ'_F	is the true stress corresponding to fracture in one reversal, and
ε'_F	is the true strain corresponding to fracture in one reversal.

Eq. (6.57) is also referred to as the Mason-Coffin relation of fatigue life and total strains. The coefficients applied in Eq. (6.57) can be found in SAE J1099 Standards (SAE, 2014). However, the strain-life method is rarely used in practice due to two main reasons: (1) it is unclear how to determine the total strain at the discontinuity, and (2) no data is available for strain-concentration factors.

6.3.4.2 Linear Elastic Fracture Mechanics Method In the linear elastic fracture mechanics method, the fatigue damage is measured by crack sizes. Fatigue cracks nucleate and grow when the stress varies. As shown in Fig. 6.20a, where the size of an initial crack is denoted as a_i, a higher range of the stress change corresponds to a quicker increase of the stress intensity. Thus, the rate of crack size growth with respect to the loading cycle is given by

$$\frac{da}{dN} = C(\Delta K_I)^m = C(\beta\Delta\sigma\sqrt{\pi a})^m \tag{6.58}$$

where

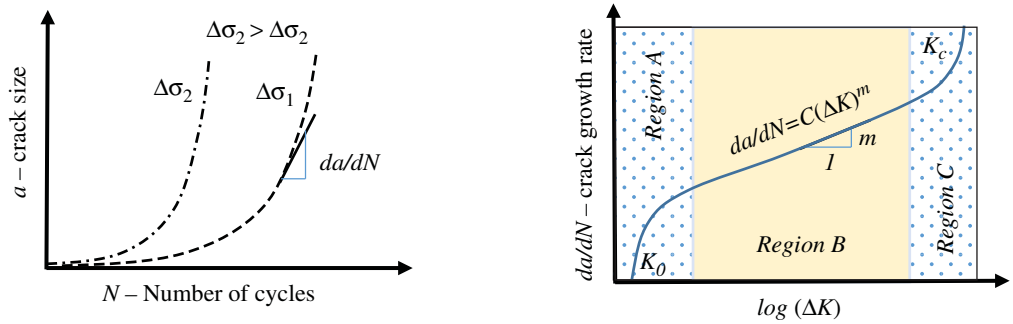
α	is the crack size,
β	is the tress intensity modification factor,
N	is the number of reversals of cyclic loading,
C and m	are the empirical material constants,
ΔK_I	is the change of stress intensity, and
$\Delta\sigma$:	is the change of stress.

Upon integrating Eq. (6.58), the number of cycles N_f corresponding to a fatigue failure is found as

$$N_f = \frac{1}{C}\int_{a_i}^{a_f} \frac{da}{(\beta\Delta\sigma\sqrt{\pi a})^m} \tag{6.59}$$

where a_i and a_f are the crack size at the beginning and the fracture state, respectively.

Because the stress intensity modification factor actually changes with the crack size, the linear elastic fracture mechanics method was adopted in only in a few of numerical tools (NASA/FLAGRO 2014) in some special areas. Fatigue analysis based on the linear elastic fracture mechanics needs some essential information, such as crack parameters and loading schedule, which is unavailable in most applications.



(a) Crack growth with the number of cycles (b) Three phases of crack growth

Figure 6.20 Linear elastic fracture mechanics method.

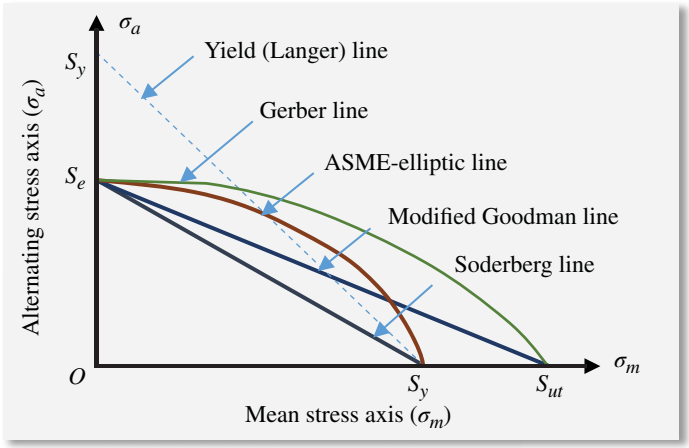
6.3.4.3 Stress-Life Method In a stress-life method, the fatigue damage is measured by *fatigue strength*. The fatigue strength is defined in terms of the number of cycles. In particular, the fatigue strength is called an *endurance limit* when the number of loading cycles exceeds the required number of loading cycles. A product has an infinite fatigue life if its fatigue strength is higher than the endurance limit. The basic relation of the fatigue strength and the number of loading cycles is commonly known as an *S-N curve*; i.e.,

$$S'_f = \frac{(fS_{ut})^2}{S_e} N^{\left(-\frac{1}{3}\log\left(\frac{fS_{ut}}{S_e}\right)\right)} \tag{6.60}$$

where

S'_f is the fatigue strength,
N is the number of fully reversed cycles,
f is the fatigue strength fraction for 10^3 loading cycles,
S_{ut} is the ultimate tensile strength, and
S_e is the endurance limit.

Fatigue strength S'_f and endurance limit S_e in Eq. (6.60) are applicable only to a fully-reversed load under standardized testing conditions. For the real-world applications, modification factors are introduced to take into account of the difference between actual and testing loading conditions. For example, if the load is not fully reversed, the design criteria in Fig. 6.21 should be applied to consider the impact of the mean stress on the fatigue behavior of material. In the case when the magnitude of a dynamic load varies, the Miner's rule is used to calculate the accumulated damage in the given loading period. The stress-life method works well when the material deforms in its elastic range (Unigovski et al., 2013).



(a) Design diagram

Design Criterion Equation

Goodman line	$\frac{\sigma_a}{S_e} + \frac{\sigma_m}{S_{ut}} = \frac{1}{n}$
Soderberg line	$\frac{\sigma_a}{S_e} + \frac{\sigma_m}{S_y} = \frac{1}{n}$
Gerber line	$\frac{n\sigma_a}{S_e} + \left(\frac{n\sigma_m}{S_{ut}}\right)^2 = 1$
ASME-elliptic line	$\left(\frac{n\sigma_a}{S_e}\right)^2 + \left(\frac{n\sigma_m}{S_y}\right)^2 = 1$

(b) Design formula

Figure 6.21 Stress-life method for fatigue analysis

6.3.4.4 Selection of Fatigue Analysis Methods There are some reasons why three fatigue analysis methods have coexisted for a long time. The advantages and disadvantages of each method are relative and depend on where and when the fatigue analysis is needed. Table 6.1 provided some general tips for users in selecting an appropriate method for fatigue analysis (Aparcio 2013).

TABLE 6.1 Guides for Selection of Fatigue Analysis Methods (Bi 2018)

Strain-Life Method	Linear Elastic Fracture Method	Stress-Life Method
• Mostly defect free, metallic structures or components. • Components where the crack initiation is the important failure criterion. • Locating the point(s) where cracks may initiate, and hence the growth of a crack should be considered. • Evaluating the effect of alternative materials and different surface conditions. • Components that are made from metallic, isotropic ductile materials, which have symmetric cyclic stress-strain behavior. • Components that experience short lives – low cycle fatigue – where plasticity is dominant.	• Precracked structures or structures which must be presumed to be already cracked when manufactured, such as welds. • Prediction of test programs to avoid testing components where cracks will not grow. • Planning inspection programs to ensure checks are carried out with the correct frequency. • To simply determine the amount of life left after crack initiation. • Components that are made from metallic, isotropic ductile materials that have symmetric cyclic stress-strain behaviors.	• Long-life or high-cycle fatigue problems, where there is little plasticity, since the S-N method is based on nominal stress. • Components where a crack initiation or crack growth modeling is inappropriate, e.g., composites, welds, plastics, and other nonferrous materials. • Situations where large amounts of pre-existing S-N data exist. • Components, which are required by a control body to be designed for fatigue using standard data. • Spot weld analysis and random vibration-induced fatigue problems.

6.4 FINITE ELEMENT ANLAYSIS (FEA) FOR STRUCTURAL ANALYSIS

FEA is to obtain an approximate solution to a structural analysis problem. Before FEA modeling, a user has to construct a virtual model of the part or assembly to be analyzed, and specify the material properties for every object in the model. The user must understand physical phenomena occurring to the model, so that the analysis type and element types can be specified appropriately. In FEA modeling, the *divide and conquer* strategy is applied to obtain the system model from an assembly of submodels of simple units. As shown in Fig. 6.22, the continuous domain of the model is decomposed into small parts known as *elements*. Elements are assembled through the interconnection of points, which are called *nodes*. Accordingly, each element is associated with a set of nodes, and the element behavior is modeled by the behaviors of discrete nodes.

Generally, the procedure of FEA modeling consists of the following steps:

Step 1: Decomposition. The continual domain is discretized into a collection of shapes or elements, the nodes for each element are specified. The assembling relations of elements as well as element-node relations are defined clearly. Since state variables on nodes are

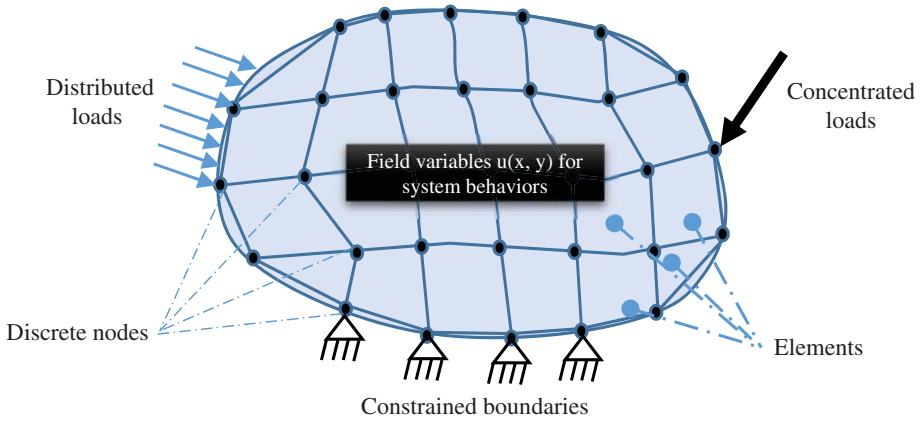


Figure 6.22 Discretization of a continual domain into nodes and elements.

defined as design variables of elements, interpolation functions are specified to describe the response of any position in an element by nodal values.

Step 2: Develop Element Models. An analysis type is selected based on the physical behaviors of the model. Design variables are selected, the mathematic model with governing differential equations is defined. The mathematic model is then converted into element models by the approximation methods, such as *direct methods*, *minimum potential energy methods*, or *weighted residual methods*.

Step 3: Assembly. Based on the stored assembly relations in the decomposition, element models in local coordinate systems are transformed into element models in a global coordinate system, and they are assembled into a system model under the global coordinate system.

Step 4: Apply Boundary Conditions and Loads. The interactions of the physical system with its application environment are defined, they are represented as boundary conditions or load conditions in the model.

Step 5: Solve for Primary Unknowns. Sufficient boundary conditions ensure the system model solvable. A system model usually consists of a large number of linear equations. A number of well-developed algorithms can be utilized to solve unknown variables from the system model.

Step 6: Calculate Dependent Variables. The design variables in an engineering system can be classified into independent variables and dependent variables. For example, stress and strain are dependent with each other, either stress or strain can be selected as independent one, and the other can be determined based on the constitutive model of materials. After independent variables are solved, postprocessing can be performed to evaluate dependent variables.

In the implementation of any FEA code, the above steps are essential to obtain the final solution to an FEA model; however, most of the activities in these steps are automatically accomplished by software. Users are required to provide only minimal information as the inputs of model to run

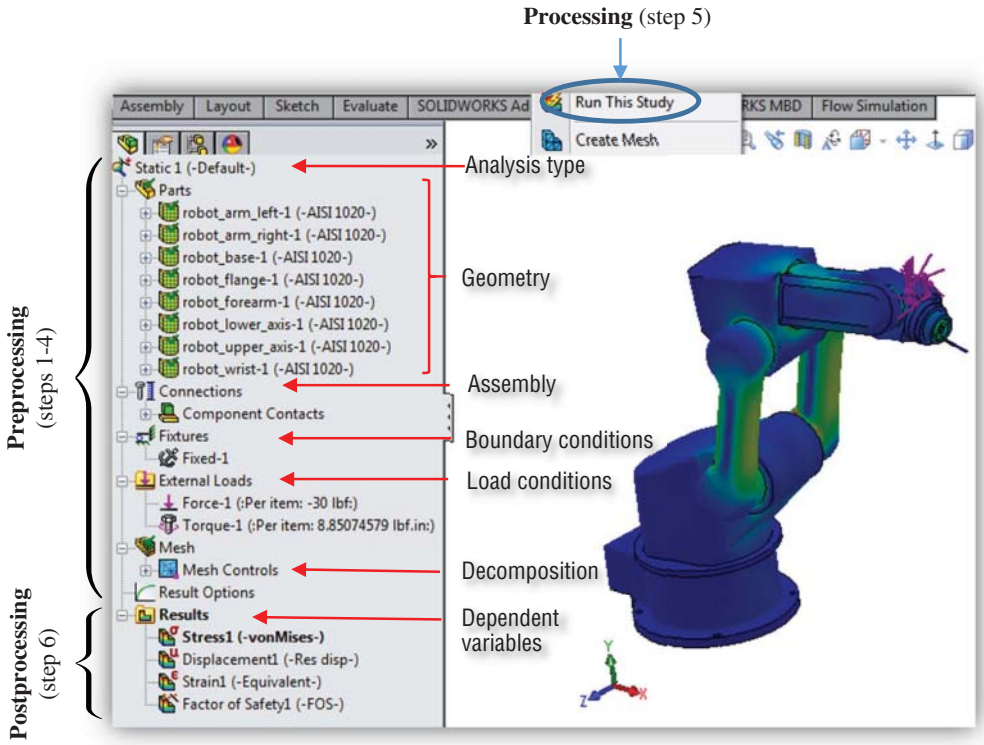


Figure 6.23 Preprocessing, processing, and postprocessing in an FEA model.

a numerical simulation. A commercial FEA code provides a graphic user interfaces (GUI) only for the tasks where users provide inputs. As shown in Fig. 6.23, GUIs of a commercial FEA code are provided for the manual intervention at three solving stages, i.e., *preprocessing*, *processing*, and *postprocessing*.

While most of activities are automatically performed by an FEA code, users are responsible to formulate design problems, provide the correct and sufficient inputs for every steps, and interpret and verify the results from the software code adequately. If the inputs of an FEA model are wrongly given, the obtained results from the simulation could mislead users.

The introduction of programming implementation in the above sections aims to understand the foundation of FEA theory; it does not intend to replace the role of any commercial FEA tools. In this section, Solidworks is used as the vehicle to illustrate how a commercial software tool can be adopted to fulfill various tasks involved in the preprocessing, processing, and postprocessing of FEA. Fig. 6.24 gives an overview of the mappings between available functional modules in Solidworks and major tasks involved in FEA modelling.

No matter what type of software architecture (i.e., structural, procedural, or object-oriented architecture) is adopted in programming, graphic user interfaces (GUIs) of a commercial FEA

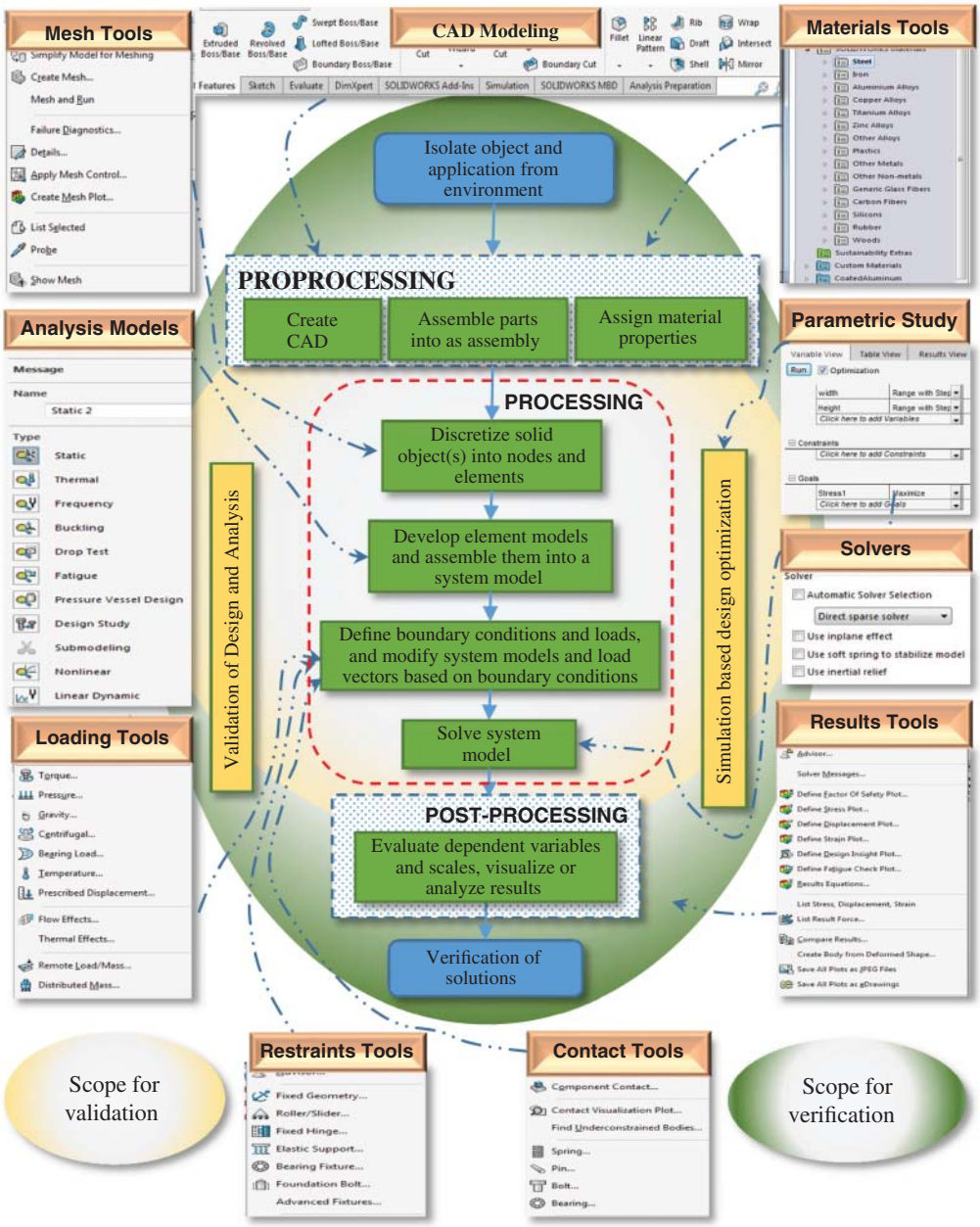


Figure 6.24 Solidworks simulation for FEA (Bi 2018).

tool are usually user-friendly, which allow users to access functional modules for FEA modeling interactively. In the following, some typically modules to support the preprocessing, processing, and postprocessing are introduced.

6.4.1 CAD/CAE Interface

FEA is a general tool to evaluate the distribution of field variable over a continual domain; a continual domain can be one dimensional (1-D), two dimensional (2-D), or three dimensional (3-D). To model a design problem, the domain must be represented by a virtual model in computer. For some simple objects, such as springs and truss members, the analyzed domain can be directly described by specifying coordinates of their intersections as *nodes* and a connection matrix of nodes for *elements*. However, objects in the real-world applications are usually very complex, sophisticated computer-aided design (CAD) tool is required to create the computer models of objects. A Computer-Aided Engineering (CAE) tool such as FEA must have an interface which allows to import and export virtual models of objects directly from and to CAD tools.

The vendor-neutral file formats in Table 6.2 provide basic representations of geometries, such as vertices, edges, and boundary surfaces of solid bodies; the models of solid objects in these formats do not include all information about how solid objects are created, such as the information about sketches and the parameters for different features of objects. This causes the difficulty to revise the geometries of objects when needed. Therefore, it is desirable to use a solid model in the native format where all of the information about the parameters and relations of solid objects

TABLE 6.2 The Common Formats of Computer Solid Models (Bi 2018)

Format	Developer	Description
IGES - Initial Graphics Exchange Specification (.igs)	U.S. National Bureau of Standards in 1080	IGES is a vendor-neutral file format that allows the digital exchange of information among computer-aided design (CAD). The information of geometries is not complete; therefore, tolerances of feature vary from one system to another.
STEP - The Exchange of Product model data (.step, .stp)	International Organization for Standardization, 1994	STEP files improve the IGES format in the sense that the tolerance data is included along with significant amounts of meta-data, such as product structure and the definition of solid features. STEP files can be geometry based or product structure based.
STL - STereoLithography (.stl)	3D Systems, 1988	STL is a polygonal file format that has been widely used for rapid prototyping. It is low fidelity in terms of geometric representation of solid object.
VRML - The Virtual Reality Ming Language (.wrl, .X3D)	Web3D Consortium, 1994	VRML files are text based and designed in a structured human-readable manner for web browsers. VRML files are widely used to transport three-dimensional models between graphics applications.

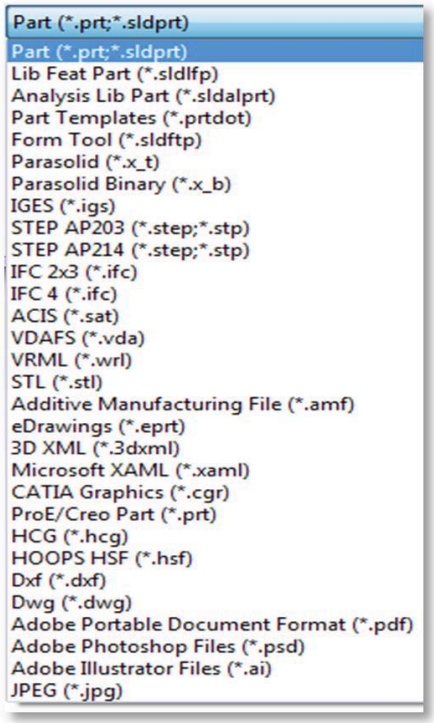


Figure 6.25 A list of file formats compatible to Solidworks 2017 (Bi 2018). (Bi 2018)

is sustained. Some leading CAD software suppliers have developed their own formats to support CAD data exchanges and parametric designs, e.g., *.x_t* and *.x_b* from Parsolid, *.sat* and *.sldlfp* from Dassault Systems, *.dxf* and *.dwg* from Autodesk, and *.jt* from Siemens PLM Software. Due to an increasing need for data exchange across products from different vendors, direct converters of a CAD file from one native format to another are available. For example, Fig. 6.25 gives a list of 31 formats that are compatible with Solidworks 2017 for importing and exporting a CAD model.

In an integrated CAD/CAE software tool, such as Solidworks, FEA tools are packed as an embedded functional module in the software platform. Therefore, parametrized solid models in a native format can be accessed by FEA tools seamlessly.

6.4.2 Materials Library

The data about material properties is essential to numerical simulation. Before running an FEA simulation, one must define all the necessary material properties specified by the given analysis type. For example, the modulus of elasticity is required for static and modal analysis; while thermal conductivity is needed for a heat transfer problem.

Most products use common industrial materials, such as iron, steel, concrete, plastics, and aluminum; the properties of those materials are well documented. A commercial FEA software is usually equipped with a materials library for commonly used industrial materials. It also provides users with the interface and template to customize material properties for solid objects. Common properties of solid objects can be classified into (1) physical properties, such as density and melting temperature; (2) mechanical properties, such as Young's modulus, Poisson's ratio, yield strength, and hardness; (3) thermal properties, such as thermal conductivity, specific heat, and coefficient of thermal expansion; (4) electric properties, such as resistivity; and (5) acoustic properties, such as compression wave velocity, shear ware velocity, and bar velocity. Depending on the types of applications, corresponding material properties are essential. For example, mechanical properties of a solid object must be given if static analysis or modal analysis is performed on object.

As shown in Fig. 6.26, the materials library in the Solidworks simulation is organized in the levels of *Library*, *Category*, and *Material*. In the structure of Solidworks material library, *custom material* has to be placed in a category of a custom material library. Therefore, one has to start by creating a custom material library, then a new category under custom library, and, finally, a new material under the custom new category.

A commercial FEA tool usually provides users with material template when new material model is needed. As shown Fig. 6.27, basic physical, mechanical, and thermal properties, such as density, elastic modules, and thermal conductivity can be input directly. If composite materials or nonlinear material models have to be defined, the software tool allows one to use custom curves or even measurement data as inputs. Fig. 6.28 shows an example interface for a user to input Strength to Number of Cycles (S-N) curves, which is essential to fatigue analysis of solid objects.

For fatigue analysis, dynamic analysis, or large displacement under plastic deflection, raw data of material properties is unlikely to come from a single source. Solidworks provides the tool called Materials Web Portal to collect material properties from the third party (Matereality LLC).

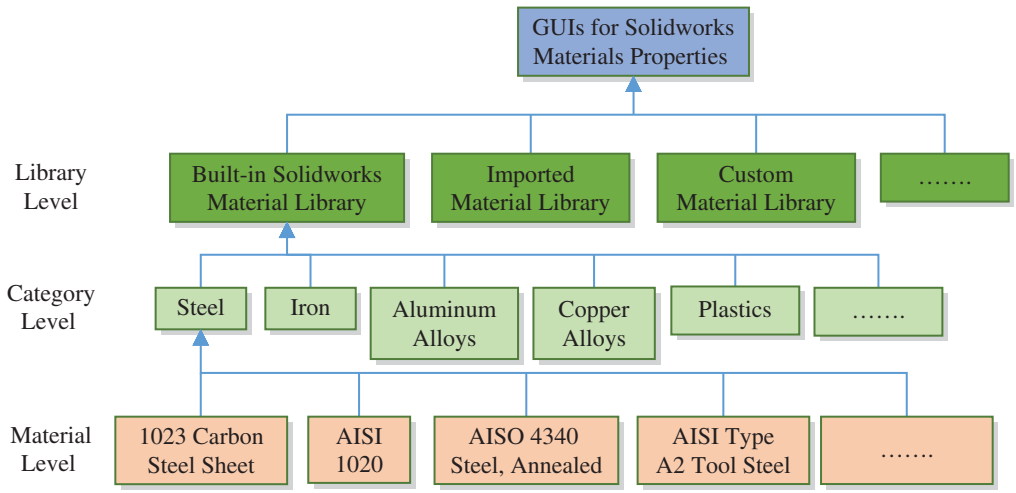


Figure 6.26 Typical structure of materials library in FEA package (Bi 2018).

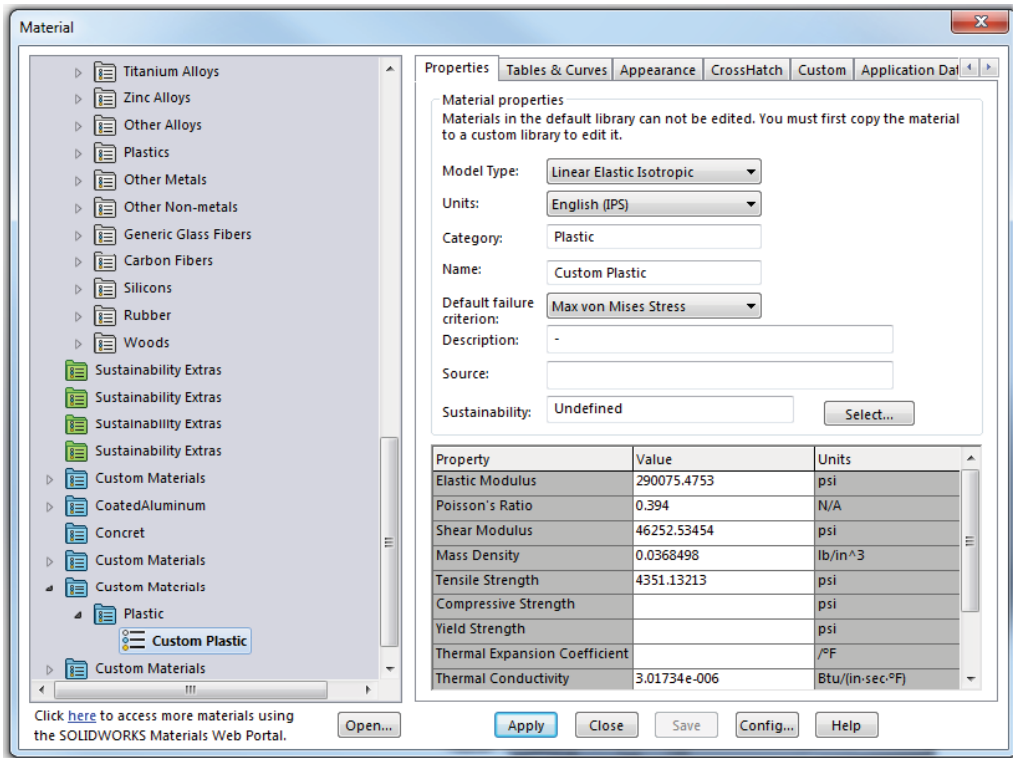


Figure 6.27 Interface to create custom material model (Bi 2018).

This portal offers the data on nonlinear materials and fatigue curves, which can be difficult to find from other sources.

6.4.3 Meshing Tool

A continual domain with infinite degrees of freedom (DoF) is represented by discretized nodes and elements with a finite DoF. A meshing tool aims to convert a continual domain into nodes and elements. It is a critical step in FEA modeling. An FEA tool is equipped with an *automatic meshing* module. It is used to estimate a global element size based on the volume, surface areas, and geometric details of a solid object, and create elements and nodes based on global element size, tolerance, and local mesh control. Note that the scale of system model directly relates to the element's size; the smaller the elements are, the higher the number of DoF that a system model has. *Local mesh control* allows one to specify divisions of selected features, such as edges, faces, and components.

An FEA tool supports many element types for different analyses. As shown in Fig. 6.29, in meshing, element types must be specified based on object shapes to avoid distorted elements. For *bulk* objects, solid elements are suitable. For *thin* objects, shell elements should be used. For

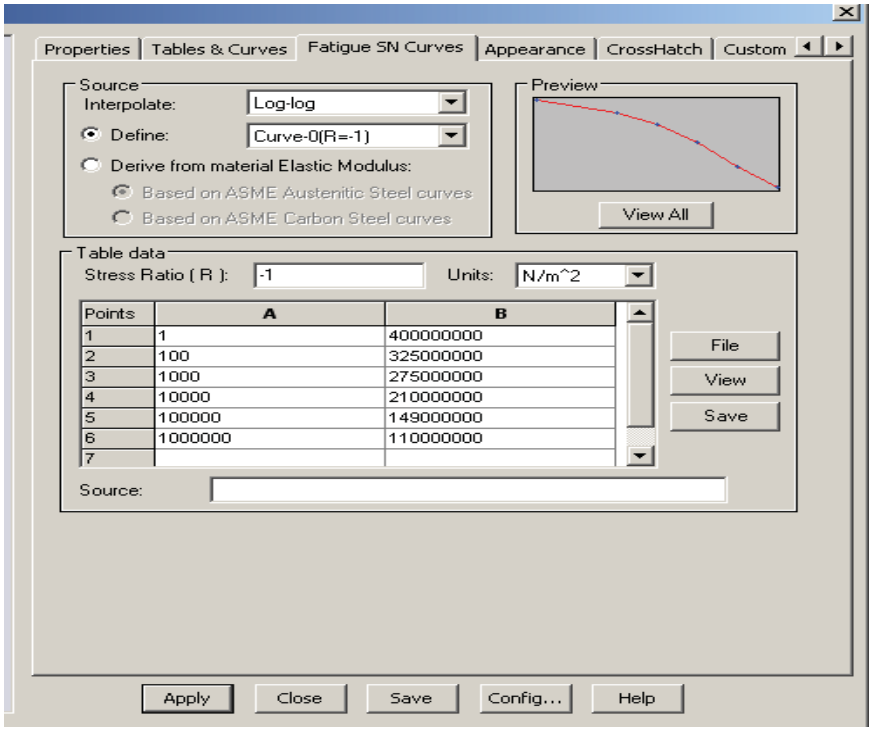
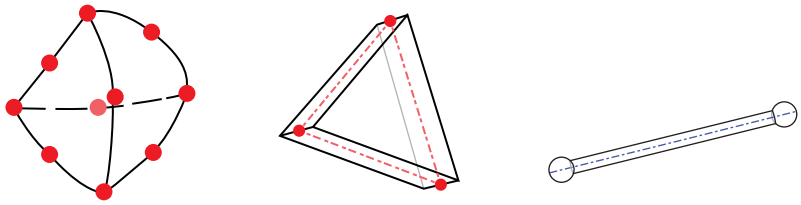


Figure 6.28 Generate S-N curve for fatigue analysis (Bi 2018).



(a) Bulk element (b) Shell element (c) Truss or beam element

Figure 6.29 Exemplified element types for different shapes (Bi 2018).

extruded or revolved trusses and beams with a constant cross-section, truss or beam elements are appropriate.

When the object to be analyzed is an assembled solid, the meshing tool might need manual intervene to (1) ensure no interference occurs at the interfaces of two objects, and (2) set up mesh control to achieve a compatible mesh if possible.

It is desirable to run interface check and eliminate all possible interferences at interfaces of solid components. For example, the Solidworks software has an *Interference detection* tool to

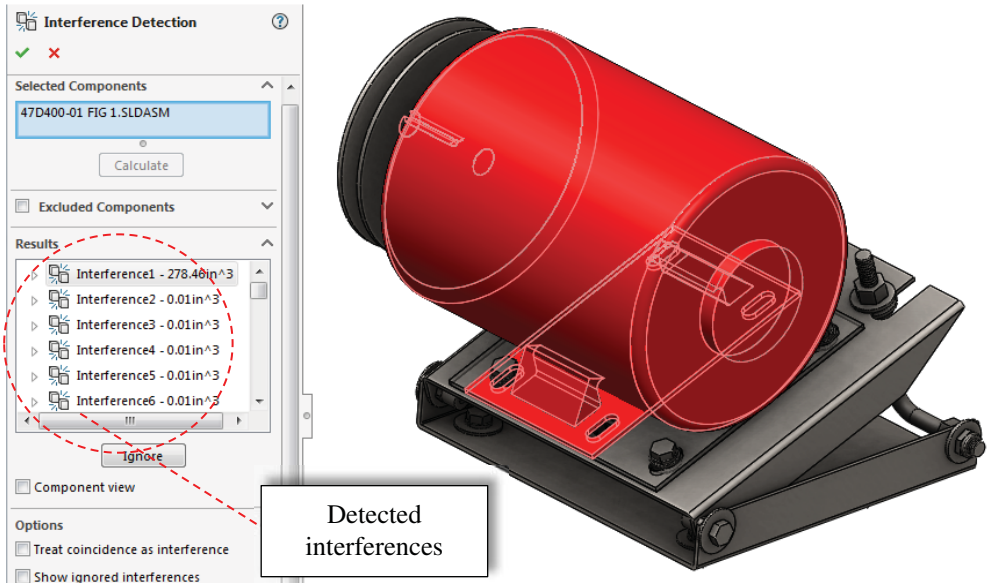


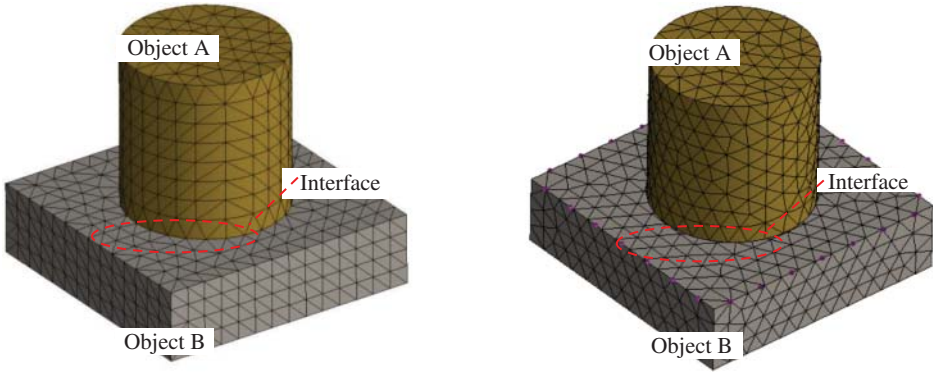
Figure 6.30 Detecting and fixing interferences in an assembled object (Bi 2018).

evaluate if there are interferences in an object group. If there are, the CAD models or assembly relations of corresponding objects have to be revised to eliminate physical intrusions of two solid bodies. Fig. 6.30 shows an example where interface detection is performed to identify interferences in assembly.

As assembled object is involved in a number of interfaces where two or multiple solids are joined together as bonded contact. During the meshing process, nodes from different solids can be joined differently to generate either a *compatible mesh* or an *incompatible mesh*. As shown in Fig. 6.31, the nodes from two or more solids have one-to-one correspondences in a compatible mesh, but such correspondences are not satisfied in an incompatible mesh. In a bonded contact, nodes on two contact surfaces can be merged or superimposed; in a no-penetration contact, two contact surfaces with the node-to-node correspondence become source and target faces. Since nodes in an incompatible mesh are restrained only by constraint equations, incompatible mesh causes potential issues of stress concentration at the bonded contact. Computation on a compatible mesh leads to better accuracy than that of incompatible mesh. In using a commercial FEA tool for a complex assembled model, a user should refine meshing parameters to obtain a compatible mesh as much as possible.

For an actual part or assembly, it is not rare that the first run of meshing processes does not succeed. If a failure occurs to the meshing process, the Failure Diagnostics module in Solidworks can be applied to diagnose the causes, a trial-and-error process is deployed to adjust element sizes, define mesh controls on critical features, and activate automatic remeshing until the mesh is generated for the entire domain of solids.

To increase the accuracy of solution, *mesh refinement* is an effective means. A mesh can be refined in two alternative ways, i.e., *h-adaptive meshing* and *p-adaptive meshing*. H-adaptive



(a) Compatible mesh (node-node at interface)

(b) Incompatible mesh (non node-node at interface)

Figure 6.31 Comparison of compatible and incompatible meshes (Bi 2018).

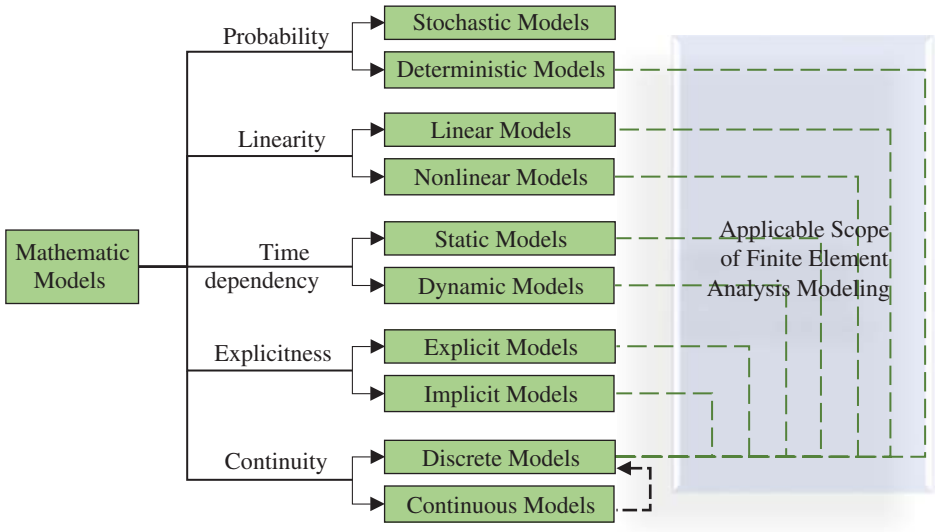


Figure 6.32 Classification of structural analysis problems (Bi 2018).

meshing refines the mesh by reducing element sizes at critical areas; while the p-adaptive meshing inserts more nodes in existing elements without the changes of element sizes. Increasing nodes in an element leads to a high order of polynomial interpolation in an element. Both the ways of mesh refinement can be performed automatically to meet the expected meshing accuracy given by users; the refinements are performed iteratively on an FEA model without a manual intervention by users.

6.4.4 Analysis Types

An FEA software tool is a generic tool to solve differential or integral equations with given boundary conditions. As long as the governing equations for a design problem are covered by the software, this problem can be solved readily by the FEA tool. Therefore, most of the FEA tools are applicable to a variety of *Analysis Types*. Table 6.3 lists some common Analysis types in the Solidworks Simulation.

TABLE 6.3 Common Analysis Types of Simulation in Solidworks (Bi 2018)

Analysis Type	Descriptions
Static analysis	Static analysis is suitable to the cases of small deformations of elastic materials subject to static loads. It is assumed that the materials of an object behavers in its elastic range, i.e., the strain has a linear relation with stress. It is used to evaluate stress distribution thus predict the static failure where the maximum stress exceeds the yield strength of materials. Static analysis will not model the behavior of materials appropriately if the stress exceeds yield strength.
Nonlinear analysis	Nonlinear analysis aims to model the scenarios where (1) both elastic and plastic deformation occur to objects, or (2) the properties of materials are nonlinear. For the first type of scenario, an object deforms in a way that the shape or stiffness of object is changed significantly depending on the stress state. For second type of scenario, the applied materials, such as plastics, rubbers, or elastomers, can be been represented with linear stress-strain curve due to possible large deformation.
Frequency analysis	Frequency analysis is for a modal analysis to evaluate natural frequencies of a structure; an excitation at one of these critical frequencies likely causes problematic vibrational response. The outcomes of a frequency analysis include (1) a list of natural frequencies and (2) mode shapes corresponding to the frequencies.
Dynamic analysis	Dynamic analysis takes into account of the dynamics of loading conditions, such as a shock or a vibration. Time-dependent loads can be defined in stress analysis. The method called modal superposition is used to analyze the responses of structure to individual inputs. The system behavior is defined by adding individual responses together. Three types of dynamic loads are (1) time-dependent acceleration or load, (2) a load or acceleration with frequency change, and (3) nondeterministic excitation including random vibration expressed by a power spectrum density (PSD) curve.
Thermal analysis	Thermal analysis is to analyze a solid model with three types of heat transfer behaviors: conduction, convection and radiation. A heat transfer model is developed based on the energy conservation where heat is transferred by conduction in a solid body, and the convection and radiation on boundary surfaces. Heat convection is measured by a convective coefficient. Note that convective coefficient is not a material property, it is affected by many environmental parameters. An input convective coefficient commonly corresponds to a laminate air or fluid flow under the natural convection. If the surrounding atmosphere is complicated, the heat transfer coefficient should be obtained separately from experiment or flow simulation.

TABLE 6.3 (*continued*)

Analysis Type	Descriptions
Flow simulation	Flow Simulation is a computational fluid dynamics (CFD) tool that allows one to model air and fluid flow around and through solid objects. Flow simulation can perform detailed thermal analysis on a variety of heating and cooling scenarios; it can perform conductive, convective, and radiative calculation simultaneously without an input of convective coefficient.
Fatigue analysis	Repeated loading and unloading causes the damage of objects over time even when the stresses are considerably less than yield strengths. This damage is called as fatigue. Fatigue is the prime cause of the failure of most of metal objects. Fatigue analysis investigates the accumulated damage on solid objects caused by repeated or random load cycles; the more cycles a load applies on an object, the more significant the fatigue damage is. A failure caused by repetitive loads is called fatigue failure. The capability of materials to resist fatigue failure is characterized by the plot of strength and number of cycles (S-N curve). Once dynamic loads are given, a fatigue analysis uses S-N curve to predict fatigue life or safety factor of design of solid objects.
Drop test	A drop test analysis aims to calculate time-dependent stresses and deformations caused by an initial impact of an object with a rigid or flexible planar surface. In drop test, it is desirable to define the materials as *elasto-plastic* one; this enables the software to account for energy lost in the dynamic simulation.

6.4.5 Tools for Boundary Conditions

To solve a set of differential equations uniquely, boundary conditions must be given in the forms of restraints and loads. The *fixtures* module in the PropertyManager of the Solidworks simulation provides the interfaces to specify the restraints of displacements on vertices, edges, or faces. Restraints can be zero or nonzero displacements. Boundary conditions of displacements are essential to the analysis types for the deformation of a solid object, such as static, frequency, dynamic, or nonlinear studies. Table 6.4 lists some common options of restraints in the Solidworks Simulation.

Table 6.5 lists common types of loads for structural analysis in the Solidworks Simulation.

Note that types of restraints relate to analysis types. If another analysis type is defined, the types of restraints and loads can be very different. For example, in an FEA model of heat transfer, the restraints and loads on solid objects are related to temperature, convection, radiation, heat flux, and heat power, which are defined on vertices, edges, faces, or components.

6.4.6 Solvers to FEA Models

An FEA model is eventually formulated as a mathematical model. A mathematic model describes design variables, their relations, and constraints. Design variables are system parameters of interest that are solved. As shown in Fig. 7.32, mathematical models can be classified (Aris 1994;

TABLE 6.4 Displacement Boundary Conditions for Structural Analysis (Bi 2018)

Restraints	Description
Fixed geometry	In a fixed geometry, DoF of the restraints varies with element types. For solid or truss elements, three translational DoFs are fixed. For shell and beam elements, both translational and rotational DoFs are fixed. No reference geometry is needed to define a fixed geometry.
Immovable	Immovable restrains all translational motions for whatever types of element. It is applicable to vertices, edges, faces, or nodes of beam elements. For solids, Immovable and fixed geometry have the same functions.
Roller/sliding	Roller/sliding defines a planar face where nodes on a contact surface can move freely into its plane; it allows the contact face be shrunk or expanded under loading. However, the motions in the normal direction of the plane are constrained.
Fixed hinge	Fixed hinge defines a round face where nodes on this face are free to rotate about its rotational axis. During the deformation, the radius and the length of the round are set.
Symmetry	When both geometries and loads are symmetric about a reference, numerical simulation can be performed on only a portion of the whole solid model to reduce computation. Symmetry is applied to define the constraints of symmetric reference to replace a full model by a partial model. For a solid mesh, it constrains one translation, for a shell mesh, it set the displacement of a translation and two rotations. Symmetry is applicable only on a flat face.

TABLE 6.5 Load Boundary Conditions for Structural Analysis (Bi 2018)

Loads	Description
Pressure	Pressure is a type of surface load. It applies uniform or varying pressure on edges or surfaces of a physical structure. If the pressure varies, an analytic function must be defined to calculate pressure value for corresponding nodes.
Force	Force can be used to define forces, moments, or torques. Force is a type of concentrated load; however, it will be modeled as a uniformly distributed load on the nodes of selected faces, edges, vertices.
Gravity	Gravity is a type of body load. It applies a linear acceleration to a solid object. It is a common load type in structural analysis and nonlinear analysis.
Centrifugal	Centrifugal is a type of body load. It applies an initial force caused by angular velocity and acceleration of solid object. The software calculates the loads based on the specified angular velocity, acceleration, and mass density of materials.
Remote loads and restraints	As far as an assembled model is analyzed, it is unnecessary to include all parts or components in the FEA model. When some parts or components are excluded, the loads and constraints on those components can be converted as equivalent ones on the simplified model by using remote loads and restraints; the converted loads or constraints can be *remote load*, *remote displacement*, and *remote mass*.

Bender 2000; Bokil 2009) based on the criteria of probability, linearity, time-dependence, and continuity. As a generic tool, FEA can be applied to solve all of them except a probabilistic mode.

- **Deterministic and probabilistic model**: In a deterministic model, every set of variable states is uniquely determined by parameters in the model as well as the previous states of these variables. The model generates same results if the initial conditions are given. A statistical model involves a number of uncertainties in which the states of variables are probability distributions of mean values.
- **Linear and nonlinear models**: If all of relations among design variables are linear, the corresponding model is linear; otherwise, it is a nonlinear model. Nonlinear systems are generally difficult to solve. A common approach to solve a nonlinear problem is linearization.
- **Static and dynamic models**: A dynamic model treats the time as another dimension of design problems; it takes into account the time-dependent changes of system states. A static model is also called a steady-state model; design variables in such a model are time-invariants, and the system is in equilibrium.
- **Explicit and implicit models**: When all of system inputs of a model are known; if the system outputs can be calculated in a sequence of steps explicitly; the corresponding model is called as an explicit model. Otherwise, if system outputs have to be solved iteratively, such a model is called as an implicit model.
- **Discrete and continual models**: A discrete model treats objects as discrete and continual model treats objects as continual domains.

Crandall (1956) classified engineering problems into three types, i.e., *equilibrium problems*, *eigenvalue problems*, and *propagation problems*. An equilibrium problem concerns the deformation of solid object under static, quasi-static or repetitive loads. An eigenvalue problem is an extension of an equilibrium problem whose solutions are characterized by a unique set of system configurations, such as resonance and bulking. A propagation problem concerns the time-dependent changes of field variables. Solidworks Simulation provides four solutions to a formulated FEA model: *Auto*, *FFEPlus*, *Direct Sparse*, and *Large Problem Direct Sparse* (Reuss 2014).

Fast Finite Elements (FFEPlus) is an iterative solver that uses implicit integration method; the solution is evolved iteratively under computation errors that are small enough to meet terminate conditions. FFEPLus is efficient when the number of DoF of a system model is large, in particular, a model with more than 100,000 DoFs; it becomes more efficient when the model size is larger. FFEPLus can be suspicious if (1) incompatible mesh is applied and any local bonded contact is not covered by global bonded contact, (2) external forces or gravity is applied in frequency analysis, (3) base excitation is considered in linear dynamic study, (4) elasticity moduli vary greatly from one solid to another, (5) the boundary conditions of pressure or temperature are imported and circular/cyclic symmetry boundary conditions are applied, and (6) nonlinear analysis.

Direct Sparse finds a solution directly using exact numerical techniques. "Sparse" refers to the sparsity (zeroes) of the matrice that represents the relations of design variables and loads. Direct Sparse achieves a good accuracy in solving small or medium-sized problems. It is faster if a computer has large memory. The Direct Sparse solver may be applied in a small FEA model, nonlinear analysis, or more accurate result. The size of an FEA model is confined according to the

analysis type, 100,000 DOF for general analysis, 50,000 DOF for nonlineat analysis, and 500,000 DOF in heat transfer problems.

Large Problem Direct Sparse (LPDS) is an enhanced Direct Sparse solver for a large FEA model. High computation is addressed by using multiple cores. A LPDS solver can be applied when the Direct Sparse solver is required, but the computer does not possess random access memory (RAM). LPDS can be used as a last resort to solving an FEA model. In addition, Solidworks Simulation has an *auto* option that an appropriate solver can be automatically be selected to solve practical problems.

6.4.7 Postprocessing

The results of an FEA model usually include a considerable large amount of data. It is difficult and tedious to review and understand the meanings of calculated results. Postprocessing tools are used to sort, visualize, and output the data, such as the distribution of stress, strain, safety factor, and temperature. Postprocessing helps in visualizing the results, identifying the weakest locations in product, and highlighting the areas of material waste.

Even though the result of an FEA model is available at the phase of postprocessing, critical thinking is needed to review and understand results. Solidwork Simulation provides many postprocessing tools for users to understand simulation results: (1) visualize the distributions and contours of field variables; (2) animate the responses of objects, such as deformations, vibrational models, and contact behaviors; (3) create flow trajectories in flow simulation; (4) make slides and create sectional views to visualize the distribution of field variables internally; and (5) use the probe tools to retrieve data at specified vertices, edges, faces, or components.

6.5 PLANNING V&V IN FEA MODELING

To practice V&V, planning is the most critical step to minimize possible errors in FEA modeling. As shown in Fig. 6.33, every step in FEA modeling generates new information about the system to be modeled. The activities in these steps are also error sources. Therefore, along with the information flow, information/data in one format is processed and converted to the information/data in another format, corresponding V&V has to be performed to ensure errors are not propagated or accumulated.

V&V relates closely to the objective of FEA simulation. Therefore, the objective of FEA simulation must be clearly stated. This begins with the identification of design variables and system parameters. The design problem must be formulated in a comprehensive way to define a complete FEA model, which includes the source of data, the assumptions from idealization, terminating conditions in solving processes, and the procedures, methodologies, tools, and criteria for V&V. In formulating an FEA problem, the free body diagram (FBD) based approach can be used to identify boundary conditions and loads. In addition, commercial FEA code often provide a taxonomy of element types. This helps users to understand software capabilities and select right element types for given analysis problems.

From the perspective of V&V, it is interesting to look into the role of the idealization in an FEA modeling process. On one hand, the idealization is based on a real-world design problem, and the

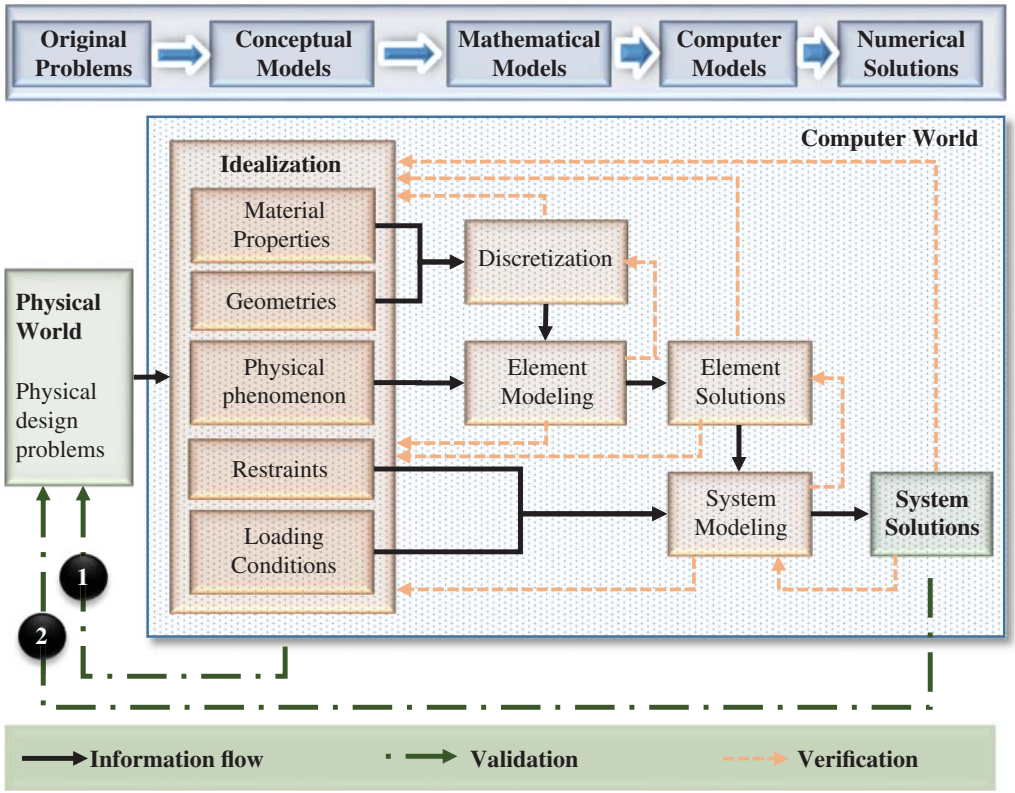


Figure 6.33 Verification and validation in FEA modeling (Bi 2018).

simplified model should be a reasonable representation of the original problem. On the other hand, the idealization is directly related to verification. In other words, the idealization must be verified to endure that the conceptual model is converted into a mathematical model adequately.

6.5.1 Sources of Errors

An FEA procedure consists of multiple modeling steps, and each step brings the possibility of new discrepancy of the computer representation from an ideal one. Understanding error sources is crucial to justify whether or not the obtained results at every step are acceptable; this helps users to select correct analysis types, element types, meshes, and solvers in minimizing errors (Shah 2002). Identifying possible discrepancies may result in an improvement of the model and the reduction of overall errors of the simulation model (Brinkgreve and Engin 2013). In this section, the quantification of error is introduced, and the error sources are discussed.

6.5.1.1 Error Quantification Solving an FEA model usually requires an iterative algorithm, in which the terminating condition must be defined to identify an acceptable solution. The

terminating conditions are mostly based on quantified errors. For a simplified comparison, an error is mostly quantified as a vector or scalar. Without losing the generality, the displacements in structural analysis are used as the quantities for the error quantification of state variables.

FEA is applied to find the distribution of state variables, such as displacements in structural analysis or associated scalar variables, such as natural frequencies in modal analysis. Assume $\boldsymbol{u}$ is a vector of state variables to be determined, the error of an approximated solution can be defined as,

$$\{\boldsymbol{\delta}\} = \{\overline{\boldsymbol{u}}\} - \{\widehat{\boldsymbol{u}}\} \tag{6.61}$$

where $\boldsymbol{\delta}$ is the error of the approximated solution, and $\{\overline{\boldsymbol{u}}\}$ and $\{\widehat{\boldsymbol{u}}\}$ are the exact and approximated solutions, respectively.

Since a continual domain has been represented by discretized nodes and elements in an FEA model. The size of vector $\{\widehat{\boldsymbol{u}}\}$ shows how many degrees of freedom are applied to approximate the quantities in a continual domain. To avoid artificial inaccuracies caused by local features in the quantification, the size of vector $\{\widehat{\boldsymbol{u}}\}$ should be reasonably large enough. For example, a point load is impossible in real life; an idealization on point load will cause an infinitely large displacement and stress at the imposed node; and the solution error should be defined for the entire solid domain rather than the local region where the point load is applied.

In the FEA implementation, various norms can be used to convert the vector of errors $\{\boldsymbol{\delta}\}$ in Eq. (6.61) into scalar parameters as summed errors. Taking an example of a system model for structural analysis,

$$[K]\{\boldsymbol{u}\} = \{\boldsymbol{F}\} \tag{6.62}$$

An error of the approximation can be defined in an energy norm as (Shah 2002),

$$\|\boldsymbol{\delta}\| = \left[\int_{\Omega} (\{\overline{\boldsymbol{u}}\} - \{\widehat{\boldsymbol{u}}\})^T \cdot [K] \cdot (\{\overline{\boldsymbol{u}}\} - \{\widehat{\boldsymbol{u}}\}) d\Omega\right]^{1/2} \tag{6.63}$$

where $\|\boldsymbol{\delta}\|$ is a scalar measure from the vector of errors relating to the approximated solution.

In addition, the variation for a relative energy norm error can be defined as,

$$\eta = \frac{\|\boldsymbol{\delta}\|}{\|\overline{\boldsymbol{u}}\|} \times 100\% \tag{6.64}$$

Eqs. (6.62)–(6.64) can be extended and applied to quantify the errors for any vector of variables.

6.5.1.2 System Inputs As shown in Fig. 6.33, to represent a real-world engineering problem by a conceptual computer model, many assumptions have to be made in the idealization and these assumptions bring numerous of errors or uncertainties. For example, materials properties are essential input for any FEA. Unfortunately, a great deal of uncertainties is raised in defining materials properties. There is a very wide range of materials used for structures with drastically different behaviors. For each material type, it may go through several response regimes, i.e., elastic, plastic, viscoelastic, cracking and localization, and fracture. While it is

TABLE 6.6 Basic properties of materials.

Assumption	Explanation
Elasticity	The stress-strain response is reversible, and consequently, the material has a preferred natural state. The natural state is taken at a reference temperature with no load; it is referred to as an unstressed and undeformed state. When a load is applied or temperature changes, the material develops nonzero stresses and strains, and moves to occupy a deformed configuration.
Linearity	The material behaves in its elastic region. The stress is proportional to the strain at any position. Doubling a stress means to double the corresponding strain, and vice versa.
Isotropy	The material properties are not sensitive to load directions. This is a good assumption for materials, such as metals, concrete, and plastics. It is inadequate for the materials with heterogeneous mixtures, such as composites and reinforced concrete. Those materials are anisotropic by nature.
Small strains	A strain is considered small when its magnitude is well within the elastic range of materials. The change of geometry can be neglected as loads are applied on the materials. If a strain exceeds certain level, nonlinear constitutive relation must be defined to model the relation of displacements and strains.

impractical and unnecessary to define the accuracy constitutive models in modeling, users are responsible to determine how the given materials are used and what assumptions should be made. In defining materials, at least the behaviors of materials in Table 6.6 should be taken into consideration.

When the default settings of materials are applied, a user should be aware of the assumptions underlying these settings. If any of the assumptions is not aligned well with the given application, one has to customize materials in FEA.

6.5.1.3 Errors of Idealization *Idealization* is to describe and abstract a physical system as a conceptual model based on the assumptions. A conceptual model is the collection of computer representations for physical objects, processes, or systems (Moorcroft 2012). Developing a conceptual model involves in (1) identifying objects, domains of interest, and the relations of objects with their applied environments; (2) determining the level of agreement between the experiment and simulation outcomes; (3) making assumptions in the representations of physical processes; and (4) specifying the failure modes of interests as well as validation metrics (Thacker et al 2004). It is the users' responsibility to develop such a conceptual model.

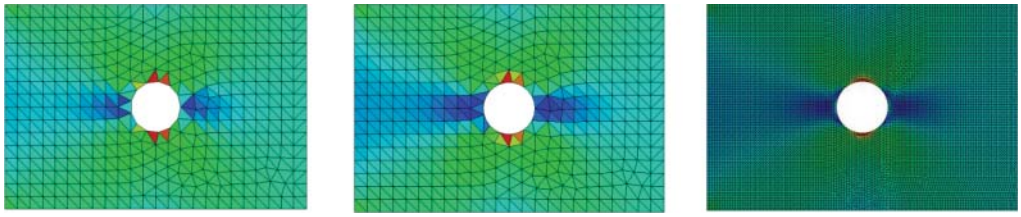
Typical tasks in the idealization are (1) the system of interest has to be isolated from its residential environment to identify its boundary conditions; (2) constitutive models and parameters have to be determined to represent material properties; (3) a virtual model is created to describe the continuous domain of physical object or system; (4) the system physical phenomenon must be clear to identify an appropriate analysis type or mathematic model of elements. Every activity involved in the idealization introduces some simplifications that could cause the discrepancies of a virtual computer model and physical system. The conceptual model should represent the original system adequately, and this can be proven by performing the validations on both inputs and outputs of FEA models.

FEA treats a continual domain as a set of discretized elements and nodes, and the state variables in an element are interpolated by shape functions. In addition, shape functions are mostly linear, quadratic, or cubic polynomial equations with a low polynomial order. Obviously, the discretization is the source of error since the solution to the continual domain is approximated by nodal values discretely. Fig. 6.34 gives an example of the strain distribution of a metal plate under an axial load. Fig. 6.34*a* is for the discontinued strain across elements in a coarse mesh. The results can be improved by using (1) quadratic elements in Fig. 6.34*b* and (2) use more fine elements in Fig. 6.34*c*. However, the errors of discretization exist for whatever sizes and types of elements an FEA model uses.

It can also be seen that a stress that crosses a shared edge of two elements is discontinued. Fig 6.35*a* shows such a discontinuity. Note that if a share edge relates to nonlinear high-order elements, even the displacement can be discontinued; Fig. 6.35*b* shows such an example.

From the perspective of FEA modeling, the way of using shape functions to construct mass or stiffness matrices of elements is an approximation of exact mathematic model in continual domain. This brings discretization errors. There is no universal rule to warrantee the appropriation of mesh size; however, the convergence study can be performed in the area of interest to test the appropriateness of mesh by a number of iterations.

6.5.1.4 Errors of Mathematic Models After the conceptual model is formulated from the idealization, a *mathematical model* has to be defined. Usually, a mathematical model in an FEA model is the representation of governing conditions with specified boundary conditions, initial conditions, and system parameters, which are required to describe the corresponding conceptual

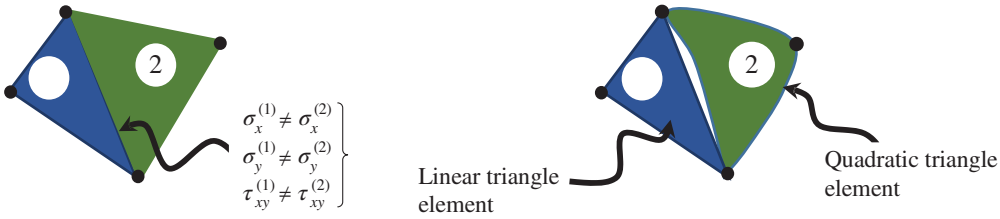


(a) Coarse mesh with linear triangle element

(b) Coarse mesh with quadratic triangle element

(c) Fine mesh with linear triangle element

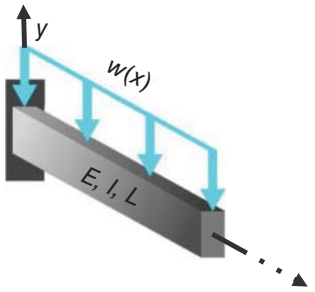
Figure 6.34 Example of strain discontinuity due to discretization (Bi 2018).



(a) Stress discontinuity

(b) Displacement discontinuity

Figure 6.35 Errors caused by a model with basic elements (Bi 2018).



(a) Conceptual model of cantilever beam

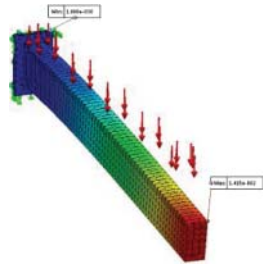
$$EI\frac{\partial^4 y}{\partial x^4} = w(x) \quad x \in [0, L]$$

$$B.C.: y|_{x=0} = 0; \frac{\partial y}{\partial x}|_{x=0} = 0;$$

$$\frac{\partial^2 y}{\partial x^2}|_{x=L} = 0 \frac{\partial^3 y}{\partial x^3}|_{x=L} = 0$$

System parameters: E, I, L

(b) Mathematical model of cantilever beam subjected to boundary conditions



(c) Numerical solution of mathematical model

Figure 6.36 Example of mathematical model (Bi 2018).

models. Taking an example of the problems in mechanics, a mathematic model is for the representation of partial differential equations for the conservation of mass, momentum, and energy; and the model also specifies the spatial and temporal domain, and initial boundary conditions, as well as material properties. On the other hand, a *computational model* refers to the numerical implementation of a mathematic model. A computational model includes a set of discretized nodes and elements, solution algorithms, and terminating criteria. Fig. 6.36 shows an example of the mathematical model for a cantilever beam under the distributed load. The model consists of a differential equation for y-axis displacement (y), boundary conditions for the nodal displacements at $x = 0$, L, and load $w(x)$, and system parameters (E, I, and L). A computational model consists of computer programs and the assumptions made in conceptual and mathematic models. To solve a computational model, the inputs of programs are constitutive models and loads, mesh types and density, analysis types, and terminating conditions.

6.5.1.5 Errors of Model or Analysis Type Element types are selected to represent the most significant features of a physical system or object. To make the complexity of model manageable, not all of the physical features are represented in details. For example, the enclosure of an airplane engine is generally modeled as shell elements, while the wall thickness of some areas is not suitable to be treated as shell elements. If these features are modeled as beam elements, the joining positions should be located at the grid points of shell elements rather than at flanges (Chen 2001).

It is the primary responsibility of an FEA user to create a computer model. An FEA modeler determines state variables and system parameters to represent real-world objects. This responsibility includes a proper validation of the model and its components. It is also the responsibility of an FEA user to document missed data and the consequences thereof to upper administrator or clients.

6.5.2 Verification

Verification concerns the mathematical and computational perspectives of an FEA model. Verification is to analyze the introduced errors at every step of FEA to see if these errors are acceptable and within the expected tolerance. As shown in Fig. 6.37, Conover et al. (2008) classified the

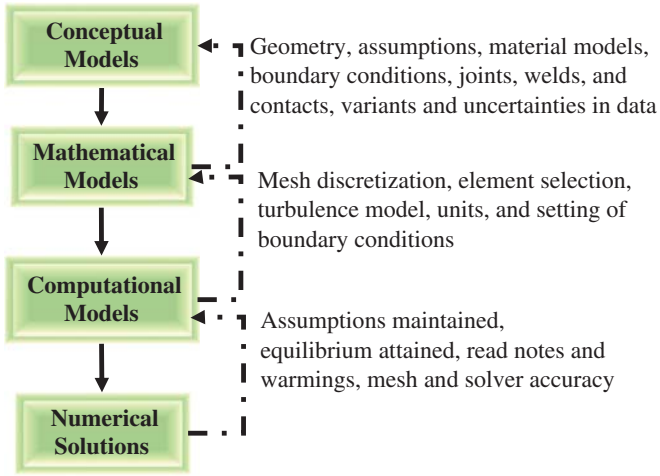


Figure 6.37 Verification at different modeling stages (Bi 2018).

activities of the verification in terms of modeling stages where errors are introduced, i.e., errors are introduced from a conceptual model to a mathematical model, computational model, and finally to the solution of numerical simulation.

As shown in Fig. 6.38, verification has to be performed at different stages for *geometric correctness*, *element types*, *mesh sizes*, *material properties*, *contact conditions*, *energy balances*, and *abnormal mesh*, such as isolated nodes and tangled meshes. To perform these verifications, Thacker et al. (2014) classified the verification in FEA modeling into two basic types. The first type is *code verification*. Code verification focuses on the identification and removal of errors in the code. The second type is *calculation verification*. Calculation verification focuses on the error quantification introduced during the application of the code to a particular simulation. The most important task in a calculation verification is the study of grid or time convergence to refine the mesh until a satisfactory solution is obtained.

6.5.2.1 Code Verification Code verification is not used to prove that the mathematic model is a right representation of physical reality. Instead, code verification is to ensure that a numerical algorithm can solve a mathematic model properly. It does not matter if the mathematical model represents the physical system correctly. If the code verification is performed, the errors from the code can be treated separately from the errors of other sources, and this simplifies sequential code validation.

The software developer should be mainly responsible for code verification. As a software product, the software development must follow the standardized procedure to ensure the functionalities and quality of products. Classic waterfall model in Fig. 6.39 can be used as the guidance for the testing and verification of software products (Wall and Kossilov 1994, IAEA 1999). The development of a software product experiences several stages from conceptual design to final products. At each of these stages, the corresponding verification must be performed to achieve results with expected level of accuracy. When the solution to a mathematic model is programmed, the code

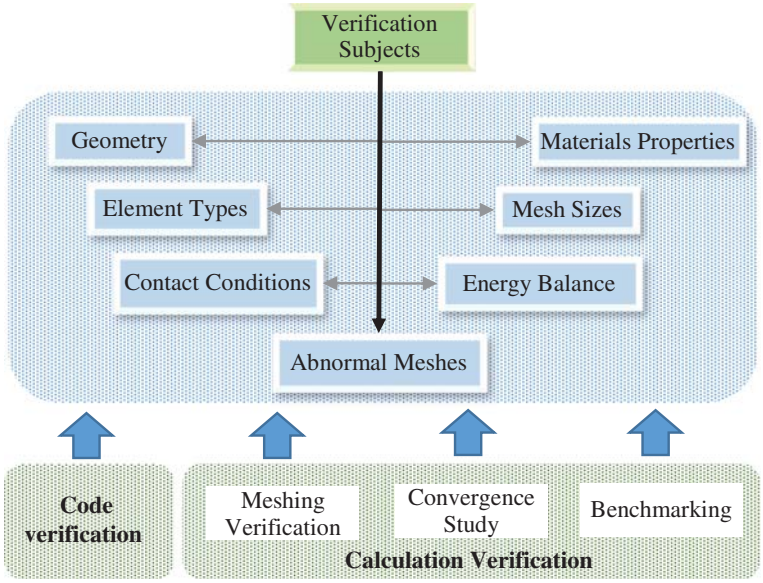


Figure 6.38 Verification subjects in an FEA model (Bi 2018).

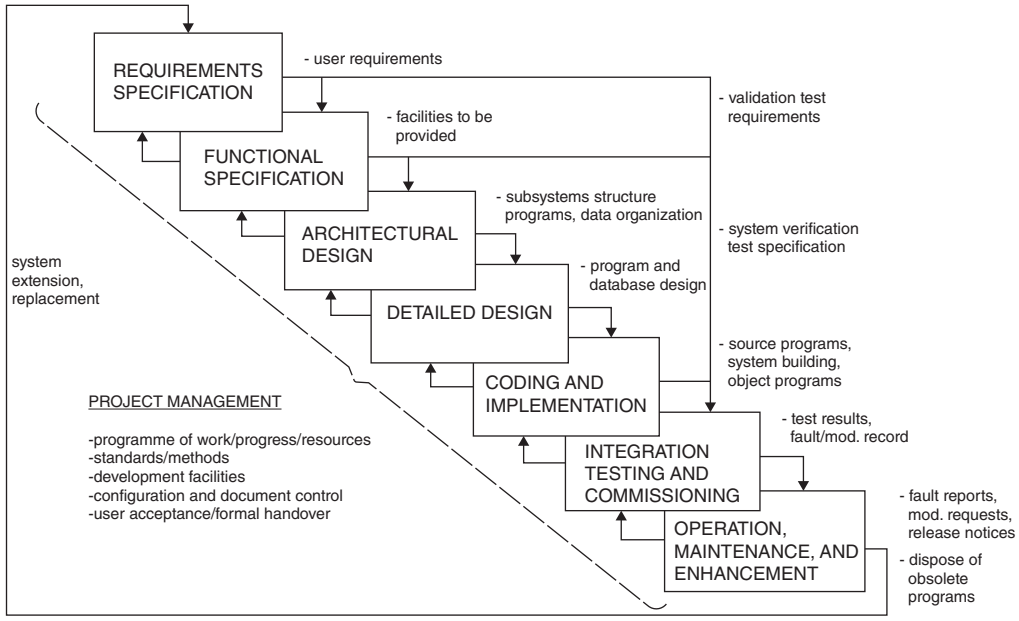


Figure 6.39 Code verification in software life cycle (Adopted from Wall and Kossilov 1994).

must be verified to identify and correct language, grammar, compilation, and assembled errors. After this, the preliminary program check-out begins by executing individual program modules to eliminate potential errors. Such tasks have to be accomplished by software developers. To ensure the functionalities and quality of software products, software users should also conduct the independent code verification to prove that the software tool has the expected functionalities for given tasks.

Numerical simulation is to solve differential equations by computers. Differential equations in a continual domain are represented by state variables on discretized nodes to achieve consistency, stability, convergence, and most important, accuracy of solutions. From this perspective, code verification can be decomposed into two basic tasks: (1) *numerical algorithm property verification*, which is used to determine if the tested algorithm has been implemented in agreement with the proven mathematic properties, such as accuracy, stability, consistency, and (2) *numerical algorithm adequacy verification,* which is used to determine the tested algorithm satisfies the accuracy, robustness, and speed requirements of its intended use (Knupp 2016).

For each verification, the mathematic model and the corresponding program are the inputs for the process of code verification. For the code verification in FEA modeling, a mathematic model includes the detailed description of governing equations, initial and boundary conditions, assumptions and applicable domains. The mathematic model also includes the inputs and data associated with system parameters and coefficients of model. As a summary, the information about mathematical model must be sufficient to generate a certain solution for the verification purpose.

Example 6.1 (Code verification). This example is developed to verify the program for the beam elements in the Solidworks. The cantilever beam in Fig. 6.40a is fixed at one end, and subjected to a concentrated load (200 lbf) on the other end, plain carbon steel is used and the cross-section is a rectangle tube with the principal moments of inertia of the area of $I_y = 4.694292\ \text{in}^2$. The analytical solution for the maximized displacement at the tip is

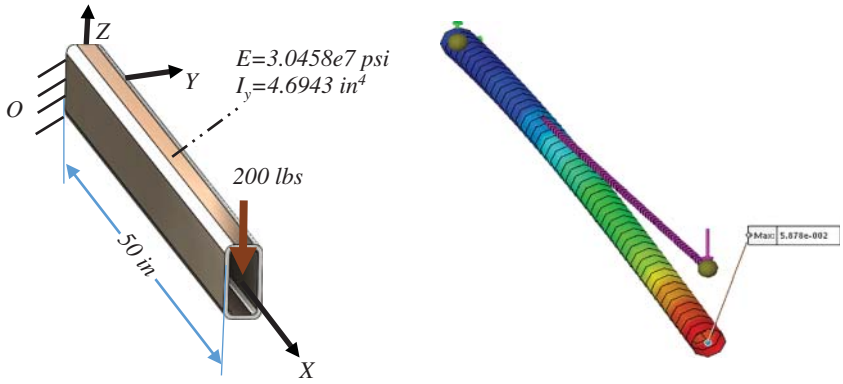
$$y_{\max} = \frac{PL^3}{3EI} = \frac{(200)(50)^3}{3(3.0458 \times 10^7)(4.6942)} = 0.0583(in)$$

SOLUTION

As shown in Fig. 6.40b, structural members for the beam are selected in the Solidworks model, and a design study is conducted by evaluating the impact of the number of elements in FEA on the maximized displacement at the tip. The obtained displacement (~ 0.0588 in) is converged and not affected by the number of elements. The accuracy from the numerical simulation can be verified as,

$$\varepsilon = \frac{|z_{\max}^{analytical} - z_{\max}^{simulation}|}{z_{\max}^{analytical}} = \left|\frac{0.0583 - 0.0588}{0.0583}\right| = 0.86\%$$

Therefore, the program has been verified to be able to obtain acceptable results for the beam.



(a) Verification problem

(b) Parametric study on the number of beam elements (from 1 to 50 elements)

Figure 6.40 Example of code verification (Bi 2018).

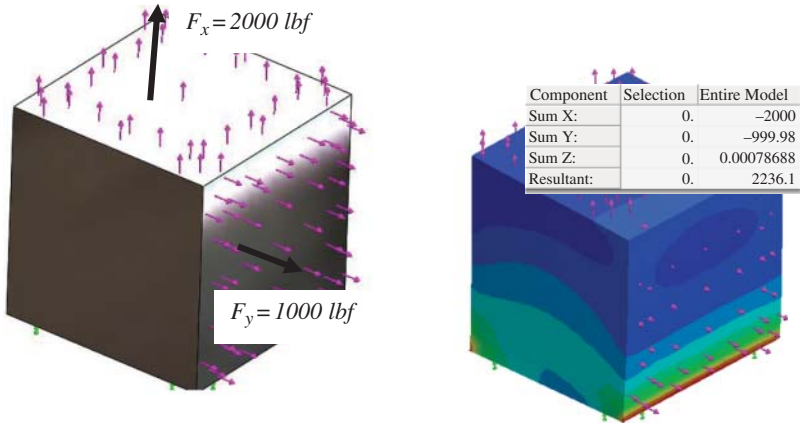
6.5.2.2 Calculation Verification Calculation verification focuses on the removal of errors introduced during the execution of computer programs and the use of software tools. Software users are responsible to perform the calculation verification. In a calculation verification, the simulation result is compared against analytical or validated solutions to determine discretization errors, input data errors, and the overall performance of simulation. Users need to capture various errors in an FEA model, such as the errors from *distorted elements*, *disconnected nodes*, *improper material* assignments, inconsistency of *various coordinate systems*, *boundary and interface conditions*, mechanical, thermal, and inertia *loadings*. Calculation verification should ensure that the software correctly yields an acceptable solution instead of accepting the general-purpose software blindly without a valid assessment.

Example 6.2 (Calculation verification). Fig. 6.41*a* shows a simple solid geometry (i.e., a cube with a size of $4 \times 4 \times 4$ in.) with the materials of plain carbon, the standard solid mesh is used for the calculation verification. The force equilibrium of the free body diagram is used as the criterion of verification. For the boundary conditions, it is assumed that the base surface is fixed, and the applied loads are $F_x = 2000$ lbf and $F_y = 1000$ lbf.

SOLUTION

As shown in Fig. 6.41*b*, the cube geometry is modeled in the Solidworks, the default mesh size and element type is used, and the boundary conditions are applied by fixing the bottom surface and applying two external forces on top surface and the lateral surface on the right side, respectively. After the simulation, the reaction forces from the fixed surface are found as $R_x = -2000$ lbf and $R_y = -999.98$ lbf. The error from the simulation is quantified as,

$$\eta = \frac{\left\| \sqrt{2000^2 + 1000^2} - \sqrt{2000^2 + 999.98^2} \right\|}{\left\| \sqrt{2000^2 + 100^2} \right\|} \times 100\% = 4.0 \times 10^{-4}\%$$



(a) A cube with two applied loads (b) List of reaction force at support

Figure 6.41 Calculation verification based on force equilibrium of free body diagram (Bi 2018).

The discrepancy of the simulation result for the force equilibrium of object is ignorable.

The criterion for the force equilibrium is widely used to verify an FEA model. If a system to be modeled is an assembled product. Any component in the assembly can be selected as an object to be verified.

6.5.2.3 Meshing Verification In an FEA model, a continual domain is represented by a mesh with discretized nodes and elements. Meshing should be verified to avoid some issues, such as large difference of stiffness. For example, it is a common practice in static analysis that the ratio of the maximum and minimum element stiffness coefficients should be less than 1.0×10^8. Otherwise, the rigidity of softer elements will be ignored in a system model, which might lead to unacceptable discrepancy of the simulation solution. Users should verify the appropriation of a mesh from many perspectives:

(1) Verify the maximized stress to see if there is an abnormal stress concentration; stress concentration may lead to the stress level beyond yield strength.
(2) Verify if all of the displacements are in expected ranges.
(3) Verify if the deformed shapes make practical sense.
(4) Verify the reaction forces against applied loads to check force equilibrium. For a steady problem, the sum of forces must be balanced by the sum of reaction forces; this can be used to identify misplaced loads, incorrect units, geometric errors or types of input; check reactions at contact pairs.
(5) Verify the bonded contacts to see if penetration occurs, and generate the plots of stress distribution to verify the reasonableness.

Example 6.3 The model in Fig. 6.40 is used again as an example for meshing verification. Beam elements are used to represent the cantilever beam. Use a parametric study for the meshing verification to prove the convergence of simulation.

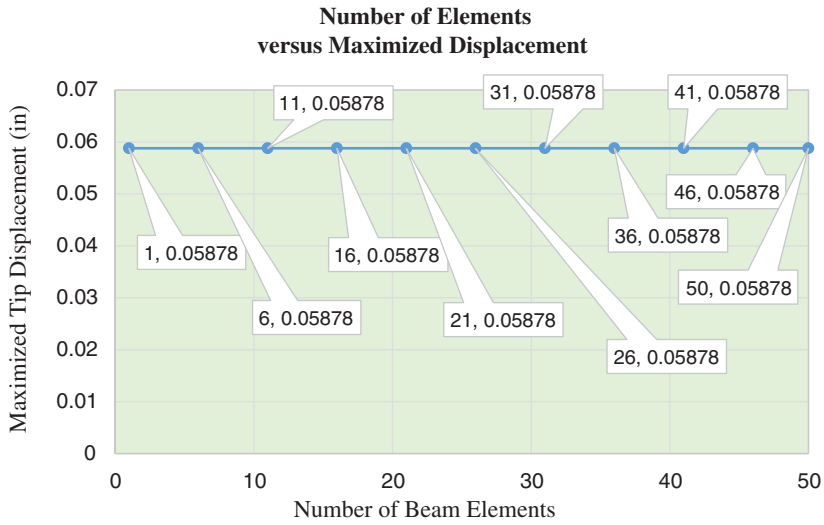


Figure 6.42 Parametric study on cantilever beam (Fig. 6.40) for mesh verification (Bi 2018).

SOLUTION

The beam is modeled in the Solidworks simulation, and a parametric study is defined where the only variable is the number of the beam elements. Fig. 6.42 has shown the result of the parametric study. The max displacement at the tip remains the same for a range of beam members from 1 to 50. This passes the meshing verification.

Due to the limits of computer memory and speed, a user often faces a trade-off between accuracy and computation time. The demand on computing resources can be alleviated by some simplifications, such as running an analysis on a partial model for symmetric or anti-symmetric objects. Fig. 6.43 shows an example of symmetric specimen subjected to a tensile load. Due to symmetric relations, only a quarter of the specimen is modeled in the simulation. However, it is worth to note that for a valid symmetric model, all of the geometries, loads, and BCs must be symmetric.

For a complex object, it is often necessary to reduce the mesh density at uncritical regions. To determine suitable mesh sizes, one should be aware that the accuracy of state variables in a specific region relates to both element sizes and gradients of state variables. Therefore, small-size elements should be used in the areas with a high derivative of state variable; for example, in the regions with estimated high stresses or fluxes. On the other hand, large elements can be used in the regions with low stresses or fluxes. Fig. 6.44 gives an example that the model includes the features of geometric discontinuities. To increase the accuracy of the simulation, the high-density meshing is applied only in local regions with geometric discontinuities. It is also worth to note that the accuracy of one element model is affected by those of surrounding elements; therefore, meshing sizes must be changed smoothly from one region to another.

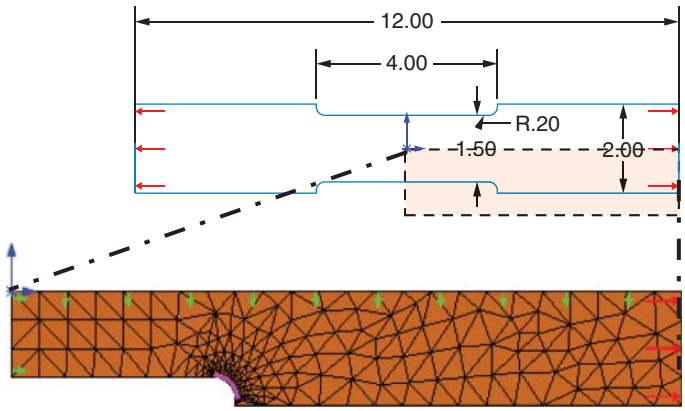
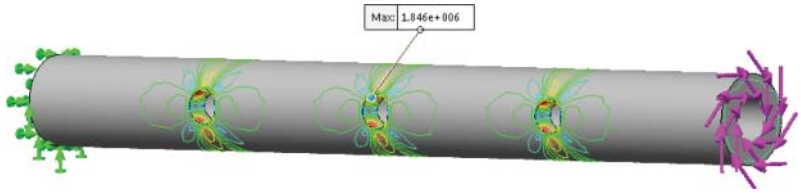


Figure 6.43 Example of using symmetric relation in computing reduction (Bi 2018).



(a) Increasing mesh density in critical regions

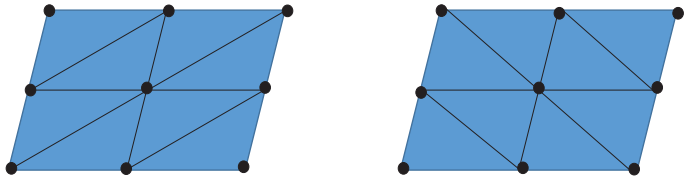


(b) High level of gradient in critical area

Figure 6.44 Estimating gradient distribution to justify mesh control (Bi 2018).

Automatic mesh generator in a commercial software tool is not visible to users. Users get limited feedbacks or guides when a meshing process fails. To find a resolution for a failure of meshing process, one may try to change the size setting of a mesh to obtain more hints about meshing failures. An assembled model fails more likely in meshing. In particular, the mesher may run out of memory because of tiny features; the decomposition on those features can cause a large number of tiny elements. If an assembled model is concerned, users should mesh individual parts before the assembled model is modeled and analyzed.

Major factors in choosing mesh sizes are (1) the balance of computation time and solution accuracy, (2) the avoidance of distorted shapes that lead to near singular stiffness matrices, (3) the representation of boundary conditions where loads are distributed properly.



(a) High aspect ratio (b) Low aspect ratio

Figure 6.45 Impact of aspect ratio on mesh quality (Bi 2018).

To verify the quality of mesh, the concept of aspect ratio can be utilized. An aspect ratio is defined as the ratio of the longest and shortest edges. The lower the aspect ratio it, the better shape the element is. Fig. 6.45 has shown that the quality of meshes can be different even with the same number of elements and nodes.

Commercial software tools, such as Solidworks and ANSYS, provide a collection of test cases to verify and validate the capabilities of the software tools. The simulation can be verified and validated by comparing the results of analytical solutions for numerous classical engineering problems (ANSYS 2013).

6.5.2.4 Convergence Study One primary question in developing an FEA model is how small the elements in a mesh should be so that an acceptable simulation result can be obtained. Note that mesh sizes in the discretization are determined subjectively, and it is hard to justify the errors caused by the discretization. Therefore, one has to ensure that the solving process be converged to correct solutions. A convergence study can be used to evaluate the impact of mesh sizes on the simulation accuracy. The mesh size must be fine enough to ensure that the simulation result will not be changed significantly by further reducing mesh sizes. The requirements of convergence can be met by considering three criteria (Burnett 1987; Pointer 2004):

(1) **Continuity condition**. The shape functions of elements must ensure that the displacement solutions across elements are continuous. Shape functions are usually required in formulating models of elements. It is the developer's responsibility to ensure the satisfaction of continuity condition.

(2) **Completeness condition**. The mesh must be free of singular nodes. The magnitude of a state variable on a singular node tends to be infinitely large; that causes a large gradient of the state variable in the element. The condition of completeness ensures that the nodal values in each element approach the same value when the element size reduces. It is the user's responsibility to verify the condition of completeness.

(3) **Convergence of energy**. For an FEA model with the satisfaction of completeness and continuity conditions, the convergence of energy warrantees that the solution to the model is converged. It is the user's responsibility to ensure the convergence of energy.

Mesh sizes relate closely to both computation and accuracy. The finer a mesh is, the better result an FEA model can obtain; however, it demands more computation. A trial and error method can

be applied to determine mesh sizes. Once an FEA solution is found, a mesh with a fine size is applied to find a new solution, two solutions are compared to see if the solution is improved by refining the mesh. The iteration will be continued until the difference of two solutions is within the specified percentage of errors.

6.5.2.5 Benchmarking A comparative reference is essential for code or calculation verification. A *benchmark* is a standard test designed to probe the accuracy or efficiency of FEA models. A benchmark problem is a well-defined example problem for which a reference solution exists, and *benchmarking* is defined as the process to evaluate the variation in results from different programmers or software codes. If there is no analytical solution to a design problem, numerically derived benchmarking solutions can be applied. The governing equations of an engineering problem are PDEs, benchmark solutions for PDEs can be found in two different methods: (1) a PDE is transformed into an ordinary differential equation (ODE), and the numerical integration is performed on ODE to find the solution; (2) the numerical integration is directly applied to a PDE. In either of two cases, the accuracy of solution must be assessed critically to qualify them for use in code or calculation verification. For a solution from the first method, the benchmarking process has been standardized to assess simulation accuracy. For a solution from the second method, it should be the last resolution for benchmarking and the code used in generating that solution has been thoroughly verified and documented (ASME 2006).The credibility of a benchmark solution can be enhanced if it has been obtained by different numerical approaches or software tools. Using a solution agreed by multiple independent sources will mitigate the risk of errors in the verification. Although benchmarking depends on how users translate a benchmark problem into a computer model and how they interpret the results, it is encouraged to benchmark different software packages against each other or against the reference solution.

Most benchmarks are simple practical problems for which no analytical solution exists. Users can use a benchmark to check if they use their own tools, define their own models but still obtain similar solutions to those solutions from the benchmarks. Since the solution is numerical simulation based, a small deviation from the reference solution is acceptable. Even larger deviations may still be acceptable, depending on the type of problem and the level of details that is provided with the benchmark. Some public benchmarks have shown that a large difference can occur; it implies the need for the follow-up validation of numerical models. In summary, benchmarks can serve for the following purposes (ANSYS 2013):

- Verify computer software and program modules.
- Train unexperienced FEA users, help them become familiar with numerical analysis, and practice FEA modeling appropriately.
- Prove FEA users' competence in solving engineering problems, in particular, their domains by FEA.
- Make users aware of differences of results even for a well-defined problem. This emphasizes the importance of validation of numerical models.
- Highlight the importance of providing correct inputs of model, for example, define appropriate constitutive models for the materials.
- Identify the limitations of the state of the art in numerical modeling in practice.

6.6 FINITE ELEMENT ANALYSIS FOR VERIFICATION OF STRUCTURAL ANALYSIS

Finite element analysis (FEA) is a general-purpose tool for stress analysis on any structures. It is especially useful in some cases that (1) no precedent empirical data or analytical solution is available; (2) the geometry of object is too complicated to be applied by stress concentration factor method; (3) multiphysics behaviors are involved in a system; (4) types of loadings and discontinuities are strongly coupled and are varied with respect to time. In applying FEA for stress analysis, it is critical to tune-up an FEA model and verify the result from the simulation model adequately to ensure the fidelity of simulations. An FEA model can be verified and validated by comparative studies where experimental data or analytical solutions for the stress calculation in some simplified cases.

The stress data included in all of the charts or formulas should be verified by the simulation of corresponding FEA models. In this section, the stress concentration in a finite-width thin element with opposite single semicircular notches in Section 2.3.2 and Chart 2.3 is used as an example to verify the FEA-based simulation method.

Fig. 6.46 shows a finite width thin element ($H \times h$) with two symmetric semicircular notches (r). Chart 2.3 shows that the formula for stress concentrations (K_{tg} and K_{tn}) are given as,

$$\left.\begin{aligned} \sigma_{nom} &= \frac{P}{hd} = \frac{P}{h(H-2r)} \\ K_{tn} &= \frac{\sigma_{\max}}{\sigma_{nom}} = 3.065 - 3.472\left(\frac{2r}{H}\right) + 1.009\left(\frac{2r}{H}\right)^2 + 0.405\left(\frac{2r}{H}\right)^3 \end{aligned}\right\} \tag{6.65}$$

$$\left.\begin{aligned} \sigma &= \frac{P}{hH} \\ K_{tg} &= \frac{\sigma_{\max}}{\sigma} = \frac{H}{(H-2r)}K_{tn} \end{aligned}\right\} \tag{6.66}$$

Note that stress concentration is not affected by material properties, and the length and width of the thin plate. To simplify the comparison, the thin plate model in Fig. 6.47 has a length of 10.00-in., a cross-section area of $h \times H = 1.00\ \text{in}^2$, and the material of the plate is set as *plain carbon steel*. The pound-in-second system is used as the unit system. Fig. 6.48 shows the corresponding FEA model: a simplified two-dimensional simulation model is accurate enough to

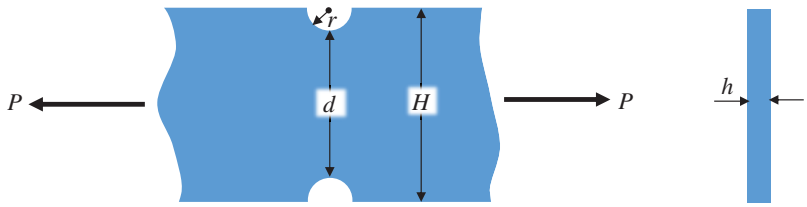
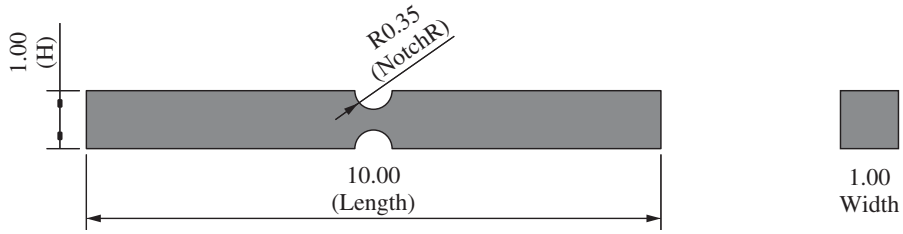


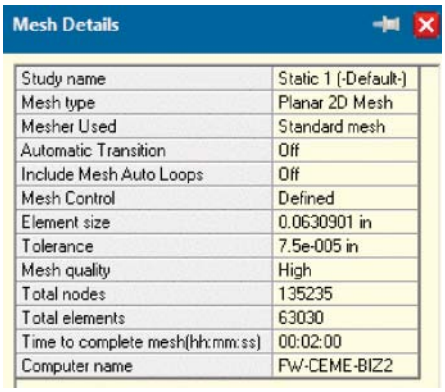
Figure 6.46 A finite-width thin element with semicircular notches subject to tensile load.



Unit: Inch-pound-second (IPS) system
Material: Plain carbon steel
Tensile load: 1.00 (lbf)
Cross-section area: $h \times H = 1.00$ in^2
Notch radius: 0.00625 – 0.35 in

Figure 6.47 A finite thin element with semicircular notches subject to tensile load.

investigate the thin plate under a tensile load. The left edge is fixed, and the right edge is free and applied by an external force of 1.00 lbf. A two-dimensional model allows to use a fine mesh where the 'mesh control' is applied at two notches with the element size of 0.00025. Note that to further reduce the computation, a one-quart model can be used and the symmetric planes on horizontal and vertical directions can be defined as *roller support*.



Mesh Details

Study name	Static 1 (-Default-)
Mesh type	Planar 2D Mesh
Mesher Used	Standard mesh
Automatic Transition	Off
Include Mesh Auto Loops	Off
Mesh Control	Defined
Element size	0.0630901 in
Tolerance	7.5e-005 in
Mesh quality	High
Total nodes	135235
Total elements	63030
Time to complete mesh(hh:mm:ss)	00:02:00
Computer name	FW-CEME-BIZ2

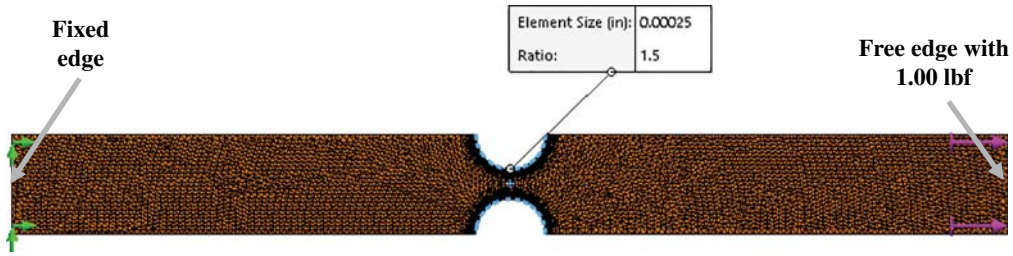


Figure 6.48 A two-dimensional FEA model of finite thin element.

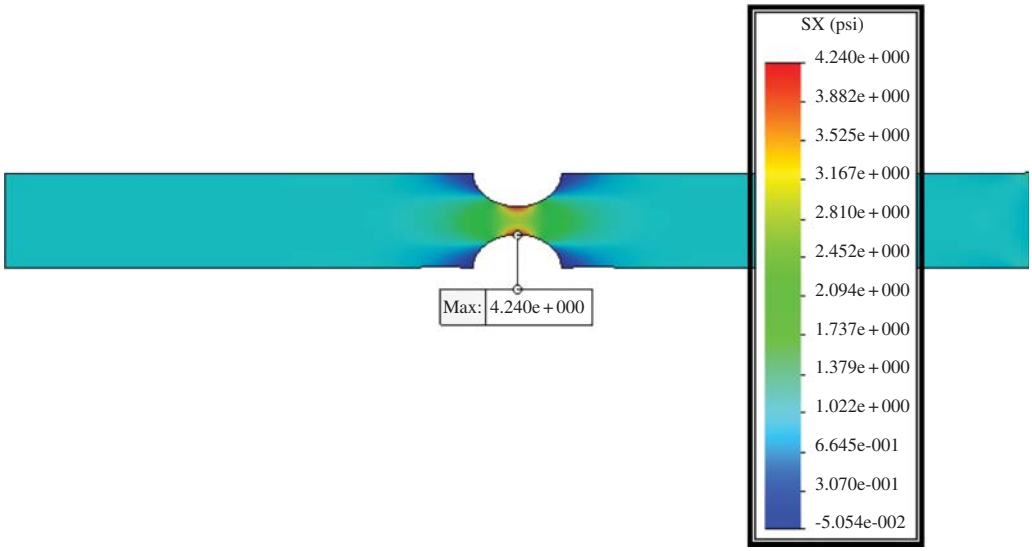


Figure 6.49 An two-dimensional FEA model of finite thin element.

Furthermore, a parametric study is developed by setting the notch radius as the variable for the range of (0.00625 in., 0.35 in.) with a step of 0.00625 in. The max normal stress along the axial direction (σ_x) in each scenario is recorded. The parametric study generates a total of 56 scenarios. Fig. 6.50 shows the comparison of the simulation result with the data included in Chart 2.3. For all of the scenarios, the maximized discrepancy between the results of simulation and empirical formula is 1.42%, which is well within the acceptable range.

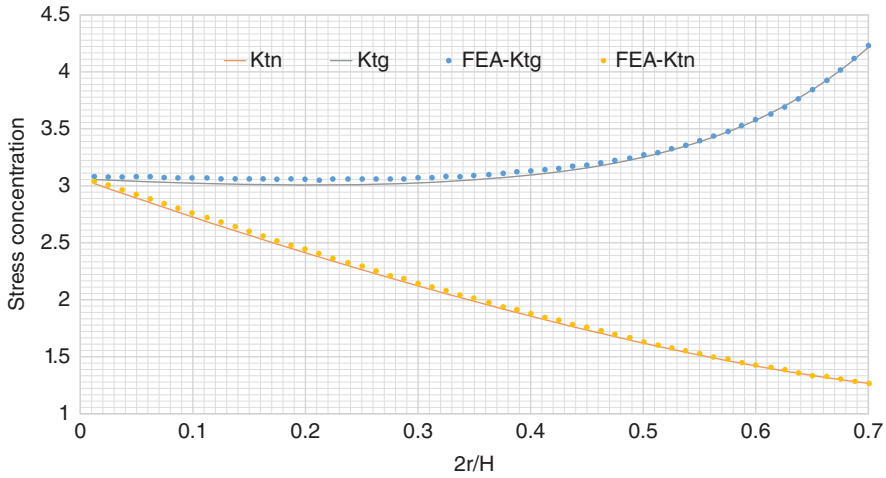


Figure 6.50 Comparison of stress concentration from the simulation and the empirical formula for single thin plate with semicircular notches subject to tensile load.

6.7 FEA FOR STRESS ANALYSIS OF ASSEMBLY MODELS

The stress concentration factor method applies only to simple parts with discontinuities. Products are mostly designed as the assemblies of parts and components. The impact of assembly relations or boundary supports on stress distributions have to be taken into consideration. An FEA-based method allows modeling the assembly relations or other boundary constraints of products adequately to analyze stresses in products. Here, a fastening assembly is used as an example to illustrate the procedure of using the FEA-based method for the stress analysis of products; the relation of the preload and the stress on the weakest position of the fastener is explored. The simulation aims at finding the allowable preload when the maximum tensile load (500 N) is applied. Note that no solution is provided in the Section 5.6 of bolts and nuts on fatigue stress concentration factors.

The fastening configuration and the main dimensions of parts are illustrated in Fig. 6.51. The materials of two plates to be joined are set as *1060 alloy*, and the materials for both the nut and bolt are set as *plain carbon steel*. In assembly modeling, the centerlines of the holes on two plate and the threads on the bolt and the nut are all aligned. The contact surfaces in the assembly are defined as *coincident*, and the nut and the bolt have a *screw* mate with a specified pitch of 2 mm. A preload is represented a restrained displacement shows the assembly model of a fastener.

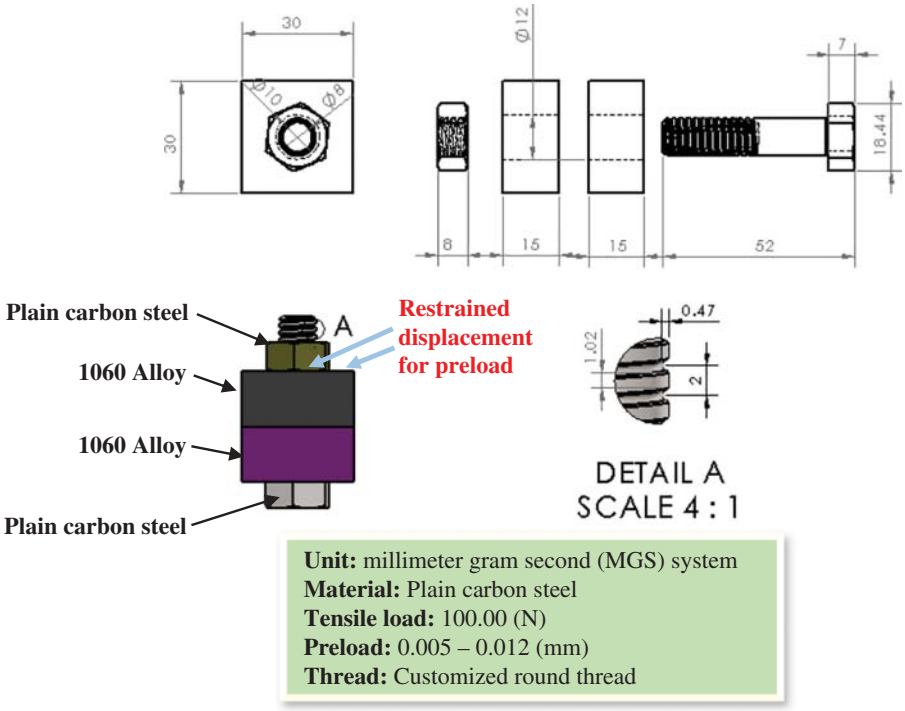


Figure 6.51 Assembly model of fastening.

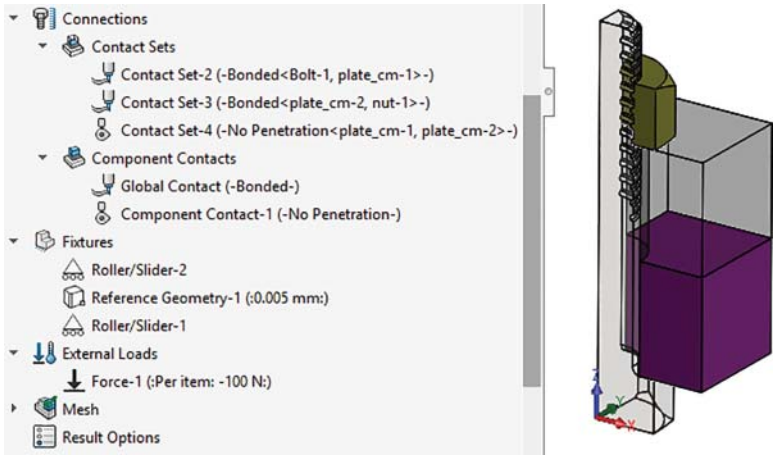
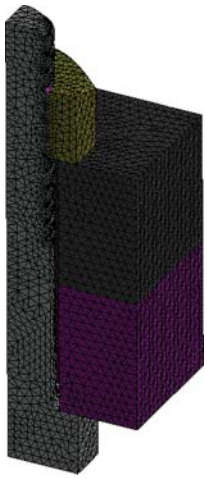


Figure 6.52 Simulation model of bolt-nut assembly.

Fig. 6.52 shows the reference simulation model. Due to the symmetry, one quarter of the assembly model is used in the simulation. The bottom surface of the lower plate is , and the surfaces cutout by symmetric planes are set as *roller support*. A *no penetration* relation is set for all of the identified contacts between the nut and the bolt, the bolt and lower plate, the lower and the upper plate, and the upper plate and the nut.

As shown in Fig. 6.53a, *mesh control* is applied to critical areas including the thread and nut. In addition, the mesher uses *curvature-based mesh* to achieve a better fit to smooth geometries.

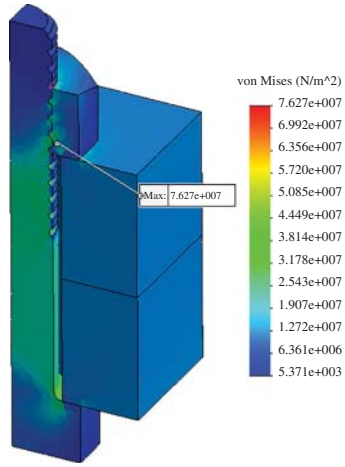


(a) Mesh with "mesh control"

Mesh Details

Study name	Static 1 (-Default-)
Mesh type	Solid Mesh
Mesher Used	Curvature-based mesh
Jacobian points	4 points
Mesh Control	Defined
Max Element Size	0.1 cm
Min Element Size	0.02 cm
Mesh quality	High
Total nodes	144952
Total elements	97195
Maximum Aspect Ratio	21.374
Percentage of elements with Aspect Ratio < 3	99.3
Percentage of elements with Aspect Ratio > 10	0.0257
% of distorted elements (Jacobian)	0
Remesh failed parts with incompatible mesh	Off
Time to complete mesh(hh:mm:ss)	00:00:09
Computer name	FW-CEME-BIZ2

(b) Details of mesh



(c) Sample stress distribution

Figure 6.53 Meshing and stress distribution of bolt-nut assembly.

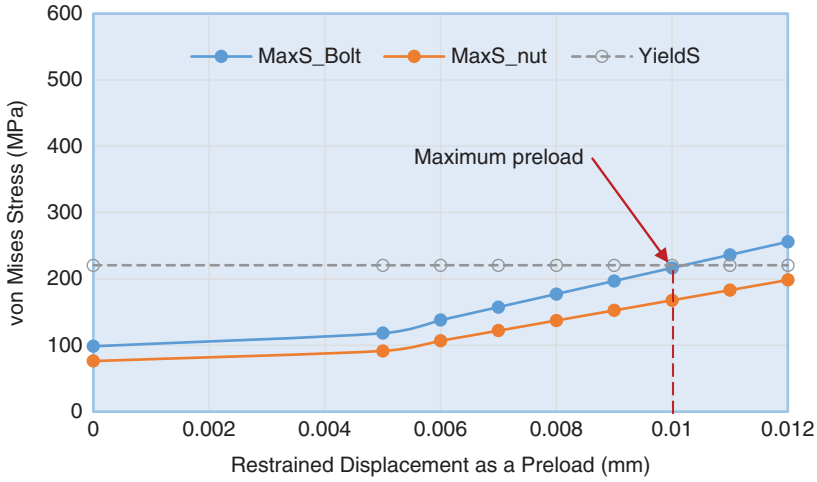


Figure 6.54 Parametric study of preload for bolt-nut assembly.

Fig. 6.53*b* shows the example statistic data of the generated mesh, and Fig. 6.53*c* gives an example of stress distribution over the thread and nut with the annotated maximum stress occurring to the nut.

The maximum stress is affected by the assembly relations of parts as well as a preload in the bolt-nut assembly. In this model, the preload in the bolt-nut assembly is represented by the initial displacement of contact bottom surface of nut to the top surface of the upper member. A parametric study is conducted to look into the relation of the maximum stress and the preload. Fig. 6.54 shows that the maximum stress from the simulation increases linearly with an increase of preload; this matches the expectation and result of the analytical model of the bolt-nut assembly. The maximum preload to avoid an initial yielding on nut should be below an initial displacement of 0.01 mm for the specified assembly.

6.8 PARAMETRIC STUDY FOR STRESS ANALYSIS

The SCF method can deal with design variables only one by one, while the stress distribution of a product mostly depends on many design variables simultaneously. An FEA method supports the parametric study where the simulation can be repeatedly performed for a number of design scenarios. In a parametric study, design variables can be geometric dimensions, materials, boundary conditions, loading conditions, or simulation settings. One design scenario corresponds to the set of given values for the selected design variables. By comparing the simulation results for these design scenarios, a parametric study allows to identify the optimized solution based on the specified design criteria. Here, the stress analysis of a wheel design is used to illustrate the procedure of developing a parametric study for a product.

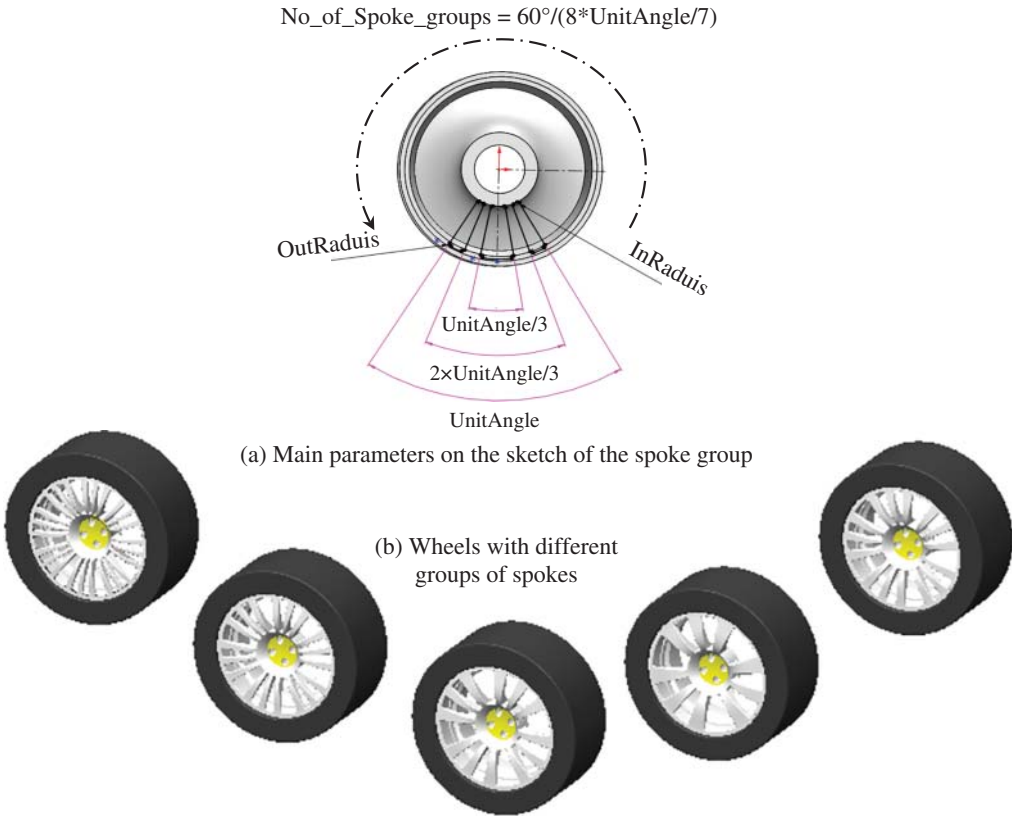
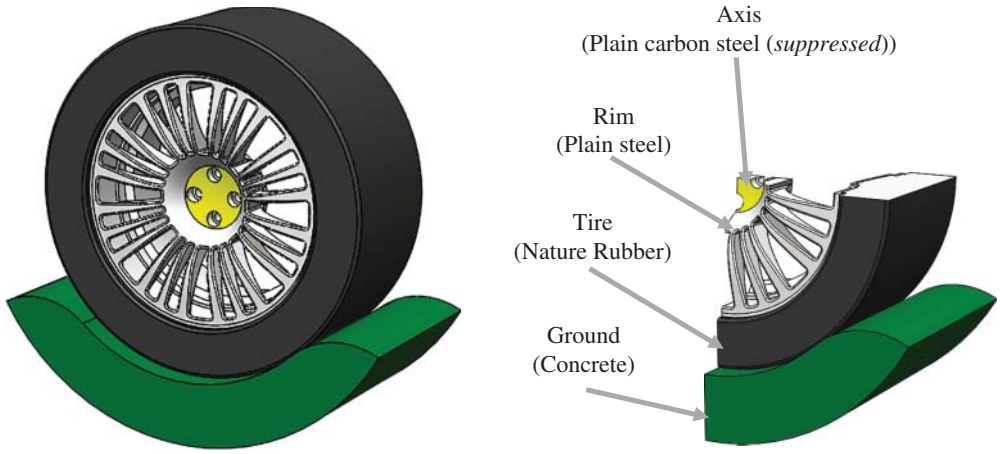


Figure 6.55 Parametric model of a wheel design.

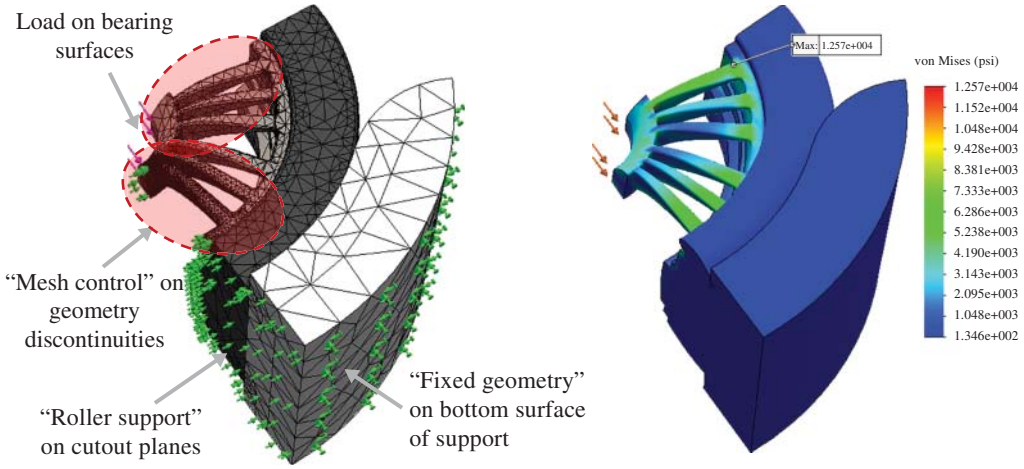
Fig. 6.55 shows the concept design of wheel. Except for the specified dimensions, the designer is interested in the impact of (1) the number of spokes and (2) the radius of the rounds on the stress on the weakest points. The goal is to minimize the total mass of rim with the required design safety factor.

The results from the parametric study are given in Fig. 6.58 and Fig. 6.59 for the maximum von-Mises stress and the total weight of the rim with respect to two design variables, respectively. The results show that both the number of spoke groups and the radii of out fillets affect the stress concentration greatly, and the maximum von Mises stress over the rim is minimized by having the minimized unit-angle of 39.38° (i.e., the maximized eight groups of spokes) and the maximized radius of out fillets. Neither of these two design variables affect the total mass of the rim significantly. The weight can be minimized by using a large number of spoke groups and a small radius of out fillets. Therefore, the proposed wheel design can be optimized at (UnitAngle = 39.38°, RoundR_2 = 0.2 in) where the von Mises stress in the rim is minimized to 12,572 psi subjected to the specified load.



(a) Wheel model with support (b) One-quart model for simplification

Figure 6.56 Wheel model with support and simplification.



(a) Mesh with "mesh control" (b) Sample stress distribution

Figure 6.57 FEA model and simulation for wheel design.

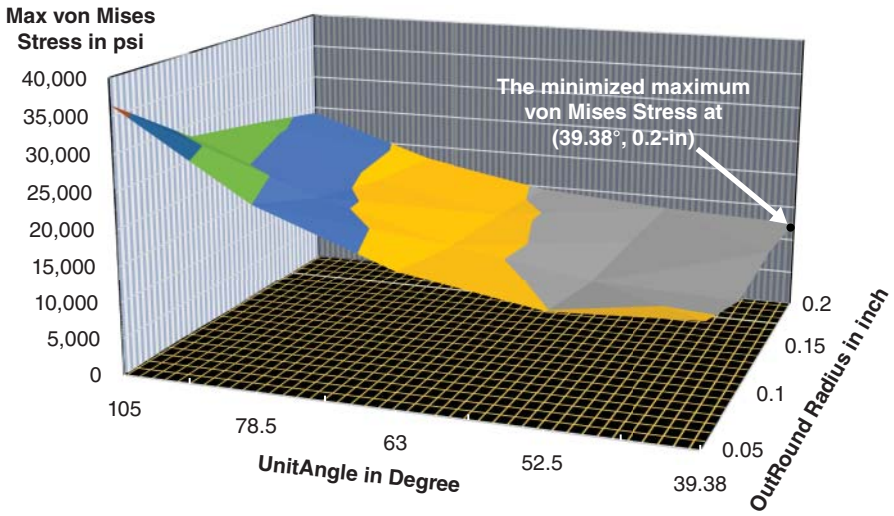


Figure 6.58 The maximum von Mises stress in rim with respect to the number of spoke groups and radius of out fillets.

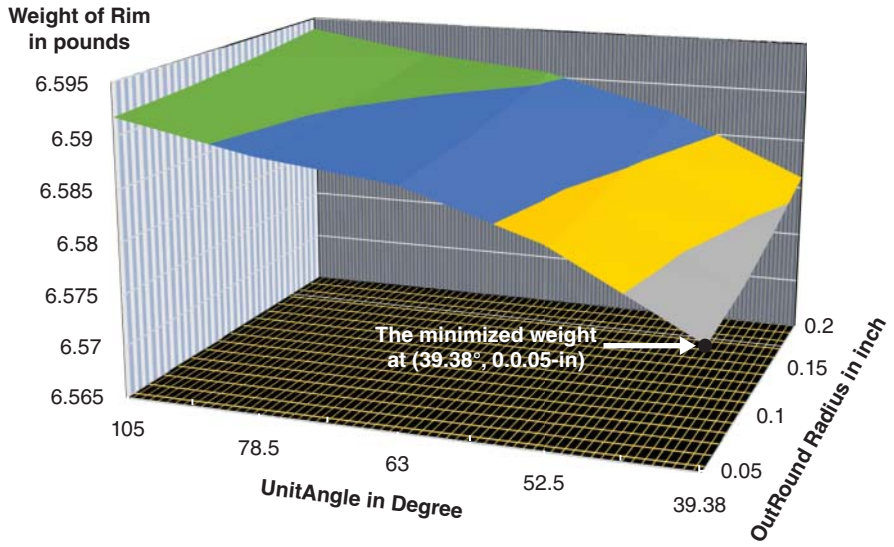


Figure 6.59 The total weight of the rim with respect to the number of spoke groups and radius of out fillets.

6.9 FEA ON STUDY OF STRESS CONCENTRATION FACTORS

Any complex structure or system consists of basic elements with a number of design features, such as holes, fillets, and notches. The details of the machine element designs affect the overall performance of a mechanical system. Therefore, the method of SCFs is fundamental to evaluate the impact of design features on system performance. However, the empirical equations, charts, and analytical models reported on in Chapter 2 to Chapter 5 are applied mostly to object individuals, homogeneous and isotropic materials, simple discontinuities, and for specified load types or simple combinations. In other words, these charts and models are inapplicable to calculate stress concentration factors in various complex cases, such as (1) a body with composites, (2) an object with advanced design features, such as spherical cavities, and sweeping or lofting features, (3) an assembly of objects by welds, and (4) the stress induced by multiple physics behaviors, such as a combination of mechanical forces and thermal loads. The FEA method presented in this chapter provides an ideal alternative to evaluate stress concentration factors in all of the complex application scenarios.

REFERENCES

ANSYS In., 2013, *ANSYS mechanical APDL element reference*, version 15.0, Southpointe, 275 Technology Drive, Canonsburg, PA, http://148.204.81.206/Ansys/150/ANSYS%20Mechanical%20APDL%20Element%20Reference.pdf.

Aparcio, C., 2013, *What is fatigue analysis*? http://simulatemore.mscsoftware.com/what-is-fatigue-analysis-msc-nastran/.

Aris, R., 1994, *Mathematical Modelling Techniques*, New York: Dover. ISBN 0-486-68131-9

ASM International, 2008, *Elements of Metallurgy and Engineering Alloys (#05224G): Chapter 14 Fatigue,* http://www.asminternational.org/documents/10192/1849770/05224G_Chapter14.pdf.

ASME, 2006, *Guide for verification and validation in computational solid mechanics*, http://jacobsschool.ucsd.edu/EEI/academic/courses/06/spring/SE207/pdf/Reference-01.pdf.

Bender, E.A., 2000, *An Introduction to Mathematical Modeling*, New York: Dover. ISBN 0-486-41180-X.

Bokil, V. A., 2009, *Introduction of mathematic modeling*, http://math.oregonstate.edu/~gibsonn/Teaching/MTH323-001S09/Supplements/IntroToModel.pdf

Brinkgreve, R. B. J., and Engin, E., 2013, *Validation of geotechnical finite element analysis*, Proceedings of the 18th International Conference on Soil Mechanics and Geotechnical Engineering, Paris 2013.

Budynas, R., and Nisbett, J. K., 2015, *Shigley's Mechanical Engineering Design*, 10th Edition, ISBN-13: 978-0073398204, McGraw Hill

Burnett, David S., 1987, *Finite Element Analysis*. Reading: Addison-Wesley Publishing Company.

Chen, G., 2001, *FE model validation from structural dynamics*, Imperial College of Science, Technology and Medicine, University of London, South Kensington, London, UK.

Conover, D., 2008, *Verification and validation of FEA simulations*, Integration of Simulation Technology into the Engineering Curriculum, Cornell University, July 25 - 26, 2008, at Cornell University, Ithaca, New York.

Crandall, S. H., 1956, *Engineering Analysis: A Survey of Numerical Procedures*, McGraw-Hill Book Co., Inc..

Gavin, H., 2012, *Geometric Stiffness Effects in 2D and 3D Frames*, http://people.duke.edu/~hpgavin/cee421/frame-finite-def.pdf.

Hamrock, B. J., Jacobson, B., and Schmid, S. R., 1999, *Fundamental of machine elements*, WCB/McGraw-Hill, ISBN 0-256-19069-0.

International Atomatic Energy Agency (IAEA), 1999, *Verification and validation of software related to nuclear power plant instrumentation and control*, Technical Report No. 384, http://www-pub.iaea.org/mtcd/publications/pdf/trs384_scr.pdf.

Knupp, P., 2016, *Code verification for phenomenological modeling and simulation software*, https://cfwebprod.sandia.gov/cfdocs/CompResearch/docs/cv.pdf.

Moorcroft, D., 2012, *Model verification and validation process*, https://www.niar.wichita.edu/niarfaa/Portals/0/Model%20Validation%20Process2.pdf.

Nanninga, N. E., 2008, *High cycle fatigue of AA6082 and AA6063 aluminum extrusions*, Doctoral Thesis, Michigan Technological University, http://digitalcommons.mtu.edu/etds/18.

NASA/FLAGRO, 2014, *Fatigue User's Guide>Crack Growth>NASA/FLAGRO*, http://www.mscsoftware.com/training_videos/patran/Reverb_help/index.html#page/Fatigue%20Users%20Guide/fat_growth.08.8.html.

Pointer, J., 2004, *Understanding accuracy and discretization error in an FEA model,* http://www.designspace.com/staticassets/ANSYS/staticassets/resourcelibrary/confpaper/2004-Int-ANSYS-Conf-54.PDF.

Reuss, B., 2014, *Solidworks Simulation 2015 – FEA Solvers*, https://www.3dvision.com/blog/entry/2014/11/26/solidworks-simulation-2015-fea-solvers.html.

SAE, 2014, *J1099, SAE Standards: technical report on low cycle fatigue properties ferrous and nonferrous of materials*, http://standards.sae.org/j1099_197502/.

Shah, C., 2002, *Mesh discretization error and criteria for accuracy of finite element solutions*, Cummins, Inc., http://simplorer.com/staticassets/ANSYS/staticassets/resourcelibrary/confpaper/2002-Int-ANSYS-Conf-9.PDF.

Shariyat, M., Sola, J. F., and Jazayeri, S. A., 2016, Experimentally validated combustion and piston fatigue life evaluation procedures for the bi-fuel engines, using an integral-type fatigue criterion, *Latin American Journal of Solids and Structures*, Vol. 13, No. 6, p. 1030–1053.

Thacker, B. H., Doebling, S. W., Hemez, F. M., Anderson, M. C., Pepin, J. E., and Rodriguez, E. A., 2004, *Concepts of model verification and validation, LA-14167-MS*, Los Alamos National Laboratory, US Department of Energy, https://www.osti.gov/scitech/servlets/purl/835920/.

Unigovski, Y. B., Grinberg, A., Gerafi, E., Gutman, E. M., Moisa, S., 2013, Low-cycle fatigue of an aluminum alloy plated with multi-layer deposits, *Journal of Optoelectronics and Advanced Materials*, Vol. 15, Nos. 7–8, pp. 863–868.

Wall, N., and Kossilov, A., 1994, *Verification and validation of software related to nuclear power plant control and instrumentation*, http://www.iaea.org/inis/collection/NCLCollectionStore/_Public/26/045/26045115.pdf.

what-when-how, 2018, http://what-when-how.com/the-finite-element-method/fem-for-frames-finite-element-method-part-1/.

INDEX

Note: Page references in *italics* refer to figures and tables. Page references in **bold** refer to charts.

Accumulative damage, 542
Acoustic properties, 543, 553
Alternative stress, 15, 522, *522*, 586
American Society of Mechanical Engineers (ASME)
  ASME-elliptic line, *546*
  on benchmarking for verification, 576
  cylindrical pressure vessel design, 463, **515**
  pressure vessel codes, 232
  Analysis types, 524, 547, 558–559, *558–559*, 563, 567
Angle section, 463, **514**
Anisotropic material, 7
Artificial neural network, 480, 483
ASME-elliptic line, 546, *546*
Assembly models, stress analysis of, 580–582, *580–582*
Auto correlation length (ACL), 480
Automatic mesh generator, 574
Axial loading (tension), 170–176, *170–176*
Axisymmetric problems, 49–51
Axles, 13, 26, 104–105, 167, 449–450

Bar with a groove, *43*, 44, 48, 64
Bar with a hole, 42, *43*
Bar with a notch, 102, **121**, **126, 127**
Bar with a shoulder fillet, **184–187**, **193**, 452
Bead reinforcement, 263, 267, **379–381**, **390, 391**
Beam with a central hole, *288*, 288–289
Beam with a circular hole, 289
Beam with an elliptical hole, 290
Benchmarking, 576

Peterson's Stress Concentration Factors, Fourth Edition. Walter D. Pilkey, Deborah F. Pilkey and Zhuming Bi.
© 2020 John Wiley & Sons, Inc. Published 2020 by John Wiley & Sons, Inc.

Bending loads, 14–15, 50, 52, 61–62, 73, 289, 465. *See also* Welds
Bending of plates with notches, 103–104
Bending of solids with grooves, 104–105, *105*
Bending of thin beams with notches, *101*, 101–103
Bending stress, 24, **419**, **423**, 445, 447, 455, 462, 478–479
Bends, 23
Biaxial stress
  circular holes with in-plane stress in infinite thin element, *219*, 219–220
  symmetrically reinforced circular hole in a biaxially stressed wide, thin element, 227–234, *229*, *231, 233, 234*
Block with cross-bores, 279, 476, *476*
Bolt head, 452–454, *453*
Bolts and nuts, design elements, *450*, 450–452, *451*
Bottom-up procedure, 3, *3*
Boundary conditions, 559
Boundary element method, *519*, 520
Box section, 463, **514**
Brace and chord members, 465–469
Brinell hardness test, 10–11
Brittle Coulomb-Mohr (BCM), *31*, 36, *39*
Brittle fracture, *9*, 17
Brittle Fracture Index, 477–478
Buckling, 17
Butt-welded joint, 480

CAD/CAE interface for FEA, *551*, 551–552, *552*
Calculation verification, 571–572, *572*, 576
Cauchy stress tensor, 26–28
Ceramic, 6, *6*, 7
Chamfers, 23, *24*
Charpy test, 16–17
Circular holes with in-plane stress, 214–246
  circular or elliptical hole in spherical shell with internal pressure, 223
  double row of circular holes in thin element in uniaxial tension, 243–244
  effect of length of element, *218*, 218–219
  equal diameter in a thin element in uniaxial tension, *236–238*, 236–241, *240*
  internal pressure, *235*, 235–236
  nonsymmetrically reinforced hole in finite-width element in uniaxial tension, 227
  radially stressed circular element with ring of circular holes, *245*, 245–246
  reinforced hole near the edge of semi-infinite element in uniaxial tension, 223–226, *225*
  single circular hole
    in an infinite thin element in uniaxial tension, *214–216*, 214–217
    in an infinite thin element under biaxial in-plane stresses, *219*, 219–220
    in an semi-infinite element in uniaxial tension, 217
    in a cylindrical shell with tension of internal pressure, 220–223, *221*
    in a finite-width element in uniaxial tension, 218
    single row of equally distributed circular holes in element in tension, 243
    symmetrically reinforced circular hole in a biaxially stressed wide, thin element, 227–234, *229*, *231, 233, 234*
    symmetrically reinforced hole in finite-width element in uniaxial tension, 226–227, *227*
    symmetrical pattern in thin element in uniaxial tension, 244–245
    thin element with circular holes with internal pressure, 246, *247*
    unequal diameter in a thin element in uniaxial tension, 241–242, *242*

Circular hole with elliptical notches, 59, *60*
Circular hole with internal pressure, 63, *63*
Circular hole with opposing semicircular lobes, 81, *81*
Circular shaft with a U-shaped groove, 107, *107*
Circular thin element with in-plane loading, 229, *229*
Circumferential groove, 44, *48*, 48–50, *49*, 58, 59, 62, 64, 90
Circumferential shoulder fillet, 175–176
Code verification, 568–570, *569*, *571*, 576
Coefficient of thermal expansion, 553
Compatible mesh, 555–556, *557*
Composite material, 2, *6*, 6–7, 19, *19*
Compound fillet, 172, *172*, 179–180
Compression strength, 8, *31*, 35–36
Compression stress, 14, 24, 36
Compression tests, 8, *8*, *11*
Compressor-blade fastening (T-head), 452–454, *453*
Computational fluid dynamics, *559*
Computational method, 45, *519*, 519–520
Computer aided design, 551. *See also* CAD/CAE interface for FEA
Computer aided engineering, 551. *See also* CAD/CAE interface for FEA
Concentrated load, *25*, 281, **409**, **410**, 461. *See also* Structural analysis
Conceptual design, 1, 568
Concrete-filled steel tube, 477
Constitutive model, 3, 535, 548, 565, 567
Constructive solid geometry, 21, *22*
Contact condition, 568, *569*
Convergence study, 566, *569*, 575–576
Coordinate transformation, 525, 527–528, 541
Countersunk holes, *276*, 276–277, *277*
Crack initiation, 78, 543, *547*
Cracklike central slit in a tension panel, 252
Crack propagation, 78
Crane hook, 462
Crane hooks, 462
Crankshaft, *168*, 461–462, **510**, **511**
Creep failures, 8, *9*
Creep-rupture, 90
Critical loading condition, 7, 23
Curvature-based mesh, 581
Curved bar, *457*, 457–458
Curved beam, 289
Cylinder stress, 26
Cylinder with an eccentric hole, 45, *45*, *46*
Cylindrical inclusion, 272–274, **403**, **404**
Cylindrical pressure vessel, 463, **515**
Cylindrical pressure vessel with torispherical ends, 463
Cylindrical tunnel, 277–278, 405, 406

Deep hyperbolic groove, *48*, 48–49, 52, 100
Deep hyperbolic notch, *91*, 91–92, 96
Deep notch, *56*, 56–57, *68*, 95
Defects, parts with (design), 471–473, *472*, *473*
Degrees of freedom, 526–527, 531, 554
Depressions in tension, *98*, 98–100, *99*
Design criteria/design rules, 30
Design elements, 439–488
  angle and box sections, 463
  bolt and nut, *450*, 450–452, *451*
  bolt head, turbine-blade, or compressor-blade fastening (T-head), 452–454, *453*
  bolts and nuts, *450*, 450–452, *451*
  charts, **489**–**515**
  crane hook, 462
  crankshaft, 461–462
  curved bar, *457*, 457–458
  cylindrical pressure vessel with torispherical ends, 463
  discontinuities with additional considerations, *476*, 476–477, *477*
  frame stiffeners, 475, *475*
  gear teeth, 445–447, *446*
  helical spring, 458–461, *459*
  lug joint, *454–456*, 454–457
  notation, 439–440

Design elements (*contd.*)
parametric studies, 480–481
parts with defects, 471–473, *472*, *473*
parts with inhomogeneous materials or composites, 471
parts with residual stresses, 478–479
parts with threads, *474*, 474–475
pharmaceutical tablets with holes, 477–478, *478*
press- or shrink-fitted members, 447–450, *448*, *449*
shaft with keyseat, *441*, 441–445, *444*
splined shaft in torsion, 445
surface roughness, *479*, 479–480
U-shaped member, 462–463
welds, *464*, 464–470, *467–470*
Design relations
for alternating stress, 72–74
for combined alternating and static stresses, *74*, 74–78, *76*
limited number of cycles for alternating stress, 78
for static stress, 69–72, *71*
Design safety. *See* Safety factors
Detailed design, 1, *569*
Deterministic method, 19–20, *557*, 561
Direct method, 548
Direct shear and torsion, 106–109, *107*
Direct sparse, 561–562
Discontinuities
design elements, *476*, 476–477, *477*
geometric, 21–23
Displacement boundary condition, 559
Distortion energy, *31–33*, 32–34
Distortion stress, 33, *33*
Distributed circular holes in an element, 243
Divide and conquer strategy, 520, 547
Double-shear method, 13
Drop test, *559*
Ductile Coulomb-Mohr (DCM), *31*, 38, *39*
Ductile fracture, 17
Dynamic analysis, 558
Dynstat test, 16–17

Edge notch, 96, 98, 103, **115**, **124, 125, 136**
Effective stress concentration factor, 64–66
Eigenvalue system, 536
Eigenvector, 28
Elastic modulus, 8, *10*, *11*, 522
Elastic shear strength, 14
Electric analog, 106, **160**, **161**
Electric properties, 553
Element with a hexagonal hole, 59, *60*
Element with an equivalent ellipse, 59–60, *60*
Element with two circular holes, 242, *242*
Element with two unequal circular holes, 242, *242*
Ellipsoidal cavities, 271–272
Ellipsoidal inclusions, 272–274
Elliptical holes in tension, 247–252, *248*, *249*
Elliptical hole with internal pressure, 263
Elongation, 8
Empirical formulas
circular hole with opposite semicircular lobes in thin element in tension, 265
deep hyperbolic groove, 52
FEA and, 579
K_t, 447, 462, **496**
K_{tn}, 94, 217
multiple stress concentration, 59
tension (axial loading), 171
End-milled keyseat, *441*, 441–442
Endurance limit, 15, *15*
Energy conservation, 480, 527, *558*
Engineering analysis methods, for FEA, *519*, 519–520
Equivalent ellipse, 59–60
Equivalent elliptical notch, 92–93, *93*
Experimental method, *519*, 519–520
Extreme Learning Machine (elm), 480

Factor of safety, 34, 69
Failure criteria of materials, 30–38, *32*, *33, 35, 37–39*
Failure diagnostics (Solidworks module), 556

Failure theory, 34
Fast Finite Elements (FFEPlus), 561
Fatigue analysis, 542–547, *543*, *545–547*
Fatigue failures, 444–445
Fatigue notch factor, 41, 67, 72–73, 448
Fatigue strength, *8*, *9*, 14–15, *15*, 77–78, 212–214
Ferrous metal, 6, *6*
Fillets, 23. *See also* Shoulder fillets
Finite difference method, 171–172, *519*, 520
Finite element analysis (FEA)
  analysis types for FEA simulation, 558, *558–559*
  CAD/CAE interface for, *551*, 551–552, *552*
  FEA modeling steps, 547–551, *548–550*
  limitations of SCFs, overview, 517–518
  materials library for FEA simulation, 552–553, *553*, *554*
  meshing tool for, 554–557, *555–557*
  parametric study for stress analysis, 582–583, *583–585*
  postprocessing, 562
  solvers to FEA models, 559–562, *560*
  for stress analysis of assembly models, 580–582, *580–582*
  structural analysis problems, *518*, 518–519
  structural analysis theory and, 520–547. *See also* Structural analysis
  on study of stress concentration factors, 586
  tools for boundary conditions, 559
  types of engineering analysis methods, *519*, 519–520
  verification for, 567–576. *See also* Verification
  for verification of structural analysis, 577–579, *577–579*
  V&V and planning in FEA modeling, 562–567, *563*, *565–567*
Finite element method, 45–46, 82, *519*, 520
Finite-width correction factors, 95
Finite-width members, 104
Finite-width thin element, 94–96, 216, 250, 263, **307**, **352, 372, 378**
Flat bar with opposite notches, *91*, 92, 98
Flat beams, 101–102
Flat-bottom grooves, 100
Flat element under biaxial tensile stresses, 239
Flat member, 92, 169, 170–171, *171*
Flat stepped bar, 172, **193**
Flow simulation, *558*, *559*, 562
Fluctuated stress, 24
Fluctuating load, 14
Force characteristics, 24, *25*
Force equilibrium, 521, 571–572
Frame stiffeners, 475, *475*
Frame structures, *523*, 523–530, *524*, *527–530*
Free body diagrams (FBD), 1, 562, 571, *572*
Frequency analysis, *558*, 561
Functionally graded material, 471
Functional requirements, 1–2, 518

Gear teeth, 445–447, *446*
General stress, 26, *27*, 52
Gerber line, *546*
Global coordinate system, *524*, 525, 548
Goodman line, *546*
Graphic method, *519*, 519–520
Graphic user interfaces (GUI), 549
Grooves
  bar with a groove, *43*, 44, 48, 64
  bending of solids with grooves, 104–105, *105*
  circular shaft with a U-shaped groove, 107, *107*
  circumferential groove, 44, *48*, 48–50, *49*, 58, 59, 62, 64, 90
  deep hyperbolic groove, *48*, 48–49, 52, 100
  flat-bottom grooves, 100
  grooved shaft, 62, *62*, *90*, **132**, **155, 162**

Grooves (*contd.*)
hyperbolic circumferential groove, *48*, 48–49, *49*
semi-infinite element with a groove, *60*, 61
shaft with a circumferential groove, *49*, *50*, 58, 104–105, *105*, *107*
shaft with double groove, *60*
small radial hole through a groove, *58*
solids with grooves, 104–105
solid with shallow grooves and shoulders, 51, *51*
in tension, 100, **134**
U-shaped circumferential groove, 44, 100, 104, 106–107, *107*
V-groove, 475
V-shaped circumferential groove, 108
V-shaped grooves, 100, 109

H-adaptive meshing, 556–557
Hardness tests, 8–13, *12*, *13*
Heat transfer, 552, 558–559, 562
Helical spring, 458–461, *459*
Helical torsion spring, 461, **509**
Hemispherical depression, 98, *98*
Hibert transform, 481
Holder-continuous surface, 481
Holes, 23, 209–437
charts, **307**–**437**
circular holes with in-plane stresses, 214–246. *See also* Circular holes with in-plane stress
hole in a cylindrical shell, 220, 223, 262, **310**, **311, 436**
hole in a finite-width element, 218, 226–227, 250–252, 263, **309**, **372**
hole in an infinite thin element, *214*, 214–217, *215*, 246, 250–252, *253–257*, 253–262, *260*
hole in a semi-infinite element, 59, 217
hole in a spherical shell, 223
holes in thick elements, 274–283, *275–277*, *279, 282, 283*
hole with opposite semicircular lobes, 265–266
notation, 209–211, *210*
stress concentration factors, 211–214, *212*
Hollow roller, 281, **409**, **410**
Hooks, crane, 462
Hot-spot stress, 466
Hydrostatic pressure, 32, 64, 277, **405**, **406**
Hydro stress, 33
Hyperbolic circumferential groove, *48*, 48–49, *49*
Hyperboloid depression, 98–99, *99*

Idealization
errors of, 565–566
role in an FEA modeling process, 562–565
Impact test, *8*, *9*, 16–17
Impurities, 2, 7, *9*, 19, 472
Inclined round hole, 269–270
Incompatible mesh, 556–557, *557*
Infinite fatigue life, 15, 545
Infinitely thick solid, 275
Infinite plate, 103–104, **149**–**151**
Inhomogeneous materials or composites (design), 471
Interference detection, 555–556
Internal pressure
circular hole with, *235*, 235–236
circular or elliptical hole in spherical shell with, 223, **311**
circular thin element with circular pattern of three/four holes with, **370**
circular thin element with eccentric circular hole with, **369**
cylinders with a circular hole subject to uniaxial tension and, 222
discontinuities and additional considerations, *476*
elliptical hole with, 263
infinite element with circular hole with, *63*, 63–64
Lamé solution and, 281, **411**

parts with defects and, 471–473, *472*, *473*
perforated flange with, **368**
single circular hole in cylindrical shell with tension, 220
thin element with circular holes with, 246, *247*
Intersecting cylindrical holes, 278–279, *279*
Isotropic material, 7, 471, *547*
Isotropic panel with a circular hole, 286
Isotropic panel with an elliptical hole, 286
Izod test, 16, 17

Joints
butt-welded joint, 480
lug joint, *454–456*, 454–457
pin and hole joint, 456
round pin joint, 268–269
tubular joints, *464*, 464–470, *467–470*
tubular N-joints, 464
X-joint, *464*, 469, *470*

Keyholes, 92–93, *93*, **144**
Keyseats
end-milled, *441*, 441–442
notation, 440
overview, 439
shaft with, *441*, 441–445, *444*
sled-runner keyseat, 441, *441*
Kinematic energy, 537

Lagrange's equation, 537
Lamé solution, 281, **411**
Large Problem Direct Sparse (SolidWorks), 561–562
Ligament efficiency, 244, **356**, **357, 361, 432**
Limiting stresses, 75, *76*
Limit safety factor, 70–71, *71*
Linear triangle element, 531, *566*
Line method, 480
Load cell, *10*, *11*
Load distribution, 24
Loads and deformation, 4, *5*
Loads and stresses, 4, *5*, 61, 83, *84*
Local and nonlocal stress concentration, 52–57, *53*, *54, 56*
Local coordinate system, 524, *524*, 548
Localized stress concentration, 52, 55–56
Local mesh control, 554
Lug joint, *454–456*, 454–457

Mason-Coffin relation, 544
Material properties
anisotropic material, 7
composite material, 2, *6*, 6–7, 19, *19*
failure criteria of materials, 30–38, *32*, *33, 35, 37–39*
functionally graded material, 471
isotropic material, 7, 471, *547*
materials properties and testing, 7–17, *8–16*
parts with inhomogeneous materials, 471
parts with inhomogeneous materials or composites, 471
Materials library for FEA simulation, 552–553, *553*, *554*
Mathematical analysis, 94, 169, **309**, **335, 336, 345, 346, 350, 355, 400**
Maximum normal stress (MNS) theory, *31*, 34–36, *35*
Maximum shear stress (MSS) theory, 28, 30–31
Mechanical structures, stress analysis of, 21–29, *22–25*, *27, 29, 30*
Members with transverse holes, 209, *210*
Meshing tool, 554–557, *555–557*
Meshing verification, 572–576, *573–575*
Mesh refinement, 556–557
Minimized potential energy method, 529, 531, 540
Modal analysis, 535–540, *536–540*
Mode I fracture, 80
Modified-Mohr (MM) theory, 37, *38*
Modules of rigidity, 522
Mohr's circle, 28–31, *29*, *30*

Moment of inertia, 224, 295, **437**, 457–458, 463, 570
Multiple notches, 96–97, *97*, 102–103, **145**
Multiple stress concentration, *57–60*, 57–61

Narrow shoulder, 171, *171*
NASA, 230, 544
Neuber approximation, 92, 109
Nodal displacement, 525, 531, 567
Nodes
  CAD/CAE interface and, 551
  code verification and, 570, 571
  defined, 547–548
  errors and, 566–568
  FEA, overview, 520
  FEA simulation and, *550*
  loads boundary conditions for structural analysis and, *560*
  meshing tool and, 554, 556–557
  meshing verification and, 572, 575
  trusses and frame structures, 524, 525, 527, 531–533
Noncircular contour, 172–175, *172–175*
Nonferrous metal, 6, *6*
Nonlinear analysis, *558*, *560*, 561
Nonsymmetrically reinforced hole, 227
No-penetration contact, 556
Notches
  bar with a notch, 102, **121**, **126, 127**
  bending of plates with notches, 103–104
  bending of thin beams with notches, *101*, 101–103
  circular hole with elliptical notches, 59, *60*
  deep hyperbolic notch, *91*, 91–92, 96
  deep notch, *56*, 56–57, *68*, 95
  defined, 23
  edge notch, 96, 98, 103, **115**, **124, 125, 136**
  equivalent elliptical notch, 92–93, *93*
  fatigue notch factor, 41, 67, 72–73, 448
  flat bar with opposite notches, *91*, 92, 98
  with flat bottoms, 96, 103, **122**, **123, 146**
  multiple notches, 96–97, *97*, 102–103, **145**
  notched-bar impact strength, 16–17
  notched bars, 98
  notched section, *41*, *42*
  notches in tension, 92–98, *93*, *97*
  notches with flat bottoms, 96, 103, **122**, **123, 146**
  notch sensitivity, 64–69, *65*, *66, 68*
  opposite single U-shaped notches, 94–95
  opposite U-shaped notches, 94, 101, *101*, **116**, **117**, 476
  plane element with a V-shaped notch, 65
  in tension, 92–98, *93*, *97*
  See also Notches and grooves; Semicircular notches
Notches and grooves, 89–166
  bending of plates with notches, 103–104
  bending of solids with grooves, 104–105, *105*
  bending of thin beams with notches, *101*, 101–103
  charts, **113–166**
  depressions in tension, *98*, 98–100, *99*
  direct shear and torsion, 106–109, *107*
  grooves in tension, 100
  notation, 89–90
  notches in tension, 92–98, *93*, *97*
  stress concentration factors, *90*, 90–92, *91*
  test specimen design for maximum K_t for a given *r/D* or *r/H,* 109
  See also Grooves
Number of cycles, 14–15, *15*, 78

Opposite shallow spherical depressions, 99–100
Opposite shoulder fillets, 170, 177
Opposite single U-shaped notches, 94–95
Opposite U-shaped notches, 94, 101, *101*, **116**, **117**, 476
Orthotropic panel with a circular hole, *284*, 286

Orthotropic panel with a crack, 286
Orthotropic thin members, *284*

P-adaptive meshing, 556–557
Parametric studies, 480–481
Parametric study for stress analysis, 582–583, *583–585*
Parts with defects, 471–473, *472*, *473*
Parts with inhomogeneous materials, 471
Parts with residual stresses, 478–479
Parts with threads, *474*, 474–475
Peak stress
  decay of stress away from, 46
  ratio of, to normal stress at a discontinuity, 40
Pharmaceutical tablets with holes, 477–478, *478*
Pin and hole joint, 456
Pin-to-hole clearance, 454
Plane and axisymmetric problems, 49–52, *50*, *51*
Plane element with a V-shaped notch, 65
Plane strain
  defined, *46*, 46–47
  model, 535, *536*
  problems, *530*, 530–535, *532*, *534*
Plane stresses, *530*, 530–535, *532*, *534*
Plane stress model, 530, *530*, 535, *536*
Plastic deformation, 64, 68, 274, 476, *558*
Plate with a row of elliptical holes, 291
Plate with a single elliptical hole, 291
Plate with elliptic holes, 471
Point method (pm), 178, 480
Poisson's ratio, **130**, **149–151, 399, 401, 421**
Polymeric materials, 6, *6*
Postprocessing, 562
Potential energy, 524–525, 529, 531, 533, 535, 537, 540, 548
Power-law index, 471
Power spectrum density, *558*
Preprocessing, *549*, 551
Press- or shrink-fitted members, 447–450, *448*, *449*
Pressure vessel code, 232
Pressure vessel nozzle, 270, *271*
Pressure vessel wall, 176, **192**, 270
Pressurized cylinder, 281–288
Principal coordinate system, 28
Principle of superposition, *61–63*, 61–64
Probability
  classification of structural analysis problems, *557*
  of failure/success, *20*, 20–21
  solvers to FEA models, 561
Processing, 549, *549*
Product design, 2–3
Propagation problem, 561
Proportional limit, 8
Pure shear stress, 255, 293, **362**, **428**

Ratio of stress to strain, 40
Reference stress, 42–45, 55, 211
Reinforced hole near the edge, 223–226
Reliability, 20–21
Repetitive loads, 542, *559*, 561
Residual stresses, *474*, 478–479
Ribs, 23
Riveting, 474, 527
Rockwell hardness test, *8*, 10, 12
Rollers, 409, 439, 578, 581
Root-mean-square (RMS), 480
Rotating disk, 52–54, *53*
Rotor, *18*, 90, *168*, 180, 450
Round-cornered equilateral triangular hole, 267
Round-cornered square hole, 265, 267, 281, 290, **390**, **391**
Round pin joint, 268–269
Rupture, *9*, 64, 66, 69n3, 78, 90, 274

Safety factors
  factor of safety, defined, 34, 69
  limit safety factor, 70–71, *71*
  stress analysis, *19*, 19–20, *20*, 83–84, *84*
  stress concentration safety factors, 78
SCFs. *See* Stress concentration factors
Second-power relation, 104

Semicircular notches
bending of plates with notches, 103, 104
bending of thin beams with notches, 101, 102
charts, **116**, **121, 127, 128, 137, 142, 151, 152, 377**
circular hole with opposite semicircular lobes in thing element in tension, 265
multiple, 97
single, 94, 96
structural analysis and, 577–579, *577–579*
Semi-infinite element with a groove, *60*, 61
Semi-infinite element with double notches, 59, *60*
Shaft with a circumferential groove, *49*, *50*, 58, 104–105, *105*, *107*
Shaft with double groove, *60*
Shaft with keyseat, *441*, 441–445, *444*
bending, 442
combined bending and torsion, 443
effect of proximity of keyseat to shaft should fillet, *443*, 443–444
fatigue failures, 444–445
torque transmitted through key, 443
torsion, 442
Shallowness, 220
Shape functions, 524, 531–534, 566, 575
Shearing, 17
Shear modulus, *14*, 285, 522
Shear strength, *9*, 13–14, 31, 44
Shear stress, *9*, 13, 24, 26, 28–31, 67, 70–74, 107–108
Shear test, 13
Shock loading, 69
Shoulder fillets, 167–208
bending, 177–178
fillets, defined, 23
notation, 167–169, *168*
reducing stress concentration at a shoulder, 180–182, *181*
stress concentration factors, *169*, 169–170
tension (axial loading), 170–176, *170–176*
torsion, 178–180, *179*
Shrink-fitted members, *448*, *449*, 449–450
Simple stress, 26, 39
Single-shear method, 13
Single V-shaped notches, 95–96
Sled-runner keyseat, 441, *441*
Small radial hole through a groove, *58*
S-N curve, *9*, 14, 545, 553, *555*, *559*
S-N diagram, 78
Soderberg line, *546*
Soderberg rule, 75, 77–78
Solid objects under loads, *4*, 4–6, *5*
Solids with grooves, 104–105
Solid with shallow grooves and shoulders, 51, *51*
Solidworks
analysis types in simulation by, 558, *558–559*
code verification, 570–571
failure diagnostics, 556
FEA model solutions, 561–562
material library, 553
overview, 549–550, *552*, 575
See also CAD/CAE interface for FEA
Source of error, 563–567, *565*, *566, 568*
Spatial decomposition, 21–22, *22*
Spherical cavities, 271–272
Spindle, 167
Splined shaft, 445, **492**
Splined shaft in torsion, 445
Static and fatigue failures, 17, *17*, *18*
Static failure, 4, *5*, 8, *9*, 14–15, 17, *17*, *18*
Stepped flat tension bar, 170, **184**–**187**
Stiffness matrix, 525, 526, 529, 530, 538, 540–542
Stochastic method, 19, 20
Strain-life method, 543–544, *547*
Streamline fillet, 173, *174*
Stress analysis, 1–87
of assembly models, 580–582, *580–582*
design relations

for alternating stress, 72–74
for combined alternating and static stresses, *74*, 74–78, *76*
limited number of cycles for alternating stress, 78
for static stress, 69–72, *71*
failure criteria of materials, 30–38, *32*, *33, 35, 37–39*
local and nonlocal stress concentration, 52–57, *53*, *54, 56*
materials properties and testing, 7–17, *8–16*
of mechanical structures, 21–29, *22–25*, *27, 29, 30*
multiple stress concentration, *57–60*, 57–61
notch sensitivity, 64–69, *65*, *66, 68*
overview, 1–2
plane and axisymmetric problems, 49–52, *50*, *51*
principle of superposition for combined loads, *61–63*, 61–64
in product design, 2–3, *3*
safety factors, 83–84, *84*
solid objects under loads, *4*, 4–6, *5*
static and fatigue failures, 17, *17*, *18*
stress concentration, 39–46, *40–43*, *45*
as three-dimensional problem, 47–49, *48*, *49*
as two-dimensional problem, *46*, 46–47
stress concentration factors and stress intensity factors, *79*, 79–83, *81–83*
types of materials, *6*, 6–7
uncertainties, safety factors, and probabilities, *19*, 19–21, *20*
Stress concentration, 39–46, *40–43*, 45
as three-dimensional problem, 47–49, *48*, *49*
as two-dimensional problem, *46*, 46–47
See also Design relations
Stress concentration factors (SCFs), *90*, 90–92, *91*
defined, 40
stress intensity factors and, *79*, 79–83, *81–83*
study of FEA on, 586
Stresses and strains, 5–6, 32, *565*
Stress intensity, *79*, 79–81, *81*
Stress intensity modification factor, 544
Stress-life method, 543, 545, *546*, *547*
Stress raiser, 50, 52, 55, 58, 59, 65–66
Stress-strain curve, *10, 11, 14*, 41
Structural analysis, 520–547
fatigue analysis, 542–547, *543*, *545–547*
modal analysis, 535–540, *536–540*
plane stresses and strain problems, *530*, 530–535, *532*, *534*
structural analysis problems, *518*, 518–519
theory, 520–547
trusses and frame structures, *523*, 523–530, *524*, *527–530*
volume force and, 520–523, *521–523*
Structural design, 1–2, 518
Superposition, *61–63*, 61–64
Surface force, 47, 520, 571
Surface modelling, 21–22, *22*
Surface roughness, *479*, 479–480
Symmetrically reinforced circular hole, 227–235, *229*, *233, 235*
Symmetrically reinforced hole, 226–227

Tangential stress, 260, 273, 274, 278, 280, **376**, **407, 408**
Tensile compression stress, 24
Tensile strength, 8, *9*, *31*, 35–36, 38, 68–70, 75, *76*
Tensile stress, *9*, *10*, 24, 34–36
Tensile tests, 8, *9*, *10*
Test specimen design for maximum K_t for a given *r/D* or *r/H,* 109
T-head, *453*, 453–454, **498–502**
Theory of critical distance, 480
Theory of elasticity, 2, 40, 45, 52, 101, 214, 275, 530
Thermal analysis, *558–559*
Thermal conductivity, 552, 553

Thin element containing two holes, 239
Thin element in pure shear, 293
Thin element with an ovaloid, 263–265, *264*
Thinness, 99, 220, 277
Threaded part, 90
Threads, parts with, *474*, 474–475
Three dimensional problem, 47–48, 551
Time dependence, 24, *25*, *518*, 561
Top-bottom procedure, 2–3
Torque transmitted through key, 443
Torsion, 442
Torsional failure, 17
Torsional loads, 15
Torsional stress, 24
Transverse hole, *210*, *275*, 291–292, **394**, **424, 437**
Trapezoidal protuberance, 171–172, **188**, **189**
Truss structures, *523*, 523–530, *524*, *527–530*
T-shaped blade fastening, 454
Tubes, 176, **394**
Tubular joints, *464*, 464–470, *467–470*
Tubular members, *71*, 222, 464
Tubular N-joints, 464
Turbine-blade, 452–454, *453*
Twisted infinite plate, 294
Two-dimensional problem, 46–47, 109
Types of materials, *6*, 6–7. *See also* Material properties

Ultimate strength, 8, *9*, 30, 72, 84
Uncertainties, *19*, 19–21, *20*
Uniaxial in-plane tension, 214, 224
Uniaxially stressed tube, 267–268
Uniaxial tension
  cylinders with a circular hole subject to uniaxial tension and, 222
  double row of circular holes in thin element in, 243–244
  equal diameter in a thin element in, *236–238*, 236–241, *240*
  nonsymmetrically reinforced hole in finite-width element in, 227
  overview, 55–57
  reinforced hole near the edge of semi-infinite element in, 223–226, *225*
  single circular holes and, *214–216*, 214–217
  symmetrically reinforced hole in finite-width element in, 226–227, *227*
  symmetrical pattern in thin element in, 244–245
  unequal diameter in a thin element in, 241–242, *242*
U-shaped circumferential groove, 44, 100, 104, 106–107, *107*
U-shaped member, 462–463
U-shaped notches
  opposite single U-shaped notches, 94–95
  opposite U-shaped notches, 94, 101, *101*, **116**, **117**, 476
  overview, 90, 92–93

Validation, 3, 244, *519*, *520, 550, 563*
Verification, 567–576
  benchmarking and, 576
  calculation verification, 571–572, *572*, 576
  code verification, 568–570, *569*, *571*, 576
  FEA for verification of structural analysis, 577–579, *577–579*
  meshing verification, 572–576, *573–575*
  overview, 567–568, *568*
V-groove, 475
Vickers hardness test, *8*, 10, 12, *12*
Volume force, 520–523, *521–523*
Von Mises effective stress, 34
Von Mises-Hencky theory, 32
V-shaped circumferential groove, 108
V-shaped grooves, 100, 109
V-shaped notch
  chart, **140**

circumferential groove and, 108
closed-form solutions for, 103
in flat-beam element, 102
grooves in tension, 100
round-bottomed, 90
V-shaped notches
plane element with a V-shaped notch, 65
single V-shaped notches, 95–96
V&V, planning in FEA modeling and, 562–567, *563*, *565–567*

Wahl factor, 458, 460
Waterfall model, 568, *569*
Weighted residual method, 548
Welds
butt-welded joint, 480
design elements, *464*, 464–470, *467–470*
Width correction factor, 252

X-joint, *464*, 469, *470*

Yielding, 17, 30–31, 34, 70
Yield strength, *9*
Young's modulus (elastic modulus), 8, *10*, *11*, 522